ICEM21

21st International Conference on EXPERIMENTAL MECHANICS

6-11 July 2025
Bologna

Books of Abstracts

Società Editrice ESCULAPIO

ISBN 978-88-9385-488-7

© Copyright 2025
Società Editrice Esculapio s.r.l.
Via Terracini, 30 – 40131 Bologna
www.editrice-esculapio.com – info@editrice-esculapio.it

Layout design: Carlotta Lenzi, Laura Brugnoli

Editors:
Dario Croccolo e Giorgio Olmi

PROGRAMME

MAIN TOPICS

01 Testing and Diagnostic
02 Thermo-Fluid Systems
03 Civil Engineering Applications
04 Sensors and Instrumentation
05 Teaching Experimental Mechanics
06 Modes of Failure
07 Nanotechnologies and Nanomaterials
08 Biomechanical Applications
09 Tribology, Surface and Interface Engineering
10 Optical Techniques
11 Impact and Crashworthiness
12 Analytical and Numerical Models
13 Composite and Advanced Materials
14 Fatigue and Fracture
15 Machine design and prototyping
16 Industrial Engineering
17 Joints and Fasteners
18 Case studies and practical applications

THEMATIC SYMPOSIA

Additive Manufactured Materials: Production, Experiments and Applications
Advances in Experimental Techniques under Impact and Shock
Dynamic Behavior of Materials
Experimental Big Data Analysis and Artificial Intelligence
Experimental Mechanics for Nondestructive Testing
Experimental techniques and monitoring systems for major structures
Experimental Techniques for Materials Characterization with special focus on Instrumented Indentation Test: to microstructure, degradation and residual stresses
Experimental testing of lightweight materials, structures and components
Non-Destructive Monitoring of Structural Integrity
Novel Applications of Experimental Mechanics
Optical Technics in Experimental Mechanics
Thermal based techniques for materials and components analysis: applications and perspectives
Thermoelastic Stress Analysis
Wood Mechanics and Timber Engineering
X-ray & Neutron Tomography and Applications

PARTNERS

EURASEM

EuraSEM European Society for Experimental Mechanics

DIN - University of Bologna

ALMA MATER STUDIORUM UNIVERSITÀ DI BOLOGNA

AIAS

aias

SPONSORS

X-sight

X-SIGHT
OPTICAL EXTENSOMETERS & DIC SYSTEMS

ITALSIGMA

ITALSIGMA

ORGANIZING COMMITTEE

Prof. Dario Croccolo (Chairman)
Prof. Giorgio Olmi (Vice-Chairman)
Prof. Massimiliano De Agostinis (Vice-Chairman)
Eng. Stefano Fini (Vice-Chairman)
Eng. Tommaso Maria Brugo (Vice-Chairman)
Eng. Mattia Mele (Vice-Chairman)
Eng. Chiara Scapecchi (Vice-Chairman)
Dr. Nicoletta Madrigali and INTRAS Congressi

INTERNATIONAL SCIENTIFIC COMMITTEE

Nikolaos Alexopoulos (Greece)
Alireza Amirkhizi (USA)
Bonnie Antoun (USA)
Leslie Banks-Sills (Israel)
Giovanni Belingardi (Italy)
Nicola Bonora (Italy)
Tore Borvik (Norway)
Sven Bossuyt (Finland)
John Botsis (Switzerland)
Elsa Caetano (Portugal)
Katia Casavola (Italy)
Luciano Lamberti (Italy)
Lorella Ceschini (Italy)
Jan Chvojan (Czech Rep.)
Terry Yuan-Fang Chen (Taiwan)
Sam Coppieters (Belgium)
Dario Croccolo (Italy)
Francesca Maria Curà (Italy)
Raj Das (Australia)
Massimiliano De Agostinis (Italy)
Patrick De Baets (Belgium)
Stefano Fini (Italy)
Motoharu Fujigaki (Japan)
Matteo Giacopini (Italy)
Francois Hild (France)
Johan Hoefnagels (Netherlands)
Dimitrios Karalekas (Greece)
Miloslav Kepka (Czech Rep.)
Mateusz Kopec (Poland)
Zbigniew Kowalewski (Poland)
Giuseppe Lacidogna (Italy)
Luciano Lamberti (Italy)
Genevieve Langdon (South Africa)
Franck Lauro (France)
Alexandre Lavrov (Norway)
David Lecompte (Belgium)
Xide Li (China)
Sara Mantovani (Italy)
Shaker A. Meguid (Canada)
Mattia Mele (Italy)
Robert Mines (UK)
Roberto Montanari (Italy)
Yoshiharu Morimoto (Japan)
Sayed A. Nassar (USA)
Christopher Niezrecki (USA)
Giorgio Olmi (Italy)
Yukitoshi Otani (Japan)
Carmine Pappalettere (Italy)
Jean-Noël Périé (France)
Bernhard Pichler (Austria)
Elzbieta Pieczyska (Poland)
Anastasios Vassilopoulos (Switzerland)
Pawel Platek (Poland)
Vikas Prakash (USA)
Gonzalo Ruiz López (Spain)
Alexis Rusinek (France)
Yoshida Sanichiro (USA)
Raffaella Sesana (Italy)
Luis Felipe Sesé (Spain)
Joaquim Silva Gomes (Portugal)
Blazej Skoczen (Poland)
Maria Strantza (USA)
Erman Tekkaya (Germany)
Luca Tomesani (Italy)
Rachel Tomlinson (UK)
Danny Van Hemelrijck (Belgium)
Wim Van Paepegem (Belgium)
Mario Vaz (Portugal)
Patricia Verleysen (Belgium)
George Z. Voyiadjis (USA)
Liliang Wang (UK)
Wei-Chung Wang (Taiwan)
Paul Wood (UK)
Sanichiro Yoshida (USA)
Qican Zhang (China)
Xiaoxin Zhang (Spain)
Andrea Zucchelli (Italy)

MAIN TOPICS

TESTING AND DIAGNOSTIC 3

Test bench for the multidimsensional excitation of disc shaped drivetrain components 5

P. Altoé, K. Wolter, S. Ott, A. Fidlin

Characterisation of a displacement-amplified piezoelectric actuator for high-frequency forcing in bearing test stand 7

G. C. Barnaby, R. T. Wragge-Morley, and P. H. Mellor

Effect of the highly accelerated stress test on the interfacial adhesion of die attach film in package structure 9

S. J. Oh, H. Jeong, J.-H. Lee, S. Kim, S. Han, H. Moon, and J.-Y. Song

Mechanical and microstructural characterization of monomaterial and bi-material components fabricated by laser powder bed fusion 11

A. Angelastro, M.A. Attolico, S. L. Campanelli, S. Carone, C. Casavola, V. Errico, P. Leo, V. Moramarco, M. Patronelli, G. Renna, C. Scaramuzzi

Simulating axial bearing loading from an e-vtol multicopter on a laboratory rig 15

R.T. Wragge-Morley, G.C. Barnaby, J.M. Yon and P.H. Mellor

THERMO-FLUID SYSTEMS 17

Magnetically maneuverable microcarrier using acoustic bubbles 19

J. Park, Y. Kim, D. Kim, S.K Chung and K.Y Lee

MODES OF FAILURE 21

Tensile plastic instability in useful deformation for volume conservation type materials forming processes in manufacturing industries 23

J. Banerjee and L. Cruz-Zapata

NANOTECHNOLOGIES AND NANOMATERIALS 25

High-performance transparent conducting electrodes on pet by blade coating and photonic curing at > 10 m/min 27

J. C. Bonner, R. T. Piper, B. Bhandar, J. W. P. Hsu

Improving the performance of the structure contracting by sound waves 29

Y. Tsuchida, Y. Tsuchiyama, S. Arikawa

Interfacial strain transfer analysis between bismuth selenide nanoflakes and flexible substrate using raman spectroscopy 31

Miaojing Wang, Huadan Xing, Rubing Li, Zhixuan Cheng, Qiu Li, Wei Qiu

BIOMECHANICAL APPLICATIONS 33

An experimental in vitro knee model to measure forces of the ACL and PCL 35

A. L. Matos, A. Ramos, and J. A. Simões

Deep learning-based nanomechanical vibration for rapid and label-free assay of epithelial mesenchymal transition 37

Shangquan Wu, Wenjie Wua, Yongpei Penga, Qingchuan Zhang

Optical coherence elastography for strain measurement of intact blood vessels 39

Cuiru Sun, Guorui Du, Haosen Wang, Jinlong Chen

TRIBOLOGY, SURFACE AND INTERFACE ENGINEERING 41

Tribological and microstructural charaterization of coatings used on C75 tool steel 43

N.Picco, M.Magnan, F.Sordetti, M.Tolazzi, M.Virgolin, A.Lanzutti

Capillary driven solder climbing due to hairline surface texture for advanced package assembly 45

Jeehoo Na, Eunhye Lee, YehRi Kim, Eunjin Jo, Dongjin Kim, Dongwoo Lee, and Tae-Ik Lee, †

OPTICAL TECHNIQUES 47

Shear characterization in soft polyurethane foams: a critical comparison among experimental approaches 49

V. Moramarco, G. Pappalettera, M. Patronelli, C. Casavola and L. Del Core

Development of stereo dic measurement on thermal energy storage tank: determination of mechanical response 51

G. Alonso Aruffo, Y. Lalau, L. Penazzi and R. Bonnaire

IMPACT AND CRASHWORTHINESS 53

Impact three-point bending test using split hopkinson bar method for cfrp ±45° angle-ply laminates 55

A. Ejiri, H. Yamada, N. Ogasawara, T. Uno, H. Yoshikawa and W. Yoneyama

Personnel blast protection of hollow pyramid structure filled with liquid 57

Yuan Li, Shufan Lu, Jiyu Tang, Tao Suo,

ANALYTICAL AND NUMERICAL MODELS 59

Benchmark of analytic vs. Monte carlo batch aqcuisition functions for machine learning optimization of experiments 61

Mark Lee, Imon Mia, William Vandenberghe, and Julia W. P. Hsu

Numerical Calibration of Tensile and Compressive Failure of Bio-Epoxy Foam Core for explicit Analysis using a Simplified Testing Approach 63

A.Harrison

Development of an automated process for material card calibration of joints for finite element simulations 65

T. Wirtz

Buckling structures in a controlled-thickness gradient: finite element method and experimental studies 67

M. Chargaoui, G. Parry, C. Coupeau

COMPOSITE AND ADVANCED MATERIALS 69

Thermal and mechanical behavior of benzoxazine/epoxy-based nanocomposites 71

E. Tikarrouchine, O. Mehelli, D.E. Tria, A. Bouteldja and M. Derradji

Effect of post treatment on mechanical properties of cellulose nanofiber sheet 73

M. Asami, A. Miyawaki and S. Arikawa

Effect of unit cell configuration on bending behavior of spreadtow woven flax/pp composites in the molten state 75

R. Hossein Abadi, U. Sachs, D. Van Hemelrijck and K.A. Kalteremidou

Delamination strategies for achieving fully freestanding ionomer-bound carbon films with enhanced mechanical reliability 77

Y. H. Kim, and T.-S. Kim

Experimental and numerical analysis of damage induced during dry drilling of multi-layer materials (CFRP/AL-7075) 79

M. F. Ameur, R. Zitoune, M.Kenane and M. Habak

FATIGUE AND FRACTURE 81

Investigation of mixed-mode test on dynamic fracture toughness of dissimilar materials interface 83

Y. Naito, Y. Tanaka and S. Arikawa

Effect of microstructure on thermal cycle damage behavior a ybta3o9/ysz dual tbc with columnar structure 85

Y. Yamazaki and T. Takizawa

Searching for the first sign - crack initiation under fatigue loading in seawater-corroded structural S355 steel 87

S.A. Elahi, R. Krankenhagen, S. Chaudhuri, R.M. Tapia, F. Mehri Sofiani, W. De Waele

A finite element methodology for the structural assessment of high-performance electric motor gears 90

S.Messina, S.G.Barbieri, F.Manni, M.Giacopini, L.Pascale

A finite element methodology for structural assessment of a gear with nitriding treatment 92

F. Manni, V. Mangeruga, S. Messina, M. Giacopini

Cyclic strain responses and crack growth in fe-mn-c twip steel under stress-amplitude controlled fatigue loading 94

Lihe QIAN, Cheng ZHENG and Jiangying MENG

Evaluation of fatigue damage development in power engineering steel after long time exploitation supported by dic technique 96

Z.L. Kowalewski, M. Kopec, A. Brodecki

MACHINE DESIGN AND PROTOTYPING 99

Development and locomotion experiment of inchworm robot for mobile additive manufacturing 101

K. Jimbo

Multivariable regression models based on numerical extended analyses for design purposes 103

D. Croccolo, M. De Agostinis, S. Fini, F. Livera, M. Mele, G. Olmi, G. Piraccini, N. Vincenzi

JOINTS AND FASTENERS 107

Low temperature and precision bonding technology using spread laser beam for thin lens package 109

Eunhye Lee, Jeehoo Na, Min-Su Kim, Byeong-Kwon Ju, and Tae-Ik Lee,†

Study of the corrosion-induced degradation of aeronautical aluminum alloys 2024 and 2198 riveted sheets 111

C. M. Charalampidou, K. Bailas, P. Papanikos, N. D. Alexopoulos

CASE STUDIES AND PRACTICAL APPLICATIONS 115

Industrial production of green ammonia (nh3) for fertilizer manufacture: case study in technical applications of green hydrogen in ammonia production 117

Nascimento, Mauricio A., Júnior, Everardes P.

THEMATIC SYMPOSIA

ADDITIVE MANUFACTURED MATERIALS: PRODUCTION, EXPERIMENTS AND APPLICATIONS 123

LPBF graded lattce structure: a micro-mechancal property study 125

K.Sleem, G. Grima, A. Santoni, M. L. Gatto, E. Santecchia, S. Spigarelli, M. Cabibbo

A Study of Loosening Phenomenon and Acceleration Ratio of Loosening in Actual Equipment Compared to Results of Laboratory-Style Bolted Joints Loosening Tests 128

S. Hareyama, K. Manabe, S. Kobayashi

Influence of 3D printing parameters on basf ultrafuse 316l steel mechanical properties 131

Pawel Platek, Natalia Daniel, Kamil Cieplak, Marcin Sarzynski

Study on stiffness change of chainmail structure for leg mechanisms 133

Sae Yamaguchi, Toshitake Tateno

Experimental validation of a FEM constitutive model for an innovative L-PBF AM Metal-Matrix-Composite 136

Matteo Crachi, Raffaella Sesana, Cristiana Delprete, Leila Belen Fraga, Sebastian D'hers

Mechanical response of 3d printed lattice structures made from paht-cf material under compression loading 142

P. Platek, M. Sarzynski, K. Cieplak, B. Dekert, P. Baranowski, M. Kucewicz

Room and high temperature behaviour of the AlSi9Cu3 alloy produced by PBF-LB and subjected to tailored heat treatments.....144

L. Tonelli, L. Castagnini, A. Martucci, I. Lagalante, M. Lombardi, A. Morri and L. Ceschini

Elastic properties of reinforced body centered cubic lattice structures.....146

M.Giacalone, S. Mantovani

Stress concentration in hybrid tpms geometries undergoing axial fatigue loads.....149

M.Mele, M. De Agostinis, D. Croccolo, S. Fini, G. Olmi, A. Paffetti, A. Morri, P. Leo, R. Nobile,

A. Pola, M. Tocci, S. Sartori

Dependence of phase angle between mechanical loading and temperature cycles in TMF on small crack propagation.....152

M. Arai, Y. Omiya and Y. Yamazaki

Elastic property analysis in triply periodic minimal surface structures through homogenization and artificial neural networks.....154

D. Croccolo, M. De Agostinis, S. Fini, M. Mele, G. Olmi, A. Paffetti

Design of lightweight cellular structures optimised for pincollar joints.....157

D. Croccolo, M. De Agostinis, S. Fini, M. Mele, G. Milan, G. Olmi, A. Paffetti

Characterization of aggregate distribution in 3d concrete printing using X-ray CT.....160

R. Yoshihara, K. Hashimoto, D. Lou and Y. Honda

Fabrication and experimental characterization of strain sensors based on inkjet printing.....162

G. De Pasquale, F. Ursi, S. Fink and A. El-Sarout

Dynamic strain sensors integrated in the fused filament fabrication of structures.....164

F. Ursi and G. De Pasquale

Evaluation of intra-filament void structure of 3D printed mortar with different printing speed.....166

K. Nakase, K. Hashimoto, K. Ota, Y. Hama, T. Sugiyama

Mechanical response of sinusoidal honeycomb auxetic structures in an additively manufactured shape memory alloy.....168

E. Avoledo, F. Scalzo, X. Wang, E. Salvati

Stress-driven design of gyroid lattices with variable thickness: a preliminary procedure applied to connecting RODS.....169

A. Ciccarella, V. Colaiuda, V. Pocetta, G. Dell'Avvocato, L. Di Angelo and E. Mancini

Microstructure evolution and tensile properties of selective laser melted additively manufactured ti-6al-4v at elevated temperatures.....171

Chong Zhao and Zhengmao Yang

Use of thermal and mechanical indicators for the fatigue damage of AlSi10Mg additive manufactured specimens.....174

R. Nobile, R. De Finis, P. Leo, G. Renna and A. De Luca

Accelerating fatigue characterization through a compact integrated testing machine and thermographic methods.....176

D. D'Andrea, D. Crisafulli, G. Risitano and D. Santonocito

Effect of plastic pre-strain on the yield surface of LPBF manufactured stainless steel 316L 179

V.P. Dubey, M. Kopec, M. Pawlik, P. Wood and Z.L. Kowalewski

Parametric study of energy absorption capabilities of a novel lattice structure 181

J. Melendez, S. Candelaria, D. Serrano, M. Menegozzo, P. Gonzales

Studies on mechanical properties of maraging M300 STEEL manufactured additively via SLM..... 183

Pawel Platek, Giorgio Olmi, Janusz Kluczyński, Marcin Sarzynski, Jacek Janiszewski, Kamil Cieplak, Judyta Sienikiewicz, Dario Croccolo

Studies on mechanical properties of maraging M300 steel manufactured additively via SLM..... 183

Pawel Platek, Giorgio Olmi, Janusz Kluczyński, Marcin Sarzynski, Jacek Janiszewski,

Kamil Cieplak, Judyta Sienikiewicz, Dario Croccolo

Initial characterization of multiple shape-memory anycubic resin 185

M. Staszczak, A.D. Lantada, A. Gradys, L. Urbański, K. Takeda and E.A. Pieczyska

Influence of processing parameters on mechanical properties of multi-material components from aluminium and copper – Manufactured by laser-based powder bed fusion..... 187

C. Singer, J. Foerster, S. Zabihzadeh, G. Schlick, C.M. Charalampidou, J. Schilp, J.S. Aristeidakis, I.S. Berglund and N.D. Alexopoulos

Influence of high strain rate and temperature on the yield behaviour of 3d printed polyamide 11..... 190

Paul Wood, Urvashi Gunputh, Marzena Pawlik, Yiling Lu, Pawel Platek, Jacek Janiszewski, Marcin Sarzynski, Alexis Rusinek

Rockwell and scratch adhesion tests for hard coatings deposited on light alloys fabricated by SLM . 192

E. Ghio, M. F. Bonilauri, G. Bolelli, A. Bertè P. Colombi, E. Cerri

Cyclic compression properties of high-strength, recoverable, light-curable 4d printing lattice reinforced with glass fibers..... 194

Junwei Pan, Jianguo Cai

ADVANCES IN EXPERIMENTAL TECHNIQUES UNDER IMPACT AND SHOCK..... 197

Synthesis of Gunfire Shock Signals Based on Shock Response Spectrum 199

Yinzhong Yan

Electromagnetic hopkinson bar: basic principles and application 202

Yazhou Guo, Zhongbin Tang, Tao Suo, Yulong Li

Key Technologies for Coaxial Ultrasonic Defect Detection Based on Frequency-Tunable Laser Transient Gratings 204

Song Yingzheng, Yue Mengmeng, Liu Ran, Li Qun

Mechanical behaviors of plain-woven composite tube under highstrainrate tensile-shear coupling loads 208

Shiling Fang, Hang Wu, Zhenqiang Zhao, Chao Zhang

A measurement of the mechanical properties of pure aluminum by instrumented Taylor impact test at ultra-high velocity using a single-stage gas gun..... 211

M. Matsumoto, C. Gao, T. Iwamoto and Y. Tanaka

Design and optimization of an emat for measuring the elliptical polarization of rayleigh wave 213

Yujie Hou, Yan Lyu, Jie Gao, Cunfu He

High velocity impact on the pre-tensioned fabric-laminate composite structure 220

J. Wei, S. H. Shang, H. X. Wang, Y. Shen, S. L. Xiao, Y.C. Yuan, Y. Li, J. G. Liu, H. Meng, J. Deng, T. J. Lu, and J. L. Gao

DYNAMIC BEHAVIOR OF MATERIALS 223

X-RAY diffraction of polyvinylidene fluoride under dynamic compression 225

R. Huber, E. Watkins, D. Dattelbaum, L. Gibson, B. Bartram, and J. Jordan

Effects of ultrasonic vibration on the kinetic state of atoms around the screw dislocation of BCC Fe....227

A. Asazuma and S. Arikawa

Experimental characterization for the ratchetting effect of isotropic soft magnetorheological elastomer 229

Y. Li, H. Deng and X. Gong

Magnetic flexible sensor with randomly distributed pine-branch microstructure for bidirectional recognition.....231

D. Li, X. Gong, H. Deng, and S. Xuan

Bionic-leaf vein inspired breathable anti-impact wearable electronics with health monitoring, electromagnetic interference shielding and thermal management 233

X. Wang, H. Deng, X. Gong and S. Xuan

Dual-modulus 3d printing magnetorheological metamaterials for negative vibration regulation 235

C. Lou, X. Lian, H. Deng, and X. Gong

Influence of temperature on microstructural evolution during the dynamic tensile extrusion of pure copper 237

S. Ricci, G. Iannitti, G. Testa, A. Ceccacci, A. Pagano, A. Ruggiero, N. Bonora

Validation of chain drive resonance models by video, audio and torque measurements 241

R.T. Wragge-Morley, G.C. Barnaby, J. Bentley, F.S. Da Silva Davidson, J Drabble, K Kythreotis, S. Lu, M. M. Wharton, T.L. Hill and B.J. Hicks

Extraordinary elastic-wave manipulations of higher-order diffractions based on non-hermitian metasurfaces.....243

Bing Li, Bochen Ren, Jiali Cheng

Anisotropic large deformation mechanical properties of oriented PMMA under different strain rates.....245

Yueming Du, Zhaolin Chen, Chao Zhang, Tao Suo

Accurate strain measurement in split Hopkinson bar testing of fibrous composites.....247

A. Gilat, and J. Seidt

Small-strain dynamic behavior of a coal mine overburden waste 249

Koushik Das, Debjit Bhowmik, Bappaditya Manna, Ramanathan Ayothiraman

Prediction of internal damage in GFRP laminates caused by repeated low velocity impacts using artificial intelligence methods.....251

D.E. Tria, H.E. Hebbouche, A. Lourari, S. Boukhaoua

Dynamic centrifuge test on the effect of vertical excitation on liquefiable ground.....253

K.R. Huang, Y. Yuan, Z.X. Fan

Celluar structure of methyl vinyl silicone rubber foam and its effect on mechanical properties.....255

Bin Dai, Yafei Yang, GuoFang Ding, Luoshi Kai and Cui Zhang

Hmx based energetic material combustion in a spherical container and its quantitative model of reaction pressure.....258

C. Pan, X. Yang, X. Huang, T. Li, H. Fu, H. Shang, P. Li

Abnormal dynamic behavior in an FCC high entropy alloy under extreme loading conditions.....260

Jianguo Li, Kun Jiang and Tao Suo

Rate-dependent failure of transversely-isotropic rock that exhibits a bi-modulus constitutive response.....263

A. T. Guthai, A. F. Fahem, and R. P. Singh

Crack growth behavior and combustion reaction evolution of the holed explosive disks.....265

X. Yang, H. Shang, T. Li, L. Yang, M. Li, Z. Wu

Assessment of impact reistance of hybrid basalt-polypropylene fiber reinforced concrete.....267

A. Syamsir, I. A. Ja'e, Z. Itam, M. A. S. N. Azlisham, and V. Anggraini

Dynamic Behavior and Impact Ignition Criterion of Ti-B-PTFE Reactive Material.....270

Zhe Peng, Rui Liu

EXPERIMENTAL BIG DATA ANALYSIS AND ARTIFICIAL INTELLIGENCE.....273

Monocular vision-based object motion measurement method.....275

Zibin Liu, Banglei Guan, Shunkun Liang, Ang Su, Zhang Li, Yang Shang, Xiaolin Liu and Qifeng Yu

A machine learning method integrating mechanical knowledge and its application in laod modeling of tunneling equipment.....277

Q. Zhang, S. Liu, M. Ma and Y. Kang

Advancing automated machining through enhanced surface roughness prediction in high entropy alloy coating processes by exploring a novel parameter acquisition using artificial neural network...279

M.Dehghanpour Abyaneh, R. Sesana, M.S. Javadi, N. Sheibanian, S. Ozbilen, R. Lupoi

Unsupervised deep learning based digital image correlation.....283

Q.W. Ma, X.N. Cheng, B. D. Li, B. F. Bai and S. P. Ma

Unsupervised Deep Learning DIC with only Single-pair image for high order displacement measurement.....285

Canyu Zhu, Shihai Lan, Tianxiang Ren, Qingchuan Zhang

Prediction of frictional moment of cylindrical roller bearing using experimental data driven artificial neural networks.....290

Y. Hou, X. Wang, Q. Li

Self-evolving synthesis of hydrogels with low interfacial adsorption mechanical properties for single-cell analysis 292

Wenhui Lu, Xiaobao Cao, Zhike Peng, Xi Shi and Songtao Hu

Unsupervised structural damage assessment method based on response correlations 295

Licheng Zhou and Yonghui Lu

Digital image correlation for deformation measurement in high-temperature environment 297

Dongcai Tan, Banglei Guan, Shunkun Liang, Ang Su, Zhang Li, Yang Shang, Xiaolin Liu and Qifeng Yu

Intelligent localization method of fatigue crack tips in numerous high-temperature DIC images 301

Lei Huang, Xing Sun, Wei He and Huimin Xie

AI-based optimization of bolted joints design 303

D. Croccolo, M. De Agostinis, S. Fini, M. Khan, M. Mele, G. Olmi, C. Scapecchi, Z. Wu, S.Nassar

Self-ecolving synthesis of light-weight and high-strength mechenical metamaterials 305

Haoran Li, Xiaobao Cao, Xi Shi, Zhike Pen, Songtao Hu

Self-evolving mechanics experiments for materials synthesis 308

Songtao Hu

Ai-based analysis of gearbox vibration-bearing strain correlation 311

X. Zhao, Y. Hou, X. Wang

Multi source experimental data driven fatigue failure analysis and life prediction of pre-corroded aluminum alloys 313

H. Song, J. Liu, W.C. Wang, J. DU

Research on the Precipitation Behavior of CrN Phase in Nitrided Martensitic Stainless Steel 315

Hongye Zhang, Zhengzhong Xi, Xiao Han, Ruijun He

Aleatory uncertainty quantification in heterogeneous materials via bayesian inference with pymc: application to single lap joints 317

F. Jan, M. Kujawa, Ł. Smakosz

Distributed experimental analysis of the state of charge for lithium-ion batteries based on thermoelastic guided wave 319

Jie Gao, Yan Lyu, Cunfu He

EXPERIMENTAL MECHANICS FOR NONDESTRUCTIVE TESTING 329

Interfacial single-side *j*-integral and increasement *j*-integral criteria based on DIC method for FRP–concrete joint 331

Wen Li, Peiyan Huang

Nondestructive testing for the estimation of the rail neutral temperature 336

S. Baktash, M. Belding, and P. Rizzo

Experimental investigation on the motorcycle swingarm deformability and stability 339

B. Almeida, A. Leite, S. Dias, M.Oliveira, I. Arce and F. Pereira

Temperature-dependent experimental characterization of a sstretchable strain sensor 342

B. Almeida, J.R. Fernandes, M.Oliveira, R. Morais and F. Pereira

A study on a nondestructive method of detecting ceramic coating debongding using NDTPEA 345

Lianyun Xu, Zhende Hou, Shaozhe Pan, Chuan Qu

Investigating the possibility to detect and characterize rail cracks at high speeds with induction thermography 348

E. D'Accardi, G. Dell'Avvocato, G. Marinelli, G. Fumarola, D. Palumbo and U. Galietti

Efficiency of PZT transducers in damage detection of structures 350

M. Dziendzikowski, K. Kowalczyk, Z. Dworakowski

Bearing diagnostic based on fault classification using autoregressive linear discriminant analysis and support vector machine.....352

M.Vanali, M.Conti, S.Pavoni

Improving the capabilities of ultrasonic inspection of railroad rails in high-speed and walking-speed testing 345

A. Z. Hosseinzadeh, C. Huang, I. Batista, and F. Lanza di Scalea

Detection of lithium-ion battery state of charge using magnetic fluxgate sensor 356

Qirui Wang, Yan Lyu,and Jie Gao

State parameter estimation of lithium-ion battery based on ultrasonic transmission characteristics..364

Binpeng Zhang, Yang Zheng, Jie Gao, Yan Lyu, Cunfu He

EXPERIMENTAL TECHNIQUES AND MONITORING SYSTEMS FOR MAJOR STRUCTURES..... 371

A novel structure health monitoring method for mesh reflectors based on the resnet network.....373

Siming Liu, Guowang Luo, Shilin Xie

Data-driven simplified prediction of vibration induced by operating metro trains.....375

Bhattacharjee. N, Sur. A, Manna. B, Banerjee. A, and Shahu. J T

A Study on Seismic Resistance Analysis of A-Type Marble Storage Racks in Eastern Taiwan 377

J. T. Liu, H. W. Mo, C. S. Lin and C. F. Chen

Determining and monitoring the forces in the cables of a suspension bridge.....379

V. Chmelko, T Koščo, M.Garan, M.Šulko

Performance of radial fins in enhancing the stability of offshore pipelines under vertical penetration 381

Debtanu Seth, Bappaditya Manna, and J.T Shahu

In situ strain gauge measurements reveal dynamic mechanical changes at the interface during plating and stripping in olidstate li metal batteries.....384

Fenghui Wang, Hongye Zhang, Zhipeng Chen, Sen Yang, Kejie Wang, Shouyu Zhang, Xinlei Cao

Failure analysis of composite wind turbine blade joint: case study.....388

S.A. Nassar, Z. Wu, J. Kent, C. Bumb, M.Y. Khan

Sequential free-oscillation test method for rocking structural systems.....390

D. Kalliontzis, A.E. Schultz, S. Sritharan

Experimental research on the static and fatigue properties of the external anchorage structure with steel anchor tube of the stayed cables.....395

Guowen Yao, Li Ying, Fengmin Chen, Guoying Kong, Xuanbo He, Yang Tang, Xuebing Hu, Yu Wang, Mark Hughes

Experimental study on mechanism of impressed current cathodic protection of galvanized steel wire for bridge cable.....400

Lianhua Wang, Guowen Yao, Xuanbo He, Yu Wang, Mark Hughes, Ling Zhao, Yang Tang, Pengyu Chen

A novel inverse technique of impact force identification for major composite strucures.....406

Junjiang Liu, Shengchuan wu, Baijie Qiao

EXPERIMENTAL TECHNIQUES FOR MATERIALS CHARACTERIZATION WITH SPECIAL FOCUS ON INSTRUMENTED INDENTATION TEST: TO MICROSTRUCTURE, DEGRADATION AND RESIDUAL STRESSES.....411

Surface characterization of plasma-treated 316l produced by l-PBF.....413

E. Bolli, S. Kaciulis, A. Lanzutti, A. Mezzi, R. Montanari, A. Palombi, N. Picco, F.Sordetti, E. Vaglio, A. Varone, C. Verona

Elastic modulus of porous materials: models and experiments.....415

M. Richetta, A. Palombi, A. Varone

Engineering applications of fimec test.....417

R. Montanari, A. Varone

Assessment of the inter-critical coarse-grain heat affected zone in welded joints of vanadium microalloyed hsla steel.....420

A. Di Schino, B.R. Rodriguez-Vargas, R. Schmidt, G. Stornelli, A. Tselikova

Electrospark deposition and ultrasonic peening treatment on al-Si10-mg selective laser melted parts: microstructure and properties.....423

P. Leo, G. Renna, A. De Luca, R. Nobile, C. Casavola, V. Moramarco, S. Carone, M.A. Attolico

Delamination and fracture of ply-angle layered composites.....425

J. Botsis and G. A. Pappas

Influence of hygroscopic absorption on the resilience of epoxy matrix composite reinforced with ceramic particles.....427

M.D.D Boudiaf, R. Roubache , M.K Harouche and S. Benhamouda

Dynamic modulus highlights microstructural changes in 3D-printed metals.....429

D. Croccolo, R. Montanari, G. Olmi, A. Palombi, M. Richetta, A. Varone

High resolution digital image correlation measurements of 316h austenitic stainless steel.....431

C. Allen, H. E. Coules and C. E. Truman

Multiscale instrumented indentation tests to determine the mechanical performance of a L-PBF 316L deposit.....433

G. Maizza, A.A.A. Hamed, A. Albanese, and M. J. Marques

Mechanism of loosening without rotation for thin plate bolted joint subjected to offset load.....435

S. Hashimura, N. Yamamoto and S. Osaka

Correlation between EBSD parameters and PL-nIIT based mechanical performances of a PBF-LB 316L deposit 437

Faisal Hafeez, Giovanni Maizza, Roberto Montanari, Alessandra Varone

Characterization of selective laser melted TI-6AL-4V samples in the As built and stress relief state 439

P. Leo, G. Renna, A. De Luca, C. Scaramuzzi, N. Soni, F. Panella, T. Primo and G. Papadia

Study of crack-susceptibility in laser welded nickel-based superalloy sheets by 3d laser welding model 441

Giovanni Maizza, Cheng Peihong, Alessandra Varone, Roberto Montanari

Development and optimization of the combustion unit of a hydrogen-fueled gas turbine for energy generation 443

Uma Nataraj Gottipati, Angelo Minotti, Vincenzo La Battaglia, Alessandro Giorgetti, Gabriele Arcidiacono

Correlation between chemical composition and mechanical surface response of biomedical patches 449

A. de Nigris, D. Gentile, L. Ambrosone

EXPERIMENTAL TESTING OF LIGHTWEIGHT MATERIALS, STRUCTURES AND COMPONENTS 451

Enhancing Mechanical Performance and Energy Release in PTFE/Al Composites through Graphene Oxide Integration 453

Ramzi Makaoui, Oussama Mehelli, Djallel Eddine Tria, Mehdi Derradji

Mechanical behaviors of carbon/epoxy-aluminum lamintes 455

Z. Jiang, J. Tsai

Ambient-temperature plasticity of hard and brittle materials at Micron-meter-size scales 457

H. Inui, K. Kishida, Z.H. Chen, L. Li, B. Paul, S. Han, Z. Wang

The peak stress method for the fatigue strength assessment of arc-welded joints made of additively manufactured stainless steel parts 459

L. Contiero, L. Vecchiato, A. Campagnolo, V. Babini, G. Meneghetti

Random fatigue life assessment: numerical and expirimental study 461

L. Rebhi, A. Bouzar Essaidi

Design of test setup to measure hoop elastic modulus of gre pipes 467

Abdullah M. Al Shabibi, Luqman S. Al Maskari, Ahmed A. Al Fadhli, Ahmed M. Al Omairi, Almuataz S. Al Shukaili

A study on fatigue enhancement in nothed aerospace components using laser shock peening 471

M.A. Attolico, G. Renna, V. Moramarco, C. Casavola

Influence of hygroscopic absorption on the resilience of epoxy matrix composite reinforced with ceramic particles 475

M.D.D Boudiaf, R. Roubache, M.K Harouche, S. Benhamouda

Experimental fatigue testing of an aluminum frame for electrically-power assisted cycles 477

E.V. Arcieri, S. Baragetti

Numerical investigation of the effect of yield strength on the behaviour of clamped circular plate under transient pressure loading 479

Swathi Kiran Anupoju, S.N. Khaderi, V. Narayanamurthy

Effect of polyhedral oligomeric silsesquioxane (POSS) on the compressive behaviour of an epoxy polymer 481

E. Georgiou, G. Quino, I. Hamerton, R.S. Trask

Development of an indoor rotor helicopter prototype employing low-cost structure and intrumentation for comparative tests of vibration control 483

A. G. Oliveira, A. A. Silva, M. C. Rodrigues, G. de C. Coêlho

Ductile fracture simulation in welded thin plate for stainless steel with multiple flaws 486

B. J. Kim, C. Y. Oh, J. H. Hwang

Full-field characterisation of pultruded rods under compression using the cradle test 488

G. Quino, C. Zhao, P. Robinson, R.S. Trask

Fatigue behaviour of hot-rolled, low carbon steel under prestrain and notch effect 490

I. Tomasi, L. Solazzi, C. Petrogalli, A. Mazzoni, G. Donzella

Patch size and overlapping optimisation for a new generation of recycled composite laminates 492

P. Bettini, F. Mongioì, L. Calervo, A. Milite, A. Zucchelli, T.M. Brugo, R. Palazzetti

Investigation of the creep deformation mechanism at room temperature on AZ31 magnesium alloy 494

S. Arikawa, K. Matsuoka, S. Yamaguchi

SPH-FEM approach for fluid-structure interaction of anisogrid lattice structures 496

E.V. Arcieri, S. Baragetti

Design and mechanical behaviors of curved-wall carbon fiber composite honeycomb sandwich structure with higher buckling resistance 498

Jian Xiong

Utilization of cenosphere and light expanded clay aggregate with micro fibre reinforced lightweight concrete 499

T.K. Shen, Z. Itam, A. Syamsir, Z. Che Muda, M.H. Zawawi, N. M. Zahari

Fatigue behavior of lack of penetration defects in welded aluminum joints 502

L. Santoro, E. Viglietti, R. Sesana

Influence of the relative angle of rotation between layers on the natural frequency of multilayer sandwich plates 505

Youlong Wang, Zhenglong Wang, Junwei Pan

In-plane compressive mechanical properties of a novel sutureinspired discrete self-locking structure .. 508

Shungang Wang, Yongxiang Tang, Yi Liu

A coupled design approach for Kirigami-inspired auxetic with tube tunable energy absorption 511

Iokkei Cai, Yu Yu, Xiaoru Li

Hexagonal Chiral Bistable Auxetic Metamaterials: Geometrical and Mechanical Analysis 514

Xiushi Li, Boyu Ma, Xueru Chen

NON-DESTRUCTIVE MONITORING OF STRUCTURAL INTEGRITY 517

Re-use of composites waste in the production of medical devices: mechanical analysis using acoustic emission 519

E. Declercq, K. Giannadakis, D.G. Aggelis, D. Van Hemelrijck, K.A. Kalteremidou

Fractal Patterns for Failure Modes of Ultra-high Performance Concrete 521

Zihan Jiang, Federico Accornero, Zhiwen Zhu

The dependence of the degree of non-additivity of mechanically loaded systems on the loading rate 523

D. Triantis, I. Stavrakas, E. D. Pasiou, S. K. Kourkoulis

CFRP self-sensing composite laminate interleaved with piezoelectric nanofibers 525

T. M. Brugo, F. Mongioì, G. Selleri, E. Maccaferri, R. Palazzetti, P. Bettini, A. Zucchelli, D. Fabiani, L. Mazzocchetti

Acoustic emission testing of reinforced concrete beams under bending loading: methodology and preliminary results 527

D. D´Angela, G. Magliulo, A. Monici, M. Del Zoppo, M. Di Ludovico, A. Prota

The garisenda tower in bologna: damage assessment results from principal component analysis, acoustic emission, and nonlinear finite element involving creep and smeared cracking 528

G. Lacidogna, P. Marin Montanari, S. Invernizzi, A. Di Tommaso

Characterization of concrete damage through ultrasonic dispersion 532

G. Lefever, N. Ospitia, N. De Belie, D.G. Aggelis

NOVEL APPLICATIONS OF EXPERIMENTAL MECHANICS 535

Flame retardancy and mschnical properties of novel halogenfree polyurethane containing chitosan from fisheries waste 537

Ming-Yuan Shen, Chin-Lung Chiang, Cing-Yu Ke

Ultrfast processing of metallic alloys at low temperature 539

M. Rahman, L. Warner, S. Todaro, D. Waryoba, A. Haque

Residual stress crowding effects on wide bandgap electronics reliability 541

N. Al-Mamun, M. Rahman, C. Chavda, M. Munshi, A. Haque, D. Wolfe, F. Ren, S. Pearton

Experimentally validated fracture of metastable materials at extremely low temperatures 543

B. Skoczeń

Electromechanical characterization of orthotropic mechanical properties in piezoelectric PVDF films using 3d digital image correlation 545

R. Elhajjar, O. Schneider, D. Schlitz

Mechanical evolution and mechanism analysis of graphite electrode using in-situ raman spectroscopy and XRD techniques 547

Haimei Xie, Bin Han, Qian Zhang, Yilan Kang

Thermal stress measurement of through-glass via substrate by enhanced exposure theory of photoelasticity 549

Po-Yu Chen, Po-Chi Sung, Wei-Chung Wang, Chien-Hsun Chu, Chen-Tsai Yang

Fully bonded FRP–concrete interfacial double shear test method and its application in interfacial fracture energy.....551

Wen Li, Peiyan Huang

Image Stitching Technology Based on Digital Image Correlation (DIC) for Measuring the Straightness of Long Components.....555

Chia-Heng Sung, Zi-Liang Tseng, Ching-Tse Chuang, Terry Yuan-Fang Chen, Ming-Tzer Lin

Determination of multiple wavelength photoelastic constants of birefringent materials by using a hyperspectral camera and image analysis.....557

Terry Yuan-Fang Chen, Tsai-Hsing Chang, and Ming-Tzer Lin

Mechanical properties of novel nano-carbon paper reinforced carbon fiber composite laminates.....560

Chin-Lung Chiang, Yu-Xiang Chiu, Ming-Yuan Shen

Design and Prototyping of a High Force Density, Low-Cost Linear Electric Motor.....565

H. Ouldhamrane, K. Touimi, Y. Achour, A. Zaoui

Nanomechanical Sensors for Detecting Disease Early Detection.....567

Qiubo Chen, Lin Zhan, Zihan Qiao, Yipeng Yang, Wenjie Wu, Chen Wang, Kainan Mei, Qingchuan Zhang, Shangquan Wu

Quantitative flow visualization of transonic diffuser flows.....569

H. Kodama, T. Yamashita, Nakao, Y. Miyazato

Evaluation of ultrashort creep tests on hydrating cementitious materials requires an evaluation protocol accounting for creep during load application.....571

S.J. Schmid, L. Zelaya-Lainez, O. Lahayne, M. Peyerl, B. Pichler

Experimental aproach for the analysis of internal strain maps on a bolted connections using digital image correlation.....573

A.J. Conde-Calabrús, L. Felipe-Sesé, A. Molina-Viedma, J.A. Almazán-Lázaro, E. López-Alba, F.A. Diaz

Use of shape memory alloy for thermal strain-absorption in aerospace applications.....575

A.E. Berrocal-Coba, M. Menegozzo, F.A. Just-Agosto, A. Cecchini-Brigi

Effect of geogrid reinforcemnt in the granular cushion layer on the behaviour of disconnected piled raft system.....577

Raut S, Halder P, Manna B, Shahu JT

Micromechanical Characterisation of Twinning and Detwinning during fatigue in Zirconium using High-Resolution Electron Backscatter Diffraction and Digital Image Correlation Techniques.....579

Weifeng Wan, Chaitanya Paramatmuni, Xiaojun Yan

Effect of initital conditions on passive scalaire mixing in turbulent wakes.....584

M. Sehaba, A. Benaissa, J. Lemay

Fatigue and tensional force determination on thin films used in semiconductor manufacturing.....586

Y.C. Lee, M., Y.W. Chen

A study on seismic resistance analysis of A-Type marble storage racks in Eastern Taiwan.....588

J.T. Liu, H.W. Mo, C.S. Lin and C. F. Chen

Experimental-computational approach to identify the tensile curve of a material during operation ..590
V. Chmelko, M.Šulko, M. Kučerková

Development of a biomechanical experimental robot for high fidelity characterization of footwear traction 592
A. Chanda, S. Gupta

Research on Shear Deformation Characteristics of Sandy Soil-Structure Interface 595
Xueying Yang

NOVEL APPLICATIONS OF EXPERIMENTAL MECHANICS 597

Deep learning-based prediction of residual stresses of a biaxially loaded infinte plate with a circular hole from photoelastic images 599
D.W. Lee, H.J. An, T.Y. Kim, B.H. An, S.M. Lee, J. Oyebanji, P. Balasubramanian

Modal characteristic identification of structure using high-speed digital image correlation method ..601
Xiongjie Che, Ruihai Xin, Nam Seo Goo

Etching selection for phase analysis in super duplex stainless steel SAF2507 603
F. Sordetti, A. Palombi, N. Picco, M. Magnan, C. Maranzana, A. Varone, A. Lanzutti

Generalized camera model calibration method based on collimator.....606
Shunkun Liang, Banglei Guan, Zibin Liu, Ang Su, Zhang Li, Yang Shang, Xiaolin Liu, Qifeng Yu

Polymer characterization using laser doppler vibrometry and ultrasonic excitation.....609
N. Hasheminejad, N. Ghaderi, A. Golmohammadi

Study of triangular underexpanded sonic jets 611
S. Kato, T. Miyaguni, S. Nakao and Y. Miyazato

Study of diamond underexpanded sonic jets 613
K. Tanaka, T. Miyaguni, S. Nakao, Y. Miyazato

Shock structures in ninja-star underexpanded sonic jets.....615
R. Uchida, T. Miyaguni, S. Nakao, Y. Miyazato

A calibration method of fringe projection profilemetry based on optical ray model correction 617
Wenxin Hu, Chen Xiong, Yan Liu

Time-gated active-imaging digital image correlation: a novel solution for ultra-high temperature deformation measurement.....620
Liping Yu, Ning Lu, Bing Pan

Coupling effect between deformation and blood condition on skin reflectance spectrum in-vivo.....625
Wang Shibin, Huo Zongze, Yu Qiaoyun, Ji Boyang, Wang Zhiyong, Li Chuanwei, Li Linan, Ma Jiangxiong

Determination of isochromatic fringes using modified matlabbased image processing techniques 627
Ramit Chugh, Shubhrata Nagpal, Shubhashis Sanyal

Inhomogeneous tensile deformation of nitrogen-added Ti-Nb based shape memory alloys 628
K. M. Golasiński, M. Maj, S. Musiał, W. Tasaki, E.A. Pieczyska, H. Y. Kim

3D motion measurement of moving points based on a monocular camera 630
Huayu Huang, Banglei Guan, Zibin Liu, Ang Su, Zhang Li, Yang Shang, Xiaolin Liu, Qifeng Yu

Applied stress modulation of brillouin oscillations at the filmsubstrate interface by picosecond ultrasonics 633
Yantao Zeng, Lin'an Li, Shibin Wang, Zhiyong Wang, Chuanwei Li

Electrowetting-actuated Liquid Iris for Switchable Aperture 635
C. Lee, S. Park, S. K. Chung, J. Lee

Quantitative measurement the warpage of printed circuit board under the electricity on by utilizing laser speckle interferometry 637
Funjun Yang, Hanyang Jiang, Yinhang Ma, Xiangyang Xu

New Photoelastic Technology and Its Applications Based on Pixelated Polarization Camera and RGB Method 639
Fei Su, Qingyi Liu

Determining the heart performance of experimental an animal based on the averaged speed using digital image correlation method 642
Chi Hung Hwang, Chun-Wei Lai, RongQing Qiu, Wei-Chung Wang, Yen-Pei Lu, Rui-Cian Weng

Snapshot full Stokes camera by RGB polarization camera for stress visualization 645
Yukitoshi Otani, Jessica Onaka, Nathan Hagen

THERMAL BASED TECHNIQUES FOR MATERIALS AND COMPONENTS ANALYSIS: APPLICATIONS AND PERSPECTIVES 647

Active and passive thermography for a non-destructive surface treatment characterization in spur gears 649
L. Corsaro, F. Curà, R. Sesana

Thermographic estimation of the fatigue limit of a titanium alloy 653
C. Colombo, A. Salerno, A. Teyssiéras, J. Fiocchi, C. Biffi

A model for assessing the effect of thickness on apparent thermal diffusivity in lock-in thermography measurements 655
L. Santoro, R. Sesana, L. Tromba

Novel Thermographic NDE approach for testing the dispersion of nanoparticles in nanocomposites ... 659
Nicola Montinaro, Guglielmo Marchesa, Donatella Cerniglia, Antonio Pantano

Energy-based approaches for a rapid fatigue characterisation of AlSi10Mg-AM 661
R. De Finis, D. Palumbo, U. Galietti

Stresses and deformations induced by curing in epoxy matrix CFRPs composite laminates 664
A. Mengozzi, M. Giacalone, E. Dolcini, S. Mantovani

Increasing damage assessment in hybrid woven composites using a novel thermographic procedure ... 667
T. Matarrese, C. Sergi, D. Palumbo, F. Sarasini, U. Galietti

Rapid fatigue characterization of single row bolted lap cfrp joints via infrared thermography 669
N. Manoharan, S. Gururaja

Temperature harmonic analysis to investigate intrinsic dissipation of fatigue loaded Ti6Al4V produced by laser powder bed fusion 671
F.W. Panella, G. Pitarresi, D. Crisafulli, R. Penna, P. Leo, G. Pollara, G. Risitano, M. Tornabene

THERMOELASTIC STRESS ANALYSIS 673

Analysis of Stress Behavior in Ti90Al(10-x)V(x) Alloy for Medical Applications using CASTEP simulations. 675
Charef Azzeddine, Karima Zitouni, Said Benramech

Numerical simulation for the thermal-mechanical response of PBX-2 explosives at different heating rates 679
Xiaoli Zhang

Operational modal shapes of plates using digital image correlation and TSA 681
A. Molina-Viedma, L. Felipe-Sesé, E. López-Alba, F. Díaz-Garrido

Thermoelastic stress analysis set up optimization via robust design 683
F. Di Carolo, U. Galietti

Assessment of fatigue crack closure via wavelet transform of infrared thermography data 685
L. Bercelli, B. Levieil, C. Doudard, S Calloch

Optimised sampling strategies for self-referenced thermoelastic stress analysis 687
G. Pitarresi, M. Tornabene, R. Cappello

Application of thermoelastic stress analysis on titanium in the presence of biaxial stresses 689
D. Palumbo, R. De Finis

Strain experimental modal analysis via a high-speed thermoelasticity-based approach 691
L. Capponi, K. Zaletelj, G. Rossi, J. Slavič

Aliasing interference and signal undersampling in thermoelastic stress analysis 693
R. Cappello, G. Pitarresi

WOOD MECHANICS AND TIMBER ENGINEERING 695

Brazilian native woods pillars stability 697
R.M.L.R.F. Brasil, A.M. Wahrhaftig, G.A. Pereira

Numerical simulation of contribution of concrete anchorage to ductility of shear walls made of cross laminated timber 699
P. Sejkot, A. Iqbal, G. Faraone

Axial-shear interaction of angle brackets in connections of cross-laminated timber 701
P. Sejkot, A. Aloisio, A. Iqbal

A nanoindentation study on diverse technical lignins for biocomposite applications 703
Luis Zelaya-Lainez, Michael Schwaighofer, Markus Königsberger, Markus Lukacevic, Sebastián Serna-Loaiza, Florian Zikeli, Michael Harasek, Anton Friedl, Olaf Lahayne, Josef Füssl

Restarting of long-term monitoring of two eight-story residential CLT buildings 705
M. Dorn, C. Amaddeo, E. Serrano

Suitability of poplar rotary cut veneers as active layers in shape changing wood bilayers.....707

S. Calvano, F. Negro, C. Cremonini, R. Zanuttini

In situ monitoring of a complex model structure built with green wood and submitted to real climate conditions.....709

S. Bouhlel, A.Cointe, E. Maurin, A. Histace, Y. Mélinge

Influence of moisture on beech and birch: compression perpendicular to grain and rolling shear properties.....711

E. Binder, E. Kuck, C. Bertram, Z. Shehadeh, M. Schweigler, C. Sandhaas, T.K. Bader

Moisture protection techniques for the narrow face of CLT during the construction phase.....713

M. Schweigler, M. Eveborn, M. Dorn, Z. Shehadeh, T.K. Bader

Effect of wood drying on axially loaded screws in oak.....715

M. Pilon, L. Bleron

Combined embedment and axial load tests of a steel dowel in various wood species.....718

R. Lemaître, T.K. Bader, M. Schweigler

Mechanics-based 3d modelling of cnc-made carpentry joints used in CLT-glulam composite flooring systems.....720

Y. Diao, C. Loss

Comparison of mechanical properties of cross laminated timberpressed on vacuum and hydraulic presses.....722

W. Plowas, R. Hairstans, B. Shirley, S. Hart

Investigating the influence of delignification and polymer infiltration on wood cell wall properties via nanoindentation.....725

J. Schindler, M. Königsberger, L. Zelaya-Lainez, A. Mariani, D. Nuvoli, J. Füssl

The effect of catenary action in restrained and reinforced glued lamindated timber members.....727

L. Esser, A. Frangi

Finite element modelling of clt-steel composite shear walls for mass timber balloon-type construction.....730

C. Leong, C. Loss

Long-term analysis of steel-timber shear connectors for composite floors.....732

M. Kamalinejad, C. Burigo, C. Loss, I. Goingo

Effect of interposed resilient soundproofing profile on timber-totimber structural connections.....734

A. Morganti, L. Barbaresi, M. Benatti, P. Brugnara, M. Zoppè, C. Luzzani, L. Pozza

X-RAY & NEUTRON TOMOGRAPHY AND APPLICATIONS.....**737**

Time resolved failure physics tomography (5D CT) on the damage behaviors by multi-modal methods.....739

S.C. Wu

Experimental and computational analyses of hydrogen embrittlement behaviour in aluminium alloys using synchrotronbased multimodal measurements.....742

H. Toda, Y. Wang, Z. Wu, H. Fujihara, M. Yamaguchi, T. Tsuru, K. Shimizu and K. Hirayama

Characterization of internal deformation and damage evolution in materials under extreme environment by using X-ray CT 744

Long Wang, Chuantao Hou, Ruisi Xing, Junbai Song, Wugang Liu, Yueping Zhang, Qiaoyu Liu, Fang Ren, Shengchuan Wu

Analysis of damage evolution in c/sic composite structures with hole under monotonic tensile loading 746

Qiaoyu Liu, Long Wang, Chuantao Hou, Zhiqiang Li, Zhouxia Jia, Baorui Liu, Yao Li, Tongzhao Wang

Void nucleation and growth behavior of tig welded AA2219 deformed at cryogenic temperatures 748

Y.N. Hu, S.C. Wu, Z.Y. Wang, Y.L. Xue, Y.N. Fu, G.Z. Kang, P.J. Withers

Carbon steel S38C axle residual stress neutron testing and life prediction 752

Tianyu Qin, Feifei Hu, S. Yuhua Su, Pingguang Xu, Shengchuan Wu

The diffraction elastic constants of railway wheel steel of highspeed train 754

X.X. Zhang

Characterization of residual stress fields in metallic materials: a combined neutron bragg edge imaging and diffraction analysis 757

Y. Su, T. Shinohara, J.D. Parker, K. Oikawa, T. Kai, W. Gong, S. Harjo, K. Aizawa, Y. Kiyanagi

The Latest Progress of HEPS and Its Hard X-Ray Imaging Beamline 759

Li Gang, Zhang Weiwei, Zhang Jie, Wang Yanping, Gao Lidan, Sun Rui, Wang Zhimao, Huang Mei, Deng Tijian, Wang Lu, Jiang Xiaoming

4D microstructural characterization of corrosion fatigue crack initiation in high-strength aluminum ally 761

Ni Ao, Songquan Tang, Shengchuan Wu

In situ X-ray tomography of failure criticality in μ-LPBF fabricated cellular lattice 764

Yuexun Liu, Shengchuan Wu, Xu Song

Move contrast x-ray imaging for in-situ/in-operando mechanical testing with high sensitivity 769

T.Q. Xiao, F.X. Wang, K. Li, X.L. Ju, M.W. Xu, Z.H. Song, C.C. Ma

POSTERS

Effect of the glass and PVB thickness on the head injury criterion 773

J. Kim, S. Ahn, J. Hwang, H. Jung

AI classification of fracture modes in metallic components 775

R. Montanari, M. Sileo

Development of an Organometallic Benzoxazine Composite for Dual Electromagnetic and Ballistic Shielding Applications 777

Abdelmalek Habes, Oussama Mehelli, Mehdi Derradji, Fouad Benaliouche, Slimane Abdous, M'hamed El Hadi Timtaoucine

Speed-dependent characteristics model of railway buffers using deep learning 781

Jun Hyeok Hwang, Hyun Seung Jung, Jin Sung Kim, Seung Ho Ahn

Development of an in-vitro model to study the cervical spine load transfer using mobi-c prosthesisa....783

A. Ramos, G. Costa, J. A. Ferreira, Y. Ledoux, and M. Mesnard

Numerical analysis of four types of star-shaped auxetic structures based on the geometric parameters of the 2D arc-starshaped structure.....785

V. Sinđelić, A. Nikolić, S. Ćirić Kostić, N. Bogojević

Effect of strain rate on compressive properties of high carbon chromium bearing steel and chromium molybdenum steel 787

K. Tateyama, R Kiya, H. Yamada, H. Fujiki

Evaluation of the relationship between fatigue fracture surfaces in rotating shafts and acoustic emission generation behavior using a non-contact ae measurement system.....789

T. Matsuo, Y. Abe

Experimental verification of the fatigue strength of a locomotive composite drive shaft.....791

J. Chvojan, J. Vaclavik

Effect of strain rate on the pullout resistance of geogrids 794

Harshal Verma, Bappaditya Manna, Partha Narayan Mishra, David Williams

Fracture toughness determination through resistance curve: a comparison between ASTM E1820 and ISO 12135 standards.....797

G. Coêlho, A. Guimarães, A. Silva, M. Dos Santos

Effect of CNF string on tensile strength of bio-degradable parts fabricated in fused filament fabrication 800

T. Tateno, A. Nishida, Y. Kiminami

Kinematic analysis of a 3-bar mechanism for gmaw welding in the flat position (G1).....802

S. Cacpata

Kinematic analysis of a mechanism designed for a thumb exoskeleton, integrating numerical, analytical, and simulation methods into autodesk software 804

D. García

Data-model coupling driven stress field measurements for structures with localized deterioration....806

Jian Zhao, Guangbo Wang

Synthetic aperture x-ray ghost imaging: enabling sub-micron pixel resolution.....808

Nixi Zhao, Jie Tang, Changzhe Zhao, Jianwen Wu, Haipeng Zhang, Han Guo, Tiqiao Xiao

Experimental methodology of fast x-ray imaging beamline at SSRF 810

Ke Li, Fei-Xiang Wang, Jianfeng Ji, Ya-Nan Fu, Guo-Hao Du, Biao Deng, Ti-Qiao Xiao, Hong-Lan Xie

Numerically study for assessement of ballistic efficiency of high hardnes perforated plates with unconventional holes 814

A. Spoiala, A.N. Rotariu, L.C. Matache, E. Trana, F. Bucur

Numerical simulation-based determination of the viscosity influence of materials subjected to dynamic loads at high strain rates 816

L.C. Matache, A.N. Rotariu, I.D. Pacurar, R.M. Mircioaga, C. Puica, M. Marmureanu, P. Somoiag

BL13HB: the new x-ray imaging and biomedical application beamline at SSRF 818

Y.L. Xue, H. Guo, G.H. Du, J.F. Ji, B. Deng, H.L. Xie, and T.Q. Xiao

Development of ptc-based composite surface heating textiles: enhanced mechanical reliability and wash durability through MWCNT compositing.....821

Ji-Hyeok Choi, Sun Hee Kim

Corrosion resistance evaluation and behavior analysis of Fe- and Ni-based alloys for molten salt reactors with molybdenum coating application.....824

Su Hyeong Kim, Ji-Hyeok Choi, Young Soo Yoon

Investigation of 316l produced by additive manufacturing for nuclear applications 828

R. Montanari, A. Palombi, M. Richetta, A. Varone, A. Zahid

Characteristics of LDHs grown on ECAP processed AZ31 alloy 830

Filippo Berto, Franco Bonollo, Alberto Fabrizi, Alessandra Fava, Paolo Ferro, Roberto Montanari, Riccardo Narducci, Ekaterina Pakhomova, Alessandra Palombi, Subhan Rasulzade, Maria Richetta, Alessandra Varone

AUTHORS

Abdous S., 777
Abe Y., 789
Accornero F., 521
Achour Y., 565
Aggelis D.G., 519, 532
Ahn S., 773, 781
Aizawa K., 757
Al Fadhli A.A., 467
Al Maskari L.S., 467
Al Omairi A.M., 467
Al Shabibi A.M., 467
Al Shukaili A.S., 467
Albanese A., 433
Alexopoulos N.D., 111, 187
Allen C., 431
Al-Mamun N., 541
Almazán-Lázaro J.A., 573
Almeida B., 339, 342
Aloisio A., 701
Altoé P., 5
Amaddeo C., 705
Ambrosone L., 449
Ameur M.F., 79
An B.H., 599
An H.J., 599
Angelastro A., 11
Anggraini V., 267
Anupoju S.K., 479
Ao N., 761
Arai M., 152
Arce I., 339
Arcidiacono G., 443
Arcieri E.V., 477, 496
Arikawa S., 29, 73, 83, 227, 494
Aristeidakis J.S., 187
Aruffo G.A., 51
Asami M., 73
Asazuma A., 227
Attolico M.A., 11, 423, 471
Avoledo E., 168
Ayothiraman R., 249
Azlisham M.A.S.N., 267
Azzeddine C., 675
Babini V., 459
Bai B.F., 283
Bailas K., 111
Baktash S., 336
Balasubramanian P., 599
Banerjee A., 23, 375
Banerjee J., 23, 375
Baragetti S., 477, 496
Baranowski P., 142
Barbaresi L., 734
Barbieri S.G., 90
Barnaby G.C., 7, 15, 241,
Bartram B., 225
Batista I., 345
Belding M., 336
Benaissa A., 584
Benaliouche F., 777
Benatti M. , 734,
Benhamouda S., 427, 475
Benramech S., 675
Bentley J., 241
Bercelli L., 685
Berglund I.S., 187
Berrocal-Coba A.E., 575
Bertè A., 192
Berto F., 830
Bertram C., 711
Bettini P., 492, 525
Bhandar B., 27
Bhattacharjee N., 375
Bhowmik D., 249
Biffi C., 653
Binder E., 711
Bleron L., 715
Bogojević N., 785,
Bolelli G., 192
Bolli E., 413,
Bonilauri M.F., 192
Bonnaire R., 51
Bonner J.C., 27
Bonollo F., 830
Bonora N., 237
Botsis J., 425
Boudiaf M.D.D, 427, 475
Bouhlel S., 709
Boukhaoua S., 251
Bouteldja A., 71
Bouzar Essaidi A., 461
Boyang J., 625
Brasil R.M.L.R.F., 697
Brodecki A., 96
Brugnara P., 734
Brugo T.M., 492, 525
Bucur F., 814
Bumb C., 388
Burigo C., 732
Cabibbo M., 125
Cacpata S., 802
Cai I., 511
Cai J., 194
Calervo L., 492
Calloch S., 685
Calvano S., 707
Campagnolo A., 459
Campanelli S.L., 11
Candelaria S., 181
Cao X., 292, 305, 384
Cappello R., 687, 693
Capponi L., 691
Carone S., 11, 423
Casavola C., 11, 49, 423, 471
Castagnini L., 144
Ceccacci A., 237
Cecchini-Brigi A., 575
Cerniglia D., 659
Cerri E., 192
Ceschini L., 144,
Chanda A., 592
Chang T., 557
Charalampidou C.M., 111, 187
Chargaoui M., 67
Chaudhuri S., 87
Chavda C., 541
Che Muda Z., 499
Che X., 601
Chen C.F., 377, 588
Chen F., 395
Chen M., 586
Chen Pengyu, 400
Chen Po-Yu, 549
Chen Q., 567
Chen T.Y., 555, 557
Chen X., 514
Chen Y.W., 586
Chen Z., 245, 384
Chen Z.H., 457
Cheng J., 31, 39, 243
Cheng X.N., 283
Cheng Z., 31
Chiang C., 537, 560
Chiu Y., 560
Chmelko V., 379, 590
Choi J.H, 821, 824
Chu C., 549
Chuang C., 555
Chuanwei L., 625, 633
Chugh R., 627
Chung S.K., 19, 549, 635, 642
Chvojan J., 791
Ciccarella A., 169
Cieplak K., 131, 142, 183,
Ćirić-Kostić S., 785
Coêlho G., 797, 483
Cointe A., 709
Colaiuda V., 169
Colombi P., 192
Colombo C., 653
Conde-Calabrús A.J., 573
Conti M., 352
Contiero L., 459
Corsaro L., 649
Costa G., 783
Coules H.E., 431
Coupeau C., 67
Crachia M., 136
Cremonini C., 707
Crisafulli D., 176, 671
Croccolo D., 103, 149, 154, 157, 183, 303, 429
Cruz-Zapata L., 23
Curà F., 649

D'Accardi E., 348
D'Andrea D., 176
D'Angela D., 527
D'hers S., 136
Da Silva Davidson F.S., 241
Dai B., 255
Daniel N., 131
Das K., 249
Dattelbaum D., 225
De Agostinis M., 103, 149, 154, 157, 303,
De Belie N., 532
de C. Coêlho G., 483, 797
De Finis R., 174, 661, 689,
De Luca A., 174, 423, 439
de Nigris A., 449
De Pasquale G., 162, 164
De Waele W., 87
Declercq E., 519
Dehghanpour Abyaneh M., 279
Dekert B., 142
Del Core L., 49
Del Zoppo M., 527
Dell'Avvocato G., 169, 348
Delpretea C., 136
Deng B., 810, 818
Deng H., 229, 233, 235
Deng J., 220
Derradji M., 71, 453, 777
Di Angelo L., 169,
Di Carolo F., 683
Di Ludovico M., 527
Di Schino A., 420
Di Tommaso A., 528
Diao Y., 720
Dias S., 339
Diaz F.A., 573
Díaz-Garrido F., 681
Ding G., 255
Dolcini E., 664
Donzella G., 490
Dorn M., 705, 713
Dos Santos M., 797
Doudard C., 685
Drabble J., 241
Du G., 39, 810, 818
DU J., 313
Du Y., 245
Dubey V.P., 179
Dworakowski Z., 350,
Dziendzikowski M., 350
Ejiri A., 55
Elahi S.A., 87
Elhajjar R., 545
El-Sarout A., 162
Errico V., 11
Esser L., 727
Eveborn M., 713
Fabiani D., 525
Fabrizi A., 830
Fahem A.F., 263
Fan Z.X., 253
Fang S., 208
Faraone G., 699
Fava A., 803
Felipe-Sesé L., 573, 681
Fernandes J.R., 342
Ferreira J.A., 783
Ferro P., 830
Fidlin A., 5
Fini S., 103, 149, 154, 157, 303
Fink S., 162
Fiocchi J., 653
Foerster J., 187
Fragab L.B., 136
Frangi A., 727
Friedl A., 703
Fu H., 258
Fu Y.N., 748, 810
Fujihara H., 742
Fujiki H., 787
Fumarola G., 348
Füssl J., 703, 725
Galietti U., 348, 661, 667, 683
Gang L., 759
Gao C., 211
Gao J., 213, 319, 356, 364
Gao J.L., 220
Garan M., 379
García D., 804
Gatto M.L., 125
Gentile D., 449
Georgiou E., 481
Ghaderi N., 609
Ghio E., 192
Giacalone M., 146, 664
Giacopini M., 90, 92
Giannadakis K., 519
Gibson L., 225
Gilat A., 247
Giorgetti A., 443
Goingo I., 732
Golasiński K.M., 628
Golmohammadi A., 609
Gong W., 757
Gong X., 229, 231, 233, 235
Gonzales P., 181
Goo N.S., 601
Gottipati U.N., 443
Gradys A., 185
Grima G., 125
Guan B., 275
Guimarães A., 797
Gunputh U., 190
Guo H., 808, 818
Guo Y., 202
Gupta S., 592
Gururaja S., 669
Guthai A.T., 263
Habak M., 79
Habes A., 777
Hafeez F., 437
Hagen N., 645
Hairstans R., 722
Halder P., 577
Hama Y., 166
Hamed A.A.A., 433
Hamerton I., 481
Han B., 547
Han S., 9
Han X., 457
Haque A., 539, 541
Harasek M., 703
Hareyama S., 128
Harjo S., 757
Harouche M.K, 427, 475
Harrison A., 63
Hart S., 722
Hasheminejad N., 609
Hashimoto K., 160, 166
Hashimura S., 435
He C., 213, 319, 364
He R., 315
He W., 301
He X., 395, 400
Hebbouche H.E., 251
Hicks B.J., 241
Hill T.L., 241
Hirayama K., 742
Histace A., 709
Honda Y., 160
Hossein Abadi R., 75
Hosseinzadeh A.Z., , 345
Hou C., 744, 746
Hou Y., 213, 290, 311
Hou Z., 345
Hsu J.W.P., 27, 61
Hu F., 752
Hu S., 292, 305, 308
Hu W., 617
Hu X., 395
Hu Y.N., 748
Huang C., 345
Huang H., 630
Huang K.R., 253
Huang L., 301
Huang P., 331, 551
Huang X., 258
Huber R., 225
Hughes M., 395, 406
Hwang C., 642
Hwang J., 773,
Hwang J.H., 486,781
Iannitti G., 237
Inui H., 457
Invernizzi S., 528
Iqbal A., 699, 701
Itam Z., 267, 499
Iwamoto T., 211
Ja'e I.A., 267
Jan F., 317
Janiszewski J., 183, 190
Javadi M.S., 279
Jeong H., 9
Ji J., 810
Ji J.F., 818
Jia Z., 746
Jiang H., 637
Jiang K., 260
Jiang Z., 455, 521
Jiangxiong M., 625
Jie Z., 759
Jimbo K., 101
Jo E., 45
Jordan J., 225
Ju B., 109
Ju X.L., 769
Jung H., 773
Jung H.S., 781
Júnior E., 117
Just-Agosto F.A., 575
Kaciulis S., 413
Kai L., 255
Kai T., 757

Kalliontzis D., 390
Kalteremidou K.A., 75, 519
Kamalinejad M., 732
Kang G.Z., 748
Kang Y., 277, 547
Kato S., 611
Ke C., 537
Kenane M., 79
Kent J., 388
Khaderi S.N., 479
Khan M., 303
Khan M.Y., 388
Kim B.J., 486
Kim D., 19, 45
Kim H.Y., 628
Kim J., 773
Kim J.S., 781
Kim M., 109
Kim S., 9
Kim SuHyeong, 824
Kim SunHee, 821
Kim T.S., 77
Kim T.Y., 599
Kim Y., 19, 45
Kim Y.H., 77
Kiminami Y., 800
Kishida K., 457
Kiya R, 787
Kiyanagi Y., 757
Kluczyński J., 183
Kobayashi S., 128
Kodama H., 569
Kong G., 395
Königsberger M., 703, 725,
Kopec M., 96, 179
Koščo T., 379
Kourkoulis S.K., 523
Kowalczyk K., 350
Kowalewski Z.L., 96, 179
Krankenhagen R., 87
Kučerková M., 590
Kucewicz M., 142
Kuck E., 711
Kujawa M., 317
Kythreotis K., 241
La Battaglia V., 443
Lacidogna G., 528
Lagalante I., 144
Lahayne O., 571, 703
Lai C., 642
Lalau Y., 51
Lan S., 285
Lantada A.D., 185
Lanza di Scalea F., 345
Lanzutti A., 413
Ledoux Y., 783
Lee C., 635
Lee D., 45
Lee D.W., 599
Lee E., 45, 109
Lee J., 635
Lee J.H., 9
Lee K.Y., 19
Lee M., 61
Lee S.M., 599
Lee T., 45, 109
Lee Y.C., 586
Lefever G., 532
Leite A., 339
Lemaître R., 718
Lemay J., 584
Leo P., 11, 149, 174, 423, 439, 671
Leong C., 730
Levieil B., 685
Li B., 243
Li B.D., 283
Li C., 625
Li D., 231
Li H., 305
Li J., 260
Li K., 769, 810
Li L., 625
Li M., 265
Li P., 258
Li Q., 31, 290
Li R., 31
Li T., 258, 265
Li W., 331, 551
Li Xiaoru, 511
Li Xiushi, 514
Li Y., 202, 220, 229746
Li Z., 275, 746
Lian X., 235
Liang S., 275, 297, 606
Lidan G., 759
Lin C.S., 377, 588
Lin M., 555, 557
Linan L., 625
Liu B., 746
Liu J., 313, 406
Liu J.G., 220
Liu J.T., 377, 588
Liu Qiaoyu, 744, 746
Liu Qingyi., 639
Liu R., 270
Liu S., 277, 373
Liu W., 744
Liu X., 275, 297, 606, 630
Liu Yan., 617
Liu Yi, 508
Liu Yuexun, 764
Liu Z., 275, 606, 630
Livera F., 103
Lombardi M., 144
López-Alba E., 576, 681
Loss C., 720, 730, 732
Lou C., 235
Lou D., 160
Lourari A., 251
Lu N., 620
Lu S., 241
Lu T.J., 220
Lu Wang, 759
Lu Wenhui, 292
Lu Yen-Pei, 642
Lu Yiling., 190
Lu Yonghui, 295
Lukacevic M., 703
Luo G., 373
Lupoi R., 279
Luzzani C., 734
Lyu Y., 213
Ma B., 514
Ma C.C., 769
Ma M., 277
Ma Q.W., 283
Ma S.P., 283
Ma Y., 637
Maccaferri E., 525
Magliulo G., 527
Magnan M., 43, 603
Maizza G., 433, 437
Maj M., 628
Makaoui R., 453
Manabe K., 128
Mancini E., 169
Mangeruga V., 92
Manna B., 249, 375, 381, 577, 794
Manni F., 90, 92
Manoharan N., 669
Mantovani S., 146, 664
Maranzana C., 603
Marchesa G., 659
Mariani A., 725
Marinelli G., 348
Marmureanu M., 816
Marques M.J., 433
Martucci A., 144
Matache L.C., 814, 816
Matarrese T., 667
Matos A.L, 35
Matsumoto M., 211
Matsuo T., 789
Matsuoka K., 494
Maurin E., 709
Mazzocchetti L., 525
Mazzoni A., 490
Mehelli O., 71, 453, 777
Mehri Sofiani F., 87
Mei H., 759
Mei K., 567
Mele M., 103, 149, 154, 157, 303
Melendez J., 181
Mélinge Y., 709
Mellor P.H., 7, 15
Meneghetti G., 459,
Menegozzo M., 181, 575
Meng H., 220
Mengmeng Y., 204
Mengozzi A., 664
Mesnard M., 783
Messina S., 90, 92
Mezzi A., 413
Mia I., 61
Milan G., 157
Milite A., 492
Minotti A., 443
Mircioaga R.M., 816
Mishra P.N., 794
Miyaguni T., 611, 613, 615
Miyawaki A., 73
Miyazato Y., 569, 611, 613, 615
Mo H.W., 588, 377
Molina-Viedma A., 573, 681
Mongioì F., 492, 525
Monici A., 527
Montanari P.M., 528
Montanari R., 413, 417, 429, 437,
441, 775, 828, 830
Montinaro N., 659
Moon H., 9
Morais R., 342
Moramarco V., 11, 49, 423, 471
Morganti A., 734

Morri A., 144, 149
Munshi M., 541
Musiał S., 628
Na J., 45, 109
Nagpal S., 627
Naito Y., 83
Nakao S., 569, 611, 613, 615
Nakase K., 166
Narayanamurthy V., 479
Narducci R., 830
Nascimento M., 117
Nassar S.A. , 303, 388
Negro F., 707
Nikolić A., 785
Nishida A., 800
Nobile R., 149, 174, 423
Nuvoli D., 725
Ogasawara N., 55
Oh C.Y., 486
Oh S.J., 9
Oikawa K., 757
Oliveira A.G., 483
Oliveira M. , 339, 342
Olmi G., 103, 149, 154, 157, 183, 303
Omiya Y., 152
Onaka J., 645
Osaka S., 435
Ospitia N., 532
Ota K., 166
Otani Y., 645
Ott S., 5
Ouldhamrane H., 565
Oyebanji J., 599
Ozbilen S., 279
Pacurar I.D., 816
Paffetti A., 149, 154, 157
Pagano A., 237
Pakhomova E., 830
Palazzetti R., 492, 525
Palombi A., 413, 415, 429, 603, 828, 830
Palumbo D., 348, 661, 667, 689
Pan B., 620
Pan C., 258
Pan J., 194, 505
Pan S., 345
Panella F.W., 671, 439
Pantano A., 659
Papadia G., 439
Papanikos P., 111
Pappalettera G., 49
Pappas G.A., 425
Paramatmuni C., 579
Park J., 19
Park S., 635
Parker J.D., 757
Parry G., 67
Pascale L., 90
Pasiou E.D., 523
Patronelli M., 11, 49
Paul B., 457
Pavoni S., 352
Pawlik M., 179, 190
Pearton S., 541
Peihong C., 441
Pen Z., 305
Penazzi L., 51
Peng Z., 270, 292
Penga Y., 37
Penna R., 671
Pereira F., 339, 342
Pereira G.A., 697
Petrogalli C., 490
Peyerl M., 571
Picco N., 43, 413, 603
Pichler B., 571
Pieczyska E.A., 185, 628
Pilon M., 715
Piper R.T., 27
Piraccini G., 103
Pitarresi G., 671, 687, 693
Platek P., 131, 142, 183, 190
Plowas W., 722
Pocetta V., 169
Pola A., 149
Pollara G., 671
Pozza L., 734
Primo T., 439
Prota A., 527
Puica C., 816
Qiao B., 406
Qiao Z., 567
Qiaoyun Y., 625
Qin T., 752
Qiu R., 642
Qiu W., 31
Qu C., 345
Quino G., 481, 488
Qun L., 204
Rahman M., 539, 541
Ramos A., 35, 783
Ran L., 204
Rasulzade S., 830
Raut S., 577
Rebhi L., 461
Ren B., 243
Ren F., 541, 744
Ren T., 285
Renna G., 11, 174, 423, 439, 471
Ricci S., 237
Richetta M., 415, 429, 828, 830
Risitano G., 176, 671
Rizzo P., 336
Robinson P., 488
Rodrigues M.C., 483
Rodriguez-Vargas B.R., 420
Rossi G., 619
Rotariu A.N., 814, 816
Roubache R., 427, 475
Ruggiero A., 237
Rui S., 759
Rusinek A., 190
Sachs U., 75
Salerno A., 653
Salvati E., 168
Sandhaas C., 711
Santecchia E., 125
Santoni A., 125
Santonocito D., 176
Santoro L., 502, 655
Sanyal S., 627
Sarasiniand F., 667
Sartori S., 149
Sarzynski M., 131, 142
Scalzo F., 168
Scapecchi C., 303
Scaramuzzi C., 11, 439
Schilp J., 187
Schindler J., 725
Schlick G., 187
Schlitz D., 545
Schmid S.J., 571
Schmidt R., 420
Schneider O., 545
Schultz A.E., 390
Schwaighofer M., 703
Schweigler M., 711, 713, 718
Sehaba M., 584
Seidt J., 247
Sejkot P., 699, 701
Selleri G., 525
Sergi C., 667
Serna-Loaiza S., 703
Serrano D., 181
Serrano E., 705
Sesana R., 136, 279, 502, 649, 655
Seth D., 381
Shahu J.T., 375, 381, 577
Shang H., 258, 265
Shang S.H., 220
Shang Y., 275, 297, 606, 630
Shehadeh Z., 711, 713
Sheibanian N., 279
Shen M., 537, 560
Shen T.K., 499
Shen Y., 220
Shi X., 292, 305
Shibin W., 525, 633
Shimizu K., 742
Shinohara T., 757
Shirley B., 722
Sienikiewicz J., 183
Sileo M., 775
Silva A., 797
Silva A.A., 483
Simões J.A., 35
Sinđelić V., 785
Singer C., 187
Singh R.P., 263
Skoczeń B., 543
Slavič J., 691
Sleem K., 125
Smakosz Ł., 317
Solazzi L., 490
Somoiag P., 816,
Song H., 313
Song J., 744
Song J.Y., 9
Song X., 764
Song Z.H., 769
Soni N., 439
Sordetti F., 43, 413, 603
Spigarelli S., 125
Spoiala A., 814
Sritharan S., 390
Staszczak M., 185
Stavrakas I., 523
Stornelli G., 420
Su A., 630
Su F., 639
Su Y., 752, 757
Sugiyama T., 166,
Šulko M., 379, 590

Sun C., 39
Sun X., 301
Sung C., 555
Sung P., 549
Suo T., 202, 245, 260
Sur A., 375
Syamsir A., 267, 499
Takeda K., 185
Takizawa T., 85
Tan D., 297
Tanaka K., 613
Tanaka Y., 83,211
Tang Jie, 808
Tang Jiyu, 57
Tang S., 761
Tang Yang, 395,400
Tang Yongxiang , 508
Tang Z., 202
Tapia R.M., 87
Tasaki W., 628
Tateno T., 133,800
Tateyama K., 787
Testa G., 237
Teyssiéras A., 653
Tijian D., 759, ,
Tikarrouchine E., 71
Timtaoucine M., 777
Tocci M., 149
Toda H., 742
Todaro S., 539
Tolazzi M., 43
Tomasi I., 490
Tonelli L., 144
Tornabene M., 671,687
Touimi K., 565
Trana E., 814
Trask R.S., 481,488
Tria D.E., 71,251,453
Triantis D., 523
Tromba L., 655
Truman C.E., 431
Tsai J., 455
Tselikova A., 420
Tseng Z., 555
Tsuchida Y., 29
Tsuchiyama Y., 29
Tsuru T., 742
Uchida R., 615
Uno T., 55
Urbański L., 185
Ursi F., 162
Vaclavik J., 791
Vaglio E., 413
Van Hemelrijck D., , 75,519
Vanali M., 352
Vandenberghe W., , 61
Varone A., 413,415,
417,429,437,441,603,828,830
Vecchiato L., 459
Verma H., 794
Verona C., 413
Viglietti E., 502
Vincenzi N., 103
Virgolin M., 43
Wahrhaftig A.M., 697
Wan W., 579
Wang C., 567
Wang F., 384
Wang F.X., 769,810
Wang G., 806
Wang H., 39
Wang H.X., 220
Wang K., 384
Wang L., 400,744,746
Wang M., 31
Wang Q., 356
Wang S., 508,633
Wang T., 746
Wang W.C., 313,549,642
Wang X., 168,233,290,311
Wang Y., 395,400,505,742
Wang Z., 457,505,633
Wang Z.Y., 748
Warner L., 539
Waryoba D., 539
Watkins E., 225
Wei J., 220
Weiwei Z., 759
Weng R., 642
Wharton M.M., 241
Williams D., 794
Wirtz T., 65
Withers P.J., 748
Wolfe D., 541
Wolter K., 5
Wood P., 179,190
Wragge-Morley R.T., , 7,15,241
Wu H., 208
Wu J., 808
Wu Shangquan, 35, 567
Wu Shengchuan, , ,
406,744,752,761,764
Wu S.C., 739,748
Wu W., 567
Wu Z., 265,303,388,742
Wua W., 37
Xi Z., 315
Xiao S.L., 220
Xiao T., 808
Xiao T.Q., 769,810,818
Xiaoming J., 759
Xie H., 301,547
Xie H.L., 810,818
Xie S., 373
Xin R., 601
Xing H., 31
Xing R., 744
Xiong C., 617
Xiong J., 498
Xu L., 345
Xu M.W., 769
Xu P., 752
Xu X., 637
Xuan S., 231,233
Xue Y.L., 748,818
Yamada H., 55, 787
Yamaguchi M., 742
Yamaguchi S., 133, 494
Yamamoto N., 435
Yamashita T., 569
Yamazaki Y., 85, 152
Yan X., 579
Yan Y., 199
Yang C., 549
Yang F., 637
Yang L., 265
Yang S., 384
Yang X., 258, 265, 595
Yang Y., 255, 567
Yang Z., 171
Yanping W., 759
Yao G., 395, 400
Ying L., 395
Yingzheng S., 204
Yon J.M., 15
Yoneyama W., 55
Yoon Y.S., 824
Yoshihara R., 160
Yoshikawa H., 55
Yu L., 620
Yu Q., 275, 297, 606, 630
Yu Y., 511
Yuan Y., 253
Yuan Y.C., 220
Yuhua Su S., 752
Zabihzadeh S., 187
Zahari N.M., 499
Zahid A., 828
Zaletelj K., 691
Zanuttini R., 707
Zaoui A., 565
Zawawi M.H., 499
Zelaya-Lainez L., 571, 703, 725
Zeng Y., 633
Zhang B., 364
Zhang C., 208, 245
Zhang H., 315, 384, 808
Zhang L., 630
Zhang Q., 37, 277, 285, 547, 567
Zhang S., 384
Zhang X., 679
Zhang X.X., 754
Zhang Y., 744
Zhao C., 171, 488, 808
Zhao J., 806
Zhao L., 400
Zhao N., 808
Zhao X., 311
Zhao Z., 208
Zheng C., 94
Zheng Y., 364
Zhimao W., 759
Zhiyong W., 625
Zhou L., 295
Zhu C., 285
Zhu Z., 521
Zikeli F., 703
Zitoune R., 79
Zitouni K., 675
Zongze H., 625
Zoppè M., 734
Zucchelli A., 492, 525

MAIN TOPICS

Testing and Diagnostic

TEST BENCH FOR THE MULTIDIMSENSIONAL EXCITATION OF DISC SHAPED DRIVETRAIN COMPONENTS

P. Altoé [1], K. Wolter [2], S. Ott [2], A. Fidlin [1]

[1] Institute of Engineering Mechanics (ITM), Karlsruhe Institute of Technology (KIT), Karlsruhe, Germany
[2] Institute of Product Engineering (IPEK), Karlsruhe Institute of Technology (KIT), Karlsruhe, Germany

1. Introduction

The various subsystems in the drivetrains of technical systems are generally subject to multidimensional vibration excitation. This is not limited to conventional or hybrid drivetrains of mobile drive systems, which experience multidimensional vibration excitation, e.g., due to the cranking in connected combustion engines. In electric drivetrains, the vibration excitation emanating from electric motors is of particular interest, in addition to the influence of external vibrations on their operation. The external vibrations can range from the coupling of rotational, axial and radial excitation in a coupled helical gear to the stochastic excitation onto a wheel hub motor. The influence on operation is becoming increasingly important in the pursuit of weight reduction, higher efficiency and good NVH behavior [1]. In order to achieve these goals during development, multidimensional couplings between subsystems are increasingly being considered in addition to purely torsional simulation models of drivetrains. The validation of these models is of central importance. However, existing test benches often only offer the option of torsional excitation. This article presents the commissioning of a new test bench that allows multidimensional excitation.

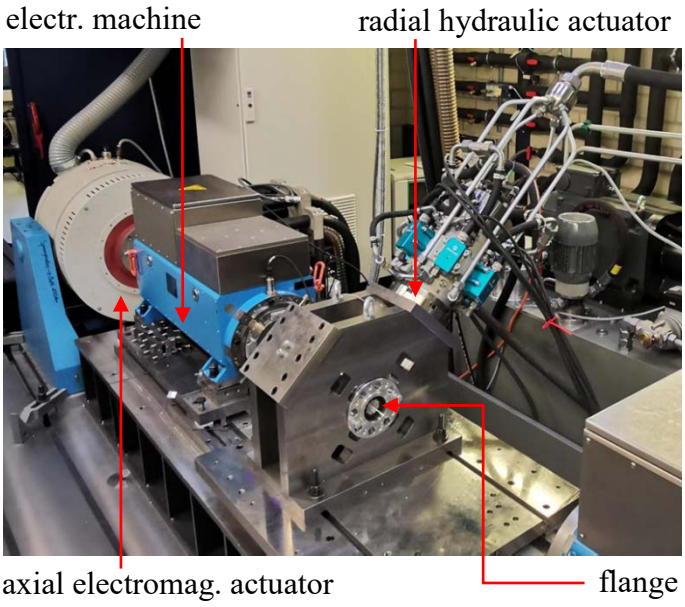

Fig. 1: Test bench for multidimensional excitation.

2. Test Bench

For the new test bench, an existing test bench [2] was extended to include radially acting vibration excitation. Fig. 1 shows the flange of the test bench to which a test specimen can be connected and excited to torsional, axial and radial vibrations. The excitation is applied via a special superposition unit that connects the flange to the torsionally acting electric machine, the axial electromagnetic shaker and the radially acting hydraulic actuator behind it. An additional actuator can be mounted on

the opposite side of the current hydraulic actuator in order to allow for radial loads in two directions in the future.

3. Results of Commissioning

Different operating points were approached for initial commissioning. At different rotational speeds (500, 1000 rpm) of the electric machine, the axial and radial actuators were open-loop controlled at a constant frequency (10, 100, 200 Hz), whereby no force or displacement closed-loop control was initially carried out. To measure the system response, the axial deflection of the flange's center and the radial deflection in the hydraulic actuator's direction were measured. Two amplitude spectra of the measurements are shown in Figure 2. The set frequencies in radial and axial directions are clearly recognizable in the spectrum. Due to a slight misalignment of the flange, frequency components of the rotational speeds in the axial deflection response are unavoidable. Furthermore, a coupling of the radial signal to the axial deflection of the flange is unavoidable without corresponding displacement control, as the radial actuator behind the flange also leads to a tilting and thus axial displacement of the flange's surface.

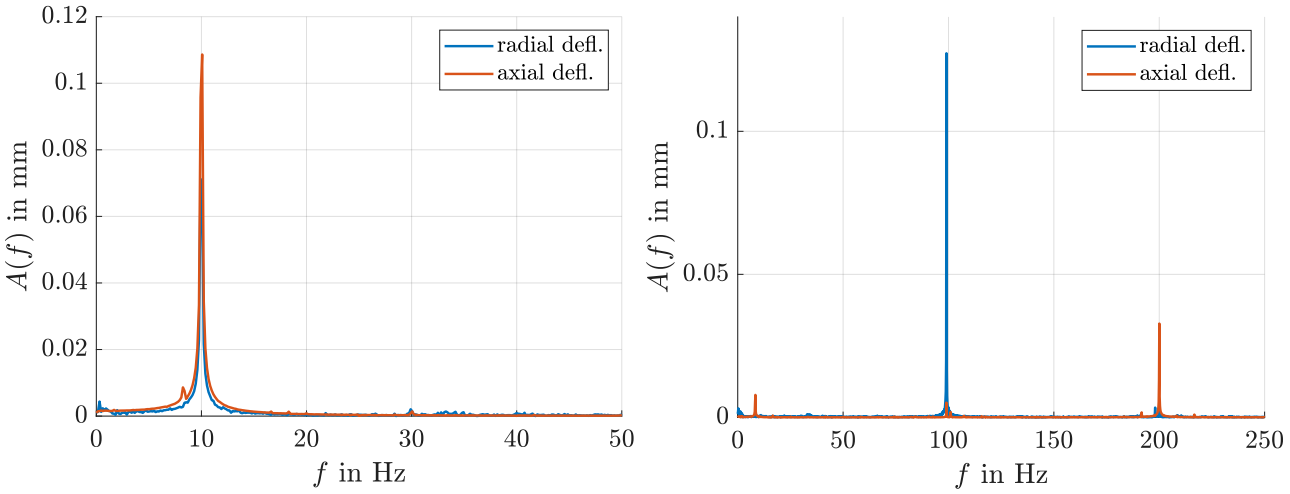

Fig. 2: Amplitude spectrum at (left) 500 rpm, 10 Hz radial, 10 Hz axial and (right) 500 rpm, 100 Hz radial, 200 Hz axial excitation.

4. Conclusion and Future Work

This article presents a novel test bench for applying multidimensional (radial, axial, torsional) excitations to drivetrain components. The results of commissioning show that the coupling of the various excitations to the flange is successful. In the future, the independent control of the different excitation types in terms of force and displacement is to be implemented.

5. Acknowledgements

The authors are grateful for the financial support of the German Research Foundation (DFG), grant DFG_INST 121384/249-1.

5. References

[1] W. Cai, X. Wu, M. Zhou, Y. Liang, Y. Wang (2021). Review and Development of Electric Motor Systems and Electric Powertrains for New Energy Vehicles. *Automotive Innovation,* **4**, 3-22.

[2] J. Berger, R. Theuerkauf, S. Ott (2018). Neue Prüf(-stands)-Konzepte ermöglichen Validierung mehrdimensional angeregter Triebstrangteilsysteme. *VDI-Berichte*, **2333**, 511-526.

CHARACTERISATION OF A DISPLACEMENT-AMPLIFIED PIEZOELECTRIC ACTUATOR FOR HIGH-FREQUENCY FORCING IN BEARING TEST STAND

G. C. Barnaby, R. T. Wragge-Morley, and P. H. Mellor
School of Electrical, Electronic and Mechanical Engineering, University of Bristol, UK

1. Introduction

Bearings used in new applications must be tested with representative loading to understand wear and failure mechanisms. Quasi-static axial, radial, and moment external loading are possible on test beds [1]. In-use loads on bearings found in some emerging applications are cyclic in nature and highly dynamic, e.g. those resulting from blade flapping in E-VTOL aircraft. Test-rig load application via a Piezoelectric Actuator (PEA) is a solution which has precedent in the literature for aerospace applications [2,3]. This study describes the test design and implementation for characterisation of a PEA for application as a high force density linear actuator for dynamic loading of test bearings. The design and characterization of a rhombus type amplifier spring is presented, which provides a blocking force and increases the displacement of the PEA at cost of the maximal forcing.

2. Materials and methods

A high frequency, high force density linear actuator for a rolling element bearing test-stand was designed using a large piezoelectric stack [4]. A containment spring is required to offer blocking force and amplify its displacement. There are many designs available, and analytical methods in the literature to determine the amplification ratio [5]. A rhombus amplifier spring has been designed with geometry for a specified amplitude ratio derived by analytical and finite element (FE) methods. To isolate the piezoelectric stack from moment loading, end caps with spherical contacts were implemented. Several tests were completed to characterize the PEA: voltage-force characteristics of PEA were determined with various preload applied by test machine (Fig. 1.); Load-extension and amplitude ratio were determined for rhombus and compared with analytical solutions from the literature [5] and FE analysis; finally, voltage-force characteristics of the amplified PEA with preload supplied by interference fit in rhombus amplifier (Fig. 2.) were determined.

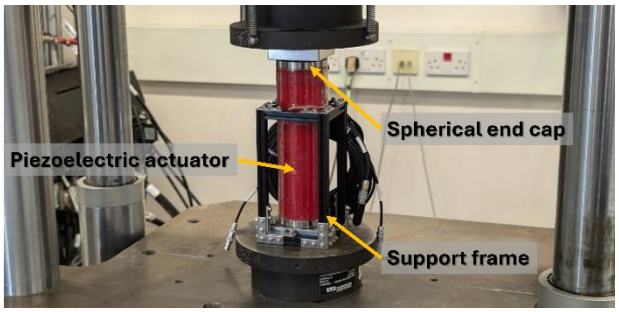

Fig. 1. Piezoelectric actuator in universal test machine

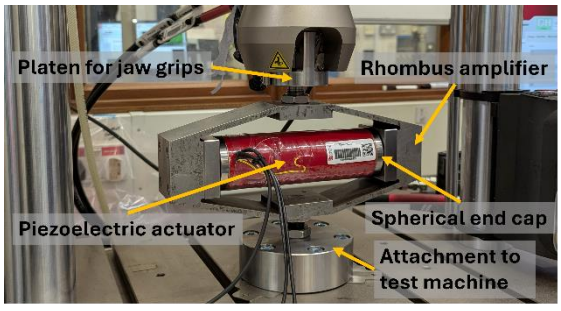

Fig. 2. Piezoelectric amplifier in rhombus amplifier with attachments in universal test machine.

3. Results and conclusions

The voltage-forcing relationship of the PEA was found to be similar under different axial pre-loading (Fig. 3.). The rhombus amplifier demonstrated both hysteresis and reduced stiffness when compared to the finite element analysis (Fig. 4.). This is hypothesized to be due to local plastic

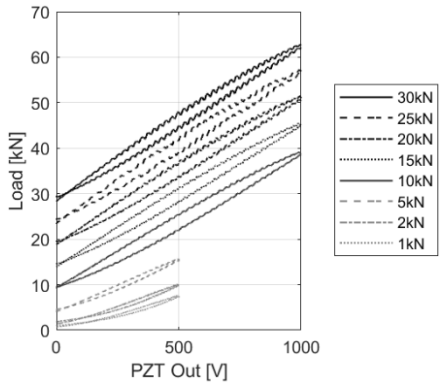

Fig. 3. Piezoelectric stack Load-Voltage characterization under varying preload

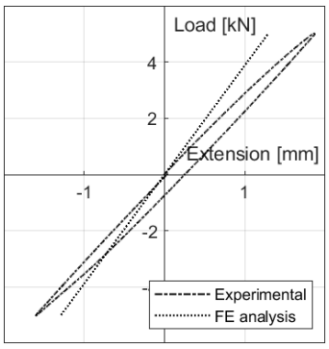

Fig. 4. Rhombus amplifier load-extension with FE result

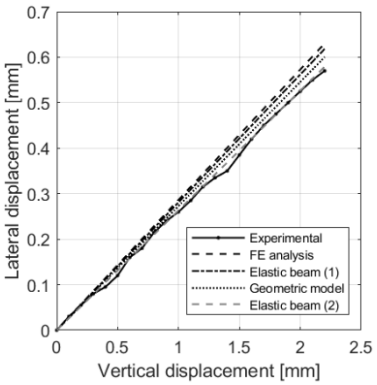

Fig. 5. Rhombus amplifier displacement amplitude with analytical results

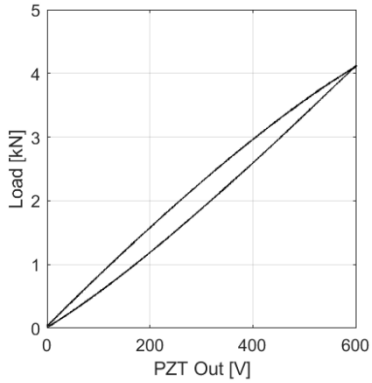

Fig. 6. Amplified piezoelectric stack Load-Voltage in compression.

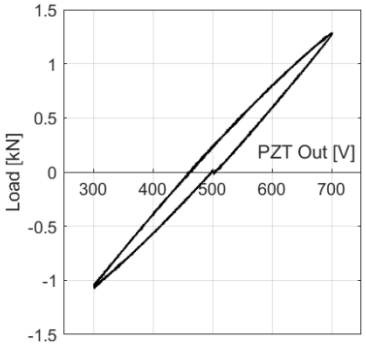

Fig. 7. Amplified piezoelectric stack Load-Voltage in compression and expansion from voltage offset.

deformation in areas of stress concentration. The displacement-amplitude ratio was also different between FE and experiment (Fig. 5.), with experimental results agreeing more closely with an elastic beam model from the literature.

The response of the amplified PEA is demonstrated in two modes. Firstly, the compressive force measured on the universal test machine holding zero displacement (Fig. 6.). This shows more than 4kN output for given 600V input. Secondly, the PEA demonstrates both compressive and tensile forcing by fluctuating its voltage output about an offset (Fig. 7.). In this example, with a 500V offset and ±200V fluctuation, +1.3kN and -1.1kN is achieved.

The presented methods and results for characterization of the PEA offer a platform for development of it as a high frequency, force-dense actuator in test stands. Data could be used in open loop control to control forcing and amplitude with voltage input, and to correct for hysteretic effects. Validated analytical approaches can be used for future hardware iterations.

4. Acknowledgements

This research was conducted under UKRI ATI project AEPEC (Reference 113253).

5. References

[1] R. T. Wragge-Morley et al. (2024). A bearing test stand to represent E-VTOL air-screw loads in vertical and forwards flight., *Joint Surfaces, Interfaces and Coatings Technologies, Plasma Tech and Tribology International Conference 2024*. Vienna, Austria.

[2] R. Jepsen, et al. (2010). Using Piezo-Electric Material to Simulate a Vibration Environment, *U.S. Patent Office*. p. 10.

[3] E. Romero, R. Jepsen, and D. L. Gregory (2013). High Force Vibration Testing with Wide Frequency Range. *U.S. Patent Office*. p. 7.

[4] R. T. Wragge-Morley, J. M. Yon, and P. H. Mellor (2023). Design of a piezo-electric actuator for dynamic testing of rolling element bearings. *ICEM 20: Experimental Mechanics in Engineering and Biomechanics*. Porto, Portugal.

[5] M. Ling et al. (2016). Enhanced mathematical modeling of the displacement amplification ratio for piezoelectric compliant mechanisms. *Smart Materials and Structures*. **25**, 1-11.

EFFECT OF THE HIGHLY ACCELERATED STRESS TEST ON THE INTERFACIAL ADHESION OF DIE ATTACH FILM IN PACKAGE STRUCTURE

S. J. Oh, H. Jeong, J.-H. Lee, S. Kim, S. Han, H. Moon, and J.-Y. Song,
Semiconductor Manufacturing Research Center, Korea Institute of Machinery and Materials (KIMM), Daejeon, Republic of Korea

1. Introduction

The development of 3D sensing LiDAR sensors for autonomous vehicles and robotics has become a key research field, particularly in enhancing the field of view (FOV), miniaturization, and weight reduction [1]. To achieve these performance goals, one promising approach is packaging of thinned IC chips, such as IR image sensors and mini-LD arrays, onto curved light weight substrates. However, the use of curved substrates introduces significant challenges, especially the potential delamination at the material interfaces, which could compromise the overall reliability and performance of the sensor. To maintain the structural integrity of the curved sensor packages, understanding the interfacial adhesion property of die attach film (DAF) is crucial for multi-layered packaging. To address the issue, optimizing the double cantilever beam (DCB) test method is adopted to accurately evaluate and enhance the bonding characteristics of these curved package structures [2]. This study aims to develop an asymmetric DCB testing method for various packaging configurations with heterogeneous materials, ensuring reliable bonding under harsh environmental conditions [3].

2. Materials and methods

The test specimens were fabricated by bonding the diced silicon (Si) and liquid crystal polymer (LCP) using DAF to duplicate the interfacial property of thinned IC chip on the curved polymeric beam. For the Si beam, a 775 μm-thick 8-inch Si wafer was diced into 0.8 mm x 4 mm after the lamination of DAF film. The LCP beam was fabricated by compression molding to a 1.95 mm thickness with the same in-plane dimensions. The beam thicknesses were determined to control the flexural modulus of each beam and thus to control mode-mixity of the asymmetric DCB specimen. After the beam fabrication, the LCP beam was bonded onto the DAF-laminated Si beam using customized thermo-compression bonder with controlled pressure of 0.13 MPa and temperature of 133 °C. After the pre-bonding, the structure was fully bonded by reflow in air ambient at 140 °C. Finally, specimens were subjected to an 85°C/85% RH highly accelerated stress test (HAST) for extended durations to simulate operational environments. Each specimen was tested under quasi-static loading conditions with sufficiently low crosshead speed to accurately evaluate the changes in interfacial adhesion energy.

3. Results and conclusions

The asymmetric DCB test successfully measured the interfacial bonding strength in the curved LCP/DAF/Si structures. By adjusting the thickness of the LCP and Si substrates to achieve identical bending stiffness, Mode-I fracture at the interface was induced, allowing for the quantitative

measurement of the interfacial bonding strength. The initial bonding strength, which exceeded 150 J/m^2 was found to drastically decrease to approximately 50 J/m^2 after exposure to a harsh environment of 85°C/85% RH for 96 hours. This result highlights the substantial degradation of interfacial adhesion property of DAF material under harsh environmental conditions and need for process optimization to enhance long-term reliability of the curved LiDAR sensor. As future work, we plan to investigate bonding strength under controlled mode-mixity conditions to derive a more comprehensive failure criterion for heterogeneous packaging structures.

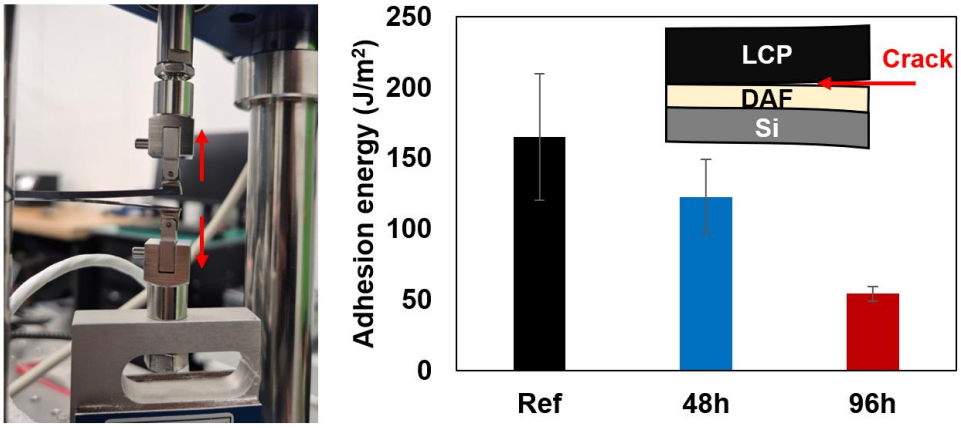

Fig. 1. Asymmetric DCB test setup and adhesion energy after the environmental test

4. Acknowledgements

The research was supported by "Development of Multi-Axis Assembly System for Curved Free-Form Electronics (20018154)" funded by MOTIE (Ministry of Trade, Industry and Energy) in Korea and by a grant of the Basic Research Program funded by the Korea Institute of Machinery and Materials (grant number: NK254A)

5. References

[1] D. Liang, C. Zhang, P. Zhang, S. Liu, H. Li, S. Niu, R. Z. Rao, L. Zhao, X. Chen, H. Li & Y. Huo (2024). Evolution of laser technology for automotive LiDAR, an industrial viewpoint. *Nat. Commun.* **15**, 7660.

[2] Y. Pan, S. J. Oh, J.-H. Kim, T.-S. Kim, K.-W. Paik, (2020). A Study on the dynamic bending property of chip-on-flex assembly using anchoring polymer layer anisotropic conductive films, *IEEE Transactions on Components, Packaging and Manufacturing Technology*, **10**, 941–948.

[3] S. J. Oh, J. H. Lee, S. M. Kim, S. Han, A.-Y. Park, H. Moon (2025). Overview of Testing Methods for Mechanical and Adhesion Properties of Materials in Semiconductor Packages. *IEEE Transactions on Materials for Electron Devices,* doi: 10.1109/TMAT.2025.3561740.

MECHANICAL AND MICROSTRUCTURAL CHARACTERIZATION OF MONO-MATERIAL AND BI-MATERIAL COMPONENTS FABRICATED BY LASER POWDER BED FUSION

A. Angelastro[1], M.A. Attolico[1], S. L. Campanelli[1], S. Carone[1], C. Casavola[1], V. Errico[1], P. Leo[2], V. Moramarco[1], M. Patronelli[1], G. Renna[2], C. Scaramuzzi[2]

[1] Department of Mechanics, Mathematics and Management, Polytechnic University of Bari, Via Orabona 4, Bari, 70125, Italy
[2] Department of Engineering for Innovation, University of Salento, via per Monteroni di Lecce, 73100, Lecce, Italy

1. Introduction

Additive manufacturing (AM) technologies have revolutionized modern manufacturing by enabling the production of components with highly complex geometries, customized designs, and integrated multi-material functionalities. Among these technologies, Powder Bed Fusion-Laser Beam (PBF-LB) stands out as a versatile method that offers exceptional control over the microstructure and properties of processed materials [1-2]. The ability to fabricate components layer by layer provides unique opportunities for tailoring material properties, especially when employing advanced alloys such as AISI 316L stainless steel and CoCrMo. These materials are widely recognized for their superior mechanical performance, corrosion resistance, and biocompatibility, making them suitable for critical applications in industries such as aerospace, automotive, and biomedical engineering.

In particular, the use of bi-material structures, such as CoCrMo-AISI 316L combinations, has opened new avenues for creating functionally graded components. These structures offer the potential to optimize performance by combining the distinct advantages of individual materials within a single part [3-5]. For instance, AISI 316L is known for its excellent ductility and corrosion resistance, while CoCrMo alloy exhibits high strength and wear resistance. The integration of such materials using PBF-LB poses unique challenges, as the process inherently involves complex thermal and mechanical interactions during layer-by-layer deposition. These interactions influence defect formation, microstructural evolution, and residual stresses, which, in turn, affect the final mechanical properties of the components [6-7].

This work focuses on the systematic characterization of AISI 316L, CoCrMo, and CoCrMo-AISI 316L specimens. The research activities include an extensive experimental campaign involving metallographic analysis, defect quantification, and mechanical testing. The primary objectives are to assess the influence of process parameters on the microstructure, defect distribution, and mechanical behavior of these materials and to provide insights into the critical factors that govern the performance of bi-material systems.

Furthermore, this study explores the relationships between manufacturing-induced microstructural features and the resulting mechanical properties, including elastic modulus, yield strength, tensile strength, and elongation at fracture. By comparing the findings with existing literature, this research highlights the impact of process conditions and material selection on component performance. These insights aim to guide the optimization of PBF-LB parameters for future applications and contribute to the development of robust methodologies for fabricating high-performance multi-material components using additive manufacturing.

2. Materials and methods

This investigation focused on evaluating the mechanical and metallographic properties of AISI 316L stainless steel, CoCrMo alloy, and CoCrMo-AISI 316L bi-material specimens produced using Powder Bed Fusion-Laser Beam (PBF-LB) additive manufacturing technology. The study encompassed material selection, specimen fabrication, defect characterization, and mechanical testing to provide a detailed understanding of the properties of these materials.

The PBF-LB process used high-purity AISI 316L and CoCrMo alloy powders with controlled particle size distributions. Specimen fabrication involved optimized process parameters based on previous metallographic analyses to ensure consistent and defect-minimized prints. The specimens were printed at a 45° orientation to the recoater blade and staggered to allow uniform powder deposition and minimize potential obstructions during fabrication. This strategic arrangement aimed to achieve optimal layering and uniform material properties.

Metallographic characterization involved preparing longitudinal-transverse (L-LT) sections of the samples by grinding and polishing, followed by chemical etching. Optical microscopy (OM) and scanning electron microscopy (SEM) were utilized to observe the microstructural features and defect morphology. Image analysis was performed using ImageJ software to quantify defect area fraction, Feret diameter, and circularity, providing insights into defect distribution and shape characteristics. Quantitative data were extracted to identify the types of defects present, such as gas-induced porosity and lack-of-fusion voids, along with their location within the layered structure.

X-ray diffraction (XRD) analysis was conducted to determine the crystalline phases present in the specimens. The analysis was carried out on sections prepared both parallel and perpendicular to the build direction, using a Rigaku D/MAX Ultima system with Cu-Kα radiation (λ=1.5406 Å). Measurements were performed in a 2θ range of 20-100°, with a scanning speed of 0.02° per step and an acquisition time of 1 second per step. This analysis provided detailed phase identification crucial for understanding internal stresses and material behavior.

Mechanical testing of the fabricated specimens followed ASTM E8 standards, using Type A specimens for tensile tests. Specimens were conditioned in a controlled environment for 24 hours before testing to standardize temperature and moisture content. Cross-sectional dimensions were measured with a centesimal caliper at three points along the reduced section to ensure accurate area calculations. Testing was conducted on an Instron 1342 machine equipped with an MTS load cell with a maximum capacity of 100 kN. Longitudinal strain was recorded using an MTS extensometer with a 20 mm gauge length and electrical resistance strain gauges. Transverse strain measurements were also taken with perpendicular strain gauges for determining Poisson's ratio.

Data acquisition was managed with the Vishay StrainSmart® System 5000 at a sampling rate of 10 Hz. The elastic modulus was calculated by linearly interpolating data between 20% and 60% of the yield stress, determined via the 0.2% offset method. The ultimate tensile strength (UTS) was identified at the maximum load, while percentage elongation at fracture (A%) was calculated from the plastic deformation at rupture. Representative stress-strain curves and a summary of mechanical properties were obtained for AISI 316L and CoCrMo specimens to compare the behavior of different material configurations under similar testing conditions.

3. Results and conclusions

The experimental investigation focused on characterizing the mechanical and metallographic properties of mono-material and bi-material components fabricated using Powder Bed Fusion – Laser Beam (PBF-LB) technology. The materials under study included AISI 316L stainless steel, CoCrMo alloy, and bi-material CoCrMo-AISI 316L specimens. Detailed analyses of defect morphology, microstructural features, and mechanical performance were conducted to assess their applicability in demanding industrial environments.

Defect analysis was performed on sections prepared by standard metallographic grinding and polishing techniques. Quantitative image analysis using ImageJ software revealed a defect density below 0.5% for both monolithic AISI 316L and CoCrMo alloy samples. The defects were primarily small spherical voids attributed to gas-induced porosity, alongside larger voids caused by lack of fusion (LoF). These defects were predominantly concentrated along stratified layers and at interfaces between adjacent layers. Morphological analysis showed that over 70% of the defects had a near-spherical shape, with a circularity factor exceeding 0.8. The defects were also characterized by their small size, with diameters typically ranging from 0 to 20 μm.

Microstructural analysis, conducted through optical microscopy (OM) and scanning electron microscopy (SEM), revealed distinct differences in the structural characteristics of the AISI 316L and CoCrMo alloy samples. In the longitudinal–long transverse (L-LT) section, both materials exhibited semicircular melt pool morphologies, a typical feature of heat conduction-dominated solidification during PBF-LB processing. SEM micrographs highlighted cellular and columnar structures resulting from rapid cooling and directional heat flow. The CoCrMo alloy samples displayed a higher prevalence of elongated columnar grains compared to AISI 316L, reflecting material-dependent thermal properties.

X-ray diffraction (XRD) analysis further elucidated the crystallographic phases present in the samples. The AISI 316L specimens exclusively exhibited peaks corresponding to the austenite phase (γ, FCC), while the CoCrMo alloy samples displayed both hexagonal close-packed (ε-HCP) and metastable face-centered cubic (γ-FCC) phases. No intermetallic compounds were detected in either material. These findings underscore the strong influence of material composition and processing conditions on the resultant microstructure.

Mechanical characterization was conducted on mono-material and bi-material specimens using static tensile tests in accordance with ASTM E8. AISI 316L stainless steel demonstrated high ductility and moderate strength, with mechanical properties aligning closely with values reported in the literature. The yield strength and tensile strength were measured at 510 MPa and 580 MPa, respectively, with a percentage elongation at fracture of 30%. Conversely, the CoCrMo alloy exhibited significantly higher tensile strength and yield stress values, at 1056 MPa and 675 MPa, respectively, but lower ductility, with an elongation at fracture of approximately 10.77%.

These results provide a comprehensive understanding of the mechanical and metallographic behavior of components fabricated using PBF-LB technology. The study highlights the suitability of AISI 316L for applications requiring high ductility and moderate strength, while CoCrMo alloy is better suited for scenarios demanding high strength and wear resistance. The low defect density and controlled microstructural characteristics further underscore the capability of PBF-LB technology to produce high-quality components tailored for specific industrial applications.

4. Acknowledgements

This work was conducted within the framework of the PRIN project, **"OPTIMA - Optimization of Performances of The Innovative Multi-material Metallic Parts Obtained by Additive Manufacturing."** The authors acknowledge the valuable support and resources provided through this initiative, which enabled the successful completion of the research activities described in this paper.

5. References

[1] DebRoy, T., Wei, H.L., Zuback, J.S., Mukherjee, T., Elmer, J.W., Milewski, J.O., Beese, A.M., (...), Zhang, W., "Additive manufacturing of metallic components – Process, structure and properties", (2018) Progress in Materials Science, 92, pp. 112-224.

[2] Tofail, S.A.M. et al., "Additive manufacturing: scientific and technological challenges, market uptake and opportunities", (2018) Materials Today, 21, 1, pp. 22-37.

[3] Wei, C., Li, L., "Recent progress and scientific challenges in multi-material additive manufacturing via laser-based powder bed fusion", (2021) Virtual and Physical Prototyping, 16, 3, 347-371.

[4] Bandyopadhyay, A., Heer, B., "Additive manufacturing of multi-material structures", (2018) Materials Science and Engineering R: Reports, 129, pp. 1-16.

[5] Guan, Jieren, Wang, Qiuping, "Laser Powder Bed Fusion of Dissimilar Metal Materials: A Review", (2023) Materials, 16, 7.

[6] Hasanov, S., Alkunte, S., Rajeshirke, M., „Review on additive manufacturing of multi-material parts: Progress and challenges", (2022) Journal of Manufacturing and Materials Processing, 6, 1.

[7] Rangasamy, N., & Rakurty, C.S. (2023). "A Review of the Residual Stress Generation in Metal Additive Manufacturing: Analysis of Cause, Measurement, Effects, and Prevention." Micromachines, 14(7), 1480.

SIMULATING AXIAL BEARING LOADING FROM AN E-VTOL MULTICOPTER ON A LABORATORY RIG

R.T. Wragge-Morley[1], G.C. Barnaby[1], J.M. Yon[1] and P.H. Mellor[1]

[1] *School of Electrical, Electronic, and Mechanical Engineering, University of Bristol, Bristol UK*

1. Introduction

Multicopter E-VTOL craft are a significant growth area [1]. Though similar in concept to a conventional rotorcraft, these vehicles have a number of additional constraints imposed by weight budget. The use of many small rotors (most concepts use at least 8) with distributed propulsion leads to shaft speeds typically an order of magnitude higher than a regular helicopter. The space and weight constraints often result in the use of direct drive rotors that are either fixed pitch or lack the complex flapping hinge, blade feathering and trailing damper arrangement found in a normal helicopter hub. The result of this is that the kinetic energy resulting from edgewise rotor dynamics in forward flight is all supported by the relatively small drive-end bearing sets of the propulsion machines.

The steady-state loading experienced in forwards flight is cyclical, and linked to the blade-pass frequency. Significant short term excursions are also to be expected during maneuvering or aerodynamic turbulence. An experimental facility has been developed to examine the performance of angular contact ball bearings subject to these loads at full scale [2]. Its purpose is to examine wear mechanisms, the impact of known faults, and effectiveness of prognostics schemes. This contribution describes the development of a generic aircraft platform model allowing pre-defined or user defined trajectories to be 'flown' in two dimensions: altitude and horizontal displacement. The implementation of this model on the test-stand is also described.

2. Materials and methods

To close the loop between bearing loading and flight dynamics, a 2D model has been developed based on standard forms of the expressions for rotor thrust and torque [3]. The model makes certain assumptions which simplify craft topology – there are two identical rows of propulsion machines and rotors, one forward and one aft resulting in an even number of identical rotors generating lift, depicted in Fig. 1. It is additionally assumed that the fixed pitch propellor geometry is such that a constant incidence angle can be assumed resulting in constant lift and drag coefficients C_L and C_D. The model does however use the International Standard Atmosphere [4] to compensate air density with altitude.

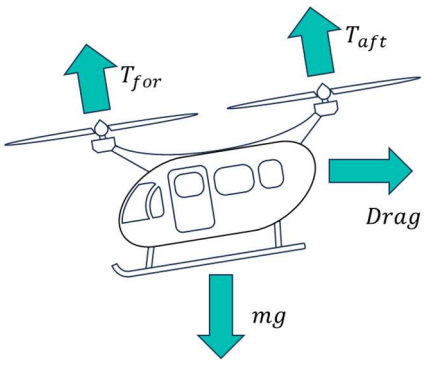

Fig. 1. Geometry of 2D multicopter

The model uses closed-loop controllers to track altitude and air-speed demands, where the rotors positions and attitudes are assumed fixed relative to the craft and air-speed is controlled by changing craft attitude. The same lift

model is used in conjunction with rotor speed and air-speed to compute the additional force imposed by the advancing blade due to 'flapping' forces.

3. Results and conclusions

The bearing test stand is instrumented with accelerometers, thermocouples and frictional moment measurement. Fig. 2. shows the spectral response of one accelerometer aligned radially to the bearings under test. The bearing is being subjected to computed axial loading, based on the 2D aircraft simulation following altitude and air speed trajectories.

Basing the simulation on user-variable parameters for number of rotors, rotor geometry, motor power and take-off weight, 'flight' performance was achieved by appropriate controller tuning, and the outputs for blade forcing are used to control the rig hardware. The rig hardware and control systems are able to track the highly dynamic forcing demand and once initial lift-off is achieved the simulated propulsion system is able to track the altitude and speed demands. The rotor speed varies slightly with power demand in flight, which can be seen in the time axis of the spectrogram. Meanwhile, the bright fringes showing the bearing element frequencies demonstrate variations of radial vibration intesity with both forcing oscillation amplitude and shaft speed. The frequencies detected were shown during instrumentation development studies to match those expected in normal operation.

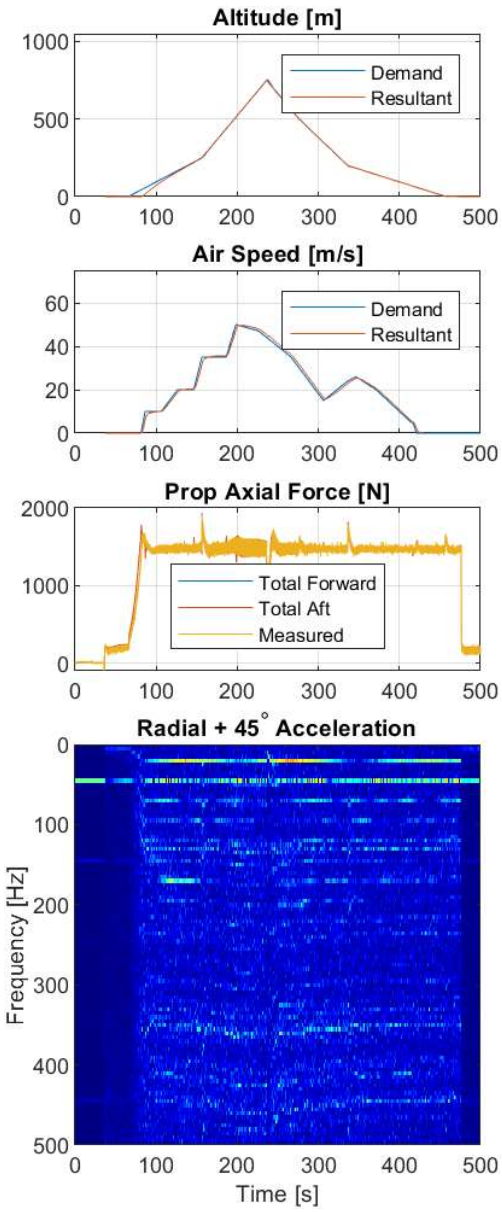

Fig. 2. Time series of simulation and experimental data for a short 'flight' hop.

4. Acknowledgements

The development of the bearing test stand was supported by UKRI ATI project AEPEC (Reference 113253).

5. References

[1] O. Ugwueze, T. Statheros, M. Bromfield and N. Horri (2023), "Trends in eVTOL Aircraft Development: The Concepts, Enablers and Challenges," in AIAA SCITECH 2023 Forum, National Harbor MD, USA.

[2] R. Wragge-Morley, G. Barnaby, J. Yon and P. Mellor (2024). A bearing test stand to represent E-VTOL air-screw loads in vertical and forwards flight. Tribology International Conference, Vienna, Austria

[3] J. Seddon and S. Newman (2011), Basic Helicopter Aerodynamics Third Edition, Chichester UK: John Wiley and Sons Ltd.

[4] International Standards Organisation, ISO 2533:1975 - Standard Atmosphere, 1975.

Thermo-Fluid Systems

MAGNETICALLY MANEUVERABLE MICROCARRIER USING ACOUSTIC BUBBLES

J. Park[1], Y. Kim[1], D. Kim[2], S.K Chung[1] and K.Y Lee[1]
[1] Department of Mechanical Engineering, Myongji University, Yongin, Republic of Korea
[2] Microsystems, Inc., Yongin, Republic of Korea

1. Introduction

According to the World Health Organization (WHO), cancer remains one of the leading causes of mortality worldwide. Among the commonly used treatment methods for cancer is the administration of drugs either orally or intravenously. While these drug administration methods are convenient, they have the disadvantage of causing side effects, such as hair loss and nausea [1]. To address these side effects, targeted drug delivery technologies using microcarriers introduced into the human circulatory system have recently gained significant attention [2]. To realize such targeted drug delivery technologies, various types of microcarriers controlled by factors such as temperature and pH changes have been actively investigated [3, 4]. However, these technologies face limitations, as it is difficult to achieve complete drug sealing, making it challenging to deliver liquid-phase drugs, which penetrate faster than solid-phase drugs in aqueous environments.

To overcome these limitations, this study proposes a microcarrier that utilizes magnetic liquid metal for transportation to target cells and acoustic bubbles for the effective manipulation of multiphase drugs. The proposed technology enables the wireless manipulation of multiphase drugs with different physical properties in aqueous environments using only acoustic bubbles, without the need for complex mechanical mechanisms.

Fig. 1. Schematic diagram of a proposed multiphase drug manipulation technology utilizing magnetic liquid metal and acoustically oscillating bubbles.

The proposed microcarrier consists of a microtube for drug manipulation and a magnetic liquid metal carrier for microcarrier control. The microtube encapsulates drugs using two bubbles of different volumes (an inner bubble and an outer bubble), while the magnetic liquid metal is loaded into the liquid metal carrier for magnetic actuation. When a magnetic field is applied to the magnetic liquid metal, the microcarrier is transported to the target cells (Figure 1(a1)). Subsequently, applying an acoustic wave at the natural frequency to the inner bubble induces oscillation, generating microstreaming flow. This process removes the outer bubble, allowing the encapsulated drug to be released and delivered to the target tissue (Figure 1(a2-a3)).

2. Results and Discussion

This study investigated the effect of the oscillation amplitude of the inner bubble on drug release by examining the oscillation properties of the inner bubble based on the lengths of the inner and outer bubbles embedded in the microcarrier. Experimental results revealed that as the length of the bubbles increased, both the oscillation amplitude and the natural frequency of the inner bubble decreased. Furthermore, it was observed that the oscillation amplitude of the inner bubble was maximized when the lengths of both the inner and outer bubbles were minimized.

Subsequently, experiments were conducted to release multiphase drugs (liquid and solid phases) with different physical properties using acoustic bubbles. First, liquid-phase drug release experiments were performed using a chemically reactive drug. The results confirmed that the encapsulated drug was released outside the microtube due to the oscillation of the inner bubble, and the released drug reacted normally with the surrounding fluid. Second, solid-phase drug release experiments were conducted using glass beads, and the release of solid drugs was experimentally verified through the oscillation properties of the bubbles (Figure 2).

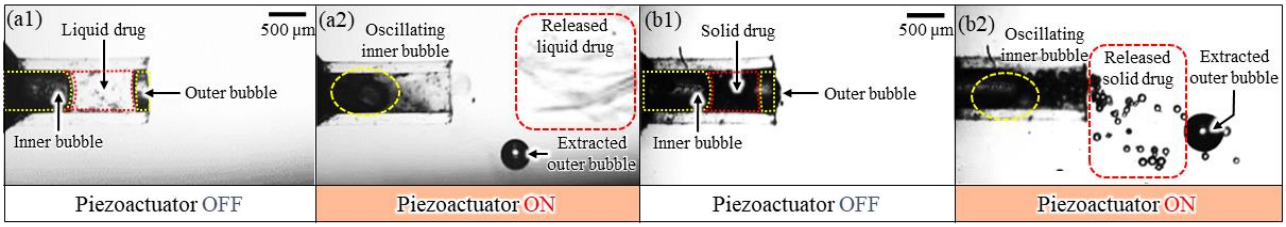

Fig. 2. Sequential snapshots of drug release using acoustic excitation of inner bubble: (a) liquid drugs and (b) solid drugs released through the oscillation of inner bubbles.

Finally, as a proof of concept, the proposed targeted drug delivery technology was demonstrated using a fabricated microcarrier in a Y-shaped channel filled with water. First, the microcarrier loaded with magnetic liquid metal was propelled to the target tissue via magnetic actuation. Subsequently, an acoustic wave was applied to the inner bubble embedded in the microtube, causing the inner bubble to oscillate and push the outer bubble outward, thereby releasing the drug. Following drug release, the remaining inner bubble generated microstreaming flow, facilitating the diffusion of the drug.

3. Conclusions

This paper proposes a multiphase drug delivery microcarrier based on acoustic bubbles and magnetic actuation to enhance drug delivery efficiency. The proposed technology, utilizing a simple microcarrier structure, enables the manipulation of various types of drugs, making it applicable not only to targeted drug delivery but also to a wide range of biomedical surgeries.

4. References

[1] A. Pearce, M. Haas, R. Viney, S. A. Pearson, P. Haywood, C. Brown, & R. Ward (2017). Incidence and severity of self-reported chemotherapy side effects in routine care: A prospective cohort study, *PLoS One*, **12**(10).

[2] T. Xu, W. Gao, L. P. Xu, X. Zhang, & S. Wang (2017). Fuel-free synthetic micro-/nanomachines, *Advanced Materials*, **29**(9).

[3] L. Zhang, J.J Abbott, L. Dong, B.E Kratochvil, D. Bell & B.J Nelson (2009). Artificial bacterial flagella: Fabrication and magnetic control. *Applied Physics Letters*, **94**, 2007-2009.

[4] H. Li, G. Go, S. Y. Ko, J. O. Park, & S. Park (2016). Magnetic actuated pH-responsive hydrogel-based soft micro-robot for targeted drug delivery, *Smart Materials and Structures*, **25**(2).

Modes of failure

TENSILE PLASTIC INSTABILITY IN USEFUL DEFORMATION FOR VOLUME CONSERVATION TYPE MATERIALS FORMING PROCESSES IN MANUFACTURING INDUSTRIES

J. Banerjee[1] and L. Cruz-Zapata[1]
[1] Department of Mechanical Engineering, University of Puerto Rico (UPRM), Mayagüez, Puerto Rico

1. Introduction

In metalworking industries, basically there are three types of manufacturing processes, namely, volume conservative processes, volume subtractive processes and volume additive processes [1]. Mostly, the materials forming processes like rolling, forging, extrusion, hydrostatic forming, electromagnetic forming, etc. are volume conservative processes where the material is neither subtracted (like machining, grinding, sandblasting, chemical-mechanical planarization (CMP), super-polishing, etc.), nor added (like assembly, welding, riveting, etc.). The plastic or permanent deformation starts at the onset of yield strength of the workpiece material and ends at the point of failure either by mechanical fracture or by thermal consequences, such as thermal fatigue, creep or catastrophic thermal impact.

Nevertheless, long before such failures, the workpiece material faces plastic instability, a bifurcation point between the stress and the strain, and the internal stress in the workpiece as well as the external load on it start falling while the strain or unit deformation keeps continuing. This is the unset of plastic instability, and the useful deformation for the workpiece stops at this critical point [2]. For any materials forming process where the workpiece material's volume remains essentially unchanged (volume conservation or volume constancy), the machine operating the process, such as a rolling mill or a forging press, must be stopped in order to reduce, if not totally eliminate, any failure of the final product in mass producing industries. Otherwise, the rejection of parts (final products or components) would increase costs, due to reducing the rate of production as well as deteriorating the product quality.

2. Application of Volume Constancy and Maximum Load at the Onset of Plastic Instability

Considering a simple uniaxial and axisymmetric forming process, such as wire-drawing, the length of the workpiece at any point during the tensile operation is L and the corresponding cross-sectional area is A. The workpiece material volume, V = L.A remains constant at any time during its plastic (permanent) deformation. Hence, the first derivative of a constant is zero. In other words,

$$dV = L\,(dA) + A\,(dL) = 0 \text{ ----(1)}$$

Now, at the point of the onset of plastic instability, the external force, F, passes through its maximum magnitude before declining due to the formation, nucleation and propagation of any internal crack or any other defects within the bulk material of the workpiece. Hence, F = S.A, S being the corresponding internal stress in the workpiece when the external force, F is maximum. Therefore, using the same argument of volume constancy, as in equation (1), at a maximum of F,

$$dF = S(dA) + A\,(dS)\text{------(2)}$$

Combining equations (1) and (2), it can be shown in a few steps, dS/S = dL/L where dL/L =de, de being a small strain. Thus,

$$dS/S = de\text{------}(3).$$

Rearranging equation (3),

$$dS/de = S\text{------}(4).$$

Equation (4) can be solved mathematically, only by knowing and applying a physical and conceptual relationship between the plastic stress, S and the corresponding plastic strain, e. Now, using the empirical Ludwik's Law for deformable solids,

$$S = K.\ e\ **\ n\ \text{----------}(5)$$

where K is the strength coefficient of the workpiece material and n is its strain-hardening or work-hardening exponent.

Substituting S from equation (5) into equation (4):

$$d\ [\ K.\ e\ **n]\ /\ de = K.\ e**n\ \text{----}(6)$$

$$K.\ [d(e**n)\ /de] = K\ [e**n]$$

$$d/de[(e**n)] = e**n$$

$$n\ [\ e**(n\ -1)] = e**n.$$

$$\text{Hence, } n = [e**n]\ /\ [\ e**\ (n-1)] = e\text{----}(7).$$

In other words, n = e. Thus, with a few simple steps as shown above, it is proved that at the point of the onset of tensile plastic instability, when the external force passes through its maximum value, the corresponding "optimum" strain, **e** is equal to the strain-hardening property, **n**, of the workpiece material. Thus, the plastic instability of a workpiece does not depend on its size or shape, but only on the plastic property, namely the strain-hardening or work-hardening.

3. Conclusions

Calculations, very similar to the one shown above for uniaxial tension, such as a simple forming process like wire drawing, can be applied to the processes of biaxial tension, like cup drawing, hydrostatic bulge forming and electromagnetic forming, where the workpiece is "thin", its thickness being much smaller as compared to its length and width [3,4]. It can also be applied for rolling of thin plates where the "lateral spread" is much smaller than its elongation. In case of compression in forging, similar analytical approach of "compressive" (instead of "tensile") instability can be applied to coining of thin disks or upsetting of small cylinders, where the effect of "barreling" or "bollarding" can be considered negligible [5].

4. References

[1] J. Banerjee (2020). The onset of plastic instability as a criterion for useful deformation in manufacturing processes. *Integrity, Reliability and Failure (IRF) International Conference, Porto, Portugal*.

[2] J. Banerjee (2022). Fundamental parameters of plasticity for the design of products in mass scale manufacturing in metalworking industries. *Proceedings of the Mechanics and Materials in Design (M2D) International Conference, Madeira, Portugal*, 203 – 204.

[3] J. Banerjee, J, Rivera-Rodriguez (2023). Hydrostatic bulge-forming: A high precision manufacturing process, *Proceedings of the 20th International Conference on Experimental Mechanics; Porto, Portugal*, 385 – 386.

[4] Z. Zheng, J. Banerjee (2001). A theoretical and computational study of electromagnetic (magnetic pulse) high velocity manufacturing processes, *Mechanical Behavior of Materials*, 12, 336 – 342.

[5] J. Velez, J. Banerjee (2012). Theoretical limits on barreling of cylinders under axisymmetric compression, *Mechanical Behavior of Materials*, 23, 131-132.

Nanotechnologies and Nanomaterials

HIGH-PERFORMANCE TRANSPARENT CONDUCTING ELECTRODES ON PET BY BLADE COATING AND PHOTONIC CURING AT > 10 M/MIN

J. C. Bonner[1], R. T. Piper[1], B. Bhandar[2], J. W. P. Hsu[2]
[1] Department of Materials Science and Engineering, University of Texas at Dallas, Richardson, TX USA
[2] Department of Physics, University of Texas at Dallas, Richardson, TX USA

1. Introduction

Transparent conducting electrodes (TCEs) are critical components for many optoelectronic applications including displays, solar cells, and wearable electronics. Good TCEs require high optical transmittance, low electrical sheet resistance, and low surface roughness. However, optimizing these properties simultaneously is challenging, as materials with high electrical conductance typically have low optical transmission.

The most common TCE material is indium tin oxide (ITO). Highly crystalline ITO films deposited on rigid glass can achieve excellent properties, but fabricating quality ITO films on flexible plastic substrates is more difficult.[1] The high-temperature processing needed for optimal ITO is incompatible with the thermal budgets of plastic materials. The ITO alternative TCE materials still require thermal annealing at high temperatures for long durations to achieve their desired properties, thus incompatible with flexible plastic substrates or roll-to-roll processing.

To address these challenges, we investigate a novel material processing method called photonic curing. Photonic curing uses millisecond, intense pulses of broadband light to locally heat and transform thin-film materials.[2] The rapid, selective heating enables the use of temperature-sensitive plastic substrates and is compatible with high-speed manufacturing. Compared to traditional thermal annealing, not only does photonic curing increase fabrication speed, it also reduces energy consumption and carbon emissions.

In this work, we demonstrate the use of blade coating and photonic curing to fabricate TCEs on flexible plastic substrates. By optimizing the photonic curing parameters, we achieve TCEs with excellent optical, electrical, and mechanical properties, overcoming the limitations of conventional thermal processing. We show that both solution deposition and photonic curing can be performed at a speed > 10 m/min. This enables the development of next-generation optoelectronic devices on low-cost, lightweight, and flexible plastic platforms.

2. Materials and methods

In this work, we fabricate hybrid TCEs on polyethylene terephthalate (PET) substrates at room temperature using solution deposition and photonic curing instead of high-temperature thermal annealing. The hybrid TCE structure consists of a multiscale silver network of metal bus lines and silver nanowires, which is overcoated with a sol-gel indium zinc oxide (IZO) film.[3] This hybrid structure leverages the high conductivity of the silver components and the planarization of the IZO to achieve the desired optical and electrical properties. Small-area (1” x 3”) samples are first fabricated and characterized for optical transmittance, sheet resistance, and surface roughness, benchmarked against commercial PET/TCEs. Bending tests were also performed to evaluate their mechanical durability. The process is then scaled up to fabricate large-area (7” x 8”) hybrid TCEs at high speeds

up to 11 m/min. Finally, the halide perovskite solar cells are fabricated on the hybrid TCEs to evaluate their performance in optoelectronic devices.

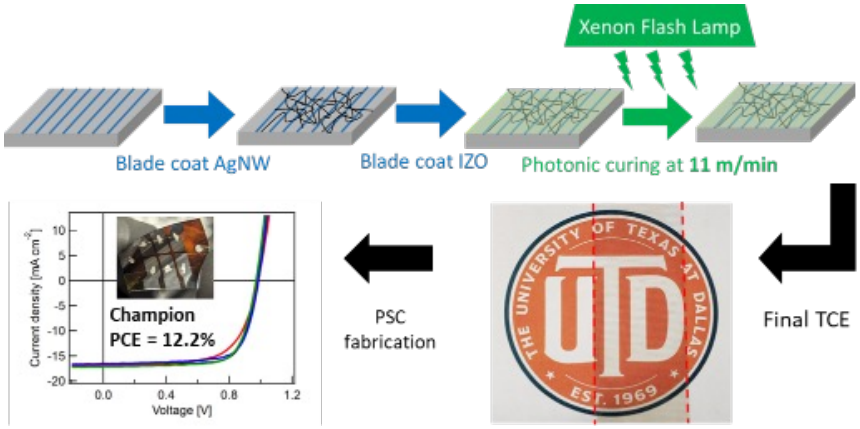

Fig. 1. (top) Workflow for fabricating hybrid TCE using blade coating and photonic curing. (bottom) Transparency of hybrid TCE and perovskite solar cell performance and picture.

3. Results and conclusions

Our hybrid TCEs achieve excellent optoelectronic properties: an average transmittance of (90 ± 0.4) % referenced to the PET substrate in the visible range, an average sheet resistance of (11 ± 0.5) Ω sq^{-1}, and an average surface roughness of (4.3 ± 0.4) nm.[4] Bending tests demonstrate a < 5% change in resistance after 2000 bending cycles at a 5 mm radius. These values outperform commercial PET/TCE substrates. The superior quality of our hybrid TCEs is demonstrated through halide perovskite solar cells, which achieve average and champion power conversion efficiencies of (10.5 ± 1.0)% and 12.2%, respectively, significantly higher than devices made on commercial PET/ITO (Table 1). The scalable potential of our fabrication method is demonstrated by maintaining high uniformity and excellent properties when scaled up to large-area samples, with photonic curing successfully performed at processing speeds of 11 m min^{-1}. This work showcases our approach as a viable pathway for high-speed manufacturing of high-performance TCEs on PET substrates for flexible optoelectronic devices.

Substrate	V_{oc} [V]	J_{sc} [mA cm^{-2}]	FF	Average PCE [%]	Champion PCE [%]
Hybrid TCE	0.982 ± 0.01	15.7 ± 0.66	0.707 ± 0.02	10.9 ± 0.53	11.8
PET/ITO	0.932 ± 0.01	12.9 ± 0.35	0.610 ± 0.02	7.34 ± 0.28	7.65

Table 1. Average *J-V* parameters along with champion power conversion efficiency of the perovskite solar cells on hybrid TCEs and PET/ITO

4. Acknowledgements

This work was funded by the U.S. Department of Energy's Office of Energy Efficiency and Renewable Energy under the Solar Energy Technologies Office Award Number DE-EE0009518.

5. References

[1] Piper R T, Xu W and Hsu J W P 2022 How Optical and Electrical Properties of ITO Coated Willow Glass Affect Photonic Curing Outcome for Upscaling Perovskite Solar Cell Manufacturing *IEEE J Photovolt* **12** 722–7
[2] Hsu J W P and Piper R T 2024 Photonic curing for innovative fabrication of flexible metal oxide optoelectronics *J Phys D Appl Phys* **57** 252001
[3] Piper R T, Xu W and Hsu J W P 2023 Silver nanowire-indium zinc oxide composite flexible transparent conducting electrodes made by spin-coating and photonic curing *MRS Adv* **8** 177–82
[4] Bonner J C, Piper R T, Bhandari B, Allen C R, Bowers C T, Ostendorf M A, Davis M, Valdez M, Lee M and Hsu J W P 2024 "Green" Fabrication of High-performance Transparent Conducting Electrodes by Blade Coating and Photonic Curing on PET for Perovskite Solar Cells *Materials and Sustainability*

EuraSEM 6-11 July 2025 ICEM21 Bologna 21st International Conference on EXPERIMENTAL MECHANICS

IMPROVING THE PERFORMANCE OF THE STRUCTURE CONTRACTING BY SOUND WAVES

Y. Tsuchida[1], Y. Tsuchiyama[1], S. Arikawa[2]
[1] Graduate School of Science and Technology, Meiji University, Japan
[2] Department of Mechanical Engineering Informatics, Meiji University, Japan

1. Introduction

Many researches have been conducted on actuators that operate by supplying non-contact energy to further reduce the size and weight of actuators. By using functional materials known as "smart materials" that respond to external stimuli, the components of actuators operating by non-contact energy supply can be minimized, enabling ultra-compact and ultra-lightweight designs. There are examples of materials deformed by magnetic field [1] and electric field [2]. While many studies add functionality to materials, this study adds functionality to structures to contract by a non-contact energy supply. The research was conducted on the structure that contract in response to sound waves of a resonant frequency. However, the factors governing contraction performance remain unclear. This study aims to improve contraction performance by experimentally and theoretically investigating which viscosity of the frame influences contraction performance.

2. Deformation principle

In this study, “unit structure” shown Fig. 1 (a) is defined two hexagonal frames and a membrane. The upper side is defined the “membrane structure,” and the lower side is defined the “non-membrane structure.” The membrane of the membrane structure resonates by sound waves of the resonant frequency, thereby enabling the frame repeats contracted and initial states as shown Fig. 1 (b). The frame of the non-membrane structure repeats the expanded and contracted states due to the tension in the membrane structure. It should be noted that these structures do not always contract independently; however, they do contract when they are formed into the unit structure. This phenomenon can be attributed to the fact that the two structures are vibrating in opposition to one another.

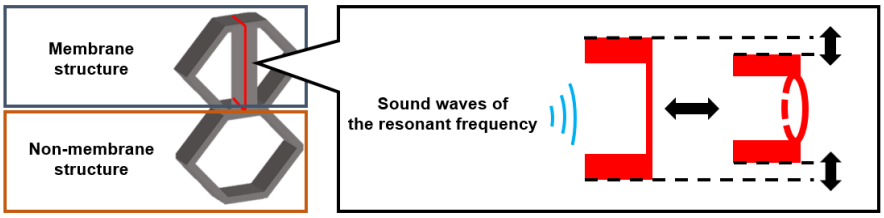

(a) Unit structure (b) Behavior of membrane

Fig. 1. Deformation principle of the structure with membrane

3. Experimental method

The objective of this investigation is to ascertain the effect of the viscosity of the frame on the behavior of membrane structure. Frames of the membrane structure were fabricated using light-cured

resin and aluminum. The experiments were conducted using a laser displacement meter to measure the displacement of the frame when these specimens were exposed to sound waves at the resonance frequency. The vibration amplitude of the frame was assessed in this experiment. Figure 2 (a) and (b) show the displacement-time profiles of frame for photocurable resin as high viscosity and aluminum as low viscosity. The result shows that the vibration amplitude of aluminum frame is more than twice that of light-curing resin. It indicates that the damping effect of the viscosity of the frame materials has a negative influencing factor on the vibration amplitude.

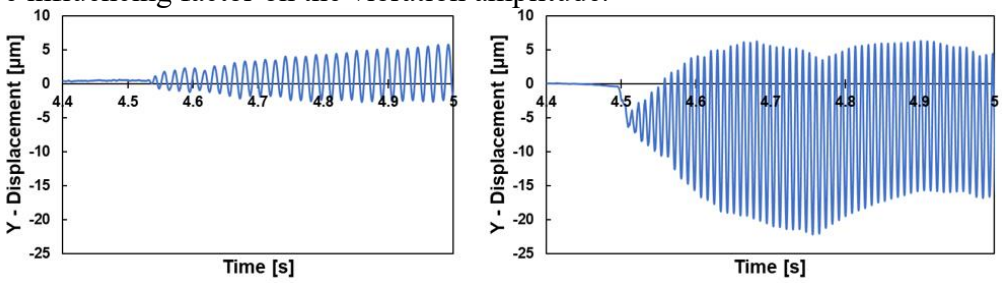

(a) Photocurable resin frame (b) Aluminum frame

Fig. 2. Displacement-time profile obtained by the experiment

4. Theoretical study

The purpose of theoretical studies is to investigate the impact of material and structural parameters on the contraction performance. The initial step is to construct a simple model (Fig. 3), wherein the frame is represented by upper square m_2 and the spring k_2 for length L, while the membrane is depicted by a mass point m_1, two rods, and the spring k_1 connected to a virtual wall. When an external force P as a sound pressure is applied to this model, the membrane deforms and the frame contracts. Vibration analysis was conducted by changing the viscosity coefficient of the frame of this model and the results are shown in Fig. 4. The results show that the higher viscosity coefficient of the frame reduces the vibration amplitude.

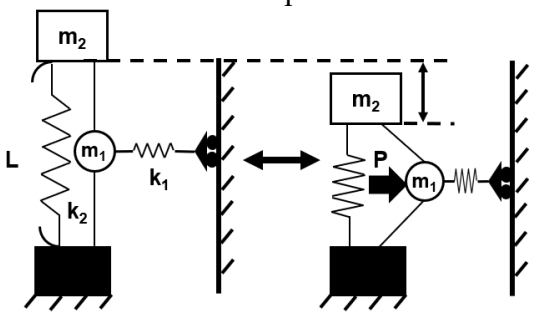

Fig. 3. Simple model of the membrane structure

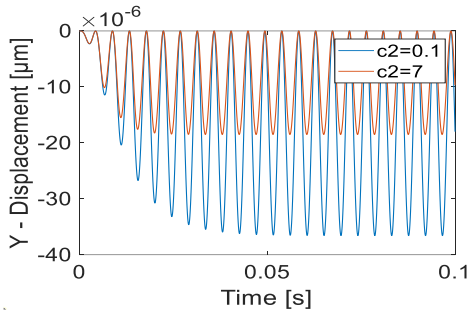

Fig. 4. Vibration behaviors for high and low viscosity

5. Conclusion

The results of experimental and theoretical studies indicate that an increase in the viscosity of the frame has a negative impact on vibration. In addition, investigations will be conducted for identifying the effects of other factors such as mass, frequency and so on.

6. References

[1] T. Shiga, Y. Hirose, A. Okada, T. Kurauchi (1993). "Bending of Ionic Polymer Gel Caused by Swelling under Sinusoidally Varying Electric Fields," Journal of Applied Polymer Science, Vol.47, pp. 113-119.

[2] Yoonho Kim, Hyunwoo Yuk, Ruike Zhao, Shawn A. Chester and Xuanhe Zhao (2018). Printing ferromagnetic domains for untethered fast-transforming soft materials, NATURE, Vol.558, pp.274-279.

INTERFACIAL STRAIN TRANSFER ANALYSIS BETWEEN BISMUTH SELENIDE NANOFLAKES AND FLEXIBLE SUBSTRATE USING RAMAN SPECTROSCOPY

Miaojing Wang[1], Huadan Xing[1], Rubing Li[1], Zhixuan Cheng[1], Qiu Li[2], Wei Qiu[1,3,4]
[1] Department of Mechanics, Tianjin University, Tianjin, China
[2] Tianjin Key Laboratory of High Speed Cutting and Precision Processing, Tianjin University of Technology and Education, Tianjin, China
[3] National Key Laboratory of Vehicle Power System, Tianjin, China
[4] Tianjin Key Laboratory of Modern Engineering Mechanics, Tianjin, China

1. Introduction

Topological insulators (TIs) are a new kind of material with insulating bulk and conducting surface states that are topologically shielded. TIs have unique features that make them potential candidates for broadband optoelectronic detectors, spintronics, and quantum computing devices [1]. As a strong TI with a layered crystal structure and a large bulk energy gap of about 0.3 eV at room temperature, Bi_2Se_3 has superior applications in electronic devices such as low-energy dissipation electronics, spintronics, thermoelectrics, and optoelectronics [2]. Based on the current studies, the electronic and photonic properties of layered TIs such as the band structure [3], electromagnetic transport [4], and light absorption, strongly depend on the lattice structure, strain and stress, and interlayer interactions. At the same time, the mechanical stability of the nanostructure-substrate composite under external loading determines the reliability and lifetime of the device. Therefore, it is crucial to understand the interfacial mechanical properties, at the micro-nano scale, of the multi-layer TI and flexible substrate structure. However, the research on interface mechanics of TI nanomaterials was only preliminary and achieved limited progress in recent years [5, 6].

This work calibrated the Raman shift-strain coefficients of A_{1g} phonon modes for Bi_2Se_3 nanoflakes with different longitudinal and transverse dimensions combined with micro-Raman spectroscopy and in-situ loading. A phenomenological model was proposed to analyze the process of interfacial re-bonding after debonding and the interfacial bonding enhancement after cyclic loading at the interface between Bi_2Se_3 nanoflakes and the flexible substrate. The influences of the longitudinal and transverse dimensions on the behaviors of interfacial bonding and hence deformation transfer between Bi_2Se_3 nanoflakes and the flexible substrate were analyzed.

2. Materials and methods

The Bi_2Se_3 nanoflakes used in this work were grown on the SiO_2/Si substrate by chemical vapor deposition and then transferred onto a 0.125mm-thick flexible polyethylene terephthalate (PET) substrate using a wet transfer method assisted by a polymethyl methacrylate film. A rapid and reliable method for layer number identification based on optical contrast was developed by correlating the microscopic images of Bi_2Se_3 samples on SiO_2/Si and PET substrates with their thicknesses given by atomic force microscope. The samples used in this work are labeled as S1 to S6 based on the layer numbers identified (S1 for 7 QLs, S2 for 8 QLs, S3 for 8 QLs, S4 for 9 QLs, S5 for 11 QLs, S6 for 13 QLs).

The PET substrate with Bi_2Se_3 nanoflakes was loaded with uniaxial tensile deformations, and the strain increased from 0 to about 1% in steps of about 0.1%. Raman spectra were collected from a region of 4×4 μm^2 at the center of each sample during initial tensile loading (the first stage) and re-tensile loading after five loading-unloading cycles (the second stage) at room temperature.

3. Results and conclusions

The Raman shifts of A_{1g}^1 and A_{1g}^2 modes detected from different samples under initial loading and reloading after 5 cycles were used to analyze the interfacial deformation transfer stages during loading. The process of interfacial bonding-debonding-rebonding was analyzed using a developed finitely elastic interface model [7]. The samples were grouped according to transverse and longitudinal dimensions to analyze the influence of the two dimensions on the interfacial deformation transfer. The influence of the transverse dimension on the interfacial bonding was attributed to the edge effect, while the influence of the longitudinal dimension on the deformation transfer showed that with the increment of the nanoflake layer numbers, the efficiency of deformation transfer from the substrate to the Bi_2Se_3 sample was gradually reduced, as shown in Fig. 1.

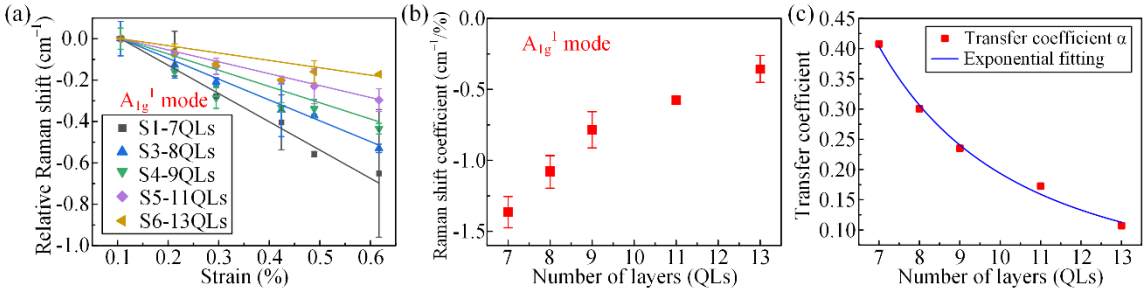

Fig. 1. Raman shifts of A_{1g}^1 mode and transfer coefficient at the Bi_2Se_3/substrate interface

4. Acknowledgements

The research presented in this paper was supported by the National Natural Science Foundation of China (Grant Nos. 12125203, 12021002, and 12041201) and the Natural Science Foundation of Tianjin (22JCYBJC01680).

5. References

[1] M. Z. Hasan, C. L. Kane (2010). Colloquium: Topological insulators. *Rev. Mod. Phys.*, **82**, 3045-3067.
[2] H. Li, H. L. Peng, W. H. Dang, L. L. Yu, Z. F. Liu (2012). Topological insulator nanostructures: Materials synthesis, Raman spectroscopy, and transport properties. *Front. Phys.*, **7**, 208-217.
[3] S. M. Young, S. Chowdhury, E. J. Walter, E. J. Mele, C. L. Kane, A. M. Rappe (2011). Theoretical investigation of the evolution of the topological phase of Bi_2Se_3 under mechanical strain. *Phys. Rev. B*, **84**, 085106.
[4] C. Schindler, C. Wiegand, J. Sichau, L. Tiemann, K. Nielsch, R. Zierold, R. H. Blick (2017). Strain-induced Dirac state shift in topological insulator Bi_2Se_3 nanowires. *Appl. Phys. Lett.*, **111**, 171601.
[5] Q. Li, Y. Wang, T. T. Li, W. Li, F. F. Wang, A. Janotti, S. Law, T. Y. Gu (2020). Localized strain measurement in molecular beam epitaxially grown chalcogenide thin films by micro-Raman spectroscopy. *ACS Omega*, **5**, 8090-8096.
[6] K. A. Niherysh, J. Andzane, M. M. Mikhalik, S. M. Zavadsky, P. L. Dobrokhotov, F. Lombardi, S. L. Prischepa, I. V. Komissarov, D. Erts (2021). Correlation analysis of vibration modes in physical vapour deposited Bi_2Se_3 thin films probed by the Raman mapping technique. *Nanoscale Adv.*, **3**, 6395-6402.
[7] H. D. Xing, X. J. Wang, C. C. Xu, H. Z. Du, R. B. Li, Z. H. Zhao, W. Qiu (2023). Spectral mechanical investigation of the elastic interface between a MoS_2/graphene heterostructure and a soft substrate. *Carbon*, **204**, 566-574.

Biomechanical applications

EuraSEM 6-11 July 2025 ICEM21 Bologna 21st International Conference on EXPERIMENTAL MECHANICS

AN EXPERIMENTAL IN VITRO KNEE MODEL TO MEASURE FORCES OF THE ACL AND PCL

A. L. Matos[1], A. Ramos[1], and J. A. Simões[2]
[1] Department of Mechanical Engineering (TEMA), University of Aveiro, Portugal
[2] Escola Superior de Artes e Design, Matosinhos, Portugal

1. Introduction

The Anterior Cruciate Ligament (ACL) and Posterior Cruciate Ligament (PCL) have important biomechanical functions in the knee joint, mainly knee stabilization. In young and active sportsmen, where changes of motion and rotation occur in the knee, injuries of the LCA are frequent worldwide [1], and in the USA more than 400 000 patients per year. Studies using cadaveric models of the knee to evaluate forces of the ACL and other ligaments [3, 4] using robotic systems, but none as in vitro. The cadaveric models present a range of values of LCA associated with the knee anatomy and other biomechanical factors. Assessing the forces on the ACL and LCP is important to study the best orientation of reconstruction, and tunnel inclination, ligament pre-load, tunnel edge and length of ligament, as well as to validate computational models.

This study presents the development of an experimental in vitro reconstruction model of a knee joint, able to replicate the native knee articulation to study the forces of the ACL and PCL at different ligament reconstruction scenarios.

2. Materials and methods

An in vitro model was designed (Figure 1) with synthetic composite bone structures such as the left tibia, femur, and patella, acquired from Sawbones, these bone analogs include cortical and cancellous bone replicas that have been validated with similar mechanical behavior of real bone [4]. The soft tissues like cartilage were designed using MRI images and reconstruction with CAD tools.

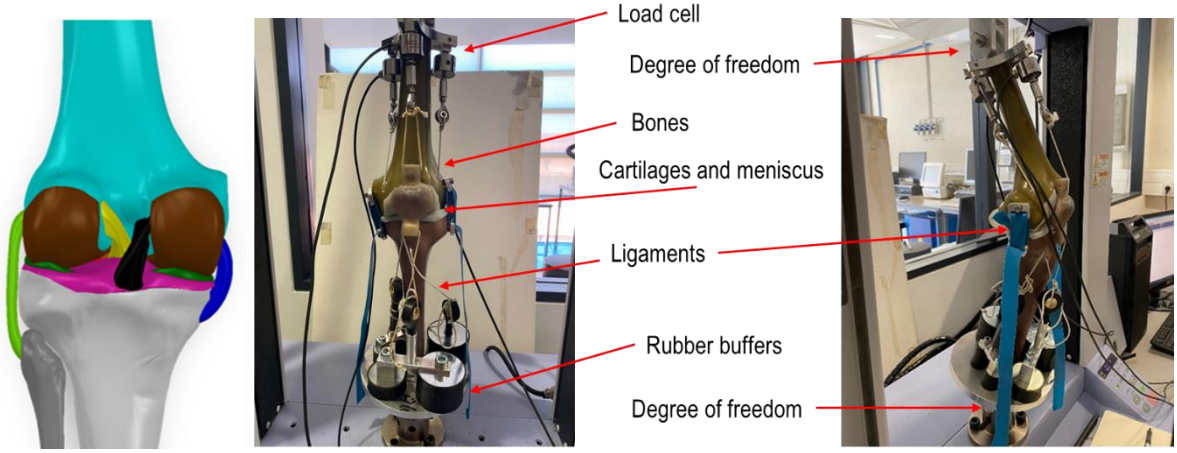

Fig. 1. Experimental in vitro model of knee joint CAD model, frontal and sagittal view.

The meniscus, ACL, PCL, and medial and lateral collateral ligaments (MCL and LCL) were modeled with realistic geometry and insertion points according to literature. The meniscus and cartilage were manufactured using additive manufacturing technology with rubber-like material with properties identical to cartilage (10MPa of elastic modulus). Cables and rubber buffers were used to replicate the ACL, PCL behavior, and patella stiffness as defined in the literature [3]. The forces of the ligaments were measured using an HBM U9B cell with 1KN maximum load, and the forces were applied using a universal testing Shimadzu machine with position control up to 90º knee flexion (Figure 1) with a velocity of 50mm/min.

3. Results and conclusions

Typical force curve of the ACL is plotted in Fig. 2, for knee in flexion. The curve behavior agrees with identical ones observed with cadaveric models [5], but with a higher maximum load, around 255N. The experimental model needs some improvements to reduce the friction of ligaments in the tunnels and cartilage mechanical behavior because it moves from the original place and increases friction in the joint. Another important aspect is the stiffness of ligaments for example the lateral ligaments, for improved biomechanical in vitro simulations and results.

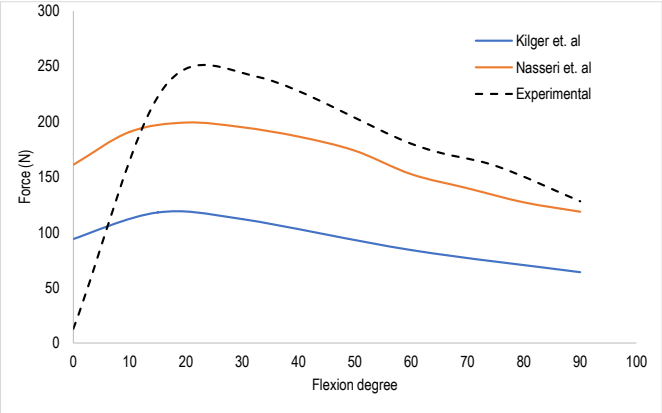

Fig. 2. Force measured in the ACL for the knee in flexion.

4. Acknowledgements

This work was supported by the projects UIDB/00481/2020 and UIDP/00481/2020 (https://doi.org/10.54499/UIDB/00481/2020) and (https://doi.org/10.54499/UIDP/00481/2020).

5. References

[1] Sanders TL, Maradit Kremers H, Bryan AJ, et al. Incidence of anterior cruciate ligament tears and reconstruction: A 21-year population-based study. American Journal of Sports Medicine. 2016;44(6):1502-1507.

[2] Li G, Papannagari R, DeFrate LE, Jae DY, Sang EP, Gill TJ. Comparison of the ACL and ACL graft forces before and after ACL reconstruction: An in-vitro robotic investigation. Acta Orthop. 2006;77(2):267-274.

[3] Mayer C, Barner K, Lorimer S, et al. Side Variations of Anterior Cruciate Ligament Coronal Angles: Implications for ACL Reconstruction. Clinical Anatomy. 2019;32(8):1102-1106.

[4] Ramos A., Soares dos Santos M.P., Mesnard M., Predictions of Birmingham hip resurfacing implant offset - In vitro and numerical models (2019) Computer Methods in Biomechanics and Biomedical Engineering, 22 (4), pp. 352 – 363.

[5] Kilger RHP, Stehle J, Fisk JA, Thomas M, Miura K, Woo SLY. Anatomical double-bundle anterior cruciate ligament reconstruction after valgus high tibial osteotomy: A biomechanical study. American Journal of Sports Medicine. 2006;34(6):961-967.

Deep learning-based nanomechanical vibration for rapid and label-free assay of epithelial mesenchymal transition

Shangquan Wu[1], Wenjie Wua[1], Yongpei Penga[1], Qingchuan Zhang[1]
[1] Department of Modern Mechanics, University of Science and Technology of China, Hefei, China.

1. Introduction

Malignant tumor invasion accounts for 90% of tumor deaths [1]. In tumor pathology, epithelial-mesenchymal transition (EMT) is the main cause of infiltrative metastasis of malignant tumors [2]. During EMT, epithelial phenotype (E-type) cells in primary cancer are transformed to mesenchymal phenotype (M-type) cells, which are more motile, invasive, and resistant to apoptotic stimuli, thereby greatly promoting the spread of cancer cells [3]. Numerous clinical studies have shown that the ratio of M-type tumor cells to E-type tumor cells in patients is highly correlated with tumor size, cancer stage, cancer recurrence rate, and survival of cancer patients [4-6]. In addition, M-type tumor cells exhibit characteristics similar to cancer stem cells (CSCs), such as increased drug efflux pumps and antiapoptotic effects, and thus possess greater drug resistance, which greatly reduces the effectiveness of cancer chemotherapy [7,8]. Thus, understanding the EMT mechanism will facilitate the design of EMT-reversal drugs, which in turn will serve for cancer treatment.

Therefore, a noninvasive and highly sensitive E/M phenotypic detection method needs to be developed for dynamically identifying the different stages of EMT and investigating the mechano-biological mechanisms of EMT. At the same time, the method is also expected to serve for personalized drug selection and treatment plan formulation for cancer patients. Cellular biomechanical signals are highly correlated with cell activities. Cell colonies consist of multiple single cells, each of which may generate nanovibrations. Therefore, the study of nanovibrational differences due to changes in cell structure will contribute to the understanding of changes in cellular characteristics during EMT and to the classification of E/M phenotype detection.

In this study, we propose an E/M phenotype classification method based on nanomechanical vibrations combined with deep learning (Fig. 1). The method was achieved with an accuracy of 92.5% using only 1 second of vibration data. In addition, we further extended the method to the screening of EMT inhibiting anticancer drugs. The present method has the advantages of being nondestructive, rapid, highly sensitive and label-free. The link between the E/M phenotype and nanovibrations embodied by this work is expected to play a role alongside current clinical assays to assist in cancer typing and anticancer drug screening.

2. Materials and methods

To investigate the nanomechanical response induced by cancer cell colonies, we built a microcantilever system (Fig. 1b). At the beginning of the experiment, the microcantilever was pressed on the cell colony with a contact depth of 5 μm. Cell colonies generated significant nanovibration with a standard deviation of 6 nm ("iii" in Fig. 1d). To achieve the E/M phenotype transition of the cells in vitro, we treated the cell colonies with culture medium containing 10 ng/ml TGF-β1 and culture medium without agents, respectively and then the measurements were performed at 24, 48 and 72 hours respectively. TGF-β1 is a widely used EMT induction reagent. Further, we use deep learning to filter out useful features for E/M phenotype classification, thus minimizing the negative impact on classification caused by background noise and useless nanovibration created by cells, especially in the budding stage of EMT (Fig. 1c).

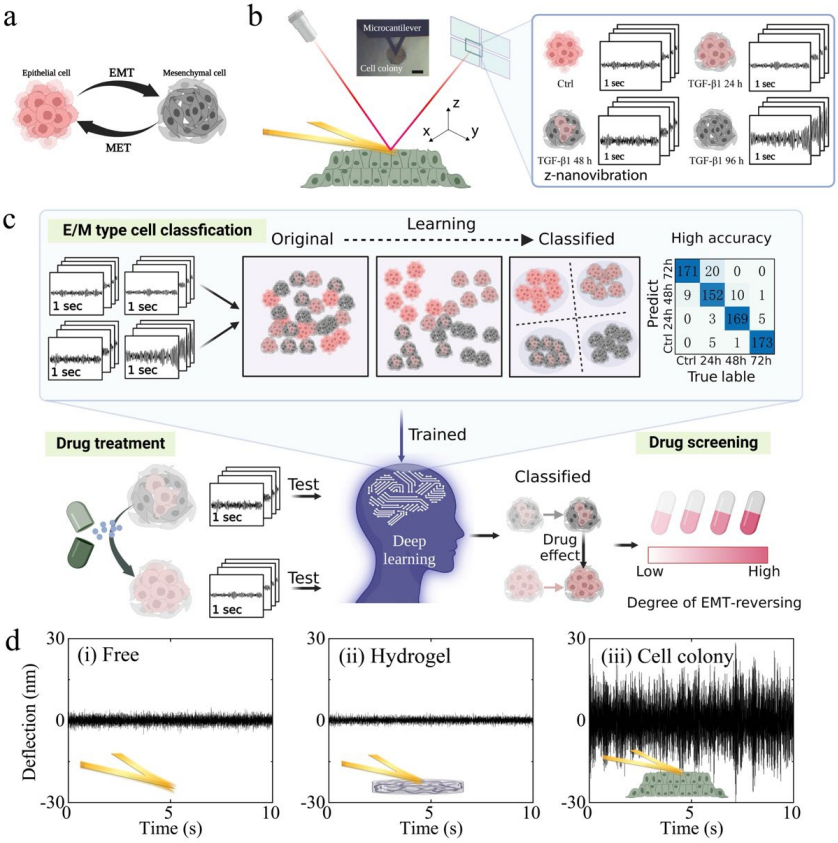

Fig. 1 Detection of E/M phenotype in cancer cell colonies using deep learning-based nanomechanical vibration.

3. Results and conclusions

We investigated cancer cell colonies from a mechanical perspective and developed an assay for classifying epithelial/mesenchymal cancer cell colonies using the biomechanical fingerprint in the form of 'nanovibration' in combination with deep learning. The classification method requires only 1 sec of vibration data and has a classification accuracy of nearly 92.5%. The method has also been validated for the screening of anticancer drugs. Compared with traditional methods, the method has advantages of being nondestructive, label-free, and highly sensitive. Furthermore, we proposed a new perspective that subcellular structure influence the amplitude and spectrum of nanovibrations, and demonstrated it using experiments and numerical simulation. These findings allow internal changes in cell colony to be manifested by nanovibrations. This work provides new perspectives and an ancillary method for cancer cell phenotype diagnosis and promotes the study of biomechanical mechanisms in cancer progression.

4. Acknowledgements

The research presented in this paper has received funding from the National Natural Science Foundation of China (Grant Nos. 12222212 and 12072339).

5. References

[1] Mehlen P, Puisieux A (2006). Metastasis: a question of life or death., *Nat. Rev. Cancer,* **6,** 449-458.
[2] Shibue T, Weinberg RA (2017). EMT, CSCs, and drug resistance: the mechanistic link and clinical implications. *Nat. Rev. Clin. Oncol.,* **14,** 611-629.
[3] Nieto MA, Huang RYJ, Jackson RA, Thiery JP (2016). Emt: 2016. *Cell*, **166,** 21-45.
[4] Li YM, *et al*. (2013) Epithelial-mesenchymal transition markers expressed in circulating tumor cells in hepatocellular carcinoma patients with different stages of disease. *Cell Death Dis*., **4**.
[5] Yu M, et al. (2013) Circulating Breast Tumor Cells Exhibit Dynamic Changes in Epithelial and Mesenchymal Composition. *Science* **339,** 580-584.
[6] Qi LN, et al. (2018) Circulating Tumor Cells Undergoing EMT Provide a Metric for Diagnosis and Prognosis of Patients with Hepatocellular Carcinoma. *Cancer Res.,* **78,** 4731-4744.
[7] Dongre A, Weinberg RA (2019). New insights into the mechanisms of epithelial-mesenchymal transition and implications for cancer. *Nat. Rev. Mol. Cell Bio.,* 20, 69-84.
[8] Yang J, et al. (2021) Guidelines and definitions for research on epithelial-mesenchymal transition. *Nat. Rev. Mol. Cell Bio.,* 22, 834-834.

OPTICAL COHERENCE ELASTOGRAPHY FOR STRAIN MEASUREMENT OF INTACT BLOOD VESSELS

Cuiru Sun, Guorui Du, Haosen Wang, Jinlong Chen
School of Mechanical Engineering, Tianjin University, Tianjin China

1. Introduction

The biomechanical properties of blood vessels play a significant role in the onset and progression of cardiovascular diseases. Conventional tensile testing of vascualr samples often compromises tissue integrity and fails to provide comprehensive, full-field strain measurements. This limitation is particularly problematic for heterogenous vascular tissues where localized variations in biomechanical properties are critical. Optical coherence elastography (OCE) shows promise in assessing the strain within the vascular wall *in vivo* [1]. However, applying an external load to pricely control vascular wall deformation presents a challenge [2]. Recently, Wang et al [3] developed a micro-motor-driven catheter and performed OCE imaging of both vascular phantoms and actual samples. Despite this advancement, the technique required averaging multiple frames to mitigate phase noise, which is impractical for clinical use due to variability of blood pressure. Moreover, the micro-motor-driven catheter is not yet available for clinical use.

In this manuscript, we propose an OCE method for the quantitative measurement of blood vessel deformation under simulated physiological conditions. We introduce a subpixel alignment based phase difference algorithm to determine the radial displacement and strain fields accurately. Vascualr phantoms and porcine blood vessels under inflation were tested to validate the proposed method. This study offers a valuable experimental technique for measuring the mechanical properties of intact vascular samples. It lays the groundwork for the development of *in vivo* OCE methods for the diagnois and treatment of cardiovascular diseases.

2. Materials and methods

An OCE system for vascular deforamtion measuremnt was integrated by an swept source optical coherence tomography (OCT) scanning system with an pusatile circulation device, as depicted in Fig. 1. The swept laser operates at a scanning speed of 50kHz, achieving an axial resolution of approximately 9μm. The pulsatile circulation device, powered by a pump, simulates the physiological pulse wave cycles ranging from 60 to 100 beats per minute found in the human body. In the experimental setup, the vascular sample is secured in a tank containing saline solution. The IVOCE catheter is introduced into the vascular sample via a three-way connector, and it is positioned at a fixed location without pull-back to capture cross-sectional images of the vascular wall as it undergoes pulsatile deformation. The interference data was pre-processed by rotation alignment and the elimination of catheter-induced jitter. Subsequently, radial strain was obtained by a phase difference algorithm based on complex domain calculation. The displacement along the imaging beam is directly proportional to the phase difference, as described by [4] :

$$\Delta d(z,t) = \frac{\Delta\Phi(z,t)\lambda}{4\pi n} \qquad (1)$$

where λ is the center wavelength of the light source, n is the refractive index of the sample, ΔΦ is the phase difference of the spectra acquired before and after the sample deformation. The strain field was obtained by derivative calculation of the displacement related terms in the complex domain.

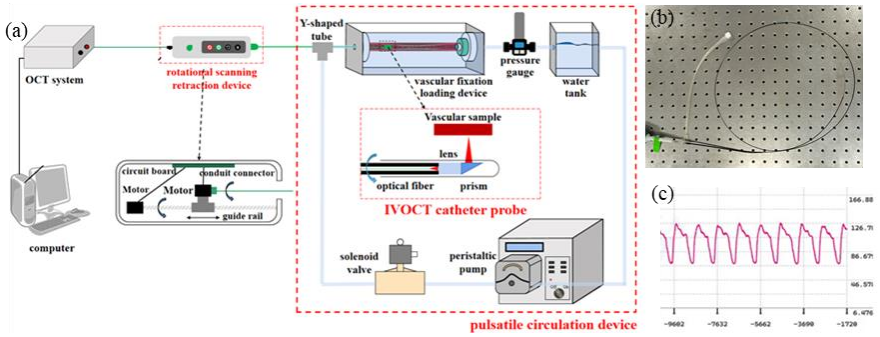

Fig. 1 OCE system for vascular deformation measurement. (a) a schematic diagram of the system; (b) a photo of the imaging catheter; (c) an example of the pulsatile pressure.

3. Results and conclusions

A vascular phantom was measured to validate the accuracy and reliability of the method. The structural image, displacement and strain maps of the phantom are shown in Fig.2. The strain distribution match well the theoretical results. Then the radial strain of a porcine vascular sample under pulsatile pressure were measured.

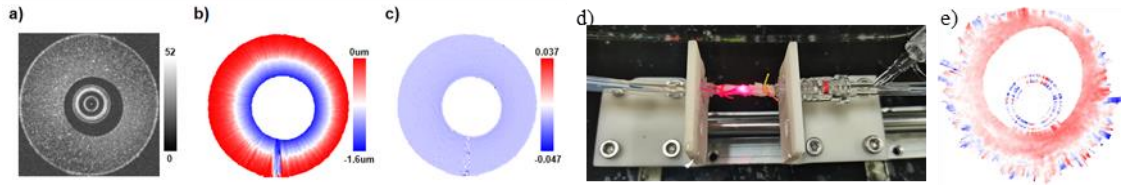

Fig. 2 Measurement results of a phantom and a porcine blood vessel. a)-c) OCT structural, phase difference and strain images of a phantom; d) porcine blood vessel sample under test; e) strain image of the blood vessel.

The vascular OCE system integrated with a radial strain calculation algorithm was demonstrated capable of measuring the radial displacements accurately. No specialized catheter stabilization is needed. The vascular deformation testing system, offers a novel experimental tool for the study of vascular biomechanics.

4. Acknowledgements

The research presented in this paper has received funding from the National Natural Science Foundation of China. No.s 12472185, 12272262, 12021002, 82241208.

5. References

[1] R.C. Chan, A.H. Chau, W.C. Karl, S. Nadkarni, A.S. Khalil, N. Iftimia, M. Shishkov, G.J. Tearney, M.R. Kaazempur-Mofrad, B.E. Bouma (2004). OCT-based arterial elastography: Robust estimation exploiting tissue biomechanics, *Optics Express,* **12**(19), 4558-4572.
[2] G. van Soest, F. Mastik, N. de Jong, A.F. van der Steen (2007). Robust intravascular optical coherence elastography by line correlations, *Phys Med Biol,* **52**(9), 2445-58.
[3] T. Wang, T. Pfeiffer, A. Akyildiz, H.M.M. van Beusekom, R. Huber, A.F.W. van der Steen, G. van Soest (2022). Intravascular optical coherence elastography, *Biomed Opt Express,* **13**(10), 5418-5433.
[4] S.J. Kirkpatrick, R.K. Wang, D.D. Duncan (2006). OCT-based elastography for large and small deformations, *Optics Express,* **14**(24), 11585–11597.

Tribology, Surface and Interface Engineering

TRIBOLOGICAL AND MICROSTRUCTURAL CHARATERIZATION OF COATINGS USED ON C75 TOOL STEEL

N.Picco[1,], M.Magnan[1], F.Sordetti[1], M.Tolazzi[2], M.Virgolin[2], A.Lanzutti[1]*

[1] *University of Udine, Polytechnic Department of Engineering and Architecture, Via delle Scienze 208, 33100 Udine (UD), Italy*
[2] *Freud S.p.A. – Bosch, Via Remigio Solari, 7, 33050 Pavia di Udine, UD*
[*] *Corresponding author: e-mail: niki.picco@uniud.it*

1. Introduction

C75 tool steel is a widely used material in various technological fields due to its low cost and high availability combined with good mechanical properties. However, the material is subject to environmental degradation, sometimes combined with tribological degradation [3], due to the considerable stresses that the tool is subjected to during machining and the presence of any foreign bodies, which can then damage the tool. A coating is therefore required to avoid these problems, with the main objective of increasing resistance to environmental and mechanical degradation. In particular, Ni-based coatings [1] and Cr-based coatings [2] are required to provide tools with the necessary anti-wear properties.

2. Materials and methods

The specimens were analyses in cross section in order to analyze both the thickness and microstructure of the coatings. Vickers microhardness tests were then carried out at different loads, from HV2 to HV0.01 in plan view, to evaluate the mechanical properties of substrate and coating system. The adhesion and abrasion resistance of the coatings was evaluated by scratch tests performed at a constant initial load of 1N, that was incremented with 1N steps until scratches were visible to the naked eye. Tribological characterization was carried out using a tribometer in a pin-on-disc configuration. The tests lasted 1 hour, at a speed of 300 rpm, with an applied load of 50 N (radius 18mm). The counter material was a C40 pin with a diameter of 6 mm. During the test, the coefficient of friction was continuously recorded using a biaxial load cell. The wear tracks were then analysed using SEM to assess the wear mechanism and a stylus profilometer to assess the depth of the wear trace, which was necessary to calculate the wear rate [4]. As an example, worn specimens are shown in Figure 1.

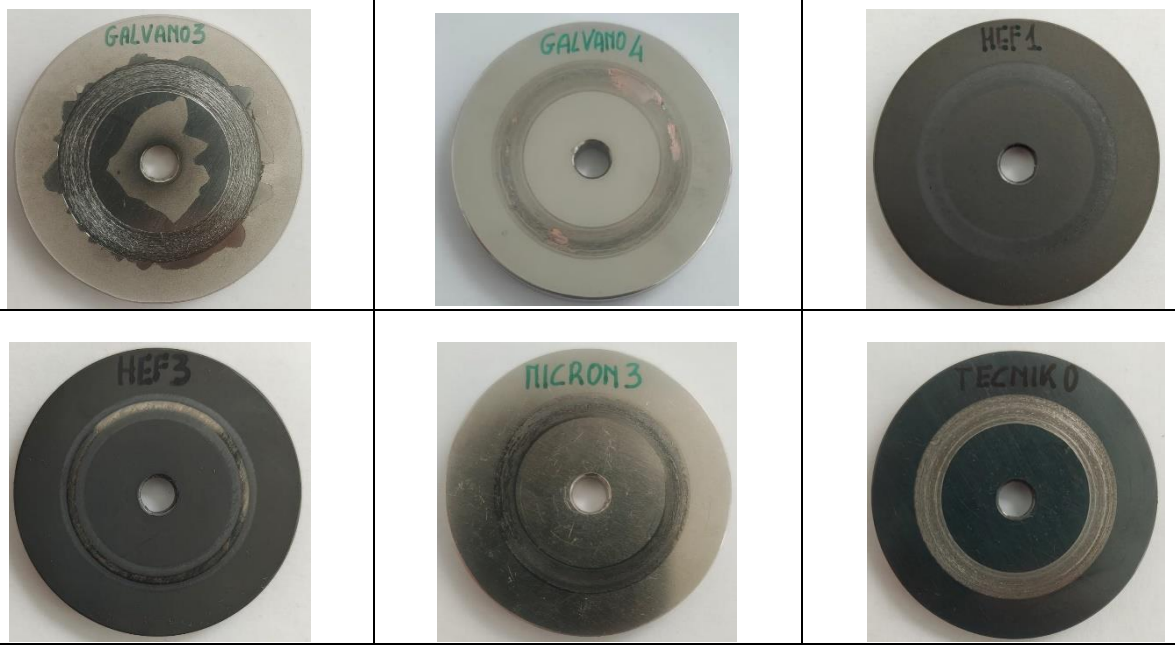

Figure 1. Traces of wear on the coated samples

3. Results and conclusions

The analyses showed that not all electroplated coatings improved the wear resistance of the steel substrate. Going into the detail of the analysis, samples with thicker coatings performed worse than those with thinner coatings. This should be related to both coating microstructure and residual stresses. By analyzing the preliminary results of the wear rate, it has been observed that some coatings, due to detrimental volume loss, presented higher wear rate, although the steel substrate was not reached. On the other hand, other coatings improved the wear resistance of the tribological system. It should be noted that in some cases the surface hardness was greatly improved by the coating material (above 1000HV).

4. References

[1] M. Kumar, A. Sidpara, V. Racherla, Improving surface finish and wear resistance of electroless nickel plating using flexible abrasive tool, Wear, Volumes 546-547, 1 June 2024, 205326, https://doi.org/10.1016/j.wear.2024.205326.

[2] A. Liang, Y. Wang, F. Wang, L. Qiang, Fantastic behavior of near zero wear of Cr-based coatings, Materials Letters, Volume 319, 15 July 2022, 132228, https://doi.org/10.1016/j.matlet.2022.132228.

[3] ASM Metals HandBook, Volume 18, Friction, Lubrication, and Wear Technology.

[4] ASM Metals Handbook, Volume 05, Surface Engineering.

CAPILLARY DRIVEN SOLDER CLIMBING DUE TO HAIRLINE SURFACE TEXTURE FOR ADVANCED PACKAGE ASSEMBLY

Jeehoo Na[1,2], Eunhye Lee[1], YehRi Kim[1], Eunjin Jo[1], Dongjin Kim[1] Dongwoo Lee[2], and Tae-Ik Lee[1,†]

[1] Advanced Packaging Integration Center (APIC), Regional Industry Innovation Department (Growth Engine), Korea Institute of Industrial Technology, Incheon 21999, Republic of Korea

[2] Applied Mechanics and Materials Design Lab, School of Mechanical Engineering, Sungkyunkwan University, Suwon 16419, Republic of Korea

[†]Email: tilee@kitech.re.kr

1. Introduction

Recently, semiconductor packaging has increasingly required high performance and miniaturization, leading to a demand for more complex interconnection technologies. Among various packaging techniques, soldering is essential for providing mechanical and electrical connections between the chip and substrate in high-density packaging technologies.[1] However, the analysis and solution are required for the solder wicking that occurs during the soldering process. Solder wicking refers to the flow of molten solder away from the intended soldering area along vias or leads. When this phenomenon occurs in advanced packaging technologies employing fine-pitch interconnections, it may compromise mechanical and electrical reliability.[2] Solder wicking can occur due to issues such as insufficient heat distribution and surface tension. This phenomenon is particularly prevalent in substrates with low thermal conductivity, where problems such as an imbalance in heat transfer arise, leading to heat being concentrated in specific areas or not being effectively transmitted.[3] This uneven heat distribution causes the solder to flow in unintended directions along the surface in areas of excessive heat transfer. When the surface of the material possesses a certain directionality, the capillary action of the liquid can be accelerated by the morphology of the surface. [4] In cases where the material intended for soldering has a textured surface with directional characteristics, the capillary action of the solder may be enhanced, leading to solder wicking. Therefore, further research is needed on this topic.

This study found that solder climbing occurs due to capillary action driven by the surface hairline texture during the soldering process. The spreading of solder paste was observed in situ using an SMT scope, depending on the surface texture. Following the soldering tests, the phenomenon of solder climbing was quantified.

2. Materials and methods

In this study, ENIG-plated specimens were fabricated with different surface roughness to observe the solder spreadability depending on the surface hairline texture. To measure the surface roughness, the surfaces of ENIG specimens were analyzed using an atomic force microscope (AFM). The specimens of each condition were then prepared by aligning them on a printed circuit board (PCB) with SAC305 solder paste applied. The spreadability of the solder according to the surface

morphology was observed in situ using an SMT scope. After the soldering test, the surface and cross-section of specimens were by optical microscope (OM) and scanning electron microscope (SEM) to quantify the solder climbing.

3. Results and conclusions

Fig. 1(a) shows that the solder climbing was observed using the SMP scope. During the soldering process, the solder spread along the surface texture at a maximum temperature of 250 ℃ after the melting point. Also, during the cooling process, the solder spread further, which is due to the capillary action driven by the surface vertical texture. The result of additional solder climbing is shown in Fig. 1(b).

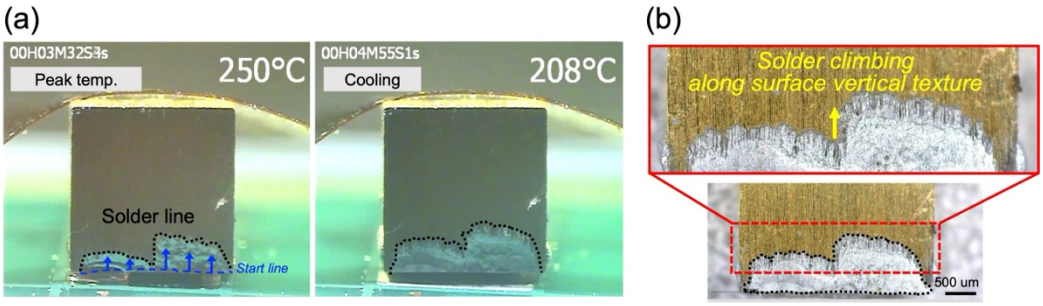

Fig. 1. (a) Observation of the soldering process via the SMT scope. (b) Result of the surface image following the soldering test.

4. Acknowledgements

This work was supported by the Technology Innovation Program (Public-private joint investment semiconductor R&D program(K-CHIPS) to foster high-quality human resources) (RS-2023-00236091, Hybrid bonding technologies for 3D package interconnects) funded by the Ministry of Trade, Industry & Energy (MOTIE, Korea) (1415187584).

5. References

[1] P. T. Vianco (2019). A Review of Interface Microstructures in Electronic Packaging Application: Soldering Technology., *Jom.*, **71(1)**, 158-177.

[2] W. Liu and E. P. Sekulic (2011). Anisotropic spreading of liquid metal on a rough intermetallic surface., *Theoret. Appl. Mech.*, **38(4)**, 365-377.

[3] L. Vargas, J. Terrazas, E. Cabrera, B. Valdez and N. Nedev (2014). Failure analysis method to study solder wicking phenomena in modern microelectronic devices., *J Mater Sci: Mater Electron.*, **25**, 609-617.

[4] G. Fischer, M. Bigerelle, K. J. Kubiak, T. G. Mathia, Z. Khatir and K. Anselme (2014). Wetting of anisotropic sinusoidal surfaces experimental and numerical study of directional spreading., *Surf. Topogr.: Metrol. Prop.*, **2**, 044003.

Optical Techniques

6-11 July 2025 ICEM21 Bologna
21st International Conference on EXPERIMENTAL MECHANICS

SHEAR CHARACTERIZATION IN SOFT POLYURETHANE FOAMS: A CRITICAL COMPARISON AMONG EXPERIMENTAL APPROACHES

V. Moramarco[1], G. Pappalettera[1], M. Patronelli[1], C. Casavola[1] and L. Del Core[2]
[1] Dipartimento di Meccanica, Matematica e Management, Politecnico di Bari, Bari, Italy.
[2] Blackshape S.p.A., Monopoli, Italy.

1. Introduction

Polyurethane foams find widespread use in various industries, including aerospace and packaging. Several standards can be found for the shear testing of rigid materials, allowing for different test setups. On the contrary, when it comes to extremely soft materials, such as open-cell polyurethane foams, no specific standards for shear testing can be referred to. Generally, existing standards for sandwich structures, such as ASTM C 273, are used. Given the complexity of open-cell soft foams, characterized by low stiffness and high deformations, proper mechanical characterization necessitates the use of contactless measurement techniques such as Digital Image Correlation (DIC).

In this study, open-cell polyurethane foams with densities of 85, 63, and 46 kg/m³ containing fire-retardant graphite are investigated. The graphite particles serve as a natural speckle pattern for DIC, avoiding artificial patterns that could bias measurements [1]. Shear properties were assessed using ASTM C 273, BS 4370, and Iosipescu shear tests. ASTM C 273 provides a standardized method for measuring the shear properties of sandwich structure cores, while BS 4370 focuses on testing rigid cellular materials. The aim of the study is to compare the stress-strain behavior and investigate the presence of secondary effects (bending, edge effects, undesired normal stresses). The elastic moduli, obtained up to 5% strain, were compared among the different tests and with engineering moduli derived from linear relationships using known moduli for compression and tension.

2. Materials and methods

Different types of setups and specimens with different aspect ratios (AR) were compared to investigate parasitic effects such as bending moment, undesired normal stresses, and the effect of free edges.

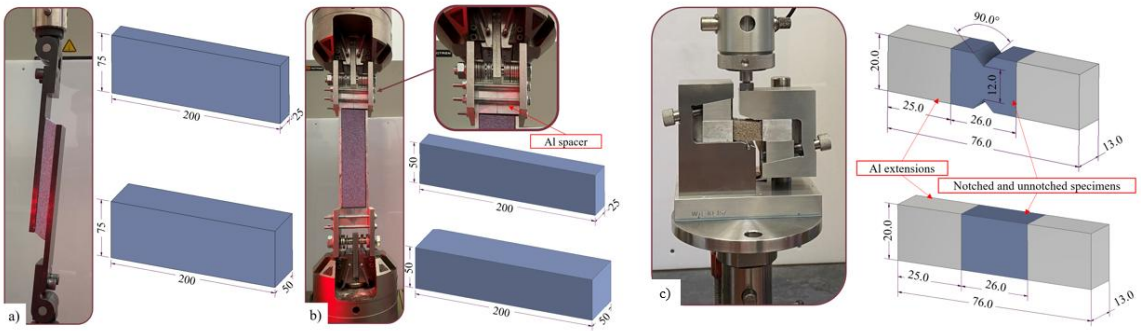

Fig. 1 a) ASTM C 273 setup and dimensions of tested specimens, b) BS 4370 setup with gripping system detail and dimensions of tested specimens, c) ASTM D 5379 setup, aluminum extensions and dimensions of notched and unnotched specimens.

It was decided to compare the results obtained from the ASTM C 273 standard, which has an inclined configuration, clearly visible in Fig. 1a, with those obtained from the BS 4370 standard (Fig. 1b. Since performing the Block Shear tests requires large blocks, up to 200 mm long and 70 mm wide, and 200 x 50 mm respectively for the ASTM C 273 and the BS 4370 standard; the results obtained from a shear setup that allows for much less material waste, namely ASTM D 5379, also known as Iosipescu (Fig. 1c), were investigated. The full-field measurement technique enables pointwise measurements and the application of virtual strain gauges. This approach allowed for a comparison between results obtained by positioning virtual strain gauges at ± 45° and those obtained from measurement points specified by the standard for extensometers placement on rigid materials.

3. Results and conclusions

ASTM C 273 with 25 mm specimens (Fig. 2a) was found to be the least affected by parasitic effects and served as the reference configuration. The 50 mm ASTM C 273 specimens (Fig. 2b) produced similar results but had slight alignment issues. BS 4370 (Fig. 2 c, d) provided reliable data but was time-intensive and more prone to alignment challenges. DIC enabled measurements at large deformations, with comparable results up to 30% strain for ASTM C 273 and BS 4370, and full comparability for the Iosipescu test (Fig. 2 e, f). Two-point measurements proved more accurate than virtual strain gauges at large deformations, particularly for softer foams. The Iosipescu test with unnotched specimens yielded comparable results to ASTM C 273 while saving material and offering good repeatability [2].

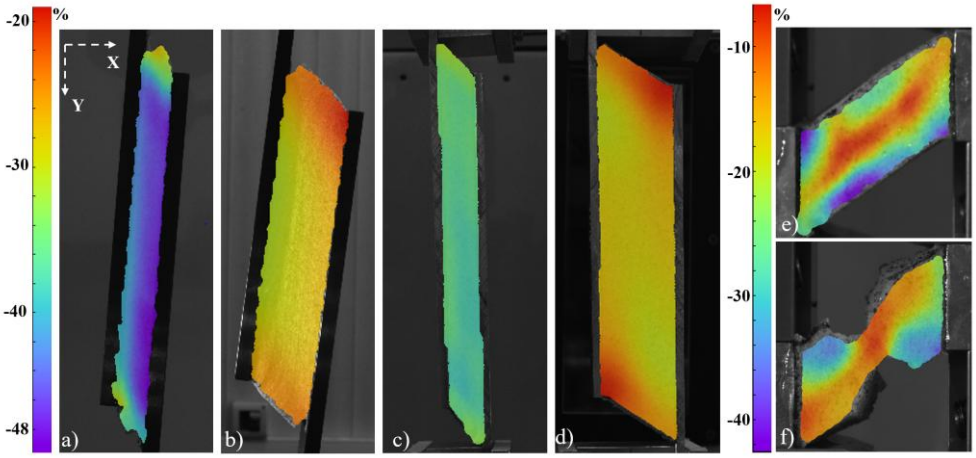

Fig. 2. Shear strain for: a) ASTM C 273 with a thickness of 25 mm; b) ASTM C 273 with a thickness of 50 mm; c) BS 4370 with a thickness of 25 mm; d) BS 4370 with a thickness of 50 mm; e) ASTM D5379 with an unnotched specimen; f) ASTM D5379 with a notched specimen.

4. Acknowledgements

The research presented in this paper was partly supported by the Italian Ministry of University and Research under the Programme *Department of Excellence* Legge 232/2016 (Grant No. CUP - D93C23000100001) and by *POC Puglia FESR/FSE 2014–2020–Asse X-Azione 10.4 -RIPARTI.*

5. References

[1] C. Casavola, L. Del Core, V. Moramarco, G. Pappalettera, M. Patronelli (2022). Experimental and numerical analysis of the Poisson's ratio on soft polyurethane foams under tensile and cyclic compression load, *Mech. Adv. Mat. Struct.*, **29**, 7172-7188. DOI: 10.1080/15376494.2021.1994061.

[2] V. Moramarco, G. Pappalettera, M. Patronelli, C. Casavola, L. Del Core (2024). Shear characterization in soft polyurethane foams: A critical comparison among experimental approaches, *Mech. Adv. Mat. Struct.*, DOI: 10.1080/15376494.2024.2341284

EuraSEM 6-11 July 2025 ICEM21 Bologna 21st International Conference on EXPERIMENTAL MECHANICS

DEVELOPMENT OF STEREO DIC MEASUREMENT ON THERMAL ENERGY STORAGE TANK: DETERMINATION OF MECHANICAL RESPONSE

G. Alonso Aruffo[1], Y. Lalau[2], L. Penazzi[3] and R. Bonnaire[3]
[1] IRCER, Université de Limoges, CNRS 7315, Limoges, France
[2] RAPSODEE, Université de Toulouse, IMT Mines Albi, Albi, France
[3] Institut Clément Ader (ICA), Université de Toulouse, CNRS, IMT Mines Albi, INSA, ISAE-SUPAERO, UPS, Campus Jarlard, F-81013 Albi, France

1. Introduction

A Thermal Energy Storage (TES) system captures thermal energy by heating or cooling a storage medium for later use in heating applications or power generation. This study focuses on TES storage tanks using the thermocline principle, with a packed bed as heat storage material. Currently, there is little to no experimental data in the literature on the response of heat storage tanks to these loads, due to the difficulty in accessing the tank surface because of thermal insulation. This work presents an experimental setup designed to measure displacement (and resulting strains) of the tanks surface using non-contact optical measurement techniques, specifically 3D stereo correlation. Results obtained by this measurement will be used to validate a digital twin.

2. Materials and methods

The TES system on which tests were performed on, isa pilot version of the industrial facility described by [1]. For the 3D stereo correlation tests, a horizontal test bench was used with two cameras (*///Allied vision*, 5 MPX resolution). The optics were of the type Kowa CCTV LENS 1"50mm/ F1.4. Images were captured using Vic-Snap (Correlated Solution ©) and post processing using the VIC-3D (Correlated Solution ©) softwares. Lighting was ensured by a MHI-type light source using a Dedolight 400D lamp. The storage system used a propane gas burner and fans to achieve thermal load up to 500°C and cooling during the tests.

Fig. 1. (left) Porthole design, (right) experimental set up integrated to the TES

This study faced two main challenges in data acquisition: accessing the external surface of the TES and dealing with environmental conditions during the experiments. Outdoor conditions such as wind, sunlight variations, and humidity could affect the quality of images obtained by 3D DIC [2-3]. These

factors can be mitigated during post-processing. This work focuses solely on developing the experimental setup to access the tank's surface.

The diameter of the porthole (Fig. 1) was chosen to ensure that the measurement area represents the average size of the heterogeneous storage material. To minimize potential heat dispersion caused by the porthole, quartz glass was mounted using high temperature resistant silicone (SILCOSET 158). It is assumed that the presence of quartz glass between the surface and the cameras can be neglected [4]. The tank surface was prepared by cleaning with acetone and ethanol before applying a speckle pattern using high temperature resistant spray paint (Nespoli).

3. Results and conclusions

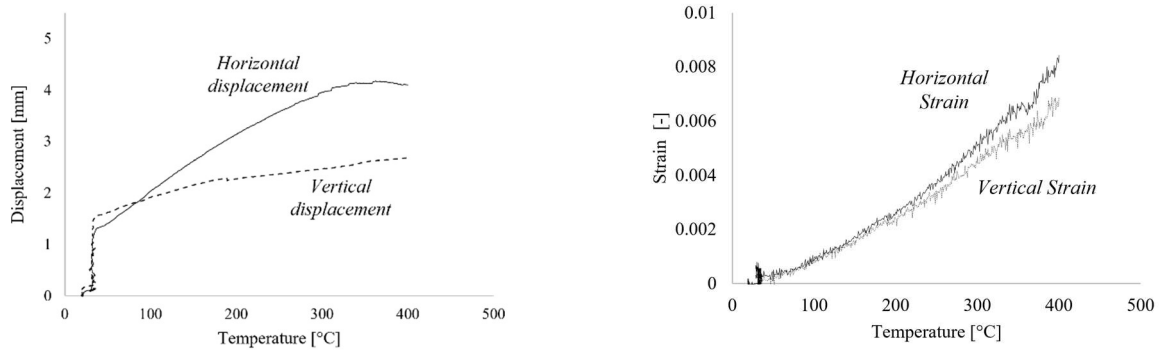

Fig. 2. Displacements and strain variation with temperature

These results were filtered to remove measurement errors related to the test environment. Details of the filtration procedure and subsequent validation are discussed in previous work [5]. The final displacement evolution fields as a function of temperature are shown in Fig. 2. The calculated strains (also in Fig. 2) indicate material elongation due to thermal expansion.

This study significantly improved our understanding of the mechanical response of thermal storage structures, which remains poorly understood and controlled. In addition to the complex experimental conditions, which added value to this work, the quality of the results obtained in terms of repeatability are a real step forward for the implementation of a numerical model.

4. Acknowledgements

The research presented in this paper has received funding from the France Relance program.

5. References

[1] Lalau, Y., Al Asmi, I., Olives, R., Dejean, G., Meffre, A., & Py, X. (2022). Energy analysis and life cycle assessment of a thermal energy storage unit involving conventional or recycled storage materials and devoted to industrial waste heat valorisation. Journal of Cleaner Production, 330, 129950.

[2] Badaloni, M., Rossi, M., Chiappini, G., Lava, P., & Debruyne, D. (2015). Impact of experimental uncertainties on the identification of mechanical material properties using DIC. Experimental Mechanics, 55, 1411-1426.

[3] Pan, B., Wu, D., & Yu, L. (2012). Optimization of a three-dimensional digital image correlation system for deformation measurements in extreme environments. Applied optics, 51(19), 4409-4419.

[4] Su, Y., Yao, X., Wang, S., & Ma, Y. (2017). Refraction error correction for deformation measurement by digital image correlation at elevated temperature. Optical Engineering, 56(3), 034106-034106.

[5] Alonso Aruffo, G., Lalau, Y., Penazzi, L., Bonnaire, R. Development of a displacement and strain measurement method using optical non-contact method in complex environments - submitted

Impact and Crashworthiness

IMPACT THREE-POINT BENDING TEST USING SPLIT HOPKINSON BAR METHOD FOR CFRP ±45° ANGLE-PLY LAMINATES

A. Ejiri[1], H. Yamada[2], N. Ogasawara[2], T. Uno[3], H. Yoshikawa[3] and W. Yoneyama[3]
[1] *Graduate School of Science and Engineering, National Defense Academy, Japan*
[2] *Department of Mechanical Engineering, National Defense Academy, Japan*
[3] *Yonex Co., Ltd, Japan*

1. Introduction

Carbon fiber reinforced plastic (CFRP) is used in sports products because of its high strength and lightweight characteristics. For example, as the swing speed of a tennis racket can reach tens of m/s, a stroke of this velocity will subject the racket to an impact load. Therefore, it is necessary to design CFRP considering the mechanical properties under high-rate deformation.

The split Hopkinson bar (SHB) method [1][2], a typical impact deformation test, is suitable for evaluation of mechanical properties under high-rate deformation. In this study, a three-point bending test is used to evaluate the modulus of elasticity for CFRP. In the impact three-point bending test, specimen with short longitudinal direction cannot be used to avoid significant shear stress. On the other hand, the use of long specimen results in high-frequency oscillations caused by inertial forces and multiple reflections of stress waves within the specimen, which complicates the analysis of test results. [3]. To deal with this problem, Ogawa and Higashida proposed a method of providing a ramp wave with a gradual rise to the specimen by placing a small piece of zinc as a buffer between the striker and the input bar [4].

However, the shape and material of this buffer should be determined taking into account the strength of the specimen. This study investigates the optimal buffer shapes for impact three-point bending tests of CFRP ±45° angle-ply laminates, with the aim of evaluating the impact bending properties of CFRP.

2. Materials and methods

In this study, CFRP laminates were fabricated by stacking unidirectional prepreg sheets composed of carbon fibers and epoxy resin. The carbon fiber was TR50S (Mitsubishi Chemical). The epoxy resin base was a mixture of jER828:jER1001 at a ratio of 40:60 (wt.%) (Mitsubishi Chemical), the curing agent was jER cure DICY7 (Mitsubishi Chemical), and the curing accelerator was DCMU99 (Hodogaya Chemical). 16 layers of this prepreg sheet were laminated with 45° and -45° fiber orientation and cured in an autoclave. Three specimens with a length of 100 mm, a width of 15 mm, and a thickness of 2 mm were cut from this CFRP angle-ply laminate.

Generally, solid round bars are used for the input and output bars in the SHB method, but circular tubes were used in this study to enhance the sensitivity of stress wave measurements. Both the input and output tubes were made of T6 tempered 6063 aluminum alloy. The input tube had an outer diameter of 20 mm and an inner diameter of 18 mm, while the two output tubes had an outer diameter of 12 mm and an inner diameter of 10 mm. Foil strain gauges (KFGS-1-120-C1-11, Kyowa Electric) were attached to the input tube at two locations. Incident and reflected waves were measured over an

extended period using the two-point stress measurement method [5]. On the other hand, foil strain gauges and semiconductor strain gauges (KSPB-1-350-E4, Kyowa Electric) were attached to the two output tubes. In this study, polytetrafluoroethylene (PTFE) is used as a buffer.

3. Results and conclusions

Figure 1 shows the strain-time relationship of the incident and transmitted waves obtained from the impact three-point bending test with and without the PTFE buffer. Without the PTFE buffer, the incident wave exhibited a square shape and the transmitted wave showed high-frequency oscillations. On the other hand, by using the PTFE buffer, gradual rising incident wave was obtained, which suppressed the high-frequency oscillations of the transmitted wave. Therefore, it was confirmed that using this buffer enables highly accurate experiments. By applying the oscillation-suppressed stress wave to the one-dimensional elastic wave propagation theory, the bending stress-bending strain relationship as shown in Fig.2 was obtained. Therefore, it is possible to evaluate non-oscillating impact bending properties by controlling the waveform of the incident wave.

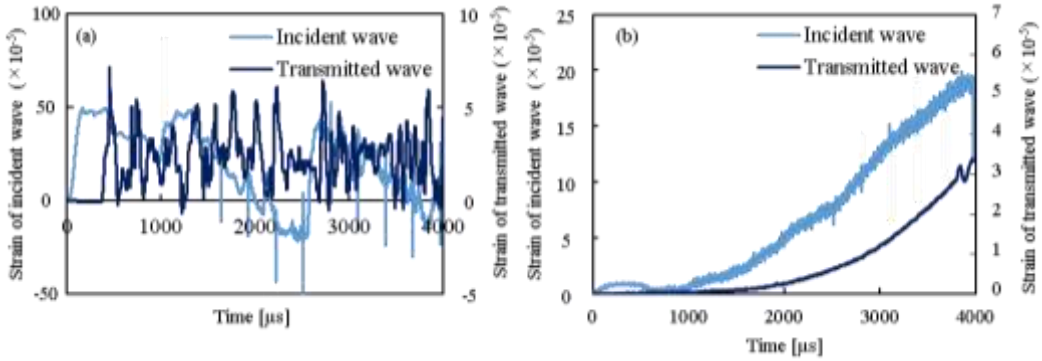

Fig.1 Relationship between strain of incident wave or strain of transmitted wave and time. (a) is the results without the PTFE buffer, while (b) is the results with the PTFE buffer.

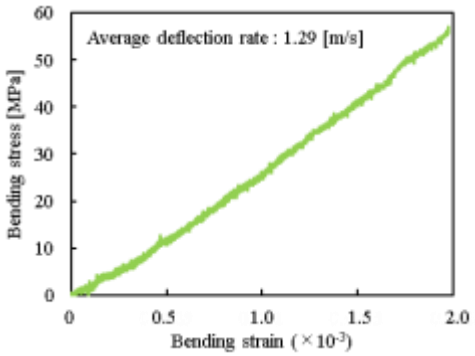

Fig. 2 Relationship between bending stress and bending strain.

4. References

[1] B. Hopkinson (1914). A Method of Measuring the Pressure in the Deformation of High Explosives by the Impact of Bullets, *Philosophical Transactions of the Royal Society A,* **213**, 437-452

[2] H. Kolsky(1949). An Investigation of the Mechanical Properties of Materials at Very High Rates of Loading, *Proceedings of the Physical Society. Section B*, **62**, 676-700

[3] T. Kusaka, T. Kurokawa, Y. Yamauchi (1994). Strain Rate Dependence of Mode II Interlaminar Fracture Toughness of Unidirectional CF/Epoxy Composite Laminates, *Journal of the Society of Materials Science*, **43**, 445–450.

[4] K. Ogawa, F. Higashida (1990). Impact Three-point Bending Tests by Applying Ramped Incident Wave, *Reinforced Plastics*, **36**, 123–129.

[5] N. Yanagihara(1977). The Measuring Method of Impact Force by the Theory of Propagation of Longitudinal Elastic Stress Wave, *Transactions of the JSME*, **43**, 4048-4052.

PERSONNEL BLAST PROTECTION OF HOLLOW PYRAMID STRUCTURE FILLED WITH LIQUID

Yuan Li[1,2], Shufan Lu[1,3], Jiyu Tang[1], Tao Suo[1,2]
[1] Institute of Extreme Mechanics and School of Aeronautics, Northwestern Polytechnical University, Xi'an, China
[2] National Key Laboratory of Strength and Structure Integrity, Xi'an, China
[3] Aircraft Strength Research Institute of China, Xi'an, China

1. Introduction

The personnel blast protection structure not only requires a small deflection of the back plate and small force transmission but also considers wearing comfort and ease of movement. Due to the strict design requirements, the current personnel's ability to resist blast shock waves is still insufficient. Two main measures are usually adopted in the current personnel protections. One is using the energy-absorbing materials, like foams, honeycombs, etc. The other one is the face shape design of the protection structures [1]. The porous materials have the advantages of being lightweight and big specific energy absorbing. Some of them are soft and widely used in personnel protection. However, these porous materials usually suffer from force enhancement while facing blast shock waves. As a result, some other materials are exploited by the researchers, like the shear-thicken fluid, polyurea, etc. Among them, liquid is a promising material [2], which can be used in different forms, like liquid foam [3], moist, liquid-filling nanomaterials, etc. On the other hand, protection structure design is also an important aspect [4]. The V shaped structure shows an effective energy dispersion effect and is widely used in the armor vehicle floor. However, they are not commonly exploited in personnel protection against blast shock waves.

Noticing the promising protection potential of the liquid and V-shaped structure, this study explores their combination to achieve a much better blast protection effect. The liquid was used in its bulk form and filled in the intervolume of the V-shaped structure. Shock tube tests were conducted to simulate the blast shock waves and also verified numerical modeling was performed to reveal the protection mechanisms.

2. Materials and methods

This study designs a new personnel shock wave protection structure by combining the respective protection advantages of V-shaped structures and liquid. Through shock tube testing and numerical modeling, shock wave protection research was conducted on the designed and additively manufactured liquid-filled pyramid structure. A nylon tube filled with silicon rubber was used to simulate the human body and fixed at the nozzle of a shock tube, as shown in Fig. 1. The designed structure was placed in front of the silicon rubber, and the pressure curves measured at the shock tube nozzle (incident pressure) and inside the silicon rubber (transmitted pressure) were compared to analyze the protective effect.

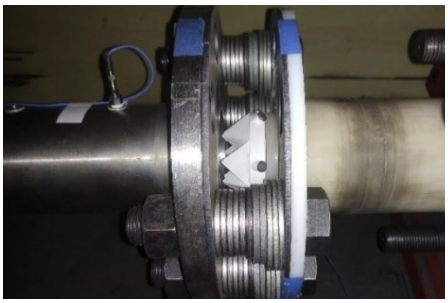

Fig. 1. Test setup of the shock tube

3. Results and conclusions

Test results show that compared to the situation of no protection (Fig. 2), the liquid-filled hollow pyramid structure can achieve a protection effect of overpressure attenuation of 26.0% and impulse attenuation of 13.1%. It also shows that under the situation of more plugs, more liquid mass was leakaged and the overpressure attenuation was improved. On this basis, the changing rules of the energy of the plug and liquid, the motion state of the pyramid shell structure, etc. were studied in detail through modeling, and the shock wave protection mechanism of the liquid-filled pyramid structure was clarified. There is a balance between the pressure attenuation by the energy dispersion and offset and the pressure enhancement by the cone valley focusing. Relevant research results can provide an important reference for improving personnel's anti-explosion shock protection level.

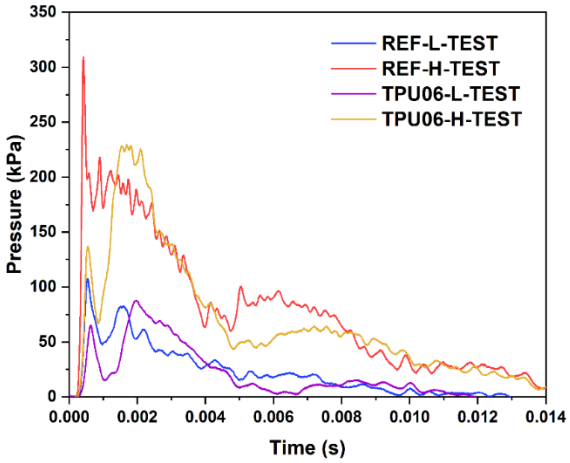

Fig. 2. Transmitted pressure curves in the silicon rubber

4. Acknowledgements

The research presented in this paper has received funding from the National Natural Science Foundation of China under grant number 12141203.

5. References

[1] Y. Li, Z. Lv, Y. Wang (2020). Blast Response of Aluminum Foam Sandwich Panel with Double V-Shaped Face Plate, *International Journal of Impact Engineering*, **144**, 103666.

[2] Y Chen, H Wei, S Constantini (2012). Blast shock wave mitigation using the hydraulic energy redirection and release technology, *Plos One*, **7**, e39353.

[3] K. Ahmeda, A.Q. Malik (2010). Experimental studies on blast mitigation capabilities of conventional dry aqueous foam, *AIP Advances*, **10**, 065130.

[4] M. Konarzewski, R. Panowicz, A. Jeschke (2023). Double-Bend and Semi-Spherical Energy Deflectors' Blast Load Efficiency—a Comparative Study, *Applied Sciences,* **13**, 6752.

Analytical and Numerical Models

BENCHMARK OF ANALYTIC VS. MONTE CARLO BATCH AQCUISITION FUNCTIONS FOR MACHINE LEARNING OPTIMIZATION OF EXPERIMENTS

Mark Lee[1], Imon Mia[2], William Vandenberghe[2], and Julia W. P. Hsu[2]
[1] Department of Physics, The University of Texas at Dallas, USA
[2] Department of Materials Science & Engineering, The University of Texas at Dallas, USA

1. Introduction

Many types of scientific or engineering experiments aim to find the optimum conditions of an unknown functional relationship between a set of experimental inputs $\boldsymbol{X}$ and an output objective $y = f(\boldsymbol{X})$, where $\boldsymbol{X}$ is a multidimensional vector of input parameters. The "black box" function $f(\boldsymbol{X})$ is unknown and usually too complicated to be accurately modeled by any specific parametric representation. In such cases, Bayesian optimization (BO) [1] using a data-based non-parametric surrogate regression model has emerged as a powerful and widely adopted machine learning (ML) method to guide empirical searches of parameter space seeking the optimal input $\boldsymbol{X}_{\text{opt}}$ that will give optimal objective value $y_{\text{opt}} = f(\boldsymbol{X}_{\text{opt}})$. BO is particularly useful when generating new samples to test $f(\boldsymbol{X})$ is expensive in cost or time, so the total number of sampled data points is typically less than a few hundred. Examples of experiments of engineering tests that have used BO ML methods include new materials synthesis and processing [2,3], mechanical design [4], new drug discovery [5], and maximizing manufacturing yield [6]. In many real-world experiments, the cost of generating and experimentally evaluating a small batch of $q > 1$ new samples at one time, where typically $q \leq 10$, only marginally exceeds the cost of a producing a single sample. It then makes sense to use batches of q new samples to test $f(\boldsymbol{X})$ and provide additional data to update the surrogate model in each BO iteration step, a process called batch BO (bBO) [7]. The goal for real experiments is to maximize confidence in the accuracy of the modeled global optimum using the fewest number of expensive batch iterations possible.

2. Methods

The central component of bBO is choice of a batch acquisition function (bAF) that suggests the statistically most promising new $\boldsymbol{X}$ to test in the next experimental batch. The present study compares the performance of analytic and Monte Carlo (MC) batch acquisition functions (bAFs) using two test functions that serve as proxies for common engineering optimization experiments. Our study evaluates the analytic upper confidence bound with local penalization (UCB/LP) bAF against parallel, stochastically calculated MC-based approaches: q-log expected improvement ($q$logEI) and q-upper confidence bound (qUCB), where q is the batch size. An additional MC bAF, q-log noisy expected improvement ($q$logNEI) is also evaluated on a test problem with noisy functional evaluations because $q$logNEI was specifically developed to handle noisy experiments.

The two test functions used, both with six input parameters (so $\boldsymbol{X}$ is a 6-dimensional vector), are the Ackley function [8] and the Hartmann [9] function. Six input parameters are used because most real experiments find adjusting between three to six parameters to be practically tractable. Ackley represents a "needle-in-haystack" challenge because it is a highly heterogeneous function, oscillating

near its minimum value through most of its domain except for a sharp peak that occupies a small fraction of its domain hypervolume. Hartmann represents a "false maximum" challenge because it has a secondary maximum with objective value nearly degenerate with its true maximum.

3. Results and conclusions

Analytic UCB/LP and MC *q*UCB both did very well finding and accurately modeling the "needle-in-haystack" maximum point on the Ackley function without noise, with UCB/LP performing slightly better overall than *q*UCB. *q*logEI, on the other hand failed to converge onto any accurate model of Ackley's maximum. On the Hartmann function without noise, all bAFs performed adequately, although all bAFs became trapped in the "false maximum" approximately one-third of the time. UCB/LP and *q*UCB performed similarly to each other while both outperformed *q*logEI in all metrics. On Hartmann with noise, all MC bAFs outperformed analytic UCB/LP, particularly in needing fewer bBO iterations to converge onto the optimal values. *q*UCB especially modeled the Hartmann maximum with reasonable accuracy and within the experimental budget even against very high noise levels. Although *q*logNEI was developed specifically to handle noisy functional evaluations, it showed no clear performance advantage over *q*UCB but required significantly longer computational time.

In many real-world experiments, nothing is known *a priori* about the general landscape of the function $f(\boldsymbol{X})$ being tested, and empirical evaluations of $f(\boldsymbol{X})$ always include noise. Results of this work indicate that *q*UCB performs very well with both needle-in-haystack and false optima functional landscapes and against fairly high levels of noise. Therefore, *q*UCB is recommended as the default choice of bAF when applying bBO for optimization of real experimental processes.

4. Acknowledgements

The research has received funding from the United States National Science Foundation under award number CMMI-2109554.

5. References

[1] X. Wang, Y. Jin, S. Schmitt and M. Olhofer (2023). Recent advances in Bayesian optimization *ACM Computing Surveys,* **55.13s** art. 287.
[2] S.Sun, N. T. Hartono, Z. D. Ren, F. Oviedo, A. M. Buscemi, M. Layurova, D. X. Chen, T. Ogunfunmi, J. Thapa, S. Ramasamy and C. Settens (2019). Accelerated development of perovskite-inspired materials via high-throughput synthesis and machine-learning diagnosis *Joule* **3** 1437.
[3] B. J. Shield, J. Stevens, J. Li, M. Parasram, F. Damani, J. I. M. Alvarado, J. M. Janey, R. P. Adams and A. G. Doyle (2021). Bayesian reaction optimization as a tool for chemical synthesis *Nature* **590** 89
[4] A. E. Gongora,B. Xu, W. Perry, C. Okoye, P. Riley, K. G. Reyes, E. F. Morgan and K. A. Brown (2020). A Bayesian experimental autonomous researcher for mechanical design *Science Advances* **6** eaaz1708.
[5] L. Colliandre and C. Muller (2024). Bayesian Optimization in Drug Discovery, in Heifitz, A (ed) Methods in Molecular Biology (Springer, Berlin) **2716** 101.
[6] S. Guler, M. Schoukens, T. D. Perez and J. Husakowski (2021). Bayesian optimization for Tuning Lithography Processes *IFAC–PapersOnLine* **54.7** 827.
[7] N. Hunt (2020). *Batch Bayesian Optimization* Thesis, MIT: dspace.mit.edu/handle/1721.1/128591.
[8] Description of Ackley function at: www.sfu.ca/~ssurjano/ackley.html.
[9] Description of Hartmann function at: www.sfu.ca/~ssurjano/hart6.html.

Numerical Calibration of Tensile and Compressive Failure of Bio-Epoxy Foam Core for Explicit Analysis using a Simplified Testing Approach

***A.Harrison*[1]**
[1] *Institute of Vehicle Concepts, Vehicle Architectures and Lightweight Design Concepts, German Aerospace Centre, Germany*

1. Introduction

There is an increased demand in many sectors to produce lightweight and sustainable structures to fulfill various requirements. One such example is within the automotive industry to provide eco-friendly vehicles whilst fulfilling structural safety requirements. In the rapidly developing industry, a reliable, quick method to model more complex behavior of materials, such as rate-dependency and failure criterion, is required for rapid prototyping and analysis via Finite Element Methods [1]. To model highly non-linear structural responses is typically laborious and requires a vast number of coupon tests that must follow strict forms and testing parameters through Quasi-static and Dynamic testing respectively. Furthermore, the numerical representation of the characterized foam material can often lead to instabilities in explicit calculations due to the unloading response, element failure and unrepresentative performance with consideration to other parts of the system. Thus, the selection of the material model is imperative to accurately and reliably represent the foam model in use.

This study aims to showcase the simplified methodology of foam testing to characterize key structural material properties and develop the numerical representation via parameter tuning in black-box optimization techniques for implementation within commercially available explicit solver, LS-DYNA.

2. Materials and methods

The material used in the study is a bio-based epoxy foam developed under the EU project r-LightBioCom in support of development of high-performance composites for use-cases in the automotive, aeronautical and infrastructure sectors. The material coupons were subjected to quasistatic and dynamic loading in compression and 3-point bending tests, using a Universal Testing Machine (UTM) and gravity driven pendulum impact machine (IMPETUS) [2], in which the force and traverse distance and the acceleration and pendulum angle were measured by the UTM and IMPETUS respectively. From the data recorded, calculation of the relevant material responses such as Stress, Strain, Energy Absorption and any rate-dependent behavior were made. The main focus of the study is not the examination of the material itself, rather the extraction of the data as input for the calibration of the numerical representation through black-box parameter tuning to replicate the material response without the requirement of standardized tests. The testing parameters are provided in Table 1.

Test Type	Speed(s) (m/s)	Fin/support Radius (mm)	Support Distance (mm)	Specimen Dimensions (LxWxH)(mm)
Compression	9.9E-6, 1, 2.5, 3	-	-	20x20x20
3-Point Bending	3.3E-6, 0.5, 1, 1.5	QS: 10, 5 DYN: 5, 2	50	60x20x20

Table 1. Testing parameters of the material calibration study

The test data was imported into VALIMAT software to form the specific parameter-model cases for the automated calibration process. The result curves act as the target for the optimization following a DOE of the variables from the parameter set, the explicit solver is induced with the boundary conditions of the testing parameters and element formulation. The mesh used 3mm type 2 fully integrated solid elements. The process chain material formulation was extended to replicate large deformations under compressive stress with isotropic behavior by integrating *MAT_163 (MODIFIED_CRUSHABLE_FOAM), in which the material is defined by yield-stress versus volumetric strain [3]. The analytical function used for parameter tuning was the curve was the 4a foam model function [4], Johnson-Cook model was used for strain-rate effects and MAT_ADD_EROSION flag was implemented at the final stage of the material calibration for tension failure induced by the bending load-case.

3. Results and conclusions

The resulting numerical material description provided good alignment in compressive performance and failure initiation through bending, as shown in Figure 1. Furthermore, the implementation of MAT_163 provided the necessary variables to accurately determine varying strain-rate performance in compression loading with failure induced by the optional erosion flag by using the maximum principle stress and plastic strain failure criteria. The complete material description was found to be suitable for both compressive and bending load-cases which are prevalent for automotive use-cases.

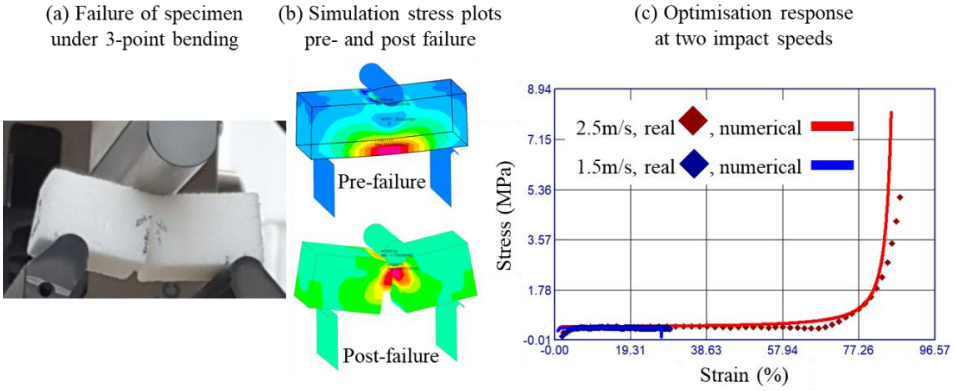

Fig. 1. (a), (b) and (c) highlighting the results from physical testing, simulation and parameter optimization respectively

4. Acknowledgements

The author would like to acknowledge Leibniz-Institut fuer Verbunwerkstoffe (IVW) for producing and supplying the material used within this study.

The research presented in this paper has received funding from European Union under Grant Agreement Project No 101091691

5. References

[1] Ramaswamy, K., Patham, B., Savic, V., and Tripathy, B., "Stable and Accurate LS-DYNA Simulations with Foam Material Models: Optimization of Finite Element Model Parameters," SAE Int. J. Mater. Manf. 10(2):226-233, 2017, DOI: 10.4271/2017-01-1338

[2] IMPETUS, [Apparatus], 4a Engineering, https://www.4a-engineering.at/4a-impetus

[3] "LS-DYNA: Keyword User's manual Volume II Material Models", LS-DYNA R11, LSTC, 2018

[4] VALIMAT, [Software], 4a foam model, https://www.4a-engineering.at/4a-valimat

DEVELOPMENT OF AN AUTOMATED PROCESS FOR MATERIAL CARD CALIBRATION OF JOINTS FOR FINITE ELEMENT SIMULATIONS

T. Wirtz
Institute of Vehicle Concepts, German Aerospace Center (DLR e.V.), Germany

1. Introduction

In the automotive industry, point and surface joining techniques are often used. These include clinching, self-pierce riveting, flow drilling screws [1] and adhesive joints. To accurately model the joints in FE-Models, especially for crash simulations, properly calibrated material cards are required. A great amount of manual effort is required for the generation of the material card parameters. Automating this process can reduce the costs currently required for the generation of validated numerical descriptions.

For this purpose, an automated process chain will be developed. Using tensile tests, performed on a universal testing machine, the quasi static characteristics of joints will be determined. The dynamic characteristics will be determined using the IMPETUS pendulum from 4a Engineering [2]. New clamping concepts and simulation models are developed to receive the static and dynamic responses of the joints. Furthermore, algorithms will be implemented that automatically determine the material card parameters of the joint connection, considering various boundary conditions, from the obtained test results. In this work, the current status of the development is shown.

2. Materials and methods

Figure 1 shows the abstracted process chain. First, suitable test specimens must be produced. These are then tested using various test methods. The selection of suitable test methods was based on the main types of loading of the joints to be tested in real use [3]. These include quasi-static and dynamic impact tests so that strain rate-dependent material behavior can be replicated. Based on the measurement results of these tests, initial values of parameters of the joint material card are determined. The determination of these starting values is a critical stage within the process chain to ensure quick realization of optimal parameters in the optimizer. The simulation results are utilized to create a metamodel. An algorithm is employed to the metamodel within a loop to accelerate the identification of optimum material parameters. Once converged, the generated material card for the joint is verified. Finally, a simulation of the shear tension and head tension test is carried out again with the previously optimized material card parameters in order to verify the functionality of the metamodel and to validate the FE model and the material card parameters with regard to the real tests and test results. If this is the case, the selected values of the material parameters are output in the form of a material card.

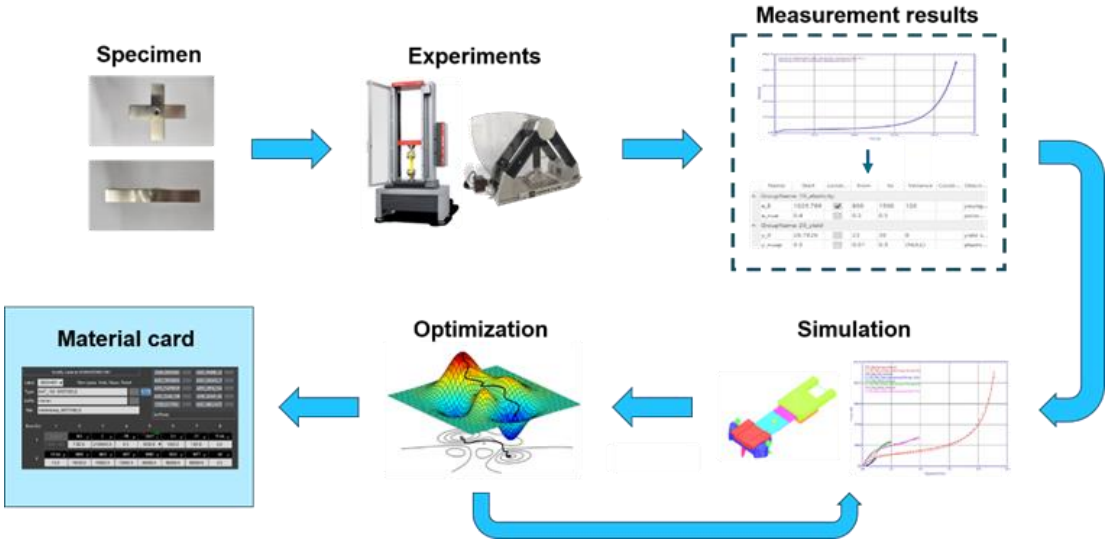

Fig. 1. Process chain of automated material card calibration [4]

3. Results and conclusions

The result of this work will be a process for automated material mapping and calibration of point and plane joints for use in explicit FE simulations. The result of this process is a strain rate dependent material card of the joint on a macroscopic level. The representative material card contains the joint, including the material of the joining partners, sheet thicknesses, selected joining method, joining material and prevailing manufacturing influences. Compared to the load cases that lead to the failure of the joint, the micromechanical failure types play a rather subordinate role, as the material card of the joints is calibrated for crash simulations [5]. Due to the process chain and testing process, the material card is validated for predominantly uniaxial stress states by means of shear tensile and head tensile tests at coupon level. However, as soon as a parameter of the joint changes, e.g. the sheet thickness of a joining partner, the calibration process must be carried out again. At the end of the development of this automated material card calibration process, it should be possible to describe a wide variety of joints in the form of a validated material card. It should be possible to choose between different joint formulations and different material cards. Due to the automation of the calibration process, a considerable reduction in development time and the associated personnel costs can be achieved. Furthermore, an increase in the quality of the determined material parameters is expected, as an automated optimization algorithm can perform more iterations and make more qualitative adjustments to the material parameters.

4. References

[1] Pischinger, Stefan (2016): Vieweg Handbuch Kraftfahrzeugtechnik, 8. aktualisierte und erweiterte Auflage, Wiesbaden: Springer Vieweg (ATZ/MTZ-Fachbuch), https://doi.org/10.1007/978-3-658-25557-2

[2] IMPETUS, [Apparatus], 4a Engineering, https://www.4a-engineering.at/4a-impetus

[3] AWS D8.9M:2012, 2012: Test Methods for Evaluating the Resistance Spot Welding Behavior of Automotive Sheet Steel Materials, ISBN: 978-0-87171-808-2

[4] Wirtz, Tim (2024): Development of an automated process for material card calibration of Punctiform and Planar joints for explicit FE-simulations, presentation on 4a Technology Days Schladming

[5] André, Victor; Costas, Miguel; Langseth, Magnus; Morin, David (2023): Neural network modelling of mechanical joints for the application in large-scale crash analyses, In: International Journal of Impact Engineering 177, DOI: 10.1016/j.ijimpeng.2023.104490

BUCKLING STRUCTURES IN A CONTROLLED-THICKNESS GRADIENT: FINITE ELEMENT METHOD AND EXPERIMENTAL STUDIES

M. Chargaoui [1], G. Parry [2], C. Coupeau [1]
[1] Institut Pprime, Université de Poitiers / UPR 3346 CNRS/ ISAE-ENSMA, 86000 Poitiers, France
[2] SIMaP, Grenoble INP / Université de Grenoble Alpes/ CNRS UMR 5266, F-3800, Grenoble, France

1. Introduction

Thin films and coating are widely used in numerous technological applications, including for instance microfluidics, microelectronics, optical devices or thermal barriers. They are commonly produced by physical vapor deposition, and exhibit large intrinsic stresses, often reaching the order of gigapascals (GPa) [1]. Under compressive stress, delamination or buckling of the film/substrate system may occur, compromising their functionality. However, buckling offers insights into the mechanical properties of the film/substrate system, such as Young's modulus, internal stress or toughness [2,3]. While the straight sided buckles in constant-thickness films are well-understood [4,5], the influence of thickness gradients remains unexplored. In this context, we investigated stressed nickel films which exhibit a controlled thickness gradient deposited by ion beam sputtering on polycarbonate substrates. Our experimental observations show that the maximum deflection of straight sided buckles oriented parallel to the thickness gradient decreases as the film thickness increases. Additionally, when those buckles oriented not parallel to the thickness gradient, they result in asymmetrical profile with shift of its maximum deflection towards the thinner part of the film. FEM simulations in the framework of elastic plate theory further investigate the effect of thickness gradient. The numerical results are presented, discussed, and compared with the experimental findings.

Keywords: Thin films, Thickness gradient, Buckling, AFM, FEM

2. Methods

2.1 Experimental details

Nickel films were deposited on polycarbonate (PC) substrate (5×2 mm^2 in surface; 10 mm length) by physical vapor deposition, with the substrate shutter moving at 2-10 µm/s to create a defined thickness gradient at deposition rate of 0.078 nm/s. Optical interferometry (Talysurf CCI 46000) was used to characterize the thickness gradient. The internal stress in the film was estimated using the Stoney's curvature method to be around $\sigma_0 = 0.8 \pm 0.1$ GPa. Spontaneous buckles appear on the sample just after deposition. The buckles are characterized by atomic force microscopy (AFM).

2.2 Mechanical modeling details

Thin films with a thickness gradient are modeled using finite element simulations in ABAQUS/Standard with a static solver. The simulation consists of a film as a 2D elastic nickel plate (E_f = 200 GPa and a Poisson's ratio ν_f = 0.31 [4]) and substrate as rigid (60 µm width × 120 µm length) with varying thickness $h(x)$ along the (Ox) axis (see Fig. 2). Large deformations are considered using the geometrical non-linear Green-Lagrange strain tensor.

3. Experimental *vs.* numerical results

The experimental straight sided buckle (see Fig.1) exhibits an unusual asymmetry ($b_+ \neq b_-$) at the centerline. This asymmetry is further investigated in FEM simulations (see Fig. 2), which reveal that the variation in film's thickness along the SS profile is the primary cause of this asymmetry.

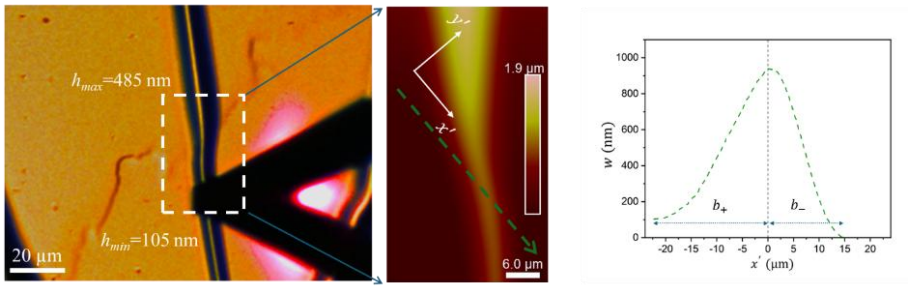

Fig. 1. Straight sided buckle lying not parallel to the thickness gradient (a) Optical image of straight sided buckle on a nickel Ni film. (b) AFM image (30×50 µm^2). (c) The profile the green arrow (Ox') at approximately 40° from the thickness gradient in (b).

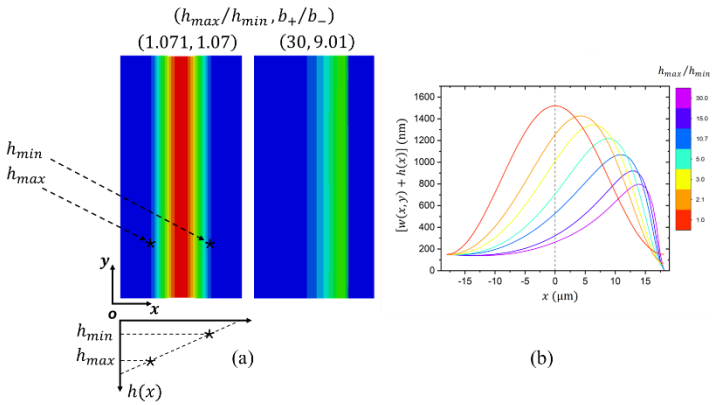

Fig. 2. Influence of a thickness gradient perpendicular (Ox) to the straight sided buckle. (a) Out-of-plane displacements with respect to the different thickness gradients (h_{max}/h_{minn}) with their resultant's asymmetry b_+/ b_-. (b) Mapping of the post-equilibrium profile of the SS buckle with respect to. FEM simulation for a nickel film (E_f= 200 GPa and ν_f = 0.31), for $2b$ = 36 µm, σ_{xx}^0 = 0.8 GPa and σ_{yy}^0 = 0 GPa.

4. Acknowledgements

This work was supported by the French government program "France 2030" (LABEX INTERACTIFS, reference ANR-11-LABX-0017-01).

5. References

[1] G. Abadias, E. Chason, J. Keckes, M. Sebastiani, G. Thompson, E. Barthel, G. Doll, C. Murray, C. Stoessel, L. Martinu, Review Article: Stress in thin films and coatings: Current status, challenges, and prospects, J. Vac. Sci. Technol. Vac. Surf. Films 36 (2018) 020801.

[2] C. Coupeau, From thin film and coating buckling structures to mechanical properties, Mater. Sci. Eng. A 483–484 (2008) 617–619.

[3] J.-Y. Faou, G. Parry, S. Grachev, E. Barthel, Telephone cord buckles—A relation between wavelength and adhesion, J. Mech. Phys. Solids 75 (2015) 93–103.

[4] C. Coupeau, R. Boijoux, Y. Ni, G. Parry, Interacting straight-sided buckles: An enhanced attraction by substrate elasticity, J. Mech. Phys. Solids 124 (2019) 526–535.

[5] G. Parry, A. Cimetière, C. Coupeau, J. Colin, J. Grilhé, Stability diagram of unilateral buckling patterns of strip-delaminated films, Phys. Rev. E 74 (2007) 066601.

Composite and Advanced Materials

THERMAL AND MECHANICAL BEHAVIOR OF BENZOXAZINE/EPOXY-BASED NANOCOMPOSITES

E. Tikarrouchine[1], O. Mehelli[1], D.E. Tria[1], A. Bouteldja[1] and M. Derradji[1]
[1] Ecole Militaire Polytechnique, BP 17, Bordj El-Bahri 16046, Algiers, Algeria

1. Introduction

Engineering continually seeks innovative solutions to meet the increasing demand for high-performance materials. Advances in manufacturing techniques now enable the development of intricate composite materials. Among the growing portfolio of high-performance materials, benzoxazine (PBz) and epoxy resins have garnered significant attention for their exceptional thermal, mechanical, and chemical properties. PBz resins are characterized by their superior thermal stability, low processing viscosity, and catalyst-free polymerization, making them highly attractive for advanced composite applications. In contrast, epoxy resins exhibit strong adhesive properties, chemical resistance, and broad versatility, rendering them a staple in coatings, adhesives, and structural applications. The tailored synthesis of these thermosetting resins allows for property optimization to meet diverse engineering demands.

Recent advancements in nanotechnology have opened new avenues to enhance the performance of PBz and epoxy matrices through the incorporation of nanofillers. Nanofillers such as multi-walled carbon nanotubes (MWCNTs) and aluminum nitride (AlN) nanoparticles significantly enhance thermal conductivity, mechanical strength, and electrical properties, while also improving thermal stability and reducing flammability [1], [2]. For epoxy resins, these improvements are well-documented; however, PBz-based nanocomposites remain underexplored, particularly regarding their behavior under dynamic loading conditions. Understanding the thermomechanical performance of these nanocomposites is critical to realizing their full potential in high-stress environments.

This study aims to bridge this gap by systematically investigating the thermomechanical behavior of PBz and epoxy nanocomposites reinforced with MWCNTs or AlN nanoparticles. Using an in-situ synthesis process, nanofillers are dispersed within the polymer matrix to maximize their interaction and impact. Thermal and mechanical properties are analyzed using Differential Scanning Calorimetry (DSC), Thermogravimetric Analysis (TGA), and Dynamic Mechanical Analysis (DMA). Additionally, dynamic loading experiments employing the Split Hopkinson Pressure Bar (SHPB) provide novel insights into PBz composites' high-strain-rate performance, a rarely studied domain [3].

This study contributes to the ongoing development of next-generation nanocomposites tailored for demanding industrial applications.

2. Materials and methods

The study used reagent-grade materials, including Bisphenol-A, DGEBA epoxy resin, and MWCNTs from Sigma-Aldrich (USA), a cycloaliphatic amine hardener from Huntsman Corporation (USA), and aluminum nitride nanoparticles (70 nm) from Nanostructured & Amorphous Materials, Inc. (USA). Aniline and paraformaldehyde were also obtained from Sigma-Aldrich (Germany). No additional purification was performed.

Thermal analysis using DSC, TGA, and DMA evaluated the curing behavior, thermal stability, and mechanical properties of benzoxazine and epoxy resins with nanofillers. DSC focused on curing Bz monomers, TGA assessed thermal stability up to 800 °C, and DMA analyzed stiffness and nanofiller effects. Mechanical tests, including quasi-static (fig. 1-a) and dynamic (fig. 1-b) regimes, were conducted on nanocomposite samples with high repeatability. Specimens were prepared with precise geometry, conditioned for uniform humidity, and sealed to maintain consistent testing conditions.

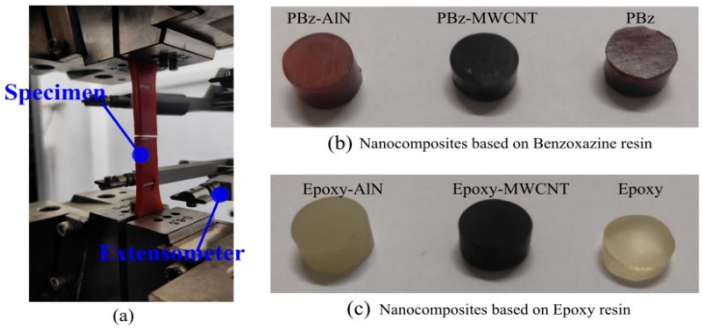

Fig. 1. Specimens of the prepared nanocomposites for a) quasi-static and b) dynamic tests.

3. Results and conclusions

This study examined the effects of AlN and MWCNT nanofillers on the mechanical (fig. 2) and thermal properties of epoxy and PBz resins. Epoxy reinforced with 1% MWCNT significantly outperforms AlN, enhancing strength and toughness, especially under dynamic conditions (fig. 2-b), due to restricted polymer chain movement by nanofillers. PBz nanocomposites exhibit superior mechanical performance, with 1% MWCNT reinforcement achieving the highest stress levels, attributed to PBz's toughness, stability, and MWCNT's exceptional mechanical properties. This highlights PBz as a key material for applications requiring high strength, stiffness, and resilience.

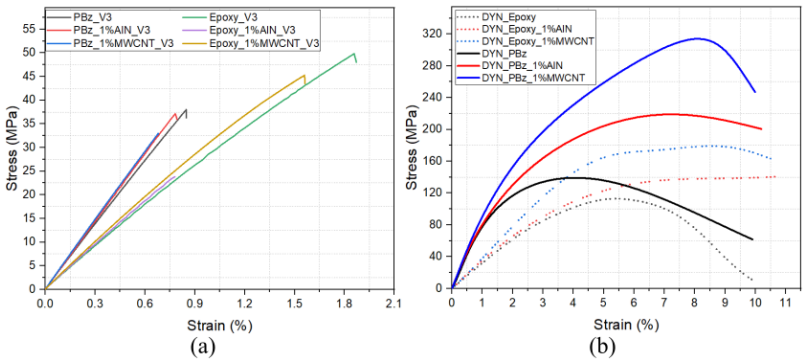

Fig. 2. Overall response of the developed nanocomposites in term of stress–strain for a) the quasi-static and b) the dynamic tests (comparison between the PBz and Epoxy based nanocomposites).

5. References

[1] Mehelli, O., Derradji, M., Habes, A., Leblalta, N.E., Belgacemi, R., Abdous, S., Izri, Y., Liu, W., 2021. Benzoxazine resin as an interesting building block for advanced neutrons shields. High Performance Polymers 33, 1116–1123

[2] Chen, W., Lu, H., Nutt, S.R., 2008. The influence of functionalized mwcnt reinforcement on the thermomechanical properties and morphology of epoxy nanocomposites. Composites Science and Technology 68, 2535–2542.

[3] Laifa, S., Tria, D.E., Derradji, M., Khalfallah, S., 2023. The synergistic effect of temperature and loading rate on the mechanical behavior of shear thickening fluid reinforced with graphene nano-platelets using split hopkinson pressure bar. Thin-Walled Structures 192, 111133.

EFFECT OF POST TREATMENT ON MECHANICAL PROPERTIES OF CELLULOSE NANOFIBER SHEET

M. Asami[1], A. Miyawaki[2] and S. Arikawa[2]
[1] Graduate School of Science and Technology, Meiji University, Japan
[2] Department of Mechanical Engineering, Meiji University, Japan

1. Introduction

In recent years, the increase in carbon dioxide emissions from the disposal and incineration of plastic products derived from fossil fuels has caused serious environmental problems such as global warming and climate change. To reduce the environmental burden, cellulose nanofiber (CNF) is attracting attention as a sustainable natural resource. CNF is a woody biomass resource obtained by breaking cellulose, the main component of wood and other plant fibers, down to nano-sized pieces. It is expected to be a material with new functions in various respects, such as lightness, strength and low linear expansion.

In previous studies, many voids were observed in the cross sections of naturally dried CNF sheet, which were considered to be the cause of reduced strength and mechanical properties [1]. Therefore, the density and strength of CNF sheet were attempted to be increase by reducing the distance between fibers and strengthening hydrogen bonds through compression. It was also considered that the improvement of crystallinity by heating and fiber reorientation by water soaking might contribute to the improvement of the mechanical properties of the CNF sheet. Although previous studies have shown that thermo-compression improves the mechanical properties of CNF sheet [2], the effects of compression and the appropriate compression stress remain to be elucidated. Therefore, evaluating the extent to which post-treatment contributes to improving the performance of CNF sheet and finding the optimal treatment method will facilitate the practical use of CNF sheet and will be a step forward toward reducing the environmental burden and realizing a sustainable society.

In this study, we aimed to improve the mechanical properties of CNF sheet, which is obtained by naturally drying CNF, through simple and sustainable approaches such as compression with heating. The permeability due to thermal compression force was also investigated.

2. Materials and methods

For the specimens used in this study, CNF sheet was made by naturally drying a 2 wt.% CNF aqueous dispersion solution at room temperature (24℃) for about 3 days. The specimens were then cut into the shape shown in Fig. 1. The post-treatment method was thermo-compression of the CNF sheet at 120℃ using a compression device and furnace. Tensile testing was performed at a crosshead speed of 1.00 mm/min. Transmittance of the post-treated CNF sheet was measured using a UV-visible spectrophotometer.

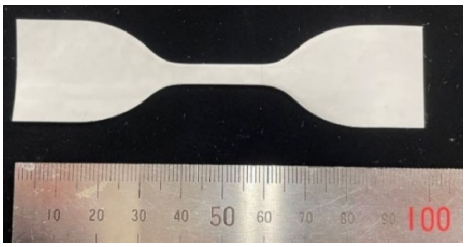

Thickness 0.05mm

Fig. 1. CNF sheet specimen

3. Results and conclusions

The maximum stress values for each of the specimens with various thermo-compression tested in tension are shown in Fig. 2(a). The stress applied by thermal compression was 0.66 MPa, 0.99 MPa, and 1.32 MPa, and the maximum tensile stress values are the average of six tests, respectively. The maximum tensile stress value for specimen with various thermos-compression conditions was 134MPa, which increased when the stress applied by thermo-compression was 0.66 MPa and 0.99 MPa, as shown in Fig. 2(a). When the stress applied by thermo-compression was 1.32 MPa, there was a sharp decrease of the maximum stress.

Figure 2(b) shows the transmittance of the CNF sheet after post-treatment. As the stress applied by thermo-compression was increased, the transmittance also increased. This is thought to be due to a decrease in defects that cause light to diffuse. On the other hand, the decrease in the maximum stress value at thermo-compression of 1.32MPa from Fig. 2(a) is thought to be due to the rupture of CNF molecules.

Through this study, it was confirmed that the mechanical properties of the CNF sheet were improved when they were subjected to thermo-compression under 1.0 MPa. It was also suggested that the mechanical properties of CNF sheet deteriorate when the stress applied by thermo-compression exceeds the optimal pressure range. Additionally, the effects of temperature on thermo-compression, the effects of water soaking and re-drying on the CNF sheet and the orientation of the CNF will be investigated.

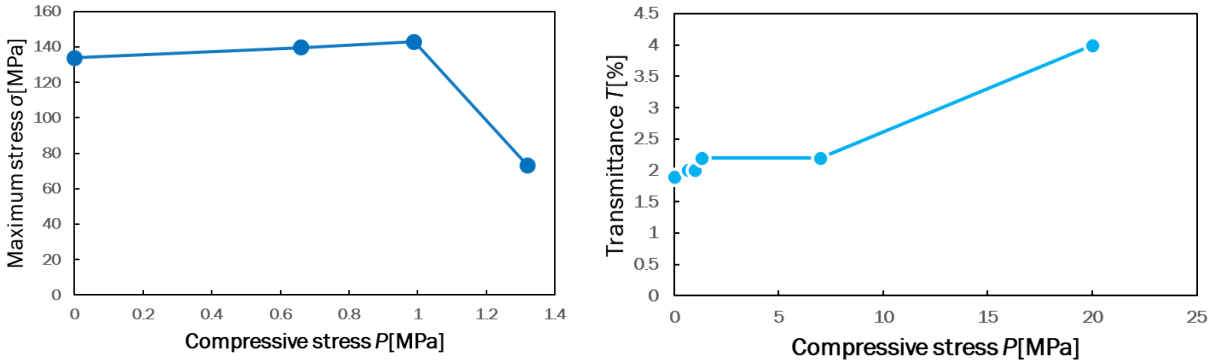

(a) (b)

Fig. 2. (a) Maximum stress value of CNF sheet with thermo-compression at 120°C (b) Transmittance of CNF sheet with thermo-compression at 120°C

4. References

[1] Haishun Du, Mahesh Parit, Xinyu Zhang, Kun Liu, Chuanling Si, Miaomiao Zhang, Zhihua Jiang, Engineering cellulose nanopaper with water resistant, antibacterial, and improved barrier properties by impregnation of chitosan and the followed halogenation, Carbohhydrate Polymers, 270, (2021).

[2] Ikramul Hasan, Jinwu Wang, Mehdi Tajvidi, Tuning physical, mechanical and barrier properties of cellulose nanofibril films through film drying techniques coupled with thermal compression, Cellulose, 28, 11345-11366, (2021).

EFFECT OF UNIT CELL CONFIGURATION ON BENDING BEHAVIOR OF SPREAD-TOW WOVEN FLAX/PP COMPOSITES IN THE MOLTEN STATE

R. Hossein Abadi[1], U. Sachs[2], D. Van Hemelrijck[1] and K.A. Kalteremidou[1]
[1] Department of Mechanics of Materials and Constructions (MeMC), Vrije Universiteit Brussel (VUB), Brussels, Belgium
[2] ThermoPlastic composites Research Center (TPRC), PO Box 770, 7500 AT Enschede, The Netherlands

1. Introduction

The use of thermoforming processes to produce thermoplastic composite parts with complex shapes has gained attention due to their ability to integrate favorable mechanical properties, efficient production rates, and economic viability. Among thermoplastic composites, those reinforced with natural fibers like flax stand out for their recyclability and environmental advantages, making them remarkably appealing to industries like automotive.

Spread-tow woven composites, made by weaving thin, flat unidirectional tapes, offer improved fiber alignment, higher fiber content, and better performance per unit weight compared to conventional woven reinforcements [1]. This structure reduces fiber crimp and resin content, resulting in a lighter composite with enhanced mechanical properties. These characteristics make spread-tow woven composites attractive for various industries.

During thermoforming, composites experience various deformation mechanisms. Out-of-plane bending is one of the deformation mechanisms during thermoforming, and its interaction with other mechanisms, such as in-plane shear, can contribute to the formation of wrinkles which can affect the structural integrity of the final product. Understanding this mechanism is essential for accurately predicting and optimizing the forming process. This paper investigates the experimental bending behavior of spread-tow woven flax/polypropylene composites under thermoforming conditions, with a particular focus on the impact of unit-cell configuration on their performance.

2. Materials and methods

Specimens were prepared from a single-ply spread-tow woven flax/PP composite (40% fiber volume fraction) with an average thickness of 0.5 mm and a tow width of 25 mm. Given the design of the bending setup to test specimens up to 25 mm wide, two specimen types were tested: one containing a full centralized unit cell (configuration (a), Fig. 1(a)) and the other including the transition-dominated region between adjacent unit cells (configuration (b), Fig. 1(b)). Bending experiments were conducted at three temperatures, using a modified rheometer equipped with a thermal chamber for precise temperature control. The developed setup at TPRC (Fig. 1(c)) based on the Kawabata bending test [2], featured a fixture where specimens rested loosely on support pins inside the fixture to minimize tensile and compressive strains [3]. The rheometer's rotating upper shaft bent the specimens, while the system measured the bending moment with high precision. Specimens were preheated for 12 minutes, to ensure uniform temperature on the specimen before testing. The test matrix is presented in Table 1.

(a) (b) (c)

Fig. 1. Specimen with (a) full central unit cell, (b) transition-dominated region, (c) bending setup.

Parameter	Value	Unit
Specimen length	35	mm
Specimen width	25	mm
Bending rate	6	°/s
Temperature	175, 190, 200	°C

Table 1. Test matrix for bending experiments.

3. Results and conclusions

The obtained moment versus rotation angle curves are plotted together in Fig. 2. The bending moment decreases with increasing temperature for both specimen types. The specimens with configuration (a) exhibit slightly higher bending resistance compared to those with configuration (b), though the differences are not significant across the tested temperatures.

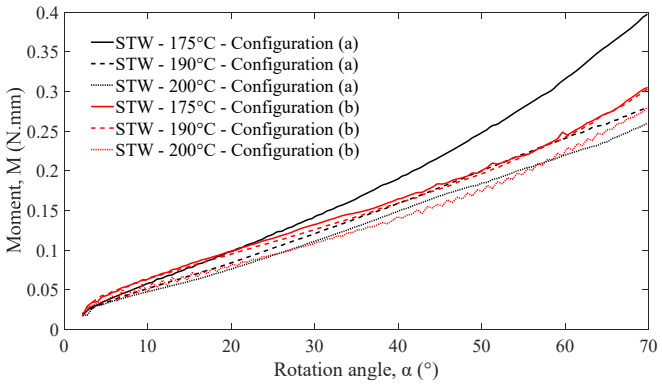

Fig. 2. Moment versus rotation angle curves for two types of specimens at varying temperatures.

4. Acknowledgements

The authors gratefully acknowledge the support of the ThermoPlastic composites Research Center (TPRC) for facilitating the necessary equipment and expertise. Furthermore, the financial contribution of the FWO Research Foundation–Flanders (file number K247524N) is gratefully acknowledged. The authors also acknowledge the material supplier W8SVR GmbH.

5. References

[1] HM. El-Dessouky and CA. Lawrence (2013). Ultra-lightweight carbon fibre/thermoplastic composite material using spread tow technology. *Composites Part B: Engineering.,* 50, 91-97.

[2] U. Sachs and R. Akkerman (2017). Viscoelastic bending model for continuous fiber-reinforced thermoplastic composites in melt. *Composites Part A: Applied Science and Manufacturing.*, 100, 333-341.

[3] S. Ropers, M. Kardos, TA. Osswald (2016). A thermo-viscoelastic approach for the characterization and modeling of the bending behavior of thermoplastic composites. *Composites Part A: Applied Science and Manufacturing.*, 90, 22-32.

DELAMINATION STRATEGIES FOR ACHIEVING FULLY FREESTANDING IONOMER-BOUND CARBON FILMS WITH ENHANCED MECHANICAL RELIABILITY

Y. H. Kim[1], and T.-S. Kim[1*]

[1] Department of Mechanical Engineering, Korea Advanced Institute of Science and Technology, Daejeon, Korea
*Email: tskim1@kaist.ac.kr

1. Introduction

Ionomer-bound carbon films, celebrated for their exceptional electrochemical properties, are vital components in advanced devices such as fuel cells, electroactive polymer actuators, and supercapacitors. However, their inherently fragile nature poses a significant challenge to achieving the long-term durability necessary for reliable operation in these applications [1]. To address these limitations, understanding the intrinsic mechanical properties of these films is critical, as it provides essential insights into their structural behavior and informs the development of optimized design strategies to enhance their durability and performance [2]. A major barrier to this objective lies in the lack of effective delamination methods and a clear understanding of the processes required to fabricate freestanding carbon films. Overcoming this barrier demands a comprehensive understanding of the free-standing fabrication process. With this foundation, careful engineering can enable the production of damage-free ionomer-bound carbon films, allowing for precise evaluation of their intrinsic mechanical properties.

This study proposes a novel technique for delaminating ionomer-bound carbon films using elevated-temperature water. Through this approach, we discovered that carbon films can be delaminated more quickly, easily, and without defects. To quantify the effectiveness of this method, we measured the critical energy release rate (G_c) and the threshold energy release rate (G_{th}) using the Double Cantilever Beam (DCB) test, confirming a reduction in interfacial energy. Subsequently, by measuring the swelling strain of the carbon film, we identified that the delamination mechanism is driven by stress concentration induced by out-of-plane deformation. Finally, we present a method for retrieving delaminated carbon films from water. This technique significantly reduces the critical tensile stress during the drying process, preventing mechanical fracture of the electrode and enabling the fabrication of freestanding ionomer-bound carbon films. This research provides foundational insights for evaluating the mechanical properties of ionomer-carbon films, offering valuable knowledge applicable across all fields where these materials are utilized.

2. Materials and methods

A high-concentration catalyst ink was prepared using carbon black (Pt/C; Vulcan XC-72, 40 wt% Pt), Nafion ionomer dispersion (Nafion D2021, Sigma-Aldrich, USA), and ethylene glycol, which were mixed in a 20 ml vial. The slurry had a solid content of approximately 11 wt%. To achieve a uniform slurry, the mixture was processed using a magnetic stirrer and ultra-tip sonication. Subsequently, 500 µl of the catalyst ink was applied onto a glass substrate and coated at a controlled

speed of 5 mm/s using a doctor blade. To ensure precise control over the coating thickness, PI tape was affixed to both ends of the glass substrate prior to the coating process. The coated film was then dried in a convection oven at 90°C for 2 hours, followed by thermal treatment at 130°C.

The fabricated specimen was prepared for a Double Cantilever Beam (DCB) test. The electrode specimen, cut using a diamond cutter, was attached alongside a dummy glass substrate of identical dimensions. The two glass substrates were bonded using epoxy adhesive and cured in a convection oven. During the bonding process, a protective layer of 3M tape was applied to prevent the epoxy from infiltrating the electrode. Aluminum loading tabs were affixed to both sides of the DCB specimen, enabling attachment to a micromechanical testing system (Delaminator Adhesion Test System, DTS Company) equipped with a linear actuator and a load cell. The DCB specimen was then immersed in a bath containing deionized (DI) water, with the temperature controlled using a hot plate.

3. Results and conclusions

Fig. 1 illustrates the critical energy release rate (G_c) and the threshold energy release rate (G_{th}) of ionomer-bound carbon films in air and deionized (DI) water at various temperatures. These results demonstrate the significant sensitivity of the interfacial energy between the carbon film and the glass substrate to environmental conditions and temperature. This sensitivity highlights the critical role of environmental factors in determining the adhesion and delamination characteristics of Ionomer-bound carbon films.

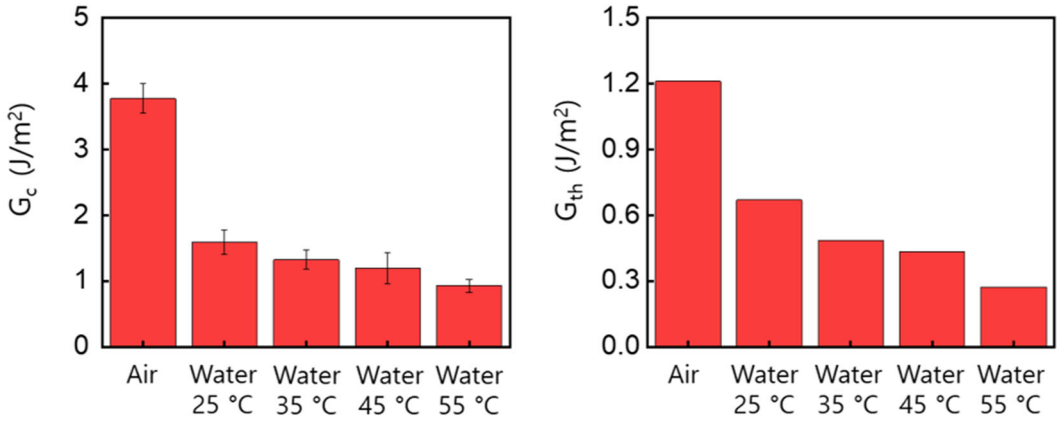

Fig. 1. The results of G_c and G_{th} in air and DI water at various temperatures

4. Acknowledgements

This work was supported by the National Research Foundation of Korea (NRF) grant funded by the Korean government (MSIT) (No. 2022R1A2C3009087)

5. References

[1] Uchiyama, T., Kumei, H., & Yoshida, T. (2013). Catalyst layer cracks by buckling deformation of membrane electrode assemblies under humidity cycles and mitigation methods. *Journal of power sources*, *238*, 403-412.

[2] Pyo, J. B., Kim, J. H., & Kim, T. S. (2020). Highly robust nanostructured carbon films by thermal reconfiguration of ionomer binding. Journal of Materials Chemistry A, 8(46), 24763-24773.

Experimental and Numerical Analysis of Damage Induced During Dry Drilling of Multi-Layer Materials (CFRP/AL-7075)

M. F. Ameur[1, 2], R. Zitoune[2], M.Kenane[3] and M. Habak[4]
[1] Ecole Nationale Supérieure des Technologies Avancées (ENSTA) Algiers, Algeria
[2]Innovative Mechanics Laboratory (LMI), Dept GMP (ENSTA) Algiers, Algeria
[3]Laboratoire des Sciences et Génie des Matériaux, FGMG, University USTHB, Algeria
[4]Laboratoire des Technologies Innovantes (LTI), IUT d'Amiens, DepGMP, University PJV, French

1. Introduction

The aviation industry is widely known for the diversity of manufacturing techniques and materials that it employs. For many years, intensive use of composite materials made of carbon fiber reinforced polymer (CFRP) and aluminum alloys have been integrated into the aeronautical industry. The use of hybrid materials such as CFRP/Aluminium, CFRP/Titanium provide the best combination of mechanical properties including low density, high strength/weight ratio and high corrosion resistance which result in energy and cost saving [1,2]. In the aircraft industry, thousands of holes are required for the assemblies of hybrid structures. In fact, for economic reasons drilling of these hybrid materials in one-shot operation is required [3-4]. To reduce the cost of manufacturing with respect to the machining process, in the last decade the process of drilling and riveting of these hybrid materials is conducted automatically using a robots or specific machine (flexible system) [5]. Among these defects, the appearance of delamination, matrix degradation, poor diameter tolerance and fiber pull-out are frequent [6,7].Therefore, the cutting parameters such as feed rate and spindle speed must be optimized [8] in order to improve the machining quality. During drilling of CFRP/Al, Zitoune et al. [9] have proposed a numerical model developed in the quasi-static frame in order to predict the critical thrust force responsible for the decohesion of the CFRP and the aluminum parts in function of the thickness of the aluminum part. The FE model should be a qualified tool to model the mechanical behavior and damage formation when machining of hybrid materials.

In this paper, an experimental and numerical study of the machinability of CFRP/Al is conducted. The 3D finite element approach was developed to model the machining behavior when dry drilling of stacked carbon fiber reinforced epoxy (carbon T700 / epoxy M21) / Aluminum alloy (Al 7075) using the ABAQUS/EXPLICIT solver. Different kinds of damage mechanisms based on the Hashin, Johnson cook and the B-K criteria have been taken into account to improve the robustness of the proposed model. The thrust forces predicted from developed 3D model have been discussed and correlated to the experimental findings in function of the machining parameters. In addition, the damage induced by the machining process has been quantified using the X-ray tomography and correlated to those predicted by the FE model.

2. Experimental procedure

The composite used for these tests is a carbon/epoxy (CFRP) T700-M21. This material is made of unidirectional prepreg. The lay-up sequence of the tested plates was quasi-isotropic with a stacking sequence of [(90/45/0/-45)3]s. Mechanicals properties of the materials (cf.table 1).

The mechanical properties of this Al 7075 are listed in Table 2. The drilling trails were carried out on a computer numerical control (CNC) machine.The cutting forces are measured using a piezo-electric dynamometer type Kistler 9257 (cf. fig.2).

3. Results and conclusions

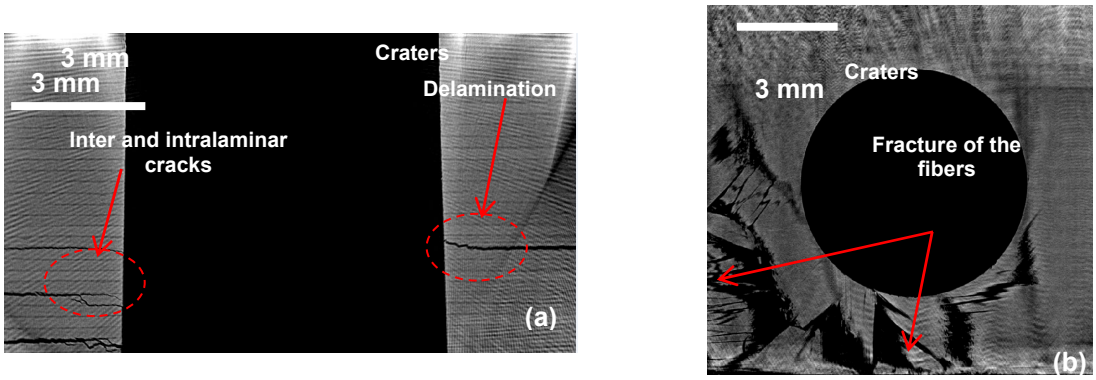

Fig.12. Images of the X-ray tomography showing the state of the last two plies from the hole exit after drilling with a feed rate of 600 mm/s and s spindle speed of 3000 rpm. With (a): cross section of the CFRP part and (b): top view showing the damage in the ply number 20.

4. Conclusion

From this experimental and 3D numerical studies of dry drilling of hybrid material made of CFRP and aluminum alloy 7075 the following conclusion can be drawn:

- The experimental analysis has shown that, the main parameter which influence the thrust force is the feed rate. This result has been confirmed by the 3D numerical model. In fact, the results of the thrust force predicted by the model are in good agreement with those recorded by the sensor force. The small gap observed between the model and the experimental at the macro scale has been related to the thermal effect.

The damage predicted by the model and based on Hashin criterion seems to be satisfactory. In fact, the X-ray tomography reveal that, when drilling is conducted with a feed rate inferior to 0.2 mm/rev (600 mm/min) no damage is generated between the layers of the CFRP and only small craters in the thickness of the plies are observed. In this case the machining can be considered as good quality. This result can be attributed to the presence of the aluminum pate on the bottom of the CFRP which can act as back plate supporting the plies and hence avoiding delmamination. However, when the machining is conducted with high feed rate (e.g. 0.2 mm/rev or 600 mm/min).

5. References

[1] R Zitoune, NCadorina, FCollombet, M Simac. Temperature and wear analysis in function of the cutting tool coating when drilling of composite structure: In situ measurement by optical fiber. Wear 2017; 376–377, Part B, 1849-1858.

[2] MF Ameur, M Habak, M.Kenane, HAouici, M Cheikh . Machinability analysis of dry drilling of carbon/epoxy composites: cases of exit delamination and cylindricityerror.Advanced Manufacturing Technology 2017 ;88 (9–12): 2557–2571.

[3] M. Ramulu, T. Branson, D. Kim. A study on the drilling of composite and titanium stacks. Composite Structures 2001; 54, 67-77.

[4] R. Zitoune, KVijayan, FCollombet , S.Le Roux. Experimental and numerical analysis on drilling of carbon fibre reinforced plastic and aluminium stacks. Composite Structures 2016;146(20),148-158.

Fatigue and Fracture

INVESTIGATION OF MIXED-MODE TEST ON DYNAMIC FRACTURE TOUGHNESS OF DISSIMILAR MATERIALS INTERFACE

Y. Naito[1], Y. Tanaka[2] and S. Arikawa[2]
[1]Graduate School of Science and Technology, Meiji University, Japan
[2]Department of Mechanical Engineering Informatics, Meiji University, Japan

1. Introduction

In order to achieve carbon neutrality, there is an urgent need to reduce carbon dioxide emissions from transportation equipment. For that, reducing fuel consumption through weight reduction is important. Dissimilar materials can be joined to complement the weaknesses of a single material to reduce weight. Dissimilar materials may have cracks or defects at the interface, and their deformation behavior is complex due to differences in physical properties between the materials. Fracture toughness evaluation is necessary because dissimilar materials may have cracks or defects. The deformation behavior is complex due to differences in the physical properties of the bonded materials, and transportation equipment is subjected to impact loading. Kojima et al. [1] reported that dynamic fracture toughness values can be calculated from measured displacement fields using a digital image correlation (DIC) method. However, while the entire fracture toughness values for the mixed-mode K_{0C} were evaluated, the stress intensity factors for each mode K_{IC} and K_{IIC} were not. In this study, a mixed-mode impact test is performed using an impact test apparatus that can change the loading direction, and the mixed-mode ratio of the stress intensity factor is investigated using measured displacement data by DIC.

2. Materials and methods

A schematic diagram of the test apparatus is shown in Fig. 1. In this study, a three-layered specimen consisting of aluminum alloy (A2017) at the center layer and acrylic resin (PMMA) as upper and lower layers bonded with an acrylic adhesive (LOCTITE AA330) was used. Impact tests were performed using the Split Hopkinson Pressure Bar (SHPB) test apparatus. The mixed-mode impact test was performed by inserting a wedge between the output bar and specimen as shown in Fig. 1. The test was conducted by changing the loading direction by using wedges with different inclination angles θ. Five types of wedges were used: θ = 15°, 30°, 45°, 60°, and 75°.The impact fracture was observed with an ultra-high-speed camera. The frame rate was 1Mfps and the image size was 926×768 pixels. The images were analyzed by DIC to obtain the measured displacement field, and the strain field was calculated by differentiating the displacement field. As an example, the x-direction displacement field obtained from DIC is shown in Fig. 2. The stress at the interface can be calculated from the strain field, and the critical stress intensity factors K_{IC} and K_{IIC} were calculated using the stress values along interface [1].

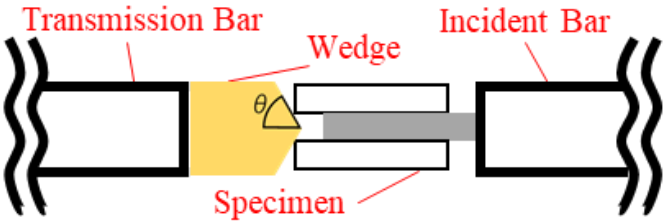

Fig. 1. Schematic diagram of a proposed set up

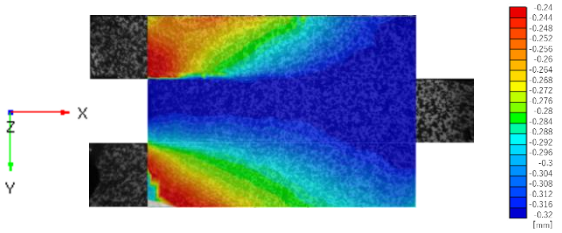

Fig. 2. x-direction displacement by DIC

3. Results and discussions

Figure 3 shows the obtained results of K_{IC} and K_{IIC} for impact tests with various wedge angles. Figure 3 indicates that a wide range of mixed-mode ratios of stress intensity factors were achieved. On the other hand, the impact test without the wedge produced larger K_{IIC} and smaller K_{IC}.Yuki et al.[2] reported that the mixed-mode ratio follows an elliptic law when the direction of tension is changed in static tensile tests on dissimilar materials. However, no such law was found in the results of this study. From now on, the measurement accuracy of the experiment needs to be improved in order to reduce the error of the data and to see fracture criterion.

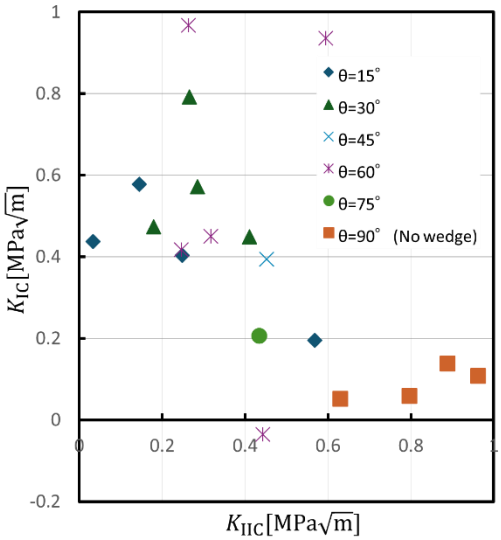

Fig. 3. Relationship between mode I and II components of critical stress intensity factor

4. Conclusion

In the present study, a wide range of mixed-mode ratios were achieved by impact testing with wedges inserted. Further improvements in measurement accuracy will be pursued to provide more detailed information on the dynamic fracture conditions of the mixed-mode.

5. References

[1] T. Kojima, Y. Kimura, S. Arikawa, M. Notomi, (2020), Evaluation of dynamic fracture toughness of a bonded bi-material interface subject to high-strain-rate shearing using digital image correlation, Enginnering Fracture Mechanics, Vol. 241, pp. 1-13, 2020

[2] R.Yuki, J. Liu, J. Xu, Y. Kim, (1994), Study on the Mix Mode Fracture Criterion of Interface Crack, Material, Vol. 43, No. 493, pp. 1206-1210

EFFECT OF MICROSTRUCTURE ON THERMAL CYCLE DAMAGE BEHAVIOR A $YbTa_3O_9$/YSZ DUAL TBC WITH COLUMNAR STRUCTURE

Y. Yamazaki[1] and T. Takizawa[2]
[1] School of Engineering, Chiba University, Chiba, Japan
[2] School of Science and Engineering, Chiba University, Chiba, Japan

1. Introduction

Thermal barrier coatings (TBCs) are used in hot sections of aero-engines and land-based gas turbines for increased efficiency and extended life of superalloy components. A typical TBC system consists of a metal bond coating (BC) with high-temperature corrosion resistance on a substrate superalloy and a ceramic top coating (TC), which is conventionally YSZ sprayed by air plasma spraying (APS) or electron-beam physical vapor deposition (EB-PVD) processes. Recently, the suspension plasma spray (SPS) technique has attracted attention as a new method of using a suspension of submicron spray powders with a solvent. Because of using submicron fine powders, the SPS technique can fabricate coatings with unique microstructures, such as columnar and cauliflower-like structures. It has appeared that the TBC system with the columnar structure TC sprayed by the SPS method is expected to have high thermal cycle resistance properties due to its unique microstructure. However, improving the thermal insulation of the TBC sprayed by the SPS technique is required. More recently, $YbTa_3O_9$ coating with superior thermal shielding properties compared with the conventional YSZ used in the TBC was developed.

In this study, the double-layered TBCs consisting of YSZ and $YbTa_3O_9$ were prepared using the SPS technique. Based on the thermal cycle fatigue test results, the effect of microstructure on the thermal fatigue property of the SPS-TBCs was discussed.

2. Materials and methods

In this study, two types of TBC with dual-top coatings were prepared. The cross-sectional SEM images of the tested coating are shown in Fig. 1. In both specimens, the substrate and the BC are IN738LC and CoNiCrAlY coating sprayed by the high velocity oxy-fuel technique. As the first layer of TC, YSZ coating with a columnar structure was sprayed on the BC by the SPS technique. The $YbTa_3O_3$ coatings with two different microstructures were sprayed as the second TC layer. One has the deposited splats microstructure with the inter-splat pores sprayed by the conventional APS technique. The other one has the columnar microstructure sprayed by the SPS technique.

The thermal fatigue tests were conducted using the test equipment, which includes infrared heaters and an air-cooling system shown in Fig. 2. The maximum temperature at the TC and substrate surfaces were 1100°C and 1000°C, respectively. The minimum temperature of both sides was 400°C. The period of a thermal cycle was almost 80 sec. Before the thermal fatigue test, the specimen was post-spray heat-treated at 1000°C for 300 hours, and then, blackbody paint was sprayed on the TC surface for infrared heating. After the 10,000 thermal cycle fatigue tests, the damage behaviors of the specimens were observed using an optical microscope and SEM.

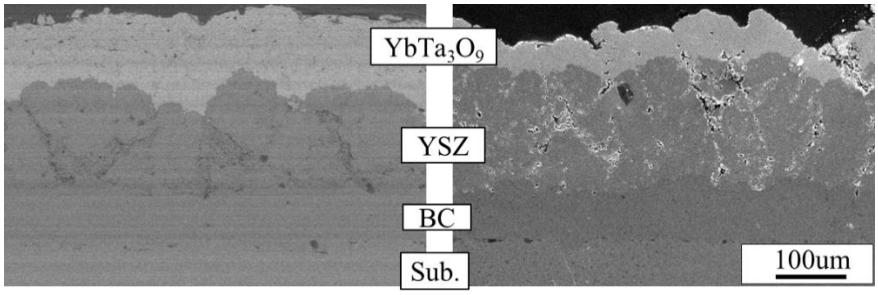

(a) APS-$YbTa_3O_9$+SPS-YSZ (b) SPS-$YbTa_3O_9$+SPS-YSZ

Fig. 1. Cross sectional microstructure of the tested coatings

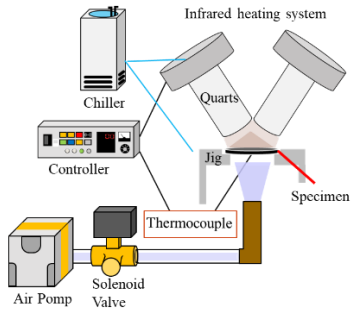

Fig. 2. Thermal test equipment

3. Results and conclusions

Figure 3 shows typical damage behaviors of the specimens after the 10,000 thermal cycle fatigue tests. In the APS-$YbTa_3O_9$+SPS-YSZ, macroscopic delamination occurred at both $YbTa_3O_9$/YSZ and YSZ/BC interfaces from the specimen edge. In addition, the partial and local spallation of the $YbTa_3O_9$ can be also observed around the specimen center. On the other hand, the SPS-$YbTa_3O_9$+SPS-YSZ, a few local and partial spallation of the $YbTa_3O_9$ occurred around the specimen edge, however, no macroscopic delamination can be observed. In addition, the interfacial cracks were also initiated at the interface between $YbTa_3O_9$ and YSZ, however, the delamination has not occurred. Comparing the thermal fatigue damage morphologies, it appears that SPS-$YbTa_3O_9$+SPS-YSZ has an excellent thermal fatigue strength than APS-$YbTa_3O_9$+SPS-YSZ.

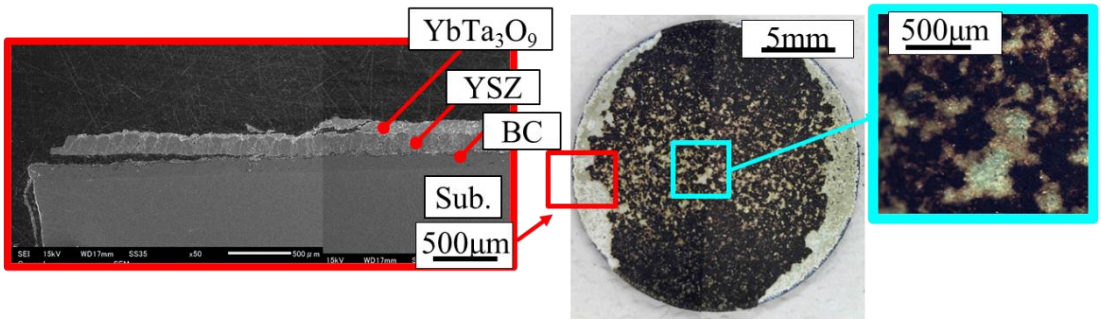

(a) APS-$YbTa_3O_9$+SPS-YSZ

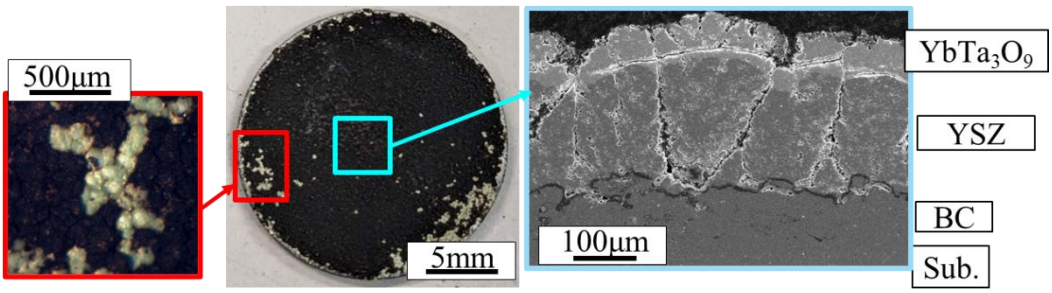

(b) SPS-$YbTa_3O_9$+SPS-YSZ

Fig. 3. Typical damage behaviors of the specimens after the 10,000 thermal cycle fatigue tests

4. Acknowledgements

The research presented in this paper has been supported by JSPS KAKENHI grant number 21K03768 and Amano Institute of Technology, Public Interest Foundation. This study was conducted with support from TOCALO for thermal spray of specimens and Mr. Okumura for thermal fatigue tests.

Searching for the first sign - crack initiation under fatigue loading in seawater-corroded structural S355 steel

S.A. Elahi[1], R. Krankenhagen[2], S. Chaudhuri[2], R.M. Tapia[2], F. Mehri Sofiani[1], W. De Waele[1]
[1] Soete Laboratory, Department of Electromechanical, Systems and Metal Engineering (EMSME), Faculty of Engineering and Architecture, Ghent University, Technologiepark 46, 9052 Zwijnaarde, Belgium
[2] Bundesanstalt für Materialforschung und -prüfung, Berlin, Germany

1. Introduction

Corrosion caused by direct contact with seawater is the most important problem for technical systems and components made of steel in the maritime sector (quote). The loss of material associated with general corrosion leads to a weakening due to the associated reduction in cross-section. Besides, stress concentrations will occur at localized areas of corrosion called corrosion pits. With repeated loading, such pit may act as a nucleation site for fatigue cracks, which ultimately lead to the degradation of the fatigue strength of the material (quote). Due to the random nature of the spatial occurrence of such localized corrosion, the prediction of service life under fatigue loading is made even more difficult. Research shows that a significant portion of fatigue life is spent in the transition of a corrosion pit to a short fatigue crack and in the growth of such short cracks [1]. As a part of the MAXWind project, numerical models are developed that incorporate the evolution of pit morphology due to corrosion [2], associated geometric stress concentration [3], and pit to crack transition [4]. Experiments that represent actual corrosion pits are thus required to verify and validate such models and to determine the model parameters.

As part of the project, structural steel coupons (used for manufacturing wind turbine monopile structures) were directly exposed to seawater in an offshore facility for 22 months. Subsequently, dog-bone shaped specimens were extracted from coupons from different corroded contact areas (underwater, water level, splash zone) for fatigue strength evaluation. This article describes selected results of fatigue tests (purely tensile at different load levels. The sample surfaces were monitored with an IR camera during the entire fatigue test. The aim of this observation was to record the spatial temperature distribution which can be correlated to the stress distribution on the sample surface. The occurrence of cracks is characterized by the appearance of closely neighboring regions with reduced (at the crack flanks) and increased (at the crack tip) internal stress [5]. The resulting temperature differences are very small but can be quantified using the lock-in technique (i.e. TSA - thermal stress analysis). In this study, different thermal signatures are considered, which can be used as an indicator for the first occurrence of macroscopic cracks.

2. Materials and methods

The surfaces of the seawater exposed steel coupons, made of S355 structural steel, were first cleaned to remove the corrosion products (Thibaux and Vanden Haute, 2022). Next, optical scanning was performed to quantify the amount and extent of corrosion pits. Following, specimens having a dog bone contour were manufactured, and the edges were polished according to the relevant standards (ref). The fatigue tests were carried out with 175, 210, 245 and 280 MPa stress range levels, a fatigue

ratio R=0.1, and a loading frequency of 10 Hz until ultimate failure. To reduce the influence of surface inhomogeneities on the thermal signature of the corroded coupons, a black coating was applied on their entire surface. The thermographic measurements were performed by a MWIR camera with 1240 x 1080 pixels. The main recording parameters are compiled in table 1:

Frame rate	Sequence of thermal recordings	Length of one thermographic recording sequence
200 Hz	Every 2000 cycles	1100 frames (corr. to 55 cycles)

Table 1. Main thermographic recording parameters

3. Results and conclusions

The figure shows exemplarily the rising of thermal contrasts in a region where the final crack appeared. The displayed thermal contrast maps are related to the thermoelastic amplitude of every detector pixel. In the highlighted region of the thermal maps, the rising stress concentration is clearly recognizable in the thermoelastic signal, notwithstanding there was no visual indication of the rising crack.

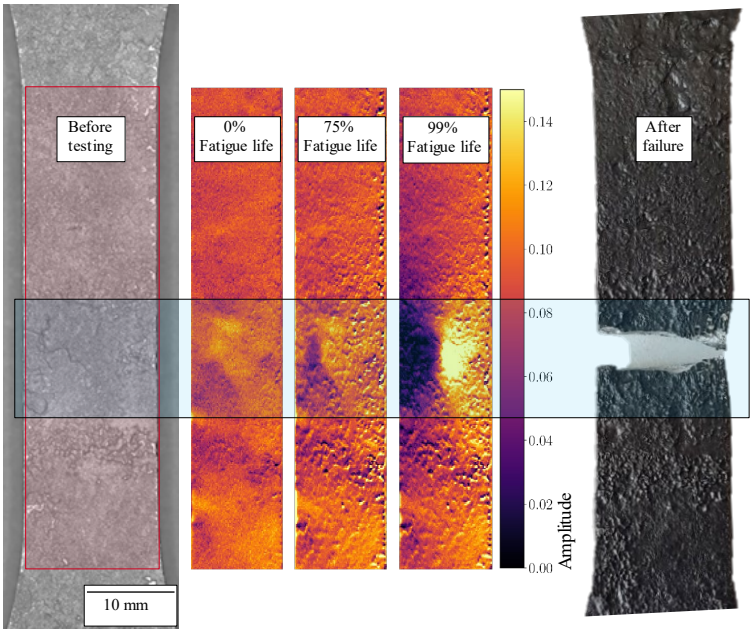

Fig. 1. Left: photograph of the specimen before testing, showing the side of the specimen from which the fatigue crack initiated. Middle: 3 thermograms showing the thermoelastic amplitude evolution due to fatigue loading. Right: photograph of the coated specimen after final failure.

The presentation will be focused on different evaluation techniques to identify the time of the very first crack initiation. These data can be used in connection with the also measured pit geometry for model verification.

4. Acknowledgements

W. De Waele would like to acknowledge the financial support of the Belgian Federal Government through the Energy Transition Fund (ETF) for the projects MAXWIND and FATCOR. S. A. Elahi would like to acknowledge the financial support of FWO for a short research stay at BAM.

5. References

1. Fatoba, O. and R. Akid, *On the behaviour of small fatigue cracks emanating from corrosion pits: Part I – The influence of mechanical factors.* Theoretical and Applied Fracture Mechanics, 2022. **117**: p. 103154 DOI: https://doi.org/10.1016/j.tafmec.2021.103154.
2. Mehri Sofiani, F., et al., *A hybrid probabilistic-deterministic framework for prediction of characteristic size of corrosion pits in low-carbon steel following long-term seawater exposure.* Corrosion Science, 2024. **232**: p. 112039 DOI: https://doi.org/10.1016/j.corsci.2024.112039.
3. Mehri Sofiani, F., et al., *Quantitative analysis of the correlation between geometric parameters of pits and stress concentration factors for a plate subject to uniaxial tensile stress.* Theoretical and Applied Fracture Mechanics, 2023. **127**: p. 104081 DOI: https://doi.org/10.1016/j.tafmec.2023.104081.
4. Elahi, S.A., et al., *Investigation of the effect of pitting corrosion on the fatigue strength degradation of structural steel using a short crack model.* Procedia Structural Integrity, 2023. **51**: p. 30-36 DOI: https://doi.org/10.1016/j.prostr.2023.10.063.
5. Anderson, T.L., *Fracture mechanics: fundamentals and applications*. Fourth Edition ed. 2017: CRC Press.

A FINITE ELEMENT METHODOLOGY FOR THE STRUCTURAL ASSESSMENT OF HIGH PERFORMANCE ELECTRIC MOTOR GEARS

S.Messina[1], S.G.Barbieri[1], F.Manni[1], M.Giacopini[1], L.Pascale[2]
[1] Department of Engineering "Enzo Ferrari", University of Modena e Reggio Emilia, Modena, Italy
[2] Ferrari SpA, e-PWT/PWT Structural Calculation Division, via Abetone Inferiore 4, I-41053 Maranello (MO), Italy

1. Introduction

The increasing demand for high-performance and powerful electric motors is pushing gearbox design to its limits. The main objective of this study is to develop a Finite Element (FE) methodology for the structural analysis of a high-performance electric motor gearbox. In particular, the high cycle fatigue life is addressed. The developed methodology simulates the full operation of gear mesh. By focusing on the movement of a single tooth, different instants of the contact history are evaluated. First, the computational domain has been defined. An untrained eye might think that it would be necessary to discretize only one tooth of one gear and all the teeth of the other [1]. A formula was found that indicates the number of discretized teeth on each gear: twice the contact ratio plus one [1]. The rest of the gear was considered as a simple cylindrical object without teeth [2]. The discretization strategy was then addressed, as it is a critical step in ensuring a successful simulation. The final results are highly influenced by the quality of the initial discretization. The goal was to create a refined discretization in the areas most relevant to the safety factor, while using a coarser discretization in less critical regions to ensure faster simulations [2]. Once the discretization was defined, various modelling strategies with progressively increasing complexity were tested. The influence of different transmission components, such as the shaft, bearings, the effect of the reaction forces from adjacent gears, and the importance of including the microgeometry were thoroughly analyzed. The simulations were performed using Marc Mentat, and the effects of thermal treatment were not considered. The fatigue analysis was carried out using the multiaxial Dang Van criterion. Additionally, the minimum number of steps required to capture the full fatigue history while ensuring the simulation remained as efficient as possible was investigated.

2. Materials and methods

The present study is based on gears made of 18NiCrMo5 steel. The methodology has been concieved considering different modelling strategies. As a start, the model has included only the mesh of the two gears with the contact in their teeth and controlled in correspondence of their rotating axes through a rigid connection [3]. The first gear, called gear 1 in the following, is linked in all the degrees of freedom except for the rotation along its axis and the other gear, called gear 2, is fixed in all the six degrees of freedom [4]. The torque is applied at the center of the link in gear 1 [4]. In the second step, the discretized shafts have been inserted in the domain. In this case the connection is performed through four rigid links, one per each shaft bearing, and the torque is applied where the actual input splined shaft is connected with the shaft of gear 1. The third model also includes the simulation of the bearing through a link with a spring with a defined stiffness and linked to the ground. The last simulation considers a change in the geometry to appreciate the influence of the microgeometry.

Results of this latest strategy have been considered in the following. In fact, the presence of microgeometry together with the influence of the shafts have been proved to be mandatory to correctly grasp the correct behavior of the gear meshing despite the consequent high computational effort. Then, a comparison between different numbers of simulation increments has been made to define the best solution to guarantee accurate results and the minimum computational time.

3. Results and conclusions

The primary outcome of this study was the development of a comprehensive FE procedure to thoroughly investigate the fatigue behavior of gear pairs in high-performance vehicles. The proposed model effectively identified the distinct contributions of each transmission component and emphasized the significant impact of microgeometry. Additionally, the analysis revealed the influence of simulation increments on the results, leading to the adoption of an optimal strategy. The most accurate simulation incorporated microgeometry, which enhanced the identification of the stress zones on the gear teeth. This accuracy highlighted the centering effect, which is crucial for gear meshing. Figure 1a shows the maximum principal value of stress distribution along the gear teeth. The results show clear differentiation in the areas of maximum stress of three contacting theet Note that, thanks to the presence of microgeometry, the maximum stress in the central thoot is perfectly centered along the tooth flank. Figure 1b illustrates the safety factor distribution along the gear teeth following the Dang Van multi-axial criterion.

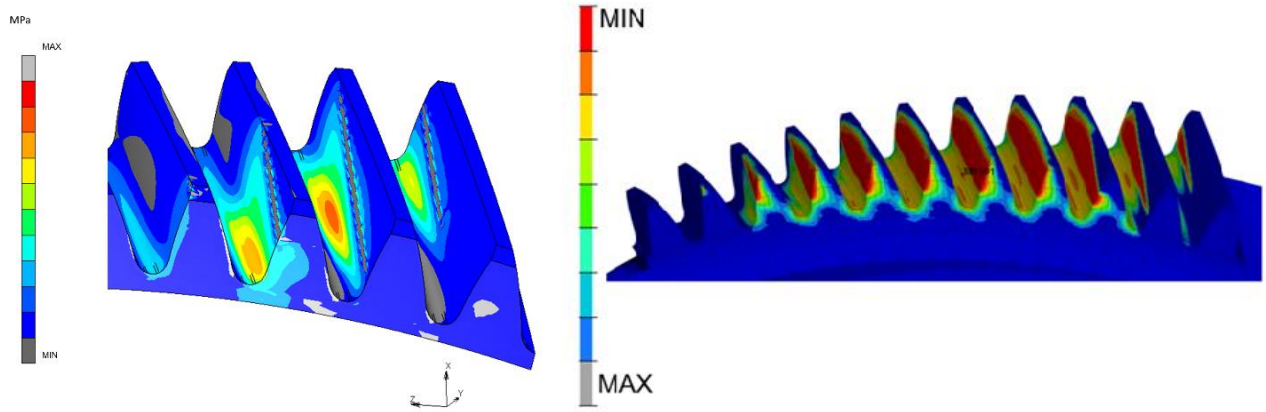

(a) (b)

Figure1: (a) Maximum principal value of stress distribution; (b) Dang Van safety factor distribution.

4. References

[1] T.J. Lisle, B.A. Shaw, R.C. Frazer (2017). External spur gear root bending stress: a comparison of iso 6336:2006, agma 2101-d04. *Ansys Finite Element analysis and strain gauge techniques, Mechanism and Machine Theory*, **111**, 1-9.

[2] Y.A. Tesfahunegn, F. Rosa, C. Gorla (2010). The effects of the shape of tooth profile modifications on the transmission error, bending, and contact stress of spur gears. *Journal of Mechanical Engineering Science*, **224,** 1749-1758.

[3] Z. Chena, M. Zenga, A. Fuentes-Aznar (2020). Computerized design, simulation of meshing and stress analysis of pure rolling cylindrical helical gear drives with variable helix angle. *Mechanism and Machine Theory*, **153**, 103962

[4] Y. Chen, C. Tsay (2002). Stress analysis of a helical gear set with localized bearing contact. *Finite Elements in Analysis and Design*, **38**, 707-723.

A FINITE ELEMENT METHODOLOGY FOR STRUCTURAL ASSESSMENT OF A GEAR WITH NITRIDING TREATMENT

F. Manni[1], V. Mangeruga[1], S. Messina[1], M. Giacopini[1]
[1] Department of Engineering "Enzo Ferrari" (DIEF), University of Modena and Reggio Emilia, Modena, Italy

1. Introduction

The transmission of power through components such as gears is a topic of great interest in engineering. The need to manufacture high-performance components requires enhancing their characteristics through surface treatments, such as nitriding. These conditionings increase hardness and create beneficial residual stress, leading to improved fatigue resistance. On one hand, surface residual stresses are typically pursued to be compressive and advantageous for surface durability. On the other hand, unavoidable tensile stresses are generated deeper in the component jeopardizing the stress state of these internal regions. As a result of this, during gear meshing, the damage may not nucleate on the surface anymore, which now benefits from favorable conditions.

Specifically, this contribution considers a particular load case in which the wheel is subjected to an anomalous overload. Following the nitriding treatment and the residual stresses released by this process it is not clear how possible local plasticizations generated by the overload can arise on the surface or on the substrate and how the fatigue resistance of the wheel can consequently be modified. The objective of this work is therefore to understand the impact of applying a plasticizing overload on the residual stress state created by nitriding. First, the nitriding surface treatment [1,2] is analysed to evaluate the residual stresses within the component. Then, a reliable strategy is proposed to impose these stresses in a Finite Element Method (FEM) model. Subsequently, the meshing of two straight-toothed gears under heavy (overload) conditions is simulated. Different meshing instants are considered, the results of the numerical forecasts are analysed the changes in the initial residual stress given by the nitriding process are highlighted.

2. Materials and methods

As a starting point, experimental analyses have been conducted on a transversal section of the gear to measure the hardness of the treated zones, from the surface to 1.55 mm towards the inside of the component. Then, these data have been correlated with the induced distortions [3,4] and, consequently, the generated stress state. This stress state has been reproduced in a FEM model to retrieve the structural behavior of the entire component. In particular, the distortions have been artificially simulated using a thermal-structural model. A normalized temperature and a consequently tuned coefficient of thermal expansion have been adopted. A numerical procedure has been developed to accurately retrieve the actual geometry of the gear after the application of this artificial thermal field. The method considered the initial positions of the nodes, their displacement caused by thermal deformation, and the target configuration needed to replicate the real geometry of the component. The meshing between two treated gears has been then simulated under the overload condition considering two different scenarios. First, the configuration capable of maximizing the distance between the contact area of the gear tooth and the root has been set up. This approach has been based on the hypothesis that the stresses capable of compromising the integrity of the tooth are induced by

its bending. However, as will be explained later, it has been necessary to analyze a second instant of the meshing cycle in which the whole meshing load is transmitted by a single pair of teeth thus possibly maximizing the damage induced by the overload.

3. Results and conclusions

Figure 1 shows the output of the simulations. Figures 1(a) and 1(d) display contact status in both configurations. Figure 1(a) refers to the first case. It can be observed that the teeth contact is in a position capable to maximize the lever arm between the contact area and the tooth root. However, the meshing is achieved through contact between two pairs of teeth. This phenomenon distributes the load between the two teeth. As a result, this configuration might not be the most critical one for the meshing. Other output parameters should be considered, such as plastic strain and the minimum principal value of stress registered after the overload removal, as shown in Figures 1(b) and 1(c) respectively. It is evident that the plastic strain is extremely limited. Indeed, the residual stress given by the nitriding process does not appear to be compromised, as depicted in Figure 1(c). Thus, a second configuration is analyzed. The simulated instant in this case has been identified by limiting the search for the maximum lever arm to cases where only one pair of tooth is engaged in meshing, as shown in Figure 1(d). Figure 1(e) shows the plasticized zone which is now significantly more extensive compared to the first case and is located precisely at the boundary between the treated and untreated areas. In addition, Figure 1(f) shows that the stress state given by the nitriding process has been significantly altered, particularly in the area just above the tooth root, where we observe a decrease in compressive stresses making it a preferential zone for crack initiation.

The methodology developed has thus proven effective in capturing the stress state of a gear subjected to surface nitriding treatment and subjected to overload. In the future, the entire meshing cycle will be simulated to provide a complete overview of the loading cycle of the gear.

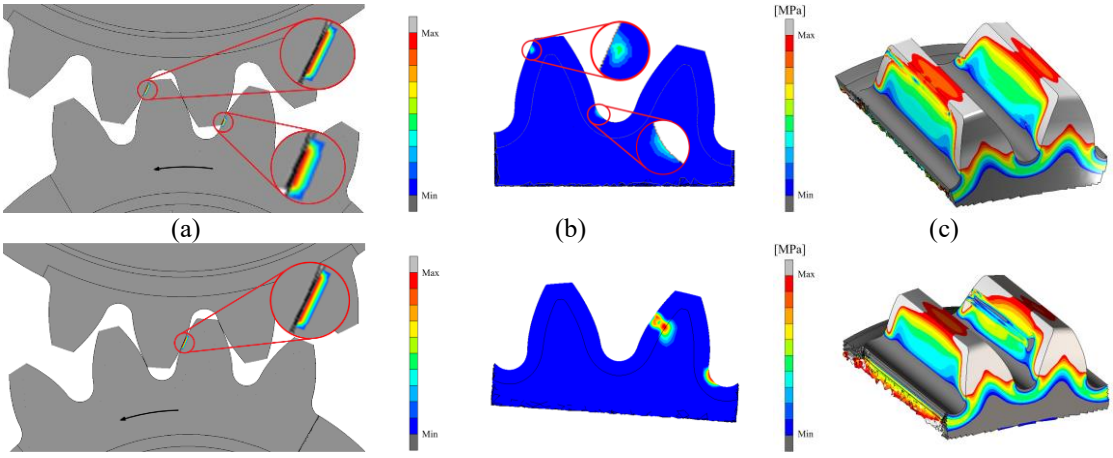

Fig. 1. Output of the simulations: (a), (d) contact status; (b), (e) equivalent plastic strain; (c), (f) minimum principal value of stress.

4. References

[1] D. Pye. Practical (2003). Nitriding and Ferritic Nitrocarburizing. ASM International.

[2] J. Dulcy L. Torchane, P. Bilger and M. Gantois (1996). Control of Iron Nitride Layers Growth Kinetics in the Binary Fe-N System, *Metallurgical and Materials Transactions A*, **27**, 1823-1835.

[3] G. Fallotb S. Jegoua and L. Barrallier (2018). Gaseous nitriding behaviour of 33CrMoV12-9 steel: Evolution of the grain boundaries precipitation and influence on residual stress development. *Surface and Coatings Technology*, **339**, 78-90.

[4] M. Kovačič J. Vižintin B. Podgornik and V. Leskovšek (2011). Residual stress field analysis and prediction in nitrided tool steel. *Materials and Manufacturing Processes*, **26**, 1097-1103.

CYCLIC STRAIN RESPONSES AND CRACK GROWTH IN FE-MN-C TWIP STEEL UNDER STRESS-AMPLITUDE CONTROLLED FATIGUE LOADING

Lihe QIAN, Cheng ZHENG and Jiangying MENG
State Key Laboratory of Metastable Materials Science and Technology,
Yanshan University, China

1. Introduction

Twinning-induced plasticity (TWIP) steels exhibit high strength, large ductility, and superior toughness at room temperature, stemming from the dynamic formation of mechanical twins during plastic deformation [1]. There are many potential applications of twinning-induced plasticity (TWIP) steels in vehicles, such as shafts, suspension swing arms, etc. TWIP steels for such applications are inevitably subjected to cyclic loading and easily cause fatigue failure in practical service. Therefore, a clear understanding of the fatigue property and failure mechanisms of TWIP steels is critical important for effective design of vehicle structures.

Studies show that the addition of element Al to Fe-Mn-C TWIP steels can increase stacking fault energy (SFE), delaying twinning nucleation and leading to the initiation of microcracks before necking [2]. Element Al can also suppress dynamic strain aging (DSA). Moreover, the addition of Al retards or alleviates hydrogen-induced delayed fracture as well [3]. Alternatively, it was reported that Al addition also affects the cyclic deformation response and fatigue mechanism of TWIP steel, though in a complex way [4], related to the strain amplitude and loading environment. Under atmospheric condition, the low-cycle fatigue (LCF) lifetime of Fe–Mn-C TWIP steel at higher strain amplitudes was worsened with Al addition, which was attributed to the suppressed deformation twinning and decreased cyclic deformation ductility. In contrast, at lower strain amplitudes, the LCF lifetime was enhanced due to Al addition. Furthermore, with the addition of Al, the Fe-Mn-C TWIP steel exhibits a decreased threshold for fatigue crack propagation [5], and enhanced cyclic softening as well as decreased LCF lifetime at both high and low strain amplitudes [6].

However, the fatigue properties of Fe-Mn-C TWIP steel with or without addition of Al under stress amplitude control are not clear. In the present work, the cyclic deformation responses, fatigue lifetimes and fatigue crack growth behavior in a Fe-Mn-C and a Fe-Mn-C-Al steel are comparatively investigated under constant stress amplitude control to clarify the effect of alloying element Al.

Experimental procedure

The steels investigated are Fe-22Mn-0.6C and Fe-22Mn-0.6C-3Al (wt. %), hereafter 0Al steel and 3Al steel, respectively. The cold-rolled plates were annealed at 950 ºC for 30 min followed by water quenching. The austenite grain sizes are ~50 μm for both steels. The yield strength, tensile strength and elongation of 0Al steel are 291, 937 and 83%, while those of 3Al steel are 343, 716 and 67%, respectively. Dog-bone plate specimens, 9 mm×8 mm×3 mm in parallel section, were prepared for conducting low-cycle fatigue (LCF) tests. Symmetrical tension-compression LCF tests were performed under stress amplitude control at 0.1Hz at room temperature. An axial extensometer with

a gauge length of 5 mm was used to measure strain. Fatigue crack length was measured using a microscope, and full-field strain distributions were in-situ acquired with digital image correlation (DIC) method. Cross-sectional microstructures of fatigue-failed specimens were examined using EBSD and TEM. Cyclic strain responses and crack growth behavior are analyzed based on crack tip region deformation field and evolved microstructure.

3. Results and conclusions

Both steels exhibit initial cyclic hardening, then cyclic saturation, followed by cyclic softening until fracture. As compared with 0Al steel, 3Al steel is more cyclically softened (Fig. 1a), and shows larger accumulative plastic strain and fatigue damage. Accordingly, at each stress amplitude, 3Al steel shows decreased fatigue lifetime ad increased fatigue crack growth rate (Fig. 1b).

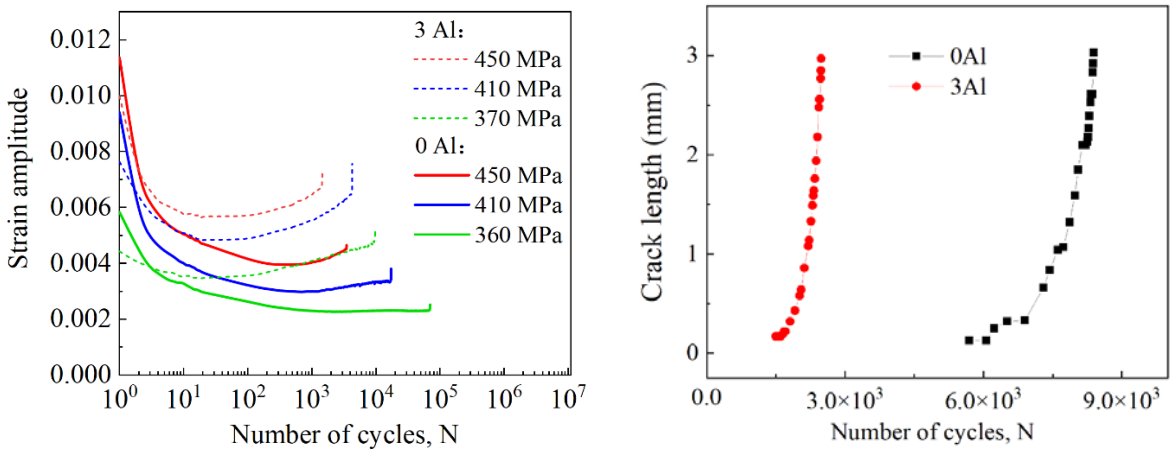

(a) (b)

Fig. 1. (a) Strain amplitude versus number of cycles fatigued at three stress amplitudes; (b) fatigue crack length versus number of cycles at a stress amplitude of 410 MPa.

4. Acknowledgements

This work was supported by the National Natural Science Foundation of China (No. 52271119).

5. References

[1] M. Madivala, A. Schwedt, S.L Wong., et al. (2018). Temperature dependent strain hardening and fracture behavior of TWIP steel. *Int. J. Plast.*, 104, 80–103.

[2] M.C. Jo, A. Zargaran, et al. (2021). Effects of Al addition on tensile properties of partially recrystallized austenitic TRIP/TWIP steels. *Mater. Sci. Eng. A*, 806,140823.

[3] K.T. Park, K.G. Jin, S.H. Han, et al. (2010). Stacking fault energy and plastic deformation of fully austenitic high manganese steels: effect of Al addition. *Mater. Sci. Eng. A*, 527, 3651–61.

[4] S.W. Song, Y.J. Kwon, T. Lee, et al. (2016). Effect of Al addition on low-cycle fatigue properties of hydrogen-charged high-Mn TWIP steels. *Mater. Sci. Eng. A*, 677, 421–30.

[5] P. Ma, L. Qian, J. Meng, et al. (2015). Influence of Al on the fatigue crack growth behavior of Fe-22Mn-(3Al)-0.6C TWIP steels. *Mater. Sci. Eng. A*, 645, 136–41.

[6] P. Guo, L. Qian, J. Meng, S. Liu, F. Zhang (2024). Effect of Al on the low cycle fatigue deformation behavior and microstructure evolution of Fe–22Mn-0.6C TWIP steel. *J. Mater. Res. Tech.*, 30, 2086–2098.

EVALUATION OF FATIGUE DAMAGE DEVELOPMENT IN POWER ENGINEERING STEEL AFTER LONG TIME EXPLOITATION SUPPORTED BY DIC TECHNIQUE

Z.L. Kowalewski[1], M. Kopec[1], A. Brodecki[1]
[1] Institute of Fundamental Technological Research Polish Academy of Sciences, Warsaw, Poland

1. Introduction

The exploitation loads and associated with them microstructural changes occurring due to high-temperature exposure significantly accelerate the development of damage dynamics [1]. Thus, this research aimed to compare the behaviour of long-time degradation of 10CrMo9-10 (10H2M) power plant steel to that of the same material in the as-received state by using different experimental and analytical approaches. The specimens machined from the as-received steel and the same material after exploitation for 280 000h at the temperature of 540°C were subjected to fatigue that was simultaneously monitored by means of the Digital Image Correlation (DIC) technique.

2. Materials and methods

The fatigue testing was performed on wire-cut specimens made of the 10H2M steel pipe in the as-received and exploited states (280 000h at the temperature of 540°C and internal pressure of 2.9 MPa).The standard tensile tests were firstly carried out at the strain rate equal to 2×10^{-4} s^{-1} in order to assess the mechanical properties of both states of the steel considered. Fatigue loading conditions were established based on these tests and mechanical parameters examined. Both, uniaxial tensile and fatigue tests were executed on the MTS 858 testing machine. The fatigue tests were stress controlled with $(\sigma_{max}- \sigma_{min})/2$ mean stress level and stress asymmetry coefficient R=0, frequency of 20 Hz, and stress amplitude in the range from 330 MPa to 430 MPa. The range of fatigue stress amplitude values was established based on the conventional yield strength $R_{0.2}$ determined on the basis of the uniaxial tensile test. The strain values necessary for the hysteresis loop determination were recorded by the conventional MTS extensometer with a gauge length of 25 mm. The fatigue development was monitored by DIC Aramis 12M equipped with lenses of a total focal length of 75 mm and calibration settings appropriate to the measuring area equal to 170x156 mm. The calibration was performed before tests using a certified GOM calibration plate. Aramis software enabled to capture DIC images automatically at σ_{max} after each of 1000 fatigue cycles.

3. Results and conclusions

The fatigue tests carried out on both material types revealed notable differences in mechanical response. The exploited material tested at the same stress amplitude was able to transfer only half of the number of cycles in comparison to the as-received one. Depending on the stress amplitude, the fatigue lifetime of the exploited material decreased from 300% to 400%. Long-term service leads to a significant decrease in the fatigue life of pipes and degradation of properties is mostly attributed to the accumulation of defects in the material during operation [2-3]. The fatigue damage development was monitored during fatigue by using DIC technique. The representative images of strain distribution for both types of steel in question were presented, and subsequently, compared for the

stress amplitude equal to 400 MPa, Fig. 1. Since the specimen geometry enforces a damage to be developed in its middle section, the effective gauge for DIC observations was significantly reduced after initial tests, as could be observed in Figure 1a-b. It should be highlighted, that at the higher stress amplitude considered, the strain recordings from the specimen surface were as high as 18%, thus, the unified strain scale was inconvenient to apply. It is easy to see, that a different strain distributions were found for both states of the material, and as a consequence, the fatigue lifetime of the exploited material was about two times lower than that of the as-received one. It should be mentioned, that for the exploited material, the significant changes in strain distribution, reflecting damage development, were found in the middle section of the specimen when half of its fatigue life was reached, Fig.1a. Subsequent cycles led to the continuous development of damage in the central region of the specimen and its failure after 2.1×10^5 cycles. On the other hand, the as-received specimen exhibited damage localization shortly before the failure as the first strain concertation area was found after 5×10^5 cycles and the specimen fractured after 5.5×10^5 cycles, Fig.1b.
Comparison of the DIC images for the material in as-received state to those obtained for the exploited one clearly identifies differences in damage mechanisms. The results clearly indicate, that DIC is a powerful tool for strain localization analysis during fatigue and identification of damage mechanisms, especially at higher magnitudes of stress amplitude.

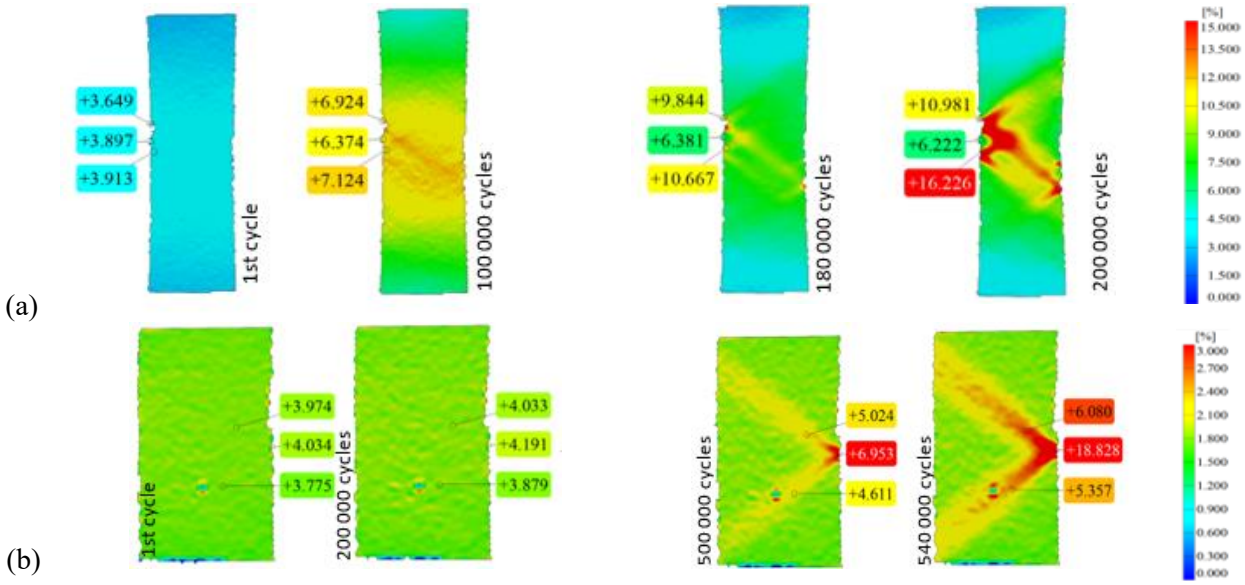

Fig. 3. DIC measurements performed on the exploited (a) and as-received (b) material for the stress amplitude equal to 400 MPa.

4. Acknowledgement

This research was funded in part by National Science Centre, Poland under grant agreement No. 2023/51/B/ST8/01751.

5. References

[1] Kopec M., Kukla D., Brodecki A., Kowalewski Z.L., Effect of high temperature exposure on the fatigue damage development of X10CrMoVNb9-1 steel for power plant pipes, Int. J. Press. Vessels Pip., 2021, 189, 104282

[2] Brodecki A., Kopec M., Kowalewski Z.L., Monitoring of fatigue damage development in as-received and exploited 10CrMo9-10 power engineering steel supported by Digital Image Correlation, Int. J. Press. Vessels Pip., 2023, 202, 104889

[3] Kopec M., Brodecki A., Kukla D., Kowalewski Z.L. Suitability of DIC and ESPI optical methods for monitoring fatigue damage development in X10CrMoVNb9-1 power engineering steel, Arch. Civ. Mech. Eng. 2021, 21 (4), 167

Machine design and prototyping

6-11 July 2025 ICEM21 Bologna
21st International Conference on EXPERIMENTAL MECHANICS

DEVELOPMENT AND LOCOMOTION EXPERIMENT OF INCHWORM ROBOT FOR MOBILE ADDITIVE MANUFACTURING

***K. Jimbo*[1]**
[1] *Department of Advanced Machinery Engineering, School of Engineering, Tokyo Denki University, Tokyo, Japan*

1. Introduction

Material Extrusion (MEX) is one of the methods of Additive Manufacturing (AM), in which material is extruded from a nozzle and layered. There are MEX type fabrication machines that have improved flexibility to produce complex parts and enable support-free fabrication by attaching a nozzle to the end of a robot arm [1]. There is also a type of AM machine that moves around to fabricate objects. Because this mobile AM is mainly used in the construction field today. In addition, researches have also been carried out into methods of using multiple machines simultaneously to improve productivity [2]. However, these are typically wheeled machines, which make it difficult to move over complex and delicate structures.

The author has proposed using the mechanism of an inchworm robot for the fabrication and locomotion of a mobile AM method [3]. The goal is to develop a mobile AM machine with a simple mechanism that uses the same link system for both fabrication and locomotion. Conventional inchworm robots use pneumatic pressure or electromagnets to hold their feet to the surface on which they move. However, these methods are unsuitable for movement over fabricated structures. To address this issue, previous research has conducted simulations and confirmed that it is possible to perform locomotion and fabrication by calculating the center of gravity (COG) of a moving robot and ensuring that the COG is always on the supporting leg. The purpose of this research is to develop an inchworm robot for use in mobile AM and to investigate its characteristics through the locomotion experiment.

2. Development and locomotion experiment of inchworm robot

The schematic diagram of the inchworm robot and a photo of the machine developed for the motion experiment are shown in Fig. 1. The characteristics of the machine are listed in Table 1.

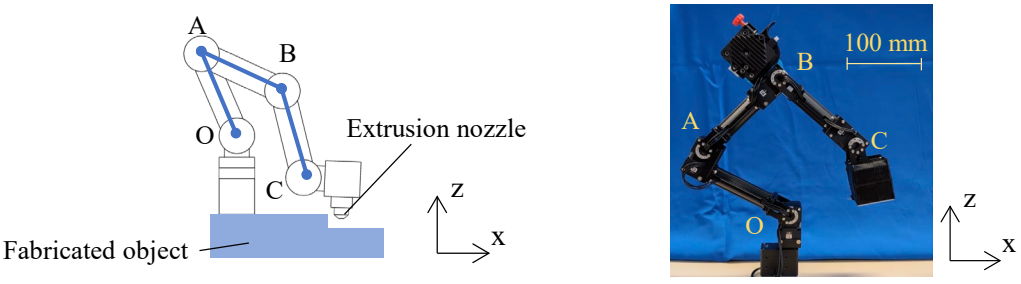

Fig. 1. Schematic of the inchworm robot for mobile AM (left) and the photo of the developed machine (right)

Table 1. Size and weight of each part of the inchworm robot

Link length	OA: 130 mm, AB: 124 mm, BC: 123 mm
Link weight	OA: 50 g, AB: 50 g, BC: 50 g
Node weight	O: 200 g, A: 100 g, B: 350 g, C: 100 g

Node B is designed to be equipped with a filament extruder. A servomotor (ROBOTIS, DYNAMIXEL XM-430) was used for driving. The body moves during locomotion through the following sequence:
(1) The front leg is raised by 30 mm and moved forward by 40 mm, then lowered by 30 mm.
(2) The posture is adjusted so that the COG is positioned above the front legs.
(3) The rear leg is raised and moved forward, then lowered.
(4) The posture is adjusted so that the COG is positioned above the rear legs.
The COG during operation was calculated using Python, and the motor was controlled using the control software (dynamixel SDK).

The photos of each posture during locomotion are shown in Fig. 2. In each posture, the COG was successfully positioned above the supporting leg, confirming that the robot could maintain stability. However, if the angular acceleration of the motors was too high, the robot would occasionally tip over during locomotion. It was also observed that the weight of the equipment influenced the control of the positions of the front and rear legs, leading to positional errors.

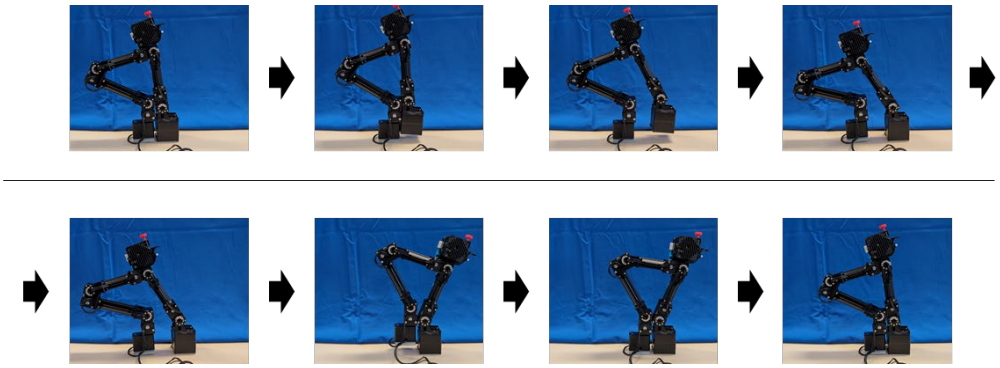

Fig. 2. Photos of each posture in the motion experiment

3. Conclusions

The inchworm robot for mobile AM was developed and experiments were conducted to evaluate its locomotion. The stability of each posture during locomotion was confirmed; however, it was found that precise motor control is essential for stable operation.

4. Acknowledgements

This work is funded by JSPS KAKENHI grant number 23K13237.

5. References

[1] A. Shah (2022). Emerging trends in robotic aided additive manufacturing, *Mater. Today*, **62** (113), 17231−7237.

[2] X. Zhang, M. Li, J. H. Lim, Y. Weng, Y. W. D. Tay, H. Pham, Q. Pham (2018). Large-scale 3D printing by a team of mobile robots, *Automat. Constr.,* **95**, 98−106.

[3] K. Jimbo (2024). Study on step motion of inchworm robot for mobile additive manufacturing, *The 43rd JSST Annual International Conference on Simulation Technology*, 84−88.

MULTIVARIABLE REGRESSION MODELS BASED ON NUMERICAL EXTENDED ANALYSES FOR DESIGN PURPOSES

D. Croccolo[1], M. De Agostinis[1], S. Fini[1], F. Livera[2], M. Mele[1], G. Olmi[1], G. Piraccini[1], N. Vincenzi[2]

[1] Department of Industrial Engineering (DIN), University of Bologna, Bologna, Italy
[2] Bucci Automations S.p.A. Division, Via Granarolo 167, 48018 Faenza RA, Italy

1. Introduction

Nowadays, with the large spread of performing computational devices, engineering has witnessed a growing adoption of numerical methods for solving complex problems, complementing or replacing traditional analytical approaches. While analytical methods can be regarded as a rigorous way to model and analyze physical systems, they are often limited by the mathematical complexity arising when applied to the actual geometries or features of real components. Problems involving irregular non-beam-like geometries, nonlinear material properties, or variable boundary conditions frequently make it unfeasible or completely impossible to work out closed-form analytical solutions.

Numerical approaches, such as the Finite Element Method (FEM), offer a flexible and powerful alternative and allow for approximate but accurate solutions for even the most complex components or devices. Their versatility makes them particularly suitable for practical applications where models can efficiently incorporate geometric and physical details that would be difficult to handle analytically [1]. A specific example of exploiting numerical methods for design purposes is the adoption of multivariable regression models for stress estimation in mechanical components. These models, based on the statistical analysis of experimental and/or numerical data, enable the correlation of independent variables with the stresses generated within a functional part and its expected response.

Finally, the validation of the obtained estimates can be carried out through an experimental approach. By fabricating samples with known geometry and applying strain gauges to their surfaces, it is possible to compare the results obtained from both the mathematical regression model and/or the numerical FEM model with those derived from the conducted experimental tests. In particular, in this study, strain gauges have been applied to the external surface of elastic collets used in automatic bar feeders. The aim was to experimentally validate the stress distribution obtained from the FEM model. This direct measurement provided a crucial comparison, ensuring that the numerical approach accurately captures the real mechanical behaviour of the component.

This synergy between numerical and statistical approaches represents a significant step forward in solving complex engineering problems. While analytical solutions, once obtained, provide immediate and often generalizable results, numerical and statistical regression methods offer flexibility and adaptability, even in the presence of complex geometries, discretization, or modelling errors. In addition, multivariable regression models make it possible to easily address inverse problems that are particularly common in the framework of mechanical design. In particular, they enable the proper determination of the design options, namely the geometries, which accomplish the specifications, e.g., the stress target value. As a further step, optimizations, as well as life or duration predictions, can finally be run.

A possible drawback is that regression models introduce some challenges, such as the need for sufficiently large and representative datasets, including the risk of overfitting or underestimating nonlinear effects. In this context, the present study aims to analyze and justify the adoption of numerical and numerical-regression approaches, with particular emphasis on multivariable linear regression models, for stress estimation in mechanical components. The study also includes an experimental validation through strain gauges applied to elastic collets in automatic bar feeders to compare the stress distribution with the FEM results.

2. Materials and methods

The present study aims to evaluate the effect of the combination of 8 geometrical parameters (from A to H) on the maximum value of the equivalent stress inside a mechanical component. This maximum value always occurs at the same location. A proper set of FEM simulations to combine every level of the chosen independent factors has been planned, following the DOE (Design Of Elements) technique of Full Factorial Design [2] [3].

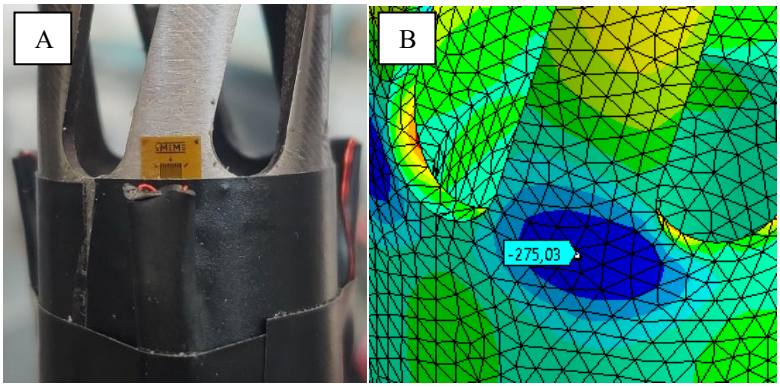

Figure 1: (A) Strain gauge applied on the external surface of an elastic collet for automatic bar feeders and (B) stress level estimated by FEM simulation

Additionally, to experimentally validate the FEM results, an experimental setup was implemented using strain gauges applied to elastic clamps as shown in Fig. 1(A). The strain gauges were bonded at critical points identified through FEM simulations, highlighted in Fig. 1(B), to ensure direct measurement of stress variations. The collected strain data were then converted into stress values using the material's known elastic properties and compared with the FEM predictions. This methodology makes it possible to achieve a direct correlation between numerical and experimental results, improving the reliability of the model.

3. Results and conclusions

The chosen regression model currently involves 64 independent variables and 68 regression points: together with main effects, all the possible combinations of five factors have also been included, in order to consider the effects of correlations between different variables' values on the resulting stress $\sigma = Y_i$. This structure of the model has been optimized, considering the high impact of multi-factor interactions on the response of the studied component. The resulting model is the following:

$$Y_i = a_0 + a_1 \cdot ABCDE + \cdots + a_{64} \cdot DEFGH$$

This regression model is characterized by a well acceptable adjusted coefficient of determination $R^2_{adj} = 0.96$ [4]. Percentage errors, as differences between the model's estimates and their corresponding FEM valuated values, have also been investigated and are under 10% as shown in Fig. 2. However, other alternative models and regression approaches are also possible and are currently being investigated.

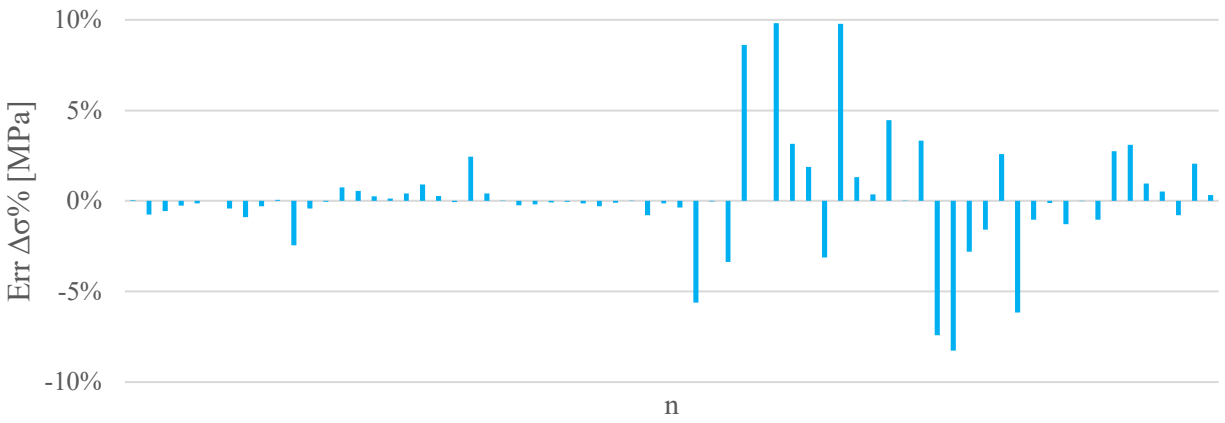

Fig. 2: Percentage errors between the regression-estimated and FEM-computed stress errors for different geometrical combinations

The experimental validation using strain gauges further confirmed the accuracy of the numerical model. The stress values obtained from experimental measurements showed a maximum deviation of less than 8% compared to the FEM predictions, providing proof of the high reliability of the developed FEM models. This result highlights the reliability of the numerical model in predicting the mechanical behaviour of the studied component and confirms the importance of combining numerical simulations with experimental verification to enhance the robustness of engineering analyses.

5. References

[1] G. Niemann, H. Winter and B.-R. Höhn, Manuale degli organi delle macchine, Tecniche Nuove, 2006.

[2] A. Rafidah, A. Nurulhuda, A. Azrina, Y. Suhaila, I. Anwar and R. Syafiq, “Comparison Design of Experiment (DOE): Taguchi Method and Full Factorial Design in Surface Roughness,” *Applied Mechanics and Materials,* vol. 660, pp. 275-279, 2014.

[3] M. Tanco, E. Viles and P. Lourdes, “Comparing Different Approaches for Design of Experiments (DoE),” in *World Congress on Engineering*, London, UK, 2008.

[4] D. C. Montgomery, E. A. Peck and G. G. Vining, Introduction to Linear Regression Analysis, 5th ed., Hoboken: Wiley, 2012, pp. 226-227.

Joints and Fasteners

LOW TEMPERATURE AND PRECISION BONDING TECHNOLOGY USING SPREAD LASER BEAM FOR THIN LENS PACKAGE

Eunhye Lee[1,2], Jeehoo Na[1], Min-Su Kim[1], Byeong-Kwon Ju[2], and Tae-Ik Lee[1,†]

[1] Advanced Packaging Integration Center (APIC), Regional Industry Innovation Department (Growth Engine), Korea Institute of Industrial Technology, Incheon 21999, Republic of Korea
[2] Display and Nanosystem Lab, Department of Electrical Engineering, Korea University, Seoul 02841, Korea

[†]Email: tilee@kitech.re.kr

1. Introduction

The advancement of electronic devices has driven the miniaturization of electronic components, leading to the progressive thinning of optical components used in such devices. Lenses are critical components in various applications, including smartphones, digital cameras, security cameras, advanced driver-assistance systems (ADAS) in vehicles, drones, augmented reality (AR), and virtual reality (VR) devices [1]. This trend highlights the increasing necessity for technologies capable of bonding lenses with precision and without deformation. Notably, high-performance camera lenses require greater reliability and highly precise bonding techniques. In camera modules, lens components are accompanied by spacers, which are positioned between lenses to prevent light reflection and scattering within the camera. Spacers are typically coated with carbon material, providing light-blocking capabilities and preventing electrostatic discharge. Epoxy, as a conventional adhesive, is widely used for bonding optical components [2]. However, bonding lenses and spacers using conventional adhesives such as epoxy poses several challenges. First, the thickness increases, making it difficult to apply to miniaturized products. Second, controlling the quantity is difficult, leading to reduced uniformity and diminished precision due to deformations or damage occurring during the bonding process. Third, due to its inherent hygroscopic properties, epoxy reduces reliability in high-temperature and humid environments [3]. Deformations or damages occurring during the bonding process can negatively affect lens performance [4]. Therefore, the development of technologies that can bond accurately and quickly while minimizing thermal damage is of utmost importance.
This study developed a precise bonding technique using a spread laser beam to minimize thermal damage and thickness variations when bonding multiple optical components within lenses. The application of polymer laser bonding significantly improved bonding quality and effectively prevented optical distortion at the lenses. Reliability was evaluated through temperature and humidity tests, demonstrating the superior reliability of laser bonding compared to conventional adhesives. Furthermore, shear testing confirmed the excellent bonding strength of the laser-bonded interfaces.

2. Materials and methods

In this study, polycarbonate(PC) was utilized to fabricate the lenses. The base material employed was polyethylene terephthalate(PET), and a donut-shaped spacer coated with carbon black was produced. To compare with laser bonding, a comparison sample was prepared using epoxy. The

epoxy used was CEMEDINE's EP330 product. The epoxy bonding was performed by applying a thin layer of epoxy to both surfaces of the spacer, placing it between the PC lenses and fixing it. After fixation, it was cured for 40 minutes. For laser bonding, the spacer was placed between the PC lenses and stabilized with a vacuum pack. After packaging, a fiber laser(continuous wave ytterbium) with a wavelength of 1064 nm was used to irradiate the laser after setting an area of 10 mm X 10 mm. The laser output and exposure time were conducted under various conditions to establish optimal parameters. To evaluate reliability, a constant temperature and humidity test was conducted, set at 85 degrees and 85% humidity. The thickness changes between the laser bonding and epoxy bonding were compared using scanning electron microscopy (SEM), and the bonding strength was assessed through shear testing.

3. Results and conclusions

Fig. 1(a) shows the process of laser bonding, and Fig. 1(b) shows the thickness variation of the laser and epoxy after bonding. Fig.1 (c) shows the bonding mechanism. When comparing the thickness after joining, the laser bonding exhibited negligible changes in thickness, whereas in the case of epoxy bonding, the presence of an adhesive layer resulted in an increase in thickness. Even after temperature and humidity testing, laser bonding proved to have superior bond strength to epoxy bonding. Laser bonding is capable of achieving thinner and more precise joints compared to epoxy bonding.

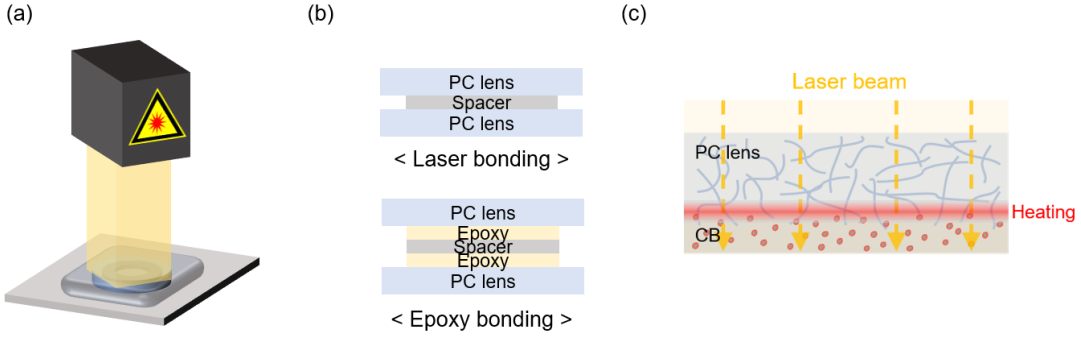

Fig. 1. (a) Laser bonding process (b) Comparison of thickness variations in epoxy bonding and laser bonding (c) Bonding mechanism

4. Acknowledgements

This research was supported by the National Research Foundation (NRF) funded by the Korean government (MSIT) (No. RS-2024-00423772).

5. References

[1] H. Kim, J. Lee, S.-M Hwang, S. Cha. (2016). Embedded camera module for automotive camera system. In *2016 Pan Pacific Microelectronics Symposium (Pan Pacific) IEEE*, pp. 1-7.

[2] J.G. Liu, B.M. Andersen, E.E. Bergmann, S.K. Fairchild (2000). Epoxy adhesives for optical element attachment in planar passive optical components. *2000 Proceedings. 50th Electronic Components and Technology Conference. IEEE*, 975-980.

[3] He Y., & Kabiri, M. (2022). In-situ characterization of moisture absorption and hygroscopic swelling of an epoxy molding compound for electronic packaging. *Journal of Thermal Analysis and Calorimetry*, **147(10)**, 5667-5675.

[4] Sidney Ray. (2012). Camera lenses. In *The Manual of Photography*, pp. 175-198.

STUDY OF THE CORROSION-INDUCED DEGRADATION OF AERONAUTICAL ALUMINUM ALLOYS 2024 AND 2198 RIVETED SHEETS

C. M. Charalampidou[1], K. Bailas[2], P. Papanikos[2], N. D. Alexopoulos[1]
[1] Research Unit of Advanced Materials, Department of Financial Engineering, University of the Aegean, Chios, Greece
[2] Department of Product and Systems Design Engineering, University of the Aegean, Syros, Greece

1. Introduction

Aircraft is composed of numerous small structural parts / components of different geometries which are assembled by various mechanical techniques to form large structures. The most common methods for joining such structural parts is through mechanical fasteners, i.e., rivets, bolts, and nuts. Other connection methods include the use of adhesives or a combination of adhesives and mechanical fasteners. Rivets, in particular, are extensively used to secure components like fuselage frames to beams. They offer several advantages such as time savings due to the easy and quick installation, cost efficiency, and superior flexibility and strength compared to adhesives [1].

The majority of the airframe consists of aluminium alloys and composite materials. During operation, numerous structural components of the aircraft are subjected to both static and dynamic loads. The mechanical strength of a riveted joint is influenced by several factors, including the rivet hole diameter, material properties, type of mechanical loading, and the design or connection methods [2-4]. Nevertheless, rivet holes tend to weaken the joint by creating areas of high stress concentration [5-6]. Failures in riveted joints can result from residual stresses introduced during the manufacturing process [7-8]. Nevertheless, multiple studies [9-11] have demonstrated that the machining quality of joint holes has a more pronounced impact on fatigue life than residual stresses.

Corrosion significantly affects the lifespan of an aircraft, particularly under loading conditions such as fatigue. According to Kermanidis et al. [13] and Charalampidou et al. [14] corrosion-induced fatigue life degradation is primarily due to the elimination of the fatigue crack initiation phase, caused by the corrosion-induced formation of pits / holes as well as by localized embrittlement due to hydrogen diffusion. Pitting corrosion typically originates from surface defects or discontinuities. Machining processes for holes and joints can create such surface imperfections, accelerating corrosion propagation. Therefore, given that many components of aircraft structures are still joined by rivets rather than welds, it is crucial to thoroughly study the corrosion mechanisms associated with riveted connections.

2. Materials and methods

The materials used were wrought aeronautical aluminium alloy 2024-T3 and 2198-T8, in 3.2 mm nominal thickness. Initially, rectangular samples (150 mm × 19 mm) were cut from the sheets through waterjet. Later, the specimens were peeled off from the sheet and smoothed on their side surfaces with the use of lathe. Holes of 4.76 mm diameter were drilled on the large flat surfaces (upper and lower) using a vertical stationary milling drilling machine. Prior to corrosion exposure, all samples were cleaned with acetone. Four (4) different cases were performed in the present experimental investigation, to simulate all possible corrosion damage cases next to the damage of the anti-corrosion coating of aircraft joints:

1. corrosion damage on all surfaces including the open-hole surface,

2. corrosion exposure on the specimens' surfaces excepting the open-hole surface,
3. corrosion damage only inside the open-hole, and
4. corrosion exposure only on the specimens' small side-surfaces (thickness area).

The experimental test results were used as validation results for the finite element analysis that was performed in the following to theoretically assess the corrosion-induced damage on the material, that is hardly dependent on the corrosion problem that was simulated with the above four different cases. In this contribution, the test specimen was modelled in ANSYS finite element software and various "artificial cracks" from corrosion-induced degradation were modeled on the specimen surface according to the different of the above four cases. The quasi-static tensile mechanical performance of pre-corroded open hole specimens was calculated for different artificial cracks geometry and the calculation results were compared against the experimental tensile results.

3. Results and conclusions

Fig. 1 shows the experimental results of elongation at fracture A_f versus corrosion exposure time for three (3) different corrosion modes of AA2024-T3 specimens. These results were obtained by calculating the average value of the numerical data extracted from at least three (3) different tensile stress-strain curves in each case. Specimens corroded only outside the hole (blue curve) showed the greatest resistance to corrosion attack in terms of A_f degradation, while the specimens corroded on all surfaces (including the open-hole) as well as those corroded only inside the open-hole presented similar behavior and resistance to corrosion.

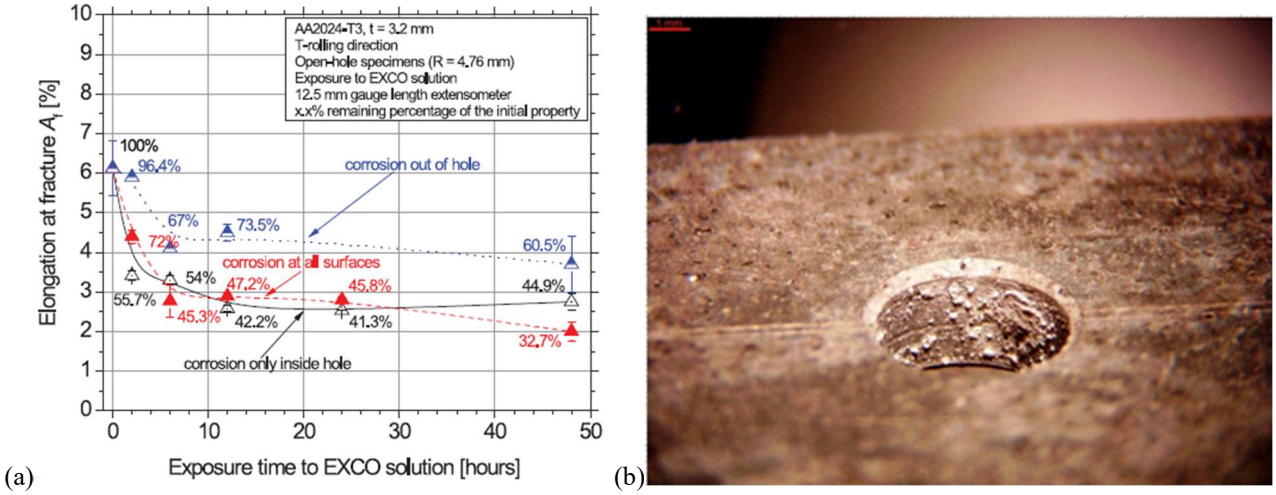

Fig. 1. (a) Experimental results for the effect of corrosion exposure on the mechanical properties and (b) stereoscopic image showing the surfaces of the specimens exposed for 2 h to EXCO solution on all surfaces and inside hole.

4. Acknowledgements

The work has been financed by the Hellenic Foundation for Research and Innovation H.F.R.I.-Project ID 03385 Acronym CorLi-Corrosion susceptibility, degradation and protec-tion of advanced Al-Li aluminium alloys.

5. References

[1] L. Han, M. Thornton, M. Shergol, A comparison of the mechanical behaviour of self -piercing riveted and resistance spot welded aluminium sheets for the automotive industry, Mater. Des. 31 (2010) 1457-67.

[3] Y. Yan, W.D. Wen, FK Chang, P. Shyprykevich, Experimental study on lamping effects on the tensile strength of composite plates with a bolt-filled hole, Compos. Part A 30 (1999) 1215–29.
[4] J.M. Minguez, J. Vogwell, Effect of torque tightening on the fatigue strength of bolted joints. Eng. Fail. Anal. 13 (2006) 1410–21.
[5] T.N. Chakherlou, R.H. Oskouei, J. Vogwell, Experimental and numerical investigation of the effect of clamping force on the fatigue behaviour of bolted plates, Eng. Fail. Anal. 15 (2008) 563–74.
[6] T.N. Chakherlou, J. Vogwell, The effect of cold expansion on improving the fatigue life of fastener holes, Eng. Fail. Anal. 10 (2003)13–24.
[7] R.G. Budynas, JK. Nisbett, Shigley's mechanical engineering design, 8th ed. London: McGraw-Hill Series in Mechanical Engineering, 2008.
[8] A. Skorupa, M. Skorupa, T. Machniewicz, A. Korbel, Fatigue crack location and fatigue life for riveted lap joints in aircraft joints in aircraft fuselage, Int. J. Fatigue. 58 (2014) 209–17.
[9] J. Mucha, The effect of material properties and joining process parameters on behaviour of self-pierce riveting joints made with the solid rivet, Mater. Des. 52 (2013) 932–46.
[10] K. Iyer, S.J. Hu, F.L. Brittman, P.C. Wang, D.B. Hayden, S.P. Marin, Fatigue of single- and double-rivet self-piercing riveted lap joints, Fatigue Fract. Eng. Mater. Struct. 28 (2005) 997-1007.
[11] DVTG Pavan Kumar, N.S. Sathiya, S. Kalyana Sundaram, S. Chandra. Further numerical and experimental failure studies on single and multi-row riveted lap joints, Eng. Fail. Anal. 20 (2012) 9-24.
[12] N. Chen, H. Luo, M. Wan, J. Chenot, Experimental and numerical studies on failure modes of riveted joints under tensile load, J. Mater. Process Technol. 214 (2014) 2049–58.
[13] Al. Th. Kermanidis, P.V. Petroyiannis, Sp.G. Pantelakis, Fatigue and damage tolerance behaviour of corroded 2024 T351 aircraft aluminum alloy, Theor. Appl. Fract. Mech. 43 (2005) 121–132.
[14] C. Charalampidou, W. Dietzel, M. Zheludkevich, S. K. Kourkoulis, N.D. Alexopoulos, Corrosion-induced mechanical properties degradation of Al-Cu-Li (2198-T351) aluminium alloy and the role of side-surface cracks, Corrosion Science 183 (2021) 109330.

Case studies and practical applications

INDUSTRIAL PRODUCTION OF GREEN AMMONIA (NH3) FOR FERTILIZER MANUFACTURE: CASE STUDY IN TECHNICAL APPLICATIONS OF GREEN HYDROGEN IN AMMONIA PRODUCTION.

Nascimento, Mauricio A. 1(*), Júnior, Everardes P. 2
[1] *IFBA/COEDIF, Federal Institute of Education, Science and Technology of Bahia, Brazil, Department of Civil Engineering*
[2] *IFBA/COEDIF, Federal Institute of Education, Science and Technology of Bahia, Brazil, Department of Environment*
(*)Email: nascimento.mauricioandrade@gmail.com

1. Introduction

The production of ammonia (NH_3) from nitrogen and hydrogen, known as the Haber-Bosch process, revolutionized agriculture by enabling the large-scale synthesis of nitrogen fertilizers. This innovation is widely recognized as one of the most important technological achievements of the last century, with profound impacts on the global economy and human well-being [1], playing a crucial role in increasing global agricultural productivity, and contributing significantly to food security and population growth.

Nitrogen fertilizers are nitrogen (N)-rich products and their basic material is NH_3. However, their use must be balanced with sustainable practices to ensure the long-term health of the soil and the environment [2], since the use of ammonia-based fertilizers introduces a significant amount of nitrogen into the terrestrial environment, even exceeding the contribution of all symbiotic and free-living nitrogen fixers [3]. This information highlights the magnitude of the impact of the ammonia fertilizer industry on nitrogen cycling in the terrestrial ecosystem, drawing attention to the need for sustainable approaches to managing the use of these fertilizers to mitigate adverse effects on the environment. Their use is associated with serious negative environmental impacts, ranging from contamination of water resources to eutrophication of aquatic ecosystems and increased greenhouse gas emissions. These impacts represent a significant concern in terms of environmental sustainability and require the adoption of effective management and mitigation measures [4].

The annual production of approximately 160 million tons of NH_3 is distributed mainly for the manufacture of fertilizers, representing about 80% of the total. These fertilizers play a crucial role in feeding more than 70% of the world's population, highlighting their relevance to global food security [5]. While countries such as the United States, India, China and European countries apply more fertilizer than necessary, in some regions of South America and Eastern Europe, as well as in most of sub-Saharan Africa, fertilizer use remains substantially below the levels needed to maximize crop yields and ensure food security for growing populations. High fertilizer import and transportation costs, combined with low crop prices, further exacerbate the lack of economic incentive to increase agricultural production in these areas [6]. Another aspect to consider regarding NH_3 production concerns the energy efficiency of production. Despite advances in energy efficiency, the ammonia synthesis process continues to face substantial challenges in terms of sustainability. Responsible for consuming between 1% and 2% of global energy and contributing to 1.6% of anthropogenic CO_2 emissions on a global scale, the urgency to develop more efficient and sustainable strategies for its production becomes evident [7]. Ammonia is obtained through a reaction between hydrogen (H_2) and nitrogen (N_2) in the presence of a catalyst under high pressure and temperature. Whereas in Brazil, H_2 is obtained through the steam reforming of natural gas, with high carbon emissions in the process.

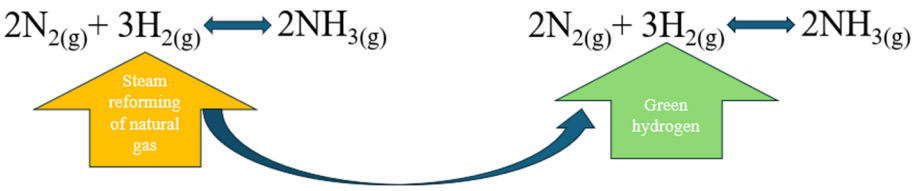

Fig 1. Ammonia (NH3) synthesis reaction proposing the replacement of natural gas as a hydrogen provider with green hydrogen produced through sustainable sources.

2. Materials and methods

This research aims to further reduce dependence on fossil fuels and mitigate climate change through the adoption of more sustainable NH_3 production methods, raising the technical possibilities of introducing green hydrogen in the production of ammonia as a substitute for natural gas as a source of hydrogen. Associated with the reduction of environmental impact (mainly resulting from the reduction of CO_2 emissions) through the beneficial use of green hydrogen as a source of hydrogen in the NH_3 manufacturing process as an alternative to natural gas, one of the commercial advantages offered also from an economic point of view, it is the fact that the transportation and marketing of green hydrogen as a source of energy for export can also be carried out through fertilizers. The development of green ammonia is a reality, evidenced by the growing number of large-scale commercial projects that aim not only to provide a more sustainable alternative to produce fertilizers, but also to contribute to the reduction of greenhouse gas emissions. The expansion of these commercial projects reflects the growing recognition of the importance of the transition to cleaner and renewable energy sources, both in the agricultural sector and in energy production [1]. Brazil is a major consumer of fertilizers, but on the other hand, it has a deficit in its domestic supply, which leads to the need for high imports to supply the country's domestic production. Around 45 million tons of fertilizers, intermediates and NPK complexes were made available to the Brazilian market in 2023. Most (around 86%) of these fertilizers used in the Brazilian agricultural sector are imported [8]. On the other hand, the country has been highlighted in international studies and consultancies, such as McKinsey and Bloomberg, due to its privileged geographical conditions (solar and wind incidence), as the main “player” in the global production of green hydrogen. Thus, the necessary increase in its domestic production has great potential associated with the exploration of green hydrogen as a renewable energy source, adding to the energy production and commercialization chain, as well as the possibility of boosting fertilizer production.

3. Results and conclusions

Since Brazil has great potential for producing green hydrogen, it is believed that this factor could influence domestic fertilizer production. This would contribute not only to decarbonizing the fertilizer production chain, specifically NH_3 production, but also to implementing the informal economy associated with agribusiness. The integration of green hydrogen energy into the Brazilian economic context has the potential to be a game-changer for the popular economy. As a catalyst for productivity, training, and integration into formal markets, green hydrogen represents not only an environmental imperative, but also a transformative force for inclusive and sustainable economic development. By embracing this opportunity, Brazil could position itself as a leader in the global search for a green and equitable future and as an exporter of fertilizers, rather than an importer, which is currently its real role. To realize these potential benefits, collaboration between the State, civil society, and the popular economy is crucial in creating an environment conducive to the widespread adoption of sustainable energy solutions. And it is precisely in the potential production of Green Ammonia that hydrogen from sustainable sources can be applied to strengthen the fertilizer industry, as a substitute for natural gas, which implies high production costs and environmental impacts in Brazil, as well as measuring development for popular economies associated with agribusiness.

4. References

[1] GENÇER, Emre, et al. Sustainable production of ammonia fertilizers from biomass. Biofuels, Bioprod. Bioref. v. 14, p. 725–733, 2020. Available on: doi: 10.1002/bbb.210. Accessed on: 06/05/2024.

[2] FAO. Global Estimates of Gaseous Emissions of NH3, NO and N2O from Agricultural Land. First version, published by FAO and IFA. Rome, 2001. Available on: https://www.fao.org/3/Y2780E/y2780e00.htm. Accessed on: 01/11/2024.

[3] CANFIELD, Donald E.; GLAZER, Alexander N.; FALKOWSKI, Paul G. The evolution and future of earth's nitrogen cycle. Science, v. 330, p. 192–196, 2010. Available on: DOI: 10.1126/science.1186120. Accessed on: 22/06/2024.

[4] LEWIS Simon L.; MASLIN Mark A. Defining the Anthropocene. Nature. v. 519, p. 171–180, 2015. Available on: doi:10.1038/nature14258. Accessed on: 04/07/2024.

[5] DAW, Jennifer; STOUT, Sherry. Building island resilience through the energy, water, food nexus. 2019.

[6] MORRIS, Michael; KELLY, Valerie A.; KOPICKI, Ron J.; BYERLEE, Derek. Fertilizer Use in African Agriculture; Lessons Learned and Good Practice Guidelines. World Bank Publications, Washington, DC, 2007. Available on: http://documents.worldbank.org/curated/en/498591468204546593/Fertilizer-use-in-African-agriculture-lessons-learned-and-good-practice-guidelines. Accessed on: 12/06/2024.

[7] ERISMAN, Jan Willem; et al. How a century of ammonia synthesis changed the world. Nat Geosci, v. 1, p. 636–639, 2008. Available on: https://doi.org/10.1038/ngeo325. Accessed on: 01/08/2024.

[8] ANDA - Associação Nacional e difusão de adubos. Relatório pesquisa Setorial – Macro Indicadores. Available on: <https://anda.org.br/pesquisa_setorial/> Accessed on: 09/07/2024.

THEMATIC SYMPOSIA

Additive Manufactured Materials: Production, Experiments and Applications

LPBF GRADED LATTCE STRUCTURE: A MICRO-MECHANCAL PROPERTY STUDY

K.Sleem, G. Grima, A. Santoni, M. L. Gatto, E. Santecchia, S. Spigarelli, M. Cabibbo*

Department of Industrial Engineering and Mathematical Sciences (DSM), Università Politecnica Delle Marche, Via Brecce Bianche, 12, 60131 Ancona, Italy.

1. Introduction

The metal lattice structure represents a novel approach for achieving excellent mechanical properties, including a high strength-to-weight ratio, high specific rigidity, high durability, and an enhanced energy absorption rate in comparison to sold bulk metal structures [1,2]. The graded lattice structure (GLS) is the result of the replication of a given type of unit cell with a gradient in cell size without changing element thickness, or with a gradient in strut thickness without changing unit cell size, along a specified direction [2]. The implementation of graded density in lattice structures is of great importance in minimizing strain and stress localization, which is achieved through an improved uniform load distribution. Furthermore, the variation in properties permits local and continuous tailoring of material stiffness, resulting in enhanced buckling resistance and ultimate load-bearing capacity [3].

The production of graded lattice structures requires the use of advanced techniques to obtain complex and neat structures. To this purpose, additive manufacturing (AM), and particularly laser powder bed fusion (LPBF) is surely one of the most promising such technique. This exhibits a remarkable level of accuracy in manufacturing geometrical customized metal lattice structures. In fact, the use of focused laser beam makes LPBF a fully reliable 3D printing process, able to selectively melt powder in a computer-driven layer-by-layer sequence [4]. Despite these significant advantages offered by LPBF, the implementation of extremely high solidification rates and the interaction between laser and powder during the printing process presents challenges in maintaining surface quality, which ultimately does impact into the surface mechanical properties of the fabricated parts.

AISI316L stainless steel is much appreciated for its large variety of applications, including aerospace and automotive structures, and biomedical applications, being a highly weldable steel, with high corrosion resistance, and sufficiently high tensile properties [5]. Concerning biomedical applications, ASI316L is considered quite a good solution for short-term implants as it can offer bone-equivalent mechanical properties, acceptable biocompatibility, and low-cost [1].

In the present study the effects of grading and size reduction of lattice structures on the surface quality and surface mechanical properties were studied by micro-mechanical tests. The investigation of surface mechanical properties, including hardness, surface elastic modulus, wear resistance and surface resilience, yield pressure, and surface creep mechanisms were mainly inferred by nanoindentation tests.

2. Materials and methods

The scaffold lattice structures were obtained by repeating rhombic dodecahedral (RD) elementary unit cells, with a 10 mm cubic volume (S10). The functional grading was achieved by varying the thickness of the unit cell strut by 0.25 mm step size, starting from the central part of the structure by a thickness of 0.25mm and increasing in the printing direction to reach the maximum thickness of 0.75mm, with a mirroring symmetry at the central horizontal axis. The resulting design

is presented in Fig. 1 below. The 7mm cubic volume scaffold (S7) was obtained by reducing the 10mm one by a factor of 0.7.

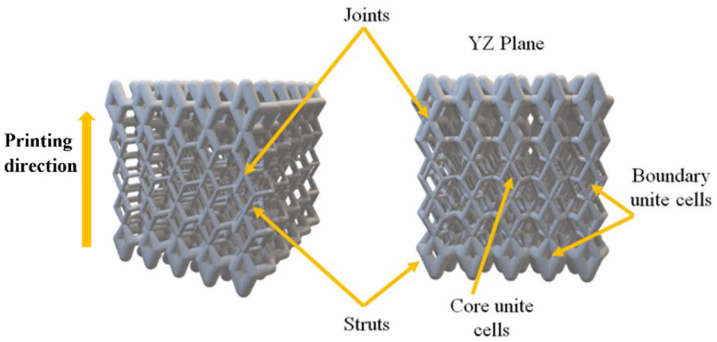

Fig. 1: Schematic view of scaffold-graded lattice structure showing the (YZ) plane and the printing direction

Microstructural analyses were performed by LEICA™ DMi8® optical microscope and by Tescan VEGA3 scanning electron microscope (SEM). Surface roughness was studied by using LEICA™ DVM6® stereo microscope. Micro-mechanical analyses of hardness, reduced elastic modulus, and creep behavior were inferred using a Hysitron Ubi®1 nanoindenter equipped with Berkovich diamond tip and TriboScan® analyzing software.

3. Results and conclusions

The variation of hardness and elastic modulus with the applied load is illustrated in Fig. 2, where a reduction in both cases with applied load was found. The estimated values of hardness were found to be consistent with that of microhardness, with the S7 scaffold displaying a higher value of hardness than the S10 scaffold in both as-built and thermal-treated conditions. This was also true for the local elastic modulus.

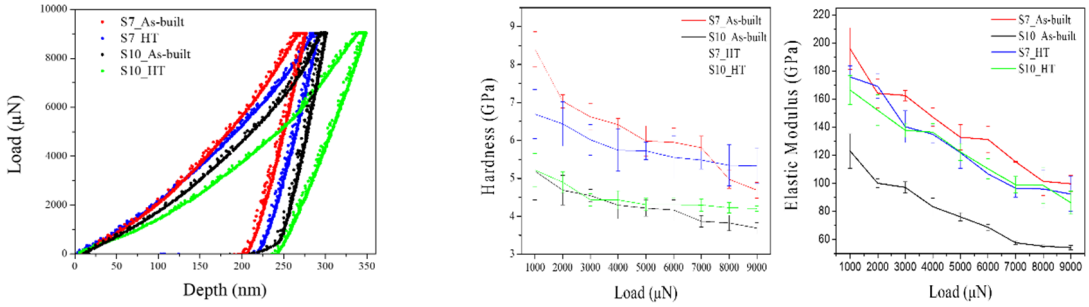

a) b) c)

Fig. 2. Load-displacement nanoindentation curves, a), variation of hardness, b), and elastic modulus, c), as a function of the applied loads, estimated by the analysis of load-displacement curves shown in a).

5. References

[1] M. L. Gatto, G. Cerqueni, R. Groppo, E. Santecchia, E. Tognoli, S. Defanti, M. Mattioli-Belmonte and P. Mengucci (2023). Improved biomechanical behavior of 316L graded scaffolds for bone tissue regeneration produced by laser powder bed fusion, *J. Mech. Behav. Biomedical Mater.,* **144**, 105989.

[2] N. Khan and A. Riccio (2024). A systematic review of design for additive manufacturing of aerospace lattice structures: Current trends and future directions, *Progr. Aerospace Sci.,* **149**, 101021.

[3] S. Daynes, S. Feih, W. F. Lu and J. Wei, Optimisation of functionally graded lattice structures using isostatic lines (2017). *Mater.&Design*, **127**, 215–223.

[4] N. Semjatov, B. Wahlmann and C. Körner (2024). Multiple interaction electron beam powder bed fusion for controlling melt pool dynamics and improving surface quality, *Additive Manuf.,* **90**, 104316.

[5] A. Saboori, A. Aversa, G. Marchese, S. Biamino, M. Lombardi and P. Fino (2020). Microstructure and mechanical properties of AISI 316L produced by directed energy deposition-based additive manufacturing: A review, *Appl Sci.,* **10**, 3310.

EuraSEM 6-11 July 2025 ICEM21 Bologna 21st International Conference on EXPERIMENTAL MECHANICS

A Study of Loosening Phenomenon and Acceleration Ratio of Loosening in Actual Equipment Compared to Results of Laboratory-Style Bolted Joints Loosening Tests

S. Hareyama[1], K. Manabe[1], S. Kobayashi[1]
[1] *System Design Department, Tokyo Metropolitan University, Japan*

1. Introduction

In laboratory tests, the loosening of bolted joints has been evaluated using the Junker-type loosening machine. This machine can be used to evaluate the relative loosening resistance of various locking devices and locking methods. On the other hand, we have proposed a loosening life evaluation method for evaluating the loosening of bolted joints used in actual equipment. In this study, we will examine how much the test results from the loosening tester are accelerated compared to the loosening life results from the actual machine.

2. Observation of Loosening Phenomenon in Actual Machine [1-2]

Figure 1 shows the axial force variation of two bolts during the initial tightening work on the actual machine (large forklift) and during transportation by truck to the customer. One bolt was tightened using anaerobic adhesive (Loctite 262), and the other was tightened using machine oil lubrication. No work was performed, and the decrease in axial force is thought to be due to initial loosening or sinkhole-type loosening.

On the other hand, Fig. 2 shows an example of the waveform during work at the customer's site. Due to the impact load, the axial force of the bolts fastened with machine oil lubrication decreases instantaneously, and the axial force remains low. On the other hand, the bolts fastened with anaerobic adhesive also show a momentary drop in axial force, but the axial force is restored to its original level immediately afterwards, indicating that the bolts are effective in preventing loosening. The tendency to loosen (the tendency for the axial force to drop) is thought to be the cumulative result of the instantaneous drop in axial force seen in machine oil lubrication.

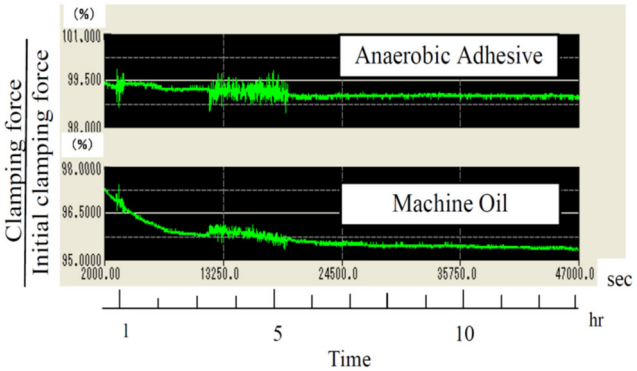

Fig. 1. Depression type loosening

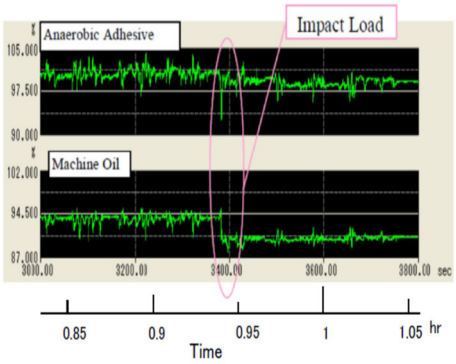

Fig. 2. Waveform of loosening phenomenon

3. Prediction of Loosening Lifetime on Bolted Joints in Actual Machine

Figure 3 shows an example of plotting the loosening tendency of actual equipment on double-log paper, and the regression line can generally be expressed by Equation (1) when the ratio of clamping force to initial clamping force is R and the operating time is H (a, b: constants). If we apply equation

(1) to the regression line of the loosening tendency of bolts tightened with anaerobic adhesives, we get equation (2). On the other hand, the regression line of bolts tightened with machine oil is equation (3). Figure 4 shows the results of these tests summarized as a diagram for evaluating loosening, and it is possible to estimate the loosening lifetime and residual clamping force in actual equipment.

$$\log R = a + b \times \log H \quad (1)$$

$$\log R = 1.992 - 0.00814 \times \log H \quad (2)$$

$$\log R = 1.980 - 0.0277 \times \log H \quad (3)$$

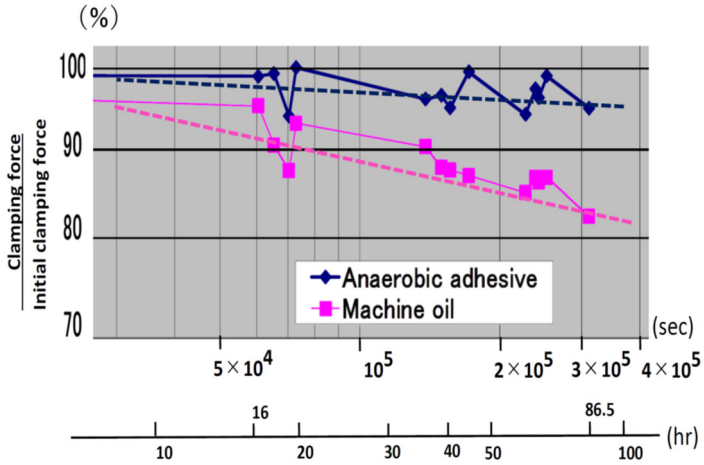

Fig. 3. Working load type loosening (Logarithmic coordinates)

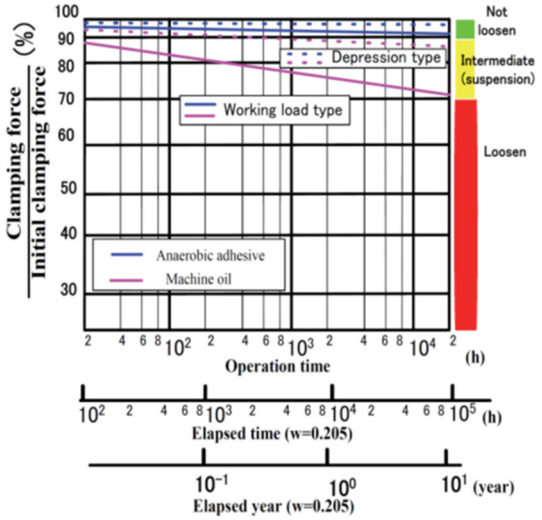

Fig. 4. Prediction of working load type loosening (Logarithmic coordinates)

4. Loosening Lifetime Relation Between Experimental Test and Actual Machine Test

Figure 5 shows the results of the Junker-type axial-perpendicular vibration loosening test for various types of bolt-nuts plotted on logarithmic coordinates [3]. Tightening method with low anti-loosening performance lose their linear trend at an early stage of the test cycle. On the other hand, tightening method with high anti-loosening performance maintain their linear trend for a long time.

Figure 6 shows the acceleration ratio of the Junker-type loosening test compared to the actual machine test, based on the results of the actual machine test in Fig. 4 and the laboratory-style loosening test in Fig. 5.

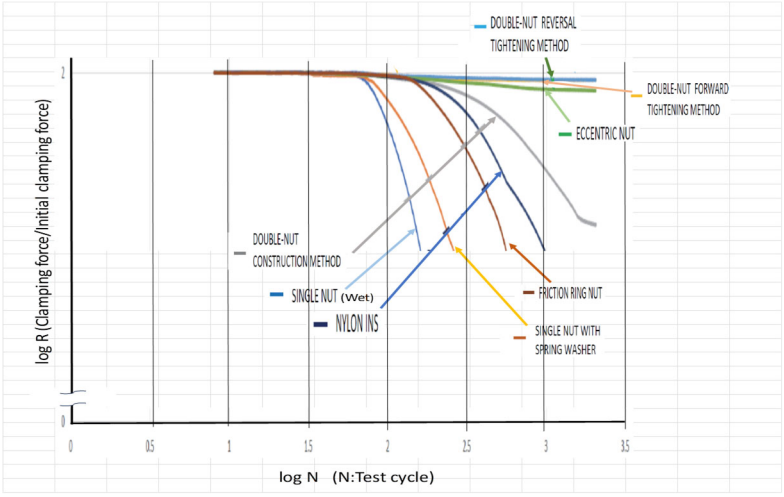

Fig. 5. Example of loosening test results by Junker-type loosening test (Logarithmic coordinates)

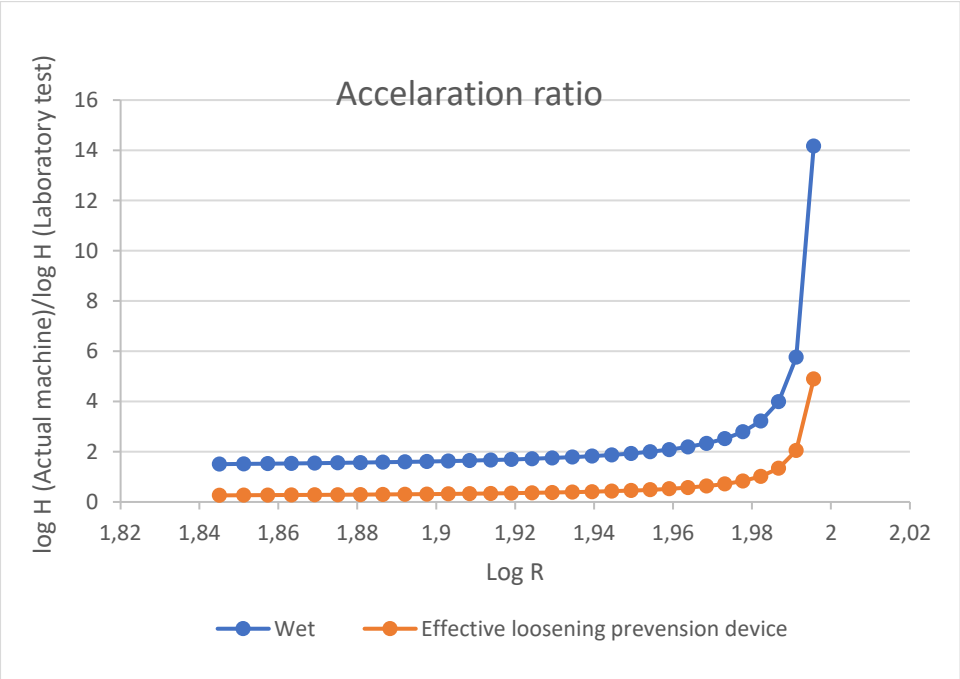

Fig. 6. Acceleration ratio between laboratory test and actual machine operation

The vibration frequency for the test in Fig. 5 is 12.5 Hz. Figure 4 shows the elapsed time or elapsed years, but in the preparation of Fig. 6, the comparison is made in terms of seconds.

Figure 6 compares the results with lubricated tightening and effective loosening. This study examined methods to determine the acceleration rate of laboratory loosening tests. Future work is to obtain similar data on more products and with more loosening methods to improve the accuracy of the acceleration ratio.

5. References

[1] Hareyama, S., Manabe, K., Nakashima, M., 2012, "The Absolute Evaluation and Loosening Life Prediction Method on Self-loosening of Bolted Joints during Actual Machine Operation," Proceedings of the ASME IMECE2012-86415

[2] Hareyama, S., Manabe, K., Kobayashi, S., 2019, "Residual Clamping Force Estimation and Lifetime Prediction to Loosening Failure of Bolted Joints" SAE Technical Paper 2019-01-1111, doi:10.4271/2019-01-1111.

[3] Hareyama, S., Manabe, K., Kobayashi, S., 2022, "Evaluation for Residual Lifetime and Remaining Axial Tension to Loosening Failure on Bolted Joints Used in Long-Life Machine and Plant Equipment," Proceedings of the ASME PVP2022-80082, pp. 1-10.

INFLUENCE OF 3D PRINTING PARAMETERS ON BASF ULTRAFUSE 316L STEEL MECHANICAL PROPERTIES

Pawel Platek[1], Natalia Daniel[1], Kamil Cieplak[1], Marcin Sarzynski[1]
[1] Faculty of Mechatronics, Armament and Aerospace, Military University of Technology, Warsaw, Poland

1. Introduction

Based on the review of current trends in additive manufacturing, a growing focus can be observed on techniques designed for the fabrication of metallic components, such as steel, lightweight metal alloys and metal composite materials [1]. Traditionally, these materials are processed using methods such as Powder Bed Fusion (PBF) and Direct Energy Deposition (DED), both of which rely on the melting of metal powders or wires using high-energy sources to proceed with them. Despite their advantages, these techniques face notable limitations, including high equipment costs and substantial production expenses. An emerging and cost-effective alternative to the mentioned groups of techniques is the Fused Filament Fabrication (FFF) technique, which is widely used [2]. In this method, standard filaments are replaced by metal filaments, which are composites of metal powders and polymer binders [3]. The process involves printing the composite material to create objects referred to as "green parts." These green parts exhibit low mechanical strength because of their heterogeneous structure and lack of melting bonds between metallic powder particles. To achieve the desired mechanical and physical properties, the green parts undergo postprocessing, which includes a two-step thermochemical treatment: catalytic debinding to remove the polymer binder, and sintering in a controlled hydrogen atmosphere. Following the debinding and sintering processes, the resulting parts exhibit high mechanical strength and physical properties comparable to those of fully metallic materials. However, this approach has few significant drawbacks, such as thermal shrinkage and relatively high porosity in the final components, that affect mechanical strength. These limitations are inherent to the FFF printing process and subsequent post-processing stages.

This study aims to evaluate the impact of the 3D printing process parameters, using the FFF technique, on the physical and mechanical properties of samples manufactured with BASF Ultrafuse 316L metal filament.

2. Materials and methods

The material samples were produced using a widely adopted 3D printer, the Prusa i3 MK3S+, with different 3D printing parameter settings defined in the PrusaSlicer software (version 2.7.4). In the technological tests and studies conducted on mechanical strength, the material used was BASF Ultrafuse 316L filament. The primary objective of the technological tests was to determine 3D printing parameters that ensure minimal material porosity after the manufacturing process. Based on these parameters, material samples compliant with ASTM E466:96 were produced to perform quasi-static tensile conditions.

Figure 1 presents a general view of the 3D printer used during the tests, along with material samples produced to identify 3D printing parameters as well as for strength investigations.

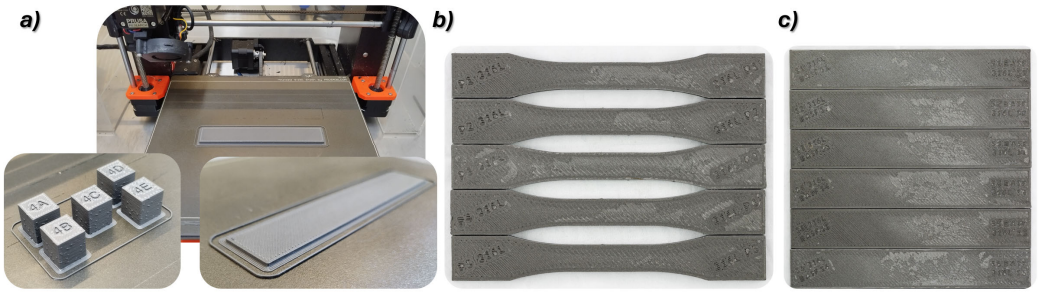

Fig. 1. Manufacturing process of material samples from BASF Ultrafuse 316L filament

3. Results and conclusions

In the first stage of the study, material samples were produced as shown in Fig.1a. These samples were created in the form of cubes using various configurations of 3D printing parameters. During the process, the nozzle temperature was sequentially varied, with values of 220, 230, 240, 250, and 260 ° C. Furthermore, the width of the deposited material was adjusted, with values of 0.55, 0.60, 0.65, 0.75, and 0.8 mm. Other parameters of the 3D printing process remained constant for each configuration. The samples underwent a thermochemical treatment, on which a set of process parameters ensuring the highest material density was identified.

In the next stage, samples for tensile tests were prepared, as depicted in Fig.1b and Fig.1c. The study assessed the strength of samples manufactured in the target geometry, specified according to ASTM E466:96, and in the form of flat, thick-walled elements from which the target shape was cut out. Both the samples for porosity evaluation and for mechanical strength tests were scaled to account for material shrinkage resulting from the applied thermochemical treatment.

On the basis of the tensile tests, stress-strain curves were obtained and fundamental strength parameters of the tested material were determined (Table 1).

	Samples “ready to test”		Samples cut out from the profile	
	Avg.	Std.dev.	Avg.	Std.dev.
E [GPa]	65	14	79	12
$R_{0.2}$ [MPa]	180	12	176	3
R_m [MPa]	405	9	483	11
A_p [%]	24.2	2.4	50	12

Table 1. Mechanical parameters of BASF Ultrafuse 316L material manufactured via FFF 3D printing technique

4. Acknowledgements

The research presented in this paper has received funding from National Centre for Research and Development as part of the Strategic Research and Development No. TECHMATSTRATEG2 /410049/12/NCBR/2019

5. References

[1] A. Bernard *et al.*, “Vision on metal additive manufacturing: Developments, challenges and future trends,” *CIRP J. Manuf. Sci. Technol.*, vol. 47, pp. 18–58, 2023, doi: 10.1016/j.cirpj.2023.08.005.

[2] S. Spiller, F. Berto, and N. Razavi, “Mechanical behavior of Material Extrusion Additive Manufactured components: An overview,” *Procedia Struct. Integr.*, vol. 41, no. C, pp. 158–174, 2022, doi: 10.1016/j.prostr.2022.05.018.

6-11 July 2025 ICEM21 Bologna
21st International Conference on EXPERIMENTAL MECHANICS

STUDY ON STIFFNESS CHANGE OF CHAINMAIL STRUCTURE FOR LEG MECHANISMS

***Sae YAMAGUCHI*[1], *Toshitake TATENO*[2]**
[1] *Graduate School of Science and Technology, Meiji University, Japan*
[2] *Department of Mechanical Engineering Informatics, Meiji University, Japan*

1. Introduction

Chain mail, which is made by interconnecting chains to each other, has been used as a self-defense garment. With the development of additive manufacturing technology, there has been a lot of research on the characteristics of structures inspired by chain mail. Yifan Wang et al. produced a chain mail structure made by connecting hollow octahedral chains in a flat shape, and investigated its physical properties [1]. The results showed that the chain mail structure they proposed had the fluidity like cloth in normal conditions, but that when it is placed in a compression bag and internal confining pressure is applied, the elastic modulus increased. In addition, Jiawen Xu et al. showed that the chainmail structure with confining pressure has higher impact resistance than the structure without confining pressure [2]. This reversible change in mechanical properties is thought to be caused by the jamming transition, a phase transition that occurs in granular material aggregates due to local geometric constraints. Chainmail structures can provide sufficient rigidity with less volume and mass than conventional granular materials such as sand.

Legged robots have the advantage of being able to run in places with poor footing, but have the disadvantage of energy efficiency. One of the reasons for their low energy efficiency is that the many motors in the leg joints consume electricity for supporting their own weight.

If it is possible to support the posture by mechanically fixing the legs when they are grounded, it will be possible to reduce power consumption. To achieve this, in this study, a chain mail structure is applied to the legs of a legged robot. In this way, the legs become fluid when they are not grounded and solid when they are grounded.

2. Prototype

In this study, chain mail structures are designed with connecting the hollow octahedral chain elements shown in Figure 1, which were used in the research of Yifan et al. [1]. Chain mail structures are constructed as a joint mechanism for the legs of a legged robot, as shown in Figure 2 and Figure 3. In this structure, the upper and lower parts are supported by two chain mail structures that are connected in a flat manner. In the fabrication of the test piece, a Fused Filament Fabrication (FFF) 3D printing machine (Ultimaker S3, manufactured by Ultimaker) was used. The material used for the fabrication of the test piece is PLA (Tough PLA White, manufactured by Ultimaker).

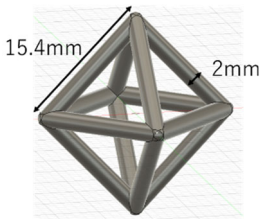

Fig. 1. CAD image of a chain element

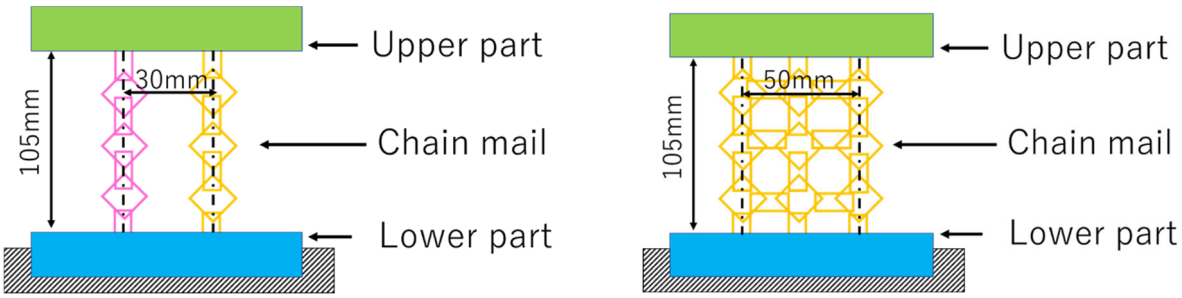

Fig. 2. Parts configuration of the test piece (left: front view, right: side view)

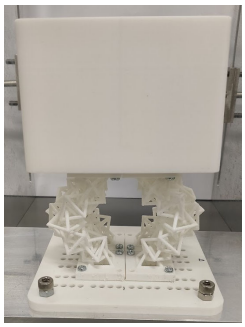

Fig. 3. Fabricated test piece

3. Experiment

In the experiment, the upper part of the test piece is pulled horizontally while a load is applied from above.

A jig (Figure 4) was attached to a universal testing machine (EZ-LX, Shimadzu Corporation), and the lower part of the test piece was fixed to the jig. The upper part of the test piece was connected to the universal testing machine via a wire that passes through a pulley on the jig (Figure 4 and Figure 5). By pulling the wire vertically upwards in the universal testing machine, a horizontal pulling force is applied to the upper part of the test piece.

Pulling force is measured until the upper part of the test piece loses its balance. Measurements are taken three times for each of the 100g, 300g and 500g loads.

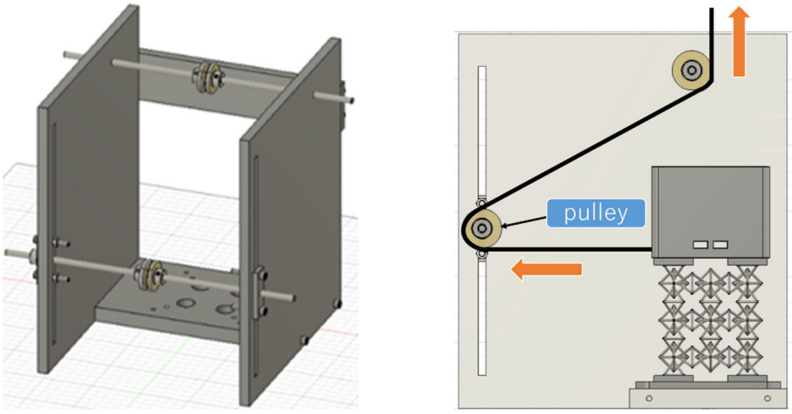

Fig. 4. CAD image and wire-pulling mechanism of the jig

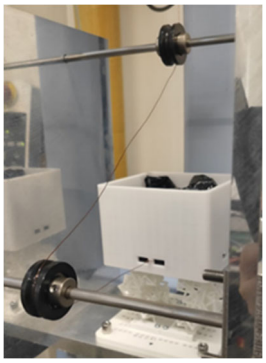

Fig. 5. The experiment setup

4. Results and discussion

In the experiment, the tensile force of wire and the stroke at that time were measured. The graph obtained from the experiment is shown in Figure 6.

From this result, it can be seen that the slope of the graph in early stages of pulling and the maximum tensile force increase as the weight is increased. This shows that the rigidity of the chain mail structure is increased by applying a load from above.

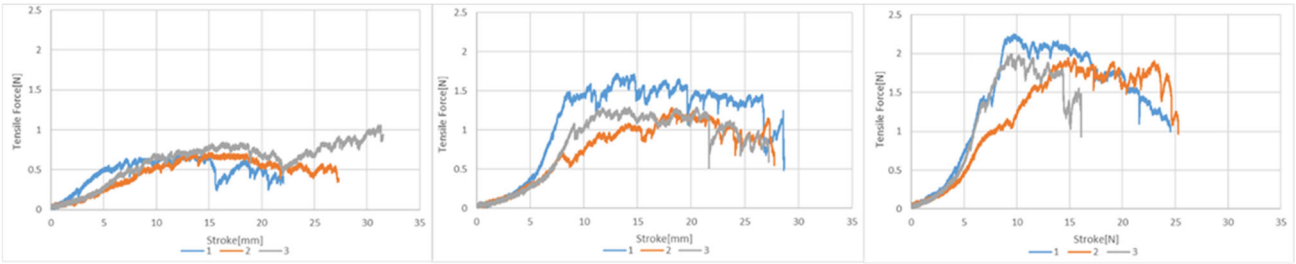

Fig. 6. Test piece experimental results

5. Conclusion

In this study, the application of chain mail structure to the legs of a legged robot was proposed. By using ability of the chain mail structure to change its mechanical properties, the reduction in the power consumption of the leg motor is expected. A prototype of the joint mechanism using chain mail was developed, and experiments were conducted. As a result, it was shown that the stiffness of the chain mail structure increases as the load from above is increased.

6. References

[1] Yifan Wang, Liuchi Li, Douglas Hofmann, José E. Andrade, Chiara Daraio (2021). Structured fabrics with tunable mechanical properties, Nature, 596, 238−243.

[2] Jiawen Xu , Yan Zhang , Yijing Huang , Lijun Chang , Taiwei Chen , Tong Ren , Zhihua Cai (2024). Dynamic response of chain mail fabrics with variable stiffness, International Journal of Mechanical Sciences, 264, Article 108840.

Experimental validation of a FEM constitutive model for an innovative L-PBF AM Metal-Matrix-Composite

Matteo Crachi[a], Raffaella Sesana[a], Cristiana Delprete[a], Leila Belen Fraga[b], Sebastian D'hers,

[a]*DIMEAS Politecnico di Torino Corso Duca degli Abruzzi 24 10129 Torino (TO) Italy*
[b]*Instituto Tecnologico de Buenos Aires Iguazu 341 C1437 Cdad. Autonoma de Buenos Aires Argentina*

Correspondence to matteo.crachi@polito.it

1. Introduction

One of the most critical components of high performance bi-propellant Liquid Rocket Engines are the thrust chambers. To keep temperature controlled and preheat the propellant, the use of regenerative cooling is widely used. The propellant is injected, mixed, and combusted inside to produce high-pressure and high-temperature gases. These gases exert extreme thermal loads on the walls of the chamber, which can easily exceed the melting point of conventional materials. To prevent failure, regenerative cooling channels are integrated into the walls allowing a portion of the propellant to flow through and absorb the heat.
Additive manufacturing (AM) is a process that involves creating three-dimensional objects by adding layers of material. It makes possible to manufacture thrust chambers, as single, integrated component, reducing the number of parts and eliminating the need for complex assembly processes.
Material selection affects the performance, reliability, and safety of the thrust chamber. To meet specific requirements, several factors must be taken into consideration. Some characteristics are thermal conductivity, thermal expansion, mechanical strength, and corrosion resistance to withstand the environment created by the combustion products [1]
Copper alloys offer high thermal conductivity and good corrosion resistance, crucial properties for the thrust chambers where harsh chemicals are involved. However, these alloys alone may not possess the required mechanical strength and stiffness needed. To overcome this limitation, high strength steel or nickel alloys are often used in conjunction with copper alloys to create Metal Matrix Composites (MMC). The combination of these materials can be tailored to have the necessary mechanical properties to withstand the high pressure and loading conditions experienced during rocket engine operation [2].
The primary aim of the present research is to delve into the mechanical properties of an innovative MMC. To address this, the present in-depth study was developed by means of Finite Element Analysis (FEA) approach, allowing to calibrate the behavior and specific properties of the Cu17-4PH MCC by means of nano indentation to compute the young modulus.

2. Materials and methods

In the present research, the investigated MMC has a custom composition of 65% copper and 35% 17-4PH stainless steel prior to the manufacturing process. Specimens for experimental testing were manufactured by means of a Concept Laser M2 machine. Process parameters were set according to the internal research group know-how, findings from previous research projects [4], and the similarity between the properties of the composites.

The research plan is composed of three parts: experimental tensile monotonic testing, nano hardening tests and numerical simulation of tensile monotonic testing. Experimental tensile tests provide stress-strain curves where the strain is measured both globally on the whole specimen and locally within the microstructure of the MMC via Direct Image Correlation. Tests are run in a SEM fixture to allow the observation of microstructural distribution of strain on MMC surface by means of DIC acquisition and analysis. This procedure aims at investigating the microstructural behavior and composition and at analyzing the Representative Volume Element (RVE) dimensions to be used in the numerical simulations. The numerical analysis replicates the tensile test with a focus on the calibration of the constitutive material model for MMC based on microstructural component distribution and to mimic the contribution of the diverse components of MMC to the global straining behavior. The calibrated constitutive models, focusing on the young modulus are then compared with the extrapolated ones by means of local nano hardness tests.

3. Results and conclusions

The FE mesh is exported to a commercial FEM software solver and employed to simulate the elastoplastic behavior of the microstructure, as shown in Figure 2, where the boundary conditions and loads are indicated. A distributed force designed to achieve 3000 N, the maximum load observed in the load-displacement curves, in 100 incremental steps, is imposed at the top of the mesh.

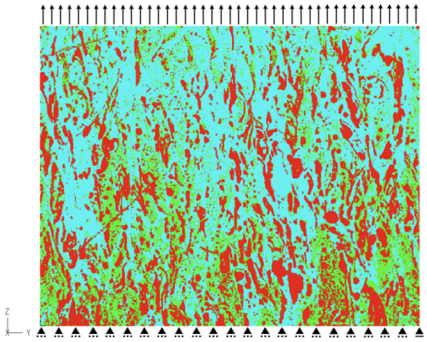

Figure 2 - FE mesh depicting the applied loads and boundary conditions used for the tensile test simulation

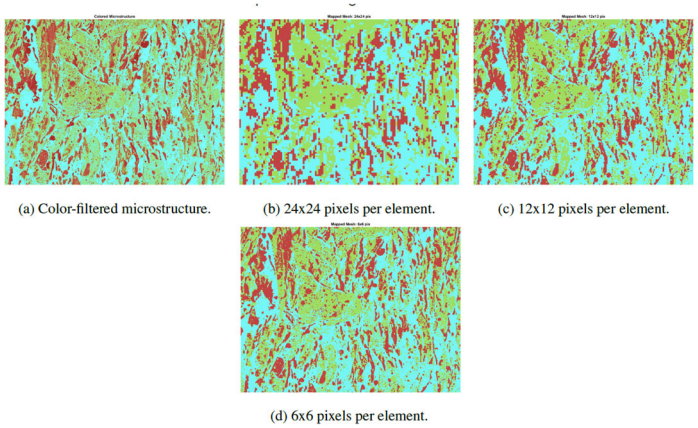

(a) Color-filtered microstructure. (b) 24x24 pixels per element. (c) 12x12 pixels per element.

(d) 6x6 pixels per element.

Figure 2 - FE mesh depicting the applied loads and boundary conditions used for the tensile test simulation

Cracks within a material microstructure can dramatically deviate the strain-stress curve from its typical trajectory. Serving as stress concentrators, these cracks intensify the local stress level, precipitating an earlier commencement of plastic deformation and ultimately, leading to fracture at

reduced overall stress levels. The material at the crack tip is subjected to significantly higher stress than the remaining material, triggering localized plastic deformation, propagation of the crack, and eventual failure.
The results garnered from simulations conducted with FEM commercial software will be presented and discussed, reporting Specimen 2 results as an example.
To accurately calibrate the mechanical properties of the MMC, a series of simulations were conducted, during which the strain hardening modulus and yield strength were systematically adjusted to align with the strain-stress curve derived from the tensile test. The strain maps obtained from FE simulation are compared to the experimental ones obtained from DIC during testing, for each specimen. Subsequently, the material properties can be adjusted. This process allows for a congruence in the elastic and plastic region across DIC and FE. The conclusive results of these simulations are illustrated in Figure 3. The curve overlapping demonstrates the accuracy of the simulation in replicating the physical test outcomes. Although the yield strength of the mix does not adhere to the rule of mixtures, the strain hardening modulus does. This property was calculated using the initial MMC proportions of 65% Cu and 35% 17-4PH.

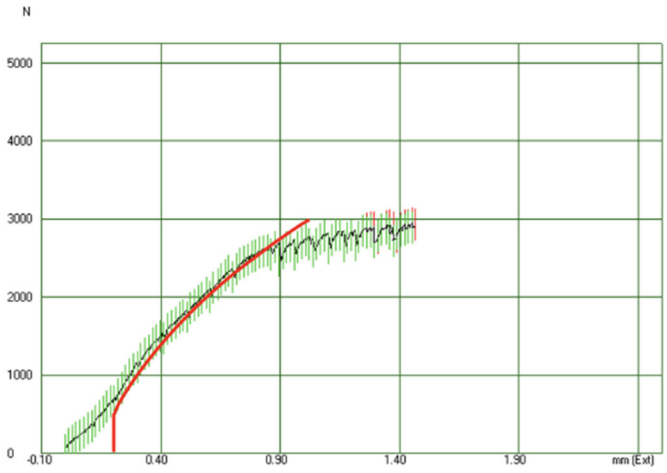

Figure 3 - Comparison of Strain-Stress curves obtained from tensile test (black) and FE simulation (red).

The two curves overlap in the linear range. The mismatches at the beginning can be attributed to settlement issues, which are also reflected in the concavity of the strain-stress curve derived from the test. The tail end of the curve does not match due to the failure of the MMC caused by crack propagation in the interfaces, as illustrated in Figure 4. Crack propagation is not included in numerical analysis.

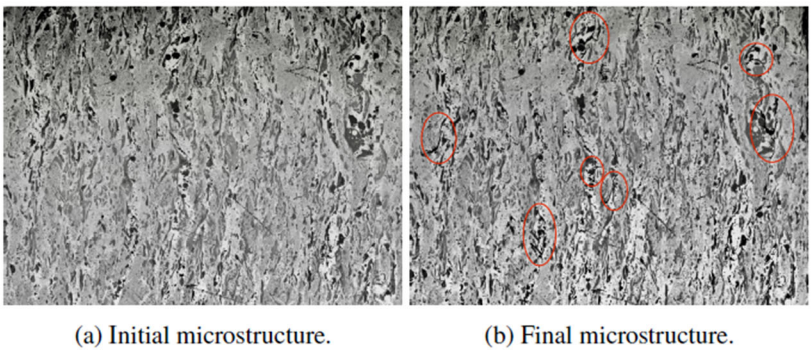

Figure 4 - Comparative microstructural analysis at the onset (left) and conclusion (right) of the tensile test, highlighting the effect of crack propagation.

The simulated curve would approach a horizontal asymptote if the stainless steel would undergo full plastic deformation. However, in Figure 5 the strain-stress bilinear behavior for each of the three materials comprising the modeled MMC is illustrated. The strain-stress curve is obtained by choosing an exemplary element from each material and extracting the data calculated at the Gauss points.

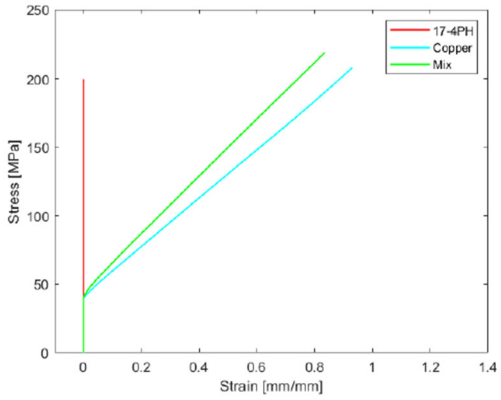

Figure 5 - Strain-stress curves for constituent materials of the MMC under tensile loads

The mean strain and its space-wise distribution is compared between the FEA and the DIC ones, as depicted in Figure 6 in the plastic field. The findings, as detailed in Table 2, confirm the validity of the DIC software for the intended analysis in this research. As illustrated in Figure 7, the strain maps from both analyses correspond in a zone free from cracks and porosity. A calculation of the mean accumulated plastic strain is made using both the DIC and numerical solver. The results of this analysis are presented in Table 2. An error margin of nearly 2% is recorded, which is considered within an acceptable range.

Model	e_{xx}	e_{xy}	e_{yy}
DIC	-2.382e-3	-1.096e-5	6.958e-3
FEA	2.222e-3	-1.250e-5	.900e-3
Error [%]	7.20	12.32	8.41

Table 2 - Comparative analysis of mean strain values derived from both DIC and FEA.

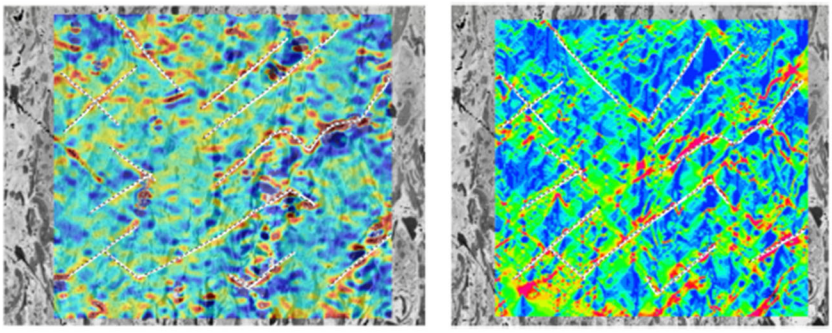

Figure 6 - Comparison of strain maps from DIC (left) and FEA (right) revealing similar patterns in strain distribution

In Figure 7 the strain pattern shows the typical characteristic of shear bands in metallic materials under high strain, which typically form a zigzag or wavy geometric pattern. The angle at which this zigzag pattern manifests in shear bands can be variable, contingent on the material and prevailing conditions. However, it forms at a 45° angle.

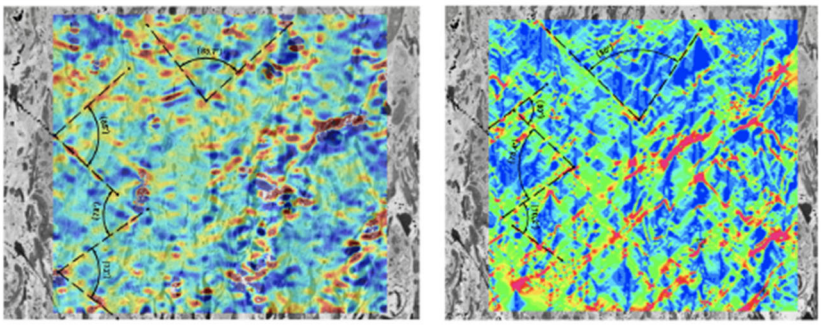

Figure 7 - Shear bands drawn on top of strain maps from DIC (left) and FEA (right).

	FEA	DIC	Relative Error
Mean Accumulated Plastic Strain	0.04639920	0.04545096	2.086%

Table 2 - Results of the mean accumulated plastic strain calculated with both DIC and FEA.

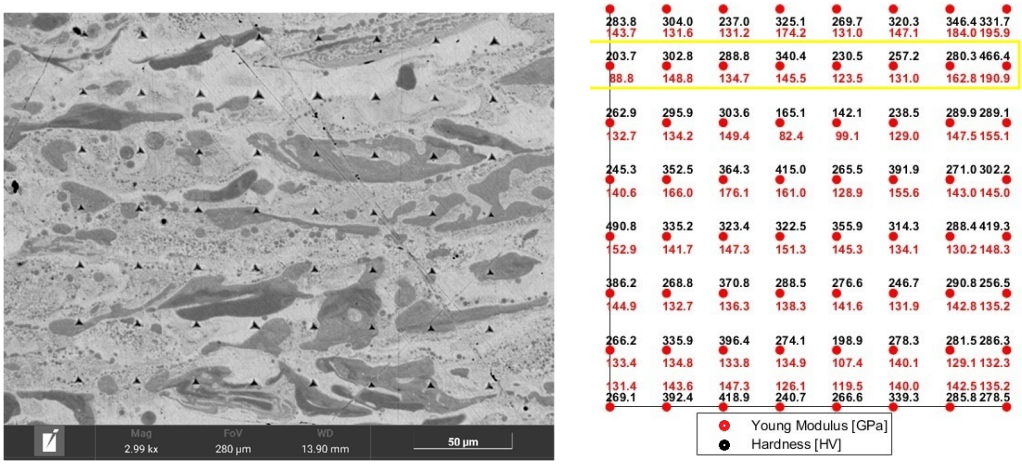

Figure 8 – Nano hardness map and Young Modulus computation

This project aimed to determine the mechanical properties of a MMC through the analysis of SEM images and nano indentation tests. The project's main objectives were successfully achieved with precision and accuracy. The strain-stress curve obtained from the tensile test of Specimen 2 was successfully corroborated using FEA and the calibrated Young Modulus validated by means of nano hardness, demonstrating a strong alignment with the rule of mixtures. This finding validates the effectiveness of FEA in accurately modelling the mechanical behavior of MMCs under tensile load by using the rule of mixtures as a first approach. The comparison of strain map distribution between DIC and FEA further reinforced the accuracy of the models used, with the mean accumulated plastic strain from both methods showing an acceptable error of almost 2\%. This close match underscores the reliability of both DIC and FEA in mapping strain distribution in MMCs. For future work and in order to gain a more comprehensive understanding of the mechanical properties and behavior of the MMC, it would be recommended to adjust and calibrate these properties through multiple tensile tests. This would ensure a more accurate and reliable understanding of the material behavior. In terms of fracture mechanics, a deeper and more detailed analysis could be obtained by calculating the stress intensity factor for multiple crack tips in an interface. This would give a more complete picture of how the MMC responds to stress and fails. Additionally, it would also be beneficial to employ a different method other than CTOD for these calculations. One such method that could be used is computational simulations with the Extended Finite Element Method (X-FEM).

5. References

[1] Michele Ferraiuolo, Michele Perrella, Venanzio Giannella, and Roberto Citarella. Thermal–Mechanical FEM Analyses of a Liquid Rocket Engines Thrust Chamber. Applied Sciences, 12(7):3443, March 2022.

[2] Andrea El Hassanin, Fabio Scherillo, Umberto Prisco, Raffaele Sansone, and Antonello Astarita. Selective laser melting of Cu-inconel 718 powder mixtures. Journal of Manufacturing Processes, 59:679–689, November 2020.

MECHANICAL RESPONSE OF 3D PRINTED LATTICE STRUCTURES MADE FROM PAHT-CF MATERIAL UNDER COMPRESSION LOADING

P. Platek[1], M. Sarzynski[1], K. Cieplak[1], B. Dekert[1], P. Baranowski[2],M. Kucewicz[2]
[1] Faculty of Mechatronics, Armament and Aerospace, Military University of Technology, Warsaw, Poland
[2] Faculty of Mechanical Engineering, Military University of Technology, Warsaw, Poland

1. Introduction

The progress in Additive Manufacturing techniques has significantly increased interest in cellular materials with regular structures as alternatives to standard materials [1]. One of the main advantages of cellular structures is the ability to define their mechanical and physical properties by selecting an appropriate unit cell shape and manufacturing the structure from a material with specific physical and mechanical properties. Currently, cellular materials are manufactured from a wide range of thermoplastic materials, metallic powders, and composites [2]. They are characterised by a high capacity for absorbing mechanical energy, damp vibrations, and suppressing noise. They are used as thermal insulators, heat exchangers, and electromagnetic shielding.

Depending on the type of unit cell used, cellular materials are classified into two basic groups: 2D and 3D [1]. Two-dimensional cellular materials are widely known and extensively used (e.g., honeycomb structures) because of the simplicity of their manufacturing process. In contrast, 3D materials such as lattice and Triply Periodic Minimal Surface (TPMS) structures are more challenging to produce due to the presence of overhanging features. They are commonly manufactured using 3D printing techniques like Powder Bed Fusion (PBF) and feedstock in the form of polymeric or metallic powders. These materials exhibit lower relative density and allow for achieving homogeneous mechanical properties compared to 2D structures.

Due to the more complex production process of 3D cellular structures, the number of publications investigating their mechanical properties remains relatively limited in comparison to 2D variants.

This study aims to present the results of research into the mechanical properties of lattice cellular structures manufactured using the Fused Filament Fabrication (FFF) 3D printing technique from a high-temperature-resistant Polyamide reinforced with chopped carbon fibre (PAHT-CF). Thanks to the identification of 3D printing parameters, lattice-type structures were successfully fabricated using a standard FFF 3D printer while maintaining high geometric accuracy.

2. Materials and methods

To produce the samples necessary for the experimental tests, a Bambu Lab P1S FFF 3D printer was used and PAHT-CF material in filament form. Figure 1 shows a general view of the 3D printer used and the material samples. The studies were carried out using both experimental and numerical approaches. Material samples were fabricated to determine the mechanical properties of PAHT-CF, followed by static tensile testing. In the subsequent phase of the study, lattice structures with varied topologies were produced and their energy absorption capacity under compression testing conditions. Additionally, simulation studies were performed using the Finite Element Analysis (FEA) method to

replicate the deformation process of the structures and to extend the scope of the research. Based on the results obtained, a specific topology variant was identified as the basis for further investigations.

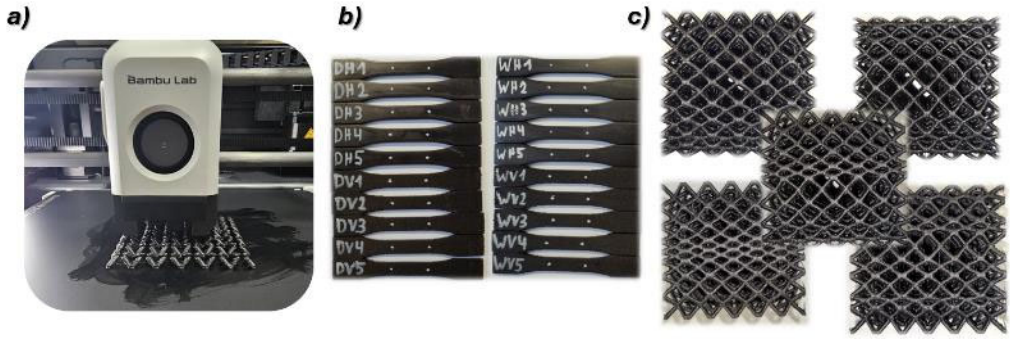

Fig. 1. Sample manufacturing process with the used of 3D printing; a) main view of used 3D printer, b) manufactured samples compliant with ASTM E466:96, c) samples of lattice structures

3. Results and conclusions

Figure 2 presents the results of experimental studies obtained from compression tests of various structural variants under quasi-static loading conditions. These results were used to validate the proposed numerical FEA model. Based on the findings, the Mixed Gradient Structure was selected for further optimisation studies.

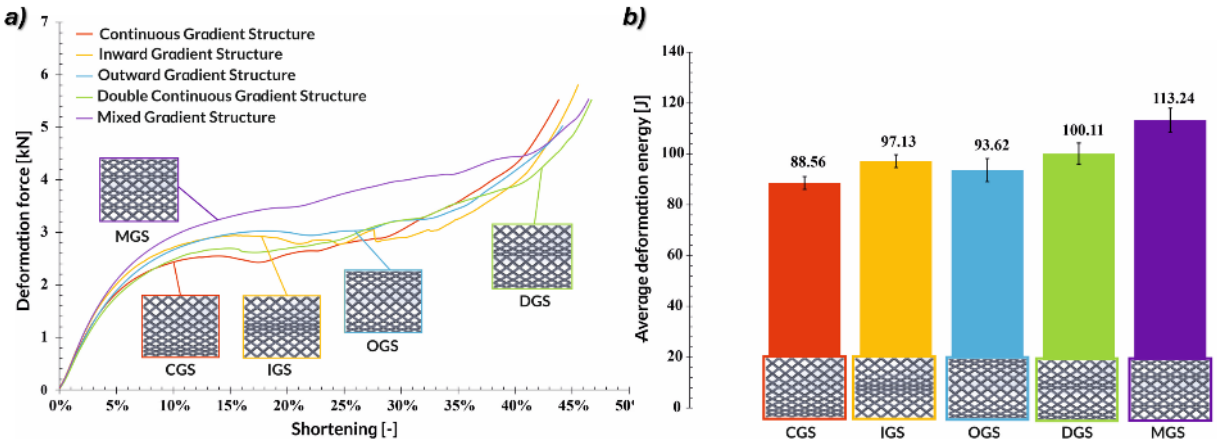

Fig. 1. Results of experimental compression tests a) – deformation force plot, b) – comparison of deformation energy values

5. References

[1] H. Yin, W. Zhang, L. Zhu, F. Meng, J. Liu, and G. Wen, "Review on lattice structures for energy absorption properties," *Compos. Struct.*, vol. 304, no. P1, p. 116397, 2023

[2] A. Nazir, K. M. Abate, A. Kumar, and J. Y. Jeng, "A state-of-the-art review on types, design, optimization, and additive manufacturing of cellular structures," *Int. J. Adv. Manuf. Technol.*, vol. 104, no. 9–12, pp. 3489–3510, 2019

[3] M. Srivastava, S. Rathee, V. Patel, A. Kumar, and P. G. Koppad, "A review of various materials for additive manufacturing: Recent trends and processing issues," J. Mater. Res. Technol., vol. 21, pp. 2612–2641, 2022

ROOM AND HIGH TEMPERATURE BEHAVIOUR OF THE AlSi9Cu3 ALLOY PRODUCED BY PBF-LB AND SUBJECTED TO TAILORED HEAT TREATMENTS

***L. Tonelli*[(1)], *L. Castagnini*[(1)], *A. Martucci*[(2)], *I. Lagalante*[(2)], *M. Lombardi*[(2)], *A. Morri*[(1)] *and L. Ceschini*[(1)]**

[(1)] *Department of Industrial Engineering (DIN), Alma Mater Studiorum - University of Bologna, Bologna (Italy)*
[(2)] *Department of Applied Science and Technology (DISAT), Politecnico di Torino, Torino (Italy)*

1. Introduction

Reducing carbon footprint in strategic sectors, particularly mobility, has become a central focus for governments, industries and academic research. Enhancing sustainability in mobility can be pursued by reducing the overall weight of aircraft or vehicles, thereby decreasing fuel and energy consumption. A widely accepted strategy involves replacing heavy alloys, such as iron-based ones, with lighter alloys, such as aluminium-based ones for structural components [2].

In recent years, the diffusion of additive manufacturing (AM) technologies has significantly expanded the potential for structural lightweighting in mobility applications. Indeed, by enabling the production of complex geometries with optimized material distribution, the overall weight of parts can be substantially reduced. Laser-based powder bed fusion (PBF-LB) is the most advanced AM technology and, combined with light alloys, it offers great potential for sustainable mobility.

However, the innovative nature of PBF-LB introduces unique microstructural features that directly affect the mechanical behaviour of manufactured components. Consequently, post-process heat treatments must be carefully tailored to this specific microstructure to obtain the desired mechanical properties. It follows that the successful adoption of aluminum alloys processed by PBF-LB for structural components necessitates a thorough characterization of their microstructural features and mechanical responses under various process and post-processing conditions.

While significant efforts have focused on Al-Si-Mg alloys, mainly AlSi10Mg and AlSi7Mg [1], the exploration of Al-Si-Cu alloys has been comparatively limited. These alloys, including AlSi9Cu3, are characterized by high strength and excellent thermal stability, making them very attractive for both the automotive and aerospace sectors. However, the literature on Al-Si-Cu alloys processed via PBF-LB is still quite limited, especially if the mechanical response at high temperatures is considered.

Based on the above, the present study aims to address this gap by providing a comprehensive characterization of the static mechanical properties of AlSi9Cu3 alloy produced by PBF-LB and subjected to tailored heat treatments, optimized within this research. Tensile properties were assessed at room temperature, and overaging hardness curves were evaluated at 200 °C, 245 °C, and 290 °C. These findings will provide a basis for future investigations into the thermal stability and high-temperature performance of this alloy.

2. Materials and methods

AlSi9Cu3 samples were produced starting from spherical pre-alloyed powders and processed on an EOSINT M270 Dual Mode PBF-LB machine, operating under Ar atmosphere and with a pre-heated building platform. The initial phase of this study focused on investigating post-process heat treatments performed on cubic samples. Both direct aging (T5) and solution treatment followed by aging (T6) were investigated. To evaluate the mechanical properties, cylindrical samples oriented in the vertical build direction were manufactured for tensile testing. After heat treatment, tensile samples were machined from the printed cylinders and subjected to uniaxial tensile tests at room temperature

using a screw tensile testing machine. Additionally, the hardness evolution under prolonged exposure at 200 °C, 245 °C, and 290 °C (overaging behavior) was characterized. The results of tensile tests and overaging behaviour were interpreted through detailed fractographic and microstructural characterizations. This comprehensive approach aimed to correlate microstructural features, including process-induced defects, to the observed mechanical performance.

3. Results and conclusions

The results of the tensile test (Fig. 1a) demonstrate the significant influence of heat treatment on mechanical behavior of the alloy. The T6 heat-treated alloy exhibits superior ultimate tensile strength (UTS) and elongation to failure (A%) compared to the as-built (AB) and T5 conditions, while maintaining comparable proof strength ($Rp_{0.2}$). The mechanical response is strongly affected by the unique microstructural features and process-induced defects, such as lack of fusion and gas pores (Fig. 1b), present in the PBF-LB AlSi9Cu3 alloy. Thus, a thorough understanding of these factors is essential for the effective design and optimization of structural components.

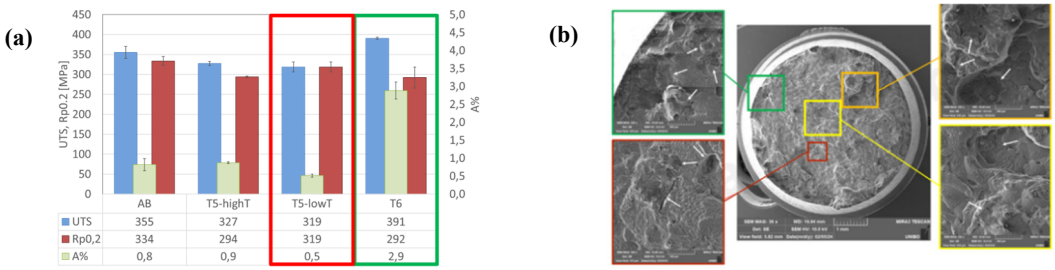

Fig. 1: Results of tensile tests (a) and representative SEM images of fracture surfaces with process-induced defects like lack of fusion and gas pores (b).

Conversely, the T6 heat-treated alloy exhibits lower thermal stability compared to the T5 condition (Fig. 2). As a result, the parameters for heat treatment should be carefully tailored to the component's working temperature.

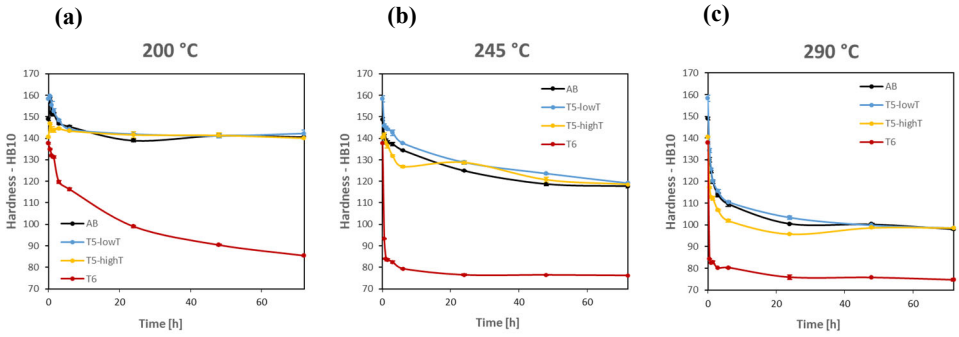

Fig. 2: AB, T5-low T, T5-high T and T6 overaging curves at 200 °C (a), 245 °C (b), 290 °C (c).

When compared to the behavior of conventional cast alloys, such as A354 and C355, the AlSi9Cu3 produced by PBF-LB emerges as a highly promising candidate for high-temperature applications.

4. Acknowledgements

Financed by the European Union - NextGenerationEU (National Sustainable Mobility Center CN00000023, Italian Ministry of University and Research Decree n. 1033 - 17/06/2022, Spoke 11 - Innovative Materials & Lightweighting).

5. References

[1] H.R. Kotadia et al.; *Additive Manufacturing*, 2021, *46,* 102155.
[2] W. Zhang, J. Xu; Materials & Design, 2022, 221, 110994.

ELASTIC PROPERTIES OF REINFORCED BODY CENTERED CUBIC LATTICE STRUCTURES

***M.Giacalone*[1], *S. Mantovani*[1],**
[1] *MilleChili Lab, "Enzo Ferrari" Engineering Department, University of Modena and Reggio-Emilia, Modena, Italy*

1. Introduction

Lattice structures have gained particular interest in the last years, as they proved helpful in biomedicine [1], as their mechanical properties may be tailored to match those of bone tissue, improving the integration of orthopedic implants. On the other hand, lattice structures may be used as functionally graded materials for lightweighting in automotive [2]. In both these cases the mechanical properties of these structures need to be carefully assessed, especially since they are related to their relative density. Besides the traditional Gibson-Ashby model [3], homogenization techniques have been developed and they are based on Finite Element (FE) simulations, starting from a representative unit cell.

The Body Centered Cubic (BCC) is among the most popular trabecular lattice with a cubic unit cell. This cell is bending dominated, as per the definition given by Gibson and Ashby. To increase the stiffness of this lattice, the BCC is reinforced with beams at the edges of the unit cell. When these beams are placed on the edges parallel to one direction, which is usually z, the lattice takes the name of BCCz. This unit cell enhances its stiffness in one direction at the expense of the mechanical properties in the transverse directions. Therefore, it may be suitable for applications in which the typical loading direction is well known.

This study presents a numerical homogenization to determine the main elastic constants of the BCCz lattice, over its relative density. This contribution is a follow up of Mantovani *et al.* [4], where the more isotropic BCCxyz cell, was considered. Some interpolating functions of prompt access, linking the main elastic constants of the BCCz lattice to its relative density are presented.

2. Materials and methods

The homogenization method starts with the CAD of a fundamental patch for the BCCz unit cell, which corresponds to 1/16 of the total cell (Fig. 1). The volume of this patch was used to calculate the relative density (ρ/ρ_s). Then, the geometry was discretized with first-order, tetrahedral elements. The full unit cell was then obtained by replicating the fundamental patch in space (Fig. 1). The cell was then subjected to periodic boundary conditions and six load cases, each with a unitary axial or shear strain. A sensitivity analysis of the mesh size was performed to assess the convergence, then, this workflow was repeated to generate 14 FE models. In each of these models, the cell size (l) was equal to 1, while the beam diameter (d) was increased to increase the relative density.

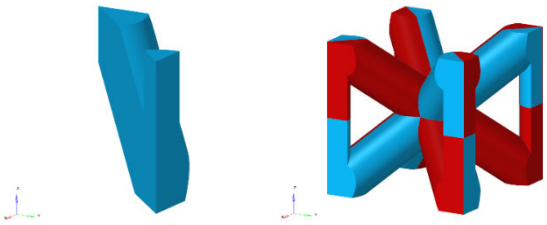

Fig. 1. BCCz Fundamental patch and full unit cell

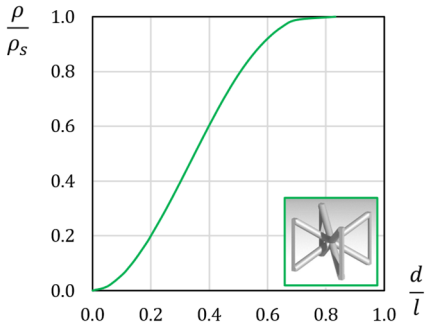

Fig. 2. Influence of the geometrical parameters on the relative density

#	$d\ [mm]$	ρ/ρ_s
1	0.05	0.015
2	0.10	0.056
3	0.15	0.119
4	0.20	0.200
5	0.25	0.293
6	0.30	0.394
7	0.35	0.499
8	0.40	0.603
9	0.45	0.701
10	0.50	0.788
11	0.55	0.861
12	0.60	0.920
13	0.65	0.963
14	0.70	0.988

Table 1. Relative density of the selected test cases

3. Results and conclusions

Fig. 3 shows the resulting elastic constants over the relative density. As it was expected, the Young's modulus along z (*i.e.* the direction of the reinforcing beams) is always higher than the Young modulus along x, because of the effect of the outer reinforcing beams. On the other hand, the shear moduli are more influenced by the diagonal beams within the cube. Therefore, the difference between the two shear moduli G_{xy}/E_s vs G_{yz}/E_s is negligible.

On the Poisson's ratios, significant variations are noticed within the relative density range (ρ/ρ_s). Within the xy plane, at extremely low relative density, the behavior of the diagonal beams resembles that of eight rods pinned together at the center of the cell, leading to a homogenized Poisson's ratio of 1.

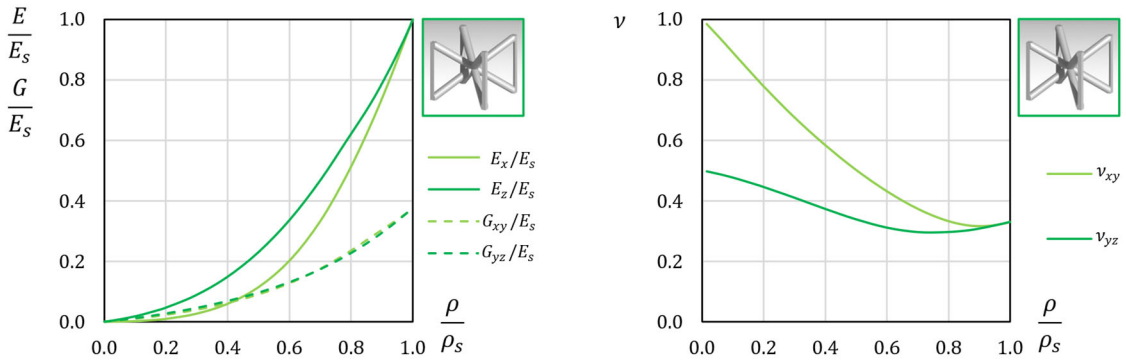

Fig. 3. Main elastic constants of the BCCz unit cell over the relative density

4. Funding

This work has been supported by the project "GOALS, Green Optimizations by Additive-manufactured Lightweight Structures", Project 20228PFA89, CUP J53D23001980006, Progetti di Ricerca di Rilevante Interesse Nazionale PRIN 2022, funded under the National Recovery and Resilience Plan (NRRP), Mission 4 Component C2 Investment 1.1 by the European Union – NextGenerationEU.

5. References

[1] S. Arabnejad, B. Johnston, M. Tanzer, and D. Pasini, 'Fully porous 3D printed titanium femoral stem to reduce stress-shielding following total hip arthroplasty', *Journal of Orthopaedic Research*, vol. 35, no. 8, pp. 1774–1783, Aug. 2017, doi: 10.1002/jor.23445.

[2] M. Abdi, I. Ashcroft, and R. D. Wildman, 'Design optimisation for an additively manufactured automotive component', *International Journal of Powertrains*, vol. 7, no. 1/2/3, p. 142, 2018, doi: 10.1504/IJPT.2018.090371.

[3] L. J. Gibson and M. F. Ashby, *Cellular Solids*. Cambridge University Press, 1997. doi: 10.1017/CBO9781139878326.

[4] S. Mantovani, M. Giacalone, A. Merulla, E. Bassoli, and S. Defanti, 'Effective Mechanical Properties of AlSi7Mg Additively Manufactured Cubic Lattice Structures', *3D Print Addit Manuf*, vol. 9, no. 4, pp. 326–336, Aug. 2022, doi: 10.1089/3dp.2021.0176.

STRESS CONCENTRATION IN HYBRID TPMS GEOMETRIES UNDERGOING AXIAL FATIGUE LOADS

M.Mele[1], M. De Agostinis[1], D. Croccolo[1], S. Fini[1], G. Olmi[1], A. Paffetti[1], A. Morri[1], P. Leo[2], R. Nobile[2], A. Pola[3], M. Tocci[3], S. Sartori[4]

[1] Department of Industrial Engineering (DIN), University of Bologna, Bologna, Italy
[2] Department of Engineering for Innovation (DEfI), University of Salento, Lecce, Italy
[3] Department of Industrial and Mechanical Engineering (DIMI), University of Brescia, Brescia, Italy
[4] Leonardo Helicopters, Cascina Costa di Samarate, Italy

1. Introduction

Additive manufacturing provides an unparalleled opportunity to fabricate complex geometries. This opportunity also paves the way for the reduction of weight in components by means of cellular solids, the fabrication of which could not be achieved by means of traditional manufacturing processes. Among cellular solids, triply periodic minimal surfaces (TPMS) have attracted considerable attention due to their distinctive properties. TPMS are intricate, three-dimensional structures that repeat periodically in all directions and have zero mean curvature, indicating that they locally minimise surface area. These structures efficiently distribute stress and offer excellent mechanical properties. Their periodic structure minimises stress concentrations, thereby improving strength-to-weight ratios and enhancing energy absorption and resilience under load. This results in controlled deformation, which improves performance and material efficiency[1].

In their exact form, TPMS are defined using the formula. However, more often, a combination of harmonic functions is used to delimit the space of TPMS. The most common structures include the Gyroid, Schwarz primitive, Diamond and I-WP, whose defining equations are summarized in Table 1

Table 1 Equations defining the base TPMS cells

Cell	Defining function
Schwarz P	$\cos x + \cos y + \cos z$
Gyroid	$\cos x \sin y + \cos y \sin z + \cos z \sin x$
Schwarz Diamond	$\sin x \sin y \sin z + \sin x \cos y \cos z + \cos x \sin y \cos z + \cos x \cos y \sin z$
I-WP	$2(\cos x \cos y + \cos y \cos z + \cos z \cos x) - (\cos 2x + \cos 2y + \cos 2z)$

The static properties of these structures have been the subject of several studies, while the issue of their fatigue behaviour has only been addressed by a limited number of researchers. Examples of characterisation include the gyroid structure [2,3] and the Schwarz structure [4].

Recently, research has indicated the potential for obtaining novel structures with distinctive properties through the combination of equations reported for fundamental structures [5]. In particular, Wang et al. demonstrated that artificial neural networks (ANN) can be effectively employed to predict the force/displacement curve of these structures under static loads [6]. This study represents a

preliminary investigation into the fatigue properties of these structures, with an analysis of the stress concentration factor Kt obtained under axial loads.

2. Materials and methods

The hybrid cells were obtained as a weighted sum of the functions in Table 1. Given that the sum of the weighting coefficients is equal to one, the combination of cells can be regarded as a problem in two variables. A full-factorial design of experiment (DoE) was conducted, in which the two variables were varied on 11 levels, resulting in a total of 121 different geometries, which also included the four base TPMSs. For the purposes of the analysis, a 4mm x 4mm x 4mm cell with a 0.8mm wall thickness was considered.

A 3x3x3 structure was initially modelled for each cell, after which a 0.01 mm elongation was imposed. The results of the simulation were then elaborated to isolate the stress results on the central cell. The maximum principal stress within the cell was extracted, and this stress was compared to the nominal one to calculate the stress intensity factor. Both modelling and calculation were run in NTop, while a Python script was used to elaborate the data.

3. Results and conclusions

Figure 1 shows the map of the stress concentration factor Kt when moving between different hybrid geometries.

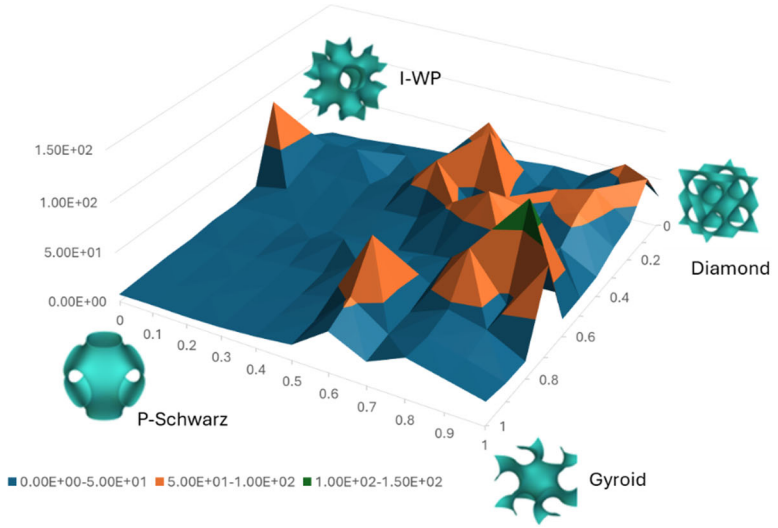

Figure 1 Map of the stress concentration factor for mixed cellular solids

As illustrated in *Figure 1*, the minimum value of Kt is observed in correspondence with the P-schwarz and I-WP geometries. A substantial pseudo-optimal region of feasibility can be discerned in the vicinity of these points, suggesting the existence of promising structural configurations with regard to fatigue behaviour. Additionally, it is possible to identify peaks in the map; these are arguably attributable to anomalous intersections in the hybrid geometry, resulting in the formation of sharp edges.

4. Acknowledgements

Financed by the European Union - NextGenerationEU (National Sustainable Mobility Center CN00000023, Italian Ministry of University and Research Decree n. 1033 - 17/06/2022, Spoke 11 - Innovative Materials & Lightweighting). The opinions expressed are those of the authors only and should not be considered as representative of the European Union or the European Commission's official position. Neither the European Union nor the European Commission can be held responsible for them.

5. References

[1] H. Yin, W. Zhang, L. Zhu, F. Meng, J. Liu, G. Wen, Review on lattice structures for energy absorption properties, Compos. Struct. 304 (2023) 116397. https://doi.org/10.1016/j.compstruct.2022.116397.

[2] G. Schultheiß, B. Heine, M. Merkel, Characterization of flexural fatigue behaviour of additively manufactured (PBF–LB) gyroid structures, Prog. Addit. Manuf. 9 (2024) 1331–1340. https://doi.org/10.1007/s40964-024-00607-y.

[3] L. Yang, C. Yan, W. Cao, Z. Liu, B. Song, S. Wen, C. Zhang, Y. Shi, S. Yang, Compression–compression fatigue behaviour of gyroid-type triply periodic minimal surface porous structures fabricated by selective laser melting, Acta Mater. 181 (2019) 49–66. https://doi.org/10.1016/j.actamat.2019.09.042.

[4] M. Gavazzoni, S. Beretta, S. Foletti, Response of an aluminium Schwarz triply periodic minimal surface lattice structure under constant amplitude and random fatigue, Int. J. Fatigue 163 (2022) 107020. https://doi.org/10.1016/j.ijfatigue.2022.107020.

[5] Z. Li, J. Li, J. Tian, S. Xia, K. Li, M. Li, Y. Lu, M. Ren, Z. Jiang, Inverse design of cellular structures with the geometry of triply periodic minimal surfaces using generative artificial intelligence algorithms, Eng. Struct. 321 (2024) 118988. https://doi.org/10.1016/j.engstruct.2024.118988.

[6] Y. Wang, Q. Zeng, J. Wang, Y. Li, D. Fang, Inverse design of shell-based mechanical metamaterial with customized loading curves based on machine learning and genetic algorithm, Comput. Methods Appl. Mech. Eng. 401 (2022) 115571. https://doi.org/10.1016/j.cma.2022.115571.

DEPENDENCE OF PHASE ANGLE BETWEEN MECHANICAL LOADING AND TEMPERATURE CYCLES IN TMF ON SMALL CRACK PROPAGATION

M. Arai[1], Y. Omiya[1] and Y. Yamazaki[2]
[1] Graduate School of Science and Engineering, Chiba University, Chiba, Japan
[2] School of Engineering, Chiba University, Chiba, Japan

1. Introduction

Recently, high efficiency gas turbine combined cycle (GTCC) systems have been used as the primary supply source for electric power systems. Although it is strongly needed to increase the proportion of renewable energy sources such as solar and wind power, there is a severe problem with the unstable power supply. Their power generation capacities are greatly affected by environmental factors such as weather changes. Therefore, the presence of the GTCC with superior starting performance becomes essential as a backup power supply of renewable energy sources. In such situations, since the operation expects increased frequent starting/stopping and frequent load fluctuation as a backup power supply, there is concern about severe damage caused by thermo-mechanical fatigue (TMF) loading in turbine blades and vane. Many efforts have been made to estimate the TMF lives of Ni-base superalloys [1]. Early growth behaviors of naturally initiated small cracks in order of sub-millimeter in size can provide some essential information for life and the remaining life prediction to the TMF and LCF failures because most part of fatigue life under TMF and LCF conditions is generally dominated by the propagation process. Especially, since the wall thickness of the superalloy blade with the cooling flow path is thin (some millimeters), the understanding of the small crack propagation mechanisms becomes important.

In this study, TMF tests were conducted under the In-Phase (IP), the Out-of-Phase (OP), and the Dwell-IP conditions on single crystal Ni-based superalloys to investigate the small crack propagation behavior of naturally generated cracks on the specimen surface. In addition, the effect of phase angle in the TMF loadings on small crack propagation was investigated.

2. Materials and methods

The material used in this study is a single crystal Ni base superalloy, CMSX-4. The propagation tests of naturally initiated small fatigue crack were conducted under the In-Phase (IP), the Out-of-Phase (OP), and the Dwell-IP types of thermomechanical fatigue loading conditions in this study. The Dwell-IP condition refers to a condition in which a high temperature tensile hold of 10 minutes is added at the maximum temperature of the IP condition. The test conditions are summarized in Table 1. All tests were performed under load-controlled conditions by means of the TMF testing machine. A triangle waveform was used for both mechanical and thermal cycling under the IP and OP conditions. The hysteresis loop during the test was measured by using the extensometer with 5 mm gauge length. The mechanical strain, ε_{mech} was evaluated from the difference between the measured total strain during the TMF tests and the thermal expansion without loading, measured before the TMF tests.

3. Results and conclusions

Typical hysteresis loops measured during TMF tests are shown in Fig. 1. As shown in Fig. 1, the elastic deformation was dominant in the cyclic deformation behavior. Although the hysteresis loops under IP and Dwell-IP conditions show almost the same deformation behavior, a creep strain of $\Delta\varepsilon_{creep}$ = 0.04% occurred due to the high temperature tensile hold under the Dwell-IP condition. In addition, the hysteresis loops exhibited a parabolic shape due to the temperature dependence of Young's modulus under all TMF test conditions. Figure 2 shows the crack propagation rates correlated with the cyclic *J*-integral range, ΔJ_f. The ΔJ_f was evaluated by Dowling's equation [2]. The crack propagation rate is higher in the order of Dwell-IP, IP, and OP conditions. The difference in crack growth rate due to the phase angle might be related to the localized creep strain at the crack tip.

Table 1 – Crack propagation test conditions.

Test type	IP	OP	Dwell-IP
Temperature range [°C]	400 - 900		
Stress range [MPa]	-550 - 400	-400 - 500	-550 - 400
Frequency [Hz]	1/400		1/1000
Hold time at maximum temp. [s]	0	0	600
Phase angle [deg.]	0	-180	0

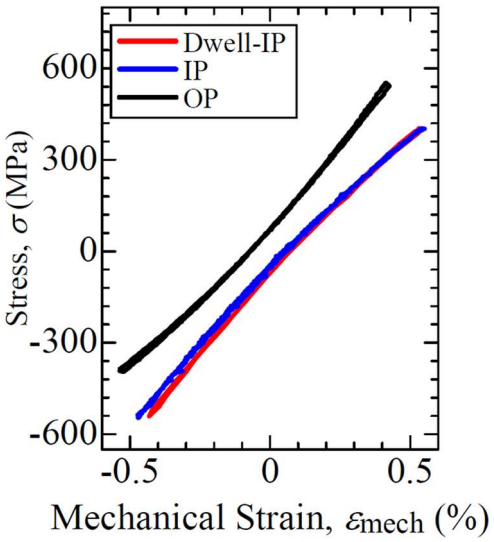

Fig. 1. Typical hysteresis loops.

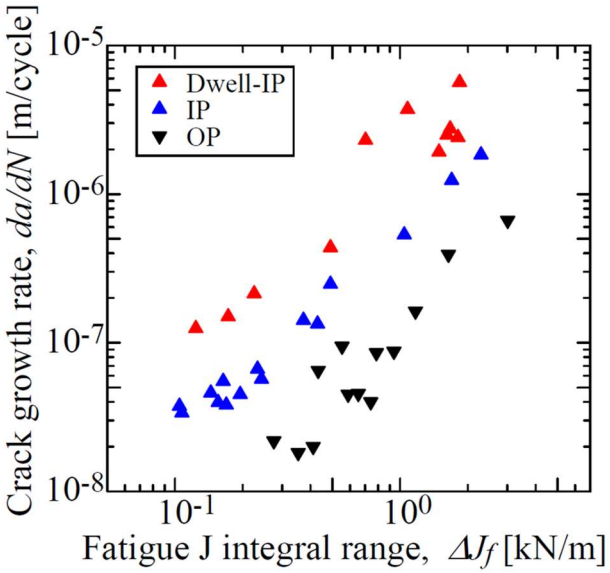

Fig. 2. Crack propagation rates correlated with ΔJ_f.

3. References

[1] J. Jones, M. Whittaker, R. Lancaster, C. Hyde, J. Rouse, B. Engel, S. Pattison, S. Stekovic, C. Jackson, H.Y. Li. (2020) The effect of phase angle on crack growth mechanisms under thermo-mechanical fatigue loading, *Int. J. Fatigue.*, **135**, 105539.

[2] N.E. Dowling. (1977) Cyclic stress-strain and plastic deformation aspects of fatigue crack growth, *ASTM STP*, **673**, 97-121.

ELASTIC PROPERTY ANALYSIS IN TRIPLY PERIODIC MINIMAL SURFACE STRUCTURES THROUGH HOMOGENIZATION AND ARTIFICIAL NEURAL NETWORKS

D. Croccolo[1], M. De Agostinis[1], S. Fini[1], M. Mele[1], G. Olmi[1], A. Paffetti[1]
[1] Department of Industrial Engineering (DIN), University of Bologna, Bologna, Italy

1. Introduction

This research introduces a detailed framework for the development, homogenization, and predictive analysis of Triply Periodic Minimal Surface (TPMS)-based unit cells, celebrated for their superior mechanical properties and lightweight nature. The process begins with the construction of TPMS cells (Primitive, Gyroid, Diamond, I-WP) and custom-defined hybrid cells through strategic combinations of percentage weights and parental cells, allowing precise geometric control.

Finite Element (FE) models of these cells are then utilized in a homogenization process to derive their effective elastic properties, facilitated by a Python script that automates data collection for training an Artificial Neural Network (ANN). This ANN accurately predicts the mechanical properties, significantly improving design process efficiency.

TPMS structures, observed in natural systems such as sea urchin skeletons and butterfly wings [1], demonstrate high specific strength and low density due to their unique minimal mean curvature. Advances in Additive Manufacturing (AM) have enabled the production of these complex structures, allowing application-specific customization [2]. Various AM methods, like Fused Filament Fabrication (FFF) and Laser Powder Bed Fusion (L-PBF), have proven effective for creating TPMS structures [3, 4].

Integration of predictive modeling, through advanced ANN models, opens new possibilities for the design and optimization of engineered materials, extending TPMS applications to areas such as thermal management and water treatment [5]. This approach not only enhances traditional engineering strategies but also incorporates cutting-edge technology, setting a new standard in material science for designing and optimizing lightweight, high-performance materials. The methodology developed offers robust and efficient tools to take advantage of the benefits of TPMS structures, driving innovative solutions in various industrial and research domains.

2. Materials and methods

In the methodology used for this research, the initial focus is on the systematic creation of TPMS-based unit cells including Primitive, Gyroid, Diamond, and I-WP geometries, as well as innovative hybrid designs. These designs were crafted through meticulous adjustments in percentage weights and a strategic selection of base cells, allowing for detailed control over their geometric configurations.

To quantitatively analyze these structures, Finite Element (FE) models were developed, serving as a crucial step for the subsequent homogenization process which aims to elucidate their effective elastic properties.

A custom Python script was used to automate the data generation and collection process, which is vital to train a sophisticated artificial neural network (ANN). This ANN plays a pivotal role in predicting the linear elastic properties of TPMS structures, thus streamlining the design process and enhancing the precision in engineering applications. The utilization of this methodology not only facilitates the detailed study of the mechanical behavior of TPMS structures but also integrates advanced manufacturing techniques to tailor these materials for specific applications, further expanding their potential in various engineering domains.

3. Results and conclusions

This study has effectively demonstrated the potential of Triply Periodic Minimal Surface (TPMS) structures to optimize mechanical properties for key industrial applications. The generation, homogenization, and predictive modeling of these structures have been explored, specifically focusing on Primitive, Gyroid, Diamond, and I-WP cells and their mixed combinations.

The proposed approach combined known TPMS cells with weighted sums, improving the design space and leading to significant improvements in stiffness, strength, and energy absorption. The homogenization process, automated through a Python-based script, efficiently extracted the effective elastic properties, aligning well with the theoretical models shown in the accompanying graph. The graph displayed in Figure 1 illustrates the normalized Young's modulus against the Volume Fraction, validating our methods against established theoretical boundaries.

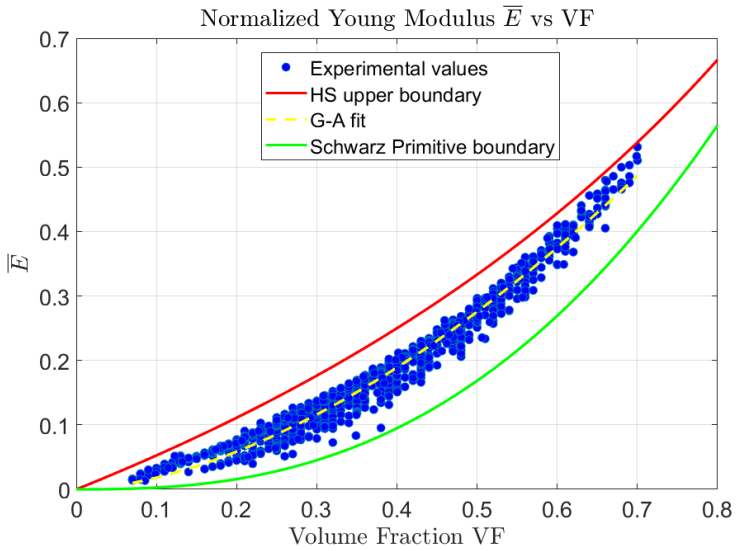

Fig. 1. Extracted normalized Young's Modulus from the homogenization process, compared to the structures' Volume Fraction.

The predictive models, particularly our Artificial Neural Network (ANN), showed high accuracy, affirming the utility of machine learning in streamlining the design process and reducing simulation costs. Future work will focus on expanding the Machine Learning models and datasets, improving predictive robustness, and integrating experimental validations with physical prototypes to advance the understanding of TPMS under practical conditions. This work underscores the versatility of TPMS structures in engineering high-performance materials, setting a foundation for further innovation in lightweight design applications.

Acknowledgements: Project funded under the National Recovery and Resilience Plan (NRRP), Mission 04 Component 2 Investment 1.5– NextGenerationEU, Call for tender n. 3277 dated 30/12/2021 Award Number: 0001052 dated 23/06/2022.

4. References

[1] S. H. Siddique, P. J. Hazell, H. Wang, J. P. Escobedo, A. A. Ameri, Lessons from nature: 3d printed bio-inspired porous structures for impact energy absorption – a review, Additive Manufacturing 58 (2022). doi:10.1016/j.addma.2022.103051.

[2] H. Yin, W. Zhang, L. Zhu, F. Meng, J. Liu, G. Wen, Review on lattice structures for energy absorption properties, Composite Structures 304 (2023) 116397. doi:10.1016/j.compstruct.2022.116397.

[3] N. Kladovasilakis, K. Tsongas, D. Tzetzis, Mechanical and fea-assisted characterization of fused filament fabricated triply periodic minimal surface structures, Journal of Composites Science 5 (2021). doi:10.3390/jcs5020058.

[4] X. Shi, W. Liao, P. Li, C. Zhang, T. Liu, C. Wang, J. Wu, Comparison of compression performance and energy absorption of lattice structures fabricated by selective laser melting, Advanced Engineering Materials 22 (2020). doi:10.1002/adem.202000453.

[5] M. G. Gado, O. Al-Ketan, M. Aziz, R. A. Al-Rub, S. Ookawara, Triply periodic minimal surface structures: Design, fabrication, 3d printing techniques, state-of-the-art studies, and prospective thermal applications for efficient energy utilization, Energy Technology 12 (2024). doi:10.1002/ente.202301287.

DESIGN OF LIGHTWEIGHT CELLULAR STRUCTURES OPTIMISED FOR PIN-COLLAR JOINTS

D. Croccolo[1], M. De Agostinis[1], S. Fini[1], M. Mele[1], G. Milan[1], G. Olmi[1], A. Paffetti[1]

[1] Department of Industrial Engineering (DIN), University of Bologna, Bologna, Italy

1. Introduction

The development of lightweight components has attracted significant interest across various engineering disciplines, and particularly in the automotive industry, where achieving an optimal balance between safety, efficiency, and the reduction of both emissions and fuel consumption is of paramount importance.

In this context, cellular solids – defined as "porous" materials composed of interconnected elements with shared edges and faces, arranged to occupy a defined volume [1] – play a pivotal role.

These metamaterials offer significant advantages, including the ability to enhance both stiffness and strength while simultaneously improving impact resistance. Furthermore, they exhibit exceptional strength-to-mass ratio, fire resistance, adjustable thermal conductivity, low moisture retention, and sound-dampening properties, rendering them highly suitable for high-performance applications [4].

Additive Manufacturing techniques have opened new possibilities for crafting such complex models that cannot be replicated with conventional fabrication methods, securing an elevated degree of control and geometric freedom [5, 6].

Following insights from literature review, this study rely on the geometric and functional redesign of the hollow part of a pin-collar steel connection (ISO 10123 e ASTM D4562-01), considering three distinct type of cells, namely BCC + CP (body-centred cubic + primitive cubic), circular honeycomb and generative shape. The primary objective is to establish which configuration, compared to the full specimen, guarantees optimal performance without compromising hybrid joint's static strength.

The introduction of cellular architectures within adhesive joints represents a novel approach that deserves a thorough investigation as it could enable the possibility to effectively transfer shocks and impacts to the hub, thereby relieving the load acting on the adhesive. This modification aim to facilitate a better overall response of the system, optimising the load distribution, improving the operational efficiency, and extending the lifespan of the components.

2. Materials and methods

The individual cells were modelled using CREO Parametric software, ensuring conformity with hub's circular profile and adherence to the constraints imposed by M-LPBF (Metal Laser Powder Bed Fusion) process. A key requirement was to maintain a minimum wall thickness of 1 mm, while optimising material efficiency.

The component's overall dimensions span from an inner diameter of 20 mm to an outer diameter of 40 mm, with the cellular architectures positioned within a diameter range of 24 to 36 mm. This configuration incorporates solid layers of 2 mm at both the inner and outer regions of each section, thereby reinforcing structural integrity. The modified collars comprise twelve circumferentially distributed cells, organised into four levels, resulting in a total of forty-eight elements.

Table 1 summarises the final mass properties of the three types of cellular solids, while the full component exhibits a total mass of 149.9 g. These values were calculated based on the properties of AISI-316L stainless steel, with a specified density of 7954 kg/m³.

Table 1. Mass properties of hollow section as a function of different cells type.

Cell type	Mass [g]	% of reduction
BCC + CP	91.7	38.82
Generative	82.8	44.76
Circular Honeycomb	129.6	13.34

The three specimens were subsequently assessed using a static simulation within a linear elastic framework in Ansys software. In this context, deformation is directly proportional to the applied load, allowing the energy absorption characteristics to be effectively represented by analysing the displacement of the component. Furthermore, it remains essential to ensure that failure occurs in the adhesive layer rather than the material itself. Cyclic symmetry constraints were implemented to reduce the computational cost.

The yield strength of the material was set to 470 MPa, and a standard LOCTITE® Hysol® 9466 epoxy resin, possessing a shear strength (τ_{ad}) of 37 MPa, was employed as the adhesive. The value of shear strength was used to determine the average adhesive force applied to the internal diameter.

3. Results and conclusions

As depicted in *Figure 1*, circular honeycomb unit elements fail to achieve a significant reduction in mass and exhibit high rigidity, rendering them less competitive for the intended energy absorption application.

Conversely, the variants featuring BCC + CP cells and generative modelling, despite minor differences in relative density, demonstrate overall superior performance. However, truss-based configurations are preferable as they yield more consistent results and offer a more repeatable design.

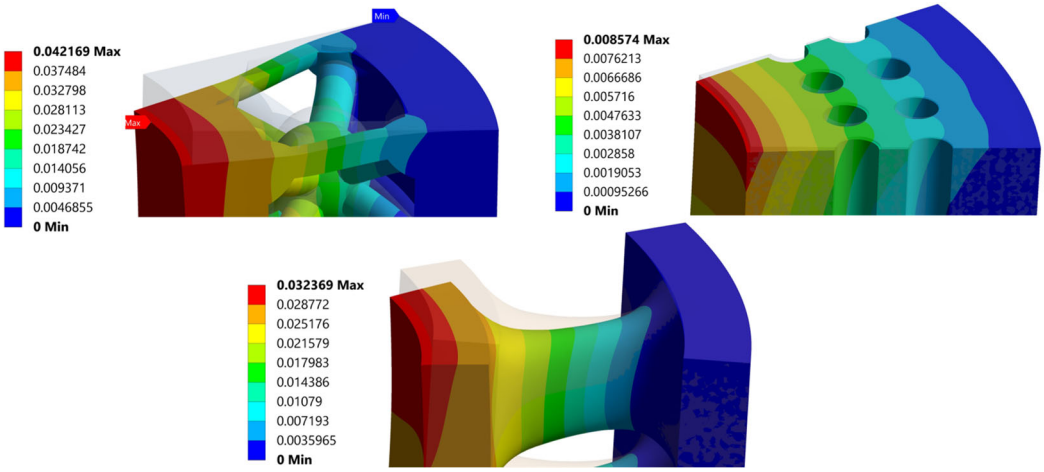

Figure 1. Displacement comparison as a function of unit cell.

Indeed, generative forms, while highly competitive, are dependent on the type of genetic algorithm embedded within the software. As a result, they display a greater degree of variability in the design, precluding the perfect scalability of outcomes when comparing cells of differing sizes. Certainly, further investigations will be required within the elastic-plastic field, also exploring dynamic scenarios, and advancing the implementation of more intricate cellular geometries.

Acknowledgements: Project funded under the National Recovery and Resilience Plan (NRRP), Mission 04 Component 2 Investment 1.5– NextGenerationEU, Call for tender n. 3277 dated 30/12/2021 Award Number: 0001052 dated 23/06/2022.

5. References

[1] G. Costanza, D. Solaiyappan, and M. E. Tata, "Properties, Applications and Recent Developments of Cellular Solid Materials: A Review," Nov. 01, 2023, Multidisciplinary Digital Publishing Institute (MDPI). doi: 10.3390/ma16227076.

[2] E. Arrieta, J. Mireles, C. Stewart, C. Carrasco, and R. B. Wicker, "Multiscale Analysis Of Cellular Solids Fabricated By EBM," 2017.

[3] D. Rosen, S. Johnston, M. Reed, and H. Wang, "Design Of General Lattice Structures For Lightweight And Compliance Applications," Jul. 2006.

[4] S. Prabhu, V. K. B. Raja, and R. Nikhil, "Applications of Cellular Materials – An Overview," Applied Mechanics and Materials, vol. 766–767, pp. 511–517, Jun. 2015, doi: 10.4028/www.scientific.net/amm.766-767.511.

[5] M. Helou and S. Kara, "Design, analysis and manufacturing of lattice structures: An overview," Int J Comput Integr Manuf, vol. 31, no. 3, pp. 243–261, 2018, doi: 10.1080/0951192X.2017.1407456.

[6] A. Changdar, S. S. Chakraborty, Y. Li, and C. Wen, "Laser additive manufacturing of aluminium-based stochastic and nonstochastic cellular materials," Jun. 01, 2024, Chinese Society of Metals. doi: 10.1016/j.jmst.2023.09.045.

[7] N. Top, İ. Şahin, and H. Gökçe, "The Mechanical Properties of Functionally Graded Lattice Structures Derived Using Computer-Aided Design for Additive Manufacturing," Applied Sciences (Switzerland), vol. 13, no. 21, Nov. 2023, doi: 10.3390/app132111667.

CHARACTERIZATION OF AGGREGATE DISTRIBUTION IN 3D CONCRETE PRINTING USING X-RAY CT

R. Yoshihara[1], K. Hashimoto[2], D. Lou[1] and Y. Honda[3]
[1] Graduate School of Engineering, Hokkaido University, Sapporo, Japan
[2] Faculty of Engineering, Hokkaido University, Japan
[3] Technical Center of Engineering, Hokkaido University, Japan

1. Introduction

3D concrete printing (3DCP) has been advancing automation of construction technology and has gained attention in recent years. In this additive manufacturing process, cementitious material is extruded from nozzle and deposited with geometric digital control. The process creates weak layer-interface region between adjacent filaments, which leads to crack along the region and anisotropy in the printed object [1]. It has been believed that the primary factor behind the formation of material heterogeneity is provided by air voids distribution during the deposition [2].

As for the conventional casting of concrete, it has been noted that local material segregation affects the mechanical properties of concrete. For instance, aggregate content is lower near interface with rebar, resulting in reduction of the mechanical properties of concrete [3]. In 3DCP, it can be assumed that heterogeneous distribution of aggregate influences the mechanical properties of 3D-printed structure. Furthermore, mortar used as 3DCP material is flowed out under applied pressure inside nozzle. The behavior of material extrusion is similar to pipe flow in the conventional pumiping of concrete. In the pumping of concrete, aggregate moves away from the interior pipe wall in accordance with velocity distribution and shear force distribution. Consequently, 2-mm-thick layer of cement paste is formed near the inner surface of pipe wall, which is known as lubrication layer [4].

Since it has been assumed that the lubrication layer is formed inside the nozzle in 3DCP [5], decrease in aggregate content and increase in cement paste content contribute to the formation of layer-interface region, which corresponds to the outside of filaments. However, there are very few studies evaluating the aggregate distribution in 3DCP. The objective of this study is to evaluate the heterogeneity of aggregate distribution in 3D-printed object. Continuous cross-sectional images are obtained using X-ray CT to quantify the volume and diameter of each aggregate.

2. Materials and methods

A lab-scale 3D printer was developed with using cartridge system. Mortar was used as the 3DCP material. Silica sand was used as the aggregate. The average aggregate diameter was approximately 500 μm. The sample preparation process is outlined in Fig. 1. Sample F was trimmed into 4mm cube from center region of filament. Similarly, Sample L was trimmed into 4mm cube from layer interface region of 3D printed object composed of two layers and two rows. A micro-CT scanner was used to obtain continuous cross-sectional images of the samples. The volume and diameter of each aggregate were calculated by image analysis. The aggregate content with a diameter of 500 μm or more was calculated for each sample. Furthermore, the cement paste content was consequently calculated by subtracting the aggregate content and the cumulative air void volume from the total volume of interest.

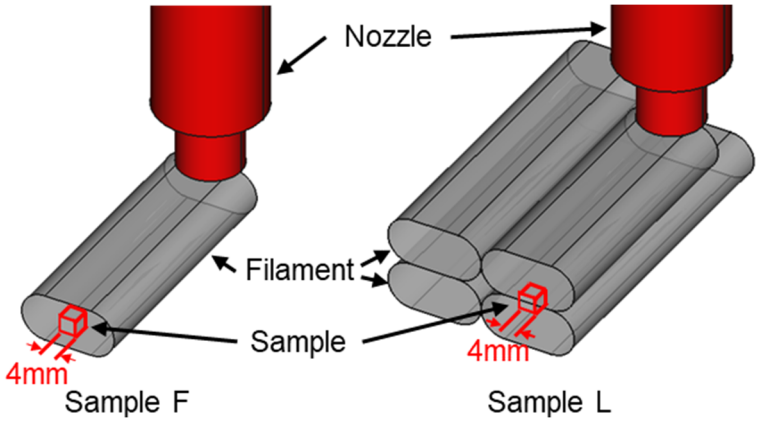

Fig. 1. Sample preparation

3. Results and conclusions

Fig. 2 shows the aggregate content in each sample type. The aggregate content in the layer-interface region is smaller than that in the center of the filament, regardless of aggregate diameter. Furthermore, the larger aggregate shows a greater reduction in content. Fig. 3 shows the cement paste content in each sample type. The cement paste content in Sample L is 1.07 times that in Sample F. These results indicate the presence of heterogeneity within the 3D-printed object. This heterogeneity is likely caused by the formation of lubrication layer inside the nozzle. It can be assumed that the lubrication layer reduces the amount of large aggregate even in the layer-interface region which corresponds to the outer side of filament.

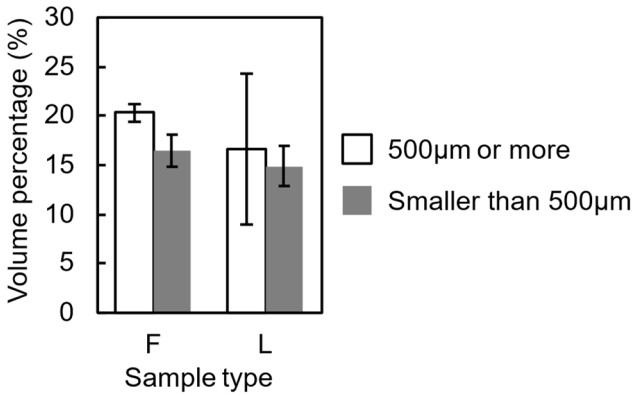

Fig. 2. Aggregate content

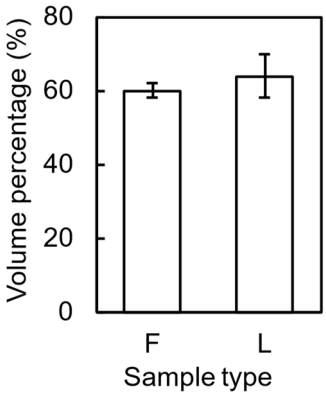

Fig. 3. Cement paste content

4. References

[1] K. Nakase, K. Hashimoto, T. Sugiyama, K. Kono (2024). Influence of print paths on mechanical properties and fracture propagation of 3d printed concrete. *Constr. Build. Mater.*, **438**, 137019.

[2] Y. Chen, O. Çopuroğlu, C. Romero Rodriguez, F. F. de Mendonca Filho, and E. Schlangen (2021). Characterization of air-void systems in 3d printed cementitious materials using optical image scanning and X-ray computed tomography. *Mater. Charact.*, **173**, 110948.

[3] C. F. de Azevedo, J. M. F. de Carvalho, J. C. Mendes, A. S. S.Castro, R. R. Barreto, R. A. F. Peixoto (2020). Compressive strength of reduced concrete specimens considering dimensional distortion of coarse aggregates. *Constr. Build. Mater.*, **257**, 119448.

[4] S. Fataei, E. Secrieru, V. Mechtcherine (2020). Experimental insights into concrete flow-regimes subject to shear-induced particle migration (sipm) during pumping. *Materials*, **13**, 1233.

[5] R. Yoshihara, K. Nakase, K. Hashimoto, T. Sugiyama, Y. Honda (2024). Evaluation of aggregate distribution heterogeneity in 3d printed concrete by means of X-ray CT. *Buildings*, **14**, 1132.

FABRICATION AND EXPERIMENTAL CHARACTERIZATION OF STRAIN SENSORS BASED ON INKJET PRINTING

G. De Pasquale[1], F. Ursi[1], S. Fink[2] and A. El-Sarout[2]
[1] Smart Structures and Systems Lab, Politecnico di Torino, Italy
[2] Fraunhofer Institute for Laser Technology ILT, 52074 Aachen, Germany

1. Introduction

Recent advancements in electronics manufacturing include the development of additive manufacturing (AM) techniques that enable components with unique features and cost-effective solutions [1]. Electronics produced through AM, often referred to as printed electronics, can be categorized into those on 3D surfaces, fully printed electronics, and in-mold electronics. The most commonly employed AM techniques for printed electronics include extrusion-based printing, inkjet printing, electrohydrodynamic (EHD) jet printing, and aerosol jet printing (AJP) [2]. Applications of printed electronics have shown promising results in manufacturing sensors, antennas, batteries, and flexible electronics. Among these, there is significant interest in using AM techniques to create affordable sensing devices with simple operational principles, such as strain gauges [3]. One intended purpose of printed strain gauges is the development of smart components equipped with integrated self-health monitoring (SHM) systems [4]. Other potential applications will involve multi-material joints for structural applications [5, 6].

This study aims to manufacture and investigate the sensing properties of a strain gauge created using Inkjet printing. The sensing device will be validated through tensile testing of a dog-bone specimen equipped with the printed strain gauge.

2. Ink-jet printed sample fabrication

The substrate is a dog-bone sample (10.46x2.65 mm^2 cross section) of AlSi10Mg alloy fabricated through laser powder based fusion (L-PBF) process with 352 W laser power, 0.03 mm layer thickness and 0.124 mm hatch distance. After manufacturing, samples are cleaned with isopropanol and treated in a plasma chamber for 5 minutes to enhance adhesion of the insulating polymer. An insulating layer of Ormocomp polymer is dispensed on the sample using a Martin dispenser, ensuring uniform coverage with a syringe and 0.34 mm needle in a spiral pattern. The dispensing speed is 15 mm/s, with a 0.26 mm track spacing and 7 mm^3/s flow, resulting in a 140 µm thick layer, which cures under 355 nm UV light for 15 minutes before sensor printing.

A sensor is printed on the insulated sample using a Fujifilm DMP inkjet printer with silver nanoparticle ink in a double chessboard pattern. The 12-nozzle cartridge operates at a resolution of 1016 dpi, with a plate temperature of 40 °C and print-head temperature of 35 °C. The printing process is executed in a four-step chessboard pattern. In this approach, the printing file is divided into four chessboard-like sub-images, which are printed one after another. This method minimizes the coffee-stain effect, allowing ink to dry independently and avoiding material concentration at edges. While it increases surface roughness, the benefits of reduced defects and improved sensor performance are deemed greater.

For sintering, an Ytterbium fibre-laser at 1070 nm and 200 W power is used with an f-theta lens (focal length = 254 mm). The focused laser beam moves over the printed sensor in a bidirectional meandering square format at 1500 mm/s, with the power set to 32 W and a sintering time of less than 5 seconds. The width of the conductive path is 0.1 mm. The path described by the conductive track consists of two meanders, each of them made of five units and measuring 0.4x0.4 mm. One meander is horizontally oriented while the other is vertically oriented (Fig 1a).

3. Characterization results

The electro-mechanical characterization of the sample is performed with the hydraulic testing system Instron 8801. Force, displacement and electrical resistance of the sensor are measured with 200 Hz sampling frequency with the DAQ QuantumX 1615B and Catman software. The resistance of the conductive track is measured with a four-wire connection to compensate the lead resistance. The load is applied with displacement-controlled mode at 0.1 mm/min up to 600 N, with clamp pressure of 90 bar. The experimental setup is reported in Fig. 1b and the resistance-force curve in Fig. 1c. In the measured force range 0-600 N (72 GPa Young's modulus) the sample strain is $\varepsilon = 0.0301\%$. The measured k-factor of the sensor is then $\Delta R/R0/\varepsilon = 1.0809$ in the range considered. The coefficient of determination of the linear regression is 0.994.

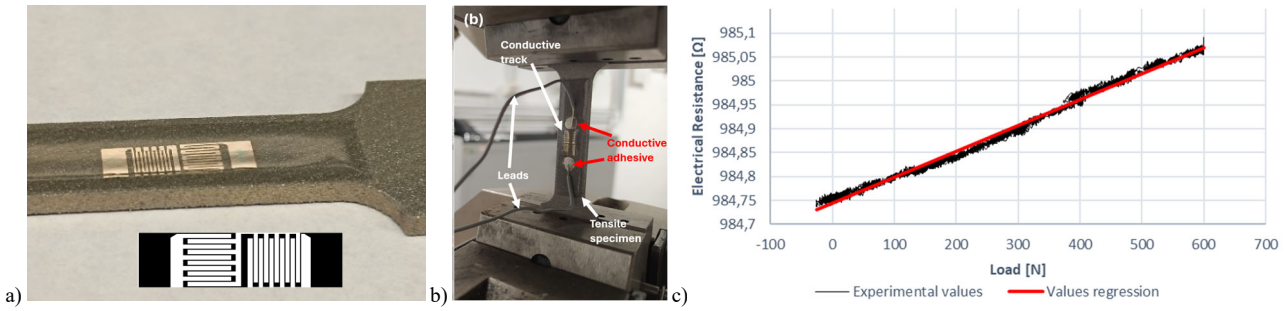

Fig. 1. Close-up of the printed sensor and design used as input for the inkjet system (a), tensile test setup (b), experimental curve and linear regression of electric output of the sensor (c).

4. Acknowledgements

Partially funded by the Horizon Europe grant "HORIZON-CL4-2022-RESILIENCE-01", Project MIMOSA (Project 101091826).

5. References

[1] S.K. Dhinesh et al. (2022). Recent trends in additive manufacturing of electronics devices. *Mater. Today Proc.*, **66**, 928–941.

[2] H.W. Tan, Y.Y. Choong, C.N. Kuo, H.Y. Low, and C.K. Chua (2022). 3D printed electronics: Processes, materials and future trends. *Prog. Mater. Sci.*, **127**, 100945.

[3] A.S. Fiorillo, C.D. Critello, and A.S. Pullano (2018). Theory, technology and applications of piezoresistive sensors: A review. *Sens. Actuators A Phys.*, **281**, 156–175.

[4] L. Duan, D.R. D'hooge, and L. Cardon (2020). Recent progress on flexible and stretchable piezoresistive strain sensors: From design to application. *Prog. Mater. Sci.*, **114**, 100617.

[5] G. De Pasquale and A. Coluccia (2023). Modeling and Experimental Validation of CFRP-Metal Joints Utilizing 3D Additively Manufactured Anchors. *ASME J. Manuf. Sci. Eng.*, **145**(11), 111004.

[6] G. De Pasquale, F.E. Altunok and F. Ursi (2023). Investigation of the Mechanical Strength of CFRP with Co-Cured Additively Manufactured Metal Inserts. *Procedia Struct. Integrity*, **47**, 573-578.

DYNAMIC STRAIN SENSORS INTEGRATED IN THE FUSED FILAMENT FABRICATION OF STRUCTURES

F. Ursi and G. De Pasquale
Smart Structures and Systems Lab, Politecnico di Torino, Italy

1. Introduction

Fused filament fabrication (FFF) is currently one of the simplest and most accessible additive manufacturing (AM) processes, widely adopted for the production of functional components across various application areas, including biomedicine, civil engineering, automotive, aerospace, and acoustics [1]. FFF can process a wide range of materials, including filler-based polymers such as carbon-based conductive polymer composites (CPCs), which are particularly effective in strain-sensing applications [2]. The use of CPCs offers a practical approach for co-printing both the structural material and the sensing system, enabling the creation of smart components. Recent studies have highlighted how the layer-by-layer manufacturing strategy, inherent to different additive processes, can be utilized as an embedding method. The integration of external elements (e.g., circuits, electronic boards, actuators) into a component has been demonstrated to be effective in fields such as sensing, robotics, and energy harvesting [3, 4]. Notably, the embedding of sensing elements represents a promising diagnostic strategy, particularly under hostile environmental conditions.

The integration of sensing elements into structural components, either as stand-alone transducers or printed conductive materials, represents an alternative approach to traditional sensors for structural health monitoring (SHM). This study aims to investigate and compare the strain-sensing performance under dynamic conditions of two different transducers embedded within a cantilever beam and integrated into the FFF process: a commercially available stand-alone piezoelectric sensor and a co-printed sensor based on conductive polymers.

2. Samples description and dynamic tests setup

The cantilever beams used as support structures were fabricated from black nylon and white PLA using the FFF process on the Ultimaker S5 system. The first sensor analyzed is the stand-alone PFC-W14 model from Advanced Cerametrics Inc. The second sensor is co-printed with the structure itself using the conductive material “FILI” provided by the Aimplas Technological Institute of Plastics. Dynamic excitation was applied using the electromechanical shaker TV 51120 (TIRAvib). The input acceleration was measured with a 353B34 ICP accelerometer (Piezotronics), while the response acceleration at the free end of the beam was recorded with the VibroONE VIO130 vibrometer (Polytec). The two sensors were characterized by correlating their electrical outputs with the frequency response function (FRF) of the structure.

The output signals from the two sensors (voltage for the PFC sensor and resistance for the co-printed sensor) were acquired using the NI 9234 module integrated into the CompactRIO 9054 analog-to-digital converter (National Instruments), with data collection and analysis performed through a custom LabVIEW application. The experimental setup is shown in Figs. 1a and 1b, while the sensors are depicted in Figs. 1c and 1d.

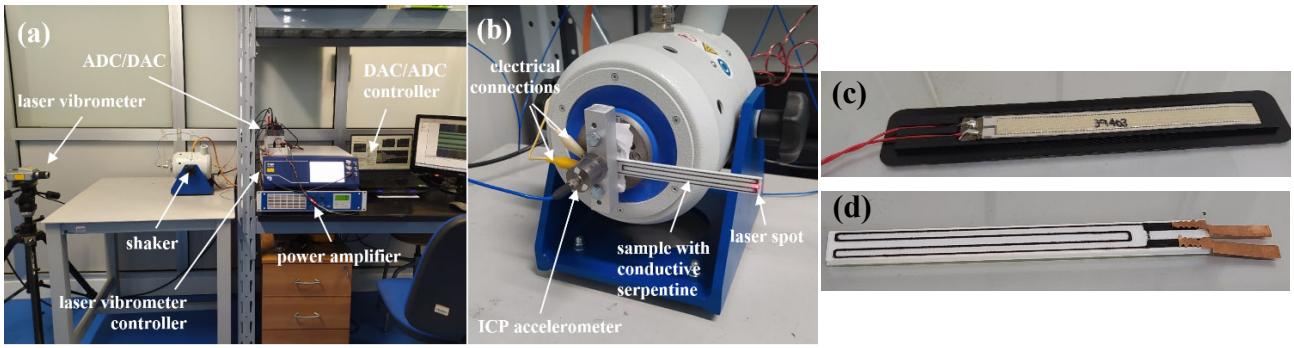

Fig. 1. Experimental setup: test bench components (a), detail of the cantilever with co-printed conductive polymer track (b), stand-alone PCF sensor (c) and co-printed sensor (d).

3. Results: FRFs and sensors outputs

The results of the dynamic tests are presented in Fig. 2a (nylon beam with the stand-alone PFC sensor) and Fig. 2b (PLA beam with the co-printed sensor). The upper diagrams illustrate the structural FRFs in terms of acceleration. The input acceleration ranges used during the tests are 1–10 m/s² for the PFC sensor and 0.5–1.5 m/s² for the co-printed sensor. The lower diagrams display the output signals of the sensors (voltage and resistance) normalized with respect to the input acceleration. A comparison of the diagrams demonstrates accurate capture of the system dynamics.

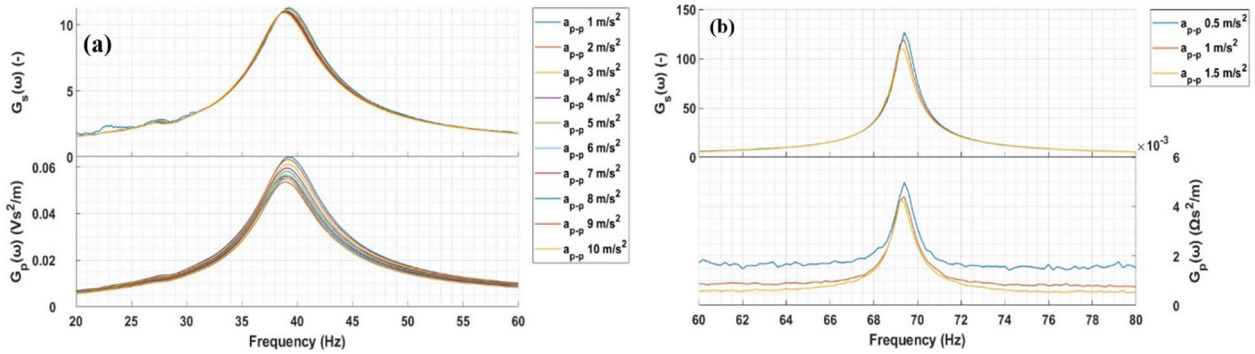

Fig. 2. Experimental results of nylon beam with PFC sensor (a) and PLA beam with co-printed sensor (b): excitation-response accelerations ratio (top) and sensors outputs normalized with input acceleration (down).

4. Acknowledgements

Funded by the Horizon Europe grant "HORIZON-CL4-2022-RESILIENCE-01", Project MIMOSA (Project 101091826).

5. References

[1] A. Cano-Vicent et al. (2021). Fused deposition modelling: Current status, methodology, applications and future prospects. *Addit. Manuf.*, **47**, 102378.

[2] M. Maurizi et al. (2019). Dynamic Measurements Using FDM 3D-Printed Embedded Strain Sensors. *MDPI Sensors*, **19**, 2661.

[3] G. De Pasquale and A. Coluccia (2023). Modeling and Experimental Validation of CFRP-Metal Joints Utilizing 3D Additively Manufactured Anchors. *ASME J. Manuf. Sci. Eng.*, **145**(11), 111004.

[4] G. De Pasquale, F.E. Altunok and F. Ursi (2023). Investigation of the Mechanical Strength of CFRP with Co-Cured Additively Manufactured Metal Inserts. *Procedia Struct. Integrity*, **47**, 573-578.

EVALUATION OF INTRA-FILAMENT VOID STRUCTURE OF 3D PRINTED MORTAR WITH DIFFERENT PRINTING SPEED

K. Nakase[1], K. Hashimoto[2], K. Ota[3], Y. Hama[4, 5], T. Sugiyama[2]
[1] Division of Field Engineering for the Environment, Hokkaido University, Japan
[2] Division of Civil Engineering, Hokkaido University, Japan
[3] Faculty of Engineering, Hokkaido University, Japan
[4] College of Design and Manufacturing Technology, Muroran Institute of Technology, Japan
[5] Division of Architecture, Hokkaido University, Japan

1. Introduction

As 3D printing construction market expands, understanding the durability of 3D printed concrete/mortar has become increasingly important [1]. Void structures of concrete generally influence their durability, and many studies have investigated them in 3D printed concrete [2]. In the material extrusion, which is the most common printing method for 3D printed concrete, undesirable voids can form due to the extrusion and deposition process of the extruded material (filament). These voids are classified into two types based on their formation: inter-filament voids and intra-filament voids [3]. Inter-filament voids occur between adjacent filaments, whereas the intra-filament voids are distributed within individual filaments. The intra-filament voids are typically smaller than inter-filament voids [3].

While inter-filament voids can be mitigated by designing appropriate mix proportions and printing procedures, intra-filament voids correspond to the voids and pores similarly formed in conventional cast concrete. Previous studies have indicated that intra-filament voids tend to elongate during the printing process particularly when the material extrusion direction is perpendicular to the printing direction [2, 4]. Therefore, it is important to evaluate the effect of printing parameters on the morphology of intra-filament voids. This study evaluates the influence of the printing speed on the shape alteration of intra-filament voids by X-ray computed tomography (CT).

2. Materials and methods

Ordinary Portland Cement (3.16 g/cm^3) and silica sand (2.68 g/cm^3) were used as the binder (C) and fine aggregate (S), respectively. The water-to-cement ratio (W/C) and sand-to-cement ratio (S/C) were set at 19.5% and 55% respectively. A superplasticizer (SP) with the SP-to-cement ratio (SP/C) of 30% was added as an admixture. It was confirmed that the air content after mixing was 6.0%.

The specimens with varying printing speeds were fabricated using a material extrusion-based 3D printer. This study used the ratio v/E, defined as the printing speed (v) divided by the extrusion volume (E) as a parameter. When the nozzle diameter and printing pitch were set to 16 mm and 24 mm respectively, the slicer software automatically set a printing speed to 3.91 mm/s. Based on this value, specimens were printed with v/E of 1.0, 1.5 and 2.0. After printing, the specimens were cut into 50 mm lengths as shown in Fig. 1.

X-ray CT was performed for a volume of interest with its voxel size of 10.56 µm, using 100 kV and 200 µA for X-ray generation. During scanning, a 0.2 mm-thick Cu filter was used to remove low-

energy X-rays and reduce the artifacts. Air voxels were extracted from the obtained images to quantify the effect of printing speed on the morphology of intra-filament voids. The elongation of intra-filament voids was evaluated in the three Cartesian directions as depicted in Fig. 2.

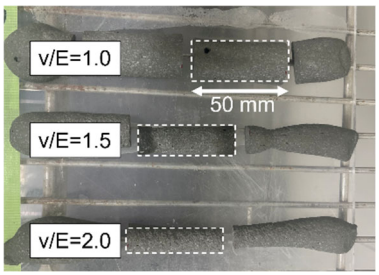

Fig. 1. Printed specimens.

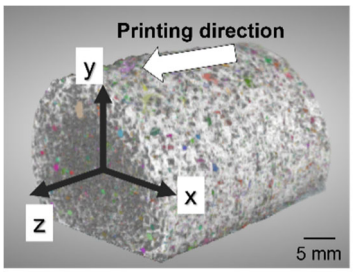

Fig. 2. Three Cartesian directions.

3. Results and conclusions

Fig. 3 shows the relationship between the equivalent spherical diameter and the z-projection diameter. In this study, the z-direction corresponds to the printing direction and the z-projection diameter refers to the difference between the maximum and minimum z-coordinate of each intra-filament void [2]. For a perfectly spherical void, the equivalent diameter and z-projection diameter are equal, resulting in a slope of 1.00. A larger z-projection diameter compared to the equivalent spherical diameter indicates elongation in the z-direction. Fig. 3 shows that as the printing speed increases, corresponding to the larger *v/E* values, the intra-filament voids become more elongated in the z-direction, i.e., the printing direction. The previous studies have suggested that this phenomenon is suggestively explained from the printing process; the pressure during extrusion causes intra-filament voids to elongate along the material flow direction [2, 4].

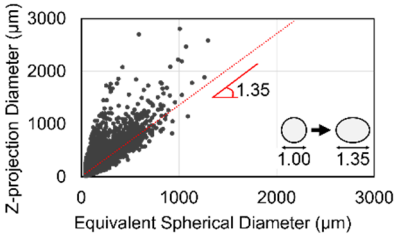

(a) v/E=1.0

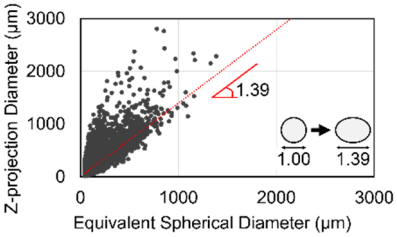

(b) v/E=1.5

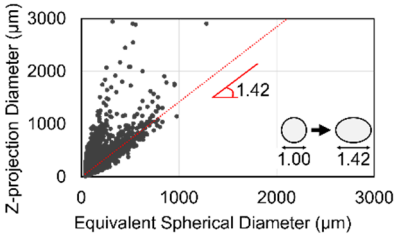

(c) v/E=2.0

Fig. 3. Relationship between equivalent spherical diameter and z-projection diameter.

4. Conclusion

This study investigated the effect of printing speed on the intra-filament void shape formed in 3D printed mortar using X-ray CT. The relationship between the equivalent spherical diameter and the projection diameter in the printing direction indicates that the shape of intra-filament void distributes in 3D printed mortar elongates in the printing direction as the printing speed increases.

5. References

[1] L., Bekaert, M., Wangler, T., Wang, Z., Mechtcherine, V. and Roussel, N. (2024). On the micro- and meso-structure and durability of 3D printed concrete elements. *Cem. Concr. Res.*, **185**, 107649.

[2] Kruger, J., du Plessis, A. and van Zijl, G. (2021). An investigation into the porosity of extrusion-based 3D printed concrete. *Addit. Manuf.*, **37**, 101740.

[3] Sun, X., Mazur, M. and Cheng, C. T. (2023). A review of void reduction strategies in material extrusion-based additive manufacturing. *Addit. Manuf.*, **67**, 103463.

[4] Nakase, K., Hashimoto, K., Sugiyama, T. and Kono, K. (2024). Influence of print paths on mechanical properties and fracture propagation of 3D printed concrete. *Constr. Build. Mater.*, **438,** 137019.

MECHANICAL RESPONSE OF SINUSOIDAL HONEYCOMB AUXETIC STRUCTURES IN AN ADDITIVELY MANUFACTURED SHAPE MEMORY ALLOY

E. Avoledo[1], F. Scalzo[1], X. Wang[2], E. Salvati[1]
[1] Polytechnic Department of Engineering and Architecture, University of Udine, Via delle Scienze 206, Udine, 33100, Italy
[2] Key Laboratory for Liquid-Solid Structural Evolution and Processing of Materials (Ministry of Education), Shandong University, Jingshi Road 17923, Jinan 250061, China

1. Abstract

This study investigates the mechanical response of a laser powder bed fusion (L-PBF) NiTi alloy, focusing on its superelastic behaviour under both uniaxial deformation and more complex conditions attained through the exploitation of miniaturised auxetic geometries. Tests were conducted at two relevant thermal conditions, i.e., below and above the martensite to austenite finish transition temperature.

Static and cyclic tests were performed using a hybrid force and deformation control approach across various temperature regimes. Precise deformation control was achieved through a newly developed control algorithm, relying on the non-contact digital image correlation (DIC), which is essential for managing large deformations and sub-millimetre gauge areas.

Additionally, a custom measurement system, incorporating a microheater and temperature sensor in a closed-loop configuration, was developed to ensure precise in-situ temperature control of the samples.

Regarding the sinusoidal honeycomb auxetic structures, the study aims to shed light on the role of fillet radius between sinusoidal and linear beams on mechanical performance. Specimens comprising one cell and two adjacent cell halves were analysed to replicate single-cell behaviour.

The outcomes of this study provide valuable insights into the future applications of this shape memory alloy, emphasising both its functional characteristics and structural integrity under quasi-static and cyclic loading conditions.

STRESS-DRIVEN DESIGN OF GYROID LATTICES WITH VARIABLE THICKNESS: A PRELIMINARY PROCEDURE APPLIED TO CONNECTING RODS

A. Ciccarella, V. Colaiuda, V. Pocetta, G. Dell'Avvocato, L. Di Angelo and E. Mancini
Department of Industrial and Information Engineering and Economics, University of L'Aquila, L'Aquila, Italy

1. Introduction

One of the critical challenges in mechanical design within the transportation sector today is achieving lightweight structures. This factor plays a vital role in meeting various goals, such as reducing fuel consumption and enhancing performance in specific domains, such as motorsports. With the advent of additive manufacturing (AM) technologies, producing lighter components, even with complex geometries, has also become feasible using conventional materials such as steel. The quest for lightweight and mechanically efficient structures has brought significant attention to bio-inspired design principles. Combining nature-inspired principles with advanced materials and manufacturing technologies holds great promise for the future of lightweight design in transportation. Mimicking these principles, lattice structures have emerged as a promising solution [1].

In the present study, triply periodic minimal surface (TPMS) structures are used, which, compared to conventional lattice structures, feature a unique surface with an average curvature of zero. This allows for a more uniform stress distribution, supporting of higher loads and resulting in more uniform deformation [2]. Abueidda et al. [3] compared the mechanical properties of some of the most popular TPMS structures, demonstrating experimentally and computationally how the gyroid structure is among the most promising, in terms of mechanical strength and energy absorption. Gyroid structures are typically characterized by a continuous and uniform repeating pattern of unit cells. By adjusting the parameters that define the individual cell, particularly the thickness, it is possible to vary the density along the structure. This study proposes a new topology optimization methodology that leverages the parametrization of cell density to achieve a variable-density structure based on stress distribution. Many studies on topology optimization using TPMS structures focus on static or quasi-static components [4]. There is a lack of topology optimization applied to dynamic components, such as connecting rods, which operate under cyclic and complex loading conditions. Building on the previous discussion, this new topology optimization methodology is applied to the real case of a connecting rod for high-speed engines.

2. Materials and methods

This section outlines the steps involved in optimizing a connecting rod with a variable density gyroid lattice structure, aiming for significant weight reduction while maintaining mechanical resistance. The initial design conditions were defined following the methodology proposed by Di Angelo et al. [5], applied to the same connecting rod geometry. A FEM simulation was conducted on the kinematic chain to calculate the Von Mises stress field on the connecting rod, serving as the foundation for the current optimization. Using the software nTopology®, gyroid lattice structure was introduced within the central region of the connecting rod. The lattice design process began by defining cell dimensions of 3×3×3 mm, ensuring precise alignment within 3 mm-thick central body of the rod. The minimum cell thickness (t_{min}) was set to 0.35 mm, corresponding to a relative density ($\rho_{rel} = \rho_{cell}/\rho_{bulk} > 0.2$) to maintain isotropic behaviour, as indicated by the Zener criterion reported in

Mancini et al [6]. The maximum cell thickness (t_{max}) was set to 1.5 mm, representing fully dense regions with ρ_{rel}=1. The thickness of the lattice cells was initially defined with a linear dependency on the Von Mises stress field (Fig.1). Subsequently, a non-linear dependency of degree n was investigated to maximize weight reduction while ensuring adequate mechanical resistance.

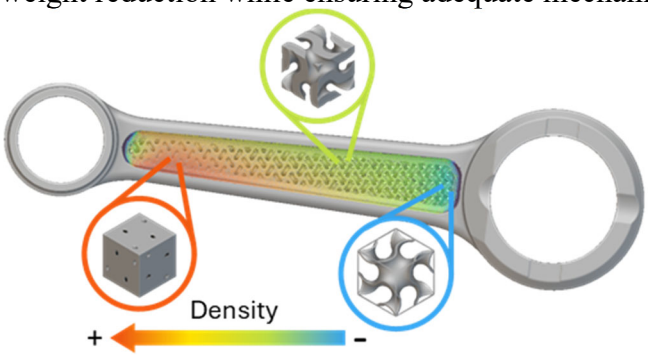

Fig. 1. Variable-density structure based on stress distribution

To further analyse the optimized designs, FEM simulations were conducted using HyperMesh® to evaluate the performance of the connecting rod within the complete kinematic chain.
To verify the proposed procedure, the component has been realized and experimentally tested confirming the mechanical properties obtained by numerical model.

3. Results and conclusions

This methodology demonstrates the effective integration of FEM simulations and lattice-based topology optimization, resulting in a connecting rod with a 6% mass reduction, three times greater than that achieved with classical topology optimization. The optimized connecting rod was subsequently manufactured using 3D printing technology to validate the proposed design, conducting experimental tests to assess its real-world performance. (Fig.2)

Fig. 2. 3D-printed steel connecting rod, produced using additive manufacturing

4. References

[1] Bandyopadhyay, Amit, Kellen D. Traxel, and Susmita Bose. "Nature-inspired materials and structures using 3D Printing." Materials Science and Engineering: R: Reports 145 (2021): 100609.
[2] Qiu, Na, et al. "Experimental and numerical studies on mechanical properties of TPMS structures." International Journal of Mechanical Sciences 261 (2024): 108657.
[3] Abueidda, Diab W., et al. "Mechanical properties of 3D printed polymeric Gyroid cellular structures: Experimental and finite element study." Materials & Design 165 (2019): 107597.
[4] Parlayan, O., Ozdemir, M., Gayir, C.E. et al. A new sensitivity-based mapping scheme for topology optimization of graded TPMS designs. Int J Adv Manuf Technol 129, 3197–3220 (2023). https://doi.org/10.1007/s00170-023-12439-1
[5] Di Angelo Luca, Edoardo Mancini, and Paolo Di Stefano. "Numerical methodology for design and optimization of a connecting rod for very high speed engines." International Journal on Interactive Design and Manufacturing (IJIDeM) (2022): 1-26.
[6] Mancini Edoardo et al. "DLP printed 3D gyroid structure: Mechanical response at meso and macro scale." Mechanics of Materials 192 (2024): 104970.

6-11 July 2025 ICEM21 Bologna
21st International Conference on EXPERIMENTAL MECHANICS

MICROSTRUCTURE EVOLUTION AND TENSILE PROPERTIES OF SELECTIVE LASER MELTED ADDITIVELY MANUFACTURED TI-6AL-4V AT ELEVATED TEMPERATURES

Chong ZHAO[1] and Zhengmao YANG[1]
[1] Wide range Flight Engineering Science and Applications Center, Institute of Mechanics, Chinese Academy of Sciences

1. Introduction

Ti6Al4V is widely used in aerospace, biomedical, and industrial applications due to its high strength, corrosion resistance, and lightweight properties [1]. However, exposure to high temperatures can degrade its mechanical performance. Additive manufacturing (AM) techniques like SLM and EBM offer advantages over conventional methods but introduce challenges such as surface roughness and anisotropy [2]. Studies have shown that microstructural differences impact mechanical properties, especially at high temperatures [3, 4]. Damage modeling, including the GTN and VA models, helps predict material behavior under stress [5]. HR-EBSD provides high-resolution strain and dislocation analysis, aiding in understanding fatigue and deformation mechanisms [6].

This research investigates the anisotropic and high-temperature mechanical properties of Ti6Al4V components produced by selective laser melting (SLM). Mechanical properties, including elastic modulus, yield strength, UTS, and elongation, were assessed at 250°C and 400°C for build orientations of 0°, 45°, and 90°. The 0° orientation showed better flow stress and ductility at 400°C. Fatigue testing revealed stress asymmetry due to residual strain, the Bauschinger effect, and texture, with fatigue life at 250°C nearly double that at 400°C. The study also explored the effects of lamellar α-Ti phase, grain boundary strengthening, and GND accumulation. Schmid factor variations correlated with material strength and fracture susceptibility, with increasing Schmid factor from 0° to 90° leading to localized deformation and reduced elongation. These findings will help optimize SLM Ti6Al4V simulation methods and improve additive manufacturing parameters.

2. Materials and methods

SLM Ti6Al4V samples were fabricated with a rotating scan pattern for isotropic properties in the building plane but remained transversely isotropic due to elongated grain structure. Three build orientations (0°, 45°, 90°) were studied. To reduce residual stress and enhance ductility, samples underwent SRA at 800°C for 2 hours. AM defects were preserved, and no HIP was performed. Samples were machined from an initial 12.5 mm diameter to a columnar shape and polished for analysis.

SLM laser power, W	350	Layer thickness, μm	60
Laser scan speed, mm/s	1250	Hatch spacing, μm	150
Overlap rate, %	75	Laser spot size, μm	50
Protective gas	Argon	Average particle diameter, μm	40

Table 1: Ti6Al4V SLM parameters.

The study investigates the anisotropy of SLM Ti6Al4V parts at 250°C and 400°C, considering strain rate sensitivity and creep behavior. Fatigue tests were conducted at these temperatures with varying tensile strains (0.6%, 0.8%, 1%). Post-fatigue samples underwent EBSD characterization, with cross-sections polished for microstructural analysis. A Zeiss Sigma 300 SEM with an Oxford EBSD detector captured phase distribution and grain orientation near fracture surfaces, using a 0.2 µm step size for accurate GND density and residual strain analysis.

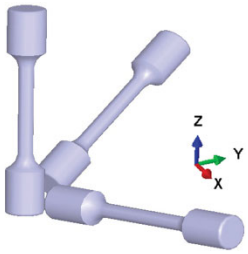

Figure 1. Drawing of the final test sample geometry.

3. Results and conclusions

The obtained data is collectively displayed in Figure 2. At 400°C, anisotropic behavior is evident, primarily due to microstructural evolution, with the 0° sample exhibiting superior flow stress and ductility. Fatigue tests reveal stress asymmetry influenced by residual strain, the Bauschinger effect, and texture, with fatigue life at 250°C nearly twice that at 400°C. A shape factor is introduced to account for grain boundary strengthening in high-aspect-ratio α-Ti lamellae, while GNDs and temperature effects on yield strength are quantified. Schmid factor variations lead to GND accumulation, affecting residual stress and strain continuity, potentially causing fracture. Intragranular misorientation activates multiple slip systems, enhancing strength, while high GND density at micro-zone boundaries may initiate cracks. Schmid factor analysis confirms increasing deformation ease from 0° to 90°, correlating with tensile test results. These findings aid in improving numerical simulations and optimizing AM parameters for enhanced mechanical performance.

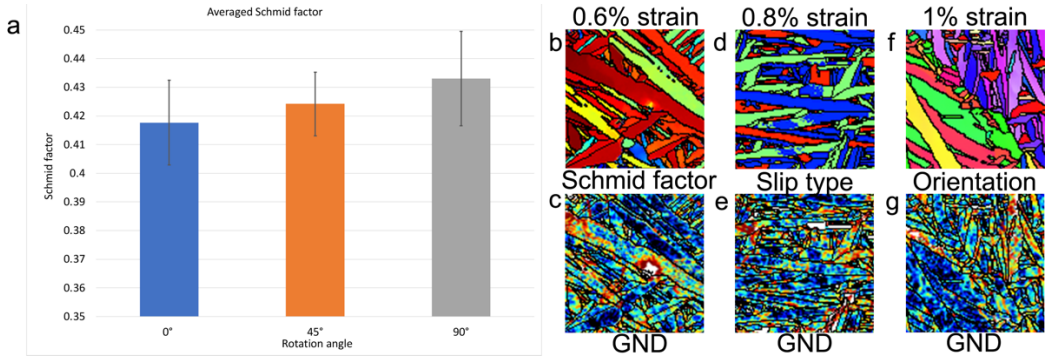

Figure 2. Misorientation and GND density analysis for the high temperaturę fatigue test. (a) average Schmid factor at different rotation angle, (b, c) Schmid factor influence, (d, e) Slip type influence, (f, g) Micro zone boundary influence.

4. Acknowledgements

The research presented in this paper has received funding from the National Natural Science Foundation of China (NSFC) (Grant No. 52105165).

5. References

[1] Mian, M.J., J. Razmi, and L. Ladani, Mechanical behavior of electron beam powder bed fusion additively manufactured Ti6Al4V parts at elevated temperatures. Journal of Manufacturing Science and Engineering, 2021. 143(2): p. 021013.

[2] Kok, Y., et al., Anisotropy and heterogeneity of microstructure and mechanical properties in metal additive manufacturing: A critical review. Materials & Design, 2018. 139: p. 565-586.

[3] Kotkunde, N., et al., Comparative study of constitutive modeling for Ti–6Al–4V alloy at low strain rates and elevated temperatures. Materials & Design, 2014. 55: p. 999-1005.

[4] Lee, W.-S. and C.-F. Lin, Plastic deformation and fracture behaviour of Ti–6Al–4V alloy loaded with high strain rate under various temperatures. Materials Science and Engineering: A, 1998. 241(1-2): p. 48-59.

[5] Chaboche, J.-L., Continuum damage mechanics: Part I—General concepts. 1988.

[6] Britton, T.B., et al., Probing Deformation and Revealing Microstructural Mechanisms with Cross-Correlation-Based, High-Resolution Electron Backscatter Diffraction. Jom, 2013. 65(9): p. 1245-1253.

USE OF THERMAL AND MECHANICAL INDICATORS FOR THE FATIGUE DAMAGE OF AlSi10Mg ADDITIVE MANUFACTURED SPECIMENS

R. Nobile[1], R. De Finis[1], P. Leo[1], G. Renna[1] and A. De Luca[1]
[1] Department of Engineering for Innovation, University of Salento, Lecce, Italy

1. Introduction

Additive manufacturing represents probably the highest potential innovation of the last years in the manufacturing of complex parts realized with metallic materials. The possibility to realize completely new geometries, both at macro and mesoscale level, increases exponentially the possible design solutions available for the community of mechanical designers. However, the effective possibility of using these solutions in industrial applications, especially in advanced sectors as for the development of critical solutions for aerospace and energy production applications, requires an intensive study of the factors that could influence the mechanical strength and failure modes of these materials.

According to these considerations, fatigue and fracture behaviour represents one of the most critical aspects of metallic materials, independently from the manufacturing process used to obtain it. This is particularly true for additive manufactured materials, which are characterized by inherent inhomogeneities due to the specific manufacturing process. Several researchers studied the mechanical properties of additive manufactured specimens considering the effects of the process parameters, as for example temperature of the chamber, orientation of the specimens, strategy of deposition, and mechanical and thermal post-treatments. Limiting the attention to AlSi10Mg material, which is the object of this work, several depth investigations can be found in literature [1, 2], in which several indications about the fatigue behaviour are reported in the high-cycle regime [3]. However, the adaptation of predictive models of the fatigue life available in literature, rather than the development of new ones, requires the study of the constitutive behaviour of AM materials subjected to cyclic loads at high load levels, which can potentially introduce a progressive and increasing deformation over time.

This work contributes to the knowledge of the cyclic behaviour of AlSi10Mg AM material considering the evolution of hysteresis cycles obtained in load control at different stress amplitude and load ratio. The specific aim is to obtain an experimental basis for the correct definition of the cyclic material behaviour under limited plasticization levels.

2. Materials and methods

In this study, AlSi10Mg static and fatigue specimens have been realized adopting a Laser Powder Bed Fusion (LBPF) technology using a Renishaw AM 400. The main parameters of the manufacturing process were the use of Meander strategy with scan rotation of 45 degrees between consecutive layers, power equal to 375W, scan speed equal to 2000mm/s and exposure time of 50µs. Building camera has been pre-heated to 250°C to reduce the residual stress and geometrical distortions. For static specimen, both horizontal and vertical orientations have been considered in order to evaluate the effect of the growth direction on the resulting mechanical properties. As no

significant effect of the orientation has been found on the static properties, only the horizontal orientation has been chosen for fatigue specimens.

The static properties of the material have been determined using a constant crosshead speed of 1 mm/min, according to ASTM E8 standard. A preliminary evaluation of the beginning of the fatigue damage of the material has been carried out adopting the classic thermographic method described in [4], in which the temperature of the steady state (ΔT steady) acquired during a stepwise loading procedure is used as an indicator of the fatigue limit of the material. To do this, stepwise fatigue tests have been characterized by a load frequency of 19 Hz, a load ratio R = 0.1 and blocks having a duration of 15000 cycles. During fatigue test, also hysteresis cycles have been recorded using an axial extensometer having a gage length of 25 mm. All the mechanical tests have been carried out on a servo-hydraulic testing machine MTS810-100 kN, while a thermal camera FLIR A700 has been used.

3. Results and conclusions

The tensile curves of the specimens having horizontal and vertical orientation have been reported in Figure 1a and allow establishing the irrelevance of the orientation on the static properties. Moreover, yield and ultimate strength are in excellent agreement with similar data reported in literature. The main results of the first two fatigue tests, carried out using a stepwise loading approach, have been expressed in terms of variation of stabilized temperature ΔT and mean strain ε_m (Fig. 1b). Even if the thermal curves are not perfectly repetitive, a change of the thermal behaviour can be traced in the range between 45-55 N/mm^2, which could be associated to damage process determined by fatigue load, in coherence with data reported in literature [1, 2]. Finally, the behaviour of the mean strain against applied stress amplitude highlights the presence of a relevant ratcheting of the material, according to the characteristic failure mode of AM material, which is determined by multiple crack initiation sites in the gage length.

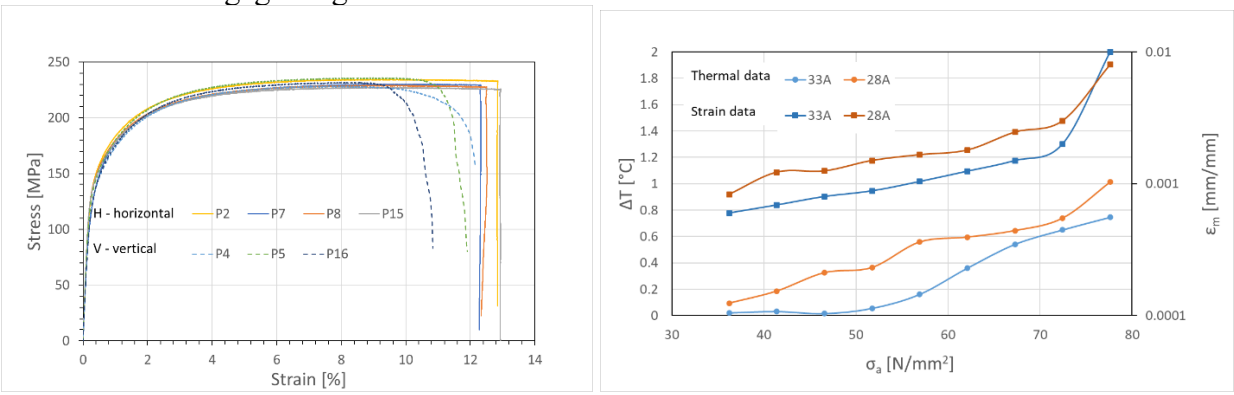

(a) (b)

Fig. 1. Static properties (a); trend of thermal and mechanical damage indicators in fatigue tests (b).

4. References

[1] M. Matušů, L. Džuberová, J. Papuga, J. Rosenthal, J. Šimota, L. Beránek (2024). Fatigue analysis and heat treatment comparison of additively manufactured specimens from AlSi10Mg alloy, *International Journal of Fatigue*, **185**, 108357.

[2] Matušů M, Šimota J, Papuga J, et al. (2024). S–N curves established from limiting energy in the case of specimens additively manufactured from AlSi10Mg, *Fatigue Fract Eng Mater Struct.*, **47**(12), 4771-4790.

[3] A. Raja, Srinivasa Rakesh Cheethirala, Pallavi Gupta, Nilesh J. Vasa, R. Jayaganthan (2022). A review on the fatigue behaviour of AlSi10Mg alloy fabricated using laser powder bed fusion technique, *Journal of Materials Research and Technology*, **17**, 1013-1029.

[4] La Rosa G, Risitano A. (2000), Thermographic methodology for rapid determination of the fatigue limit of materials and mechanical components, *Int J Fatigue*, **22**(1), 65-73.

ACCELERATING FATIGUE CHARACTERIZATION THROUGH A COMPACT INTEGRATED TESTING MACHINE AND THERMOGRAPHIC METHODS

D. D'Andrea[1], D. Crisafulli[1], G. Risitano[1,2], and D. Santonocito[1,2]
[1] Department of Engineering, University of Messina, Messina, Italy
[2] Knowow S.r.l. – Spinoff Accademico, Messina, Italy

1. Introduction

In industrial contexts, understanding the mechanical behavior of materials is crucial for accelerating the design process of mechanical devices and components. While this principle applies to conventionally produced materials such as metals, plastics, and composites, it becomes even more critical for Additive Manufactured (AM) materials. Indeed, in AM varying process parameters can result in significantly different mechanical properties, necessitating a thorough characterization of the material behavior [1].

Mechanical characterization, particularly fatigue assessment, typically requires testing a large number of samples, which is time-intensive and resource-consuming. To address this challenge, innovative testing methodologies are essential to significantly reduce testing time while maintaining high accuracy in determining both the fatigue limit and fatigue life of materials.

Since 2000, the use of infrared thermography (IR) has provided a rapid method for assessing the fatigue limit and obtaining the full S-N curve of engineering materials [2]. Techniques such as the Risitano Thermographic Method (RTM) [3] and the more recent Static Thermographic Method (STM) [4] have demonstrated significant reductions in the number of specimens required. Meanwhile, advances in infrared sensor technology have made these methods more cost-effective and precise [5]. However, limitations still exist due to the need for multiple devices—such as a universal testing machine (UTM) and an infrared camera—as well as expertise in data analysis.

To overcome these challenges, the Fast Fatigue Machine (FFM) has been developed. The FFM integrates a compact UTM, an IR camera, and a Digital Image Correlation (DIC) acquisition system into a single device. This innovative system enables rapid and quasi-automatic data analysis, providing precise information about fatigue limits and S-N curves in a fraction of the time required by conventional fatigue testing campaigns.

The present study aims to compare fatigue data obtained using the FFM with those derived from a traditional UTM paired with an IR camera for the same material batch. The results demonstrate a significant reduction in testing time and material usage, highlighting the efficiency and effectiveness of the FFM in modern fatigue assessment.

2. Materials and methods

The compact specimen design represented in Figure 1a from [6], was adopted both for static and fatigue testing. It was obtained by Multijet Fusion (MJF) AM process, developed by HP, from PA12 powder on a HP-5200 printer with a "balanced" printing profile.

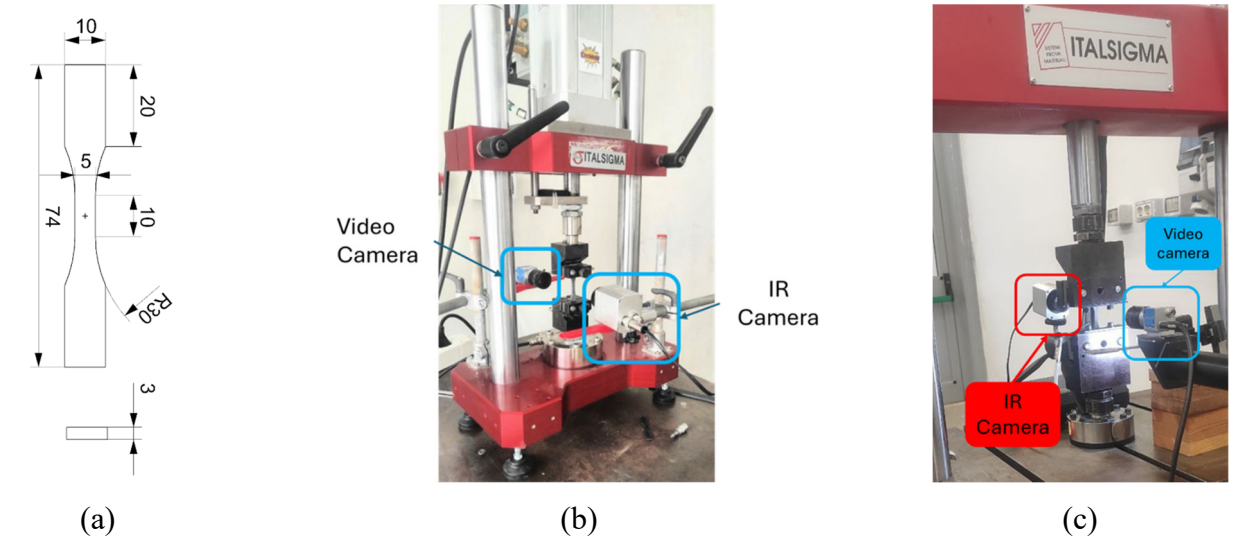

Figure 1. a) PA12 specimen's geometry; b) FFM setup; c) Italsigma FPF25 setup

Two experimental setups have been used: the first one (Figure 1b), which is also the focus of this work, consists of FFM, a pneumatic benchtop testing machine designed by University of Messina's academic spin-off Knowow S.r.l. in collaboration with Italsigma S.r.l. The system is equipped with a 2.5 kN load cell and it is set up to apply full field measurement techniques such as IR thermography and DIC through the insertion of two dedicated camera supports. The second one (Figure 1c) consists of an Italsigma FPF25, a servo-hydraulic UTM equipped with 25 kN load cell. IR images were captured using an IRtech XT model thermal imaging camera while images for DIC analysis were acquired with a Basler acA2440-35uc video camera. Static tensile tests have been carried out at a displacement velocity of 2.4 mm/min and analyzed following ASTM D638 standards guidelines. Stepwise fatigue tests were performed under stress control adopting a stress ratio R= 0.1 and a frequency of 1 Hz. Data from static and fatigue tests were analyzed with iterative algorithm developed in Python language.

3. Results and conclusions

Preliminary results demonstrate how air usage as a working fluid does not affect results of static tensile tests on plastics, since they don't require high pressures to reach failure.
Fatigue tests are also not affected by it, even if load waveform results distorted while respecting maximum and minimum values imposed. Future analysis will focus on distortion effects to scientifically confirm this affirmation.

In Table *1* S-N data discussed by Avanzini et al. [6] and the one deriving from a traditional fatigue characterization have been compared to Thermographic Methods results.

	Avanzini et al.	FFM	FPF25
Fatigue limit by CA [MPa]	27.7	//	//
Fatigue limit by RTM [MPa]	//	26.0	25.4
Limit Stress by STM [MPa]	//	25.1	25.5

Table 1. Fatigue results comparison

It was observed how STM and RTM lead to a fast estimation of fatigue limit, which corresponded with good approximation to the ones proposed in literature. Besides, RTM allowed to evaluate the entire S-N curve deriving from thermal data. FFM demonstrated how simpler mechanical testing system are reliable for this kind of studies and how Thermographic Methods represents a valid alternative to get insights in fatigue properties of material. Full field measurements techniques predisposition of FFM make it a useful tool for industrial applications, in which it is fundamental to have material properties in a short time.

4. References

[1] N. Sanaei, A. Fatemi, Defects in additive manufactured metals and their effect on fatigue performance: A state-of-the-art review, Prog Mater Sci 117 (2021). https://doi.org/10.1016/j.pmatsci.2020.100724.

[2] P. Corigliano, F. Cucinotta, E. Guglielmino, G. Risitano, D. Santonocito, Fatigue assessment of a marine structural steel and comparison with Thermographic Method and Static Thermographic Method, Fatigue Fract Eng Mater Struct 43 (2020). https://doi.org/10.1111/ffe.13158.

[3] G. La Rosa, A. Risitano, Thermographic methodology for rapid determination of the fatigue limit of materials and mechanical components, Int J Fatigue 22 (2000) 65–73. https://doi.org/10.1016/S0142-1123(99)00088-2.

[4] A. Risitano, G. Risitano, Determining fatigue limits with thermal analysis of static traction tests, Fatigue Fract Eng Mater Struct 36 (2013) 631–639. https://doi.org/10.1111/ffe.12030.

[5] G. Pitarresi, R. Cappello, G. Catalanotti, Quantitative thermoelastic stress analysis by means of low-cost setups, Opt Lasers Eng 134 (2020). https://doi.org/10.1016/j.optlaseng.2020.106158.

[6] A. Avanzini, D. Battini, S. Pandini, Static and fatigue behavior in presence of notches for polyamide 12 (PA12) additively manufactured via Multi Jet Fusion™ process, Int J Fatigue 161 (2022) 106912. https://doi.org/10.1016/J.IJFATIGUE.2022.106912.

[7] S.N. Olufsen, M.E. Andersen, E. Fagerholt, μDIC: An open-source toolkit for digital image correlation, SoftwareX 11 (2020) 100391. https://doi.org/https://doi.org/10.1016/j.softx.2019.100391.

EFFECT OF PLASTIC PRE-STRAIN ON THE YIELD SURFACE OF LPBF-MANUFACTURED STAINLESS STEEL 316L

V.P. Dubey[1], M. Kopec[1], M. Pawlik[2], P. Wood[2] and Z.L. Kowalewski[1]
[1] Institute of Fundamental Technological Research, Polish Academy of Sciences, Pawinskiego 5B, 02-106 Warsaw, Poland
[2] Institute for Innovation in Sustainable Engineering, College of Science and Engineering, University of Derby, DE22 1GB, UK

1. Introduction

In recent years, additive manufacturing (AM) offers a revolutionary approach for fabricating complex-shaped, high-performance components with minimal material waste and post processing through a layer-by-layer deposition of materials. Stainless steel 316L (SS316L) belongs to the materials of an austenitic structure. It is widely used in such industries as aerospace, medical, and energy due to its exceptional corrosion resistance, biocompatibility, and mechanical properties. Additionally, its low thermal conductivity, high melting point, and other distinctive attributes make it well-suited for additive manufacturing [1]. The mechanical characterization is still primarily performed by means of uniaxial testing methods, whereas, it provides limited data concerning the mechanical strength and damage of materials in a single direction which does not simulate into real-world multiaxial stress conditions [2]. To fully understand material's behaviour, including initial texture or anisotropy, yield surface identification in the biaxial or triaxial stress space is important.

Therefore, in this research the yield surface approach in the biaxial stress space based on the offset yield point definition was applied to assess the variation of mechanical properties in the as-printed and pre-deformed material. An experimental investigation was conducted to understand the physical mechanism accountable for plastic deformation caused by monotonic tension in AM SS316L in vertical build orientation.

2. Materials and methods

The SS316L was additively manufactured using the Renishaw AM 250 system (Laser Powder Bed Fusion technology) with powder feedstock. The round tubes were printed in Z – vertical orientation following the parameters in Table 1. After printing, specimens underwent stress relief at 470°C for 6 hours while still attached to the build plate, then were detached via wire cutting and then machined into tubular specimens.

The mechanical testing was performed on the MTS 858 biaxial testing machine at room temperature, with Vishay 120Ω strain gauges bonded on the tubular specimens to measure and control axial, shear and hoop strains. Tensile pre-deformation was applied at 0.35%, 0.5%, and 0.8% plastic strain. After reaching each pre-strain value, specimen was linearly unloaded to zero stress and then yield points were determined using sequential probes in the plane stress state, where strain-controlled loading was applied until a limited plastic strain (0.0015%) was reached, followed by stress-controlled unloading. The procedure was performed along 17 strain paths (0° to 360° in increments) in the axial-shear strain plane. Yield points at 0.001% plastic offset strain were determined from each stress-strain curves. The yield surface was obtained by fitting the experimental yield points to the Szczepinski anisotropic yield equation using the least squares method [3].

Region	Layer thickness [μm]	Hatch distance [mm]	Beam Comp [mm]	Focal point [mm]	Power [W]	Point distance [μm]	Exposure time [μs]	Scan speed [mm/s]	Energy density [J/mm^3]
Volume Fill Hatch	50	0.11	0.025	0	195	60	80	750	47.27
Scanning strategy	Meander								

Table 1. Process parameters applied during additive manufacturing

3. Results and conclusions

Figure 1(a) shows the material characteristics of Z-vertical build SS316L in the form of stress-plastic strain curves during pre-straining of the material. It can be observed that each curve initially exhibits an elastic region followed by plastic deformation. After unloading to zero stress, the material does not return to its original strain but retains permanent plastic deformation. Figure 1(b) depicts an evolution of the initial yield surface (as-printed) in the biaxial stress space that were obtained from experimental results at 0.001% plastic offset strain. The initial yield surface confirms the presence of initial anisotropy with a shift in the compression direction. The tensile plastic pre-strain leads to the softening of the material. A lowest degree of this effect was obtained after 0.5% plastic deformation.

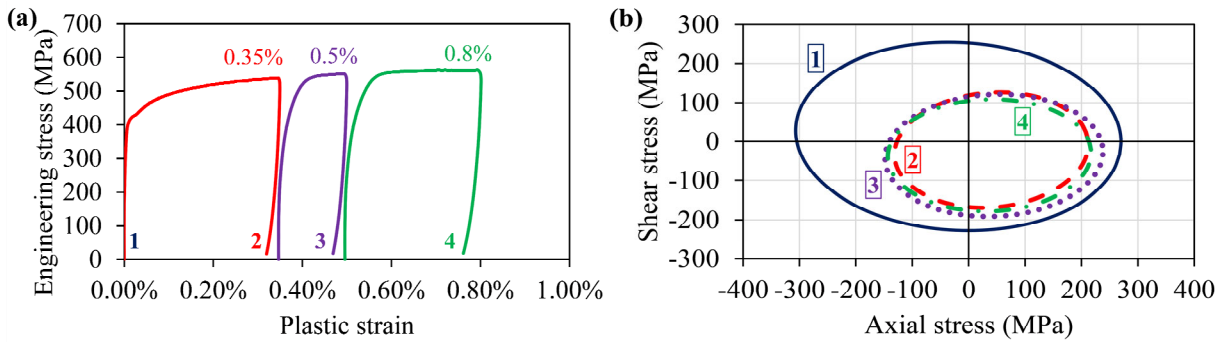

Fig. 1. Material response of SS316L (Z-vertical build) subjected to tensile plastic pre-strain equal to: 0.35% (2), 0.5% (3) and 0.8% (4) **(a)** and evolution of the initial yield surface (1) of Z-build SS316L due to such pre-deformation **(b)**.

4. Acknowledgements

This work was funded partly by the National Science Centre through the grants no. 2019/35/B/ST8/03151 and 2023/51/B/ST8/01751.

5. References

[1] M. Kopec, U.F. Gunputh, W. Macek, Z.L. Kowalewski and P. Wood (2024). Orientation effects on the fracture behaviour of additively manufactured stainless steel 316L subjected to high cyclic fatigue. *Theor. Appl. Fract. Mech.*, **130**, 104287.

[2] M. Kopec, V.P. Dubey, M. Pawlik, P. Wood, and Z.L. Kowalewski, (2024). Experimental identification of yield surface for additively manufactured stainless steel 316L under tension–compression-torsion conditions considering its printing orientation. *Manufacturing Letters*, **41**, 28-32.

[3] V.P. Dubey, M. Kopec, M. Łazińska and Z.L. Kowalewski (2023). Yield surface identification of CP-Ti and its evolution reflecting pre-deformation under complex loading. *Int. J. Plast.*, **167**, 103677.

PARAMETRIC STUDY OF ENERGY ABSORPTION CAPABILITIES OF A NOVEL LATTICE STRUCTURE

J. Melendez[1], S. Candelaria[1], D. Serrano[1], M. Menegozzo[1], P. Gonzales[2]
[1] Department of Mechanical Engineering, University of Puerto Rico, Mayaguez, Puerto Rico, USA
2 Department of Mathematical Sciences, University of Puerto Rico, Mayaguez, Puerto Rico, USA

1. Introduction

Advancements in additive manufacturing have revolutionized the design of honeycomb cores, by enabling the creation of complex, organic-like geometries and material combinations that were previously limited by traditional manufacturing constraints. This technology accelerates the development and testing of optimized designs for both scientific and non-scientific applications. Additive manufacturing has the potential to enhance the development of innovative honeycomb-like core structures, which are widely used in composite structures for their high strength-to-weight ratio and energy absorption capabilities. By leveraging additive manufacturing, new multifunctional core structures can be designed with optimum mechanical, acoustic, and fatigue lifetime properties under loads acting along multiple directions, without sacrificing weight efficiency. This study aims to design and optimize a novel core structure, evaluate its practicality through numerical analysis, and validate its performance via physical testing of 3D-printed samples.

This work contributes to the research efforts presented in [1] by investigating how geometric changes affect the energy absorption capabilities of a novel lattice structure. Early tests suggest that lattice could be a promising multifunctional core configuration for high-impact applications in automotive, aerospace, and military fields. The research presented aims to provide insights to guide future development of a groundbreaking lattice structure.

2. Materials and methods

In the present study, a numerical simulation approach was used to replicate a physical compression test, focusing on the load-bearing capabilities of the innovative lattice structures shown in Figure 1. The preliminary work presented defines the diameter of the center feature as *X*. Changes in the value of *X* influence the inner support structures' angles and lengths. The simulations used GRANTA's Library's ABS Plastic material for the lattices, with frictionless contact between the lattices and rigid compression plates. The bottom plate was fixed. The analysis' initial conditions had no pre-stressing and an initial velocity equal to zero. To assess the load bearing capabilities, the compressive plate was assigned a velocity of 8 m/s (Ramped) and timed to compress each lattice up to 70 percent of its original dimension. Ten samples were analyzed to generate "Axial Compression vs Load Reaction" curves and analyzed for densification and energy conservation (by limiting the kinetic energy to guarantee quasi-static loading conditions). Energy absorption was finally estimated per lattice. The results were compared with a datum honeycomb geometry configuration core structure.

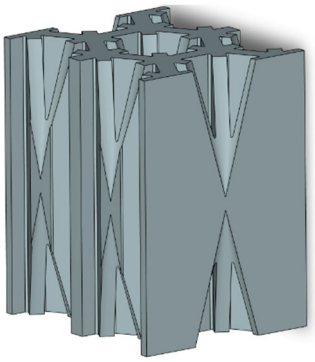

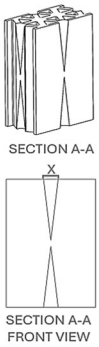

Geometry	X mm
a	0
b	3.124
c	4.112
d	5.01
e	5.908
f	6.806
g	7.704
h	8.602
i	9.5
Datum	N/A

Figure 1. Innovative Core Structure Geometry and cross-sectional view identifying *X*.

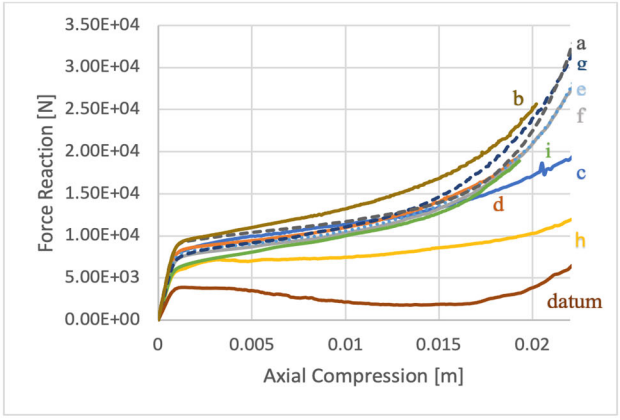

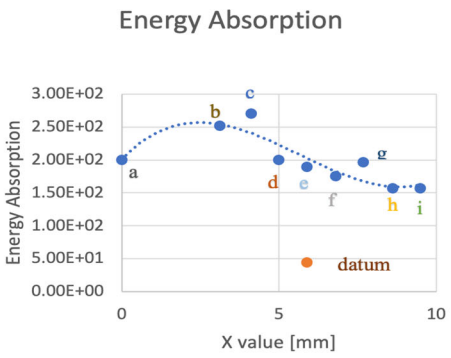

Figure 2. (a) Force Reaction and (b) Energy absorption as a function of X

3. Results and conclusions

This study presents numerical simulations of axial compression experiments on lattice geometries, analyzing the impact of changing the geometric variable *X* on load-bearing and energy absorption capabilities. The first observation is that the novel structure outperforms the honeycomb datum in all accounts. Results show that as *X* increases, the lattice's energy absorption increases and then decreases. This suggests that the geometric innovation enhances the cell's performance, though the added mass from decreasing *X* may also influence energy absorption, it suggests that an optimum value may be obtained. Future studies should explore density-based comparisons and validate these findings through experimental testing. Additionally, further research will investigate compression along other axes and use machine learning to predict and optimize the behavior of multipurpose lattice cells for improved efficiency.

4. References

[1] Candelaria Caraballo, Samir, Marco Menegozzo, and David Serrano Acevedo. 2025. "An Innovative Approach to Tailor Sandwich Core Structures for Multi-Directional Loading Scenarios" *Materials* 18, no. 3: 599. https://doi.org/10.3390/ma18030599

STUDIES ON MECHANICAL PROPERTIES OF MARAGING M300 STEEL MANUFACTURED ADDITIVELY VIA SLM

Pawel Platek[1], Giorgio Olmi[2], Janusz Kluczyński[3], Marcin Sarzynski[1], Jacek Janiszewski[1], Kamil Cieplak[1], Judyta Sienikiewicz[1], Dario Croccolo[2]

[1] Faculty of Mechatronics, Armament and Aerospace, Military University of Technology, Warsaw, Poland

[2] Department of Industrial Engineering (DIN), Alma Mater Studiorum – University of Bologna, Bologna, Italy

[3] Faculty of Mechanical Engineering, Military University of Technology, Warsaw, Poland

1. Introduction

One of the most prospective AM techniques in high-tech industries is Selective Laser Melting (SLM), which used a high-energy laser to selectively melt and fuse metal powders. Among many commercially available metal powders, the Maraging M300 steel is one of the most popular materials due to its exceptional combination of high strength, low carbon content, and excellent hardenability [1]. Furthermore, an additional heat treatment process, makes it possible to increase its mechanical properties, including high hardness, superior wear resistance, and good toughness. These attributes make Maraging M300 widely applicable in aerospace, space exploration, automotive, tooling as well as defence industries [2]. SLM-based production of Maraging M300 steel offers significant advantages over conventional manufacturing techniques, such as machining or casting. The ability to fabricate complex geometries directly from a digital model reduces both material waste and time consumption with positive outcomes from the point of view of echo-sustainability. However, despite these benefits, the mechanical properties of SLM-processed Maraging M300 steel may differ from those achieved through traditional methods.

Therefore, a comprehensive understanding of how the SLM technique influences the microstructure and mechanical performance of Maraging M300 steel is essential for refining its properties and expanding its industrial applications. Continued research in this area will facilitate the development of optimised processing strategies, ensuring enhanced performance and broader usability of this material.

The main goal of this study is to analyse the mechanical strength of Maraging M300 steel produced additively using the SLM technique. The conducted research involved an assessment of the material's mechanical properties under both static and dynamic loading conditions, as well as fatigue testing.

2. Materials and methods

The tensile test specimens were fabricated using the SLM Solution 125 HL system (SLM Solutions AG, Lübeck, Germany) with commercially available Maraging M300 steel powder, distributed by Carpenter, featuring a particle size of 30–63 µm. Additional trials were conducted before manufacturing the test specimens to optimise process parameters and minimise material porosity. Subsequently, three types of specimens were produced to be used in quasi-static loading tests (ASTM E466:96), fatigue tests (ISO 1143), and (non-standarized) dynamic tests. The main view

of the aforementioned samples is shown in Figure 1. The specimens used in the tests were not subjected to any additional heat treatment processes.

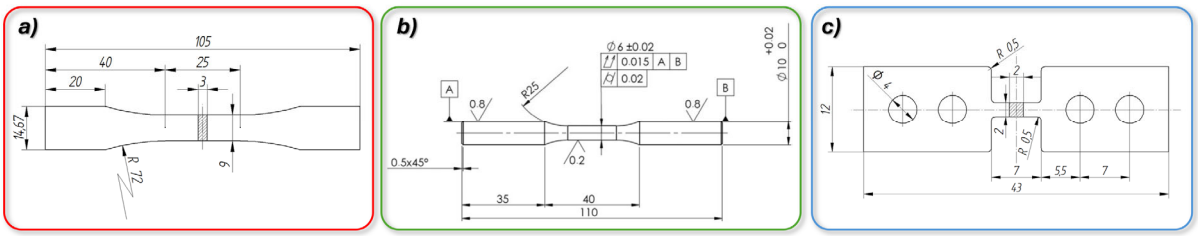

Fig. 1. Main view of material samples used in conducted strength tests a) – quasi-static tensile test, b) – fatigue tests, c) – dynamic SHPB tensile tests

3. Results and conclusions

The mechanical testing results reflect the properties of Maraging M300 steel in its as-built condition after the manufacturing SLM process, taking into account the influence of the applied load type. For tests conducted under quasi-static loading conditions, the obtained results differ from the data available in the literature [1]. However, the fatigue test results demonstrated a significant impact of structural defects on the achievable fatigue strength lifespan [2]. In dynamic loading tests, it was observed that Maraging M300 steel exhibits high sensitivity to loading rate. To precisely determine the factors affecting mechanical strength, additional fractographic analyses were performed by optical and stereoscopic microscopes and SEM. The captured images revealed the presence of defects in the specimens, primarily in the form of porosity, which significantly influenced the test results.

Consequently, for structural components manufactured using the AM SLM technique and subjected to dynamic or cyclic loading, it is recommended to apply additional heat treatment, such as HIP (Hot Isostatic Pressing), to minimise the impact of structural defects on mechanical properties.

Parameter	**Obtained results**	**Literature Data** [1]
E [GPa]	138 ± 5	163 ± 4.4
$R_{0,2}$ [MPa]	834 ± 79	1212 ± 99
R_m [MPa]	1035 ± 64	1290 ± 1.9
A_p [%]	13 ± 4	13.3 ± 0.1
HRC	32.5 ± 1.5	39.9 ± 0.1

Table 1. Results of quasi-static tensile tests of Maraging M300 steel manufactured via SLM

4. Acknowledgements

The research presented in this paper has received funding from National Centre for Research and Development as part of the Strategic Research and Development No. TECHMATSTRATEG2 /410049/12/NCBR/2019

5. References

[1] Kempen, K.; Yasa, E.; Thijs, L.; Kruth, J.P.; Van Humbeeck, J. *Microstructure and Mechanical Properties of Selective Laser Melted 18Ni-300 Steel.* In Proceedings of the Physics Procedia; Elsevier B.V., 2011; Vol. 12, pp. 255–263.

[2] Croccolo, D.; De Agostinis, M.; Fini, S.; Olmi, G.; Robusto, F.; Ćirić-Kostić, S.; Morača, S.; Bogojević, N. *Sensitivity of Direct Metal Laser Sintering Maraging Steel Fatigue Strength to Build Orientation and Allowance for Machining*. Fatigue Fract Eng Mater Struct 2019, 42, 374–386.

6-11 July 2025 ICEM21 Bologna
21st International Conference on EXPERIMENTAL MECHANICS

INITIAL CHARACTERIZATION OF MULTIPLE SHAPE-MEMORY ANYCUBIC RESIN

M. Staszczak[1], A.D. Lantada[2], A. Gradys[1], L. Urbański[1], K. Takeda[3] and E.A. Pieczyska[1]
[1] *Institute of Fundamental Technological Research, Polish Academy of Sciences, Poland*
[2] *Universidad Politécnica de Madrid (UPM), Madrid, Spain*
[3] *AICHI Institute of Technology (AIT) Toyota-city, Japan*

1. Introduction

The Shape Memory Polymers (SMP) are multifunctional materials that can change their shape under external stimuli, usually temperature [1-2]. The temperature is usually glass transition temperature T_g for Polyurethane Shape Memory Polymers (PU-SMP) [3, 4] or shape memory epoxy (SMEp) [5], characterised by a relatively high strength and beneficial shape memory properties which enables various applications in the medical or industrial instruments and daily life. Particularly interesting is a new generation of multiple Shape Memory Epoxy (SMEp) that demonstrate the ability to memorize more than two shapes. The property significantly broadens the functionality of SMPs making them attractive for applications from robotics to biomedicine. The multiple shape memory effect (SME) can be achieved through additive manufacturing (AM), particularly 4D printing.

2. Materials and methods

The research concerns SMP specimens made from anycubic resin, a mix of some epoxies and acrylates, which were printed using Digital Light Processing (DLP) technique. Various times of polarization, i.e. 2 s, 6 s, 8 s and 10 s per layer, were used.

3. Results and concluding remarks

The comparison of the mechanical behavior of the specimens obtained by the 4D printing with various exposure times per layer during the loading till rupture with a strain rate of 10^{-2} s^{-1} at room temperature is presented as force-displacement and stress-strain curves in Fig. 1a and Fig. 1b, respectively.

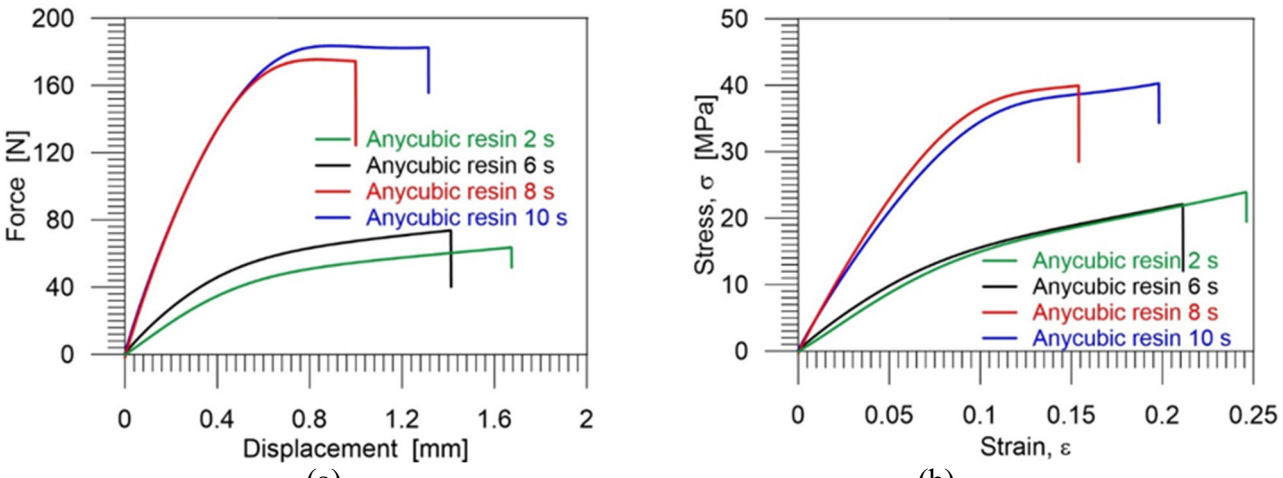

(a) (b)

Fig. 1. Comparison of (a) force-displacement and (b) stress-strain curves for anycubic resin specimens

In addition, the shape memory properties of the specimens were investigated in the thermomechanical loading program performed in the thermal chamber of the Instron testing machine. At the initial stage, the specimen was heated to $T_h = T_g + 20°C$ at 12 °C/min. After that, tension loading was applied with a strain rate of 10^{-2} s^{-1} at $T_g + 20°C$ until a maximum programmed strain was reached. Next, the specimen was cooled to low temperature T_l , which corresponded to either room temperature (24 C°) or T_g - 20°C depending on the specimen, while maintaining the maximum strain (ε_m) to fix its temporary shape. Then the specimen was unloaded to zero-force at T_l with a strain rate of 10^{-2} s^{-1}, demonstrating the shape fixity. Finally, the specimen was reheated from T_l to T_h at a heating rate of 12 °C/min in no-load conditions, leading to the shape recovery.

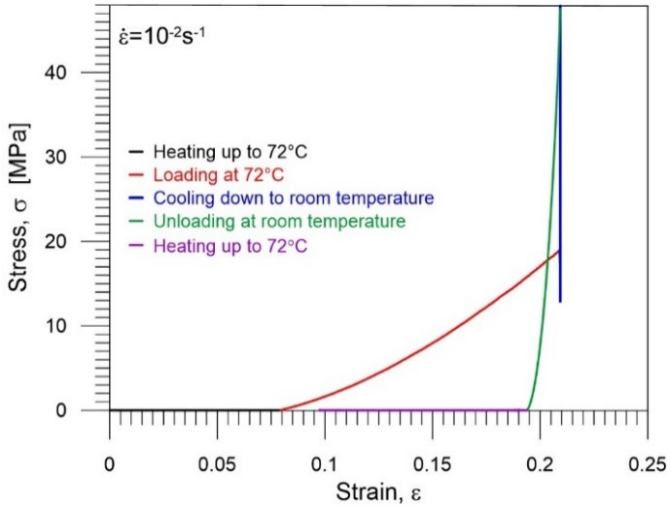

Fig. 2. Stress vs. strain curve obtained during thermomechanical loading program [6] of the specimen with 10 s per layer; particular colors of curves mark subsequent stages of the program.

The example of the stress vs. strain curve obtained during the thermomechanical loading program [6] of the specimen with the exposure time of 10 s per layer is shown in Fig. 2. The shape fixity and shape recovery parameters, obtained for anycubic specimens with different exposure times per layer, demonstrated high sensitivity of the DLP parameters used, on the SMEp application parameters.

4. Acknowledgements

The research has been supported by the 16th Call of the KMM-VIN Research Fellowship Programme and the Polish National Science Centre under Grant UMO-2024/53/B/ST8/03931.

References

[1] Lendlein A. and Kelch S., Shape-memory polymers, *Angew. Chem. Int. Ed.*, 2002, 41, 2034–2057.
[2] H. Tobushi, R .Matsui, K. Takeda and E.A. Pieczyska (2013). *Mechanical Properties of Shape Memory Materials*, Nova Science Publishers, New York.
[3] Staszczak M., Urbański L., Cristea M., Ionita D., Pieczyska E.A.(2024). Investigation of Shape Memory Polyurethane Properties in Cold Programming Process Towards Its Applications, *Polymers*, ISSN:2073-4360, DOI:10.3390/polym16020219, **16**, 2, 219-1-219-20.
[4] Staszczak M., Urbański L., Gradys A., Cristea M., Pieczyska E.A.(2024). Nucleation, Development and Healing of Micro-Cracks in Shape Memory Polyurethane Subjected to Subsequent Tension Cycles, *Polymers*, ISSN:2073-4360, DOI:10.3390/polym16131930, **16**, 13, 1-22.
[5] Nabavian Kalat M., Staszczak M., Urbański L., Fernandez C., Vega C., Cristea M., Ionita D., Lantada A., Pieczyska E.A. (2023). Investigating a shape memory epoxy resin and its application to engineering shape-morphing devices empowered through kinematic chains and compliant joints, *Materials and Design*, 10.1016/j.matdes.2023.112263, ***233***, 112263, 1-15.
[6] Tobushi, H.; Hara, H.; Yamada, E.; Hayashi, S. (1996). Thermomechanical properties in a thin film of shape memory polymer of polyurethane series. *Smart Mater. Struct.*, ***5***, 483-491.

INFLUENCE OF PROCESSING PARAMETERS ON MECHANICAL PROPERTIES OF MULTI-MATERIAL COMPONENTS FROM ALUMINIUM AND COPPER – MANUFACTURED BY LASER-BASED POWDER BED FUSION

C. Singer[1], J. Foerster[1], S. Zabihzadeh[2], G. Schlick[1], C.M. Charalampidou[3], J. Schilp[4], J.S. Aristeidakis[5], I.S. Berglund[5] and N.D. Alexopoulos[3]

1 Fraunhofer Research Institute for Casting, Composite and Processing Technology IGCV, Am Technologiezentrum 10, 86159 Augsburg, Germany

2 Swiss Centre for Electronics and Microtechnology (CSEM), Additive manufacturing and component reliability, Neuchâtel, Switzerland

3 University of the Aegean, Department of Financial Engineering and Management, Research Unit of Advanced Materials, 82100 Chios, Greece

4 University of Augsburg, Chair of Digital Manufacturing, Am Technologiezentrum 8, 86159 Augsburg, Germany

5 QuesTek Europe AB, Råsundavägen 18A, 169 67 Solna, SWEDEN

1. Introduction

Nowadays Additive Manufacturing (AM) is gaining ground for producing metallic parts and products. Over the past years, the exploitation of AM processes aims to produce highly complicated mono-material parts in a short time and as a monolithic component. For metallic materials the most common process is powder fusion of metal using a laser beam (PBF-LB/M). Recently, the possibility to manufacture parts with more than one material on the same part using PBF-LB/M has gained increasing attention. The variation of the material's chemical composition throughout a component, also referred to as multi-material components, enables for a more flexible design of the product, e.g. [1, 2]. Examples from the open literature include the combination of mechanical strength as well as temperature resistance or even thermal conductivity properties, e.g. [3-5]. Other examples involve the trade-off between hardness measurements and toughness values [6, 7] or in another cases the sensor integration [8, 9] by AM of dissimilar materials. The multi-materials concept aims to manufacture sustainable-by-design new products with higher performance in e.g. mechanical or thermal properties as well as weight reduction, allowing for the efficient and sustainable use of critical raw materials.

In the present contribution, a multi-material combination of CW106C powder, referred hereafter as CuCr1Zr, and EN AW-4046 powder, referred hereafter as AlSi10Mg, with sharp transition zones, printed in different directions and manufacturing sequences of the two materials, is investigated. For the validation of the approach and the characterization of the transition zones, the manufactured samples were investigated and characterized using optical microscopy, scanning electron microscopy, hardness profile measurements and tensile tests. Furthermore, the density of the transition zones was analysed by image data processing. CALPHAD based computational tools were employed to predict microstructural evolution and solidification behaviour upon AM processing of the sharp transition zone, providing insight and supporting experimental investigations. The feasibility of the presented methods is shown and the production of defect-free transition zones with controlled expansions for multi-material solutions via PBF-LB/M is presented.

2. Materials and methods

The present study simulates the production phase of high performance automotive – power electronics sensing / cooling end-products. In this product, Al and Cu alloys were used, where the Cu alloy could serve as functional material for electricity or heat conduction purposes. CuCr1Zr was selected to serve for heat conduction purposes, while adding Chromium (Cr) and Zirconium (Zr) to the Cu matrix increases material strength as well as heat and wear resistance without significantly affect its heat and electric conductivity capabilities. The Al alloy AlSi10Mg, was selected as the main structural material of the product/component. It is a precipitation-hardenable cast alloy with good electric conductivity and increased chemical stability in corrosive environments.

All samples were manufactured on a customized SLM280HL PBF-LB/M machine (Nikon SLM Solutions Group AG, Germany). The system has a divided recoating system and a suction unit to apply and remove different powder materials and Argon was used as inert gas and a silicone rubber lip as a recoating device. Different process parameters were used to produce the interfaces, namely laser power in [W] and scan speed in [mm/s]. For the validation, various cuboid samples were prepared with the two different build sequences (CuCr1Zr built on AlSi10Mg and vice versa) with transition zones in the z-direction. Additionally, samples with their transition zones in the x–y plane were fabricated using different parameter combinations in the transition zone. These multi-material test specimens were manufactured for quality analysis and evaluation of the components by determining the density and mixing in the joint zone, as well as through mechanical tests such as hardness measurements. Additionally, reference samples were also manufactured for comparison purposes.

3. Results and conclusions

Initially, the manufactured samples were investigated and characterized using optical microscopy to select the process window for achieving the most defect-free interfaces possible between the two metallic materials. For the intended defect-free interfaces of the produced materials, the geometrical dimensions of the interfaces as well as hardness profile measurements were performed. Furthermore, the density of the transition zones was analysed by image data processing. Finally, calculation results indicate the formation of brittle phases in the transition zone, which may limit processability. The feasibility of the presented method is shown and to produce defect-free transition zones with controlled expansions for multi-materials via PBF-LB/M is pursued.

4. Acknowledgements

The authors gratefully acknowledge the financial support of the HORIZON Research and Innovation Actions, European Health and Digital Executive Agency for the implementation of the project «MULTI-MATERIAL DESIGN USING 3D PRINTING» having an acronym “MADE-3D” of the act HORIZON-CL4-2022- RESILIENCE-01 with Grant Agreement code 101091911.

5. References

[1] M. Schneck, M. Horn, M. Schmitt, C. Seidel, G. Schlick, G. Reinhart (2021). Review on additive hybrid- and multi-material-manufacturing of metals by powder bed fusion: State of technology and development potential. *Prog. Addit. Manuf.*, **6**, 1–14.

[2] DIN EN ISO/ASTM TR 52912:2020.: Additive manufacturing– Design – Functionally graded additive manufacturing. Beuth Verlag GmbH, Berlin

[3] Schneck M, Horn M, Schindler M, Seidel C (2022) Capability of multi-material laser-based powder bed fusion-development and analysis of a prototype large bore engine component. Metals 12(1):44. https:// doi. org/ 10. 3390/ met12 010044

[4] Ringel B, Zaepfel M, Herlan F, Horn M, Schmitt M, Seidel C (2022) Advancing functional integration through multi-material additive manufacturing: Simulation and experimental validation of a burner nozzle. Mater Today Proc 70(2):296–303. https:// doi.org/ 10. 1016/j. matpr. 2022. 09. 241

[5] P. Kindermann, M. Strasser, M. Wunderer, I. Uensal, M. Horn, C. Seidel (2023). Cold spray forming: a novel approach in cold spray additive manufacturing of complex parts using 3D-printed polymer molds. *Prog. Addit. Manuf.*, **22**, 413.

[6] M. Schmitt, A. Gottwalt, J. Winkler, T. Tobie, G. Schlick, K. Stahl (2021). Carbon particle in-situ alloying of the case-hardening steel 16mncr5 in laser powder bed fusion. *Metals*, **11**, 896.

[7] M. Lehmann, C. Kolb, J. Gschloessl, M. Zaeh (2023). Using particle-loaded inks to selectively change the material properties in binder-jetted WC-Co parts. *J. Mater. Sci.*, **58**, 16089–16104.

[8] M. Binder, C. Anstaett, M. Horn, F. Herzer, G. Schlick, C. Seidel (2018). Potentials and challenges of multi-material processing by laser-based powder bed fusion. *Solid Freeform Fabric Proc*., **29**, 376-387.

[9] C. Singer, M. Schmitt, G. Schlick, J. Schilp (2022). Multi-material additive manufacturing of thermocouples by laser-based powder bed fusion. *Procedia Cirp,* **112**, 346–351.

[10] M. Horn, J. Schweiger, T. Schroeder, L. Langer, J. Trimpl, K. Erdelt (2023). Additive Multimaterialfertigung von Metallen in der Doppelkronentechnik. *Quintessenz Zahntechnik*., **49**, 808–817.

INFLUENCE OF HIGH STRAIN RATE AND TEMPERATURE ON THE YIELD BEHAVIOUR OF 3D PRINTED POLYAMIDE 11

Paul Wood[1], Urvashi Gunputh[1], Marzena Pawlik[1], Yiling Lu[1], Pawel Platek[2], Jacek Janiszewski[2], Marcin Sarzynski[2], Alexis Rusinek[3]

[1] Institute for Innovation in Sustainable Engineering, College of Science and Engineering, University of Derby, Derby, United Kingdom
[2] Military University of Technology, Faculty of Mechatronics, Armaments and Aerospace, 2 gen. Sylwestra Kaliskiego, 00-908 Warszawa
[3] Laboratory of Microstructure Studies and Mechanics of Materials – UMR CNRS 7239, Lorraine University, 57070 Metz, France

1. Introduction

Polyamide 11 (PA11) is widely used in industrial sectors that include healthcare, automobiles, and oil and gas. PA11 is a bio-based and biocompatible semicrystalline nylon polymer formulated from the oil of caster beans which is a renewable source. The volume fraction of the crystalline phase in PA11 is just above 20% but can vary depending on the prior thermal processing conditions and heat treatment. The balance is the amorphous phase. The main glass transition (T_α) of PA11 is ~45 °C. But T_α depends on the strain rate in which the polymer material is subjected. At high strain rates the T_α is raised. According to the WLF equation T_α for PA11 at 2000 s^{-1} could reach ~75 °C. In many amorphous polymers the effect of lowering the temperature on the properties such as elastic modulus and yield stress is same as increasing the strain rate. This observation has enabled the strain rate and temperature dependent elastic modulus and yield stress of polymers to be described using the time-temperature (or strain rate-temperature) superposition principle [1].

In the glassy region below T_α the mobility of the polymer chains become more restricted, but they are not completely immobile due to secondary relaxations. PA11 has two secondary relaxations ($T < T_\alpha$) that can account for an increase in the strength properties. The T_β relaxation occurs at -50 °C (2) and the T_γ relation at -120 °C. Below T_β the PA11 may be become brittle as in the case of the amorphous polymer PMMA, that displayed a higher yield stress with increasing strain rate above its T_β, but below its T_β it was brittle and fractured before yield could be reached [3].

The large-deformation properties of the PA11 such as yield, and ductility are strongly influenced by the size of the spherulites in the microstructure [2]. If the cooling rate of PA11 from the melt is very rapid e.g. 100 °C/s the resulting microstructure was shown to develop tiny isolated spherulites with size below 4 µm that were surrounded by a mainly non spherulitic structure. A slow cooling of the melt e.g. 0.1 °C/s, resulted in larger spherulites up to 20 µm filling the entire microstructure and this happens because crystallization starts at a higher temperature e.g. 165 °C, than under a slow cooling from the melt. Irrespective of the cooling rate from the melt the crystallinity of the PA11 microstructure was found to be broadly similar. The cooling rate in selective laser sintering was reported to be rapid [4] and attributed to the fresh powder particles being swept over the preceding layer. We believe the temperature of the powder bed and the laser scan time for each layer will influence the cooling rate. The first objective of this study is to conduct quasi-static and dynamic compression tests on selective laser sintered (SLS) PA11 in the design range of interest to determine the mechanical behaviour of the 3D printed material as a function of temperature and strain rate.

The original Eyring model describes the yield stress (σ_y) of a polymer with dependency on temperature (T) and strain rate ($\dot{\varepsilon}$). Bauwens-Crowet et. al. [5] had shown that the Eyring plots of σ_y / T versus log ($\dot{\varepsilon}$) obtained at different temperatures and strain rates can be shifted to create a master curve at a selected reference temperature (T_r). The cooperative model [3] broadens the applicability of the Eyring model because it can describe temperature and strain rate effects on the elastic modulus and yield stress over a wider range including the T_α and T_β relaxations. The cooperative model was enhanced [6] to describe the yield behaviour of semi-crystalline polymers by using an effective activation volume and effective activation energy. This empirically based model uses micromechanics to discern the amorphous and crystalline phase volume fractions in the polymer. The second objective of this study is to identify a suitable model that can capture the behaviour of the PA11 semi-crystalline polymer in the design range of interest.

2. Materials and methods

SLS 3D printed samples were prepared using virgin powder feedstock. High strain rate compression tests were performed at low strain rate (0.001 s^{-1}), intermediate strain rate (0.5 s^{-1}) and at high strain rate (to 2000 s^{-1}), and at temperatures -20, +20 and +50 °C for each strain rate level using 3 material samples at each level tested. Tension tests were performed at room temperature at low strain rate (0.001 s^{-1}) and intermediate strain rate (0.333 $^{-1}$).

3. Results

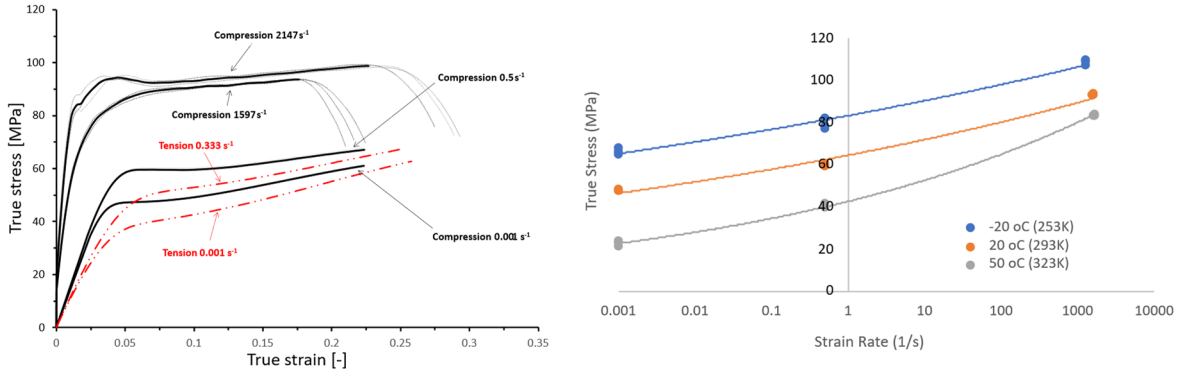

The left figure shows the effect of strain rate at room temperature in tension and compression and the right figure shows the effect of temperature and strain rate on yield stress.

4. References

[1] Siviour et. al., High Strain Rate Mechanics of Polymers: A Review. J. dynamic behavior mater. 2, 15–32 (2016). https://doi.org/10.1007/s40870-016-0052-8

[2] Jariyavidyanont et. al., (2019). Thermal Properties of Biobased Polyamide 11. In: Di Lorenzo, M., Androsch, R. (eds) Thermal Properties of Bio-based Polymers. Advances in Polymer Science, vol 283. Springer, Cham. https://doi.org/10.1007/12_2019_47

[3] J. Richeton et. al., Influence of temperature and strain rate on the mechanical behavior of three amorphous polymers: Characterization and modeling of the compressive yield stress, International Journal of Solids and Structures, 2006, https://doi.org/10.1016/j.ijsolstr.2005.06.040.

[4] Esposito et. al., Changes in polyamide 11 microstructure and chemistry during selective laser sintering, Additive Manufacturing, 2021, https://doi.org/10.1016/j.addma.2021.102445.

[5] Bauwens et. al., 1969. Tensile yield-stress behavior of poly(vinyl chloride) and polycarbonate in the glass transition region. Journal of Polymer Science: Part A-2 7.

[6] Gueguen et. al., Micromechanically based formulation of the cooperative model for the yield behavior of semi-crystalline polymers. Acta Mater. 2008, 56, 1650–1655.

ROCKWELL AND SCRATCH ADHESION TESTS FOR HARD COATINGS DEPOSITED ON LIGHT ALLOYS FABRICATED BY SLM

E. Ghio[1], M. F. Bonilauri[2], G. Bolelli[2,3,4], A. Bertè[5] P. Colombi[5], E. Cerri[1]

[1] *D.I.S.T.I., University of Parma, v. G. Usberti 181/A, 43124, Parma, Italy*
[2] *Dept. Engineering "Enzo Ferrari", University of Modena e Reggio Emilia, v. P. Vivarelli 10/1, 41125, Modena, Italy*
[3] *InterMech MO.RE. University of Modena and Reggio Emilia, v. P. Vivarelli 2, 41125, Modena, Italy*
[4] *Consorzio INSTM, Local Unit: Università di Modena e Reggio Emilia, v. P. Vivarelli 10/1, 41125, Modena, Italy*
[5] *LAFER S.p.A., Strada Di Cortemaggiore 31, 29122, Piacenza, Italy*

1. Introduction

Generally, Ti6Al4V components are produced through conventional manufacturing (CM) processes, including forging, casting and rolling, and through subsequent post-processes conferring the final shape. In contrast, Powder-based Additive Manufacturing processes, such as Laser Powder Bed Fusion (L-PBF), enable the direct production of near-net-shape metallic components by adding metal powders layer-by-layer [1]. The Ti6Al4V alloy is also characterized by limited wear resistance, which can be improved through the deposition of hard coatings [2]. To achieve a successful hard coating for various industrial applications, the adhesion strength to the substrate is the most important aspect to investigate. There are several qualitative and quantitative characterization methods, including indentation and scratch tests, to guarantee the reproducibility of the deposition process [3]. More specifically, the Rockwell indentation test, according to the VDI 3198 standard [4], is a well-established, cost effective and quick mechanical method to investigate the adhesion and brittleness of a hard coating on a substrate. A conical diamond indenter is impressed into the coating surface, and the failures caused by the extreme shear stresses induced at the coating/substrate interface and by the bending stresses within the coating must be compared to a failure chart with six adhesion classes (HF1-HF6). However, the quality control method for assessing the coating/substrate adhesion becomes more accurate and effective when using a scanning electron microscope (SEM) to investigate the failure mechanisms of deposited coating. The scratch test has been investigated in detail, and several studies have appeared where the failure modes were described. The recent review by Randall [5] showed that the scratch adhesion test is a rather mature method to be applied both in laboratory and production settings. Few authors investigated the comparability between the results of the Rockwell indentation and the scratch adhesion tests. This paper aims to evaluate the comparability between the results of scratch and Rockwell indentation tests applied to two types of thin-film coatings deposited on SLMed Ti6Al4V substrates with different surface roughness. The films were chosen for their technological interest in tribological applications: an AlCrN layer deposited by High- Power Impulse Magnetron Sputtering, and a DLC-based film deposited by hybrid Magnetron Sputtering – Physical Vapour Deposition and Plasma Enhanced Chemical Vapour Deposition.

2. Materials and methods

Substrate samples were manufactured by Laser-Powder Bed Fusion (L-PBF) using a Ti6Al4V Extra-Low Interstitials (ELI) feedstock powder. Different roughness levels were induced on the surface by grinding paper and measured by a 3-D profilometer. Two types of coatings were deposited

on all types of substrates: a Diamond-Like Carbon (DLC)-based coating and an AlCrN coating. Depositions were carried out at an industrial facility to obtain representative samples of the current state. A Rockwell indentation test, defined by the VDI 3198 standard, was used to establish the coating/substrate adhesion. Rockwell imprints were also investigated through focused ion beam scanning electron microscopy (FIB-SEM). The results obtained by the Rockwell indentation were then compared to the scratch adhesion results. Scratch tests were performed with a Micro-Combi Tester apparatus equipped with a conical diamond indenter having a 120° opening angle and a 200 µm-radius rounded tip.

3. Results and conclusions

In-situ cross sections of the two coatings obtained by FIB milling of the samples after the Rockwell indentation tests are illustrated in Fig. 1a and b and the mechanical data are summarized in fig. 1c. The films showed good adhesion regardless of the surface roughness and the microstructure of the L-PBF and rolled Ti6Al4V. The results show that no significant correlations were found between the results of the scratch test (critical load) and the VDI 3198 Rockwell indentations (number of cracks per unit length around the indent). Nevertheless, the films were similarly damaged through cracks and delaminations during both the scratch test and the Rockwell indentation. Only the scratch test was able to reveal a slightly negative correlation between roughness and adhesion strength through a modest increase in the critical load for delamination.

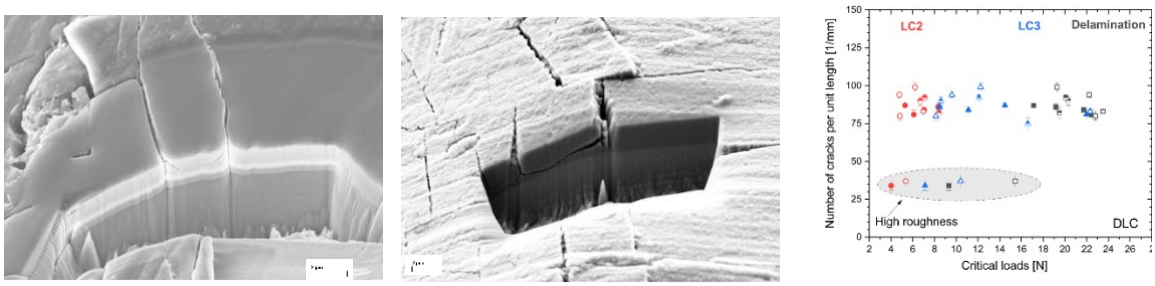

Fig. 1. SEM micrographs of deposited a) DLC and b) AlCrN coatings and c) relationship between VDI results and scratch tests.

4. Acknowledgements

The project was granted by National Recovery and Resilience Plan (NRRP), Mission 4, Component 2, Investment 1.5. – Call for tender No. 3277 of 30/12/2021 of Italian Ministry of University and Research founded by European Union – NextGenerationEU.

5. References

[1] E. Ghio, E. Cerri, *Materials* 15 (2022) 2047. https://doi.org/10.3390/ma15062047.
[2] K.G. Budinski, *Wear* 151 (1991) 203–217. https://doi.org/10.1016/0043-1648(91)90249-T.
[3] P.R. Chalker, S.J. Bull, D.S. Rickerby, *MSE A* 140 (1991) 583–592. doi.org/10.1016/0921-5093(91)90482-3.
[4] V.D.I. Normen, VDI 3198, VDI-Verlag (1991) 1–8.
[5] N.X. Randall, *Surf Coat Technol* 380 (2019) 125092. https://doi.org/10.1016/J.SURFCOAT.2019.125092.

CYCLIC COMPRESSION PROPERTIES OF HIGH-STRENGTH, RECOVERABLE, LIGHT-CURABLE 4D PRINTING LATTICE REINFORCED WITH GLASS FIBERS

***Junwei Pan*[1], *Jianguo Cai*[1]**
[1] *Department of Civil Engineering, Southeast University, Nanjing, China*

1. Introduction

Light-curable additive manufacturing (AM) technologies, most notably stereolithography (SLA) and digital light processing (DLP), have unlocked the rapid, monolithic fabrication of architected lattice structures with sub-micrometer resolution and bespoke mechanical performance. In SLA, ultra-high precision is achieved via point-by-point laser scanning [1], whereas DLP leverages full-layer projection to accelerate build rates without compromising feature fidelity [2]. Periodic lattices such as the Octet-truss and Box geometries exhibit exceptional strength-to-weight ratios and programmable deformation modes, and have been employed in lightweight load-bearing components, energy-absorption systems, and biomedical scaffolds [3]. However, the intrinsically low elastic modulus and limited fatigue resistance of unreinforced photopolymers constrain their use under cyclic or large-strain loading. Although incorporation of micro- and nanoscale fillers, such as graphene oxide, carbon fibers, and ceramic particulates, can enhance stiffness or strength, these approaches often introduce processing complexity, suboptimal dispersion, diminished light transmittance, and weakened interfacial bonding, with concomitant losses in toughness [4].

Glass fiber powder has recently emerged as a cost-effective, mechanically robust inorganic reinforcement: its high specific surface area promotes strong fiber–resin adhesion, its chemical stability and corrosion resistance confer durability, and its tunable light-scattering properties preserve uniform curing depth [5]. Nonetheless, research to date has predominantly addressed thermosetting matrices, leaving the performance of glass fiber-reinforced DLP-printed lattices, particularly under large-strain, multi-cycle compression, largely unexplored. Similarly, the domain of photoactivated 4D-printed composites has been dominated by thermoplastic shape-memory polymers, and the influence of inorganic fillers on reversible, recoverable photopolymer architectures remains poorly understood.

To address these challenges, we have developed a temperature-responsive, glass fiber-reinforced photopolymer and employed a structure–material co-design strategy to fabricate Octet-truss and Box lattices via DLP. Through systematic cyclic mechanical and thermal compression testing, we quantify strength retention, energy-absorption efficiency, and dimensional recovery, revealing how fiber reinforcement and lattice topology synergistically enhance fatigue resilience and reversible deformation. These findings establish design principles for durable, high-performance 4D-printed materials suitable for adaptive, energy-absorbing applications.

2. Materials and methods

This study used digital light processing (DLP) to fabricate tensile and lattice specimens from a transparent, tough photosensitive resin (ANYCUBIC) reinforced with glass fiber (GF) powder (Hebei Minerals, max length ~80 μm). Seven resin mixtures with GF contents of 0 to 30 wt% were prepared.

Resin and GF were manually mixed, then ultrasonically agitated for 30 min (80 W, 40 kHz) to ensure uniform dispersion. Sedimentation and viscosity tests confirmed adequate mixing and printability despite increased viscosity with GF content.

Samples were printed on an ANYCUBIC HALT-RAY printer at 50 μm layer thickness, with base exposure of 70 s for 3 layers and 3 s for subsequent layers; build speed was 3 mm/s. Lattices (Octet-truss and Box) had 5×5×5 cells of 10 mm size, tensile specimens measured 170×6×2 mm. Samples with the same GF content were printed in single batches.

Mechanical tests used a 10 KN universal tester at 5 mm/min. Quasi-static compression was performed on lattices to assess GF effects on strength and deformation. Octet-truss samples underwent cyclic compression and thermal recovery to evaluate fatigue and shape-memory properties. SEM at 500× magnification examined fiber dispersion and interface quality in low-GF and high-GF samples.

3. Results and conclusions

The stress–strain curves in Fig. 1g show that the compressive response of the lattice structures varies with glass fiber content. Peak load and energy absorption data (Fig. 1h) reveal an overall improvement with increasing glass fiber loading, particularly notable at 30 wt%. Despite minor microstructural inhomogeneity observed in SEM images (Fig. 1c, 1e), all specimens exhibited stable deformation (Fig. 1f), and no defects due to printing or filler addition were found (Fig. 1b, 1d). These results indicate that fiber reinforcement enhances both strength and toughness without compromising print quality. Therefore, glass fiber-reinforced resin systems show promise for structural applications requiring tunable mechanical performance.

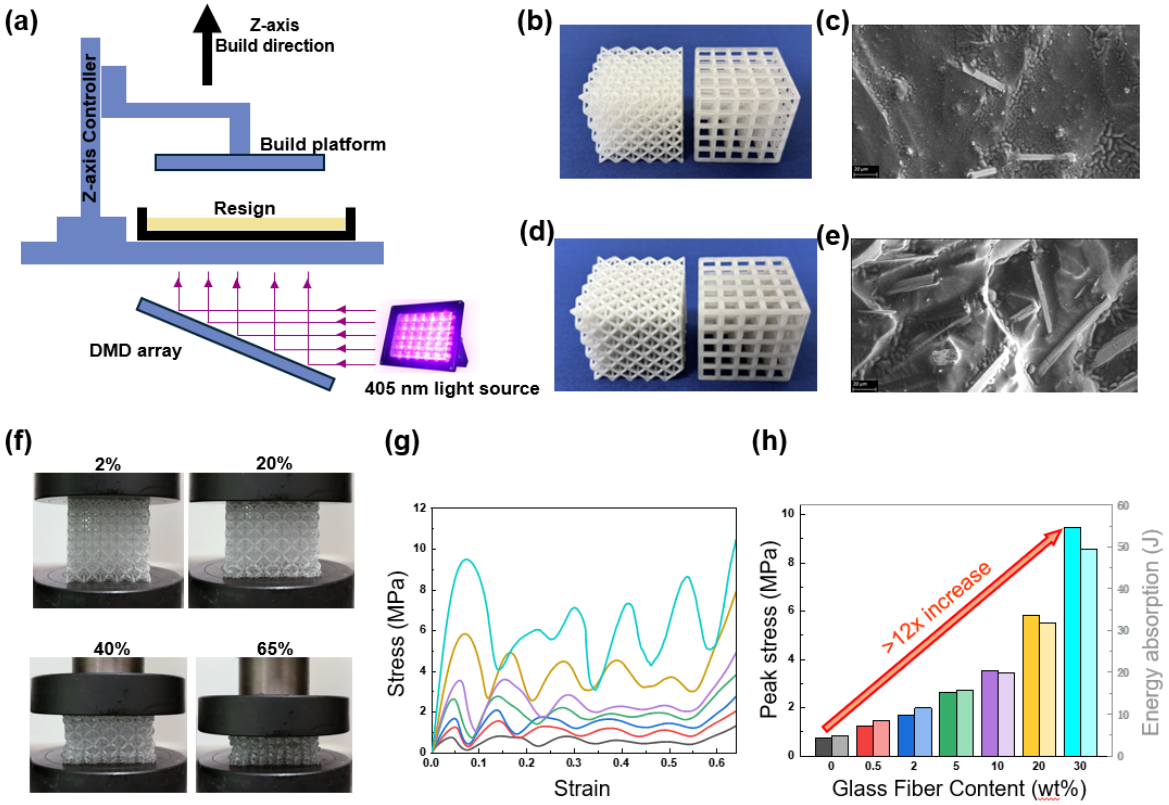

Fig. 1. Compressive mechanical properties of light-cured lattice structures: (a) DLP printing principle, (b) Lattice specimens with 0.5% glass fiber contents, (c) SEM micrograph of 0.5 wt% specimen, (d) Lattice specimens with 30% glass fiber contents, (e) SEM micrograph of 30 wt% specimen, (f) Deformation and load-bearing capacity at different strain levels, (g) Stress-strain curves of specimens, (h) Peak load-bearing capacity and energy absorption of specimens.

4. Acknowledgements

The work presented in this article was supported by the National Natural Science Foundation of China (52478306, 52478145), Jiangsu Provincial Department of Science and Technology Projects (Grant No. BE2023801) and Aeronautical Science Foundation（2024Z006069001）

5. References

[1] Xiao R., Ding M., Wang Y., Gao L., Fan R., Lu Y. (2021). Stereolithography (SLA) 3D printing of carbon fiber-graphene oxide (CF-GO) reinforced polymer lattices. *Nanotechnology*, 32(23), 235702.

[2] Zhang G., Song D., Jiang J., Li W., Huang H., Yu Z., Peng Z., Zhu X., Wang F., Lan H. (2023). Electrically assisted continuous vat photopolymerization 3D printing for fabricating high-performance ordered graphene/polymer composites. *Composites Part B: Engineering*, 250, 110449.

[3] Wang N., Meenashisundaram G.K., Kandilya D., Fuh J.Y.H., Dheen S.T., Kumar A.S. (2022). A biomechanical evaluation on Cubic, Octet, and TPMS gyroid Ti6Al4V lattice structures fabricated by selective laser melting and the effects of their debris on human osteoblast-like cells. *Biomaterials Advances*, 137, 212829.

[4] Hao Q., Liu S., Wang X., Zhang P., Mao Z., Zhang X. (2024). Progression from graphene and graphene oxide to high-performance epoxy resin-based composite. *Polymer Degradation and Stability*, 110731.

[5] Mo Z., Jiang X., Zhu X., Ding J., Ban B., Sun J., Chen J. (2024). Facile purification of glass fiber powder by sedimentation for enhanced epoxy resin composites. *Colloids and Surfaces A: Physicochemical and Engineering Aspects*, 695, 134259.

Advances in Experimental Techniques under Impact and Shock

Synthesis of Gunfire Shock Signals Based on Shock Response Spectrum

Yinzhong Yan
[1] *School of Civil Aviation, Northwestern Polytechnical University, Xi'an, Shaanxi 710072, China*
[2] *Yangtze River Delta Research Institute of Northwestern Polytechnical University, Taicang 710060, China*

1. Introduction

Gunfire shock refers to the transient, high-rate repetitive excitations that materials and structures experience during the firing of guns[1], e.g. aircraft artillery. This type of shock is characterized by its relatively short duration but can occur repeatedly if multiple rounds are fired. The gunfire shock environment poses significant challenges as it can damage the structural and functional integrity of materials and equipment exposed to it. Common structural failures include junction friction changes, permanent mechanical deformation, accelerated material fatigue, and cracking in brittle (optical) materials. In terms of functional failures caused by gunfire shock, the performance of device components can change temporarily during shock or permanently after shock, affecting properties such as insulation resistance, magnetic and electrostatic field strength, and piezoelectric activity. Thus, gunfire shock testing of device under laboratory exciter is necessary to provide a degree of confidence in how devices withstand the gunfire shock environment.

Gunfire shock testing in the lab requires time-history signal data for exciters like electrodynamic shakers. MIL-STD-810H[1] suggests three methods for synthesizing gunfire shock signals: (1) measured data replication, (2) shock response spectrum (SRS) synthesis, and (3) stochastic synthesis. When in-service gunfire shock data is available, the time waveform replication (TWP) method is recommended, as it reproduces the measured environment most accurately. Measured signals may need tailoring for conservative testing. Studies in 1994 by Smallwood[2] and Merritt[3] introduced pulse ensemble approaches for replicating gunfire time traces using measured data. Merritt used short-time Fourier spectrum, while Smallwood applied the product model for non-stationary random vibration and band-limited temporal moments. Smallwood later advanced synthesis methods using wavelets, manipulating wavelet coefficients to generate new, realistic signals[4] and scaling measurements for conservative testing. The Karhunen-Loève (K-L) expansion method[5] offers a compact approach for simulating general non-stationary environments. Sherf et al.[6] analyzed gunfire shocks and proposed a synthesis method based on signal maxima statistics. When measured data is unavailable, as in new aircraft designs or device installations, stochastic synthesis is used. The sine-on-random (SOR) method[7] is common but inadequate, as its rise time and duration do not match real gunfire shocks. Thus, stochastic synthesis is a last resort for gunfire shock signal generation. However, there is currently no open method for gunfire shock synthesis from SRS specifications.

This study aims to provide a comprehensive method for synthesising gunfire shock signals from SRS specifications. The proposed method consists of three primary processes. Based on the shock-waveform dictionary technique, temporal characteristics, such as the initial rise time and duration of single-shot shocks and the repetition intervals of multi-shot shocks, are all controllable.

2. Materials and methods

The proposed method synthesizes gunfire shock signals in three steps. First, an intermediate SRS is constructed to guide the synthesis of single-shot shocks, ensuring they meet temporal and spectral requirements while accounting for resonance effects. Second, single-shot shocks are generated using a shock-waveform dictionary, allowing precise control over rise time, duration, and displacement. Lastly, multi-shot signals are created by concatenating single-shot shocks and compensating for low-frequency discrepancies with noise generated via a filter bank. This approach ensures the final signal meets SRS specifications while replicating the realistic characteristics of gunfire shocks.

3. Results and conclusions

Figure 1 illustrates the synthesized multi-shot gunfire shock signal and its compliance with the specified SRS. Part (a) shows the time-history of the acceleration signal, consisting of 20 individual shocks separated by 15-millisecond intervals. The distinct temporal features of each shock, such as rise time and duration, are preserved, while the added low-frequency noise ensures a realistic representation of the gunfire environment. Part (b) compares the SRS of the synthesized signal to the specification within a ±3 dB tolerance band. The SRS aligns closely with the specification across all frequencies, with minimal deviation. Resonance effects in the low-frequency range are effectively compensated by the noise addition. The largest error is 2.2 dB, and the average error is only 0.45 dB, demonstrating high accuracy.

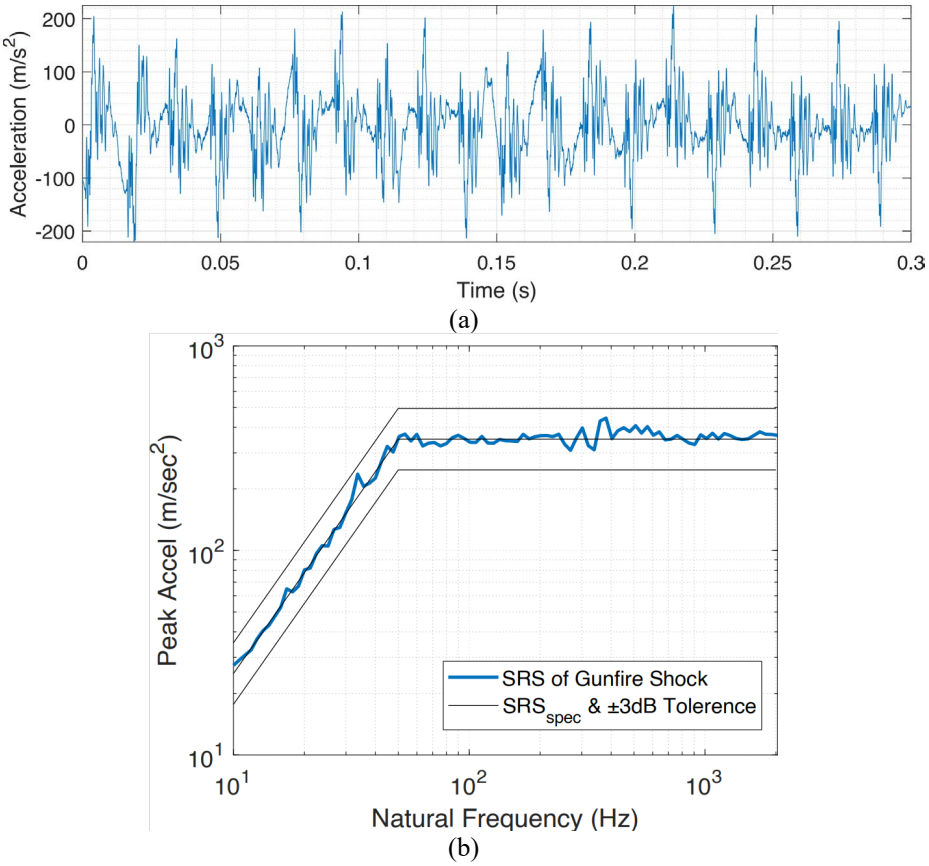

Fig. 1. The synthesized multi-shots gunfire shock: (a) Time history and (b) SRS comparison.

4. Acknowledgements

This work is supported by the National Natural Science Foundation of China (No. 12302487 and No. U2241274), the Suzhou Leading Talents Program for Innovation and Entrepreneurship (No. ZXL2023160) and the Basic Research Program of Taicang (No. TC2023JC07).

5. References

[1] MIL-STD-810H, Environmental Engineering Considerations and Laboratory Tests, Department of Defence, Washington D.C, USA, 2019.

[2] D. O. Smallwood, Gunfire characterization and simulation using temporal moments, Tech. rep., Sandia National Labs., Albuquerque, NM (United States) (1994).

[3] R. G. Merritt, Simulation of ensemble oriented nonstationary processes, part 2, in: Annual Technical Meeting-Institute of Environmental Sciences, Vol. 40, Institute of environmental sciences, 1994, pp. 318–318.

[4] D. O. Smallwood, Characterization and simulation of gunfire with wavelets, Shock and Vibration 6 (2) (1999) 59–72.

[5] D. Smallwood, Characterization and simulation of gunfire with Karhunen-Loeve expansion, Journal of the IEST 47 (1) (2004) 47–50.

[6] Z. Sherf, P. Hopstone, G. Ostrovski, R. Klein, D. Yehuda, Problems in the analysis of a shock sequence with application to gunfire analysis and simulation, Journal of the IEST 45 (1) (2002) 161–177.

[7] M. T. Hale, Synthesis of a time history based on the sine-on-random prediction methodology defined in MIL-STD-810 method 519, Journal of the IEST 60 (1) (2017) 31–41.

ELECTROMAGNETIC HOPKINSON BAR: BASIC PRINCIPLES AND APPLICATION

Yazhou Guo[1,3*], Zhongbin Tang[1,3], Tao Suo[1,3], Yulong Li[1,2,3]
[1]School of Aeronautics, Northwestern Polytechnical University, Xi'an 710072, China
[2]School of Civil Aviation, Northwestern Polytechnical University, Xi'an 710072, China
[3] National Key Laboratory of Aircraft Configuration Design, Northwestern Polytechnical University, Xi'an 710072, China

1. Introduction

Hopkinson bar, since being invented by Hopkinson in 1914[1], has become the most popular experimental apparatus in the field of impact dynamics. This apparatus had widely applied to test the mechanical properties of materials at strain rates ranging 10^2-$10^4 s^{-1}$. However, in light of the original design of split Hopkinson bar is to load the specimen by one single stress wave (compression, tension or torsion)[2], its makes it difficult to measure the material behavior under multi-pulse or multi-axial loadings. Plenty of researchers have been put into the multi-axial dynamic tests through modification of the traditional Hopkinson bar apparatus and the design of special shaped specimens. Recently, we reported a new technique similar to the traditional Hopkinson bar, the E-Hopkinson bar, except that the stress waves are generated directly by electromagnetic forces. This electromagnetic force is adopted to generate stress pulse directly instead of gas gun or elastic energy release. The stress pulse generator is in contact with the incident bar and there is no mechanical motion of projectile (in fact, there is no projectile) during the whole loading process. Moreover, the generation of stress wave is controlled by electronic unit. As a result, the repeatability of loading time can be as good as less than few microseconds. With such time accuracy, two or more stress pulse generators can be combined together to loading one specimen.

In this investigation, we introduced briefly the basic principles of the E-Hopkinson bar technique and some recent experimental works which cannot be performed by traditional Hopkinson bar apparatus using this technique.

2. Basic principles and applications

The basic idea of the proposed E-Hopkinson bar system in this work is based on the principles of the RLC (Resistance-Inductance-Capacitance) circuit. In general, an E-Hopkinson bar system should include three main units: the charging unit, the discharging unit and the Hopkinson bar unit, as shown in Figure 1. Details of the components and design of each unit can be found in our previous works [3]. Based on the principles we apply the E-Hopkinson bar technology to symmetric dynamic compression/stretching of materials, interlaminar fracture of composites, dynamic Bauschinger effect of metals, mechanical testing at moderate strain rates (10^0-$10^2 s^{-1}$) and dynamic multi-axial testing.

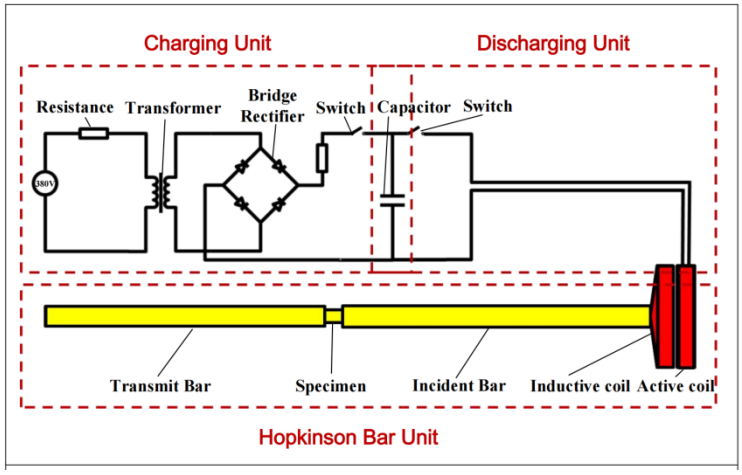

Figure 1. Schematic of the E-Hopkinson bar system

3. Summary

In this work, we introduced a technique called E-Hopkinson bar that proposed for testing the dynamic mechanical behavior of materials. The E-Hopkinson bar use electromagnetic force to generate stress pulse directly, rather than air gun or elastic energy release. Therefore, the time point at which the specimen is loaded by the stress wave can be accurately controlled (within several microseconds). By far, this technique has been applied in symmetrically dynamic compression/tension of materials, interlaminar fracture of composites, dynamic Bauschinger effect of metals, intermediate strain rate tests and dynamic multi-axial test.

4. Acknowledgements

The authors acknowledge the financial support by National Natural Science Foundation of China (NSFC Contracts Nos. 11527803, 11922211, 11832015 and 11672354) and the 111 Project (No. BP0719007). Authors declare no conflict of interests.

5. References

[1] Hopkinson, B., A method of measuring the pressure produced in the detonation of high explosives or by the impact of bullets. Philosophical Transactions of the Royal Society of London A, 1914. 213(497-508): p. 437-452.

[2] Chen, W.W. and B. Song, Split Hopkinson (Kolsky) bar: design, testing and applications. 2010: Springer Science & Business Media.

[3] Nie, H.L., T. Suo, B.B. Wu, Y.L. Li, and H. Zhao, A versatile split Hopkinson pressure bar using electromagnetic loading. International Journal of Impact Engineering, 2018. 116: p. 94-104.

Key Technologies for Coaxial Ultrasonic Defect Detection Based on Frequency-Tunable Laser Transient Gratings

Song Yingzheng[1], Yue Mengmeng[2], Liu Ran[1]*, Li Qun[1]*

[1]State Key Laboratory for Strength and Vibration of Mechanical Structures, School of Aerospace Engineering, Xi'an Jiaotong University, Xi'an 710049, Shaanxi, China

[2]Key Laboratory of Ultra-Fast Photoelectric Diagnostics Technology
Xi'an Institute of Optics and Precision Mechanics, Xi'an, Shaanxi 710119, China
No. 17, Xinxi Road, Gaoxin District

*[1]*Corresponding e-mail: qunli@mail.xjtu.edu.cn TEL: +8602982667535.*

1. Introduction

Laser ultrasound has emerged as a rapidly developing novel detection technology in recent years, demonstrating broad application prospects and significant demand in quality control and management throughout the entire life cycle of equipment. As early as 2008, the National Research Council Canada (NRC) and Lockheed Martin Corporation jointly developed a Laser Ultrasonic Inspection System (LUIS), primarily deployed by the U.S. military for detecting disbond defects in wings, fuselage components, and other critical areas during routine maintenance of F-22 fighter jets [1]. Shortly thereafter, U.S.-based PaR Systems and UK-based Photonic Solutions introduced commercial-grade laser ultrasonic inspection systems, marking significant advancements in industrial applications [2,3]. To address the application requirements of frequency-tunable and flexible array-line laser ultrasonic sources, this project proposes a novel concept of frequency-tunable laser transient grating based on acousto-optic diffraction, focusing on key technologies for coaxial ultrasonic detection using tunable laser transient gratings. Technically, the proposed method replaces conventional fixed-period phase masks with acousto-optic gratings generated through acousto-optic diffraction. By utilizing self-matching interference between diffraction orders of excitation light, it achieves frequency-tunable laser transient gratings, thereby enabling continuous frequency tuning of excited ultrasonic surface waves.

Compared with linear laser sources, frequency-tunable grating sources demonstrate higher sensitivity in specific scenarios. For instance, when detecting strip-shaped defects with large inclination angles relative to the horizontal plane, the tunable grating source exhibits superior signal-to-noise ratio, whereas conventional linear laser sources struggle to identify such defects. Furthermore, the tunable grating laser source can accurately and sensitively distinguish variations in displacement curves caused by strip-shaped defects with different lengths, angles, and depths. This characteristic renders the proposed method particularly valuable for advancing nondestructive testing technologies.

2. Materials and methods

In this study, a technical innovation was implemented by replacing conventional fixed-period phase masks with an acousto-optic grating based on acoustic diffraction. This approach utilizes self-matching interference between diffracted orders of the excitation laser to generate a frequency-tunable laser-induced transient grating, enabling continuous tuning of the excitation frequency for ultrasonic surface waves. Structurally, an optical 4f system was designed and optimized to achieve coaxial laser ultrasound excitation and detection, significantly improving system usability.

Furthermore, fundamental mechanisms were investigated, including the interaction between the laser-induced transient grating and thermoelastic/ultrasonic effects, as well as the correlation between transient grating diffraction spectra and material structural properties. Computational simulations were performed on experimental materials to analyze displacement profiles under varying defect conditions. Defect distributions within the materials were characterized by interpreting defect echo signals derived from ultrasonic wave reflections.

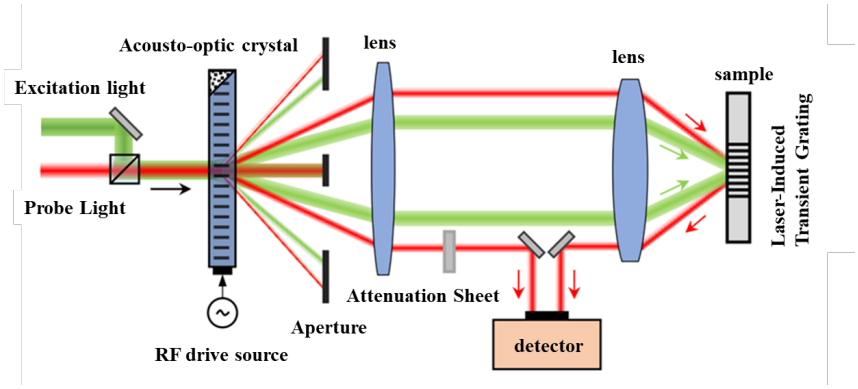

Fig. 1. Schematic Diagram of Frequency-Tunable Laser-Induced Transient Grating Coaxial Ultrasonic Detection

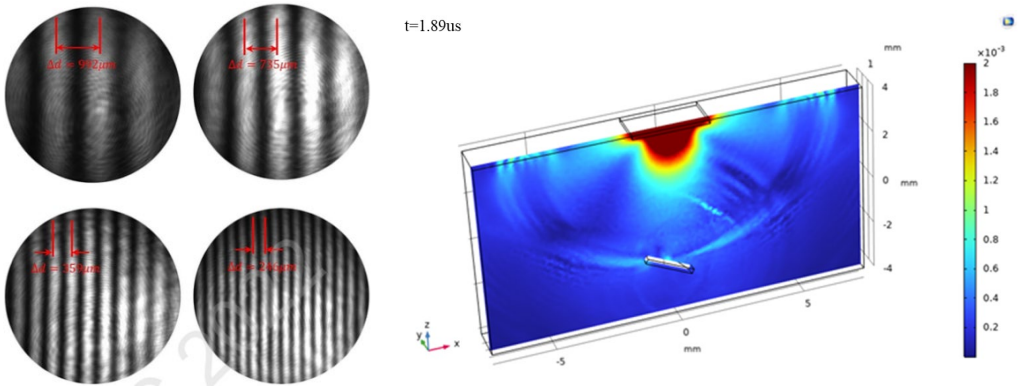

Fig. 2. Grating Light Source Configuration and Stress Visualization in Simulated Defect Analysis

3. Results and conclusions

Under equivalent energy conditions, the tunable frequency grating laser ultrasonic (TFGL-U) technology demonstrates superior detection sensitivity in specific scenarios. Particularly for strip-shaped defects with steep inclination angles relative to the horizontal plane, TFGL-U achieves significantly enhanced signal-to-noise ratio (SNR) advantages over conventional line-source laser ultrasonic systems. This advancement enables breakthrough detection capabilities where traditional line-source methods fail to identify defects entirely. As shown in Figure 3.

The defect characterization capabilities of TFGL-U exhibit distinct parametric correlations:

Dimensional sensitivity: Echo signal amplitudes show proportional relationships with defect lengths. As shown in Figure 4.

Angular response: Echo signal phase angles in time-domain curves systematically vary with defect inclination angles. As shown in Figure 5.

Depth resolution: Both amplitude and time-width characteristics of echo signals correlate with defect burial depths. As shown in Figure 6.

These systematic correlations establish TFGL-U as a comprehensive detection methodology with high sensitivity to defect geometry (size), spatial configuration (position and angle), and burial characteristics. The multi-parameter discriminative capability, combined with its non-contact nature

and material adaptability, positions tunable frequency grating laser ultrasonics as an advanced nondestructive testing (NDT) technology for high-precision defect characterization.

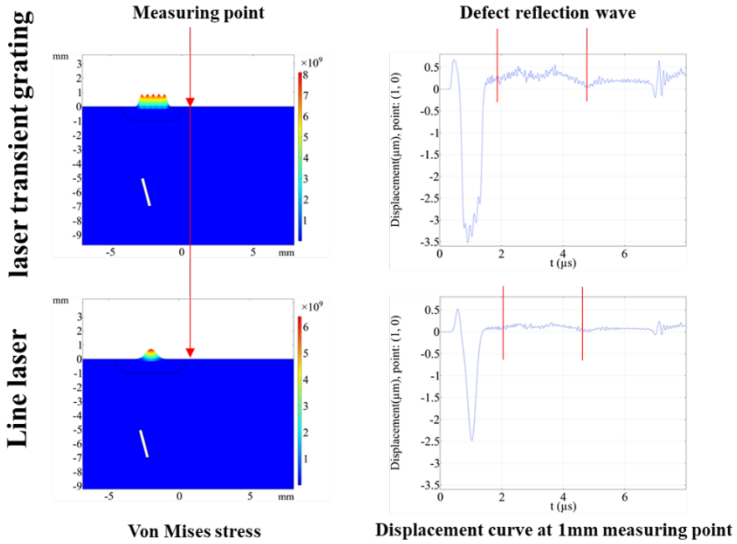

Fig. 3. Defect echo contrast: Grating > Line source (equal energy)

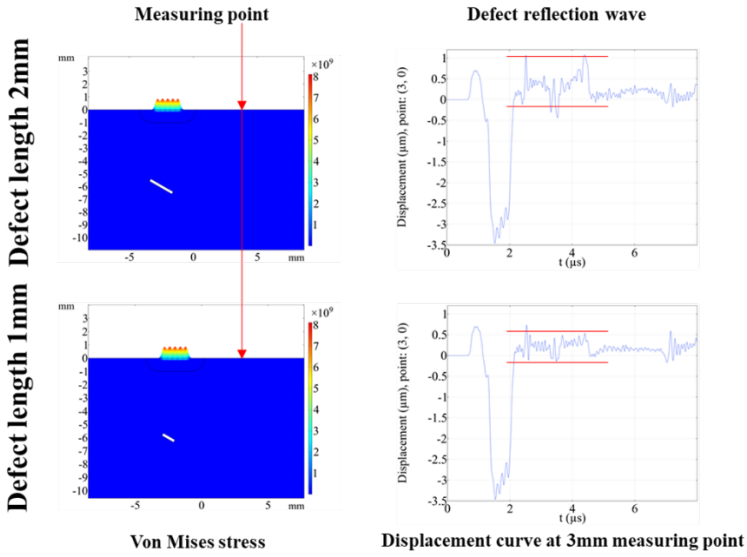

Fig. 4. Defect length-dependent echo amplitude variations.

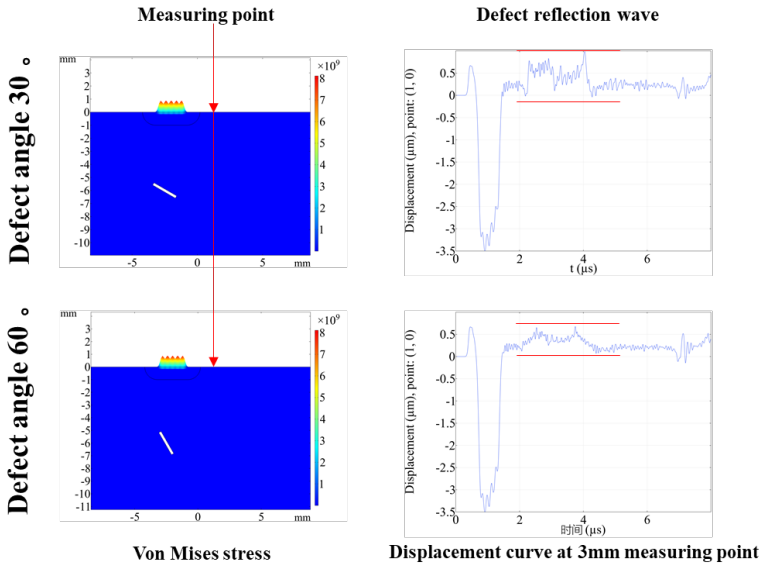

Fig. 5. Echo Angle vs. Incident Angle in Defect Scattering

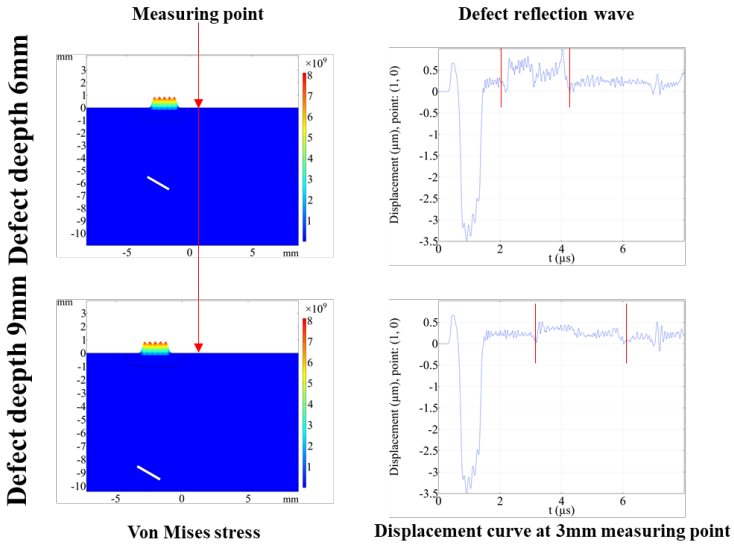

Fig. 6. Defect depth-dependent echo propagation length variation.

4. Acknowledgements

This research was supported by the National Natural Science Foundation of China (62205369、12402089)he computation was performed using the high performance computing (HPC) platform of Xi'an Jiaotong University.

5. References

[1]Osterkamp M A, Kaiser D L. Application of laser ultrasonics for the nondestructive inspection of complex composite aerospace structures[J]. LU, 2008.

[2] Products: Tempo 2D-Multi-component Receiver[EB/OL]. Photonic Solutions Company official website; https://www.photonicsolutions.co.uk/company.php?comp=6743, 2021-12-23.

[3]Technologies:LaserUT[EB/OL].PaRSystemsCompanyofficialwebsite;https://www.par.com/technologies/non-destructive-testing/laser-ultrasonic-testing/,2021-12-23.

MECHANICAL BEHAVIORS OF PLAIN-WOVEN COMPOSITE TUBE UNDER HIGH-STRAIN-RATE TENSILE-SHEAR COUPLING LOADS

Shiling Fang[1,2,3] Hang Wu[1,2,3] Zhenqiang Zhao[1,2,3*] Chao Zhang[1,2,3,4]
[1]School of Aeronautics, Northwestern Polytechnical University, Xi'an, Shaanxi, China 710072
[2]Joint International Research Laboratory of Impact Dynamics and Its Engineering Applications, Xi'an, Shaanxi, China 7100723.
[3]National Key Laboratory of Strength and Structural Integrity, Xi'an, 710072, China
[4] School of Civil Aviation, Northwestern Polytechnical University, Xi'an, Shaanxi, China 710072

1. Introduction

Composites widely utilized in engine blades and various aerostructures, are frequently subjected to dynamic loads such as explosions, impacts, and bird strikes. The strain rate significantly affects the mechanical properties of composites, prompting numerous studies [1-5] aimed at characterizing these properties under different strain rates and proposing advanced constitutive models and failure criteria. However, most of these studies have focused on uniaxial loading conditions. In contrast, composites in aerospace applications often experience coupled loading environments. Additionally, composites exhibit pronounced anisotropic mechanical properties and multi-scale structural characteristics, leading to complex stress states in various aerostructures. However, limited by the development of dynamic experimental technology, research on the mechanical behavior of composites under complex dynamic loads remains largely theoretical, and the lack of relevant mechanical property data and insufficient knowledge of the failure mechanism of materials have seriously restricted the level of advanced composites for impact resistance applications.

Based on the newly developed E-Hopkinson Bar system, this paper proposes a high-strain-rate tensile-shear coupling test technique for composites, successfully realizes the multi-axial loading of composites under dynamic conditions, and systematically explores the influence of tensile and shear effects on the mechanical properties and failure mechanisms of composites.

2. Materials and methods

This paper utilizes T300/6511 plain weave composites supplied by Weihai Guangwei Composites Co., Ltd. The material is fabricated into round tube specimens to facilitate both tensile and shear loading, thereby minimizing size effects and ensuring effective control of stress triaxiality during the tensile and shear processes. In order to make the stress distribution of the specimen in the loading process, it is necessary to ensure that the stress difference between the inner and outer diameter of the specimen is less than 15%. Additionally, to prevent excessive distortion of the specimen gauge length prior to failure during the test, it is necessary to conduct pretests to determine the appropriate specimen gauge length. The size of the specimen used in this test is shown in Fig. 1(a), designed for 8mm gauge length, and reserved 70mm bonding area to ensure the reliability of the adhesive bonding. The experiment begins with a quasi-static test conducted on the Water-Bai Hydraulic tensile and torsion static tester to investigate the material's uniaxial and multiaxial behavior under static conditions. Based on the static test results, dynamic high-strain-rate tests are performed using the E-

Hopkinson system, pioneered by Liu et al. [6], to explore the mechanical properties and damage mechanisms of the material under various stress ratios, strain rates, and loading time sequences.

3. Results and conclusions

The damage morphology obtained from the test is shown in Fig. 1(b), where C denotes the ratio of tensile to shear stresses, and the results show that the tensile action weakened the shear strength of the specimen, and the torsion action weakened the shear strength of the specimen, in other words, in the tensile-shear composite loading, with the increase of torsion load ratio, the slope of the tensile stress-strain curve was reduced, and at the same time, the slope of the torsional stress-strain curve was reduced with the increase of the tensile load ratio. Overall, it seems that the breaking strength of plain-woven composite tube specimens is greater than quasi-static under dynamic conditions, and the strain rate effect is more pronounced as the stress ratio decreases, i.e., the ratio of torsional load in the composite loading load increases.

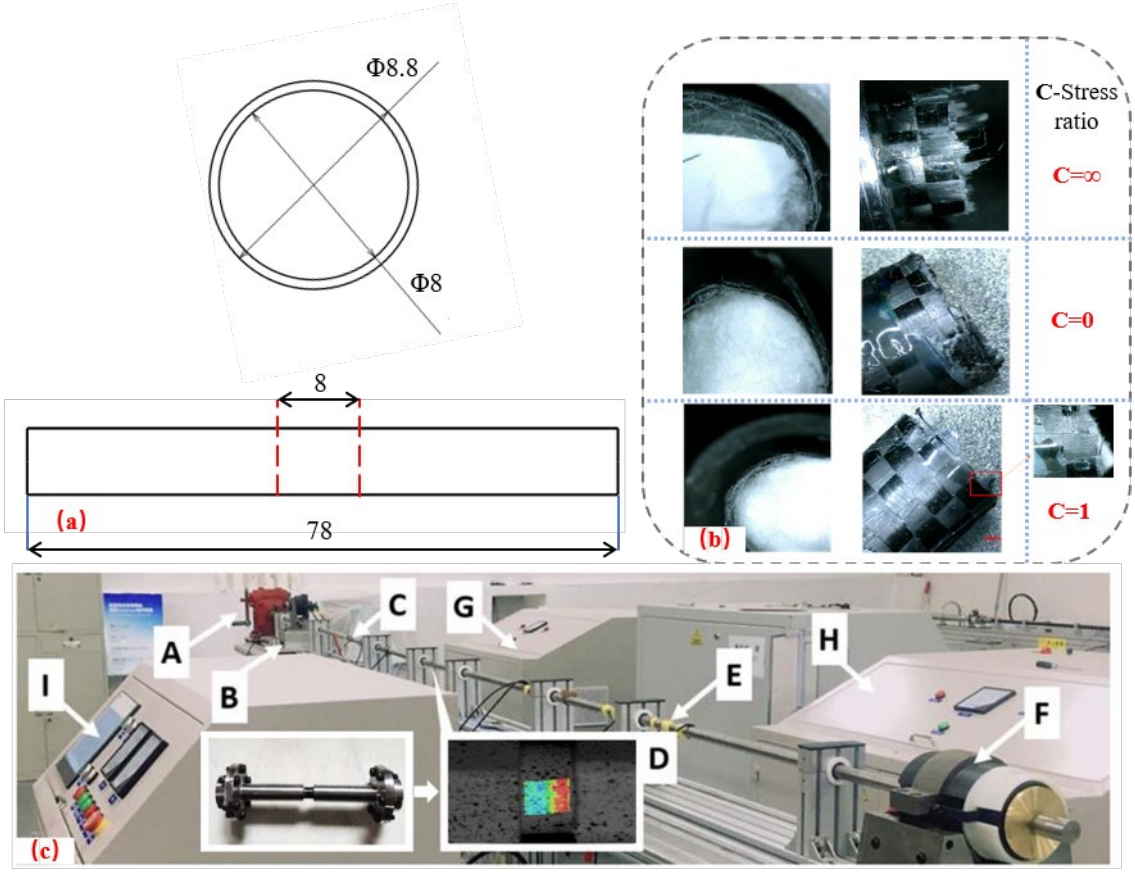

Fig. 1 (a) Specimen size design (b) Damage morphology of high strain rate specimen (c) Dynamic tension-shear experimental platform based on E-Hopkinson bar

4. References

[1] Daniel I M, Werner B T, Fenner J S. Strain-rate-dependent failure criteria for composites[J]. Composites Science & Technology, 2011, 71(3): 357-364.

[2] Daniel I M. Yield and failure criteria for composite materials under static and dynamic loading[J]. Progress in Aerospace Sciences, 2016, 81(Feb.): 18-25.
[3] Daniel I M, Luo J J, Schubel P M, et al. Interfiber/interlaminar failure of composites under multi-axial states of stress[J]. Composites Science & Technology, 2009, 69(6): 764-771.
[4] Daniel I M. Constitutive behavior and failure criteria for composites under static and dynamic loading[J]. Meccanica, 2015, 50(2): 429-442.
[5] Schaefer J D, Daniel I M. Strain-Rate-Dependent Yield Criteria for Progressive Failure Analysis of Composite Laminates Based on the Northwestern Failure Theory[J]. Experimental Mechanics, 2018, 58(3):487-497.
[6] Liu, C., Wang, W., Suo, T., Tang, Z., Guo, Y., Li, Y., 2022. Achieving combined tension-torsion split Hopkinson bar test based on electromagnetic loading. Int. J. Impact Eng 168, 104287.

A MEASUREMENT OF THE MECHANICAL PROPERTIES OF PURE ALUMINUM BY INSTRUMENTED TAYLOR IMPACT TEST AT ULTRA-HIGH VELOCITY USING A SINGLE-STAGE GAS GUN

M. Matsumoto[1], C. Gao[2], T. Iwamoto[3] and Y. Tanaka[3]
[1]Graduate School of Advanced Science and Engineering, Hiroshima University, Japan
[2]College of Science and Technology, Ritsumeikan University, Japan
[3]Academy of Science and Technology, Hiroshima University, Japan

1. Introduction

The authors have instrumented a classical Taylor impact test [1] by a Hopkinson pressure bar and a high-speed camera, and an evaluation method [2] which enables to measure a stress-strain curve of the material is proposed. However, the impact velocity has not achieved the range beyond the ultra-high level in the test due to the limitation of the compressed air. When increasing the velocity, the high-frequency component in the impact force wave is possible to miss due to insufficient bandwidth of an amplifier for the measurement. In this study, a single-stage light gas gun using helium gas as the driven gas is adopted in the instrumented Taylor impact (ITI) test to increase the impact velocity. In addition, piezoelectric films [3] are attached on the surface of the Hopkinson bar as a sensor to measure the impact force waves at the ultra-high velocity with high frequencies. The deformation behavior of pure aluminum at the ultra-high velocity is evaluated with the results from a strain gauge.

2. Experimental method

Fig. 1 shows the breech of the single-stage light gas gun manufactured in this study. The gas gun is designed based on the study by Sawaoka [4]. High-pressurized helium gas from a helium cylinder at 14 MPa of a maximum pressure is filled in the tank. By opening the solenoid valve, the compressed air supplied from the rear side of the specimen pushes it forward. Then, the gas is instantaneously released from the supply ports. Fig. 2 shows a schematic illustration of apparatus for the ITI test used. The components of the apparatus consists of almost the same as the previous study [2]. The air gun is replaced by the gas gun explained above. The specimen is pure aluminum (A1070). When the specimen impacts the Hopkinson pressure bar, the force wave can be measured by the strain gauge and the sensors made of the film glued on the surface of the bar. Polyvinylidene fluoride (PVDF) film (KUREHA chemical), with 80 μm in thickness is used. Two sensors are glued in a similar manner to the gauge and connected directly to an oscilloscope (YOKOGAWA DL2700). As shown in Fig. 2, the sensors and strain gauges are attached at 50 and 65 mm from the impact face, respectively.

3. Results, discussion and summary

Fig. 3 shows waves obtained by the strain gauge and PVDF sensors. In this figure, the red line is the stress by the gauge and the blue line is the output voltage from PVDF sensor. The impact velocity is 573.6 m/s. Because the wave obtained by PVDF sensor shows a steeper rise than the

gauges, the high frequency component can be captured as expected. Fig. 4 shows photograph of the deformed specimen. The figure shows a photo of the deformed specimen after the test. The plastic deformation progresses to be almost flat, and the petals are fractured after the deformation to become larger shape. In this study, a single stage light gas gun with helium gas was adopted for the ITI test, and a test at a higher impact velocity was attempted. In addition, two PVDF sensors were applied to measure force wave with higher accuracy and high frequency.

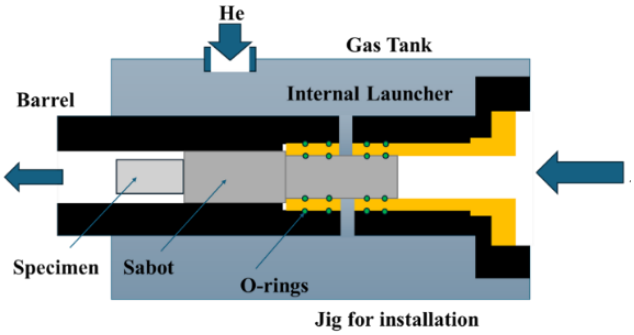

Fig. 1. A schematic illustration of the designed and manufactured single-stage light gas gun

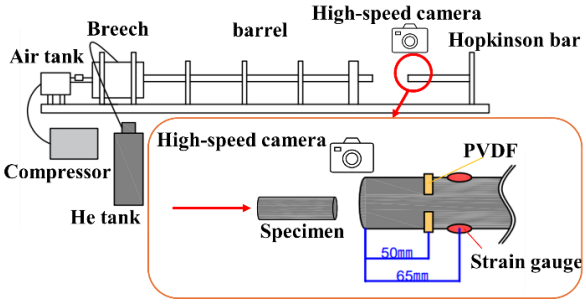

Fig. 2. A schematic illustration of the apparatus for Taylor impact test at ultra-high velocity

4. Acknowledgments

The material used in this study was provided by the Light Metal Education Foundation. This study was supported by the Amada Foundation with Grant No.AF-2023037-C2 and the 33rd Iron and Steel Research Promotion Grant.

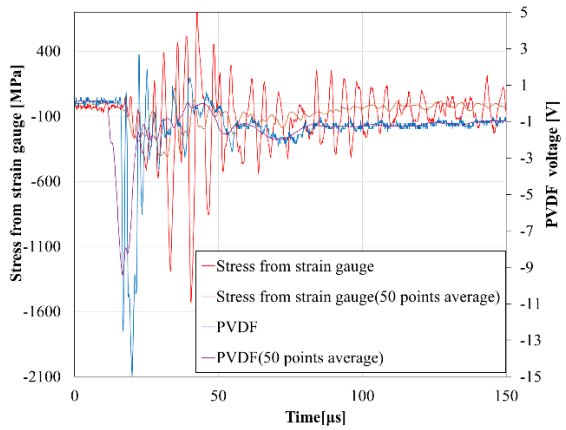

Fig. 3. Time histories of stress obtained by the strain gauges and output voltage from PVDF

Fig. 4. Photographs of the deformed specimen after the test

5. References

[1] GI. Taylor (1970). The use of flat-ended projectiles for determining dynamic yield stress theoretical considerations, *Proc. Roy. Soc. London*, **194**, 289-299.
[2] C. Gao, T. Iwamoto (2021). Instrumented Taylor impact test for measuring stress-strain curve through single trial, *Int. J. Impact Eng.*, **157**,103980.
[3] Y. Tanaka, E. Shintaku, Y. Fujimoto (2010). Development of contact-type sensor using piezoelectric film for guided wave measurement, *Int. J. Appl. Electromang. Mech.*, **33**, 1237-1244.
[4] A. Sawaoka (1975). Fundamental Techniques for Hypervelocity Impact (Part I), *J. High. Press. Inst. Jpn.*, **13**, 141-146. (in Japanese).

DESIGN AND OPTIMIZATION OF AN EMAT FOR MEASURING THE ELLIPTICAL POLARIZATION OF RAYLEIGH WAVE

Yujie Hou[1], Yan Lyu[2], Jie Gao[2], Cunfu He[2]
[1] College of Mechanical & Energy Engineering, Beijing University of Technology, Beijing, China
[2] School of Information Science and Technology, Beijing University of Technology, Beijing, China

1. Introduction

The trajectory of the mass of a Rayleigh wave is an ellipse, and the ratio of the horizontal to vertical axis of the ellipse is known as the elliptic polarization of the Rayleigh wave [1]. It has been shown that the sensitivity of the polarization of a Rayleigh wave to stress is about one order of magnitude greater than the wave speed [2]. Michael Junge [3] and others used the high sensitivity of Rayleigh wave polarization to stress changes to measure the stress-strain state of specimens. James Ayers [4-5] and others proposed a technique for damage identification based on the direction of elliptical polarization. There are many sensors and measurement methods for Rayleigh wave polarization, mainly including laser measurement, piezoelectric measurement and electromagnetic acoustic measurement. In particular, laser measurements utilize multi-angle measurements from a Doppler laser vibrometer to capture in-plane and off-plane displacement components of Rayleigh waves [6]. However, it is very sensitive to the surface quality of the specimen, the optical system is more complex and easily affected by the ambient temperature and humidity, which is costly in practice. The use of piezoelectric sensors can also be used to directly measure the two components of polarization, but due to the need to use the coupling agent for its measurement, it is difficult to ensure that the coupling layer is consistent throughout the measurement process, and poor consistency. Electromagnetic acoustic transducer (EMAT) can directly measure the polarization two-component information, EMAT transducer composition cost is low, and it does not need to be in direct contact with the specimen, avoiding the disadvantages of using coupling agent. In this study, a Rayleigh wave polymagnetic type polarization measurement electromagnetic acoustic transducer (Magnetic concentrate type polarization measurement, MC-PM-EMAT) structure is proposed, which makes use of the fringe effect of the magnetic field to significantly enhance the magnetic field strength at the coil and improve the transducer's transducer efficiency.

2. Materials and methods

The Rayleigh wave, in contrast to linearly polarized bulk waves (shear and longitudinal waves) that exhibit particle motion solely in one direction, follows an elliptical trajectory. As shown in Fig. 1, ultrasonic Rayleigh waves propagate along the surface of a plate infinite domain medium with displacement components in both in-plane and off-plane directions [7]. The elliptic trajectory equation for a Rayleigh wave can be expressed as follows.

$$\begin{cases} u_1(t) = u_{1,\max}(z=0)\sin(-\omega t) \\ u_3(t) = u_{3,\max}(z=0)\cos(-\omega t) \end{cases} \tag{1}$$

where $u_{1,max}(z=0)$ and $u_{3,max}(z=0)$ are the maximum in-plane and out-of-plane displacements at $z=0$ on the surface of the semi-infinite domain medium, respectively. It can be determined from Eq. (1) that the Rayleigh waves cause the surface plasmas to vibrate according to a counterclockwise elliptical trajectory.

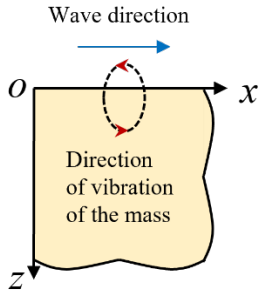

Fig. 1. Schematic diagram of Rayleigh wave propagation trajectory

(1) *Magnetic field structure design*

In order to realize the measurement of elliptical polarization of Rayleigh waves, the designed EMAT should have the ability to measure both in-plane and out-of-plane displacements. In order to achieve this purpose, two magnet structures are usually used to measure the in-plane and out-of-plane displacements of the surface wave, and then the measurement of the elliptical polarization of the Rayleigh wave is realized by combining the elliptic trajectory equations of the Rayleigh wave with the signals of the measured in-plane and out-of-plane displacements.

Currently, the magnet structure and flux density distribution of the traditional in-plane and out-of-plane displacements show the phenomenon of small in the middle and large on both sides. Although this magnet structure can effectively achieve the measurement of in-plane and out-of-plane displacements of the Rayleigh wave, but by the influence of the magnetic field strength, the transducer efficiency of this EMAT is low, and the actual measurement results have poor signal-to-noise ratios.

Effective measurement of surface signals can only be achieved by EMAT when the direction of the static magnetic field is perpendicular to the direction of vibrational displacement of the Rayleigh wave plasmas. Therefore, by designing the magnetic field direction of the permanent magnet, decoupled measurements of Rayleigh wave elliptically polarized in-plane and out-of-plane displacements can be realized. In order to solve the problem of traditional polarimetric measurement of EMAT, considering the edge effect of magnets, two polymagnetic magnet array structures are proposed in this study, as shown in Fig. 2. This polymagnetic design can greatly enhance the magnetic field strength at the receiving coil to improve the transducer's transducer efficiency. As can be seen from the Fig. 2, magnet opposites attract will strengthen the magnetic field at the in-plane displacement receiving coil, and magnet repulsion will strengthen the magnetic field at the out-of-plane displacement receiving coil.

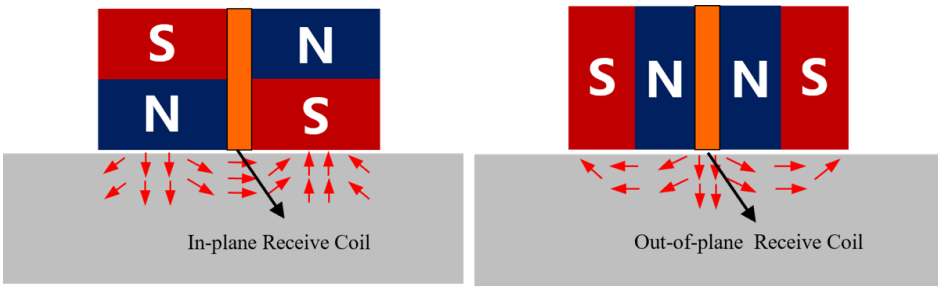

Fig. 2 Magnetic concentrate type EMAT structure

(2)*Geometric structural design*

The magnetic field structure described in 2.1 above already enables the measurement of Rayleigh wave elliptical polarization, and also improves the magnetic field strength at the receiving coil by using the edge effect of the magnet. In order to further improve the amplitude of the received signal and obtain the optimal combination of geometrical structure parameters for MC-PM-EMAT, this study extracts the key parameters under the above proposed structure, analyses the influence of each parameter on the receiving performance and selects the optimal parameter combination.

Considering the large variety of combinations of structural parameters of this sensor and the large amount of finite element simulation calculations, the orthogonal design of experiments method was adopted to study the optimization of the geometric design of this sensor. In this study, the in-plane and out-of-plane receiving voltage peak-to-peak UPP of the sensor is investigated in conjunction with the geometrical features of the sensor, the width of the permanent magnet w_1, the height of the permanent magnet h, the spacing of the two magnets w_2, the diameter of the receiving coils d_1, the distance of the magnets and the receiving coils from the aluminum plate d_2. These five parameters were analyzed for influencing factors and orthogonal tests were conducted using orthogonal table $L_{16}(45)$. The range of parameters is selected according to the common realistic specifications, and the five parameters are selected as w_1: 20-35 mm, w_2: 2-8 mm, h: 10-25 mm, d_1: 0.1-0.4 mm, and d_2: 0.1-0.4 mm.

In this study, the Rayleigh wave out-of-surface voltage amplitude was selected for the analysis of the influencing factors. The effect of each factor on the received Rayleigh wave signal amplitude was assessed by calculating the arithmetic mean k_i (i=1,2,3,4) of each factor at the same level of and the difference between the maximum and minimum values of the corresponding k_i as the extreme deviation r, as shown in table I below.

TABLE 1. ANALYSIS OF ORTHOGONAL TEST FOR MC-PE-EMAT

Table Head	Analysis of orthogonal test for MC-PE-EMAT				
	w_1	w_2	h	d_1	d_2
k_1	2.7925	3.1425	2.4575	4.1250	3.1375
k_2	2.1850	2.4225	1.5150	2.2625	2.3725
k_3	1.5175	1.8825	2.2225	1.3675	1.5000
k_4	2.2500	1.2975	2.5500	0.9900	1.7350
r	1.2750	1.8450	1.0350	3.1350	1.6375

From the table, it can be seen that the polar deviation r of each factor is in the order of d_1 (3.150) > w_2 (1.8450) > d_2 (1.6375) > w_1 (1.2750) > h (1.0350) from the largest to the smallest, and the largest influence on the amplitude of the received surface wave signals is the diameter of the receiving coil. It can be seen that when the width of the permanent magnet is k_1 level, 20 mm wide, the received signal amplitude is the largest, and at the same time, in order to ensure the consistency of the signal measurements within the surface wavefront and away from the surface, the height of the permanent magnet is also selected to be 20 mm. Therefore, the optimal combination of geometrical structure parameters for the MC-PM-EMAT is 0.1 mm diameter of the receiving coil, 2 mm spacing between the two magnets, 0.1 mm distance between the magnets and the receiving coil and the aluminum plate, 20 mm width of the permanent magnet and 20 mm height of the permanent magnet. The simulation process of MC-PM-EMAT involves the multi-field coupling problem of electric field, magnetic field, and force field. In this section, a multi-physics field simulation model of MC-PM-EMAT is developed based on COMSOL Multiphysics software.

As shown in Fig. 3, the simulation model consists of 3 main parts, which are piezoelectric inclined probe, MC-PM-EMAT and aluminum alloy object under test. The main parameters of the materials in the simulation are shown in Table 2 below. In order to get a purer surface wave, so the piezoelectric slant probe is used to excite the surface wave in the measured object. The size of the piezoelectric

sheet is 8 mm×0.62 mm and the size of the wedge is 16 mm×10 mm. In order to ensure the generation of pure surface wave signals in the specimen, the angle of incidence θ of the angular acoustic beam transducer must be greater than or equal to the second critical angle. This is obtained according to Snell's law. here θ is the angle of incidence in the wedge, θ_S is the angle of refraction of the transverse wave in the aluminum plate, V_W is the wave speed of the longitudinal wave in the wedge and V_S is the wave speed of the transverse wave in the aluminum plate.

The wave velocity of the longitudinal wave of the wedge in the piezoelectric inclined probe is 2077 m/s, and the wave velocity of the transverse wave in the aluminum plate is 3103 m/s. The second critical angle to make the transverse wave fully reflective can be calculated from Snell's law to be 42.02°, and in order to ensure the purity of the surface wave, the tilt angle of the wedge is set to be 43° in the simulation. The excitation signal is a 5-cycle Hanning window modulated sine wave signal with a frequency of 2.5 MHz, and the propagation of the Rayleigh wave from the piezoelectric inclined probe to the surface of the aluminum plate is achieved by setting the piezoelectric sheet terminals with the ground terminal and the coupling between the electric field and the solid mechanical field. The aluminum alloy test object is used to realize the propagation of surface waves in the plate, in which the size of the aluminum plate is 120 mm × 40 mm. The left and right sides and the lower boundary of the aluminum alloy specimen are set as low-reflection boundaries to reduce the interference of reflections from other waveforms.

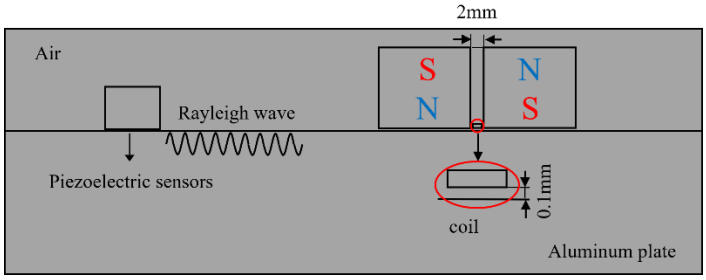

Fig. 3 Schematic geometrical model of magnetic concentrate type EMAT finite element simulation

TABLE 2. MAIN PARAMETERS OF THE MATERIAL IN THE SIMULATION

Main parameters of the material in the simulation	
parameter	**value**
Piezo sheet density	7500 kg/m^3
Wedge Poisson's ratio	0.35
Young's modulus of wedge	3.20 GPa
Density of wedge	1190 kg/m^3
Magnet residual flux density	1 T
Magnet conductivity	7x10^5 S/m
Aluminium plate conductivity	3.77x10^7 S/m
Density of aluminium sheet	2700 kg/m^3
Young's modulus of aluminium sheet	70x10^9 Pa
Poisson's ratio of aluminium plate	0.33
Coil conductivity	6x10^7 S/m

MC-PM-EMAT is used to measure the in-plane and out-of-plane displacement signals of elliptical polarization of surface waves, in which the dimensions of the permanent magnet are 20 mm×20 mm, the distance between the two permanent magnets is 2 mm, and the dimensions of the coil are 2 mm×0.1 mm, and the diameter of the coil of a single round conductor is 0.1 mm with a total

of 20 turns. The lifting distance of both the permanent magnets and the coil is 0.1 mm. The permanent magnets provide the static magnetic field for the model, and the static magnetic field is achieved by setting the magnetization model of the residual flux density of the magnets, which is set to be 1 T in the present study. The external current density setting is also added, and the law of electromagnetic induction is utilized to couple the solid mechanics module and the magnetic field module to realize the energy conversion from the force field to the magnetic field and then to the electric field conversion.

Finally, mesh and study setup was performed. The geometrical model is divided using a free triangular mesh, and the mesh size of the aluminum plate specimen is close to one-tenth of the wavelength of the Rayleigh wave. The study consists of three parts: steady state, coil geometry analysis and transient. The time step in the transient study needs to satisfy the sampling theorem, which is set to one-fiftieth of the period in this model.

3. Results and conclusions

Rayleigh waves propagate along the upper surface of the aluminum plate, and their energy is mainly concentrated in a wavelength range, which is consistent with the known theory of surface wave propagation. Through the use of COMSOL finite element simulation software on the MC-PM-EMAT Rayleigh wave in-plane and out-of-plane components of the voltage signal measurement, the receiving coil and piezoelectric inclined probe distance of 65 mm, intercept the received surface wave signal to obtain the results of the measurement are shown in Fig. 4 below.

It is known that when a Rayleigh wave propagates along an isotropic solid surface, its trajectory is an ellipse perpendicular to the surface and parallel to the propagation direction. The elliptical trajectory is divided into the synthesis of the in-plane and out-of-plane components to extract the in-plane and out-of-plane voltage signals in the receiving coil. Plotting the Rayleigh wave elliptic trajectories by taking the maximum single period of the in-plane and out-of-plane components of the received Rayleigh wave signal as the x-component and y-component of the elliptic polarization, respectively. The phase difference between the in-plane and out-of-plane components of the Rayleigh wave signal is $\pi/2$, and the actual measured elliptical polarization of the Rayleigh wave has a small amplitude deflection, which produces a certain angle of deflection due to the following reasons: the received voltage in the simulation is the acquisition of the voltage in a rectangular area, not a single point of the voltage extraction, and the superposition of the multiple points leads to the phase difference between the two components is not $\pi/2$; the superimposition of the reflections from the bottom surface the body wave.

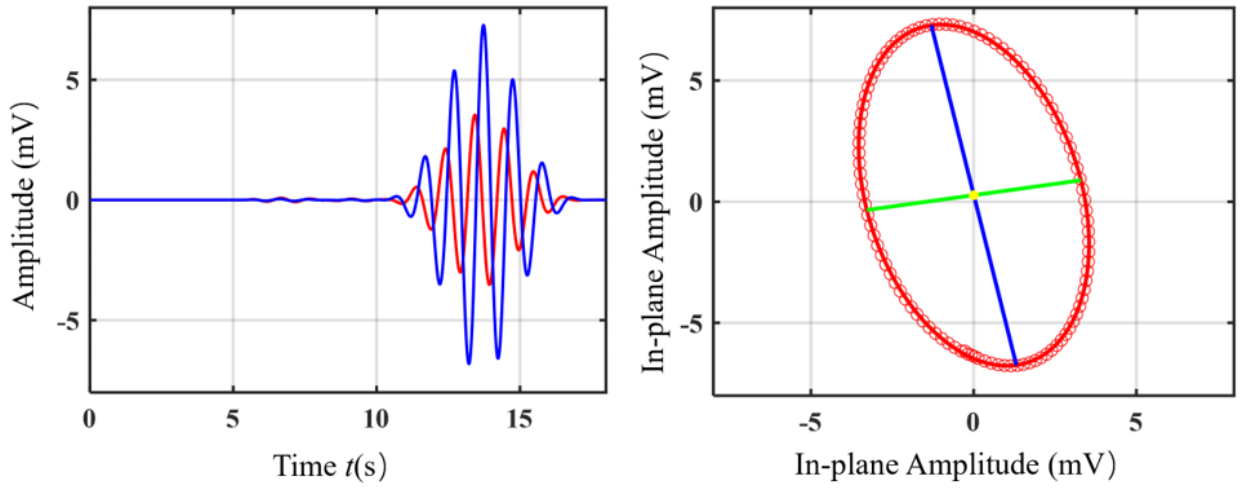

Fig. 4 Rayleigh wave elliptical polarization simulation measurements

In order to validate the above MC-PM-EMAT configuration and realize the measurement of Rayleigh wave elliptical polarization, the relevant EMAT was fabricated for ultrasound experiments. The MC-PM-EMAT consists of two sensors with magnets magnetized in different directions, each of which consists of two N52-type NdFeB permanent magnets, a 6-turn wire-wound linear single coil, a top cover, a housing, and a BNC connector, as shown in Fig. 11 below. The magnet dimensions are 30 mm × 20 mm × 20 mm (L × W × H), the coil diameter is 0.1 mm, and the spacing between the magnets is 2 mm. Since the in-plane and out-of-plane components of the Rayleigh wave polarization are measured independently, the magnet configurations for the in-plane component are isobaric, and a large repulsive force is generated due to the large magnet dimensions. Therefore, the magnet shell configuration is used to make the distance between the two repulsive magnets reach 2 mm, and in order to ensure the consistency of the measurement, the measurement of the out-of-plane component is encapsulated in the same shell.

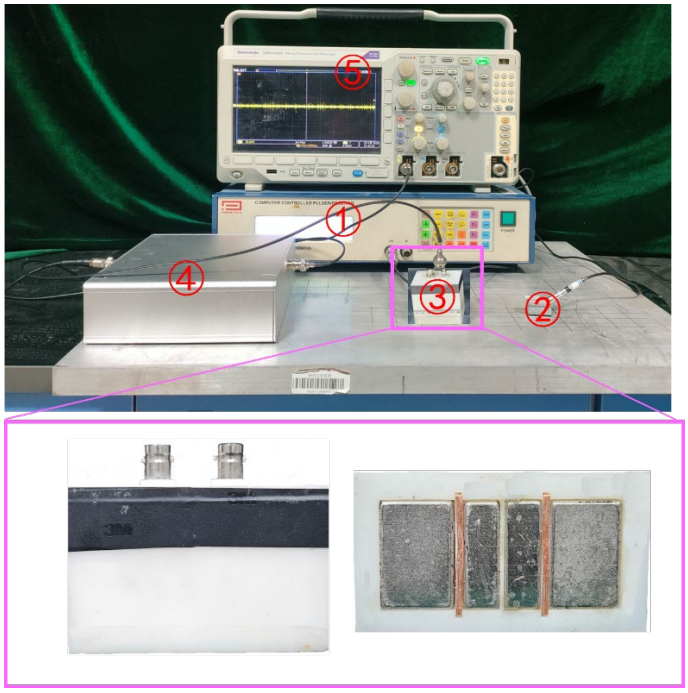

Fig. 5 Experimental measurement system

Figure 5 shows the experimental measurement system of MC-PM-EMAT, which is mainly composed of pulse excitation receiver (Olympus 5800PR) (1), a piezoelectric slant probe (Shantou 2.5 MHz) (2), MC-PM-EMAT (3), an in-house preamplifier (4), and an oscilloscope (Tektronix MDO 3022) (5). Experimental measurements were carried out on the upper surface of an aluminum plate specimen with a thickness of 30 mm. A piezoelectric inclined probe with a centre frequency of 2.5 MHz was excited by a pulse excitation receiver and the MC-PM-EMAT was placed at the same level as the piezoelectric inclined probe, the received Rayleigh wave signals were amplified by a self-developed preamplifier, and then the Rayleigh waveforms were displayed on the oscilloscope with data storage.

In this study, experiments on the reception of MC-PM-EMAT for elliptical polarization of Rayleigh waves were carried out, and the received Rayleigh wave signals were intercepted to obtain the measured signals of the in-plane component voltages of the two sensors in Fig. 6. The in-plane component of the largest magnitude single-cycle signal in the received signal is used as the x-component of the ellipse, and the out-of-plane component is used as the y-component of the ellipse for the plotting of the elliptic polarization, and then the elliptic polarization is fitted using the least-squares method to obtain the elliptic polarization of the polymagnetized surface wave shown in Figure 14 below. The feasibility of the MC-PM-EMAT developed in this institute was verified.

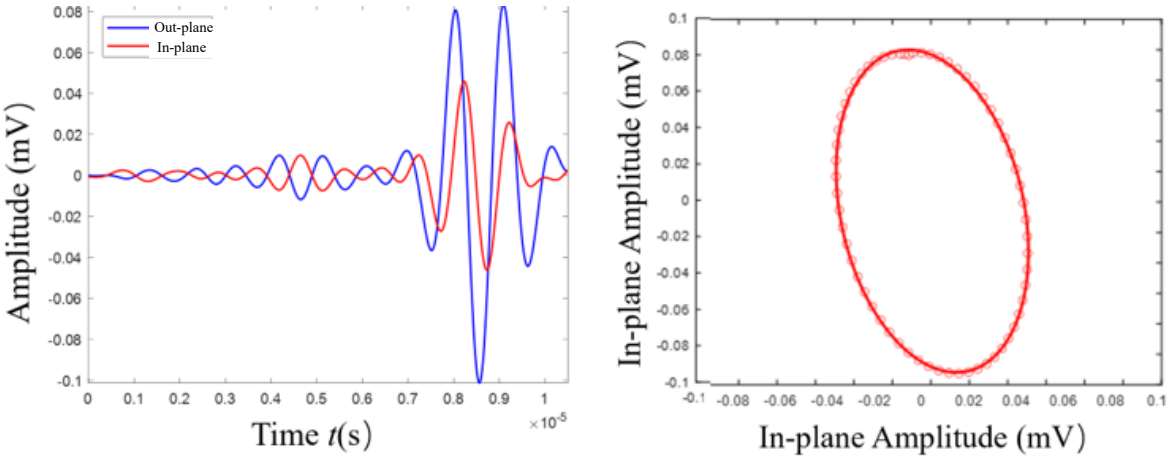

Fig. 6 Experimental measurement results

In this study, a Rayleigh wave elliptically polarized measurement electromagnetic acoustic sensor is developed, which consists of two permanent magnets and a linear single coil, using the edge-concentration effect of the magnets, the magnetic field strength at the coil can be significantly enhanced, which in turn enhances the transducer's transducer efficiency. The MC-PM-EMAT was further developed and the elliptical polarization measurement performance of the sensor was experimentally investigated. The feasibility of elliptical polarization measurements with the MC-PM-EMAT is verified. The sensor provides an important sensing tool for further development of detection techniques based on polarization characteristics.

4. Acknowledgements

This work is supported by the National Natural Science Foundation of China (No. 52235012 and No.12272015) and National Key R&D Program of China (No. 2022YFC3005002 and No. 2023YFF0716601).

5. References

[1] [1] HE C F, DENG P, LV Y, et al. A high signal-to-noise ratio electromagnetic surface acoustic wave sensor and its application in thick wall pipeline detection [J]. Chinese Journal of Mechanical Engineering, 2017, 53(04): 59-66.

[2] DU Q L, LIU Z P, LIU S J. Analysis of influencing factors and numerical simulation of horizontal-to-vertical spectral ratio method [J]. Journal of Earthquake and Tsunami, 2019, 14(01): 205000.

[3] MICHAEL J, QU J M, JACOBS L J. Relationship between Rayleigh wave polarization and state of stress [J]. Ultrasonics, 2006, 44(3): 233-237.

[4] AYERS J T, APETRE N, RUZZENE M. Multiple component mode conversion coefficients via Lamb wave polarization measurements [J]. Health Monitoring of Structural and Biological Systems, 2011(7984): 798411.

[5] AYERS J T, OWENS C T, SWENSON E, et al. Elliptical trajectory orientation of Lamb wave polarization as a damage localization parameter in aerospace structures [J]. Review of Progress in Quantitative Nondestructive Evaluation, 2012(1430): 1153-1160.

[6] MONTINARO N, EPASTO G, CERNIGLIA D, et al. Laser ultrasonics inspection for defect evaluation on train wheel [J]. NDT & E International, 2019(107): 102145.

[7] AYERS J, APETRE N, RUZZENE M. Measurement of Lamb wave polarization using a one-dimensional scanning laser vibrometer (L) [J]. Acoustical Society of America, 2011, 129(2): 585-588.

HIGH VELOCITY IMPACT ON THE PRE-TENSIONED FABRIC-LAMINATE COMPOSITE STRUCTURE

J. Wei[1], S. H. Shang[1], H. X. Wang[1], Y. Shen[1], S. L. Xiao[1], Y.C. Yuan[1], Y. Li[1], J. G. Liu[1], H. Meng[1, 2], J. Deng[1, 2], T. J. Lu[1, 2], and J. L. Gao[1, 2, *]

[1] College of Aerospace Engineering, Nanjing University of Aeronautics and Astronautics, No. 29 Yudao Street, Nanjing 210016, China
[2] State Key Laboratory of Mechanics and Control for Aerospace Structures, Nanjing University of Aeronautics and Astronautics, No. 29 Yudao Street, Nanjing 210016, China

1. Introduction

In recent years, with the renewal of high-performance fiber materials and the ongoing optimization of weaving and manufacturing technologies, fabrics and composites have been developed with higher specific strength and stiffness, ballistic limit, and energy absorption [1-2]. These materials have been widely used in the armor protection of vehicles and personal bulletproof vests.

This study proposes a composite structure composited of prestressed flexible fabric and fiber-reinforced laminates to resist high-speed bullet impact. Through the use of fiber-reinforced laminates at the front, the structural lateral stiffness is increased, and the local impact deformation is reduced. By placing a flexible fabric at the rear, the energy absorption of the structure is increased. The energy absorption and ballistic limit of the structure is further improved by applying a certain amount of prestress to the ends of the flexible fabric. Moreover, existing research has been limited to the effects of uniaxial prestress on the ballistic performance of flexible fabrics or fiber-reinforced laminates [3-4]. This study investigates the impact behavior of the composite structure with biaxial prestress. The effect of preload on the ballistic limit of the composite structure is characterized. This study represents an initial exploration of the engineering application of prestressed fabric-laminate composite structures in the field of protective engineering and provides experimental data for further modeling and optimization design of composite structures.

2. Materials and methods

The composite structure specimen in this study comprises an aramid fiber fabric and a laminated plate, with detailed dimensions shown in Fig. 1. The fabric features symmetrical warp and weft, with a yarn linear density of approximately 1900 dtex. The aramid plate measures 50 mm × 50 mm in planar dimensions and has a thickness of 3 mm, yielding a surface density of approximately 3.99 kg/m^2 . The laminated plate is constructed by hot-pressing 12 layers of prepreg material. The aramid plate is centrally positioned on the fabric and bonded using epoxy resin.

In this study, a first-stage light gas gun was used to conduct high-speed impact experiments, with the experimental setup as shown in Figure X. Prior to the experiment, a specially designed clamping device was used to fix the composite structure specimen inside the target chamber, where the prestress within the structure was applied and regulated. The projectile was an 8 mm steel ball, and its velocity was characterized using a high-speed camera. Another high-speed camera was set up on the side of

the target chamber at an oblique rear position to the specimen to capture in real-time the deformation and failure process of the composite structure, as well as the penetration process of the projectile.

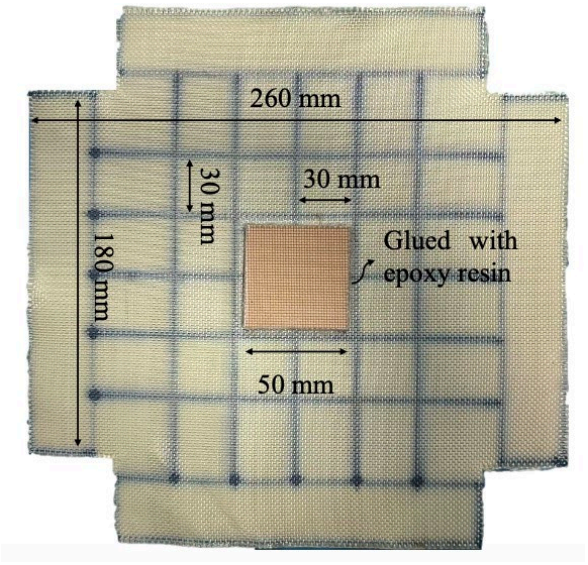

Fig. 1. Real picture of the fabric-laminate composite structure specimen

3. Results and conclusions

The ballistic limit of the composite structure under various preload conditions was determined by fitting the relationship between residual velocity and impact velocity using the Lambert-Jonas formula.

$$v_r = \begin{cases} 0 & 0 \le v_i \le v_0 \\ \alpha\left(v_i^{\beta} - v_0^{\beta}\right)^{1/\beta} & v_i \ge v_0 \end{cases} \tag{1}$$

As illustrated in Fig. 2, the ballistic limit velocity of the structure initially increases and then decreases as the preload is increased. Specifically, the ballistic limit of the structure in the absence of preload is 435.06 m/s. This limit reaches a maximum value of 458.45 m/s at a preload of 500 N, and subsequently declines. At a preload of 2000 N, the ballistic limit decreases to 401.51 m/s.

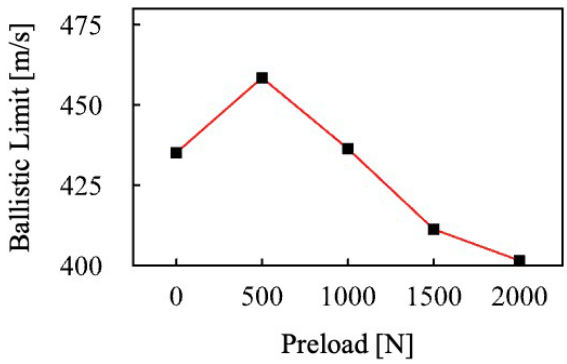

Fig. 2. Ballistic limit of composite structure with different preloads

4. Acknowledgements

We would like to acknowledge the financial support provided by the National Natural Science Foundation of China (12302472, 12202188, 52361165626, 11872072, 12002157), the Science and Technology Support Program of Jiangsu Province (BK20230874), China Postdoctoral Science Foundation Funded Project (2022M721609), the Fundamental Research Funds for the Central Universities (NS2024002) and the Priority Academic Program Development of Jiangsu Higher Education Institutions. Additionally, we are grateful for the research funding from the State Key Laboratory of Mechanics and Control for Aerospace Structures (Nanjing University of Aeronautics and Astronautics) (Grant No. MCAS-I-0124G05, MCAS-I-0124G02), as well as the Aeronautical Science Fund of China (Grant No. 2023Z057052005).

5. References

[1] J. Gao, N. Kedir and W. Chen (2022). Characterization of failure of single carbon nanotube fibers under extreme transverse loading. *Mater. Des.*, **215**, 110482.

[2] T. Xu and R.J. Farris (2007). Comparative studies of ultra high molecular weight polyethylene fiber reinforced composites. *Polym. Eng. Sci.*, **47**(10), 1544-1553.

[3] E. Tapie, E.S.L. Tan, Y.B. Guo, and V.P.W. Shim (2017). Effects of pre-tension and impact angle on penetration resistance of woven fabric. *Int. J. Impact Eng.*, **106**, 171-190.

[4] M.V. Zhikharev, S.B. Sapozhnikov, O.A. Kudryavtsev, and V.M. Zhikharev (2019). Effect of tensile preloading on the ballistic properties of GFRP. *Compos. Part B-Eng.*, **168**, 524-531.

Dynamic Behavior of Materials

X-RAY DIFFRACTION OF POLYVINYLIDENE FLUORIDE UNDER DYNAMIC COMPRESSION

R. Huber[1], E. Watkins[2], D. Dattelbaum[1], L. Gibson[1], B. Bartram[1], and J. Jordan[1]
[1] Los Alamos National Laboratory, Los Alamos, NM, USA
[2] Oak Ridge National Laboratory, Oak Ridge, TN, USA

1. Introduction

Studying polymers under one-dimensional (1D) shock compression via gas gun planar impact has traditionally been diagnosed with streak cameras or, more recently, optical velocimetry.[1-2] Optical velocimetry provides the means to observe the arrival times, t, of the shockwaves at interfaces, with known material thickness, x, to determine shock velocity, U_s ($U_s = \Delta x/\Delta t$).[3] This method also captures the particle velocity, u_p, profile, which, regarding polymers, can elucidate different material properties, such as viscoelastic behavior or decomposition regions.[4-5] To better understand the structural effects of shockwaves, we combined x-ray diffraction with dynamic compression to directly observe the polymer transformations that correlate to the known u_p profiles. This work was performed at the Dynamic Compression Sector (DCS), at the Advanced Photon Source (APS), at Argonne National Laboratory.

Previously, the authors have studied and published x-ray diffraction at DCS on high density polyethylene (HDPE) and polytetrafluoroethylene (PTFE).[6-7] For HDPE and PTFE, we observed polymer chain compression up to the transition region, where the polymer reaches a pressure when decomposition products form. In this work, we will explore how polyvinylidene fluoride (PVDF) reacts to shock driven compression from 1.8 to 31.5 GPa with x-ray diffraction and optical velocimetry.

2. Materials and methods

PVDF was purchase from Port Plastics (Albuquerque, NM) as Kynar® 740. The initial density of the material was 1.78 g/cm^3. PVDF samples were machined into disks that measured 3 mm thick by 10 mm in diameter.

DCS Hutch 35-ID-E has a dual 33 mm bore single-stage powder gun (PG) and a two-stage light gas gun (2SLGG). These gas guns can reach 0.5–2.6 for the PG and 2.8–5.7 km/s for the 2SLGG.[8] The gas guns are paired to the APS bunch clock, where an ~80 ps x-ray packet is delivered to the beamline every 154.3 ns. This x-ray packet, at 23.6 KeV (0.5254 Å), is directed through the dynamically compressing polymer. These x-rays are captured on a scintillator that converts the x-rays to visible light, the image is then passed through an image intensifier and split to the CCD cameras. For each gas gun shot, four images were recorded. A total of five shots were performed on PVDF.

3. Results and conclusions

The PVDF transition region begins at 31.7 GPa, five shots were performed to observe polymer chain compression between 1.8 and 31.5 GPa.[9] Figure 1 shows an example of the optical velocimetry spectrogram and the two-dimensional (2D) diffractograms for shot 20-4-063, where a LiF impactor was launched into the PVDF samples resulting in a pressure of 11.06 GPa. The optical velocimetry spectrogram in Figure 1A shows a clean rise and flat top at the free surface. If a rounded or multi-wave profile was observed, that would imply a reaction present during shock compression.

The 2D x-ray diffractograms show the static diffraction pattern (Figure 1B, before dynamic compression) and the dynamic diffraction pattern (Figure 1C). The static 2D diffraction pattern appears to be lower signal-to-noise than the dynamic pattern. The static pattern is allowed to average over multiple x-ray pulses, where the dynamic pattern is captured, in time, with only one ~80 ps x-ray packet. These 2D x-ray diffractograms are then radially integrated to produce one-dimensional (1D) x-ray diffraction patterns. Those diffraction patterns represent the crystalline segments of the polymer. We will discuss the quantification of the crystalline and amorphous sections of these materials and compare them to their bulk Hugoniot loci to observe how the polymer segments are affected during dynamic compression.

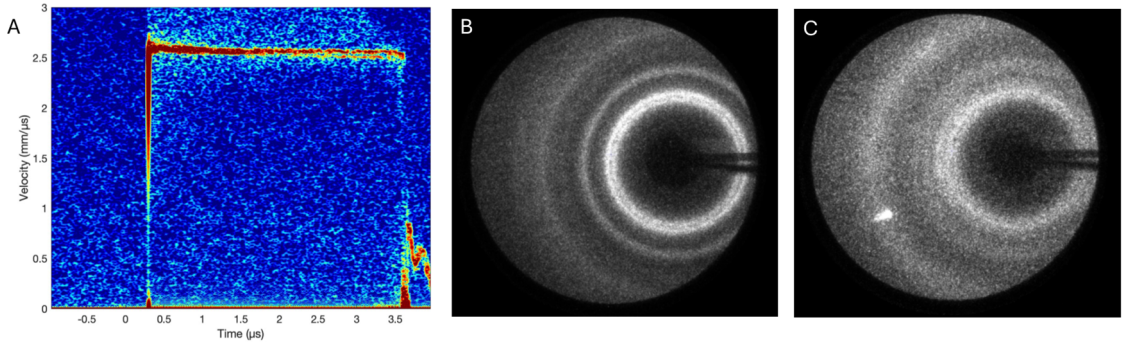

Fig. 1. A) Optical velocimetry spectrogram from Shot 20-4-063, LiF impactor into the PVDF sample. B) 2D x-ray diffractogram showing the static diffraction of PVDF. C) 2D x-ray diffractogram showing the dynamic diffraction of PVDF.

4. Acknowledgements

The results in this work were supported by the DOE/NNSA Dynamic Materials Properties Campaign. This publication is based upon work performed at the Dynamic Compression Sector, which is operated by the Washington State University under the U.S. Department of Energy (DOE)/National Nuclear Security Administration Award No. DE-NA0003957. This research used resources of the Advanced Photon Source, a DOE Office of Science User Facility operated for the DOE Office of Science by Argonne National Laboratory under Contract No. DE-AC02-06CH11357. This work was conducted at Los Alamos National Laboratory, an affirmative action/equal opportunity employer, which is operated by Los Alamos National Security, LLC, for the National Nuclear Security Administration of the U.S. Department of Energy under Contract No. DE-AC52- 06NA25396

5. References

[1] Marsh, S.P., LASL Shock Hugoniot Data, Report, 1980.
[2] Strand OT, *et al.* (2006) Compact system for high speed velocimetry using heterodyne techniques. Rev Sci Instrum 77(8):083108
[3] J.W. Forbes, Shock Wave Compression of Condensed Matter, Springer Berlin, Heidelberg, 2012.
[4] D. M. Dattelbaum, J. D. Coe, Shock-driven decomposition of polymers and polymeric foams, Polymers 11 (2019).
[5] R. C. Huber, *et al.*, Polyimide dynamically compressed to decomposition pressures: Two-wave structures captured by velocimetry and modeling, Journal of Applied Physics 133 (2023).
[6] R. C. Huber, *et al.*, In situ x- ray diffraction of high density polyethylene during dynamic drive: Polymer chain compression and decomposition, Journal of Applied Physics 130 (2021).
[7] R. C. Huber, *et al.*, Capturing Polymer Chain Compression and Shock Driven Decomposition of Polytetrafluoroethylene During Dynamic Shock Compression with In Situ X-Ray Diffraction, Journal of Dynamic Behavior of Materials (2023).
[8] D. Capatina, *et al.*, DCS - a high flux beamline for time resolved dynamic compression science – design highlights, AIP Conference Proceedings 1741 (2016) 030036.
[9] [9] W.J. Carter, S.P. Marsh, Hugoniot Equation of State of Polymers, Technical Report LA-13006 MS, Los Alamos National Laboratory, 1995.

EFFECTS OF ULTRASONIC VIBRATION ON THE KINETIC STATE OF ATOMS AROUND THE SCREW DISLOCATION OF BCC Fe

A. Asazuma[1] and S. Arikawa[2]
[1] *Graduate School of Science and Technology, Meiji University, Japan*
[2] *Department of Mechanical Engineering Informatics, Meiji University, Japan*

1. Introduction

There is an effect called the ultrasonic vibration-assisted forming effect. It is a phenomenon, in which the flow stress decreases intensely when ultrasonic vibration is superimposed during the plastic deformation. It includes three effects, which are the “Stress superposition effect”, “Residual effect” and “Acoustic softening effect”. This study focuses on the acoustic softening effect, including microstructure changes, such as dislocation sliding.

It is reported that the acoustic energy required to produce the same degree of softening is 10^7 times less than the thermal energy [1]. One reason for this is that acoustic energy, generated by ultrasonic vibration, is preferentially absorbed by micro-defects such as dislocations. In this regard, the acoustic softening effect has been validated using molecular dynamics simulations [2]. The results demonstrate that the kinetic energy of the atoms increases and dislocations are activated when ultrasonic vibrations are applied to aluminum under deformation. Similar phenomena are considered to occur for various other metals [3]. However, how the dislocation absorbs acoustic energy and becomes more mobile is not fully understood.

For the edge dislocations in BCC Fe, the density difference above and below the slip plane caused by the presence of extra atomic planes affects the shape of the interatomic potential, leading to a difference in the intensity of motion and dislocation energy absorption. In this study, the effect of the ultrasonic vibration on the kinetic state of atoms around the screw dislocation of BCC Fe is investigated using the molecular dynamics method.

2. Simulation methods

The molecular dynamics simulations are conducted by LAMMPS [4] using the screw dislocation inserted model shown in Fig. 1 which slip direction <111> adopted to the *x*-axis, slip plane (110) to the *xz* plane. The model size is 97.5 Å × 99.6 Å × 75.9 Å and it contains 52800 atoms. Vacuum gaps are introduced at the top and bottom of the model in the *y*-axis direction, therefore the model has two free surfaces. Periodic boundary conditions are applied in the three-dimensional directions of the model. Introduced screw dislocation is shown in Fig. 1 (b) and it is at an easy-core position.

When a screw dislocation exists, the area around the dislocation core is severely distorted. The distortion affects the potential field of the atoms around the dislocation core. When interatomic potentials differ between atoms, it is expected that the ease with which the atoms vibrate will vary. Yield motion is relative motion between the atoms around the dislocation core, therefore, it is considered that the dislocation motion is more likely to occur due to the greater difference in the intensity of the motion around the dislocation core. Intensity of motion can be evaluated in terms of kinetic energy or mean square velocity.

When the screw dislocation slips, there is a relative motion between atoms 1 and 2 shown in Fig.1 (c). The mean square velocity of atoms 1 and 2 is evaluated.

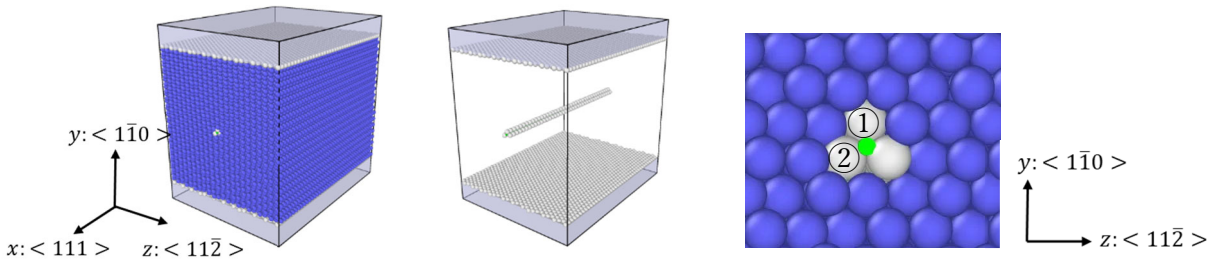

(a) (b) (c)

Fig. 1. The model used for molecular dynamics analysis

3. Results and conclusions

Two kinds of *xy*-shear stress for deformation are produced, one with ultrasonic vibration application in the *xy*-shear component and another without vibration. stress-time curve is shown in Fig. 2. As a result, the yield stress is reduced by about 108 MPa. It can be said that the acoustic softening effect could be represented using molecular dynamics simulations.

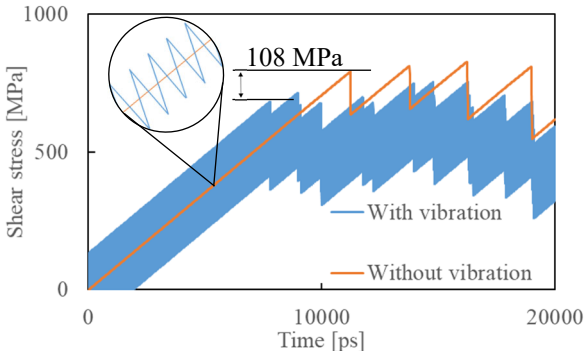

Fig. 2. Stress-time curve with and without vibration

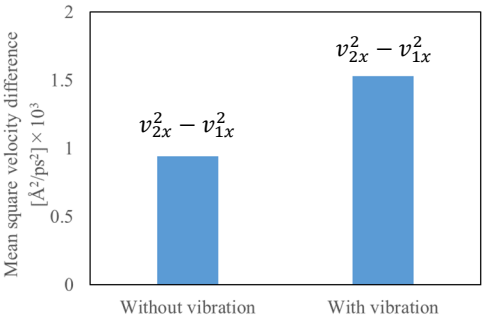

Fig. 3. Difference in mean square velocity between atoms 1 and 2

The kinetic states of atoms around the screw dislocation are shown in Fig. 3. Figure 3 compares the difference in mean square velocity in <111> direction between atoms 1 and 2. It can be seen that when the ultrasonic vibration is applied, the difference in the slip direction tends to be greater than the model without vibration. This indicates that the intensity of the motion differs between atoms 1 and 2, and the difference widens when acoustic energy is applied. The line of atoms in the position of atom 2 is considered to absorb energy.

4. References

[1] B. Langenecker (1966). Effects of ultrasound on deformation characteristics of metals, *IEEE Transactions on Sonics & Ultrasonics*, **13**, 1-8.

[2] Y. Zhao, J. Zhai, Y. Guan, F. Chen, Y. Liu, Y. Li, J. Lin (2022). Molecular dynamics study of acoustic softening effect in ultrasonic vibration assisted tension of monocrystalline/polycrystalline coppers, *Journal of Materials Processing Technology*, **307**, 117666.

[3] R.K. Dutta, R.H. Petrov, R. Delhez, M.J.M. Hermans, I.M. Richardson, A.J.Böttger (2013). The effect of tensile deformation by in situ ultrasonic treatment on the microstructure of low-carbon steel, *Acta Materialia*, **61**, 1592-1602.

[4] LAMMPS Molecular Dynamics Simulator: https://lammps.sandia.gov/

6-11 July 2025 ICEM21 Bologna
21st International Conference on EXPERIMENTAL MECHANICS

EXPERIMENTAL CHARACTERIZATION FOR THE RATCHETTING EFFECT OF ISOTROPIC SOFT MAGNETORHEOLOGICAL ELASTOMER

Y. Li, H. Deng* and X. Gong*
CAS Key Laboratory of Mechanical Behavior and Design of Materials, Department of Modern Mechanics, University of Science and Technology of China, Hefei, Anhui, 230027, PR China
**E-mail: hxdeng@ustc.edu.cn; gongxl@ustc.edu.cn*

1. Introduction

Magnetorheological elastomer (MRE) is a type of smart material that has the unique ability to sense and respond to magnetic field stimulation, known as the magnetorheological (MR) effect. This characteristic of MRE presents significant potential for applications in vibration control. MRE-based vibration control devices often experience asymmetric cyclic loading during normal operation. As a specialized particle-filled polymer material, MRE exhibits notable stress softening under cyclic loading, a phenomenon referred to as the ratchetting effect [1-4]. This behaviour results in significant differences in the mechanical performance of MRE-based vibration control devices during short-term versus long-term loading. Previous experimental studies on traditional polymer materials have primarily focused on how various loading conditions—such as load level, loading rate, load peak and temperature—affect ratchetting effect [1, 2]. The physical mechanisms underlying ratchetting effect are generally attributed to internal factors, including the entanglement and sliding of molecular chains, as well as friction between the matrix and the filler. These factors ultimately manifest as stress softening during cyclic loading at the macroscopic level. However, a review of the literature indicates a gap in research on the ratchetting effect of MRE. If the impact of this behaviour is not taken into account, the performance of MRE-based vibration control devices may be overestimated, directly affecting their safety and hindering the long-term development of MRE-based applications. Therefore, to address the existing research gap, this study conducted an experimental characterization of the ratchetting effect in isotropic soft magnetorheological elastomer (s-MRE), examining the effects of strain rate, strain amplitude, pre-strain value, and magnetic field conditions on ratchetting effect. This research aims to enhance the understanding of the MRE ratchetting effect, thereby better guiding the design and application of MRE-based devices.

2. Materials and methods

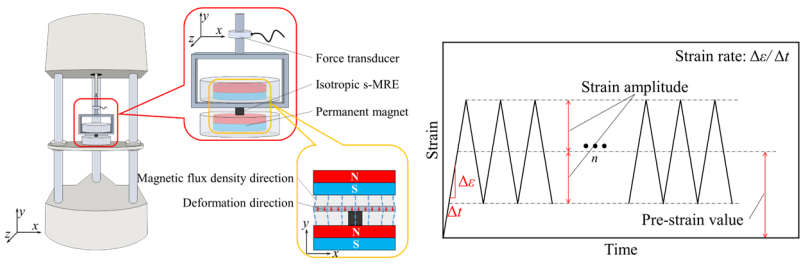

Fig. 1. Schematic diagram of the equipment and loading conditions for cyclic loading.

The isotropic s-MRE samples utilized in this study were prepared through a process involving raw material mixing, injection molding, and vulcanization treatment. To investigate the specific effects of mechanical loading factors alongside magnetic field conditions on ratchetting effect, a standardized and systematic cyclic loading test was conducted. The same test was conducted three times, and the results were averaged to ensure their reliability. Based on the experimental data obtained, the evolution curve of the absolute ratchet behaviour, defined during the cyclic loading process, was established for the analysis of the ratchetting effect. The calculation rule of the absolute ratchet effect is shown in Eq. 1, where $\sigma_{\max,i}$ and $\sigma_{\min,i}$ represent the peak stress and valley stress in the i-th cycle, respectively.

$$\Delta\sigma_{\text{avg},i} = 0.5\left(\sigma_{\max,1} + \sigma_{\min,1}\right) - 0.5\left(\sigma_{\max,i} + \sigma_{\min,i}\right) \tag{1}$$

3. Results and conclusions

Fig. 2 illustrates the evolution curve of the absolute ratchet behaviour. The results indicate that the ratchetting curves show significant differences under various mechanical loading conditions. The different mechanical loading factors tested collectively influence both the level and evolution of ratchetting effect. Notably, at higher strain rates, ratchetting effect stabilizes at a higher level and requires more cycles to achieve this stability. When the pre-strain value remains constant, variations in strain amplitude result in only minor changes to the absolute ratchet behaviour. However, once the pre-strain value increases, the absolute ratchet behaviour exhibits a distinct increasing trend. Furthermore, the changes in the curve under different magnetic field conditions are minimal, suggesting that magnetic field conditions have little significant impact on the level and evolution of ratchetting effect.

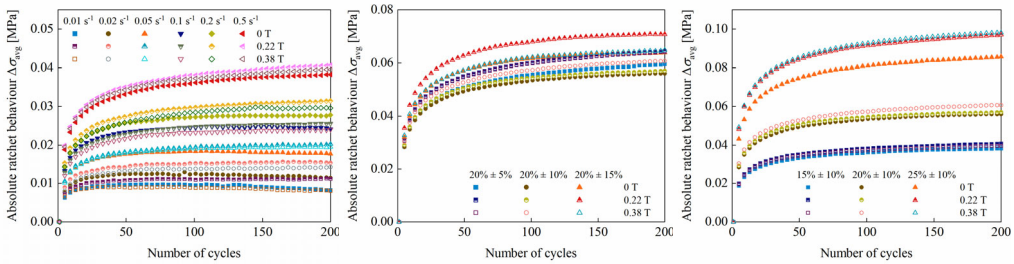

Fig. 2. Under different experimental settings, the evolution curve of absolute ratchet behaviour with the number of cycles.

4. Acknowledgements

The research presented in this paper has received funding from the National Natural Science Foundation of China (12202434, 12427802) and the Fellowship of China Postdoctoral Science Foundation (2022M713045).

5. References

[1] T. Barriere, X. Gabrion, S. Holopainen, J. Jokinen (2020). Testing and analysis of solid polymers under large monotonic and long-term cyclic deformation, *International Journal of Plasticity*, **135**, 102781.

[2] P. Ma, K. Chen, J. Liu, Y. Chen, G. Kang (2023). Experimental study on pure-shear cyclic deformation of dielectric elastomer at different temperatures, *Polymer Testing*, **129**, 108262.

[3] Z. Liang, J. Li, K. Chen, C. Yu, Q. Kan (2024). Multiple relaxation mechanism-based thermo-mechanical constitutive model describing cyclic shape memory effect of shape memory polyurethane, *Acta Mechanica Sinica*, **40**, 423347.

[4] A. Avanzini (2008). Mechanical characterization and finite element modelling of cyclic stress-strain behaviour of ultra high molecular weight polyethylene, *Materials and Design*, **29**, 330–343.

MAGNETIC FLEXIBLE SENSOR WITH RANDOMLY DISTRIBUTED PINE-BRANCH MICROSTRUCTURE FOR BIDIRECTIONAL RECOGNITION

D. Li, X. Gong*, H. Deng*, and S. Xuan*

CAS Key Laboratory of Mechanical Behavior and Design of Materials, Department of Modern Mechanics, University of Science and Technology of China, Hefei, Anhui, 230027, PR China
**E-mail: gongxl@ustc.edu.cn; xuansh@ustc.edu.cn; hxdeng@ustc.edu.cn*

1. Introduction

The rapid development of artificial intelligence technology has brought great changes to our daily life. Traditional semiconductor sensors have a certain degree of rigidity thus they cannot meet the requirements of large deformation in practical applications [1]. In contrast, flexible sensors have been widely used in smart wearable devices because of their advantages of high sensitivity, large monitoring range, and easy deformation [2]. Most flexible sensors exhibit good response when monitoring stretching, compression, or bending stimuli, but all have only a single electrical response mode and do not respond multifunctionally or selectively to multimodal signals [3]. However, the more complex joint motions of the human body are characterized by multiple mechanical states (stretching, bending, and compression) during movement. Therefore, the flexural deformation behavior of flexible sensors attracted increasing interest [4]. In conclusion, the development of a flexible sensor capable of generating completely different resistance change signals for different bending direction stimuli has become a new research direction for smart wearable products.

This study reports a magnetic thin-film sensor (MP-Ag-MP) consisting of magnetic PDMS matrix and conductive Ag nanowires film with pine-branch microstructure. The sensor has diametrically opposed electrical signal responses to bending stimuli in different directions, thus enabling the differentiated monitoring of in-plane and out-of-plane bending. The MP-Ag-MP sensor can also respond promptly to different magnetic field directions and intensities, which demonstrates excellent magnetic sensing performance. The sensor can be applied to monitor various human joint motions and construct a Morse code encryption-decryption system. Furthermore, a stress-magnetic bi-functional control system integrated with Bluetooth transmission function can be designed to wirelessly control the motion of the smart cart. As a result, this randomly distributed pine-branch microstructure endows the wonderful bi-directional sensing function and provides high potential application in smart wearable devices.

2. Materials and methods

Fig. 1 shows the fabrication process of the stress-magnetic bi-functional sensor with randomly distributed pine-branch microstructure. First, PDMS and NdFeB particles were mixed evenly and uniformly coated onto a sandpaper. After peeling off from the sandpaper, the magnetic film with a ridge-like microstructure was obtained. Subsequently, silver nanowires were dropwisedly coated on the magnetic film several times, then it was encapsulated.

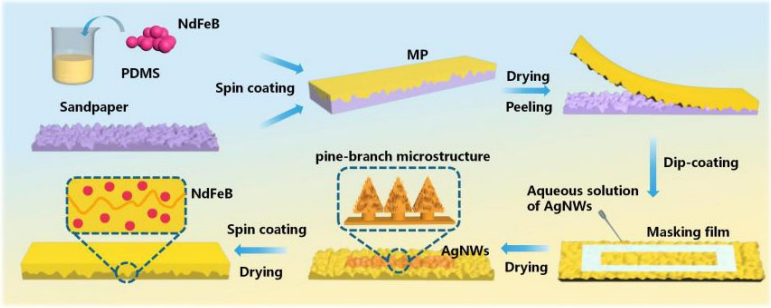

Fig. 1. The fabrication process of the MP-Ag-MP sensor

3. Results and conclusions

The bending behavior of MP-Ag-MP sensor is divided into two types: in-plane bending and out-of-plane bending. In-plane bending is defined as bending toward the direction of the downward concavity of the conductive layer (Fig. 2), and Out-of-plane bending is opposite. More notably, since the sensor generates completely opposite positive and negative electrical response signals for both in-plane and out-of-plane bending, the sensor has the potential to be applied in distinguishing bending direction. Therefore, an intelligent wireless control system for cart motion is designed. The sensor can be simply attached to the wrist or use a magnet field to control the car moving. As a result, the MP-Ag-MP thin-film sensor with pine-branch microstructure shows high application potential in the field of smart wearable devices.

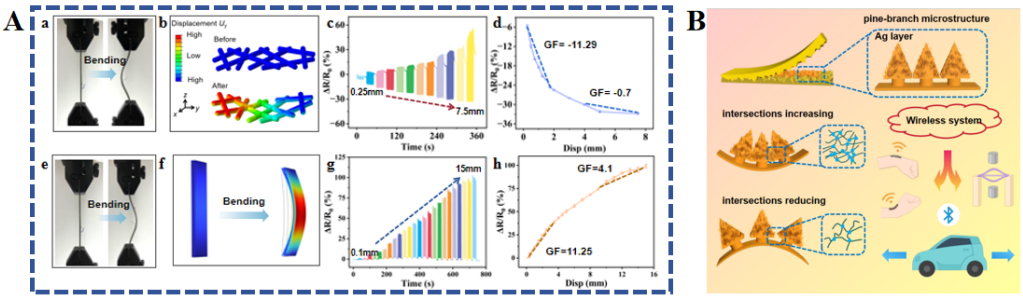

Fig. 2. The bending properties and applications of the MP-Ag-MP sensor

4. Acknowledgements

The research presented in this paper has received funding from the National Natural Science Foundation of China (Grant Nos. 12072338, 12132016, 12427802).

5. References

[1] T. Q Trung , N. E. Lee (2016). Flexible and Stretchable Physical Sensor Integrated Platforms for Wearable Human-Activity Monitoring and Personal Healthcare. *Adv. Mater.*, **28**, 4338-4372.

[2] O. A. Araromi, M. A. Graule, K. L. Dorsey (2020). Ultra-sensitive and Resilient Compliant Strain Gauges for Soft Machines. *Nature*, **587**, 219-224.

[3] Y. Cheng, R. Wang, J. Sun (2015). A Stretchable and Highly Sensitive Graphene-based Fiber for Sensing Tensile strain, Bending, and Torsion. *Adv. Mater.*, **27**, 7365-7371.

[4] D. Yang, H. K. Nam, T. S. D Le (2023). Multimodal E-Textile Enabled by One-Step Maskless Patterning of Femtosecond-Laser-Induced Graphene on Nonwoven, Knit, and Woven Textiles. *ACS Nano*, **17**, 18893-18904.

BIONIC-LEAF VEIN INSPIRED BREATHABLE ANTI-IMPACT WEARABLE ELECTRONICS WITH HEALTH MONITORING, ELECTROMAGNETIC INTERFERENCE SHIELDING AND THERMAL MANAGEMENT

X. Wang, H. Deng*, X. Gong* and S. Xuan*
CAS Key Laboratory of Mechanical Behavior and Design of Materials, Department of Modern Mechanics, University of Science and Technology of China, Hefei, Anhui, 230027, PR China.
**E-mail: hxdeng@ustc.edu.cn; gongxl@ustc.edu.cn; xuansh@ustc.edu.cn*

1. Introduction

Breathable and stretchable conductive materials are ideal for healthcare wearable electronic devices. However, the tradeoff between the sensitivity and detection range of electronic sensors and the challenge posed by simple-functional electronics limits their development. Various conductive structures have been applied to enhance the sensitivity and detection range of electronic sensors. The macroscopic material structure design, including kirigami and precrack, is an essential method to improve the performance of the sensors [1]. Furthermore, incorporating new conductive materials into the base materials is also an innovative approach [2]. In particular, transition metal carbide ($Ti_3C_2T_x$ MXene), a novel class of two-dimensional (2D) layered material, is particularly attractive for wearable electronic devices due to its outstanding metallic conductivity, high specific surface area, abundant surface groups, and mechanical flexibility. Nonetheless, the film formed by the 2D MXene often exhibited low ductility and flexibility, which will cause a loss of detection range and cycle life. Incorporating biomimetic design principles in sensing materials enables devices to possess inherent response characteristics and additional derived functionalities [3]. In nature, the leaf veins have evolved a hierarchically interconnected network structure to achieve an optimal balance between material transportation and mechanical stability. Drawing inspiration from leaf veins, the integration of 1D nanowires into 2D nanosheets to construct a conductive network holds great promise for enhancing the synergy between microscopic conductive networks [4].

Here, inspired by a bionic-leaf vein conductive path, we develop a breathable, flexible multifunctional sandwich composite with sensing, Joule heat, anti-impact, and electromagnetic interference (EMI) shielding. Interestingly, benefiting from the bionic-leaf vein conductive path, an electronic device with high sensitivity and wide detection range is fabricated. The in-plane bending, out-of-plane bending, and stretching can be distinguished by exporting different kinds of resistance changes. The wearable electronic device is integrated into the Bluetooth sensing glove to cooperate with machine learning to recognize the grasp signals of different objects. Finally, the sensing and Joule heating arrays are incorporated into the multifunctional belt for precise and controllable thermal management and hammer alarm. The sensor holds great potential in smart healthcare, body monitoring, and human-computer interaction.

2. Materials and methods

The preparation of the flexible multifunctional sandwich composite consists of three steps: 1) Alternately assembling AgNWs and MXene on the non-woven fabric to form a conductive fabric; 2) Mixing polyborosiloxane (PBS) and VMQ to create a perforated polyborosiloxane elastomer (PBSE) film; 3) Wrapping the conductive fabric with the PBSE film to form a sandwich structure. The effects

of the bionic structure on its stretching sensing, electromagnetic shielding, and electrothermal properties were investigated.

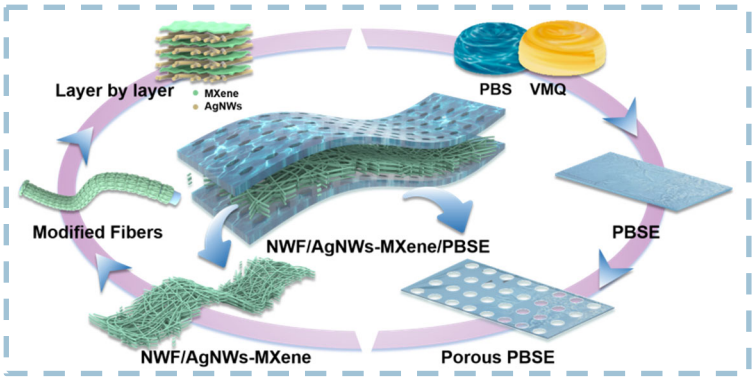

Fig. 1. Schematic of preparation process of porous conductive sandwich composite.

3. Results and conclusions

The synergy of 1D AgNWs and 2D MXene ensured a wide detection range (Strain=57%) and high sensitivity (GF=1158.1) of sensing. In addition, the sensor exhibited interesting bidirectional resistance changes to distinguish in-plane bending and out-of-plane bending stimuli. Moreover, the high conductivity and intercalated structure formed by AgNWs and MXene allowed sandwich composite multiple reflections and absorption of EMI waves and desired EMI shielding performance (41.46 dB). Meanwhile, sandwich composite exhibited precise and controllable Joule heating (input direct voltage=2 V, temperature=39.8 °C). An excellent anti-impact performance was provided due to the shear stiffening of PBSE.

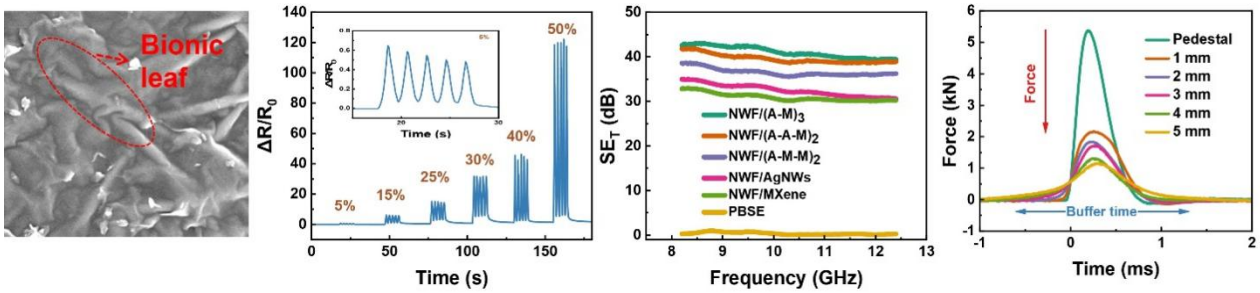

Fig. 2. Bionic-leaf vein microstructure and characterization of sensing, EMI shielding and anti-impact properties.

4. Acknowledgements

Financial supports from the National Natural Science Foundation of China (Grant Nos. 12072338, 12132016, and 12427802) are gratefully acknowledged.

5. References

[1] Y. Bai, L. Yin, C. Hou, Y. Zhou, F. Zhang, Z. Xu, K. Li, Y. Huang (2023). Response regulation for epidermal fabric strain sensors via mechanical strategy, *Adv. Funct. Mater.*, **33**, 2214119.

[2] H. An, T. Habib, S. Shah, H. Gao, M. Radovic, M.J. Green, J.L. Lutkenhaus (2018). Surface-agnostic highly stretchable and bendable conductive MXene multilayers, *Sci. Adv.*, **4**, eaaq0118.

[3] Y. Liu, K. He, G. Chen, W.R. Leow, X. Chen (2017). Nature-inspired structural materials for flexible electronic devices, *Chem. Rev.*, **117**, 12893–12941.

[4] M. Cheng, M. Ying, R. Zhao, L. Ji, H. Li, X. Liu, J. Zhang, Y. Li, X. Dong, X. Zhang (2022). Transparent and flexible electromagnetic interference shielding materials by constructing sandwich AgNW@MXene/wood composites, *ACS Nano*, **16**, 16996–17007.

DUAL-MODULUS 3D PRINTING MAGNETORHEOLOGICAL METAMATERIALS FOR NEGATIVE VIBRATION REGULATION

C. Lou, X. Lian*, H. Deng*, and X. Gong*
CAS Key Laboratory of Mechanical Behavior and Design of Materials, Department of Modern Mechanics, University of Science and Technology of China, Hefei, Anhui, 230027, PR China
**E-mail: xylian@ustc.edu.cn; hxdeng@ustc.edu.cn; gongxl@ustc.edu.cn*

1. Introduction

There is nowadays an increasing interest in Metamaterials, exhibiting excellent ability of manipulating and controlling waves propagation. The characteristics of most presented metamaterials cannot be artificially adjusted due to the fixed material property [1]. To further develop the application potential of metamaterials, the intelligent metamaterials have attracted more and more attention in recent years. As a classical intelligent material, magnetorheological elastomer (MRE) could be used to fabricate magnetorheological metamaterial (MRM), whose characteristic can be adjusted under external magnetic field [2-3]. In the fabrication process of MRMs, MRE is mostly prepared by the traditional molding method, and then the MRMs are obtained by artificial integration, resulting in the complex preparation processes and simple MRE structures. As an emerging additive manufacturing technology, 3D printing technology can programmatically print various complex structures [4]. However, due to the low bond strength between different materials, dual-modulus 3D printing of MRMs is still a challenge, which is of great significance for further development of MRM. In addition, due to the controllable stiffness behavior of MRE, MRMs have been investigated in the field of vibration isolation. The MRMs with periodic structures presented bandgaps that could manipulate the transmission of vibration. Due to the magnetorheological effect of MRE, the stiffness of laminated MRE was just increased under external magnetic field. The bandgaps of MRMs were broadened and raised under external magnetic field. While it is more attractive to investigated a negative regulation MRM, whose bandgaps can be broadened and lowered under external magnetic field, which is of great concern in engineering practices.

This study proposes a dual-modulus negative regulation MRM, which could lower the starting frequency and increase the ending frequency of MRM bandgap by changing structure stiffness under external magnetic field, resulting in a wider bandgap of negative regulation MRM. The theoretical model and transmission spectrum of the MRM with periodic structure were presented, and the effect of stiffness to the transmission spectrum was further evaluated.

2. Materials and methods

The experimental samples of negative regulation MRM were manufactured by dual-modulus 3D printing technology based on HMRE powders and LMRE powders. The mechanical performance of HMRE and LMRE are tested by a dynamic mechanical analyzer (DMA, ElectroForce 3200, TA Instruments, USA) and universal tensile instrument (Criterion™ Model 43, MTS Co., LTD, China) with a 500 N force sensor module. The loading rate was set at 0.1 mm/s.

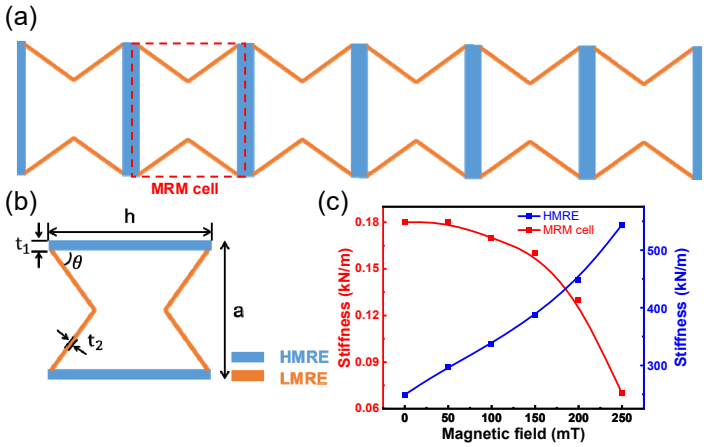

Fig. 1. Schematic diagram of (a) the negative regulation MRM and (b) the MRM cell, (c) the stiffness of MRM cell and HMRE under different magnetic fields.

3. Results and conclusions

By substituting the lumped mass and stiffness into the above equations, the starting frequency of the bandgap for the infinite-sized negative regulation MRM without external magnetic field was obtained as 67.5 Hz, and the ending frequency was 2507.9 Hz (Fig. 2). The bandgap of MRM was broadened and the starting frequency was lowered by applying an external magnetic field.

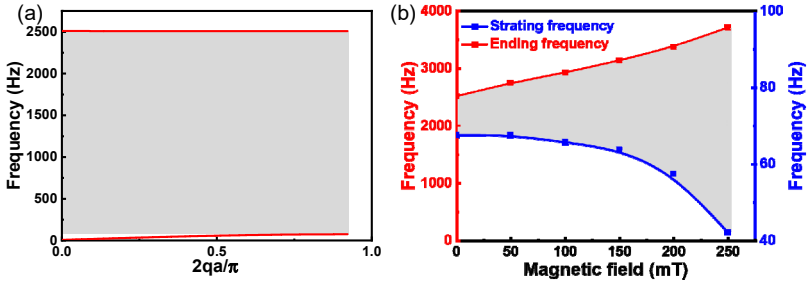

Fig. 2. Dispersion relation and band gap (gray) of the negative regulation MRM (a) without external magnetic field, (b) under different magnetic field.

4. Acknowledgements

The research presented in this paper has received funding from National Natural Science Foundation of China (Nos. 12372187, 12402228, 12427802, and 12132016), the Fundamental Research Funds for the Central Universities (No. WK2480000010), the Fellowship of China Postdoctoral Science Foundation (No.2024M753103), the CAS Talent Introduction Program (No. KJ2090007006), and the Anhui Provincial Natural Science Foundation (No. 2408085QA014).

5. References

[1] R. Xu, Y. He, X. Li, M. Lu, Y. Chen (2023). Snap-fit mechanical metamaterials. *Appl. Mater. Today*., **30**,101714.

[2] C. Willey, V. Chen, K. Scalzi, P. Buskohl, A. Juhl (2020). A reconfigurable magnetorheological elastomer acoustic metamaterial. *Appl. Phys. Lett.*, **117**, 104102.

[3] Z. Chen, S. Sun, L. Deng, J. Yang, S. Zhang, H. Du, W. Li (2022). Investigation of a new metamaterial magnetorheological elastomer isolator with tunable vibration bandgaps. *Mech. Syst. Signal Process*., **170**, 108806.

[4] X. Cao, S. Xuan, Y. Gao, C. Lou, H. Deng, X. Gong (2022). 3D printing ultraflexible magnetic actuators via screw extrusion method. *Adv. Sci.*, **9**, 2200898.

INFLUENCE OF TEMPERATURE ON MICROSTRUCTURAL EVOLUTION DURING THE DYNAMIC TENSILE EXTRUSION OF PURE COPPER

S. Ricci[1], G. Iannitti[1], G. Testa[1], A. Ceccacci[1], A. Pagano[1], A. Ruggiero[1], N. Bonora[1]
[1] Department of Civil and Mechanical Engineering (DICeM), University of Cassino and Southern Lazio, Cassino, Italy

1. Introduction

Understanding how microstructural evolution influences mechanical response and performance in dynamic environments is essential in those applications where materials are required to perform under extreme conditions. Gray et al. [1] designed the Dynamic Tensile Extrusion (DTE), which has been used to investigate materials' formability and fragmentation in extreme conditions [2]–[4], such as those experienced in shaped charged devices. The test involves launching a spherical or bullet-shaped projectile into a conical die, whose shape is designed to induce a velocity difference between the tip and the tail of the sample, promoting its dynamic extrusion. In these conditions, the material undergoes significant adiabatic deformation, even higher than 500%, with strain rates between 10^5-10^6 s^{-1}. Several studies have been developed to understand the role of the initial microstructure and its changes due to excessive straining in pure copper during DTE. The initial grain size was found to strongly influence material ductility in these conditions. Gray et al. [1] highlighted that the dynamic tensile ductility is an inverse function of the grain size in coarse-grained (CG) Oxygen Free-High Conductivity (OFHC) Cu. This behavior was related to the higher propensity of finer grain structures to exhibit phenomena such as strain localization and texture evolution. Park et al. [5-6] compared the response of CG and ultrafine-grained (UFG) Cu, with the latter characterized by either elongated or equiaxial grains. They also confirmed the strong influence of the initial grain size on material extrusion, with CG Cu exhibiting the highest ductility, whereas equiaxial UFG reached lower deformation levels before failure. As also reported by Gray et al. [1], significant elongation of the microstructure along the extrusion direction was found after the test, together with the development of a double fiber texture of <111> and <100> along the same direction and mechanical twinning. As opposed to UFG structures, no recrystallization was found in CG Cu. Hörnqvist et al. [7] investigated the response of OFHC Cu samples with an initial grain size of 47 µm, employing an extrusion velocity of 400 ms^{-1}. Microstructural investigations were carried out on the fragment that remained in the die, and they confirmed the presence of a significantly deformed and texturized microstructure. Furthermore, meta-dynamic recrystallization (mRDX) occurred in those parts of the sample that underwent significant straining. The experimental investigation was coupled with numerical modeling, whose results highlighted that the conditions developed during the test (adiabatic temperature rise, extremely high deformation, and strain rates) promoted mDRX during straining, whereas subsequent grain growth took place during the cooling phase after the test. Lee et al. [8] compared the response of UFG and fine-grained (FG) Cu at similar projectile velocities. In both materials, ductility was found to increase with the grain size, contrary to CG Cu. Microstructural analysis performed on the recovered jets revealed significant microstructural changes during the test (grain elongation, texture development) and the presence of mDRX, which was found to be more pronounced as the initial grain size decreased and also responsible for anticipated failure. However, there has been little investigation into the role of temperature in promoting and influencing

microstructural changes and evolution in these conditions. Thus, this work aims at assessing the impact of temperature on the dynamic tensile extrusion of OFHC Cu by performing DTE tests at approximately 400 ms^{-1}, with different initial temperatures ranging from room temperature to 400 °C. Systematic microstructural investigations were carried out to determine microstructural changes and their extension into the recovered fragments and the occurrence of mDRX. Numerical simulations were also performed to further explore the conditions that sustain microstructural evolution.

2. Materials and methods

DTE tests were performed on OFHC Cu (commercial pure, 99.98%). Samples were machined into a bullet shape [9] from half-hardened bars and subjected to an annealing process consisting of holding the material at 450 °C for 0.5 hours in an Argon inert atmosphere [7]. After this process, the material presents a random texture with several annealing twins and a grain size of 47 μm, as reported in [7]. DTE tests were performed in vacuum, using a single-stage gas gun placed at the University of Cassino and Southern Lazio with He as propellant gas, following the procedure reported in [10]. The extrusion die had been custom-designed to allow for sample heating and temperature monitoring before firing. After the test, fragments were recovered in ballistic gel, their shape and size recorded, and then microstructural investigations were carried out with a FEI/Philips XL-30 SEM, which mounts an Oxford C-Nano EBSD probe.

3. Results and conclusions

Preliminary numerical simulations have been conducted to evaluate the influence of the initial temperature on the sample's final deformation levels. 2D axisymmetric simulations have been carried out with the FEM software MSC Marc, based on the computational framework developed in [11], validated to accurately predict the dynamic extrusion behavior of OFHC Cu across different launching velocities at room temperature. The selected material model for the description of the Cu sample is the Mechanical Threshold Stress (MTS), and material parameters are also reported in [11]. Figure 1 highlights the substantial deformation experienced by the material during the extrusion process, and, by increasing the initial temperature, material ductility is significantly enhanced.

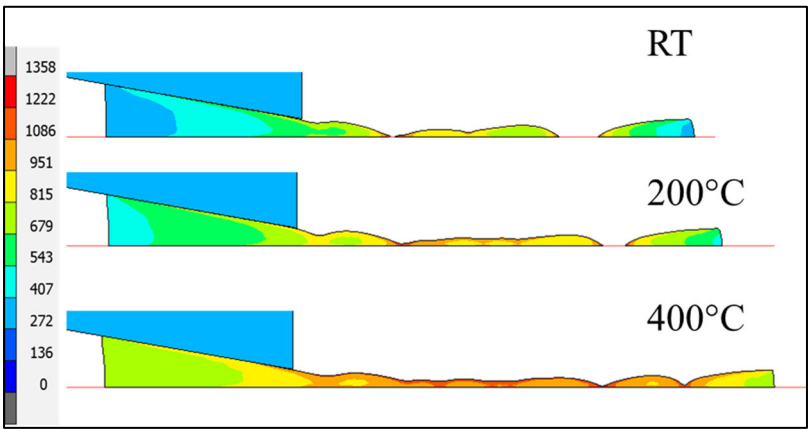

Fig. 1. Temperature maps of the extruded jets at 80 ms after firing at different initial temperatures.

Following the procedure and employing the parameters reported in [9], the Zener-Hollomon factor was calculated at five distinct locations on the sample that remained in the die. The results illustrated in Figure 2 suggest that, by increasing the initial temperature, the critical level of deformation for DRX, ε_{cr}, is met in a more extended area of the sample.

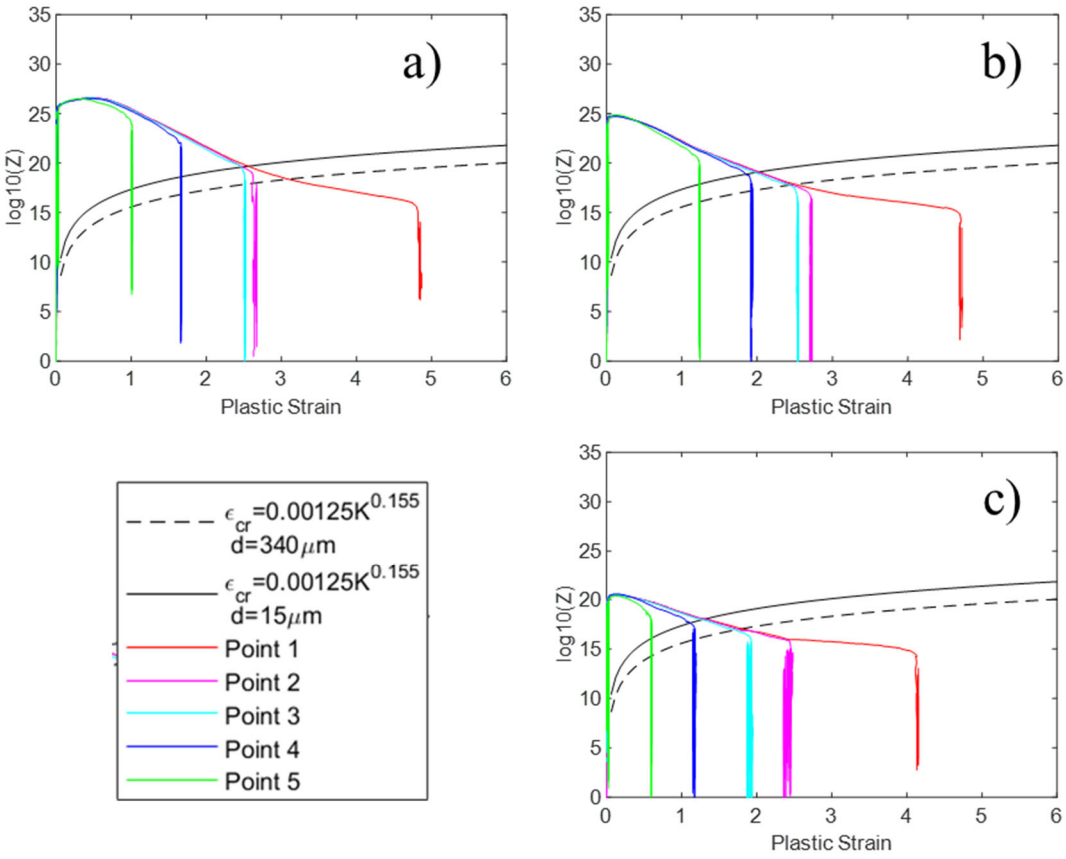

Fig. 1. Evolution of the Zener–Hollomon (K) parameter with plastic strain for five different locations along the axis of the fragment that remained in the die, a) room-temperature, b) 200 °C, and c) 400 °C. Point 1 is at 0.5 mm from the tip, and points 2-5 are at 2.5, 4, 8, and 12 mm, respectively.

5. References

[1] G. T. Gray *et al.*, "Influence of shock prestraining and grain size on the dynamic-tensile- extrusion response of copper: Experiments and simulation," *AIP Conf. Proc.*, vol. 845 I, no. 2006, pp. 725–728, 2006, doi: 10.1063/1.2263424.

[2] J. P. Escobedo *et al.*, "Influence of texture and test velocity on the dynamic, high-strain, tensile behavior of zirconium," *Acta Mater.*, vol. 60, no. 11, pp. 4379–4392, 2012, doi: 10.1016/j.actamat.2012.05.001.

[3] Y. Cao *et al.*, "Microstructure evolution and mechanical properties at high temperature of selective laser melted AlSi10Mg," *J. Mater. Sci. Technol.*, vol. 62, pp. 162–172, 2021, doi: 10.1016/j.jmst.2020.04.066.

[4] L. Park, S. Woo, Y. Lee, K. Lee, and Y. Sun Yi, "Comparison of dynamic tensile extrusion behaviour of WCu composites made by different processes," *EPJ Web Conf.*, vol. 183, pp. 2–5, 2018, doi: 10.1051/epjconf/201818303004.

[5] K. T. Park, L. J. Park, H. Jun Kim, S. Bong Kim, and C. Soo Lee, "Dynamic tensile extrusion behavior of coarse grained and ultrafine grained OFHC Cu," *Mater. Sci. Eng. A*, vol. 569, pp. 61–70, 2013, doi: 10.1016/j.msea.2013.01.015.

[6] K. T. Park, L. Park, H. J. Kim, S. B. Kim, and C. S. Lee, "Analysis on dynamic tensile extrusion behavior of UFG OFHC Cu," *IOP Conf. Ser. Mater. Sci. Eng.*, vol. 63, no. 1, 2014, doi: 10.1088/1757-899X/63/1/012144.

[7] M. Hörnqvist, N. Mortazavi, M. Halvarsson, A. Ruggiero, G. Iannitti, and N. Bonora, "Deformation and texture evolution of OFHC copper during dynamic tensile extrusion," *Acta Mater.*, vol. 89, pp. 163–180, 2015, doi: 10.1016/j.actamat.2015.01.053.

[8] K. Lee, S. Woo, S. B. Kim, S. Lee, L. Park, and K. T. Park, "Deformation and microstructural evolution of ultrafine- And fine-grained OFHC Cu during dynamic tensile extrusion," *J. Mater. Res. Technol.*, vol. 9, no. 5, pp. 10746–10757, 2020, doi: 10.1016/j.jmrt.2020.07.090.

[9] G. Testa *et al.*, "Modelling and simulation of dynamic recrystallization (DRX) in OFHC copper at very high strain rates," *AIP Conf. Proc.*, vol. 1793, 2017, doi: 10.1063/1.4971659.

[10] N. Bonora, G. Testa, A. Ruggiero, G. Iannitti, N. Mortazavi, and M. Hörnqvist, "Numerical Simulation of Dynamic Tensile Extrusion Test of OFHC Copper," *J. Dyn. Behav. Mater.*, vol. 1, no. 2, pp. 136–152, Jun. 2015, doi: 10.1007/s40870-015-0013-7.

[11] S. Ricci, G. Testa, G. Iannitti, A. Ruggiero, and N. Bonora, "On The Role of Constitutive Modeling and Computational Parameters in the Numerical Simulation of Dynamic Tensile Extrusion Test," *J. Dyn. Behav. Mater.*, vol. 8, no. 4, pp. 453–472, 2022, doi: 10.1007/s40870-022-00352-9.

6-11 July 2025 ICEM21 Bologna
21st International Conference on EXPERIMENTAL MECHANICS

VALIDATION OF CHAIN DRIVE RESONANCE MODELS BY VIDEO, AUDIO AND TORQUE MEASUREMENTS

R.T. Wragge-Morley[1], G.C. Barnaby[1], J. Bentley[1], F.S. Da Silva Davidson[1], J Drabble[1], K Kythreotis[1], S. Lu[1], M. M. Wharton[1], T.L. Hill[1] and B.J. Hicks
[1] School of Electrical, Electronic, and Mechanical Engineering, University of Bristol, UK

1. Introduction

Bush and bush-roller chains are multi-body systems that comprise many individual links in contact by non-conformal cylindrical contacts between pins and bushes. In many applications such as automotive timing chain, chain guides are used to control tension and dynamical behaviour of chains. However, there are certain power-transmission applications where the chain spans are free – principally in the final-drives of bicycles and motorcycles. The focus of this study is the resonant behaviour of the tight span of a chain drive transmitting power.

Models exist describing the resonant behaviour of chain drives [1, 2] which often model the chain span as a heavy string. More recent contributions have applied the Galerkin Method to derive modeshapes of axially translating and accelerating strings [3, 4], whilst further realism has been added by the introduction of viscoelastic string models to represent damping [5]. Some approaches model the string in a quasi-static state, whilst others model it in translational motion. The transverse vibration of the tight chain span is generally assumed to be driven by the polygonal action of the smallest cog on the span [6]. The presence of excessive vibration in the span is undesirable in most power transmission applications as it increases noise, friction and wear.

2. Materials and methods

This work makes use of several methods to validate the efficacy of chain resonance models form the literature. Instrumentation techniques include the use of digital image correlation (DIC) in high-speed camera imagery and long exposure still photography; high bandwidth torque measurement on an advanced chain transmission dynamometer [7], and acoustic emission from the chain drive – the equipment for these studies is illustrated in Fig 1. Further studies were conducted using a quasi-static test-setup excited via a shaker and measured with a laser doppler vibrometer. The chains under investigation are all ½” pitch bicycle chains running on cycling chainrings and sprockets.

Fig. 1. High speed camera and acoustic emission equipment in chain drives test-cell

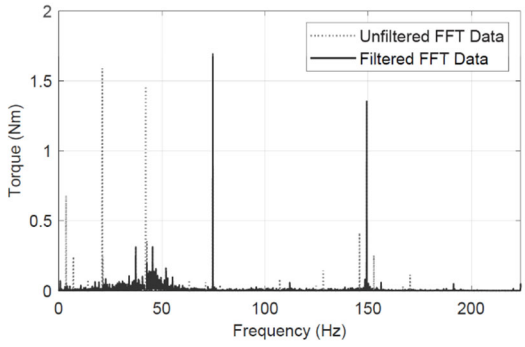

Fig. 2 FFT of high bandwidth torque Transducer signal before and after filtering to remove known system frequencies

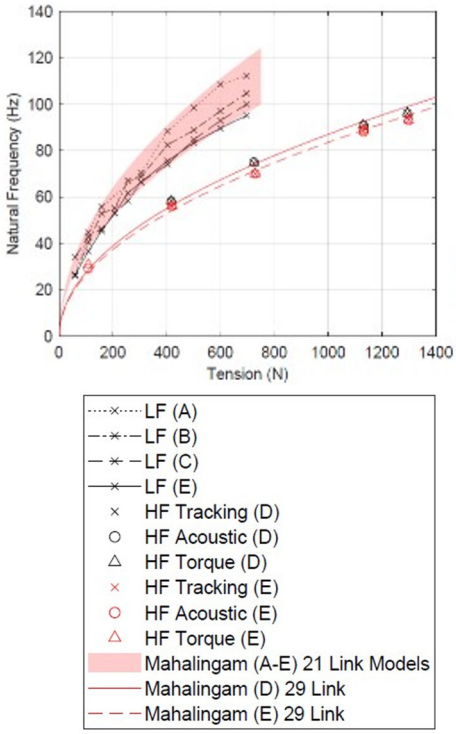

Fig. 3 Comparison of observed resonant frequencies against analytical models for several different roller chains observed in stationary (LF) and axially translating (HF) experiments with different monitoring techniques

In addition to the studies validating dynamics modelling approaches, research has been conducted to demonstrate the impact of chain resonance on power transmission efficiency, targeting a track-cycling application.

The torque transducer outputs from the TPM dynamometer have a bandwidth of 1000Hz, which is greater than the expected natural frequencies of the chain spans under tension, illustrated in Fig. 2. This means that the torque measurements from the test-bed can be used to accurately identify the presence of resonant modes in the driveline. However, it is necessary to remove by filtering a variety of other frequencies associated with the electrical machines (winding slot, rotor bar pass, synchronous and slip frequencies), line frequencies from power electronics and artefacts from bearings. The presence of chain vibration and tooth interaction frequencies in the filtered and unfiltered data are illustrated in Fig 2.

3. Results and conclusions

Several different methods with differing levels of cost and complication have been successfully applied to the validation of chain span resonance models. Fig 3. Shows good agreement for both stationary and axially translating chains of different lengths using each method, errors between analytical results and measurements were found to be of the order of 2.0-2.5% for DIC tracking, acoustic emission and torque data analysis of an axially translating chain span. In the stationary rig, the correlation was less good, with errors of typically 5.75-8.70%, attributable to the presence of more complex modeshapes in a slightly shorter chain span between excitation nodes. Measurable reductions in power transmission efficiency when span resonance occurs under high load have been demonstrated.

4. Acknowledgements

This research was supported by the British Cycling Federation, Renold Chain, Hottinger Bruel & Kjaer UK Ltd. and a UKRI studentship funded as part of DTP 2018-19 University of Bristol EP/R513179/1.

5. References

[1] S. Mahalingam (1957). Transverse vibrations of power transmission chains, *British journal of Applied Physics,* **8-4,** 145-148.

[2] Fuglede, N.; Thomsen, J. J. (2016). Kinematic and dynamic modeling and approximate analysis of a roller chain drive. *Journal of Sound and Vibration,* **vol. 336**, 447-470.

[3] J.A. Wickert; C. D. Mote Jr. (1990). Classical Vibration Analysis of Axially Moving Continua. *ASME Journal of Applied Mechanics,* **57-3**, 738-744.

[4] M. Pakdemirli; A.G. Ulsoy; A. Ceranoglu (1994). Transverse Vibration of an Axially Accelerating String. *Journal of Sound and Vibration*, **169-2**, 176-196.

[5] Li-Qun Chen; Jean W. Zu; Jun Wu; Xiao-Dong Yang (2004). Transverse vibrations of an axially accelerating viscoelastic string with geometric nonlinearity. *Journal of Engineering Mathematics*. **48**, 171-182.

[6] S. Mahalingam (1958). Polygonal action in chain drives. *Journal of the Franklin Institute*. **265-1**, 23-28.

[7] G. C. Barnaby (2023). Experimental and modelling methods for high-accuracy performance characterisation of chain drives. *University of Bristol PhD Thesis*.

EXTRAORDINARY ELASTIC-WAVE MANIPULATIONS OF HIGHER-ORDER DIFFRACTIONS BASED ON NON-HERMITIAN METASURFACES

***Bing Li*[1*], *Bochen Ren*[1], *Jiali Cheng*[1]**
[1] *School of Aeronautics, Northwestern Polytechnical University, Xi'an, Shaanxi, 710072, China*
**corresponding author: bingli@nwpu.edu.cn*

1. Introduction

The past decades have witnessed the remarkable development and explosive implications of meta-structures in elastic-wave steering under the Hermitian systems that disregard material loss. However, the reality of practical applications is inevitably intertwined with loss, leading to the dissipation of elastic wave energy. Traditionally, such losses were viewed as detrimental, potentially compromising the performance of elastic wave devices. Yet, a paradigm shift has emerged from recent groundbreaking research, which has uncovered the potential of strategically engineered loss/gain within non-Hermitian systems to facilitate remarkable wave steering phenomena [1-3]. Through the meticulous design of loss and gain media, complex wave-matter interactions can be realized, encompassing unidirectional wave propagation, band merging, and enhanced sensing capabilities. This novel perspective paves the way for innovative applications in acoustics, seismology, and materials science, where the judicious use of loss and gain can be harnessed to achieve unprecedented control over elastic waves [2-4].

The advent of non-Hermitian metasurfaces has opened new frontiers for elastic wave control, offering a reduced structure footprint in low-dimensional designs. Despite their promise, metasurfaces face inherent limitations stemming from their gradient index characteristics, which can constrain their capabilities. Achieving highly efficient wave manipulation in advanced artificial materials, with a focus on ultra-compact dimensions and easy fabrication, remains an open challenge.

2. Design and results

This work proposes a design strategy that leverages non-Hermitian modulation to surmount these obstacles. The proposed non-Hermitian metagratings (NHMGs) [4], characterized by their subwavelength unit cells, enable a suite of extraordinary elastic-wave manipulations, including the skin-like effect, asymmetric propagation, and perfect absorption. Building upon these capabilities, we have further engineered a cloaking device based on NHMG, as depicted in Fig. 1, which can effectively shield arbitrary-shaped targets from detection [4]. Our research not only expands the repertoire of elastic wave manipulation techniques in non-Hermitian materials but also offers an ultra-compact solution for wave control, holding significant potential for engineering applications.

3. Acknowledgements

The authors acknowledge the support from the National Natural Science Foundation of China (NSFC) (Grant No. 12272298).

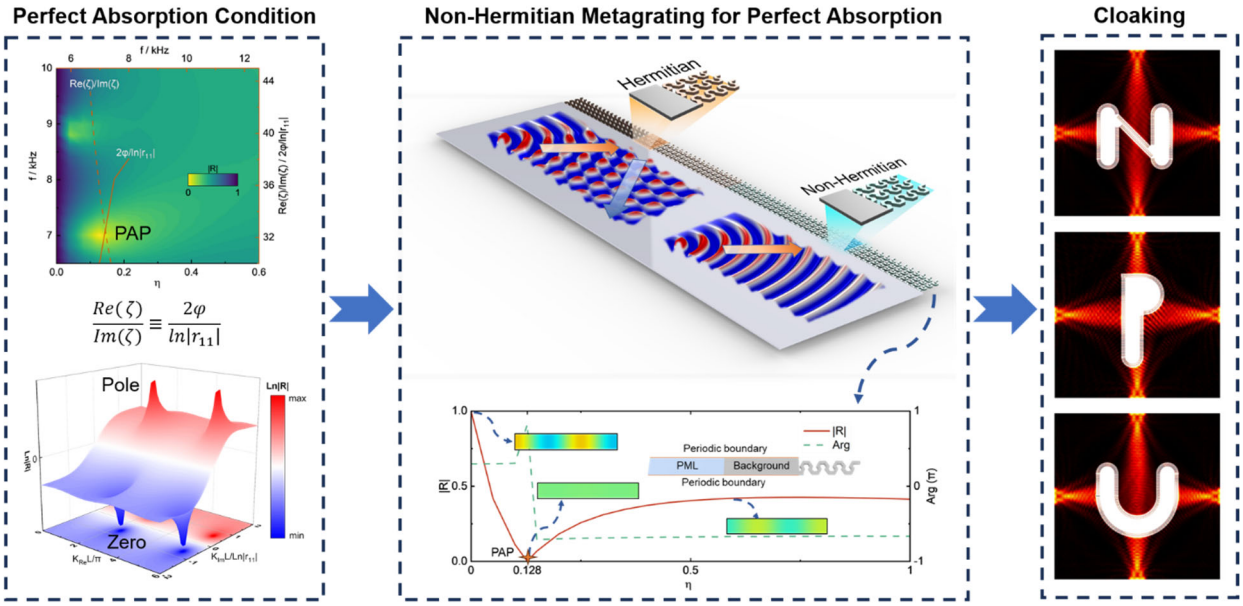

Fig.1 Non-Hermitian metagrating for perfect absorption and arbitrary-shaped target cloaking

4. References

[1] Zhu W., Fang X., Li D., Sun Y., Li Y., Jing Y. & Chen H (2018). Simultaneous observation of a topological edge state and exceptional point in an open and non-Hermitian acoustic system, *Physical Review Letters*, **121**(12), 124501.

[2] Cao L., Zhu Y., Wan S., Zeng Y., & Assouar B (2022). On the design of non-Hermitian elastic metamaterial for broadband perfect absorbers, *International Journal of Engineering Science*, **181**, 103768.

[3] Li B., Hu Y., Chen J., Su G., Liu Y., Zhao M., & Li Z (2020). Efficient asymmetric transmission of elastic waves in thin plates with lossless metasurfaces, *Physical Review Applied*, **14**(5), 054029.

[4] Cheng J., Hu Y., Li B (2024). Non-Hermitian metagrating for perfect absorption of elastic waves, *Materials Horizons*, **11**(7), 1658-1667.

6-11 July 2025 ICEM21 Bologna
21st International Conference on EXPERIMENTAL MECHANICS

ANISOTROPIC LARGE DEFORMATION MECHANICAL PROPERTIES OF ORIENTED PMMA UNDER DIFFERENT STRAIN RATES

Yueming Du[1,2], Zhaolin Chen[1,2], Chao Zhang[1,2], Tao Suo[1,2]
[1] School of Aeronautics, Northwestern Polytechnical University, Xi'an 710072, PR China
[2] National Key Laboratory of Strength and Structural Integrity, Xi'an 710072, PR China

1. Introduction

Poly(methyl methacrylate)(referred to as PMMA), is an amorphous polymer with sort of advantages, such as low density, high transparency and excellent mechanical properties. It has been widely used in aviation, automobile, construction and other commercial fields. Compared with unoriented PMMA, the impact resistance, crack resistance and fracture toughness of oriented PMMA are significantly improved. Having a better understanding of the mechanical behavior of directed PMMA is necessary to promote its potential application in many engineering fields and is a key point for the safety and reliability of aircraft when subjected to hail and bird strikes. Therefore, in order to study the anisotropic large-deformation mechanical behavior of oriented PMMA, uniaxial in-plane and out-of-plane compressive and tensile experiments under low and high strain rates were carried out for PMMA with different orientation degrees.

2. Materials and methods

The orientation degrees of the PMMA in both directions are essentially the same. The orientation degree is defined as $\phi = (A/a - 1) \times 100\%$, where a is the effective side length of the square PMMA sheet excluding the clamping length before stretching, and A is the effective side length after stretching. To evaluate the influence of orientation degree, oriented PMMA sheets with three different orientation degrees ($\phi = 65\%$, 72%, and 85%) were selected for this research. In-plane compression, in-plane tension, out-of-plane compression, and out-of-plane tension tests were conducted.

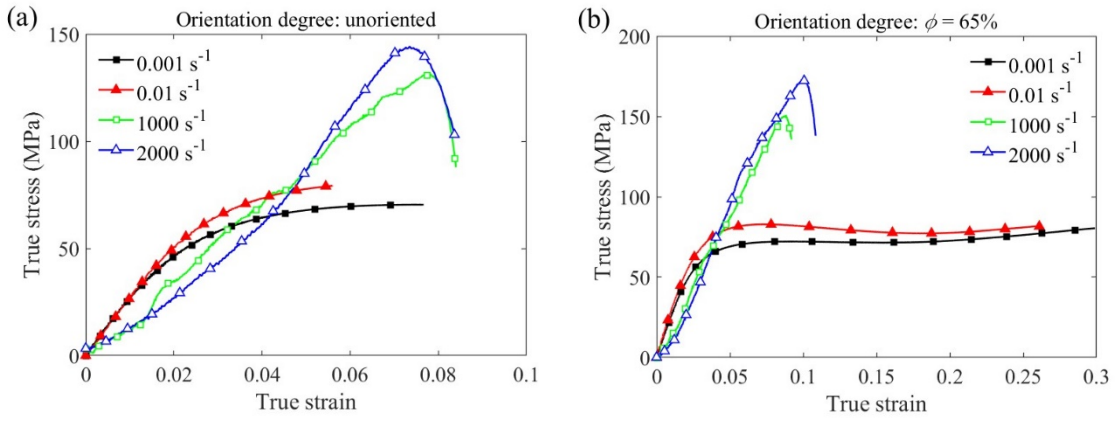

Fig. 1. The stress-strain curves of in-plane tensile experiments of PMMA under different strain rates: (a)unoriented; (b) the orientation degrees of 65%.

3. Results and conclusions

Fig. 1 shows the stress-strain curves of in-plane tensile experiments of unoriented PMMA and 65%-orientation degree PMMA under different strain rates. As can be seen from these figures, both unoriented and orientated PMMA show that the yield strength increases with the increase of strain rate. For the unoriented case, the fracture strain of the material is less than 8%, but for the oriented material, the resistance to tensile fracture is greatly improved, especially for the low strain rate case. Therefore, it shows that the process of orientation can greatly enhance the tensile mechanical behavior of the material.

In Fig. 2, it can be observed that under in-plane tensile load of low strain rate, the crack of unoriented PMMA is perpendicular to the tensile direction. But the failure of oriented PMMA is sometimes more than one crack, and multiple cracks and splits often occur. In addition, with the increase of orientation, the degree of orientation of the molecular chain along the loading direction increases, and the deflection angle of cracks gradually increase. This phenomenon also corresponds to the increase of toughness shown in the stress-strain curve above. In the stress-strain curve of in-plane tension, the fracture strain increases gradually with the increase of orientation. Corresponding to the area under the curve, it shows that the tensile fracture toughness of the material increases with the increase of orientation degree.

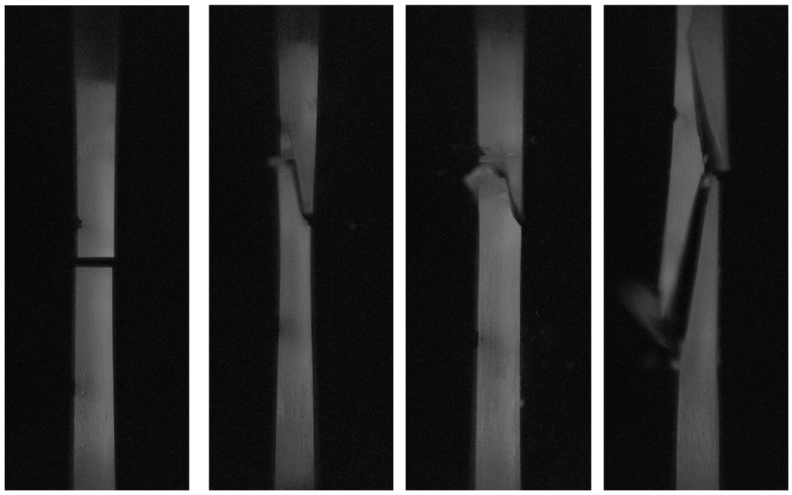

Fig. 2. The crack of PMMA under in-plane tensile load: (a)unoriented; (b) 65%; (c)72%; (d)85%.

4. Acknowledgements

The presented work is financially supported by the National Natural Science Foundation of China (Grant Nos. 12025205, 12141203, and 12302228).

5. References

[1] Cai W, Wang P. Fractional modeling of temperature-dependent mechanical behaviors for glassy polymers. International Journal of Mechanical Sciences 2022;232.

[2] Wang J, Xu Y, Zhang W. Finite element simulation of PMMA aircraft windshield against bird strike by using a rate and temperature dependent nonlinear viscoelastic constitutive model. Compos Struct 2014;108:21–30.

[3] Yu P, Yao X, Tan S, Han Q. A macro-damaged viscoelastoplastic model for thermomechanical and rate-dependent behavior of glassy polymers. Macromol Mater Eng 2016;301(4):469-485.

[4] Cole K C, Ben Daly H, Sanschagrin B, Nguyen K T, Ajji A. A new approach to the characterization of molecular orientation in uniaxially and biaxially oriented samples of poly(ethylene terephthalate). Polymer 1999;40(12):3505-3513.

ACCURATE STRAIN MEASUREMENT IN SPLIT HOPKINSON BAR TESTING OF FIBROUS COMPOSITES

A. Gilat, and J. Seidt
Department of Mechanical and Aerospace Engineering, The Ohio State University
Columbus, OH 43210

1. Introduction

The Split-Hopkinson Bar (SHB) technique is frequently used for testing metals at high strain rates in the range of 500 to 5,000 s^{-1}. In this technique a short specimen is placed (compression) or attached (tension) between two metal bars (incident and transmitter). The specimen is loaded by a wave that is generated in the incident bar. Once the specimen is loaded, most of the wave is reflected back to the incident bar and part of the wave passes through the specimen to the transmitter bar. Traditionally, the strain in the specimen during the test is determined from analyzing the reflected wave in the incident bar. The amplitude of this wave is proportional to the difference between the particle velocities of the ends of the incident and transmitter bars where the specimen is placed. The average strain rate in the specimen is the difference in the particle velocity divided by the specimen's gage length. The strain is obtained by integrating the strain rate. This determination is accurate if the relative motion between the ends of the bars is identical to the change in length of the specimen (no relative motion between the specimen ends and the bars), and if the strain in the specimen is uniform. The force in the specimen is determined from the wave measured in the transmitter bar. Compression tests are the easiest to conduct with the SHB technique since the specimen is just placed between the two bars. In tension the specimen geometry is more complicated (dog-bone shaped) such that the motion between the incident and transmitter bar cannot be all attributed to deformation in the gage section of the specimen. In addition, the specimen has to be attached to the bars. This can affect the state of stress and deformation in the specimen and might disturb the transmission of the waves. In recent years the Digital Image Correlation (DIC) technique has been introduced for accurate non-contact full-field measurement of strains directly on the surface of specimens. The results show that in compression at strains larger than about 0.02 the strains determined from the waves agree with the DIC measured strains. In tension there are large discrepancies that depend on the specimen geometry.

Testing of fibrous composites with the SHB technique requires special attention due to the nonhomogeneous structure of the material, the requirement of specimens of small size, and the brittleness of the material. Small fibrous composite specimens are difficult to machine and attach to the testing apparatus. Brittle composites fracture at strain of less than 5% and sometimes at strains of the order of 1% or less. Determining such small strains in SHB experiments from the waves in the bars is not accurate due to wave dispersion and the effects of the specimen boundary and attachment method on the waves.

2. Experimental method

The present paper examines the challenges in obtaining accurate stress strain curve when testing fibrous composite using the split Hopkison bar technique. The focus is on the measurement of strain and strain rate. The strain and strain rate are measured on the surface of the specimen by using DIC and the measurements are compared with the ones that are determined in the traditional way from the recorded waves. The DIC measurements are done by using Shimadzu HPV-X2 high-speed video

cameras (frame rate of up to 5,000,000 fps and 400×250 pixel resolution). Compression tests have been done with specimens machined from T800/F3900 unidirectional laminates in the 0° and 90° directions, and tensile tests have been done with specimens machined in the 90° direction.

3. Results and conclusions

As an example, Figure 1 shows the waves recorded in a compression SHB test with specimens machined in the 0° direction. The recorded wave in the transmitter bar, which correspond to the force in the specimen, shows that the specimen fractures 19 µs after the loading starts. This means that when using the traditional SHB analysis the strain rate and strain are determined from the first 19 µs of the reflected wave in the incident bar. This initial portion of the wave might not accurately correspond to the actual deformation of the specimen. The strain rate, strain, and stress that are determined from the waves are displayed in Figure 2. The figure shows also the strain that is measured by DIC. It can be seen that there are significant differences between the two measurements. The stress strain response from this test is shown in Figure 3. The figure shows the curves that use the strain determined by the wave and strain measured by DIC. The figure also shows stress strain curves from quasi-static tests. The stress strain curve that is determined from the reflected wave shows a significant strain rate sensitivity with higher stiffness (which is not realistic) and higher stress. The stress strain curve that is determined from the DIC measurement has the same stiffness as the quasi-static curves with slightly higher maximum stress.

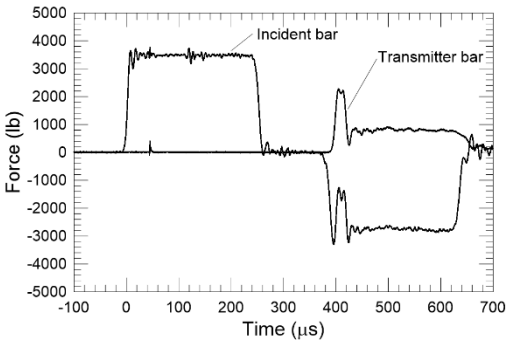

Fig. 1. Waves recorded in a test.

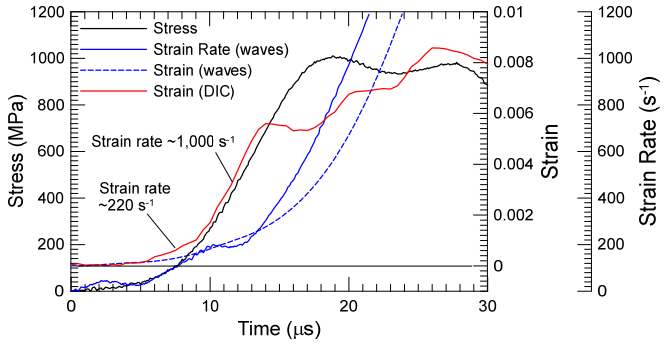

Fig. 2. History of stress, strain rate and strain

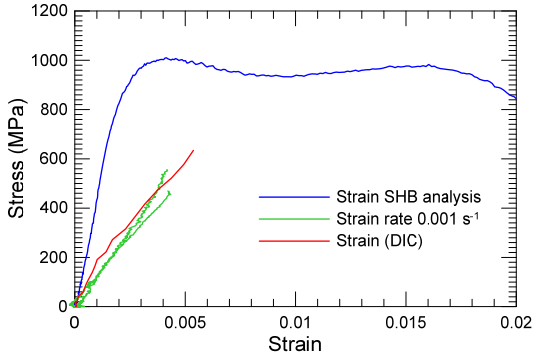

Fig. 3. Compression stress strain curves of T800/F3900 unidirectional laminates in the 0° direction.

4. Acknowledgements

The research was supported by the U.S.A. Federal Aviation Administration, Grant No. 11-G-004. The authors are grateful to Mr. William Emmerling, and Dr. Daniel Cordasco from the FAA for their support and involvement.

SMALL-STRAIN DYNAMIC BEHAVIOR OF A COAL MINE OVERBURDEN WASTE

Koushik Das[1], Debjit Bhowmik[2], Bappaditya Manna[1], Ramanathan Ayothiraman[1]
[1] Department of Civil Engineering, Indian Institute of Technology Delhi, New Delhi, India
[2] Department of Civil Engineering, National Institute of Technology Silchar, Assam, India

1. Introduction

Overburden wastes are produced in granular form during blasting for mining all over the world. Granular sand-sized sandstone particles are produced typically from the coal mining. Globally, one major social and environmental concern is how to dispose and utilize such granulated overburden waste. One of the main causes of the significant amount of natural resources being consumed is the rapid infrastructure development. Several researchers have studied various aspects of using granulated sandstone as aggregate to produce new concrete, thus reducing the problem of waste and helping to preserve natural aggregate resources [1]. From both an economic and environmental perspective, the use of waste materials in civil engineering practice is always appreciated. There is no significant study available that has utilized such an overburden waste from coal mines for various applications in geotechnical engineering. A comprehensive understanding of the dynamic behavior of a material is necessary for the designs of geotechnical structures, including foundations, pavements, and earth-retaining structures subjected to dynamic loads. Therefore, investigation of of dynamic behavior is essential to evaluate its potential as a geomaterial and utilizing it for various geotechnical applications.

2. Investigation Method

In the present study, a fixed-free-type longitudinal Resonant Column Apparatus (RCA) following ASTM D4015–2021 specifications [2] has been utilized to evaluate the dynamic properties of granulated sandstone such as shear modulus (G) and damping ratio (D) for a range of shear strain levels and confining pressures.

2.1 Material Used

Sandstone, as a granulated overburden waste, is collected from a coal mine in India. The specific gravity is determined to be 2.57 and natural moisture content 5.6 %. Particles finer than 4.75mm sieve is considered for the study (D_{10}~ 0.25 mm, D_{30}~ 0.45 mm, D_{50} ~ 0.6 mm, D_{60} ~ 0.8 mm).

2.2 Sample Preparation and Test Procedures

A split mould with a rubber membrane is used to prepare samples (70 mm diameter, 140 mm height) by filling it with a measured dry mass of sample in compacted layers to achieve the uniform relative density. Negative suction pressure maintains the sample's shape until the minimum confining pressure is applied, after which suction is replaced with backpressure. Confining pressure is provided via an air compressor. Harmonic torsional excitation is applied using an electromagnetic system and the excitation frequency is swept from 10–190 Hz to identify the resonant frequency, with finer adjustments near resonance. Shear modulus is calculated from the resonant frequency at maximum shear strain. Damping tests are conducted by applying transient forces and analyzing free vibrations

using the logarithmic decrement method over 10 cycles. Tests are performed at 50, 100, and 150 kPa confining pressures with strain levels ranging from 10^{-4}% to 10^{-2}%.

3. Results and Discussions

The investigation results are greatly dependent on the level of strain as well as the confining pressure it is subjected to. The shear modulus increases with the increase in confining pressure, as anticipated from an increase in particle-to-particle contacts. The shear modulus is normalized with the maximum shear modulus (G_{max}) corresponding to the smallest strain level to obtain the modulus degradation curve, as presented in Figure 1(a). The modulus decreases as the shear strain increases. With an increase in confining pressure, the rate of modulus degradation is less. Several researchers have reported similar observations for other geomaterials [3–5].

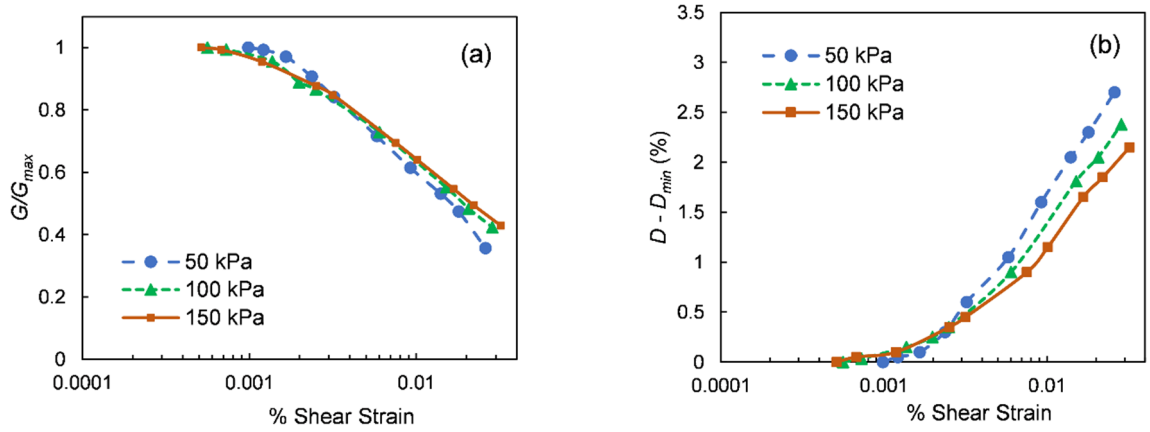

Fig.1. (a) Modulus degradation curve and (b) Damping curve

Similarly, damping ratio is normalized comparing with minimum damping ratio (D_{min}) at smallest strain level as presented in Figure 1(b). It is evident that, as the shear strain increases, damping value increases as anticipated, as evidenced by the similar observations of numerous researchers [3–5]. Damping is less for higher confining pressure as evident from an increase in stiffness of the sample. The shear modulus and damping ratio obtained in this laboratory investigation provides insights to understand the material behaviour in dynamic loading conditions under a range of shear strain enabling comparison with different geomaterials to assess the possibilities of utilizing such a mining waste for various geotechnical applications with economical and environmental benefits.

5. References

[1] Nuaklong P, Sata V, Chindaprasirt P (2015). Influence of recycled aggregate on fly ash geopolymer concrete properties. https://doi.org/10.1016/j.jclepro.2015.10.109.

[2] ASTM D4015 (2021). Test Methods for Modulus and Damping of Soils by Fixed-Base Resonant Column Devices. https://doi.org/10.1520/D4015-21.

[3] Senetakis K, Anastasiadis A, Pitilakis K, Souli A (2012). Dynamic behavior of sand/rubber mixtures, part II: Effect of rubber content on G/Go-γ-DT curves and volumetric threshold strain. *ASTM Special Technical Publication*;1540 STP:248–64. https://doi.org/10.1520/JAI103711.

[4] Anastasiadis A, Senetakis K, Pitilakis K, Gargala C, Karakasi I (2012). Dynamic Behavior of Sand/Rubber Mixtures. Part I: Effect of Rubber Content and Duration of Confinement on Small-Strain Shear Modulus and Damping Ratio. *Testing and Specification of Recycled Materials for Sustainable Geotechnical Construction*:221–47. https://doi.org/10.1520/STP154020120011.

[5] Das S, Bhowmik D (2020). Dynamic Behaviour of Sand–Crumbed Rubber Mixture at Low Strain Level. *Geotechnical and Geological Engineering*;38:6611–22. https://doi.org/10.1007/S10706-020-01458-4/FIGURES/12.

PREDICTION OF INTERNAL DAMAGE IN GFRP LAMINATES CAUSED BY REPEATED LOW VELOCITY IMPACTS USING ARTIFICIAL INTELLIGENCE METHODS

D.E. Tria[1], H.E. Hebbouche[1], A. Lourari[1], S. Boukhaoua[1]
[1] Ecole Militaire Polyechnique, BP17, Bordj el Bahri,16111, Algiers, Algeria.

1. Introduction

Composite structures used in aerospace and offshore applications frequently experience repeated low-velocity impacts in localized regions during service [1]. These impacts gradually lead to matrix cracking, delamination, and fiber fractures, which compromise structural integrity and increase the risk of unexpected failure [2]. Artificial intelligence (AI)-based methods have shown significant potential for automating damage assessment, including damage classification, quantification, and predicting the remaining useful life of structures. For instance, Zargar and Yuan [3] demonstrated the use of a physics-inspired deep learning (DL) model to characterize impact damage by analyzing the evolution of impact-generated propagating waves. Similarly, Fotouhi et al. [4] utilized DL techniques for quantitatively assessing microscale damage (e.g., matrix cracking) and macroscale damage (e.g., impact and erosion). By analyzing images of impacted and non-impacted surfaces, their model achieved validation accuracies of 96% and 87%, respectively, underscoring the potential of DL to automate visual inspections. However, their findings also emphasized the need for improved datasets and customized classifiers to enhance DL model performance. While a single low-velocity impact may not visibly damage composite structures, repeated impacts often lead to cumulative effects, making maintenance and safety assurance more challenging. Fiber-reinforced composites, widely valued for their lightweight, high strength, and stiffness, are particularly susceptible to low-velocity impacts due to their limited transverse load-bearing capacity. Although much research has addressed single-impact scenarios [1-5], repeated impacts better reflect real-world conditions, where cumulative damage can surpass that caused by a single high-energy impact.

This study focuses on understanding the damage accumulation and failure mechanisms in glass fiber-reinforced epoxy composite laminates subjected to repeated low-velocity impacts. By combining experimental data with AI-driven tools, this research provides a robust framework for assessing damage, offering cost-effective inspection solutions, improving durability, and enhancing the safety of aerospace structures.

2. Materials and methods

Experiments were conducted using an instrumented drop-weight tower, applying localized impacts at energy levels of 6J and 25J with hemispherical, conical, and truncated-conical impactors. Mechanical responses were characterized through force-time, displacement-time, and energy-time curves, and visual inspection images of damage zones. For each impact, key metrics, including delamination area, energy absorption, peak impact force, bending stiffness, maximal displacement, and impact duration, were analyzed. Based on this experimental data, an artificial intelligence (AI) methodology was developed to predict damage dimensions and their influence on mechanical properties. A database was constructed from the experimental results, capturing diverse damage profiles induced by repeated low-velocity impacts. This database served as input for training deep learning and machine learning models, which were tested in both parallel and sequential architectures.

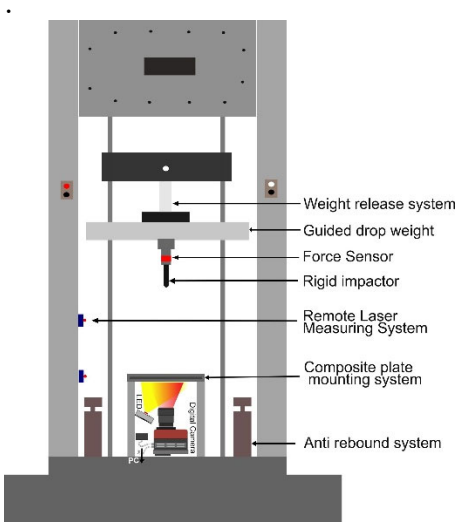

Fig.1. Drop weight tour system.

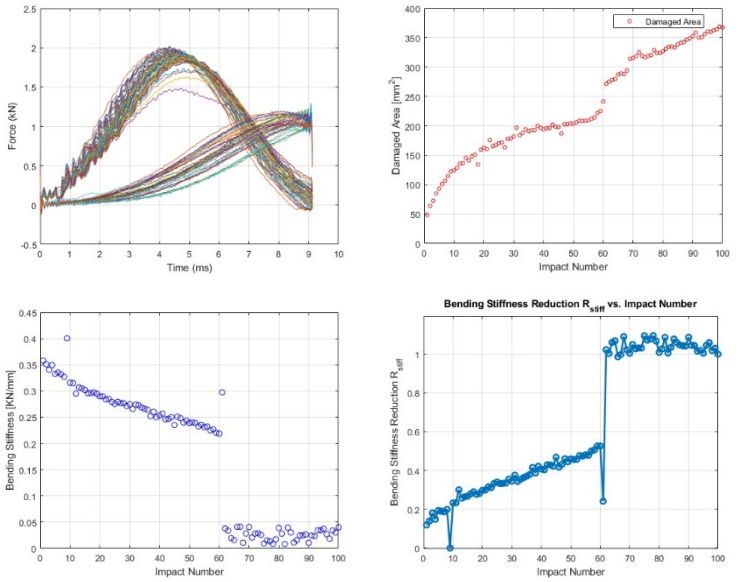

Fig. 2. Low velocity impact data.

3. Results and conclusions

The results revealed that delamination growth ceased after a certain number of impacts, while bending stiffness continued to decrease due to progressive fiber rupture. The evolution of delamination areas varied with impactor geometry and laminate thickness, underscoring the need for advanced methods to predict damage progression and assess structural integrity. The AI models demonstrated high reliability and efficiency in predicting internal damage characteristics and assessing the residual performance of composite structures.

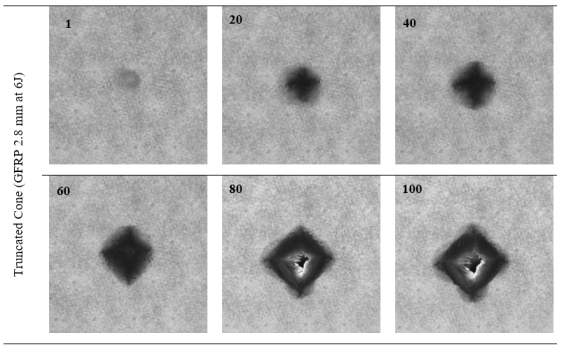

Fig. 3. Visual inspection images showing damage area evolution.

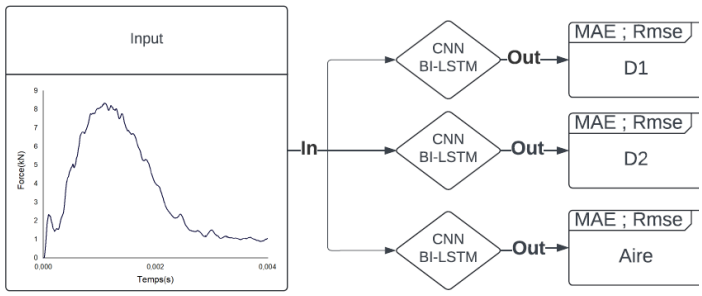

Fig. 4. Combined CNN and Bi-LSTM models for predicting damaged area size.

4. References

[1] Zhou J, Liao B, Shi Y, Zuo Y, Tuo H, Jia L. Low-velocity impact behavior and residual tensile strength of CFRP laminates. Compos Part B-Eng 2019; 161:300-13..J.

[2] Cao Y, Cao Z, Zhao Y, Zuo D, Tay TE. Damage progression and failure of single-lap thin-ply laminated composite bolted joints under quasi-static loading. Int J Mech Sci 2020; 170:105360.

[3] Zargar SA, Yuan FG. Impact diagnosis in stiffened structural panels using a deep learning approach. Struct Health Monit 2021;20:681–91.

[4] Fotouhi S, Pashmforoush F, Bodaghi M, Fotouhi M. Autonomous damage recognition in visual inspection of laminated composite structures using deep learning. Compos Struct 2021;268:113960.

[5] Paolino DS, Cavatorta MP, Belingardi G. Effect of thickness on the damage tolerance of lass/epoxy laminates subject to repeated impacts. P I Mech Eng C-J Mec 2017; 232:1363-73.

6-11 July 2025 ICEM21 Bologna
21st International Conference on EXPERIMENTAL MECHANICS

DYNAMIC CENTRIFUGE TEST ON THE EFFECT OF VERTICAL EXCITATION ON LIQUEFIABLE GROUND

K.R. Huang[2], Y. Yuan[1, 2], Z.X. Fan[2]
[1] State Key Laboratory of Disaster Reduction in Civil Engineering, Shanghai, China
[2] Department of Geotechnical Engineering, Tongji University, Shanghai, China

1. Introduction

Liquefaction induced earthquake damage occurred frequently in saturated ground. In the 2010-2011 Canterbury earthquake sequence, spatially extensive liquefaction induced failures occurred in Christchurch, which were accompanied by strong vertical ground acceleration [1]. In general, the liquefaction failure of saturated sand ground is triggered by horizontal seismic excitation. Previous research [2] has suggested that the influences of the vertical acceleration on soil liquefaction were negligible in fully coupled dynamic numerical simulation. Similarly, Tsaparli et al. [3] investigated vertical acceleration amplification and ensuing liquefaction with finite element analysis and found that vertical motion propagation through saturated sand deposit may lead to significant deviatoric stresses, plasticity and possibly liquefaction. Based on dynamic centrifuge tests, Wang et al. [4] believed that although the effect of vertical excitation on soil liquefaction can be ignored, its influence on the internal force of the structure is significant. Obviously, the effect of vertical earthquake on liquefiable ground needs further research.

This study conducted a dynamic centrifuge test on saturated sand deposit and deals with the seismic response of liquefiable ground under vertical earthquake. The results indicated that the oscillation of excess pore pressure is more pronounced with vertical motion. The effect of the vertical earthquake on the horizontal acceleration response of the liquefiable ground is slight.

2. Materials and methods

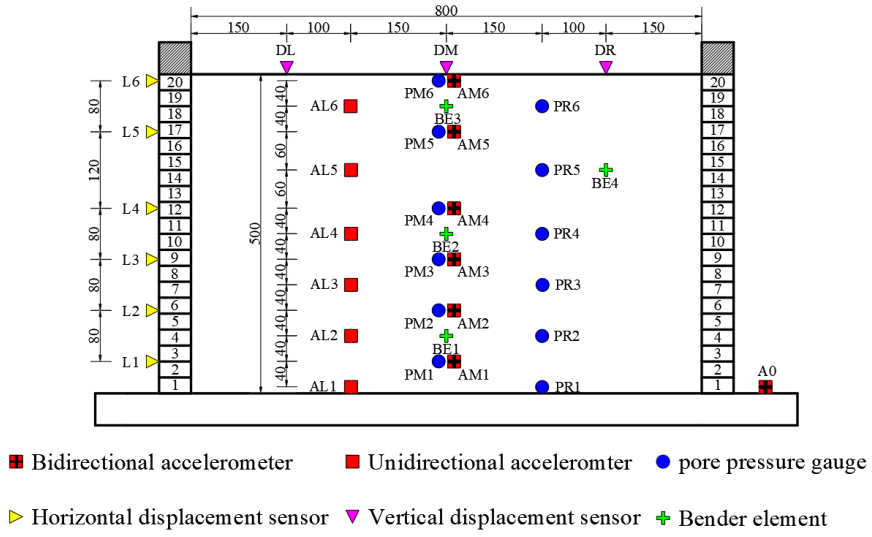

Fig. 1. The measurement scheme and instrumentation layout

Fujian intermediate sand with particle size between 0.5mm and 1.0mm was selected for centrifuge test. The model ground with a height of 500mm was prepared by the air pluviation method inside a laminar container. The relative drop height was controlled to obtain target relative density of 50% for model ground. The centrifugal accelerations was set at 50g to match pressure of prototype deposit. After four identical horizontal sinusoidal waves with 15 cycles, horizontal and vertical excitations were applied simultaneously. Four types of sensors were installed to capture the dynamic response of the model ground. The accelerometers and pore pressure transducers were positioned intensively to measure the acceleration and pore pressure response. The lateral displacement and settlement of the ground were obtained from displacement sensors. Pairs of bender elements were placed to measure the variation of shear velocity of saturated sand deposit. The measurement scheme and instrumentation layout is shown in Fig. 1.

3. Results and conclusions

Acceleration response and excess pore pressure ratio of liquefiable ground under horizontal unidirectional excitation and horizontal and vertical bidirectional seismic excitation are plotted in Fig. 2. The effect of the vertical earthquake on the horizontal acceleration response of the liquefiable ground is slight. The oscillation of excess pore pressure is more pronounced with vertical motion.

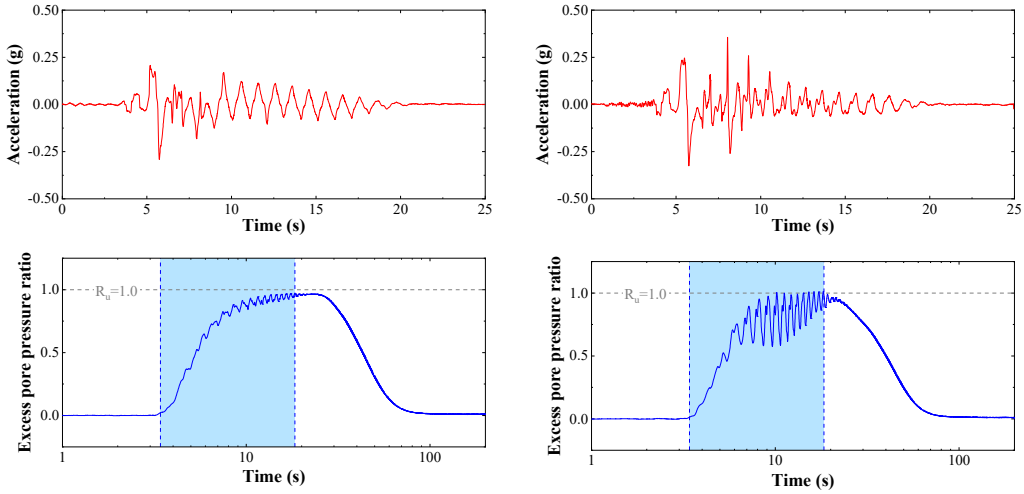

(a) unidirectional (b) bidirectional

Fig. 2. Acceleration response and excess pore pressure ratio of liquefiable ground:

4. Acknowledgements

The authors acknowledge support from the National Natural Science Foundation of China (52061135112).

5. References

[1] R.P. Orense, T. Kiyota, S. Yamada, M. Cubrinovski, Y. Hosono, M. Okamura and S. Yasuda (2011). Comparison of liquefaction features observed during the 2010 and 2011 Canterbury earthquakes. *Seismological Research Letters*, **82**, 905–918.

[2] H. Liu and E.X. Song (2005). Seismic response of large underground structures in liquefiable soils subjected to horizontal and vertical earthquake excitations. *Computers and Geotechnics*, **32**, 223-244.

[3] V. Tsaparli, S. Kontoe, D.M. Taborda and D.M. Potts (2017). An energy-based interpretation of sand liquefaction due to vertical ground motion. *Computers and Geotechnics*, **90**, 1-13.

[4] R. Wang, T. Zhu, J.K. Yu and J.M. Zhang (2022). Influence of vertical ground motion on the seismic response of underground structures and underground-aboveground structure systems in liquefiable ground. *Tunnelling and Underground Space Technology*, **122**, 104351.

CELLUAR STRUCTURE OF METHYL VINYL SILICONE RUBBER FOAM AND ITS EFFECT ON MECHANICAL PROPERTIES

Bin Dai[1], Yafei Yang[1], GuoFang Ding[1], Luoshi Kai[1] and Cui Zhang[1]
[1] Institute of Chemical Materials, Chinese Academy of Engineering Physics, Mianyang, China

1. Introduction

Due to both the excellent performance of silicone rubber and lightweight of foam materials, silicone rubber foam material are excellent to be used as vibration damping, sound insulation, heat insulation, sealing materials. Used for positioning and shock absorbing between the precision parts is one of most important applications, so it required to have the capacities of good elastic recovery, low compression set and long term load holding, all the features are associated with the compression stress-strain and stress-relaxation properties of the silicone rubber foam materials. Schneider et al. [1-5] had obtained the stress-relaxation data at different temperatures after a long-term study on the stress-relaxation properties of silicone rubber foam materials.In recent years, we have carried out a series of studies on the preparation, structure and performance of silicone rubber foam material[6-9], and got the conclusions that foam materials with spherical cell have better mechanical properties. Referred to our previous work, we prepared spherical cell aperture silicone rubber foam materials with different cell sizes by the way of physical foaming to study the relationship between the cell size with the compression stress-strain property and compression stress-relaxation property, meanwhile, we monitored the changing of cell in the dynamic compression process by using micro-focus CT technology.

2. Materials and methods

Using polymethylvinylsiloxane as a raw rubber, silica as reinforcing filler, and spherical urea with different sizes prepared by ourselves as cell-forming agent, four kinds of foam materials with different cell diameters after heat vulcanization were obtained , the porosity was about 50%, the density was 0.55g/cm^3.

In this study, we designed a special dedicated compression device, using microfocus CT technology to observe the three-dimensional structure change internal the cell of silicone rubber foam materials(12mm in sample diameter, thickness of 4.5mm) in the process of dynamic compression, obtained the regular pattern of deformation of cell structure and the porosity.

3. Results and conclusions

The mechanical properties of methyl vinyl silicone rubber foam materials with different cell diameters of the spherical cell structure were investigated. The results showed that the cell diameter had significant effects on the mechanical properties,the foam materials with cell diameter range 300~450μm had the best compression stress property and stress-relaxation property. The changing of cell shape of the spherical cell foam materials in the process of dynamic compression were analyzed by using micro focus uCT technology, with obtaining the parameters of cell volume, porosity and so on.

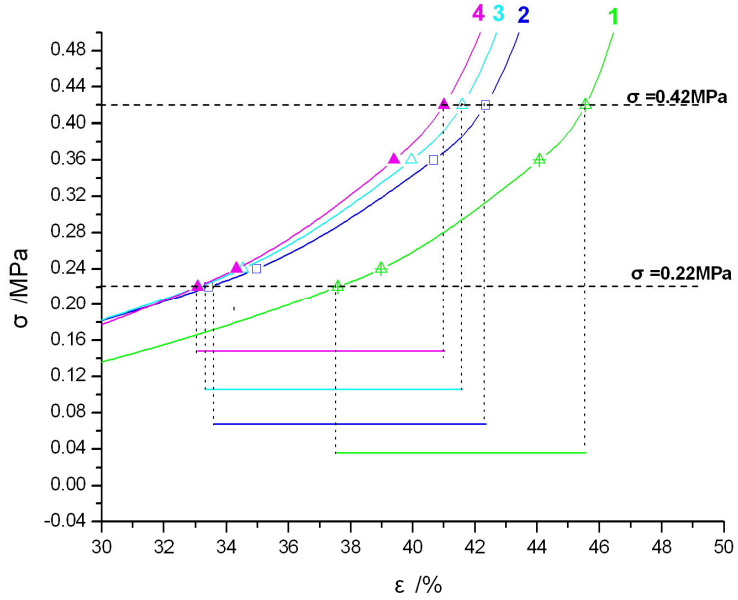

Fig. 1. The compression σ-ε curve of silicone rubber foam materials with different cell diameters
(1. 100~200μm 2. 200~300μm 3. 300~450μm 4. 450~600μm 5. 600~800μm)

Compression state	A	D	I
average pore size /um	146.2	145.4	105.6
average wall thickness /μm	295.6	659.3	219.7
average cell number	589	493	351
average cell density /mm2	13.1	10.4	6.8
the average bubble cell area /μm2	25132.7	24383.3	10802.4
The average size of hole wall /μm2	196242	224568	333090

Table 1. The changing of cell parameter in the compression process of samples

5. References

[1] Schneider .J W . Stress erlation of cellular Siliecone material[R], USA :Bendix K ansas City Division, 1980
[2] Schneider .J W . Stress erlation of cellular Siliecone material[R], USA :Bendix K ansas City Division, 1981
[3] Schneider .J W . Stress erlation of cellular Siliecone material[R], USA :Bendix K ansas City Division, 1982
[4] Schneider .J W . Stress erlation of cellular Siliecone material[R], USA :Bendix K ansas City Division, 1984
[5] Schneider .J W . Stress erlation of cellular Siliecone material[R], USA :Bendix K ansas City Division, 1985

[6] Chen Meihua, Luo Shikai, Zhao Qi, Lei Wei hua, Li Yan, Study on the influence of the molecular weight of si licone rubber on the performance of silicone foam, *New Chemical Materials*, 2011,**39**(8):65-68
[7] Ding Guo fang, Cao Jun, Zhang Chang sheng, Luo Shi kai, Study on influence of blowing agent particle size on properties of the silicone rubber foams, *New Chemical Materials*, 2012, **40**(11) : 120-122
[8] Sha Yan song, Zhang Chang sheng, Luo Shi kai, Performance research on BPO crosslinked silicone rubber foam material, *New Chemical Materials*, 2013,**41**(1) : 54-56
[9] Sha Yan song, Zhang Chang sheng, Li Jing li, Luo Shi kai, Effects of Cell Structure on Properties of Silicone Rubber Foam Material, *Materials for Mechanical Engineerring*, 2013, **37**(2):25-28

HMX BASED ENERGETIC MATERIAL COMBUSTION IN A SPHERICAL CONTAINER AND ITS QUANTITATIVE MODEL OF REACTION PRESSURE

C. Pan, X. Yang, X. Huang, T. Li , H. Fu, H. Shang, P. Li

Institute of Fluid Physics, China Academy of Engineering Physics, Mianyang, China

1. Introduction

Charges was ignited with non-shock accidentally, possibly developed into deflagration and even detonation, resulting in disastrous consequences. If an engineering model can be proposed to describe the charge reaction evolution process and quantify the charge reaction intensity, which was of great significance for evaluating the charge safety. Therefore, recently models related to the explosive combustion reaction have been investigated, involving the simple laminar burning, single crack convection theory, phenomenological model and simulation method, etc. However, there is no unified theory or method that can completely reveal and predict a series of complex phenomenon in charge combustion reaction process. Hill [1] established a phenomenological model to directly solve the combustion reaction pressure and describe the charge reaction intensity, which is worth learning and feasible. However, Hill phenomenological model has many assumptions and limitations, and its key criterion: the critical pressure criterion for burning crack propagation lacks the description of the burning crack influence mechanism.

2. Model establishment

In this work, a constrained charge combustion reaction evolution model of is established with fracture toughness and reaction pressure as the main parameters based on the Visco-Scram theory [2], which can describe the combustion gaseous product pressurization and shell constraint strength during combustion evolution. The critical pressure criterion for burning crack propagation was as follows.

$$\Phi = \frac{S_c}{S_{max}} = [1 - c(\frac{{K_{IC}}^2}{Pl_0})^a]^b \tag{1}$$

A General formula for calculating reaction pressure was proposed, which can be solved analytically based on Euler method, as follows.

$$\frac{dP}{dt} = \frac{\rho_{e0}\alpha}{12m_e(t)} \frac{(3M_0+2\eta P)^2}{3M_0+(4\eta-1)P} \left[\frac{6P}{(3M_0+2\eta P)} + \rho_{e0}\omega R_p T_p S_c(P)\right] P^{\beta-1} \tag{2}$$

3. Results and conclusions

The retrieved curves are plotted together in **Fig. 1**, along with dots indicating the experimental data. The statistical test indicates the differences among the curves are not significant, i.e. they are confounded by the experimental uncertainty. Therefore, the results were then sorted out, to determine a unique fatigue limit.

The model reliability of charge reaction combustion evolution was verified via central ignition experiment of highly constrained spherical 95% HMX-based explosive PBX-1, as shown in Fig.1. Compared to Hill's model, the present model was more consistent with experimental tests, including laminar combustion accumulated pressure, shell response and burning cracks accelerated pressurization, which can be seen in **Fig. 2**. Moreover, the present model can better reflect the slow pressurization characteristics dominated by explosives surface laminar combustion. This study can help the engineering simulation analysis and essential physical mechanisms explanation on constrained explosives combustion reaction.

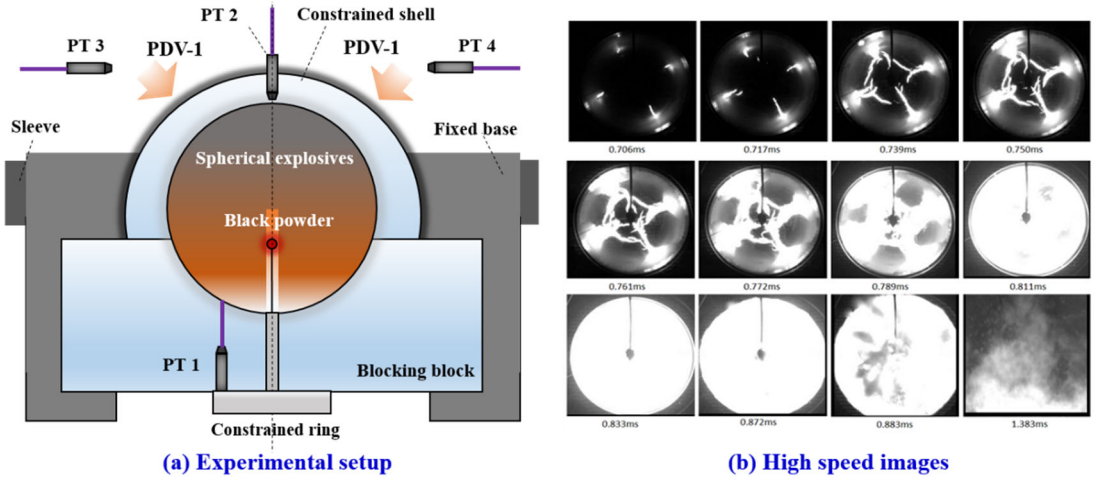

Fig. 1. Schematic experimental setup of spherical explosives with strong confinement.

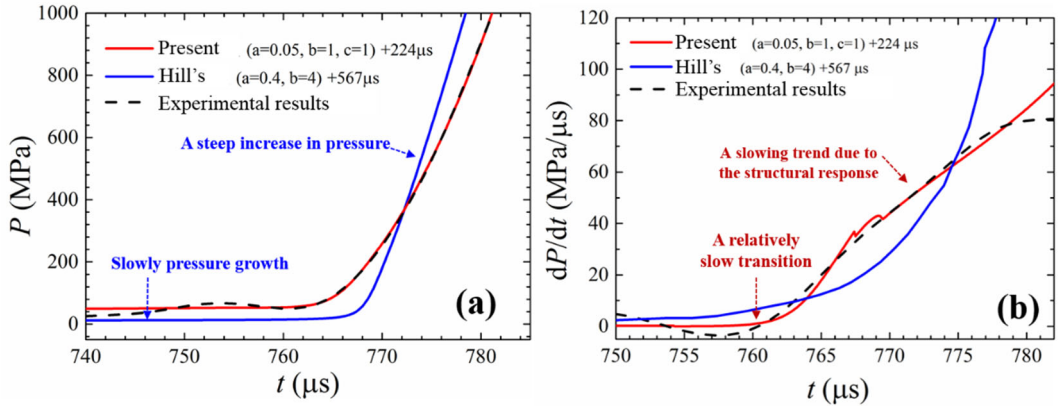

Fig. 2. Comparison of calculated and experimental reaction pressure and pressure growth rate: (a) reaction pressure; (b) reaction pressure growth rate.

4. Acknowledgements

The research presented in this paper has received funding from the NSFC program No.12402445 and National Key Laboratory Foundation (2024CXPTGFJJ06404).

5. References

[1] LG. Hill. Burning crack networks and combustion bootstrapping in cookoff explosions(2006). A*IP Conference Proceedings,* 845: 531-534.

[2] JG. Bennett, KS. Haberman, JN. Johnson, et al. A constitutive model for the non-shock ignition and mechanical response of high explosives(1998). *J Mech Phys Solids*, 46(12): 2303-2322.

Abnormal dynamic behavior in an FCC high entropy alloy under extreme loading conditions

Jianguo Li[1,2,3,4,5*], Kun Jiang[1] and Tao Suo[1,2,3,4,5*]

[1] School of Aeronautics, Northwestern Polytechnical University, Xi'an, China
[2] Institute of Extreme Mechanics, Northwestern Polytechnical University, Xi'an, China
[3] Shaanxi Key Laboratory of Impact Dynamics and its Engineering Application, Xi'an, China
[4] Joint International Research Laboratory of Impact Dynamics and its Engineering Application, Xi'an, China
[5] National Key Laboratory of Strength and Structural Integrity, Xi'an, China

Ever more extreme environments in advancing industrial applications motivate efforts to design new generation of alloys with excellent mechanical properties. High entropy alloys (HEAs) are considered as promising candidates for bearing extreme loadings. However, the reported results of correspondence between extremely mechanical behaviors and micromechanisms are still in infancy. Here we showed mechanical responses over wide strain rate and temperature ranges and microscopic observations recovered from dynamic uniaxial tension of face-centered cubic (FCC) HEA to reveal plasticity mechanisms transition under various loading conditions. As shown in Fig.1, with an increasing strain during the extreme dynamic tension a sequence of mechanisms, including twinning, detwinning-induced localization, nanoscale body-centered cubic (BCC) phase transformation and symbiotic amorphization, were progressively activated for continued plasticity. At strains over 35%, twin boundaries hindrance to localized band propagation and more dislocations emitting from BCC phases even collectively caused a second sharp rise in hardening. Additionally, the plasticity kept

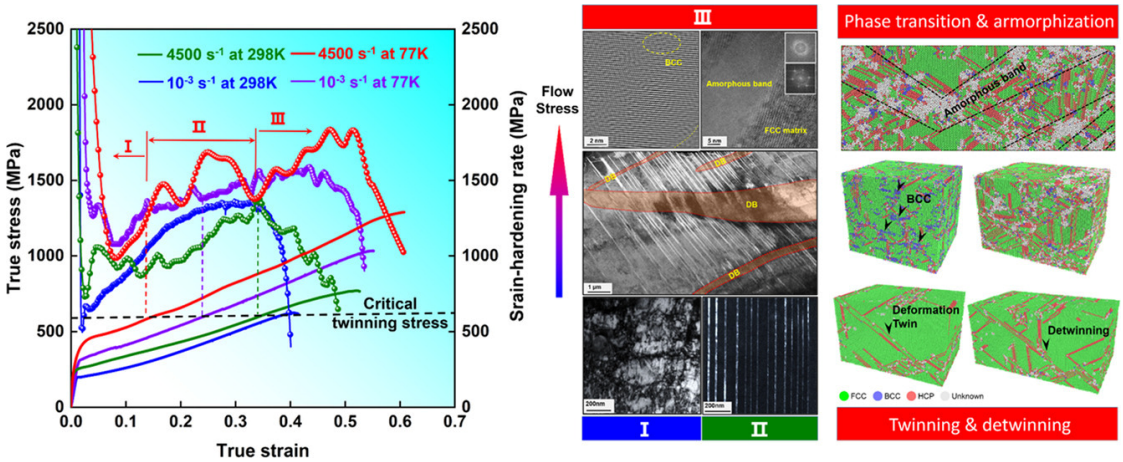

Fig.1. The typical mechanical responses of $Al_{0.1}CoCrFeNi$ HEA under various loading conditions.True stress-strain curves and the evolution of work hardening rate with increasing strain. Microscopic observations reveal the transition of dominated plasticity mechanisms from dislocation slip to deformation twins, and further to nanoscale phase transformation as well as solid-state amorphization transition under extreme tension. MD simulation results showing the amorphization transformation mechanism for this FCC HEA.

increasing during crystal to amorphization transition, which should be promoted by severe lattice distortion in super-dense dislocations areas. By combining large scale molecular dynamic simulations, the causes of phase transition to BCC lattice structure or even to amorphous bands were explained in depth. The thorough uncovering of these brand-new mechanisms can help understand the plasticity and amorphization of HEAs under the extreme loadings.

We also investigated the dynamic compressive behavior of this Al0.1CoCrFeNi HEA via a series of split Hopkinson pressure bar (SHPB) experiments at 77 K and room temperature. As stated above about its tension behavior, due to its strong strain hardening, remarkable strain rate sensitivity and moderate temperature dependence, the FCC high/medium entropy alloys (H/MEAs) usually are believed to have remarkable resistance to shear localization even under forced dynamic shear. However, when dynamically loaded at 77 K, its dynamic compressive failure was found to be caused by crack propagation within the primary adiabatic shear bands (ASBs) along the directions of maximum shear stress. Detailed examination of the specimens using electron backscatter diffraction (EBSD) and transmission electron microscopy (TEM) revealed convincing microstructural evidences for massive dynamic recrystallization (DRX) prior to ASB. We suggested that the expansion and coalescence of these DRX softened regions served as the root cause for the occurrence of ASBs and the final catastrophic fracture of specimens. The severe local shear flow, substantial adiabatic temperature rise and extremely fast quenching within the ASB resulted in ultrafine grains therein. Our results and analyses provided a plausible understanding of the formation mechanisms of ASBs in the FCC HEA under impact loading.

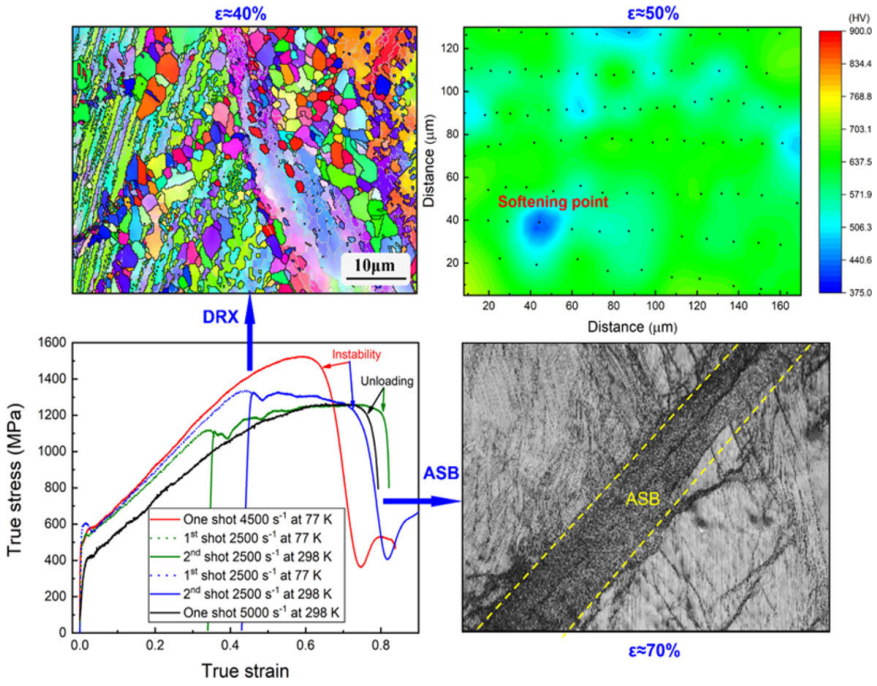

Fig.2 Typical true stress-strain curves of Al0.1CoCrFeNi under dynamic compression at different temperatures by one-shot load or interrupted loads. The green and blue curves were from interrupted dynamic tests, i.e., preloaded to 30% and 40% strains respectively at 77 K, and then loaded at 298 K. Two specimens that failed by ASB (marked by “Instability”).EBSD showing massive DRX grains in the dynamically deformed specimen to a strain of 50% at 77 K, and microhardness distribution after dynamic loading at 77 K to a strain of 50% reveals the softening effect and hence promoting the formation of ASBs.

Keywords
High entropy alloy, Extreme dynamic loading, Dynamic behavior, Plasticity mechanisms, Solid state amorphization, Adiabatic shear band, Dynamic recrystallization, Molecular dynamic simulations.

Acknowledgements
This work was financially supported by National Natural Science Foundation of China (Grant Nos. 12025205, 12102363 and 11972310). J. L also thanked the financial support from the Fundamental Research Funds for the Central Universities (Grant No. G2021KY05102).

References
[1] Kun Jiang, Qian Zhang, Jianguo Li, Xiaoyan Li, Feng Zhao, Bing Hou, Tao Suo (2022) Abnormal hardening and amorphization in an FCC high entropy alloy under extreme uniaxial tension, *International Journal of Plasticity*, **159**, 103463. https://doi.org/10.1016/j.ijplas.2022.103463
[2] Kun Jiang, Jianguo Li, Xiukai Kan, Feng Zhao, Bing Hou, Qiuming Wei, Tao Suo (2023) Adiabatic shear localization induced by dynamic recrystallization in an FCC high entropy alloy, *International Journal of Plasticity*, **162**, 103550. https://doi.org/10.1016/j.ijplas.2023.103550

RATE-DEPENDENT FAILURE OF TRANSVERSELY-ISOTROPIC ROCK THAT EXHIBITS A BI-MODULUS CONSTITUTIVE RESPONSE

A. T. Guthai[1], A. F. Fahem[2], and R. P. Singh[3]
[1]Corning Research and Develop Division, Corning Inc., Corning, New York, USA
[2]Department of Mechanical Engineering, College of Engineering, University of Al-Qadisiyah, Al-Diwaniyah, Iraq
[3]School of Mechanical and Aerospace Engineering, and School of Materials Science and Engineering, College of Engineering, Architecture and Technology, Oklahoma State University, Tulsa, Oklahoma, USA

1. Introduction

Shale is a clastic (clay-containing) sedimentary rock that serves as the primary resource to produce hydrocarbons from rock sources. Typically, hydraulic fracturing is used for releasing the trapped organic matter from shale. Thus, a fundamental characterization of the dynamic failure evolution of shale, as a function of loading rate, is necessary for tuning the fracture response to maximize extraction efficiency and minimize the use of water for the hydraulic fracturing process.

The layered nature of shale, as a sedimentary rock, along with the inclusion organic mat- ter and the pre-existence of microstructural defects lead to an overall transversely-isotropic response [1, 2]. As expected, the constitutive response of shale is affected by both the loading rate, the degree of confinement, and material anisotropy [3, 4]. While the constitutive response of shale has been characterized extensively under both quasi-static and dynamic loading conditions, the effect of loading rate on the failure response, as a function of anisotropy is not well studied. In addition, recent studies have demonstrated that shale can exhibit a bi-modulus response, where the constitutive properties are affected by the tensile or compressive state of stress [5]. The effect of this constitutive response on the dynamic failure properties is yet to be examined in detail.

In this work we report of the failure response of shale as a function of loading rate. The quasi-static, and dynamic, tensile and compressive strengths are determined for the two orthogonal principal material directions given as parallel and perpendicular to the bed- ding plane of the sedimentary rock microstructure. The rate-dependent failure response is then compared for three different kinds of shale to illustrate the effects of the bi-modulus constitutive response and the level of transverse-isotropy on the failure behavior.

2. Materials and methods

The failure response was studied using a Brazilian disk specimen configuration subjected to diametral compressive loading. The test specimens were fabricated from three different shales from the Arkoma Basin in Coal County and the Anadarko Basin in Canadian and Kingfisher Counties of Oklahoma, USA. The three materials exhibit variations in the level of transverse-isotropy and bi-modulus response under quasi-static loading conditions, as determined by a prior study. The as-received core samples were cut into a disk geometry of diameter, D ≈ 25.4mm, and thickness, t ≈ 5mm, to provide a t/D ratio of 0.2, as per ASTM-D3967[6]. The machining was done using a low-speed metallographic saw and coring drill to minimize surface induced damage that could affect the failure process.

Diametral compression experiments under quasi-static loading conditions were conducted using a screw-driven mechanical test frame under displacement control. The load vs displace- ment data was recorded until failure, and the strength was determined using the peak failure load. Diametral compression experiments under dynamic loading conditions were conducted using a split-Hopkinson pressure bar and once again the strength was determined using the peak failure load. Both types of experiments were conducted for loading orientations along both principal material directions to determine the direction- and bi-modulus-dependent failure strength. High-speed imaging during the dynamic loading tests allowed for characterization of the failure process and identification of the time of failure initiation.

3. Results and conclusions

In general, it was observed the both the compressive and tensile strengths were higher for the dynamic loading condition. The differences in the compressive and tensile strengths, however, were dependent on the loading rate and on the shale microstructure. This indicates that certain shales can exhibit greater strength anisotropy as the loading rate increases. This difference is due to inertial effects that govern the initiation of failure from pre-existing flaws that are inherent to these shales.

Further details of the quantitative results, the load-dependent fracture behavior, and the interplay between constitutive properties and the fracture behavior will be discussed at the conference presentation.

4. Acknowledgements

This material is based upon work supported by the Department of Energy under Award Number DE-FE0031777. This report was prepared as an account of work sponsored by an agency of the United States Government. Neither the United States Government nor any agency thereof, nor any of their employees, makes any warranty, express or implied, or assumes any legal liability or responsibility for the accuracy, completeness, or usefulness of any information, apparatus, product, or process disclosed, or represents that its use would not infringe privately owned rights. Reference herein to any specific commercial product, process, or service by trade name, trademark, manufacturer, or otherwise does not necessarily constitute or imply its endorsement, recommendation, or favoring by the United States Government or any agency thereof. The views and opinions of authors expressed herein do not necessarily state or reflect those of the United States Government or any agency thereof.

5. References

[1] Gautam, R. & Wong, R. C. Transversely isotropic stiffness parameters and their measurement in Colorado shale. *Canadian Geotechnical Journal*, **43**, 1290–1305, 2006.

[2] Wong, R. C. K., Schmitt, D. R., Collis, D. & Gautam, R. Inherent transversely isotropic elastic parameters of over-consolidated shale measured by ultrasonic waves and their comparison with static and acoustic in situ log measurements. *Journal of Geophysics and Engineering*, **5**, 103–117, 2008.

[3] Sayers, C. M., Van Munster, J. G. & King, M. S. Stress-induced Ultrasonic Anisotropy in Berea Sandstone. *International Journal of Rock Mechanics and Mining Sciences & Geomechanics Abstracts*, **27**, 429–436, 1990.

[4] Omovie, S. J. & Castagna, J. P. Relationships between Dynamic Elastic Moduli in Shale Reservoirs. *Energies*, **13**, 6001, 2020.

[5] Fahem, A. F., Thumbalam Guthai, A. & Singh, R. P. Full-Field Strain Measurement Integrated with Two Dimension Regression Analysis to Evaluate the Bi-Modulus Elastic Properties of Isotropic and Transversely Isotropic Materials. *Experimental Mechanics*, **64**, 53–71, 2024.

[6] D18 Committee. Test Method for Splitting Tensile Strength of Intact Rock Core Specimens. http://www.astm.org/cgi-bin/resolver.cgi?D3967-23.

6-11 July 2025 ICEM21 Bologna
21st International Conference on EXPERIMENTAL MECHANICS

CRACK GROWTH BEHAVIOR AND COMBUSTION REACTION EVOLUTION OF THE HOLED EXPLOSIVE DISKS

X. Yang[1], H. Shang[1], T. Li[1], L. Yang[1], M. Li[1], Z. Wu[1]
[1] *Institute of Fluid Physics, China Academy of Engineering Physics, Mianyang, China*

1. Introduction

When the confined high explosives (HE) hit by fragments, fall and collide by accident, non-shock initiation may occur and undergo a high-intensity reaction, resulting in catastrophic consequences. Different from the traditional detonation process, the essence of the non-shock initiation reaction is the combustion reaction initiated by the local high temperature caused by the thermal decomposition of HE. When the restraint is strong enough, the transient high pressure produced by the coupling effect of dynamic crack propagation and combustion reaction will lead to rapid breakage of HE, resulting in a sharp increase in the combustion surface area and a high intensity reaction [1]. The complex coupling effect of charge and restraint structure makes it difficult to predict the formation location, propagation direction and path of the crack in the charge.

To this end, an experimental technique of the holed explosive disks central ignition with adjustable preloading is established. The characteristic parameters such as reactive crack growth velocities are obtained after ignition under different constraints (preloading) and inertial constraints (charge size). We quantitatively compare and analyze reactive crack growth and combustion reaction process. The influencing factors and mechanisms of reaction evolution revealed in this work will provide support for the evaluation of charge reaction intensity.

2. Materials and methods

The schematic experimental setup for the propagation behavior and evolution of the central ignition reaction of the holed explosive disks is shown in Fig. 1. The explosive disks with holes is installed in the cylindrical shell. A high-power (200 W) laser beam is used for ignition. In order to ensure reliable ignition, moderate amount of black powder is added in the center hole of the disk. Two sizes of explosive disks are used in our study, of which the diameters (D) and thicknesses (H) are listed in Table 1. Therefore, two corresponding cylindrical shells are designed, of which the inner diameters are 100 mm and 150 mm. The cover plate and the cylindrical shell are tightened by bolts, which is used to adjust the clamping force. The clamping force is transmitted to the explosive disk through a quasi-static force sensor and the partition plate, realizing the adjustable and controllable preloading on the surface of the explosive disk.

	D (mm)	*H* (mm)	Pre-pressure (MPa)	Radial confinement
D100-H20-P4	100	20	4	Yes
D100-H20-P7			7	Yes
D100-H20-P9	150	20	9	No
D150-H20-P4			4	Yes
D150-H20-P10			10	Yes

Table 1. Experimental design

Two pressure transducers (PT1 and PT2) are installed on the end of the charge with the size of D150-H20 to measure the combustion pressure, while space constraints prevent end pressure measurement on a D120-H20 charge. PT3 and PT4 are installed on the surface of the charge. The expansion velocity of the confinement shell and cover plate is measured by Photonic Doppler velocimetry (PDV) to assist in the analysis. The experimental process is photographed by a high-speed camera from the sapphire window and the total crack evolution is obtained by image analysis.

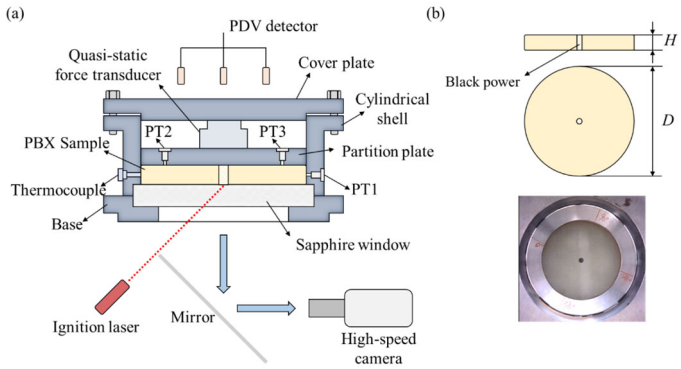

Fig. 1. (a) Schematic experimental setup of thin charges spherical explosives with radial confinement and pre-pressure. (b) Schematic and physical diagram of the explosive disk.

3. Results and conclusions

The times-series images of D100-H20-P4 experiment are shown in Fig. 2 (a). The black power is ignited at -0.70 ms. Three main cracks can be observed at -0.483 ms due to the action of the product gas with high temperature and high pressure, which is produced by the combustion of black powder. With the development of combustion reaction, three cracks extend to the boundary of the charge. The propagation velocity of high temperature gas in the crack can be obtained by obtaining the position of the flame tip propagating in the crack at different time, and the corresponding results is shown in Fig. 2 (b). The zero moment is defined by the time when the PDV probe is triggered, that is, the time when the shell is deformed.

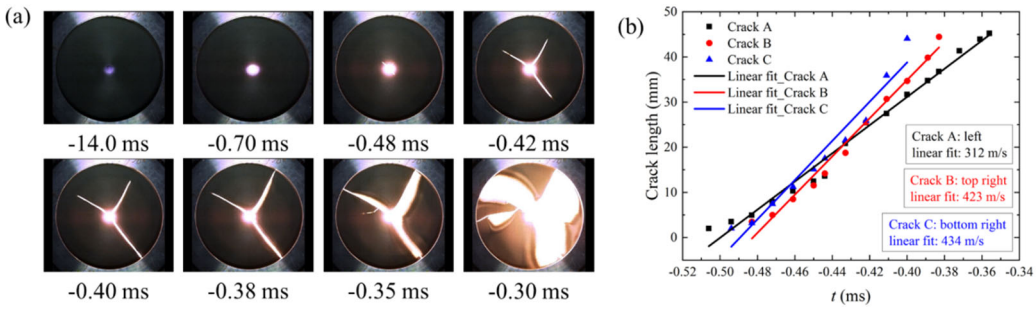

Fig. 2. Experimental results of D100-H20-P4: (a) Time-series images, (b) crack growth rate.

4. Acknowledgements

The research presented in this paper has received funding from the National Key Laboratory of Shock Wave and Detonation Physics (No. 2024CXPTGFJJ06404).

5. References

[1] L.G. Hill (2006). Burning crack networks and combustion bootstrapping in cookoff explosions., AIP Conference Proceedings., **845**, 531-534.

ASSESSMENT OF IMPACT REISTANCE OF HYBRID BASALT-POLYPROPYLENE FIBER REINFORCED CONCRETE

A. Syamsir[1,2], I. A. Ja'e[1,3], Z. Itam[1], M. A. S. N. Azlisham[1], and V. Anggraini[2]

1. *Institute of Energy Infrastructure, Universiti Tenaga Nasional, Jalan IKRAM-UNITEN, 43000, Kajang, Selangor, Malaysia*
2. *Faculty of Engineering, Universitas Putra Indonesia YPTK, Padang 25145, Indonesia*
3. *Department of Civil Engineering, Ahmadu Bello University, Zaria 810107, Nigeria*

1. Introduction

Conventional concrete, despite being the most widely used construction material, suffers from poor tensile resistance, which adversely affects its ability to withstand loading from sudden impacts.

Over the years, various strategies have been explored to improve the performance of conventional concrete, specifically its tensile-related performance through the incorporation of different types of fibres [1-3]. For example, Krishna et al[4] investigates the influence of macro polypropylene and hooked end steel fibre on concrete for rigid pavement construction. Their findings indicate improvement in toughness indices by up to 14 times along with approximately 20 -25% reduction in shrinkage.

Previous studies has identified 1.5% basalt fibre as the optimal volume fraction[1], significantly enhancing split tensile and impact resistance. Thus, this study seeks to further explore this performance by examining the effect of incorporating polypropylene alongside basalt fibre.

In this context, this study investigates the influence of hybrid basalt and polypropylene fibre (BPPF) on the impact resistance of fibre-reinforced concrete incorporated with silica fume. The objective is to improve the tensile behaviour of the concrete, thereby bolstering its impact performance under low-velocity impact loading. The research examines basalt fibre ranging from 0% – 1.5%, as well as BPPF content from 0% -3%. The concrete specimens were experimentally assessed through tensile strength test and low velocity impact resistance test.

2. Materials and methods

Material used includes grade 42.5 ordinary Portland cement, fibrillated basal and polypropylene fiber, portable water and silica fume. Table 1 presents the properties of the fiber used.

Table 1: Properties of the fiber

Type	Diameter (µm)	Density (g/cm^3)	Tensile strength (MPa)	Elastic modulus (GPa)	Ultimate elongation (%)
Polypropylene fibre	12	0.91	365-600	2.4-3.2	25-60
Basalt fibre	15	2.65	3300-4500	80-100	2.4-3.0

Grade 30 concrete mix containing different volume fractions of fiber as shown in Table 2 were used, with 550kg of cement, 1485kg of aggregate, 0.45 water cement ratio and 5kg single dose of silica fume.

Cylindrical specimen of dimension 150mm x 300mm was cured in clean water and tested for split tensile strength after 28 days. For each of the concrete mixes, three specimens were produced and the average value used for the assessment.

The Impact resistance was assessed by testing 75mm x 150mm cylindrical specimens at 28 days curing age. Each specimen was tested by dropping an 8.5kg cylindrical weight through a 450mm height onto the specimen. In each case, the number of blows at the manifestation of first crack and at failure were recorded and analysed.

Table 2: Volume fractions of fibers used in concrete mix design

Mix	PC	BF (1)	BF (2)	BF(3)	BFPP (1)	BFPP(2)	BFPP(3)	BFPP(4)	BFPP(5)
BF (%)	0	0.5	1.0	1.5	0.5	0.5	1.5	1.5	1.5
PP (%)	0	0	0	0	1.5	0.5	0.5	1.0	1.5
Silifa Fume (%)	0	5	5	5	5	5	5	5	5

3. Results and conclusions

The results as shown in Figure 1 demonstrated about 25% improvement in tensile strength, while concrete produced with hybrid BPPF exhibited improved crack resistance. The highlighted improvement is attributed to the combined influence of the varying tensile strengths of the fibres and the enhanced densification of the concrete matrix due to the production of extra C-S-H from silica fume. Additionally, the enhanced impact resistance underscores the potential for using hybrid BPPF reinforced concrete in applications where dynamic impact loading is critical importance.

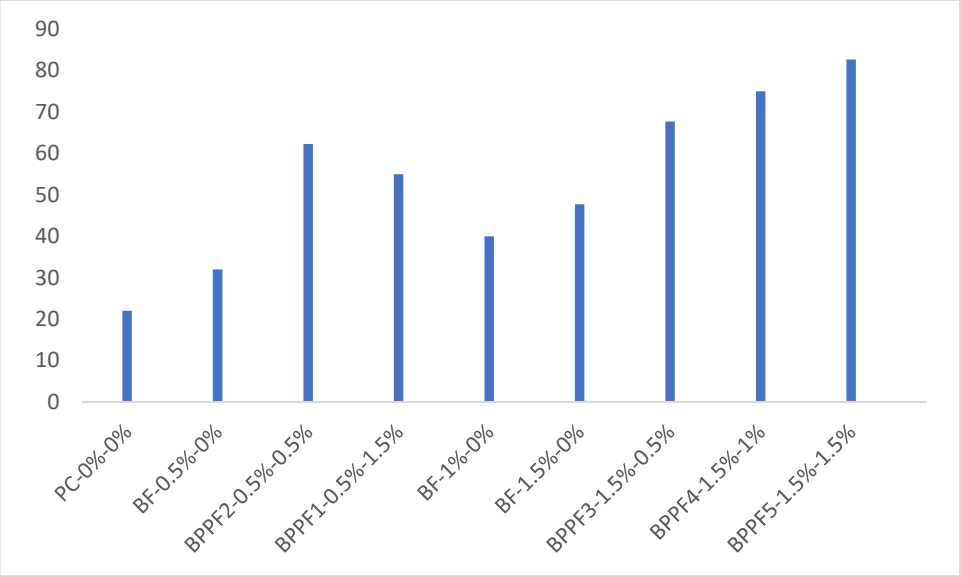

Fig. 1. Variation in impact resistance with varying content and composition of fiber

4. Acknowledgements

The research presented in this paper was supported by UNITEN through the Higher Institution Centre of Excellence (HICoE), Ministry of Higher Education (MOHE), Malaysia under the project code 2024001HICOE as referenced in JPT(BPKI)1000/016/018/34(5)

5. References

[1] Ja'e, I.A. *et al.*,(2024) Optimisation of mechanical properties and impact resistance of basalt fibre reinforced concrete containing silica fume: Experimental and response surface assessment, *Developments in the Built Environment,* vol. 17, p. 100368. doi: https://doi.org/10.1016/j.dibe.2024.100368.

[2] Ja'e, I.A. *et al.*,(2025) Structural performance of lightweight fibre-reinforced oil palm shell concrete subjected to impact loadings under varying boundary conditions, *Case Studies in Construction Materials,* vol. 22, p. e04240. doi: https://doi.org/10.1016/j.cscm.2025.e04240.

[3] Ja'e, I.A. *et al.*,(2024) Modelling and optimisation of the structural performance of lightweight polypropylene fibre-reinforced LECA concrete, *Results in Engineering,* vol. 24, p. 103149. doi: https://doi.org/10.1016/j.rineng.2024.103149.

[4] Goel, P., Kumar, R., and Bhattacharjee, B.,(2022) Hybrid fiber reinforced concrete composite for construction of rigid pavements, *Journal of Cement Based Composites,* vol. 1, p. 5630.

Dynamic Behavior and Impact Ignition Criterion of Ti-B-PTFE Reactive Material

***Zhe Peng*[1], *Rui Liu*[1],**
[1] *School of Mechatronical Engineering, Beijing Institute of Technology, Beijing, China*

1. Introduction

Energetic structural materials (ESMs) are composite materials consisting of two or more components such as thermite compositions, intermetallic compounds, metal/polymer mixtures, metastable molecular compounds. These materials exhibit inert behavior under ambient conditions but undergo rapid intercomponent reactions with substantial energy release when subjected to intense dynamic loading[1]. Recent advances in metal/polymer reactive materials have predominantly focused on incorporating one or multiple metallic additives into PTFE to develop novel reactive systems. In 2024, Zhu Z.R. et al[2]. synthesized Ti-PTFE-W specimens and characterized their dynamic compression behavior under high strain rates via SHPB tests. The research validated the feasibility of Ti-based reactive materials.

The high exothermicity of PTFE-Ti interactions enhances the reactivity between Ti and B, thereby achieving substantial energy release. Additionally, there is a lack of a unified criterion to definitively determine whether ignition will occur. To evaluate ignition in Ti-B-PTFE reactive materials, the impact ignition criterion $p^n r$ is adopted to establish an effective ignition threshold framework[3-4].

In this study, Ti-B-PTFE reactive materials were fabricated via cold pressing, and their microstructural characteristics were characterized using scanning electron microscopy (SEM) and XRD. The dynamic mechanical properties and ignition behavior of the Ti-B-PTFE composites were systematically investigated through SHPB experiments. Based on the experimental results, a highly accurate and reliable ignition criterion for Ti-B-PTFE reactive materials was established.

2. Materials and methods

The Ti-B-PTFE reactive materials with varying PTFE content were fabricated using titanium powder (25 μm particle size), boron powder (1 μm particle size), and PTFE powder (1 μm particle size). The weight percentages of the three components in the three formulations are listed in Table 1. The powders were homogeneously blended in a V-shaped mixer. The mixed Ti-B-PTFE powders were uniformly loaded into a steel mold with an inner diameter of 5 mm. Cylindrical specimens (Φ5 mm × 5 mm) were obtained via cold-pressing under a consolidation pressure of 1000 MPa. The microstructural characteristics of the Ti-B-PTFE composites were analyzed using a ZEISS Gemini SEM 300 field-emission scanning electron microscope (Carl Zeiss AG, Germany)

To investigate the dynamic mechanical properties of Ti-B-PTFE reactive materials under intermediate to high strain rate conditions (10^2-10^4 s^{-1}), dynamic compression tests were performed using a SHPB system. The specimens for dynamic compression were cylindrical with dimensions of Φ5 mm × 5 mm. To investigate the dynamic ignition behavior of Ti-B-PTFE reactive materials and establish a robust methodology for determining their ignition thresholds, SHPB experiments were conducted using striker bars of varying lengths (300 mm, 200 mm, and 100 mm). The high-speed camera (Fastcam Nova S16, frequency: 150,000 frames per second) was employed to capture the dynamic deformation and failure process of the material.

3. Results and conclusions

In this study Ti-B-PTFE reactive materials were designed and fabricated.and systematically The microstructure, thermal reaction properties, dynamic mechanical properties, and dynamic ignition behavior of these materials were investigated. Simultaneously, a highly accurate and reliable ignition criterion for Ti-B-PTFE reactive materials was established. The specific conclusions are as follows:

1) Ti-B-PTFE reactive materials exhibit strain rate sensitivity. As the strain rate increases, the yield strength of the 5% PTFE specimen rises from 17.8 MPa to 23.6 MPa, the yield strength of the 10% PTFE specimen increases from 26.9 MPa to 33.1 MPa, and the yield strength of the 15% PTFE specimen enhances from 42.8 MPa to 49.2 MPa. Additionally, at similar strain rates, higher PTFE content in the material leads to increased yield strength.

2) DSC analysis was employed to elucidate the reaction process of Ti-B-PTFE reactive materials under an argon atmosphere. Initially, Ti reacts with PTFE, liberating substantial heat. This exothermic reaction furnishes the necessary thermal energy to drive the solid - phase reaction between Ti and B. Analysis of combustion residues obtained from dynamic compression experiments detected reaction products including TiB_2, TiB, and TiC. These experimental results confirm that the proposed ignition mechanism of Ti - B - PTFE reactive materials under dynamic compression conditions is consistent with the results of DSC experiments.

3) Analysis of the dynamic ignition behavior of Ti-B-PTFE reactive materials reveals that as the loading strain rate increases, the ignition delay time decreases, and the reaction intensity amplifies, resulting in more violent combustion of the material. Experimental results show that longer striker bars are associated with extended combustion durations in Ti-B-PTFE reactive materials. Moreover, specimens with low PTFE content did not exhibit ignition during experiments. In contrast, specimens with higher PTFE concentrations experienced enhanced reaction intensity, accompanied by a notable prolongation of the combustion duration.

4) For Ti-B-PTFE reactive materials, the fitting-derived parameters of the dynamic ignition criterion $p^n\tau$ accurately predict ignition occurrence. The ignition difficulty of reactive materials decreases with increasing PTFE content, and the 15% PTFE formulation exhibits higher ignition susceptibility.

4. References

[1] Dreizin, E.L., Schoenitz, M. Mechanochemically prepared reactive and energetic materials: a review [J]. Mater Sci 52, 11789–11809 (2017).

[2] Zhu R Z, Zhang W Z, Tian X W, et al. Mechanical Property and Constitutive Model of a Ti/PTFE/W[J]. Journal of Physics: Conference Series,2024,2891(8):082016-082016.

[3] Walkerfe, Wasleyrj. Critical energy for shock initiation of heterogeneous explosives[J]. Explosive Stoffe , 1969,17(1):9-14.

[4] Chen W X ,Wang X J ,Tang K , et al. Study on shock initiation of the charge covered by metal plate with penetrated notch[J]. Journal of Physics: Conference Series,2020,1507(3):

Experimental Big Data Analysis and Artificial Intelligence

MONOCULAR VISION-BASED OBJECT MOTION MEASUREMENT METHOD

Zibin Liu[1,2], Banglei Guan[1,2,*], Shunkun Liang[1,2], Ang Su[1,2], Zhang Li[1,2], Yang Shang[1,2] , Xiaolin Liu[3] and Qifeng Yu[1,2]

[1]College of Aerospace Science and Engineering, National University of Defense Technology, Changsha, China

[2] Hunan Provincial Key Laboratory of Image Measurement and Vision Navigation, Changsha, China

[3] College of Physics and Optoelectronic Engineering, Shenzhen University, Shenzhen, China

**Corresponding author*

1. Introduction

Object motion parameter measurement is a crucial task in the field of optical measurement [1]. By accurately measuring the motion parameters of objects, such as velocity, acceleration, and displacement, we can provide key data for subsequent kinematic and dynamic analysis, thereby achieving a comprehensive understanding of the object's motion state. Traditional motion measurement methods often rely on high-precision sensors, such as Inertial Measurement Units (IMUs) and optical tracking systems, but these methods typically require complex hardware equipment or are difficult to apply in some scenarios.

With the rapid development of computer vision technology, monocular vision-based object motion measurement methods have gradually become an important alternative. Monocular vision methods utilize the two-dimensional image information captured by cameras to recover the motion parameters of objects in 3D space through image processing and algorithmic derivation. Compared to traditional methods, monocular vision offers the advantages of low equipment cost, flexible application, and no dependence on physical contact, especially in scenarios where sensors cannot be installed or remote monitoring is required, it demonstrates unique advantages.

This study proposes a monocular vision-based method for object motion measurement, which aims to accurately estimate the motion parameters of an object in 3D space. The method begins by extracting key 2D image features of the object from monocular images, such as corners [2], lines [3] or distinctive patterns. These 2D features are then combined with the known 3D structure of the object, allowing the relative position and orientation of the object with respect to the observing camera to be estimated. This method, leveraging optical measurement techniques, relies solely on a monocular camera to estimate motion parameters without the need for costly sensors or direct physical interaction with the object, thus providing a cost-effective and non-intrusive solution for motion analysis.

2. Methods

This method achieves object motion measurement based on a monocular camera. The key idea is to estimate the relative pose between the object and the camera by matching 2D feature points from the image with 3D feature points on the object. The relative pose can be described using three degrees of freedom for rotation and three degrees of freedom for translation.

The process begins by extracting 2D feature points of the object from the monocular image. These feature points typically correspond to regions with distinct edges or unique textures in the image, which effectively capture the object's state. Once the 2D feature points are extracted, the next step is to match them with the corresponding points in the object's 3D model. To achieve this, the 3D structural information of the object must first be obtained, typically through modeling, laser scanning, or other 3D reconstruction techniques. Afterward, a correspondence relationship between the 2D feature points and the 3D model is established, followed by the formulation of constraint equations. The relative position between the camera and the object can then be computed by solving the constraint equations linearly, obtaining the rotation and translation.

3. Results and conclusions

We conduct both simulated and real-world experiments to validate the accuracy and reliability of the algorithm. The pose error of the object is described by the re-projection error, which reflects the difference between the estimated pose and the actual observation. In the simulated experiment, the re-projection error is 0.57 pixels, while in the real-world experiment, the error slightly increases to 0.85 pixels. To visually demonstrate the algorithm's accuracy, we re-project the 3D model of the target object onto the image plane and display the re-projected images from the simulated and real-world experiments, as shown in Fig. 1 (a) and (b), respectively. It is clear that the difference between the re-projected model and the actual image is small, confirming the effectiveness and accuracy of the algorithm under different experimental conditions.

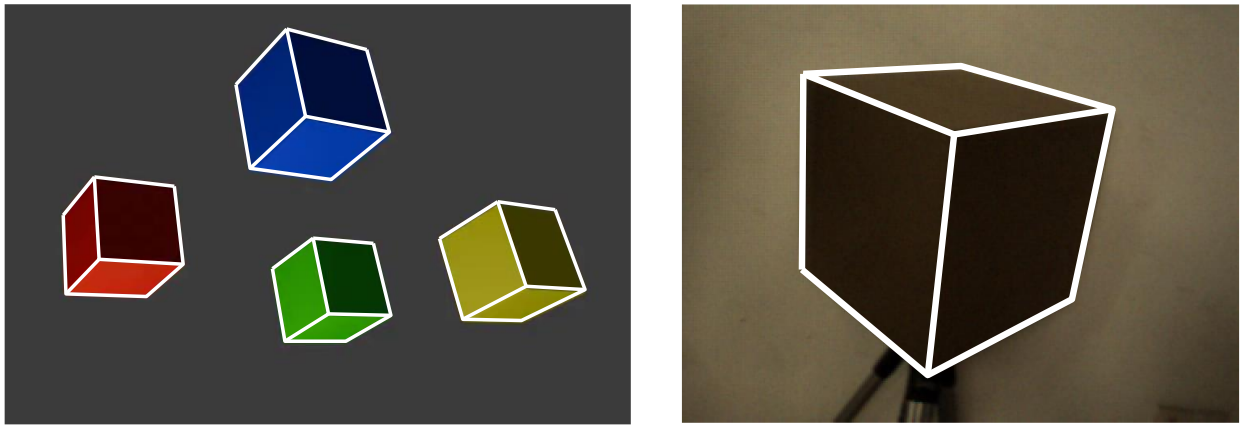

(a) The reprojection results of the simulated object. (b) The reprojection results of the real object.

Fig. 1. Schematic diagrams of pose re-projection for the simulated and real experiments.

4. Acknowledgements

The authors would like to acknowledge the funding support provided by project 12372189 by the National Natural Science Foundation of China and project 2023JJ20045 by the Hunan Provincial Natural Science Foundation for Excellent Young Scholars.

5. References

[1] Zibin Liu, You Li, Chunhui Wang, Liang Liu, Banglei Guan, Yang Shang, and Qifeng Yu (2024). AstroPose: Astronaut pose estimation using a monocular camera during extravehicular activities, Sci. China Technol. Sci., 1-13.

[2] Rublee, Ethan and Rabaud, Vincent and Konolige, Kurt and Bradski, Gary (2021). ORB: An efficient alternative to SIFT or SURF, Proc. IEEE Int. Conf. Comput. Vis., 2564-2571.

[3] Chi Xu, Lilian Zhang, Li Cheng anb Reinhard Koch (2017). Pose estimation from line correspondences: A complete analysis and a series of solutions, IEEE Trans. Pattern Anal. Mach. Intell., 39, 1209–1222.

A MACHINE LEARNING METHOD INTEGRATING MECHANICAL KNOWLEDGE AND ITS APPLICATION IN LAOD MODELING OF TUNNELING EQUIPMENT

Q. Zhang[1], S. Liu[1], M. Ma[1] and Y. Kang[1]
[1] Department of Engineering Mechanics, Tianjin University, Tianjin, China

1. Introduction

With the rapid advancement of experimental mechanics techniques, the volume of test data has grown exponentially. Extracting the key evolutionary information of mechanical parameters from this massive and complex dataset has become a new challenge in experimental mechanics data analysis [1]. Artificial intelligence (AI) methods, which can directly learn the operational laws of complex systems from data, are gradually being applied in this field to address these challenges.

In the modeling of mechanical parameters for certain types of engineering equipment, AI methods still face numerous challenges in practical applications. In such scenarios, the equipment is large-scale, and the core control variables are closely related to mechanical interactions. Modeling these control variables based on in-situ data is fundamental to ensuring safe operation as well as enabling future intelligent control. However, the numerous coupled influencing factors, harsh operational environments, and substantial interference result in high-dimensional, and noisy in-situ data. In this context, purely data-driven methods often struggle to achieve ideal generalization performance. Additionally, these scenarios demand real-time response and involve high risks, which necessitate a modeling approach that is robust to noisy data, lightweight, and traceable.

Mechanical research, through its rigorous theoretical framework, provides deep insights into the essence of physical phenomena without being entirely dependent on data. Therefore, integrating mechanical knowledge with AI to establish scientifically grounded intelligent learning models presents a potential solution to these complex challenges [2].

In response to the aforementioned requirements, this paper proposes a machine learning method that integrates mechanical knowledge. The proposed method consists of three interrelated modules: a knowledge-driven module, a data-driven module, and an integration layer. The knowledge-driven module aims to extract and represent the underlying mechanical logic inherent in the equipment system. The integration layer incorporates this underlying logic into the data-driven approach, guiding it to meet the comprehensive modeling requirements of the scenario. The data-driven module leverages empirical engineering data and iteratively optimizes the framework to derive a concrete engineering model.

2. Methods

The knowledge-driven module is based on the dimensional analysis method. By considering the physical meaning of variables and their intrinsic dimensional relationships, the underlying logic of interactions among key variables is extracted in the form of dimensionless π factors.

The integration layer embeds the π factors into the loss function, constraining the data-driven model to optimize within a dimensionless physical space spanned by the π factors. Within this constrained model framework, the integration layer further encodes the underlying logic into the regularization terms. By designing an L_1 sparse regularization, a sparsity-driven optimization approach guided by the underlying logic is formed. This strategy, combined with the π factors' ability to fundamentally represent different physical processes of the system, directs the model to focus on

the dominant physical processes. As a result, even under low-quality data conditions, the model learns the most influential aspects of system behavior, avoiding overfitting to noise. Additionally, the π factors, derived from traceable theoretical foundations, capture the primary nonlinear interactions between key variables in complex systems. This relationship is not only transferable to similar operating conditions, enhancing the model's generalizability, but also allows the data-driven component to utilize a lightweight, traceable model.

The data-driven component, considering the non-smooth nature of the objective function in the integration layer, employs a coordinate descent method for optimization.

3. Results and conclusions

The aforementioned method is applied to establish a core mechanical control parameter model for the total thrust of Tunnel Boring Machines (TBMs), which are the most widely used large-scale equipment in current underground engineering. The study uses the tunnel construction section of Line 9 of the Tianjin Metro in China as a case study. The collected dataset contains 933 samples, including thrust and 12 key influencing factors related to it.

Fig. 1(a) illustrates the variation of the measured and predicted values along the tunneling direction. Fig. 1(b) presents the performance of the proposed method compared with six other commonly used machine learning methods in terms of model complexity and accuracy. The results indicate that the proposed method maintains consistency with the measured results in both the overall trend and key transition points, even with the limited engineering field data. Furthermore, the model established using the proposed method achieves an average prediction error that is at least 9.2% lower compared to other methods, with a model complexity that is at most only 1% of that of the other methods.

This method enhances the applicability of machine learning methods in intelligent control scenarios, also promoting the intelligent development of experimental mechanics.

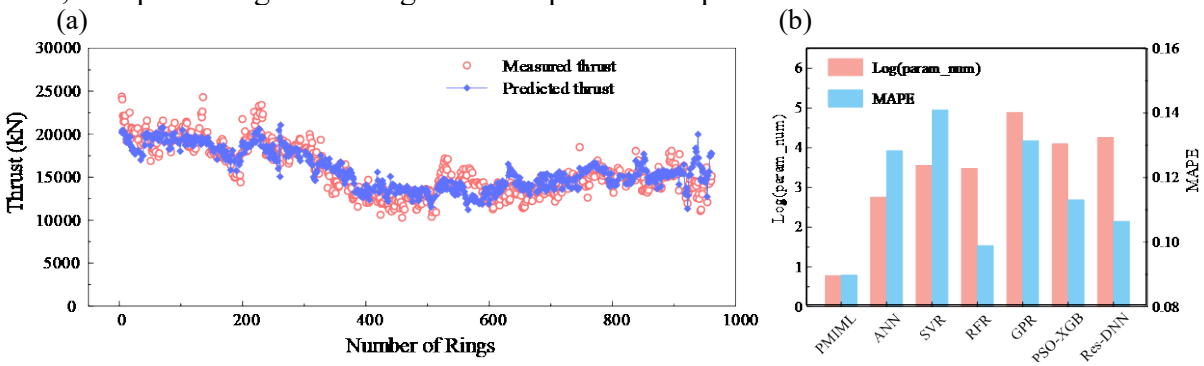

Fig. 1. Analysis of TBM thrust prediction results for Tianjin Metro Line 9 project.

4. Acknowledgements

This study was funded by National Natural Science Foundation of China [Grant Nos. 12372186] and National Key R&D Program of China [No.2022YFC3802301].

5. References

[1] N.R. Brodnik, C. Muir, N. Tulshibagwale, J. Rossin, M.P. Echlin, C.M. Hamel, S.L.B. Kramer, T.M. Pollock, J.D. Kiser, C. Smith, S.H. Daly (2023). Perspective: Machine learning in experimental solid mechanics, J. Mech. Phys. Solids, **173**, 105231.

[2] G.E. Karniadakis, I.G. Kevrekidis, L. Lu, P. Perdikaris, S. Wang, L. Yang (2021). Physics-informed machine learning, Nat. Rev. Phys., **3** (6), 422-440.

Advancing automated machining through enhanced surface roughness prediction in high entropy alloy coating processes by exploring a novel parameter acquisition using artificial neural network

M.Dehghanpour Abyaneh[1,2], R. Sesana[1], M.S. Javadi[3], N. Sheibanian[1,2], S. Ozbilen[4], R. Lupoi[4]
[1]DIMEAS, Department of Mechanical and Aerospace Eng., Polytechnic of Turin, Corso Duca degli Abruzzi 24, 10129 Turin, Italy.
[2] TN ITALY, Central Laboratory, Corso Torino 378, 10064 Pinerolo, Torino, Italy.
[3]Department of Mechanical Engineering, Amirkabir University of Technology, 424, Hafez Ave., Tehran, Iran.
[4]Department of Mechanical, Manufacturing & Biomedical Engineering, Trinity College Dublin, the University of Dublin, Parsons Building, Dublin, D02, Ireland.

1. Introduction

The advancement in metallurgical science has led to the creation of alloys with superior and more specific properties compared to individual metals. Traditionally, alloys primarily consist of one main element, restricting the compositional diversity and freedom. A revolutionary concept introduced by J. W. Yeh and B. Cantoris, known as "HEA" (High Entropy Alloy), diverges from this norm by incorporating a minimum of five primary elements, each making up 5-35% in atomic percentage [1].

Elements present in lesser amounts, under 5%, are considered secondary alloying elements [1,2]. Presently, the focal area of research is on alloys comprising elements like Al, Co, Cr, Cu, Fe, and Ni, as well as those derived from these by additional elements or substitutions. The potential for discovering new alloys remains vast [2]. HEAs are recognized for their structural and functional capabilities, owing to a high mixing entropy that encourages the formation of solid solutions with uncomplicated microstructures [2]. These alloys are associated with heightened strength and hardness, improved stress and strain tolerance, and reduced temperature sensitivity [1, 2].

The unique blend of multiple primary elements in HEAs contributes to outstanding mechanical and chemical properties, such as enhanced strength, wear resistance, high-temperature resilience, structural stability, and resistance to corrosion and oxidation, without necessitating special manufacturing processes. HEAs' remarkable attributes and microstructural characteristics stem from several "core effects," including high mixing entropy, lattice distortion, sluggish diffusion, and a cocktail effect [1, 2, 5]. Notably, Al0.5CoCrCuFeNi alloy variants, through specific processing, have exhibited superior fatigue strength compared to many traditional alloys [4].

HEAs' tribological performance is influenced by their chemical composition; elements like Al, Fe, and Nb refine the grain structure and promote the formation of BCC phases, while Mn and Cr aid in developing hard phases [5]. The addition of C, N, B, and Si enhances the formation of compounds or facilitates phase transitions, leading to increased hardness and wear resistance. The phase composition significantly influences the wear resistance of HEAs, with complex and ordered phases outperforming conventional alloys of comparable hardness [2].

Consequently, HEAs are being increasingly utilized in developing highly wear-resistant coatings through various deposition techniques, further enhanced by incorporating ceramic particles into the metal matrix for greater hardness and wear rate reduction [1, 3, 6].

In this study, we extend our previous work on the application of Artificial Neural Networks (ANN) to the field of metallurgy, with a specific focus on High Entropy Alloys Cold Sprayed Coating (HEAs). The unique compositional complexity and superior properties of HEAs present a challenging yet promising landscape for leveraging ANN in predicting and optimizing their mechanical and chemical properties.

2. Materials and methods

The concept behind the neural network is to simulate human brain functionality like training and learning by mathematical and statistical formulation. For emulation of a human neural network, an artificial neural network consists of simple computing units called neurons, each unit connects via weighted connectors, and the optimum computing weight related to specific inputs call learning the artificial neural network is a part of a machine learning procedure that produces unique computational implements based on a statistical approach to solve real-world problems.

In this study an experimental data set, including 20 different conditions, was collected in this study [7]. The data set includes seven different parameters. Five of them are input measured before the setup experiments procedure, and two of them are surface roughness.

Input Parameters					**Output Parameters**	
Cut off(mm)	No. Cut off	Type	Temperature	Alloy Type	Ra (mean)	Rz (mean)
0.25	5	Parallel	650	Al0.1-HEA	5.81366667	28.5756667
0.25	5	Parallel	750	Al0.1-HEA	4.487	21.1253333
0.25	5	Parallel	650	Al0.2-HEA	4.367	21.1023333
0.25	5	Parallel	750	Al0.2-HEA	5.85066667	27.221
0.25	5	Parallel	850	Al0.2-HEA	5.09333333	24.5886667
0.25	5	Parallel	650	Al0.5-HEA	6.35733333	26.447
0.25	5	Parallel	750	Al0.5-HEA	5.73133333	27.1643333
0.25	5	Parallel	650	MN-HEA	5.58666667	26.569
0.25	5	Parallel	750	MN-HEA	5.55	26.206
0.25	5	Parallel	850	MN-HEA	5.78666667	25.1653333
0.25	5	Perpendicular	650	Al0.1-HEA	6.01	28.1073333
0.25	5	Perpendicular	750	Al0.1-HEA	5.20733333	24.9916667
0.25	5	Perpendicular	650	Al0.2-HEA	5.64533333	26.4616667
0.25	5	Perpendicular	750	Al0.2-HEA	5.87	27.531
0.25	5	Perpendicular	850	Al0.2-HEA	4.90933333	25.63
0.25	5	Perpendicular	650	Al0.5-HEA	6.62833333	30.1833333
0.25	5	Perpendicular	750	Al0.5-HEA	5.73266667	27.8073333
0.25	5	Perpendicular	650	MN-HEA	5.21666667	24.469
0.25	5	Perpendicular	750	MN-HEA	5.505	25.162
0.25	5	Perpendicular	850	MN-HEA	5.609	24.718

TABLE 1. The data used in this research including input parameters and Average values of the roughness parameters.

3. Results and conclusions

Fig. 1 depicts the performance of the network, which proves that the artificial neural network is reliable for forecasting Roughness of parts with different input parameters. For Ra, the training R-value obtained is 0.89039, for validation or all data is 0.75559, for testing the R-value is 0.41119. The training R-value of Rz obtained is 0.91267, for validation 0.81112, for testing the R-value is 0.94439.

(a)

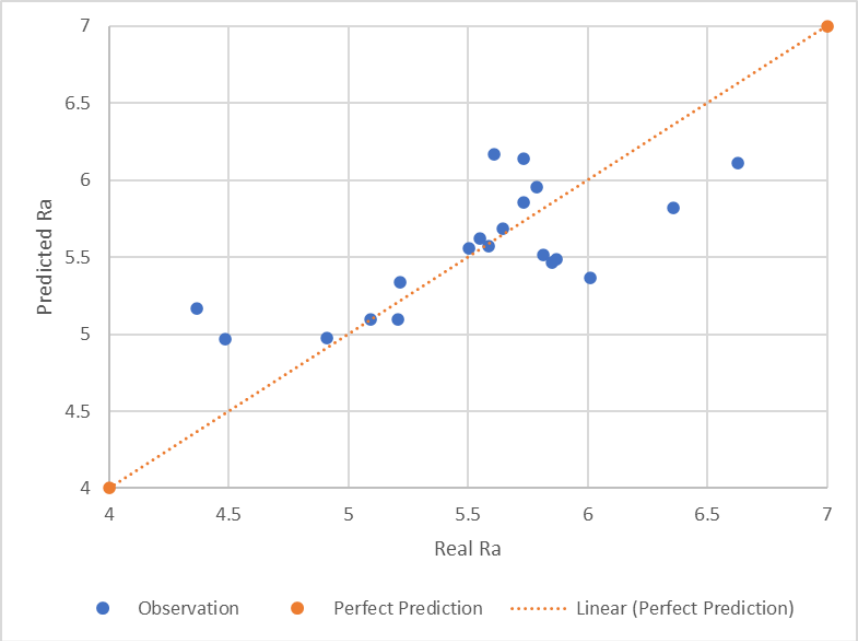

(b)

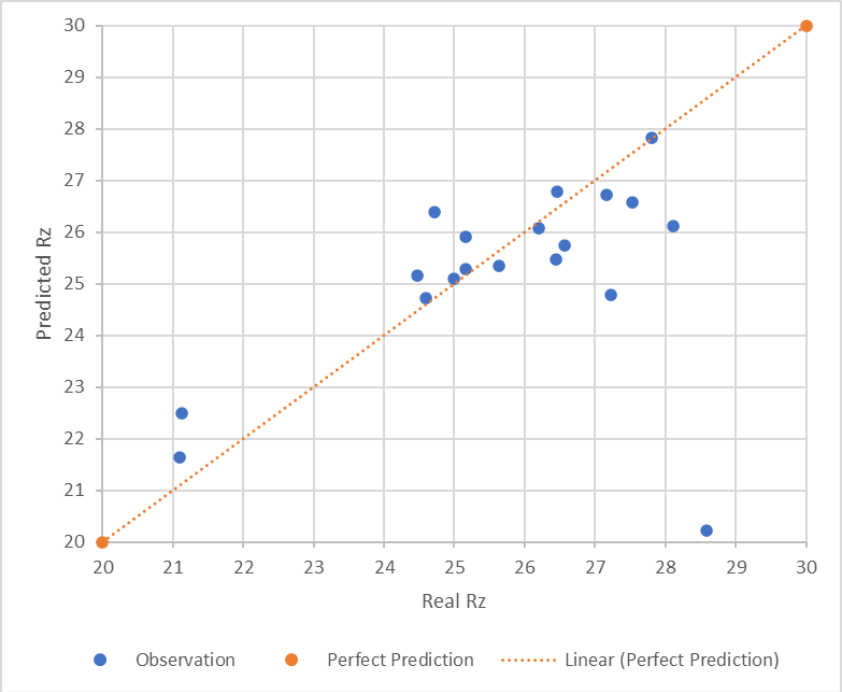

Fig. 4. Comparing predicted data and real ones for a. Ra and b.Rz.

4. Acknowledgements

The research mentioned here is funded by the European Commission, REA through its Marie Sklodowska Curie European Individual Fellowship to one of the authors (SÖ), [Project No: 101018482] (Nov. 2021- Oct. 2023), which is gratefully acknowledged.

This publication is also part of the project PNRR-NGEU which has received funding from the MUR-DM117/2023 for one of the writers (MD), [Project No: MUR DM 117/Tsubaki Nakashima – Recovery, reuse and reduction of waste sludge in the pro-duction of balls and rolls for rolling bearings] (Nov. 2023- Oct. 2026), which is grate-fully acknowledged. This publication is finally part of the project PNRR-NGEU which has received funding from the MUR-DM352/2023 for one of the writers (NS), [Project No: MUR DM 352/TN Italy – Ceramic coatings for the production of balls for hybrid bearings] (Nov. 2022- Oct. 2025), which is gratefully acknowledged.

The following are also thanked for their contribution to the experimental part: Dr. Brendan Twamley of TSBI, TCD (XRD), Mr. John Fitzgerald of NHTC of Ireland, Robert Dunbar (OM, metallography, sample preparation), TCD workshop personnel (sample cutting, machining), Giacomo Cappelli (help in CS tests).

5. References

[1] Murty, B.S., et al., High-entropy alloys. 2019: Elsevier.
[2] Tsai, M.-H. and J.-W. Yeh, High-entropy alloys: a critical review. Materials Research Letters, 2014. 2(3): p. 107-123.
[3] Yin, S., et al., Deposition of FeCoNiCrMn high entropy alloy (HEA) coating via cold spraying. Journal of Materials Science & Technology, 2019. 35(6): p. 1003-1007.
[4] Nikbakht, R., et al., Cold spray deposition characteristic and bonding of CrMnCoFeNi high entropy alloy. Surface and Coatings Technology, 2021. 425: p. 127748.
[4] Nikbakht, R., et al., Cold spray deposition characteristic and bonding of CrMnCoFeNi high entropy alloy. Surface and Coatings Technology, 2021. 425: p. 127748.
[5] Wu, J., Y. Chen, and H. Zhu, A review on the tribological performances of High-Entropy Alloys. Advanced Engineering Materials, 2022. 24(8): p. 2101548.
[6] Sesana, R., et al., Cold spray HEA coating surface microstructural characterization and mechanical testing. Results in Materials, 2024. 21: p. 100540.
[7] Eren, B., M.A. Guvenc, and S. Mistikoglu, Artificial intelligence applications for friction stir welding: A review. Metals and Materials International, 2021. 27: p. 193-219.

UNSUPERVISED DEEP LEARNING BASED DIGITAL IMAGE CORRELATION

Q.W. Ma[1], X.N. Cheng[2], B. D. Li[2], B. F. Bai[1] and S. P. Ma[2]

[1] Department of Mechanics, School of Aerospace Engineering, Beijing Institute of Technology, Beijing, China

[2] Department of Engineering Mechanics, School of Naval Architecture, Ocean and Civil Engineering, Shanghai Jiaotong University, Shanghai, China

1. Introduction

Digital Image Correlation (DIC) is a robust, non-contact method for full-field deformation measurement widely used in photomechanics [1]. Traditional DIC deformation field analysis based on subset image matching which requires manual selection of calculation parameters. It will cause the difficulty in non-uniform field measurements when we want to obtain both high spatial resolution and high measurement resolution [2]. Meanwhile, DIC analysis is an inverse problem that needs to be processed by optimizing method, so the measurement efficiency is very low, which limits its usage in many applications. Deep Neural Networks (DNN) have high-order fitting capabilities, so they could achieve better characterize of the deformation modes for the deformation field. Recent works have offered some insights by introducing a deep learning approach to DIC, that is using a deep Convolutional Neural Network (CNN) to represent the process of deformation field analysis [3-5]. The neural network model can directly predict the full-field displacement with the speckle image pair as the input and the displacement field as the output, which means that the deformation field is directly inferred from the reference image and deformation image. These approaches have avoided setting parameters to some extent and skipped the optimization process for correlation. This kind of method called supervised deep learning based DIC (SL-DIC) and it is much faster than the traditional method.

However, the generalization and accuracy of SL-DIC are contingent on the scope and variety of the dataset because it requires training with a large number of simulated speckle images and displacement fields with known deformations. The simulated datasets of speckle images may not replicate the influence of lighting variations, noise, and distortions, etc., in actual measurement, leading to a significant difference in gray-level distribution between the simulated and real experiments. As a result, neural network models trained on simulated datasets may underperform when applied to speckle images in real experiments.

This paper proposes an unsupervised learning neural network based DIC (USL-DIC) method that circumvents the need for standard deformation fields and achieves high precision analysis of deformed fields. It constructs a loss function based on the photometric consistency assumption and allows the neural network model to directly extract displacement information from the images.

2. Method and verification

The USL-DIC developed in this paper is based on U-Net, and its principle and structure are shown in Fig.1(a). The U-Net (w, b) network structure is a contracting path - expansive path structure. The contracting path consists of four blocks, each of which uses two convolution operations, two batch normalizations, and two ReLU operations. The number of channels in the feature map processed by

each block is doubled, and then a Max Pooling down-sampling operation is performed to halve the size and save the feature map. The calculation of the loss function only requires the reference image and the deformed image, as well as the displacement field predicted by neural network itself. It does not require displacement ground truth and the model can learn itself based on the given physical laws. Then, the constraint of displacement continuity is introduced into the optimization process (USLC-DIC), that is, the original predicted displacement field output by the last layer of the U-net model is down-sampled by a step size s to form two sparse displacement field grids of m/s × n/s (Fig.1(b)).

The results in Fig.1(c) show that the displacement results calculated by USLC-DIC has low error value in all regions. It can also be seen that the error of USLC-DIC is significantly lower than that of subset-DIC in non-uniform deformation areas, and slightly higher in uniform displacement areas.

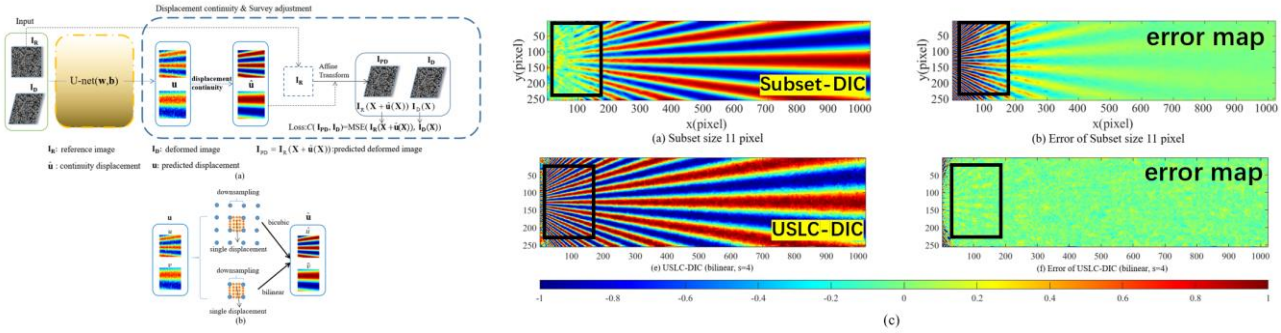

Fig. 1. Net structure and results of USLC-DIC: (a) photometric consistency assumption and displacement continuity constraint model; (b) calculation process of displacement continuity; (c) comparison of displacement results between subset-DIC and USLC-DIC

3. Conclusions

An unsupervised deep learning based DIC with displacement continuity constraint (USCL-DIC) method is presented which can directly solve the displacement field of 'reference image-deformed imag'. It eliminates the requirement for extensive training in traditional supervised deep learning based DIC and achieves an accurate displacement analysis. The displacement continuity constraint incorporated into the optimization process could help to mitigate the influence of noise and enhance the robustness of the measurements.

4. Acknowledgements

The research presented in this paper has received funding from the National Natural Science Foundation of China (Grant Nos. 12272046, 12132009)

5. References

[1] T.C. Chu, W.F. Ranson, M.A. Sutton, W.H. Peters (1985). Applications of digital-image-correlation techniques to experimental mechanics. *Exp. Mech*., **25**, 232–244.

[2] M. Grédiac, B. Blaysat, F. Sur (2017). A critical comparison of some metrological parameters characterizing local digital image correlation and grid method. *Exp. Mech*., **57**, 871–903.

[3] S. Boukhtache, K. Abdelouahab, F. Berry, B. Blaysat, M. Grédiac, F. Sur (2020). When Deep Learning Meets Digital Image Correlation. *Opt. Lasers Eng*., **136**, 106308.

[4] S.H. Lan, Y. Su, Z.R. Gao, Y. Chen, H. Tu, Q.C. Zhang (2022). Deep learning for complex displacement field measurement. *SCIENCE CHINA: Technological Sciences*, **65**, 3039–3056.

[5] X.N. Cheng, S.H. Zhou, T.Z. Xing, Y.C. Zhu, S.P. Ma (2023), Solving digital image correlation with neural networks constrained by strain-displacement relations. *Opt. Express*, **31**, 3865–3880.

Unsupervised Deep Learning DIC with only Single-pair image for high order displacement measurement

Canyu Zhu[a], Shihai Lan[a,b], Tianxiang Ren[a], Qingchuan Zhang[a]*

[a] CAS Key Laboratory of Mechanical Behavior and Design of Materials, Department of Modern Mechanics, University of Science and Technology of China, Hefei 230027, China

[b] School of Electronic Engineering and Automation, Guilin University of Electronic Technology , Guilin, 541004, China

Abstract

Digital Image Correlation (DIC) is the most widely used non-contact full-field strain measurement method, but due to the influence of subset calculations in principle, measuring complex deformation with high strain gradients within the subset remains a challenge. DIC based on neural networks performs well in complex deformation measurement scenarios, but its measurement accuracy and generalization ability depend on extensive training sets. This paper proposes a DIC method based on unsupervised learning that requires only a single pair of images. Unlike traditional unsupervised algorithms of optical flow estimation or Particle Image Velocimetry (PIV), the shape function in traditional DIC is incorporated into the loss function. This allows the use of only the reference image and the deformed image as input dataset, and the correct displacement field can be output after parameter optimization through training. This method does not require additional training sets to measure high-order strain fields like traditional neural networks-based DIC. The proposed method has demonstrated promising results in simulation experiments for high-order strain measurement and does not require additional datasets of the same type. In the measurement of the star-shaped displacement fields, its accuracy is better than the traditional DIC based on the subset, and it maintains convergence even when the strain is large, a situation where traditional DIC fails to converge. In addition, compared with the network obtained by supervised training as a pre-trained model, the method proposed in this paper can achieve superior results. The methods of the article can theoretically be applied to the result optimization of other networks beyond those discussed in this paper.

1 Introduction

Digital Image Correlation (DIC)[1-3] is the most widely used non-contact full-field strain measurement method. This method has the advantages of simple experimental equipment, low environmental requirements, wide measurement range, and high accuracy. It has been widely used in non-contact displacement and strain measurements.[4] Its working principle is to track the movement of speckle patterns on the material surface. These patterns are captured in the image and then measured for displacement and strain through sub-pixel correlation matching.

Traditional DIC selects the subsets around the points to be measured in the image and fits the displacement fields of the subsets with a first or second order function to accurately obtain the sub-pixel displacement. When the subset deforms into a complex high-order displacement field, it will face the problem of under-matching, resulting in systematic errors that make the measured displacement field smooth and increase random errors. Smaller subset sizes can reduce the systematic errors caused by under-matching, but it will decrease the robustness of DIC and increase random errors[5, 6]. Consequently, traditional DIC struggles to measure high-order strains in stress concentration areas[7, 8], such as PLC deformation bands[9], complex displacement fields in cell force measurements[10], crack tip displacement fields[5, 11], etc.

In 2020, an improved optical flow method[12] based on Convolutional Neural Network (CNN) was proposed for DIC, demonstrating superior performance over traditional DIC in the measurement of high-order displacement fields[13]. This innovation has since garnered attention in the DIC field. Subsequent improvements to the DIC neural network by scholars have expanded its applicability. Boukhtache and have lightened this network[14]. Yang and others have enhanced the large deformation measurement capability of deep learning DIC[14]. Wang proposed a new dataset to enhance the complex deformation field measurement capability of deep learning DIC[15].DIC based on the deep learning has been implemented in practical applications. Lan improved the network that outputs displacement fields in two directions at the same time to output a single direction displacement field to improve accuracy, and the use of the improved UDIC-NET for cell force measurement has yielded better results than traditional DIC, underscoring the potential of deep learning-based DIC in measuring complex deformation fields[16].

Current DIC networks all contain encoder and decoder parts of the U-Net architecture. The encoder extracts features from reference and deformed images, while the decoder magnifies the encoder's feature maps to obtain the final displacement fields prediction. Convolution kernels can extract features from images, specific types of deformation will present specific features, corresponding to specific displacements. The neural network learns and summarizes experience, so it can predict specific deformation features. Since CNN is good at extracting features from small areas, it can bypass the limitations imposed by traditional calculation methods based on subsets.

However, deep learning DIC faces several challenges. Firstly, neural networks require extensive data for training to ensure generalization ability[15]. For deformation types not present in the dataset, the output results may lack accuracy. Secondly, obtaining real data for datasets can be challenging, leading to a reliance on simulated datasets of speckle patterns and displacement fields. Moreover, even if the dataset encompasses all possible cases, it cannot guarantee optimal results. For instance, in the measurement of complex displacement fields, if the dataset contains more high-order displacement fields, the model will tend to output high-order displacement fields, resulting in larger errors in the low-order displacement field part. Conversely, if the dataset contains more low-order displacement fields, high-order displacement fields may be smoothed. If the dataset contains displacement fields of both types, the results may be slightly inferior to the results of training separately. This contradiction also exists in the measurement of large and small displacements. Therefore, for a new experimental scenario, it may be challenging to determine the credibility of the measurement results, as we do not know whether the displacement case is in the dataset. Traditional DIC methods allow us to estimate the credibility of the results by observing the difference in displacement measurements when reducing the subset size, based on the conclusion of high-order strain error analysis. However, deep learning DIC methods lack such a method to estimate the credibility of the results.

Unsupervised learning offers a potential solution to this problem. The dataset for unsupervised learning does not require truth displacement fields, and training can be completed with speckle images

before and after deformation, allowing the introduction of real experimental images as datasets while the real displacements are unknown. Wang has conducted research on deep learning DIC predicated on unsupervised learning[17]. Analogous unsupervised learning studies have been undertaken in the realms of optical flow estimation[18, 19] and particle image velocimetry (PIV)[20]. However, a significant amount of real experimental data is still needed for training, which can be time-consuming and costly for many DIC experiments.

In light of unsupervised learning, we propose a novel digital image correlation method that requires only a single pair of images to optimize the neural network, thereby achieving accurate measurement of the input high-order deformation. In the process similar to unsupervised training, we use only one pair of deformed image and reference image as the dataset and set a special calculation method of the loss. Take loss function in unsupervised optical flow method as an example, we generate a warped image with the reference image and output displacement fields, subtract the warped image and the actual deformed image pixel by pixel, and use the Mean Squared Error(MSE) as the loss. Then, optimize the parameters according to the loss until the loss converges. This approach yields a model that outputs a result for the input pair of deformed image and reference image, and this result minimizes the loss. Additionally, for the method proposed in this paper, the standard of high-quality speckles differs from traditional DIC, and the discussion in this paper is also based on the optimized standard for the method.

The principles underpinning our approach have been successfully applied in image denoising[21, 22], and single-pixel measurement[23], underscoring the unique influence of the neural network's structure on the optimization of input and output. Since the dataset is small, the selection of the loss function is of paramount importance. We have explored the effects of different loss functions on the results in this paper. Furthermore, our method can be employed to optimize pre-trained models, thereby enhancing the results or verifying their credibility.

The remainder of this paper is organized as follows: Chapter 2 provides an overview of the network utilized and the training strategy. Chapter 3 presents the results of different losses without pre-training, the rationale for proposing losses, and the impact of speckles on images. Chapter 4 discusses the results of different losses after introducing pre-training and analyzes these results. Chapter 5 offers a comparison of the results of star-shaped displacement field measurement and traditional DIC. Finally, Chapter 6 provides a summary of our findings and conclusions.

2 Conclusion and discussion

This paper proposes an innovative Digital Image Correlation (DIC) method based on unsupervised learning that requires only a single pair of images. The advantage of this method is its capability to compute high-order strain fields like neural network-based DIC without additional training sets. The key of this method is the design of the loss function, which incorporates the shape function akin to traditional DIC and implicitly associates adjacent pixels to an enhancement constraint, thereby facilitating convergence in an unsupervised learning scenario devoid of additional datasets.

While the proposed method may be more time-intensive than traditional DIC and the extant deep learning DIC, it offers significant advantages. In comparison to traditional DIC, it can adeptly capture high-frequency displacement details, with minimal errors in both the high-order displacement and smooth displacement components. Furthermore, it retains convergence even under conditions of larger displacement gradients where traditional DIC fails to converge.

In contrast to deep learning DIC, our method does not necessitate a dataset, thereby circumventing the challenges associated with obtaining training datasets and the training time and skill. Additionally,

this method can be employed in conjunction with pre-trained models to optimize their output, thereby achieving superior results.

Since the principle of this method is to obtain the displacement field by minimizing the preset loss function, it have a principle similar to traditional DIC, thereby offering interpretability compared to supervised training DIC. Furthermore, the credibility of the results can be validated by reducing the subset and observing the difference of the measurement results. This adds an additional layer of reliability to the proposed method.

Data availability

The source code of this research is available in Github at https://github.com/USTC-PMLAB/USDICNET.git; other data will be made available on request.

Acknowledgments

This work was supported by the National Natural Science Foundation of China (Grant Nos. 12232017 and 32061160475), and the National Science and Technology Major Project (Grant No. J2019-V-0006-0100).

References

[1] W.H. Peters, W.F. Ranson, DIGITAL IMAGING TECHNIQUES IN EXPERIMENTAL STRESS-ANALYSIS, Optical Engineering, 21 (1982) 427-431.
[2] T. Chu, W. Ranson, M.A. Sutton, Applications of digital-image-correlation techniques to experimental mechanics, Experimental mechanics, 25 (1985) 232-244.
[3] B. Pan, K. Qian, H. Xie, A. Asundi, Two-dimensional digital image correlation for in-plane displacement and strain measurement: a review, Measurement science and technology, 20 (2009) 062001.
[4] Y. Gao, T. Cheng, Y. Su, X. Xu, Y. Zhang, Q. Zhang, High-efficiency and high-accuracy digital image correlation for three-dimensional measurement, Optics and Lasers in Engineering, 65 (2015) 73-80.
[5] X. Xu, Y. Su, Q. Zhang, Theoretical estimation of systematic errors in local deformation measurements using digital image correlation, Optics and Lasers in Engineering, 88 (2017) 265-279.
[6] M. Bornert, F. Brémand, P. Doumalin, J.-C. Dupré, M. Fazzini, M. Grediac, F. Hild, S. Mistou, J. Molimard, J.-J. Orteu, Assessment of digital image correlation measurement errors: methodology and results, Experimental mechanics, 49 (2009) 353-370.
[7] H.W. Schreier, M.A. Sutton, Systematic errors in digital image correlation due to undermatched subset shape functions, Experimental Mechanics, 42 (2002) 303-310.
[8] X. Xu, Y. Su, Y. Cai, T. Cheng, Q. Zhang, Effects of various shape functions and subset size in local deformation measurements using DIC, Experimental Mechanics, 55 (2015) 1575-1590.
[9] G.F. Xiang, Q.C. Zhang, H.W. Liu, X.P. Wu, X.Y. Ju, Time-resolved deformation measurements of the Portevin–Le Chatelier bands, Scripta Materialia, 56 (2007) 721-724.
[10] J. Huang, X. Pan, X. Peng, T. Zhu, L. Qin, C. Xiong, J. Fang, High-efficiency cell–substrate displacement acquisition via digital image correlation method using basis functions, Optics and lasers in engineering, 48 (2010) 1058-1066.
[11] Y. Belrhiti, O. Pop, A. Germaneau, P. Doumalin, J. Dupré, H. Harmuth, M. Huger, T. Chotard, Investigation of the impact of micro-cracks on fracture behavior of magnesia products using wedge splitting test and digital image correlation, Journal of the European Ceramic Society, 35 (2015) 823-829.

[12] A. Dosovitskiy, P. Fischer, E. Ilg, P. Hausser, C. Hazirbas, V. Golkov, P. Van Der Smagt, D. Cremers, T. Brox, Flownet: Learning optical flow with convolutional networks, Proceedings of the IEEE international conference on computer vision2015, pp. 2758-2766.
[13] S. Boukhtache, K. Abdelouahab, F. Berry, B. Blaysat, M. Grediac, F. Sur, When deep learning meets digital image correlation, Optics and Lasers in Engineering, 136 (2021) 106308.
[14] S. Boukhtache, K. Abdelouahab, A. Bahou, F. Berry, B. Blaysat, M. Grédiac, F. Sur, A lightweight convolutional neural network as an alternative to DIC to measure in-plane displacement fields, Optics and Lasers in Engineering, 161 (2023) 107367.
[15] Y. Wang, J. Zhao, DIC-Net: Upgrade the performance of traditional DIC with Hermite dataset and convolution neural network, Optics and Lasers in Engineering, 160 (2023) 107278.
[16] S. Lan, Y. Su, Z. Gao, Y. Chen, H. Tu, Q. Zhang, Deep learning for complex displacement field measurement, Science China Technological Sciences, 65 (2022) 3039-3056.
[17] Y. Wang, C. Zhou, Unsupervised CNN-based DIC method for 2D displacement measurement, Optics and Lasers in Engineering, 174 (2024) 107981.
[18] S. Meister, J. Hur, S. Roth, Unflow: Unsupervised learning of optical flow with a bidirectional census loss, Proceedings of the AAAI conference on artificial intelligence2018.
[19] Z. Ren, J. Yan, B. Ni, B. Liu, X. Yang, H. Zha, Unsupervised deep learning for optical flow estimation, Proceedings of the AAAI conference on artificial intelligence2017.
[20] M. Zhang, M.D. Piggott, Unsupervised learning of particle image velocimetry, High Performance Computing: ISC High Performance 2020 International Workshops, Frankfurt, Germany, June 21–25, 2020, Revised Selected Papers 35, Springer2020, pp. 102-115.
[21] D. Ulyanov, A. Vedaldi, V. Lempitsky, Deep image prior, Proceedings of the IEEE conference on computer vision and pattern recognition2018, pp. 9446-9454.
[22] S. Laine, T. Karras, J. Lehtinen, T. Aila, High-quality self-supervised deep image denoising, Advances in Neural Information Processing Systems, 32 (2019).
[23] J. Li, B. Wu, T. Liu, Q. Zhang, URNet: High-quality single-pixel imaging with untrained reconstruction network, Optics and Lasers in Engineering, 166 (2023) 107580.
[24] Y. Su, Q. Zhang, X. Xu, Z. Gao, Quality assessment of speckle patterns for DIC by consideration of both systematic errors and random errors, Optics and Lasers in Engineering, 86 (2016) 132-142.
[25] B. Pan, H. Xie, Z. Wang, K. Qian, Z. Wang, Study on subset size selection in digital image correlation for speckle patterns, Optics express, 16 (2008) 7037-7048.

PREDICTION OF FRICTIONAL MOMENT OF CYLINDRICAL ROLLER BEARING USING EXPERIMENTAL DATA DRIVEN ARTIFICIAL NEURAL NETWORKS

Y. Hou[1], X. Wang[1,2], Q. Li[3]

[1] Frontiers Science Center for Smart High-speed Railway System, Beijing Jiaotong University, Beijing, China

[2] School of Mechanical, Electronic and Control Engineering, Beijing Jiaotong University, Beijing, China

[3] Beijing Key Lab of Traffic Data Analysis and Mining, Beijing Jiaotong University, Beijing, China

1. Introduction

The rolling bearing plays a key role in drivetrains supporting the shafts or gears and transmitting load at very low friction. Still, the rolling bearings are is a major contributor to the power loss and heat generation in drivetrains [1]. The power loss and heat generation are caused by the bearing friction. Accurate prediction of the bearing frictional moment contributes to the correct determination of the power loss and heat generation rate for the designer and engineer.

Complex correlations exist between the frictional moment of bearings and multiple operating parameters such as the shaft speed, roller-raceway contact load, rolling-sliding ratio and lubricating property [2]. In order to understand these correlations and predict the frictional moment of rolling bearings, some physical models have been developed based on empirical experience in the past decades [2]. However, due to the complex hydrodynamic sliding forces, it's very difficult to develop a simple and general formulation to evaluate the bearing friction under rolling-sliding conditions. To deal with the complex frictional behavior under a wide range of bearing operating conditions, the neural network model has been used to replace the conventional physical model [3,4]. However, most previous neural network models used for dealing with the rolling bearing frictional behavior were trained by the data from physical calculation models, which actually improved efficiency rather than authenticity of the prediction.

The novelty of this study is to accurately predict the frictional moment of cylindrical roller bearings (CRBs) under a wide range of operating conditions based on the experiment and artificial neural networks (ANN). An experimental system is built for the synchronous test of the frictional moment and its related operating parameters of CRBs. An ANN model is designed and then trained by the experimental data with measured shaft speed, radial load distribution, cage slip ratio and lubricant property as input variables and the measured frictional moment as the target variable. The prediction performance of the experimental data driven ANN model is validated under both the pure rolling and rolling-sliding operations of the test CRB. This experimental data driven ANN model contributes to the efficient and accurate evaluation of power loss and the antifriction design of CRBs.

2. Materials and methods

To train and test an ANN model using actual data for predicting the desired bearing frictional moment values, the frictional moment, inner ring speed, radial load distribution among rollers, cage slip and lubricant property were synchronously measured during the experiment (Fig. 1(a)). An ANN model was designed for predicting the frictional moment of CRBs by using the experimentally measured operating data of the test CRB (Fig. 1(b)).

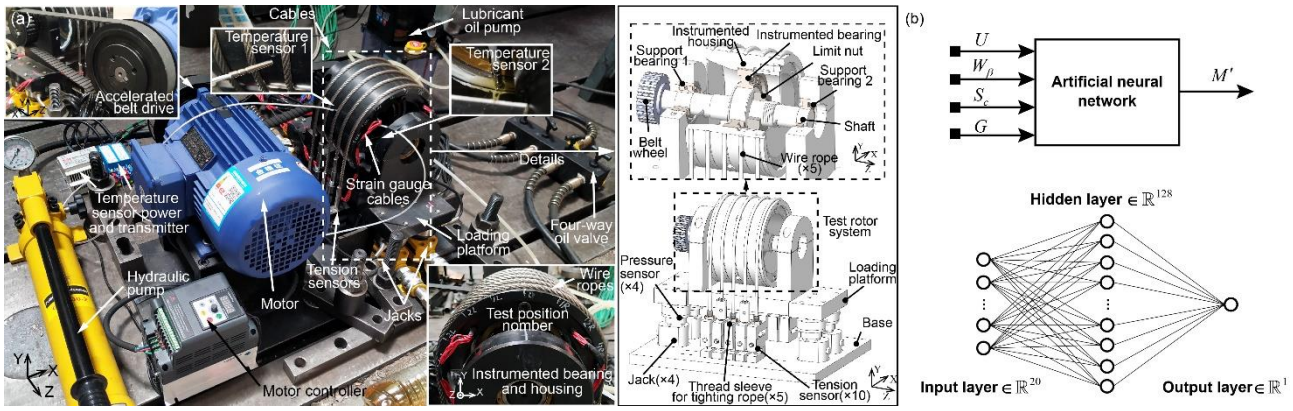

Table 1. Experimental design (involving MS1 heat-treated machined peened samples)

3. Results and conclusions

A total of 304 combined test conditions were carried out and provided 182 samples as the training set and 122 samples as the test set. The prediction results of frictional moments based on both the training set and test set are observed to agree well with the measured ones (Fig.2(a)). Compared with the conventional physical models of SKF and ISO, the ANN model trained by using the measured data provides better predictions of the CRB frictional moment under a wide range of operating conditions (Fig.2(b))..

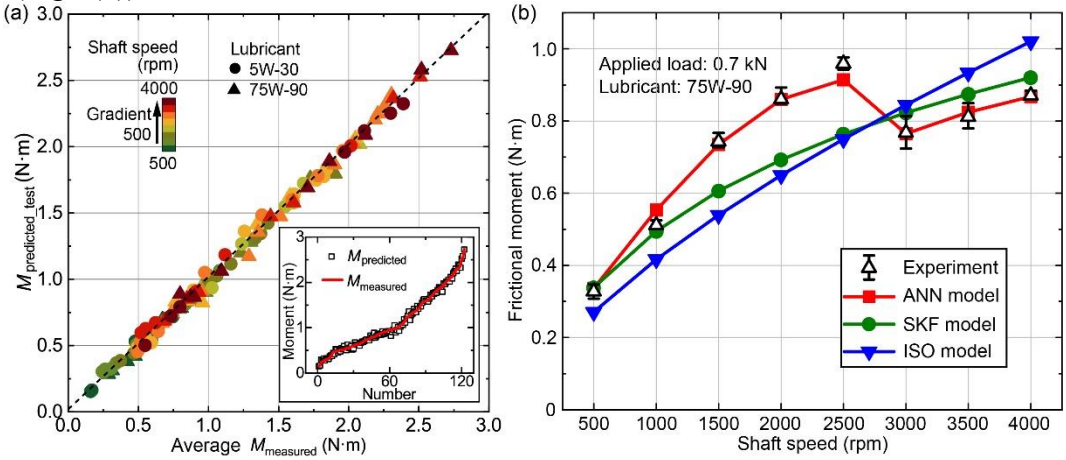

Fig. 1. (a) Comparison between the measured frictional moment and the prediction results from the ANN model based on the test set, (b) Comparison between predicted frictional moments by using ANN, SKF and ISO model

4. Acknowledgements

This research is supported by the Joint Funds of the National Natural Science Foundation of China (Grant No. U1834202).

5. References

[1] H. Matsuyama, H. Dodoro, K. Ogino, H. Ohshima, and K. Toda (2004). Development of super-low friction torque tapered roller bearing for improved fuel efficiency, *SAE Technical Paper Series,* No. 2004-01-2674.

[2] M. Masjedi and M. M. Khonsar (2013). Theoretical and experimental investigation of traction coefficient in line-contact EHL of rough surfaces. *Tribol. Int.*, **70**, 179–189.

[3] H. R. F. Fotso, C. V. A. Kazé, and G. D. Kenmoé (2021). Real-time rolling bearing power loss in wind turbine gearbox modeling and prediction based on calculations and artificial neural network, *Tribol. Int.*, **163**, 107171.

[4] F. Meng, J. Gong, S. Yang, L. Huang, H. Zhao, and X. Tang (2021). Study on tribo-dynamic behaviors of rolling bearing-rotor system based on neural network, *Tribol. Int.*, **156**, 106829.

SELF-EVOLVING SYNTHESIS OF HYDROGELS WITH LOW INTERFACIAL ADSORPTION MECHANICAL PROPERTIES FOR SINGLE-CELL ANALYSIS

Wenhui Lu[1], Xiaobao Cao[2], Zhike Peng[3], Xi Shi[1] and Songtao Hu[*1]
[1] State Key Laboratory of Mechanical System and Vibration, School of Mechanical Engineering, Shanghai Jiao Tong University, Shanghai 200240, China
[2] Guangzhou National Laboratory, Guangzhou 510320, China
[3] School of Mechanical Engineering, Ningxia University, Yinchuan 750021, China
**Corresponding author: E-mail: hsttaotao@sjtu.edu.cn*

1. Introduction

Single-cell protein analysis allows for a deeper understanding of the single-cell resolution, offering the potential to reveal cellular heterogeneity and enhance the exploration of biological phenomena and disease biology. Hydrogels are utilized as functional carriers in various forms, and they have been successfully applied in genomics and transcriptomics. However, the high interfacial protein adsorption of hydrogels leads to considerable false positives and reduced detection sensitivity, forming a significant bottleneck for the application of single-cell protein analysis.

Free radical polymerization is a widely employed method for preparing hydrogels, allowing for the adjustments in physicochemical properties by varying the types and ratios of monomers [1]. Adam D. Celiz et al. utilized 141 types of acrylamides and their derivatives to create 909 polymers aimed at identifying novel materials for culturing human pluripotent stem cells [2]. Hassan M. Rostam et al. constructed a homopolymer library based on 141 acrylamide and its derivative monomers to evaluate the effects of various polymers on macrophage polarization and to investigate their ability to modulate macrophage phenotypes and responses to implanted foreign bodies [3]. Doreen Chan et al. combined 11 types of acrylamide monomers at a 25% ratio to create a library of 172 different polymers and assessed their ability to resist contamination from serum and platelet-rich plasma [4]. The capacity of the constructed hydrogel copolymer combination library is constrained by the manual operations, limiting the performance of the synthesized hydrogels. To synthesize hydrogels with ultra-low interfacial adsorption mechanical properties, it is essential to have a sufficiently large library, which presents a high-dimensional screening challenge.

Here, we reported a self-evolving experimental platform for synthesizing hydrogels with ultra-low interfacial adsorption mechanical properties. This platform integrates nine automated workstations to enable can-do capabilities and employs synergy-enhanced Bayesian optimization as its AI brain to tackle small-data challenges. Using this paradigm, we synthesized hydrogels with an ultra-low interfacial adsorption mechanical index of 0.2537, achieving nearly a 10^4-fold reduction in experimental workload. Additionally, comparison with conventional hydrogels using sandwich ELISA shows a nearly 9-fold improvement in detection sensitivity.

2. Materials and methods

We proposed a robotic platform for synthesizing hydrogels with ultra-low interfacial adsorption mechanical properties (Fig. 1). The synthesis system was constructed based on the photo-crosslinkable principle and consisted of a liquid handling workstation, a shaking workstation, a light-curing workstation, and a storage workstation, ultimately realizing stable curing of hydrogels. The characterization system was built upon the bicinchoninic acid protein assay method and comprised a metal bath workstation, a rotary cleaning workstation, an incubation workstation, and a microplate reader workstation, thereby enabling quantification of non-specific protein adsorption. Additionally, the mobile robot was designed to serve as the connective device among these workstations.

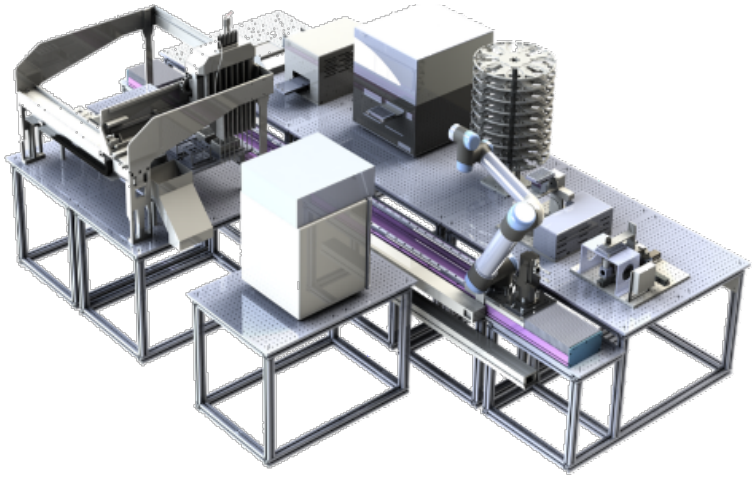

Figure 1. Composition of three systems and nine key workstations

Besides the robotic platform to run synthesis and characterization taskflows sequentially to collect standardized data, we also developed the artificial intelligence as the brain to analyze the collected data, redesign hydrogel formulations, thus enabling a human-like self-evolving paradigm (Fig. 2).

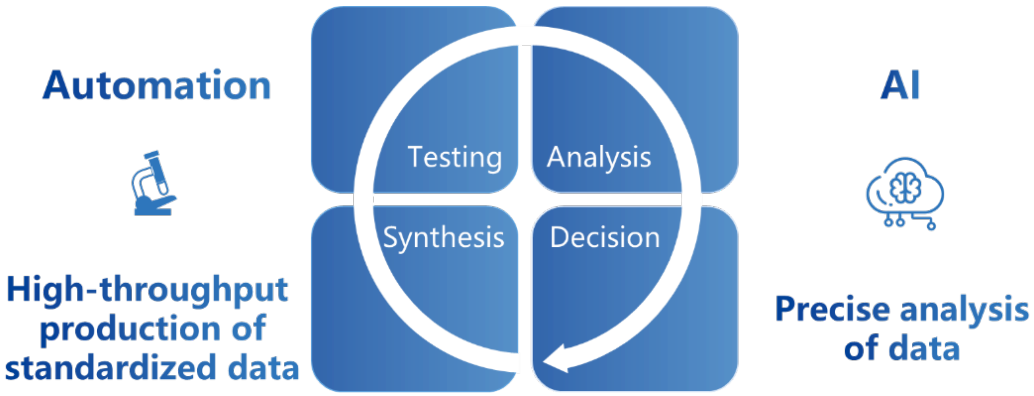

Figure 2. Synthesis-Testing-Analysis-Decision cycle

3. Results and conclusions

The standard antigen concentration detection curves using beads as carriers are plotted in Fig. 3. The self-evolving synthesized hydrogels exhibited nearly a 9-fold increase in detection sensitivity, highlighting the significant potential of the self-evolving synthesized hydrogels in single-cell protein analysis.

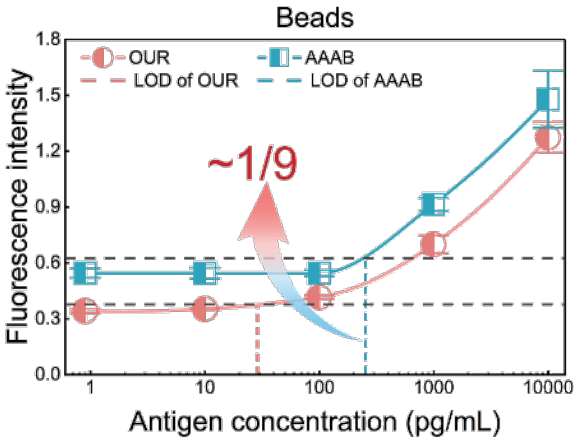

Fig. 3. Standard antigen concentration detection curves using beads as carriers

4. Acknowledgements

The research presented in this paper has received funding from the National Natural Science Foundation of China (12272226), Natural Science Foundation of Shanghai (23ZR1430200), National Natural Science Foundation of China (12232013) and Major Project of Guangzhou National Laboratory (GZNL2024A03003).

5. References

[1] Li, R., Sun, Y., Cai, Z., Li, Y., Sun, J., Bi, W., Yang, F., Zhou, Q., Ye, T., & Yu, Y. (2021). Highly bioactive peptide-HA photo-crosslinking hydrogel for sustained promoting bone regeneration. *Chem. Eng. J.*, **415**, 129015.

[2] Celiz, A. D., Smith, J. G. W., Patel, A. K., Hook, A. L., Rajamohan, D., George, V. T., Flatt, L., Patel, M. J., Epa, V. C., Singh, T., Langer, R., Anderson, D. G., Allen, N. D., Hay, D. C., Winkler, D. A., Barrett, D. A., Davies, M. C., Young, L. E., Denning, C., & Alexander, M. R. (2015). Discovery of a novel polymer for human pluripotent stem cell expansion and multilineage differentiation. *Adv. Mater.*, **27**, 4006–4012.

[3] Rostam, H. M., Fisher, L. E., Hook, A. L., Burroughs, L., Luckett, J. C., Figueredo, G. P., Mbadugha, C., Teo, A. C. K., Latif, A., Kämmerling, L., Day, M., Lawler, K., Barrett, D., Elsheikh, S., Ilyas, M., Winkler, D. A., Alexander, M. R., & Ghaemmaghami, A. M. (2020). Immune-instructive polymers control macrophage phenotype and modulate the foreign body response in vivo. *Matter*, **2**, 1564–1581.

[4] Chan, D., Chien, J., Axpe, E., Blankemeier, L., Baker, S. W., Swaminathan, S., Piunova, V. A., Zubarev, D. Yu., Maikawa, C. L., Grosskopf, A. K., Mann, J. L., Soh, H. T., & Appel, E. A. (2022). Combinatorial polyacrylamide hydrogels for preventing biofouling on implantable biosensors. *Advanced Materials*, **34**, 2109764.

UNSUPERVISED STRUCTURAL DAMAGE ASSESSMENT METHOD BASED ON RESPONSE CORRELATIONS

Licheng Zhou and Yonghui Lu

State Key Laboratory of Subtropical Building and Urban Science, School of Civil Engineering and Transportation, South China University of Technology, Guangzhou 510640, China

1. Introduction

Structural damage assessment for civil engineering structures has become an important research topic and has gained much attention for decades in the field of structural health monitoring (SHM). Currently, many researchers have focused on unsupervised learning structural damage identification methods. The most important merit of these methods is that they only use structural response data in undamaged conditions to train and do not require damage labels. Some unsupervised learning methods can localize damage, such as feature-based methodologies[1,2] and autoregressive (AR) model-based methods[3,4]. For feature-based methodologies, although the damage localization effect on practical engineering structures is good, it has the disadvantages of too many artificially extracted features, a large amount of calculation, and a complex feature selection process, which make this method have certain limitations in practical engineering applications. AR model-based methods can automatically extract features from structural response data, but they have certain limitations on the type of structure or load conditions. However, it is noteworthy that these methods can be improved if both the correlations among sensors were considered and advanced deep learning networks were employed instead.

Therefore, this study proposes an unsupervised structural damage assessment method, which applies bidirectional long short-term memory (BiLSTM) networks to establish the response correlations among sensors. The proposed method only uses structural response data in undamaged conditions to train the response correlation model and considers the response correlations among sensors, enabling it to automatically identify and localize damage in an unsupervised manner for practical civil engineering structures under operational and ambient excitations.

2. Methods

The proposed method first divides the sensor into several sensor clusters and uses BiLSTM networks to establish a response correlations model for each sensor cluster. Specifically, the response correlations model for each sensor cluster reconstructs the acceleration response of a certain sensor by using the acceleration response of adjacent sensors in the sensor cluster. Then, reconstruction errors between the true and reconstructed responses are taken as damage-sensitive features. Finally, the damage is identified and localized through changes in the reconstruction errors of different sensor clusters.

3. Results and conclusions

The effectiveness and accuracy of the proposed damage identification method are verified by conducting a numerical beam-like bridge experiment. As is shown in Fig. 1, the span of the beam-

like bridge is l = 3 m, and the cross-sectional dimension is 120 mm×60 mm. The wall thickness of the beam is 3 mm. Four damage locations were set on the beam to verify the effectiveness of the proposed method. The ambient excitation was simulated by applying 100 Hz white Gaussian noise vertically at nineteen nodes of the model. Five virtual vertical accelerometer sensors were arranged at the bottom of the beam to collect the acceleration response.

This beam-like bridge model considers 3 sensor clusters, and the corresponding reference sensors are sensors 2, 3, and 4, respectively. The damage identification results of the beam-like bridge are presented in Fig. 2. This result shows the damage position can be determined based on the identified damages from the sensor clusters. In other words, if the damage is identified in a certain sensor cluster, it means that this damage occurs near the reference sensor for that sensor cluster. In a word, considering the three sensor clusters of the beam-like bridge model comprehensively, not only can the damage be identified, but also the location of the damage can be accurately localized.

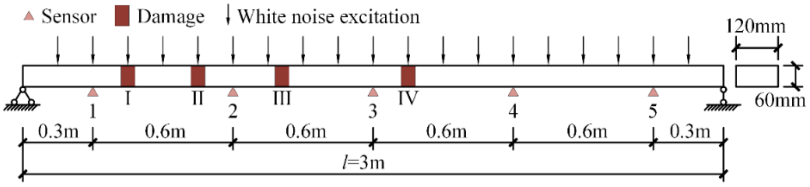

Fig. 1. Sketch of the beam-like bridge model.

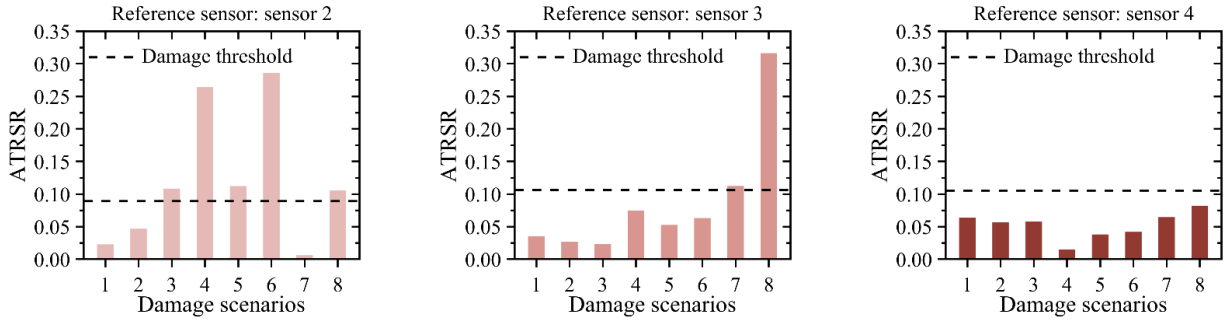

Fig. 2. Damage identification results of the beam-like bridge for the proposed method with (a) sensor cluster 1, (b) sensor cluster 2, and (c) sensor cluster 3.

4. Acknowledgements

This research has been supported by the National Natural Science Foundation of China (Grant Nos. 11972162, 11932007, 12072115, and 12072116), the Natural Science Foundation of Guangdong Province, China (Grant No. 2023A1515012942), and the State Key Laboratory of Subtropical Building and Urban Science, South China University of Technology (Grant No. 2022KA05).

5. References

[1] M. Kaloop, J. Hu (2015). Stayed-cable bridge damage detection and localization based on accelerometer health monitoring measurements. Shock Vib., **2015**, 1–11.

[2] V. Alves, A. Cury (2023). An automated vibration-based structural damage localization strategy using filter-type feature selection. Mech. Syst. Signal Process, **190**, 110145.

[3] A. Entezami, H. Shariatmadar (2018). An unsupervised learning approach by novel damage indices in structural health monitoring for damage localization and quantification. Struct. Health Monit., **17**, 325–45.

[4] K. Roy, B. Bhattacharya, S. Ray-Chaudhuri (2015). ARX model-based damage sensitive features for structural damage localization using output-only measurements. J. Sound Vib., **349**, 99–122.

DIGITAL IMAGE CORRELATION FOR DEFORMATION MEASUREMENT IN HIGH-TEMPERATURE ENVIRONMENT

Dongcai Tan[1], Banglei Guan[1*], Shunkun Liang[1], Ang Su[1], Zhang Li[1], Yang Shang[1], Xiaolin Liu[2] and Qifeng Yu[1]

[1] College of Aerospace Science and Engineering, National University of Defense Technology, Changsha, China

[2] College of Physics and Optoelectronic Engineering, Shenzhen University, Shenzhen, China

** Corresponding Author*

1. Introduction

With the rapid development of aerospace vehicles, accurate measurement of high-temperature structural deformation has become increasingly important. Thermal deformation measurement is of great importance for evaluating the thermal mechanical performance indicators of materials. Traditional contact-based deformation measurement methods are difficult to apply in high-temperature environments because components cannot withstand high temperatures. Therefore, the development of non-contact ultra-high-temperature deformation measurement methods is extremely important. The digital image correlation method is a widely used non-contact deformation measurement method that has the advantages of non-contact, full-field measurement, high precision, and strong environmental adaptability and has obvious advantages and application value in ultra-high-temperature environment deformation measurement. [1-3] employs light sources with varying wavelengths and adaptive narrow band filters to mitigate the decorrelation caused by thermal radiation, thereby enhancing the accuracy of deformation measurement. [4-6] utilize digital image technology to investigate the impact of creep effect on fatigue behavior [4], plastic deformation of metal foils under high temperature and tensile loads [5], as well as strain measurement and structural health monitoring [6] in high temperature environments. However, their research did not encompass the actual process of thermal deformation measurement due to factors such as temperature rise, air flow from high temperature regions to low temperature regions, changes in air density, and alterations in air refractive index. These factors significantly compromise the accuracy of measuring high temperature deformation fields.

This study uses a combination of simulation and ray tracing algorithms to analyze the deflection laws of light in high-temperature fields and real-time compensates them into the measurement results of high-temperature deformation. To verify the precision of the refractive index compensation for the deformation measurement results, we set up a binocular stereo vision measurement system and used a high-power blue light source and corresponding narrowband filter to weaken the interference of thermal radiation. The experimental results show that the measurement system can collect clear images in high-temperature environments, and the measurement results closely align with simulation outcomes at 1100℃, which can meet the measurement needs of components in high-temperature environments. This research not only improves the precision of high-temperature deformation measurement but also provides an effective technical means for measurement in high-temperature environments.

2. Materials and methods

In the experiment, we designed and manufactured an aluminum alloy S-bend specimen to simulate a key structural component in aerospace vehicles. To measure the high-temperature deformation of the S-bend specimen, we adopted a monocular spectrometry technique by cleverly configuring optics so that a single camera could simulate the function of a binocular stereoscopic vision system. This method effectively solved the time-temperature synchronization problem in traditional binocular stereoscopic measurement systems, where the two cameras may experience time synchronization errors due to temperature differences in high-temperature environments. Meanwhile, the technique also avoided measurement errors introduced by relative vibrations between cameras. In this study, Zhang's calibration method [7] is used to calibrate the monocular camera through the checkerboard calibration board, and part of the calibration pictures are shown in Figure 1. The calibration results of relative extrinsic parameter of the stereo vision measurement system are shown in Table 1.

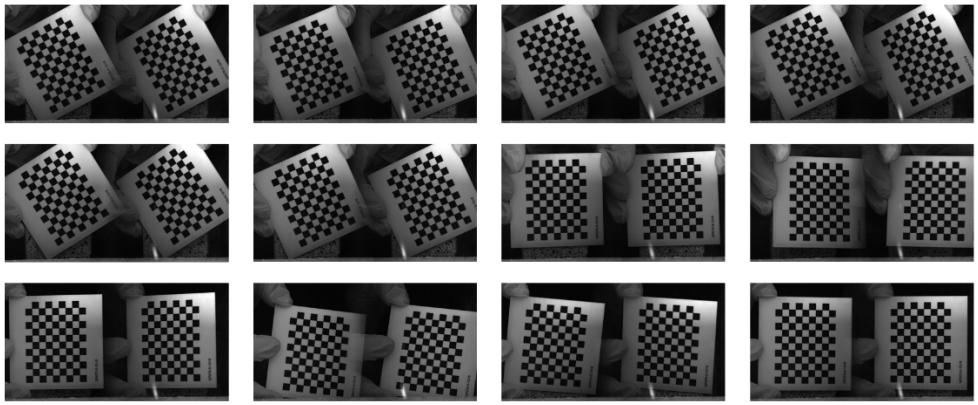

Fig. 1. Partial calculation pictures

translation vector/mm			orientation parameters/°		
T_x	T_y	T_z	θ_x	θ_y	θ_z
-123.40	0.82	17.69	-0.184	18.583	-0.312

Table 1. Relative extrinsic parameter of the stereo vision measurement system

3. Results and conclusions

Figure 2 shows the partial thermal deformation results of the S-bend test piece calculated by the digital image correlation method under high-temperature conditions. In this figure, DT represents the total displacement of the test piece. During the experiment, the test piece was heated from room temperature and gradually increased to 500°C for the first time, then successively increased to 700° C, 900°C and 1100°C. After each temperature increase to the set temperature, the heating furnace was kept at that temperature for 20 minutes to ensure that the test piece temperature reached the set value.

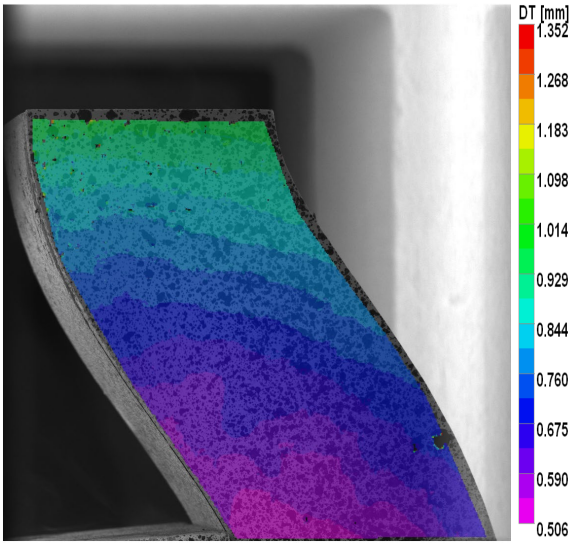

Fig. 2. Partial deformation calculation results

Figure 3 shows the deformation at the center position of the test piece. The deformation results were compared with the simulation results obtained by software. In terms of deformation trends and numerical values, a good fit was achieved.

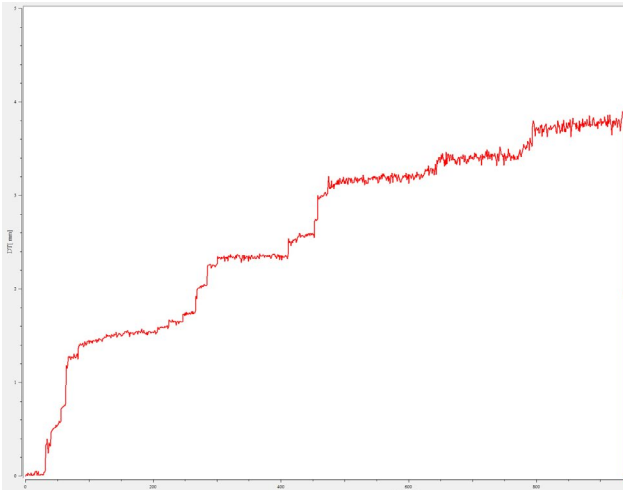

Fig. 3. The deformation results at the center of the specimen

4. Acknowledgements

This research has been supported by the Hunan Provincial Natural Science Foundation for Excellent Young Scholars under Grant 2023JJ20045, and the National Natural Science Foundation of China under Grant 12372189.

5. References

[1] T. Q. Thai, R.S. Hansen, A. J. Smith, et al (2019). Importance of exposure time on DIC measurement uncertainty at extreme temperatures, *Exp. Tech.*, **43**, 261-271.

[2] A. Doitrand, R. Estevez, M. Thibault, P. Leplay (2020). Fracture and cohesive parameter identification of refractories by digital image correlation up to 1200℃, *Exp. Tech.*, **60**, 577-590.

[3] E. K. Nickerson, R. B. Berke (2018). Ultraviolet diffraction assisted image correlation (UV-DAIC) for single-camera 3D strain measurement at extreme temperatures, *Exp. Tech.*, **58**, 885-892.
[4] A. V. Movahedi-Rad, T. Keller, A. P. Vassilopoulos (2019). Creep effects on tension-tension fatigue behavior of angle-ply GFRP composite laminates, *Int. J. Fatigue*, **123**, 144-156.
[5] Q. Zheng, N. Mashiwa, T. Furushima (2020). Evaluation of large plastic deformation for matals by a non-contacting technique using digital image correlation with laser speckles, *Mater. Des.*, **191**, 108626.
[6] Y. Pang, B. K. Chen, S. F. Yu, S. N. Lingamanaik (2020). Creep effects on tension-tension fatigue behavior of angle-ply GFRP composite laminates, *Opt. Lett.*, **45**, 2331-2334.
[7] Z. Z. You(2000). A flexible new technique for camera calibration. *IEEE Trans. Pattern Anal. Mach Intell.*, **22**, 1330-1334.

INTELLIGENT LOCALIZATION METHOD OF FATIGUE CRACK TIPS IN NUMEROUS HIGH-TEMPERATURE DIC IMAGES

Lei Huang[1], Xing Sun[1], Wei He[2*] and Huimin Xie[3*]
[1] School of Mechanical Engineering and Mechanics, Xiangtan University, Xiangtan, China
[2] College of Mechanical and Vehicle Engineering, Hunan University, Changsha, China
[3] AML, School of Aerospace Engineering, Tsinghua University, Beijing, China
** Corresponding author. Email: hewei2008@hnu.edu.cn & xiehm@mail.tsinghua.edu.cn*

1. Introduction

In recent years, there has been growing interest in leveraging deep learning (DL) for solving complex problems in fracture mechanics, particularly those related to fatigue crack propagation. Fatigue fracture is a critical failure mode in structural materials, it can occur under cyclic loads significantly below the yield stress, leading to catastrophic failures in components such as turbine blades. The ability to monitor and characterize fatigue crack behavior is therefore of paramount importance for ensuring safety and performance[1].

Digital Image Correlation (DIC) has proven to be a robust optical measurement technique for studying fatigue fracture. By integrating DIC with fracture mechanics, key parameters such as stress intensity factors (SIFs) and crack closure effects can be accurately evaluated[2]. However, accurate localization of crack tips from DIC images remains a challenge due to limitations in image quality.

To address these challenges, recent studies have explored automatic crack tip localization methods. With the advent of deep learning, DL-based approaches have emerged as promising alternatives[3,4]. Unlike traditional methods, deep learning models can directly map displacement fields to crack tip locations without depending on physical models, offering advantages in speed, accuracy, and robustness to noise.

This study builds on previous advancements by proposing a novel deep learning framework for crack tip localization using the U-Net architecture. Transfer learning (TL) is employed to overcome the limitations of small datasets, enhancing the network's ability to generalize across different geometries, fabrication processes, and service environments. The proposed method is validated by analyzing its accuracy in varying conditions, demonstrating its potential to revolutionize fatigue crack analysis through automated and efficient crack tip localization.

2. Methods and principle

The displacement field and crack path near the crack tip can be obtained by DIC technique combined with optical microscopy[5], from which labeling data can be obtained and a dataset for deep learning can be built. The crack tip localization model is constructed based on U-Net neural network, and the training process is divided into pre-training and transfer learning training, and the transfer learning adjusts the hidden layer of the network by fine-tuning the pre-training model using a smaller experimental dataset to improve its generalization performance under different conditions. The effectiveness of transfer learning is demonstrated by the performance of the pre-training model and the transfer learning model on the validation set, as shown in Figure 1.

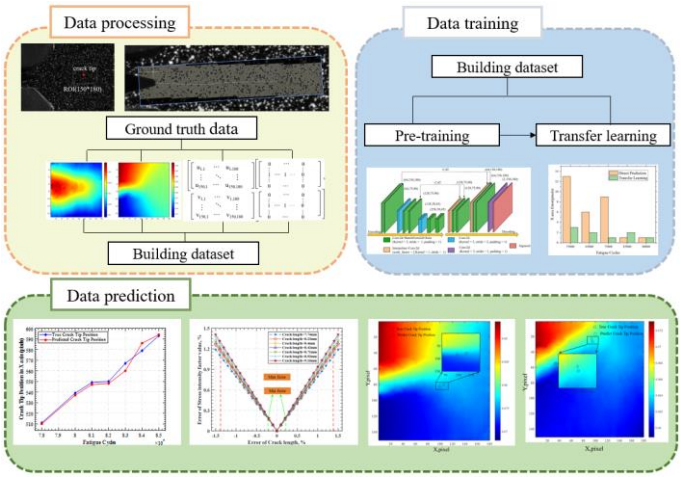

Figure 1. Localization method

3. Results and conclusions

Based on the proposed model in this paper, the crack tip location in the crack extension direction is predicted and compared with the real value, and the results are shown in Fig. 2. The geometry size, fabrication process, and service environment generalization performance of the proposed model are tested on the test set. The results show that the average error of the crack tip position localized by the model is 0.08 mm, and the localization time is within 0.2 s. The results are shown in Fig. 2.

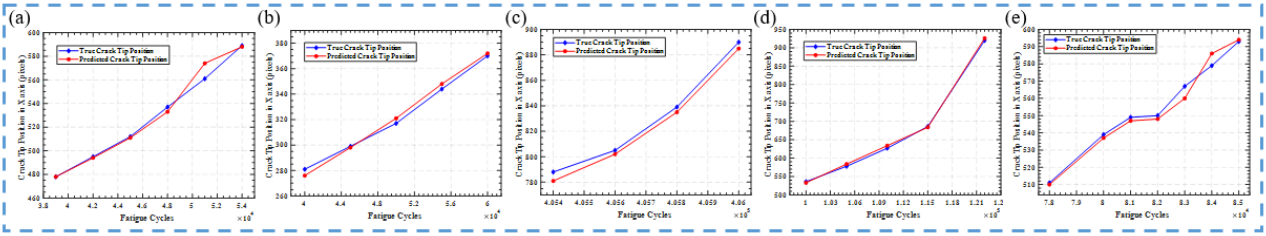

Fig. 2. The results of model generalization performance: (a) geometry size, (b)、(c) fabrication process, (d)、(e) service environment.

4. Acknowledgements

This work was supported by the National Natural Science Foundation of China (No. 12032013, 12272131, 12327801), and the Science and Technology Innovation Program of Hunan Province (2024RC3048).

5. References

[1] Neto D M, Borges M F, Antunes F V, et al. Mechanisms of fatigue crack growth in Ti-6Al-4V alloy subjected to single overloads[J/OL]. Theoretical and Applied Fracture Mechanics, 2021, 114: 103024.
[2] Duan Q Y, Li J Q, Li Y Y, et al. A novel parameter to evaluate fatigue crack closure: Crack opening ratio[J/OL]. International Journal of Fatigue, 2020, 141: 105859.
[3] Strohmann T, Starostin-Penner D, Breitbarth E, et al. Automatic detection of fatigue crack paths using digital image correlation and convolutional neural networks[J/OL]. Fatigue & Fracture of Engineering Materials & Structures, 2021, 44(5): 1336-1348.
[4] Li Y, Ni T, Zhang F, et al. U-Net learning for the automatic identification of the sandstone crack tip position to determine mixed-mode stress intensity factors utilizing digital image correlation method[J/OL]. Theoretical and Applied Fracture Mechanics, 2023, 127: 104028.
[5] Additive manufacturing - Opening stress intensity factor determination of metal components - Digital image correlation method[Z].

AI-BASED OPTIMIZATION OF BOLTED JOINTS DESIGN

D. Croccolo[1], M. De Agostinis[1], S. Fini[1], M. Khan[1,2], M. Mele[1], G. Olmi[1], C. Scapecchi[1], Z. Wu[2], S. Nassar[2]

[1]Department of Industrial Engineering (DIN), University of Bologna, Bologna, 40136, Italy
[2]Department of Mechanical Engineering, Oakland University, Rochester, MI 48309, USA

1. Introduction

This study takes advantage of Genetic Algorithms (GA) to optimize bolted joints design subjected to external loads and bending moments. Optimization variables include the number of bolts, layout, and bolt size. The optimization objective is to achieve a uniform combined stress distribution in all the bolts and reduce weight and cost of an end plate-to-beam connection.

Among the various optimization techniques, those based on evolutionary algorithms are preferred for their robustness and ability to handle multiple variables, such as genetic algorithms, which are known for their effectiveness in finding global optimal solutions to engineering problems [1-2]. In a recent research publication [3], a genetic algorithm was used to optimize the screws layout to minimize the acceleration/vibrations in an electronic circuit component. From the analytical and FEA analysis, the optimization led to a 67% reduction in the acceleration, from 43.9 m s^{-2} to 14.4 m s^{-2}. In an aerospace application [4], genetic algorithm was applied to optimize the bolt layout to reduce the stresses at the hole edge of an aircraft wing. In the new layout, the maximum hole edge stress and number of bolts were decreased by 31% and 10% respectively. Likewise, Lu et al. [5] used [the grey wolf] algorithm to optimize the arrangement of nickel steel plate connectors with a triangular bolt pattern. The findings indicate a 24% optimization rate compared to the original structure layout.

However, a limited number of studies are conducted on the development of optimization tools for threaded fasteners based on Artificial Intelligence (AI) algorithms. In this study, a tool is developed using genetic algorithms in order to optimize bolt locations, size, and number for a given geometry and loading condition, in order to achieve uniform stress and load distribution in all bolts. The effect of elastic interaction between bolts [during inititial preloading] is taken into account for its effect on clamp load scatter in rectangular and circular flanges [6]. Moreover, a machine learning (ML) model was trained using finite element analysis (FEA) simulations to predict the optimal joint parameters.

2. Materials and methods

Initially, a simple cantilever beam was considered for the analysis, as shown in Figure 1. The beam can be subjected to six different types of loads, including two bending moments (Mx and My), one torsional moment (Mz), two shear forces (Fx and Fy), and one normal force (Rn). Forces were applied at the free end of the beam, and four cases were analysed: shear (Fy) and bending moment along the x-axis, shear (Fx) and bending moment along the y-axis, combined shear and bending moments along both the axes and a torsion.

In the first step, a tentative bolt size is estimated by assuming that bolts are not preloaded (in a loosened state) and using the following equation 1.

$$F_i = \frac{R_{t_i}}{\mu \cdot z} + R_{n_i} \quad (1)$$

Where, F_i is the initial load on each bolt, R_{t_i} and R_{n_i} are tangential and normal components of forces, μ is the coefficient of friction, and z is the number of surfaces in contact. Once the F_i is found for specific loading conditions and bolt positions, the suitable bolt size is chosen from the bolt's dataset.

After picking the appropriate bolt size for initial bolt positions, the genetic algorithms are then implemented in python to find the best bolt locations to minimize the size and to uniformly distribute stress among all bolts. Once the best positions and sizes of bolts are individuated, the stresses are analysed to make sure that they do not exceed the yield stress of the selected bolt size or joint material.

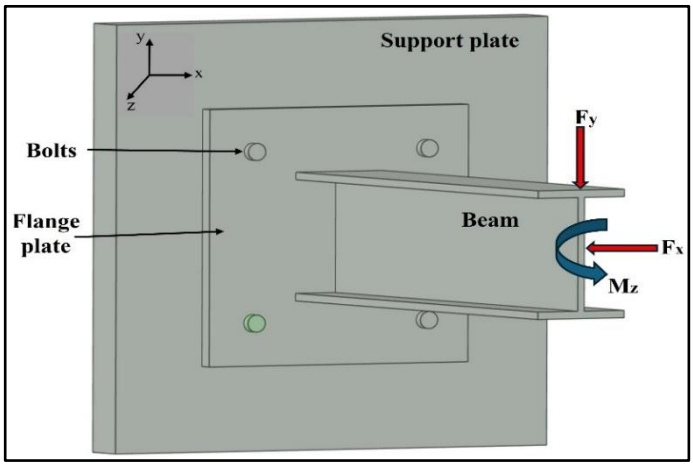

Fig. 1. Beam-flange connection subjected to external loads.

3. Results and conclusions

The preliminary results from the genetic algorithm for bending moments and torsion are presented in Figure 2. For bending along the x-axis with four bolts, the algorithm suggests placing all four bolts on the top side of the beam to better withstand the bending moments. Similarly, for bending along the y-axis, it recommends positioning the bolts on the opposite side to the direction of the applied load. For combined bending moments along the x and y axes, the algorithm recommends placing the bolts at the corners, on the opposite sides to the applied loads. In the case of torsion, the optimal bolt placement is at each corner of the flange, to provide maximum polar inertia.

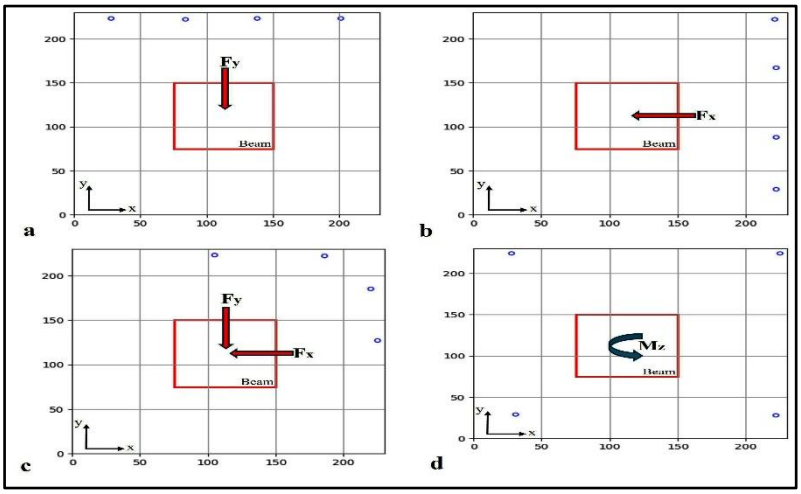

Fig. 2. Bolt positions after optimization; (a) shear and bending along x; (b) shear and bending along y; (c) combined shear and bending along x and y; (d) torsion along z.

Acknowledgements: *Project funded under the National Recovery and Resilience Plan (NRRP), Mission 04 Component 2 Investment 1.5– NextGenerationEU, Call for tender n. 3277 dated 30/12/2021 Award Number: 0001052 dated 23/06/2022.*

4. References

[1] C. He, Y. Zhang, D. Gong, and X. Ji, "A review of surrogate-assisted evolutionary algorithms for expensive optimization problems," *Expert Systems with Applications,* vol. 217, 2023. https://doi.org/10.1016/j.eswa.2022.119495.

[2] M. Gen and L. Lin, "Genetic algorithms and their applications," in *Springer handbook of engineering statistics*: Springer, 2023, pp. 635-674. https://doi.org/10.1007/978-1-4471-7503-2_33.

[3] B. Shen, Z. Pan, H. Lin, and W. Li, "Bolt layout optimization design based on genetic algorithm," in *IOP Conference Series: Materials Science and Engineering*, Beijing, China, 22-24 March, 2019, vol. 576, no. 1: IOP Publishing. https://doi.org/10.1088/1757-899X/576/1/012005.

[4] W. Xiao, E. He, Y. Hu, and S. Aeronautics, "A new method of optimizing bolts layout in connector based on improved genetic algorithm," *Journal of Northwestern Polytechnical University,* vol. 35, no. 3, pp. 414-421, 2017.

[5] X. Lu, M. Zhu, Y. Liu, S. Wang, Z. Xu, and S. Li, "Triangular position multi-bolt layout structure optimization," *Applied Sciences,* vol. 13, no. 15, p. 8786, 2023. https://doi.org/10.3390/app13158786.

[6] Nassar, S. A., and Yang, X, "Novel Formulation of Bolt Elastic Interaction in Gasketed Joints." ASME. *Journal of Pressure Vessel Technology*. October 2009; 131(5): 051204. https://doi.org/10.1115/1.3151814.

SELF-ECOLVING SYNTHESIS OF LIGHT-WEIGHT AND HIGH-STRENGTH MECHENICAL METAMATERIALS

Haoran Li[1],Xiaobao Cao[2], Xi Shi[1], Zhike Pen[3], Songtao Hu[*1]
[1] State Key Laboratory of Mechanical System and Vibration, School of Mechanical Engineering, Shanghai Jiao Tong University, Shanghai 200240, China
[2] Guangzhou National Laboratory, Guangzhou 510320, China
[3] School of Mechanical Engineering, Ningxia University, Yinchuan 750021, Ningxia, China

1. Introduction

Light-weight, high-strength materials are in high demand in fields such as aerospace, transportation, and civil construction. Mechanical metamaterials, as a kind of structural material, have attracted widespread research for their high specific strength and specific stiffness[1]. In recent years, plate lattice metamaterials have been shown to surpass Hashin-Shtrikman limitation, demonstrating significant potential[2]. However, the design and optimization of plate lattice metamaterials faces substantial challenges. Firstly, due to nonlinear properties of structures and random defects during manufacturing processes, the predictions of computational methods such as Finite Element Analysis often deviate significantly from real-world results, necessitating reliance on mechanical testing to evaluate the quality of designs[3]. Secondly, the high-dimensional parameter space requires extensive experimental exploration, thus traditional trial-and-error methods and labor-intensive synthesis are insufficient to address this issue. Automated experiment, a combination of automated laboratory processes and artificial intelligence, offers a solution to these challenges. Some automative labs have been developed in biology, chemistry and materials[4], proven able to accelerate experiments and scientific discovery. However, reports on automated experiments are scarce in the field of mechanical research. Snapp, et al.[5] reported a Bayesian experimental autonomous researcher for toughness optimation of 3D print structre, which ignored the multi-objective optimization needs of material mechanical properties. Additionally, No work has been reported on the automated synthesis and optimization of mechanical metamaterials.

Here, we present a self-evolving robotic platform for synthesizing and optimizing plate lattice metamaterials. Along with 10 key workstations for automated systhesize and experiment, we developed a multi-objective Bayesian optimization algorithm with soft-constraint as the AI brain to provide directional suggestions for subsequent automated experiments. Through this self-evolving paradigm, the robotics platform autonomously conducted 58 iterations with 696 mechanical tests. And finally constructed a Pareto front for the three objectives. The results show that under the guidance of the AI brain, the model converged to a stable Pareto front in just 30 iterations, reducing the number of experimental trials by more than 1000 times compared to traditional grid search methods.

2. Materials and methods

The robotic platform is designed and assembled in our laboratory, consisting of 10 key workstations for autonomous synthesis and characterization. The parametric design of plate lattice

materials is automatically completed using Abaqus and manufactured with 3D printers (Form3+, Formlabs). Application programming interfaces (APIs) are developed for both self-built and commercial workstations, ensuring seamless communication interconnection. All programs are implemented using Python.

Fig. 1. Self-evolving robotic platform for mechanical metamaterials synthesis

3. Results and conclusions

The robotic platform autonomously conducted 58 iterations over 110 hours, performing 696 mechanical tests to construct the Pareto front for the three objectives: porosity, compressive strength, and shear strength (as shown in the Figure 2).

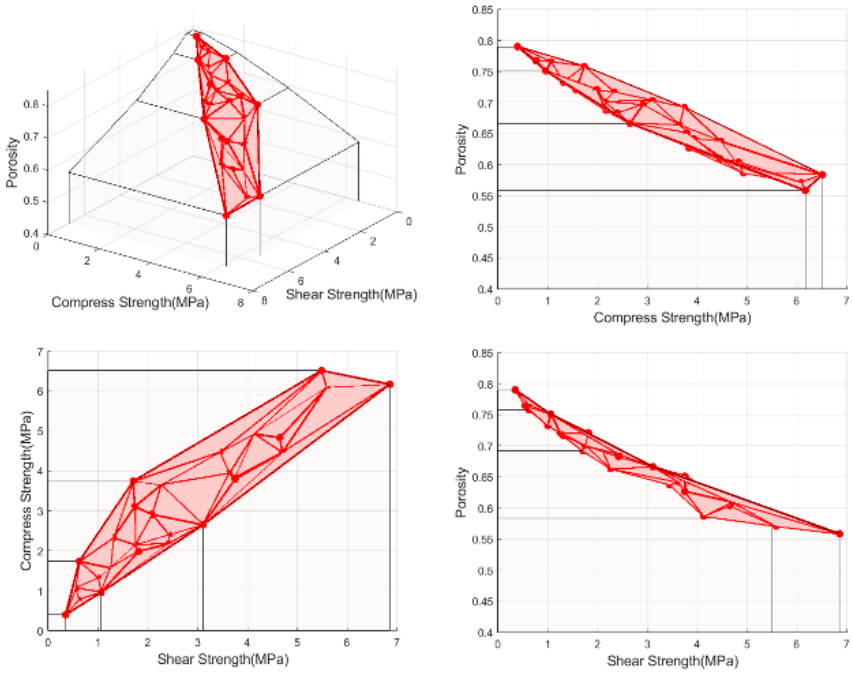

Fig. 2. Pareto front of porosity, compressive strength, and shear strength

4. Acknowledgements

The research presented in this paper has received funding from the National Natural Science Foundation of China (12272226), Natural Science Foundation of Shanghai (23ZR1430200), National Natural Science Foundation of China (12232013) and Major Project of Guangzhou National Laboratory (GZNL2024A03003).

5. References

[1] X. Yu, J. Zhou, H. Liang, Z. Jiang, and L. Wu, "Mechanical metamaterials associated with stiffness, rigidity and compressibility: A brief review," *Prog. Mater Sci.*, vol. 94, pp. 114–173, May 2018.
[2] J. B. Berger, H. N. G. Wadley, and R. M. McMeeking, "Mechanical metamaterials at the theoretical limit of isotropic elastic stiffness," *Nature*, vol. 543, no. 7646, Art. no. 7646, Mar. 2017.
[3] A. E. Gongora *et al.*, "A Bayesian experimental autonomous researcher for mechanical design," *Sci. Adv.*, vol. 6, no. 15, p. eaaz1708, Apr. 2020.
[4] A. Angelopoulos, J. F. Cahoon, and R. Alterovitz, "Transforming science labs into automated factories of discovery," *Science Robotics*, vol. 9, no. 95, p. eadm6991, Oct. 2024,.
[5] K. L. Snapp *et al.*, "Superlative mechanical energy absorbing efficiency discovered through self-driving lab-human partnership," *Nat Commun*, vol. 15, no. 1, p. 4290, May 2024.

SELF-EVOLVING MECHANICS EXPERIMENTS FOR MATERIALS SYNTHESIS

Songtao Hu*[1]

[1] *State Key Laboratory of Mechanical System and Vibration, School of Mechanical Engineering, Shanghai Jiao Tong University, Shanghai 200240, China*

**Corresponding author: E-mail: hsttaotao@sjtu.edu.cn*

1. Introduction

Mechanical experiments, which focus on various mechanical parameters to assess behavior and performance, play a crucial role in optimizing material performance, enhancing structural stability, and refining engineering design. Current mechanical experiments typically demand significant effort in the laboratory to synthesize and characterize materials, analyze results, design modified materials, and repeat this process until the desired characteristics are achieved, making it a highly time-consuming and labor-intensive endeavor. Fortunately, the marriage of automation and artificial intelligence (AI) offers a new solution. Automation increases experimental throughput while ensuring the standardization of data, thereby achieving a can-do capability. AI analysis and decision-making provides directional suggestions for subsequent automated experiments with the aid of expert experience or simulations, significantly reducing the number of required experiments and thereby achieving a can-think capability. By integrating can-do and can-think capabilities, we can attain human-like self-evolving. In recent years, similar concepts have emerged across the fields of biology [1], chemistry [2-3], and materials science [4] to address aforementioned problems. However, self-evolving mechanics experiments are little addressed.

Here, we demonstrate self-evolving mechanical experiments by successfully synthesizing light-weight, high-strength mechanical metamaterials and hydrogels with low interfacial mechanical adhesion. In addition to the automation integration of key workstations to achieve the “can-do” capability, we developed specifical algorithms as the AI brain to provide directional suggestions for subsequent automated experiments, ensuring the “can-think” capability (Fig. 1). Self-evolving mechanics experiments not only guarantee the outstanding mechanical properties of synthesized materials, but also significantly reduces the number of required experiments. As for the hydrogel, we synthesized hydrogels with an ultra-low interfacial adsorption mechanical index of 0.2537, achieving nearly a 10^4-fold reduction in experimental workload; As for the mechanical metamaterials, the robotics platform autonomously conducted 58 iterations within 110h. Results show that the model can converge to a stable Pareto front in just 30 iterations, achieving a multi-objective optimization and nearly a 10^3-fold reduction in experimental workload.

Fig. 1. Schematic of self-evolving robotic platform for mechanics experiments and materials synthesis: Automation achieves a can-do ability and AI analysis achieves a can-think ability

2. Materials and methods

Two robotic platforms are designed and assembled in our laboratory for the synthesis of both soft and hard materials with excellent mechanical properties (Fig. 2). Low-adhesion hydrogels and light-weight, high-strength mechanical metamaterials were selected as they represent advanced materials in their respective categories. The platforms consist of several key workstations for autonomous synthesis and characterization. Application programming interfaces (APIs) are developed for both self-built and commercial workstations, ensuring seamless communication interconnection. And the GUI is developed using C++ framework with Visual Studio IDE and encompasses fundamental functions, including taskflow updates, taskflow memory management, taskflow monitoring, and error alerts.

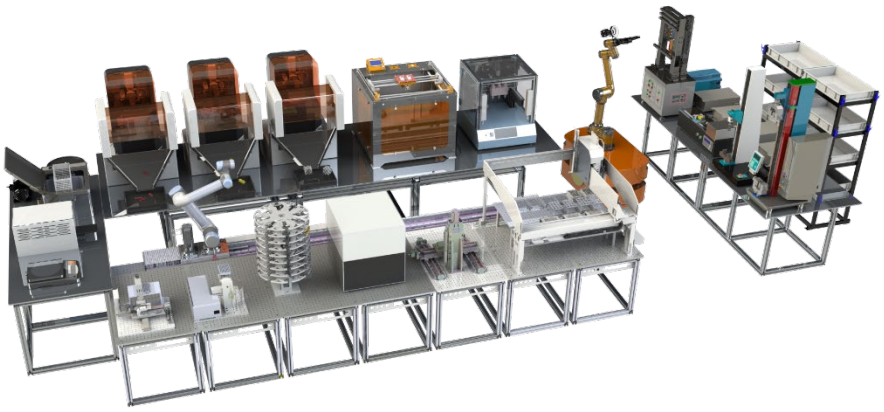

Fig. 2. Composition of robotic platforms for the synthesis of both soft and hard materials with excellent mechanical properties

4. Acknowledgements

The research presented in this paper has received funding from the National Natural Science Foundation of China (12272226), Natural Science Foundation of Shanghai (23ZR1430200), National Natural Science Foundation of China (12232013) and Major Project of Guangzhou National Laboratory (GZNL2024A03003).

5. References

[1] Huang, Y., Sheth, R. U., Zhao, S., Cohen, L. A., Dabaghi, K., Moody, T., Sun, Y., Ricaurte, D., Richardson, M., Velez-Cortes, F., Blazejewski, T., Kaufman, A., Ronda, C., & Wang, H. H. (2023). High-throughput microbial culturomics using automation and machine learning. *Nature Biotechnology*, **41**, 1424–1433.

[2] Zhu, Q., Huang, Y., Zhou, D., Zhao, L., Guo, L., Yang, R., Sun, Z., Luo, M., Zhang, F., Xiao, H., Tang, X., Zhang, X., Song, T., Li, X., Chong, B., Zhou, J., Zhang, Y., Zhang, B., Cao, J., Zhang, G., Wang, S., Ye, G., Zhang, W., Zhao, H., Cong, S., Li, H., Ling, L., Zhang, Z., Shang, W., Jiang, J., & Luo, Y. (2023). Automated synthesis of oxygen-producing catalysts from Martian meteorites by a robotic AI chemist. *Nature Synthesis*, **3**, 319–328.

[3] Zhao, H., Chen, W., Huang, H., Sun, Z., Chen, Z., Wu, L., Zhang, B., Lai, F., Wang, Z., Adam, M. L., Pang, C. H., Chu, P. K., Lu, Y., Wu, T., Jiang, J., Yin, Z., & Yu, X.-F. (2023). A robotic platform for the synthesis of colloidal nanocrystals. *Nature Synthesis*, **2**, 505–514.

[4] MacLeod, B. P., Parlane, F. G. L., Morrissey, T. D., Häse, F., Roch, L. M., Dettelbach, K. E., Moreira, R., Yunker, L. P. E., Rooney, M. B., Deeth, J. R., Lai, V., Ng, G. J., Situ, H., Zhang, R. H., Elliott, M. S., Haley, T. H., Dvorak, D. J., Aspuru-Guzik, A., Hein, J. E., & Berlinguette, C. P. (2020). Self-driving laboratory for accelerated discovery of thin-film materials. *Science Advances*, **6**, eaaz8867.

AI-BASED ANALYSIS OF GEARBOX VIBRATION-BEARING STRAIN CORRELATION

X. Zhao[1], Y. Hou[2], X. Wang[2,3]

[1] *School of Mechanical, Electronic and Control Engineering, Beijing Jiaotong University, Beijing, China*

[2] *Frontiers Science Center for Smart High-speed Railway System, Beijing Jiaotong University, Beijing, China*

[3] *School of Mechanical, Electronic and Control Engineering, Beijing Jiaotong University, Beijing, China*

1. Introduction

High-speed transmission system is a coupling system of gears - shafts - bearings - box and other components, of which the gearbox and bearings are the key components. Under actual operating conditions, the transmission system is subject to internal excitation from gears and bearings as well as external excitation from the track, and thus the transmission system exhibits different dynamic behaviors under different rotational speeds and torques [1]. Gearbox vibration acceleration can express the dynamic behavior of the transmission system directly, and the gearbox bearing strain signal contains rich information about the operating state of the bearing. Therefore, focusing on gearbox vibration acceleration and bearing strain is of great significance to the study of gearbox vibration behavior and reliability assessment. Nevertheless, it is difficult to install the measurement points on the bearings. Therefore, it is proposed to explore the relationship between the vibration acceleration and bearing strain of the gearbox using neural network.

The innovation of this study lies in employing the convolutional neural network (CNN) and the long short-term memory network (LSTM) to investigate the relationship between the vibration acceleration and bearing strain of the gearbox. Meanwhile, Principal Component Analysis (PCA) is introduced to achieve the domain-invariant representation of the measured data to accommodate the working conditions of different rotational speeds and torques and enhance the generalization of the model. The contact load inversion method based on the outer ring strain distribution test proposed in the literature [2] will be utilized to obtain the normal load distribution inside the bearing for the diagnosis and analysis of early bearing failures.

2. Materials and methods

The gearbox model used for the test was the VOITH-SE380, and the test bearing was a wheel-tested cylindrical roller bearing at the input end of the gearbox, model SKF-NU214(Fig.1). The test bench can realize the simultaneous action of internal and external excitation.

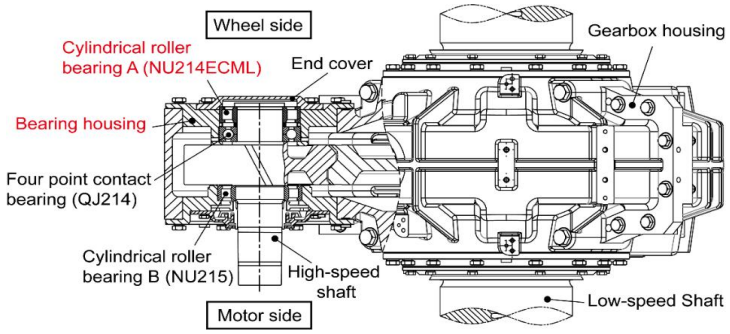

Fig.1 Test Gearbox and Bearings

Gearbox vibration acceleration measurement points are selected to constrain the modal response of the larger position of the arrangement of three-way acceleration sensor(Fig.2(a)).The principle of bearing strain measurement is to groove the inner surface of the gearbox bearing housing and arrange 17 strain measurement points in the outer ring of the test bearing(Fig.2(b)).

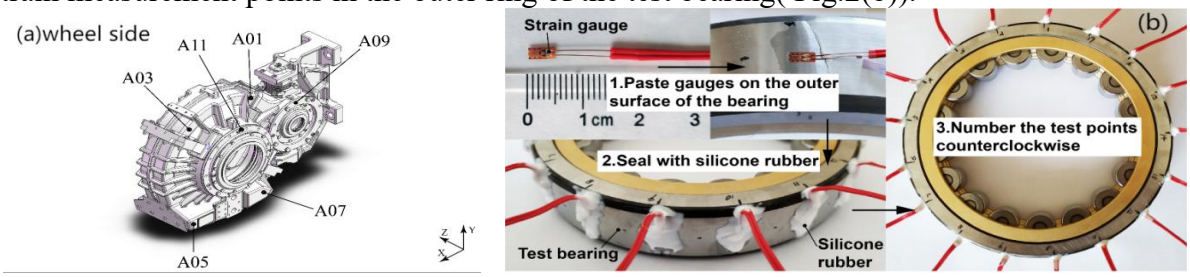

Fig.2 (a) Gearbox acceleration measurement point , (b) Bearing strain measurement points

As a type of recurrent neural network, the LSTM network addresses gradient issues in learning long-term dependencies. However, it has difficulties with local feature extraction. Therefore, the CNN-LSTM was chosen for its capacity to extract local and spatial features while maintaining long - term dependencies, using different kernel sizes for multi-scale feature extraction. The global parameter sharing of CNN also reduces training costs.

3. Results and conclusions

The dataset is measured data at 750 rpm with a linear increase in torque. The dataset was divided into training, validation, and test sets in a 3:1:1 ratio. Extract the statistical features of vibration acceleration and bearing strain signals (e.g., mean, variance, magnitude, etc.) to form a feature matrix and perform principal component analysis. The vibration acceleration of the gearbox serves as the feature input, while the bearing strain acts as the target label, enabling the precise prediction of bearing strain states. LSTM and CNN-LSTM networks are used for training, the training results of the LSTM on the test set presented in Fig. 3.

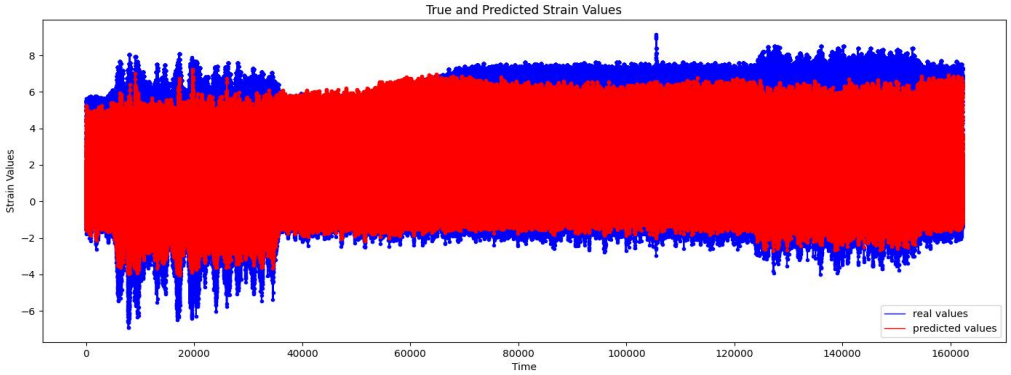

Fig.3 LSTM network test set prediction effect

4. Acknowledgements

This research is supported by the Joint Funds of the National Natural Science Foundation of China (Grant No. 12302238 and U1834202).

5. References

[1] Zhou Y, Wang X, Que H, et al. Torque effect on vibration behavior of high-speed train gearbox under internal and external excitations[J]. Railway Engineering Science, 2024,32(2):229-243.

[2] Hou Y, Wang X. Measurement of load distribution in a cylindrical roller bearing with an instrumented housing: Finite element validation and experimental study[J]. Tribology International, 2021,155:106785.

MULTI SOURCE EXPERIMENTAL DATA DRIVEN FATIGUE FAILURE ANALYSIS AND LIFE PREDICTION OF PRE-CORRODED ALUMINUM ALLOYS

H. Song[1], J. Liu[1], W.C. Wang[1], J. DU[1]
[1] Sino-European Institute of Aviation Engineering, Civil Aviation University of China, China

1. Introduction

Aluminum alloys (AA) are widely utilized in transport aircraft due to excellent mechanical properties [1]. These alloys are also susceptible to localized corrosion in aircraft service environments, which promote fatigue crack initiation and propagation [2]. It is critical to gain insight into the fatigue failure behavior of pre-corroded aluminum alloys and accurately predict the fatigue life. To date, the cross-scale, temporal-spatial experimental analysis of fatigue damage evolution in pre-corroded aluminum alloys are still lacking, and the dominated micro-crack initiation forms and relevant mechanisms also need to be figured out. Besides, conventional mechanical models for fatigue life prediction commonly simplified the corrosion pits to regular notches or cracks [3], without considering the complex local micro-morphology of corrosion pits and generally have insufficient accuracy. A data-driven fatigue life prediction model combined with corrosion macro/micro morphology and loading condition is lack and required [4].

To this end, fatigue tests were carried out on pre-corroded aluminum alloys, the damage evolution characteristics and failure mechanism were integrally investigated through multi-source experimental information involving corrosion morphology measured by optical 3D surface metrology, strain fields and damage severity curves obtained by 3D-DIC, SEM fractography, and material microstructure characterized by EBSD. Combined with the obtained experimental data, a data-driven fatigue life prediction model based on machine learning (ML) was established for pre-corroded aluminum alloy, inputting characteristic parameters of corrosion macro-morphology and local corrosion micro-morphology, and loading condition parameters.

2. Materials and methods

Al-Li alloy 2050-T8 are investigated in this work. The experimental process includes corrosion pit preparation, 3D morphology measurement, speckle spraying, fatigue tests, DIC observation, and SEM/EBSD characterization. The experimental strategy described above provide multi-source experimental information involving 3D corrosion morphology, 3D-DIC strain fields, SEM fractography, and EBSD material microstructure, which are important to clearly understand the damage characteristics and failure mechanism of pre-corroded aluminum alloy. The obtained multi-source experimental data, which contains many key influence parameters to determine the fatigue crack initiation and fatigue life, is also helpful for fatigue life prediction modelling. Based on experimental analysis, a data driven model was developed to predict the fatigue life of pre-corroded aluminum alloy, in which multi-source factors such as corrosion morphology parameters and loading parameters can be selected as the input, while fatigue life is the output.

3. Results and conclusions

Experimental results show that corrosion pit induces fatigue macro-cracks formation, and the identified nucleation time, amount, and specific location are diverse for different experimental conditions. Different dominated fatigue micro-crack initiation forms and corresponding mechanisms were analyzed, such as Corrosion Micro-Pit, Corrosion Jut-In, Corrosion Tunnel, and Pit Sub-surface, with the mechanisms of local stress/strain concentration or local material embrittlement. Corrosion Micro-Pits are the preferred location for crack initiation which is also correlated with high grain misorientation angles and large grain sizes. The developed data-driven life prediction method can successfully predict the fatigue life of pre-corroded aluminum alloy. The importance analysis reveals that the selected parameters are all strongly correlated with the fatigue life.

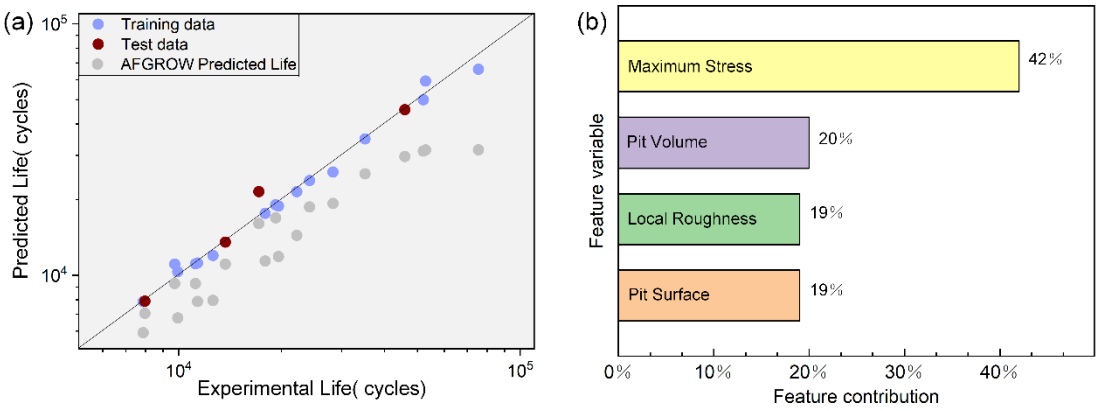

Fig. 1. (a) Predicted fatigue life of training data and test data using the ML model, (b) Percentage importance of the features in predicting fatigue life according to the ML model.

4. Acknowledgements

The research presented in this paper has received funding from the National Natural Science Foundation of China (NSFC, Grant Nos. 12372188 and 11972364)

5. References

[1] R.J.H. Wanhill, G.H. Bray (2014). Aerostructural design and its application to aluminum-lithium alloys. *Butterworth-Heinemann*., 27-58.

[2] M. Guérin, J. Alexis, E. Andrieu, C. Blanc, G. Odemer (2015). Corrosion-fatigue lifetime of Aluminium-Copper-Lithium alloy 2050 in chloride solution [J]. *Materials & Design*., **87**, 681-692.

[3] P. Hu, Q. Meng, W. Hu, F. Shen, Z. Zhan, L. Sun (2016). A continuum damage mechanics approach coupled with an improved pit evolution model for the corrosion fatigue of aluminum alloy. *Corrosion science.*, **113**, 78-90.

[4] H. Song, J. Liu, H. Zhang, J. Du (2023). Multi-source data driven fatigue failure analysis and life prediction of pre-corroded aluminum–lithium alloy 2050-T8. *Engineering Fracture Mechanics*., **292**, 109626.

Research on the Precipitation Behavior of CrN Phase in Nitrided Martensitic Stainless Steel

Hongye Zhang[1,*], Zhengzhong Xi [1], Xiao Han [2], Ruijun He [2]

[1] School of Technology, Beijing Forestry University, Beijing, China
[2] AECC Beijing Institute of Aeronautical Materials, Beijing, China
**Email: zhanghy@bjfu.edu.cn*

Abstract: The classical nitriding of martensitic stainless steel results in compressive residual stresses and a hardened layer. The generation of stresses is directly related to the volumetric changes induced by phase transformations during nitrogen diffusion, while the hardness is associated with the formation of nitrides. In this work, the evolution of the microstructure within the nitrided layer during the plasma nitriding process of AISI 422 martensitic stainless steel is investigated using transmission electron microscopy. Additionally, the precipitation behavior of CrN in the Fe-Cr-N system is simulated using the phase-field method. The study reveals that elemental segregation zones, predominantly composed of Cr and N, initially form within the martensite phase. As the nitrogen concentration in the nitrided layer increases, these solute elements precipitate and transform into semi-coherent CrN phases. The CrN phases continue to grow and coarsen, eventually undergoing coherent instability and transforming into incoherent CrN phases. Incoherent CrN phases can also form through the transformation of M23C6 at grain boundaries in the original matrix. The precipitation of semi-coherent CrN phases generates a coherent strain field, which varies with the thickness of the CrN phase; a thicker CrN phase results in a greater compressive strain. The quantitative characterization of the coherent strain field induced by semi-coherent CrN phases and the simulation of their growth and evolution provide valuable insights for optimizing the mechanical properties of nitrided AISI 422.

Keywords: Nitriding, Coherent strain field, Phase field, CrN.

1. Introduction

Currently, nitriding is increasingly finding industrial applications in fields such as gears and bearings. High hardness, high compressive residual stresses, and enhanced surface fatigue properties represent the optimal pathways for the industrial application of nitrided components. The mechanical properties of the nitrided layer are directly related to the microstructural changes and precipitation phenomena occurring during nitrogen diffusion. As nitriding progresses, residual compressive stresses arise within the material due to phase transformations or precipitations [1-2]. These microstructures have been studied by many scholars, but in most cases, the focus has been on binary alloys or synthetic alloys, with relatively little research on industrial alloys [3-4]. The objective of this paper is to investigate the microstructure and precipitation hardening behavior of the nitrided layer in AISI 422 using transmission electron microscopy (TEM). Furthermore, the experimental results will be validated through phase-field simulations.

2. Materials and methods

In this work, AISI 422 martensitic stainless steel was subjected to nitriding treatment to modify its surface and form a hardened nitrided layer. Detailed analyses of the chemical composition, phase composition, and orientation relationships of the nitrided microstructure were conducted using

scanning electron microscopy, TEM, and energy-dispersive X-ray spectroscopy. The growth and evolution of coherent CrN phases in the iron matrix were simulated using the phase-field method. Geometric phase analysis (GPA) was employed to calculate and compare the strain data around precipitates of different thicknesses with the results of the phase-field simulations. The findings of this study provide quantitative strain data, offering insights into the mechanical behavior of AISI 422 martensitic stainless steel at the nanoscale after ion nitriding.

3. Results and conclusions

During the initial stages of nitriding, GP zones composed of chromium and nitrogen form, which subsequently transform into semi-coherent CrN phases. As the nitriding depth increases, the precipitate phases undergo a transition from continuous precipitate (CP) to discontinuous precipitate. The near-surface compound layer is primarily composed of Fe4N phases, and the volumetric changes associated with phase transformations release some of the compressive residual stresses. The strain fields induced by the semi-coherent CrN phases have been quantitatively described using GPA. With increasing precipitate thickness, the compressive strain on the matrix increases. Subsequently, the residual stress gradually decreases with the incoherent transformation of the CP phases and turns into tensile residual stress at the surface due to the precipitation of a large number of γ'-Fe4N phases.

To accurately analyze the growth and evolution of precipitate phases, we conducted two-dimensional phase-field simulations of coherent CrN growth within the Fe-Cr-N system. After nucleation, the precipitate phases were primarily short rod-shaped due to the influence of anisotropic interface energy and elastic energy. As the N concentration increased, the aspect ratio of the precipitate phases gradually decreased, and higher N concentrations favored the formation of CP phases with larger widths and shorter lengths.

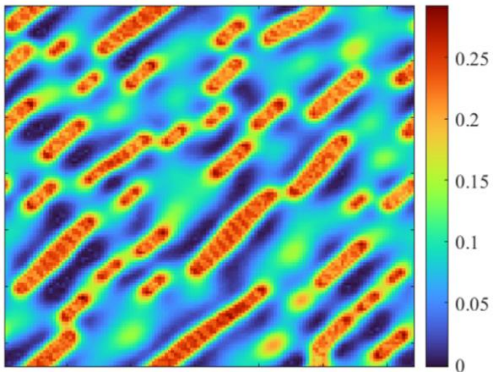

Figure 1. Simulation snapshot of rod-like CrN growth (Cr Concentration Map).

4. References

[1] D. T. Pierce, G. Muralidharan, A. Trofimov, J. Torres, H. Wang, J. A. Haynes, K. Sebeck, E. Gingrich, G. Byrd, M. Tess (2022). Evaluation of thermal processing and properties of 422 martensitic stainless steel for replacement of 4140 steel in diesel engine pistons, Materials & Design, 214, 110373.

[2] J. Sun, J. Li, J. M. Xie, Y. Yang, W. P. Wu, X. Zhou, S. H. Zhang, Q. M. Wang (2022) . Properties of rapid arc discharge plasma nitriding of AISI 420 martensitic stainless: effect of nitriding temperatures, Journal of Materials Research and Technology, 19, 4804–4814.

[3] R. Yang, G. Wu, X. Zhang, W. Fu, N. Hansen, X. Huang (2019). Gradient microstructure in a gear steel produced by pressurized gas nitriding, Materials, 12, 3797.

[4] Y. Xie, G. Miyamoto, T. Furuhara (2022). Nanosized Cr-n clustering in expanded austenite layer of low temperature plasmanitrided Fe-35Ni-10Cr alloy, Scripta Materialia, 213, 114637.

ALEATORY UNCERTAINTY QUANTIFICATION IN HETEROGENEOUS MATERIALS VIA BAYESIAN INFERENCE WITH PYMC: APPLICATION TO SINGLE LAP JOINTS

F. Jan[1], M. Kujawa[1], Ł. Smakosz[1]
[1] Gdańsk University of Technology, G. Naruowicza 11/12, Gdańsk, 80-233, Poland

1. Introduction

Reliability analysis and structural design optimization require accurate calibration of the numerical model to make realistic predictions about structural behavior under loading. Both deterministic and probabilistic methods, enabled by surrogate modeling and increased computing power, infer model parameters from experimental measurements. Probabilistic inversion determines the probability distribution of unknown parameters if uncertainties are well-defined. These include epistemic uncertainties [1,2] (from measurement errors and ignorance, reducible with more data) and aleatory uncertainties (inherent variability, irreducible [3]). This work focuses on identifying aleatory uncertainties in heterogeneous materials, where spatial variations in mechanical parameters affect structural behavior. Laboratory tests on identical material specimens highlight this. The identification process seeks to match the model response distribution with observed data, addressing a stochastic inversion problem. One method involves choosing a probability density function (PDF) for aleatory quantities and calculating statistical moments using techniques like maximum likelihood or perturbation [4]. Bayesian identification of these hyperparameters treats these moments as uncertain variables [5].

2. Materials and methods

This study evaluates the mechanical properties of adhesive-bonded single lap joints (SLJs) subjected to uniaxial tension. The SLJ specimens were fabricated, following EN485-2 guidelines, with AA-6063-T4 aluminum adherends bonded using structural epoxy adhesive DP 490. The analytical analysis focuses on energy-based models, considering a tensile loading (P) on the SLJ.

Bayesian inference for a stochastic problem using PyMC has been used to integrates uncertainty into parameter estimation [6], combining prior knowledge with experimental data to reduce epistemic uncertainty and provide a well-posed solution to the inverse problem. Consider a stochastic problem

$$z(x,\omega) = y(x) + \varepsilon(\omega)$$

and its posterior distribution according to Bayes' rule

$$p(x|z) = \frac{p(z|x)p(x)}{p(z)} = \frac{p(z\,|\,x)p(x)}{\int_x p(z|x)p(x)\,d(x)}$$

Using Hierarchical modelling the extension has been of multi-level setting is done by introducing hyperparameters θ: $p(x,\theta) = p(x|\theta)p(\theta)$ and according to Bayes' rule the corresponding joint posterior distribution up to a normalization constant is $p(x,\theta|z) \propto p(z|x,\theta)p(x|\theta)p(\theta)$.

The joint prior and posterior distribution upto a normalization constant is given as:

$$p(x_1, \dots, x_n, \theta) = \left(\prod_{i=1}^{n} f(x_i|\theta)\right) p(\theta)$$

$$p(x_1, \dots, x_n, \theta|z_1, \dots, z_n) \propto \left(\prod_{i=1}^{n} f(z_i|x_i)\right)\left(\prod_{i=1}^{n} f(x_i|\theta)\right) p(\theta)$$

The marginalized likelihood function is defined as and the corresponding marginalized posterior distribution is simplified into

$f(z_1, \dots, z_n|\theta) = \prod_{i=1}^{n} \int f(z_i|x_i) f(x_i|\theta) d\mathbf{P}(x_i)$; $p(\theta|z_1, \dots, z_n) \propto f(z_1, \dots, z_n|\theta) p(\theta)$

The sampling of the marginalized posterior is more complex and requires advanced MCMC techniques.

3. Results and conclusions

The mean values of hyperparameters converge to the true values and the identified uncertainty about these values decreases with an increasing number of measurements as it is obvious from Fig. 1.

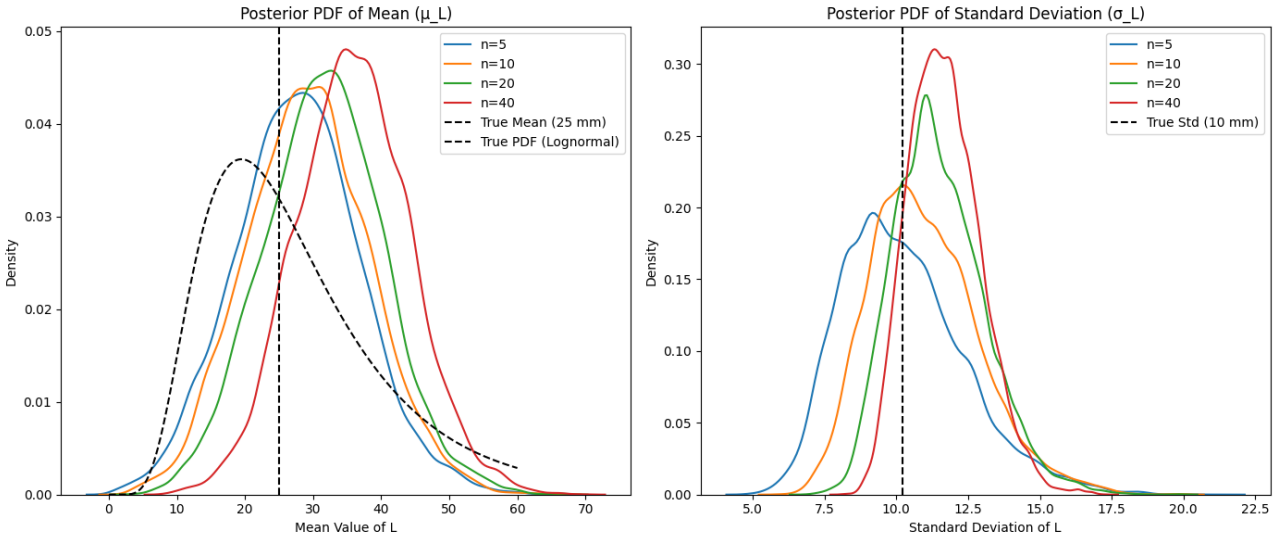

Fig. 1. Identified hyperparameters' distribution for different numbers of measurements.

5. References

[1] P. Mantovan, E. Todini, Hydrological forecasting uncertainty assessment: Incoherence of the GLUE methodology, Journal of Hydrology, 330 (2006) 368-381.
[2] K. Beven, P. Smith, J. Freer, Comment on "Hydrological forecasting uncertainty assessment: Incoherence of the GLUE methodology" by Pietro Mantovan and Ezio Todini, Journal of Hydrology, 338 (2007) 315-318.
[3] W. L. Oberkampf, S. M. DeLand, B. M. Rutherford, K. V. Diegert, K. F. Alvin, Error and uncertainty in modeling and simulation, Reliability Engineering & System Safety, 75 (2002) 333-357.
[4] J. R. Fonseca, M. I. Friswell, J. E. Mottershead, A. W. Lees, Uncertainty identification by the maximum likelihood method, Journal of Sound and Vibration, 288 (2005) 587-599.
[5] A. Gelman, J. B. Carlin, H. S. Stern, D. B. Rubin, Bayesian data analysis, second ed., Chapman & Hall/CRC, 2009
[6] A. Tarantola, Inverse problem theory and methods for model parameter estimation, Philadelphia, PA: Society for Industrial and Applied Mathematics, 2005.

DISTRIBUTED EXPERIMENTAL ANALYSIS OF THE STATE OF CHARGE FOR LITHIUM-ION BATTERIES BASED ON THERMOELASTIC GUIDED WAVE

Jie Gao[1], Yan Lyu[1], Cunfu He[1]
[1] School of Information Science and Technology, Beijing University of Technology, Beijing, China

1. Introduction

Lithium-ion batteries (LIBs) are now becoming a green energy source representing the future development trend by reliability and safety [1]. Now, the capacity of lithium-ion battery anode materials has reached a bottleneck. Silicon carbon lithium-ion battery (Si/C-LIB) have been gradually used in smartphones and electric vehicles due to their greater capacity and energy density [2]. However, Si/C-LIBs are also prone to lithium precipitation, gas production, swelling and other failures during cycling. It is important to utilize effective testing methods to detect the abnormal state of the battery. Traditional testing methods include atomic force microscopy, neutron diffraction, nuclear magnetic resonance and so on [3]. With the continuous development of battery testing field, ultrasonic testing method is considered to have greater potential. Through the wave propagation in the LIB, the changes in mechanical parameters during the cycling process can be accurately captured. And then the state parameters of LIBs can be characterized [4].

With the rising demand for lithium-ion battery testing, researchers have utilized ultrasonic testing methods to detect the state parameters of LIBs. Hsieh et al [5] proposed an experiment approach based on time of flight in LIBs. It analyzed the relationship between the change of sound velocity and SOC/SOH and then realized SOC/SOH ultrasonic measurement. Currently, guided waves have been applied to LIBs testing in many studies due to their low energy loss, designability, as well as their small sensor area and large coverage area. Ladpli et al [6] generated guided wave signals in LIBs by pitch-catch approach. Then it developed an acoustic model to simulate the changes of electrodes' modulus and density during cycling. They found that guided wave time domain signal (the amplitude and time of flight) is strongly correlated with the SOC and SOH, which can effectively realize the prediction of state parameters. Zhao et al [7] proposed an estimation method of the SOC and SOH based on ultrasonic guided wave. A comprehensive evaluation of the SOC and SOH of LIBs was achieved by time-frequency domain signals (amplitude, time of flight and power spectral density).

Previously, we have numerically calculated the guided wave propagation in multi-layered porous structures based on the Biot theory and global matrix method. We have also analyzed the influence of the SOC on the guided wave propagation in LIBs. In this study, a guided wave testing method for the SOC inhomogeneity of the Si/C-LIBs is developed. The intrinsic connection between the difference in the time domain parameters of the multi-regional and the SOC is experimentally analyzed. It realized the acoustic experimental testing of the SOC evolutionary stage and the multi-regional SOC inhomogeneity of Si/C-LIBs under different temperatures and C rates.

2. Materials and methods

To accurately capture the guided wave propagation in the Si/C-LIB under temperature field, a thermoelastic guided wave testing system was constructed. Two piezoelectric sensors with a center

frequency of 125 kHz were arranged on the surface of the Si/C-LIB. One end is responsible for stimulating, the other end is responsible for receiving, and the interval between the two is 75mm. The SWC-2 (Olympus longitudinal wave coupling agent) was used to coat the bottom of the excitation and reception sensors. It is different from the traditional longitudinal wave coupler. The main ingredient in its ingredient list is brown sugar. Compared with the water-soluble polymer colloid, it has a better coupling effect. Nevertheless, to ensure the consistency and tightness of the coupling during the experimental process, we added epoxy resin glue to SWC-2 at a ratio of 1:3. Subsequently, a function generator was used to connect the sensors at the excitation end to stimulate the five-cycle Hanning window-modulated 125 kHz, peak-to-peak 20V sinusoidal signal. The receiving end is connected to an oscilloscope to display the received time domain signals. The sampling frequency is set to 250MS/s. The experimental process focuses on the internal state changes in the thickness direction of the Si/C-LIB. In the experiment process, the internal state change in the thickness direction of the Si/C-LIB is emphasized. So the A0 mode of excitation dominated by off-plane displacement is selected. The sensor is the thickness vibration type. Its thickness is 10mm, diameter is 9mm. To realize the effective cycle of charging and discharging of Si/C-LIBs, Neware CT-4004-5V100A charging and discharging instrument is used. It can not only realize the cycle settings of Si/C-LIBs such as constant current/constant voltage or constant voltage modes, but also extract the electrical parameters. During the charging process, the protocol selected is constant current and constant voltage charging. The protocol selected for the discharging process is constant current discharging, with a 5-minute shelf time in between the change from charging to discharging process. In addition, the system also contains three parts: the automatic acquisition program of the oscilloscope, the displacement acquisition equipment in the thickness direction and the temperature acquisition equipment. It should be noted that all the above experimental environments were carried out in a preheated programmable constant temperature and humidity chamber.

To realize the synchronous acquisition of acoustic-thermal-expansion parameters during the cycling process, a set of testing device is designed in combination with the structural characteristics of Si/C-LIBs. Considering that the Si/C-LIB is a symmetric structure formed by stacking positive electrode-separator-negative electrode, the temperature sensor is selected to be arranged at the lower surface of the Si/C-LIB on the basis of the acoustic sensor arranged at the upper surface. In addition, an expansion measurement device is introduced to capture the amount of surface expansion change. It contains two independently designed acrylic plates, as well as an auto-acquisition-capable digital micrometer. They are in direct contact with the surface of Si/C-LIBs and extract the displacement during the cycling process.

The discharge process at three C rates (0.5C, and 0.75C) is selected as an example to investigate the effects of time domain signals (amplitude and time of flight) of the A0 mode for different SOC and discharge multiplicities. Fig.1(a) shows the relationship between the SOC and the time domain signals at different discharge multiplicities. Where the horizontal coordinate represents the time at which the time domain signals are received at different SOC of the Si/C-LIB, and the vertical coordinate is the amplitude of the received signals. The gradual transition from red to peach, blue to cyan, and blue to purple represents the time domain signals corresponding to different SOC at 0.5C, and 0.75C, respectively. And we obtain the guided wave time domain signal at different SOC (SOC=100%, 80%, 60%, 40%, 20%, 0%). It can be seen that the acoustic signals under different multiplicity and SOC conditions can be effectively extracted. The time domain signal evolution rules can be clearly observed. The amplitude of the guided wave decreases with the decrease of the SOC at different discharge multiplicities. Subsequently, it uses the black dashed line to show the shift pattern of the time domain signal. At this time, the wave packet continued to shift to the right along with the discharge process, that is to say, the time of flight is increasing. This also demonstrates the potential of utilizing thermoelastic guided waves for SOC testing under different service conditions. It is worth noting that due to the change in viscoelastic behavior during cycling, resulting in a significant change in amplitude with SOC. The enhancement and relaxation of lattice strain affects

the material damping and its attenuation characteristics as ions are transferred between the two electrodes. Typically, more rigid and dense materials have lower material damping and less intrinsic attenuation. As a result, the amplitude of the guided wave signal is larger at higher SOC.

Subsequently, the time domain signals extracted during the charging and discharging process were processed. The amplitude and time of flight of the A0 mode wave packet maximum were selected and plotted. So as to obtain the relationship between the SOC and the acoustic parameters at different cycle multiplicities and temperatures, as shown in Fig.1(b). Where the horizontal coordinate represents the cycle time of the Si/C-LIB and the vertical coordinate represents the amplitude and time of flight extracted at the maximum of the wave packet, respectively. The solid lines with blue circle, square, diamond, triangle, and pentagram represent the amplitude signals collected at 10°C, 15°C, 20°C, 25°C, and 30°C, respectively. The solid lines with red circle, square, diamond, triangle, and pentagram represent 10°C, 15°C, 20°C, 25°C, and 30°C, respectively. The results show that the change rule of the time domain signal during the charging and discharging cycle is very stable. During the charging process, the amplitude rises along with the increase of the SOC, and the time of flight shows a decreasing trend. In the discharge process, as the SOC decreases, the amplitude and the time of flight show the opposite rule. It is worth noting that an increase in temperature leads to a decrease in the amplitude and an increase in the time of flight received during the complete cycle of the Si/C-LIB. In addition, no direct effect of the charging and discharging multiplicity on the amplitude and time of flight was found at 0.5C, and 0.75C charging and discharging multiplicity for the time being. To better observe the correlation between SOC and the time domain signal under different conditions (temperature, charging and discharging multiplicity), the discharging time and amplitude/time of flight were extracted and fitted with the help of a primary function. This also indicates that the use of thermoelastic guided wave parameters to characterize the SOC of Si/C-LIBs has a large potential even under the action of temperature field. It is worth noting that the charging mode we used was constant-current constant-voltage charging and the discharging mode was constant-current discharging, as described in the experimental setup.

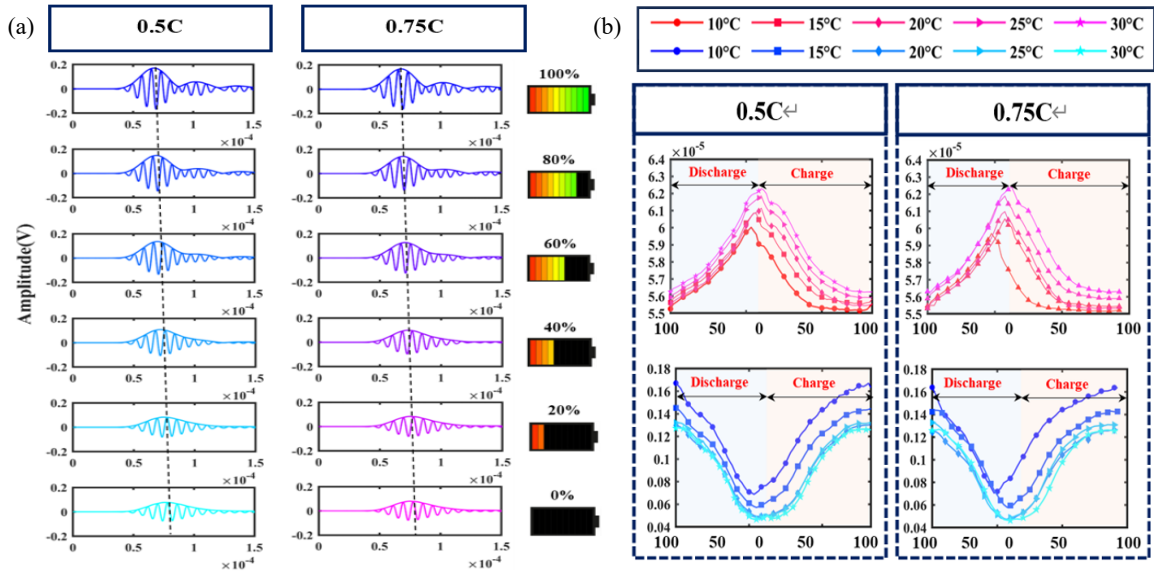

Fig. 1. Time domain signal under different discharge rates and SOC

To clarify the connection between the charging and discharging process and the acoustic characteristic parameters of the Si/C-LIB at different temperatures and cycle multiplicities, we extracted the current and voltage parameters at three C rates of 0.25C, 0.5C, 0.75C, and at five temperatures, namely, 10°C, 15°C, 20°C, 25°C, and 30°C, as shown in Fig. 2. Where the horizontal coordinate represents the cycle time of the Si/C-LIB, and the vertical coordinate represents the current

and voltage during charging and discharging, respectively. Combining the current-voltage relationship with the cycle time, the battery capacity can be mapped to each acoustic characterization parameter.

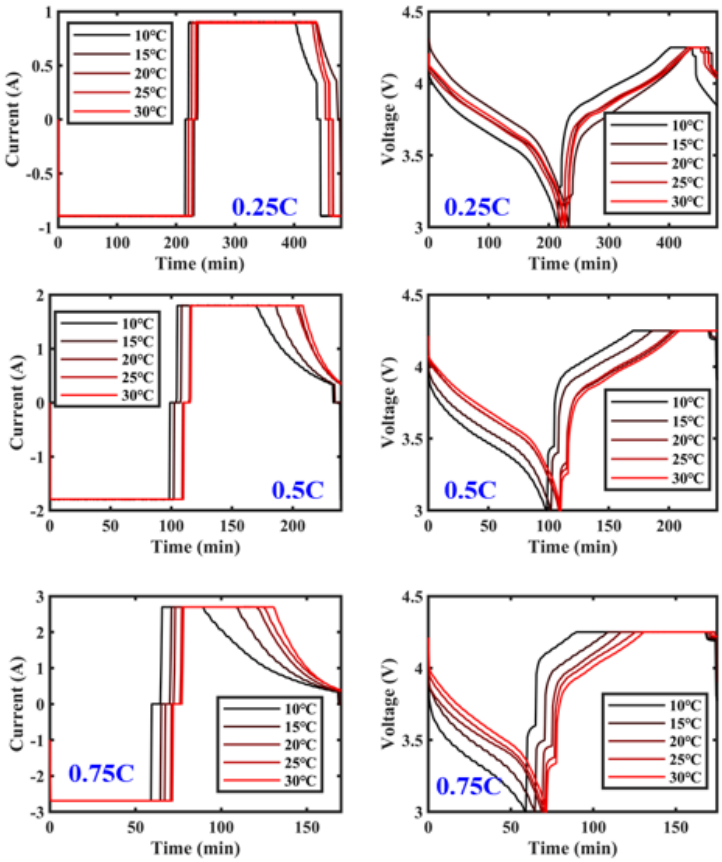

Fig. 2. Electrical parameters during cycling process

Due to the uneven distribution of SOC during the cycling process, the local electrochemical performance is prone to rapid attenuation. After verifying the effectiveness of thermoelastic guided wave in Si/C-LIB SOC testing, we develop a method for SOC inhomogeneity testing method. This is beneficial to improve the potential of battery failure warning and SOC characterization. The distance between sensors is 75 mm, and the distribution of sensors is shown schematically in Fig. 3.

Subsequently, the acoustic signals of each receiver sensor can be extracted at different temperatures and charge/discharge multiplicities. However, considering the inevitable distinction in the parameters captured by each sensor in the Si/C-LIB, we focus on the differences in the time domain signals received by each sensor under different SOC.

Then, the time domain parameters of multiple receiving ends during the cycling process were mainly extracted. The time domain parameters and SOC of Si/C-LIBs were observed under different cycle conditions. The potential of guided wave testing in characterizing the SOC inhomogeneity is further verified. For example, a set of acoustic signals was collected every 3 minutes at a charge/discharge multiplication rate of 0.75C. The amplitude along with the time of flight received by each sensor at 10°C, 15°C, 20°C, 25°C, and 30°C were extracted as shown in Fig.3. Where S1 with a purple square solid line, S2 with a light blue circular solid line, S3 with a dark blue pentagram solid line, S4 with a yellow triangular solid line, and S5 with a red rhombus denote the signals received by sensors 1-5 (-20°, -10°, 0°, 10°, and 20°), respectively. It can be seen that the amplitude received by each sensor decreases and the time of flight increases during the discharging process, while the evolution of the time domain signal received during the charging process follows the opposite pattern. Interestingly, this acoustic rule remains stable across multiple receiving ends. In

addition, observing the time domain signals received in different regions, it can be found that there is large distinction in the signals between the sensors. It is noteworthy that under the temperature conditions of 10°C, 15°C, 20°C, 25°C, and 30°C, the amplitude at S2 is relatively high, while the amplitude at S3 is relatively low.

However, the time of flight at S3 during the cycling process had a slight elevation relative to the remaining four regions, and the time of flight at S5 decreased slightly. When the sensors are in the stable coupling state, we measured the distance between five groups of sensors at the excitation end and the sensors at the receiving end. The difference of the distance is within 1mm. If we consider from the perspective of propagation distance, based on the measured group velocity between the two, we can estimate that the difference in propagation distance between S3 and S5 is about 3mm-3.5mm. It does not correspond to the actual distance between the sensors. We believe that the overall lower time of flight of S5 is not due to the difference in distance between the sensors, but rather due to the intrinsic material differences between the different regions.

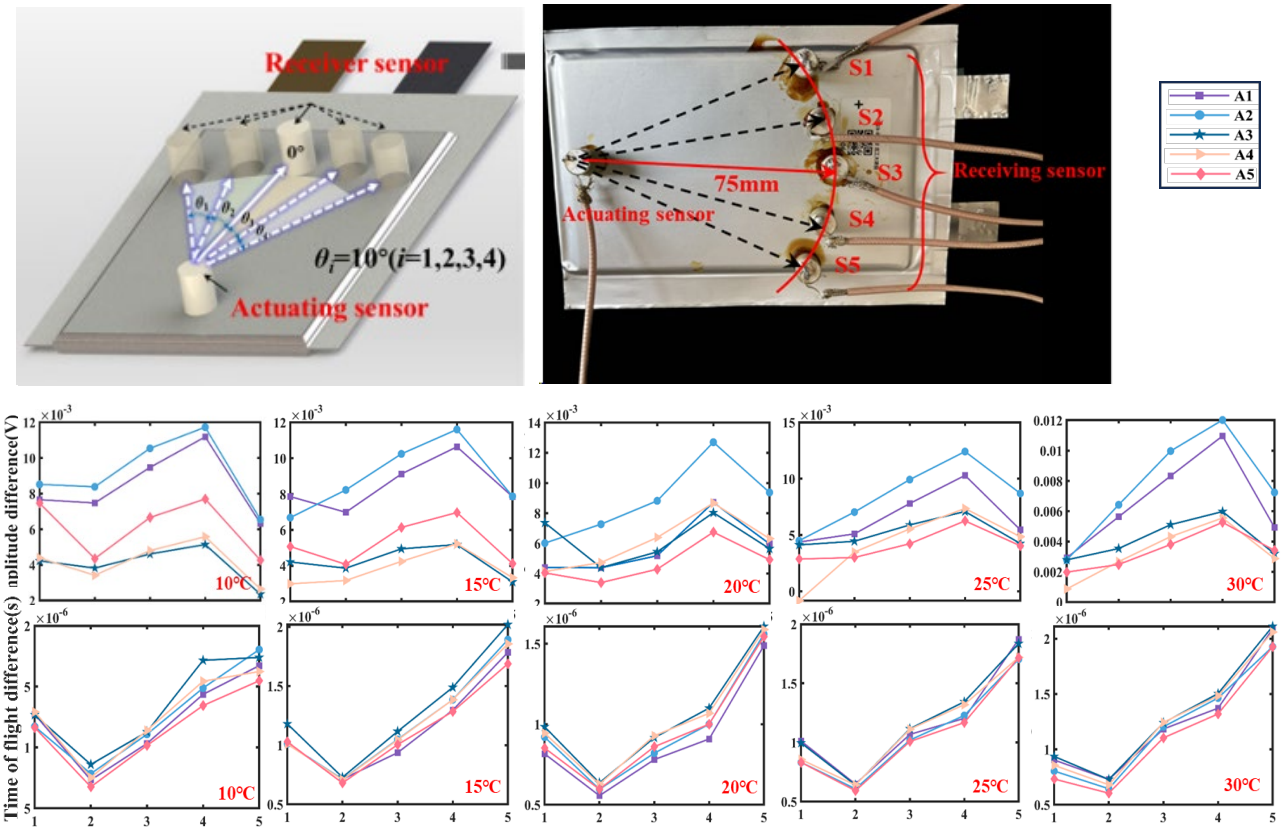

Fig. 3 Time domain signal differences of different SOC evolution stages and receiving regions with different SOC evolution stage

Using the time domain signals extracted at 0.75C charge/discharge multiplier and at 10°C, 15°C, 20°C, 25°C, and 30°C temperatures, the acoustic parameters of each sensor for different SOC are processed by the difference. The amplitude difference and the time of flight difference of each SOC evolution stage at different temperatures can be obtained, as Fig. 3 shows. Among them, A1 with a purple square solid line, A2 with a light blue circular solid line, A3 with a dark blue pentagram solid line, A4 with a yellow triangular solid line, and A5 with a red rhombus denote the SOC evolution stages of 80%~100%, 60%~80%, 40%~60%, 20%~40%, and 0%~20%, respectively. The amplitude difference of the received signal is the largest when the SOC evolution stage is 20%~40%. When the SOC is discharged from 100% to 20%, the amplitude difference shows an increasing trend. When the SOC is discharged from 20% to 0%, the amplitude difference shows a decreasing trend. Meanwhile,

the time of flight difference decreases when the SOC is discharged from 100% to 60%, and increases when the SOC is discharged from 60% to 0%. The time of flight difference reaches the maximum value when the Si/C-LIB is in the empty state. In the discharging process of the SOC from 100% to 60%, the time of flight difference is relatively small.

3. Results and conclusions

In order to analyze the offset law of characteristic parameters of acoustic waves during the cycling process of lithium-ion batteries, 20 charge/discharge cycle measurements of lithium cobalt-acid batteries were carried out at room temperature by using an ultrasonic guided wave detection system, as shown in Fig. 4. During charging, the ToF tends to decrease and the corresponding sound intensity amplitude increases, and the opposite pattern is observed during discharging.

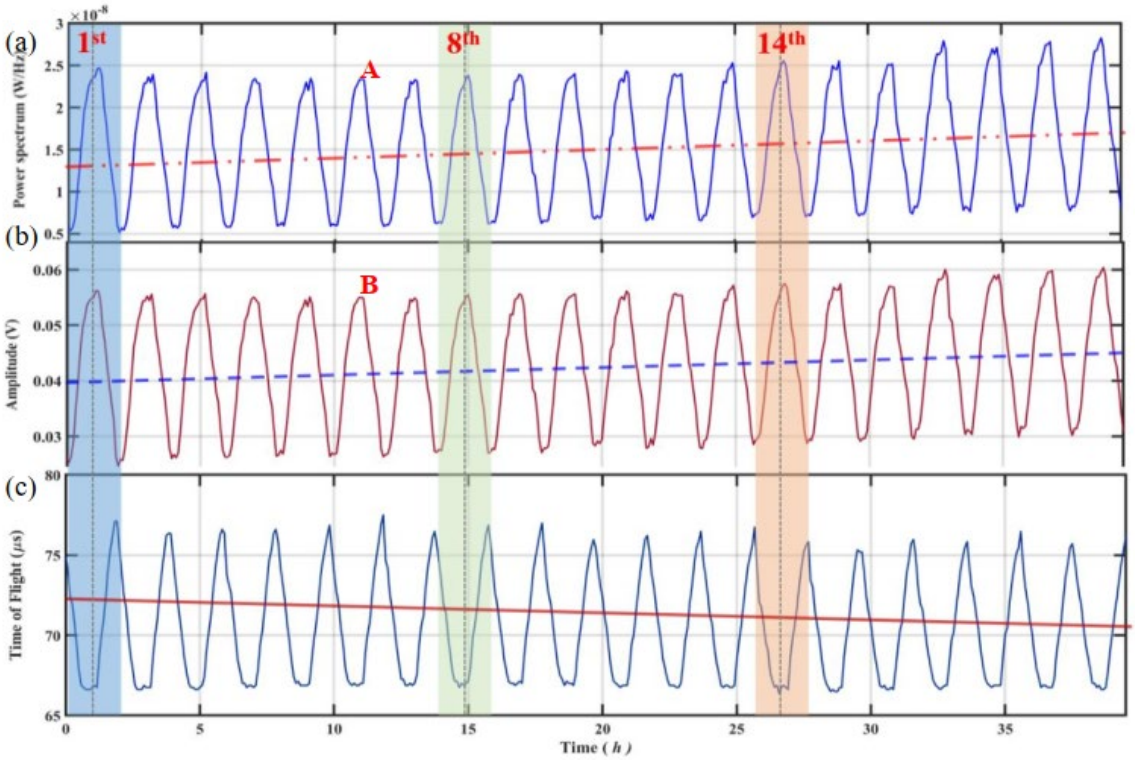

Fig. 4 Curve of acoustic parameters for lithium-ion battery during cycle

It can be seen that, in the cycle times of 1, 8 and 14, the characteristic parameters in both time and frequency domains show ideal patterns, i.e., the amplitude and power spectral density gradually increase in the charging process and become smaller and smaller in the transition time; while the overall charging process shows the opposite pattern. Similarly, the above pattern also effectively reflects the robustness of the detection means and the stability of the acquisition system. In addition, with the increasing number of cycles, the transition time of the A0 mode during the cycling process gradually decreases, while the sound intensity amplitude and power spectral density(PSD)gradually increase, as shown by the dotted line in the figure.

Based on the above least squares support vector machine algorithm, the prediction of the charge state is first performed for the customized lithium cobalt-acid battery. As can be seen from the previous section, with the help of the constructed ultrasonic guided wave detection system, the acoustic characteristic parameters of the lithium-ion battery were extracted in real time for 20 cycles, and a total of l=475 sets of data were collected, i.e., the sample set S={ToFi, SAi, PSDi,Ui, Ai, Ri},i=1,2,.....l, which contains the acoustic characteristic parameters of the lithium-ion battery Transition Time ToF, sound intensity amplitude SA, power spectral density PSD, as well as electrical parameters voltage U,

current I and resistance R, while the output term yi is the charge state of the lithium-ion battery at different moments. At this point, the sample set is divided into two subsets, in which the first 15 cycles (i.e., the first 357 sets of data) are used as the training set, which is substituted into the least-squares support vector machine established above for training. In order to verify the generalization ability and accuracy of the proposed model, the last five cycles (i.e., the last 118 sets of data) are used as the test set. It should be noted that the selected kernel function in the regression model is a Gaussian radial basis kernel function, and the width of the kernel function σ and the regularization parameter γ need to be set at first, as the key parameters for modeling,γ is a compromise between minimizing the training error and minimizing the model complexity, which has a greater impact on the generalization ability of the least-squares support vector machine model, while σ is a parameter that directly affects the number of support vectors. A smaller kernel function width will generate a large number of support vectors, which will result in oversaturation of the model, while a larger kernel function width will result in fewer support vectors, thus over-simplifying the model and reducing the accuracy.

In order to find the desired guess parameters accurately and efficiently in a sufficiently large space, this study introduces a simulated annealing-based particle swarm optimization (PS-B-SA) algorithm to achieve gradient-based inverse optimization from pre-global optimization to post-local depth optimization. The main working principle is shown in Fig.5.

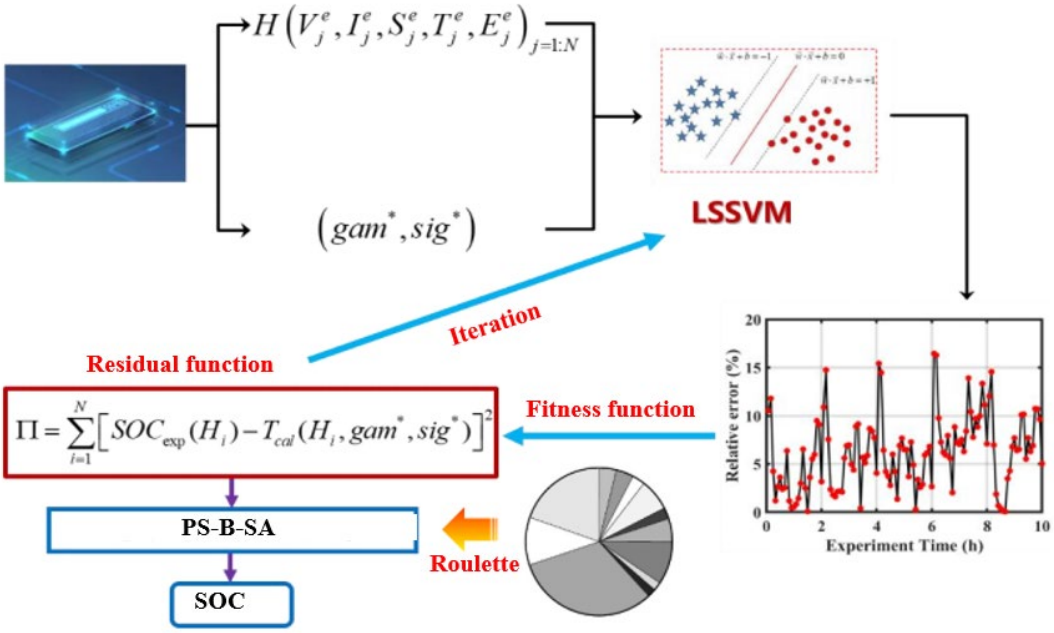

Fig. 5 Inversion diagram of key parameters of commercial lithium-ion battery

It can be seen from Fig. 6 that the stability of the inversion values of the two parameters is better, so the average values of the inversion results of the key parameters are extracted separately, and the final result of the kernel function width σ is 140.56, and the final result of the regularization parameter γ is 1.57. Finally, the above results are substituted into the established full-parameter least-squares support vector machine evaluation model and compared with the experimental measurements, as shown in Figs. 7. shown. It can be seen that the evaluation results obtained based on the above characterization algorithm have a maximum error of about 2% compared with the experimental measurements.

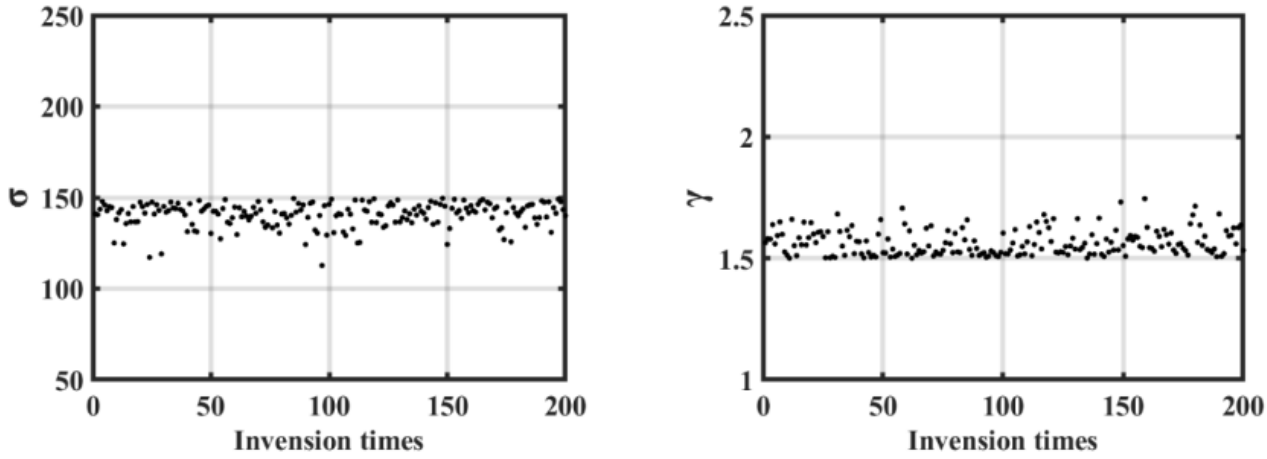

Fig. 6 Inversed results of key parameter σ/γ

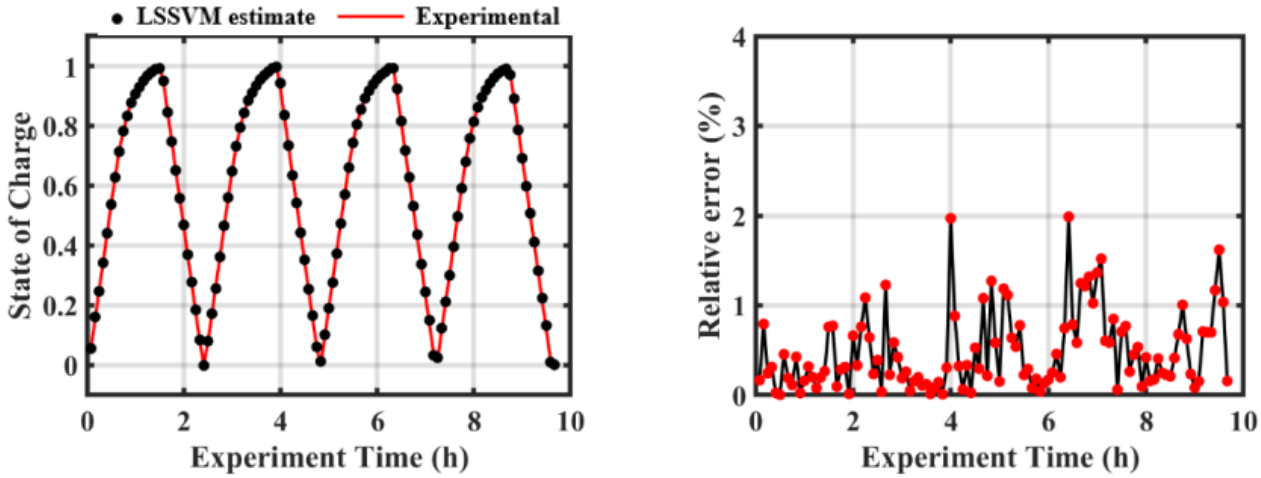

Fig. 7 Evaluation results of commercial Lithium-ion battery SOC based on hybrid algorithm

The focus of this study is to develop a distributed ultrasonic testing method for the SOC of Si/C-LIBs under complex working conditions. It can be concluded that the testing method could accurately capture the relationship between the acoustic behavior with the battery SOC. Furthermore, the mapping relationships between the multi-regional acoustic parameters, different SOC evolution stages and the SOC inhomogeneity are deeply investigated by the distributed thermoelastic guided waves testing method. The results show that when the SOC is in the 40%~100% interval at the discharging process, the inhomogeneity of the corresponding SOC evolution stage is weaker than other intervals. Combining the least squares support vector machine and the particle swarm optimization algorithm based on simulated annealing, a characteristic adaptive inversion characterization method of lithium-ion battery operation state is developed to independently optimize the key parameters (kernel function width σ, regularization parameter γ) in the intelligent inversion model to improve the quantitative reliability of the lithium-ion battery state parameter inversion model.

4. Acknowledgements

This work is supported by National Natural Science Foundation of China (No. 12402216, 12072004), Beijing Municipal Education Commission and Beijing Natural Science Foundation (No. KZ202110005005).

5. References

[1] Woeste R, Drude ES, Vrucak D, Klöckner K, Rombach E, Letmathe P, et al. A techno-economic assessment of two recycling processes for black mass from end-of-life lithium-ion batteries. Appl Energy 2024;361:122921.

[2] Zhao M, Zhang J, Zhang X, Duan K, Dong H, Lanceros-Méndez S, et al. Application of high-strength, high-density, isotropic Si/C composites in commercial lithium-ion batteries. Energy Stor Mater 2023;61:102857.

[3] Yamagishi Y, Kominami H, Kobayashi K, Nomura Y, Igaki E, Yamada H. Molecular-Resolution Imaging of Interfacial Solvation of Electrolytes for Lithium-Ion Batteries by Frequency Modulation Atomic Force Microscopy. Nano Lett 2022;22(24):9907-9913.

[4] Meng K, Chen X, Zhang W, Chang W, Xu J. A robust ultrasonic characterization methodology for lithium-ion batteries on frequency-domain damping analysis. J Power Sources 2022;547:232003.

[5] Hsieh AG, Bhadra S, Hertzberg BJ, Gjeltema PJ, Goy A, Fleischer JW, et al. Electrochemical-acoustic time of flight: in operando correlation of physical dynamics with battery charge and health. Energ Environ Sci 2015;8(5):1569-1577.

[6] Ladpli P, Kopsaftopoulos F, Chang FK. Estimating state of charge and health of lithium-ion batteries with guided waves using built-in piezoelectric sensors/actuators. J Power Sources 2018;384:342-54.

[7] Zhao G, Liu Y, Liu G, Jiang S, Hao W. State-of-charge and state-of-health estimation for lithium-ion battery using the direct wave signals of guided wave. J Energy Storage 2021;39:102657.

Experimental Mechanics for Nondestructive Testing

INTERFACIAL SINGLE-SIDE *J*-INTEGRAL AND INCREASEMENT *J*-INTEGRAL CRITERIA BASED ON DIC METHOD FOR FRP–CONCRETE JOINT

Wen Li, **Peiyan Huang******

School of Civil Engineering and Transportation, South China University of Technology, Guangzhou 510640, China

Corresponding authors: *liiween@scut.edu.cn; **pyhuang@scut.edu.cn

1. Introduction

The *J*-integral calculation of the crack using digital image correlation (DIC)-measured displacement fields has been widely applied across various materials [1-4]. However, when there is a significant difference in thickness between the materials on either side of the interface, the classical *J*-integral method becomes inadequate. This limitation arises primarily because DIC technology often struggles to accurately measure the displacement field near the interface on the thinner side, making it impossible to define a complete *J*-integral contour near the crack front. To address this challenge, We proposed a single-side *J*-integral method in a previous publication [5], offering a novel approach to characterize interfacial crack propagation behavior in bi-materials with substantial thickness differences.

This work focused on FRP–concrete joints as the study subject. Utilizing the double-shear test method for fully bonded FRP–concrete interface developed in earlier research [6], we applied the single-side *J*-integral method [5] to investigate interfacial crack propagation. Recognizing the heterogeneous nature of concrete, characterized by microcracks and micropores, we introduced the ΔJ criterion for identifying the instability of interfacial crack propagation. The single-side fracture energy threshold parameter was derived using the proposed fracture energy testing method in previously research[7]. The single-side *J*-integral method and the Δ*J* criterion were validated using specimens with four different pre-cracked interface lengths. The results indicated that the discrepancy between the experimentally measured single-side *J*-integral threshold and the experimentally obtained single-side fracture energy was within 20%, demonstrating the reliability of the proposed method.

2. Methods

2.1 The Single-Side *J*-Integral Method for Interface Crack Analysis

This paper presents a schematic diagram of the single-side *J*-integral method for interface crack analysis, as illustrated in Fig.1 , where #1 and #2 represent two different materials. The theoretical expression for the single-side *J*-integral, detailed in Eq. (1), aligns with the classical *J*-integral formulation. In this method, the integration path is defined solely within the displacement field on the thicker side near the interface.

$$J = \int_{\Gamma} w \cdot dy - \left(T_x \frac{\partial u_x}{\partial x} + T_y \frac{\partial u_y}{\partial x}\right) ds \tag{1}$$

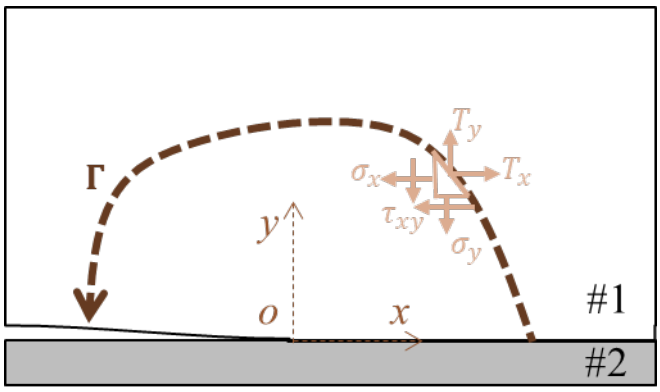

Fig.1 Schematic diagram of single-side *J*-integral of the interface

In this study, the single-side *J*-integral path is drawn on the displacement field adjacent to the concrete side of the interface. On one hand, numerous experimental [8], numerical [9], and theoretical analyses [10, 11] have established that interface macrocracks typically result from the coalescence of multiple interface microcracks. On the other hand, concrete's inherent microcracks and micropores, which were also included in the single-side counter. So the value of the single-side *J*-integral reflects contributions from both interface cracks and microcracks within the concrete. Then the single side *J*-integral can be calculated as a summation of *J*-integral contributions from interface microcracks ($\sum J_{in-y}$) and concrete microcracks ($\sum J^{ic}{}_{C-y}$). The incasement mode can be characterized as:

$$\Delta J_{side} = \Delta \sum J_{in-y} + \Delta \sum J^{ic}{}_{C-y} \tag{2}$$

2.2 Loading on the FRP–concrete Interface

(1) Concrete Microcracks:

The number of microcracks within the concrete increases from sparse to numerous, with their propagation directions becoming increasingly disordered. Within the integration path, the *J*-integrals of these concrete microcracks ($\sum J^{ic}{}_{C-y}$) tend to cancel out as displacement increases, resulting in a plateau phase in *J*-integral vs. displacement curve (see Fig.2 (a)).

(2) Interface Microcracks:

Interface microcracks gradually coalesce into macrocracks. The direction of propagation shifts from disorderly to orderly, leading to an increase in the superposed *J*-integral values ($\sum J_{in-y}$), as depicted in Fig.2 (b).

2.3 Proposed Criterion for Instability

Based on this hypothesis, the criterion for interface crack instability is defined as follows:

$$\left|\Delta J_{side_2}\right| \approx G_{side-c} \tag{3}$$

Where $G_{\text{side}-c}$ represents the energy release rate threshold on the concrete side near the interface. $G_{\text{side}-c}$ has the relationship with the interfacial fracture energy G, which was come from Täljsten model (1996) [12], as follows:

$$G_{\text{side}} = \frac{E_F t_F}{E_C t_C + E_F t_F} G \tag{4}$$

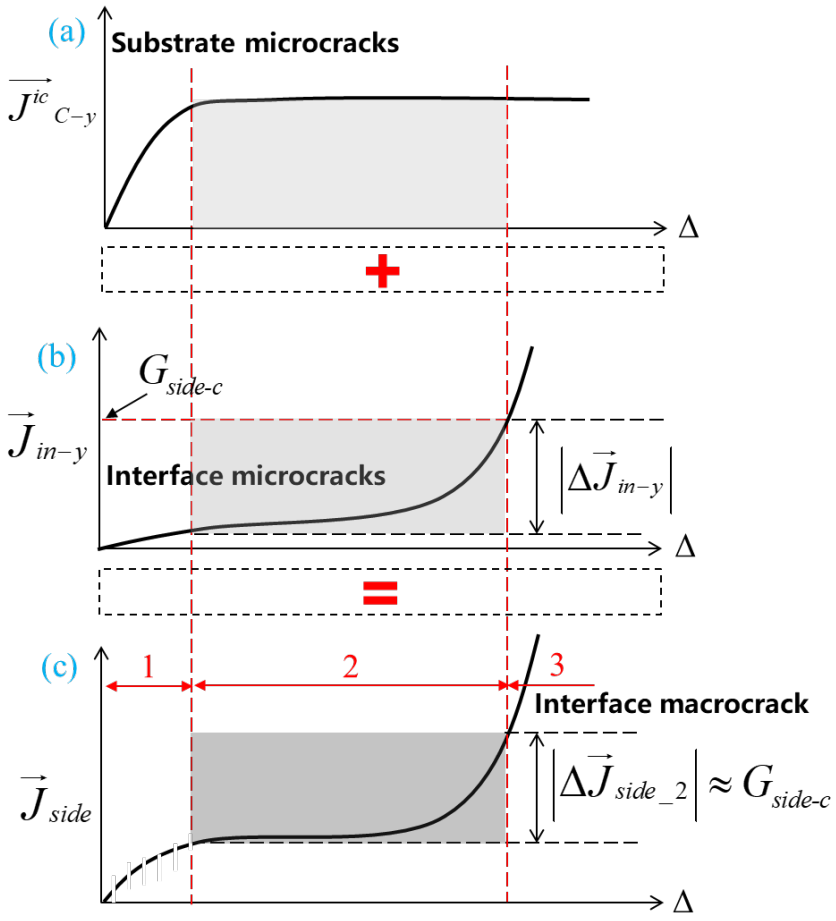

Fig.2 Single-side *J*-integral–displacement curves

3. Results and conclusions

For a specimen with a pre-cracked interface length of a = 40mm, periodic single-side *J*-integral paths were established on the concrete side of the fully bonded FRP–concrete interface, as shown in Fig.3 (a). The strain fields at loading displacements of 0.682mm and 2.215mm are illustrated in Fig.3 (a) and Fig.3 (b), respectively. The integration paths are characterized by disordered concrete microcracks (see Fig.3 b), with no macrocracks evident at displacement (see Fig.3 (c)).

The computed single-side *J*-integral from the 4 paths versus displacement curves are presented in Fig.3 , showing incremental values of single-side *J*-integrals in the second phase of 0.0291N/mm，0.0515N/mm，0.0384N/mm，0.0595N/mm. The errors relative to the energy release rate threshold on the concrete side (G_{side-c}=0.0335 N/mm) recorded a 33.2% discrepancy. Results for three additional specimens (a = 0 mm, 20 mm, 60 mm) yielded an overall error of 15.8% [5], underscoring the predictive capability of the proposed method.

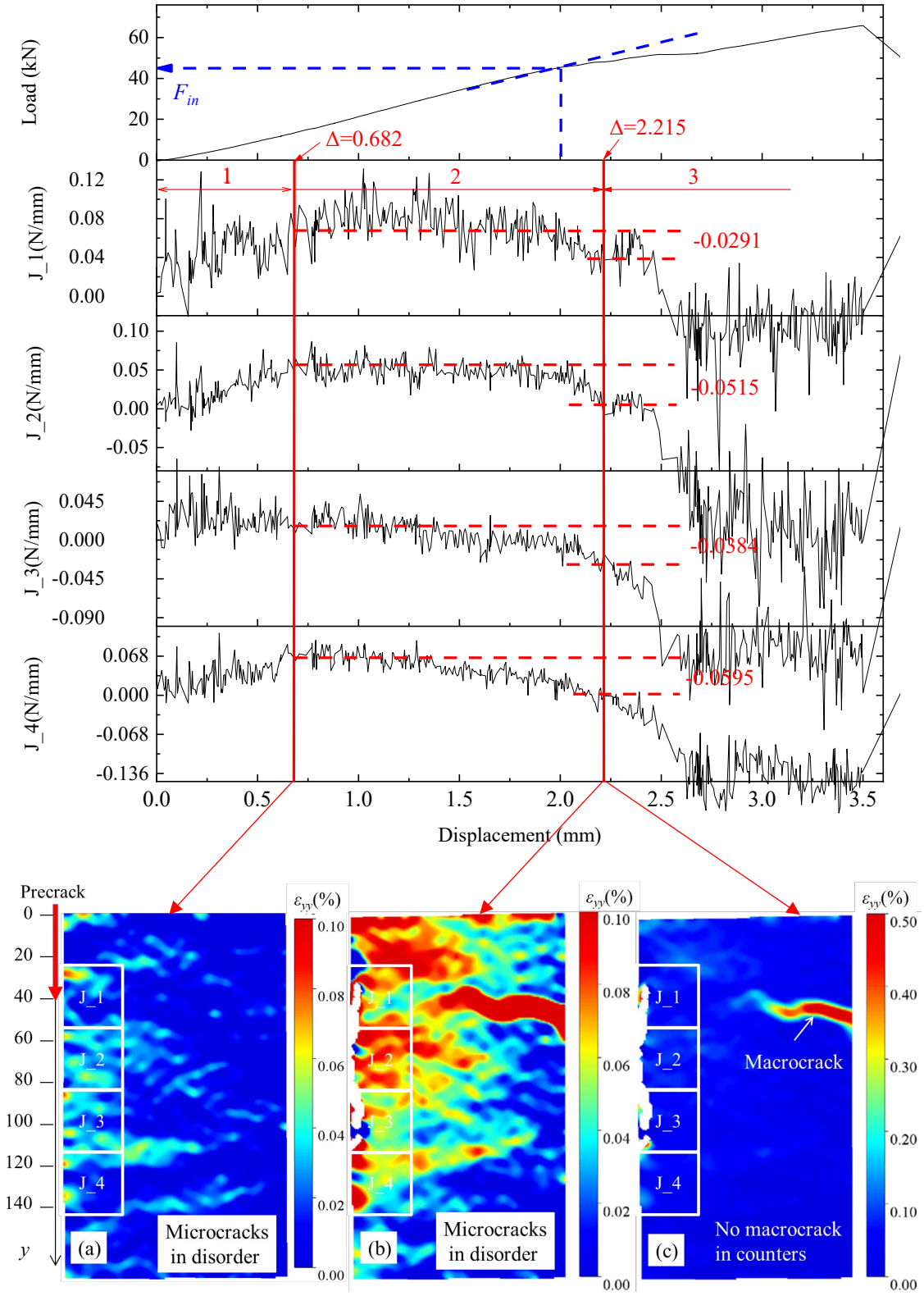

Fig.3 Load–displacement curves, single-side *J*-integral–displacement curves, and the strain fields on the concrete block of specimen III (a = 40 mm)[5]

Future work as follows:

(1) Generalization of G_{side-c}:

Further exploration is needed to develop theoretical expressions for the energy release rate (G_{side-c}) in various bimaterials under different loading modes (Mode I, Mode II, Mode III, or mixed-mode).

(2) Oscillations in *J*-Integral Displacement Curves:

Significant oscillations in single-side *J*-integral displacement curves hinder the assessment of crack propagation behavior; thus, smoother computational methods should be developed.

(3) Applicability to General Bi-materials:

The single-side *J*-integral method requires extension to other general bi-materials to evaluate its broader applicability.

4. Acknowledgements

This research was supported by the National Natural Science Foundation of China [Nos: 12302240, 11627802, 51678249, 11872185].

5. References

[1] Barhli SM, Mostafavi M, Cinar AF, Hollis D, Marrow TJ. J-Integral Calculation by Finite Element Processing of Measured Full-Field Surface Displacements. Experimental Mechanics. 2017; 57(6):997-1009.

[2] Koko A, Earp P, Wigger T, Tong J, Marrow TJ. J-integral analysis: An EDXD and DIC comparative study for a fatigue crack. International Journal of Fatigue. 2020;134.

[3] Montenegro DM, Canal LP, Botsis J, Zogg M, Studart AR, Wegener K. On the validity of the J-integral as a measure of the transverse intralaminar fracture energy of glass fiber-reinforced polyurethanes with nonlinear material behavior. International Journal of Solids and Structures. 2018;139-140:15-28.

[4] Becker TH, Mostafavi M, Tait RB, Marrow TJ. An approach to calculate theJ-integral by digital image correlation displacement field measurement. Fatigue & Fracture of Engineering Materials & Structures. 2012;35(10):971-84.

[5] Li W, Huang P, Chen Z, Yao G, Chen D. Single-side J-integral method for interfacial cracks. International Journal of Solids and Structures. 2022;241:111476.

[6] Li W, Huang P, Chen Z, Zheng X, Yang Y, Guo X. Bond behavior of fully bonded CFRP-concrete interface with improved double shear tests. Journal of Building Engineering. 2021;43:102866.

[7] Li W, Huang P, Chen Z, Zheng X. Testing method of critical energy release rate for interfacial mode II crack. Engineering Fracture Mechanics. 2021;248:107708.

[8] Michels J, Zile E, Czaderski C, Motavalli M. Debonding failure mechanisms in prestressed CFRP/epoxy/concrete connections. Engineering Fracture Mechanics. 2014;132:16-37.

[9] Li W, Wang Y, Huang P, Li D, Zeng L, Guo X. Finite element analyses of failure of fiber reinforced polymer-concrete interface considering the concrete tension–compression softening effect. Theoretical and Applied Fracture Mechanics. 2024;131:104427.

[10] Li W, Huang P, Chen Z, Cui H, Guo X, Wu B. Bond–slip model considering the interface shear stress reversal phenomenon and data dispersion for FRP–concrete interface. Engineering Fracture Mechanics. 2022;268:108492.

[11] Li W, Huang P, Chen Z, Guo X, Wu B. The shear stress reverse phenomenon in FRP sheet–concrete interface. Construction and Building Materials. 2022;344:128192.

[12] Täljsten B. Strengthening of concrete prisms using the plate-bonding technique. 1996.

NONDESTRUCTIVE TESTING FOR THE ESTIMATION OF THE RAIL NEUTRAL TEMPERATURE

S. Baktash[1], M. Belding[1,2], and P. Rizzo[1]
[1]Department of Civil and Environmental Engineering, University of Pittsburgh, 3700 O'Hara Street, 729 Benedum Hall, Pittsburgh, PA 15261.

[2] Department of Electrical and Computer Engineering, University of Pittsburgh, 3700 O'Hara Street, 1124 Benedum Hall, Pittsburgh, PA 15261.

1. Introduction

This short article describes one of the latest advancements of a monitoring/inspection technique for the estimation of localized longitudinal stress in continuous welded rails (CWR). The technique is based on the use of vibration measurements and machine learning (ML). A finite element analysis is conducted to model the relationship between the boundary conditions and the longitudinal stress of any given CWR to the vibration characteristics of the rail. The results of the numerical analysis are used to train a ML algorithm that is then tested using field data obtained by an array of accelerometers polled on the track of interest. The proposed technique was tested in the field. A commercial FEM software was used to model the rail track as a short rail segment repeated indefinitely and under varying boundary conditions and stress. A ML model was developed to infer the rail neutral temperature and the local resistance of rails to vertical and lateral displacement. The results of the experiments demonstrated that the success of the technique is dependent on the accuracy of the model and the ability to properly label the modes of the detected frequencies. This study builds upon previous research conducted at the University of Pittsburgh and the interested reader is referred to [1-7] for more details about the proposed technique.

2. Materials and methods

A finite element model (FEM) was implemented using a commercial software. The model simulated the dynamic vibration of CWR under varying longitudinal stresses and lateral and vertical resistances. The CWR was modeled as ~5-meter-long rail segment supported by eight crossties, with resistance at the seating areas modeled as periodically distributed translational springs. These springs simulated the lateral and vertical stiffness provided by rail fasteners, baseplates, and spikes. The rail was assumed fixed longitudinally whereas it was evaluated within a range of lateral and vertical support stiffnesses and axial stresses, characterized by temperature variations with respect to the neutral temperature ($\Delta T = T_R - T_N$) (see Table 1). Vibrations were induced by applying a force function equivalent to the mechanical impact of a hammer. The frequency content of these vibrations was calculated using power spectral density (PSD), capturing the relationship between support conditions, longitudinal stress, and vibration modes. The results of the finite element analysis were used to generate a synthetic dataset to train an artificial neural network (ANN). To assess the capability of the ANN's to estimate the neutral temperature and (eventually) the lateral resistance of the rail, the dataset was divided into two groups: one representing the central values ("core cases") of

the ranges listed in Table 1, and one comprising the lowest and the highest range ("extreme cases"). The scope of such partition is to evaluate whether the ANN is able to extrapolate the results when case scenarios external to the trained range is presented.

Table 1 – Variables considered in the finite element model of the rail

Parameter	min value	max value	No. of simulations (values of the parameters)
K_y (kN/mm)	0.1	100	**22** (0.1, 0.3, 0.5, 0.7, 1, 1.5, 2, 3.5, 5, 7.5, 10, 15, 20, 25, 30, 40, 50, 60, 70, 80, 90, 100)
K_z (kN/mm)	0.1	100	**22** (0.1, 0.3, 0.5, 0.7, 1, 1.5, 2, 3.5, 5, 7.5, 10, 15, 20, 25, 30, 40, 50, 60, 70, 80, 90, 100)
$\Delta T=T_R-T_N$ (°C)	−15	+15	**13** (-15, -12.5, -10, …, 10, 12.5, 15)

3. Results and conclusions

In this short article results related with the following analysis are presented. The ANN was trained using the "extreme cases" dataset, whereas the unseen "core cases" dataset was presented to the trained network to predict the rail neutral temperature. Figure 1 compares the actual ΔT to the ΔT predicted by the ANN. The graph contains also the bisector line which represent the perfect case in which the predicted and the actual neutral temperatures match, and two dashed lines, which represent an offset of ± 2.78 °C (=5 °F) with respect to the bisector. In addition, the graph presents the Mean Absolute Error (MAE), equal to:

$$MAE = \frac{1}{n}\sum_{i=1}^{n}\left|Y_i - \hat{Y}_i\right| \quad (1)$$

In Eq. (1), n represents the total number of samples for each dataset, Y_i is the ground true ΔT, and $\hat{Y}_i$ is the predicted ΔT. MAE was considered because it measures the mean absolute residual error between the predicted value and target without penalizing outliers.

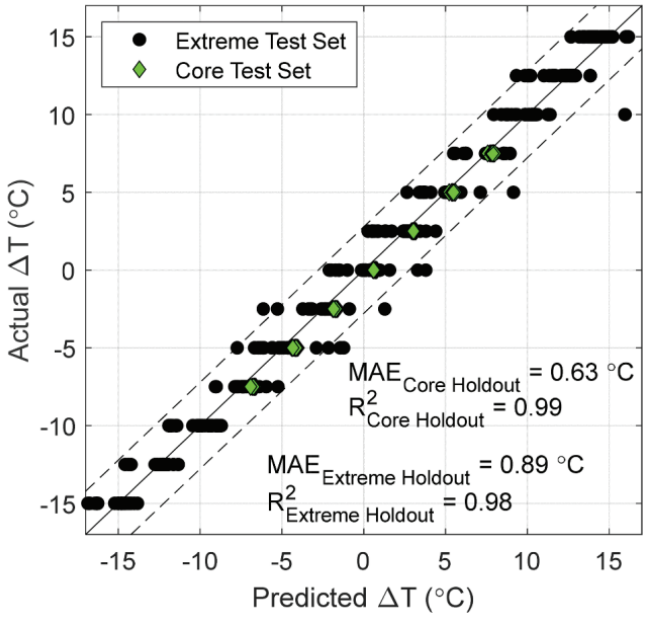

Figure 1 - True temperature variation vs predicted ΔT when the ANN is trained with the "extremes" data and tested with the "core" data. The term holdout indicates data never seen by the ANN prior to testing. The black dots refer to the 25% of training set never seen by the ANN prior to testing. The green diamonds refer to the "core" dataset. The dashed lines parallel to the bisector identify a discrepancy of ± 2.5°C with respect to the effective neutral temperature.

The results demonstrate that the proposed vibration-based nondestructive testing (NDT) method effectively quantifies the influence of lateral and vertical resistance as well as longitudinal stress on the vibration characteristics of CWR (see Fig. 1). The analysis revealed that, while temperature-induced stress has a relatively small effect on vibration modes compared to support conditions, advancements in machine learning and computational power can help identify localized areas where the track exhibits reduced overall resistance relative to surrounding regions, making it more susceptible to localized buckling. Furthermore, the study confirmed that excitation and detection on the railhead provide the best signal-to-noise ratio for field applications, with the rail web offering a practical alternative for sensing setups. The findings also highlighted challenges in generalizing machine learning predictions to scenarios with softer support conditions, emphasizing the need for additional data points in future studies.

4. Acknowledgements

This work was supported by the Association of American Railroads (AAR) under the University Grand Challenge Master Contract No. 20-0701-007537, Modification 4, Task Order 01, PO 100034 (Dr. Anish Poudel as Technical Monitor). The authors acknoweldge the contribution of Dr. Alireza Enshaeian in the creation of the original version of the finite element model used here.

5. References

[1] Enshaeian, A., Luan, L., Belding, M., Sun, H., & Rizzo, P. (2021). A contactless approach to monitor rail vibrations. *Experimental Mechanics*, ***61***, 705-718.

[2] Belding, M., Enshaeian, A., & Rizzo, P. (2022). Vibration-based approach to measure rail stress: Modeling and first field test. *Sensors*, ***22***(19), 7447.

[3] Belding, M., Enshaeian, A., & Rizzo, P. (2023). A Machine learning-based approach to determining stress in rails. *Structural Health Monitoring*, ***22***(1), 639-656.

[4] Enshaeian, A., Belding, M., & Rizzo, P. (2023). Stress Evaluation in Rails Based on Vibration Data and Artificial Intelligence. *Transportation Research Record*, ***2677***(8), 705-720.

[5] Belding, M., Enshaeian, A., Hager, C., & Rizzo, P. (2023). Machine Learning for the Nondestructive Prediction of Neutral Temperature in Continuous Welded Rails. *Research in Nondestructive Evaluation*, ***34***(3-4), 121-135.

[6] Belding, M., Enshaeian, A., & Rizzo, P. (2023). Nondestructive rail neutral temperature estimation based on low-frequency vibrations and machine learning. *NDT & E International*, ***137***, 102840.

[7] Belding, M., Enshaeian, A., & Rizzo, P. (2024). Nondestructive estimation of neutral temperature in rails: a comparative study of machine learning strategies. *Materials Evaluation*, ***82***(1), 67-78.

EXPERIMENTAL INVESTIGATION ON THE MOTORCYCLE SWINGARM DEFORMABILITY AND STABILITY

B. Almeida[1], A. Leite[1], S. Dias[1], M.Oliveira[2] , I. Arce[3,4] and F. Pereira[4]
[1]University of Trás-os-Montes and Alto Douro, Engineering Department, Vila Real, Portugal
[2]A.J.P. Motos S.A., Lousada, Portugal
[3]INEGI, Institute of Mechanical Engineering, Porto, Portugal
[4]University of Trás-os-Montes and Alto Douro, Engineering Department, Center for the Research and Technology Agro-Environmental and Biological Sciences, CITAB, Vila Real, Portugal

1. Introduction

Motorcycles are the most common type of motor vehicle in many parts of the world with the growing emphasis on sustainable transportation [1]. Recent innovations focus on producing lightweight designs, as reducing the weight of motorcycles not only decreases fuel consumption but also enhances sustainability by minimizing resource use and emissions.

One critical component in this context is the swingarm, which connects the rear wheel to the chassis and accommodates the rear suspension system. The swingarm plays a vital role in maintaining stability under various load condition [2]. Its flexibility is particularly crucial in electric motorcycles, where different weight distribution affects stability properties.

The use of modeling and numerical methods, combined with experimental approaches, has greatly improved the understanding of motorcycle stability. These methods allow the identification of mechanical properties of structural components [3]. These approaches predict component behavior under various load and environmental conditions, allowing design adjustment to improve safety, durability, and efficiency.

Topology optimization is a valuable apparatus in this process, as it redefines the shape of a component by removing unnecessary material while preserving essential mechanical performance [4]. This technique allows a reduction of production costs, time and manufacturing efficiency.

This study aims to characterize the mechanical properties of an electric motorcycle swingarm using a specially designed test bench, combined with finite element simulations. The findings will be further enhanced by applying topology optimization to refine the design. By enhancing understanding of swingarm stiffness and deformation underload, this research contributes to the development of safer, more efficient electric motorcycles and supports advancements of sustainable transportation.

2. Materials and methods

The swingarm was specifically designed for an electric motorcycle with a symmetric, bulky and compact design, weighing 4.1kg. The experimental testing procedure was conducted on a custom-designed test bench for static tests (Fig. 1) to evaluate the bending stiffness and deformation of the swingarm using an Instron 8801 machine. The swingarm structure was fixed at both ends, and the load was applied at the suspension connection point through a pin connection attached to the load cell. A 5000 kg load cell, aligned with the actuator axis, was used to measure the force applied by the actuator.

To validate the results of numerical simulation with finite element method, the experimental results were used. These simulations predicted stress and strain distribution in the swingarm under various load conditions. Additionally, topology optimization was applied to refine swingarm design.

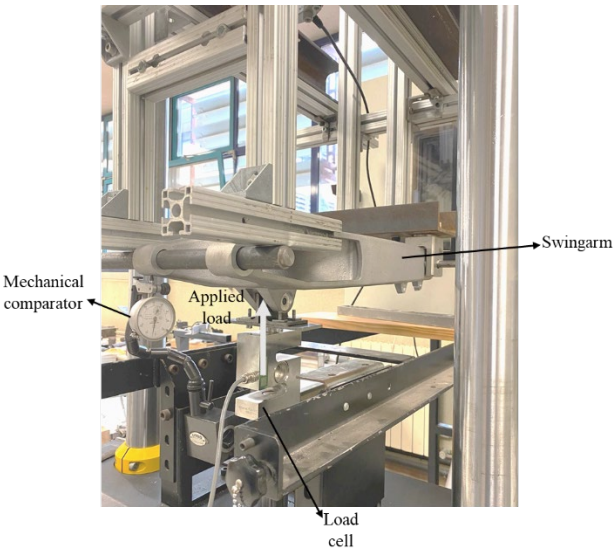

Fig. 1. Test bench

3. Results and conclusions

The results of topology optimization are presented in Fig.2, showing a 13% reduction in weight. Numerical and experimental tests were performed on the original design to evaluate its structural performance, focusing on the stress field. These results provide as a baseline for validating the optimized design, highlighting its potential for enhanced performance in mechanical applications.

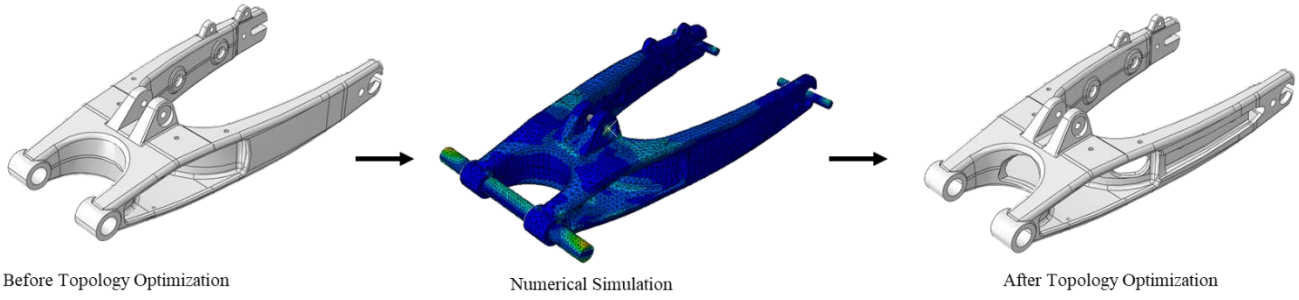

Fig. 2. Comparison of two swingarm designs: original (left) and optimized (right) for weight reduction

4. Acknowledgements

The study was developed under the project A-MoVeR – "Mobilizing Agenda for the Development of Products & Systems towards an Intelligent and Green Mobility", operation n.º 02/C05-i01.01/2022.PC646908627-00000069, approved under the terms of the call n.º 02/C05-i01/2022 – Mobilizing Agendas for Business Innovation, financed by European funds provided to Portugal by the Recovery and Resilience Plan (RRP), in the scope of the European Recovery and Resilience Facility (RRF), framed in the Next Generation UE, for the period from 2021 -2026.

5. References

[1] S. Ahmed and M. K. Gupta, "Investigations on motorbike frame material and comparative analysis using generative design and topology optimization," *Materials Today: Proceedings*, vol. 56, pp. 1440–1446, Jan. 2022, doi: 10.1016/j.matpr.2021.12.040.

[2] G. Risitano, L. Scappaticci, C. Grimaldi, and F. Mariani, "Analysis of the Structural Behavior of Racing Motorcycle Swingarms," Apr. 2012. doi: 10.4271/2012-01-0207.

[3] L. Taraborrelli, V. Favaron, and A. Doria, "The effect of swingarm stiffness on motorcycle stability: experimental measurements and numerical simulations".

[4] L. Frizziero *et al.*, "IDeS Method Applied to an Innovative Motorbike—Applying Topology Optimization and Augmented Reality," *Inventions*, vol. 7, no. 4, Art. no. 4, Dec. 2022, doi: 10.3390/inventions7040091.

TEMPERATURE-DEPENDENT EXPERIMENTAL CHARACTERIZATION OF A STRETCHABLE STRAIN SENSOR

B. Almeida[1], J.R. Fernandes[2], M.Oliveira[3], R. Morais[4] and F. Pereira[4]
[1]University of Trás-os-Montes and Alto Douro, Engineering Department, Vila Real, Portugal
[2]University of Trás-os-Montes and Alto Douro, Physics Department, Chemistry Centre - Vila Real, CQ-VR, Vila Real, Portugal
[3]A.J.P. Motos S.A., Lousada, Portugal
[4]University of Trás-os-Montes and Alto Douro, Engineering Department, Center for the Research and Technology Agro-Environmental and Biological Sciences, CITAB, Vila Real, Portugal

1. Introduction

Nowadays, stretchable strain sensors have been developed with various materials, including silicone polymers, particularly rubber-like materials. Stretchable strain sensors have numerous applications including health monitoring, electronic skin, motion detection, and monitor stress and deformation of mechanical components [1]. These sensors convert any variation such as deformation and elongation into an electrical signal such as changes in electrical resistance [2].

Silicone polymers offer exceptional physical properties, such as bio-compatibility, non-toxicity, thermal stability, and resistance to environmental conditions [3]. Among them, Ecoflex™ Shore 00-30 is a commercially available rubber-like material, with a low viscosity and a four-hour curing time, it can endure significant stretching, returning to its original form without tearing or distortion [3].

The different types of Ecoflex have been extensively studied, revealing their mechanical behavior, including time-dependent stress relaxation and strain-induced stress softening [4]. However, the influence of temperature on their tensile properties remains underexplored. Temperature variations can significantly affect the material's stiffness, energy dissipation, and failure mechanisms, highlighting the need for a comprehensive investigation of how tensile properties evolve under different thermal conditions. Understanding these effects is crucial for optimizing the use of Ecoflex in applications that involve varying environmental temperatures and complex deformation states [4].

This study aims to understand the influence of temperature on the tensile properties of Ecoflex™ Shore 00-30, to optimize the performance of a stretchable strain sensor in various applications. These insights are expected to contribute to the advancement of stretchable strain sensors with enhanced reliability and performance.

2. Materials and methods

In this study, Ecoflex™ Shore 00-30 was supplied in two liquid components: which were combined in a 1:1 weight ratio and mixed for 3min. The resulting mixture was poured into a sensor mold and placed in a vacuum oven at 52ºC and 6 bar for 1 hour to remove entrapped air and minimize bubble formation. Four samples were prepared for each experiment, subjected to different temperature treatments: nonheated, heated at 70°C for 2 hours, and heated at 70°C for 4 hours.

Tensile tests were conducted using an Instron Micro-Tester 5848, where each specimen was subjected to a controlled, increasing force while its deformation was measured (Figure 1). The face of the each specimen were marked with black points and recorded using a smartphone camera to

capture the material's response during the experiment. The recorded videos were converted in images and then processed using an algorithm developed in MATLAB, to measure displacement and determine the strain values over time (Figure 2).

Fig. 1. Tensile test

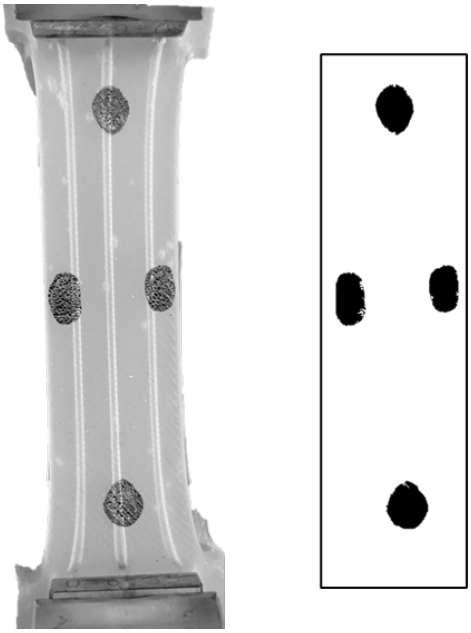

Fig. 2. Greyscale image (left) and binary image (right)

3. Results and conclusions

The results showed that the modulus of elasticity remained consistent across the diferent tested conditions, demonstrating the mechanical stability of the polymeric material. The average modulus for test condition at ambient temperature was 0.066MPa, after 2 hours at 70ºC 0.067MPa and after 4 hours at 70ºC 0.067MPa (Figure 3). Each result for each condition as minimal standard deviations, highlighting the efficiency of developed algorithm. These findings indicate that the sensors maintain vigorous mechanical properties, making them suitable for applications in environments with temperature fluctuations.

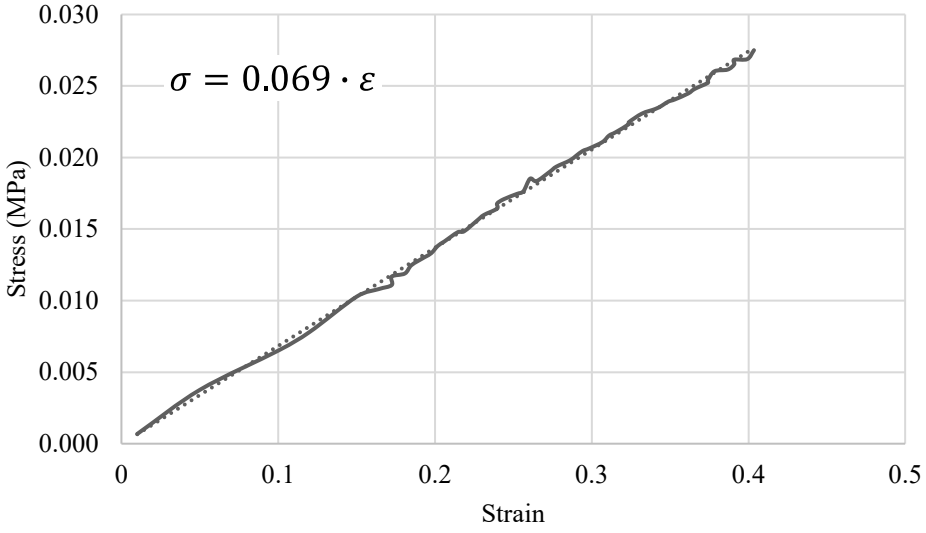

Fig. 3. An example of a stress-strain curve

4. Acknowledgements

The study was developed under the project A-MoVeR – "Mobilizing Agenda for the Development of Products & Systems towards an Intelligent and Green Mobility", operation n.º 02/C05-i01.01/2022.PC646908627-00000069, approved under the terms of the call n.º 02/C05-i01/2022 – Mobilizing Agendas for Business Innovation, financed by European funds provided to Portugal by the Recovery and Resilience Plan (RRP), in the scope of the European Recovery and Resilience Facility (RRF), framed in the Next Generation UE, for the period from 2021 -2026.

5. References

[1] A. del Bosque, X. F. Sánchez-Romate, A. Gómez, M. Sánchez, and A. Ureña, "Highly stretchable strain sensors based on graphene nanoplatelet-doped ecoflex for biomedical purposes," *Sensors and Actuators A: Physical*, vol. 353, p. 114249, Apr. 2023, doi: 10.1016/j.sna.2023.114249.

[2] H. J. Lee, R. Joyce, and J. Lee, "Liquid Polymer/Metallic Salt-Based Stretchable Strain Sensor to Evaluate Fruit Growth," *ACS Appl. Mater. Interfaces*, vol. 14, no. 4, pp. 5983–5994, Feb. 2022, doi: 10.1021/acsami.1c21376.

[3] Z. Liao, M. Hossain, and X. Yao, "Ecoflex polymer of different Shore hardnesses: Experimental investigations and constitutive modelling," *Mechanics of Materials*, vol. 144, p. 103366, May 2020, doi: 10.1016/j.mechmat.2020.103366.

[4] "Strain rate, temperature and deformation state effect on Ecoflex 00-50 silicone mechanical behaviour - ScienceDirect." Accessed: Sep. 25, 2024. [Online]. Available: https://www.sciencedirect.com/science/article/pii/S0167663623000066#b16

6-11 July 2025 ICEM21 Bologna
21st International Conference on EXPERIMENTAL MECHANICS

A STUDY ON A NONDESTRUCTIVE METHOD OF DETECTING CERAMIC COATING DEBONGDING USING NDTPEA

Lianyun Xu, Zhende Hou, Shaozhe Pan, Chuan Qu
Department of Mechanics, School of Mechanical Engineering, Tianjin University, Tianjin 300072, China

1. Introduction

We proposed a nondestructive testing method based on electro-acoustic technique (NDTPEA) to detect internal defects of dielectric materials, which can identify the defects from the original stress wave generated at the internal defect surface [1-3] . Because forming an insulating coating on a metal substrate surface can improve the performance of the metal, which is used in wide range of areas. One of the challenges is to detect coating debonding existed during the coating production process. In this manuscript, we successfully detected the ceramic coating debonding from a metal substrate using the NDTPEA.

2. Materials and methods

When a metal specimen with coating made of insulate materials is placed in a high direct electric field as shown in Fig. 1(a) the coating is polarized. If there are no debondings between the coating and metal substrate, an equal number of charges with opposite signs will be induced on the upper and lower coating surfaces, as shown in Fig. 1(b). When a narrow electric voltage pulse is input through capacitor C to cause a sudden change in the amplitude of the applied high voltage or electric field, the charges on the upper and lower surfaces are excited to vibrate and form pulse stress waves, which will propagate upside into the metal substrate and down through the coating respectively. The two stress pulses will propagate into the lower electrode successively. On the lower side of the lower electrode, there is a polyvinylidene fluoride piezoelectric film (PVDF). The film receives the pulse stress waves propagated through the bottom electrode.

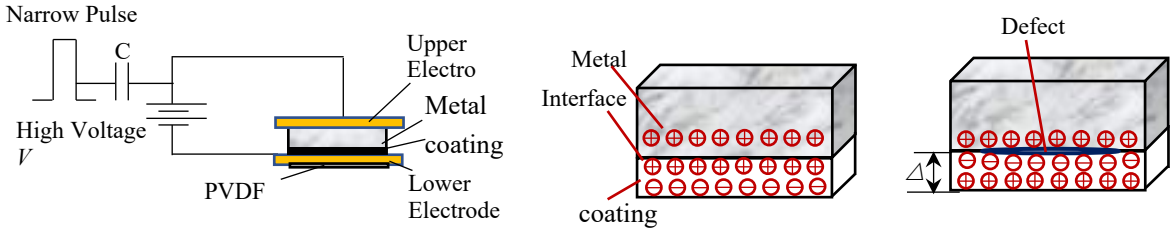

Fig. 1 (**a**) Specimen in the electric field. (**b**) Charge distribution of dielectric materials without defect. (**c**) Charge distribution of dielectric materials with defect

Fig.2(a) shows the schematic diagram of the stress waves received. Pulse A (first pulse) is the stress wave generated by the charge on the lower surface of the coating and Pulse B (second pulse) is the stress wave generated by the charge on the coating upper surface. If there are a debonding between the coating and metal substrate, the pulse stress waves only propagate in one direction. That is that the waves are only down through the coating, then then amplitudes of the waves received by the PVDF are higher than those in Fig2(a), as shown in Fig. 2(b).Time t_0 is the time for the stress

wave to travel through the entire thickness of the coating from the upper surface to the lower surface. Its value decreases with the decrease of the coating thickness. If the coating thickness becomes more thin the two pulses can connect each other.

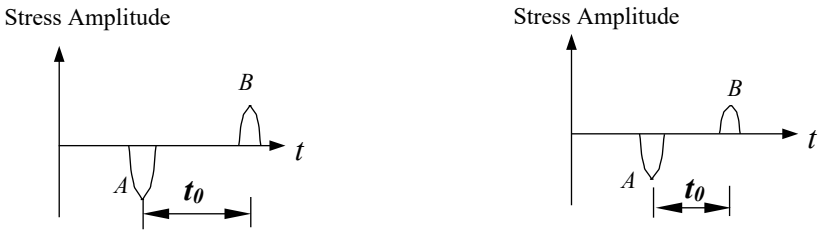

Fig. 2. (a) Stress pulse wave without debonding between coating and metal substract.
(b) Stress pulse wave with debonding between coating and metal substrac

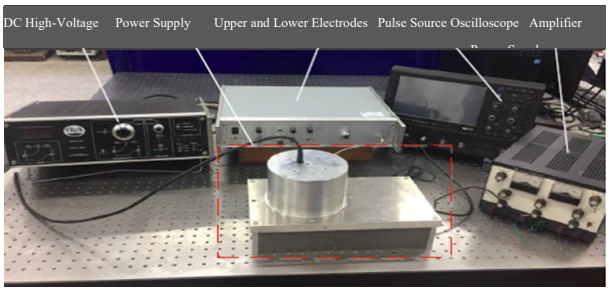

Fig. 3. Experimental test device

3. Results and conclusions

The specimen substrate was a steel circular plate of diameter 40mm and thickness 3mm. A 0.3mm thick ceramic film was adhered to the substrate as the coating. Two specimens were prepared. One is that the ceramic film surface was totally adhered to the substrate surface as a specimen without debonding. The other was only adhered around the substrate edge area and central area was not adhered as the debonding.

The two specimens have been tested and Fig. 4 and Fig. 5 show the measured pulse stress waves

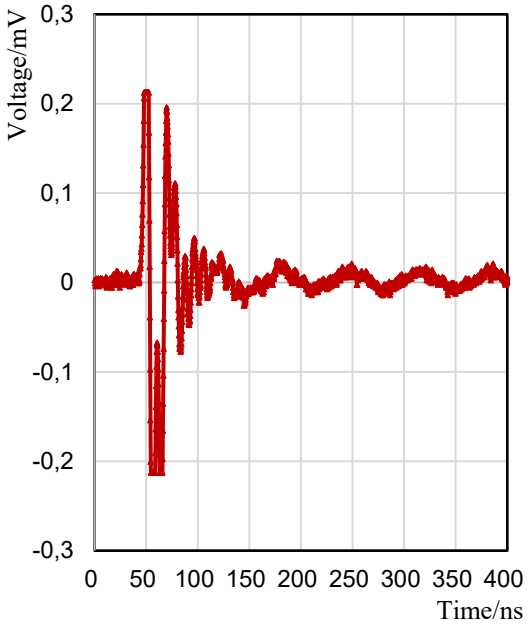

Fig. 4.Stress waves from with debonding

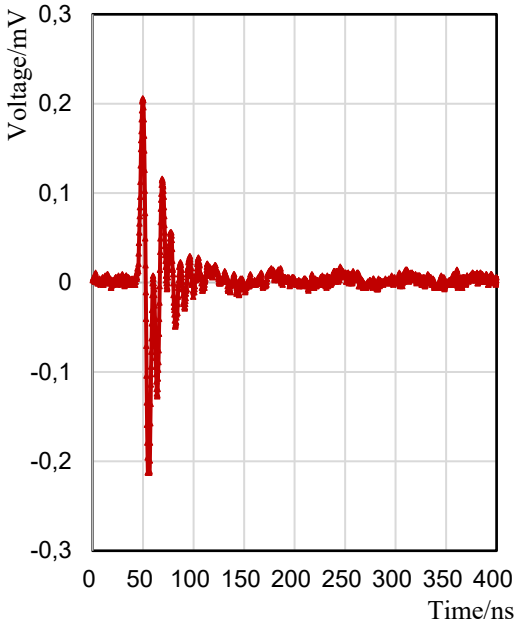

Fig. 5. Stress waves from without debonding

respectively. Fig. 4 denotes the result of the specimen with debonding and Fig5 shows that without debonding. It is clear that the curve amplitudes in fig.4 are higher than those in Fig.5, which means that the method can be used to detect the debonding of coating.

4. Acknowledgements

This work was supported by the National Natural Science Foundation of China under grant 12272263.

5. References

[1] Honarvar F, Varvani-Farahani A (2020) A review of ultrasonic testing applications in additive manufacturing: Defect evaluation, material characterization, and process control. Ultrasonics 108: 106227
[2] Garnier C, Pastor ML, Eyma F et al (2011) The detection of aeronautical defects in situ on composite structures using Non-Destructive Testing. Compos Struct 93: 1328-1336
[3] Xu, L; Hou, Z and Kang, H(2022)A Method for Detection of Internal Defects of Dielectric Materials Based on Pulsed Electro-Acoustic Technique.EXPERIMENTAL MECHANICS 62(3): 417-426

INVESTIGATING THE POSSIBILITY TO DETECT AND CHARACTERIZE RAIL CRACKS AT HIGH SPEEDS WITH INDUCTION THERMOGRAPHY

E. D'Accardi[1], G. Dell'Avvocato[2], G. Marinelli[3], G. Fumarola[3], D. Palumbo[1] and U. Galietti[1]
[1] Department of Mechanics, Mathematics and Management (DMMM), Polytechnic University of Bari, Via Edoardo Orabona n. 4, 70125 Bari, BA, Italy
[2] University of L'Aquila, Industrial and Information Engineering and Economics, Piazzale Ernesto Pontieri 1, Monteluco di Roio, 67100 L'Aquila, AQ, Italy
[3] Tesmec Rail, Giovanni Rutigliano SNC, 70020 Bitetto, BA, Italy

1. Introduction

Rail defects caused by rolling contact fatigue pose significant risks to railway safety and reliability. Non-destructive testing (NDT) is essential for detecting these defects, but traditional methods like ultrasonic testing and visual inspection have limitations. Ultrasound requires direct contact, while visual inspection requires clear surface access, which can be challenging in real operating conditions, and is limited to surface defects.

Induction thermography has emerged as an effective alternative to traditional NDTs [1-3], offering the possibility of non-contact inspections of surface and subsurface cracks. This study uses induction thermography to identify transverse cracks and head checks in real rail components. Unlike previous research conducted at low speeds in lab settings, this work explores high-speed on-site applications, reflecting real-world conditions.

The results show that defects can be detected at speeds up to 20 km/h [4-5], surpassing previous studies limited to 1-4 km/h [1-3]. Tests were conducted on rail sections with real cracks, using coils of different shapes to improve heating and enhance defect visibility.

A post-processing method was developed to address challenges with limited data capture at high speeds, to ensure accurate crack detection, regardless of speed. This study demonstrates that induction thermography is a practical solution for high-speed rail inspections, enhancing safety and efficiency in rail diagnostics and maintenance.

2. Materials and methods

The system includes a cooled FLIR infrared sensor, an infrared mirror, an induction system, and linear guides driven by a motor to move the rail. The IR sensor and excitation source were controlled by a custom system developed by Diagnostic Engineering Solutions (DES) for this project. Due to a non-disclosure agreement and the ongoing nature of the project, specific technical details about the set-up and hardware cannot be fully disclosed. For a detailed overview of the set-up and component images, refer to the previous publication [4-5].

The excitation system uses a commercial inductor capable of adjusting pulse duration and power up to 4.2 kW. Operating frequencies ranged from 150 to 400 kHz, depending on the capacitors and coil used. Based on the results obtained in previous works [4-5], a rectangular coil was designed to cover the entire rail width in one scan. The coil's geometric parameters are shown in [4].

Four rail sections, each approximately 20 cm long, were tested without covering the inspected surface (emissivity ~ 0.3). They contained typical rail defects and, in particular, transverse cracks.

3. Results and conclusions

A post-processing procedure for analysing thermal data was used to assess the effectiveness of the technique and proposed setup for crack detection.

Extracting specific profiles from the same position in each frame, made it possible to represent different rail parts at the same cooling stage. Columns from the thermal frames were selected to create new images showing the entire rail at different cooling times. Past studies have applied similar methods [1, 4-5] to process data after testing.

This method works well at moderate rail speeds, as fast thermal cameras can capture the whole rail without missing details. At higher speeds (above 5 km/h), a specific area (region of interest) is used to ensure accurate tracking of the rail as it moves very fast [4-5]. After reconstruction, a median filter has been applied in order to reduce the influence of non-uniform heating, obtaining a direct measure of the thermal contrast around the defect area. The choice of the kernel size has been optimized considering the defect dimension.

The obtained results are shown in Figure 1, confirming that it is possible to detect cracks and specific rail typical defects up to 20 km/h.

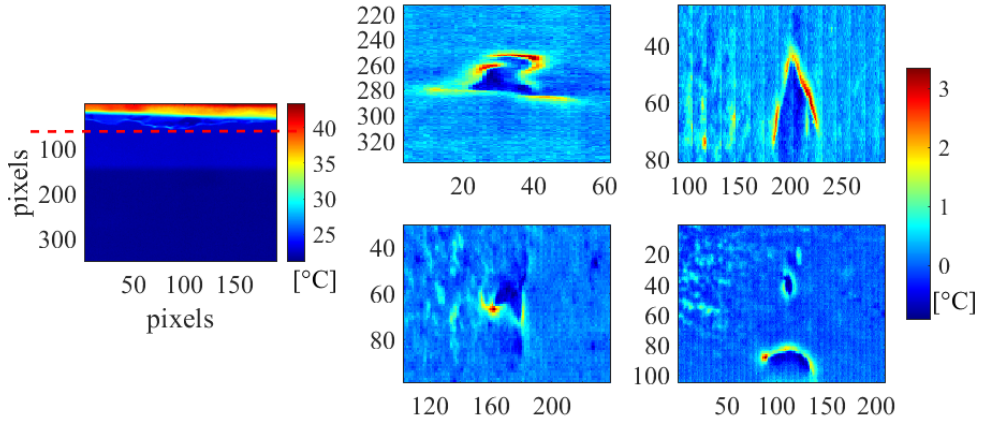

Figure1. Examples of detected cracks considering different rail track inspection at 20 km/h.

4. Acknowledgements

The research presented in this paper has been supported by Puglia Region within the Project: 'S30KXH0 – Tesmec Rail DIREC-T, DIAGNOSTICA DELL'INTEGRITÀ DI ROTAIE CON METODI DI CONTROLLO NON DISTRUTTIVI INNOVATIVI'.

5. References

[1] Tuschl C, Oswald-Tranta B, Eck S. Inductive thermography as non-destructive testing for railway rails. Appl Sci. 2021;11(3):1003. doi: 10.3390/app11031003.

[2] Zhang X, Peng J, Zhang Q, et al. Nondestructive analysis of rolling contact fatigue cracks using induced scanning thermography. Opt Express. 2022;30(24):42982–42994. doi: 10.1364/OE.469656.

[3] Netzelmann U, Walle G, Ehlen A, et al. NDT of railway components using induction thermography. In AIP conference proceedings. 42nd Annual Review of Progress in Quantitative Nondestructive Evaluation: Incorporating the 6th European American Workshop on Reliability of NDE; 26–31 July 2015; Minneapolis, Minnesota. Vol. 1706, AIP Publishing; 2016 February.

[4] D'Accardi, E., Dell'Avvocato, G., Masciopinto, G., Marinelli, G., Fumarola, G., Palumbo, D., & Galietti, U. (2024). Evaluation of typical rail defects by induction thermography: experimental results and procedure for data analysis during high-speed laboratory testing. *Quantitative InfraRed Thermography Journal*, 1–22. https://doi.org/10.1080/17686733.2024.2340060.

[5] D'Accardi, E., Dell'Avvocato, G., Masciopinto, G., Fumarola, G., Marinelli, G., Palumbo, D., & Galietti, U. (2024, June). Scanning inductive and line laser thermography for surface crack detection and characterization in railway rails. In *Thermosense: Thermal Infrared Applications XLVI* (Vol. 13047, pp. 134-145). SPIE.

EFFICIENCY OF PZT TRANSDUCERS IN DAMAGE DETECTION OF STRUCTURES

M. Dziendzikowski[1,2], K. Kowalczyk[2], Z. Dworakowski[3]
[1] Airworthiness Division, Air Force University of Technology, Warsaw, Poland
[2] Faculty of Materials Science and Engineering, Warsaw University of Technology, Warsaw, Poland
[3] Department of Robotics and Mechatronics, AGH University of Science and Technology, Krakow, Poland

1. Introduction

Among various approaches to SHM, PZT ceramic sensors have proven to be a technology with universal application capabilities [1,2]. Elastic waves excited by PZT sensors can interact with any mechanical discontinuities caused by damage and can also penetrate various joints and interfaces. However for successful application of PZT sensors significant effort towards system optimization is needed. Most importantly, the network geometry should be tailored to particular geometry of monitored element as well as location of potential damage. However also other parameters, e.g. type of the excitation signal, or signal characteristics used for structure assessment as well as signal acquisition time can have significant influence on sensitivity to damage. Based on sparsely distributed PZT networks, it can be difficult to estimate precisely sensitivity regions of PZT sensors with respect to damage. For that purpose full elastic wavefield measurements with use of laser vibrometer are used. Based on such data it is possible to precisely vizualize regions of enhanced and reduced sensitivity. In addition, different type of damage, e.g. cracks or corrosion material loss of metallic structures as well as impact damage of composite materials may result in different efficiency of PZT sensors towards their detection. In the presentation damage indices efficiency in detection of different type of damage as well as influence of signal acquisition time on the obtained spatial distributions of damage indices is considered.

2. Materials and methods

Elastic waves were acquired with use of Polytec PSV-500 Laser Scanning Vibrometer equipped with PSV-I-550 Extra Scanning Head (Fig. 1). Signals were acquired with respect to predefined rectangular scan grid consisted of thousands of scanning points, separated by approximately 2-3 mm. The data were acquired from the surface of the specimen opposite to the surface on which sensor was installed and damage introduced. Based on set of signals acquired before and after introduction of a simulated damage it was possible to determine map of Damage Indices defined for every point of the scanning grid.

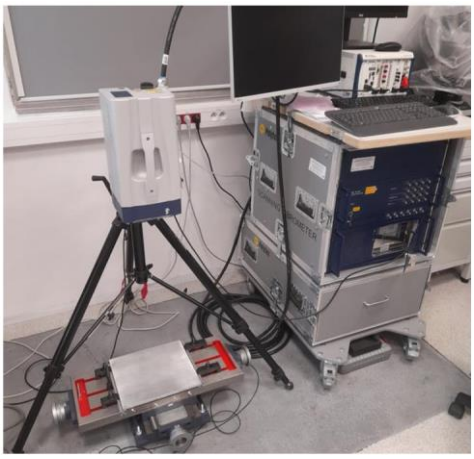

Fig. 1. Experimental setup for elastic waves acquisition with use of laser scanning vibrometer

3. Results and conclusions

The acquired data were analysed with respect to type of signal characteristic used for damage characterization as well as signal acquisition window T. In Figure below a correlation Damage Index for two different acquisition time ranges $T = (0,t_0)$ and $T = (0,3t_0)$. For t_0 only the incident $S0$ and $A0$ modes are present in the signal as shown in, whereas for longer acquisition time $t1$ multiple reflections from specimen edges occurred and contributed to Damage Index distribution in the monitored area.

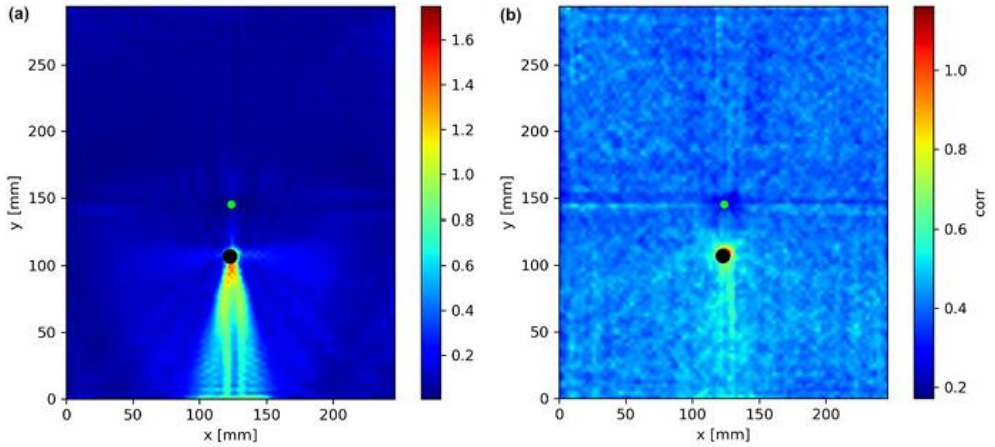

Fig. 2. Correlation damage index maps obtained for two different acquisition time ranges $T = (0,t_0)$ and $T = (0,3t_0)$

4. Acknowledgements

The work presented in this paper was supported by the National Centre for Research and Development in Poland, under project number LIDER13/0132/2022.

5. References

[1] Giurgiutiu, V. Structural health monitoring: with piezoelectric wafer active sensors 2nd ed.; Academic Press, 2014.

[2] Su, Z.; Ye, L. Identification of damage using Lamb waves: from fundamentals to applications, ; Vol. 48, Springer Science & Business Media, 2009.

BEARING DIAGNOSTIC BASED ON FAULT CLASSIFICATION USING AUTOREGRESSIVE LINEAR DISCRIMINANT ANALYSIS AND SUPPORT VECTOR MACHINE

M.Vanali, M.Conti, S.Pavoni
Department of Systems and Industrial Technologies (DISTI), University of Parma, Parma, Italy

1. Introduction

Bearings are critical components in rotating machinery, responsible for minimizing friction and ensuring efficient motion transfer between moving parts. Their failure can result in costly unplanned downtime, extensive damage to equipment, and significant safety hazards in industrial operations. Consequently, predictive maintenance of bearings has become a crucial focus in the field of condition monitoring, aiming to identify potential issues well in advance of catastrophic failures. The diagnostics of bearings involves the detection and analysis of faults, which are typically characterized by changes in vibration patterns. Traditional diagnostic methods often rely on manual feature extraction and domain expertise, but these approaches may struggle to manage the complexity and variability of real-world scenarios. Machine learning techniques offer a powerful alternative, enabling automated feature extraction, pattern recognition, and classification. By leveraging algorithms capable of processing large datasets, machine learning facilitates the identification of subtle patterns indicative of specific fault types, improving both accuracy and efficiency in diagnostics. In this study, we utilize Linear Discriminant Analysis (LDA) and Support Vector Machines (SVM) to classify various types of bearing damage [1]. LDA is a dimensionality reduction technique that projects data into a lower-dimensional space while preserving class separability. This helps in visualizing and distinguishing features corresponding to different fault categories. SVM, on the other hand, is a robust classifier that constructs hyperplanes to separate data points with maximum margin, ensuring accurate classification even in the presence of complex and overlapping distributions. The combined use of LDA and SVM offers several advantages: LDA reduces noise and emphasizes discriminative features, while SVM excels at handling non-linear boundaries and small sample sizes. This approach is particularly suited for the bearing diagnostics domain, where the ability to distinguish between closely related fault types is paramount. The objective of this study is to demonstrate the effectiveness of this methodology in classifying faults such as inner race, outer race, and rolling element defects, providing a reliable framework for predictive maintenance in industrial applications.

2. Dataset and methods

This study employs the Case Western Reserve University (CWRU) bearing dataset, a well-established benchmark in the field of bearing fault diagnostics. The dataset includes vibration signals collected under varying load conditions and fault scenarios, such as inner race defects, outer race defects, and rolling element damage. These signals were recorded using accelerometers mounted on the test rig, ensuring high-quality and consistent data. To prepare the data for analysis, autoregressive (AR) coefficients are extracted from the raw vibration signals. These coefficients capture the dynamic

characteristics of the signals, providing a compact and informative representation of the underlying system behavior [2]. The extracted AR coefficients are then projected onto Linear Discriminant Analysis (LDA) coordinates to enhance class separability, emphasizing differences between the fault types. Finally, a Support Vector Machine (SVM) classifier is applied to the LDA-transformed data. The SVM constructs decision boundaries to classify the projected coefficients with high precision, enabling accurate identification of the specific bearing fault type.

Class	*Fault Size [mils]*		
Brinelling (Rolling Element)	7	14	21
Inner Race	7	14	21
New		\	
Outer Race	7	14	21

Table 1. Different typology of faults in CWRU Dataset

3. Results and conclusions

The LDA successfully separates the autoregressive coefficients associated with different types of bearing damage, as evident from the Fig. 1. The subsequent SVM-based classification achieves high accuracy, demonstrating the effectiveness of the combined LDA-SVM approach for bearing fault diagnostics. This methodology provides a robust framework for predictive maintenance in industrial applications.

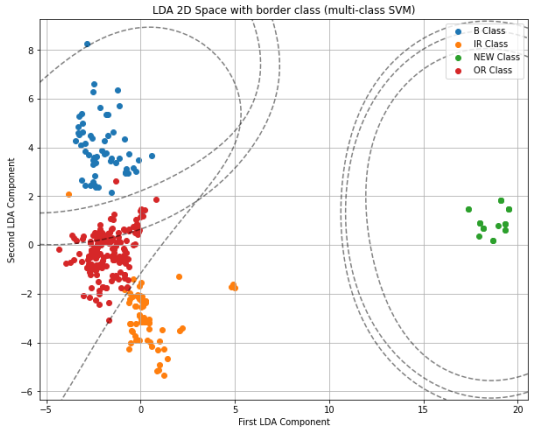

Fig. 1. LDA 2D Space with border class (multi-class SVM)

4. References

[1] Tao Xiong and V. Cherkassky, “A combined SVM and LDA approach for classification,” in *Proceedings. 2005 IEEE International Joint Conference on Neural Networks, 2005.*, IEEE, pp. 1455–1459. doi: 10.1109/IJCNN.2005.1556089.

[2] D. Zhang and W. Sui, “The Application of AR Model and SVM in Rolling Bearings Condition Monitoring,” 2011, pp. 326–331. doi: 10.1007/978-3-642-21402-8_53.

IMPROVING THE CAPABILITIES OF ULTRASONIC INSPECTION OF RAILROAD RAILS IN HIGH-SPEED AND WALKING-SPEED TESTING

A. Z. Hosseinzadeh[1], C. Huang[1], I. Batista[1], and F. Lanza di Scalea[1]
[1] Experimental Mechanics, NDE & SHM Laboratory, Department of Structural Engineering, University of California San Diego, La Jolla, CA 92093, USA

1. Introduction

Ultrasonic testing is commonly used to detect internal defects in railroad rails. Rails are inspected regularly by hi-rail vehicles with ultrasonic Rolling Search Units (RSUs) operating at speeds up to 30 mph. After initial detection, flaws are typically verified with handheld ultrasonic probes to assess their size and orientation. Ongoing research in many laboratories worldwide is aimed at improving the performance of ultrasonic rail inspections in terms of practicality and reliability of defect detection. This paper highlights two key advancements: (1) enabling high-speed rail inspections with "smart trains" and (2) enhancing ultrasonic flaw imaging at walking speeds. These efforts are being pursued at UC San Diego in collaboration with the US Federal Railroad Administration, BNSF Railway, and MxV Rail, Inc.

2. Materials and methods

The first topic focuses on a new non-contact ultrasonic testing prototype that allows flaw detection at revenue speeds (e.g., 60 mph). When fully developed, this technology will enable trains to conduct inspections during regular operations, reducing traffic disruptions and taking advantage of multiple passes over the same rail segment (the 'redundancy concept'). Figure 1 shows the main concept of this technique and the developed prototype. An array of non-contact air-coupled ultrasonic transducers are used to *passively* reconstruct the transfer function (or Green's function) of a rail segment located between receivers A and B, $G_{AB}(f)$, using normalized cross-power spectrum operator [1]. By isolating $G_{AB}(f)$, any discontinuity in the rail (e.g., defect, weld, or join) can be potentially detected as changes in the transfer function (e.g. drop in the amplitude). Although the natural excitation by the train's rolling wheels can be suitable for the purpose of the present method, a controlled acoustic source is also added to the prototype to generate continuous guided waves and guarantee a high Signal-to-Noise Ratio (SNR). This method has been prototyped and tested in different field tests, and at different test speeds.

The second topic consists of research on ultrasonic Synthetic Aperture Focusing Techniques (SAFT) for rail flaw imaging [2] using a transducer array mounted on an RSU wheel (see Figure 2(a)). SAFT presents various advantages over the conventional Phased-Array (PA) technique in terms of hardware simplicity, focusing ability and achievable test speed. A new RSU imaging prototype is being developed based on SAF advancements such as sparse firing, multi-mode detection, and eigen-filter analysis. These techniques help eliminate artifacts, like reflections from the wheel-rail interface and railhead bottom flange, thereby improving flaw detection and quantification.

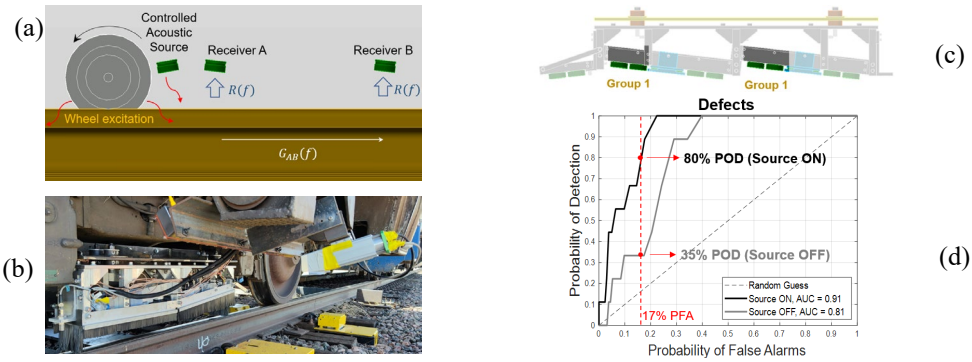

Fig. 1. High speed ultrasonic rail inspection. (a) main concept, (b)-(c) prototype's sensing head, (d) ROC curve results for internal defects during a test run at the Transportation technology Center in Pueblo, CO at 40 mph.

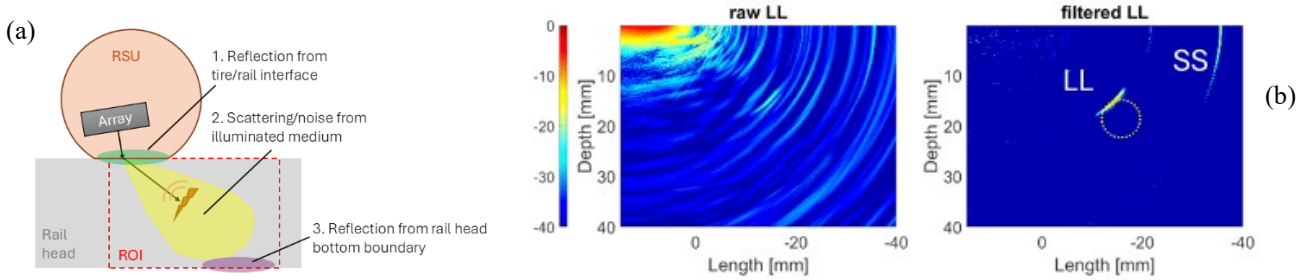

Fig. 2. Rail flaw ultrasonic imaging system. (a) Schematic of an imaging transducer inside a Rolling Search Unit for rail scanning, (b) application of recursive SVD filter to the ultrasound video showing the defect (side drilled hole) in the middle of the image.

3. Results and conclusions

Figure 1(d) shows the results of the high-speed inspection prototype conducted at the Transportation Technology Center at a speed of 40 mph in terms of receiver Operating Characteristic (ROC) curves. This result refers to internal defects independently verified in the test track. The plot shows that the active acoustic source is beneficial. Also, a typical performance of the system during those tests was 80% POD with 17% PFA. Ongoing work is aimed at improving this performance.

Figure 2(b) shows the results of the latest version of the rail flaw imaging prototype. The left figure shows a frame of the raw ultrasound video. The right figure shows the filtered frame after the application of a recursive Singular Value Decomposition (SVD) filter. This filter eliminates the video artifacts (reflections at the tire-rail interface, scattering from the rial surface, and reflections from the rail head bottom boundary) by projecting out the highest eigenvectors of the Casorati data matrix.

4. Acknowledgements

The research presented in this paper have received funding from the US Federal Railroad Administration (FRA) (project managers: M. Brice and R. Wilson), BNSF Railway (in-kind support), and MxV Rail, Inc. (project manager: A. Poudel).

5. References

[1] F. Lanza di Scalea, X. Zhu, M. Capriotti, A. Y. Liang, S. Mariani, and S. Sternin (2018). Passive extraction of dynamic transfer function from arbitrary ambient excitations: application to high-speed rail inspection from wheel-generated waves. *Nondestruct. Eval. Diagn. Progn. Eng. Syst.*, **1**, 011005.

[2] C. Huang, F. Lanza di Scalea (2024). Application of sparse synthetic aperture focusing techniques to ultrasound imaging in solids using a transducer wedge. *IEEE Trans Ultrason Ferroelectr Freq Control.*, **71**, 280–294.

DETECTION OF LITHIUM-ION BATTERY STATE OF CHARGE USING MAGNETIC FLUXGATE SENSOR

Qirui Wang[1], Yan Lyu[2],and Jie Gao[2]
[1] College of Mechanical and Energy Engineering, Beijing University of Technology, Beijing, China
[2] School of Information Science and Technology, Beijing University of Technology, Beijing, China

1. Introduction

Electric vehicles and renewable energy sources, as the two example of modern technologies developing by energy storage systems, are researched worldwide. Lithium-ion batteries are the most commonly used among all the energy storage technologies. Compared to other technologies, Lithium-ion batteries have longer life cycles, higher charge/discharge rates and high energy density, resulting in their suitability for a wide range of industrial scenarios [1]. Therefore, the reliable condition monitoring systems are required to monitor their state parameters. The state of health (SOH) and the state of charge (SOC) are pivotal parameters for ensuring the healthy and safe operation of lithium-ion batteries. Particularly within battery packs, inconsistent SOC can significantly influence battery safety and longevity.

Non-destructive monitoring and evaluation of lithium-ion battery state parameters constitute a formidable challenge within the domain of battery diagnostics. A variety of sophisticated imaging technologies have been introduced to offer insights into the in situ or operational status of batteries. X-ray imaging, with its profound transmission capabilities, has characterized the structural evolution within lithium-ion battery materials [2]. Neutron imaging has provided a window into the internal dynamics of lithium-ion batteries, including the distribution of lithium ions, the growth of dendrites, and the production of gases [3]. Ultrasound imaging has been put forth to visualize the electrolyte wetting process and to estimate the SOC of lithium-ion batteries through acoustic parameters such as flight time and amplitude [4]. These imaging techniques have enabled the detection and analysis of the internal structural behavior of lithium-ion batteries. However, their application in the detection and evaluation of lithium-ion batteries has been restricted by the inherent limitations of their imaging principles. However, the application of these imaging techniques in detecting and evaluating lithium-ion batteries is constrained by limitations inherent in their imaging principles.

Magnetic resonance imaging technique was proposed in 2018 by Ilott et al [5]. The tiny magnetic field variation is measured to detect the SOC and of lithium-ion battery as well as internal defects, induced by changes in electrode material magnetic susceptibility. Subsequently, magnetic resonance imaging technology was also applied to research on the detection of internal current distribution, SOC and SOH of lithium-ion battery. The high cost of the equipment limited the popularization and application of this technology. Magnetic field imaging technique, which use magnetic field sensors to directly measure the external induced magnetic field of the cell, has been widely used of detecting lithium-ion battery in recent years. The performance of cells can be assessed by analyzing the detected induced magnetic field. Bergholz et al. utilized an anisotropic magneto resistive (AMR) sensor to measure the externally induced magnetic field of a lithium-ion battery during constant-current discharge. They further analyzed the relationships between changes in magnetic susceptibility and

state of charge (SOC) in 2013 [6]. The AMR sensor is also applied to obtained the internal current distribution of the cell by the magnetic field image inversion above the cell [9]. Hu et al. adopted a sensitive atomic magnetometry to measure weak transient currents inside the cell at the end of discharge, and the two-dimensional magnetic susceptibility maps corresponding to the discharge capacity of the cell were obtained from a regularized inversion of the measured magnetic field in 2020 [7]. Chen et al. obtained the distribution map of the magnetic field utilizing the magnetoelectric sensors by scanning the surface of the power battery during charging [8]. The location of the anomalous magnetic field was identified by comparing the difference between healthy and faulty cells. Bason et al. used a 4×4 magnetometer array to map the magnetic field distribution of a single cell and analyze the current distribution [10]. Javadipour et al. utilized the magnetic field images captured by fluxgate magnetometers to analyze the current distribution at different SOHs [11].

Existing studies have demonstrated that the variation in external induced magnetic field of the cell can provide insights into the changes in current distribution, SOC and SOH. This is due to that any battery behavior affecting current, such as lithium plating and bubble defects, can be sensitively detected by magnetic field sensors. Although the aforementioned studies have primarily focused on the analysis of SOH and current density, further advancements in the study of SOC in lithium-ion batteries have yet to be achieved. In this study, a three-dimensional model was established to clarify the relationship between the current density and the external magnetic field. The magnetic flux density adopted by magnetic fluxgate sensor variation and to analyze relevant the charge-discharge cycle. During the discharge process, magnetic field imaging corresponding to representative SOC is used to visualize the impact of SOC on the full-cell magnetic field. By investigating the magnetic field distribution and its correlation with SOC, this research lays a valuable foundation for further magnetic characterization analysis and assessment of lithium-ion batteries.

2. Modeling for Lithium-ion Battery

This study centers on lithium-ion batteries featuring graphite anodes and LiMn2O4 cathodes. A three-dimensional model of a single-layer cell are constructed , as illustrated in Fig. 1. Given that the thickness of the single-layer cell is on the micrometer scale, the scale in the model is set to a ratio of X:Y:Z = 1:1:50. The cell with a capacity of 363 mAh is simulated to be charged from 0% to 100% State of Charge (SOC) at a rate of 1C. This simulation model is designed to be adaptable, allowing for adjustments in size parameters and the selection of different positive and negative electrode materials. In theory, the SOC across diverse types of lithium-ion batteries are facilitated to characterization.

During the simulation, the current density on the electrode surface is extracted, contributing to the formation of the external magnetic field of the lithium-ion battery in simulation. The mapping relationship between the magnetic field distribution on the surface of the single-layer lithium-ion battery and its current density is foundational and central to the concept of magnetic field imaging for lithium-ion batteries. Detailed size parameters of the single-layer cell model are provided in Table 1.

The magnetic field generated by a lithium-ion battery is influenced by two main contributors: surface currents in the electrodes and charge transfer currents in the electrolyte. This research specifically examines the current density originating from the positive electrode, which can be characterized using a concept akin to Ohm's law to describe electron conduction within the electrode :

$$\nabla \cdot \boldsymbol{J}_{\boldsymbol{S}} = 0 \tag{1}$$

where $\boldsymbol{J}$s is the current density vector in the electrode, and described as:

$$\boldsymbol{J}_S = -\sigma_S \nabla \phi_S \tag{2}$$

where σ_s is the electrical conductivity and φ_s is the electric potential in the electrode.

The magnetic field at a distance r above the battery can be computed with the Biot-Savart law, which requires the current density in (1) at each point in the geometric shape to be considered:

$$\boldsymbol{B}(\boldsymbol{r}) = \frac{\mu_0 d}{4\pi} \int \frac{\boldsymbol{J}_S(\boldsymbol{r}') \times (\boldsymbol{r}-\boldsymbol{r}')}{|\boldsymbol{r}-\boldsymbol{r}'|^3} d^3\boldsymbol{r}' \tag{3}$$

where $\boldsymbol{r}$ is the position in space at which the magnetic field is calculated, $\boldsymbol{r}'$ is the position of the current density and $\mu 0$ is the permeability of free space.

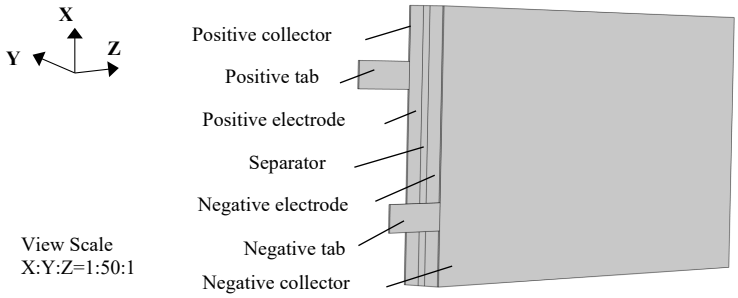

Fig. 1. Three-dimensional model of lithium-ion battery

Simulation parameters	
Parameters [unit]	Value
Battery capacity (mAh)	364
Initial voltage (V)	4.25
Battery height (mm)	120
Battery width (mm)	90
Tab height (mm)	30
Tab width (mm)	10
Tab thickness (μm)	5
Nagetive thickness (μm)	60
Positive thickness (μm)	60
Separator thickness (μm)	30

Table 1. Basic parameters of the cell model

The correlation between the current density of lithium-ion batteries and the external magnetic field are elucidated in Fig. 2. The flow of current between components during discharge are depicted in Fig. 2 (a). The current inputs from the negative tab, traverses through the negative electrode, separator, and positive electrode from the negative collector, proceeds to the positive collector, and ultimately converges at the positive tab for output. The intensity of the current is indicated by the color of the arrows within the figure. Notably, the maximum current density is observed at the tabs.

The presence of current within the battery gives rise to a magnetic field in the space as depicted in Figure 2 (b), and the magnetic flux density is employed to characterize the distribution of the magnetic field. It is observed that the maximum magnetic flux density is at the tabs, with a simulated value of 600 nT. The flux density diminishes along the Z-axis away from the tabs, which corresponds to the distribution of the maximum current density. Consequently, the intrinsic correlation between the magnetic field and current density validates the accuracy of equation (3).

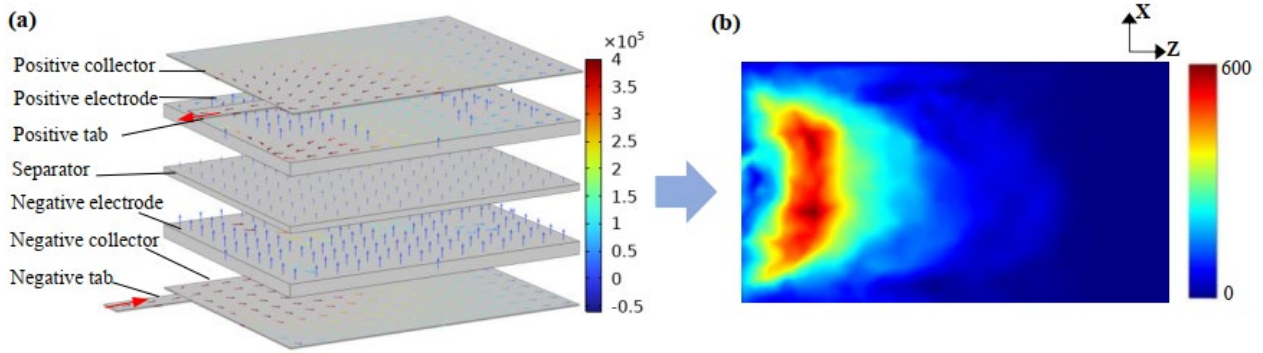

Fig. 2. The current density and magnetic field in lithium-ion battery during discharge (a) Electrode current density (b) Magnetic field in X-Y plane

3. Measurement using magnetic fluxgate sensor

3.1 The SOC and the magnetic field signal

The experimental subject is the lithium-ion pouch cell with capacity of 5600mAh. A fluxgate sensor depicted in Fig. 3(c) is employed to capture the spatial magnetic field of the battery during charge and discharge processes. The fluxgate sensor operates on the principle of detecting changes in magnetic reluctance induced by variations in the magnetic field, using an induction coil to sense these changes and thereby inferring the strength and direction of the magnetic field.

Fig. 3 illustrates the variation in magnetic flux density components Bx, By and Bz with changes in the SOC. The battery underwent a single cycle of operation under constant current-constant voltage charging and constant current discharging at a rate of 1C. Data from the initiation of charging (with separate data for constant current and constant voltage) and discharging were used as the initial values for differentiation, meaning that Fig. 3(a) describes the change in magnetic flux density during the battery cycling process. The constant current charging and constant voltage discharging are plot in first column, while constant current discharging is in second column. It can be observed that the battery reaches an upper voltage limit of 4.2V at an SOC of 85%. The trend of ΔBx, ΔBy and ΔBz is decreasing during charging, with varying degrees of change, and the magnetic field of z-axis sharp changes due to the stronger variation corresponding current. During constant voltage charging, the current depicted by the orange dashed line with sharp fluctuation influences the magnetic field, which follows the same trend. During the discharge phase, the magnetic flux density components ΔBy and ΔBz exhibit a general upward trend, whereas ΔBx manifests an initial increase followed by a subsequent decrease, correlating with the variations in the battery's internal conduction current. Consequently, it is inferred that a decline in the SOC is accompanied by the generation of a more intense magnetic field. Fig.3 (b) presents the measured and simulated magnetic flux densities as black and red solid lines, respectively. The simulation outcomes were derived from the model detailed in Section II, Part A. Given the experimental setup with a 5mm thickness, the lower current in this dimension resulted in a comparatively reduced Bx component. In the context of this specific battery, the By component is more substantial, whereas Bz exhibits a more pronounced variation particularly

during the discharge cycle. The simulated and measured data align in their general characteristics; however, discrepancies in the numerical values of magnetic flux density are observed, attributable to the single-layer model's limited capacity.

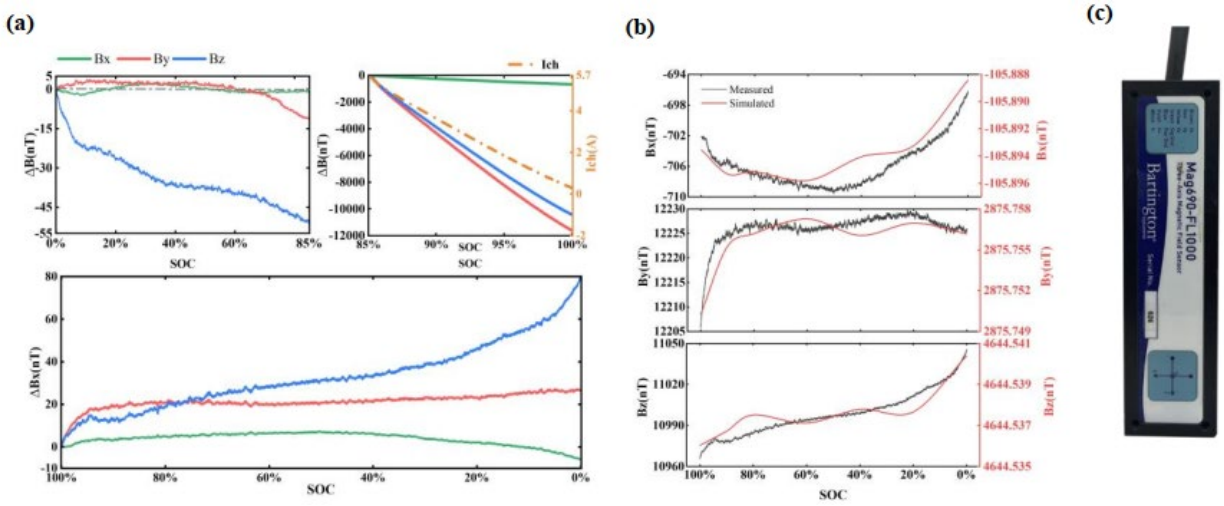

Fig. 3. The relationship between magnetic field and SOC (a) Changes in magnetic signal within one charge discharge cycle (b) Experimental and simulation results during discharge process (c) Magnetic fluxgate sensor

It has been observed that the magnetic field is inherently generated by electric current. In comparison to the magnetic field variations resulting from current fluctuations, those attributable to alterations in the SOC are exceedingly minor. Consequently, the magnetic field signals emitted by batteries operating at disparate C-rates are markedly different. Figure 4 elucidates the influence of various C-rates on the relationship between SOC and magnetic field intensity.

Fig.4 delineates the Bx, By, and Bz throughout the discharge cycle at 0.5C, 0.75C, 1C, 1.25C, and 1.5C rates. Analysis reveals a linear escalation of the magnetic field in conjunction with an increase in current. Notably, the gradient of By with respect to C-rate is substantially steeper than those of Bx and Bz, suggesting a more significant change in magnitude. Given the minimal variation in the magnetic field induced by varying SOC relative to that generated by fluctuating current, the magnetic flux densities at SOC intervals of 25%, ranging from 100% to 0%, The magnetic flux densities were plotted against Bx-SOC, By-SOC, and Bz-SOC for discharge conditions of 0.75C, 1C, and 1.25C. The relationship between magnetic flux density and SOC across different C-rates is consistent, with magnetic flux density intensifying as SOC diminishes. Although the distribution of magnetic flux density across various SOC levels is non-uniform, further research is required to explore these discrepancies. It is concluded that magnetic field detection technology is viable for SOC measurement under any C-rate condition, including state detection under complex operational scenarios.

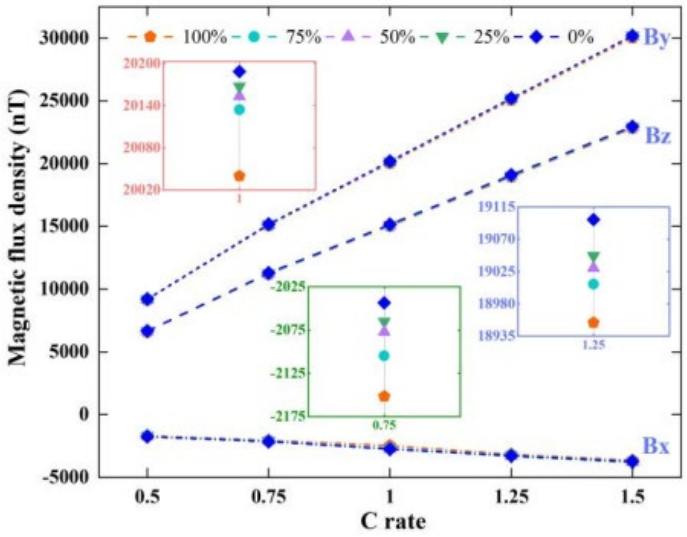

Fig. 4. The relationships of the charging current and the magnetic flux density

3.2 The magnetic field imaging corresponding the SOC

In the realm of battery diagnostics, visualization is essential for gaining insights into the in situ or operational status of a battery, including the uniformity of performance across various regions. Fluxgate sensors, capable of online data acquisition, facilitate real-time imaging, thereby enabling not only offline evaluations but also continuous online monitoring of the State of Charge (SOC) across the entire battery.

Fig.5 illustrates the variations in the magnetic field of entire-cell as it transitions from a fully charged to a depleted state under a constant current of 7A. The magnetic flux density and the corresponding variation are respectively depicted in Fig.5 (a) and (b), and the direction of the magnetic field component is consistent with Fig. 1. The extreme variability in magnetic flux density across the entire surface of the battery, as illustrated in Fig.5 (a), results in SOC imaging that is indistinguishable among different states. Therefore, the variation in magnetic flux density is analyzed as a characteristic parameter. The magnetic flux density alterations at 80% SOC, relative to the initial value at 100% SOC, are depicted in Fig.5 (b) and designated as I. Successive differential variations at SOC of 60%, 40%, 20%, and 0% are annotated as II, III, IV, and V, respectively. This analytical approach offers a detailed comprehension of the magnetic field of the battery in correlation with its SOC.

The variation in magnetic flux density with decreasing SOC is evident from the color intensity in Figure 5(b), where the transition from light to dark corresponds to an increase in density. The maximum variation in ΔBx is observed at the tabs in column V, which is consistent with the darkest regions in the Bx of Fig.5 (a). For ΔBy, the imaging in column I exhibits a complex-valued blue in the lower right corner, and this area expands and deepens in hue as the discharge, particularly in column V, suggesting inconsistent magnetic flux density trends across the battery's regions during discharge. The distribution of ΔBz mirrors that of Bz, with the imaging indicating peak values near the tabs and a gradual decrease along the z-axis.

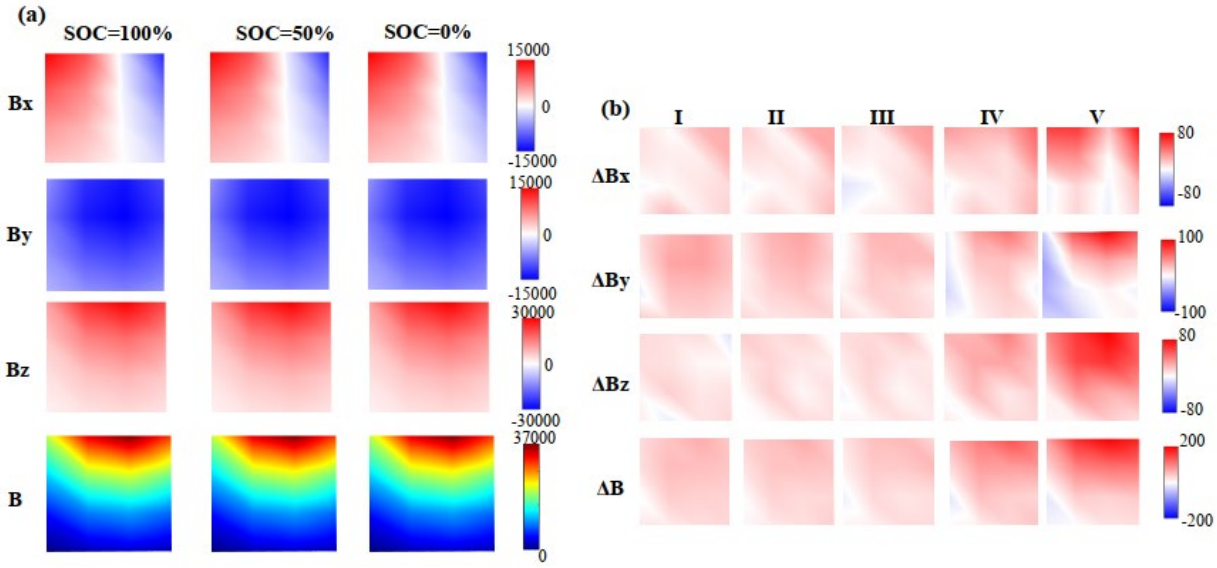

Fig. 5. Magnetic field corresponding the SOC during discharge (a) Magnetic field (b) The variation

4. Conclusion

The feasibility of monitoring and evaluating the SOC in lithium-ion batteries by magnetic field imaging technology is demonstrated in this research. A three-dimensional model for a single-layer cell is established, and the current distribution is obtained for the lithium-ion battery at specific SOC. The relationship between current density and external magnetic field is clarified. Then the variation trend of magnetic flux density during the complete cycle of charge and discharge is analyzed based on the data captured by magnetic fluxgate sensor, and it is good consistency with simulation results. Furthermore, the influence of different C rates on the magnetic field data during the discharge process was discussed. Magnetic fields imaging corresponding to various SOC during the charging phase have been acquired. Comparative analysis of the magnetic field fluctuations across different SOCs reveals discernible trends. It is observed that the magnetic field intensity escalates as the SOC diminishes, thereby validating the approach's feasibility in detecting SOC in the entire-cell. The outcomes of this study lay a substantial foundation for future enhancements in the assessment and prediction of lithium-ion batteries. Subsequent research will focus on developing a comprehensive database that maps the relationship between SOC and magnetic field data, and will incorporate a meta-learning model for training purposes. The implementation of these findings is anticipated to enhance the efficacy of battery management systems and overall battery performance, culminating in the development of more efficient and sustainable energy storage solutions.

5. Acknowledgements

This work was supported by National Key Research and Development Program of China (No. 2022YFC3005002), National Natural Science Foundation of China (No. 12072004), Beijing Municipal Education Commission and Beijing Natural Science Foundation(No.KZ202110005005).

6. References

[1] H. Popp, M. Koller, S. Keller, G. Glanz, R. Klambauer and A. Bergmann, “State estimation approach of lithium-ion batteries by simplified ultrasonic time-of-flight measurement,” IEEE Access, vol. 7, pp. 170992-171000, November 2019.

[2] A. Pfrang, A. Kersys, A. Kriston, D. U. Sauer, C. Rahe, S. Kabitz and E. Figgemeier, "Long-term cycling induced jelly roll deformation in commercial 18650 cells," J. Power Sources, vol. 392, pp. 168-175, July 2018.

[3] B. Michalak, H. Sommer, D. Mannes, A. Kaestner, T. Brezesinski and J. Janek, "Gas evolution in operating lithium-ion batteries studied in situ by neutron imaging," Sci. Rep. vol. 5, pp. 1-9, Octorber 2015.

[4] J. Gao, L. Zhang, Y. Lyu, F. Shi, B. Wu and C. He. "Ultrasonic guided wave measurement and modeling analysis of the state of charge for lithium-ion battery," J. Energy Storage, vol. 72, pp. 1-14, November 2023

[5] A. J. Ilott, M. Mohammadi, C. M. Schauerman, M. J. Ganter and A. Jerschow, "Rechargeable lithium-ion cell state of charge and defect detection by in-situ inside-out magnetic resonance imaging," Nat. Commun. vol. 9, pp. 1-7, May 2018.

[6] T. Bergholz, T. Nuñez, J. Wackerl, C. Korte, D. Stolten, "Magnetography: a novel characterization tool for Li-ion-batteries," Mater. Res. Soc. Symp. Proc. vol. 1544, pp. 1-7, December 2013.

[7] Y. A. Hu, G. Z. Iwata, M. Mohammad, E. V. Silletta, A. Wickenbrock, J. W. Blanchard, D. Budker, A. Jerschow, "Sensitive magnetometry reveals inhomogeneities in charge storage and weak transient internal currents in Li-ion cells," Proc. Natl. Acad. Sci. USA, vol. 117, pp. 1066710672, May 2020.

[8] R. Chen, J. Jiao, Z. Chen, Y. Wang, T. Deng, W. Di, et al. "Power batteries health monitoring: a magnetic imaging method based on magnetoelectric sensors". Materials, vol.15, pp. 1-11 , March 2022.

[9] F. Brauchle, F. Grimsmann, O. von Kessel and K. P. Birke, "Direct measurement of current distribution in lithium-ion cells by magnetic field imaging," J. Power Sources, vol. 507, pp. 1-11, September 2021.

[10] Mark G. Bason, Thomas Coussens, Matthew Withers, Christopher Abel, Gary Kendall, Peter Krüger, " Non-invasive current density imaging of lithium-ion batteries", J Power Sources, vol 533, pp. 1-5, June 2022.

[11] Javadipour M and Mehran K, "Analysis of current density in the electrode and electrolyte of lithium - ion cells for ageing estimation applications," IET Smart Grid, vol 2, pp. 176-189, June 2021.

[12] Hannan M A, Hoque M M, Mohamed A, et al. Review of energy storage systems for electric vehicle applications: Issues and challenges[J]. Renewable and Sustainable Energy Reviews, 2017, 69: 771-789.

STATE PARAMETER ESTIMATION OF LITHIUM-ION BATTERY BASED ON ULTRASONIC TRANSMISSION CHARACTERISTICS

Binpeng ZHANG[1], Yang ZHENG[1,*], Jie GAO[2], Yan LYU[2], Cunfu HE[2]
[1] Key Laboratory of Nondestructive Testing and Evaluation, State Administration for Market Regulation, China Special Equipment Inspection and Research Institute, Beijing, 100029, China
[2] Faculty of Information Technology, Beijing University of Technology, Beijing, 100124, China

1. Introduction

Lithium-ion battery has a complex electrochemical reaction in the cycle process, and it is a nonlinear system coupled with multiple physical fields such as electrochemical, mechanical and thermal[1,2]. Therefore, it is difficult to accurately estimate the state parameters. Traditional electrical methods have some estimation limitations, such as the difficulty in identifying the distributed inhomogeneity of the state parameters of battery, which makes it difficult to maintain the accuracy of measurement and estimation[3,4]. In order to overcome the above drawbacks, machine learning algorithms such as support vector machines(SVM)[5], Kalman filters(KF)[6] and neural networks(NN)[7] have been introduced into the estimation of state parameters, and have achieved good estimation results. However, these intelligent estimation algorithms still have some weakness[8,9], such as the kernel function of SVM must meet the Mercer condition, and it is difficult to select regularization parameters and kernel functions. The KF is limited in the application of nonlinear system, and the algorithm requires high accuracy of the initial state estimation. And the network structure parameters of the NN algorithm are difficult to determine, and the parameters need to be adjusted and selected by empirical and experimental methods.

As an improved support vector machine method, Relevance Vector Machine (RVM) is based on Bayesian framework for model training, and the active correlation decision theory based on prior parameter structure is used to eliminate sample data that is not related to the estimation target to achieve model sparsity[10]. Compared with the KF algorithm, SVM and NN algorithm, RVM can effectively overcome the weakness of difficult selection of regularized parameters and the limitation of kernel functions by Mercer conditions. In addition, RVM has significant advantages in solving high-dimensional and nonlinear classification problems[11]. Thus, it becomes one of the popular algorithms in machine learning research.

In this research, RVM is employed for the estimation of state parameters of Lithium-ion battery. Firstly, the ultrasonic transmission nondestructive testing platform was used to perform multi-cycle cycles on the lithium-ion battery, and the acoustic characteristic parameter in the cycling process was extracted in real time, so as to explore the feasibility of the RVM in SOC estimation. Subsequently, the acoustic characteristic parameter training dataset for SOH was extracted under the condition of high discharge rate cycling, and the applicability of RVM in SOH estimation was studied.

2. RVM model

In a RVM model, for a given sample training dataset $D=\{x_i,t_i\}_{i=1}^{N}$, where x_i is defined as the input vector on the R^N, t_i is the corresponding scalar output, and N is the number of training samples. The output of the RVM can be expressed as[12]:

$$y(x_i,\omega_i)=\sum_{i=1}^{N}\omega_i K(x,x_i)+\omega_0 \tag{1}$$

where $\omega=[\omega_0, \omega_1, \omega_2, \dots, \omega_N]$ is weight vector, ω_0 is bias and $K(x, x_i)$ is a kernel function.

According to Bayesian theory, if the training data $P(t|x)$ obeys the Gaussian distribution, and the mean is 0 and the variance is σ^2. Then, the probability of likelihood estimation of the training sample can be expressed as:

$$P\left(t|\omega,\sigma^2\right)=\left(2\pi\sigma^2\right)^{-\frac{N}{2}}e^{-\left(-\frac{1}{2\sigma^2}\|t-\varphi(x)\omega\|^2\right)} \tag{2}$$

where $\varphi(x)$ is a N+1-dimensional nonlinear basis function, can be express as $\varphi(x_i)=[1, K(x_i, x_1), K(x_i, x_2), K(x_i, x_3),\dots, K(x_i, x_N)]$.

At the same time, in order to reduce the complexity of the model and avoid the phenomenon of over-learning, under the framework of Bayes theory, hyperparameter α is introduced to make the weight coefficient ω_i obey the Gaussian distribution with the mean of 0. Based on this, the likelihood estimation of the weight vector ω can be expressed as:

$$P\left(\omega|\alpha\right)=\prod_{i=0}^{N}\sqrt{\frac{\alpha_i}{2\pi}}^{-\frac{\alpha_i}{2}\omega_i^2} \tag{3}$$

where $\alpha=[\alpha_0, \alpha_1, \alpha_2, ..., \alpha_N]^T$ represents the N+1-dimensional hyperparameter vector, and α_i corresponds to ω_i one by one.

Since the likelihood probabilities of both the training sample and the weight vector obey the Gaussian distribution, the posterior probability of the weight vector also obeys the Gaussian distribution. Based on this, the covariance cov and mean μ of the posterior probability of the weight vector can be expressed as:

$$\begin{aligned}\mathrm{cov}&=\frac{1}{\sigma^{-2}\Phi^T\Phi+\Lambda}\\ \mu&=\sigma^{-2}\,\mathrm{cov}\,\Phi^T t\end{aligned} \tag{4}$$

where $\Lambda=diag(\alpha_0,\alpha_1,\alpha_2,\cdots,\alpha_N)$,

$\Phi=\left[\varphi(x_1),\varphi(x_2),\cdots,\varphi(x_N)\right]^T$.

The above formula is iterated repeatedly until the obtained parameters α and σ^2 meet the convergence conditions. In the process of optimization, it is found that most of the hyperparameter α tends to infinity, the corresponding weight coefficient ω_i tends to 0, so that the kernel function and training samples are reduced. Meanwhile, the remaining training samples corresponding to the non-zero weight coefficient ω_i are retained which is called the related vector.

Furthermore, according to the optimal parameters α_{op} and σ^2_{op} obtained by iterative optimization, and combined with the posterior distribution of the weight vector, the estimated value and estimated variance after iterative learning can be obtained:

$$\begin{aligned}y_*&=\mu_*=\mu^T\varphi(x_*)\\ \sigma_*^2&=\sigma_{op}^2+\varphi(x_*)^T\,\mathrm{cov}\,\varphi(x_*)\end{aligned} \tag{5}$$

where y_* represents the average value of the weight coefficient and can be used as an estimate of t_*.

3. Dataset acquisition

In this section, the ultrasonic non-destructive testing platform (in our previous research, and shown in Ref.13) was used to perform multi-cycle continuous cycles of lithium-ion battery. By

extracting ultrasonic transmission characteristics in real time, the relationship between acoustic characteristics and battery state parameters was explored. During the experiment, a thickness-oriented piezoelectric transducer was used to excite and receive ultrasonic signals, with a center frequency of 200kHz, a diameter of 8mm, and a thickness of 4.5mm. In addition, it should be noted that during the acquisition of the parameter set used for SOC estimation, the Lithium-ion battery cycled for 30 cycles with a constant-current constant-voltage charging protocol of 1C and a constant current discharge protocol of 1C. During the acquisition of the SOH estimation dataset, the Lithium-ion battery was cycled in a 1C constant-current, constant-voltage charging protocol and a 1.5C constant-current discharging protocol until the SOH of the battery decayed to approximately 80%. In addition, a 5 minute rest is set after each complete cycle to eliminate polarization during the lithium-ion battery cycle.

3.1 SOC estimation parameter set

Fig.1 shows the capacity change curve of the Lithium-ion battery over 30 cycles. It can be seen that the capacity of the battery hardly changes during the whole cycle, that is, the SOH of the Lithium-ion battery remains unchanged during the acquisition of the SOC estimation parameter set.

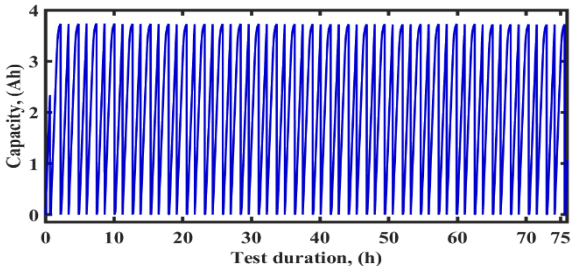

Figure 1. The capacity characteristic of the battery during 30cycles

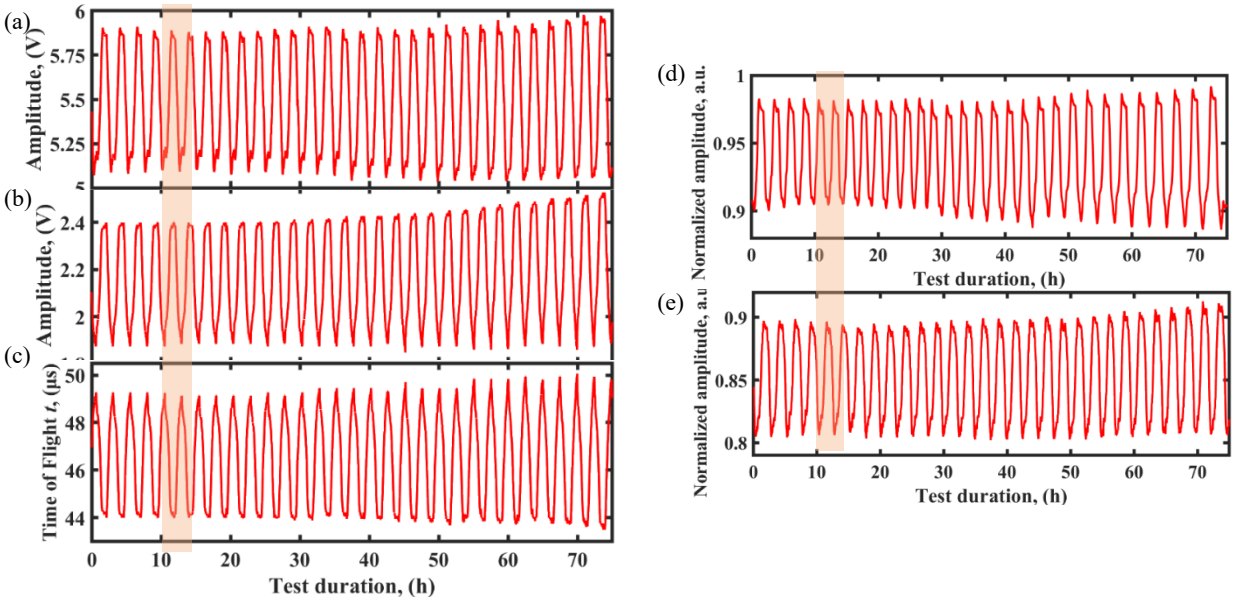

Figure 2. The curve of the acoustic parameters for battery during 30 cycles.
(a) Fast P-wave amplitude (TAF) curve, (b) Slow P-wave amplitude (TAS) curve, (c) Slow P-wave TOF curve, (d) Normalized frequency-domain fast P-wave amplitude (FAF) curve, (e) Normalized frequency-domain slow P-wave amplitude (FAS) curve.

The time-domain amplitude of the fast P-wave (TAF), the time-domain amplitude (TAS) and ToF of the slow P-wave, and the frequency-domain amplitude of the fast (FAF) and slow (FAS) P-waves of the transmitted signal during 30 cycles were extracted (the time-domain signal processing method

and the means of frequency-domain information extraction are the same as those in the previous study, which can be referenced in Ref.13), and the curve of acoustic characteristic parameters changing with the cycle time was drawn, as shown in Fig.2.

According to Fig.2, it can be found that during the charging and discharging process of the battery, acoustic characteristic parameters show regular oscillation behavior, that is, during the charging process (the shaded part in Fig.2), TAF, FAF and TAS show an increasing trend, ToF shows a decreasing trend, and vice versa during the discharge process.

3.2 SOH estimation parameter set

Under the cycle of 1C constant-current and constant-voltage charging protocol and 1.5C constant-current discharge protocol, the capacity curve of Lithium-ion battery is shown in Fig.3. It can be seen that with the increase of cycle times, the capacity of the battery shows a decreasing trend, and the SOH of the battery gradually becomes smaller. Moreover, after 180 cycles, the capacity of the battery is attenuated from the initial 3.645Ah to 2.767Ah, and the SOH of the battery decreases to 75.91%, that is, the health state of the battery has been significantly attenuated.

In order to explore the relationship between acoustic characteristic parameters and the SOH of the battery, the average value of acoustic characteristic parameters in each complete cycle during 180 cycles was extracted as the characteristic parameters used for SOH estimation under the cycle, and the change curve of acoustic characteristic parameters during 180 complete experiment cycles was drawn, as shown in Fig.4. Observing Fig.4(a), it can be found that with the SOH decreases, TAF and TAS show a decreasing trend, and ToF shows an increasing trend. Observing Fig.4(b), it can be found that FAF and FAS also show a decreasing trend as the SOH decreases.

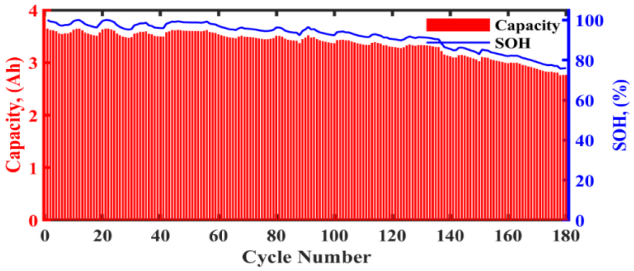

Figure 3. The capacity attenuation characteristic and health state change curve of the customized battery during cycling

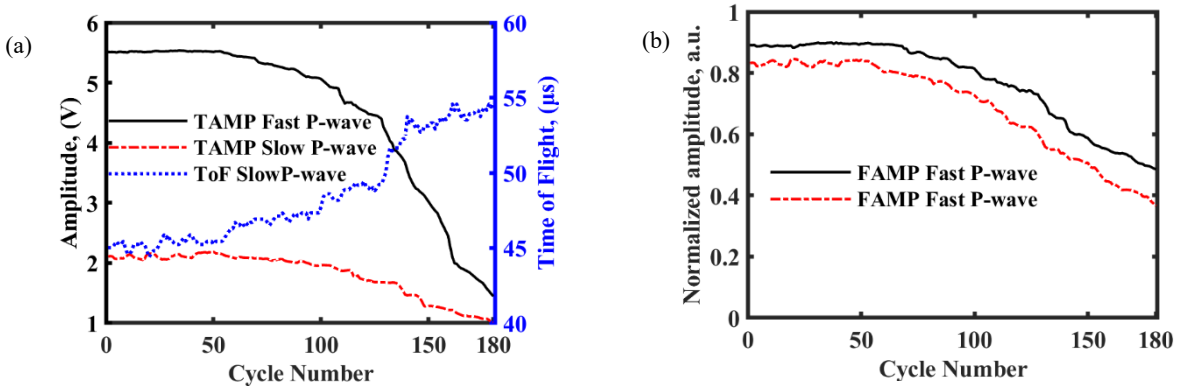

Figure 4.The curve of acoustic characteristic parameters in the charging and discharging cycle of lithium-ion battery.
(a) Time domain characteristic parameters, (b) Frequency domain characteristic parameters

4. Result and discussion

Based on RVM model and the above acoustic characteristic parameters, the SOC of Lithium-ion battery is estimated. It should be pointed out that a total of N=2225 sets of data were collected in 30 cycles of lithium-ion batteries, and each set of data contained complete acoustic characteristic parameters, that is, the sample set D={TAF$_i$, TAS$_i$, TOF$_i$, FAF$_i$, FAS$_i$}, i=1, 2, ..., N. Moreover, the capacity parameters collected by the charge and discharge equipment are used as output items, that is, the output item y_* is the SOC of the lithium-ion battery at different times.

In order to verify the generalization ability and accuracy of RVM model in SOC estimation, the data set was divided into a training group with 1784 sets of data from the first 24 cycles and a test group with 441 sets of data from the last 6 cycles. In addition, in the kernel selection of RVM model, Gaussian radial basis function is used as the training kernel function. In the key parameter setting of the model, the kernel width coefficient κ is set to 3, the initial hyperparameter α is set to 0.2, the initial variance σ^2 is set to 0.9, and the number of iterations is 200. The estimated results are shown in Fig.5. The red solid line indicates the SOC of the lithium-ion battery collected by the charge and discharge device at different times, the blue solid point indicates the estimated result of RVM model, and the red solid point indicates the relative error of the estimated result of RVM model. It can be seen that on the basis of the established estimate parameter set, the relative error of the estimated results of the SOC obtained by using RVM model is within about 4%, and the estimation results are in good agreement with the overall trend of the experimental results.

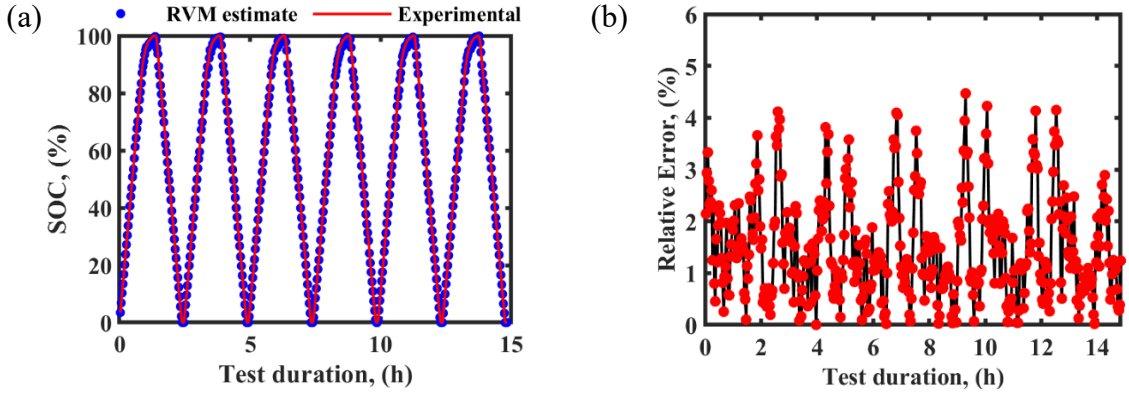

Figure 5. Estimation results of the SOC of lithium-ion batteries based on RVM model. (a) Estimation results, (b) Relative error

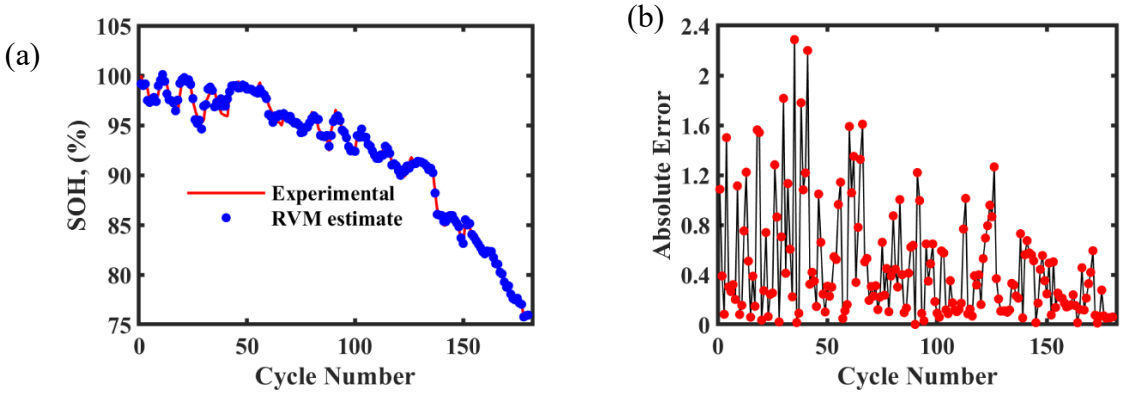

Figure 6. Estimation results of the SOH of lithium-ion batteries based on RVM model. (a) Estimation results, (b) Absolute error

5. Conclusion

In this research, based on the acoustic characteristic parameters extracted from the lithium-ion battery in multiple cycles, the state parameters of the lithium-ion battery were estimated by establishing a sample training database and employing a Relevance Vector Machine model. The experimental results show that the acoustic characteristic parameters of Lithium-ion battery show a regular increasing or decreasing trend with the change of state parameters. The estimation results show that the Relevance Vector Machine model can realize the accurate prediction of the state parameters of Lithium-ion batteries, in which the relative error of the SOC estimation results is within 4% and the absolute error of the SOH estimation results is within 2%.

Although the above results show that the Relevance Vector Machine model has a certain accuracy in estimating state parameters, its estimation accuracy still needs to be improved. In the future work, we will consider introducing a group search algorithm (such as Sparrow Search Algorithm, SSA) to iteratively optimize the key parameters (such as kernel function width, etc.) of the Relevance Vector Machine model, so as to further improve the accuracy in the state parameter estimation of lithium-ion batteries.

6. Acknowledgements

This work is financially supported by Science Youth Foundation of CSEI (Grant No. 2024nei01, 2021Qingnian14).

5. References

[1] Chiasson J., Vairamohan B.. Estimating the state of charge of a battery[J]. *IEEE Transactions on Control Systems Technology*, 13(3):465-470, 2005.

[2] Bach T. C., Schuster S. F., Fleder E., et al. Nonlinear aging of cylindrical lithium-ion cells linked to heterogeneous compression[J]. *The Journal of Energy Storage*, 5:212-223, 2016.

[3] Piller S., Perrin M., Jossen A.. Methods for state-of-charge determination and their applications[J]. *Journal of Power Sources*, 96(1):113-120, 2001.

[4] Zou Y., Hu X., Ma H., Ebenli S.. Combined State of Charge and State of Health estimation over lithium-ion battery cell cycle lifespan for electric vehicles[J]. *Journal of Power Sources*, 273: 793-803, 2015.

[5] Alvarez Anton J. C., Garcia Nieto P. J., Blanco Viejo C., et al. Support Vector Machines Used to Estimate the Battery State of Charge[J]. *IEEE Transactions on Power Electronics*, 28(12):5919-592, 2013.

[6] R. Xiong, H. He, F. Sun, et a1. Evaluation on State of Charge estimation of batteries with adaptive extended kalman filter by experiment approach[J]. *IEEE Transactions on Vehicular Technology*, 62: 108-117, 2013.

[7] Zhang S., Zhai B., Guo X., et al. Synchronous estimation of state of health and remaining useful lifetime for lithium-ion battery using the incremental capacity and artificial neural networks[J].*Journal of Energy Storage*, 26: 100951, 2019.

[8] Zhang W., Li X., Li X.. Deep learning-based prognostic approach for lithium-ion batteries with adaptive time-series prediction and on-line validation[J]. *Measurement*, 164: 108052, 2020.

[9] Yang D., Wang Y., Pan R., et al. State-of-health estimation for the lithium-ion battery based on support vector regression[J]. *Applied Energy*, 227: 273-283, 2018.

[10] Tipping M. E.. Sparse Bayesian learning and the relevance vector machine[J]. *Machine Learning Research*, 1(3):211-244, 2001.

[11] Gholami B., Haddad W. M., Tannenbaum A. R.. Relevance Vector Machine Learning for Neonate Pain Intensity Assessment Using Digital Imaging[J].*IEEE transactions on biomedical engineering*, 57(6):1457, 2010.

[12] Kong W., Li H., Huang X., et al. Gas evolution behaviors for several cathode materials in lithium-ion batteries[J].*Journal of Power Sources*, 142(1–2):285-291, 2005.

[13] Zhang BP, Lyu Y, Gao J, et al. Ultrasonic characterization of multi-layered porous lithium-ion battery structure for state of charge[J]. *Ultrasonics*, 134: 107060, 2023.

Experimental techniques and monitoring systems for major structures

A NOVEL STRUCTURE HEALTH MONITORING METHOD FOR MESH REFLECTORS BASED ON THE RESNET NETWORK

Siming Liu[1], Guowang Luo[1], Shilin Xie[1(*)]
[1] State Key Laboratory for Strength and Vibration of Mechanical Structures, Xi'an Jiaotong University, Xi'an 710049, China
[(*)]Email: slxie@mail.xjtu.edu.cn

1. Introduction

Mesh reflectors, known for their large aperture, light weight, and high stowage efficiency, have garnered significant attention from researchers worldwide. However, during extended on-orbit operations, the mesh reflectors are subjected to complex loads, including high-low temperature cycles, space debris impacts, and radiation, leading to serious structural damages such as truss damages and cable stiffness degradations. Such damages can severely deteriorate the mesh reflector accuracy, thereby affecting the antenna's electrical performance. Therefore, structural health monitoring of mesh reflectors is crucial.

Previous researches have primarily focused on detecting truss damages by applying excitations and measuring responses with accelerometers [1]. However, in the low-damping space environment, it is challenging for mesh reflectors to dissipate the vibrational energy generated by these excitations. In addition, beyond truss damages, cable damages are another critical concern that directly compromises the mesh reflector accuracy. Consequently, there is a need for a comprehensive structural health monitoring method that can simultaneously detect damages in both cables and truss without interrupting the normal service of the mesh reflectors.

Mesh reflectors are composed of pre-tensioned cable nets and surrounding truss structures. When structural damages occur, the force equilibrium within these components is disrupted and redistributed. Monitoring the force changes before and after damages can thus reveal information about structural integrity. Inspired by this concept, a novel structural health monitoring approach for mesh reflectors based on the ResNet network was proposed. Due to the difficulty of traditional inversion methods in distinguishing whether force changes are caused by cable damages or truss damages, the ResNet neural network is introduced to conduct an in-depth analysis of the force data. By embedding force sensors into the cables and truss, changes in internal forces can be monitored. These changes are then input into the ResNet network to identify damage locations and degrees. Additionally, transfer learning is incorporated to enhance the generalization capability of the ResNet network. The effectiveness of the method is validated through simulations and experiments.

2. Methods

The structural health monitoring approach for mesh reflectors based on the ResNet network is presented in Fig. 1.

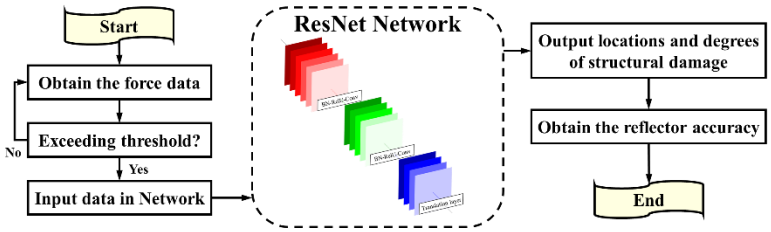

Fig. 1. The structural health monitoring approach

3. Results and conclusions

The results are presented in Fig. 2. In Fig. 2(a), the red lines represent the failure structure, while the yellow ones represent the degraded structure. In Fig. 2(c) and (d), the displacement deviation between actual nodes and ideal nodes in reflector are presented in the cloud charts. The structural health monitoring approach for mesh reflectors based on the ResNet network could accurately predict the locations and degrees of damages in mesh reflector structure.

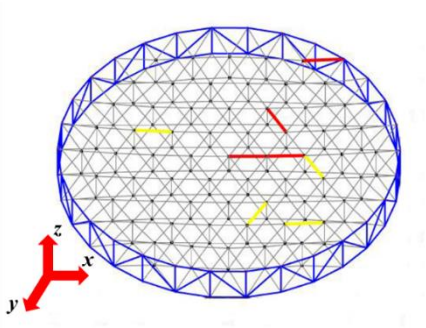

(a) Structual damages in mesh reflector.

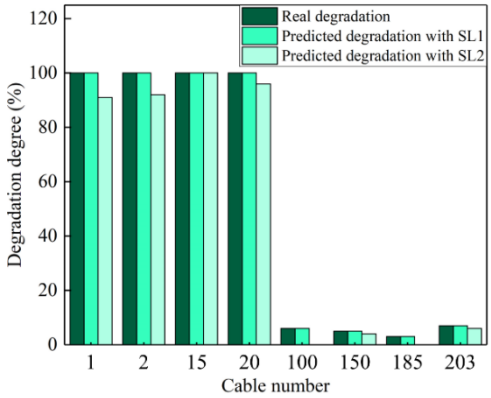

(b) Comparison of actual damage degrees and prediction ones.

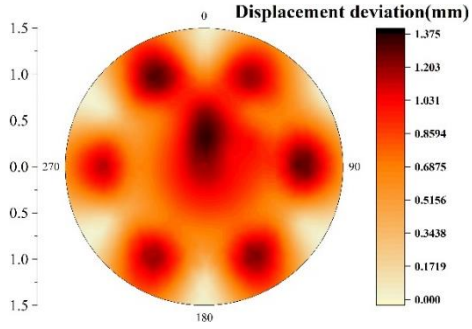

(c) The displacement deviation cloud chart of FEM.

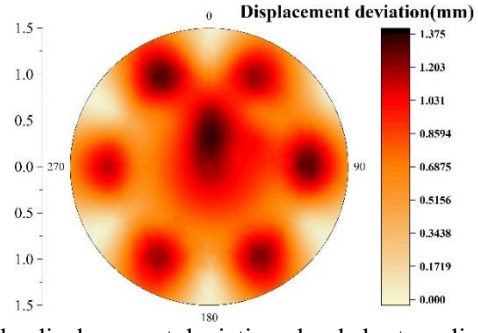

(d) The displacement deviation cloud chart predicted by the ResNet method with SL1.

Fig. 2. Fatigue curves in the finite life domain for the three sample sets

4. Acknowledgements

The financial supports from the National Natural Science Foundation of China (Grant No. 11872290) and National Natural Science Foundation of China (Grant No. 12072247) for this study are gratefully acknowledged.

5. References

[1] Angeletti, F., et al., A Study on Structural Health Monitoring of a Large Space Antenna via Distributed Sensors and Deep Learning. Sensors, 2023. **23**(1): 368.

DATA-DRIVEN SIMPLIFIED PREDICTION OF VIBRATION INDUCED BY OPERATING METRO TRAINS

Bhattacharjee. N [1], ***Sur. A*** [2], ***Manna. B*** [1], ***Banerjee. A*** [1], ***and Shahu. J T*** [1]
[1] *Department of Civil Engineering, Indian Institute of Technology Delhi, New Delhi, India*
[2] *Ayesa, Noida, India*

1. Introduction

The accelerated urbanization and industrialization of modern cities have heightened dependence on mass transit railway systems, leading to environmental concerns such as ground-borne vibrations from train movements. These vibrations affect nearby structures and residents, driving extensive research into their prediction and mitigation. While [1] highlights the environmental impact, [2] developed models addressing vehicle-track-soil interaction. Experimental studies reinforce the need for effective yet tedious solutions. Thereby, Artificial Neural Network (ANN) models have emerged as reliable tools for accurately predicting ground vibrations, which are crucial for safeguarding structures and enhancing resident comfort. This study develops a simplified ANN model to predict ground vibration velocity induced by metro trains in underground urban tunnels. Using numerically simulated data validated with field measurements, the model offers an accurate and efficient method for analyzing vibration transmission in train-track tunnel-soil systems.

2. Methodology

A numerical model of a double tunnel-soil system has been developed to simulate train-induced ground vibrations under two scenarios: (a) a train running on a single track and (b) trains running simultaneously on both tracks. The model calculates vertical vibration velocity at the ground surface above the tunnel crown using a two-step coupled theoretical approach. Validated with field measurements from the northern region of India, the model is simplified for adaptability by assuming a single soil layer with averaged properties. Using MATLAB's Neural Net Fitting Toolbox, a database is then generated by varying shear wave velocity, train speed, and tunnel depth to train an artificial neural network (ANN). The ANN architecture is effectively trained and validated to predict vibration velocities from metro train movement accurately.

3. Results and conclusions

The numerical simulation, validated against field study results, demonstrated a strong agreement across the frequency spectrum, as shown in Fig. 1(a). Fig. 1(b) presents the vibration signal's Continuous Wavelet Transform (CWT), illustrating its multiscale decomposition into the time-frequency domain. The analysis reveals that the dominant frequencies are below 10 Hz, corresponding to the train's characteristic frequency determined by its speed. Fig. 2(a) illustrates the ANN architecture used to train the data derived from the numerical results, while Fig. 2(b) demonstrates the model's efficacy with an R-value exceeding 0.99, confirming its high accuracy and reliability.

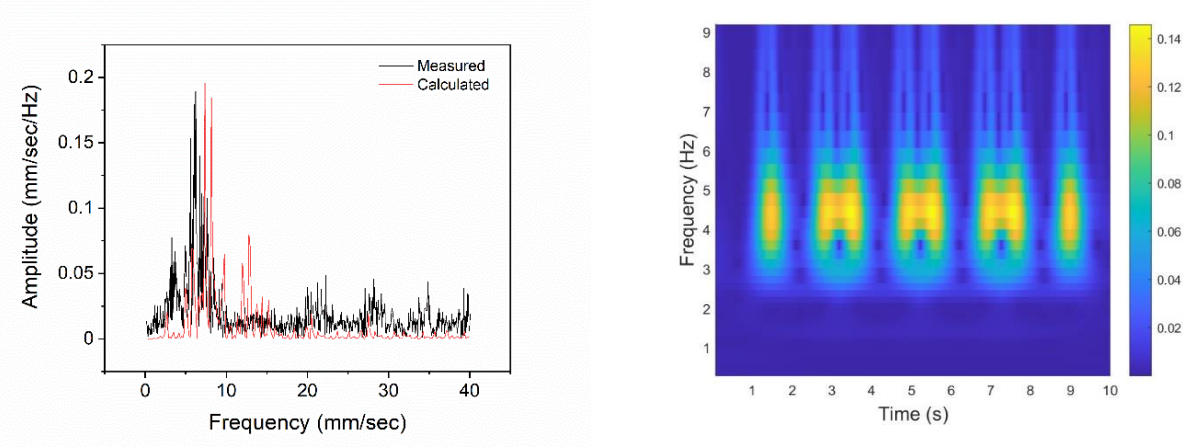

(a) (b)

Fig. 1 a) Verification of the Numerical results with the experimental case study; b) CWT representation of the signal;

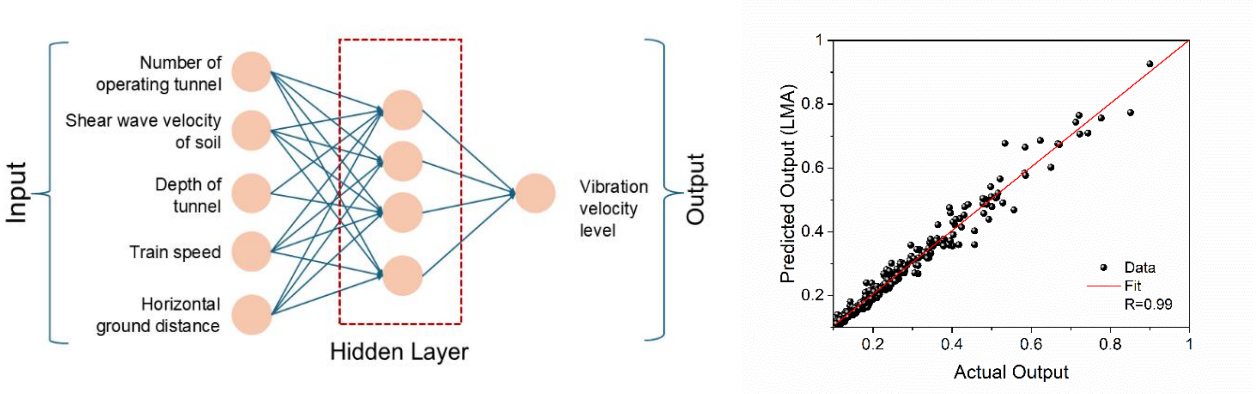

(a) (b)

Fig. 2 a) ANN architecture; b) *R*-value of ANN architecture

4. Acknowledgements

The authors acknowledge the Core Research Grant (Grant No. CRG/2020/003893) and the Department of Science and Technology, Ministry of Science and Technology, India, for their valuable financial support of this research.

5. References

[1] Faizan, A. A., Kırtel, O., Çelebi, E., Zülfikar, A. C., & Göktepe, F. (2022). Experimental validation of a simplified numerical model to predict train-induced ground vibrations. Computers and Geotechnics, 141, 104547.

[2] Auersch, L. (2020). Simple and fast prediction of train-induced track forces, ground and building vibrations. Railway Engineering Science, 28(3), 232-250.

A Study on Seismic Resistance Analysis of A-Type Marble Storage Racks in Eastern Taiwan

J. T. Liu[1], H. W. Mo[1], C. S. Lin[1]* and C. F. Chen[2]
[1] Department of Mechanical Engineering, National Kaohsiung University of Science and Technology, Kaohsiung, Taiwan
[2] Stone & Resource Industry R&D Center, Hualien, Taiwan

1. Introduction

Taiwan is located in the Pacific Ring of Fire and suffers from frequent seismic activity, so earthquake engineering and disaster prevention are crucial. Hualien, located in eastern Taiwan, is rich in marble resources. Since the 1950s, the stone industry has been developed and has become a key industry in the region. The earthquake on April 3, 2024 (hereinafter referred to as 0403 Hualien earthquake) caused stone products in Hualien to collapse, damaged storage racks, crushing equipment, and halted production. The factory now faces the urgent task of cleaning up a large amount of damaged stone and finding ways to safely and properly store the marble in the future. Frequent and strong earthquakes in Taiwan pose a major challenge to the seismic resistance of marble storage racks.

This study uses computer-aided engineering analysis (CAE) and finite element method (FEM) to simulate typical seismic conditions to evaluate the structural performance and seismic resistance of stone storage racks. We only use the modal parameters obtained from the response data through experimental modal analysis (EMA) to verify the reliability of the FEM of the stone slab A-type storage rack, and then the corresponding strength analysis can be implemented.

2. Materials and methods

The aim of this study is to introduce modal testing techniques for the validation of the FEM of stone storage racks, in order to verify the results of finite element analysis (FEA) and further enhance the seismic performance of the racks during earthquakes. The reliability of the FEM will be validated using the modal parameters obtained from EMA, as well as harmonic analysis and modal analysis in ANSYS. Field measurements, combined with the results of EMA, will be used to appropriately adjust the geometry and contact conditions, enhancing the reliability of the FEM and the analysis results. By analyzing the structural strength of the storage rack, the consistency of failure locations will be examined, providing a reference for structural adjustments. In addition, we have also proposed improvements to original storage racks to significantly modify the seismic resistance of the stone storage racks.

3. Results and conclusions

A structural seismic strength analysis has been conducted using the 0403 Hualien earthquake signal as excitation, simulating the stress and deformation of the rack during an earthquake. The results of FEA show that the maximum stress of traditional A-type storage racks when stimulated by actual earthquake signals far exceeds the yield stress of the material, and the location of its occurrence is also consistent with the location of actual damage to the disaster-damaged storage rack. Finally, some proposed improvements to original storage racks effectively reducing the maximum stress of the stone storage rack to below the yield and tensile strength of the structural material.

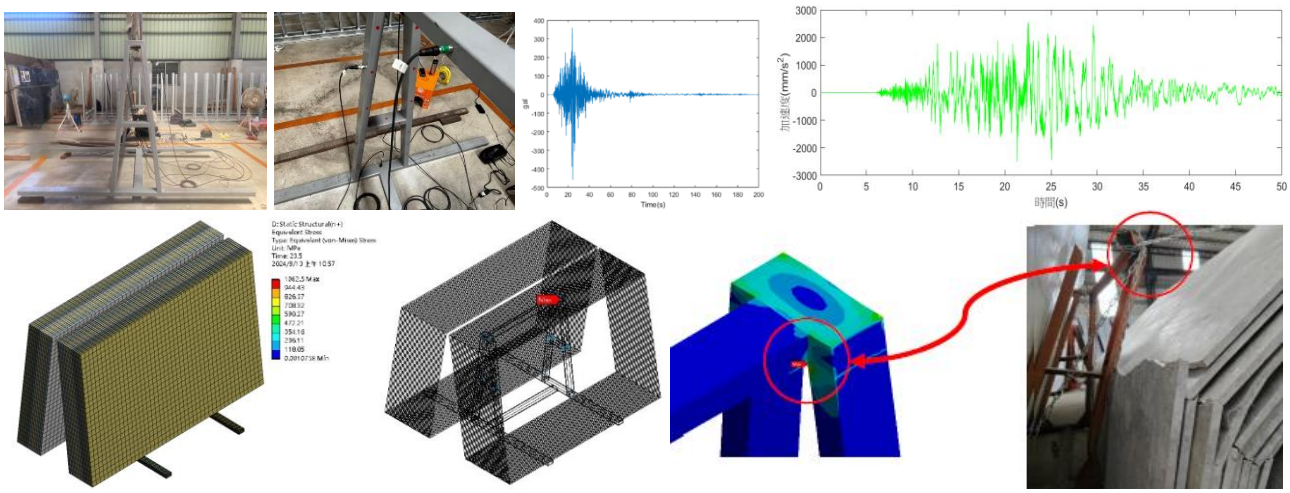

Fig. 1. EMA site, 0403 Hualien earthquake north-south signal and the location of its occurrence is consistent with the location of actual damage to the disaster-damaged A-type storage rack

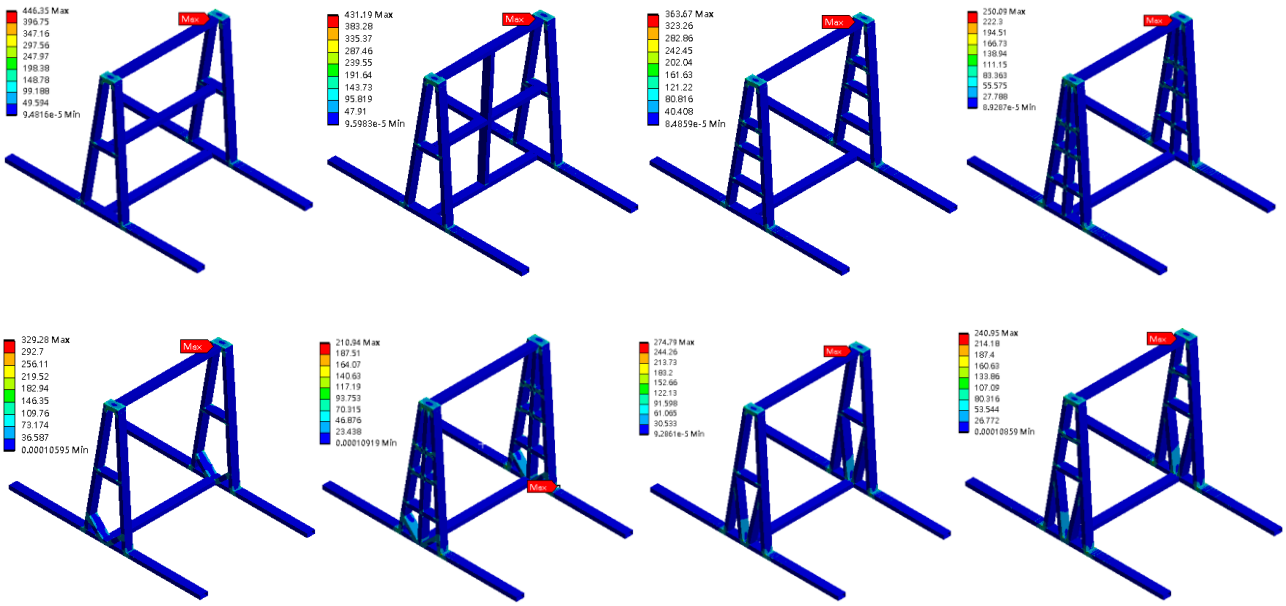

Fig. 2. A-type stone storage rack structure improvement and stress analysis

4. Acknowledgements

This research was supported in part by Stone & Resource Industry R&D Center of Taiwan under grant 113-B002-322A6-146 and 113-B002-322A6-205. The authors also wish to thank Sun Stone Company Ltd for providing the stone exhibition site in Kaohsiung and assistance to conduct the verification of the stone storage rack model in this study.

5. References

[1] Huang, T.-Y., "Updating Finite Element Model by Experimental Modal Data-The Technique and Application," Journal of Technology, Vol. **16**, No. 2. Pp. 335-344, 2001.

[2] Allemang, R. J., "The modal assurance criterion – twenty years of use and abuse," Sound and vibration, Vol. **37**, Iss. 8, pp. 14-23, 2003.

DETERMINING AND MONITORING THE FORCES IN THE CABLES OF A SUSPENSION BRIDGE

V. Chmelko[1], T Koščo[1], M.Garan[1], M.Šulko[1]

[1] Slovak University of Technology, Faculty of Mechanical Engineering, Namestie Slobody 17, 812 31 Bratislava, Slovakia

1. Introduction

Important structures such as bridges, transport structures, pressure equipment in the power industry, energy structures, ... require continuous monitoring of their health and integrity due to their cost and importance in the infrastructures of countries..

Diagnosis of the condition and serviceability of the bridge after several years of operation was a challenge implemented on the SNP Bridge in Bratislava. The diagnostics focused on the identification of the chemical composition of the rope material and its metallographic analysis directly during the operation on the bridge. The procedure and results will be presented in the paper.

Fig. 1. Bridge SNP in Bratislava and exciting of cables during operation.

2. Results and conclusions

The design forces in the ropes are known, their actual values at present have been determined by a specific procedure using the modal properties of the rope bundles as well as the individual ropes. The differences in the prestresses of the individual ropes are significant and will be presented (Fig. 2).

A major challenge was to determine the evolution of the forces in the cables over an extended period of operation in which temperature and weather conditions would be documented. A system for long-term monitoring of the evolution of forces in the ropes will be presented. The analysis of the results allows to determine the influence of weather and operational factors on the evolution of the forces in the cables, which are a key element of the bridge structure as it has no pillar in the river.

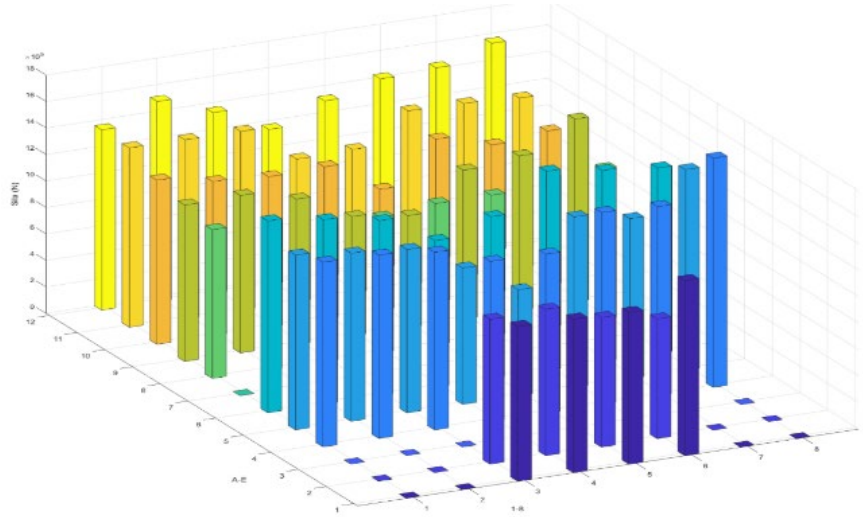

Fig.2 Forces in the ropes in the anchor chamber

3. References

[1] Fang Z, Wang JQ. Practical formula for cable tension estimation by vibrationmethod. J Bridge Eng 2012. https://doi.org/10.1061/(ASCE)BE.1943- 5592.0000200.

[2] Zui H, Shinke T, Namita Y. Practical formulas for estimation of cable tension by vibration method. J Struct Eng 1996;122(6):651–6.

[3] Koščo, T., Margetin, M., Šulko, M., Chmelko, V. (2024) Bridge cable tension estimation using the vibration method. Structures 63, 106332; https://doi.org/10.1016/j.istruc.2024.106332

[4] Koščo, T., Margetin, M., Chmelko, V. (2024) Diagnostics of prestressed ropes after multiannual operation – Bridge SNP Bratislava. ce/papers 7 (2024), No. 3-4; https://doi.org/10.1002/cepa.3081

6-11 July 2025 ICEM21 Bologna
21st International Conference on EXPERIMENTAL MECHANICS

Performance of Radial Fins in Enhancing the Stability of Offshore Pipelines under Vertical Penetration

Debtanu Seth [1]***, Bappaditya Manna***[1]***, and J.T Shahu***[1]
[1] *Department of Civil Engineering, Indian Institute of Technology, New Delhi, India*

1. Introduction

This study examined the on-bottom stability of surface-laid submarine pipelines during vertical penetration, focusing on thermal-induced buckling. Laboratory model tests were performed using a scaled-down pipe section on a uniform Kaolin clay bed, under 2D plane strain conditions within a specialized tank with observation windows. The research revealed a significant improvement in penetration resistance and stability along with an expansion in the failure mechanism below the pipe section after incorporating fins into the pipe design. These radial fins also altered the earth pressure distribution beneath the vertically loaded pipe. Thus, the enhancement of submarine pipeline stability and resistance to vertical penetration was conclusively demonstrated through strategically placed radial fins, with valuable insights being provided for future pipeline design and deployment strategies.

2. Methodology and Problem Statement

The vertical penetration resistance of a surface-laid pipe-section was investigated through multiple small-scaled model tests, with different fin configurations being examined across two soil types. A pipe-section was positioned on top of a soft soil bed and vertically loaded by an actuator via a tie rod. Four fin configurations were tested, with load-displacement behavior and pressure variations being monitored by transducers. Gradual soil flow and deformation patterns around the pipeline were captured by an advanced camera and light system. Load-displacement behaviors across soil types were compared to propose an optimized fin configuration. Pressure distribution around the pipe circumference was visualized through two-dimensional plots. Pipe-soil interactions were further elucidated using displacement contours derived from image analysis. The angle of the failure surface with the vertical plane and surface-heaving phenomenon surrounding the penetrating pipe section were comprehensively explored, with detailed graphical representations being presented. The pipes with various fin configurations were shown in figure 1.

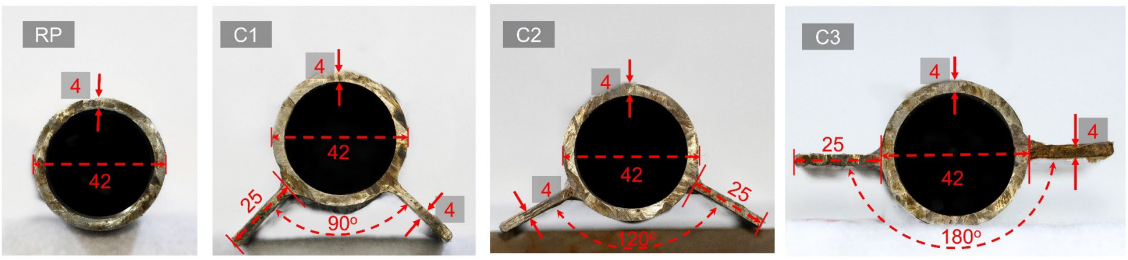

(a) (b) (c) (d)

Fig. 1. Various pipe configurations characterized by the angular fin distance (a) RP (b)C1, (c) C2, and (d) C3.

3. Results and conclusions

The results from the load displacement behaviour showed an increase in the penetration resistance with the increasing vertical penetration up to an initial peak, followed by a secondary rise in the penetration resistance with much gentler slope as can be seen from the Figure 2. The Pressure at the pipe bottom increased with the increase in vertical penetration. The highest pressure was observed at the fin bottom followed by the pipe haunch and the invert as can be seen from the Figure 3. Moreover, from the resultant displacement field it was observed that the highest soil displacement occurred below the pipe section. Additionally, the size of the failure expanded with increasing angular distance between the radial fins as illustrated in Figure 4.

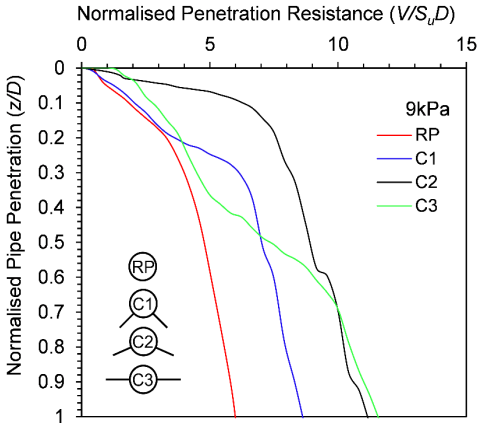

Fig. 2. Load-displacement behaviour.

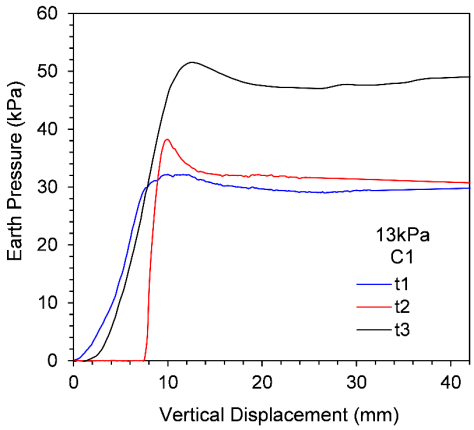

Fig. 3. Pressure variation at the pipe invert (t1), haunch (t2) and the fin bottom (t3) for a C1pipe on 13 kPa seabed.

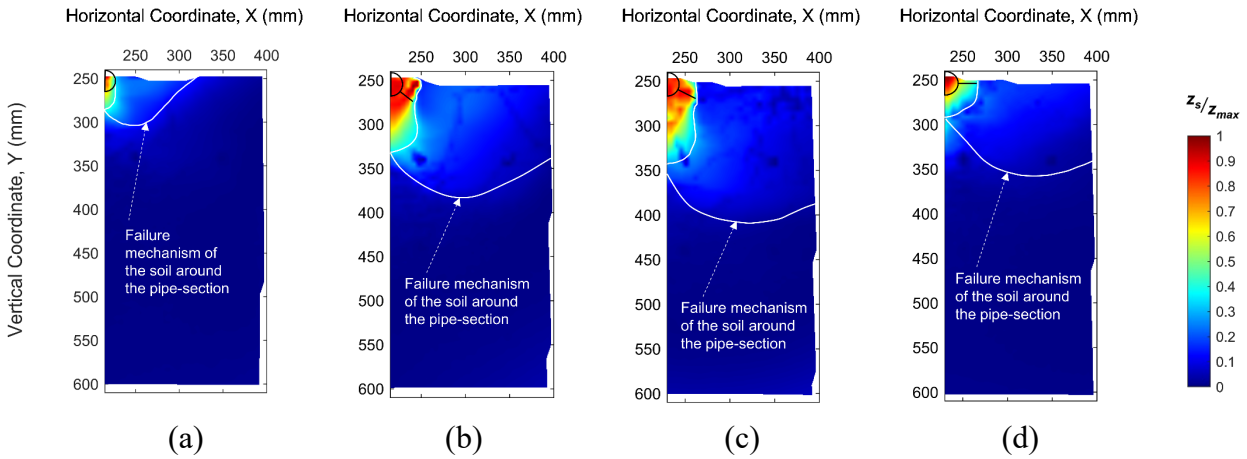

Fig. 4. Resultant displacement field within the soil below the pipe for (a) Regular, (b) C1, (c) C2 and (d) C3 pipes.

5. References

[1] Tom, J. G., O'loughlin, C. D., White, D. J., Haghighi, A., & Maconochie, A. (2017). The effect of radial fins on the uplift resistance of buried pipelines. Géotechnique Letters, 7(1), 60-67.

[2] Stanier, S. A., Blaber, J., Take, W. A., & White, D. J. (2016). Improved image-based deformation measurement for geotechnical applications. Canadian Geotechnical Journal, 53(5), 727-739.

IN SITU STRAIN GAUGE MEASUREMENTS REVEAL DYNAMIC MECHANICAL CHANGES AT THE INTERFACE DURING PLATING AND STRIPPING IN SOLID-STATE LI METAL BATTERIES

Fenghui Wang[1], Hongye Zhang[1], Zhipeng Chen[1], Sen Yang[1], Kejie Wang[1], Shouyu Zhang[1],Xinlei Cao[1]

[1]Department of Engineering Mechanics, Bio-Inspired and Advanced Energy Research Center, Northwestern Polytechnical University, Xi'an 710129, Shaanxi, China.

1. Introduction

To address the safety issues and limited energy density of lithium-ion batteries due to the use of liquid electrolytes, the development of future lithium batteries can be driven by solid-state electrolytes. The intrinsic advantages of high capacity and low reduction potential of lithium metal, as well as the non-flammability of solid electrolytes, make solid-state lithium metal batteries promising to meet the demand for high safety and high specific energy density [1-3]. Moreover, solid electrolytes have sufficient mechanical strength to inhibit the growth of lithium dendrites and prevent battery short circuits, and their thermal stability can prevent thermal runaway, resulting in superior safety performance [4, 5]. Among the solid electrolytes studied so far, inorganic ceramic electrolytes have received extensive research due to their excellent room-temperature ionic conductivity. However, the interactions between solid-solid contacts and the unstable chemical-mechanical properties in all-solid-state batteries have hindered the development of all-solid-state batteries [6, 7].

The chemical-mechanical instability of solid-solid contact interfaces may originate from the penetration of lithium metal into the solid electrolyte, the formation of interfacial layers between the solid electrolyte and the electrode, and the pore formation caused by uneven deposition, delamination, and peeling of lithium, leading to contact loss [8, 9]. Therefore, to better improve the solid-state electrolyte and the interfacial properties between the solid-state electrolyte and the electrode, it is necessary to investigate the underlying mechanics and the coupling with the electrochemical performance of the entire battery [10-12]. However, due to the uniqueness of solid-solid interfaces, the use of in situ techniques to study so-called chemical mechanical deformation has become a challenge. In recent years, various characterization methods have been used to study the interface between the electrode and the solid-state electrolyte [13-19]. For non-destructive inspection of Li plating, the Li-plating in practical applications of battery systems exhibits no signals such as voltage and current that can be easily obtained [20]. The methods used so far are usually based on specialized instruments, such as high-precision coulometry and microcalorimetry, which are more suited to basic research than to practical applications [21].

In this study, we demonstrate a novel approach to strain measurement in batteries. In situ real-time strain measurements utilizing strain gauges are employed to monitor the dynamic physical changes occurring in all-solid-state batteries during Li plating and stripping, as well as the resultant mechanical alterations. Strain gauge sensors are a widely adopted sensor technology in engineering. The fundamental principle involves the precise measurement of minor deformations on the object's surface, enabling the assessment of stress conditions and structural integrity. Resistive strain gauges

are characterized by small size and flexible operation, meanwhile, they have high accuracy and sensitivity, which can monitor the growth of Li dendrites in real time under non-destructive conditions. When Li plating and stripping events take place, the deformation occurring in both the electrode and electrolyte is monitored in real time using strain gauges. This research explores the utilization of poly (vinylidene fluoride)-hexafluoropropylene (PVDF-HFP) as the polymer matrix and garnet-type LLZTO, renowned for its exceptional Li stability and high Li-ion conductivity, as the ceramic filler in the preparation of composite electrolytes. Solid-state Li metal batteries have garnered significant interest due to their distinctive attributes, including high energy density and superior safety [1-3]. Central to these advancements, solid-state electrolytes (SSEs) are pivotal in enhancing the electrochemical performance of solid-state Li batteries [10]. Among various candidates, polyvinylidene fluoride (PVDF) based solid-state polymer electrolytes (SPEs) emerge as particularly promising. Their remarkable flexibility, robust mechanical properties, and superior processing capabilities position them as frontrunners in the development of next-generation solid-state Li batteries [22-24].

2. Materials and methods

The strain generated during battery cycling was measured by using strain gauges of type BE120-3AA from AVIC Electronic Measurement. The strain gauges are 6 mm long, 3 mm wide and 100 μm thick. The strain gauges were adhered to the center of the Cu foil collector side with 502 adhesive. Anhydrous ethanol is used to clean the surface before pasting, the glue should be applied evenly, and after pasting, the surface should be lightly pressed for more than 6 s before releasing. During strain gauge operation, the button cell is required to fasten a ring spacer at the bottom of the Cu foil to leave space for strain gauge deformation, and it should be ensured that there is a good sealing inside the cell. The connection is made entirely with high transmission performance shielded six-core cables, which provide high stability and reliability of data acquisition. The DH3816N multi-channel strain acquisition tester is used to provide 72 strain test channels, to satisfy the demand of simultaneous strain testing. Strain data are stored and recorded by a computer connected with the collector. In particular, temperature compensation is added to each channel of the strain gauge acquisition system that minimizes the temperature effect on the strain gauges during battery operation. The sampling frequency is 5s each time.

3. Results and conclusions

In order to research the strain response during Li plating and stripping, strain tests were initially performed on a solid-state Li metal battery assembled in the laboratory. This battery comprises a Li metal negative electrode, a copper wafer positive electrode, and a PVDF-HFP/LLZTO composite solid-state electrolyte. During discharge, Li from the negative side plates onto the copper wafer. Consequently, the side of the copper wafer that contacts the electrolyte experiences compressive stress, bending away from the Li electrode; conversely, the collector side of the copper wafer endures tensile stress. At this juncture, measurements from strain gauges yield positive values due to increased tensile stress on the copper wafer resulting from deposited Li mass. However, the limited intrinsic Li diffusion rate ($<10^{-11}$ cm^2 s^{-1}) leads to the formation of voids at the interface [25-27]. The accumulation of these voids leads to an uneven distribution of surrounding electric fields which accelerates subsequent Li plating processes at adjacent interfaces - ultimately culminating in dendrite formation [28, 29]. When stripping occurs on the copper wafer's surface where dendrites have formed alongside "dead Li" and residual solid electrolyte interphase (SEI), small tensile stresses persist on its collector side preventing recovery to its original position. Following multiple cycles of operation, mechanical changes induced by uneven lithiation at this interface are captured in real time by means of strain gauges.

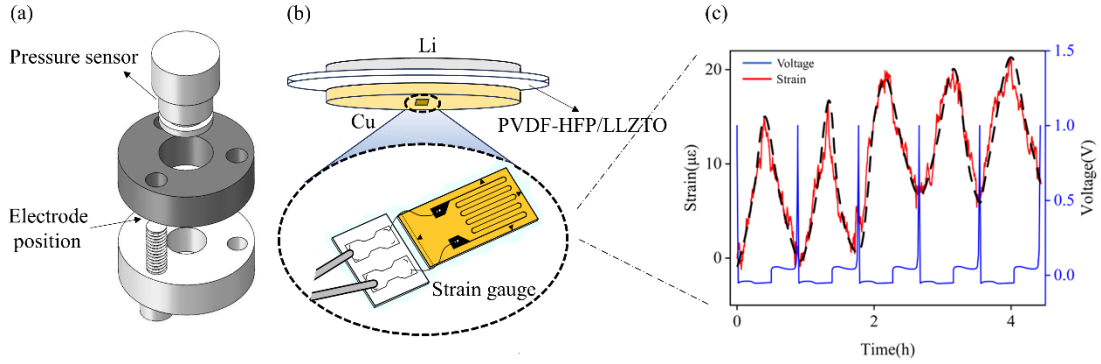

Fig. 1. The schematic diagram of the battery device and strain test

4. Acknowledgements

The authors are grateful for the support by National Natural Science Foundation of China under grants #11572253 and #11972302.

5. References

[1] L.-Z. Fan, H. He, C.-W. Nan (2021). Tailoring inorganic–polymer composites for the mass production of solid-state batteries. Nature Reviews Materials, 6, 1003-1019.
[2] A.M. Abakumov, S.S. Fedotov, E.V. Antipov, J.M. Tarascon (2020). Solid state chemistry for developing better metal-ion batteries. Nat Commun, 11, 4976.
[3] S. Randau, D.A. Weber, O. Kötz, R. Koerver, P. Braun, A. Weber, E. Ivers-Tiffée, T. Adermann, J. Kulisch, W.G. Zeier, F.H. Richter, J. Janek (2020). Benchmarking the performance of all-solid-state lithium batteries. Nature Energy, 5, 259-270.
[4] C. Fang, X. Wang, Y.S. Meng (2019). Key issues hindering a practical lithium-metal anode. Trends in Chemistry, 1, 152-158.
[5] W. Xu, J. Wang, F. Ding, X. Chen, E. Nasybulin, Y. Zhang, J.-G. Zhang (2014). Lithium metal anodes for rechargeable batteries. Energy Environ. Sci., 7, 513-537.
[6] M. Armand, J.M. Tarascon (2008). Building better batteries. Nature, 451, 652-657.
[7] X. Zhang, X. Cheng, Q. Zhang (2016). Nanostructured energy materials for electrochemical energy conversion and storage: A review. Journal of Energy Chemistry, 25, 967-984.
[8] H. Wu, H. Jia, C. Wang, J.G. Zhang, W. Xu (2020). Recent progress in understanding solid electrolyte interphase on lithium metal anodes. Advanced Energy Materials, 11, 2003092.
[9] W.-W. Wang, Y. Gu, C.-X. Liu, J. Yan, B.-W. Mao (2023). Exploring the role of LiI additive in regulating the morphology of lithium deposition by in situ AFM. The Journal of Physical Chemistry C, 127, 12492-12501.
[10] K.J. Kim, M. Balaish, M. Wadaguchi, L. Kong, J.L.M. Rupp (2020). Solid-state Li–metal batteries: challenges and horizons of oxide and sulfide solid electrolytes and their interfaces. Advanced Energy Materials, 11,2002689.
[11] B. Ozdogru, S. Padwal, B. Bal, S. Harimkar, B. Koohbor, Ö.Ö. Çapraz (2022). Coupling between voltage profiles and mechanical deformations in LAGP solid electrolyte during Li plating and stripping. ACS Applied Energy Materials, 5, 2655-2662.
[12] J.A. Lewis, J. Tippens, F.J.Q. Cortes, M.T. McDowell (2019). Chemo-mechanical challenges in solid-state batteries. Trends in Chemistry, 1, 845-857.
[13] L. Porz, T. Swamy, B.W. Sheldon, D. Rettenwander, T. Frömling, H.L. Thaman, S. Berendts, R. Uecker, W.C. Carter, Y.M. Chiang (2017). Mechanism of lithium metal penetration through inorganic solid electrolytes. Advanced Energy Materials, 7, 1701003.
[14] E. Kazyak, R. Garcia-Mendez, W.S. LePage, A. Sharafi, A.L. Davis, A.J. Sanchez, K.-H. Chen, C. Haslam, J. Sakamoto, N.P. Dasgupta (2020). Li penetration in ceramic solid electrolytes: operando microscopy analysis of morphology, propagation, and reversibility. Matter, 2, 1025-1048.

[15] H. Zhang, X. Zhang, Z. Shen, X. Peng, F. Wang, F. Xu, X. Zhao (2024). Ultrasound overcomes dendrite puncture in Li metal batteries. Journal of Energy Storage, 85,110976.
[16] K.J. Harry, D.T. Hallinan, D.Y. Parkinson, A.A. MacDowell, N.P. Balsara (2014). Detection of subsurface structures underneath dendrites formed on cycled lithium metal electrodes. Nat Mater, 13, 69-73.
[17] Y.-C. Hsieh, J.H. Thienenkamp, C.-J. Huang, H.-C. Tao, U. Rodehorst, B.J. Hwang, M. Winter, G. Brunklaus (2021). Revealing the impact of film-forming electrolyte additives on lithium metal batteries via solid-state NMR/MRI analysis. The Journal of Physical Chemistry C, 125, 252-265.
[18] F. Shi, A. Pei, A. Vailionis, J. Xie, B. Liu, J. Zhao, Y. Gong, Y. Cui (2017). Strong texturing of lithium metal in batteries. Proc Natl Acad Sci U S A, 114, 12138-12143.
[19] S. Lv, T. Verhallen, A. Vasileiadis, F. Ooms, Y. Xu, Z. Li, Z. Li, M. Wagemaker (2018). Operando monitoring the lithium spatial distribution of lithium metal anodes. Nat Commun, 9, 2152.
[20] W. Huang, Y. Ye, H. Chen, R.A. Vilá, A. Xiang, H. Wang, F. Liu, Z. Yu, J. Xu, Z. Zhang, R. Xu, Y. Wu, L.-Y. Chou, H. Wang, J. Xu, D.T. Boyle, Y. Li, Y. Cui (2022). Onboard early detection and mitigation of lithium plating in fast-charging batteries. Nature Communications, 13, 7019.
[21] Y. Liu, Y. Zhu, Y. Cui (2019). Challenges and opportunities towards fast-charging battery materials. Nature Energy, 4, 540-550.
[22] X. Zhang, T. Liu, S. Zhang, X. Huang, B. Xu, Y. Lin, B. Xu, L. Li, C.W. Nan, Y. Shen (2017). Synergistic coupling between $Li_{6.75}La_3Zr_{1.75}Ta_{0.25}O_{12}$ and poly(vinylidene fluoride)induces high ionic conductivity, mechanical strength, and thermal stability of solid composite electrolytes. J Am Chem Soc, 139, 13779-13785.
[23] S. Li, S.Q. Zhang, L. Shen, Q. Liu, J.B. Ma, W. Lv, Y.B. He, Q.H. Yang (2020). Progress and perspective of ceramic/polymer composite solid electrolytes for lithium batteries. Adv Sci (Weinh), 7, 1903088.
[24] B. Cheng, P. Du, J. Xiao, X. Zhan, L. Zhu (2024). Improving the ionic conductivity and anode interface compatibility of LLZO/PVDF composite polymer electrolytes by compositional tuning. ACS Appl Mater Interfaces, 16, 31648-31656.
[25] Z.-X. Wang, Y. Lu, C.-Z. Zhao, W.-Z. Huang, X.-Y. Huang, W.-J. Kong, L.-X. Li, Z.-Y. Wang, H. Yuan, J.-Q. Huang, Q. Zhang (2024). Suppressing Li voids in all-solid-state lithium metal batteries through Li diffusion regulation. Joule, 8, 2794-2810.
[26] M. Jäckle, K. Helmbrecht, M. Smits, D. Stottmeister, A. Groß (2018). Self-diffusion barriers: possible descriptors for dendrite growth in batteries?. Energy & Environmental Science, 11, 3400-3407.
[27] U.B. W. Frank, C. Elsässer, and M. Fähnle (1996). First-principles calculations of absolute concentrations and self-diffusion constants of vacancies in lithium. PHYSICAL REVIEW LETTERS, 77, 518-521.
[28] Y. Lu, C.Z. Zhao, H. Yuan, X.B. Cheng, J.Q. Huang, Q. Zhang (2021). Critical current density in solid-state lithium metal batteries: mechanism, influences, and strategies. Advanced Functional Materials, 31, 2009925.
[29] V. Raj, V. Venturi, V.R. Kankanallu, B. Kuiri, V. Viswanathan, N.P.B. Aetukuri (2022). Direct correlation between void formation and lithium dendrite growth in solid-state electrolytes with interlayers. Nat Mater, 21, 1050-1056.

6-11 July 2025 ICEM21 Bologna
21st International Conference on EXPERIMENTAL MECHANICS

FAILURE ANALYSIS OF COMPOSITE WIND TURBINE BLADE JOINT: CASE STUDY

S.A. Nassar[1], Z. Wu[1] , J. Kent[2], C. Bumb[2], M.Y. Khan[1,3]
[1] Department of Mechanical Engineering, Oakland University, Rochester, Michigan, USA
[2] One Power Company, Findlay, Ohio, USA
[3] Department of Industrial Engineering (DIN), University of Bologna, Bologna, Italy

1. Introduction

Failure analysis is presented for a ruptured large-diameter bolted composite-to-metal joint of a wind turbine blade during normal operation (Fig. 1). Although it is recognized that threaded fasteners are widely used for clamping structural joints in many automotive, aerospace, and infrastructure applications, the high concentration at the threat roots can dramatically reduce their fatigue performance under dynamic loads [1-2]. Investigated flanged joint has a total of 54 preloaded threaded studs to clamp the composite blade flange to respective metal hub flange on the wind turbine tower. At the opposite end on the nut, each stud is held in the composite blade flange by a T-bolt. As shown by Fig. 1 (b), during the initial installation, the stud would clamp together a stack of a) composite blade flange, b) metal hub flange, c) a bearing, and d) a stiffener plate.

Consistent with widely reported findings in the literature, SEM testing and visual inspection of the failure surfaces of ruptured flange studs in this study (Fig. 2) show that fatigue failure is mostly taking place at the first fully engaged thread [3-4]. Bolt fatigue failure is often accelerated by a decay/loss of its preload, which would dramatically increase its cyclic load amplitude due to a localized joint separation. Suspected loss of stud preload in this study may be attributed to a large scatter in stud preloading among the 54 studs at initial assembly due to bolt elastic interaction, frictional variation, non-flat contact between clamped parts, temperature fluctuation, ….etc. [5-6].

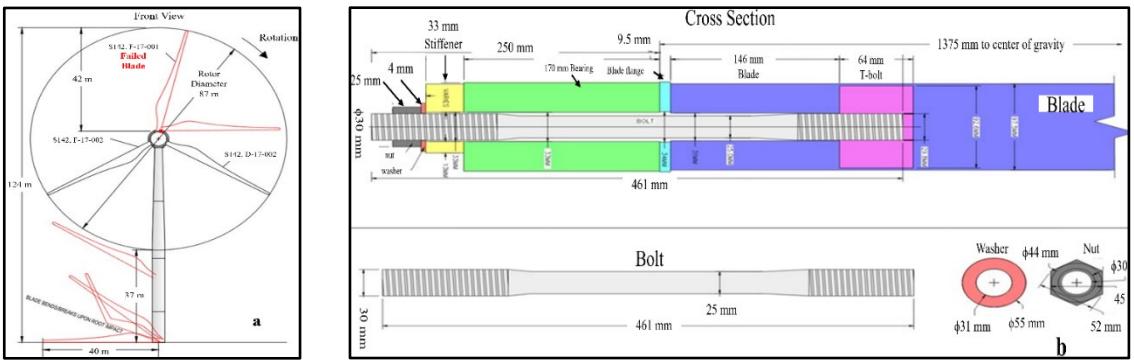

Fig. 1. (a) Front view of wind turbine (b) Cross section: stud and clamped parts

2. Materials and methods

A novel wireless technology is procured to strain gage a stud that continuously measures and transmits real-time data on stud tension F_z as well as operational bending moments M_x and M_y to receiver/display in control room on the ground level; sample data on F_z, M_x, M_y is shown in Fig. 3.

3. Results, observations, and tentative conclusions

Numerous studs suffered ultimate failure. SEM inspection of fracture surfaces (Fig. 2) of several studs shows the classical signs of slow growth of a fatigue crack (smooth beach marks) that are followed by a rough brittle fracture surface leading to the final stage of stud fatigue rupture. Additionally, it was noted that there was visible lubricant egress in clamped connections, indicating that there may not be full joint contact throughout the blade-to-hub interface. More than 50% of the observed gaps correlated to the area of associated bolt fatigue failure in the failed blade. The presence of a significant air gap in the flanged assembly as a result of a lack of flatness of the retrofitted stiffener plate was determined to be the primary cause of significant loss of localized clamping around respective nearby stud(s), which eventually led to stud fatigue failure due to exposure to high in-service force and moment amplitudes.

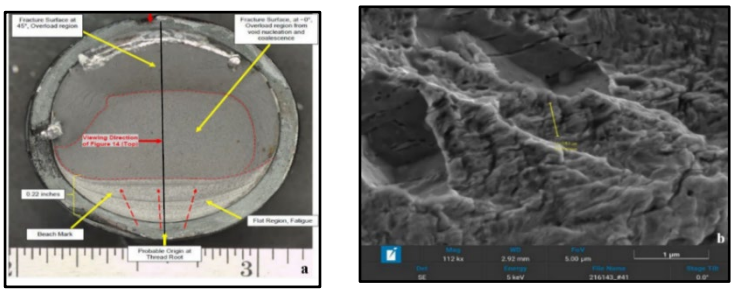

Fig. 2. (a) Fractured sample, (b) SEM of fractured sample

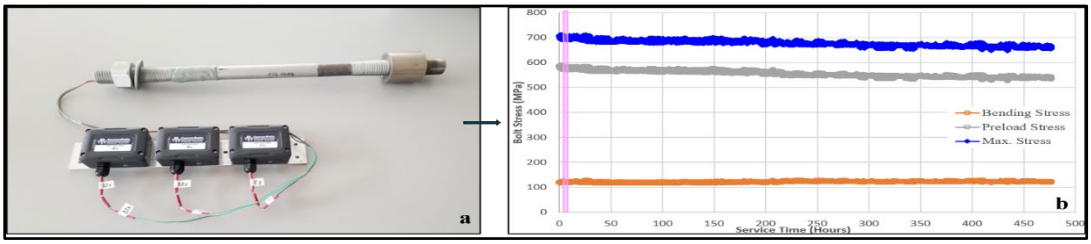

Fig. 3. (a) Stain gauges connected to stud; (b) Axial and bending stresses vs time relation

Finally, the data obtained from the strain gauges is used to plot the preload loss over time and bending moments on the blade (Fig. 3). An average 10% preload loss was observed after 500 hours. At this rate of preload decay, the residual clamp load is would be less than 50% of its presumed initial value at installation every 6 months; should that rate of preload decay continue, undesirable increased probability of cyclic localized joint gapping and/or separation. This would lead to cyclic bending moments and shear force amplitudes that accelerate stud fatigue failure.

4. Acknowledgement

NSF IUCRC center for Composite and Hybrid Material Interfacing (CHMI)-Industrial Advisory Board (IAB), for funding this research at the Oakland University site of CHMI.

5. References

[1] Piccatto, A, Belingardi, G, Wu, Z, & Nassar, SA. "Multi-Axial Fatigue of Sheet Metal Joints Under Clamp Load and Cyclic Bending." *Proceedings of the ASME 2017 IMECE. Volume 2: Advanced Manufacturing*. Tampa, Florida, USA. November, 2017. V002T02A092. ASME. https://doi.org/10.1115/IMECE2017-72691.

[2] Toribio, J., González, B., Matos, JC. *et al.* Fatigue behaviour of bolted joints. *Met. Mater. Int.* **18**, 553–558 (2012). https://doi.org/10.1007/s12540-012-4001-3.

[3] Pilkey, Walter D., Deborah F. Pilkey, and Zhuming Bi. *Peterson's stress concentration factors*. John Wiley & Sons, 2020. https://doi.org/10.1002/9781119532552.

[4] Croccolo, D.; De Agostinis, M.; Fini, S.; Mele, M.; Olmi, G.; Scapecchi, C.; Tariq, M.H.B. Failure of Threaded Connections: A Literature Review. *Machines* **2023**, *11*, 212. https://doi.org/10.3390/machines11020212.

[5] Nassar, S. A., and Alkelani, A. A. "Clamp Load Loss due to Elastic Interaction and Gasket Creep Relaxation in Bolted Joints." ASME. *J. Pressure Vessel Technol*. August 2006; 128(3): 394–401. https://doi.org/10.1115/1.2218343.

[6] Nassar, S.A., Yang, X. "Novel Formulation of Bolt Elastic Interaction in Gasketed Joints." ASME. *J. Pressure Vessel Technol*. October 2009; 131(5): 051204. https://doi.org/10.1115/1.3151814

SEQUENTIAL FREE-OSCILLATION TEST METHOD FOR ROCKING STRUCTURAL SYSTEMS

D. Kalliontzis[1], A.E. Schultz[2], S. Sritharan[3]
[1]Department of Civil Engineering, University of Houston, Houston, Texas, USA
[2]School of Civil & Environmental Engineering, and Construction Management, University of Texas at San Antonio, San Antonio, Texas, USA: corresponding author
[3]Iowa State University, Ames, Iowa, USA

1. Introduction

Physical testing of large-scale structural systems poses challenges that are often solved only by testing of large specimens with controlled force histories of large magnitude. In the case of testing for natural hazards such as earthquake or wind effects, the loads must be imposed in controlled cycles, often at high loading rates. However, for a certain class of earthquake resistant structural system, including the rocking system, these demands can be met with a simpler test method, the Sequential Free-Oscillation (SFO) test method. Yielding systems, such as steel and reinforced concrete structures, in which yielding members or reinforcement undergo large plastic demands, cyclic histories of large-magnitude forces are needed with controlled displacements. However, for rocking systems (e.g., pillars, walls and blocks that rest on their foundations), tests can be conducted under free oscillation states without the need for controlled force or displacement histories. Thus, free oscillation testing greatly simplifies the laboratory demands.

This study presents results from a testing program that successfully utilized the SFO test method for rocking structures made with either precast concrete or concrete masonry [1]. In both cases the walls were post-tensioned to a concrete foundation by means of unbonded prestressing steel elements to limit the uplift. The prestressing steel also served to complete an internal couple that generated the resistance to overturning from lateral excitation. In addition, it generated frictional resistance between the top of the foundation and the bottom of the walls. As such, no reinforcement was needed across the wall-foundation interface other than the unbonded prestressing steel. Both wall systems were loaded by imposing an initial static displacement at the top of the wall that was released suddenly, allowing the walls to oscillate freely at their natural frequency. By controlling, and sequentially increasing the top lateral displacement of the walls, a full range of responses was studied. A variety of contact and non-contact sensors was used to monitor wall performance under the SFO tests. Additionally, soft layers were used under a portion of the wall-foundation interface to enhance the impact damping of the walls and protect the corners from damage.

2. Test method

2.1 Specimens

The precast concrete rocking members were built and tested at the Structural Laboratory of Iowa State University. The members had width, length and height dimensions of 177.8 mm, 711.2 mm and 2,425.7 mm, respectively, and were tested on a reinforced concrete foundation that had width, length and height dimensions of 1,270 mm, 1,270 mm and 609.6 mm, respectively. To ensure full contact

between the rocking member and the foundation base, a 25.4 mm thick non-shrink grout layer was used at the top of the foundation base. A rubber layer with thickness ranging from zero (i.e., no rubber) to 25.4 mm was also placed on the top of the grout layer. A wood frame was placed as shown in Figure 1 to prevent any unexpected out-of-plane movement of the member; gap distances of 25.4 mm in the front and back sides of the member were initially allowed between the member and the wood frame to ensure no contact during planar rocking motions. More details of this test setup are available elsewhere [1].

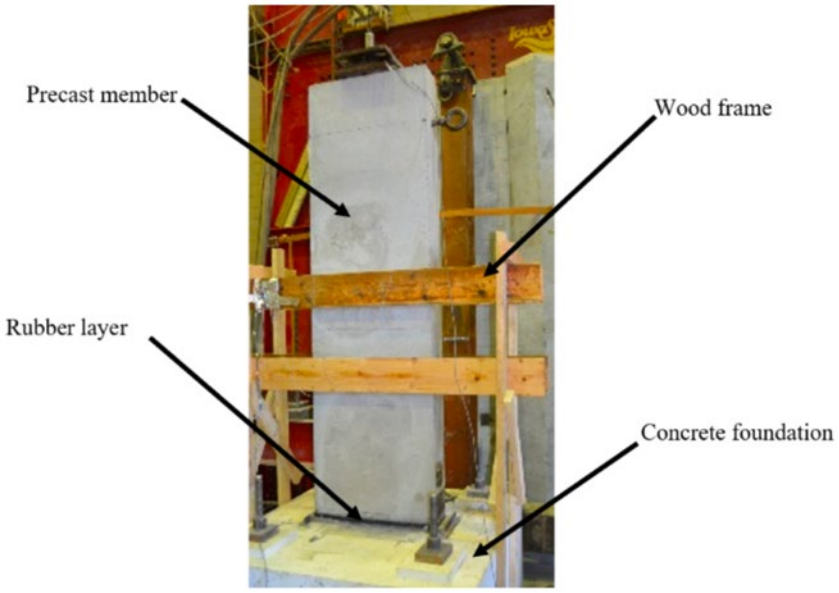

Fig. 1 Precast concrete rocking structure [1]

A masonry rocking wall was built and tested at the Theodore V. Galambos Laboratory of the University of Minnesota as shown in Figure 2. The wall was built using 6-inch (152-mm) hollow concrete masonry units (i.e., blocks) and was fully grouted. The masonry had a height of 2,438 mm and a length of 1,418 mm. The target masonry compressive strength f'_m for the masonry assembly was 20.8 MPa (i.e., 3 ksi) and the wall was post-tensioned using two unbonded threaded steel bars (ASTM A354 Grade BD), which were spaced symmetrically in the wall, resulting in a distance of 292.1 mm from the wall ends, for each bar. Each bar had a diameter of 15.9 mm (i.e., 5/8 inches), minimum specified yielding strength of 896.3 MPa (i.e., 130 ksi), minimum specified ultimate strength of 1034.2 MPa (i.e., 150 ksi), and maximum strain capacity of 0.14 mm/mm. The bars were inserted into PVC ducts with diameters of 38.1 mm (i.e., 1.5 inches) to eliminate bond with grout. Two fiber-reinforced rubber pads manufactured by Fabreeka® [2] with 203.2 mm × 19.05 mm were placed at the compression toes of the wall. The pads were as wide as the wall thickness and had a length of one-half of a masonry unit.

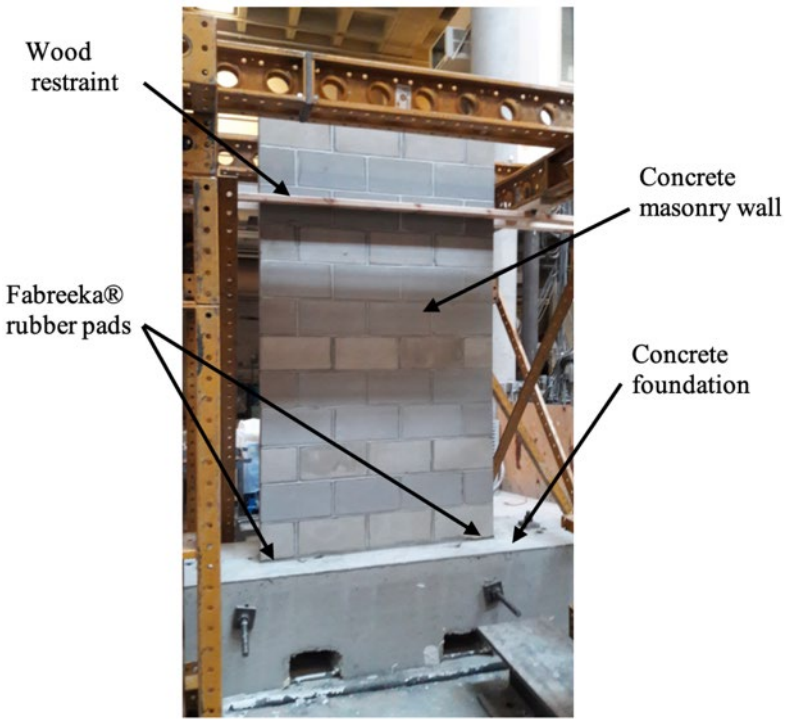

Fig. 2 Concrete masonry rocking wall [1]

2.2 Interface materials

The precast concrete rocking members tested at Iowa State University had one of four different member-to-foundation configurations. The first one was tested using a grout layer with specified compressive strength of 70 MPa as the member-to-foundation interface. The subsequent three members utilized one of three classes of

neoprene rubber with shore hardness (SH) of 50, 70 and 90. All rubber layers had width and length dimensions of 177.8 mm and 711.2 mm, respectively, matching the cross-section of the wall. The rubber layers with SH of 70 and 90 had a thickness of 25.4 mm, and three thicknesses were used for the rubber layer with SH of 50: 25.4mm, 12.7 mm and 6.35 mm.

The concrete masonry rocking wall tested at the University of Minnesota was designed to minimize damage at the compression rocking toes. A resilient solution was selected in which Fabreeka® preformed fabric pads were placed at the toe regions with a mortar layer being cast in between the pads. Fabreeka® rubber pads have a working strength of 10,000 psi, limit creep to approximately 5% of the original pad thickness, have a relatively high damping ratio of 14%, are impermeable to most oils, steam, water, mildew and brine, and feature an effective temperature range from -65°F to 200°F [2]. In addition to improving the responses of the toes, this solution allows cost-effective replacement of the Fabreeka® pads, in the event of a damaging loading event. A thickness of 19.05 mm (3/4 inches) was selected here for the pads as this thickness can be easily accommodated in the first mortar joint of a masonry wall (i.e., above the foundation).

2.3 Sequenced free-oscillation (SFO) test procedure

The SFO test procedure consists of imparting an initial excitation to a structure or structural member and allowing it to oscillate freely until the motion is damped out. The initial excitation can be a displacement or a velocity, but the former is more easily applied. For a vertical cantilever structure, such as the vertically post-tensioned rocking structures in this study, the lateral displacement at the top is the ideal choice to impart the initial excitation. In this study, the initial displacement was imparted by a force actuator that was oriented horizontally to displace the top of the rocking members to predefined initial top lateral drifts (ITLDs). The hydraulic actuator was powered by a pump and manifold controlled in a closed-loop system and was connected to the top of the rocking member by means of a quick-release device [3]. The quick-release device is designed for safely releasing an object or line under load, and it was released manually to initiate the free oscillations. For the Iowa State tests, ITLDs equal to 1%, 2% and 3% top drifts (i.e, displacement expressed as a percentage of structure height) were used, and in the Minnesota tests, ITLDs of 0.5%, 0.75%, 1.0%, 1.5% and 2.0% were used.

Instrumentation used during the tests included a variety of displacement transducers (LVDT and string potentiometers), positioning systems utilizing light emitting diodes (LEDs) that were attached to the surface of the rocking members, load cells, and accelerometers to track the performance of the rocking members. The data acquisition system used sampling frequencies as high as 500 Hz (Iowa State tests) and 1,650 Hz (Minnesota tests).

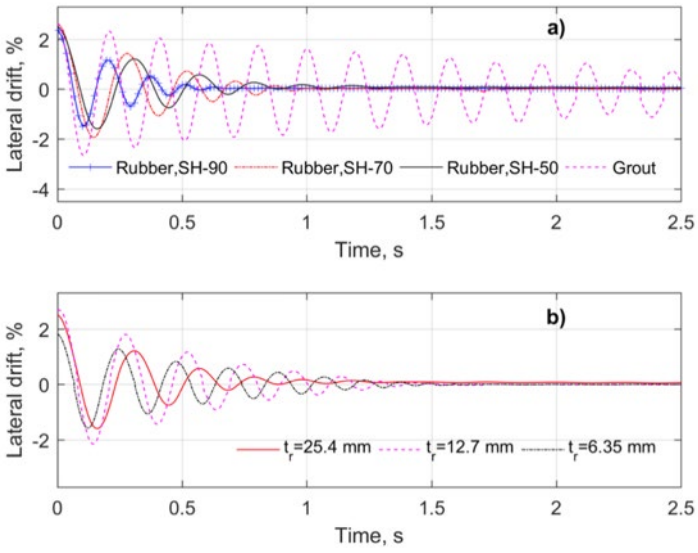

Fig. 3 Responses of precast concrete rocking member, a) 25.4 mm thick rubber layer; b) SH = 50 rubber layer

3. Results and conclusions

3.1 Dynamic response

The SFO test method can provide detailed time histories of top drift, as shown in Figure 3 for the precast concrete rocking structure tests with ITLDs of 2%. Part (a) of the figure compares all test systems with 25.4 mm thick interface layer. The responses of the systems with rubber interfaces indicate significantly faster decay than does the system with grout interface. The lateral drift amplitudes of the former approach zero after about 1.0 second, while the system with grout continues to oscillate for several seconds. Part (b) of the figure compares the three lateral drift responses of the systems that used rubber interfaces with SH of 50 and three different layer thicknesses: 25.4 mm, 12.7 mm and 6.35 mm. Period lengthening is larger for systems with thicker rubber interfaces.

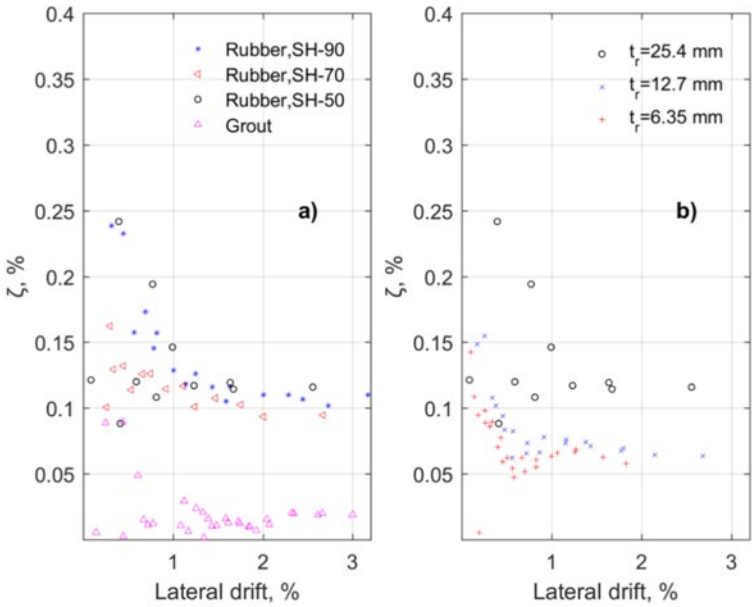

Fig. 4 Equivalent viscous damping of precast concrete rocking member: a) t_r = 25.4; b) SH = 50

3.2 Equivalent viscous damping

The overall damping capabilities of the precast concrete test systems were investigated by quantifying the corresponding equivalent viscous damping. Equivalent viscous damping, ζ, can be quantified using the logarithmic decrement of the angle of rotation of the base of a rocking member [4]. For the case of two impacts, the estimates of ζ due to total energy loss over a full rocking cycle are presented in Figure 4 as a function of lateral drift amplitudes of the test systems. In part (a), grout is observed to provide measured values of ζ that are significantly lower than the systems with rubber layers, and for several drift amplitudes, they differ by an order of magnitude. Additionally, for practical purposes, there is no significant effect of SH of the rubber on ζ. However, part (b) of the figure indicates that ζ can increase significantly with increasing thickness of the rubber layer.

Total damping is related to total energy loss which includes not only the energy loss from impacts, but other sources as well. These sources include friction from any sliding at the member-to-foundation interface, plasticity of localized regions at the compression toes, and plasticity from flexure along the height of the member. Using the measured structural responses of the concrete masonry rocking wall, the damping ratio from impacts was computed. Figure 5 compares this ratio with the total equivalent damping ratio obtained from the logarithmic decrement method. These values for

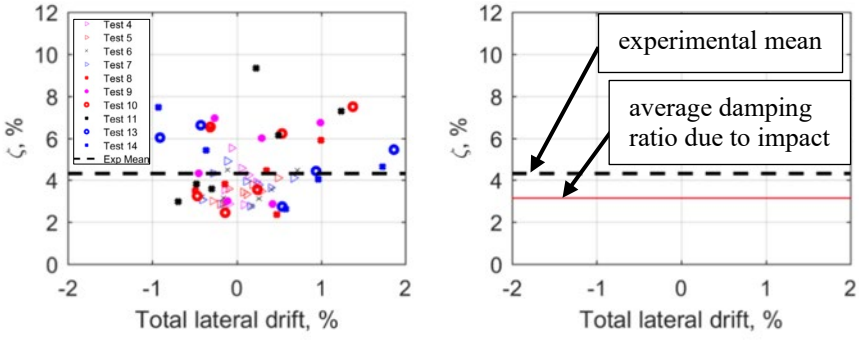

Fig. 5 Damping ratios in concrete masonry rocking wall [1]

total equivalent damping are shown for all tests in part a) and the mean value from the experiments is compared with the damping from impacts in part b).

3.3 Residual Drift

Figure 6 illustrates the residual lateral drifts of the concrete masonry wall due to horizontal sliding at the rocking interface. It is shown that these drifts were negligible during the first four tests and remained below 0.05% in all tests with ITLDs up to 1.5%. Higher residual drifts were recorded in the three tests with ITLDs of 2%. Due to all tests, the accumulated residual lateral drift was estimated experimentally to be 0.62%, which agreed with visual inspection of the rocking interface upon completion of the SFO tests. The cause of these residual drifts was investigated and found to be produced during the initial monotonic phase of the SFO tests when the wall is loaded to an initial ITLD before being released into free oscillation. No sliding oscillations took place during the free vibration motions, and the sliding drifts reduced rapidly upon initiation of the dynamic motions and within the first two free vibration cycles.

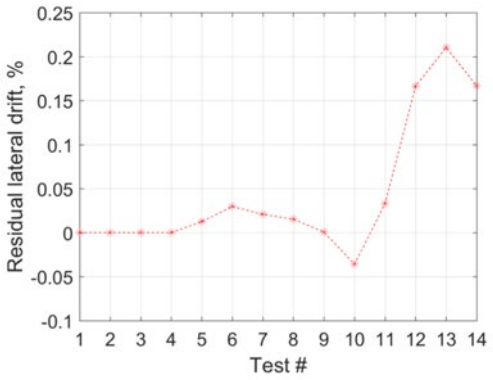

Fig. 6 Residual drift of concrete masonry rocking wall due to horizontal sliding

4. Acknowledgements

The authors acknowledge the support for the first author from the Department of Civil, Environmental, and Geo- Engineering at University of Minnesota, Twin Cities, as well as the Department of Civil, Construction and Environmental Engineering at Iowa State University.

5. References

[1] D. Kalliontzis (2018). Behavior of Precast Concrete and Masonry Wall Systems with Jointed Connections Subjected to Lateral Loads., *Ph.D. Dissertation, Univ. of Minnesota*, Aug., 383 pp.
[2] Fabreeka (2015). Fabreeka® Pads, Reducing structure-borne noise & Impact shock and vibration, 16 pp.
[3] Sea Catch. https://www.seacatch.com/.
[4] A. Chopra (2023). *Dynamics of Structures: Theory and Applications to Earthquake Engineering*, 6th ed., Pearson (March 1, 2023), ISBN-13: 9780137602605.

EXPERIMENTAL RESEARCH ON THE STATIC AND FATIGUE PROPERTIES OF THE EXTERNAL ANCHORAGE STRUCTURE WITH STEEL ANCHOR TUBE OF THE STAYED CABLES

Guowen Yao[1], Li Ying[1, 2], Fengmin Chen[2], Guoying Kong[3], Xuanbo He[1], Yang Tang[1], Xuebing Hu[1], Yu Wang[4], Mark Hughes[4]

[1] School of Civil Engineering, Chongqing Jiaotong University, Chongqing, China 400074
[2] China Railway Changjiang Traffic Design Group Co., LTD, Chongqing, China 401121
[3] Chongqing Fengjian Expressway Co., LTD, Chongqing, China 404100
[4] School of Science, Engineering and Environment, University of Salford, Manchester M5 4WT, UK

1. Introduction

As one of the key components of cable force transmission of cable-stayed bridges, the cable-girder anchorage structure has problems such as dense structural welds, a complex force transmission mechanism, and local stress concentration [1].

Wang et al. [2] Based on the morphology of etch pit distribution on actual corroded plate members and taking cylindrical etch pits as the foundation, considering the randomness of etch pit positions and sizes, they respectively established finite element models of stiffened and unstiffened plate members after corrosion and studied the compressive bearing capacity of plate members after corrosion. Zhao et al. [3, 4] established finite element models considering the randomness of corrosion and studied the impacts of randomly distributed etch pits on the tensile and shear properties of steel plates. They also put forward the variation law of the bearing capacity of steel plates with the degree of corrosion. Wang et al. [5] Conducted accelerated corrosion of stud connectors by electrifying NaCl solution and found that the fatigue life of corroded specimens was between 30% and 80% of that of uncorroded specimens. With the increase in the corrosion rate of stud connectors, the maximum slip values of specimens under each cycle all increased, indicating that the corrosion of stud connectors would significantly deteriorate their fatigue performance. Cao et al. [6] Carried out push-out tests of 8 groups of stud connectors under the coupling effect of corrosion and fatigue. The results showed that the coupling of corrosion and load accelerated the development of strain and the decline of stiffness of the composite structure. It was recommended to use the modified long-term elastic modulus of concrete to calculate the long-term performance of the steel-concrete composite structure. Chen et al. [7] Evaluated the bearing capacity, beam stiffness, and fatigue life of samples with different corrosion rates for 10 steel-concrete composite beams respectively. The corrosion of stud connectors was significantly unfavorable to the bearing capacity and stiffness of composite beams. Moreover, with the increase in the corrosion rate, the fatigue life of composite beams decreased more sharply, with a maximum reduction of 29.69%.

The new external steel anchor pipe anchorage structure studied in this paper has the advantages of convenient cable system detection, maintenance, and replacement construction. Based on a cable-stayed bridge, a 1:2 scale model test of the external steel anchor pipe anchorage structure was carried out to study the stress, deformation law, and fatigue performance of the anchorage structure and to provide support for the design optimization and construction of the anchorage structure of cable-stayed bridges [8-10].

2. Static and fatigue experiments

The spatial finite element model of cable-stayed bridge is established by Midas Civil finite element software (Fig. 1). The most unfavorable load position is determined by considering the cable force and live load cable force amplitude. Finally, the segment of WS26 stay cable with the largest cable force is determined as the key research object. According to the bridge traffic volume prediction model, the Monte Carlo statistical simulation method is used to analyze the fatigue load spectrum of the cable-stayed bridge through the MATLAB computer programming language. According to the fatigue linear damage theory, combined with BS5400, AASHTO and other related design specifications, it is clear that the fatigue test amplitude of the scale model of the external steel anchor pipe anchorage structure is 300 kN [11-15].

Based on the similarity theory, the design scheme of 1:2 scale model for fatigue test of anchorage structure of cable-stayed bridge is proposed under the condition of equal stress. The ANSYS finite element model is established, and the design details of the scale model are calculated and determined by the equivalent comparison of the stress of the original bridge segment model and the test model. Based on the comprehensive analysis of the fatigue performance and test requirements of the cable-girder anchorage zone of practical engineering bridges, a reasonable fatigue test scheme is proposed.

The static and fatigue tests of the cable-girder anchorage structure were carried out in the State Key Laboratory of Bridge and Tunnel Engineering in mountainous areas, and the stress, deformation law and fatigue performance of the external steel anchor pipe anchorage structure were revealed (Fig. 2).

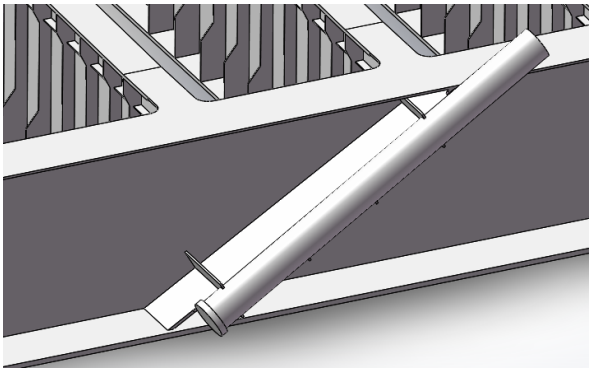

Fig. 1. Three-Dimensional Diagram of the External Steel Anchor Pipe Anchorage Structure

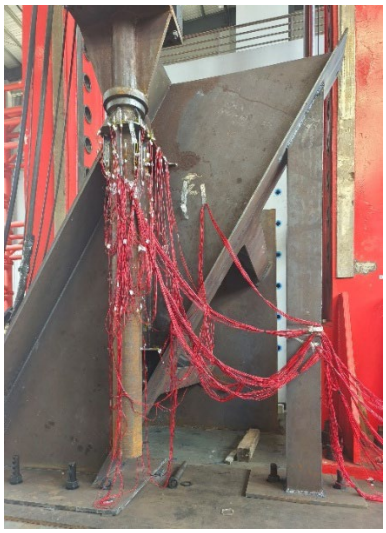

Fig. 2. SJ3 Measuring Points Layout Schematic

3. Results and conclusions

The test results indicate that the concentrated force exerted by the cable on the steel anchor pipe is transmitted to the main girder web via the anchorage web, and the stress concentration within the anchorage structure is progressively alleviated by means of the stable plate and the intermediate stiffening rib. Under the ultimate bearing capacity condition, the stress at the measuring point adjacent to the chamfered edge of the anchorage web near the steel anchor pipe surpasses the material strength design standard value. After local structural optimization, the stress at the measuring point near the chamfer edge of the anchorage web is reduced to 262 MPa, the maximum equivalent stress of the anchorage web is 228 MPa, the maximum stress of the steel anchor pipe is 152 MPa, and the maximum equivalent stress of the steel anchor pipe stiffener is 236 MPa. No cracks were found in the weld, and the static performance met the requirements (Fig. 3).

Following 2.8 million cycles of fatigue loading, the stress of the primary force transmission weld in the scale model remained essentially unaltered, and no fatigue cracks were detected in any of the components. The stress test results are consistent with the finite element structural analysis results, indicating that the overall performance of the anchorage structure is good and has a large safety reserve (Fig. 4). According to the relevant design specifications at home and abroad, the fatigue performance of the external steel anchor pipe anchorage structure is evaluated. The maximum equivalent stress of the scale model at the fatigue checking point of the connection weld between the anchorage web and the steel anchor pipe is 48.45 MPa, which meets the fatigue strength requirements of engineering applications.

Finally, based on the test results, an optimization scheme for the design of the external steel anchor pipe anchorage structure is proposed, along with more stringent technical specifications for the processing and installation precision of the steel anchor pipe anchorage structure.

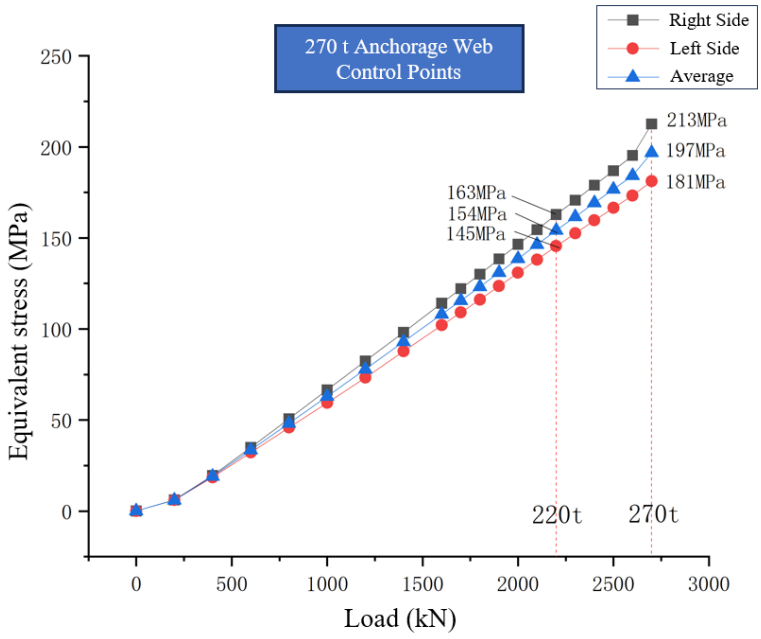

Fig. 3. The Equivalent Stress of A-4 and B-3 under Static Loading

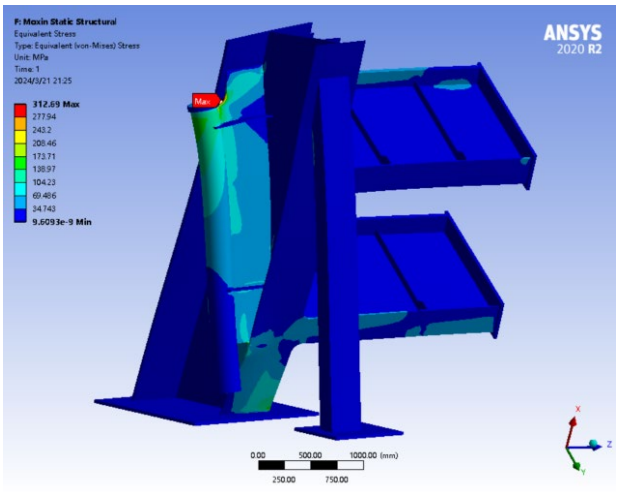

Fig. 4. The Von Mises Stress under the Maximum Cable Force of the Model

4. Acknowledgements

The research presented in this paper has received funding from the National Natural Science Foundation of China (Grant no. 52178273), the Innovation and Development Joint Project of Natural Science Foundation of Chongqing, China (Grant no. CSTB2023NSCQ-LZX0077), the Natural Science Foundation of Chongqing (Grant no. cstc2021jcyj-msxmX1159), the Chongqing Talent Plan Project (Grant no. cstc2022ycjh-bgzxm0124), the Chongqing Graduate Research Innovation Project (Grant no. CYB23244), the Team Building Project for Graduate Tutors in Chongqing (Grant No. JDDSTD2022003) and the Joint Training Base Construction Project for Graduate Students in Chongqing (Grant No. JDLHPYJD2020004).

5. References

[1] China Journal of Highway and Transport. Review on China's bridge engineering research. China Journal of Highway and Transpor, 2021, 34(02): 1-97.
[2] Wang R, Ajit Shenoi R, Sobey A. Ultimate Strength Assessment of Plated Steel Structures with Random Pitting Corrosion Damage [J]. Journal of Constructional Steel Research, 2018, 143: 331-342.
[3] Zhao Z, Zhang H, Xian L, et al. Tensile Strength of Q345 Steel with Random Pitting Corrosion Based on Numerical Analysis [J]. Thin-Walled Structures, 2020, 148: 106579.
[4] Zhao Z, Zhang N, Wu J, et al. Shear Capacity of Steel Plates with Random Local Corrosion [J]. Construction and Building Materials, 2020, 239: 117816.
[5] Wang W L, Chen J, Jin W L. Experimental investigation of corroded stud shear connectors subjected to fatigue loading [J]. Journal of Materials in Civil Engineering, 2016, 29(1): 04016175.
[6] Cao, GH, Yang, L, Zhang, W, et al. Long-Term Mechanical Properties of Steel–Concrete Connectors Subjected to Corrosion and Load Coupling [J]. Journal of Materials in Civil Engineering, 2018, 30(5): 04018058.
[7] Chen, J, Zhang, HP, Yu, QQ. Static and fatigue behavior of steel-concrete composite beams with corroded studs [J]. Journal of Constructional Steel Research, 2019, 156: 18-27.
[8] Yao G W, Liu Ch Y, Wu G Q. Study on cable corrosion damage mechanism under acid rain environment load coupling [J]. Journal of Chongqing Jiaotong University (Natural Science Edition), 2016, 35 (6): 6-10.
[9] Lu Y Y, Hu J Y, Li S, et al. Active and passive protection of steel reinforcement in concrete column using carbon fibre reinforced polymer against corrosion [J]. Electrochimica Acta, 2018, 278: 124-36.
[10] Wu J X, Liu E D. Research on the causes of bridge suspender fracture and early warning technology [J] Western Transportation Science and Technology, 2013, (5): 51-5.

[11] American association of state highway and transportation officials. AASHTO LFRD bridge design specification [S]. Washington, D. C. American Association of state highway and transportation officials, 2007.
[12] British Standards Institution (BSI). BS5400 Steel, Concrete and Composite Bridges: Part 10, Code of Practice for Fatigue [S]. London: BSI, 1980.
[13] British Standards Institute (BSI). BS5400 Steel, Concrete and Composite Bridges: Part 3, Code of Practice for the Design of Steel Bridges [S]. London: BSI, 1982.
[14] European Committee for Standardization. EN 1993-1-9 Eurocode 3 Design of Steel Structures Part 1.9: Fatigue [S]. Brussels: CEN, 2005.
[15] American Association of State Highway and Transportation Officials (AASHTO). AASHTO LRFD 2012 Bridge Design Specifications (6th Edition) [S]. Washington, D. C: AASHTO, 2012.

EXPERIMENTAL STUDY ON MECHANISM OF IMPRESSED CURRENT CATHODIC PROTECTION OF GALVANIZED STEEL WIRE FOR BRIDGE CABLE

Lianhua Wang[1, 2], Guowen Yao[1], Xuanbo He[1], Yu Wang[3], Mark Hughes[3], Ling Zhao[1], Yang Tang[1], Pengyu Chen[1]

[1] School of Civil Engineering, Chongqing Jiaotong University, Chongqing 400074
[2] China Railway 23rd Bureau Group Corporation Limited, Sichuan Chengdu 610000
[3] School of Science, Engineering and Environment, University of Salford, Manchester M5 4WT, UK

1. Introduction

High-strength galvanized steel wire has been widely used in large-span prestressed structures, cable-supported bridge structures and other large-scale and multi-configuration practical projects. Galvanized steel wire in service environment is vulnerable to the corrosion of acid rain, oxygen, chloride ions and other corrosive substances [1].When the steel wire is in a humid environment rich in oxides for a long time, the galvanic cell reaction will be formed, resulting in electrochemical corrosion [2].Under the coupling effect of alternating load and environmental corrosion, the durability of steel wire is rapidly degraded, especially the damage of bridge structure caused by the fracture of steel wire in the anchorage section of cable due to corrosion fatigue [3], which poses a great threat to the service safety of bridge. Therefore, it is necessary to explore an effective method to delay the corrosion of steel wire.

Impressed current cathodic protection (ICCP), as a method to inhibit the corrosion of steel structures, has been widely used in pipelines [4], ships [5], marine engineering [6], reinforced concrete [7] and other structures. The principle is to apply direct current to the corroded metal structure to inhibit the migration of electrons in the structure, thereby delaying corrosion. Su et al. [8] studied the effect of ICCP on the fatigue performance of corroded reinforced concrete beams. The results show that ICCP can effectively prevent the corrosion of steel bars and significantly improve the fatigue life of reinforced concrete beams. Wei et al. [9] studied the application of carbon fiber reinforced polymer as an anode material in the ICCP system of chloride-contaminated concrete and evaluated the cathodic protection efficiency of steel bars by measuring open circuit potential and instantaneous power-off potential. It is proposed that the protection current density should be less than 20 mA/m^2 during the ICCP protection process. Bahekar et al. [10] used weight loss method and open circuit potential to evaluate the cathodic protection efficiency of steel bars in concrete. They found that the corrosion rate of steel bars decreased with the increase of protection current density. At present, few scholars have used ICCP to prevent the corrosion of galvanized steel wire. In order to cut in, ICCP is adopted for galvanized steel wire under the coupling effect of prestress and corrosion conditions. By analyzing the variation law of mechanical properties of galvanized steel wire under different working conditions, the reasonable protection potential of steel wire ICCP is explored, which provides reference for the corrosion protection of steel wire.

2. Prestressed steel wire ICCP test

The test galvanized steel wire was produced by China Baowu Iron and Steel Group Co., Ltd., with a length of 100 cm, a diameter of 5 mm, a tensile strength of 1,680 MPa, and a surface galvanized layer thickness of 0.2 mm. The chemical composition is (expressed in mass fraction): C 0.82% -

0.85%, Si 0.12% -0.21%, Mn 0.60% -0.90%. In order to make the steel wire reach a high corrosion level in a short time, the steel wire was immersed in a chlorine salt solution for accelerated corrosion for 720 h. The test solution was configured according to the specification artificial atmosphere corrosion test-salt spray test [11]. The composition of the solution is as follows (expressed in mass fraction) : NaCl 5%, H_2O 94.37%, $CuCl_2 \cdot 2H_2O$ 0.03%, CH_3COOH 0.60%.

The safety factor of the cable structure is greater than 2.5 [12], and the allowable stress of the steel wire should be less than 40 % of the standard strength (f_{ptk}), that is, the applied prestress should be less than 670 MPa. Therefore, the stress-free state (0 MPa), the maximum stress state (670 MPa) and the stress state between them (335 MPa) are selected as the prestress applied to both ends of the steel wire. According to the research on steel wire ICCP [13], the steel wire was divided into four groups in this test. One group did not take protection (hereinafter referred to as class A steel wire), and the other four groups were set to -1,000 mV, -1,100 mV, -1,200 mV (hereinafter referred to as class B, C, D steel wire). The galvanized steel wire was used as the cathode, the aluminum plate was used as the auxiliary electrode, and the copper sulfate electrode was used as the reference electrode. The prestressed cathodic protection system device is shown in Fig. 1, and the equipment required for the experiment is shown in Table 1. For reduce the discreteness of the experimental results, four groups of parallel samples were carried out under the same experimental conditions. Two groups were used for appearance observation and tensile test, and the other 2 groups were used for fatigue test.

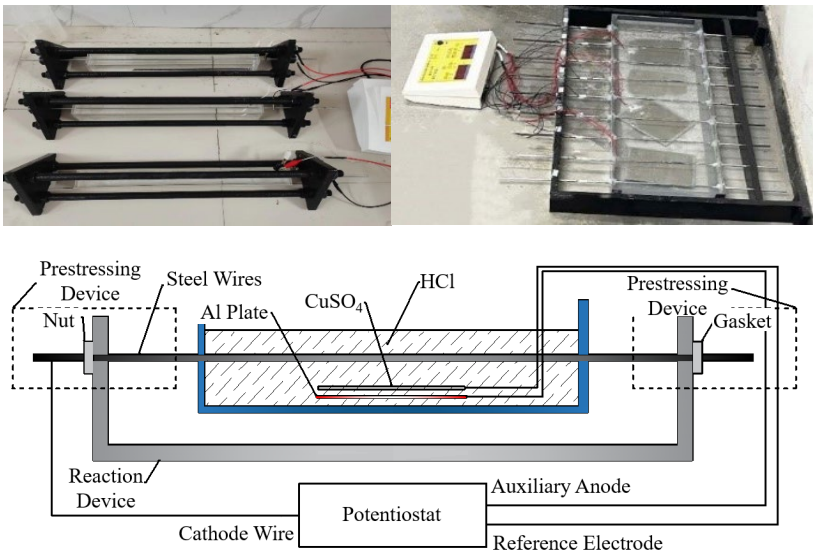

Fig. 1. Prestressed Cathodic Protection System Device

Equipment	Type	Technical Parameter	Quantity
Constant potential rectifier	DJS-292B	/	1
Electronic balance	SL500ZN	Accurate to 0.01 g	1
Graduated scale	/	Accurate to 0.01m	1
High-definition digital Camera	Nikon D7000	/	1
Electron microscope	SK2700H	/	1
Calomel reference electrode（SCE）	/	Saturated KCl filling solution	4
Universal testing machine	WAW-1000	Maximum load：1,000kN	1

Table 1. Test equipment and materials

After the test, the macroscopic appearance of the steel wire was observed by a high-definition digital camera, and the steel wire with the most serious corrosion, that is, the steel wire under the 670 MPa prestressing condition, was selected. The electron microscope was used to amplify 20 times and 50 times, respectively, for microscopic appearance observation. After the corrosion appearance of the steel wire is recorded, the rust is removed, the weight of the steel wire is weighed by an electronic balance, and the average corrosion rate of each steel wire is calculated. The WAW-1000 universal testing machine was used to carry out uniaxial tension on the steel wire, and the tensile test was carried out according to the requirements of the Metallic Materials Tensile Test Part 1 [14]. After obtaining the load-displacement curve of the steel wire, the ultimate load, yield load and elongation were further obtained. The steel wire with a prestress of 670 MPa was selected for the fatigue test, which was carried out by SDS-250 electro-hydraulic servo fatigue test machine. The upper limit of alternating stress was set to 0.4 f_{ptk} (f_{ptk} is the standard value of tensile strength), the stress amplitude was 360 MPa, and the frequency f was 10 Hz [15]. The test was stopped when the number of steel wire fracture or fatigue reached 2 million times, and the fracture appearance of the steel wire fracture was analyzed by electron microscope scanner.

3. Results and conclusions

There are a large number of rust layers and pits on the surface of unprotected steel wire, and the area of rust layer increases with the increase of prestress (Fig. 2). The application of protective potential can effectively delay the corrosion of steel wire (Fig. 3). During the corrosion protection process, the sensitivity of steel wire ductility to ICCP is higher than that of steel wire strength, which is mainly reflected in that ICCP significantly increases the elongation of steel wire, but the increase of yield load and ultimate load is relatively limited (Fig. 4).

ICCP significantly improves the fatigue life and ductility of steel wires, and the reasonable protection potential is -1,100 mV. The more positive protection potential than -1,100 mV cannot provide sufficient corrosion protection for the steel wire, and the more negative protection potential than -1,100 mV will lead to hydrogen embrittlement of the steel wire and reduce its fatigue life and ductility (Fig. 5). The application threshold of the protection potential should be controlled within a reasonable protection range to avoid over-protection of the steel wire.

The corrosion protection of the galvanized steel wire is jointly participated by the galvanized layer SACP and the external power supply ICCP [16]. The electron transport of SACP is driven by the potential difference between different metals, and the electron transport of ICCP is driven by the protection potential. The contribution of the two to the corrosion protection of the steel wire changes with the development of the corrosion process.

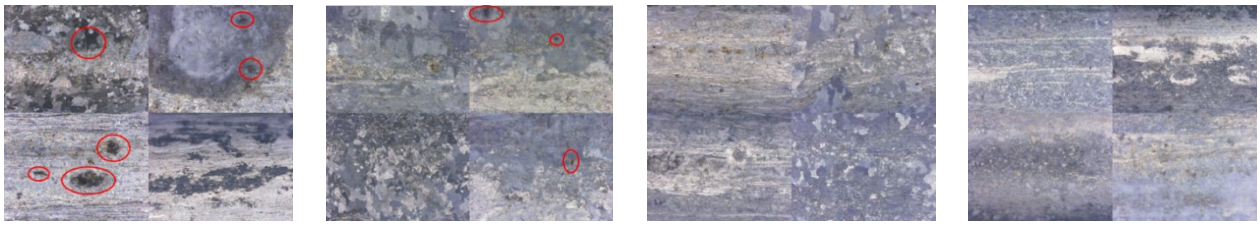

(a) Class A steel wire (b) Class B steel wire (c) Class C steel wire (d) Class D steel wire

Fig. 2. Micromorphology of steel wire

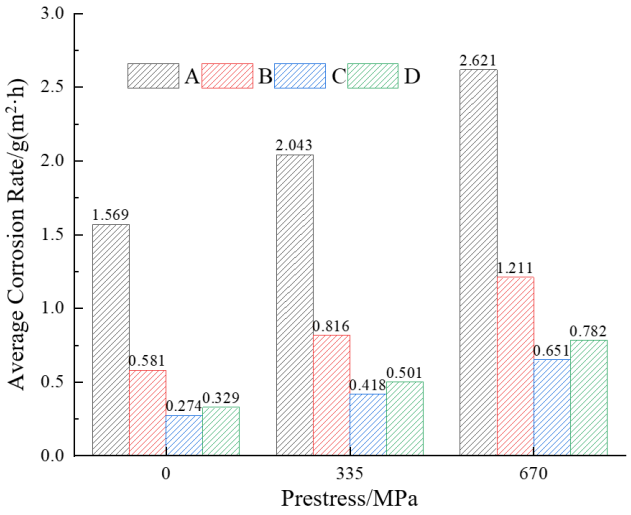

Fig. 3. Average corrosion rate

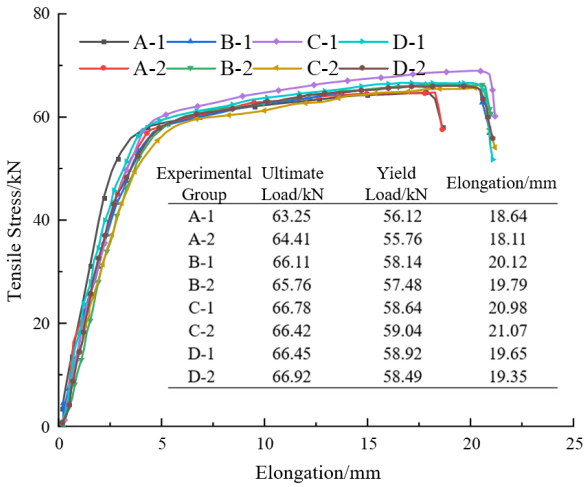

Experimental Group	Ultimate Load/kN	Yield Load/kN	Elongation/mm
A-1	63.25	56.12	18.64
A-2	64.41	55.76	18.11
B-1	66.11	58.14	20.12
B-2	65.76	57.48	19.79
C-1	66.78	58.64	20.98
C-2	66.42	59.04	21.07
D-1	66.45	58.92	19.65
D-2	66.92	58.49	19.35

(a) 0 MPa

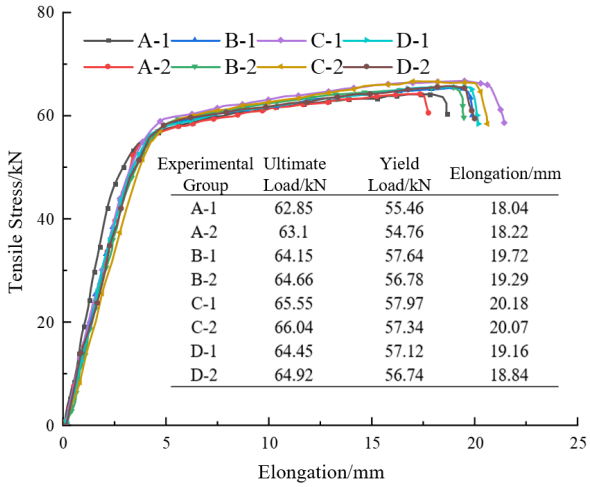

Experimental Group	Ultimate Load/kN	Yield Load/kN	Elongation/mm
A-1	62.85	55.46	18.04
A-2	63.1	54.76	18.22
B-1	64.15	57.64	19.72
B-2	64.66	56.78	19.29
C-1	65.55	57.97	20.18
C-2	66.04	57.34	20.07
D-1	64.45	57.12	19.16
D-2	64.92	56.74	18.84

(b) 355 MPa

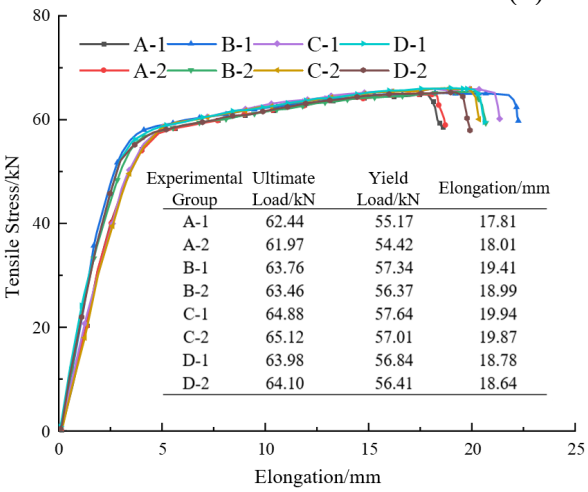

Experimental Group	Ultimate Load/kN	Yield Load/kN	Elongation/mm
A-1	62.44	55.17	17.81
A-2	61.97	54.42	18.01
B-1	63.76	57.34	19.41
B-2	63.46	56.37	18.99
C-1	64.88	57.64	19.94
C-2	65.12	57.01	19.87
D-1	63.98	56.84	18.78
D-2	64.10	56.41	18.64

(c) 670 MPa

Fig. 4. Load-deformation curves

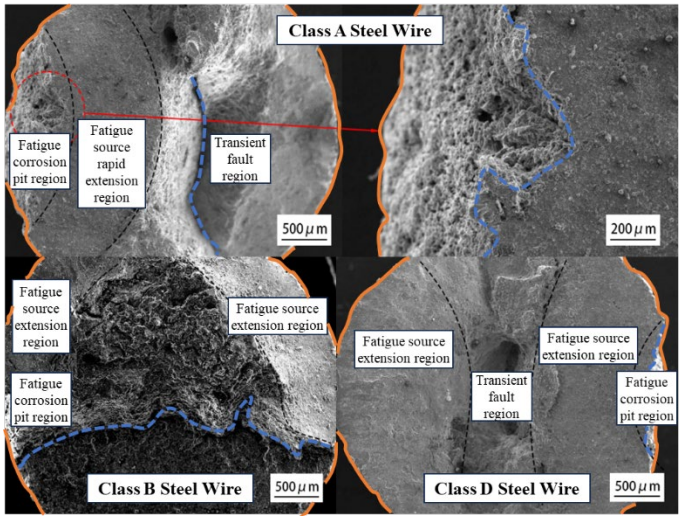

Fig. 5. Cross section of steel wire

4. Acknowledgements

The research presented in this paper has received funding from the National Natural Science Foundation of China (Grant no. 52178273); the Innovation and Development Joint Project of Natural Science Foundation of Chongqing, China (Grant no. CSTB2023NSCQ-LZX0077); the Natural Science Foundation of Chongqing (Grant no. cstc2021jcyj-msxmX1159); the Chongqing Talent Plan Project (Grant no. cstc2022ycjh-bgzxm0124); the Chongqing Graduate Research Innovation Project (Grant no. CYB23244); the Team Building Project for Graduate Tutors in Chongqing (Grant No. JDDSTD2022003); the Science and Technology Demonstration Project of the Chinese Ministry of Transport of safe and intelligent construction of Fengjian Expressway in the Three Gorges Reservoir Area (Grant No. 2021-581); the State Key Laboratory of Mountain Bridge and Tunnel Engineering, Chongqing Jiaotong University (Grant No. SKLBT- 2216).

5. References

[1] Yao G W, Liu Ch Y, Wu G Q. Study on cable corrosion damage mechanism under acid rain environment load coupling [J] Journal of Chongqing Jiaotong University (Natural Science Edition), 2016, 35 (6): 6-10.

[2] Lu Y Y, Hu J Y, Li S, et al. Active and passive protection of steel reinforcement in concrete column using carbon fibre reinforced polymer against corrosion [J]. Electrochimica Acta, 2018, 278: 124-36.

[3] Wu J X, Liu E D. Research on the causes of bridge suspender fracture and early warning technology [J] Western Transportation Science and Technology, 2013, (5): 51-5.

[4] Tang Y, Ding Sh. Intelligent monitoring technology for cathodic protection potential of long oil and gas pipelines [J] Natural gas industry, 2022, 42 (5): 46.

[5] Liu Y W, Zhang Y. Numerical analysis of flow accelerated corrosion of ship hull in seawater [J] Journal of Harbin Engineering University, 2021, 42 (1): 145-51.

[6] Hou Y, Tian Y, Zhao Zh P, et a.l Research progress in corrosion and protection of aluminum alloys for offshore engineering [J] Surface Technology, 2022, 51 (5): 1-14.

[7] Guo B, Qiao G, Li D, et al. Multi-species reactive transport modeling of electrochemical corrosion control in saturated concrete structures including electrode reactions and thermodynamic equilibrium [J]. Construction and Building Materials, 2021, 278.

[8] Su MN, Wei LL, Liang HS, et al. Fatigue behaviour and design of corroded reinforced concrete beams intervened by ICCP-SS [J]. Composite Structures, 2021, 261.

[9] Wei L, Zhu J H, Dong Z, et al. Anodic and Mechanical Behavior of Carbon Fiber Reinforced Polymer as a Dual-Functional Material in Chloride-Contaminated Concrete [J]. Materials, 2020, 13(1): 222.

[10] BAHEKAR P V, GADVE S S. Impressed current cathodic protection of rebar in concrete using Carbon FRP laminate [J]. Construction and building materials, 2017, 156: 242-251.
[11] The State Administration of Market Supervision and Administration and the State Standardization Administration Commission Corrosion test in artificial atmosphere Salt spray test: GB/T 10125-2021 [S] 2021.
[12] Code for Design of Highway Cable stayed Bridge: JTG/T 3365-01-2020 [S] 2020.
[13] Pengyu, C. Research on impressed current cathodic protection method of bridge cable structure [D]. Chongqing Jiaotong University, 2020.
[14] The State Administration of Market Supervision and Administration and the State Standardization Administration Commission Metallic materials Tensile test Part 1: Room temperature test method: GB/T 228.1-2021 [S] 2021.
[15] State Administration of Market Supervision and Administration, China National Standardization Administration Hot dip galvanized or zinc aluminum alloy steel wire for bridge cables: GB/T 17101-2019 [S] 2019.
[16] Guowen Y, Xuanbo H, Jiawei L, et al. Test Study of the Bridge Cable Corrosion Protection Mechanism Based on Impressed Current Cathodic Protection[J]. Lubricants, 2023, 11(1): 30-30.

AN NOVEL INVERSE TECHNIQUE OF IMPACT FORCE IDENTIFICATION FOR MAJOR COMPOSITE STRUCURES

Junjiang Liu[1], Shengchuan wu[1], Baijie Qiao[2]
[1] State Key Laboratory of Rail Transit Vehicle System(RVL), Southwest Jiaotong University, China
[2] School of Mechanical Engineering, Xi'an Jiaotong University, China

1. Introduction

Composite materials are being widely employed for the manufacture of aircraft components, because of their high specific strength and stiffness, as well as light weight properties[1]. However, composite structures are very susceptible to foreign object debris such as hail, birds and tools. Furthermore, the composite structures are subjected to barely visible impact damage, like delaminations and debonding. Such damage is difficult to detect and can seriously impair structural integrity[2]. The consequent reduction in residual strength may lead to fatal accidents. The knowledge of impact forces including the impact location and time-history can offer significant information for structural health monitoring, fatigue analysis and the design of composite structures[3]. Generally, it is hard to measure impact forces directly. For one thing, installing force transducers may change the dynamic properties of composite structures. For another, the locations of impact events are not known in advance. Impact Force Identification(IFI) technique is getting favored to obtain the impact forces using measured responses, such as acceleration, displacement and strain. Such method is relatively easy to operate and changes little to the monitored structure.

In this contribution, we establish a novel non-convex group sparse regularization model of IFI problem regularized by the mixed $\ell_{2,p}(0<p<1)$-norm. This model considers not merely sparsity but also the group sparsity of impact forces. In this model, non-convex functions are employed to promote sparsity and improve amplitude accuracy. Besides, group sparsity structure is encoded to decrease the DOF in the solution. The novel mixed model enables simultaneously localizing impacts and reconstructing impact time-history with a single sensor herein. It is well-known that the non-smooth and non-Lipschitz $\ell_{2,p}$ minimization is a great challenge in algorithm design. We resolve the model using the Alternating Direction Method of Multipliers(ADMM) framework[4]. The ADMM separates the original complex problem into easy-to-solve sub-problems: the least squares one and the non-convex regularized one. One can obtain a closed-form solution of the least squares sub-problem. To cope with the non-convex regularized sub-problem, i.e., the $\ell_{2,p}$ regularized minimization for any value of $p(0<p<1)$, we derive a generalized group thresholding operator. Notably, the ADMM solver owns high scalability to solve the models with any group structure configuration including the fully overlapping group structure used in this paper.

In Section 2, we state the inverse problem formulation of IFI which is described as a set of linear equations in time domain. And then we elaborate the novel non-convex group sparse regularization model of IFI and the way to solve it. Experimental validations of the proposed method are respectively conducted on a large composite fuselage structure in Section 3.

2. Inverse analysis and algorithms

Generally, for a multi-input and multi-output(MIMO) LTI system, the responses gathered by n_r sensors can be calculated by[5],

$$\begin{bmatrix} \mathbf{x}_1 \\ \mathbf{x}_2 \\ \vdots \\ \mathbf{x}_{n_r} \end{bmatrix} = \begin{bmatrix} \mathbf{H}_{1,1} & \mathbf{H}_{1,2} & \cdots & \mathbf{H}_{1,n_f} \\ \mathbf{H}_{2,1} & \mathbf{H}_{2,2} & \cdots & \mathbf{H}_{2,n_f} \\ \vdots & \vdots & \ddots & \vdots \\ \mathbf{H}_{n_r,1} & \mathbf{H}_{n_r,2} & \cdots & \mathbf{H}_{n_r,n_f} \end{bmatrix} \begin{bmatrix} \mathbf{f}_1 \\ \mathbf{f}_2 \\ \vdots \\ \mathbf{f}_{n_f} \end{bmatrix} \tag{1}$$

then, (1) can be rephrased compactly as,

$$\mathbf{x} = \mathbf{H}\mathbf{f} \tag{2}$$

with the output vector $\mathbf{x} \in \Re^{n_r \cdot N}$, the transfer matrix $\mathbf{H} \in \Re^{n_r \cdot N \times n_f \cdot N}$, and the input vector $\mathbf{f} \in \Re^{n_f \cdot N}$.

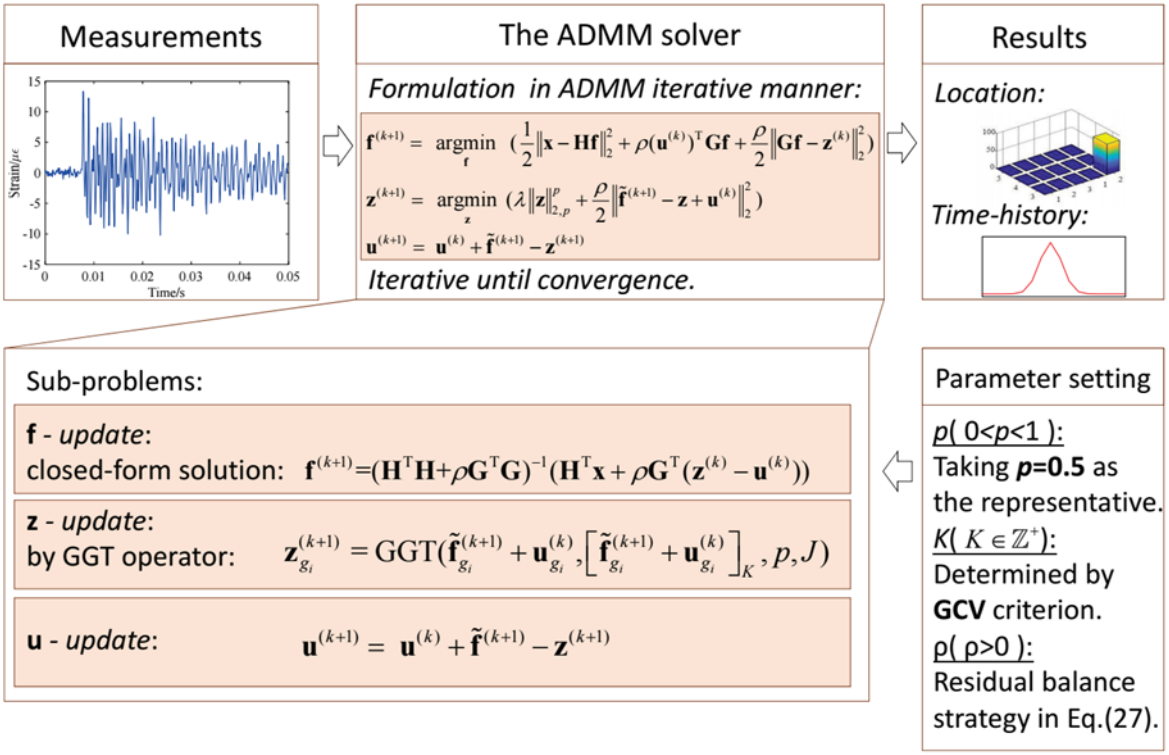

Figure 1 Overview of the proposed method for impact force identification. Taking the strain responses as the inputs, the ADMM solver can output the impact localization and time-history reconstruction results at the same time.

Computing $\mathbf{f}$ with a given $\mathbf{x}$ can be reduced to the process of deconvolution. Generally, the transfer matrix $\mathbf{H}$ is ill-conditioned, and the measurement vector $\mathbf{x}$ is known but with errors. Therefore, a naive inverse or pseudo-inverse solution easily runs far away from the exact one. Regularization technique commonly helps compute a good approximate solution by adding more correct prior information. The more prior information is encoded in regularization, the fewer DOFs there are in the solution, and the better identification performance can be obtained. Therefore, in this paper we propose a novel regularization technique as follows,

$$\underset{\mathbf{f}}{\text{minimize}}\frac{1}{2}\left\|\mathbf{x}-\mathbf{H}\mathbf{f}\right\|_2^2+\lambda\left\|\mathbf{f}\right\|_{2,p}^p \tag{3}$$

Finally, we give the resolution procedure of the proposed method of impact force identification as depicted in Figure 1.

3. Results and conclusions

In this section, we further validate our methods in a laboratory operating condition. As in the simulation study, $\ell_{2,p}$ is also compared to several state-of-the-art methods, namely ℓ_p regularization, group-Lasso and Lasso methods. A composite laminated structure has the same geometry as the plate in the simulation, and also 3×3 locations are monitored as depicted in Figure 2.

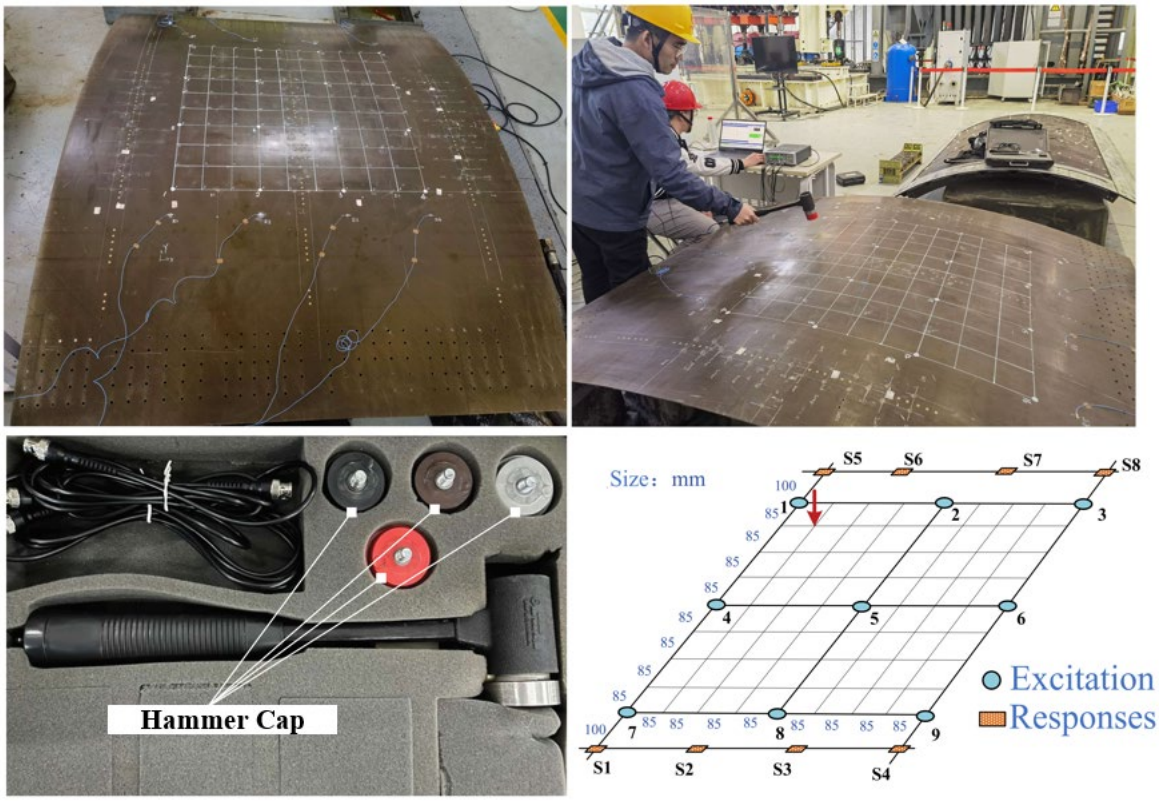

Figure 2 The composite structure under experimental test.

We use the responses from the single sensor S3 to identify the impact force acting on an potential location. The impact localization and time history reconstruction are accomplished simultaneously. Also, $p=0.5$ is adopted here for $\ell_{2,p}$ and ℓ_p methods. Figure 3 provides the localization results of four methods. $\ell_{2,p}$ can precisely localize the impact. $\ell_{2,1}$ is comparable to $\ell_{2,p}$ to some extent but the identified impact force of $\ell_{2,1}$ has an underestimated amplitude. The other two methods without group sparsity tend to generate false impacts on the non-impact locations. Form Figure 4, one can find that the impact time-history reconstructed using $\ell_{2,p}$ can almost perfectly fit the referenced one.

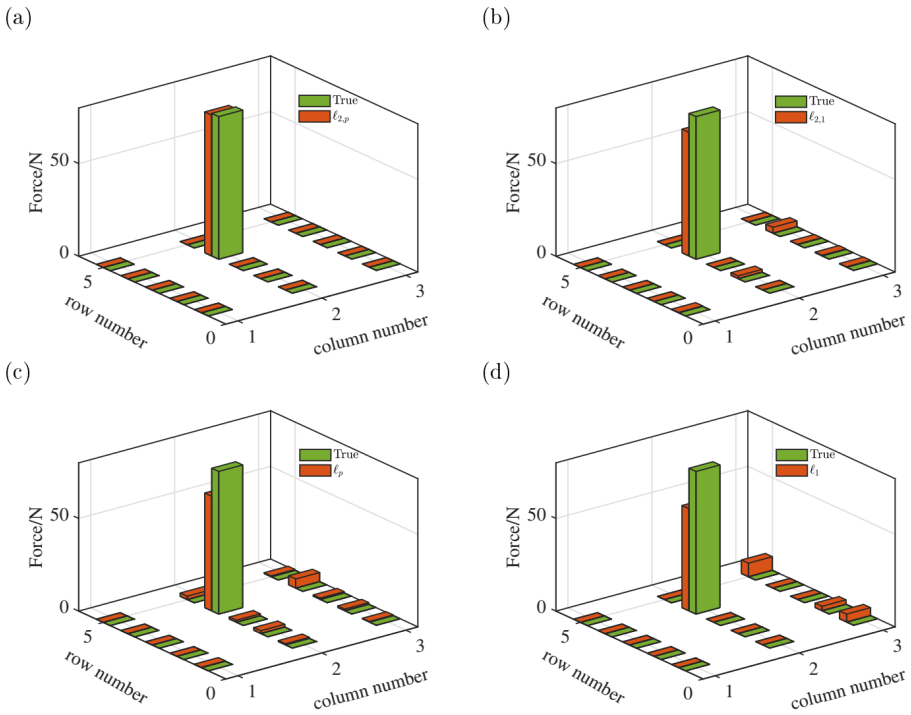

Figure 3 Localization results in experimental study of: (a) $\ell_{2,p}(p=0.5)$, (b) group Lasso, (c) $\ell_p(p=0.5)$ and (d) Lasso. Methods without group sparsity produces identified results with more false impacts at non-impact locations.

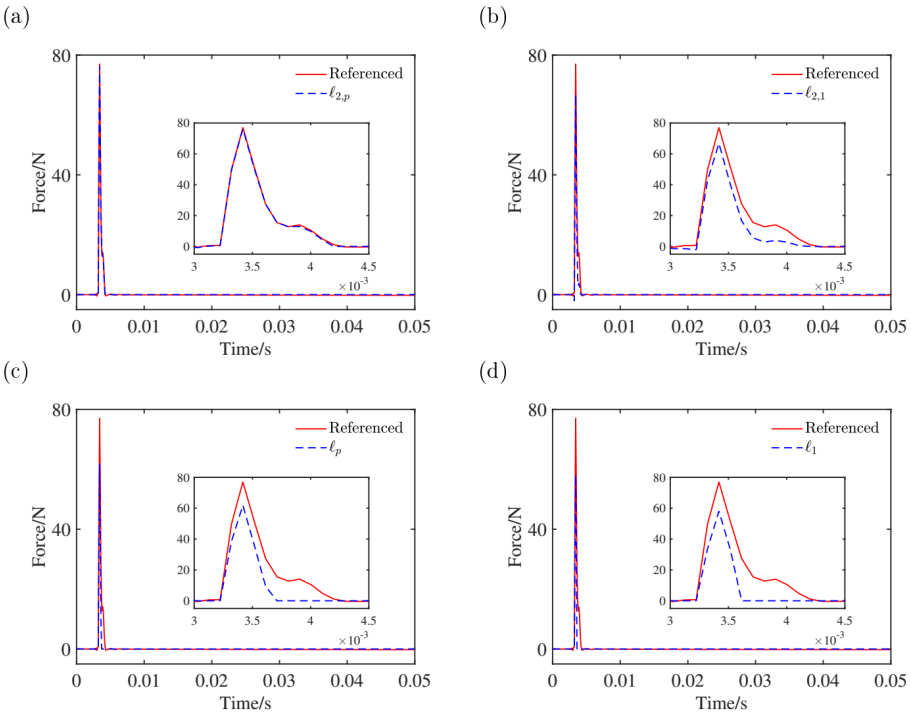

Figure 4 Time-history reconstruction results in experimental study of: (a) $\ell_{2,p}(p=0.5)$, (b) group Lasso, (c) $\ell_p(p=0.5)$ and (d) Lasso. The proposed method produces estimations with best impact-force profile in this case.

4. Acknowledgements

The research presented in this paper has received funding from the independent project of State Key Laboratory of Rail Transit Vehicle System(2025RVL-T19)

5. References

[1] De Oliveira R, Ramos C A, Marques A T. Health monitoring of composite structures by embedded FBG and interferometric Fabry–Pérot sensors[J]. Computers & structures, 2008, 86(3-5): 340-346.

[2] Baker A A. Composite materials for aircraft structures[M]. AIAA, 2004.

[3] Davies G A O, Olsson R. Impact on composite structures[J]. The Aeronautical Journal, 2004, 108(1089): 541-563.

[4] Boyd S, Parikh N, Chu E, et al. Distributed optimization and statistical learning via the alternating direction method of multipliers[J]. Foundations and Trends® in Machine learning, 2011, 3(1): 1-122.

[5] Liu J, Qiao B, Wang Y, et al. Non-convex sparse regularization via convex optimization for impact force identification[J]. Mechanical Systems and Signal Processing, 2023, 191: 110191.

Experimental Techniques for Materials Characterization with special focus on Instrumented Indentation Test: to microstructure, degradation and residual stresses

SURFACE CHARACTERIZATION OF PLASMA-TREATED 316L PRODUCED BY L-PBF

E. Bolli[1], S. Kaciulis[1], A. Lanzutti[2], A. Mezzi[1], R. Montanari[3], A. Palombi[3], N. Picco[2], F. Sordetti[2], E. Vaglio[2], A. Varone[3], C. Verona[3]

[1]ISMN-CNR, P.O. Box 10, 00015 Monterotondo Stazione, Rome, Italy
[2]Polytechnic Department of Engineering and Architecture, University of Udine, Via delle Scienze 208, 33100 Udine, Italy
[3]Department of Industrial Engineering, University of Rome "Tor Vergata", Via del Politecnico 1, 00133 Roma, Italy

1. Introduction

To improve wear resistance of austenitic stainless steels, low-temperature carburizing treatments are required. Among them, plasma-assisted carburizing showed promising results and has been employed to treat 316 L produced through Laser Powder Bed Fusion (L-PBF). The result of treatments carried out for 7 hours, in gas mixtures containing different amounts of CH_4 and H_2, is the formation of a layer of expanded austenite (S-phase) covered by a Diamond-Like Carbon (DLC) over-layer [1]. Tribological tests demonstrated that the DLC over-layer has detrimental effects on wear resistance [2]. To prevent its formation, shorter treatments with soaking time ranging from 30 to 120 minutes in 2.5 % CH_4 plus H_2, have been carried out. The mixture chosen for these experiments is the one leading to best wear behaviour [3]. Atomic Force Microscopy (AFM), X-ray diffraction (XRD), Raman spectroscopy were employed for the microstructural examination of the samples.

2. Materials and methods

316L samples, cut from blocks 3D printed with the strategy described in [1], have been plasma-treated in a microwave plasma enhanced chemical vapour deposition reactor in an atmosphere of 2.5 % CH_4 plus H_2, for 30, 45, 60, 90 and 120 minutes.

X-Ray Diffraction (XRD) measurements were made by using Mo-Kα radiation (λ = 0.07093 nm) in step-scanning mode with steps of 0.005° (2θ degrees) and counting time of 5 s per step. The amount of carbon in the S-phase C_γ (wt%) was determined by the means of the Ridley's equation:

$$a_\gamma = a_{0\gamma} + \alpha C_\gamma \tag{1}$$

where $a_{0\gamma}$ and a_γ are the lattice parameters of the untreated austenite and S-phase, respectively, and the constant α = 0.0044 nm/wt%.

Raman spectra were collected at room temperature and in air by employing a laser wavelength of 785 nm. AFM images were acquired in dynamic force mode to identify the presence of the DLC.

3. Results

In XRD spectra (Fig. 1 a) the peaks {111} and {200} of treated samples present a shift towards lower angle, due to the variation of the lattice parameter a_γ, caused by an excess of C in interstitial positions. From Eq. (1), the carbon content is 2.3 - 2.4 wt.% for all the samples, suggesting that the formation of S-phase occurs even after short treatments. Up to 120 minutes of treatment no DLC can be detected by Raman spectroscopy (Fig 1 b).

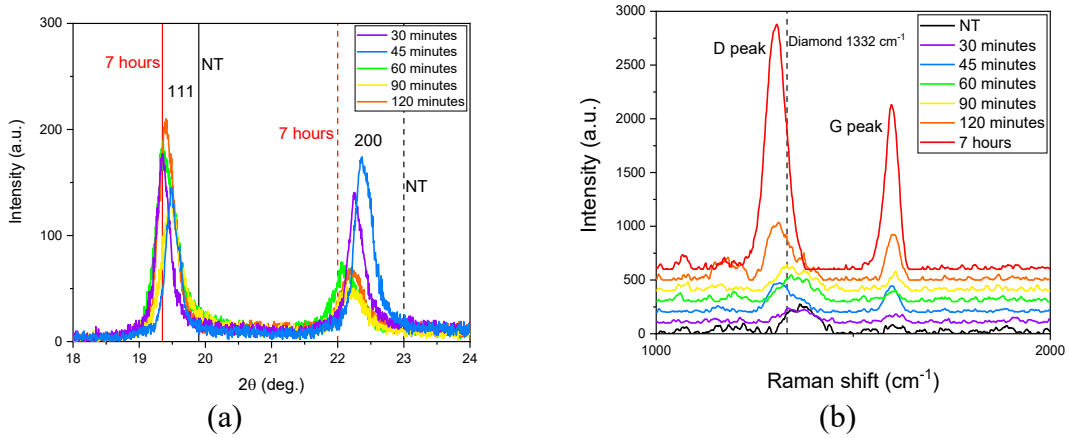

Fig. 1. XRD (a) and Raman (b) spectra of samples treated for increasing time up to 120 minutes.

AFM images in Fig. 2 (a-b-c-d) confirm data from Raman spectroscopy, namely only traces of DLC are observed in samples treated up to 120 minutes.

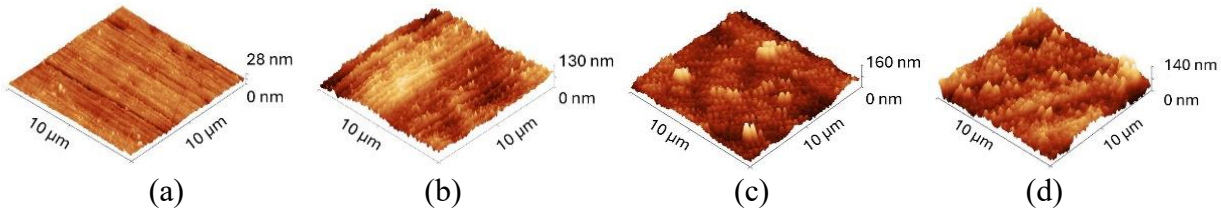

Fig. 2. AFM images of the surface of the as-received sample (a) and after 90 (b), 120 (c) minutes and 7 hours (d) of treatment.

4. Conclusions

The main results of this work can be summarized as follows.
(i) The S-phase forms in the first stages of the treatment: after 30 minutes the C content is comparable to that obtained after 7 hours.
(ii) After the S-phase reaches is C saturation limit, the C atoms can no longer enter the steel matrix and start to deposit on the surface to form a DLC over-layer that grows with increasing treatment time.
(ii) The conditions to optimize the wear resistance are the following: plasma gas atmosphere of 2.5 % CH_4 + H_2 and treatment for 90 minutes.

5. References

[1] R. Montanari, A. Lanzutti, M, Richetta, J, Tursunbaev, E. Vaglio, A. Varone, C. Verona (2022). Plasma Carburizing of Laser Powder Bed Fusion Manufactured 316 L Steel for Enhancing the Surface Hardness. *Coat*, **12**, 258.

[2] E. Bolli, S. Kaciulis, A. Lanzutti, A. Mezzi, R. Montanari, A. Palombi, F. Sordetti, E. Vaglio, A. Varone, C. Verona (2024). Surface characteristics and tribological behavior of 3D-printed 316 L steel after plasma assisted low temperature carburizing. *Surf and Coat Technol*, **477**.

[3] A. Palombi, R. Montanari, A. Varone, C. Verona, E. Bolli, S. Kaciulis, A. Mezzi, A. Lanzutti, F. Sordetti, E. Vaglio (2024) 3D-printed 316 L stainless steel: optimization of low temperature plasma assisted carburizing. *Metallurgia Italiana*. **115**, 25–31.

ELASTIC MODULUS OF POROUS MATERIALS: MODELS AND EXPERIMENTS

M. Richetta[1], A. Palombi[1], A. Varone[1]
[1] Department of Industrial Engineering, University of Rome Tor Vergata, Rome, Italy

1. Introduction

Porous materials are extensively used in many engineering applications and the knowledge of their elastic characteristics is of fundamental relevance in industrial design. Some models which consider the porosity as an ideal regular microstructure and the relative equations describing the Young's modulus vs. porosity have been considered (see Fig. 1a). The values predicted by the models have been then compared to Mechanical Spectroscopy (MS) data collected by investigating different metals (aluminium and titanium alloys prepared by Additive Manufacturing, sintered steel and tungsten).

2. Materials and methods

The MS results were obtained by using an automated vibrating reed analyzer (VRA 1604) with bar-shaped samples (28 mm x 7 mm x 0.46 mm), mounted in cantilever, excited by flexural vibrations and operating in conditions of resonance (resonance frequency in the range of kHz) under a 10^{-6} mbar pressure and at a strain amplitude of 10^{-6}. The dynamic modulus E was determined from the resonance frequency *f* by means of the following relationship:

$$E = \left(\frac{2\pi\sqrt{12}}{m^2}\right)^2 f^2 \rho \frac{L^4}{h^2} \Omega \qquad 1)$$

where $\Omega = 1.000 + 6.585\left(\frac{h}{L}\right)^2$ is a geometrical correction factor that becomes ≈ 1 if L/h > 20, m is a constant depending on the vibration mode, h the thickness of the probe, L its length, and ρ the density of the material.

3. Results and conclusions

The results show that the values of dynamic modulus of different metallic materials given by MS are in good agreement with data from tensile tests [1].

The values of the relative modulus $E_r = E / E_0$, i.e., the ratio between the elastic modulus E of the porous material and the modulus E_0 of the same pore-free material, predicted by different models are similar for materials with low porosity ($p < 0.2$) and isolated pores whereas they strongly diverge if $p > 0.2$ and interconnected pores are present. Moreover, such models fail to correctly describe the elastic behavior of materials also with low porosity ($p \approx 0.1$) like in sintered steels if the pores have a preferred orientation and an irregular shape (Fig. 1b).

On these grounds, it is concluded that, in the case of materials with irregular shape of pores, a different approach may be considered by means of FEM simulations based on the 3D reconstruction

of real spatial microstructures obtained from tomography techniques employing either X-ray or FIB/SEM.

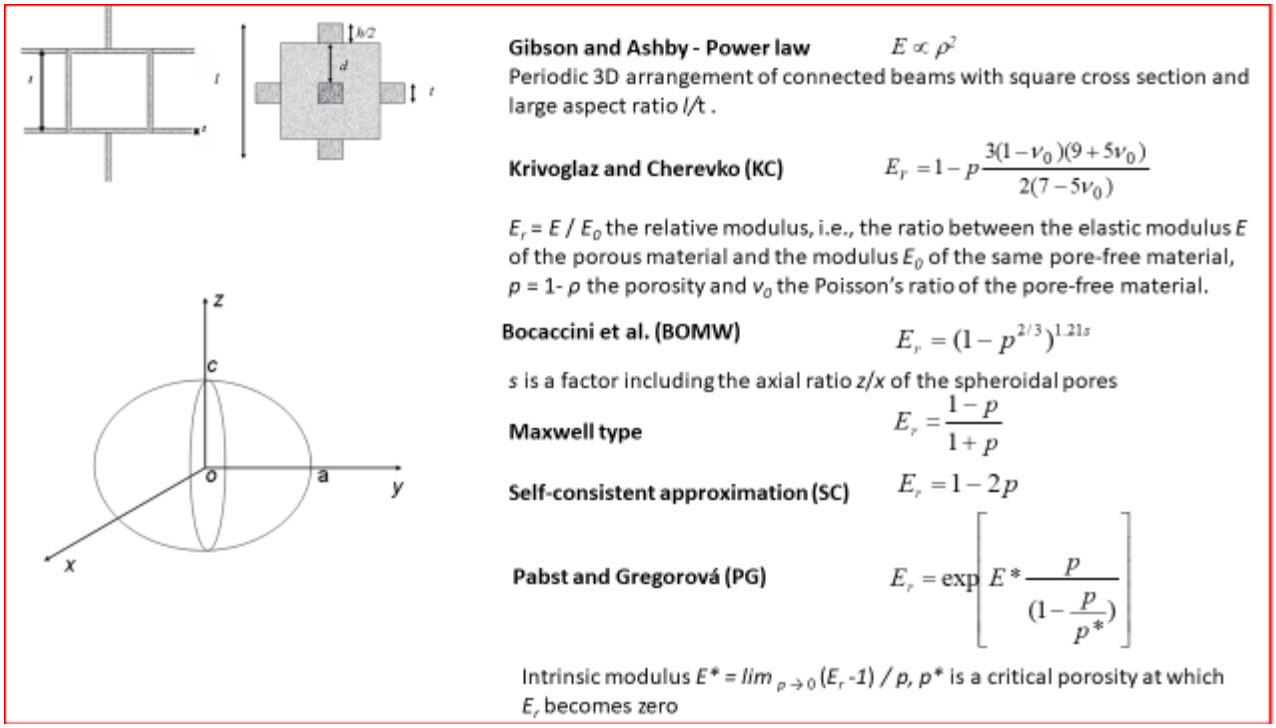

(a)

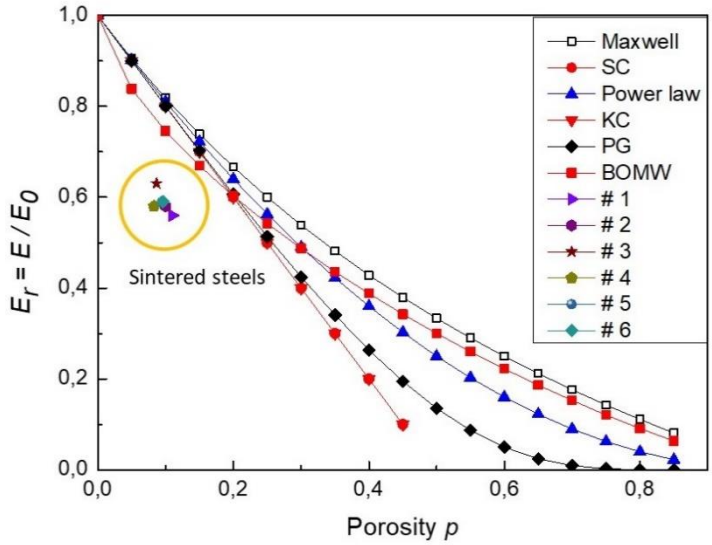

(b)

Fig. 1. Models describing the relationship between modulus and porosity (a). Trends of *Er* vs. porosity *p* calculated with the following expressions: Maxwell-type approximation, self-consistent (SC) approximation, power law, Krivoglaz and Cherevko (KC), Pabst and Gregorova (PG), and Bocaccini et. al. (BOMW) in the specific case of spherical pores (b).

4. References

[1] M. Richetta, A. Varone (2021) A focus on dynamic modulus: effects of external and internal morphological features. *Metals*, **11**, 40.

6-11 July 2025 ICEM21 Bologna
21st International Conference on EXPERIMENTAL MECHANICS

ENGINEERING APPLICATIONS OF FIMEC TEST

R. Montanari[1], A. Varone[1]
[1] Department of Industrial Engineering, University of Rome Tor Vergata, Rome, Italy

1. Introduction

FIMEC (Flat-top cylinder Indenter for Mechanical Characterisation) is an instrumented indentation test that was originally developed for measuring the mechanical properties of irradiated materials, in particular the candidates for applications in future nuclear fusion reactors [1-2]. A cylindrical punch of sintered tungsten carbide (diameter =1 mm and axial length = 1.5 mm) is commonly employed in FIMEC test but punches of smaller size (down to 0.5 mm) are also used, depending on the material characteristics and the zone to examine. The test provides applied load vs. penetration depth curves and can be performed at different temperatures from -196 °C up to +600 °C. The properties which can be determined from FIMEC test are yield stress, elastic modulus, ductile to brittle transition temperature (DBTT), surface creep and stress relaxation [3]. It allows to determine the local properties of mechanical parts of complex geometry. Therefore, it has been used to determine the mechanical properties of metallic materials in several applications of industrial interest. Some selected case studies are presented.

2. Case studies

(i) *Evaluation of the local mechanical properties in a carter of complex geometry*

Components of complex shape are commonly produced through foundry processes and not homogeneous cooling rates often give rise to different local mechanical characteristics in different zones of the same piece. The case presented here is that of a carter made of aluminum EN-AB46100 alloy. About one hundred of FIMEC tests have been performed in different areas of the carter (Fig.1) to determine the local yield stress and on this basis the die sections have been suitably modified to get more homogeneous mechanical properties.

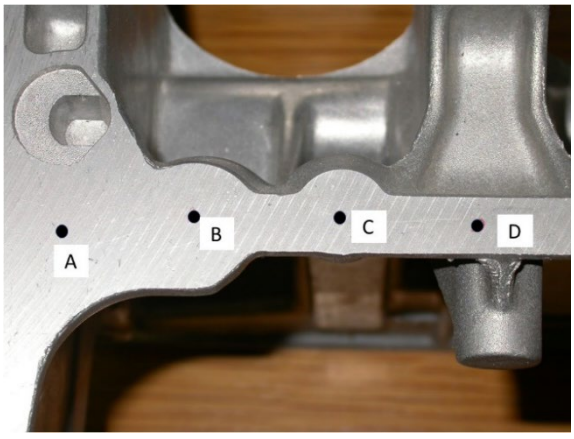

Fig. 1. Several FIMEC tests have been performed in different positions of a carter to determine on a local scale the yield stress.

(ii) *Measure of the local mechanical properties of MZ and HAZ in welded joints*

FIMEC test has been used to assess the quality of GTAW welded joints of the duplex stainless steel UNS S31803 with biphasic structure [4]. After welding the joints have been heat treated at 1050 °C for 600 s (ASTM A928/A928M. Fig. 2 shows how yield stress and microstructure change in different zones of the welded joint.

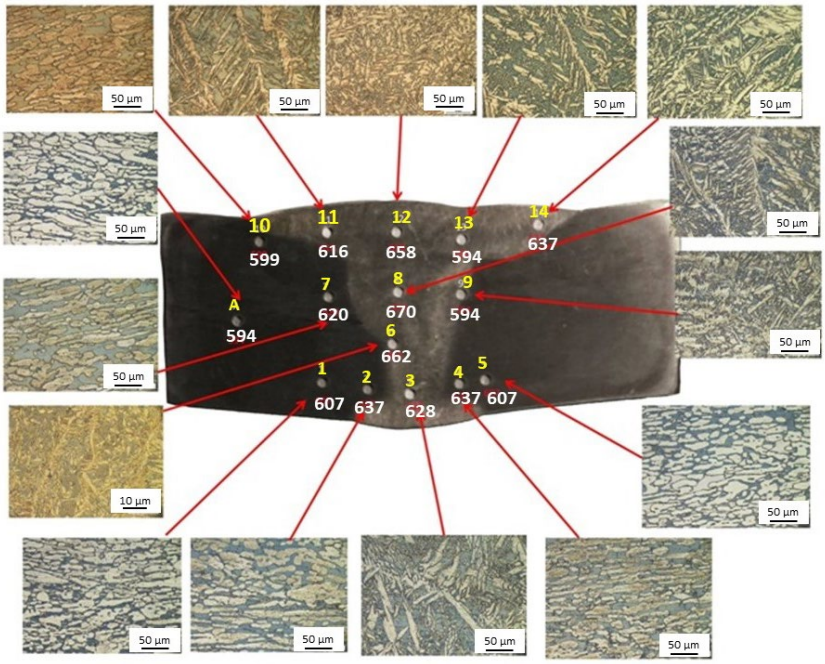

Fig. 2. Local microstructure of the joint in areas close to the positions where 15 FIMEC indentation tests were performed (yellow). For each position the yield stress is reported (white).

(iii) *Yield stress in longitudinal and transverse sections of AZ31 alloy subjected to four ECAP passes*

Billets obtained by Equal Channel Angular Pressing (ECAP) usually exhibit anisotropic mechanical behavior, however owing to their shape it is quite difficult to perform tensile tests by using samples cut along the transverse direction. The results of FIMEC tests on both sections showed that yield stress is always higher (~ 10 %) in the transverse section.

3. Conclusions

The case studies demonstrate the great versatility of the FIMEC test which provides information not available by employing conventional experimental techniques such as tensile, bending and hardness tests. On the basis of theoretical knowledge and large amount of experimental data FIMEC has become a technique mature for application on large scale in industrial practice.

5. References

[1] P. Gondi, R. Montanari, A. Sili (1994). Small scale non-destructive stress-strain and creep tests feasible during irradiation. *J. of Nuclear Materials*, **212-215**, 1688-1692.

[2] P. Gondi, A. Donato, R. Montanari, A. Sili (1996). A miniaturized test method for the mechanical characterization of structural materials for fusion reactors. *J. of Nuclear Materials*, **233-237**, 1557-1560.

[3] B. Riccardi, R. Montanari (2004) Indentation of metals by flat-ended cylindrical punch. *Materials Science & Engineering A*, **381/1-2**, 281-291.

[4] G. Angella, A. Fava, R. Montanari, M. Richetta, A. Varone (2017). Flat-Top Cylinder Indenter Examination of Duplex Stainless Steel 2205 after Different Heat Treatments. *Metals*, **7**, 178-191.

ASSESSMENT OF THE INTER-CRITICAL COARSE-GRAIN HEAT AFFECTED ZONE IN WELDED JOINTS OF VANADIUM MICROALLOYED HSLA STEEL

A. Di Schino[1], B.R. Rodriguez-Vargas[1], R. Schmidt[2], G. Stornelli[1], A. Tselikova[2]
[1] *Department of Industrial Engineering (DIN), University of Perugia, Terni, Italy*
[2] *2Vantage Alloys AG, Zug, Switzerland*

1. Introduction

The energy sector requires the development of advanced materials that can withstand extreme operating conditions. High Strength Low Alloy (HSLA) steels meet these requirements due to their high strength/weight ratios, good mechanical properties and excellent weldability [1]. The addition of micro-alloying elements, such as vanadium, promotes the formation of nitrides and carbides, increasing the mechanical strength. The presence of these elements also helps to prevent the formation of brittle microstructural constituents during welding process. In fact, HSLA steels are subjected to extreme thermal gradients during welding, resulting in microstructural changes in the heat-affected zone (HAZ) [2]. The choice of welding process and operating parameters is critical to achieve a high-quality joint. Gas Metal Arc Welding (GMAW) is a versatile process, suitable for several material thicknesses. However, particularly in thick welds where excessive heat input is a problem, special attention must be paid to the HAZ. The high thermal gradients involved in welding lead to partial or complete austenitization in the HAZ, followed by rapid cooling, resulting in the formation of brittle phases [3]. In addition, in multi-pass welds, successive thermal cycles further alter the microstructure of the sub-regions of the HAZ. Of these, the Inter-Critical Coarse-Grain HAZ (ICCGHAZ) is a critical sub-region of the Coarse-Grain HAZ (CGHAZ) that is subjected to further heating in the inter-critical temperature range (between Ac_1 and Ac_3) [4]. Partial austenitization, mainly in pearlite/bainite colonies, occurs in ICCGHAZ. During cooling, these carbon-rich regions transform into perlite/bainite and martensite-austenite (M/A) constituents. Several studies have been conducted to understand the complexity of microstructure of this sub-region [5,6]. The formation of brittle phases, such as M/A, is of particular concern as it can lead to a reduction in the toughness. In addition, the distribution, morphology and volume fraction of this phase is influenced by the chemical elements of the micro-alloy. These characteristics have a direct effect on the mechanical behavior of the entire welded joint. Wu et al. [7] demonstrated that ultrafine ferrite and V(C,N) precipitates, formed during welding, play a significant role in enhancing the toughness of welded joints. V(C,N) precipitates contribute to refining the size of M/A islands to below 1 μm. Furthermore, the carbon content within the M/A islands is reduces, resulting in softening and improved toughness. This study investigates the effect of vanadium addition on the microstructural evolution of the ICCGHAZ of HSLA steel welds produced by robotic GMAW. The results are compared with those of a standard S355 steel of C-Mn composition without microalloying elements.

2. Materials and methods

Steel plates with a thickness of 15 mm were used as base metal (BM) for the welded joints. Table 1(a) shows the chemical composition of the tested steels, S355 steel (EN10025-2) and a variant containing 0.1 wt% of vanadium (V-Variant). ER70S-6 filler wire (1.2 mm diameter) was used for welding. The joints were manufactured by a robotic GMAW process in 1G position, using a V-groove butt joint configuration with a 30° bevel angle and 85% Ar-15% CO_2 shielding gas (18 L/min). Seven weld passes were performed with spray transfer mode. The nominal welding parameters are shown

in Table 1(b). The welded samples were prepared metallographically and analyzed under optical and stereoscopic microscopes after chemical etching (Nital 2% and LePerà reagent). Microhardness tests were performed in the ICCGHAZ (wilson hardness tukon 2500) with a load of 500 gF.

(a)	Chemical composition (wt.%) – Fe to balance			
	C	Mn	V	Si
S355 steel	0.16	1.45	-	0.03
V-Variant	0.16	1.45	0.10	0.03

(b)	Nominal welding parameter				
	Current (A)	Voltage (V)	Welding speed (mm/min)	Wire feed speed (mm/s)	Heat input (kJ/mm)
	160	17	290	450	0.55

Table 1. (a) Chemical composition and (b) Nominal welding parameters

3. Results and conclusions

Figure 1(a) shows the macrostructure of fully penetrated welds, free from defects such as cracks, porosity, or undercuts, with a uniform geometry. The figure also identifies the Weld Zone (WZ) and HAZ, including the ICCGHAZ.

The microstructure of the ICCGHAZ, shown in Figure 1(b), is primarily characterized by bainite (B) with small islands of M/A with both and granular morphologies. The M/A phase is highlighted as white islands by the LePerà etching. As observed in previous studies, the V-Variant contains finely dispersed vanadium precipitates [4]. Compared to S355 steel, the V-Variant exhibits a lower volume fraction of the M/A phase. This is because the presence of V promotes the formation of precipitates, reducing the carbon content available for the development of brittle phases.

The Vickers hardness profile in Figure 1(c) reveals an increase in hardness in the ICCGHAZ compared to the BM (respectively 181 ± 4 HV for S355 steel and 209 ± 6 for V-Variant). In the V-Variant, this increase is attributed to the combined contributions of the M/A phase and the precipitation state. Conversely, the hardness increase in S355 steel is exclusively due to the presence of the brittle M/A phase. In conclusion, in the V-variant, the combination of hard and soft regions in the microstructure, coupled with fine V-rich precipitates, ensures suitable performance under various loading conditions.

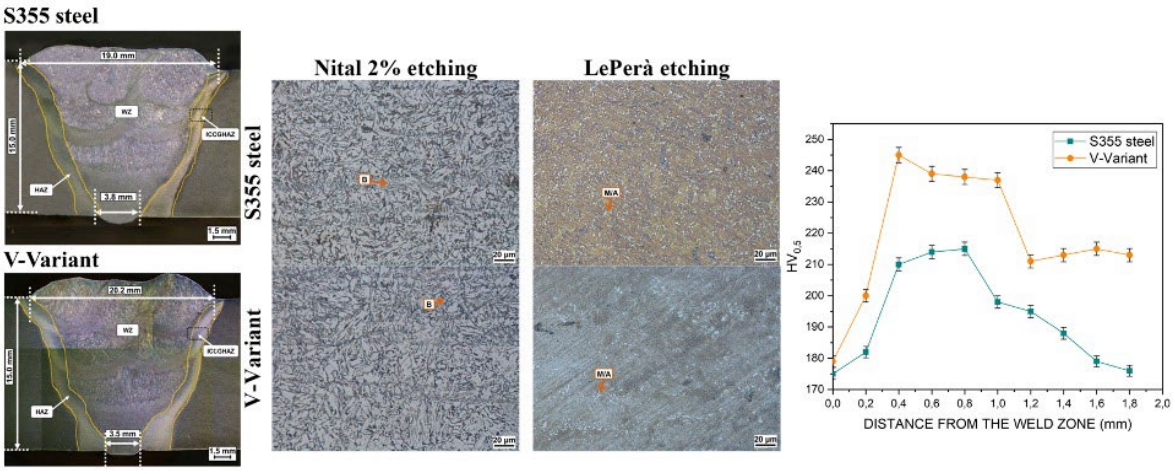

Fig. 1. (a) Macrostructure of the cross-sections of the weld joints, (b) Micrographic analysis of the ICCHHAZ, images obtained by means of Nital-2% and LePerà etchings, (c) Vickers hardness profile of the ICCGHAZ of the welded joints.

5. References

[1] S. Roy, N. Romualdi, K. Yamada, W. Poole, M. Militzer, L. Collins (2022). The Relationship Between Microstructure and Hardness in the Heat-Affected Zone of Line Pipe Steels. *JOM*, **74**, 2395–2401.

[2] I. Miletić, A. Ilić, R.R. Nikolić, R. Ulewicz, L. Ivanović, N. Sczygiol (2020). Analysis of Selected Properties of Welded Joints of the HSLA Steels. *Materials*, **13(6)**, 1301.

[3] B.C. Kim, S. Lee, N.J. Kim, D.Y. Lee (1991). Microstructure and Local Brittle Zone Phenomena in High-Strength Low-Alloy Steel Welds. *Metall. Trans.* A, **22**, 139–149.

[4] G. Stornelli, A. Tselikova, D. Mirabile Gattia, M. Mortello, R. Schmidt, M. Sgambetterra, C. Testani, G. Zucca, A. Di Schino (2023). Influence of Vanadium Micro-Alloying on the Microstructure of Structural High Strength Steels Welded Joints. *Materials*, **16(7)**, 2897.

[5] C. Li, Y. Wang, Y. Chen (2011). Influence of Peak Temperature during In-Service Welding of API X70 Pipeline Steels on Microstructure and Fracture Energy of the Reheated Coarse Grain Heat-Affected Zones. *J Mater Sci*, ***46***, 6424–6431.

[6] J.-B. Ju, W. Kim, J. Jang (2012). Variations in DBTT and CTOD within Weld Heat-Affected Zone of API X65 Pipeline Steel. *Mater. Sci. and Eng.: A*, ***546***, 258–262.

[7] H. Wu, D. Xia, H. Ma, Y. Du, D. Gao, X. Gao, L. Du (2022). Study on Microstructure Characterization and Impact Toughness in the Reheated Coarse-Grained Heat Affected Zone of V-N Microalloyed Steel. *J. Mater. Eng. Perform.,* **31**, 376–382.

ELECTROSPARK DEPOSITION AND ULTRASONIC PEENING TREATMENT ON Al-Si10-Mg SELECTIVE LASER MELTED PARTS: MICROSTRUCTURE AND PROPERTIES

P. Leo[1], G. Renna[1], A. De Luca[1], R. Nobile[1], C. Casavola[2], V. Moramarco[2], S. Carone[2], M.A. Attolico[2]

[1] Department of Innovation Engineering, University of Salento, Lecce, Italy
[2] Department of Mechanics Mathematics and Management, Politecnico di Bari, Bari, Italy

1. Introduction

Electro spark deposition (ESD) is an innovative "green" technology suitable to be used for metal coating deposition and for repairing surface cracks in metallic components [1-2]. The high cooling-rates involved in the process, produces coating with a very fine microstructure and features similar to that observed in Selective Laser Melting (SLM) process [1-3]. Coating deposition or repair procedure can be further improved by Ultrasonic Peening Treatment (UPT). UPT, based on shot peening technology, is one of the most promising methods for the cold treatment of metallic materials because induces surface compressive residual stresses, reducing also the roughness and porosity. As a consequence, corrosion resistance, fatigue strength and overall fatigue life of metallic materials are increased [4]

This study intends to evaluate the potential of ESD and UPT technologies for surface modification of Al-Si10-Mg SLM parts. Surface modifications, both for repairing or coating, should serve to extend the life in service of the parts promoting sustainability.

2. Materials and methods

In this study, Al-Si 10-Mg ESD coatings have been applied on homologue substrate. The substrate (AB) has been processed by SLM using a Renishaw AM 400 and the Meander strategy with scan rotation of 45 degrees between consecutive layers, power equal to 375W, scan speed to 2000mm/s and exposure time 50µs. For the ESD, the power level was set to 135W and the deposition has been executed with crossed orthogonal mode between consecutive layers. For UPT application, the intermediate available level of ultrasonic Energy was employed and the time of treatment was set equal to 30s.The microstructure has been characterized by Nikon Ephipot 200 Optical Microscope (OM) and Zeiss EVO Scanning Electron Microscope (SEM). Porosity analysis has been developed by optical microscope and Image J software. The size of the voids has been evaluated and supplied as area percentage. The corrosion resistance was evaluated after grinding the exposed surface using a Gamry Instrument 1010. The measurements were carried out in an aqueous solution of 3.5% NaCl at room temperature. For the roughness evaluation, Fringe projection non contact tecnique was utilized while the residual stress measurements has been evaluated by using the XStress 3000 G3R diffractometer.

3. Results and conclusions

Fig. 1a, shows the microstructure of the coating cross section after Keller etching as result from OM analysis. The typical layer structure developed during each single electrode pass is highlighted. The porosity level (area percentage) has been found equal to 3,3 ± 0,5 %. SEM analysis better defines

the microstructure (Fig.1b). The features of the coating remind those of the Selective Laser Melted substrate [3]. Coarser microstructure due to remelting of the previous layer and cellular microstructure can be observed (Fig.1b). Not any cracks or discontinuities have been detected along the interface length with the substrate (Fig.1b). After processing the coating with UPT, significant evolution has been observed at the coating surface due to plastic deformation and eutectic phase fragmentation. Moreover, the porosity level of the coating (area percentage) has been reduced to 1,8 ± 0,5 % while the roughness (Ra) decreased from 21.68±0.41 µm to 4.69±0.04 µm. Regarding the residual stress analysis (Fig.2), the ESD coating shows high tensile stress while, after UPT, surface compression stress has been detected with an average value of approximately -90 MPa. Finally, corrosion resistance of the substrate was unaffected by ESD coating but slightly improved after UPT.

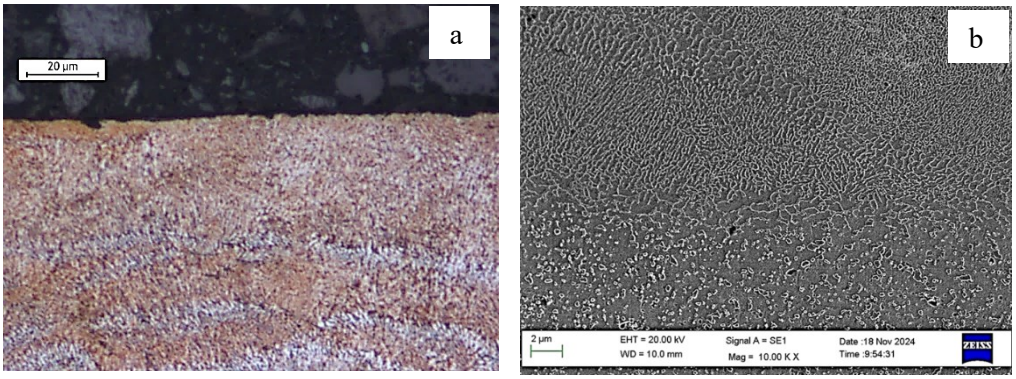

Fig. 1: microstructure of ESD coating as result from OM (a) and SEM analysis (b)

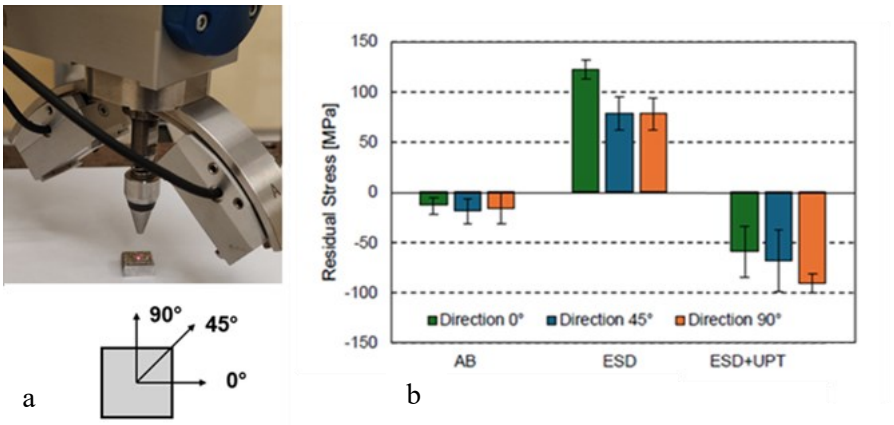

Fig.2: Definition of measurement directions (a) and comparison of normal residual stress values measured along the three measurement directions for each type of sample analyzed (b).

Acknowledgements

The research presented in this paper has received funding from Italian Ministry of University and Research under the Program PRIN PNRR-2022 (P2022ZJF9R)

5. References

[1] P. Leo, G. Renna (2019). Coatings via Electrospark Deposition in A357 alloy: microstructure and defectiveness. *La metallurgia italiana.*, **111**, 22-31.

[2] P. Leo, G. Renna, G. Casalino (2017). Study of the direct metal deposition of AA2024 by electrospark for coating and reparation scopes. *Appl. Sci.*, **7**, 1-15

[3] P. Leo, G. Renna, N.Soni, F. De Pascalis, T. Primo, A. Del Prete (2024). On the Effect of Exposure Time on Al-Si10-Mg Powder Processed by Selective Laser Melting, *Metals*, **14**, 1–18.

[4] M. Malaki, H. Ding (2015). A review of Ultrasonic peening treatment, *Mat.Des.*, **87**, 1072-1086.

DELAMINATION AND FRACTURE OF PLY-ANGLE LAYERED COMPOSITES

J. Botsis[1] and G. A. Pappas[2]
[1]EPFL, School of Engineering, Lausanne, CH-1015 Switzerland
[2]ETHZ, Dept. of Mechanical and Process Engineering, Zurich, CH-8092 Switzerland

1. Introduction

Multidirectional laminates (MD) are often used in components of advanced structures. Several works in the literature show that delamination of these materials is complicated with a multitude of fracture and damage phenomena dependent on constituent materials, ply-angle and loading conditions, amongst others. While the standardized methods [1] are adequate for composite materials with a unidirectional layout (UD), they have not been very successful in MD layouts [2]. This is evident by the inconsistency on published data in the literature. What complicates the accurate and realistic measurements of fracture toughness in layered composites, is the intrinsic presence of fiber bridging during delamination fracture in both UD and MD layouts, with the latter often lacking symmetric crack fronts, but also show crack growth on different interlaminar planes.

In this presentation, experimental results on fracture toughness at initiation and resistance to fracture evolution during delamination and collateral intra-ply fracture on DCB specimens based on [2], are discussed. The following antisymmetric layouts are considered (+30°//−30°, +45°//−45° and +60°//−60°). The results are compared with (0°//0°) layout. The standardized data reduction methods are used to evaluate the Energy Release Rate (ERR). In addition, the ERR is calculated with the use of the path-independent *J*-integral using recorded loads and the crack mouth opening angle at the point of load application.

2. Materials and methods

In this work, DCB specimens were manufactured with Gurit™ SE 70, unidirectional, carbon/epoxy prepreg system. Overall, four groups of specimens, each one defined by the interface angle, were produced i.e., 0°//0°, +30°//−30°, +45°//−45° and +60°//−60° ("//" indicates the location of the initial pre-crack plane). The 0°//0°, 20-ply thick, UD was produced and defined as a reference for interlaminar fracture testing of the antisymmetric interfaces, varying both in orientation and number of plies. The number of plies and their sequences were designed so that the flexural compliances of all specimens' beams, of width B and thickness H, were highly similar, but also reducing the bowing of the crack front, relating to minimal skewness. Details of the specimen preparation and the material properties can be found in [2,3]. The total ERR, J_{total}, is considered as the sum of ERR at initiation, $J_{I,i}$, and the contribution of bridging, $J_{I,b}$, measured based on the reaction load, P, and crack mouth opening angle at the point of load application, θ, i.e., $J_{total} = J_{I,i} + J_{I,b} = \left[2P\sin\left(\theta/2\right)/B\right]$. This calculation is insensitive to inaccuracies on the measurement of the crack length (especially with bowed crack fronts observed in MD laminates) and independent of any compliance fitting as well as any geometrical non-linearities,

3. Results and conclusions

The load-displacement curves for the different interfaces and the corresponding ERR are shown in Fig. 1. Notice the discontinuous crack propagations. During loading, delamination did not grow smoothly, but in intervals of slow growth followed by jumps and arrests.

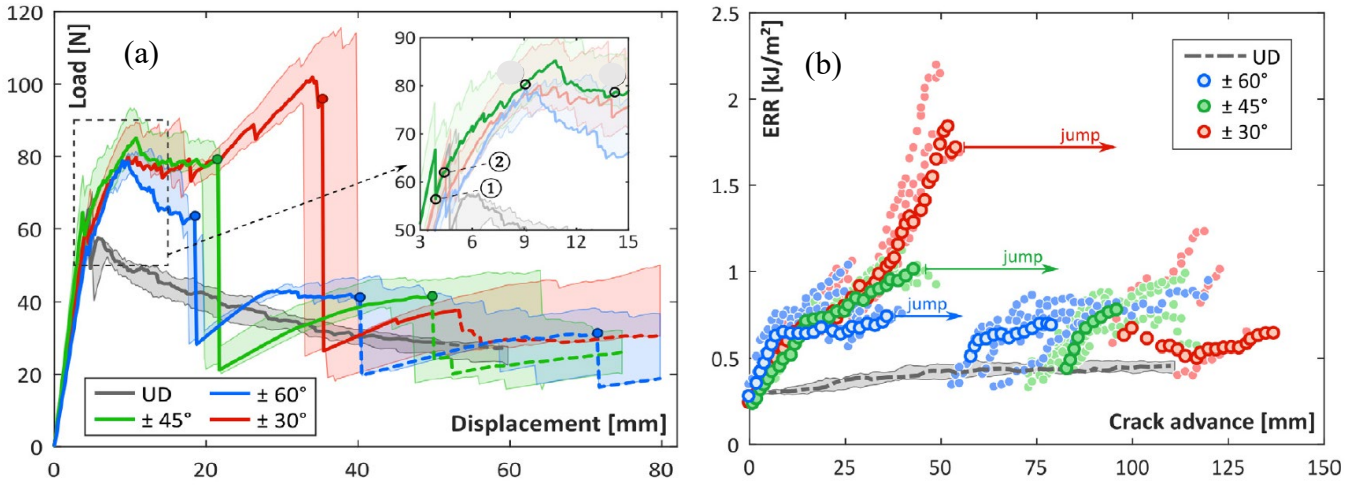

Fig. 1. (a) Load-displacement curves for four interfaces and (b) evolution of ERR vs crack advance. Lines in (a) show representative specimen and shaded zones indicate the range of results of all specimens. The dots in (a) show the point of the first crack jump and the dashed lines indicate the data after the second jump [2]. The circles in (b) correspond to the representative specimens in (a).

The insert in Fig. 1(a) indicates the pop-in point and the point of nonlinearity considered for the *J*-values at initiation. Interestingly, the initiation values are, $J_{I,i} \cong 0.29$ kJ/m^2, independent of the interface angle. Overall, it is important to notice that in the tested MD layouts, the maximal loads and resistance to delamination are well higher than the corresponding UD data. Delamination of MD laminates under Mode II and mixed Mode I and II demonstrate similar trends [3,4].

4. Acknowledgements

The research presented herein has received funding from the EPFL, Lausanne, Switzerland.

5. References

[1] ASTM Standard D5528-01, Standard Test Method for Mode I Interlaminar fracture Toughness of Unidirectional Fiber-Reinforced Polymer Matrix Composites, ASTM International; 2007.

[2] C. Blondeau, G. Pappas and J. Botsis (2019). Influence of ply-angle on fracture in anti-symmetric interfaces of CFRP laminates, *Compos. Struct.*, 216, 464–476.

[3] G. Pappas and J. Botsis (2016). Intralaminar fracture of unidirectional carbon/epoxy composite: experimental results and numerical analysis, *Int. J. Solids Struct.*, 85-86, 114-124.

[4] M. Herráez, N. Pichler, G. Pappas, C. Blondeau and J. Botsis (2020). Experimental and Numerical Modelling on Angle-Ply Laminates under Remote Mode II Loading, *Compos. - A: Appl. Sci.*, 134, 105886.

[5] N. Pichler, M. Herráez and J. Botsis (2020). Mixed-mode fracture response of anti-symmetric laminates: Experiments and modelling, *Compos. B: Eng.*, 197, 108089.

INFLUENCE OF HYGROSCOPIC ABSORPTION ON THE RESILIENCE OF EPOXY MATRIX COMPOSITE REINFORCED WITH CERAMIC PARTICLES

M.D.D Boudiaf[1], R. Roubache[2] , M.K Harouche[1] and S. Benhamouda[1]

[1] Ecole Militaire Polytechnique, Laboratoire Génie des Materiaux, Bordj el Bahri, Alger, Algerie
[2] Institute for Research and Development of Weapon Systems and Mobility Means/1RM

1. Introduction

Polymer Matrix Composites (PMO) are widely used in various industrial applications today[1]. These materials offer unique mechanical properties that allow for lightweight structures, thereby increasing energy efficiency[2]. However, the hygro-thermo-mechanical environment to which these structures are exposed can impact their durability[3] . Indeed, water absorption by hydrophilic organic matrices can lead to a reduction in the polymer network's rigidity and cause swelling.

This matrix expansion, counteracted by typically hydrophobic reinforcements, can result in significant internal mechanical stresses that may be detrimental to the structure[4]. Aging of polymers can lead to slow changes (reversible or irreversible) in the material's properties due to their inherent instability or environmental influences. Generally, water diffuses into the molecular network, acting as a plasticizer, lowering the glass transition temperature and affecting the mechanical properties (rigidity modules, fracture properties, etc.)

2. Materials and methods

1. Samples elaboration

Epoxy/kaolin samples were prepared according to an optimized experimental procedure from a previous study to achieve better dispersion and avoid particle agglomeration and sedimentation. The steps of this procedure are as follows: heating the epoxy resin and kaolin powder mixture to 40°C with mixing for 10 minutes at 3000 rpm, then adding the hardener and continuing mixing for 2 min. The mixture is poured into molds and left to dry for 24 hours at room temperature, then cured in an oven at 60°C for 4 hours. Samples with different filler contents (1%, 3%, and 5%) and particle sizes ($d<63$ µm, $63<d<100$ µm, and $100<d<125$ µm) were prepared

2. Experimental methodology

Gravimetric measurements of samples in immersion or in a humid environment are used to monitor the progress of moisture uptake. After different immersion times, water absorption characteristics of the composites are determined by the mass percentage of water absorbed Mt.Impact tests were performed using a pendulum impact tester according to ASTM D256.

3. Results and conclusions

Based on the figures1 , it is clear that the resilince modulus decreases as water absorption increases, until a saturation value is reached. However, this gap gradually narrows with the increase in moisture absorption, up to the saturated state. Moreover, when comparing figures a, b, and c, it is observed that the decrease in Young's modulus is faster for the more heavily loaded composites. This indicates that the difference between the dry and saturated states increases with the loading rate. In the dry state, the most heavily loaded composite shows the highest Young's modulus, whereas in the saturated state, the least loaded composite has the highest value. This inversion occurs approximately halfway through the saturation process.

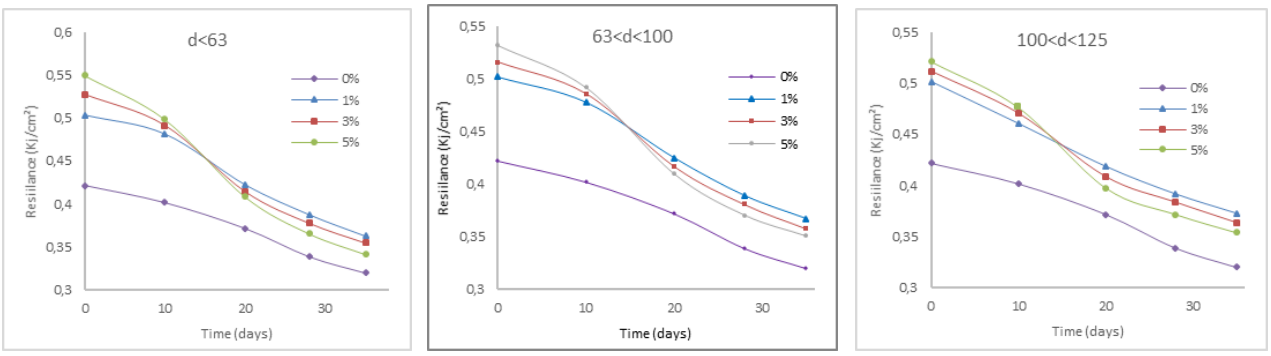

Figure 1 : impact resistance Charpy test of composite materials (epoxy-kaolin) of all models.

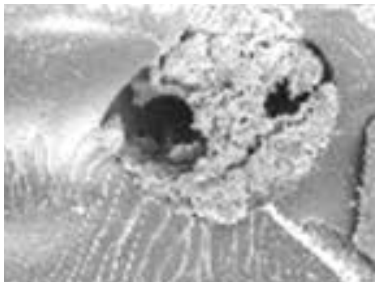

Figure 1: particle deterioration

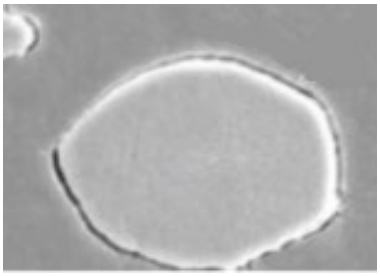

Figure 3: matrix-particle debonding

From 2 and 3 we observe the phenomenas that leads to characteristics loss. In figure 2 we see the total degradation of the kaolin particle caused to water absorbtion. In figure 3 we observe a total matrix-particle decohesion due to volume increase of the matrix caused by water absorbtion.

Conclusion

This study has shed light on the complex interaction between hygroscopic absorption and the mechanical properties of epoxy/kaolin composites. The results highlight the crucial role of powder weight ratio and particle size in determining water absorption behavior and its subsequent impact on the mechanical performance of these materials. The knowledge gained from this research can inform the design and development of epoxy/kaolin composites with enhanced durability and performance in moisture-rich environments.

Key Findings

1. The total surface area of powder particles-matrix interfaces is the main parameter determining water absorption and influencing mechanical characteristics.
2. Increasing the powder ratio increases water absorption and decreases the saturation time limit.
3. Using smaller particles increases water absorption and decreases the hygroscopic saturation time.
4. At saturation the mechanical characteristics decrease with an increase in powder weight ratio.
5. For particle size influence at saturation, an inversion of the studied characteristics is observed. In the dry state, the composite with the smallest particles has the best characteristics. However, with increasing water absorption, the decrease is greater for the composite with the smallest particle size, leading to an inversion at a certain water absorption rate. At saturation, the composite with the smallest particles has the lowest characteristics.

5. References

[1] K.J. Brookes (2016). Maraging steel for additive manufacturing-Philipp Stoll's paper at DDMC., *Met. Powder Rep.*, 71, 149–152.

[2] D. Croccolo, M. De Agostinis, S. Fini, G. Olmi, A. Vranic and S. Ciric-Kostic (2016). Influence of the build orientation on the fatigue strength of EOS maraging steel produced by additive metal machine. *Fatigue Fract. Eng. Mater. Struct.*, 39, 637–647.

[3] D. Croccolo, M. De Agostinis, S. Fini, G. Olmi, F. Robusto, S. Ćirić-Kostić, S. Morača and N. Bogojević (2019). Sensitivity of direct metal laser sintering Maraging steel fatigue strength to build orientation and allowance for machining, *Fatigue Fract. Eng. Mater. Struct.*, 42, 374–386.

[4] D. Croccolo, M. De Agostinis, S. Fini, G. Olmi, F. Robusto, S. Ćirić-Kostić, A. Vranic and N. Bogojevic (2018). Fatigue Response of As-Built DMLS Maraging Steel and Effects of Aging, Machining and Peening Treatments, *Metals*, 8, 1–21.

DYNAMIC MODULUS HIGHLIGHTS MICROSTRUCTURAL CHANGES IN 3D-PRINTED METALS

D. Croccolo[1], R. Montanari[2], G. Olmi[1], A. Palombi[2], M. Richetta[2], A. Varone[2]
[1] Department of Industrial Engineering (DIN), University of Bologna, Bologna, Italy
[2] Department of Industrial Engineering, University of Rome Tor Vergata, Rome, Italy

Corresponding author: Roberto Montanari; Mail: roberto.montanari@uniroma2.it

1. Introduction

Mechanical Spectroscopy (MS) consists in the measurement of dynamic modulus and damping vs. a physical parameter (temperature, strain, magnetic field etc.). The formal theory lying behind MS can be found in the classic book of Nowick and Berry [1] while an exhaustive collection of data on the topic taken from the literature is reported in ref. [2]. MS has proven to be a useful experimental technique for investigating the microstructure of metals and it is important for a variety of engineering fields. MS has the advantage, with respect to quasi-static techniques, of being more sensitive in revealing small microstructural variations. In this work dynamic modulus evolution vs. temperature has been used to investigate microstructural modification occurring in metals prepared by additive manufacturing. Three typical cases are reported.

2. The method

The tests were carried out by means of the automated vibrating reed analyzer (VRA 1604, CANTIL s.r.l, Bologna, Italy). Bar-shaped samples (28 mm × 7 mm × 0.46 mm) were mounted in a cantilever and excited by flexural vibrations. The measurements were made in conditions of resonance with resonance frequency f in the range of kHz, under a 10^{-6} mbar pressure and at a strain amplitude of ~10^{-6}. A single electrode was used to excite and reveal the sample vibrations. The tests were performed by increasing the temperature with a heating rate of 1°C/min. Dynamic modulus E has been calculated from the resonance frequency f by means of the relationship:

$$E = \left(\frac{2\pi\sqrt{12}}{m^2}\right)^2 f^2 \rho \frac{L^4}{h^2} \Omega \qquad (1)$$

where ρ is the density of the material, m = 1.875 a constant depending on the vibration mode, L and h are the length and thickness of the probe, respectively. Ω is a geometrical correction factor that becomes ≈ 1 if $L/h > 20$, as in present experiments.

3. Results

Case 1- Ti6Al4V alloy manufactured by Laser Powder Bed Fusion (L-PBF). As shown in Fig. 1 (a), the material exhibits few pores of large size (40-50 μm). Dynamic modulus E monotonically decreases as temperature increases up to 820 °C (Fig. 1 b). In the plot, E is normalized to the value E_0 at room temperature before the test. After cooling at room temperature E exhibits the original value indicating that the microstructure is stable and did not undergo significant variations during heating.
Case 2- Maraging stainless steel CX prepared by Direct Metal Laser Sintering (DMLS). After printing, the microstructure consists of austenite and martensite and the porosity is very low (99%).

The material was tested in as-built condition and after a heat treatment of 3 hours at 530 °C (Fig. 1 c). In the first test run, the dynamic modulus of the as-built material shows an anomaly starting from ~ 230 °C that is no longer present in the second run. The slight modulus increase can be ascribed to the closure of pores of very small size. On the contrary, after the heat treatment, the steel has a monotonous decrease in the first run and successive runs exhibit substantially the same trend. The decrease of modulus vs. temperature is greater than the one observed in the as-built sample because the microstructure is different: the heat treatment caused the reversion of martensite to austenite. Thus, the treated steel is fully austenitic and austenite has a lower modulus than martensite.

Case 3- AlSi10Mg alloy prepared by Laser Powder Bed Fusion (L-PBF). The material is used in the automotive and aerospace industry and a drawback is represented by the evolution of porosity with temperature. Figure 1 (d) displays the anomalous trend of dynamic modulus in the 1st test run. Instead of a monotonic decrease, modulus starts to increase at ~ 170 °C (point S), a maximum is observed at ~ 210 °C (point F), then it decreases again. This behavior is no longer observed in the successive test runs. After the 1st run the modulus results to be increased of about 7% while the density of the material varies from 2.39 g/cm^3 (as-printed material) to 2.52 g/cm^3. In the successive test runs the density does not change. The test demonstrates that first heating induces the closure of the nanometric pores, as shown by the micrographs in Fig. 1 (e) and (f), taken before and after heating, respectively.

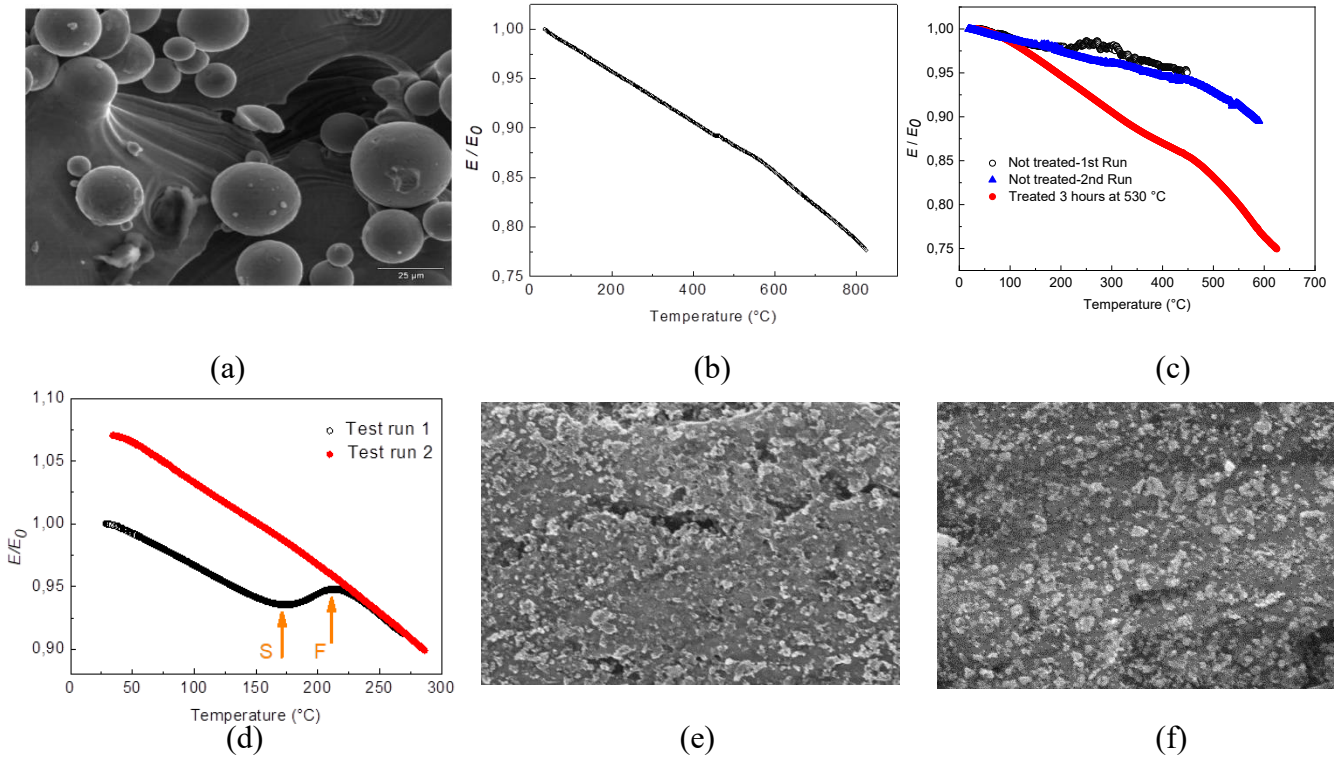

Fig. 1- Ti6Al4V manufactured by L-PBF: pores of large size (a) and E/E_0 vs. T curve (b); maraging steel CX prepared by DMLS: E/E_0 vs. T curve (c); AlSi10Mg alloy prepared by L-PBF: E/E_0 vs. T curve (d) and microstructure before (e) and after (f) the first MS test run.

3. References

[1] A.S. Nowick, B.S. Berry, Anelastic Relaxation in Crystalline Solids, Academic Press, New York, 1972.

[2] M.S. Blanter, I.S. Golovin, H. Neuhäuser, H.-R. Sinning, Internal Friction in Metallic Materials, Springer Series in Materials Science, Springer Verlag, Berlin Heidelberg, 2007.

EuraSEM 6-11 July 2025 ICEM21 Bologna
21st International Conference on EXPERIMENTAL MECHANICS

HIGH RESOLUTION DIGITAL IMAGE CORRELATION MEASUREMENTS OF 316H AUSTENITIC STAINLESS STEEL

C. Allen, H. E. Coules and C. E. Truman
Department of Mechanical Engineering, University of Bristol, Bristol, UK

1. Introduction

A significant research effort is underway to link mesoscale models of materials to continuum models [1,2]. The mesoscale models, which typical consider a domain encompassing 100s of grains, have the potential to incorporate the effects of microstructure and texture on material performance and failure. The continuum models accurately predict bulk performance and structural effects. Linking the two can be accomplished through a numerical solver such as finite element analysis. In the research presented here, the mesoscale model is provided by a Crystal Plasticity Finite Element (CPFE) model [3] which is embedded in a continuum ABAQUS model through a sub-modelling framework. To accomplish this, however, the displacements and strains around the periphery of the mesoscale sub-model are required to enable the correct application of boundary conditions in the ABAQUS model.

This background provides the motivation for the experiments which are reported in this paper. High Resolution Digital Image Correlation (HR-DIC) was used to investigate plastic deformation at the inter- and intra-granular scale. Electron Back Scatter Diffraction (EBSD) maps were collected from one smooth (uniaxial) and one notched (multiaxial) specimen of 316H stainless steel which were subsequently deformed. This permitted grain resolved strain maps to be obtained.

2. Materials and methods

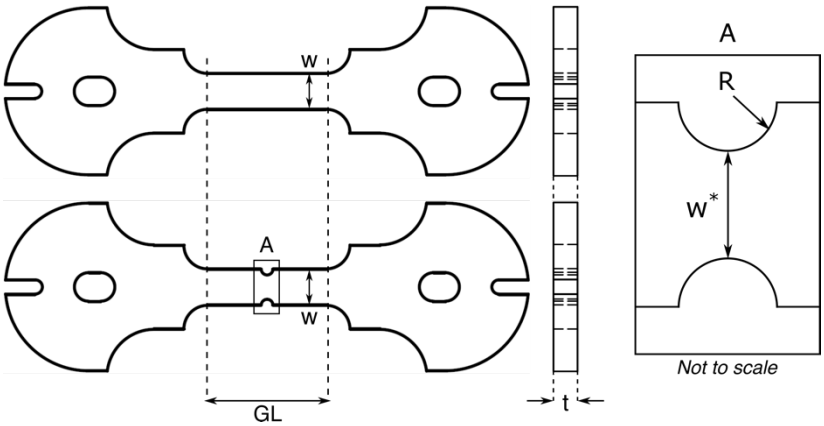

Fig 1. Smooth and notched planar specimens with key dimensions marked

Two specimen geometries were utilised for this experiment. A smooth sided specimen and a specimen with two semi-circular notches on either side of the specimen at the same position along the gauge length, Fig. 1. Both specimens were planar. In-situ tensile tests on both specimen geometries were performed at room temperature using a Tescan and Newtec In-situ Testing (TANIST) system which

consisted of a NewTec Scientific MT1000 tensile testing rig [4] coupled to a TESCAN S8000 FEG-SEM.

3. Results and conclusions

The results show there is reasonable agreement between simulations and experimental results when considering the loading direction strain. A lack of subsurface microstructure information is the most likely reason for discrepancies. The EBSD maps collected are two dimensional slices through the granular morphology. A grain that has a large area on the two-dimensional EBSD map could have a small volume and morphology that has been unaccounted for. Equally, a small grain could have a large volume. This unmeasured relation between granular volume and morphology cannot be implemented in a numerical model.

Nevertheless, HR-DIC has demonstrated it is a powerful technique for investigating deformation at the intragranular level with incredibly high resolution. Notwithstanding the inability to account for out-of-plane morphology, the experimental methodology presented in this paper has provided a significant advancement towards a validated multiscale modelling framework.

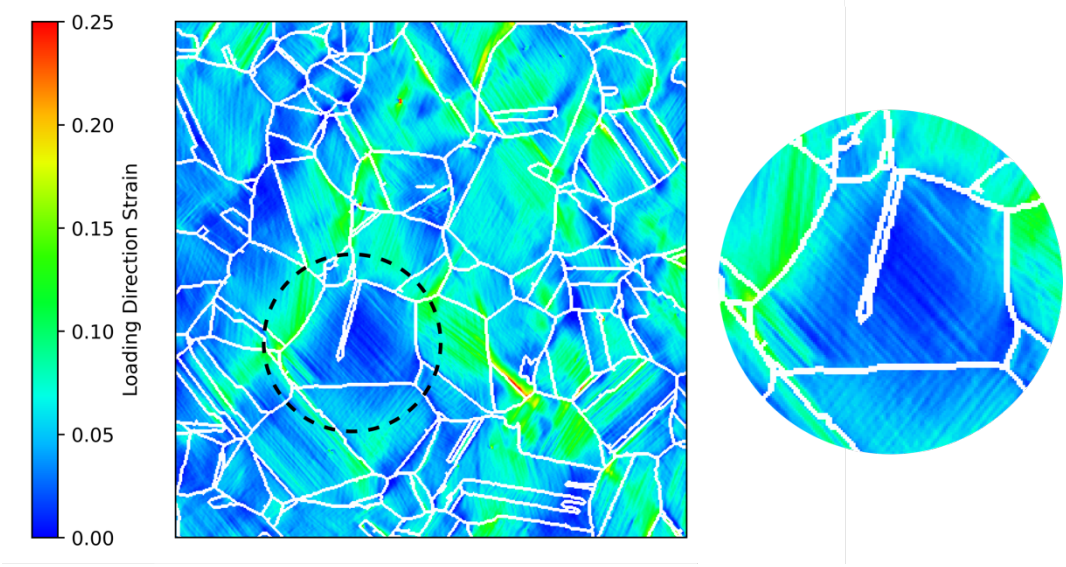

Fig 2. Experimental strain map at a macroscopic engineering stress of 270 MPa for the smooth bar

4. Acknowledgements

The research presented in this paper has received funding from EDF Energy and the Engineering and Physical Sciences Research Council (EPSRC) through the Nuclear Energy Futures Centre for Doctoral Training (CDT).

5. References

[1] C. Allen (2025). Creep-plasticity interaction in high temperature reactor materials, *PhD thesis*.
[2] C. Allen, H. Coules and C. E. Truman (2024). Continuum and crystal plasticity coupled finite element modelling to explore complex loading conditions, *Mats and Fab, Transactions of the ASME.*
[3] D. Agius, A. A. Mamun, C. A. Simpson et al (2020). Microstructure-informed, predictive crystal plasticity finite element model of fatigue-dwells, *Comp. Mats. Sci..*, **183**, 109-115.
[4] NewTec Scientific, MT1000 Information Sheet, 2023. Available: https://newtec.fr/en/mt-1000/.

MULTISCALE INSTRUMENTED INDENTATION TESTS TO DETERMINE THE MECHANICAL PERFOMANCE OF A L-PBF 316L DEPOSIT

G. Maizza[1], A.A.A. Hamed[1], A. Albanese[1], and M. J. Marques[2,3]
[1] Dipartimento di Scienza Applicata e Tecnologia (DISAT), Politecnico di Torino, Torino, Italy
[2] Departamento de Engenharia Química e Biológica, Faculdade de Engenharia, Universidade do Porto, Porto, Portugal
[3] Univ Coimbra, CFisUC, Department of Physics, Coimbra, Portugal

1. Introduction

Laser powder bed fusion (L-PBF) is currently one of the established methods of producing and repairing components with complex geometries made from metallic materials, such as 316L stainless steel [1]. The 316L alloy is currently used extensively in various industrial sectors due to its excellent combination of mechanical properties and resistance to corrosion. During the L-PBF process, the material undergoes very rapid melting, solidification and remelting resulting in steep temperature gradients across the deposit. The deposit is composed of a heterogeneous microstructure and significant residual stresses (RS) [2]. In a previous work the dual nano/macro-scale instrumented indentation tests (nIIT / MIIT) were used to analyze the mechanical properties in a L-PBF 316L deposit under constant peak load for both the nano- and the macro-scale ranges [3]. The importance of L-PBF microstructure and the complexity of the induced RS was also underlined [3]. The current IIT ISO standard [4] is limited to extracting the indentation properties for only RS-free alloys. Hence, it cannot be applicable to additive manufactured materials, thereby alternative IIT approaches are needed. In addition, nanoindentation properties are naturally affected by indentation size effect (ISE) [5]. The same reference reported various ISE models including the Bernhardt's indentation law which is considered in this study. A unique feature of the Bernhardt's law is that it describes the loading indentation curve of many metals and alloys with high accuracy. Another important feature of such law is that its quadratic-term's coefficient can be considered as a load-independent hardness [6].

In this study, an ad-hoc nano-macro IIT mapping method has been applied (Fig. 1a) over the Z-Y plane surface (Z, building direction) of a L-PBF 316L deposit using variable peak loads. Possible effects imparted by the deposit-scale fiber anisotropy on the indentation properties have been investigated. The indentation data from the multi-load IIT map has been post-processed in terms of the standard indentation properties [4] and the Bernhardt's law parameter (denoted as *loading stiffness rate, LSR*). The contour plots of the above indentation properties have been discussed in the effort of establishing a prior correlation between them and the local microstructure and L-PBF parameters.

2. Materials and methods

An initial deposit, 120 mm (length, X direction), 17 mm (width, Y direction) and 17 mm (height, Z direction) was built by L-PBF on a mild steel substrate, 135 mm (length, X), 31 mm (width, Y) and 26 mm (height, Z) using an AISI 316L pre-alloyed powder. The samples for indentation and metallographic examination have been extracted from the original deposit by transversally cutting to X direction using electro-discharge machining. A Y-Z surface region of 5.5 x 5.5 mm^2, centered in the sample, was divided into 4x4 cells (Fig. 1a) with a total of 576 nIITs and 9 MIITs. Each cell contained four 3x3 nIIT matrices carried out with a variable peak load (50, 100, 150, and 200 mN)

and constant loading rate of 120 mN/min and a holding time of 10s. The MIITs were performed at the gap between the cells under three peak loads (50,100, and 150 N), constant loading and unloading rates of 1 and 4 N/s, respectively, and a holding time of 30s.

3. Results and conclusions

The contour plot of the standard indentation hardness (not included) follows the periodic variation of the hardness as hills (yellow,) and valleys (blue) depending on small or large loads respectively which clearly underlines the ISE. As such, this parameter does not allow any correlation between hardness (function of load) and microstructure. Conversely, as the LSR is only marginally affected by ISE, its contour plot (Fig. 1b) tracks the changes of the mechanical properties and performances across the microstructure more accurately. The oscillating residuals (Fig. 1c), defined by the difference in the measured and best-fitted load to depth ratio versus depth (F/h vs. h) curves, reveal how the L-PBF-induced RS are relaxed during the indentation process (via an inflection point in the data). Inevitably, such RS relaxation affects the indentation properties, especially in the macro-range.

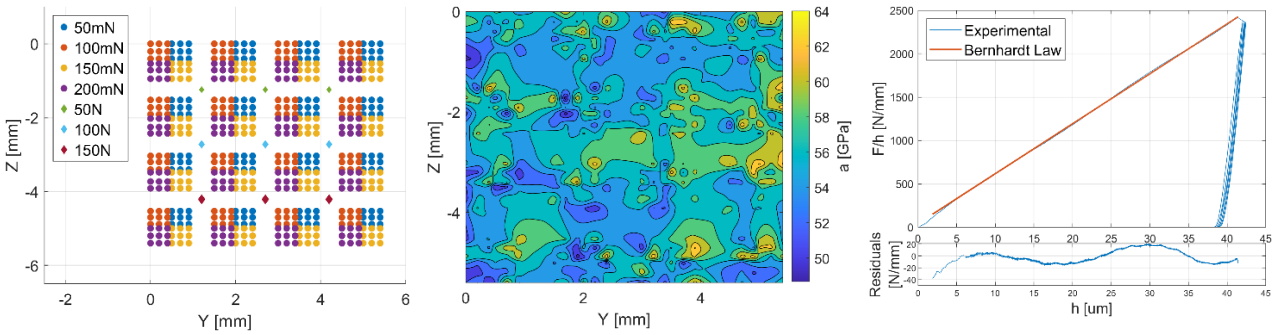

(a) (b) (c)

Fig. 1. Nano-macro IIT over the Y-Z plane, (Y, transverse direction; Z, building direction): (a) designed multi-load pattern (b) contour plot of load stiffness rate (LSR). (c) F/h vs. h experimental and Bernhardt's law fitting curves in the macroscale and fitting residuals (inset).

4. Acknowledgements

This study was carried out thanks to MICS project (Made in Italy – Circular and Sustainable) Extended Partnership and received funding from the European Union Next-GenerationEU (PIANO NAZIONALE DI RIPRESA E RESILIENZA (PNRR)) – MISSIONE 4 COMPONENTE 2, INVESTIMENTO 1.3 – D.D. 1551.11-10-2022, PE00000004). This manuscript reflects only the authors' views and opinions, neither the European Union nor the European Commission can be considered responsible for them.

5. References

[1] D'Andrea, D., 2023. Additive manufacturing of AISI 316L SS: a review. *Metals*, *13*(8), p.1370.

[2] Xie, D., Lv, F., Yang, Y., Shen, L., Tian, Z., Shuai, C., Chen, B. and Zhao, J., 2022. A review on distortion and residual stress in additive manufacturing. *Chinese Journal of Mechanical Engineering: Additive Manufacturing Frontiers*, *1*(3), p.100039.

[3] Maizza, G., Hafeez, F., Varone, A. and Montanari, R., 2024. Nanoscale and Tensile-Like Properties by an Instrumented Indentation Test on PBF-LB SS 316L Steel. *Materials*, *17*(1), p.255.

[4] ISO14577-1. Metallic materials—instrumented indentation test for hardness and materials parameters. Geneva: International Organization for Standardization; 2002.

[5] Bull, S.J., 2003. On the origins and mechanisms of the indentation size effect. *International Journal of Materials Research*, *94*(7), pp.787-792.

[6] Gubicza, J., Juhász, A., Tasnádi, P., Arató, P. and Vörös, G., 1996. Determination of the hardness and elastic modulus from continuous Vickers indentation testing. *Journal of materials science*, *31*, pp.3109-3114.

6-11 July 2025 ICEM21 Bologna
21st International Conference on EXPERIMENTAL MECHANICS

MECHANISM OF LOOSENING WITHOUT ROTATION FOR THIN PLATE BOLTED JOINT SUBJECTED TO OFFSET LOAD

S. Hashimura[1], N. Yamamoto[2] and S. Osaka[2]
[1] School of Engineering, Shibaura Institute of Technology, Tokyo, Japan
[2] Graduate School of Mechanical Engineering, Shibaura Institute of Technology, Tokyo

1. Introduction

Accidents due to bolt loosening are still occuring even though many researches with regard to bolt loosening have been conducted. This indicates that many issues which we have to study are still remaining. The loosening for comparatively thick plate bolted joints has been studied so far, but the researchs have not been almost discussed on the loosening for thin plate bolted joints as shown in Fig. 1[(1)]. For example, if the thin plate bolted joint is subjected to the offset load such as Fig. 1, the bolt recieves an additional tensile force in addition to the clamp force. After the offset load is unloaded, most engineers will consider that the bolt clamp force return to the origin. Actually does the clamp force return to the origin? For the problems, we have investigated whether the clamp force return to the origin or not[(2)]. As the results, we discovered a new type of the bolt loosening phenomenon, when the offset loads were repeatedly applied to a thin plate bolted joint. In this study, we have investigated the loosening mechanism, and the effect of plastic deformation on a new bolt loosening.

2. Experiments and FE analysis

Figure 2 shows an experimental set up for the thin plate bolted joint. The offset loads $P/2$ were loaded to both side of a thin plate bolted joint. The bolt used was a hexagon head bolt M8×30 with half thread. The clamp force was measured using a strain gauge inserted into the bolt and the initial clamp force was set to 10 kN. The thin plate specimens were made of a high tension steel 590 MPa class and the size was 150 mm×30 mm×2.3 mm. The upper plate was a hollow rectangular block made of S50C tempered steel. Two washers with 6.5 mm thickness were used. After the bolted joint was tightened, the offset load was applied while increasing 0.1 kN per cycle to the thin plate with a triangular wave to 1.0 kN. FE analyses were also conducted using an elastic model and an elasto-plastic model to elucidate an effect of plastic deformation.

3. Results and conclusions

Figure 3 shows a behaviour of the clamp force F in an experimental result, the abscissa is the offset load P and the ordinate is the clamp force F. It can be seen in Fig. 3 that F was decreased in each cycles although F

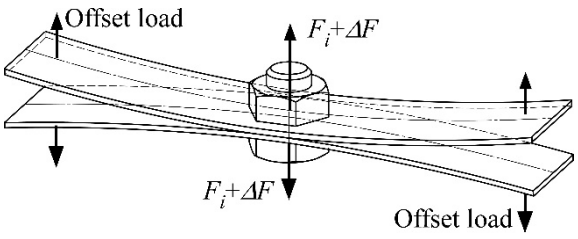

Fig. 1 Thin plate bolted joint subjected offset load.

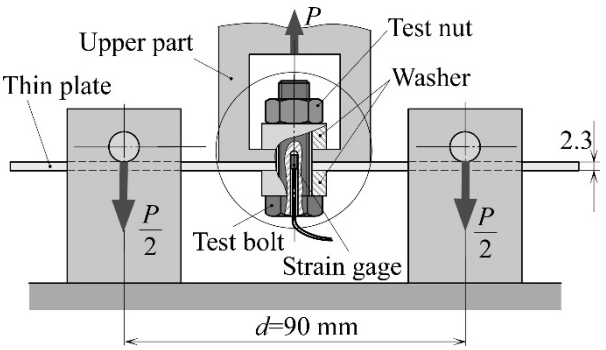

Fig. 2 Experimental setup

was not decreased until the third cycle. We can also see an interesting behaviour in Fig. 3. For example, the clamp force F, which decreased during the unloading of the fourth cycle, increases during the loading of the fifth cycle by following the route taken during the unloading of the fourth cycle. Also in the other cycles, F followed the route taken during the unloading of the previous cycle in the same manner. We also confirmed that F was not decreased if P did not exceed that in the previous cycle. And the clamp force F, which the offset load P was loaded, was gradually increased with an increase in P although F was not increased until the third cycle. The cause is considered that P was expended to pull the bolted joint in addition to bending the thin plate after the third cycle although P was expended to bend the thin plate until the third cycle.

Figure 4 shows behaviours of the clamp force F in elastic and elasto-plastic FE analyses. Light gray circles show F in the first cycle of elastic analysis and dark gray circles show F in the second cycle of elastic analysis. Black circles show F in the elasto-plastic analysis. F in the first cycle of the elasto-plastic analysis is completely hidden behind the elastic analysis symbol. The abscissa and the ordinate are the same as Fig. 3. It can be seen in Fig. 4 that the behaviours of the clamp force F in the elastic analysis were almost the same as those of the experiment. As the result of in the elastic analysis, it was seen that the clamp force reduction was caused by the bending of the thin plate, which caused the contact surface to slip, but the friction between the contact surface prevented the contact situation from returning to the origin. It was also seen in Fig. 4 that the behaviour of F in the elasto-plastic analysis was almost the same as that in the elastic analysis although the clamp force reduction in the second cycle was slight larger than that in the elastic analysis. The result indicates that the plastic deformation did not significantly contribute the clamp force reduction. The clamp force reductions in the experiment was almost twice of those in the analyses in a comparison of Fig. 3 and Fig. 4. Since the plastic deformation did not mainly effect on the reduction from Fig. 4, it is considered that the cause is except for the plastic deformation.

4. Conclusions

In this study, we have investigated the loosening mechanism, and the effect of friction coefficient between plates and plastic deformation on a new type of bolt loosening. The conclusions obtained in this study are summarized as follows.

1. The clamp force reduction was caused by the bending of the thin plate, which caused the contact surface to slip, but the friction between the contact surface prevented the contact situation from returning to the origin.
2. The plastic deformation was not main cause of the clamp force reduction.

5. References

[1] S. Hashimura and D. F. Socie (2006), “A study of loosening and fatigue of bolted joints under transverse vibration”, SAE Technical Papers; 72, 716, 1297-304.

[2] N. Yamamoto, T. Ohno and S. Hashimura (2024), “Loosening phenomenon on thin plates bolted joint due to offset load”, *Journal of Advanced Joining Processes*, 10, 100247

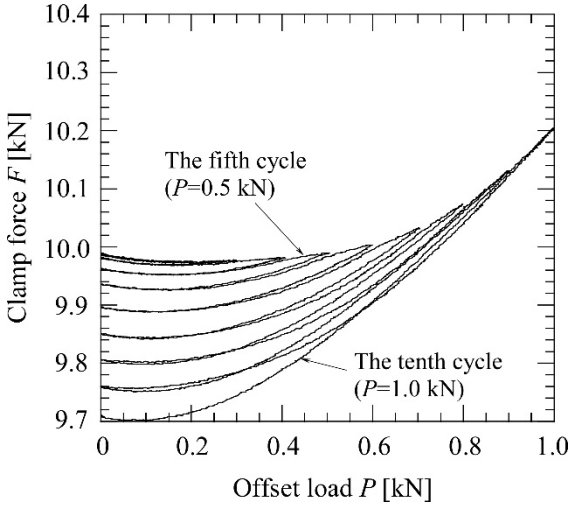

Fig. 3 Clamp force behaviors in the experiment

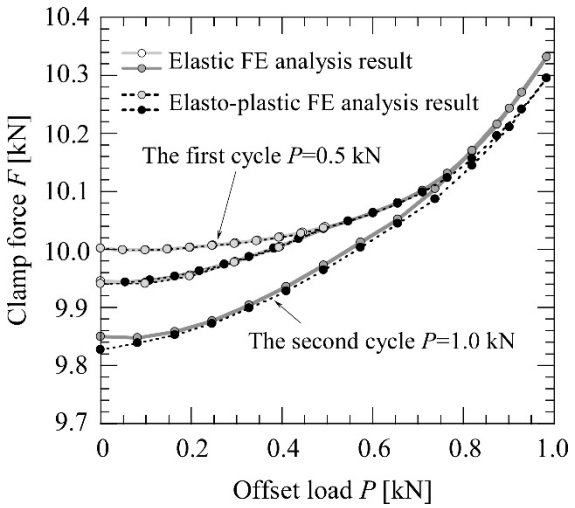

Fig. 4 Clamp force behaviors in the FE analyses

Correlation between EBSD parameters and PL-nIIT based mechanical performances of a PBF-LB 316L deposit

Faisal Hafeez[1,2], Giovanni Maizza[1], Roberto Montanari[2], Alessandra Varone[2]
[1] Department of Applied Science and Technology, Politecnico di Torino, Italy
[2] Department of Industrial Engineering, University of Rome Tor Vergata, Italy

1. Introduction

The laser powder bed fusion (L-PBF) of 316L alloy is widely investigated because of its attractive industrial interest to aerospace, medical, automotive, chemical, marine and power plants. The optimization of the performance of highly complex components in shape and microstructure has been a challenge owing to the large number of external and internal process parameters. Amongst these the highly researched ones are volumetric energy density (VED), scanning strategy and building direction. External parameters strongly affect the microstructure of the material, through its morphology, residual stresses (RS), crystallographic texture, and other sources of heterogeneities [1]. In turn, the solidification process depends on internal parameters such as the thermal gradient, solidification rate and cooling rate. Residual stresses and crystallographic texture are important contributions to mechanical properties albeit very difficult to quantitatively discern and correlate on the final components.

The instrumented indentation testing (IIT) enables sensing the elastoplastic response of materials at nano, micro and macro scale in a relatively quick and quasi-nondestructive manner [2]. Fully automated devices allow for fast grid mapping of nanoindentations with high resolution in even highly heterogeneous materials. However, special processing tools for data management, statistics, and for handling outliers are required. In our study, physically founded *performance line nanoindentation* (PL-nIIT) scheme has been applied to a LB-PBF 316L deposit to efficiently extract the inherent nanoindentation properties. An ad-hoc methodology has been designed to define the macro-scale mechanical performance of the given deposit both locally and globally being relevant from an engineering viewpoint for design, optimization or benchmarking. The effect of RS and texture has been discussed that may have caused the indentation properties to appear dubious.

2. Materials and methods

A pre-alloyed powder (LPW-316-AABE) of 44-88 µm average particle size was deposited, via LB-PBF, with 350 W laser power and 300 mm/min scanning speed over a substrate plate of AISI 1020 steel. An alternate X- and Y-direction scanning strategy with 90° interlayer rotation was employed. A sample was extracted from the original build block upon slicing and successive preparation (grinding, mirror-polishing) for nanoindentation measurements and metallographic inspection. The etched microstructure was observed by means of optical microscopy (DMI 3000 M, Leica, Wetzlar, Germany), scanning electron microscopy (FEI SEM-EDX Sirion 400 NC, Oregon USA), and electron backscattered diffraction (EBSD TESCANS 9000G, Tescan group, Brno, Czech Republic). The PL-nIIT scheme consists of 264 nanoindentation in total, distributed along five performance lines (H1, H2, D1, D2 and V), and performed in load control (100 mN peak load, 2 s dwell time and 0.5 mN/s of loading/unloading rates). Partitioning of the nano-indented PL into smaller segments permits the definition of six key performance zones (PZs) in the sample (S1, S2, E1, E2, D and C, see Figure 1a), and the associated macro-mechanical response. The same zones have been analyzed by means of EBSD to extract the most relevant microstructure parameters such as, grain size (based on area,

equivalent circle area, perimeter), aspect ratio, Schmid's factor (SF), low angle grain boundaries (LAGBs), inverse pole figures and kernel average misorientation (KAM).

3. Results and Conclusions

The layered microstructure of the deposit, observed on Y-Z plane, consisted of a mix of equiaxed grains in the X-direction and large columnar grains in the Y-direction. The PL-nIIT scheme underlined the paths (PLs) of lowest and highest cooling rate as well as the most and the least strong and stiff PZs of the deposit. The substrate, via its dilution (i.e., compositional gradient formed in the melt pool with the adjacent layers), and its conduction cooling effects, contributed dominantly on the final mechanical performances, both at local (the PZs, see Figure 1b) and global (the core C) scale. The vertical V line was the one with the highest cooling rate, therefore, it was the strongest and stiffest direction. The H2 line senses the highest heterogeneity between its two edges with the left (E1) edge being the softest and the most compliant PZ in the whole deposit. The latter has been identified as a hot spot with a large fraction of grains oriented in the <001> direction.

The (EBSD) structural parameters at the six PZs show a fair correlation with the measured indentation properties. KAM maps and LAGBs (see Figure 1c for CZ) account for the intragranular dislocation densities and the cellular sub-grain structures, respectively. A dislocation pile-up in a grain gives rise to the cellular sub-grain structures which act as LAGBs. These LAGBs hinder the dislocation motions thus causing an increase in the strength. In C and S1 zones, KAM and LAGB are high, therefore, a large value of indentation modulus was observed which is an indication of compressive residual stresses. The EIT values were low (< 190), for the zones where the KAM and LAGBs were relatively lower. This latter case can be explained by the fact that high temperatures assist the dislocations to pass through the sub-grain boundaries [3]. This effect was more prominent at the E1 region in H2 performance line.

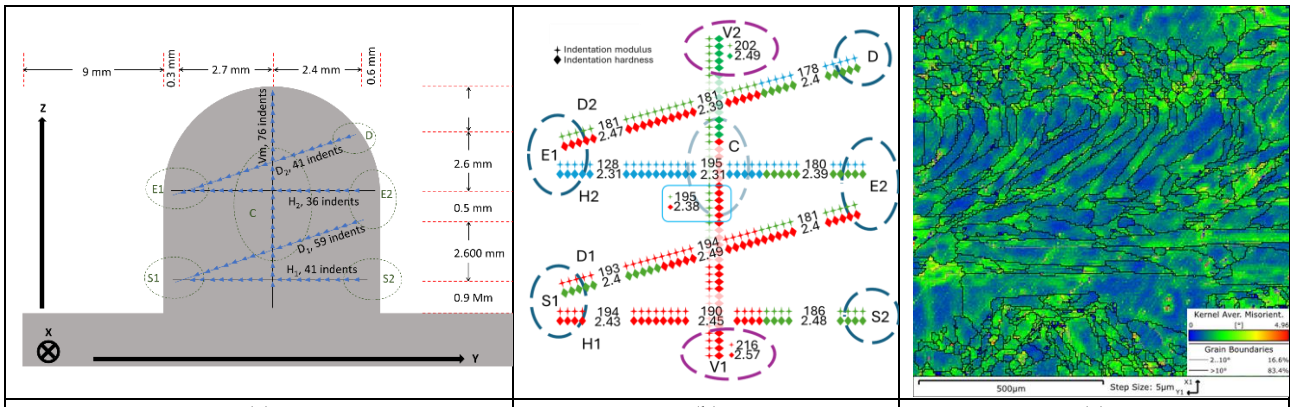

(a) (b) (c)

Figure 1. (a) Schematics of the PL-nIIT scheme with the geometrical notation, (b) measurements carried out via the methodology specified in (a), (c) KAM x GB maps captured at the core region of the investigated deposit.

4. References

[1] T. Larimian, B. AlMangour, D. Grzesiak, G. Walunj, and T. Borkar, "Effect of Laser Spot Size, Scanning Strategy, Scanning Speed, and Laser Power on Microstructure and Mechanical Behavior of 316L Stainless Steel Fabricated via Selective Laser Melting," *J. Mater. Eng. Perform.*, vol. 31, no. 3, pp. 2205–2224, Mar. 2022, doi: 10.1007/S11665-021-06387-8

[2] G. Maizza, F. Hafeez, A. Varone, and R. Montanari, "Nanoscale and Tensile-Like Properties by an Instrumented Indentation Test on PBF-LB SS 316L Steel," *Mater. 2024, Vol. 17, Page 255*, vol. 17, no. 1, p. 255, Jan. 2024, doi: 10.3390/MA17010255.

[3] R. S. Thanumoorthy *et al.*, "Effect of Build Orientation on Anisotropy in Tensile Behavior of Laser Powder Bed Fusion Fabricated SS316L," *J. Mater. Eng. Perform.*, vol. 33, no. 15, pp. 7930–7943, Aug. 2024, doi: 10.1007/S11665-023-08490-4

CHARACTERIZATION OF SELECTIVE LASER MELTED Ti-6Al-4V SAMPLES IN THE AS BUILT AND STRESS RELIEF STATE

P. Leo[1], G. Renna[1], A. De Luca[1], C. Scaramuzzi[1], N.Soni[1], F. Panella[1], T. Primo [1]and G. Papadia
[1] Department of Innovation Engineering, University of Salento, Lecce, Italy

1. Introduction

Ti–6Al–4V alloy is characterized by excellent mechanical properties, corrosion resistance, and biocompatibility. That alloy is applied in many fields, such as for aerospace, medical, and other high-performance industries. Moreover, heat treatments are usually applied to improve the service properties of the components [1, 2]. If produced according to the traditional methods, those components are characterized by high cost of manufacturing that can be reduced by using Additive Manufacturing (AM) process [1,2]. When additively manufactured, to achieve mechanical properties comparable to the wrought counterparts, a proper microstructure, roughness and porosity level are required. In particular, when processed by Selective Laser Melting (SLM) process, this alloys exhibit high yield stress but associated to low tensile elongation that does not allow their use for critical structural applications [2]. So, post-SLM heat treatment is very significant for overcoming that limit. This study intends to characterize Ti-6Al-4V parts processed by SLM in terms of microstructure, porosity, roughness, corrosion resistance and mechanical properties both in the as built state and after the post-process heat treatments as applied by the manufacturer. The previous analysis will serve to define the starting point for further improvements of the properties by handling process parameters of building and post building phases.

2. Materials and methods

Gas atomized Ti–6Al–4Vpowder was used to process cubes (10mm edge) and dog bone tensile test specimens (ASTM E8). The samples were built by SLM using a Renishaw AM 400 and the Meander strategy with scan rotation of 67 degrees between consecutive layers was applied. The Energy Density [2] resulted equal to 66 J/mm^3. After the building process, some of the samples were stress relieved (SR) according to the industrial thermal cycle with a heating rate of 2,8°C/min to 500°C plus holding time of 5 h at 500°C and air cooling to room temperature. The other samples were characterized in the as built (AB) state. The microstructure has been characterized after Kroll etching (95mL H2O, 4mL HNO3, 2mL HF) by Nikon Ephipot 200 Optical Microscope (OM) and Zeiss EVO Scanning Electron Microscope (SEM). Porosity analysis has been developed by optical microscope and Image J software. The corrosion resistance was evaluated in both the state after grinding the exposed surface using a Gamry Instrument 1010. The measurements were carried out in an aqueous solution of 3.5% NaCl at room temperature. X-ray diffractometry by a Rigaku D/MAX-Ultima X-ray system with Cu (Kα) X-radiation was used to further characterization of the samples.

3. Results and conclusions

Fig. 1a, b shows the microstructure of the cube sample from OM analysis. Due to the fast cooling rate, the microstructure is composed of Martensite α’ plateles throughout the sample, with a prevalence of columnar grains in the plane parallel to the laser beam. That martensite is characterized by high V content and dislocation density, sometime twins [1,3] leading to higher stress but low

elongation [4]. Moreover, after SEM analysis (Fig.1c) fine particles has been observed possibly due to in situ decomposition of Martensite by diffusion process activated by the cyclic heat up and cool down [2], responsible for further hardening and brittleness. Nevertheless, XRD analysis of the as-built sample has not shown any phase different from the HCP crystal structure (Fig.2 a), maybe due to the low amount of the precipitated particles or to the limit of the instrument. The porosity level (area percentage) was quite low, varying from 0,15% to 0,07% respectively in in the plane parallel and perpendicular to the laser beam. After the SR, the samples remain mainly martensitic but a significant decrease in tensile elongation, that was already low is the as built state, was induced by the SR (Fig. 2b). Indeed, at the SR temperature (500°C) despite the recovery of dislocations and mitigation of the residual stresses, decomposition of the martensites has to continue with β particles precipitation and possibly also secondary hardness due Ti3Al α2 [5] with further decreasing in ductility. In both the state, also an increasing of Oxigen content should be considered as cause of brittleness [4].

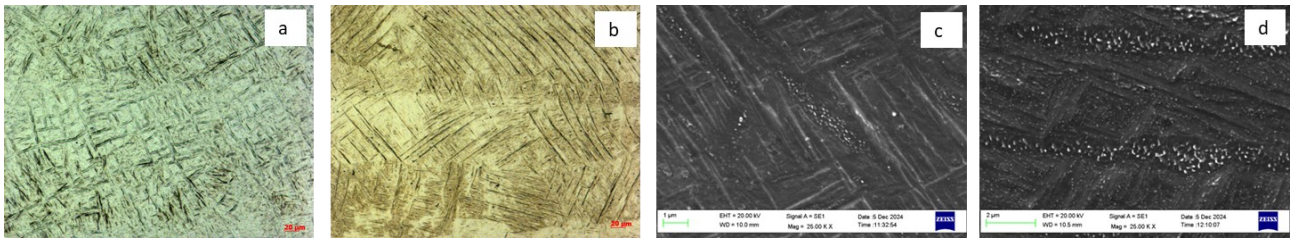

Fig. 1: OM microstructure (a, b) of AB cubic sample in orthogonal (a) and parallel plane (b) to beam directions and SEM microstructure (c, d) of AB (c) and SR (d) samples.

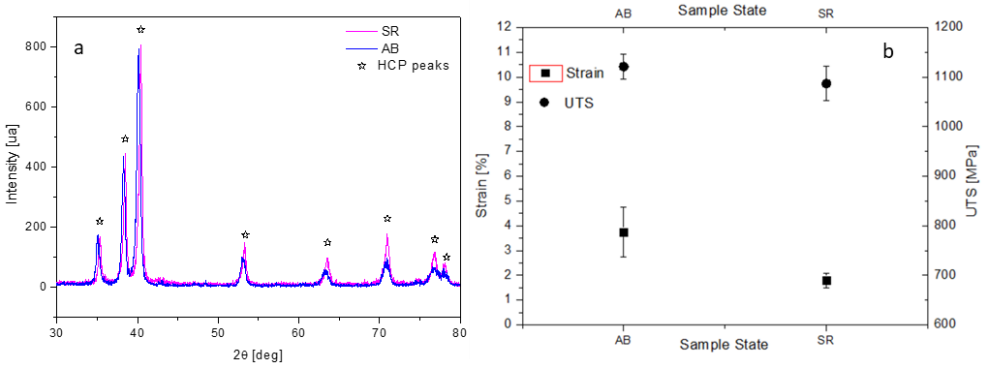

Fig.2: XRD spectra (a) and tensile test data (b) for the AB and SR samples.

5. References

[1] I.J. Polmear (1995). Light Alloys, Metallurgy of the Light Metals, 3rd ed., Arnold Publishers, London 146.

[2] W. Xu, M. Brandt, S. Sun, J. Elambasseril, Q. Liu, K. Latham, K. Xiad, M. Qiana (2015). Additive manufacturing of strong and ductile Ti–6Al–4V by selective laser melting via in situ martensite decomposition, *Acta Materialia*, 85, 74–84.

[3] P. Krakhmalev, G. Fredriksson, I. Yadroitsava, N. Kazantseva, A. du Plessis, I. Yadroitsev (2016). Deformation Behavior and Microstructure of Ti6Al4V Manufactured by SLM. *Physics Procedia,* **83**, 778 – 788.

[4] H.K. Rafi, N.V. Karthik, Haijun Gong, Thomas L. Starr, and Brent E. Stucker (2013). Microstructures and Mechanical Properties of Ti6Al4V Parts Fabricated by Selective Laser Melting and Electron Beam Melting. *Journal of Materials Engineering and Performance*, **3872**, 22(12).

[5] J. Songa, Y.Hana, M. Fanga, F. Hua, L. Keb, Y. Lic, L. Leic, W. Lua (2020). Temperature sensitivity of mechanical properties and microstructure during moderate temperature deformation of selective laser melted Ti-6Al-4V alloy. *Material Characterization,* **165**, 110342.

STUDY OF CRACK-SUSCEPTIBILITY IN LASER WELDED NICKEL-BASED SUPERALLOY SHEETS BY 3D LASER WELDING MODEL

Giovanni Maizza[1(*)], Cheng Peihong[2], Alessandra Varone[2], Roberto Montanari[2]
[1] Department of Applied Science and Technology (DISAT), Politecnico di Torino, Torino, Italy
[2] Department of Industrial Engineering, University of Rome "Tor Vergata", Rome, Italy

1. Introduction

While nickel-based superalloys continue to serve specially demanding engineering sectors (e.g., aerospace, petrochemical and energy) their safe welding remains a struggling challenge [1]. High energy-density sources (e.g., laser and electron beam) are especially suited for welding superalloys. However, the large number of process parameters along with the rapidity and the strong localization of the welding phenomena hinder the quick setup of the process, especially for complex geometries. Unsound microstructure, residual stresses, distortions, and eventually cracks near the heat affected zone (HAZ), are frequently encountered upon welding nickel-superalloys. Systematic trial-and-error experimental optimization of the welding process is often unaffordable due to the multiple involved parameters and their inherent wide process window. Finite element (FE) modeling, on the other hand, offers a valuable research alternative to quickly and economically find the requested optimal process conditions for the specified superalloy and joint geometry. First, laser welding models must be calibrated while simulating the essential thermo-mechanical phenomena with a restricted number of experimental process parameters typically within a narrow process window. Then it is employed to explore the same parameters within a much wider process window to ultimately to find the optimal welding process setup. The computed evolution and distribution of temperature and stress-strain fields finally enable to assess the structural integrity and the mechanical performance of the welded joint while minimizing the prospected residuals stress and distortion [2].

In this study, a 3D one-way transient thermo-mechanical FE model was developed to predict the thermal and stress-strain fields during the pulsed laser welding of Ni-based superalloys sheets. These were then systematically analyzed as a function of sheet restraint strength as a means of mitigating distortions and residual stresses leading to potential cracks.

2. Materials and methods

A laser device (Nd:YAG, 1.25 kW, 250 µm focused beam diameter) was used for bead-on-plate welding tests on IN792 superalloy sheets (2.0 mm thickness, clamped at their four corners) under pulsing mode ($\tau_{on} = 10\,ms$ and $\tau_{off} = 6\,ms$), $2080\,W$ maximum power ($P_{ave} = 1250\,W$), $25\ {}^{mm}/_{s}$ scanning rate and 200 °C preheating temperature of baseplate [3]. The weld pool was modeled as a full-penetrated hourglass geometry. The weld pool geometry resulted from a prior calibration procedure consisting of: a) qualitative matching, against the experimental weld pool geometry, b) quantitative matching, by minimizing the error between the computed and measured temperatures at six locations away from the surface bead centerline. In the simulations the thermal and mechanical properties were assumed temperature dependent.

The constitutive law governing the mechanical behavior at high temperature assumed a solid-state superalloy under elastic-ideal-plastic (no strain-hardening) condition [4] during realization of a full-length bead, i.e., up to 60 s. The mechanical field does not influence the thermal field. Vice versa at any (thermal) time instant during laser scanning the temperature field is used to update the mechanical properties in the mechanical model to compute the stress-strain field [1-2,4-5]. The molten pool and HAZ regions were tracked in the contour plots by the melting point of the alloy and the 650 °C contour lines respectively. The thermal boundary conditions are of convection and radiation types.

3. Results and Conclusions

The predicted temperature field fitted well with the experimental temperatures at the six locations (three in Fig. 1a). The validity of the computed stress-strain field was assessed by comparison with other references [1-2,5]. Full quantitative verification of the computed thermal stress-strain field was not possible owing to the difficulty of measuring stresses or strains at high temperatures in so short time. While the predicted longitudinal thermal stress (Fig. 1b) reached its maximum value at the fused zone boundary, the transversal thermal stress was negligibly small, which agrees with other welding models and different alloys [1-2]. Within the given welding system [5], both σ_{xx} and σ_{yy} attained the maximum tensile and compression stress values in the fused zone, then both steeply decreased and increase transversally (y-direction, Fig. 1b) respectively in a small region $(0.94 - 1.8\ mm)$ wide across the HAZ. Expectedly, all thermal stresses turn to zero towards the base material.
The FE laser welding model enabled us to identify the critical regions of major distortions and residual stresses in the welded joint and suggested useful countermeasures to mitigate them by acting on sheet restraints. However, predictions were very sensitive to the accuracy of high temperature properties.

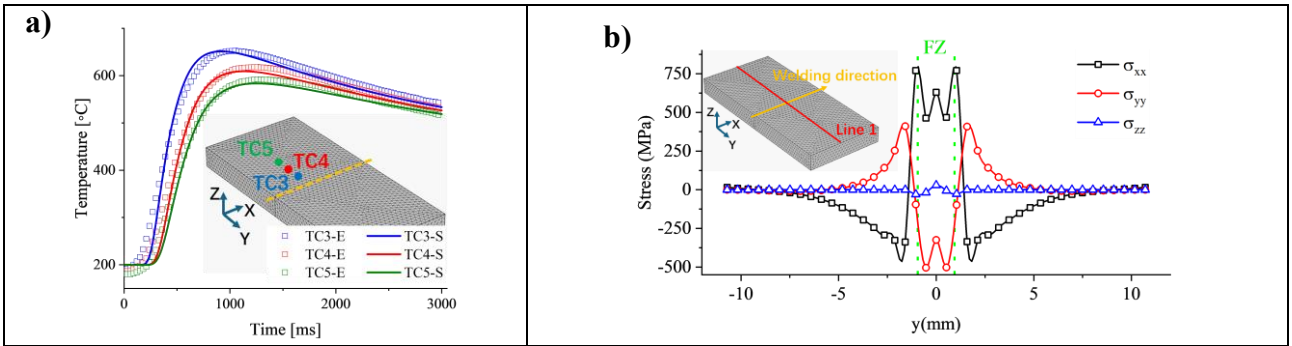

Figure 1. a) Predicted against computed thermal histories b) predicted normal thermal-stress components along Line 1 after 60 s.

4. Acknowledgements

The research presented in this paper has received funding from the European Union via the Euratom Research and Training Programme (Grant Agreement No 101052200—EUROfusion).

5. References

[1] Ferro, P., Zambon, A. and Bonollo, F., 2005. Investigation of electron-beam welding in wrought Inconel 706—experimental and numerical analysis. *Materials Science and Engineering: A*, *392*(1-2), pp.94-105.

[2] Ma, N., Deng, D., Osawa, N., Rashed, S., Murakawa, H. and Ueda, Y., 2022. *Welding deformation and residual stress prevention*. Butterworth-Heinemann.

[3] Barbieri, G., Cognini, F., de Crescenzo, C., Fava, A., Moncada, M., Montanari, R., Richetta, M. and Varone, A., 2024. Process Optimization in Laser Welding of IN792 DS Superalloy. *Metals*, *14*(1), p.124.

[4] Danis, Y., Lacoste, E. and Arvieu, C., 2010. Numerical modeling of Inconel 738LC deposition welding: Prediction of residual stress induced cracking. *Journal of Materials Processing Technology*, *210*(14), pp.2053-2061.

[5] Yukio Ueda, You Chul Kim, Min Gang Yuan, 1988, A Predicting Method of Welding Residual Stress Using Source of Residual Stress, *Quarterly Journal of The Japan Welding Society, 6(1)*, pp.59-64

DEVELOPMENT AND OPTIMIZATION OF THE COMBUSTION UNIT OF A HYDROGEN-FUELED GAS TURBINE FOR ENERGY GENERATION

Uma Nataraj Gottipati[1-2], Angelo Minotti[2], Vincenzo La Battaglia[1], Alessandro Giorgetti[1], Gabriele Arcidiacono[3]
[1]Department of Industrial, Electronic and Mechanical Engineering, Roma Tre University, Rome, 00146, Italy
[2] MIEEG S.r.l. – Colleferro (RM)
[3] Department of Engineering Science, Guglielmo Marconi University, Rome, 00193, Italy
* Correspondence: umanataraj.gottipati@uniroma3.it

1. Introduction

To achieve the Net Zero Scenario, low-emission fuel production and delivery must be expedited. Liquid fuels (liquid biofuels, ammonia, and synthetic liquid hydrocarbon fuels) and gaseous fuels (biogases, hydrogen, and synthetic methane) are the two types of low-emission fuels. Low-emission fuels are essential for decarbonising parts of the energy system where electrification or other alternatives are more expensive or difficult since many of them are compatible with the machinery and infrastructure that are now dependent on fossil fuels [1]. A wide range of power outputs at various fuel-air ratios are made possible by hydrogen fuel's ability to burn in mixture with an equivalence ratio of 0.1 (lean conditions) to 7 (rich conditions). This could significantly help the heat and power generation sector transition to a more sustainable and low-carbon energy system. It is important to keep in mind, though, that the lower limit of flammability decreases with increasing temperature and increases with high pressure. Hydrogen has a reduced flammability limit in a tiny gas turbine of more than 0.1 due to these opposing effects, which also reduces the challenges of decarbonisation as a carbon-free energy carrier that may be utilised as fuel, an energy storage option, and fuel for dispatchable power generation to counteract renewable energy sources' sporadic nature [2,3,4,5,6]. However, there are contemporary issues that need to be resolved because of the distinct physical and combustion properties of hydrogen, which set it apart from other common gaseous fuels like biogas and natural gas. Compact heat and power generators, up to 300kW, are called micro gas turbines (MGTs) [7,8,9,10,11,12]. As such, they offer a great fallback for future distributed power generation systems. By developing micro gas turbines powered by carbon-free fuels, the effects of global warming will be lessened and carbon-free electricity with zero CO2 emissions will be produced [13,14,15]. This paper is the continuous development of a previous paper [16] where the conceptual H2 turbine-based power system is reported. This system is capable of operating at high RPMs (up to +100.000RPM) and is solely focused on accelerating the clean energy transition with high-performance, hydrogen-fuelled microscale power systems while aiming for low emissions from the outlet.
Here fluid-structural investigations, of the patented combustion unit, adopting detailed H2-air reactive mechanism, LES turbulence model and different nickel superalloys material properties are reported.

2. The Combustion Unit and the Methodology

The patented combustion unit of the MIEEG power generator system is designed to provide extended residence times, perfect mixing, complete combustion and natural thermal protection, although the small dimensions, see fig.1. It connects the compressor outlet and turbine inlet, by means of specially designed manifolds. According to the power requirements, the number of combustion chambers can change to fit the high-level system. The combustion unit shall assure reliability, for long operativity times, under harsh environment due to the very high H2-combustion temperatures, even greater than 3000K, oxidation and embrittlement; in addition, NOx emissions shall be maintained below specific values [16-31].

To overcome those difficulties, investigations have been carried out assuming distinct nickel superalloys (e.g. Inconel and UDIMET) and very lean mixture conditions, which has several benefits such as preventing backfires and acting as a self-cooling system.

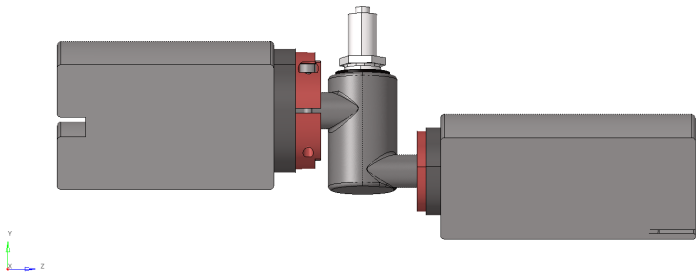

Figure 1 MIEEG Combustion System (MCS)

To design the combustion unit, we started adopting a loop methodology adopting the MODE FRONTIER software. The main operating, boundary conditions and constraints have been identified and imposed. In particular, the compressor and turbine dimensions, velocities, working pressure, the RPM, the output power, the temperature at the turbine inlet (TIT) section, were the main parameters. The loop, see fig.2, is based, fundamentally, on changing the H2-air equivalence ratio, and carrying out reactive fluid dynamics analysis adopting as checking point that the TIT shall not exceed 1500K. Once the final equivalence ratio was found, then the relative structural analysis was performed. To do that, different software has been adopted, among them ANSA, CAD, ANSYS Fluent and ANSYS Mechanical.

Numerical Analysis is performed using the ANSYS CHEMKIN H2-Air detailed mechanism (9 species and 21 reactions), the Large Eddy Simulations (LES) turbulence model, the Eddy dissipation concept and polynomial real properties of the materials.

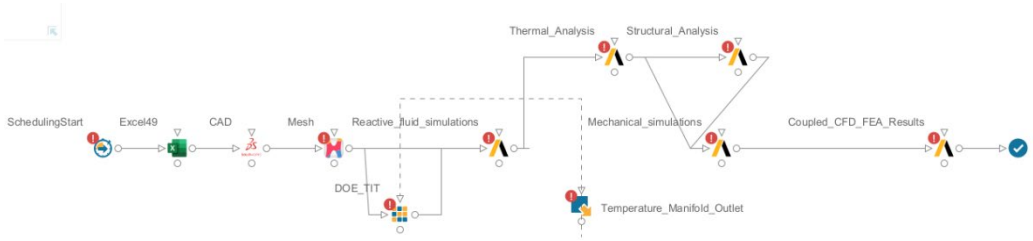

Figure 1 Design Methodology

3. Results and conclusions

Among pile of DOE configurations, the present section reports the results related to the combustion unit made of UDIMED700 (material properties in Table 1), and H2-Air equivalence ratio equal to 0.25.

Table1: UDIMET 700 properties

Density (kg/m^3)	7800 - 8000
Yield strength (elastic limit) (MPa)	865 - 1070
Specific stiffness (MN. m /Kg)	27.2 – 29.8
Maximum service temperature (°C)	797 - 1120
Melting Point (°C)	1210 - 1400
Thermal Conductivity (W/m. °C)	18 - 21
Specific heat (J/Kg. °C)	400 - 480
Fatigue Strength at 10^7 cycles (MPa)	500 – 780
Emissivity [ε]	0.2-0.3

The following Figures 3 reports the temperature maps inside the chamber at the meridian x-y plane. The temperature reaches a peak value of 2600K in the core of the chamber while is close to 1400K throughout the outlet manifold, which is connected to the turbine.

The pressures and temperatures results have been therefore interpolated in Ansys Mechanical to figure out the temperature map of the solid wall, addressing also convection and radiation (see fig.4), as well as the stress analysis (see fig.5), with the final goal to compare with the UDIMET700's strength.

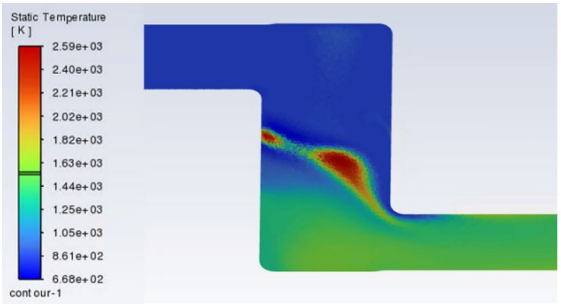

Figure 2 Temperature maps: x-z plane (left); x-y plane (right).

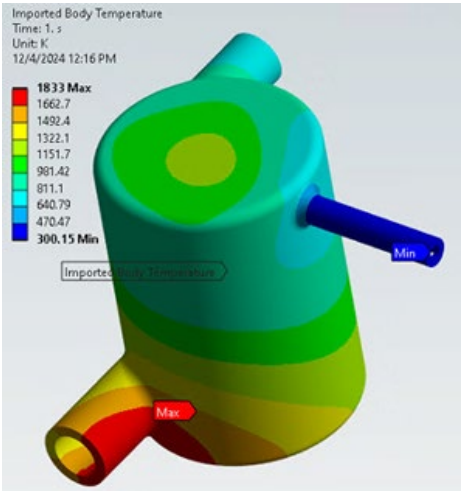

Figure 4 Solid wall temperature map [K]

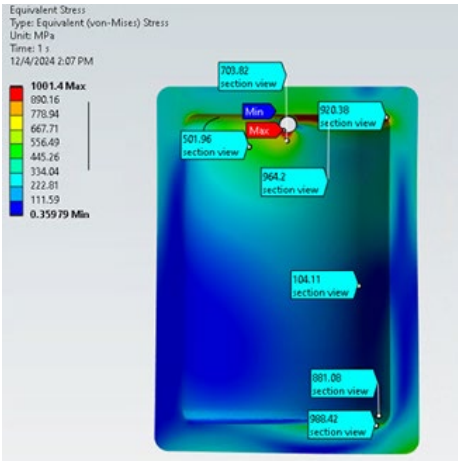

Figure 5 Mechanical equivalent stress [MPa]

The above-mentioned results show that UDIMET 700 can face the pressure stresses of the combustion event while its melting temperature is lower than the simulated one in some points of the chamber.
Apart from the obvious bias coming from the numerical simulations, that could permit us to accept values greater than the theoretical melting temperature, this investigation suggested us to adopt internal coatings to improve creep and fatigue behavior.
On this light, EBC (environmental barrier coating) plus TBC (thermal barrier coating) are under investigations and experimental tests are planned by Q3-2025. Simultaneously, more accurate fluid dynamic simulations, that include emissivity from combustion products, are in progress.

4. Acknowledgements

5. References

[1] The Future of Hydrogen – Analysis - IEA Available online: https://www.iea.org/reports/the-future-of-hydrogen.

[2] Aliberti, D.; Ortenzi, F.; La Battaglia, V.; Marini, S.; Vellucci, F. Evaluation of the Efficiency of a Hybrid ICE Vehicle Fuelled 12 with Hydrogen Compared with a Fuel Cell Vehicle, Based on a Simulation Model. Journal of Physics Conference Series **2023**, 13 2648, 012082, doi:10.1088/1742-6596/2648/1/012082.

[3] Banihabib, R.; Lingstädt, T.; Wersland, M.; Kutne, P.; Assadi, M. Development and Testing of a 100 kW Fuel-Flexible Micro Gas 19 Turbine Running on 100% Hydrogen. *International Journal of Hydrogen Energy* **2024**, *49*, 92–111, 20 doi: 10.1016/j.ijhydene.2023.06.317.

[4] Banihabib, R.; Assadi, M. A Hydrogen-Fueled Micro Gas Turbine Unit for Carbon-Free Heat and Power Generation. *Sustaina-22 bility* **2022**, *14*, 13305, doi:10.3390/su142013305.

[5] Moroshkina, A.; Ponomareva, A.; Mislavskii, V.; Sereshchenko, E.; Gubernov, V.; Bykov, V.; Minaev, S. Activation Energy of 38 Hydrogen–Methane Mixtures. Fire **2024**, 7, 42, doi:10.3390/fire7020042.

[6] Makaryan, I.A.; Sedov, I.V.; Salgansky, E.A.; Arutyunov, A.V.; Arutyunov, V.S. A Comprehensive Review on the Prospects of 40 Using Hydrogen–Methane Blends: Challenges and Opportunities. Energies **2022**, 15, 2265, doi:10.3390/en15062265.

[7] Rolo, I.; Costa, V. a. F.; Brito, F.P. Hydrogen-Based Energy Systems: Current Technology Development Status, Opportunities and Challenges. *Energies* **2023**, *17*, 180, doi:10.3390/en17010180.

[8] Barati, S.; De Santoli, L.; Lo Basso, G. Modeling and Analysis of a Micro Gas Turbine Fuelled with Hydrogen and Natural Gas 17 Blends. *E3S Web of Conferences* **2021**, *312*, 08012, doi:10.1051/e3sconf/202131208012.

[9] Di Gaeta, A.; Reale, F.; Chiariello, F.; Massoli, P. A Dynamic Model of a 100 kW Micro Gas Turbine Fuelled with Natural Gas and Hydrogen Blends and Its Application in a Hybrid Energy Grid. *Energy* **2017**, *129*, 299–320, doi: 10.1016/j.energy.2017.03.173.

[10] Xu, Z.; Lu, Y.; Wang, B.; Zhao, L.; Chen, C.; Xiao, Y. Experimental Evaluation of 100 kW Grade Micro Humid Air Turbine Cycles Converted from a Microturbine. *Energy* **2019**, *175*, 687–693, doi: 10.1016/j.energy.2019.03.036.

[11] Lim, H.-S.; Bang, J.-S.; Choi, B.-S.; Park, M.-R.; Park, J.-Y.; Seo, J.; Hwang, S.-C.; Sohn, J.L.; Kim, B.O. Secondary Flow Stabilization of 100 kW-Class Micro Gas Turbine. *Journal of Mechanical Science and Technology* **2017**, *31*, 1753–1761, doi:10.1007/s12206-017-0323-x.

[12] Devriese, C.; Pennings, W.; De Reuver, H.; Bastiaans, R.; De Paepe, W. The Preliminary CFD Design of a Compressor and Combustor System Towards a 100 kW Hydrogen Fuelled Micro Gas Turbine. *Volume 8: Microturbines, Turbochargers and Small Turbomachines; Steam Turbines* **2019**, doi:10.1115/gt2019-91342.

[13] Funke, H.H. -w.; Boerner, S.; Keinz, J.; Kusterer, K.; Kroniger, D.; Kitajima, J.; Kazari, M.; Horikawa, A. Numerical and Experimental Characterization of Low NOx Micromix Combustion Principle for Industrial Hydrogen Gas Turbine Applications. *Volume 2: Combustion, Fuels and Emissions, Parts a and B* **2012**, doi:10.1115/gt2012-69421.

[14] Iki, N.; Kurata, O.; Matsunuma, T.; Inoue, T.; Tsujimura, T.; Furutani, H.; Kobayashi, H.; Hayakawa, A.; Okafor, E. NOx Reduction in a Swirl Combustor Firing Ammonia for a Micro Gas Turbine. *MDPI* **2018**, doi:10.1115/gt2018-75993.

[15] Alavandi, S.K.; Etemad, S.; Baird, B.D. Low Single Digit NOx Emissions Catalytic Combustor for Advanced Hydrogen Turbines for Clean Coal Power Systems. *Volume 2: Combustion, Fuels and Emissions, Parts a and B* **2012**, doi:10.1115/gt2012-68128.

[16] Gottipati, U.N.; Minotti, A.; La Battaglia, V.; Giorgetti, A.; Department of Industrial, Electronic and Mechanical Engineering, Roma Tre University, Rome, 00146, Italy; MIEEG S.r.l. – Colleferro (RM) Design Challenges in the Development of a Hydrogen-Fueled Micro Gas Turbine Unit for Energy Generation. *Proceedings* **2023**, *70*, 2.

[17] Iki, N.; Kurata, O.; Matsunuma, T.; Inoue, T.; Tsujimura, T.; Furutani, H.; Kobayashi, H.; Hayakawa, A.; Okafor, E. NOx Reduction in a Swirl Combustor Firing Ammonia for a Micro Gas Turbine. .... **2018**, doi:10.1115/gt2018-75993.
[18] Cha, C.L.; Hwang, S.S. Numerical Study on Combustion Characteristics of Hydrogen Gas Turbine Combustor Using Cross Flow Micro-Mix System. *Journal of the Korean Society of Combustion* **2019**, *24*, 17–25, doi:10.15231/jksc.2019.24.3.017.
[19] Cadorin, M.; Pinelli, M.; Vaccari, A.; Calabria, R.; Chiariello, F.; Massoli, P.; Bianchi, E. Analysis of a Micro Gas Turbine Fed by Natural Gas and Synthesis Gas: MGT Test Bench and Combustor CFD Analysis. *Journal of Engineering for Gas Turbines and Power* **2012**, *134*, doi:10.1115/1.4005977.
[20] Cao, H.L.; Xu, J.L. Thermal Performance of a Micro-Combustor for Micro-Gas Turbine System. *Energy Conversion and Management* **2007**, *48*, 1569–1578, doi: 10.1016/j.enconman.2006.11.022.
[21] Cha, C.L.; Hwang, S.S. Numerical Study on Combustion Characteristics of Hydrogen Gas Turbine Combustor Using Cross Flow Micro-Mix System. *Journal of the Korean Society of Combustion* **2019**, *24*, 17–25, doi:10.15231/jksc.2019.24.3.017.
[22] Hernandez, S.R.; Wang, Q.; McDonell, V.; Mansour, A.; Steinthorsson, E.; Hollon, B. Micro Mixing Fuel Injectors for Low Emissions Hydrogen Combustion. *Volume 2: Combustion, Fuels and Emissions, Parts a and B* **2008**, doi:10.1115/gt2008-50854.
[23] Funke, H.H. -w.; Boerner, S.; Krebs, W.; Wolf, E. Experimental Characterization of Low NOx Micromix Prototype Combustors for Industrial Gas Turbine Applications. *Volume 2: Combustion, Fuels and Emissions, Parts a and B* **2011**, doi:10.1115/gt2011-45305.
[24] Lee, J.A. Hydrogen Embrittlement of Nickel, Cobalt and Iron-Based Superalloys. In *Elsevier eBooks*; 2012; pp. 624–667.
[25] Gray, H.R. Embrittlement of Nickel-, Cobalt-, and Iron-Base Superalloys by Exposure to Hydrogen. *NASA Technical Note* **1975**.
[26] Rapp, R.A.; Devan, J.H.; Douglass, D.L.; Nordine, P.C.; Pettit, F.S.; Whittle, D.P. High Temperature Corrosion in Energy Systems. *Materials Science and Engineering* **1981**, *50*, 1–17, doi:10.1016/0025-5416(81)90082-3.
[27] Sabol, G.P.; Stickler, R. Microstructure of Nickel-Based Superalloys. *Physica Status Solidi (B)* **1969**, *35*, 11–52, doi:10.1002/pssb.19690350102.
[28] Zhang, Z.; Moore, K.L.; McMahon, G.; Morana, R.; Preuss, M. On the Role of Precipitates in Hydrogen Trapping and Hydrogen Embrittlement of a Nickel-Based Superalloy. *Corrosion Science* **2018**, *146*, 58–69, doi: 10.1016/j.corsci.2018.10.019.
[29] Rezende, M.C.; Araujo, L.S.; Gabriel, S.B.; Santos, D.S.D.; De Almeida, L.H. Hydrogen Embrittlement in Nickel-Based Superalloy 718: Relationship between Γ′ + Γ″ Precipitation and the Fracture Mode. *International Journal of Hydrogen Energy* **2015**, *40*, 17075–17083, doi: 10.1016/j.ijhydene.2015.07.053.
[30] Khalid, H.; Mansoor, B. Hydrogen Embrittlement in Nickel-Base Superalloy 718. In *Springer eBooks*; 2022; pp. 279–306.
[31] Li, X.; Zhang, J.; Fu, Q.; Akiyama, E.; Song, X.; Wang, Y.; Li, Q.; Zou, N. Tensile Mechanical Properties and Fracture Behaviors of Nickel-Based Superalloy 718 in the Presence of Hydrogen. *International Journal of Hydrogen Energy* **2018**, *43*, 20118–20132, doi: 10.1016/j.ijhydene.2018.08.179.

6-11 July 2025 ICEM21 Bologna
21st International Conference on EXPERIMENTAL MECHANICS

CORRELATION BETWEEN CHEMICAL COMPOSITION AND MECHANICAL SURFACE RESPONSE OF BIOMEDICAL PATCHES

A. de Nigris[1], D. Gentile[1], L. Ambrosone[1]
[1] Department of Medicine and Health Sciences, University of Molise, 86100Campobasso, Italy

The surface properties of a material are highly dependent on both the manufacturing process and the chemical composition. The combination of these two traits gives rise to the specific mechanical properties of the artifact. This aspect assumes a particularly important role in the biomedical field, where the adhesion between surfaces at the biological tissue/biomaterial interface and their mechanical properties are crucial for drug delivery [1,2]. In addition, surface mechanical response also plays a basic role in the bioavailability and biocompatibility of the material.

Therefore, to design and produce novel materials means to control their microstructure in order to assess the required compatibility with the result of the manufacturing process. Nanoindentation is a useful tool for characterizing the surface at the nanoscale [3] and it offers several key insights that can aid in understanding and optimizing the interactions between the biomedical drug eluting devices and the tissue [4]. The technique, generally based on loading and unloading cycles, as shown in Fig. 1, allows not only to investigate the topography of the surface with nanometer resolution but also to detect heterogeneity in surface features caused by the presence of different phases [5].

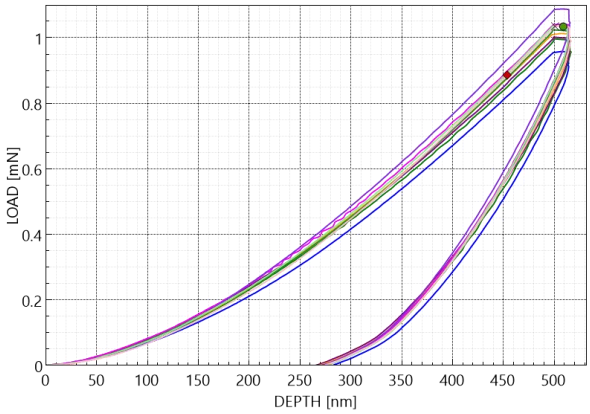

Fig. 1. Nanoindentation cycles of the biopolymeric film.

In this research four different combinations of polymeric composites 1) sodium alginate/gelatine, 2) sodium alginate/gelatine/free indocyanine green 3) sodium alginate/gelatine/empty liposomes and 4) sodium alginate/gelatine/liposomes containing indocyanine green patches were bioprinted and analyzed via nanoindentation. Various solicitations with different penetrating tips were performed on the samples. Fig. 2 highlights the fluctuations of the mechanical properties of the patch, such as Modulus and Hardness during the application of the load.

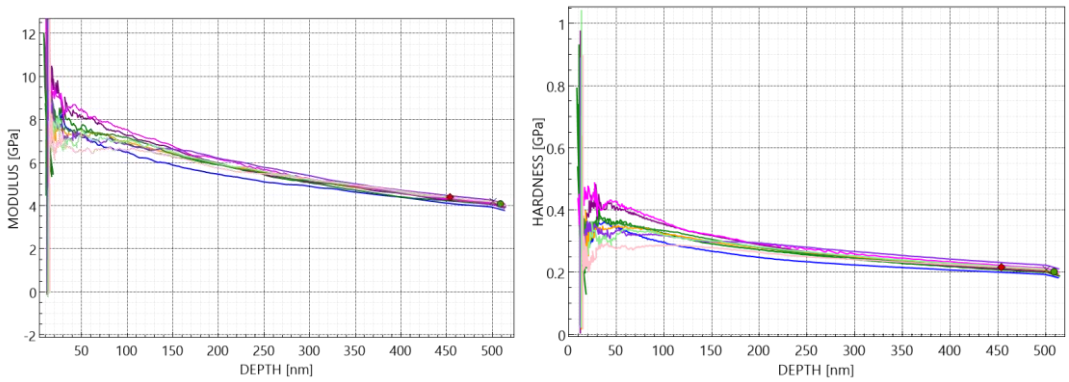

Fig. 2. Constitutive mechanical properties measurements probed during the loading/unloading phases. (a) Elastic Modulus (GPa) and (b) Hardness (GPa)

Comparison of the results among different compositions allows for the understanding of the fine surface morphology which influences cell adhesion, proliferation, and migration [6]. The increase in complexity of the chemical structure of the patches affects their intrinsic architecture, resulting in devices with tunable compliance.

5. References

[1] A., Minó, G. Cinelli, G. Paventi, G.Testa, F. Passaro, F. Lopez, L. Ambrosone, (2022). Poly (Lactic-co-glycolic) Acid and Phospholipids Hybrid Nanoparticles for Regeneration of Biological Tissue. *ChemEngineering*, **6(1)**, 10

[2] A. de Nigris, A. Minó, G. Cinelli, M. Colella, F. Lopez, L. Ambrosone (2024). Kinetic Model of Fluorescein Release through Bioprinted Polylactic Acid Membrane. Biomimetics, 9(6), 342.

[3] M. L. Oyen (2015). Nanoindentation of hydrated materials and tissues. *Current Opinion in Solid State and Materials Science*, **19(6)**, 317-323.

[4] E. Siamantouras, C. E. Hills, P. E. Squires, K. K. Liu (2015). Nanomechanical investigation of soft biological cell adhesion using atomic force microscopy. *Cellular and Molecular Bioengineering*, **8**, 22-31.

[5] M. E. Dokukin, I. Sokolov (2012). On the measurements of rigidity modulus of soft materials in nanoindentation experiments at small depth. *Macromolecules*, **45(10)**, 4277-4288.

[6] A. Kubiak, T. Zieliński, J. Pabijan, M. Lekka (2020). Nanomechanics in monitoring the effectiveness of drugs targeting the cancer cell cytoskeleton. *International Journal of Molecular Sciences*, **21(22)**, 8786.

Experimental testing of lightweight materials, structures and components

Enhancing Mechanical Performance and Energy Release in PTFE/Al Composites through Graphene Oxide Integration.

Ramzi Makaoui [1], Oussama Mehelli[2], Djallel Eddine Tria[3], Mehdi Derradji[2]*

[1]*Laboratoire Génie des matériaux, UER Matériaux et Structures, Ecole Militaire Polytechnique, Bordj El-Bahri 16046, Algiers, Algeria*

[2]*Laboratoire Génie des procédés, UER Procédés Énergétiques, Ecole Militaire Polytechnique, Bordj El-Bahri 16046, Algiers, Algeria*

[3]*Laboratoire Dynamique des Systémes Mécaniques, UER Matériaux et Structures, Ecole Militaire Polytechnique, Bordj El-Bahri 16046, Algiers, Algeria*

1. Introduction

Reactive materials have gained significant attention in various fields as energetic materials, especially for enhancing the performance of weapons, warheads, projectiles, and reactive armors. Among these, fluoropolymer/metal composites are highly favorable due to their exceptional mechanical properties and energetic characteristics, demonstrating excellent mechanical stability under standard conditions and remarkable reactivity with intense energy release under high strain rates or high-velocity impacts. A notable composite in this category is PTFE/Al, a typical reactive material [1]. For instance, Xu et al. investigated integrating Fe particles into PTFE/Al composites to enhance mechanical performance and reaction sensitivity, finding that incorporating 30% by weight of Fe significantly improved strength and reaction sensitivity [2]. Similarly, Zhou et al. explored the effects of adding CuO micro- and nano-sized particles to PTFE/Al composites, examining their influence on mechanical properties and reaction characteristics through quasi-static, drop hammer, and SHPB dynamic tests. They observed that micro-sized particles provided optimal strength, while adding CuO enhanced the material's reaction sensitivity. Their results, supported by the Johnson-Cook model in SHPB tests, reinforced the conclusion that the reactive material exhibited enhanced performance [3].

This study aims to investigate the effect of graphene oxide (GO) on the mechanical performance and energy release capabilities of PTFE/Al composites. For the first time, GO is being integrated into PTFE/Al composites, offering unique potential due to its exceptional thermal conductivity, electrical conductivity, and mechanical strength. While previous studies have explored various additives, the incorporation of GO introduces a novel approach to enhancing both mechanical stability and reactivity under high strain rates.

2. Materials and methods

In the present study, PTFE powder (average particle size of 25 µm) and Al powder (particle size range 7-15 µm) were sourced from Aladdin Chemical Company, achieving a stoichiometric composition of 73.5 wt.% PTFE and 26.5 wt.% Al. Four sample sets were prepared with varying GO contents (0%, 1%, 2%, and 3%), cold-pressed, and sintered. Calorimetric analysis assessed the

combustion energy of different PTFE/Al/GO ratios using a calorimetric bomb. Mechanical properties were evaluated through quasi-static compression tests using a Zwick/Roell 50 kN machine, followed by dynamic testing with a SHPB setup under 2500 s^{-1} strain rate.

3. Results and conclusions

As elucidated in Fig 1, The incorporation of GO enhances reactivity and thermal performance, with higher GO content resulting in improved characteristics. Fig.2 and Fig.3 displays that under both quasi-static and dynamic loading, GO promotes strain hardening and increases the toughness of the composites. GO-modified materials exhibit superior stiffness and elasto-plastic behavior, effectively delaying crack initiation under high-strain rates. Overall, this research underscores the potential of GO in the development of lightweight, high-performance reactive materials for military and civilian applications.

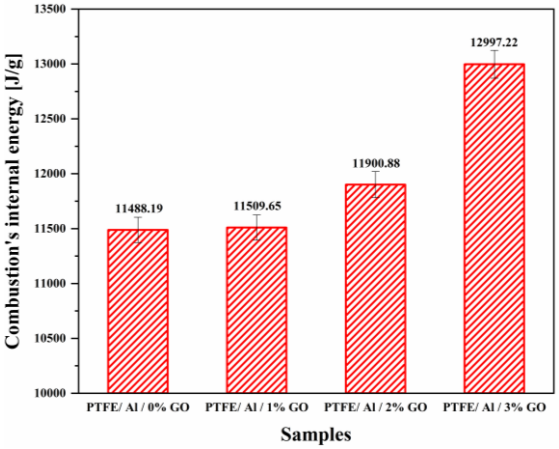

Fig.1. Energy release of PTFE/Al composites with increasing GO ratio.

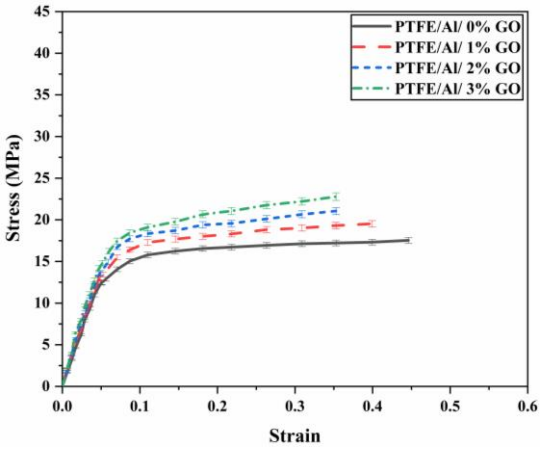

Fig.2. Quasi-static compression stress-strain curves of PTFE/Al/GO composite.

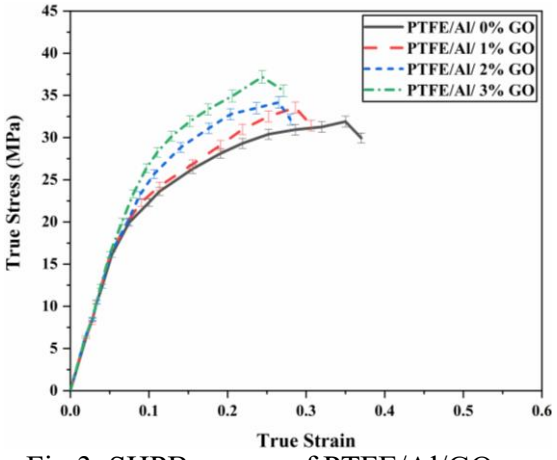

Fig.3. SHPB curves of PTFE/Al/GO composite under dynamic impact.

4. References

[1] Hastings, D.L. and E.L. Dreizin,(2018). *Reactive structural materials: preparation and characterization,* Advanced Engineering Materials.**20**,1700631.

[2] Xu, X.-c., et al.,(2023). *Mechanical properties, impact initiation characteristics and energy release effect of Al/PTFE reactive materials enhanced by Fe particles,* Transactions of Nonferrous Metals Society of China.**33**,683-700.

[3] Zhou, J., et al.,(2019). *Experimental Study of Mechanical Properties and Impact-Induced Reaction Characteristics of PTFE/Al/CuO Reactive Materials,* Materials (Basel).**13**,66.

MECHANICAL BEHAVIORS OF CARBON/EPOXY-ALUMINUM LAMINTES

Z. Jiang and J. Tsai
[1] *Department of Mechanical Engineering, National Yang Ming Chiao Tung University, Hsinchu, Taiwan, 300*

1. Introduction

There is nowadays an increasing interest in carbon/epoxy-aluminum laminates [1], since they illustrate the combined features of fiber composites and metals. Fiber composites exhibit stiffer and stronger behavior; on the other hand, the metal is relatively ductile. In past decades, modeling the mechanical behaviors of carbon/epoxy-aluminum laminates only considers the nonlinear behavior of metal without including the nonlinear behavior of fiber composites [2]. However, the fiber composite laminates depending on the stacking sequence may have nonlinear behaviors [3]. Thus, to comprehensively characterize the mechanical behavior of carbon/epoxy-aluminum laminates, the nonlinearity of the ingredient materials should be taken into account.

This study fabricated the carbon/epoxy-aluminum laminates containing different layup of fiber composites and aluminum layers. Subsequently, the tensile tests were performed on the samples to obtain the stress-strain curves. The nonlinear constitutive model [4] that comprises nonlinear constitutive models for both the metal and fiber composites was employed to characterize the nonlinear behavior of the carbon/epoxy-aluminum laminates. The model predictions were compared with the experimental data

2. Materials and methods

In this study, the carbon/epoxy-aluminum laminates with three different layup sequences, i.e. $[Al/(0/90)_4]_s$, $[Al/(45/-45)_4]_s$ and $[Al(0/90/45/-45)_2]_s$ were fabricated. To enhance the bonding properties between the fiber composites and aluminum plates, the surface treatment were conducted on aluminum sheets [5]. Subsequently, the tensile tests were performed in the carbon/epoxy-aluminum laminates to obtain the stress-strain curves. On the other hand, in the constitutive model of the carbon/epoxy-aluminum laminates, the nonlinear behaviors of the carbon fiber-epoxy composites were characterized using one parameter plastic model [3] in which the corresponding parameters were obtained from off-axis tensile tests. More specifically, by collapsing the effective stress-effective plastic strain curves obtained from off-axis tests, parameter a_{66} was derived. Nevertheless, for the aluminum, the nonlinear mechanical behaviors were modeled using J_2 flow rule [6]. The parameters were obtained by curve-fitting the tensile stress strain curves. The material properties for fiber composites and aluminum measured from experiments were listed in Table 1. The constitutive curve of the carbon/epoxy-aluminum laminates were predicted by combining the nonlinearly behaviors of each layer in accordance with classical laminated plate theory. It is noted that in the modeling, the thermal residual stress generated during the curing process was considered as the initial stress within each layer. Through the iteration process, the nonlinear stress-strain curves of the carbon/epoxy-aluminum laminates can be obtained [4].

Material							
Aluminum	E (GPa)		G (GPa)	ν	γ		α $(MPa)^{-\gamma}$
	57.7		21.8	0.32	18.78		2.12E-43
Composites	E_1 (GPa)	E_2 (GPa)	G_{12} (GPa)	ν_{12}	a_{66}	n	B $(MPa)^{-n}$
	138.7	9.1	5.5	0.29	1.6	5.09	1.54E-13

Table 1. Mechanical properties of fiber composites and aluminum.

3. Results and conclusions

The stress and strain curves for the $[Al/(45/-45)_4]_s$ laminate are plotted in Fig. 1, along with dots indicating the experimental data. The result indicates the differences between the model prediction and experimental data are not significant. Therefore, the nonlinear behaviors of carbon/epoxy-aluminum laminates can be characterized with the laminated theory together the nonlinearity of the ingredient materials.

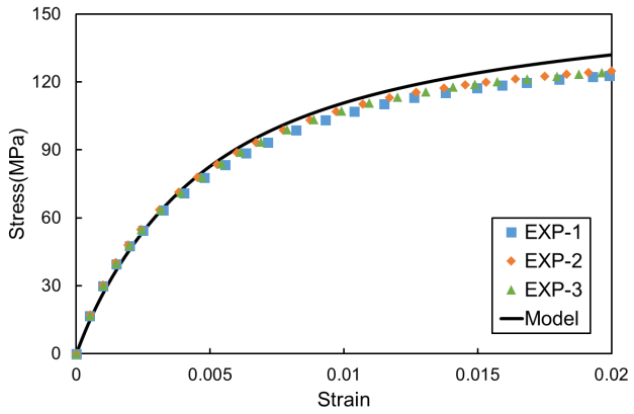

Fig. 1. Stress and strain curves of $[Al/(45/-45)_4]_s$ laminates

4. References

[1] T. Sinmazçelik, E. Avcu, M. Bora and O. Çoban (2011). A review: Fibre metal laminates, background, bonding types and applied test methods, *Mater. Des.*, **32**, 3671-3685.

[2] G. Wu and J. Yang (2005). Analytical modelling and numerical simulation of the nonlinear deformation of hybrid fibre–metal laminates, *Model. Simul. Mater. Sci. Eng.*, **13**, 413.

[3] J. Tsai and H. Wang (2007). Modeling nonlinear rate dependent behaviors of composite laminates, *J. Chin. Inst. Eng.*, **30**, 141-148.

[4] Z. Jiang and J. Tsai (2024). Characterizing nonlinear constitutive behaviors of fiber metal laminates, *Model. Simul. Mater. Sci. Eng.*, **32**, 075007.

[5] M. Allah, D.Hegazy, H. Alshahrani, T. Sebaey and M. El-baky (2023). Fiber metal laminates based on natural/synthesis fiber composite for vehicles industry: An experimental comparative study, *Fibers Polym.*, **24**, 2877-2889.

[6] J. Chen and C. Sun (1989). Modeling of orthotropic elastic-plastic properties of ARALL laminates, *Compos. Sci. Technol.*, **36**, 321-337.

AMBIENT-TEMPERATURE PLASTICITY OF HARD AND BRITTLE MATERIALS AT MICRON-METER-SIZE SCALES

H. Inui[1], K. Kishida[1], Z.H. Chen[1], L. Li[1], B. Paul[2], S. Han[1] and Z. Wang[1]
[1] Department of Materials Science and Engineering, Kyoto University, Kyoto, Japan
[2] High Temperature Materials Development Section, Materials Processing and Corrosion Engineering Division, Bhabha Atomic Research Centre, Trombay, Mumbai, India

1. Introduction

There are many hard materials that are considered to be candidates for structural applications under extreme conditions such as very high temperatures. This stems from the fact that many of them possess peculiar properties such as high hardness, high melting temperature, and so on. But, one of the common characteristics for these hard materials is their brittleness. They usually fail in cleavage without showing any plastic deformation at ambient temperature. So, even, fundamentals for plasticity such as operating slip systems and their CRSS values have yet to be known for many of them. If we assume that fracture in these hard materials occurs in a brittle manner at a pre-existing micro-crack, the effective defect size of the microcrack to cause fracture is believed to vary with the fracture toughness (K_{IC}) at a given fracture stress. If the fracture stress is fixed at 1 GPa, the effective defect size of the micro-crack is calculated to be 320 nm for K_{IC} of 1 $MPam^{-1/2}$, but this value increases to about 8 mm if the K_{IC} values is increased to 5 $MPam^{-1/2}$. Then, there is a chance for these hard materials to plastically deform in the form of micropillars of the micron-meter size even at ambient temperature. Since the discovery of the testing method by Uchic et al. in 2004, micropillar compression tests have extensively been used to explore the deformation mechanisms of small volumes, in most cases, of metallic materials with fcc (face-centered cubic), bcc (body-centered cubic) and, to a lesser extent, hcp (hexagonal close-packed) structures. Significant progress has been made in recent years in understanding the deformation behavior of small volumes of these metallic materials. In particular, the specimen-size dependent strength has been proved to arise from the size-dependent operation stress of the weakest single-arm dislocation sources due to the stochastics of dislocation source lengths.

We have investigated the compression deformation behavior of transition-metal borides [1], carbides [2] and silicides [3,4] as well as some ceramics such as SiC [5] as typical examples of hard materials in the micropillar form with the specimen size ranging from 0.5 to 10 μm at room temperature. Those hard materials include transition-metal (M) borides of the MB_2-type such as ZrB_2 and TiB_2, transition-metal silicides of the M_5Si_3-type such as Mo_5Si_3, Nb_5Si_3 and Mo_5SiB_2 and those of the MSi_2-type such as $MoSi_2$, VSi_2, $CrSi_2$, $NbSi_2$ and $TaSi_2$.

2. Results and conclusions

Although none of them listed above deform plastically at room temperature in the bulk form, plasticity is clearly observed at room temperature for all of them in the micropillar forms. This is very surprising in particular for transition-metal borides of the MB_2-type and those silicides of the M_5Si_3-type, since they usually need more than 1300°C for their plastic deformation to occur in the bulk form. Because of such a high temperature, slip systems have never been identified with confidence for these

transition-metal borides and silicides. However, plasticity observed in the micropillar form at room temperature has made us to clearly identify their operative slip systems with their CRSS (critical resolved shear stress) values. The operative slip system identified for ZrB_2 is only {1-100}<11-23>, while two different slip sytems, {1-100}<0001> and {1-100}<11-20> are identified for TiB_2. The CRSSs for these slip systems do not depend much on the specimen size. The room-temperature bulk CRSS values for these slip systems obtained as the average valuesare 3.01, 1.72 ans 5.17 Gpa, respectively.

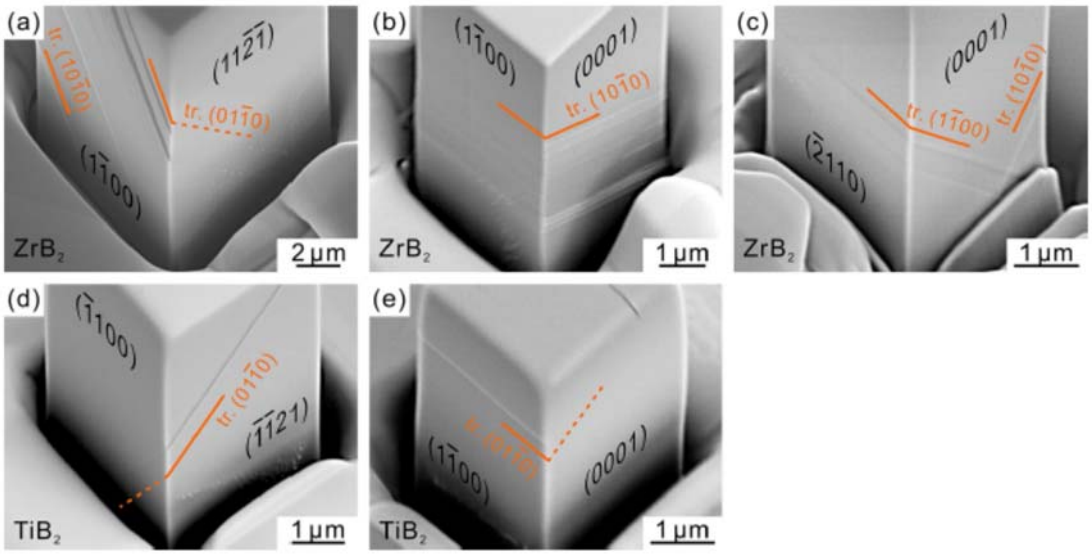

Fig. 1. SEM secondary electron images of deformed micropillar specimens taken diagonally from the above (inclined by 30 from the loading axis) for (a-c) ZrB_2, (d,e) TiB_2 with (a,d) [11-26], (b,e) [11-20] and (c) [0-110] orientations [1].

4. Acknowledgements

This work was supported by Grant-in-Aids for Scientific Research on Innovative Areas on High Entropy Alloys through the grant number JP18H05450 and JP18H05451, in part by JSPS KAKENHI (Grant numbers JP22H00262 and JP23K17338) and by JST Spring (Grant number JPMJSP2110).

5. References

[1] Z.H. Chen, B. Paul, S. Majumdar, N.L. Okamoto, K. Kishida, H. Inui, S. Otani (2021), Room-temperature deformation of single crystals of TiB_2 and ZrB_2 with the hexagonal AlB_2 structure investigated by micropillar compression. *Sci. Rep.*, **11**,14265.

[2] K. Kishida, M. Morisaki, M. Ito, Z. Wang, H. Inui (2023), Room-temperature deformation of single crystals of WC investigated by micropillar compression. *Acta Mater.*, **260**, 119302.

[3] K. Kishida, S. Nakatsuka, H. Inui (2022), Room-temperature deformation of single crystals of transition-metal disilicides ($TMSi_2$) with the $C11_b$ (TM=Mo) and C40 (TM=V, Cr, Nb and Ta) structures investigated by micropillar compression. *Acta Mater.*, **223**, 117468.

[4] K. Kishida, Z.H. Chen, H. Matsunoshita, T. Maruyama, T. Fukuyama, Y. Sasai, H. Inui, M. Heilmaier (2022). Plastic deformation of bulk and micropillar single crystals of Mo_5Si_3 with the tetragonal $D8_m$ structure. *Int.J. Plasticity*, **155**, 103339.

[5] K. Kishida, Y. Shinkai, H. Inui (2020). Room temperature deformation of 6H-SiC single crystals investigated by micropillar compression. *Acta Mater.*, **187**, 19-28.

THE PEAK STRESS METHOD FOR THE FATIGUE STRENGTH ASSESSMENT OF ARC-WELDED JOINTS MADE OF ADDITIVELY MANUFACTURED STAINLESS STEEL PARTS

L. Contiero [1], L. Vecchiato[1], A. Campagnolo[1], V. Babini[2], and G. Meneghetti[1]
[1] Department of Industrial Engineering, University of Padova, Padova, Italy
[2] Antonio Zamperla S.p.a., Altavilla Vicentina, Vicenza, Italy

1. Introduction

In the current industrial context, the adoption of components produced through additive manufacturing (AM) technologies is extraordinarily growing thanks to the reduction of wasted time and materials, the customization, and, mainly, the design of lightweight structures having complex geometries. In industrial sectors such as automotive, aerospace and amusement park industry, there is an increasing interest mainly in metal components produced by Laser Powder Bed Fusion (LPBF). However, the AM technologies have some drawbacks, among them it is worth mentioning the limited printing volumes and the high costs. To overcome these limitations, two AMed parts or an AMed part with a traditionally manufactured one can be joined by arc-welding, to obtain homogeneous or dissimilar joints, respectively. The homogeneous joints meet the demand of larger AMed components while the dissimilar joints enable the reduction of manufacturing costs since only the customized or geometrically complex part of the component is produced through AM technology. More in detail, an AMed part can be produced to be a part of an existing structure, to which it must be joined. The so obtained dissimilar welded joint allows taking advantage of the different manufacturing techniques for integrating an increased number of functions in each part. Both homogeneous and dissimilar welded joints, when introduced into real structures will undergo in-service cyclic loading conditions, therefore a fatigue strength assessment is required. Nevertheless, International Standards and Recommendations for fatigue assessment do not cover welded details including AMed parts, therefore an experimental characterization followed by a recalibration of the fatigue criteria is necessary.

The present research takes place in this scenario and focuses on the fatigue strength assessment of homogeneous and dissimilar arc-welded joints made of 316L steel. To this aim, experimental fatigue data relevant to butt-welded joints tested under axial loading and exhibiting failure from the weld toe have been collected from the literature.

2. Materials and methods

Experimental fatigue data were taken from the literature [1–3]and were referred to arc-welded butt-joints made of 316L steel and involving additively manufactured parts, both in the homogeneous and dissimilar configurations, this joint geometry being the only one investigated in the literature. More in detail, the data come from the papers by Braun et al. [1],Selmi et al.[3] and Chierici et al.[2]. In such works, the AMed parts were produced with LPBF technology either in the vertical [1,2]or in the horizontal [1,2] directions, whereas the wrought parts welded into the dissimilar joints were obtained through hot rolling process. The considered joints were tested under pure axial loading with loading ratio R between 0 and 0.5, namely with the loading axis aligned or orthogonal with respect to the printing direction for vertical and horizontal parts, respectively. Only joints exhibiting fatigue failures from the weld toe have been considered in the further analyses.

Initially, the data have been expressed in terms of number of cycles to failure (N_f) as a function of the nominal stress range ($\Delta\sigma$) and compared with the fatigue design curve according to Eurocode 3[4]. Later on, the experimental data were re-analyzed using the Peak Stress Method (PSM) which is an engineering local approach that allows to rapidly estimate Notch Stress Intensity Factors at the weld toe and weld root by linear elastic FE analyses with coarse meshes. Such an approach allows to summarize the fatigue strength of welded joints in a single design scatter band, regardless of the joint geometry. To do this, first the weld toe side of the butt joints has been idealized as a sharp V-notch, then a linear elastic FE model has been defined in Ansys® environment adopting a 2D coarse mesh pattern. The opening peak stress has been calculated at the weld toe side and adopted to convert the experimental results into the equivalent peak stress range ($\Delta\sigma_{eq,peak}$), according to the procedure described in detail in Ref. [5]. Finally, the experimental data have been compared with the design scatter bands previously calibrated on fatigue data generated by WR-WR welded joints made of structural steels [5] and WR-WR welded joints made of austenitic stainless steels [6], respectively.

3. Results and conclusions

The comparison between the experimental data and Eurocode 3 highlighted that the FAT class and the inverse slope suggested by Eurocode 3[4], which is focused on structural steels, did not match the behavior of joints with AMed parts made of stainless steels. On the other hand, the experimental data resulted in agreement with the design scatter band previously fitted on fatigue results generated by testing wrought-wrought butt-welded joints made of austenitic stainless steel.
The comparison between the experimental data and PSM-based design scatter bands confirmed what observed in terms of nominal stresses: the results of welded joints with AMed parts made of 316L steel are not in agreement with those relevant to structural steels WR-WR joints, while they are in good agreement with those of austenitic stainless steels WR-WR joints.
Finally, it has been demonstrated that the PSM-based design scatter band calibrated on stainless steels WR-WR joints [6] can be applied for the fatigue strength assessment of joints with AMed parts, regardless the joint geometry.

4. Acknowledgements

This study was carried out within the MICS (Made in Italy – Circular and Sustainable) Extended Partnership and received funding from the European Union Next-Generation EU (PIANO NAZIONALE DI RIPRESA E RESILIENZA (PNRR)–MISSIONE 4 COMPONENTE 2, INVESTIMENTO 1.3– D.D. 1551.11-10-2022, PE00000004). This manuscript reflects only the authors' views and opinions, neither the European Union nor the European Commission can be considered responsible for them.

5. References

[1] Braun M, Schubnell J, Sarmast A, Subramanian H, Reissig L, Altenhöner F, et al. Mechanical behavior of additively and conventionally manufactured 316L stainless steel plates joined by gas metal arc welding. Journal of Materials Research and Technology 2023;24:1692–705. https://doi.org/10.1016/j.jmrt.2023.03.080.
[2] Chierici M, Menghini A, Kanyilmaz A, Gökhan Demir A, Castiglioni CA, Berto F, et al. Fatigue characterization of hybrid manufacturing of steel construction parts via arc welding of LPBF-produced and hot-rolled stainless steel. n.d.
[3] Selmi H, Brousseau J, Caron-Guillemette G, Goulet S, Desjardins J, Belzile C. Weldability of 316L Parts Produced by Metal Additive Manufacturing. Journal of Manufacturing and Materials Processing 2023;7. https://doi.org/10.3390/jmmp7020071.
[4] Eurocode 3 : design of steel structures. BSI; 2010.
[5] Meneghetti G, Campagnolo A. State-of-the-art review of peak stress method for fatigue strength assessment of welded joints. Int J Fatigue 2020;139. https://doi.org/10.1016/j.ijfatigue.2020.105705.
[6] Contiero L, Vecchiato L, Campagnolo A, Babini V, Meneghetti G, Zamperla A. Stima della vita a fatica basata sul Peak Stress Method di giunzioni saldate dissimili testa-a-testa in AISI 316L tra piatti ottenuti da Additive Manufacturing e laminati. n.d.

RANDOM FATIGUE LIFE ASSESSMENT: NUMERICAL AND EXPIRIMENTAL STUDY

***L. Rebhi*[1], *A. Bouzar Essaidi*[1]**
[1] *Laboratoire Mécanique des Structures, Ecole Militaire Polytechnique, Algeria*

Abstract

Throughout their service life, machines, equipment, vehicles and buildings are subject to loads, most of which vary over time. An important task in estimating the service life of a structure or component is to analyze the operational loads in its different parts. In the case where these structures are subject to random excitations, the notion of PSD is essential for the estimation and calculation of the integrity and service life of these structures. In this work, several methods for fatigue life assessments based on the frequency response are put into practice. These methods have been applied to real model of a structure. Finally, a real laboratory test was carried to assess the effectiveness of these frequency-based methods in comparison to the time-domain calculation method.

Keywords: random fatigue, finite element analysis, stress modal analysis.

1. Introduction

In the context of random loads, such as those arising from environmental conditions, operational stresses, or seismic activity, accurately predicting structural fatigue life becomes increasingly challenging. The stochastic nature of these loads necessitates the application of advanced models and methodologies to evaluate material strength and crack propagation. These approaches must not only account for load variability but also deliver reliable and robust predictions of structural longevity. The fatigue life prediction of structures under random loads has been the subject of many research studies found in the literature. These latter are classified into two categories.

In the first category, the issue was addressed using temporal methods. The root mean square (RMS) model has been applied to predict fatigue life in aluminum alloy specimens under random loading, with improved accuracy achieved using Forman's equation [1]. A two-scale temporal asymptotic homogenization method has been developed to model fatigue as a multiscale phenomenon in the time domain, decomposing the problem into micro- and macro-chronological scales [2]. Neural stochastic differential equations have been employed to combine classical differential equation models with machine learning for random fatigue modeling [3]. However, the application of temporal methods for fatigue life prediction under random loading conditions presents several limitations, including significant computational demands and a lack of insight into the frequency domain.

The second category deals with frequency-domain methods for fatigue life assessment. In the frequency-domain method, random loads are often characterized using power spectral density (PSD) functions, which describe the distribution of load energy over different frequencies. This method transforms the time-domain load history into the frequency domain using techniques like Fourier transforms. Spectral methods for fatigue life prediction under wide-band random loading have gained significant attention in recent years. These methods utilize the power spectral density (PSD) of stress processes to estimate fatigue life, avoiding time-consuming simulations [4]. They

can be applied to various types of random processes, including Gaussian and non-Gaussian, stationary and non-stationary, and narrow-band and wide-band [5]. While traditional frequency-domain techniques have limitations, newer approaches offer improved accuracy for wide-band random loading. Recent advancements include the development of artificial neural network models, which incorporate bandwidth parameters and material properties to enhance prediction accuracy [6]. However, the effectiveness of spectral methods depends on how well their underlying assumptions align with real-world conditions, emphasizing the importance of understanding each method's applicability range to avoid estimation errors [7].

The present study compares various methods for calculating fatigue life under random loading conditions, with the objective of assessing and contrasting their performance. It aims to highlight the advantages and limitations of different techniques, ranging from traditional fracture mechanics to statistical and probabilistic approaches, providing comprehensive insights and practical recommendations for both industrial applications and academic research. A key aspect of this research is its reliance on empirical testing to validate the theoretical models. The incorporation of experimental results ensures that the analysis is grounded in practical reality, enhancing the robustness and relevance of the findings. By leveraging both theoretical approaches and real test data, the study delivers actionable recommendations that can improve the reliability of fatigue life predictions in engineering applications.

2. Numerical Modelling

In this section, the impact of random vibrations on service lives is explored through an example of a structure subjected to random base excitation. This scenario provides a realistic context to evaluate the effects of vibrations on the durability of structures to resist these dynamic constraints. The problem concerns a well-known reference structure, a cantilever beam, clamped along the left edge. An excitation in terms of acceleration is applied to its fixed end. The beam is modeled using quadrilateral finite elements as illustrated in figure1.

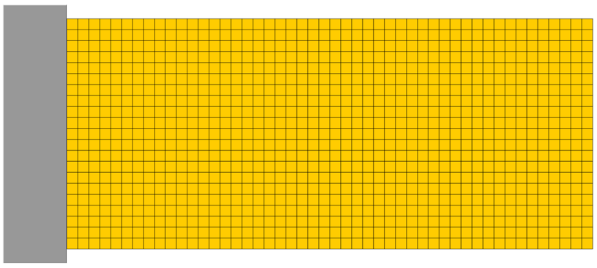

Fig.1. Finite element model of the beam

The applied excitation is in the form of white noise (see Figure 2) with an amplitude equal to 1000 (g2/Hz).

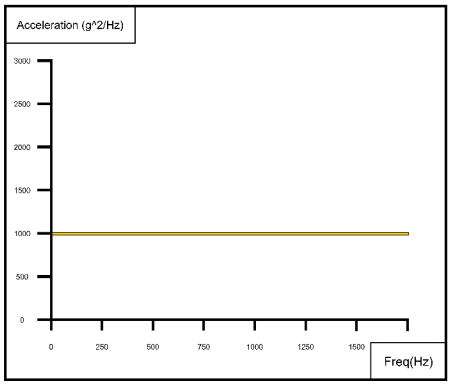

Fig.2. Input acceleration PSD of the base excitation

To evaluate the fatigue life of the specimen, a co-simulation approach was employed, integrating ANSYS and MATLAB software. This process was conducted in multiple distinct, yet complementary, stages.

Initially, the geometric and mechanical parameters of the specimen were established, with careful specification of all material and dimensional properties. This foundational step is essential for ensuring the accuracy of later analyses.

A modal analysis of the structure was subsequently conducted, enabling identification of the specimen's natural frequencies and corresponding modal shapes. Specifically, the stress modal analysis (SMA) method was applied to detect hot spots within the part most susceptible to experiencing high stress and, therefore, at higher risk of premature fatigue failure.

After identifying critical regions (hot spots), a spectral analysis was performed to assess the structure's response to random dynamic loads. This approach allowed for the extraction of the power spectral density of the von Mises equivalent stresses within these critical areas, offering a detailed frequency-domain representation of stress distribution for an in-depth evaluation of fatigue behavior. To estimate fatigue life, several frequency-domain techniques were employed, correlating the spectral information with the load cycles experienced by the component, thus providing a durability estimate under stochastic operational conditions. For comparative analysis, Miner's rule, combined with rainflow cycle counting, was also applied after converting the power spectral density (PSD) signal into the time domain.

Figure 3 provides the illustrating diagram of the process for calculating the structure's fatigue life based on co-simulation methodology.

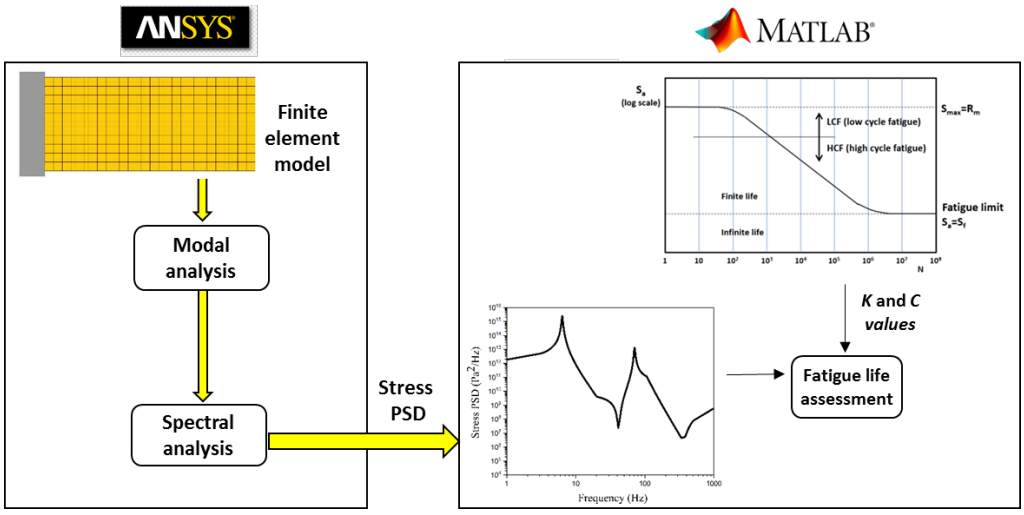

Fig.3. Illustrative diagram of the fatigue life assessment

3. Materials and methods

In order to obtain an assessment of the fatigue life of the specimen modeled in the numerical section, a fatigue life test was carried out. The excitation acceleration profile, shown in Figure 2, was applied to the base of the specimen by means of an electromagnetic exciter. Professional hardware and software, equipped with a control loop, were employed to generate the excitation based on a specified power spectral density, while the corresponding dynamic responses in terms of acceleration PSD were measured using accelerometers. The response measurement points were strategically selected on the clamped node and the free end of the specimen. Figure 4 illustrates the measurement and analysis chain used in the experiment.

	$C\ (MPa^k)$	K	$S_u(MPa)$	$RMS(MPa)$
Aluminum	6.85310^{19}	7.30	446	10

Table 1. Material parameters [8] and RMS for the fatigue-life calculation.

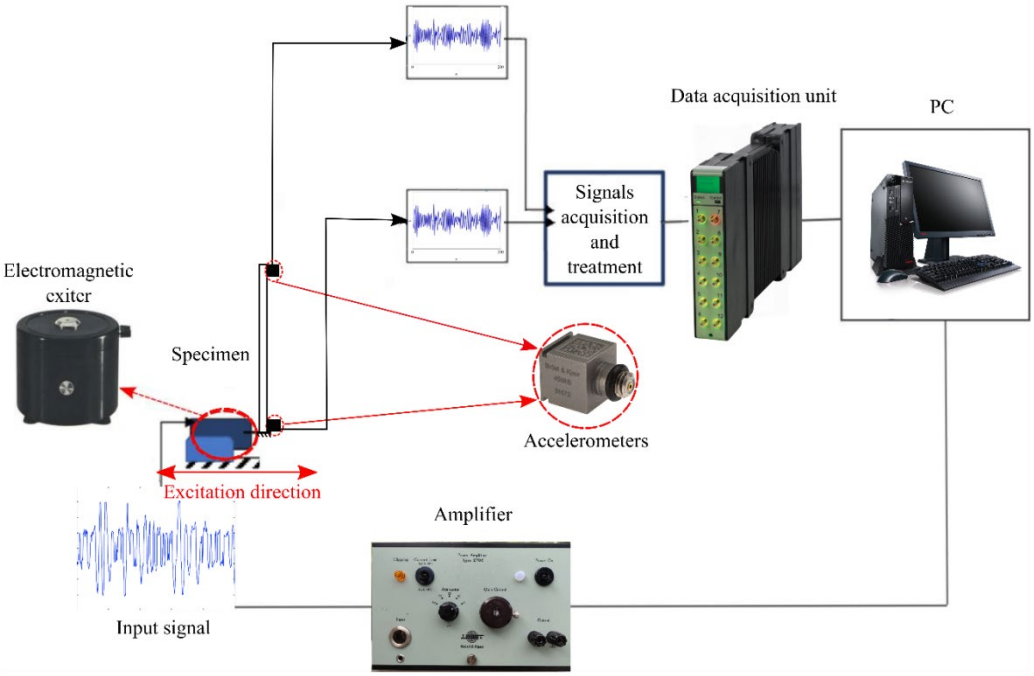

Fig. 4. Measurement chain of the fatigue test

The test setup included a computer for control and data acquisition, acceleration sensors, and a shaker system, as illustrated in Figure 5.

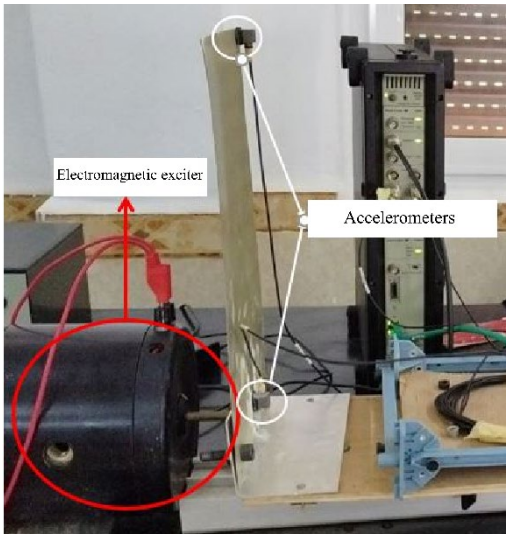

Fig. 5. The random fatigue test setup

4. Results and conclusions

Figure 6 illustrates the stress mode shapes contour of the first six modes in term of (von Mises stress). It can be seen that the positions of the maximum values of each mode are totally different. In order to locate the fatigue hotspots, the SMSs are being further investigated. Since the excitation frequency, ranging from 1 to 1750 Hz covers the first six modes, the modal stress distributions of these six modes are observed.

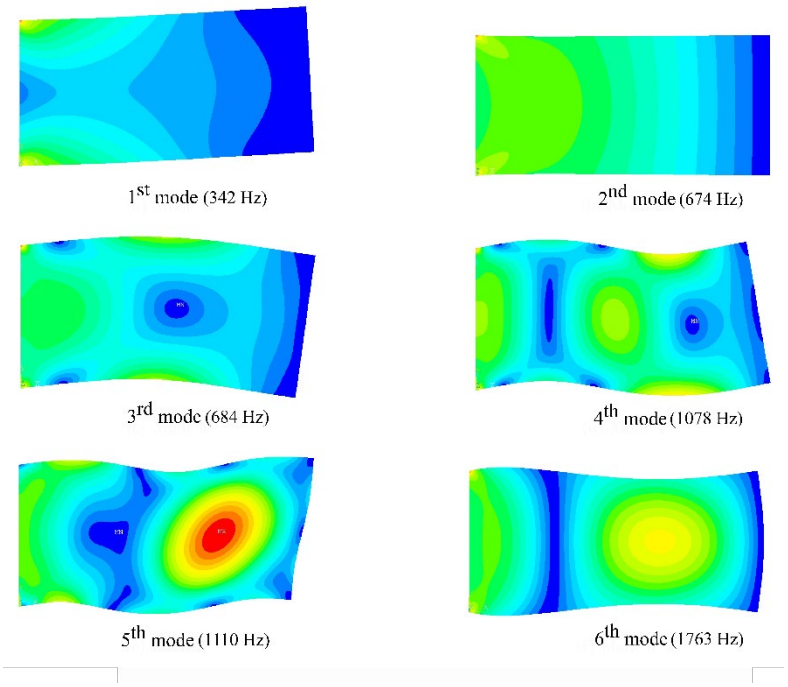

Fig. 6. Stress mode shapes of the specimen

Method	$\alpha_{0.75}$	*Tovo-Benasciutti*	*Dirlik*	*Narrow band*	*Wirsching-Light*	*Zhao et Baker*	*Miner*	*Experimental*
Fatigue life (seconds)	$2.29.10^4$	$2.90.10^4$	$2.87.10^4$	$2.63.10^4$	$3.27.10^4$	$3.31.10^4$	$1.27.10^5$	$3.02.10^4$

Table 2. Comparison of fatigue life value.

The fatigue life results derived from various methods, alongside the experimentally obtained values, are presented in Table 2. These findings reveal that frequency-based methods provide a more accurate estimation of fatigue life when compared to the time-based approach, particularly the one utilizing Miner's rule. This highlights the reliability of frequency-domain techniques in predicting fatigue performance, offering an alternative to traditional time-domain analyses.

The accuracy of predictions is a critical criterion for comparing different methods. The Dirlik method is widely regarded as highly accurate, particularly for wide-band spectra. The Wirsching-Light method, with its empirically derived correction factor, enhances accuracy for moderately wide spectra. In contrast, the $\alpha_{0.75}$ method and the narrow-band approach, while less precise, are simpler to implement. The methods proposed by Tovo and Benasciutti, as well as Zhao and Baker, achieve improved accuracy through their combinatorial and statistical methodologies.

6. Conclusion

This comparative study on the calculation of the fatigue life of structures subjected to random loading provides a comprehensive overview of the methods available in this field. Through an in-depth review of the state of the art on fatigue and random vibrations, we were able to contextualize our research and grasp the fundamental challenges associated with this domain. The comparative analysis of these methods highlighted key aspects, including the strengths, limitations, and the most suitable applications for each approach. For instance, some methods demonstrated higher accuracy for wide-band spectra, while others proved more effective for medium to narrow-band spectra.
In conclusion, this study represents a significant contribution to the understanding and advancement of practices in the estimation of fatigue life under random loading conditions. It offers valuable insights for optimizing calculation methods and paves the way for future research aimed at refining existing approaches and exploring innovative solutions for even more accurate and efficient fatigue life predictions.

7. References

[1] S.T. Kim, D. Tadjiev, H.T. Yang (2005). Fatigue Life Prediction under Random Loading Conditions in 7475-T7351 Aluminum Alloy using the RMS Model. International Journal of Damage Mechanics, 15(1), 89–102.
[2] C. Oskay, J. Fish (2004). Fatigue life prediction using 2-scale temporal asymptotic homogenization. International Journal for Numerical Methods in Engineering, 61(3), 329–359.
[3] A. Joanni, U. Hipp (2022). Random Fatigue Modeling using Neural Stochastic Differential Equations. 2022 Annual Reliability and Maintainability Symposium (RAMS), 1–4.
[4] G. Petrucci, B. Zuccarello (2004).Fatigue life prediction under wide band random loading. Fatigue & Fracture of Engineering Materials & Structures, 27(12),1183–1195.
[5] J. Hu (1995). Life prediction and damage acceleration based on the power spectral density of random vibration. Journal of the IEST, 38(1), 34–40.
[6] H. Sun, Y. Qiu, J. Li (2021). A novel artificial neural network model for wide-band random fatigue life prediction. International Journal of Fatigue, 157, 106701.
[7] D. Benasciutti, R. Tovo (2018). Frequency-based analysis of random fatigue loads: Models, hypotheses, reality. Materialwissenschaft Und Werkstofftechnik, 49(3), 345–367.
[8] M. Mrsnik, J. Slavic, M. Boltezar (2013). Frequency domain methods for a vibration-fatigue-life estimation application to real data. International journal of fatigue, 47, 8–17.

DESIGN OF TEST SETUP TO MEASURE HOOP ELASTIC MODULUS OF GRE PIPES

Abdullah M. Al Shabibi, Luqman S. Al Maskari, Ahmed A. Al Fadhli, Ahmed M. Al Omairi, Almuataz S. Al Shukaili

Department of Mechanical and Industrial Engineering, Sultan Qaboos University, Muscat, Oman

1. Introduction

Glass Reinforced Epoxy (GRE) pipes have gained widespread use in various industries, including oil and gas, chemical processing, and marine applications. GRE pipes are a thermosetting type of polymer made by folding many continuous fiberglass threads with cured amine epoxy resin. This manufacturing process gives the GRE pipes strong thermal and mechanical properties. GRE pipes are also known for their low internal resistance of flowing fluids making them good alternatives to carbon steel pipes. Furthermore, GRE pipes are popular because of their non-conductive, lightweight and easy to install nature making them suitable for use in many applications. Ensuring the structural integrity of these pipes is of prime importance for safe and efficient operations. A testing and inspection procedure for GRE pipes is essential in providing standard tests to ensure the quality of GRE pipes.

There are several well established testing protocols for GRE pipes. The ASTM D2412 presents a standard procedure to determine the pipe's stiffness and deflection characteristics under different loading conditions [1]. The elastic strength of GRE pipes in the longitudinal direction can be determined using the ASTM D2105 test method [2]. Hydrostatic tests are another reliable method for ensuring the strength of the GRE pipes. The ASME B31 code provides a guideline in conducting piping pressure tests [3]. The Pressure tests can be carried out either with liquid, usually water (hydrostatic), or gas, usually dry nitrogen. Furthermore, mechanical characterization of GRE pipes has been investigated by many researchers. Mertiny et al. [4] experimentally studied the effect of the winding angle on the strength of composite pipe. Tarakcioglu [5] investigated the fatigue behavior of glass/epoxy filament wound pipes under internal pressure The mechanical behavior of GRE pipe under axial monotonic loading was studied by [6] using acoustic emission and tensile test to determine their failure mode.

This study aims at designing and fabricating an experimental setup that is capable of measuring the hoop tensile strength and Poisson’s ratio of GRE pipes. The pipe is loaded by a hydraulic pressure and constrained in axial direction by a system of aluminum flanges and steel rods. The stress was then calculated using the measured values of pressure and strains.

2. Experimental setup

The experimental setup consists of a test specimen, a hydraulic pump and measurement instrumentations. The test specimen is made of 0.5 m long GRE pipe, two blind flanges and steel rods. Figure 1 shows the assembled test specimen where he two flanges are closing the two ends of the pipe. Steel rods are utilized to connect the flanges and to prevent the pipe from expanding the

axial direction. The pump is then connected through a hose to one of the flanges to provide the hydraulic pressure.

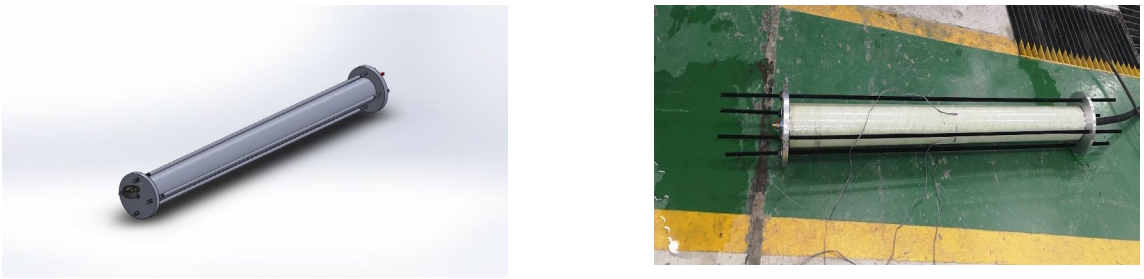

Fig. 1. Assembled test specimen

Two types of measurement instrumentations are utilized in this test: pressure transducer and strain gauges. The pressure transducer is connected to one of the flanges to measure the real-time hydraulic pressure and the strain gauges are attached to the pipe outer surface and oriented in the hoop and axial directions to obtain the corresponding strains in these two directions. All measurement instrumentations are connected to a data logger for real-time monitoring of the experimental data. Figure 2 shows the placement of the strain gauges on the GRE pipe's outer surface.

Fig. 2. Strain gauges attachment to GRE pipe surface

3. Results and conclusions

This experimental test is aimed at setting a procedurę for determining the Hoop tensile modulus and Poisson's ratio of a GRE pipe following the API 15HR standard. The Hook's relation is used to calculate the elastic modulus of the GRE pipe in the hoop direction:

$$E_h = \frac{\sigma_h}{\varepsilon_h} \qquad (1)$$

Where E_h is the Elastic Hoop Modulus, σ_h is the hoop stress, and ε_h is the measured hoop strain. Knowing the internal pressure and the pipe geometry, the hoop stress can be calculated through the following equation as in the API 15 HR standard:

$$\sigma_h = P\frac{R_o^2+R_i^2}{R_o^2-R_i^2} \qquad (2)$$

Where P is the internal pressure, R_i the pipe inner radius, and R_o is the pipe outer radius. The inner and outer radius of the pipe are measured and found to be 0.04975 m, and 0.05425 m, respectively.

The Poison's ratio for the pipe can be calculated using the following relation:

$$v = -\frac{\varepsilon_a}{\varepsilon_h} \qquad (3)$$

Where ε_a is the strain measured in the axial direction.

Figures 3 and 4 show a plot of hoop and axial strain versus applied pressure. As anticipated the relation is almost linear for the targeted range of the applied pressure. The test was repeated three times for three different specimens and an average value of 19.1 GPa has been found for the Elastic Hoop Modulus and 0.38 for the Poisson's ratio. The setup has demonstrated to be a reliable tool for measuring one of the most critical Mechanical Property of GRE pipes.

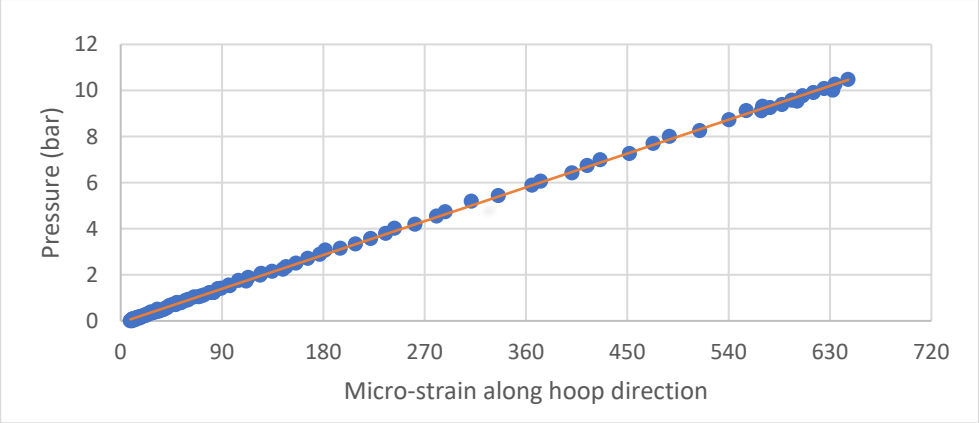

Fig. 3. Attached the strain gauges in GRE pipe surface

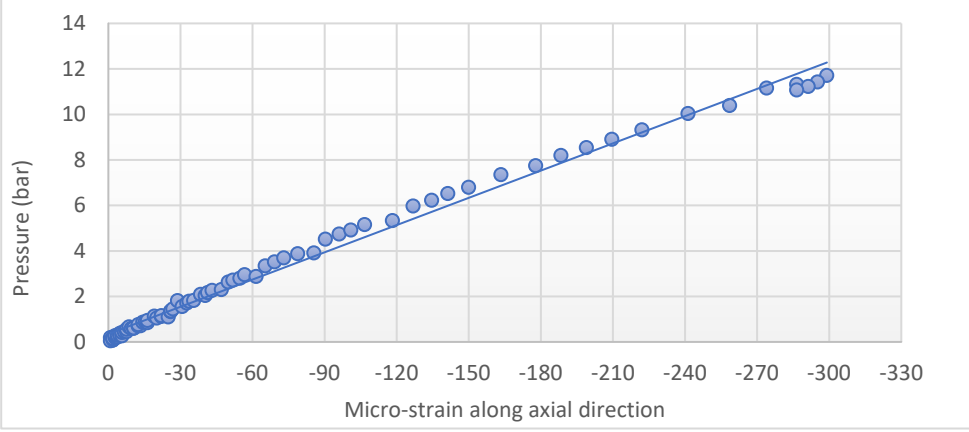

Fig. 4. Attached the strain gauges in GRE pipe surface

5. References

[1] ASTM D2412 (2002). Standard test method for determination of external loading characteristics of plastic pipe by parallel-plate loading. *American Society for Testing and Materials*, U.S.A.

[2] ASTM D2105 (2014). Standard Test Method for Longitudinal Tensile Properties of Fiberglass, (Glass-Fiber-Reinforced Thermosetting-Resin) Pipe and Tube. *American Society for Testing and Materials*, U.S.A.

[3] ASME B31 (2016). ASME Code for Piping. *American Society for Testing and Materials*, U.S.A.

[4] M. Martens and F. Ellyin (2000). Biaxial monotonic behavior of a multidirectional glass fiber epoxy pipe, *Composites*, **Part A 31**, 1001–1014.

[5] N. Tarakcioglu (2005). Fatigue failure behavior of glass/epoxy ±55 filament wound pipes under internal pressure, *Composites Science and Technology*, **65**, 703–708.

[6] A. Ben Khalifa, M. Zidi and L. Abdelwahed (2012). Mechanical characterization of glass/vinylester ±55° filament wound pipes by acoustic emission under axial monotonic loading, *Comptes Rendus Mecanique*, **340**, 453–460.

A STUDY ON FATIGUE ENHANCEMENT IN NOTHED AEROSPACE COMPONENTS USING LASER SHOCK PEENING

M.A. Attolico[1], G. Renna[2], V. Moramarco[1], C. Casavola[1]
[1] Department of Mechanics, Mathematics and Management, Polytechnic University of Bari, Via Orabona 4, Bari, 70125, Italy
[2] Department of Engineering for Innovation, University of Salento, via per Monteroni di Lecce, 73100, Lecce, Italy

1. Introduction

Ensuring the structural integrity of aerospace components under cyclic loading is critical to their performance and safety. Aluminum alloys, particularly the 7xxx series, are extensively used in the aerospace industry due to their exceptional mechanical properties and corrosion resistance. Among these, aluminum alloy 7050-T7451 stands out for its high strength-to-weight ratio, making it ideal for applications where weight reduction is essential. However, its fatigue performance can be significantly compromised when subjected to surface treatments, such as anodizing, which are commonly applied to enhance corrosion resistance [1].

Tartaric-Sulfuric Acid Anodizing (TSA), a widely used anodizing process, forms a protective oxide layer on the aluminum surface, improving its durability against environmental degradation [2]. However, this anodic layer introduces surface defects such as microvoids and tensile residual stresses, which act as preferential sites for crack initiation, reducing fatigue life. In high-cycle fatigue (HCF) regimes, this reduction becomes more pronounced, necessitating advanced surface treatments to counterbalance the detrimental effects.

Laser Shock Peening (LSP) has emerged as a promising technology to enhance fatigue life by inducing compressive residual stresses in the material's surface and subsurface regions. This treatment delays crack initiation and slows propagation under cyclic loads. Unlike conventional shot peening, LSP provides precise control over the residual stress distribution and can be tailored for specific geometries [3-4]. However, the presence of geometric discontinuities, such as notches, poses additional challenges in achieving uniform stress fields. This study evaluates the effectiveness of LSP in mitigating the adverse effects of TSA anodizing on the fatigue behavior of aluminum alloy 7050-T7451 components with notched geometries. By addressing these challenges, the study contributes to the development of robust surface treatment strategies for aerospace applications.

2. Materials and methods

The material under investigation was aluminum alloy 7050-T7451, machined into specimens with a circular notch geometry featuring a radius of 43.7 mm. This notch configuration was selected to achieve a stress concentration factor (Kt) of 1.5, representative of critical areas in aircraft components prone to fatigue failure (Figure 1). The study analyzed four distinct surface treatment conditions to evaluate their impact on fatigue performance.

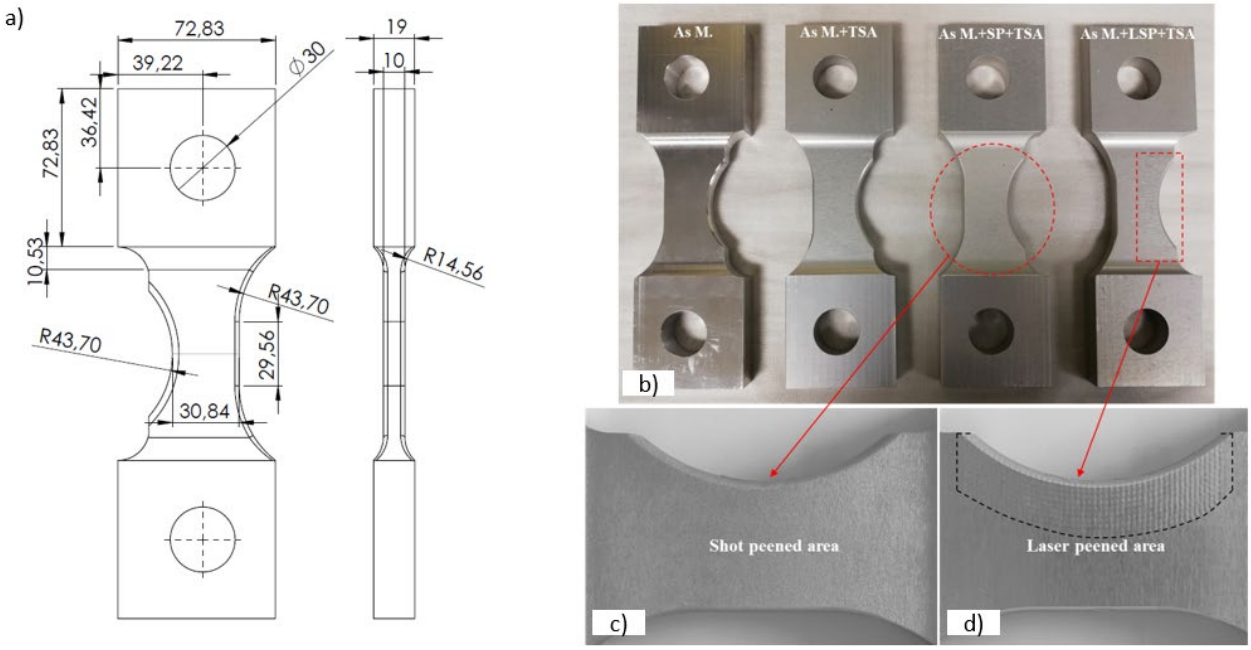

Fig. 1. a) Geometric properties of single edge notch fatigue specimen; b) overall view of each type of component; c) magnified view of the shot peened region of As M.+SP+TSA components; d) magnified view of the laser shock peened region of As M.+LSP+TSA components.

The as-machined (As M.) specimens served as the baseline, providing insights into the untreated material's fatigue characteristics. Another group underwent Tartaric-Sulfuric Acid Anodizing (TSA), which deposited a 2 µm-thick protective oxide layer. This process was included to assess the typical reduction in fatigue performance associated with anodizing. In the third group, shot peening was applied before anodizing (SP+TSA) to introduce compressive residual stresses, providing a comparative standard for conventional peening techniques. The fourth group involved Laser Shock Peening (LSP), where a Nd:YLF laser with a pulse energy of 2.5 J and a spot diameter of 2 mm was used to treat the notch region. The laser parameters included a 33% overlap to ensure consistent stress distribution, and the TSA process followed LSP treatment in this group.

Residual stress measurements were conducted using X-ray diffraction (XRD) with the $\sin^2\psi$ method. A grid of 13×11 points around the notch provided detailed stress maps for each treatment. Fatigue tests were performed under uniaxial cyclic loading at a stress ratio (R) of 0.1, with the maximum number of cycles set at 3×10^6 or until failure. Post-test analyses included Scanning Electron Microscopy (SEM) to identify crack initiation sites and investigate failure mechanisms.

3. Results and conclusions

Residual stress measurements revealed that both shot peening and laser shock peening induced significant compressive stresses in the treated regions. For LSP-treated specimens, average residual stresses reached approximately -280 MPa near the surface, with the stress field extending beyond the treated area. However, at the notch fillet, a reduction in compressive stresses was observed, likely due to the curvature of the surface. In contrast, shot peened specimens showed a more uniform stress distribution across the notch region. A representative residual stress map is shown in Figure 2.

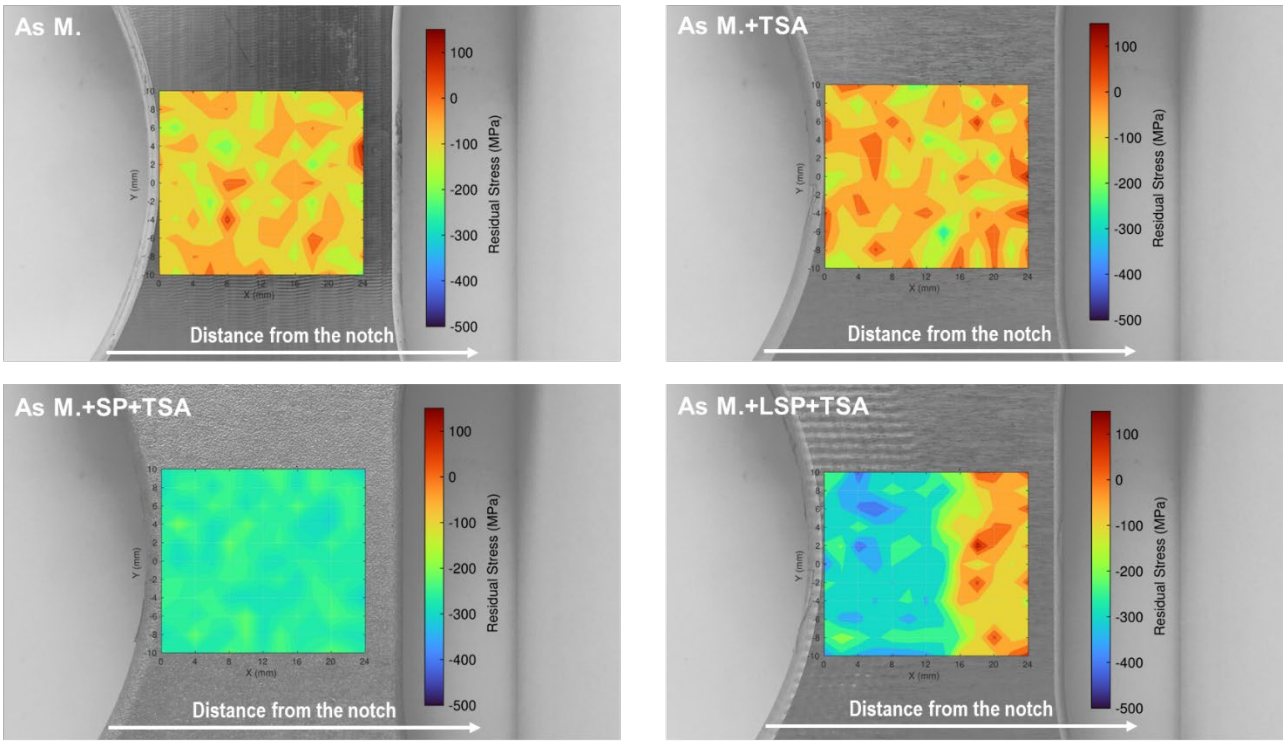

Fig. 2. Residual stress maps on the front surfaces of single-edge notched components; a) As M.; b) As M.+TSA; c) As M.+SP+TSA and d) As M.+LSP+TSA.

Fatigue test results demonstrated that surface treatments significantly improved the fatigue life of the specimens compared to the untreated (As M.) and TSA-only groups. Shot peening combined with TSA anodizing (SP+TSA) exhibited the best overall fatigue performance, with increased resistance to crack initiation and propagation. While LSP-treated specimens (LSP+TSA) also showed a marked improvement over untreated samples, their performance was slightly lower than SP+TSA specimens, particularly at higher stress levels. This discrepancy was attributed to the reduced compressive residual stresses at the notch fillet in LSP-treated specimens.

Figure 3 illustrates the S-N curves for the four specimen groups, highlighting the superior performance of LSP and SP treatments compared to untreated and TSA-only samples.

SEM analyses of fracture surfaces revealed that cracks in TSA-treated specimens typically initiated at surface defects, such as pore clusters, resulting from the anodizing process. In LSP-treated specimens, cracks initiated at the notch fillet, where residual stresses were lower. However, the presence of compressive stresses in the subsurface regions slowed crack propagation, contributing to the observed fatigue life improvement.

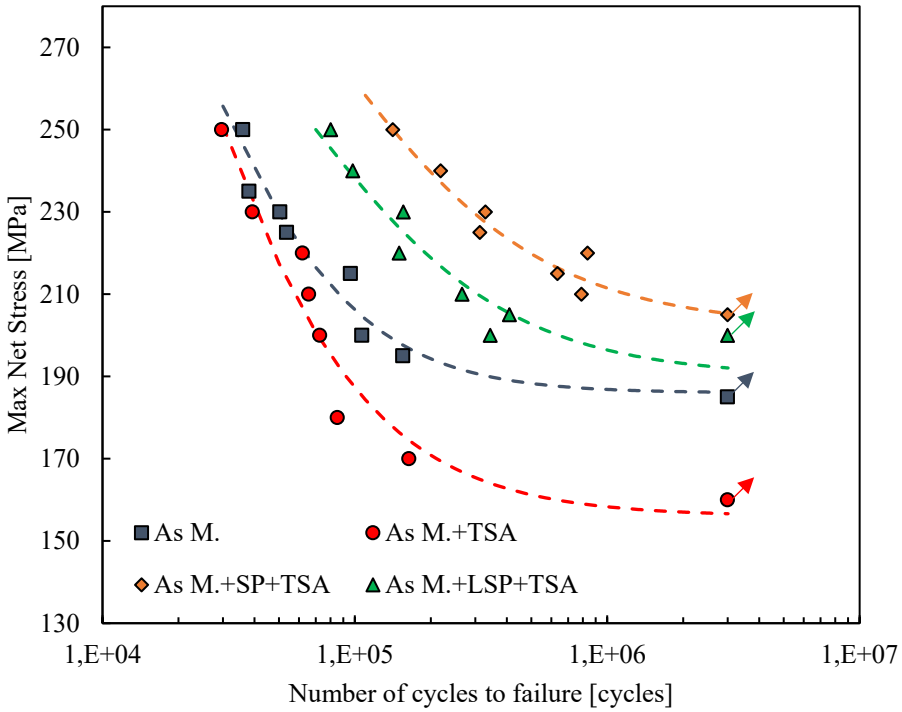

Fig. 3. S-N fatigue curves of single edge notched components under constant amplitude uniaxial cyclic loading.

4. Acknowledgements

The authors would like to thank Airbus Operations GmbH - ZAL Tech Center for providing the materials necessary to conduct this study.

5. References

[1] Hughes AE, Birbilis N, Mol JMC, Garcia SJ, Zhou X, Thompson GE. High Strength Al-Alloys: Microstructure, Corrosion and Principles of Protection.
[2] Martínez-Viademonte M.P., et al., "A review on anodizing of aerospace aluminum alloys," *Coatings*, 2020.
[3] Gujba A.K., et al., "Laser peening process and its impact on material properties," *Materials*, 2014.
[4] Peyre P., et al., "Laser shock processing of aluminum alloys," *Materials Science and Engineering*, 1996.

INFLUENCE OF HYGROSCOPIC ABSORPTION ON THE RESILIENCE OF EPOXY MATRIX COMPOSITE REINFORCED WITH CERAMIC PARTICLES

M.D.D Boudiaf[1], R. Roubache[2] , M.K Harouche[1] and S. Benhamouda[1]

[1] Ecole Militaire Polytechnique, Laboratoire Génie des Materiaux, Bordj el Bahri, Alger, Algerie
[2] Institute for Research and Development of Weapon Systems and Mobility Means/1RM

1. Introduction

Polymer Matrix Composites (PMO) are widely used in various industrial applications today[1]. These materials offer unique mechanical properties that allow for lightweight structures, thereby increasing energy efficiency[2]. However, the hygro-thermo-mechanical environment to which these structures are exposed can impact their durability[3] . Indeed, water absorption by hydrophilic organic matrices can lead to a reduction in the polymer network's rigidity and cause swelling.

This matrix expansion, counteracted by typically hydrophobic reinforcements, can result in significant internal mechanical stresses that may be detrimental to the structure[4]. Aging of polymers can lead to slow changes (reversible or irreversible) in the material's properties due to their inherent instability or environmental influences. Generally, water diffuses into the molecular network, acting as a plasticizer, lowering the glass transition temperature and affecting the mechanical properties (rigidity modules, fracture properties, etc.)

2. Materials and methods

1. Samples elaboration

Epoxy/kaolin samples were prepared according to an optimized experimental procedure from a previous study to achieve better dispersion and avoid particle agglomeration and sedimentation. The steps of this procedure are as follows: heating the epoxy resin and kaolin powder mixture to 40°C with mixing for 10 minutes at 3000 rpm, then adding the hardener and continuing mixing for 2 min. The mixture is poured into molds and left to dry for 24 hours at room temperature, then cured in an oven at 60°C for 4 hours. Samples with different filler contents (1%, 3%, and 5%) and particle sizes ($d<63$ µm, $63<d<100$ µm, and $100<d<125$ µm) were prepared

2. Experimental methodology

Gravimetric measurements of samples in immersion or in a humid environment are used to monitor the progress of moisture uptake. After different immersion times, water absorption characteristics of the composites are determined by the mass percentage of water absorbed Mt.Impact tests were performed using a pendulum impact tester according to ASTM D256.

3. Results and conclusions

Based on the figures1 , it is clear that the resilince modulus decreases as water absorption increases, until a saturation value is reached. However, this gap gradually narrows with the increase in moisture absorption, up to the saturated state. Moreover, when comparing figures a, b, and c, it is observed that the decrease in Young's modulus is faster for the more heavily loaded composites. This indicates that the difference between the dry and saturated states increases with the loading rate. In the dry state, the most heavily loaded composite shows the highest Young's modulus, whereas in the saturated state, the least loaded composite has the highest value. This inversion occurs approximately halfway through the saturation process.

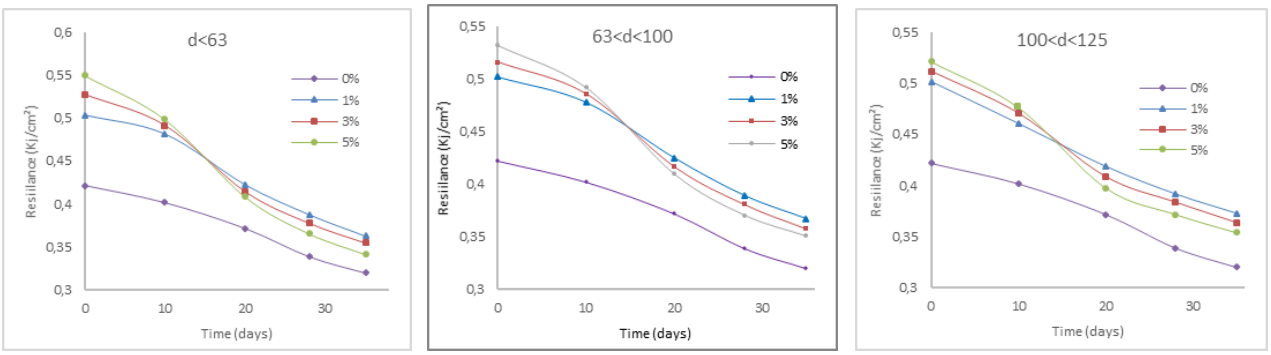

Figure 1 : impact resistance Charpy test of composite materials (epoxy-kaolin) of all models.

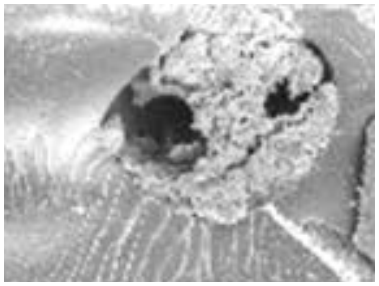

Figure 1: particle deterioration

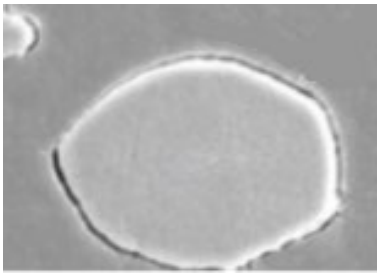

Figure 3: matrix-particle debonding

From 2 and 3 we observe the phenomenas that leads to characteristics loss. In figure 2 we see the total degradation of the kaolin particle caused to water absorbtion. In figure 3 we observe a total matrix-particle decohesion due to volume increase of the matrix caused by water absorbtion.

Conclusion

This study has shed light on the complex interaction between hygroscopic absorption and the mechanical properties of epoxy/kaolin composites. The results highlight the crucial role of powder weight ratio and particle size in determining water absorption behavior and its subsequent impact on the mechanical performance of these materials. The knowledge gained from this research can inform the design and development of epoxy/kaolin composites with enhanced durability and performance in moisture-rich environments.

Key Findings

1. The total surface area of powder particles-matrix interfaces is the main parameter determining water absorption and influencing mechanical characteristics.
2. Increasing the powder ratio increases water absorption and decreases the saturation time limit.
3. Using smaller particles increases water absorption and decreases the hygroscopic saturation time.
4. At saturation the mechanical characteristics decrease with an increase in powder weight ratio.
5. For particle size influence at saturation, an inversion of the studied characteristics is observed. In the dry state, the composite with the smallest particles has the best characteristics. However, with increasing water absorption, the decrease is greater for the composite with the smallest particle size, leading to an inversion at a certain water absorption rate. At saturation, the composite with the smallest particles has the lowest characteristics.

5. References

[1] K.J. Brookes (2016). Maraging steel for additive manufacturing-Philipp Stoll's paper at DDMC., *Met. Powder Rep.*, 71, 149–152.

[2] D. Croccolo, M. De Agostinis, S. Fini, G. Olmi, A. Vranic and S. Ciric-Kostic (2016). Influence of the build orientation on the fatigue strength of EOS maraging steel produced by additive metal machine. *Fatigue Fract. Eng. Mater. Struct.*, 39, 637–647.

[3] D. Croccolo, M. De Agostinis, S. Fini, G. Olmi, F. Robusto, S. Ćirić-Kostić, S. Morača and N. Bogojević (2019). Sensitivity of direct metal laser sintering Maraging steel fatigue strength to build orientation and allowance for machining, *Fatigue Fract. Eng. Mater. Struct.*, 42, 374–386.

[4] D. Croccolo, M. De Agostinis, S. Fini, G. Olmi, F. Robusto, S. Ćirić-Kostić, A. Vranic and N. Bogojevic (2018). Fatigue Response of As-Built DMLS Maraging Steel and Effects of Aging, Machining and Peening Treatments, *Metals*, 8, 1–21.

EXPERIMENTAL FATIGUE TESTING OF AN ALUMINUM FRAME FOR ELECTRICALLY-POWER ASSISTED CYCLES

E.V. Arcieri[1] and S. Baragetti[2]
[1] Department of Management, Information and Production Engineering (DIGIP), University of Bergamo, Dalmine (BG), Italy

1. Introduction

Environmental pollution caused by fossil-fuel-powered cars and motorcycles is a significant global concern. The emissions from these vehicles contribute to global warming and deteriorate air quality, leading to negative health impacts, particularly respiratory issue. Bicycles, as a sustainable transportation alternative, offer a solution to these problems. However, the physical exertion required for cycling can discourage many people from using traditional bicycles. The introduction of electrically-power assisted cycles (EPACs) represents a significant step toward sustainable mobility, offering an ecological alternative to traditional motor vehicles and a convenient, versatile option for cyclists, that promotes a more sustainable and healthier form of mobility [1].

The frame of a bicycle plays a vital role as the central structure that supports all other components. It is designed to absorb forces from pedaling, braking, rider weight and ground irregularities. In the case of EPACs, additional loads are due to the weight of the electric motor, battery, and associated control systems. The material selection for the frame is crucial in achieving a balance between weight and strength. Materials such as aluminum offer excellent strength-to-weight ratios and are commonly used to manufacture lightweight frames, improving energy efficiency and performance [2]. This approach, derived from the aerospace and automotive industries, helps reduce energy consumption and contribute to environmental sustainability.

The aim of this study is to test the durability of an aluminum EPAC frame under cyclic loading. The stresses in the frame were measured during the conducted test in order to identify the most stressed components.

2. Materials and methods

The tested EPAC frame was made of 6061-T6 aluminum alloy. The fatigue test was carried out on a frame + dummy fork system according to the UNI EN ISO 15194:2023 standard [3]. The fork was designed according to the stiffness requirements prescribed by the standard. The frame was secured at the rear drop-outs so that it was not restrained in a rotary sense. Dynamic forces of 600 N in a forward direction (tension loading) and 600 N in a rearward direction (compression loading) were applied to the front fork drop-outs for 100,000 cycles. The fork was free to move in the front/rear direction under the applied force but was constrained in the normal direction. Uniaxial strain gauges were placed at specific locations on the frame, far from the welds which connect the various parts, to measure the strains. The measured values of strains were then multiplied by the Young's modulus of the material, E = 69 GPa [4], to estimate the stresses in the frame parts.

3. Results and conclusions

The tested EPAC frame successfully resisted 100,000 cycles of the applied load without developing any cracks or fractures. Based on the data provided by the strain gauges, the most stressed areas of the frame were the top and down tubes, while the seat tube experienced very low stresses. This indicates that the down and top tubes are the primary load-bearing components under the considered loading condition, whereas the seat tube remains substantially unstressed.

Measured stresses (MPa)		
Position	Tension loading	Compression loading
Top tube (top)	-5	4
Top tube (down)	6	-4
Top tube (right)	1	-1
Down tube (down)	7	-8
Down tube (right)	-4	4
Seat tube (front)	-1	1
Seat tube (rear)	0	0

Fig. 1. Experimental setup (boundary conditions) and stresses measured during the test.

4. Acknowledgements

Funded by the European Union – Next Generation EU, PNRR - M4C2 INV. 1.4 National Center for Sustainable Mobility – MOST (CN00000023 - CUP F13C22000690001)

5. References

[1] L. Stilo, D. Segura-Velandia, H. Lugo, P.P. Conway and A.A. West (2021). Electric bicycles, next generation low carbon transport systems: A survey. *Transp. Res. Interdisc. Perspect.*, **10**, 100347.

[2] S.-Y. Lee, C.-P. Jiang, C.-K. Lee, W.-H. Huang, Y.-C. Cheng (2023). Optimization of design and fatigue simulations for an electric assisted bicycle frame using uniform design and grey relational analysis. *J. Strain Anal. Eng. Des.*, **58**, 3-16.

[3] UNI EN ISO 15194:2023, Cycles – Electrically power assisted cycles – EPAC Bicycles.

[4] W. Tong, K. He, X. Wang, X. Xu and M. Wang (2022). Mechanism of 6061 aluminum material erosion in USEMM. *Int. J. Adv. Manuf. Technol.* **118**, 895–906.

NUMERICAL INVESTIGATION OF THE EFFECT OF YIELD STRENGTH ON THE BEHAVIOUR OF CLAMPED CIRCULAR PLATE UNDER TRANSIENT PRESSURE LOADING

Swathi Kiran Anupoju [1], S.N. Khaderi [1], V. Narayanamurthy [2]
[1] *Mechanical and Aerospace Engineering, Indian Institute of Technology Hyderabad, India*
[2] *Research Centre Imarat, Hyderabad, India*

1. Introduction

Clamped circular plates are used as diaphragms, end-enclosures, and circular panels that must withstand high pressure and dynamic loading. They are also often studied and optimized for vibration performance in aerospace structures. They are frequently employed in pressure relief components in pressure vessels and tanks. Usually, clamped circular plates are subjected to static uniform pressure loading in structural applications and dynamic pressure loading in applications like rupture discs and pressure relief valves. Testing of the plates for uniform static pressure can be carried out by increasing the pneumatic or hydraulic pressure of a chamber closed by the test plate. In contrast, generating a dynamic pressure load requires a lot of effort. A few techniques involved in testing the plates under dynamic pressure load are using TNT explosives and developing an underwater blast simulator in which no explosives are employed. The type of load generated using explosives or underwater simulators [1] is an exponentially decaying load and many researchers have studied the behavior of different configurations of plates when subjected to these loads [2]. In contrast, the pressure loading generated in static testing is gradually increasing. However, no proper testing technique is available to develop a gradually increasing dynamic pressure load. So, it is necessary to develop an experimental method to study the clamped plates under dynamic loading. An appropriate technique is proposed in this work to develop a gradually increasing uniform dynamic pressure load to test the clamped circular plates and study the effect of yield strength on their dynamic behavior.

2. Materials and methods

The main objective of this experimental setup is to develop transient pressure loading on a clamped circular plate. The loading and unloading span of the pressure is aimed to be between 1– 10 ms. The schematic of the experiment is shown in Figure 1, where a thick cylinder is closed at one end by the clamped circular plate and the other end by a heavy piston. The piston starts to move toward the plate in the cylinder after being provided with some initial velocity using a dynamic source with a rapidly expanding compressed gas from an accumulator. The pressure in the air column increases as the piston moves forward, and this pressure is purely transient. The same pressure is applied on the clamped circular plate, the behavior of which can be investigated for different loading rates. A numerical investigation of this technique has been carried out using ABAQUS EXPLICIT. A combined Eulerian-Lagrangian (CEL) technique is employed in numerical investigation to study the interaction between air and clamped circular plates. The numerical model consists of a quarter symmetry model of the experimental set-up, i.e., piston, air, and clamped circular plate. The steel piston is assumed to be a rigid body in the numerical study; the air is considered the ideal gas to

investigate the circular plates made up of stainless-steel SS 304 in this study. The material properties of SS304 are extracted from the uniaxial tension test and implemented in the numerical model.

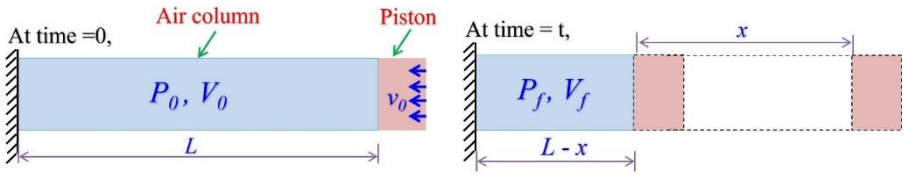

Figure 1 Schematic showing the technique to develop transient pressure loading on a circular plate

3. Results and conclusions

The out-of-plane displacement of the clamped circular plate measured at the center of the plate during the simulation is plotted along with the Von-Mises stress on the plate evolved with time in the Figure 2. The wiggles observed in the out-of-plane displacement plot in the early stages of loading are caused by the first mode of vibrations. After a while, these wiggles will vanish, and we can observe a steep rise in the displacement because of the plate bulging. The plastic yielding of the circumference of the clamped plate is the reason for the vanishing of initial wiggles. Wiggles are observed in the plot before yielding if we use a material with more yield strength. A physical experimental setup is subsequently developed based on this technique, and the effect of other parameters such as impact velocity, length of the air column, and plate material are investigated.

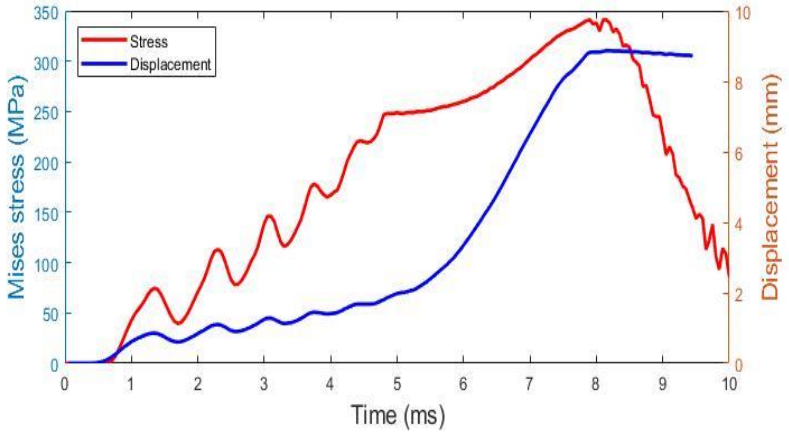

Figure 2 Evolution of out-of-plane displacement at the center of the plate and Mises stress with time

4. Acknowledgements

The research presented in this paper has received funding from the Ministry of Education India along with the Defence Research Development Organisation, India.

5. References

[1] H. D. Espinosa, S. Lee, and N. Moldovan, “A novel fluid structure interaction experiment to investigate deformation of structural elements subjected to impulsive loading,” Exp Mech, vol. 46, no. 6, pp. 805–824, Dec. 2006, doi: 10.1007/s11340-006-0296-7.

[2] S. Chung Kim Yuen, G. N. Nurick, G. S. Langdon, and Y. Iyer, “Deformation of thin plates subjected to impulsive load: Part III – an update 25 years on,” Int J Impact Eng, vol. 107, pp. 108–117, Sep. 2017, doi: 10.1016/J.IJIMPENG.2016.06.010.

[3] V. Aune, G. Valsamos, F. Casadei, M. Larcher, M. Langseth, and T. Børvik, “Numerical study on the structural response of blast-loaded thin aluminium and steel plates,” Int J Impact Eng, vol. 99, pp. 131–144, Jan. 2017, doi: 10.1016/j.ijimpeng.2016.08.010.

EFFECT OF POLYHEDRAL OLIGOMERIC SILSESQUIOXANE (POSS) ON THE COMPRESSIVE BEHAVIOUR OF AN EPOXY POLYMER

E. Georgiou[1], G. Quino[1,2], I. Hamerton[1], and R.S. Trask[1]
[1] Bristol Composites Institute, University of Bristol, Bristol, BS8 1TR, UK
[2] The Composites Centre, Department of Aeronautics, Imperial College London, SW7 2AZ, UK

1. Introduction

Owing to their good mechanical, chemical and thermal properties, epoxy resins are one of the most widely used thermoset polymers for a variety of engineering applications [1]. Epoxies are commonly utilised as structural polymers, high-performance adhesives and coatings in the aerospace, wind energy and marine sectors, but can also be found in electronic components such as automotive sensors and cameras [2]. Whilst the high degree of chemical cross-linking results in desirable outcomes with regards to the material modulus, strength and glass transition temperature, the high crosslink density makes epoxies brittle, vulnerable to fracture and notch sensitive [2], [3], [4].

Toughening of epoxies has been extensively studied over recent years, with the goal being to build upon the benefits of such resins and tailoring towards a particular application. The addition of a second phase as reinforcement is a common approach to modify the behaviour of polymers, particularly for advanced composites applications [3]. Various micro and nanoscale fillers have been used to modify epoxies, including carbon nanotubes (CNTs), graphene, nanoclays, silica, thermoplastics and reactive rubbers [4], [5]. With the modification of polymers comes two critical industry considerations: polymer processability and the justification of increased cost due to the filler *via* the achieved benefit in properties. Nanosized particles tend to offer a better balance in properties and often result in significant improvements even at low loading. They also have a lesser effect on viscosity when compared to micron sized fillers [2]. Whilst both nanosilica and graphene produce large increases in properties for relatively low loadings, nanosilica tends to outperform graphene in terms of strength and modulus [4]. When considering these factors, it is therefore unsurprising that nanosilica is a widespread choice for modifying epoxies for a variety of applications.

This study considers the effect of the addition of a functionalised polyhedral oligomeric silsesquioxane (POSS), which is the smallest available form of nanosilica, on the compressive behaviour of an epoxy polymer. Compressive behaviour is studied since it is critical to the design of fibre reinforced polymer (FRP) composites. With the compressive behaviour of a FRP often governed by matrix or fibre-matrix interface shearing, the study and enhancement of a resins ability to laterally support fibres experiencing compression is essential to improving the strength of the composite.

2. Materials and methods

A commercially available epoxy resin, Araldite© LY 556 was mixed with amine hardener XB 3473; both were supplied by Huntsman Corporation (USA). This was modified with Gylcidyl POSS (EP0409) which was purchased from Hybrid Plastics (Hattiesburg, USA). Glycidyl POSS has been incorporated into the baseline epoxy at four different percentage weights (wt%) loadings. The compressive behaviour of these samples has been compared to the unmodified epoxy.

Samples were cast into cylindrical rods using the manufacturers recommended cure cycle and then machined to a 6 mm diameter and 6mm height. Six samples of each material configuration were prepared for Digital Image Correlation by applying black speckles onto a white background.

Tests were conducted using a Shimadzu AGS-X machine fitted with a 10kN load cell at a strain rate of 0.001 /s. Compression platens of diameter 30 mm were used. Each platen was covered with Teflon tape 3M 5480 (3M, USA) to minimise friction between the platens and samples.

3. Results and conclusions

Figure 1 shows the effect of increasing POSS content on the compressive response of the baseline epoxy resin, where a representative sample from each batch is presented. Each batch exhibited a similar response in the compressive stress-strain curve. Increasing the POSS content increased the strain hardening effect, implying that POSS could increase the resistance to chain alignment in the molecular structure [6]. However, this did not have a significant effect on the elastic modulus (within 10% difference). Pultruded composite rods will be manufactured using resin systems informed by these tests, and the data will provide evidence to evaluate how the modified matrix system performs in a composite under compressive loading.

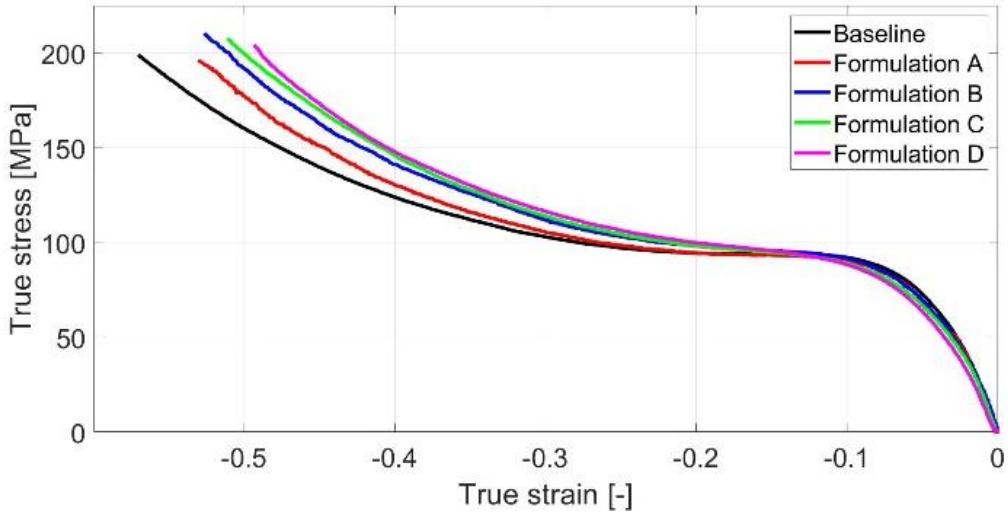

Figure 1: Axial true stress vs true strain curves for an epoxy containing different wt% POSS.

4. Acknowledgements

The authors would like to acknowledge the funding provided by the UK Engineering and Physical Sciences Research Council (EPSRC) programme Grant EP/T011653/1 NextCOMP, Next Generation Fibre-Reinforced Composites: A Full-Scale Redesign for Compression, a collaboration between Imperial College London and University of Bristol.

5. References

[1] H. Chi *et al.*, '*Nanoscale Adv*, vol. 4, no. 4, pp. 1151–1157, doi: 10.1039/d1na00757b.
[2] S. Sprenger, *Polymers*, vol. 12, no. 8, Art. no. 8, Aug. 2020, doi: 10.3390/polym12081777.
[3] K. Mishra, G. Pandey, and R. P. Singh, *Polymer Testing*, vol. 62, pp. 210–218, Sep. 2017, doi: 10.1016/j.polymertesting.2017.06.031.
[4] N. Domun, H. Hadavinia, T. Zhang, T. Sainsbury, G. H. Liaghat, and S. Vahid, *Nanoscale*, vol. 7, no. 23, pp. 10294–10329, Jun. 2015, doi: 10.1039/C5NR01354B.
[5] M. Sheinbaum, L. Sheinbaum, O. Weizman, H. Dodiuk, and S. Kenig, *Composites Part B: Engineering*, vol. 165, pp. 604–612, May 2019, doi: 10.1016/j.compositesb.2019.02.020.
[6] G. Quino, J. Gargiuli, S. Pimenta, I. Hamerton, P. Robinson, and R. S. Trask, *Polymer Testing*, vol. 125, p. 108137, Aug. 2023, doi: 10.1016/j.polymertesting.2023.108137.

DEVELOPMENT OF AN INDOOR ROTOR HELICOPTER PROTOTYPE EMPLOYING LOW-COST STRUCTURE AND INTRUMENTATION FOR COMPARATIVE TESTS OF VIBRATION CONTROL

A. G. Oliveira[1], A. A. Silva[1], M. C. Rodrigues[2], G. de C. Coêlho[1]
[1] Academic Unity of Mechanical Engineering, Federal University of Campina Grande, Campina Grande, Brazil
[2] Department of Mechanical Engineering, Federal University of Paraiba, João Pessoa, Brazil

1. Introduction

The vibration phenomena are present in helicopters and observed in various aircraft models, regardless of scale. [1] demonstrates in a review paper, supported by [2] and technical papers, among others, that the rotor corresponds to the main source of vibration. First of all, any experimental apparatus to study and test systems to vibrating control in helicopters, requires a rotor model in real scale or with a prototype in reduced dimensions, equipped with the basic mechanism to mimic the real aircraft rotor[3], [4], [5]. In order to verify the effectiveness of a proposed device to reduce vibration, as detailed in [6], named SMA Pitch Link, it was necessary design an indoor two-bladed helicopter prototype in reduced scale with the basic mechanism to tilt and rotates de blades, using low-cost instrumentation to control rotation and measure acceleration. After a battery of tests, in long-term experiments, the results prototype helps to demonstrate the effectiveness of proposed device to vibration reduction.

2. Materials and methods

The Fig.1 exhibits the main parts of helicopter rotor prototype. In general view, Fig.1a show the structure with the helicopter rotor attached on the inertial table and isolated by a metallic net. The acquisition control system employs the platform of Labview installed in a computer with an acquisition board National USB6210. The acceleration was measured with a low-cost dual-axis accelerometer ADXL202, illustrated in Fig.1c.[7]The blades were produced by rapid prototyping, printed in PLA Polymer. Due dimensional limitations of PLA (Polyacitic acid) printer each blade was printed in parts (Fig.1d) after assembled. The blades are installed in the rotor mechanism of helimodel T-Rex500 adapted, from employed pitch shifting mechanism (Fig. 1f). The kinematics analysis of rotor mechanism was based in [8]. In Fig.1g is illustrated the electromechanics system to perform the pitch movement by swashplate.

In addition to the accelerometer measurements, the main shaft rotation was measured by a proximity sensor installed on the main shaft. All of the sensor's output were analog signals injected in the USB6210. The interface to collects measurements and export the captured signal do digital files were made in Labview program.

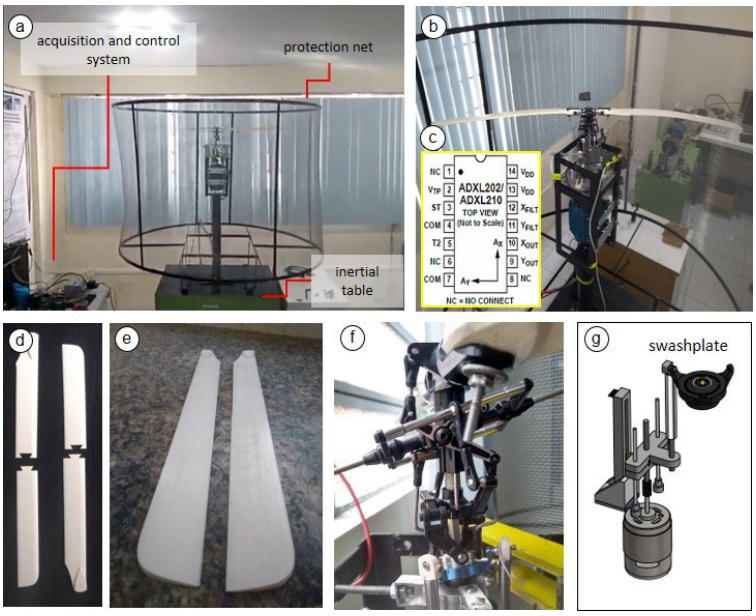

Fig. 1. Main parts of helicopter rotor prototype: a) general view of prototype; b) detail of rotor; c) accelerometer illustration; d) blades build by rapid prototyping; e) blades prepared for installation; f) mechanism of blade pitch angle shifting; g) mechanism designed to pitch control.

3. Results and conclusions

The Fig.2a exhibits the interface programmed in Labview software for Windows. A part of the block diagram is illustrated in Fig.2b. The digital resources were explored to perform the signal pos-processing and save all the parameters in a txt file. The Fast Fourier Transform (FFT), depicted in the Fig. 2c is generated from txt file and processed in Matlab. In this case, the output signal aids to compare the acceleration amplitudes employing the proposed vibration control device pitch link of [9]

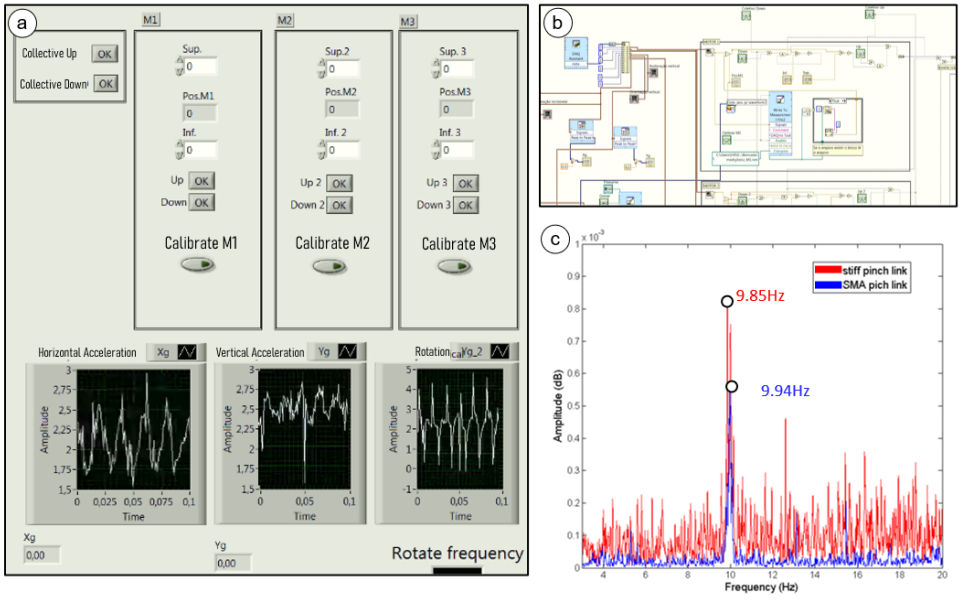

]

Fig. 2. Output measurements and digital interface: a) Labview interface for Windows; b) Labview block diagram; c) FFT of dynamic response.

4. Acknowledgements

The authors gratefully acknowledge the financial support provided by the CNPq Brazilian research agency (grant number 408131/2018-7). The authors also thank the Integrity and Inspection Research Group (Post-Graduate Program on Mechanical Engineering of the Federal University of Paraiba), the Vibration and Instrumentation Laboratory (LVI) and Multidisciplinary Laboratory of Smart Materials and Structures (LaMMEA) of the Federal University of Campina Grande, the National Institute of Science and Smart Structures INCT/EIE (Process CNPq n. 406148/2022-8) and, multidisciplinary team of intelligent metals for advanced engineering application (NISMART) (FAPESQ-PR, TO No. 044/2023)

5. References

[1] W. A. Welsh, "Helicopter Vibration Reduction," in *Morphing Wing Technologies*, Elsevier, 2018, pp. 865–892. doi: 10.1016/B978-0-08-100964-2.00027-7.

[2] A. R. S. BRAMWELL, G. DONE, and D. BALMFORD, *Bramwell's helicopter dynamics*, Second. Oxford: Butterworth-Heinemann, 2001.

[3] A. Yücekayali, A. Ezertaş, and Y. Ortakaya, "Whirl Tower Testing and Hover Performance Evaluation of a 3 Meter Radius Rotor Design," *7th AIAC Ankara International Aerospace Conference*, vol. 7, no. September 11-13, p. 1, 2013.

[4] K. Richter, E. Schiilein, B. Ewers, J. Raddatz, and A. Klein, "Boundary layer transition characteristics of a full-scale helicopter rotor in hover," *Annual Forum Proceedings - AHS International*, vol. 1, no. May, pp. 482–486, 2016.

[5] F. K. Straub, V. R. Anand, B. H. Lau, and T. S. Birchette, "Wind tunnel test of the SMART active flap rotor," *Journal of the American Helicopter Society*, vol. 63, no. 1, pp. 1–16, 2018, doi: 10.4050/JAHS.63.012002.

[6] A. G. Oliveira, A. A. Silva, M. C. Rodrigues, E. N. D. Grassi, C. J. de Araújo, and R. P. B. do Reis, "Helicopter vibration control employing superelastic pitch link with shape memory alloy," *Journal of Vibration and Control*, Nov. 2024, doi: 10.1177/10775463241259568.

[7] A. Devices, "ADXL202 Dataheet," 1999, *All Datasheet.com*. [Online]. Available: www.alldatasheet.com

[8] P. Rosata, "Identification of a small-scale helicopter dynamic model," Università di Pisa, 2015.

[9] A. Oliveira, "Vibration control of a helicopter rotor blade by employing a superelastic NiTi SMA pitch link," Federal University of Paraiba, João Pessoa, 2022. Accessed: May 10, 2023. [Online]. Available: https://repositorio.ufpb.br/jspui/handle/123456789/23383

DUCTILE FRACTURE SIMULATION IN WELDED THIN PLATE FOR STAINLESS STEEL WITH MULTIPLE FLAWS

B. J. Kim[1], C. Y. Oh[2] and J. H. Hwang[1]

[1] Department of Mechanical Engineering, Pukyong National University, Busan, South Korea
[2] Korea Institute of Materials Science, Changwon, South Korea

1. Introduction

Welding is a key method for assembling structures across industries, including critical systems in nuclear power plants. Ensuring structural soundness requires thorough evaluation of weld joints.

Previous studies by B. Bezensek [1] and F. Iwamatsu et al. [2] focused on through-thickness defects in base materials, but research on similar defects in welds is limited. Defects can occur in both base materials and welds, with varying types, and different mechanical properties of welds can cause distinct fracture behaviors. To address this, the Korea Institute of Materials Science (KIMS) recently conducted ductile fracture tests on welded plates with through-thickness defects [4].

In this study, the effect of through-thickness defects on the fracture behavior of welded plates was analyzed using finite element analysis. The simulation results were validated through comparison with ductile fracture test data.

2. Ductile fracture test on welded plates

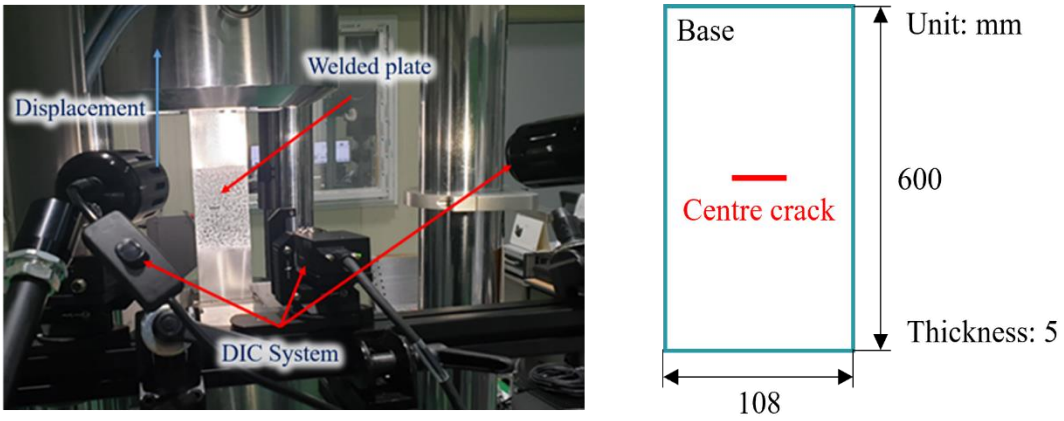

(a) (b)

Fig. 1. Information on ductile fracture test (a) test environment (b) schematic diagram of welded plates specimen

The ductile fracture tests on welded plates with weld defects, conducted by KIMS, used SA240 (SS304) stainless steel. The tests included single and multiple aligned/non-aligned defects in base and weld materials, using M(T) specimens. Displacement was controlled at 2 mm/min, and deformation was analyzed using a DIC system. The test setup is shown in Fig. 1(a).

3. Simulation of ductile fracture test

The material properties were obtained through standard tensile specimens (ASTM E8/E8M), and the comparison of the test results is shown in Fig. 2(a). Finite element analysis of ductile fracture tests on welded plates under static loading was conducted using the stress-modified fracture strain model based on research by Park et al. [3]. The strain at each stress state was calculated, and the material was defined to fracture when the strain reaches the fracture strain.

$$\varepsilon_f = A\exp\left(-1.5\frac{\sigma_m}{\sigma_e}\right)+B \quad \text{Eq. (1)}$$

The relationship between fracture strain and triaxiality in the failure criterion is given by Eq. (1). The coefficients A and B are material constants defined through testing, and triaxiality is the ratio of hydrostatic stress (σ_m) to equivalent stress (σ_e). The failure criterion equation, based on the test simulation results, is shown in Fig. 2(b).

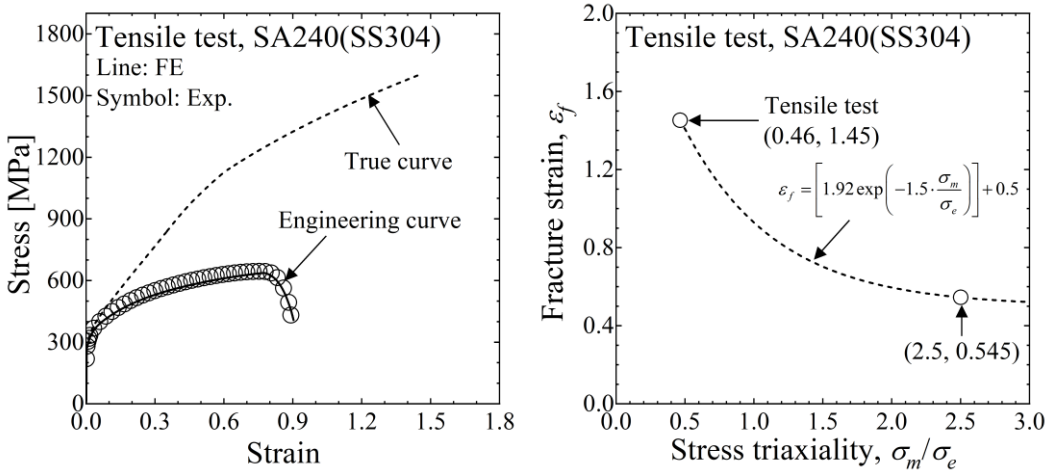

(a) (b)

Fig. 2. Result of simulation of ductile fracture test (a) True and engineering stress-strain curve with FE result for SA240(SS304) (b) Determined fracture strain model

4. Results and conclusions

In this study, ductile fracture tests on welded plates with through-thickness defects were simulated using finite element analysis, and a failure criterion was established. Further fracture behavior analysis will be conducted through damage analysis.

5. Acknowledgements

This research was supported by Korea Institute for Advancement of Technology (KIAT) grant funded by Korea Government (Ministry of Education-Ministry of Trade, Industry and Energy) (P-0028004, Future Automobile Technology Convergence Innovation Talent Training Program in 2024)

6. References

[1] B. Bezensek. (2007). Flaw alignment criteria based on limit load solutions for non-aligned through-wall flaws, *Proc. of ASME Pressure Vessels and Piping Division Conference.*, PVP2007–26041.

[2] F. Iwamatsu, K. Miyazaki, H. Takazawa and K. Saito (2013). Evaluation procedure of limit load for non-aligned multiple flaws, *Proc. of ASME Pressure Vessels and Piping Division Conference.*, PVP2013–97466.

[3] E. K. Park, J. H. Hwang, Y. J. Kim and P. S. Lam (2022). On determination of model parameters for strain based ductile tearing simulation, *Eng. Fract. Mech.,* **272**, 108698.

[4] C. Y. Oh, S. K. Jeong and J. Y. Jeon (2024). Experimental study of ductile fracture for non-aligned flaws in welded plate, *Trans. of the SMiRT 27*.

FULL-FIELD CHARACTERISATION OF PULTRUDED RODS UNDER COMPRESSION USING THE CRADLE TEST

G. Quino[1,2], C. Zhao[1], P. Robinson[1], R.S. Trask[2]
[1] Department of Aeronautics, Imperial College London, London, United Kingdom
[2] Bristol Composites Institute, University of Bristol, United Kingdom

1. Introduction

Pultrusion manufacturing of continuous fibre composites typically results in superior fibre alignment, enhancing mechanical properties, including compressive strength. However, accurately measuring their axial compressive properties is challenging. Direct compression tests of pultruded rods often result in premature failure near the grips due to unavoidable stress concentrations [1], [2]. Additionally, such tests involve complex experimental setups that are highly sensitive to tolerances and misalignments.

This work presents "the cradle test", a novel approach to characterise the compression behaviour of composite pultruded rods, with a simple setup that consistently induces compression failure. The cradle test consists of a polymeric beam that "cradles" a pultruded rod, which is adhesively bonded in position [3], [4]. The assembly is subjected to four point bending loading, making the pultruded rod undergo compression (See Fig. 1). Since this configuration does not allow to directly measure the force acting upon the pultruded rod specimen, we developed a technique based on full-field Digital Image Correlation (DIC) measurements to calculate the force acting upon the rod during testing.

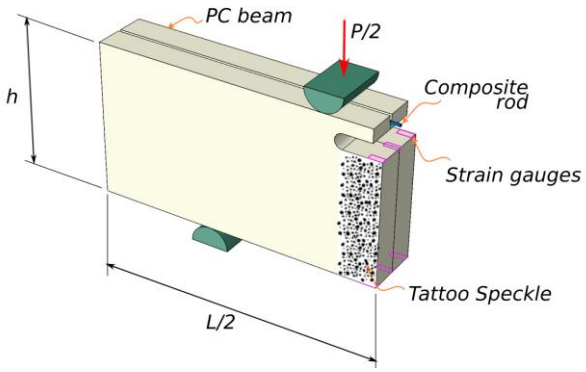

Fig. 1. Schematic showing half of the cradle test assembly.

2. Materials and methods

We characterised the compressive performance of a commercial 0.8 mm diameter carbon fibre/epoxy pultruded composite rod, under quasi-static loading, by using the cradle test. The design of the experiment was carefully conducted via extensive finite element simulations to ensure bending limits, linearity, and the structural integrity of the beam. The axial strain in the rod was determined from DIC analysis. The strain components measured by DIC on the surface of the beam, were used

to evaluate the stress state along a path across the midplane of the beam. The stress components were then integrated to estimate the force acting upon the rod. Speckle quality on the beam was controlled by using the "tattoo speckle" technique detailed in [5].

3. Results and conclusions

The method achieved consistent compression failure within the gauge length of the specimens (Fig. 2). The measured Young's modulus E= 136.4 ± 10.8 GPa was in good agreement with the one measured in uniaxial tensile experiments (E= 134 ± 5 GPa), validating the technique. The proposed method provides a practical alternative to characterise the compressive behaviour of materials with high axial stiffness.

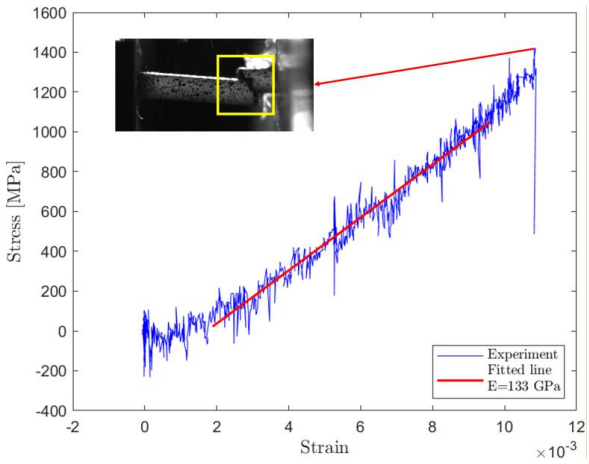

Fig. 2. Compression stress *vs.* strain curve obtained following our data reduction method.

4. Acknowledgements

The authors kindly acknowledge the support of the Department of Aeronautics, Imperial College London and the funding for this research provided by UK Engineering and Physical Sciences Research Council (EPSRC) programme Grant EP/T011653/1, Next Generation Fibre-Reinforced Composites (NextCOMP): a Full-Scale Redesign for Compression a collaboration between Imperial College London and the University of Bristol. For the purpose of open access, the authors have applied a Creative Commons Attribution (CC BY) license to any author accepted manuscript version arising.

5. References

[1] S. R. Vankar, A. N. Kaore, and C. S. Yerramalli, "Methodology for testing the compressive strength of pultruded composites," *Journal of Reinforced Plastics and Composites*, vol. 42, no. 11–12, pp. 544–557, Jun. 2023, doi: 10.1177/07316844221133293.

[2] C. Soutis, "Compression testing of pultruded carbon fibre-epoxy cylindrical rods," *J Mater Sci*, vol. 34, pp. 3441–3446, 2000, Accessed: May 26, 2021. [Online]. Available: https://link.springer.com/article/10.1023%2FA%3A1004832606677

[3] G. Quino, P. Robinson, and R. S. Trask, "Design of a bending experiment for mechanical characterisation of pultruded rods under compression," *Proceedings of the 20th European Conference on Composite Materials*, vol. Vol 3-Char, pp. 167–172, 2022, doi: 10.5075/epfl-298799_978-2-9701614-0-0.

[4] G. Quino, C. Zhao, C. Weng, B. Zhang, P. Robinson, and R. S. Trask, "Improvements on the 'cradle test' for the mechanical characterisation of pultruded rods under compression," *Proceedings of the 21st European Conference on Composite Materials - Special Sessions, ECCM21*, vol. 8, no. July, pp. 1202–1205, 2024, doi: 10.60691/yj56-np80.

[5] G. Quino, Y. Chen, K. R. Ramakrishnan, F. Martínez-Hergueta, G. Zumpano, A. Pellegrino, and N. Petrinic, "Speckle patterns for DIC in challenging scenarios: rapid application and impact endurance," *Meas Sci Technol*, vol. 32, no. 1, p. 015203, Jan. 2021, doi: 10.1088/1361-6501/abaae8.

FATIGUE BEHAVIOUR OF HOT-ROLLED, LOW CARBON STEEL UNDER PRE-STRAIN AND NOTCH EFFECT

I. Tomasi[1], L. Solazzi[1], C. Petrogalli[1], A. Mazzoni[2], G. Donzella[1]
[1] Department of Mechanical and Industrial Engineering (DIMI), University of Brescia, Brescia, Italy
[2] Moovero R&D Centre Europe, Maclodio (BS), Italy

1. Introduction

The concept of the fatigue behaviour of steel is well established in the scientific literature due to the multiple industrial fields where this material is used. One of the families of this material widely adopted is low-carbon steel, which offers a good compromise between mechanical properties and ease of processing. Despite the extensive literature on the fatigue life of these materials (examples in [1]) and specific conditions under fatigue loads, the authors aim to further investigate the fatigue life of hot-rolled low-carbon steel under different stress ratios (R), subjecting the material to stress beyond its yield strength. Moreover, another aspect being tested is the notch effect. As reported in [2], the fatigue stress intensity factor changes with different values of R, but the plastic field is not mentioned. Another aspect to analyse is the influence of pre-straining: by stretching the specimen to a defined strain value, the question arises as to how pre-straining affects the fatigue limit. Regarding the influence of the pre-strain effect, the literature contains many studies (two examples are provided in [3,4]), but limited work has been reported on the combination of both effects. These conditions are typical, for example, in wheel rims, which have been previously analysed [5].

2. Materials and methods

The present study focused on DD11 hot-rolled low-carbon steel, in accordance with the UNI EN 10111:2008 standard. The experimental plan began with tensile tests on smooth and notched specimens. Subsequently, the S-N curve of the material was obtained based on the ISO 12107 standard, observing both the high-cycle fatigue (HCF) regime and the fatigue limit. Using the Walker method as the mean stress theory, the S-N curve for R= -1 was derived from curves with different stress ratios (R). Next, the fatigue limit of notched specimens was studied at R=0.1 and compared to the fatigue limit of the base material under the same stress ratio.

Experimental tests conducted			
Specimen ID	Type of specimen	Stress ratio R	Type of experimental test conducted
C	Smooth	0.1	Tensile strength, HCF S-N curve, fatigue limit
D		0.2	HCF S-N curve
F		0.01	HCF S-N curve
G	Notched	0.1	Tensile strength, Fatigue limit
J	Notched, pre-strain 1.5 %		Fatigue limit

Table 1. Experimental design (through Instron 8501 as tensile test machine and Rumul Mikrotron resonant machine as fatigue test machine).

Finally, notched specimens with pre-strain applied were tested to determine their fatigue limit and compare the results with the previously obtained values. Table 1 provides a summary of the experimental tests conducted.

3. Results and conclusions

Table 2 presents the fatigue limits from the experimental tests cataloged as C, G, and J, as well as the evaluated fatigue limit of the base material at R = -1. Figure 1 illustrates the high-cycle fatigue (HCF) S-N curve of the base material at different stress ratios. Numerical analyses were conducted to generalize the results using the stress-strain curve of the material obtained from the tensile tests. A K_t of the notch equal to 2.35 was determined, consistent with the literature. Additionally, Figure 1 displays the S-N curves for the base material at various stress ratios.

Specimen ID	Stress ratio R	Fatigue limit evaluated or estimated (*)	Number of specimens tested
C	0.1	143.25	29
D	0.2	150.23*	15
F	0.01	139.57*	15
G	0.1	121.25	16
J	0.1	111.67	15
Base material	-1	195.4*	/

Table 1. Experimental results obtained.

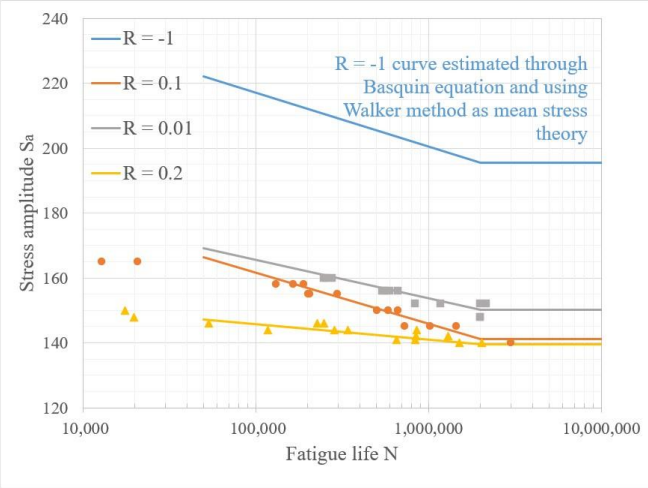

Fig. 1. Fatigue curves and data in the finite life domain for the base material in three different stress ratios.

4. Acknowledgements

The research is financed by the European Union - NextGenerationEU (National Sustainable Mobility Center CN00000023, Italian Ministry of University and Research Decree n. 1033 - 17/06/2022, Spoke 11 - Innovative Materials & Lightweighting). The opinions expressed are those of the authors only and should not be considered as representative of the European Union or the European Commission's official position. Neither the European Union nor the European Commission can be held responsible for them. CUP: D83C22000690001

5. References

[1] Handbook, A. S. M. "Volume 19: Fatigue and fracture." Geauga County: ASM International (1996).
[2] Liao, Ding, et al. "Recent advances on notch effects in metal fatigue: A review." Fatigue & Fracture of Engineering Materials & Structures 43.4 (2020): 637-659.
[3] Le, Quochung, et al. "Effect of prestrain paths on mechanical behavior of dual phase sheet steel." International journal of fatigue 31.4 (2009): 607-615.
[4] Sivaprasad, S., et al. "Effect of prestrain on fracture toughness of HSLA steels." Materials Science and Engineering: A 284.1-2 351 (2000): 195-201
[5] Mazzoni, Alberto, and Luigi Solazzi. "Experimental field test on a multipiece steel wheel and influence of the material properties on its fatigue life evaluation." Engineering Failure Analysis 135 (2022): 106106.

PATCH SIZE AND OVERLAPPING OPTIMISATION FOR A NEW GENERATION OF RECYCLED COMPOSITE LAMINATES

P. Bettini[1], F. Mongioì[2], L. Calervo[1], A. Milite[1], A. Zucchelli[2], T.M. Brugo[2] and R. Palazzetti[1]
[1] Politecnico di Milano, Milan, Italy
[2] University of Bologna, Bologna, Italy

1. Introduction

Composite manufacturing processes generate significant waste due to the raw material being supplied in sheet form. After cutting the desired geometries, the unused portions of the sheet are typically discarded, leading to the disposal of up to 35% of the purchased material. This results in both economic losses and negative environmental impacts. The literature includes a few studies addressing the application of unused prepreg scraps. For instance, Nilakantan et al. [1] describe various intermediate product forms derived from unused uncured scraps, including Resold Prepreg Roll Form (RPRF), Regular Cutout Form (RCF), Loose Chip Form (LCF), and Reused Scrap Roll Form (RSRF). Similarly, Jin et al. [2] utilized rectangular platelets of varying aspect ratios, randomly oriented, to create recycled panels with quasi-isotropic mechanical properties. Ko et al. [3] produced Single Edge Notch Tension (SENT) specimens to study mode I intra-laminar fracture and size effects in Discontinuous Fiber Composites (DFC). Another example involves a recycling strategy for offcuts generated during laser-assisted tape placement [4]. In general, studies have shown that the flexural properties of discontinuous fiber composites, created by chopping material into randomly oriented rectangular platelets, increase with platelet length but remain significantly lower than those of the original material.

This paper proposes a method to regularly assemble prepreg scraps into a new equivalent lamina, which can be utilized in the conventional lamination process. It outlines the initial steps taken to determine the optimal patch size and overlapping length for this new material. The results of this work aim to define the optimal patch size and overlapping length necessary to ensure maximal mechanical properties.

2. Materials and methods

HexPly M49/42%/200T2X2/CHS-3K has been used to cut the patches and manufacture the specimens. Patches have been cut out and regularly displaced to manufacture samples for 4-point bending (4PB) tests. The patches had been cut out of various dimensions and manually deposed following two different patterns, named “without overlap” (NO-OV) and “with overlap” (OV), to create two “equivalent laminae”: the first having 0.47 mm thickness, while the second 0.94 mm.

The sizes of the patches have been determined to ensure a minimum overlapping surface, determined as the minimum surface area that would ensure that the overlapping area would not be the weak zone under axial load. For the material used here, the minimum superposition length had been calculated in 5 mm: however, a minimum superposition length of 10 mm has been chosen.

3. Results and conclusions

Flexural Strength and Modulus have been calculated according to the relevant standard and presented for each configuration in Figure 3.

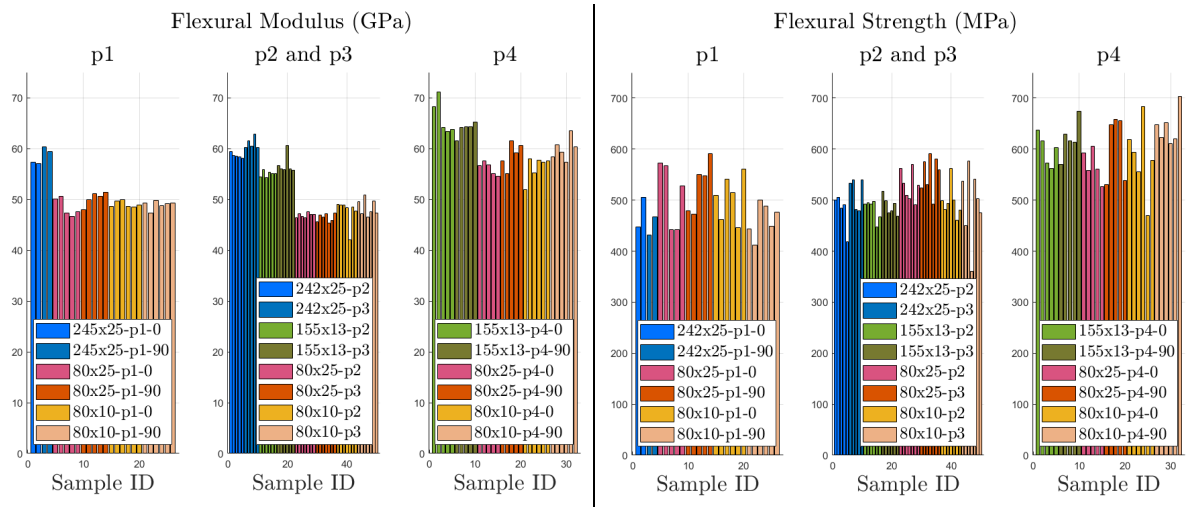

Fig. 1. Flexural Modulus (left) and Strength (right) of the tested samples.

At first glance it appears clear that the standards used for the experiments have a significant impact on the Flexural Modulus, rather than on the Flexural Strength of the samples. In particular, the longer the samples, the higher the stiffness, which agrees with [5]. However, the variability within each group seems quite low, especially on the stiffness side.

Compared to the unpatched material, the new one exhibits around 75% of the stiffness and 50% of the strength

Three different crack propagation behaviours have been observed: (i) the crack propagates breaking fibers layer after layer until a large delamination happens (39% of the total failures); (ii) fracture propagating through the whole thickness splitting the sample in two (45%), and (iii) after the first failure, the crack stops and does not propagate (16%).

4. Acknowledgements

This work has been supported by the project "SELF-RE-PREG: Self-Sensing Interleaving for Recycled Prepreg" funded by the MUR Progetti di Ricerca di Rilevante Interesse Nazionale (PRIN) Bando 2022PNR - grant P2022SLZY4, CUP D53D23018700001.

5. References

[1] G. Nilakantan and S. Nutt. (2018). Reuse and upcycling of thermoset prepreg scrap: Case study with out-of-autoclave carbon fiber/epoxy prepreg, *Journal of Composite Materials*, **52**(3):341–360.

[2] B. C. Jin, X. Li, A. Jain, C. González, J. LLorca, and S. Nutt (2017). Optimization of microstructures and mechanical properties of composite oriented strand board from reused prepreg, *Comp Struc*, **174**,389–398.

[3] S. Ko, J. Yang, M. E. Tuttle, and M. Salviato (2019). Effect of the platelet size on the fracturing behavior and size effect of discontinuous fiber composite structures, *Comp Struc*, **227**.

[4] A. Kumar Bandaru, T. Anderson, and P. M. Weaver (2024). Recycling CF/PEEK offcut waste from laser assisted tape placement: Influence of overlaps and gaps, *Comp Part A*, **180**.

[5] C. Zweben, W. S. Smith, and M. W. Wardle (1979). Test Methods for Fiber Tensile Strength, Composite Flexural Modulus, and Properties of Fabric-Reinforced Laminates. *Composite Materials: Testing and Design (Fifth Conference)*, 228–262.

6-11 July 2025 ICEM21 Bologna
21st International Conference on EXPERIMENTAL MECHANICS

INVESTIGATION OF THE CREEP DEFORMATION MECHANISM AT ROOM TEMPERATURE ON AZ31 MAGNESIUM ALLOY

S. Arikawa[1], K. Matsuoka [2] and S. Yamaguchi[1]
[1] Department of Mechanical Engineering Informatics, Meiji University, Japan
[2] Graduate School of Science and Technology, Meiji University, Japan

1. Introduction

Magnesium alloys are expected to be used as structural materials for transport equipment due to their high specific strength. Therefore, it is important to know the material properties to ensure long-term reliability. For long-term use, fatigue, stress relaxation, and creep properties are important. Twinning deformations occur because the slip system is limited in HCP metals, such as magnesium. Slip-induced grain boundary slips occur in magnesium alloys under very low strain rates of deformations at room temperature [1]. Furthermore, creep deformations occur even at room temperature for magnesium alloys [2]. Therefore, the deformation mechanisms and properties under low strain rates and long-term loadings at room temperature should be known for the reliability.

In this study, the creep deformation property and mechanism of AZ31 magnesium alloy at room temperature were investigated.

2. Materials and methods

Specimens were cut out from rolled AZ31 plates along the rolled direction. The photo of the specimen and the microstructure are shown in Fig. 1. The dimensions of the parallel part were 10 mm in length, 3 mm in width, and 1 mm in thickness. The yield strength and the maximum strength were 150 MPa and 242 MPa, respectively.

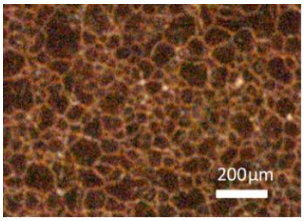

(a) Specimen (b) Optical microscope image

Fig. 1. AZ31 specimen

Constant load creep tests were conducted for 7 days at 24 ℃. The stress conditions were set to 120 MPa, 135 MPa, 193.5 MPa, and 217.5 MPa, which are 0.80, 0.90, 1.29, and 1.45 times the yield strength. Plastic strain gages were used for the strain measurements.

3. Results and conclusions

Obtained creep test results are shown in Fig. 2 (a). The enlarged view of the creep curve of the state below the yield strength is shown in Fig. 2 (b). Creep strains occur for all conditions of stresses.

The steady-state creep rates are 5.96×10^{-10}, 1.90×10^{-9}, 6.39×10^{-9}, and 3.70×10^{-8} for the stress conditions of 0.80YS, 0.90YS, 1.29YS, and 1.45YS, respectively. The creep stress index is 5.98. Stress relaxation will also occur even in a state below the yield point because creep deformation occurs at the stress below the yield strength. Additionally, the deformation states of the micro structures are observed by scanning electron microscopy for investigating the creep deformation mechanism.

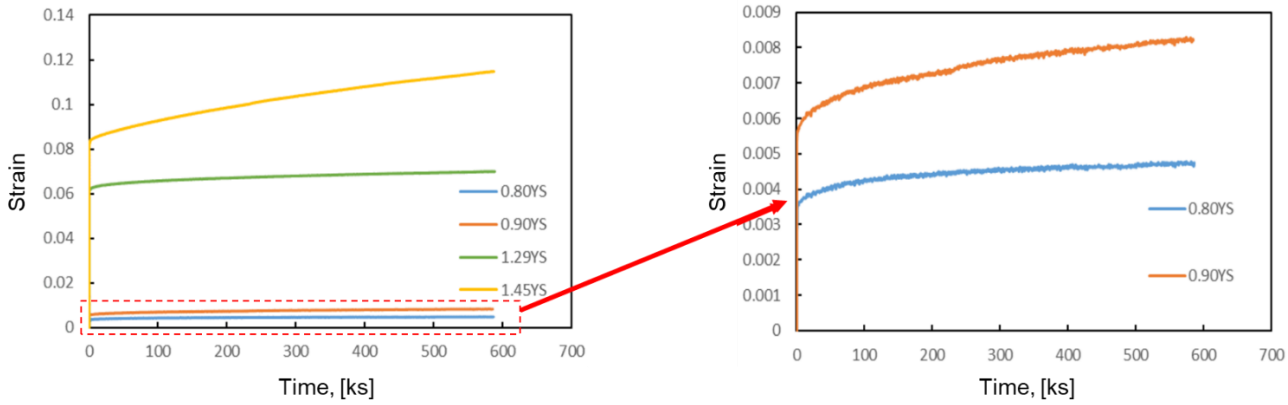

(a) all results (b) stresses below the yeild strength

Fig. 2. Strain vs time curve of creep tests

4. References

[1] J. Koike, R. Ohyama, T. Kobayashi, M. Suzuki and K. Murayama (2003). Grain-Boundary Sliding in AZ31 Magnesium Alloys at Room Temperature to 523 K. *Materials Transactions*, **44-4**, 445-451.

[2] T. Matsunaga, T. Kameyama, K. Takahashi and E. Sato (2009). Constitutive Relation for Ambient-Temperature Creep in Hexagonal Close-Packed Metals. *Materials Transactions*, **50-12**, 2858-2864.

SPH-FEM APPROACH FOR FLUID-STRUCTURE INTERACTION OF ANISOGRID LATTICE STRUCTURES

E.V. Arcieri[1] and S. Baragetti[2]
[1] Department of Management, Information and Production Engineering (DIGIP), University of Bergamo, Dalmine (BG), Italy

1. Introduction

Anisogrid lattice structures have emerged as a promising solution for lightweight, high-performance components due to their efficient use of materials, enabled by additive manufacturing techniques, which lead to a favorable strength-to-weight ratio [1-2]. Their structural response depends not only on the material used for manufacturing the structure, but also on the geometry of the single module and on the presence of defects associated with the manufacturing process. These defects are more present and influential in additively manufactured components [3]. These structures are of particular interest in many industrial applications, such as aerospace, where optimized geometries and high strength-to-mass ratios are required.

This study is part of the PRIN 2022 PNRR project "Innovative Multiphysical Approach to Aerospace Metamaterials Design", that is currently in progress. The aim of the present work is to develop a preliminary finite element model for analyzing the fluid-structure interaction of anisogrid lattice structures under fluid impact conditions.

2. Materials and methods

The study is conducted using a finite element method (FEM) software to model both the structure and the fluid. A single anisogrid module was investigated. The module has an octahedral shape, which has been shown in [4] to offer specific energy absorption capabilities. An upper and a lower skin are modelled providing a sandwich geometry. The structure is modelled using beam elements for the ribs in the core and shell elements for the skins. Constraints are applied at the connections between beam and shell elements to ensure reliable load distribution and to avoid stress concentrations that could arise from localized interactions.

The fluid is modelled using the Smooth Particle Hydrodynamics (SPH) technique. In this particle-based approach, the fluid is discretized into particles, each carrying properties such as mass and velocity. The interaction of these particles is governed by fluid dynamics principles, and the quantity of each particle is determined using kernel approximations based on the properties of neighboring particles.

The anisogrid structure is made of an aluminum alloy, assumed to be homogeneous, isotropic, and elastic to study the structural response in the elastic field. The perimeter of the lower skin is fixed, and gravitational load and impact speed are defined. Contact interaction properties between the module and the fluid are defined, even if friction effects are excluded from the simulation.

3. Results and conclusions

The FEM+SPH approach is used to model the fluid-structure interaction of a single module of an anisogrid lattice structure (Fig.1). This ongoing research activity wants to establish a framework for evaluating the behavior of anisogrid lattice structures under dynamic conditions caused by fluid impacts, offering a powerful tool for designers.

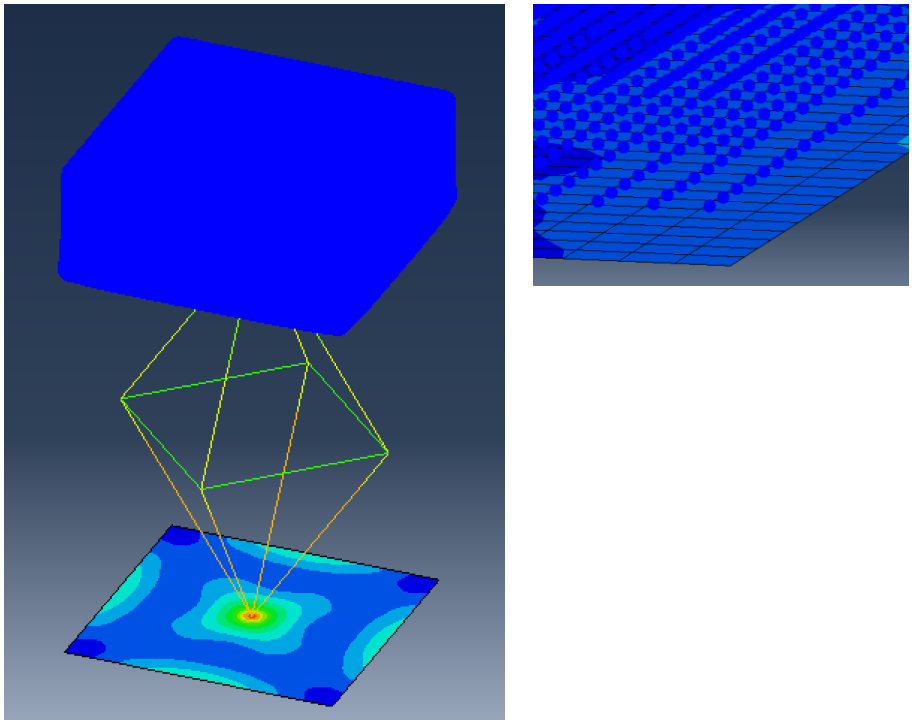

Fig. 1. Finite element model for the fluid-structure interaction behavior, with a detail of the fluid modelled with SPH approach.

4. Acknowledgements

Study conducted within the project “Innovative multiphysical approach to aerospace metamaterials design” - PRIN 2022 PNRR, funded by the European Union – Next Generation EU, Mission 4, Component 2, Investment 1.1 (MUR P20227JSS3_03 - CUP F53D23009910001).

5. References

[1] V.V. Vasiliev, A.F. Razin (2006). Anisogrid composite lattice structures for spacecraft and aircraft application. *Compos. Struct.* **76**, 182-189.

[2] G. Totaro, Z. Gürdal (2009). Optimal design of composite lattice shell structures for aerospace applications. *Aerosp. Sci. Technol.* **13**, 157-164.

[3] M.C. Brennan, J.S. Keist, T.A. Palmer (2021). Defects in metal additive manufacturing processes. *J. Mater. Eng. Perform.* **30**, 4808–4818.

[4] A.I.H. Nasrullah, S.P. Santosa and T. Dirgantara (2020). Design and optimization of crashworthy components based on lattice structure configuration. *Struct.* **26**, 969-981.

Design and mechanical behaviors of curved-wall carbon fiber composite honeycomb sandwich structure with higher buckling resistance

Jian Xiong*[1]

[1] *Center for Composite Materials and Structures, Harbin Institute of Technology, Harbin 150001, PR*

**Presenting author: jx@hit.edu.cn*

Lighter and stronger structures have always been the goals pursued by designers in many industrial fields. In order to solve the problem that low-density carbon fiber composite honeycomb is prone to buckling failure and limit its bearing capacity，a curved-wall carbon fiber reinforced polymer (CFRP)honeycomb is designed by substituting the curved walls with circular cross sections for the straight edges of traditional hexagonal honeycomb. The honeycomb was fabricated using the modified tailor-folding method. The deformation and failure modes of curved-wall CFRP honeycomb were investigated by analytical model, experiments and finite element analysis (FEA). A failure mechanism map conducted by the analytical model was used for studying the transition between dominant failure modes of honeycomb structure under key geometric parameters. The analytical model demonstrated a satisfactory correlation with the experimental results and simulations. The specific strength was employed to investigate the load-weight efficiency of curved-wall CFRP honeycomb under different geometric parameters, aiming to identify the most optimal lightweight structure configuration. The results revealed that the design of curved cell walls strengthens the buckling resistance of CFRP honeycomb. With the increase of the central angle of the circular arc, the out-of-plane compressive strength of curved-wall CFRP honeycomb increased by 50% and 148%, respectively. The CFRP honeycomb with curved-walls also had a higher specific compressive strength. The optimal geometric parameters of curved-wall CFRP honeycomb structure can be obtained by characterizing the influence of the central angle of the circular arc on the structure's out-of-plane compression characteristics. This study can serve as a guide for designing and optimizing lightweight structures.

Keywords: Composite; Sandwich structures; Honeycomb; Bucking; Mechanical property

UTILIZATION OF CENOSPHERE AND LIGHT EXPANDED CLAY AGGREGATE WITH MICRO FIBRE REINFORCED LIGHTWEIGHT CONCRETE

T.K. Shen[1], Z. Itam[2,*], A. Syamsir[2], Z. Che Muda[3], M.H. Zawawi[2], N. M. Zahari[2]
[1] Department of Civil Engineering, Universiti Tenaga Nasional, 43000 Kajang, Selangor, Malaysia
[2] Institute of Energy Infrastructure, Universiti Tenaga Nasional, 43000 Kajang, Selangor, Malaysia
[3] Faculty of Engineering and Quantity Surveying, INTI-International University, Nilai, Malaysia

1. Introduction

Lightweight concrete (LWC) has been a major attention in construction field for the last few years. It has been a highlight all because of its numerous advantages compared to normal weight concrete. There is a saying "Who doesn't like discount" which fit perfectly with LWC condition, its reduction of many aspects: dead loads that lead to smaller cross sections of structural members. Plus, it leads to convenient fabrication and cost cutting which involved shipping, transportation and overall construction cost. Furthermore, lightweight concrete compromises excellent durability or resilience to frost and chemical attack with lower permeability [1], better fire resistance [2], and enhanced thermal conductivity [3]. As per studies, the range for the unit weight of LWC would be from 1200 kg/m3 to 1800 kg/m3 [1]. While for structural lightweight concrete, the range would be 1120 kg/m3 to 1920 kg/m3 by recommendation from the ACI Committee 213 [3]. Thus, the proper selection and proficient application of lightweight filler (LWF) materials is very crucial in order to attain the desired weight with satisfactory mechanical and structural characteristics.

From studies, water and soil contaminations are caused by the enormous production of fly ash during the coal combustion process in the thermal treatment plan which can influence the ecological cycle [4]. As reported, India single-handedly delivers 166 million tons of fly ash per annum, by any means they managed to utilize effectively of 56% of fly ash and the rest is flat out become the concern for the society [5]. Therefore, the use of fly ash is now considered as a construction material, and it is unharmed to the nature if disposal occurred as it could preserve the natural resources for the future generation. Nowadays, the substitution of concrete by fly ash has been a highlight in the construction industry. That is all because the aggregates dominated 70% of total volume of concrete matrix and now fly ash could be replacing both natural fine aggregates (NFA) and natural coarse aggregates (NCA) as per research.

Fly ash cenosphere (FAC) is a small element or component from production of fly ash during the coal combustion in the thermal treatment plant. FAC is the hollow alumina-silicate microsphere with size of 10 to 400 µm and it has the shell thickness for about 5 % to 10 % of its diameter [6]. Moreover, the color of FAC is greyish white and has similar chemical composition as fly ash. By means of chemical composition, it is categorized as valued industrial waste by product and being promoted as sustainable development. Numerous parameters that properties of FAC are depending on, which included type of coal, grinding procedures or methods and combustion and withdraw process. In addition, as an essential of composite materials, FAC has a broad scope of structural and non-structural applications [7-9], as it enhances implied force resistance, provides greater insulation and lastly diminishes shrinkage and density. Because of the advantages of lightweight and filled pore

structure properties, it is suitable for construction of durable bridge decks, pavements and highways. Addition applications of FAC composite involve freeze and thaw resistant, noise isolation proof barriers and sufficient acoustic damping asphalt concrete matrices.

In recent years, the utilization of cenosphere with the combination of fiber mix to form reinforced lightweight concrete has been introduced into the industry. With the utilization of cenosphere, construction industry could possibly eliminate the concerns or issues stated with LWC. It is due to cenosphere having great potential as aggregates for the creation of high strength lightweight concrete. Further, it could attract great interest for structural applications due to reduction in many aspects especially concrete self-weight.

2. Materials and methods

This present study follows the methodology outlined in Figure 1. The materials used in this study include:

- Cement: Ordinary Portland Cement (OPC) C25, complying with ASTM Type 1 standards.
- Aggregates: Natural fine and coarse aggregates were partially replaced with 40% LECA and 40% FAC.
- Light Expanded Clay Aggregate (LECA): A lightweight, porous aggregate produced through thermal expansion of clay, with an average bulk density of 400-600 kg/m³.
- Fly Ash Cenosphere (FAC): Hollow alumina-silicate microspheres with a shell thickness of 5-10% of their diameter, offering improved workability and lower density.
- Jute Fibre: A natural micro fibre reinforcement added at 0.3% of the total volume to improve tensile strength and crack resistance.

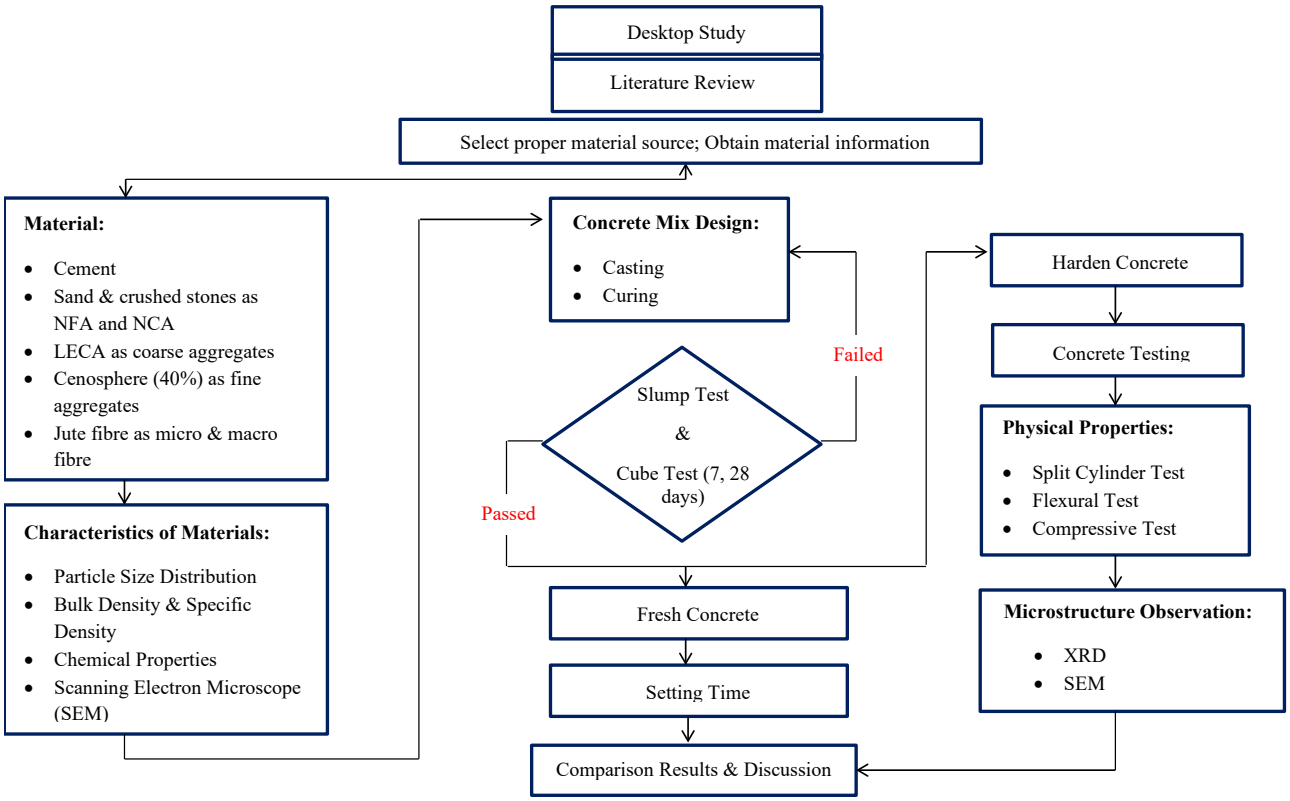

Figure 1. Methodology Flow Chart

3. Conclusions

This study demonstrates that the combination of 40% LECA, 40% FAC, and 0.3% jute fiber in LWC provides an optimal balance of strength, weight reduction, and durability. Key findings include:

- A 20% reduction in density while maintaining structural integrity.
- Enhanced compressive strength due to improved particle packing.
- Increased split tensile and flexural strength from jute fiber reinforcement.

The results suggest that this LWC formulation is a promising alternative for sustainable and high-performance concrete applications, particularly in areas requiring lightweight yet strong structural components. Future research should focus on thermal conductivity assessments and long-term durability studies to further validate its industrial applicability.

4. Acknowledgements

The authors would like to express their gratitude to Universiti Tenaga Nasional (UNITEN) for providing laboratory facilities and technical support. This work was also supported by through the Higher Institution Centre of Excellence (HICoE), Ministry of Higher Education (MOHE), Malaysia under the project code 2024001HICOE as referenced in JPT(BPKI)1000/016/018/34(5).

5. References

[1] Z. Li, Advanced Concrete Technology, John Wiley & Sons Inc, 2011.
[2] ACI 216.1, Standard Method for Determining Fire Resistance of Concrete and Masonry Construction Assemblies, 1997.
[3] ACI 213, Guide for Structural Lightweight-Aggregate Concrete, 2003.
[4] Z.T. Yao, X.S. Ji, P.K. Sarker, J.H. Tang, L.Q. Ge, M.S. Xia, Y.Q. Xi, A comprehensive review on the application of coal fly ash, Earth-Sci. Rev. 141 (2015) 105–121.
[5] Central Electricity Authority, Report on Fly ash Generation at Coal/Lignite Based Thermal Power Stations and its Utilization in the Country for the Year 2015–2016, New Delhi, March, 2016.
[6] D. Montgomery, S. Diamond, The influence of fly ash cenospheres on the details of cracking in fly ash-bearing cement pastes, Cem. Concr. Res. 14 (1984) 767–775.
[7] E. Raask, Cenospheres in pulverized-fuel ash, J. Inst. Fuel 41 (1968) 339–344.
[8] J.B. Ashby, J. Carroll, Australian cenosphere, in: J.D. Spencer, C.E. Whieldon (Eds.), Proceedings 5th International Ash Utilization Symposium, American Coal Ash Association, Atlanta, Georgia, 1979, pp. 134–139.
[9] G.L. Fisher, D.P.Y. Chang, M. Brummer, Fly ash collected from electrostatic precipitators: microcrystalline structures and the mystery of the spheres, Science 192 (1976) 553–555.

FATIGUE BEHAVIOR OF LACK OF PENETRATION DEFECTS IN WELDED ALUMINUM JOINTS

L. Santoro[1,2], E. Viglietti [1], R. Sesana[1,2]
[1] Department of Mechanical and Aerospace Engineering (DIMEAS), Politecnico di Torino, Torino, Italy
[2] Advanced Joining Technologies (J-TECH), Politecnico di Torino, Torino, Italy

1. Introduction

Fatigue failure remains a critical issue in welded structures, where stress concentrations and manufacturing defects significantly affect durability. Recent advances in numerical methods have introduced the Average Strain Energy Density (ASED) approach as a robust tool for predicting fatigue strength and crack initiation in notched components [1] [2] [3]. In parallel, experimental investigations—particularly in aluminum alloy joints—have emphasized the detrimental role of welding defects such as lack of penetration [4] [5]. The present study integrates the ASED method with four-point bending tests to assess the fatigue behavior of welded Al-6060T6 joints. By combining finite element simulations with controlled experimental tests, this work aims to provide a comprehensive evaluation of fatigue life and crack growth mechanisms in joints affected by defect-induced stress perturbations.

2. Materials and Methods

Numerical Analysis and ASED Formulation:

The theoretical framework is based on the ASED method, which evaluates the averaged strain energy density within a predefined control area around critical stress regions. Finite element simulations were performed under four-point bending conditions to obtain the strain energy density distribution and stress intensity factors for butt-ground welded joints. The formulation, originally developed for evaluating fatigue in notched components [6], was adapted to model the behavior of welded aluminum joints under cyclic loading. The finite element analysis is based on the Abaqus contour integral method for fracture mechanics analysis, implemented for static crack evaluation and fatigue crack growth prediction. A Python-based automation framework was developed to model crack propagation under plane stress conditions, integrating contour integral calculations, singularity modeling, and adaptive meshing strategies. The analysis is based on a series of static analysis made at a constant increment of crack growth.

Experimental Setup:

Fatigue tests were conducted on Al-6060T6 welded specimens using a vibraphone capable of high-frequency cyclic loading. Specimens were prepared both in a “defect-free” condition and with simulated lack of penetration defects produced by precise incisions (with depths of 2 mm, 1.5 mm, and 1 mm). The staircase method was employed to iteratively adjust the dynamic force until failure, enabling the construction of S-N curves (Wöhler curves) that capture the fatigue life at various stress levels. Detailed measurements of crack surface areas and cycle counts provided insight into the effect of defects on the structural integrity of the welds.

3. Results and Conclusions

Experimental Findings:

The fatigue tests showed that specimens with lack of penetration defects exhibited a marked reduction in fatigue life. The S-N curves for defective joints were systematically shifted compared to defect-free samples, with the severity of the life reduction correlating to the incision depth.

Finite Element and ASED Results:

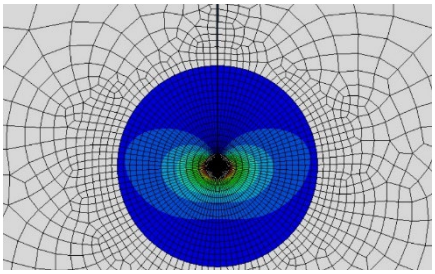

Numerical simulations revealed that the fatigue behavior of a defected specimen could be reliably predicted using the ASED criterion, with some limitations but various advantages. On the right, a result of the strain energy density contour located in the control area for a fixed crack length is represented. The first advantage of the criterion is precisely the evaluation of the stress intensity factors within a control area, where here only a fine mesh is required, limiting the computational time requirement.

The ASED criterion applied in Abaqus gives a fast evaluation of fatigue behavior, taking 24 seconds for one static analysis of a crack length of 2.2mm and a control area with a radius of 0.7mm, using Abaqus/CAE 2023. The simulations were conducted on a system equipped with an Intel Core i7-1165G7 processor (4 cores, 8 threads, 2.8 GHz) and 8 GB of RAM, running a 64-bit operating system. Resulting in a 16 minute analysis if considering 10 different applied forces with a crack growth from 2.2 to 2.8mm with a step of 0.2mm, compared to the XX required by the experimental results.

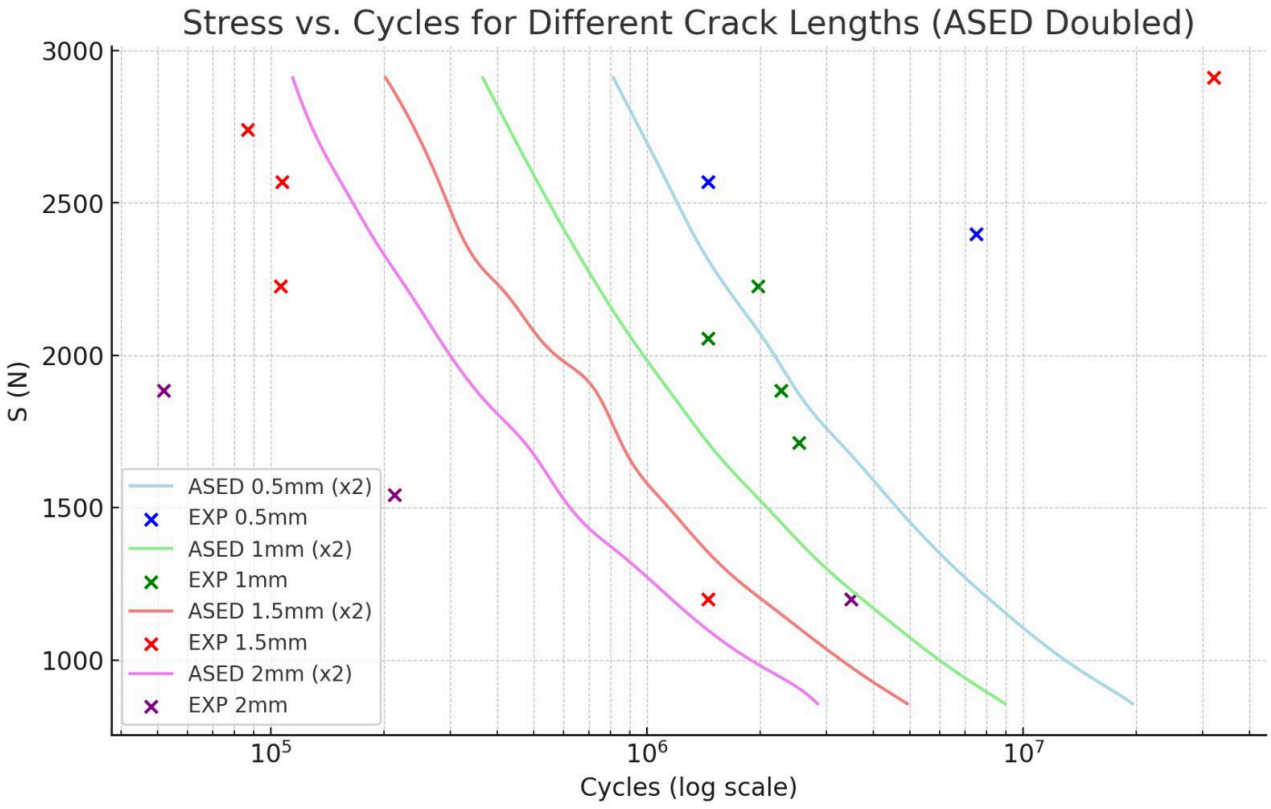

As a result, the ASED criterion data obtained predicts the trend of experimental data. The limitations of the analysis, which make it at the same time with less computational time and required complexity, mainly reside in the two-dimensional evaluation, in considering the lack of penetration defect as a crack, and in the fact that given the mechanical properties of the material, the control radius required by the material is much greater than the thickness of the specimen studied, causing a loss of accuracy in respecting some specific crack lengths, especially 0.5 and 2 mm. Other possible causes due to experimental conditions In any case, by integrating the ASED method with targeted experimental testing, the study demonstrates an effective methodology for evaluating fatigue behavior in welded aluminum joints. The findings underscore that even minor welding defects can significantly compromise fatigue performance, and that energy-based numerical methods can serve as powerful predictors of fatigue life and crack initiation in such critical structures.

4. References

1. Lazzarin, R.Z.P., and Zambardi, A., "A finite-volume-energy based approach to predict the static and fatigue behavior of components with sharp v-shaped notches," *International Journal of Fracture*, 112 (2001) 275–298.

2. F. Berto M. Zappalorto P. Lazzarin, P. Livieri. Local strain energy density and fatigue strength of welded joints under uniaxial and multiaxial loading. Engineering Fracture Mechanics, 75:1875–1889, 2008. Fracture Mechanics, 75:1875–1889, 2008.

3. F. Berto F.J. G´omez, M. Elices. Local strain energy to assess the static failure of u-notches in plates under mixed mode loading. International Journal of Fracture, 145:29–45, 2007.

4. Kah, P., Rajan, R., Martikainen, J. *et al.* Investigation of weld defects in friction-stir welding and fusion welding of aluminium alloys. *Int J Mech Mater Eng* **10**, 26 (2015)

5. Xu, Xianglai & Liu, Qingyong & Qi, Sun & Hou, Hongliang & Wang, Jing & Ren, Xueping. (2021). Effect of incomplete penetration defects on mechanical and fatigue properties of friction-stir-welded 6802-T6 joint. Journal of Materials Research and Technology. 15

6. M. Rashidi Moghaddam, M.R. Ayatollahi, F. Berto, The application of strain energy density criterion to fatigue crack growth behavior of cracked components, Theoretical and Applied Fracture Mechanics, Volume 97, 2018, Pages 440-447, ISSN 0167-8442

INFLUENCE OF THE RELATIVE ANGLE OF ROTATION BETWEEN LAYERS ON THE NATURAL FREQUENCY OF MULTILAYER SANDWICH PLATES

Youlong Wang[1], Zhenglong Wang[1] and Junwei Pan[1]
[1] Department of Civil Engineering, Southeast university, Nanjing, China

1. Introduction

The grid plate (GP) is a common sandwich structure [1], due to its light weight and high strength, it is widely used in the fields of construction and aerospace [2]. The existing improvements on sandwich plates are mainly focused on material optimization [3] and core structure improvement [4]. Few people have studied the mechanical properties of laminated plates deeply. However, some studies in recent years have shown that the laminated design can significantly improve the structural stiffness and strength, and has better energy absorption, better impact resistance and a series of other properties [5]. Further research is needed on the compressive strength, stiffness, self-vibration response and other characteristics of the laminate.

This study proposes a circular laminate GP sandwich structure with relatively rotating core layers. GP laminated plates have two different types: double-layer core structure and three-layer core structure. The relative angle between the upper and lower core layers ranges from 0 degrees to 45 degrees. By analyzing the effect of interlayer rotation angle on the natural frequency and compressive strength of laminated plates through natural frequency test, compression test and finite element verification, this study aims at providing references for the vibration design and engineering innovation of sandwich plates.

2. Materials and methods

In this study, 3D printing technology was used to prepare double-layer laminates with different inter-layer rotation angles of 0, 9, and 45 degrees, and natural frequency tests and quasi-static compression tests were performed on them. The printer used is P1S (Bambu lab, China), and the printing material is polylactic acid (PLA). The specific material parameters are shown in Table 1.

Young's modulus E	Density ρ	Poisson's ratio μ
2360 MPa	1.31 g·cm^{-3}	0.42

Table 1. 3D printing material parameters

The natural frequency test set consists of function generator (Keysight, USA), power amplifier (Siao Technology), Lead Zirconate Titanate (PZT) low-frequency sensor (Hebei Jingyi Electronics, China). Using Matlab to perform Fast Fourier Transform (FFT) on the obtained acceleration data to extract natural frequencies of plates.

In quasi-static compression test, the 100 kN microcomputer-controlled electronic universal testing machine (SUNS, China) was used, and the loading speed is 1 mm·min^{-1}.

The finite element software COMSOL was used to simulate the natural frequency of the structure obtained from the test. The first 9 natural frequency of the GP rotated plate with double core layers and three core layers was solved in the range of 0-45 degrees with a 5-degree interlayer rotation angle as an interval.

3. Results and conclusions

Test results of laminated plates at different relative rotation angles between layers are plotted together in Fig. 1. The test data show that when there is a rotation between layers, the natural frequency of the laminate will change significantly. Besides, the change in the natural frequency will not significantly change the compressive strength of the structure. The design of the interlayer angle can change the natural frequency of the laminate in specific situations without affecting its load-bearing capacity.

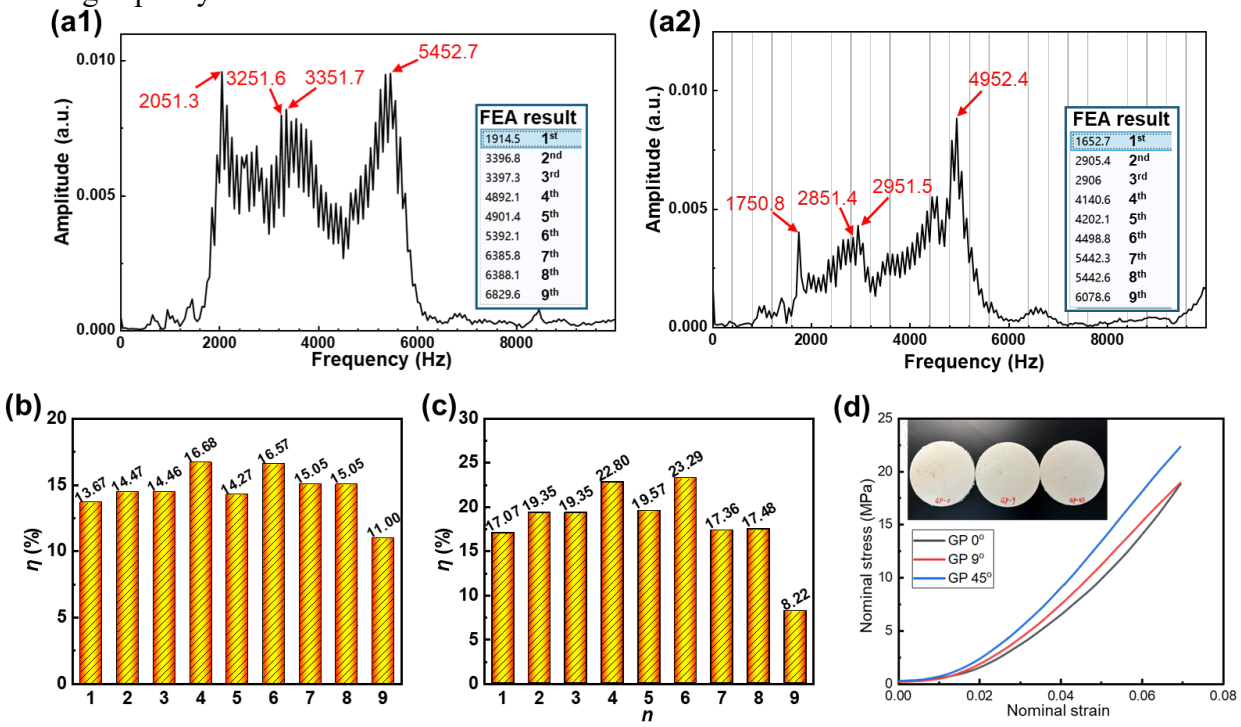

Fig. 1. Test results of laminated plates at different relative rotation angles between layers. (a) Natural frequency test and FEA results for a two-layer laminate plate. (a1) 0° ,(a2) 9°. (b) Maximum change rate of first 9 natural frequencies of double-layer plate at different rotation angles. (c) Maximum change rate of first 9 natural frequencies of tri-layer plate at different rotation angles. (d) Compression test of double-layer plates.

4. Acknowledgements

The research presented in this paper has received funding from Southeast university researching funding.

5. References

[1] He, M., & Hu, W. (2008). A study on composite honeycomb sandwich panel structure. Materials & Design, 29(3), 709-713.

[2] Sabir, R., Khan, A. A., Hasham, H. J., & Khan, I. A. (2018). Buckling Load Prediction in Ortho-Grid Plates for Aerospace Structures. Journal of Failure Analysis and Prevention, 18, 647-658.

[3] Tran, H. Q., Vu, V. T., Nguyen, V. L., & Tran, M. T. (2023). Free vibration and nonlinear dynamic response of sandwich plates with auxetic honeycomb core and piezoelectric face sheets. Thin-Walled Structures, 191, 111141.
[4] Zhang, Z. J., Han, B., Zhang, Q. C., & Jin, F. (2017). Free vibration analysis of sandwich beams with honeycomb-corrugation hybrid cores. Composite Structures, 171, 335-344.
[5] Chang, M. S. (2010). An investigation on the dynamic behavior and thermal properties of MWCNTs/FRP laminate composites. Journal of Reinforced Plastics and Composites, 29(24), 3593-3599.

IN-PLANE COMPRESSIVE MECHANICAL PROPERTIES OF A NOVEL SUTURE-INSPIRED DISCRETE SELF-LOCKING STRUCTURE

Shungang Wang[1], Yongxiang Tang[1], Yi Liu[1]
[1] Department of Civil Engineering, Southeast University, Nanjing, China

1. Introduction

Currently, the exploration of thin-walled structures' mechanical properties has focused on unleashing their optimal compressive potential through topological optimization design of structural units [1,2]. Furthermore, such structures demonstrate promising application prospects in industrial production owing to their modular assembly capability and lightweight yet high-strength characteristics. Particularly, self-locking configurations overcome the limitations imposed by integrated manufacturing on structural complexity and application scenarios: The approach enables 3D printing of small-sized, geometrically simple unit components, followed by assembly of complex configurations through groove interlocking between modular blocks [3], ultimately achieving macro-scale regulation of assembly dimensions based on practical requirements. During out-of-plane compression, thin-walled structures may exhibit either layer-wise densification patterns or diagonal densification modes (X/V-shaped configurations) throughout their deformation process. The deformation pathways of these structures are fundamentally governed by the geometric attributes of their constituent units [4,5] .

Inspired by biological cranial sutures, this study proposes a novel self-locking thin-walled structure utilizing interlocking dentition-like grooves (Fig. 1a). The interlocking grooved components can be derived from basic square frames through specific geometric relationships. Adjacent-order components can be assembled into composite structures, with the origin-first-order combination designated as Combo 01. Other configurations follow analogous nomenclature (e.g., Combo 12 and Combo 23) based on their constituent component orders.Through integrated experimental and numerical simulation approaches, we systematically investigated the influence of key geometric parameters – including the number of dentition-like grooves, aspect ratio, and wall thickness – on the compressive performance and deformation evolution of the assembled structure.

2. Materials and methods

This study employed 3D printing technology with PLA filament to fabricate three porous structures (Combo 01, Combo 12, Combo 23) and ASTM D638-02a standard dog-bone specimens. Quasi-static compression tests were conducted using a universal hydraulic testing machine to obtain mechanical response data, while finite element models were established in Abaqus CAE for verification analysis. Focusing on eight fundamental assembly configurations, we specifically selected the first three structures for geometric parametric studies. Through systematic variation of aspect ratios and wall thickness parameters, a computational model containing 29 geometric variants was ultimately developed. All models were discretized using S4R shell elements with a characteristic mesh size of 2 mm. The influence of geometric parameters on energy absorption characteristics was

quantified through specific energy absorption (SEA) metrics, while deformation mechanisms were elucidated by analyzing Poisson's ratio evolution and force-displacement response curves.

3. Results and conclusions

All images in Fig. 1b were derived from finite element simulations and uniaxial compression tests. Statistical analysis revealed distinct deformation patterns: Combo 01 exhibited layer-wise densification initiating from the platen-contacting layer, while Combo 23 demonstrated middle-layer-initiated progressive compaction with S-shaped protrusion deformation between layers due to self-locking groove interactions. Combo 12 transiently displayed diagonal compression-expansion coupling before experiencing catastrophic disintegration caused by insufficient interlocking resistance. Regarding energy absorption performance, wall thickness showed a positive correlation with specific energy absorption (SEA), whereas the aspect ratio exhibited an inverse relationship with SEA. This indicates that smaller dentition groove angles (associated with reduced aspect ratios) enhance the assembled structure's specific energy absorption capacity (Fig. 1c).

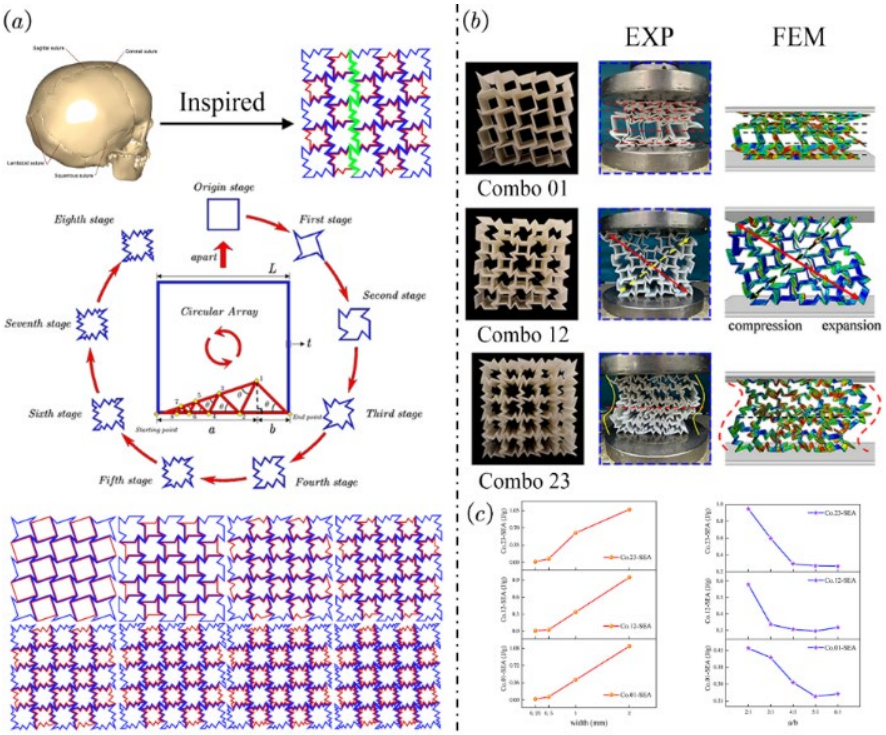

Fig. 1: Mechanical performance of bioinspired cranial suture structural components **(a)** Geometric configuration of the structural unit **(b)** Deformation patterns and finite element simulation comparisons of Combo 01, Combo 12, and Combo 23 specimens under quasi-static compression **(c)** Effects of wall thickness and aspect ratio on SEA

4. Acknowledgements

The work presented in this article was supported by the National Natural Science Foundation of China (52478306, 52478145), Jiangsu Provincial Department of Science and Technology Projects (Grant No. BE2023801) and Aeronautical Science Foundation（2024Z006069001）

5. References

[1] Huang, J., Zhang, Q., Scarpa, F., Liu, Y., & Leng, J. (2018). Multi-stiffness topology optimization of zero Poisson's ratio cellular structures. *Composites Part B: Engineering*, *140*, 35-43.

[2] Niu, H., Lu, J., Qin, R., Wang, X., Li, Q., Li, T., & Chen, B. (2025). A self-locked chiral honeycomb: in-plane compression behavior and energy absorption. *European Journal of Mechanics-A/Solids*, 105580.

[3] Deng, J., Zhao, W., Wang, J., Li, J., Wu, B., Li, X., ... & Pan, X. (2024). A novel design of an I-shape self-locked thin-walled system with mortise and tenon joints. *Thin-Walled Structures*, *201*, 111966.

[4] Cuan-Urquizo, E., & Guerra Silva, R. (2023). Fused filament fabrication of cellular, lattice and porous mechanical metamaterials: a review. *Virtual and Physical Prototyping*, 18(1), e2224300.

[5] Wang, H., Xie, S., Jing, K., Zhang, J., & Zhou, H. (2024). Mechanical properties of phenolic foam composite meta-aramid honeycomb under various directional loads and thermal environments. *Mechanics of Advanced Materials and Structures*, 1–18.

A COUPLED DESIGN APPROACH FOR KIRIGAMI-INSPIRED AUXETIC WITH TUBE TUNABLE ENERGY ABSORPTION

Iokkei Cai[1], Yu Yu[1], Xiaoru Li[1]
[1] Department of Civil Engineering, Southeast University, Nanjing, China

1. Introduction

Auxetic effect [1], manifesting a negative Poisson's ratio (NPR) effect under external loading, exhibits anomalous deformation behavior, that is, transverse contraction during uniaxial compression and lateral expansion under tensile deformation. An increasing number of research of auxetic tubular structures were conducted[2] since the distinctive energy dissipation mechanisms arise from the auxetic effect[3]. However, auxetic tubes are prone to buckling and outward peeling failure behaviors due to the inward concave phenomenon during compression, leading to premature failure. Thereby, the auxetic tube structure still faces issues of limited design flexibility, inadequate stiffness, and insufficient energy absorption capacity.

Some studies have employed tube coupling strategies to improve structural stiffness and energy absorption performance, whereas conventional coupling tubes predominantly utilize material-filled methodologies[4]. The filling coupling structures lead to excessive quality. Moreover, due to the excessive stiffness difference between the two coupled structures and the mismatch in deformation stiffness under axial compression, energy absorption capacity and deformation are typically dominated by the filler material.

To address these challenges, a novel kirigami-inspired auxetic tube named KTACT and a coupling approach were first proposed and designed. The coupling tube (CT) was composed of the KTACT and HCT. The experiment (EXP) and finite element analysis (FEA) method were implemented for analyzing the mechanical properties. The findings demonstrate that the kirigami-inspired tube and CT have the potential to be adopted in engineering fields that require enhanced energy absorption under uniaxial compression and high design flexibility.

2. Materials and methods

All the designed tubes were manufactured by the FFF (Fused Filament Fabrication) technique, and the 3D printer is Bambu Lab P1S, the printing layer thickness is set as 0.08 mm. The chosen material is Nylon PA12, the material properties as shown in Table 1. As it has excellent ductility and resistance to breakage, and is potential for engineering applications.

Density ρ	Young's modulus E	Poisson's ratio ν
1154kg/m³	700MPa	0.3

Table 1. Material properties of Nylon.

The universal testing machine was used to conduct a uniaxial quasi-static compression test. The compression speed was set as 5mm/min.

Commercial software Abaqus CAE was used to establish the finite element modeling and

analyze the deformation and force during the compression process. The compression speed was set as 100mm/min. The model was meshed with S4R elements with a global size of 1.5mm.

3. Results and conclusions

The comparison of deformation processes between EXP and FEA was provided in Fig. 1. (a), (b). CT-30-45-6.6-7-7 exhibits auxetic behavior only in the initial stage(Fig. 1. (e)). And then, transforming into a positive Poisson's ratio. When displacement reaches 40mm, folding occurs , shown as a peak in Fig.1. (c), while compression continues until densification failure. In contrast, CT-30-45-10-7-7 exhibits negative Poisson's ratio characteristics throughout compression, showing significant lateral contraction under compression, displaying inward concave deformation with a peak (Fig.1. (d)), and the compression process continued until densification failure occurred. As depicted in Fig. 1. (f), (g), the enhancement of coupling effect in force-displacement curve performance arised is significant. Fig. 1. (h) illustrated the effect of relative density on the SEA, the result indicated the energy absorption design flexibility by changing geometric parameter.

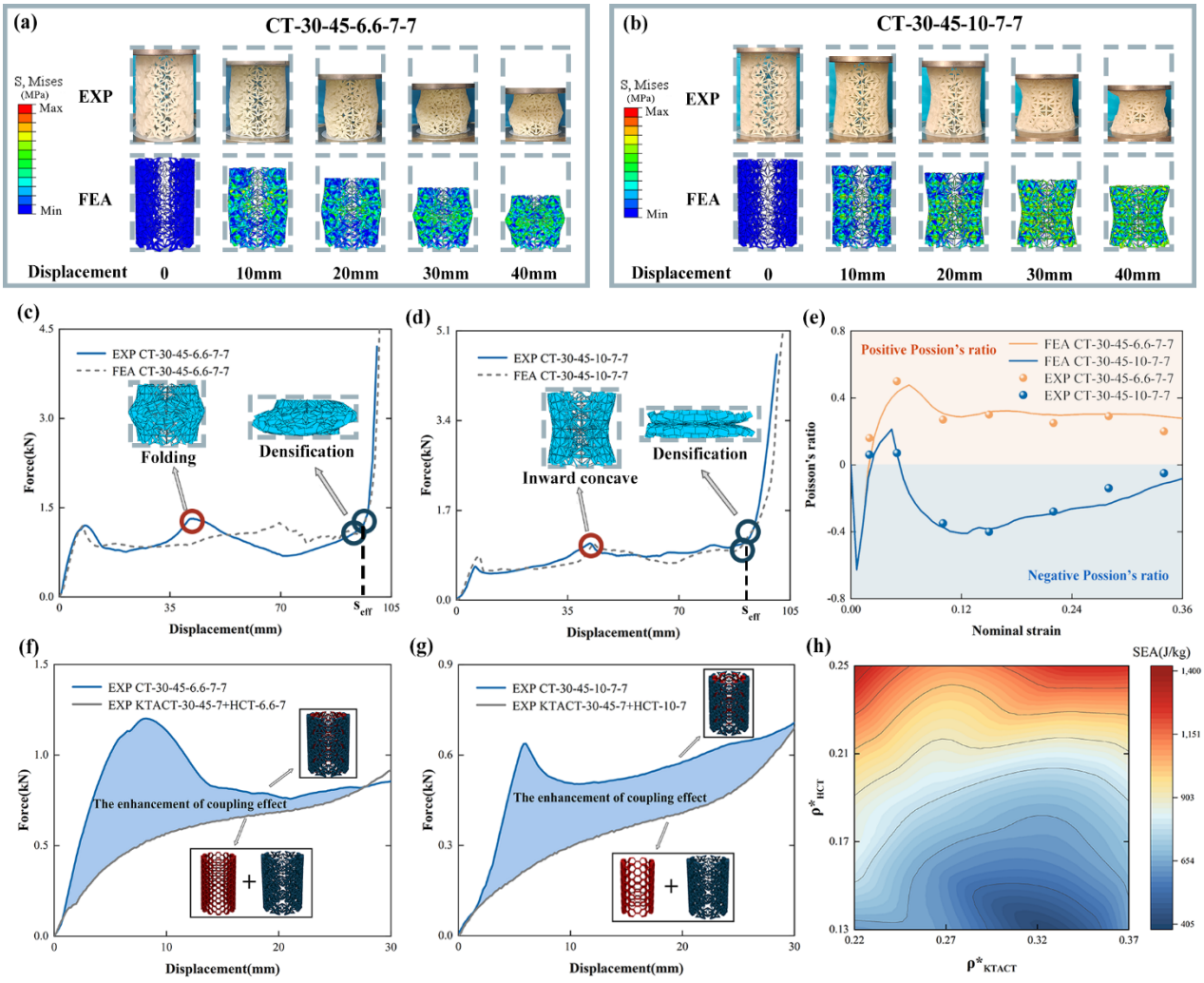

Fig. 1. The comparison of deformation processes between EXP and FEA: (a) CT-30-45-6.6-7-7; (b) CT-30-45-10-7-7; The comparison of force-displacement curve between EXP and FEA: (c) CT-30-45-6.6-7-7; (d) CT-30-45-10-7-7; (e) The comparison of Poisson's ratio between EXP and FEA; (f), (g) The comparison between CT and KTACT+HCT; (h) The effect of relative density α on the SEA

4. Acknowledgements

The work presented in this article was supported by the National Natural Science Foundation of China (52478306, 52478145), Jiangsu Provincial Department of Science and Technology Projects (Grant No. BE2023801) and Aeronautical Science Foundation（2024Z006069001）

5. References

[1] Bohara, R. P., Linforth, S., Nguyen, T., Ghazlan, A., & Ngo, T. (2023). Anti-blast and-impact performances of auxetic structures: A review of structures, materials, methods, and fabrications. *Engineering structures*, *276*, 115377.

[2] Gao, D., Wang, S., Zhang, M., & Zhang, C. (2021). Experimental and numerical investigation on in-plane impact behaviour of chiral auxetic structure. *Composite Structures*, *267*, 113922.

[3] Chen, Z., Wu, X., Xie, Y. M., Wang, Z., & Zhou, S. (2020). Re-entrant auxetic lattices with enhanced stiffness: a numerical study. *International Journal of Mechanical Sciences*, *178*, 105619.

[4] Ren, X., Zhang, Y., Han, C. Z., Han, D., Zhang, X. Y., Zhang, X. G., & Xie, Y. M. (2022). Mechanical properties of foam-filled auxetic circular tubes: Experimental and numerical study. *Thin-Walled Structures*, *170*, 108584.

Hexagonal Chiral Bistable Auxetic Metamaterials: Geometrical and Mechanical Analysis

Xiushi Li[1], Boyu Ma[1], Xueru Chen[2]
[1] School of Civil Engineering, Southeast University, Nanjing, China
[2] School of Foreign Languages, Southeast University, Nanjing, China

1. Introduction

Mechanical metamaterials attain unusual mechanical properties through microstructural design. Auxetic metamaterials, a special class of mechanical metamaterials, exhibit negative Poisson's ratio behavior—expanding transversely when stretched and contracting when compressed. Recently, auxetic metamaterials with multistable architectures have attracted increasing attention for use in self-locking structures [1] and energy absorption [2] systems, owing to their shape-morphing and programmable characteristics.

However, the designs of bistable metamaterial unit cells are predominantly derived from the only three possible edge-to-edge regular tessellations—those based on equilateral triangles [3], squares [4], and regular hexagons. In the present research, a novel metamaterial configuration is introduced based on a periodic isogonal tiling using non-edge-to-edge convex regular polygons [5], featuring a tiling pattern where each triangle is surrounded by three hexagons. The regular hexagon serves as the central element in the conjugate configuration. Along each edge of the regular hexagon, a segment ratio vector is imposed in a rotationally symmetric fashion. From the terminal point of this vector, a straight line is constructed at an angle α with respect to the adjacent hexagonal edge. This geometric operation defines a rotationally symmetric segmentation, partitioning the original hexagon into a central regular hexagon and a surrounding set of congruent quadrilateral elements. This segmentation yields a chiral unit geometry, incorporating peripheral triangles around the modified hexagon to form a distinctive metamaterial structure.

Building on this geometric foundation, the metamaterial configuration consists of a chiral unit composed of a central hexagon (CH), rotationally symmetric hexagons (RSH), and peripheral triangles (PT). Driven by two geometric parameters, this structure exhibits programmable mechanical behavior, whereby variations in these parameters lead to distinct geometric features and mechanical responses. Accordingly, we proceed to investigate these characteristics in detail.

2. Materials and methods

Traditional finite element analysis is computationally expensive when applied to a large set of parametric configurations, which limits its practicality for tasks such as configuration optimization and selection. To address this, the present study adopts a geometric analysis approach based on simplified geometric models and mechanical assumptions, enabling the prediction of deformation and strain responses with greater efficiency.

During parameter scanning, we focus on three characteristic responses. The rotation angle corresponds to the angular position at the second stable state and reflects the configuration's posture in that state. The area strain is defined as the maximum strain observed during deformation, indicating

the extent of elastic deformation. The scale factor measures the ratio of the element area in the second stable state to its initial area, capturing the overall change in structural size.

To implement this geometric analysis, we first propose the central-rigid peripheral-elastic (CRPE) model. In this model, the central hexagon and the rotationally symmetric hexagons are assumed to be rigid bodies, while the peripheral triangles are ideal elastic bodies. All elements are connected via ideal pin joints. Under this assumption, we perform rotational enumeration of the rotationally symmetric hexagons to simulate their rigid-body rotation about the pin joints and record the area variation of the elastic peripheral triangles. The rotation angle at the area extremum is extracted as the stable rotation angle, from which the scale factor is calculated. Simultaneously, we record the maximum area strain experienced by the peripheral triangles during the entire deformation process.

As a complementary idealization, we also propose an alternative deformation mode—the peripheral-rigid central-elastic (PRCE) model. In this model, the peripheral triangles and rotationally symmetric hexagons are regarded as rigid bodies, and the central hexagon is modeled as an ideal elastic element, also connected by ideal pin joints. Under this configuration, we examine the area variation of the central hexagon and identify the maximum area strain it undergoes.

To more accurately represent the elastic deformation behavior of the real structure, the maximum area strains from both models are weighted and combined to yield a representative cooperative strain indicator, which serves to evaluate the overall elastic response of the structure.

3. Results and conclusions

Based on over 4,000 computed configurations, we produced visual maps of the rotation angle, area strain, and scale factor, as illustrated in the Fig. 1. The finite element results for selected configurations with varying parameters exhibited a strong positive correlation with the area strains obtained from geometric analysis, supporting the validity of the geometric approach. As shown in the figure, the range of area strain is approximately from 0 to -1, and the scale factor ranges from 1 to 1.4, demonstrating significant potential for future applications.

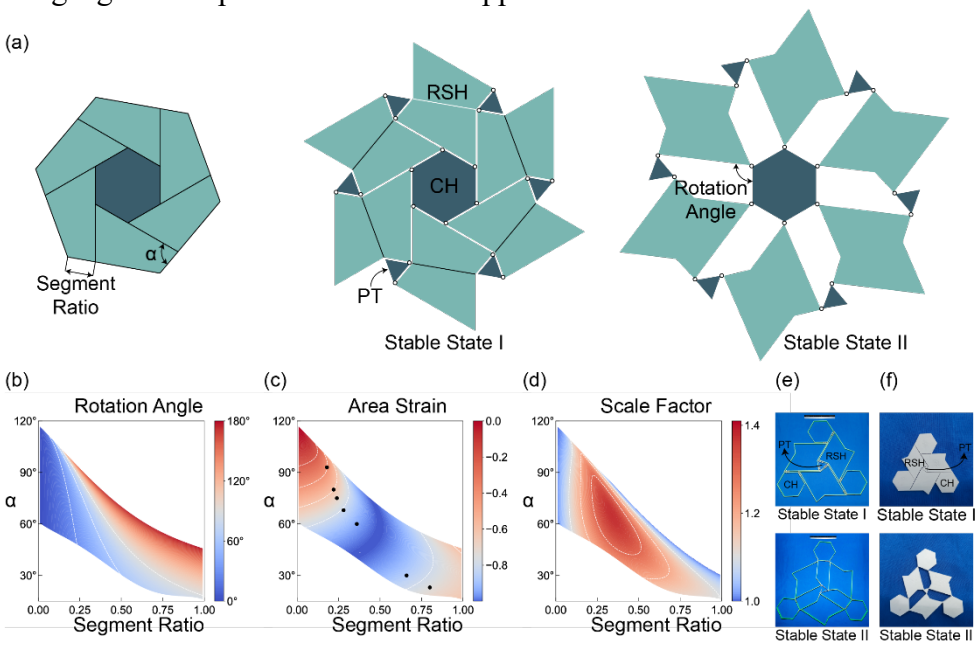

Fig. 1. (a) Geometry with key parameters (left), unit cell in stable states I and II (middle and right). (b–d) Rotation angle (b) and scale factor (d) at stable state II, and maximum area strain during deformation (c, black dots = FEM-verified), all plotted over segment ratio and α. (e) FDM-printed PLA frame model showing bistability, with hinges as moment-free mechanical joints. (f) FDM-printed TPU kirigami model showing bistability, with hinges made of thin flexible regions subjected to bending moments during deployment.

4. Acknowledgements

This research was supported by the Jiangsu Provincial College Student Innovation and Entrepreneurship Training Program.

5. References

[1] Q. Zhang, N. Pan, S. Liu et al. (2024). Self-locking Kirigami surfaces via controlled stretching, Commun. Eng., 3, 26.
[2] T. R. Giri, R. Mailen (2021). Controlled snapping sequence and energy absorption in multistable mechanical metamaterial cylinders, Int. J. Mech. Sci., 204, 106541.
[3] A. Rafsanjani, D. Pasini (2016). Bistable auxetic mechanical metamaterials inspired by ancient geometric motifs, Extreme Mech. Lett., 9 (Part 2), 291–296.
[4] A. S. Meeussen, A. Corvi, K. Bertoldi (2025). A new design strategy for highly multistable kirigami metamaterials, Adv. Funct. Mater., DOI: 10.1002/adfm.202421638.
[5] B. Grünbaum, G.C. Shephard (1977). Tilings by regular polygons., Math. Mag., 50, 227–247.

Non-Destructive Monitoring of Structural Integrity

RE-USE OF COMPOSITES WASTE IN THE PRODUCTION OF MEDICAL DEVICES: MECHANICAL ANALYSIS USING ACOUSTIC EMISSION

E. Declercq[1], K. Giannadakis[2], D.G. Aggelis[1], D. Van Hemelrijck[1], K.A. Kalteremidou[1]
[1] Department of Mechanics of Materials and Constructions, Vrije Universiteit Brussel, Brussels, Belgium
[2] Orfit Industries, Vosveld 9A, B-2110 Wijnegem, Belgium

1. Introduction

The popularity of composite materials has been increasing due to their ability to combine the advantageous properties from different materials. They offer the perfect solution for low weight and high strength and stiffness. The composites exist in both laminate and sandwich form. One of the most common manufacturing processes is using prepreg sheets. These are cut into the correct shape, and a hand lay-up method is used to form the final product which is then cured. After cutting the prepreg, a lot of waste in uncured form remains in many cases.

In the past, researchers have used composite waste to create products for less demanding applications. Nilakantan and Nutt [1] discussed the different possibilities to reuse or upcycle aerospace prepreg waste. A first step in the upcycling process was to cut rectangles out of the scrap prepreg, which could be used for manufacturing smaller objects or as reinforcement. The remainder of the scrap prepreg was cut into small pieces and pressed together to create a new laminate. These new parts could be used for decorative purposes, e.g. the interior of a car or a phone case, but also for recreative purposes, e.g. to manufacture a skateboard. Khalid et al. [2] reviewed the possibilities of upcycling and recycling after the prepreg has been cured. They demonstrated cases where the whole structure can be reused (e.g. reusing an entire wind turbine blade), the size of the used material can be reduced (e.g. recovery in small fiber- or powder form for construction use), and applications where the material can be completely recycled. When the material is recycled the process attempts to break down the matrix in order to recover the fibers. However, this often results in a loss of fiber performance and in sizing removal [3].

This study aims to recreate the original product by reusing uncured prepreg waste and analyze how the shape of the scrap can alter the mechanical performance. The product will be used for medical applications thus will have to also meet certain health requirements.

2. Materials and methods

In this research carbon- and glass fiber epoxy fabric prepregs (twill 2/2) were used to create both laminates and sandwich panels. The different composite plies were made out of scrap prepreg that was cut into different shapes: small hexagons (A = 12.5 cm²), big hexagons (A = 25 cm²), diamonds and randomly sized rectangles. To be able to compare the results, reference plates were also constructed using the original prepreg materials. For each laminate type, the shaped parts were placed next to each other with a small overlap of ~ 0.5 cm to ensure proper contact. For the laminates, multiple layers were stacked in a staggered pattern on top of each other, as shown in Figure 1. For the sandwich panels, the same process was used but the composite plies were placed on both sides of a foamed core.

After the manufacturing process, coupons were cut out of the panels and used for tensile and bending tests. These tests were performed following the ASTM D3039/D3039M – 14 [4] and ASTM D7264/D7264M – 15 [5] standards respectively. Acoustic measurements were performed during all tests using Acoustic Emission (AE) and Digital Image Correlation (DIC) was employed for the tensile tests in order to determine the strain distribution on the surface of the specimens.

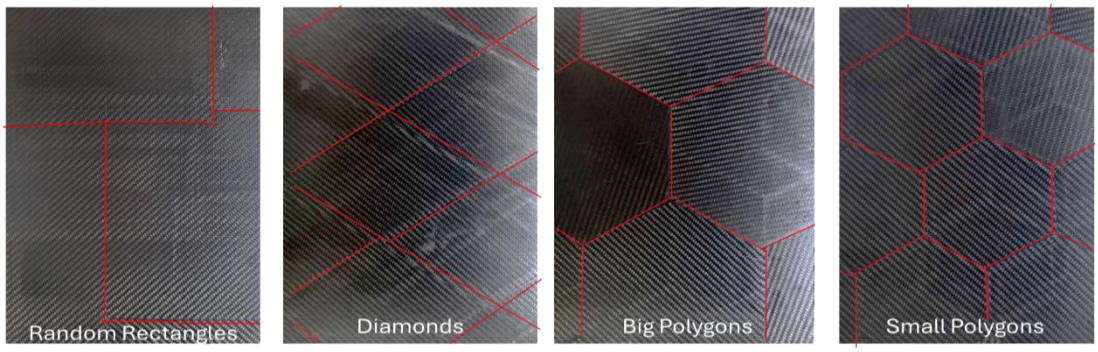

Figure 1: Laminates manufactured out of scrap prepreg in different shapes.

3. Results and conclusions

The hexagonal shapes proved less effective in the tensile tests with respect to the obtained strength and stiffness, and had a more stochastic behavior in the bending tests for both the carbon and glass laminates and sandwich panels. This performance can be explained by the random fiber orientation of the different hexagonal patterns within each layer as well as between the different layers, which was a consequence of considering the industrial requirements aiming to limit the manufacturing time as much as possible.

The diamond- and random rectangle shaped laminates presented surprisingly similar flexural- and tensile stiffnesses compared to the reference plates, but demonstrated a tensile strength corresponding to approximately 65% of the reference laminate's strength.

The next step of the research is a full analysis of the mechanical and acoustic results of all specimens. Based on the outcomes, a single shape will be chosen to undergo a full CT scan, a radio-attenuation test and a water-equivalent test, necessary for the intended medical application. The duration of the production process will also be considered towards a more sustainable solution.

4. Acknowledgements

This research is part of the SmartWeld project, which has received funding from Innoviris Brussels through Eureka and the Clusters programme and SMART Cluster. The authors acknowledge Orfit Industries for material supply and granting access to their manufacturing facilities.

5. References

[1] Nilakantan, G. & Nutt, S. (2015). Reuse and upcycling of aerospace prepreg scrap and waste. Reinforced Plastics, 59(1), 44-51.
[2] Khalid, M. Y., Arif, Z. U., Ahmed, W., & Arshad, H. (2022). Recent trends in recycling and reusing techniques of different plastic polymers and their composite materials. Sustainable Materials and Technologies, 31, e00382.
[3] Karuppannan Gopalraj, S., Kärki, T. (2020). A review on the recycling of wastes carbon fibre/glass fibre-reinforced composites: Fibre recovery, properties and life-cycle analysis. SN Applied Sciences, 2, 1, 21.
[4] ASTM D3039/D3039M – 14, Standard Test Method for Tensile Properties of Polymer Matrix Composite Materials.
[5] ASTM D7264/D7264M – 15, Standard Test Method for Flexural Properties of Polymer Matrix Composite Materials.

6-11 July 2025 ICEM21 Bologna
21st International Conference on EXPERIMENTAL MECHANICS

Fractal Patterns for Failure Modes of Ultra-high Performance Concrete

ZIHAN JIANG, FEDERICO ACCORNERO, ZHIWEN ZHU

Department of Civil Engineering and Smart Cities, Shantou University, Shantou, China

1. Introduction

Size effect describes material strength and ductility as dependent on the characteristic size of the structure. Specifically, small-size specimens show higher apparent strength than large-size samples. In the past years, several size effect laws for concrete have been proposed [1]. Carpinteri's MFSL is based on the fractal properties of the cracking process, describing the fracture of quasi-brittle materials in a non-integer dimensional space [2]. Additionally, numerical simulations have become a supplementary method for exploring the size effect in cementitious materials [3]. In particular, acoustic emission (AE) techniques can provide new insights into the concrete size effect on the energy release rate through the fractal theory [4].

This paper presents an experimental investigation of damage using the AE technique. Ultra-high performance concrete (UHPC) and plain concrete specimens with different sizes are tested to investigate the size effect. The emitted energy is experimentally detected during snap-back instabilities of concrete specimens in compression. In particular, the size effect, as well as the total number of AE events, is employed to evaluate the damage domain and its fractal dimension.

2. Materials and methods

The compression tests are carried out on nine plain concrete specimens (3×3) having characteristic size equal to 75, 150, and 300 mm, and slenderness 0.5, 1, and 2 (Fig.1). The adopted AE system is the ÆMISSION® equipped with piezoelectric sensors working in the range 10kHz-1MHz. The sensor is glued with silicone resin on the specimen surface as depicted in Fig.2.

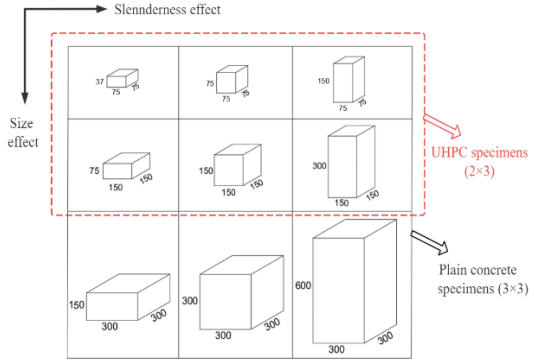

Figure 1 Specimen sizes (mm)

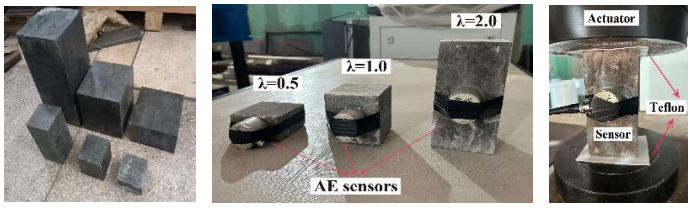

Figure 2 AE sensor layout

3. Results and conclusions

The total number of AE events and loading history from UHPC and plain concrete specimens are shown in Fig.3. As the specimen size increases, the compression strength decreases, and the fracture behaviour exhibits a ductile-to-brittle transition. In addition, as the specimen slenderness increases, the final collapse shows a crushing-to-cracking failure transition.

In Fig.4, N_{max} is represented as a function of the specimen volume, fitting the experimental data. For plain concrete specimens, the slope in the log-log plane equal to 0.73, i.e. a fractal dimension equal to 2.19, emphasizes that the energy emission occurs in a fractal domain close to a plane (crack surface, 2-D). For fibre-reinforced concrete (UHPC) specimens, a slope in the log-log plane equal to 0.92 is found, i.e. the fractal dimension is equal to 2.76, the fracture occurring in a domain close to a volume (3-D) due to the higher ductility given by the fibre-reinforcements to the concrete matrix.

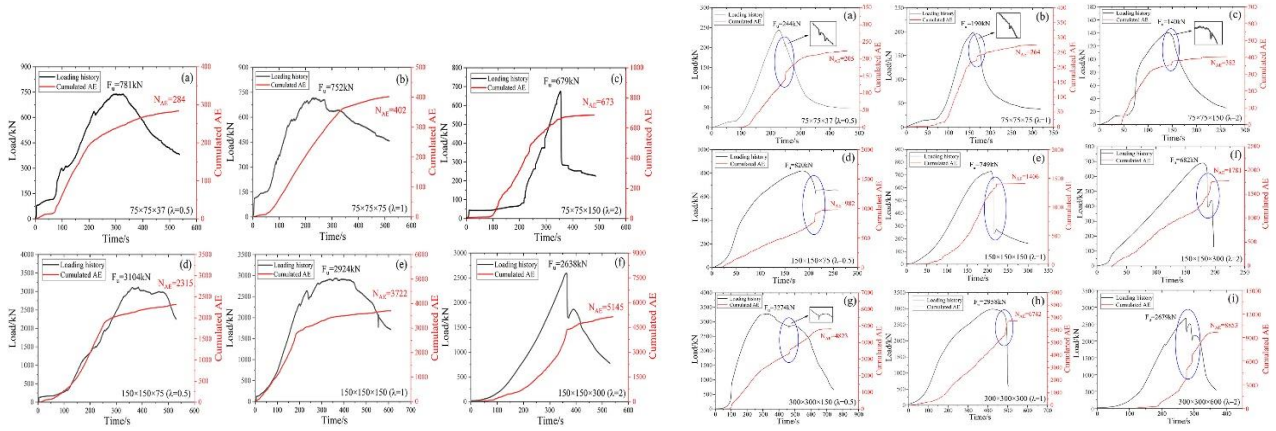

(a) UHPC (b) Plain concrete

Figure 3 AE monitoring of test specimens

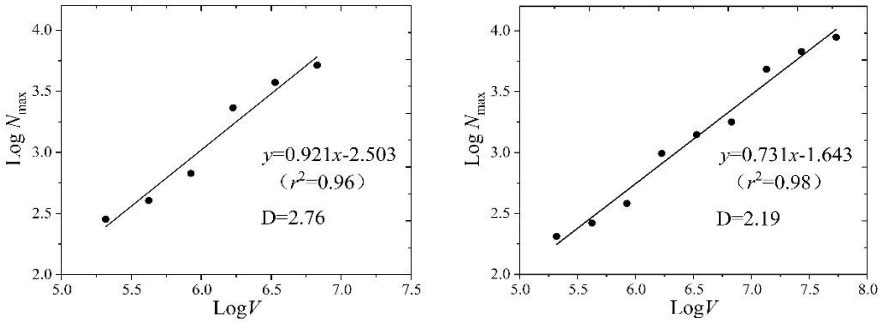

(a) UHPC (b) Plain concrete

Figure 4 Size-slenderness scale in damage evolution.

4. Acknowledgements

This research has been supported by the National Natural Science Foundation of China (grant no. 52278509) and the STU Outstanding Young Talents programme (grant no. 140-09423016).

5. References

[1] Carpinteri A, Chiaia B, Ferro G. Structures, size effects on nominal tensile strength of concrete structures: multifractality of material ligaments and dimensional transition from order to disorder. Mater Struct 1995;28(6):311–317.

[2] Carpinteri A, Chiaia B. Multifractal scaling laws in the breaking behaviour of disordered materials. Chaos, Solit and Fractals 1997;8(2):135–150.

[3] Sinaie S. Application of the discrete element method for the simulation of size effects in concrete samples. Int J Solids Struct 2017;108:244–253.

[4] Carpinteri A, Lacidogna G, Pugno N. Structural damage diagnosis and life-time assessment by acoustic emission monitoring. Engng Fract Mech 2007;74:273–289.

THE DEPENDENCE OF THE DEGREE OF NON-ADDITIVITY OF MECHANICALLY LOADED SYSTEMS ON THE LOADING RATE

D. Triantis [1], I. Stavrakas [1], E. D. Pasiou [2], S. K. Kourkoulis [2]

[1] University of West Attica, Dept. of Electrical & Electronics Engineering, Electronic Devices and Materials Lab., Ancient Olive Grove Campus, 250 Thivon Avenue, 122 44, Athens, Greece
[2] National Technical University of Athens, School of Applied Mathematical and Physical Sciences, Dept. of Mechanics, Lab. for Testing and Materials, Zografou Campus 157 73, Athens, Greece

1. Introduction

Considering that fracture is a manifestation of the non-linear processes characterizing complex dynamical systems, it is reasonable to approach the phenomenon using advanced statistical tools rather than traditional Statistical Mechanics [1,2], given that the response of such systems (at non-equilibrium stages) is not compatible to the thermodynamic principle of additivity. This incompatibility is attributed to the non-independent nature of the processes responsible for fracture, which, after specific load levels tend to produce well-organized and mutually interacting networks (sub-systems) of micro-cracks. In this context, Boltzmann-Gibbs (BG) Statistical Mechanics (and the BG entropy concept, S_{BG}) must be properly modified to cope with such phenomena that are characterized by long-range interactions and memory effects (i.e., by non-additivity), giving birth to the discipline of Non-Extensive Statistical Mechanics (NESM). Among various NESM formulations, the one most broadly used is that introduced by Tsallis [1], based on an extended definition of entropy, as $S_q=k(1-\Sigma_{i=1}^{w}P_i^q)/(q-1)$, where k is Boltzmann's constant, P_i the probability of the i^{th} configuration, w the number of possible configurations, and, q the entropic index, quantifying the degree of non-additivity of the system [1]. While S_{BG}, is maximized by the Gaussian (distribution), S_q is maximized at distributions denoted as q-Gaussians, described as [2]:

$$P(\chi,\beta) = A_q e_q\left(-\beta_q \chi^2\right) \quad (1)$$

In Eq.(1) A_q and β_q are constants while $e_q(z)$ stands for the q-exponential function, given as [1,2]:

$$e_q(z) = [1+(1-q)z]^{\frac{1}{1-q}} \quad (2)$$

Within the frame of the above argumentation, an attempt is described here to explore the potential dependence of the degree of non-additivity of a mechanically loaded system (i.e., specimens made of brittle rock) on the loading rate imposed externally, by quantifying the respective values of the q-index.

2. Materials and methods

To achieve the target of this study, advantage is taken of experimental data gathered from a protocol (described analytically in ref.[3]) comprising uniaxial compression tests with prismatic specimens made of Dionysos marble (which is used for the needs of the restoration project of the Athenian Acropolis). The acoustic activity was recorded using sensors of the R6α type. The principal characteristic of that protocol is that the loading rates imposed varied within a broad interval, ranging from 34 to 350 kPa/s.

The quantity used, to study the self-organized state of the fracture process, is the amplitude, A, of the AEs, in terms of the so called "*variable returns*" parameter [4,5] (quantifying, in fact, the fluctuations of the amplitudes), defined as $(\delta A)_i=A(t_{i-1})-A(t_i)$, where $A(t_i)$ is the amplitude of the signal recorded

at the instant t_i. Usually, $(\delta A)_i$ is normalized over the variance σ, as $(\Delta A)_i=[(\delta A)i-\mu]/\sigma$ (μ is the respective mean value). The interval of $(\Delta A)_i$ values $[(\Delta A)_{min}, (\Delta A)_{max}]$ is then divided into ten sub-intervals of equal width. For each one the Probability Density Function (PDF) of the distribution of $(\Delta A)_i$ is determined in terms of the mean value δ of each sub-interval. Combining Eqs.(1), (2) the PDF reads as:

$$PDF(\delta, \beta_q) = A_q\left[1-(1-q)\beta_q\delta^2\right]^{\frac{1}{1-q}} \quad (3)$$

3. Results, discussion and conclusions

The experimental data are then fitted by means of Eq.(3) using commercial available software. A very good correlation is revealed, as it can be seen in Fig.1a, in which the q-Gaussian distributions are plotted for the four classes of loading rates imposed, which were equal to 34, 84, 140 and 350 kPa/s.

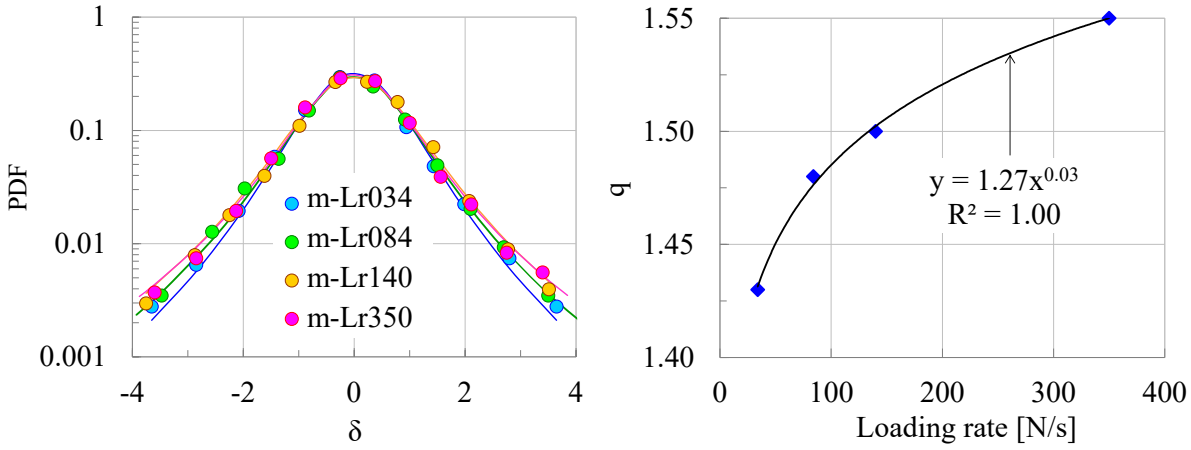

Fig. 1. (a) The q-Gaussians for the four classes of specimens; (b) Dependence of q on the loading rate.

The respective values of q, as obtained from the fitting procedure, are plotted in Fig.1b, against the loading rate imposed. It is clearly seen that a monotonously increasing trend characterizes the response of q, suggesting, that the degree of non-additivity of the fracture process is an increasing function of the loading rate. The dependence of q on the loading rate seems to be governed by a power law (see Fig.1b), however additional protocols are necessary before definite conclusions are drawn.

A similar, positive correlation of the displacement rate (rather than of the loading rate) with q, was highlighted recently by Shan et al. [5], in terms of the evolution of the electric potential, for specimens made of various rocks. In that study, the potential use of q as pre-failure index was, also, suggested.

Concluding, it could be stated that increasing the loading/displacement rate the damage mechanisms activated within the bulk of a mechanically loaded system are intensified, leading to denser networks (subsystems) of micro-cracks, or, equivalently to further deviation of the process from additivity.

4. References

[1] C. Tsallis (2009). Nonadditive entropy and nonextensive statistical mechanics - An overview after 20 years, *Braz. J. Phys*., **39**, 337–356.

[2] S. Umarov, C. Tsallis, S. Steinberg (2008). On a q-central limit theorem consistent with nonextensive statistical mechanics, *Milan J. Math.*, **76(1)**, 307–328.

[3] D. Triantis, I. Stavrakas, E.D. Pasiou, S.K. Kourkoulis (2024). Exploring the acoustic activity in brittle materials in terms of the position of the acoustic sources and the power of the acoustic signals-Part II: Applications, *Forces Mech.*, **15**, 100265.

[4] D. Tsuji, H. Katsuragi (2015). Temporal analysis of acoustic emission from a plunged granular bed, *Phys. Rev. E*, **92**, 042201.

[5] Shan T. et al. (2024). Failure evolution and disaster prediction of rock under uniaxial compression based on non-extensive statistical analysis of electric potential, *J Mining Sci. Technol*., **34**, 975-993.

CFRP SELF-SENSING COMPOSITE LAMINATE INTERLEAVED WITH PIEZOELECTRIC NANOFIBERS

T. M. Brugo[1], F. Mongioi[1], G. Selleri[2], E. Maccaferri[3], R. Palazzetti[4], P. Bettini[4], A. Zucchelli[1], D. Fabiani[2], L. Mazzocchetti[3]

[1]Department of Industrial Engineering, University of Bologna, Bologna, Italy
[2]Department of Electrical Engineering, University of Bologna, Bologna, Italy
[3]Department of Industrial Chemistry, University of Bologna, Bologna, Italy
[4]Department of Mechanics, Polytechnic di Milano, Milan, Italy

1. Introduction

Aerospace engineering is increasingly using carbon fiber composites instead of metal alloys for improved performance, weight reduction, and environmental compliance. However, these composites face challenges like hidden damage compromising structural integrity. Structural Health Monitoring (SHM) systems employ sensors within or on laminate layers to detect impacts. However traditional sensors can alter mechanical properties or face durability issues.
Advanced techniques use low-invasive piezoelectric materials, such as PZT fibers and nanoparticles [1], [2] or piezoelectric polymers like P(VDF) films, to enhance monitoring while minimizing disruptions. P(VDF) nanofibers improve toughness and reduce damage, while carbon fibers' electrical properties provide non-intrusive electrode alternatives [3].
This study focuses on modifying CFRP laminates by interleaving P(VDF-TrFE) piezoelectric nanofibers and using CFRP plies as electrodes, aiming to enable damage detection without sacrificing mechanical properties. Experimental testing will assess these functionalized laminates against traditional ones.

2. Materials and methods

The study utilized two electrospinning processes to fabricate nanofibers from P(VDF-TrFE) and Nylon-6,6. The first contributes to the laminate's sensing capabilities, while the second acts as an insulating layer to prevent short-circuiting between electrodes. The nano-modified self-sensing composite laminate features a stacking sequence of [(CFRP-90°)/(CFRP-0°)/Nylon-6,6 nanofiber/(CFRP-90°)/(CFRP-0°)/P(VDF-TrFE) nanofiber]s. Thin copper wires (80 µm) connect the CFRP plies to the acquisition circuit. Two orthogonal unidirectional CFRP plies (90° and 0°) with interleaved copper wires serve as electrodes. External CFRP plies act as shield electrodes to reduce triboelectric noise, while Nylon-6,6 membranes insulate them from signal electrodes. The piezoelectric nanofiber mat at the midplane work as a charge generator and insulator. This study, in addition to evaluating the sensor performances of the nano-interleaved laminate, compares its mechanical properties with those of reference laminates that lack nanofibers. The reference laminates share the same CFRP ply dimensions and stacking sequence as the self-sensing laminates, but without the inclusion of nanofibers, following the sequence [90°/0°/90°/0°]s.

3. Results and conclusions

The sensing capabilities of the nano-modified composite laminates were evaluated using a pre-impact test with a low force that preserved laminate integrity. In Figure 1 it can be observed as the piezoelectric output closely correlated with the contact force (R^2=0.98) measured by the impactor load cel, with a sensitivity of 227.2 mV/kN.

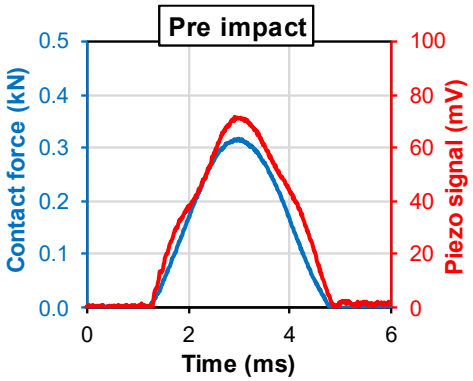

Figure 1. Contact force vs piezo-signal graphs of the pre-impact tests of the nano-modified laminates. Reprinted from [4].

The impact resistance of nano-modified and reference laminates was evaluated by performing a Low-Velocity Impact (LVI) test with an impact energy of 3 J. Figure 2 shows half of the laminates cross-section, with damage symmetrical to the impact point. As can be observed in the reference, cracks spread between the laminate plies, resulting in extensive delamination with a total length of 16.8 mm, which is three times greater than the delamination observed in the nano-modified laminate (5.3 mm).

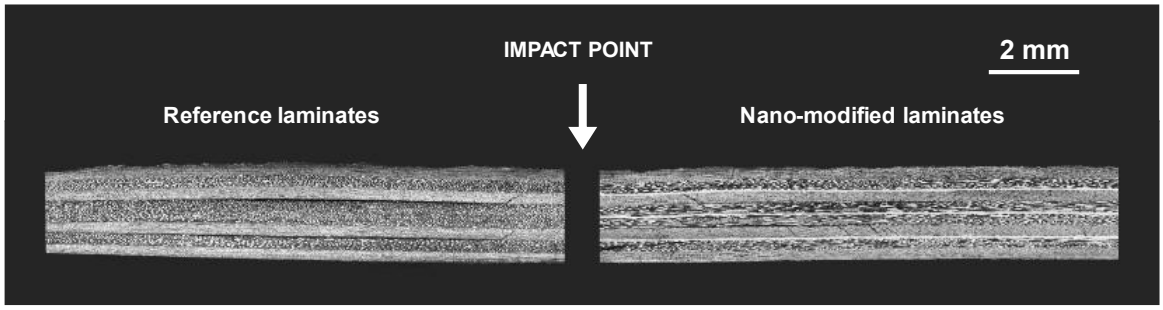

Figure 2. Micrographs analyses of the cross-section of both the reference and nano-modified laminates, after the LVI tests. Reprinted from [4].

5. References

[1] H. P. Konka, M. A. Wahab, and K. Lian, "The effects of embedded piezoelectric fiber composite sensors on the structural integrity of glass-fiber-epoxy composite laminate," Smart Mater. Struct., vol. 21, no. 1, 2012, doi: 10.1088/0964-1726/21/1/015016.

[2] M. E. Gino et al., "On the design of a piezoelectric self-sensing smart composite laminate," Mater. Des., vol. 219, p. 110783, 2022, doi: 10.1016/j.matdes.2022.110783.

[3] Y. Yu, Y. Shi, H. Kurita, Y. Jia, Z. Wang, and F. Narita, "Carbon Fiber-Reinforced Piezoelectric Nanocomposites: Design, Fabrication and Evaluation for Damage Detection and Energy Harvesting," Compos. Part A Appl. Sci. Manuf., vol. 172, no. January, p. 107587, 2023, doi: 10.1016/j.compositesa.2023.107587.

[4] F. Mongioì, et al., "CFRP cross-ply self-sensing composite laminate based on polymeric nanofibers interleaving" ECCM 21 proceedings, Vol. 6 – Multifunctional and Smart Composites, doi: 10.60691/yj56-np80.

ACOUSTIC EMISSION TESTING OF REINFORCED CONCRETE BEAMS UNDER BENDING LOADING: METHODOLOGY AND PRELIMINARY RESULTS

D. D'Angela[1], G. Magliulo[1,2], A. Monici[3], M. Del Zoppo[1], M. Di Ludovico[1], and A. Prota[1]
[1] Department of Structures for Engineering and Architecture, University of Naples Federico II, Italy
[2] Construction Technologies Institute (ITC), National Research Council (CNR), Italy
[3] E.T.S. Sistemi Industriali, Italy

This study presents the methodology and preliminary findings of acoustic emission (AE) tests conducted on reinforced concrete (RC) beams subjected to four-point bending loading up to failure. The experimental campaign investigated beams with different internal longitudinal and transverse reinforcement and composite retrofitting conditions, addressing both flexural and shear failure mechanisms. The primary objective was to identify the initiation of cracking damage through AE analysis, with the goal of developing damage criteria for structural health monitoring applications. AE data were analyzed using a range of techniques, from basic AE feature elaboration to advanced methods, with a focus on AE entropy assessment, considering Shannon and Kullback–Leibler formulations. These measures were correlated with cracking damage initiation and evolution, identifying potential trends, also associated with the retrofitting condition. The study offers methodological insights and identifies preliminary AE-based indicators for detecting early-stage damage in RC beams under bending loads, contributing to the development of more effective monitoring strategies.

THE GARISENDA TOWER IN BOLOGNA: DAMAGE ASSESSMENT RESULTS FROM PRINCIPAL COMPONENT ANALYSIS, ACOUSTIC EMISSION, AND NONLINEAR FINITE ELEMENT INVOLVING CREEP AND SMEARED CRACKING

G. Lacidogna [1], P. Marin Montanari[1], S. Invernizzi [1], A. Di Tommaso[2]
[1] Department of Civil, Environmental, and Building Engineering (DISEG), Politecnico di Torino, Torino, Italy
[2] Academy of Sciences of Bologna, Bologna, Italy

1. Introduction

The Garisenda Tower, along with the neighboring Asinelli Tower, is arguably the symbol of the city of Bologna. They are the sole remnants of about one hundred towers that spawned the city's skyline in medieval times. As such, the monitoring of their state of health has been of great interest to the scientific community for more than a century – one example being the studies of Prof. Cavani in the beginning of the 20th century [1]. The Garisenda Tower, famous for its impressive lean that can be seen with naked eye, nowadays it is object of Structural Health Monitoring (SHM) with a multitude of devices, including: a 30m long pendulum installed on the inside to measure the planar displacement of the tower's top, Fiber Optical Strands (FOS) installed in the walls of the basement to measure their vertical deformation, and piezoelectric Acoustic Emission (AE) sensors, also installed on the walls of the basement, to detect elastic waves generated by microcracking of the wall material (see Figs.1 and 2). This rich experimental setup allows for the investigation of the tower stability and damage assessment in many ways [2]. In this work, attention is focused on three key analyses: the first is a principal component analysis (PCA) study that investigates the relationship strength between AE data and other SHM data, such as temperature in the vicinity of the tower, pendulum displacement, and FOS strain, among others. The second and third analyses correspond to numerical studies (nonlinear finite element analyses) that assess damage and its sources (Fig.3). A first study using the Smeared Crack approach for the masonry walls and the selenite stone allows to understand which zone of the tower (especially the basement) is more damaged, considering two loading conditions: the Garisenda's self-weight and an increase in the tower leaning that could happen due to foundation failure, for example. From this first study, a second study is carried out by enriching the material model for masonry and selenite with a viscoelastic formulation to account for creep. Strain rates are obtained from the deformation of the FOS. This second numerical analysis aims to give an estimate of the time needed for collapse to occur due to viscous effects.

2. Materials and methods

In this work, Principal Component Analysis (PCA) [3,4] is used to put together AE activity with environmental effects and structural stability indicators. The analysis considers data from a four-year monitoring period. Building from past experiences with numerical damage modelling of historic masonry towers [5], including with the Smeared Crack approach [6], nonlinear 3D finite element (FE) models were constructed using the commercial package DIANA [7] (Fig.3).

In these models, the deadweight of the tower was combined with a tilting analysis to simulate increase in lean, by applying a rigid body rotation to the tower frustum and the surrounding soil. This finite element model is further enhanced with a viscoelastic material formulation, to take creep into account, as this effect is a known challenge for masonry and historic structures [8–10].

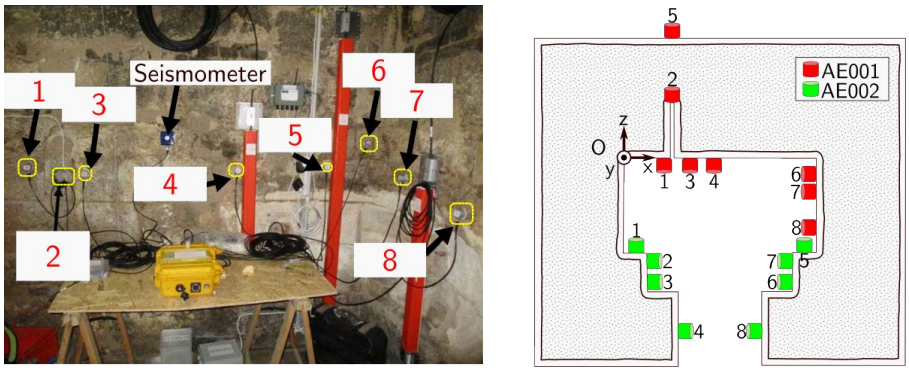

Fig. 1. *In-situ* picture of the AE sensors in the base of the Garisenda tower (left) and a schematic depiction of their position (right).

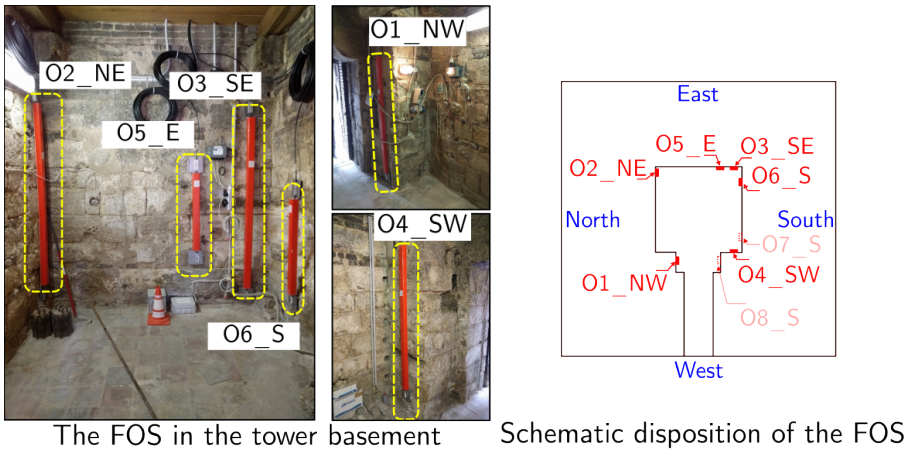

Fig. 2. *In-situ* picture of the FOS in the base of the Garisenda tower (left) and a schematic depiction of their position (right).

3. Results and conclusions

It is shown how the AE activity is generally related to negative values of FOS strains, which represent compression of the base, and to displacements of the pendulum in the South-East direction, which is the direction of leaning of the Garisenda. Moreover, such activity occurred in general in colder periods of the year. Regarding the FE models, the results could identify a critical lean angle of the tower, where collapse is imminent. Lastly, the creep analysis could give a rough

assessment of the risk of collapse by creep effects by identifying when the tower could reach a critical state (tertiary creep).

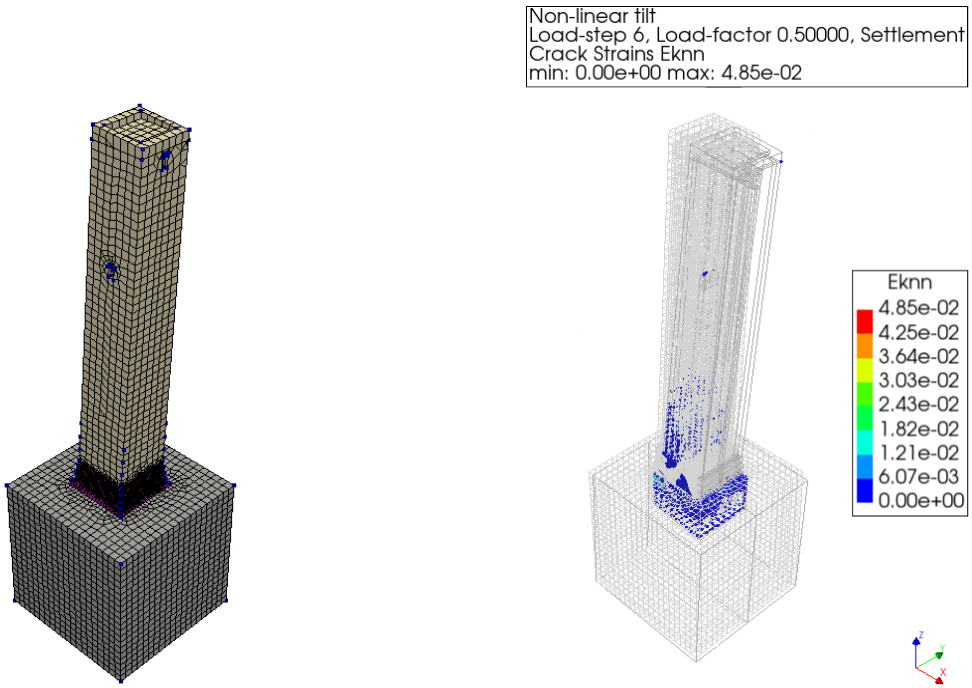

Fig. 3. The finite element mesh of the Garisenda tower (left) and crack strains due to the tilting condition obtained from the nonlinear model (right).

4. Acknowledgements

The research presented in this paper has received funding from the Municipality of Bologna. The authors express their gratitude to the Municipality for enabling the realization of this study. They would also like to extend their appreciation to Arch. Manuela Faustini Fustini and Eng. Vincenzo Daprile for their indispensable and expert collaboration.

5. References

[1] Cavani, F. (1901). Movimenti della sommità rispetto alla base nella torre Garisenda di bologna, Memorie Della Regia Accademia Delle Scienze Dell'Istituto Di Bologna – Classe Di Scienze Fisiche, serie VI(Tomo VII), 317–330.

[2] Marin Montanari, P., Lacidogna, G., Invernizzi, S., Di Tommaso, A., Carpinteri, A. (2024). Experimental and Numerical Damage Assessment of the Garisenda Tower: Investigation by AE, Thermal, Seismic, and Permanent Strain Analyses., In: Rainieri, C., Gentile, C., Aenlle López, M. eds., *Proceedings of the 10th International Operational Modal Analysis Conference (IOMAC 2024)*, vol. **514**, Cham, Springer Nature Switzerland, 3–14.

[3] Mario Azzara, R., De Roeck, G., Girardi, M., Padovani, C., Pellegrini, D., Reynders, E. (2018). The influence of environmental parameters on the dynamic behaviour of the San Frediano bell tower in Lucca, *Engineering Structures*, **156**, 175–187. DOI: 10.1016/j.engstruct.2017.10.045.

[4] Moropoulou, A., Polikreti, K. (2009). Principal Component Analysis in monument conservation: Three application examples, *Journal of Cultural Heritage*, **10(1)**, 73–81. DOI: 10.1016/j.culher.2008.03.007.

[5] Invernizzi, S., Lacidogna, G., Olivetti, G.C., Tommaso, A.D., Carpinteri, A. (2023). Garisenda Tower in Bologna (Italy): structural assessment and numerical simulation, *International Journal of Masonry*

Research and Innovation, **1(1)**, p. 1. DOI: 10.1504/IJMRI.2023.10053441.
[6] Carpinteri, A., Invernizzi, S., Lacidogna, G. (2005). In situ damage assessment and nonlinear modelling of a historical masonry tower, *Engineering Structures*, **27(3)**, 387–395. DOI: 10.1016/j.engstruct.2004.11.001.
[7] Home - DIANA. (2024). Available at: https://dianafea.com/.
[8] Taliercio, A. (2009). An overview of masonry creep., Tallinn, Estonia, 197–208.
[9] Binda, L. ed. (2008). Learning from failure: long-term behaviour of heavy masonry structures, Southampton, WIT Press.
[10] Verstrynge, E., Schueremans, L., Van Gemert, D., Wevers, M. (2009). Monitoring and predicting masonry's creep failure with the acoustic emission technique, *NDT & E International*, **42(6)**, 518–523. DOI: 10.1016/j.ndteint.2009.03.001.

CHARACTERIZATION OF CONCRETE DAMAGE THROUGH ULTRASONIC DISPERSION

G. Lefever[1], N. Ospitia[1,2], N. De Belie[2], D.G. Aggelis[1]
[1] Department of Mechanics of Materials and Constructions, Vrije Universiteit Brussel, Belgium
[2] Magnel-Vandepitte Laboratory, Department of Structural Engineering and Building Materials, Ghent University, Ghent, Belgium

1. Introduction

Ultrasonic methods have been widely applied for concrete quality evaluation [1]. This paper proposes dispersion (dependence of wave velocity on frequency) measurements to provide a direct physical relation between the wave velocity and the elastic modulus of the material as well as the typical heterogeneity or void size. The use of dispersive wave parameters improves the characterization, since wave velocity at various wavelengths interacts in a distinct manner with the different heterogeneity/damage scales. Therefore, even if differences between damaged and healthy material for some frequencies are small, results become clearer when considering the whole available frequency band. Velocity and attenuation measurements for different frequencies have proven their sensitivity to the degree of damage, as well as repair effectiveness in concrete structures [2,3]. However, further studies are needed to establish a reasonable interpretation of the shape of the dispersion curve and its connection to microstructural parameters of the material.

2. Materials and methods

The material was cementitious mortar including 6% vol. of Expanded Polystyrene (EPS) spheres with a mean diameter of approximately 5 mm. The specimens' dimensions were 400x60x60 mm³. A specimen without EPS was also produced and tested for reference. The specimens were tested 4 months after mixing, when the hydration is expected to be completed. Concerning the ultrasonic experiment, a waveform generator produced an excitation of 250 kHz. This was fed to the emitter, a wideband sensor with a broad frequency response from 100-400 kHz around the peak sensitivity of 250 kHz and was placed in contact with the specimen. The air-coupled receiver is a "Fabry-Pérot" laser interferometer, sensitive to the periodic variations of the refractive index of air under the excitation of the wave and was placed on the opposite side of the specimen. A photograph during the experiment is shown in Fig. 1a. The calculation of the phase velocity vs. frequency curve follows the procedure of Sachse and Pao [4].

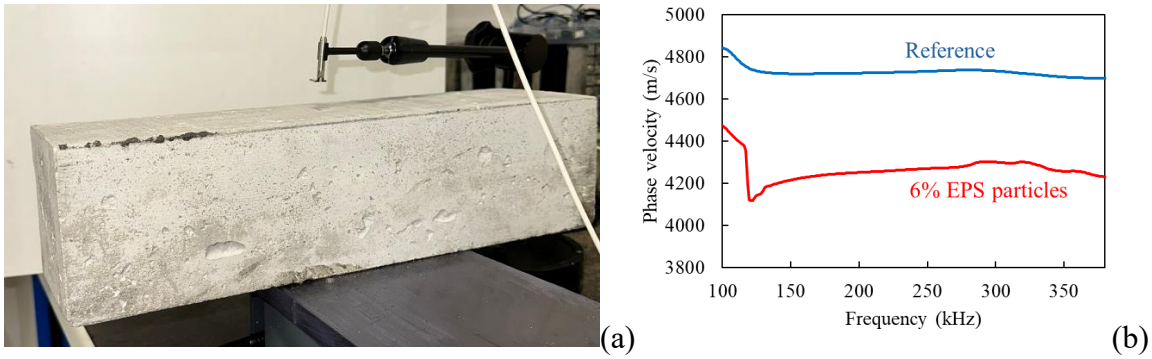

Fig. 1. (a) Snapshot during the ultrasonic test, (b) Wave velocity vs. frequency curves for reference material and material with 6% light particles.

3. Results and conclusions

Typical dispersion curves are shown in Fig. 1b. The reference mortar (0% voids) exhibits a relatively smooth curve without strong variations in the phase velocity with values around 4700 m/s up to 350 kHz. For the 6% void case, the velocity curve is positioned at lower level with a minimum at 120 kHz, while for higher frequencies the velocity comes closer to 4300 m/s. The results show that heterogeneity impacts not only the level of the velocity, but the shape of the dispersion curve which can be related to the typical size of the inclusions.

4. Acknowledgements

The authors wish to thank the Research Foundation - Flanders (FWO Vlaanderen) for the support through postdoctoral mandates 1249924N and 1299923N.

5. References

[1] T. Naik, V. Malhotra, J. Popovics, The ultrasonic pulse velocity method, in: V. Malhotra, N. Carino (Eds.), Handbook on Nondestructive Testing of Concrete, second ed., CRC Press, 2003, pp. 8-1–8-19.

[2] Ahn E., Kim C., Choi H., Shin M., Assessment of crack repairing in concrete using air-coupled surface-wave technique: Experimental and numerical investigations (2024) *Construction and Building Materials*, **441**, art. no. 137552

[3] Shiotani T. S. Momoki, H. K. Chai, D.G. Aggelis. Elastic wave validation of large concrete structures repaired by means of cement grouting (2009) *Construction and Building Materials*, **23** (7), pp. 2647 – 2652.

[4] Wolfgang Sachse, Yih-Hsing Pao, On the determination of phase and group velocities of dispersive waves in solids, *Journal of Applied Physics* **49** (1978) 4320-4327.

Novel Applications of Experimental Mechanics

FLAME RETARDANCY AND MSCHNICAL PROPERTIES OF NOVEL HALOGEN-FREE POLYURETHANE CONTAINING CHITOSAN FROM FISHERIES WASTE

Ming-Yuan Shen[1], Chin-Lung Chiang[2*], Cing-Yu Ke[3]

[1] Graduate Institute of Precision Engineering, National Chung-Hsing University, Taichung, Taiwan
[2] Department of Chemical and Materials Engineering, National Chin-Yi University of Technology, Taichung, Taiwan
[3] Department of Safety, Health and Environmental Engineering, Hung-Kuang University, Taichung, Taiwan

1. Introduction

Polyurethane (PU) had excellent tensile strength, chemical resistance, abrasion resistance, low-temperature tolerance and oil resistance [7-10]. Owing to its unique physical and chemical properties, PU polymers were widely used in coatings, packaging materials, medical devices, the textile industry, automobile manufacturing, paints, footwear, adhesives, and thermoplastic elastomers [1-2]. However, PU was highly flammable and prone to dripping when melting, posing risks of secondary fires. Developing green, ecofriendly, halogen-free flame retardants for PU was essential.

This study employed recycled fisheries waste and green, halogen-free materials to prepare flame retardants containing carbon, nitrogen, and phosphorus. The prepared flame retardants were integrated into 3-aminopropyltriethoxysilane-modified PU (Si-PU) to fabricate composite materials. The objective of the study was to enhance flame resistancy of the composites and the effect of additives on mechanical properties for PU composites

2. Synthesis of Si-PU/CS-PMPI-MPP composites

First, 5.08 g CS, 5.08 g PMPI, and 20.33 g MPP were placed into a 100-mL serum bottle, to which 50 mL of THF solvent was added and stirred for reaction at a temperature of 80 °C for 4 h, forming CS-PMPI-MPP shown in Scheme 1. Subsequently, 12.89 g IPDI and 20 g polyol were placed into a four-necked separation reaction vessel under a nitrogen atmosphere at a temperature of 80 °C, with mechanical stirring facilitated by a magnetic stirrer. The metal catalyst 1 g DBTDL was then added for reaction, and after 2 h, the prepolymer within the reaction vessel was reacted with 12.84 g APTS, also for 2 h, forming Si-PU. For comparison, using a similar reaction method, the prepolymer reacted with a chain extender (7.6 g 1, 4-butanediol) to form pristine PU. The temperature was then reduced to 50 °C. Subsequently, 80 mL of THF was added, and CS-PMPI-MPP was gradually introduced, with observations made regarding solvent evaporation or reduction and viscosity increase. Finally, the viscosity-enhanced Si-PU/CS-PMPI-MPP was placed into a Teflon mold, degassed in a vacuum oven, and dried in an oven for 12 h at 80 °C. Subsequently, the finished product was removed and cooled at room temperature, completing the preparation of Si-PU/CS-PMPI-MPP.

3. Results and conclusions

Fig. 1 present the UL-94 and LOI test results for pristine PU and the Si-PU/CS-PMPI-MPP composite. After ignition, the flame quickly spread across pristine PU, causing dripping that ignited cotton, resulting in the pristine PU being given a Fail grade. In contrast, during the vertical burning process, PU modified with APTS overcame the original PU's propensity for dripping. With the increase of CS-PMPI-MPP concentration to 40 wt%, the combustion time did not exceed 30 s after two ignitions, achieving a UL-94 rating of V-1. The LOI test results were consistent with the UL-94 outcomes. That was, pristine PU and the Si-PU/CS-PMPI-MPP 40 wt% composite displayed LOI values of 18.2 % and 26.5 %, respectively, indicating superior flame retardancy in Si-PU/CS-PMPI-MPP 40 wt% composite.

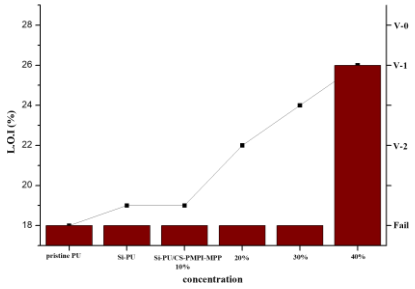

Fig. 1. LOI and UL-94 of pristine PU, Si-PU, and Si-PU/CS-PMPI-MPP 10%–40%

Fig. 2 illustrated the mechanical properties of pristine PU, Si-PU, and the Si-PU/CS-PMPI-MPP 40 wt% composite, including (a) tensile strength and (b) elongation at break. Both Si-PU and the Si-PU/CS-PMPI-MPP 40 wt% composite exhibited a decrease in elongation at break but a significant increase in tensile strength. The tensile strength of pristine PU was 1.79 MPa with an elongation at break of 368%. For Si-PU, the tensile strength was 6.72 MPa and the elongation at break reduced to 22%. The Si-PU/CS-PMPI-MPP 40 wt% composite had a tensile strength of 7.48 MPa and an elongation at break of 35%. Compared with pristine PU, the tensile strength of the Si-PU/CS-PMPI-MPP 40 wt% composite increased by 318%.

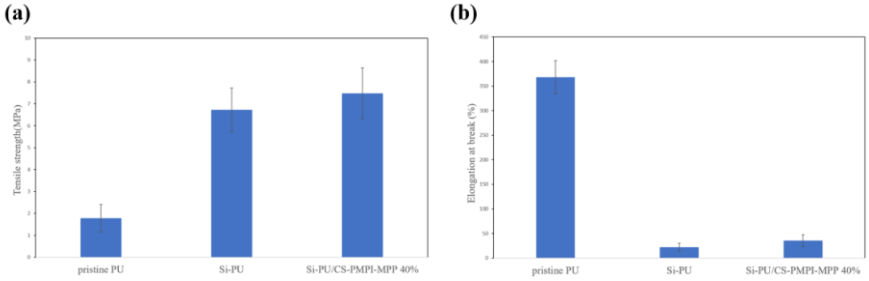

Fig. 2. Effects of flame retardants on mechanical properties of PU composites. (a) Tensile strength, and (b) elongation at break.

4. Acknowledgements

The authors would like to express their appreciation to the National Science and Technology Council for financial support of this study under Grant NSTC 113-2221-E-167 -014 -MY3

5. References

[1] M. Zajac, H. Kahl, B. Schade, T. R€odel, M. Dionisio, M. Beiner (2017), Relaxation behavior of polyurethane networks with different composition and crosslinking density, *Polymer*, **111**, 83-90.

[2] J. Pagacz, E. Hebda, B. Janowskic, D. Sternikd, M. Jancia, K. Pielichowski(2018), Thermal decomposition studies on polyurethane elastomers reinforced with polyhedral silsesquioxanes by evolved gas analysis, *Polym. Degrad. Stab.*, **149**, 129-142.

EuraSEM 6-11 July 2025 ICEM21 Bologna | 21st International Conference on EXPERIMENTAL MECHANICS

ULTRFAST PROCESSING OF METALLIC ALLOYS AT LOW TEMPERATURE

M. Rahman, L. Warner, S. Todaro, D. Waryoba and A. Haque
Department of Mechanical Engineering, Pennsylvania State University, University Park, PA, USA

1. Introduction

Annealing and recrystallization are the most impactful processing steps for microstructural and properties control of materials. They are also the most energy and time-consuming processes. Steel, for example, takes over 1000 °C temperature and several hours. Even with very high temperature, the processing takes very long time since thermal diffusion is random in nature. The motivation of this research is to achieve microstructural and defect control at very low homologous temperature (<0.2) and in a minute or less.

We introduce a non-thermal stimulus to achieve ultrafast annealing or recrystallization at very low temperature. We propose to exploit the electron wind force (EWF), which EWF originates from the momentum transfer of electrons. In the defect-free lattice, electron scattering generates resistive or Joule heating. However, whenever they encounter a defect, they transfer their momentum, and the defect experiences a mechanical force. We will show that the EWF is unique from two perspectives (a) extreme localization to the defects and grain boundaries and (b) cathode-to-anode directionality, similar to convection-diffusion. Our proposed EWF-based technique requires only two electrodes to pass pulsed current through the specimen. The amplitude of these current pulses is 100-5000 Amp; however, the pulse width is only 40-50 micro-seconds. Infrared thermometry is used to monitor the specimen temperature during processing.

2. Materials and methods

The present study dealt with two alloys; Zr_{50}-Ti_{50} and FeCrAl. ZrTi alloys are lightweight, strong, and resistant to corrosion. They are suitable for aerospace, medical devices, coatings and surface applications. FeCrAl alloys are attractive for nuclear power applications including accident tolerant fuel cladding, structural components for fast fission reactors, and as first wall and blanket structures for fusion reactors.

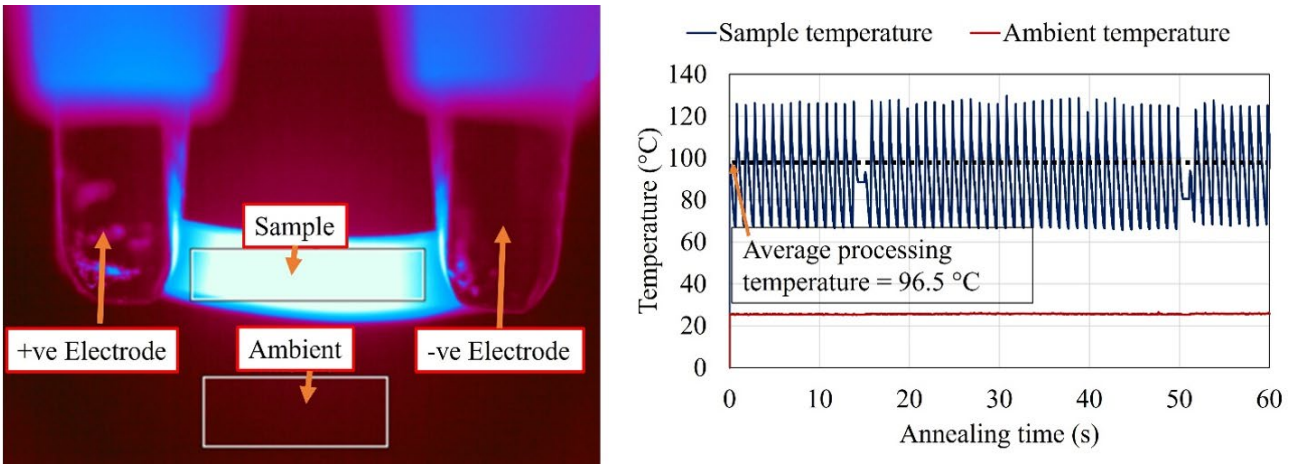

Figure 1. (left) Thermograph image and (right) temperature profile of FeCrAl for 1 minute of annealing period with a current density of 3307.7 A/(mm^2).

3. Results and conclusions

The zirconium-titanium alloy study investigates the microstructural transformations and associated property enhancements in a Zr50-Ti50 alloy annealed at only 120 C. Microanalysis with electron backscatter diffraction (EBSD) and X-ray diffraction (XRD) show the formation of alpha lath structure, typically observed in much higher thermal annealing temperatures. EBSD and XRD analyses revealed the formation and/or growth of the lath structure, with notable changes in pole distributions and the appearance of a distinct peak at 52.5° in the XRD spectrum. Nanoindentation data showed an increase in the average hardness from ~7 to ~8 GPa and a corresponding increment in the reduced modulus from 127 to 148 GPa.

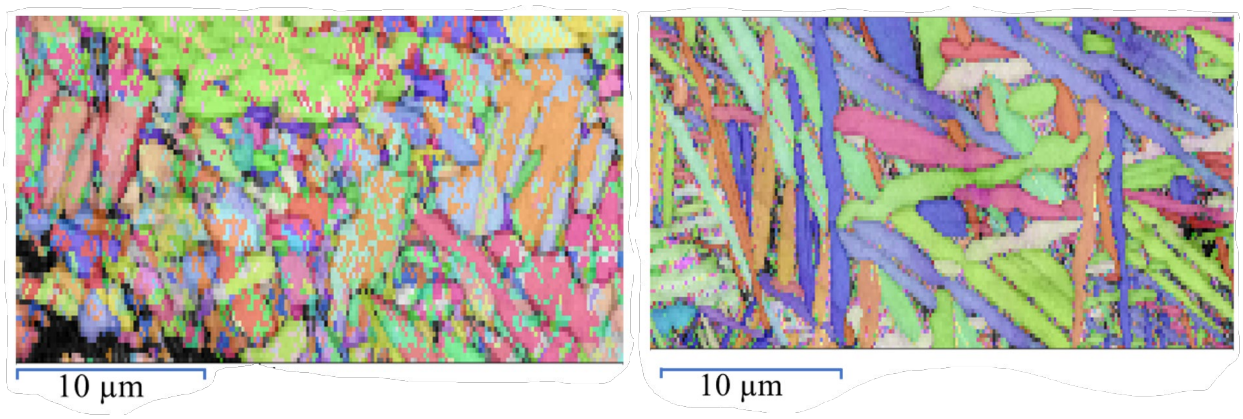

Figure 2: Recrystallization of ZrTi of alloy from (left) initial to (b) EWF annealed at 120 °C.

The FeCrAl processing study investigates low temperature recrystallization of very high density dislocation network (80% low-angle grain boundaries). At average temperature of 100 °C, the specimen could be effectively annealed in 1 min at a current density of 3300 A/mm^2. In comparison, conventional thermal annealing requires at least 750 °C and 1.5 h. For specimens with 50% thickness reduction (85% low-angle grain boundaries), the electron wind force was again unable to anneal the defects even at 3300 A/mm^2 current density and average temperature of 100 °C. Intriguingly, allowing average concurrent temperature of 200 °C eliminated almost all the low-angle grain boundaries at a current density of 700 A/mm^2, even lower than that required for the 25% thickness reduced specimens.

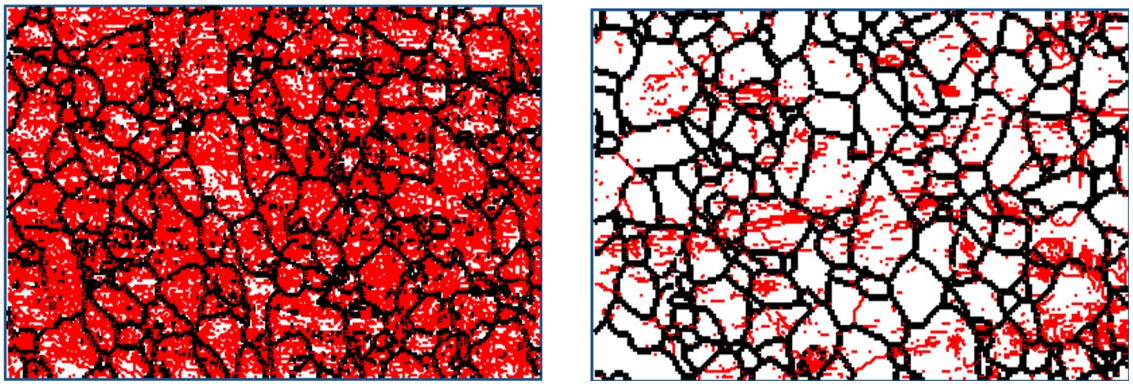

Figure 3. Grain boundaries for (left) initial cold rolled and (right) EWF annealed 96.5°C; Red color indicates low angle grain boundaries-LAGBs ($2° \leq \theta \leq 10°$). Conventional annealing takes 750°C for about 1.5 hours.

4. Acknowledgements

The research presented in this paper has received funding from the US Army Research Office through award #W911NF-23-1-0359.

RESIDUAL STRESS CROWDING EFFECTS ON WIDE BANDGAP ELECTRONICS RELIABILITY

N. Al-Mamun[1], M. Rahman[1], C. Chavda[1], M. Munshi[1], A. Haque[1], D. Wolfe[2], F. Ren[3] and S. Pearton[4]

1 Dept of Mechanical Engineering, Penn State University, University Park, PA
2 Dept of Materials Science & Engineering, Penn State University, University Park, PA
3 Dept of Chemical Engineering, University of Florida, Gainesville, FL
4 Dept of Material Science and Engineering, University of Florida, Gainesville, FL

1. Introduction

Crowding of electric field and temperature dictates reliability of electronics. Abruptness in geometry or materials dissimilarity concentrates the field, becoming birthplace for degradation. Decades of research has mitigated crowding effects, but the gap between predicted and actual reliability in harsh environments persists for wide bandgap devices. Residual mechanical stress has also been studied for decades. Residual stress is 'built-in' due to lattice and thermal mismatch, even before any biasing. It has been mostly ignored because it is small (200-500 mega-Pascals) for silicon technology. Our core hypothesis is that residual stress crowding drives the gap between predicted and actual reliability of wide bandgap devices. Very high elastic modulus and thermal expansion of WBG materials amplify mismatch stress to develop extreme crowding effect. It can exceed 3000 mega-Pascals in GaN high electron mobility transistors (HEMT), dwarfing thermal or inverse piezoelectric stresses. We propose to account for the residual stress crowding and demonstrate enhanced reliability of WBG devices. We also propose a novel room temperature annealing process to reduce (or reverse) residual and operational stress or degradation in WBG devices in few seconds.

2. Materials and methods

The present study dealt with wide bandgap SiC and GaN transistors and diodes. The specimens were tested in pristine and irradiated (heavy ion, gamma and proton) conditions. Residual stress mapping was performed with both high resolution Synchrotron and transmission electron microscopy TEM).

3. Results and conclusions

Figure 1a shows the Synchrotron and Figure 1b the TEM results for a pristine and a degraded GaN HEMT. A unique aspect of residual stress crowding is its manifestation across length-scales. We see extremely high magnitude stresses localized in both tension (red color) and compression (blue). The atoms in these regions (shown with arrows), whether in tension or compression, are far away from the equilibrium position. This makes them more vulnerable to high temperature or radiation compared to lower stress (shown with circles). Figure 1c shows similar mapping for a degraded HEMT with proliferated defects.

Since radiation exposure can be precisely controlled, it can be exploited to study degradation parametrically. Figure 2 shows our results for GaN HEMTs first degraded by $5x10^6$ rad at $60x10^3$ rad/hr. dose rate of gamma radiation and then rejuvenated using electron wind force (EWF). The threshold voltage and transconductance are shown, but all other properties deteriorated by the radiation. EWF annealing could completely reverse the damage as all these properties recovered to the pristine level. More importantly, 95% of the rejuvenation was completed in the first second of pulsing, suggesting the ultrafast nature of the process.

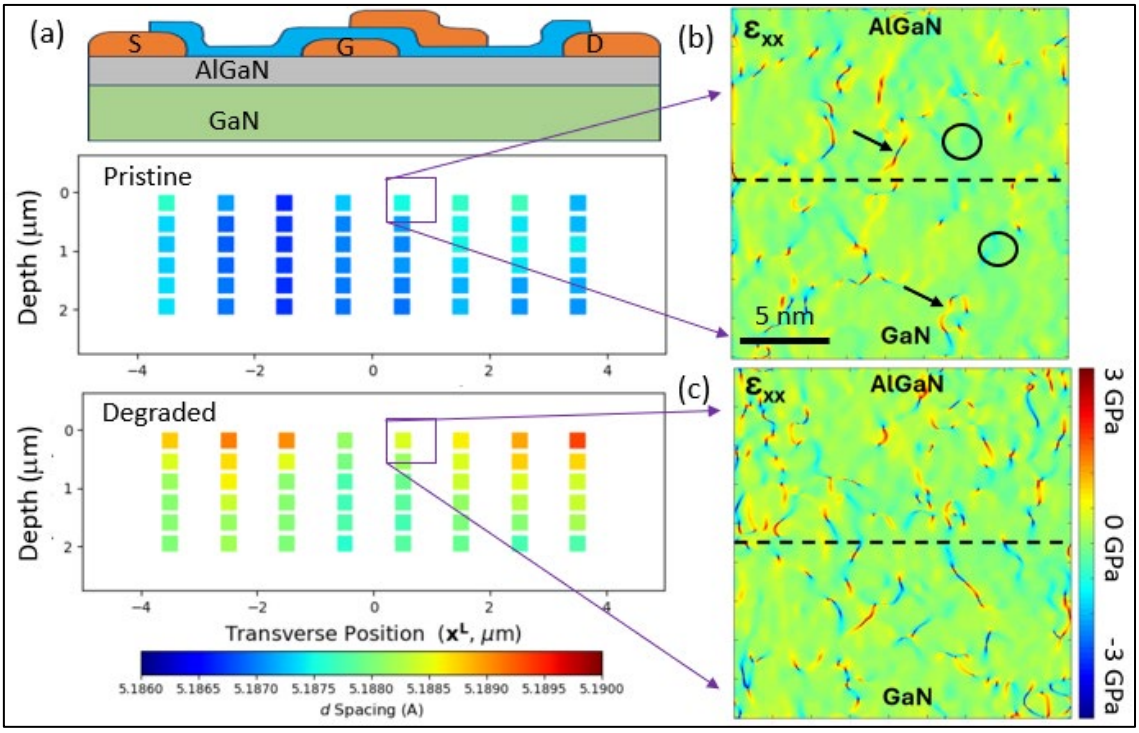

Figure 1. (a) Synchrotron stress mapping of pristine and electrically stressed GaN HEMT (b, c) High resolution stress mapping with geometric phase analysis of electron diffraction data.

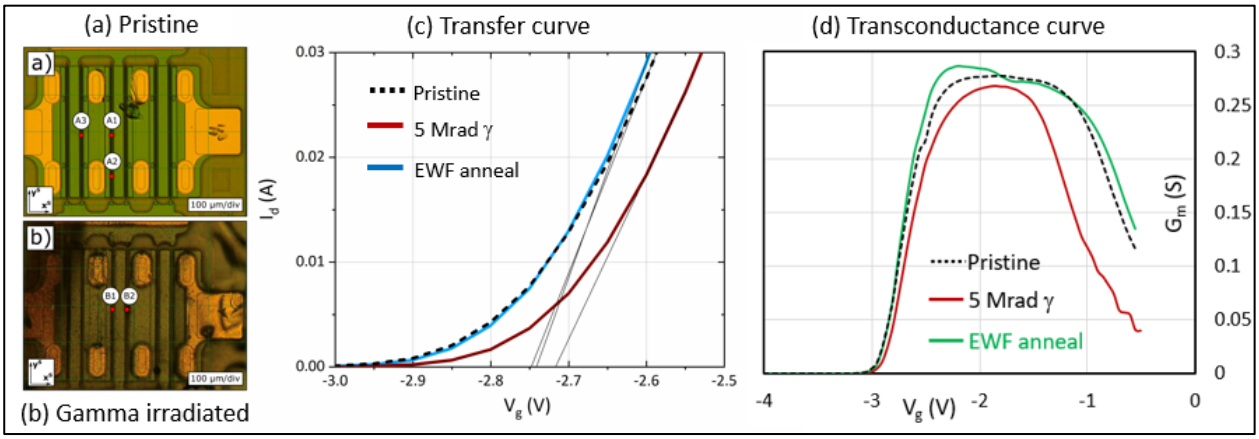

Figure 2. (a) Pristine GaN HEMT (b) after 5 Mega-rad gamma radiation (c) transfer function and (d) transconductance curve for before and after radiation damage and EWF annealing.

We also studied feasibility of preventive maintenance in electronics, which are replaced when aged or degraded. With a novel ultrafast and room temperature annealing, we rejuvenated transistors or diodes in 1 second and without heating. This may benefit safety-critical power electronics applications where the device density is not as high as integrated circuits. Our study involved SiC MOSFET which survived 10 MRad gamma radiation dose with our preemptive annealing.

4. Acknowledgements

The research presented in this paper has received funding from the Defense Threat Reduction Agency (DTRA) as part of the Interaction of Ionizing Radiation with Matter University Research Alliance (IIRM-URA) under contract number HDTRA1-20-2-0002.

EXPERIMENTALLY VALIDATED FRACTURE OF METASTABLE MATERIALS AT EXTREMELY LOW TEMPERATURES

***B. Skoczeń*[1,2]**
[1] *Research Center – Laboratory of Extremely Low Temperatures, Cracow University of Technology*
[2] *Department of Applied Mechanics and Biomechanics, Faculty of Mechanical Engineering, Cracow University of Technology, Cracow, Poland*

1. Introduction

Fracture is one of the key issues for metastable materials operating at extremely low temperatures. A broad class of these materials, in particular the stainless steels, show evidence of ductile fracture. The stainless steels exhibit at low temperatures two distinct phenomena: the intermittent plastic flow [2] and the plastic strain induced fcc-bcc phase transformation [1]. As the classical models of fracture do not include the phase transformation, a new model including the stress and the strain fields as well as the plastic strain induced phase transformation in the vicinity of the crack tip, is developed. Thus, a solution comprising distribution of the secondary phase near the crack tip is presented. Moreover, the effect of the intermittent plastic flow on fracture in two-phase continuum is highlighted. The numerical solution is cross checked with the experimental data obtained in liquid helium (4.2 K).

Another key issue at temperatures close to absolute zero is the lattice thermodynamics. When approaching absolute zero, the thermal conductivity, the thermal contraction coefficient as well as the specific heat tend to zero, which is consistent with the third law of thermodynamics. The heat transport in the lattice is based on two fundamental mechanisms: the phonon mechanism and the free electrons. As the specific heat tends to zero with temperature, the derivative of temperature w.r.t. heat (dT/dQ) tends to infinity. Thus, any small dissipation of energy in the lattice produces near absolute zero a significant increase of temperature. Such effect is called the thermodynamic instability.

2. Phenomena in metastable materials at temperatures close to absolute zero

Intermittent plastic flow (IPF) represents oscillatory mode of plastic deformation [2] that occurs below a critical temperature: T_0 for the materials with high stacking fault energy (HSFE) and T_1 for the materials with low stacking fault energy (LSFE). This phenomenon is strongly related to the thermodynamic instability of crystal lattice at the temperatures close to absolute zero. Until now, the mechanism of the intermittent plastic flow has been explained on the basis of the production of lattice barriers in the weakly excited lattice. As the edge dislocations show a tendency to pile up on the lattice barriers, and the amount of thermal energy stored in the lattice is not sufficient to catalyze the process of climbing over the obstacles or the cross-slip, the dislocation pile-ups become sessile. Moreover, as soon as the resolved shear stress at the head of dislocation pile-up reaches the level of the cohesive strength, the barriers are broken and the liberated dislocations may freely glide in the lattice. This is observed in the form of drop of stress at a constant total strain.

Plastic flow in the metastable materials (stainless steels) at extremely low temperatures is usually accompanied by a dynamic evolution of the microstructure, resulting from the plastic strain induced fcc-bcc phase transformation [1]. In the course of the phase transformation, the parent fcc phase (γ-

austenite) is transformed into the secondary bcc phase (α'-martensite) forming a two-phase continuum. The martensite platelets, embedded in the austenitic matrix, affect the surrounding fcc lattice and induce local distortions. Therefore, the plastic strain induced fcc-bcc phase transformation results in a significant evolution of the material properties and strong nonlinear hardening. The classical sigmoidal curve representing the volume fraction of secondary phase is valid for a wide range of temperatures, however, at extremely low temperatures the phase transformation rate is very high, therefore a simplified, linearized kinetics can be applied.

3. Fracture at extremely low temperatures

In order to analyze fracture, several models are available: the Griffith model based on the elastic approach, the Irwin model comprising the elastic-plastic response in front of the crack tip, as well as the Dugdale cohesive zone model, also of elastic-plastic nature. The major problem of the Irwin model consists in the fact, that it is based on the elastic - perfectly plastic approach, and constant yield stress is assumed inside the plastic zone. A realistic approach entails the need to take into account the hardening. There is however no closed form analytical solution, based on the plastic flow theory, that takes the hardening of the material into account. Hutchinson solved the problem of hardening by means of the Hencky-Ilyushin deformation theory, including its linear form. An extrapolation of the Hutchinson model to the version including the phase transformation is developed by means of the tangent stiffness obtained from the constitutive model. The derived distribution of the amount of secondary phase in front of the crack tip was compared with the experimental data (Fig. 1), obtained by means of the magnetometric methods, applied to the surrounding of the crack tip in a compact specimens loaded in liquid helium (4.2 K). Also, the effect of the intermittent plastic flow on the macrocrack propagation is shown [2]. Finally, the evolution of the microstructure along the macrocrack trajectory and in the vicinity of the crack tip is demonstrated [1].

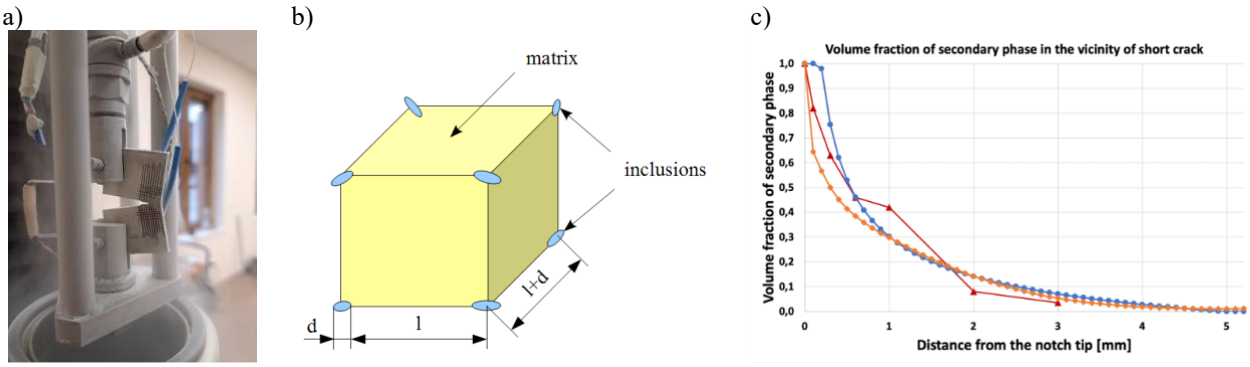

Fig. 1. Fracture of metastable materials in liquid helium (4.2 K): experiment vs analytical model

4. Acknowledgements

The research has been supported by the project of the National Science Centre (NCN), Poland: UMO-2021/41/B/ST8/01284.

5. References

[1] K. Nalepka, B. Skoczeń, R. Schmidt, M. Ciepielowska, E. Schmidt, R. Chulist (2023). Microstructure evolution in the context of fracture in austenitic steels under complex loads at cryogenic temperatures. *Materials Characterization*, **197**: 112654.

[2] K. Nalepka, B. Skoczeń, R. Schmidt, W. Zwolinska-Faryj, E. Schmidt, R. Chulist (2024). Physical mechanism of the intermittent plastic flow at extremely low temperatures. *Int. J. Plast.*, **177**: 103994.

ELECTROMECHANICAL CHARACTERIZATION OF ORTHOTROPIC MECHANICAL PROPERTIES IN PIEZOELECTRIC PVDF FILMS USING 3D DIGITAL IMAGE CORRELATION

R. Elhajjar, O. Schneider, and D. Schlitz
College of Engineering & Applied Science, University of Wisconsin-Milwaukee, USA

1. Introduction

Polyvinylidene fluoride (PVDF) films, when subjected to mechanical stretching at elevated temperatures under applied electric fields, develop remarkable piezoelectric properties that make them invaluable for sensing and actuation applications. Recent advances in micromachining techniques have enabled the fabrication of complex metamaterial structures from these films, which can achieve high strains and motion control. However, the inherent orthotropic nature of poled PVDF films, resulting from the manufacturing process, presents unique challenges in predicting and optimizing their performance in such applications. PVDF polymer piezoelectric materials offer distinct advantages over their ceramic counterparts, particularly in applications requiring flexibility and biocompatibility. Their lower density and superior mechanical flexibility allow them to withstand significantly higher strains without failure, making them ideal for dynamic applications. PVDF polymers can be quickly processed and shaped into complex geometries through standard manufacturing techniques, offering a cost-effective alternative to ceramics. However, careful design is needed to overcome the trade-offs. PVDF materials exhibit lower piezoelectric coefficients than ceramics, reducing electromechanical coupling efficiency. They also have limited operating temperature ranges and orthotropic stiffness values.

2. Materials and methods

This study investigates poled PVDF piezoelectric film mechanical and electromechanical response through a novel combination of measurement techniques. We employ three-dimensional Digital Image Correlation (3D DIC) to capture the full-field deformation response of the material under various loading conditions. This non-contact optical technique enables precise measurement of both in-plane and out-of-plane displacements and strains, providing unprecedented insight into the material's behavior. The specimens were prepared with a speckle pattern optimized for DIC tracking, ensuring high-quality displacement and strain measurements across the entire gauge length. Force measurements were conducted using a high-precision load cell with temperature compensation, allowing for accurate stress-strain relationships across different loading angles relative to the film's stretch direction. The testing apparatus was designed to maintain precise alignment and minimize parasitic loads or moments during testing. Load data was synchronized with the DIC measurements through a custom data acquisition system, enabling direct correlation between applied forces and resulting deformations.

Mechanical characterization encompasses tensile testing at angles ranging from 0° to 90° relative to the machine direction, with particular attention paid to the transition regions where property variations are most pronounced. The 3D DIC measurements reveal complex deformation patterns, including out-of-plane warping and localized strain concentrations that would be impossible to detect

with conventional strain measurement techniques. This detailed strain field analysis provides crucial insights into the failure mechanisms and their dependence on loading orientation. We measured the three primary in-plane piezoelectric strain coefficients (d_{31}, d_{32}, and d_{36}) using custom-designed electrode configurations and precise voltage control to complete the material characterization. The piezoelectric response was simultaneously monitored using the 3D DIC system, allowing for direct observation of the coupling between electrical stimulation and mechanical deformation. This approach provides a more complete understanding of the electromechanical coupling mechanisms than previously available.

3. Results and conclusions

The experimental results are compared with theoretical predictions based on classical lamination theory and off-axis transformation equations. Special attention is paid to validating these analytical models in predicting the global response and local deformation patterns observed through DIC. Testing single-element metamaterial structures fabricated from poled PVDF using 3D DIC provided crucial insights into their deformation mechanics and electromechanical coupling behavior (Figure 1). The 3D DIC measurements reveal complex out-of-plane motions and strain localizations that traditional point measurements would miss, particularly at geometric features and material transitions within the metamaterial element. These measurements enable the validation of finite element models and provide a detailed understanding of how the orthotropic properties of the base PVDF film influence the metamaterial element's performance. The full-field strain data also helps identify potential failure modes and optimal geometric configurations by highlighting areas of strain concentration and mechanical instabilities. The full-field measurements provide a detailed understanding of strain concentrations and electromechanical coupling behavior, which is essential for designing efficient metamaterial structures that exploit PVDF's unique flexibility and piezoelectric properties.

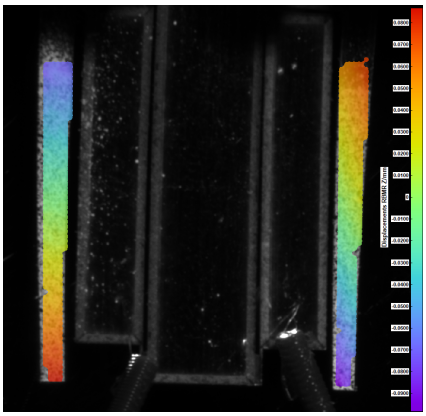

Fig. 1. Deformation at high voltage in a single metamaterial unit made from poled PVDF film

4. Acknowledgements

The research presented in this paper has received funding from the University of Wisconsin-Milwaukee Discovery and Innovation Grant (DIG) Program

5. References

[1] G. D. Jones et al. (2005). Characterization, performance, and optimization of PVDF as a piezoelectric film for advanced space mirror concepts (No. SAND2005-6846). Sandia National Laboratories (SNL), Albuquerque, NM, and Livermore, CA (United States).

[2] A.M. Vinogradov, & F. Holloway, (1997). Mechanical testing and characterization of PVDF, a thin film piezoelectric polymer. *Journal of advanced materials*, ***29*** (1).

MECHANICAL EVOLUTION AND MECHANISM ANALYSIS OF GRAPHITE ELECTRODE USING IN-SITU RAMAN SPECTROSCOPY AND XRD TECHNIQUES

Haimei Xie[1,2,3], Bin Han[1], Qian Zhang[1,2,3], and Yilan Kang[1,2,3]
[1] School of Mechanical Engineering, Tianjin University, Tianjin 300350, P.R. China
[2] Tianjin Key Laboratory of Modern Engineering Mechanics, School of Mechanical Engineering, Tianjin University, Tianjin 300350, P.R. China
[3] National Key Laboratory of Vehicle Power System, Tianjin 300350, P.R. China

1. Introduction

Understanding lithium storage mechanisms in electrode materials is crucial for the development of high-performance energy storage devices. Since the microstructure significantly affects energy storage performance, it is essential to measure the microstructural changes during lithium storage, and further analyzing how microstructures deform and correlating these changes with lithium storage performance is scientifically important for advancing high-performance electrode materials.

Research show that the electrode cycling performance of lithium-ion batteries can be modified by constraining the structural deformation, chemical doping, and structural coating. Meanwhile, researchers have employed experimental methods and simulations to study lithium storage mechanisms in electrode materials, recognizing that a deep understanding of lithium storage behavior requires insights into the microstructure and its changes during electrochemical processes. Various spectroscopic techniques have been applied to experimentally study the microstructure of electrode materials, include Raman spectroscopy, X-ray diffraction (XRD), and synchrotron radiation techniques. Song and Xie et al. employed in-situ Raman measurements to investigate the evolution of microstructural strains in graphene electrodes during lithiation-delithiation cycles, elucidating relationships among the cycling rate, microstructure, defects, layer number, deformation, and capacity[1,2]. Dominguez et al. conducted in-situ XRD to measure lattice strain evolution in crystalline germanium nanoparticles over the first three lithiation-delithiation cycles, demonstrating high reversibility[3]. In summary, the three-dimensional (i.e., interlayer and in-plane) deformation of the internal microstructure and its evolution during electrochemical processes remain poorly understood. The interactions between mechanical information, such as stress and strain, and lithium storage mechanisms require further investigation. Elucidating these interactions is crucial for optimizing electrode performance and developing advanced electrode materials.

The paper comprises in-situ experimental research on the three-dimensional deformation and microscopic lithium storage mechanisms in graphite electrodes. A comprehensive experimental approach is adopted, combining XRD and Raman spectroscopy techniques with electrochemical characterization. In-situ XRD measurements reveal multiple stages (i.e., phase transitions) and interlayer spacing changes. In-situ Raman measurements reveal the evolution of C-C bond lengths and strains within the graphite microstructure. Galvanostatic intermittent titration technique (GITT) measurements and electrochemical impedance spectroscopy (EIS) provide information on solid-state diffusion and impedance. Based on the experimental data, the evolution and interactions of the voltage potential, phase transitions, and three-dimensional microstructural deformation are analyzed. Moreover, the microscopic lithium storage mechanisms of layered graphite electrodes are discussed, providing experimental support for the development of high-performance materials.

2. In-Situ Experiments on the Microstructural Deformation

XRD is effective for obtaining structural information related to the size and spacing of layers or

nanoscale phases in crystalline materials. By measuring changes in the diffraction angle of the (002) peak for graphite, interlayer spacing parameters of the graphite lattice during lithiation and delithiation are determined using Bragg's law, expressed as follows:

$$d = \frac{n\lambda}{2\sin\theta}, \tag{1}$$

where d is the interlayer spacing, θ is the diffraction angle, λ is the wavelength of X-rays, set at 1.54059 Å, and n is the diffraction order.

Raman spectroscopy is effective for measuring the in-plane deformation of graphite. Combining the lattice dynamics equation and the theory of elasticity, the quantitative relationship between the Raman shift and in-plane strain is given by the following equation:

$$\varepsilon = -\frac{\Delta\omega}{2\omega_0\gamma}, \tag{2}$$

3. Results and conclusions

The three-dimensional strain evolution and deformation characteristics during the charge-discharge process is analyzed in detail, and the results are shown in Figure 1. The microstructural evolution of the three-dimensional strain with normalized capacity, along with potential curves and phase structure information, is presented.

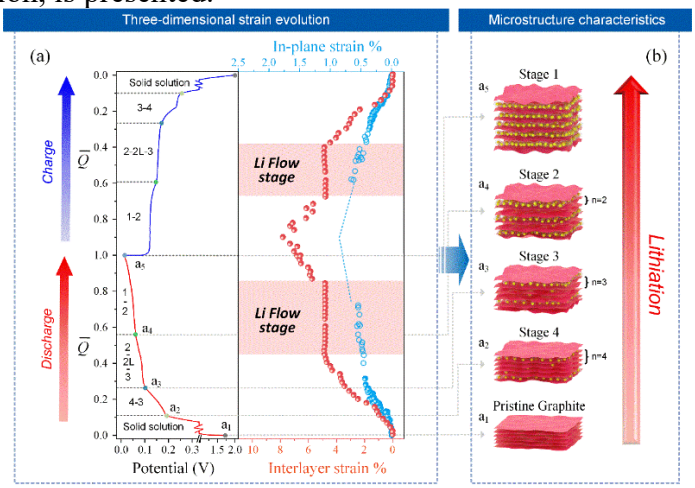

Fig. 1. Evolution of the three-dimensional microstructural strain and deformation characteristics.

4. Acknowledgements

This work was financially supported by the National Natural Science Foundation of China (grant numbers 12472183, 12041201 and 12021002)

5. References

[1] H.M. Xie, H.B. Song, J.G. Guo, Y.L. Kang, W. Yang, Q. Zhang, In Situ Measurement of Rate-Dependent Strain/Stress Evolution and Mechanism Exploration in Graphene Electrodes during Electrochemical Process, Carbon, 144 (2019) 342-350.

[2] H. Song, H. Xie, C. Xu, Y. Kang, C. Li, Q. Zhang, In Situ Measurement of Strain Evolution in the Graphene Electrode during Electrochemical Lithiation and Delithiation, The Journal of Physical Chemistry C, 123 (2019) 18861-18869.

[3] D. Zapata Dominguez, C.L. Berhaut, A. Buzlukov, M. Bardet, P. Kumar, P.-H. Jouneau, A. Desrues, A. Soloy, C. Haon, N. Herlin-Boime, S. Tardif, S. Lyonnard, S. Pouget, (De)Lithiation and Strain Mechanism in Crystalline Ge Nanoparticles, ACS Nano, 16 (2022) 9819-9829.

THERMAL STRESS MEASUREMENT OF THROUGH-GLASS VIA SUBSTRATE BY ENHANCED EXPOSURE THEORY OF PHOTOELASTICITY

Po-Yu Chen[1], Po-Chi Sung[1], Wei-Chung Wang[1], Chien-Hsun Chu[2] and Chen-Tsai Yang[2]
[1] Department of Power Mechanical Engineering, National Tsing Hua University, Hsinchu, Taiwan R.O.C.
[2] Electronic and Optoelectronic System Research Laboratories, Industrial Technology Research Institute, Hsinchu, Taiwan, R.O.C.

1. Introduction

In recent years, semiconductor packaging processes have been rapidly developed. To optimize size and enhance energy efficiency, the focus of chip design has been gradually transitioned from two-dimensional to three-dimensional integrated circuit (3D IC). Due to the excellent material properties such as low thermal expansion and high [1], glass has been applied as one of the primary materials for interposers. Through-glass via (TGV) is a technique involving electrical discharge machining, etching, and other processing procedures to fabricate the micro-scale holes through the thickness of glass substrate. Then, electrodes are plated on the inner walls of these holes to connect the circuits of different layer components on both sides of the TGV substrate. However, the TGV processing may cause higher residual stress around the hole edges. The cracks may be initiated at the locations with higher residual stresses during subsequent package processing or thermal conduction. Thus, the failure of TGV substrate may be further induced. Stress measurement of each hole of the TGV substrate is thus crucial for the semiconductor manufacturer. This study focuses on stress measurement around the hole edges under thermal conditions. Since glass is the material with low photoelastic effect, the low-level stress of glass cannot be measured by the conventional photoelastic methods accurately. Therefore, the patented measurement method enhanced exposure theory of photoelasticity (EEToP) [2] proposed by the Photomechanics Laboratory at National Tsing Hua University was employed and the full-field stress state of TGV glass substrate was successfully measured with spatial resolution of 0.65 μm under heating conditions.

2. Measurement methods

EEToP can be used to enhance the light intensity of specimens under low-level stress by extending the camera exposure time in the dark-field images in the traditional four-step phase-shifting technique (FPT). The limitation of conventional photoelastic methods on low-level stress measurement has been thus overcome. In the traditional FPT, the angles of polarizer and analyzer are rotated and four photoelastic images are captured. Two extra dark-field images with enhanced exposure are captured in EEToP. Therefore, the original FPT was modified to six-step FPT, total eight images are captured in EEToP to obtain the full-field stress state of the specimen.

In this study, EEToP was employed with a tenfold magnification of light intensity imaging setup and a heating chamber (Chain-Logic International Corporation) to form a precise optical stress measurement module with heating capability to determine the stress state of the TGV substrate.

3. Results and conclusions

The test specimen was a TGV substrate of 150 mm x 150 mm with about one thousand holes of diameter 102.1 μm prepared by both laser modification and etching by Industrial Technology Research Institute in Taiwan. The stress states of the TGV substrate at different temperatures were measured by the EEToP module. As an example, the stress measurement result at 25.5 °c is shown in Fig. 1. Obviously, there are significant residual stresses around the TGV hole. As shown in Fig. 2, the substrate stress linearly increases from 5.09 MPa to 11.33 MPa when the substrate temperature rises from 25.5 °c to 100 °c.

In the near future, the EEToP module will be used to encompass stress measurement of all holes in the TGV substrate. The measured stress results can be beneficial for the design and manufacturing of holes.

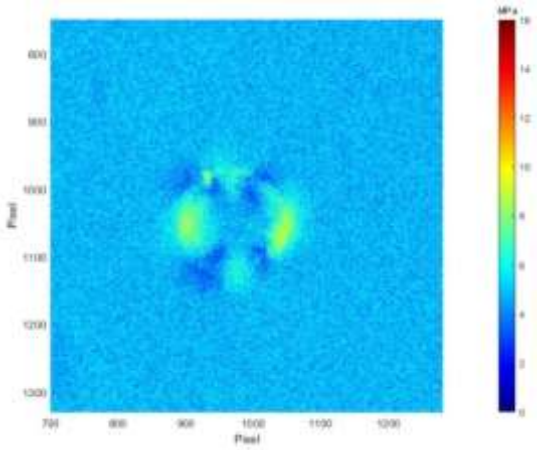

Fig. 1. The stress distribution of a hole of diameter 102.1 μm at 25.5 °c.

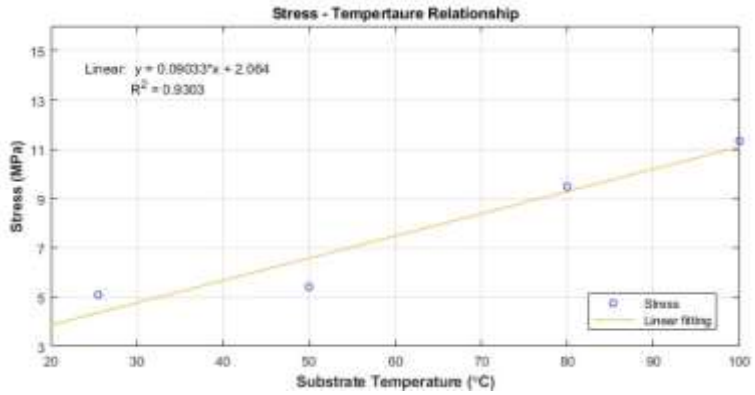

Fig. 2. The relationship between substrate stress and substrate temperature.

4. Acknowledgements

This paper was supported in part by the National Science and Technology Council (Grant no. NSTC 113-2823-8-007-004), Taiwan, Republic of China.

5. References

[1] V. Sukumaran *et al.*, "Design, Fabrication, and Characterization of Ultrathin 3-D Glass Interposers With Through-Package-Vias at Same Pitch as TSVs in Silicon," *IEEE Transactions on Components, Packaging and Manufacturing Technology,* vol. 4, no. 5, pp. 786-795, 2014, doi: 10.1109/TCPMT.2014.2303427.

[2] W. C. Wang, P. C. Sung, Z. Y. Lu, Y. L. Yeh, P. Y. Chen, "Stress Measurement Method and System for Optical Materials," United States Patent, Patent Application Number: 15/618,145, Patent Number: 10067012, Application Date: 2017/6/09, Issued Date: 2018/09/04.

FULLY BONDED FRP–CONCRETE INTERFACIAL DOUBLE SHEAR TEST METHOD AND ITS APPLICATION IN INTERFACIAL FRACTURE ENERGY

Wen Li**, **Peiyan Huang**
School of Civil Engineering and Transportation, South China University of Technology, Guangzhou 510640, China
Corresponding authors: *liiween@scut.edu.cn; **pyhuang@scut.edu.cn

1. Introduction

The bond width ratio (β) between fiber-reinforced polymer (FRP) and concrete is a critical parameter in models predicting interface behavior, including interface capacity models, fracture energy models, effective bond length models, and machine learning–based models. Experimental evidence indicates that when $\beta \geq 2/3$ (especially at $\beta = 1$) [1, 2], significant triangular spalling or concrete splitting frequently leads to failure in interfacial shear tests. This underscores the need for a straightforward and effective experimental method to evaluate FRP–concrete interfaces with large bond width ratios.

To address this, this study introduces an improved double-shear test method specifically tailored for fully bonded ($\beta = 1$) FRP–concrete interfaces [3]. The key modifications include: (1) Fastening Caps: Additional fastening caps at the free end of the concrete block to constrain axial displacement. (2) Clamping Devices: Peripheral clamping devices installed at both loaded ends and one free end of the concrete block to prevent lateral displacement and mitigate concrete splitting.

Moreover, given the limitations of existing Mode II interface fracture energy models—which are predominantly empirical or semi-empirical and exhibit significant variability in predictions [4-8]—this study also develops a new experimental method for assessing Mode II fracture energy based on energy release rate definitions. This method utilizes the enhanced double-shear test setup and specimens with varying pre-crack lengths [9].

2. Methods

2.1 Experimental Setup

The fully bonded FRP–concrete double-shear specimen and loading setup are depicted in Fig.1. Key distinctions from traditional double shear tests include:

(1) Bond Width: The width of the FRP matches the width of the concrete block.

(2) Clamping Devices: These devices are installed at both loaded ends and one free end of the concrete block.

(3) Fastening Caps: These caps are added to the free end of the concrete block to ensure successful FRP debonding from the lower concrete block.

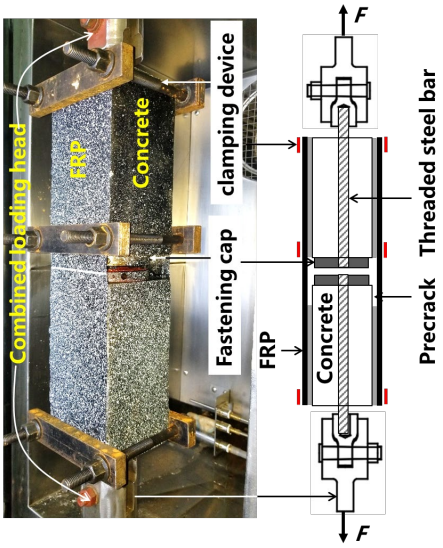

Fig.1 Loading and clamping device of double shear specimen[9]

Exploratory experiments [3] and numerical analyses [10] have confirmed the following outcomes: (1) Without Clamping Devices: The lower concrete block experiences splitting during testing. (2)Without Fastening Caps: Triangular spalling occurs in the concrete blocks.

2.2 Fracture Energy Testing

Four groups of specimens with pre-crack lengths of 0 mm, 20 mm, 40 mm, and 60 mm were prepared. Load-displacement curves were obtained through experimentation, and the fracture energy was calculated as the area difference under these curves, as shown in Fig.2.

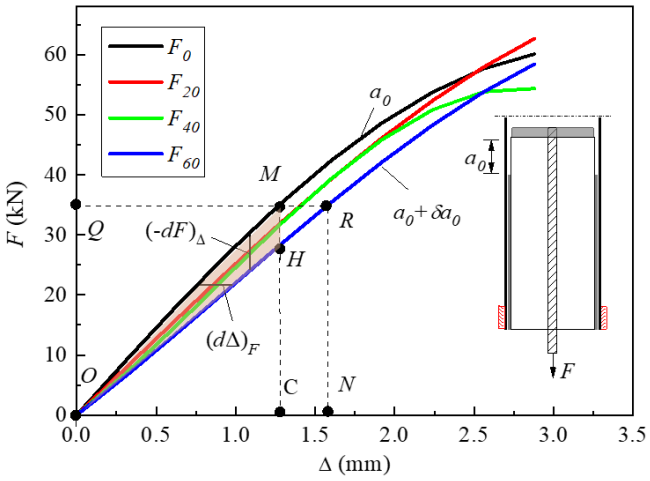

Fig.2 The fitting load-displacement curves of the specimens with different pre-crack lengths[9]

3. Results and conclusions

3.1 Test Results

One typical result for a fully bonded FRP–concrete double-shear specimen without pre-cracks is illustrated in Fig.3. The FRP debonds cleanly from the concrete block, with no occurrences of splitting or triangular spalling. Using this method, the Mode II fracture energy of the FRP–concrete interface was measured to be 1.10±0.10N/mm.

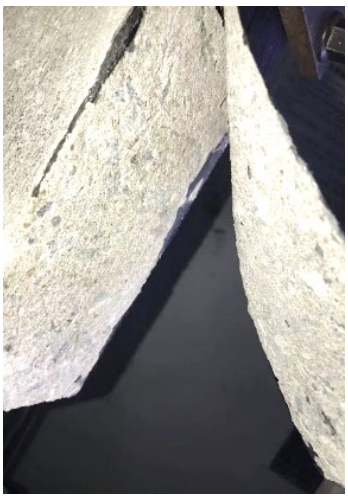

Fig.3 Failure surface of fully bonded FRP–concrete interfacial double shear test[3]

3.2 Comparison with Existing Models

Experimental results were compared to existing fracture energy models, as shown in Fig.4. notably: (1) Täljsten [11], Dai et al. [4], and Wu et al. [5]: Their predictions were closer to experimental results, with errors within 20%. (2) Neubauer et al. [6] and Lu et al. [8]: Their predictions varied significantly from experimental outcomes, with errors nearing 50%.

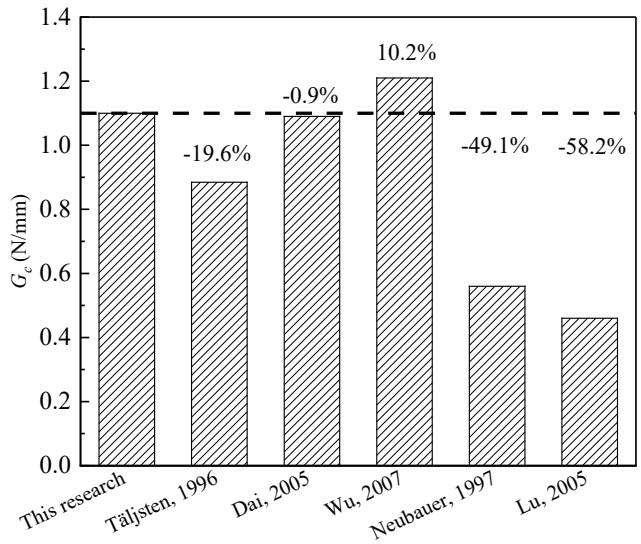

Fig.4 Comparison of the critical energy release rates calculated by different models with the testing results[9]

The primary reason for these discrepancies lies in parameter selection: Models by Neubauer et al. [6] and Lu et al. [8] depend on concrete tensile strength, which is inherently lower and less stable than compressive strength. In contrast, models by Dai et al. [4], and Wu et al. [5] are based on compressive strength, leading to more reliable predictions.

3.3 Future Work

Based on the fully bonded FRP–concrete interface double-shear test method, we have further explored the following research directions: Shear Stress Reversal Phenomenon at the Interface[12, 13] and Interface Single-Side J-Integral Method[14]. Future research will focus on examining the influence of the bond width ratio (β) on various interface behaviors, including load capacity, stiffness, fracture energy, bond-slip relationships, and effective bond length.

4. Acknowledgements

This research was supported by the National Natural Science Foundation of China [Nos: 12302240, 11627802, 51678249, 11872185].

5. References

[1] Yao J, Teng JG, Chen JF. Experimental study on FRP-to-concrete bonded joints. Composites Part B: Engineering. 2005;36(2):99-113.
[2] Ko H, Matthys S, Palmieri A, Sato Y. Development of a simplified bond stress-slip model for bonded FRP-concrete interfaces. Construction and Building Materials. 2014;68:142-57.
[3] Li W, Huang P, Chen Z, Zheng X, Yang Y, Guo X. Bond behavior of fully bonded CFRP-concrete interface with improved double shear tests. Journal of Building Engineering. 2021;43:102866.
[4] Dai J, Ueda T, Sato Y. Development of the nonlinear bond stress-slip model of fiber reinforced plastics sheet-concrete interfaces with a simple method. Journal of Composites for Construction. 2005;9(1):52-62.
[5] Wu Z, Niu H. Prediction of crack-induced debonding failure in R/C structures flexurally strengthened with externally bonded FRP composites. Doboku Gakkai Ronbunshuu E. 2007;63(4):620-39.
[6] Neubauer U, Rostasy F. Design aspects of concrete structures strengthened with externally bonded CFRP-plates. Proceedings of the seventh international conference on structural faults and repair, 8 July 1997 volume 2: concrete and composites1997.
[7] Blaschko M, Niedermeier R, Zilch K. Bond failure modes of flexural members strengthened with FRP. Second International Conference on Composites in InfrastructureNational Science Foundation1998.
[8] Lu X, Teng J, Ye L, Jiang J. Bond–slip models for FRP sheets/plates bonded to concrete. Engineering Structures. 2005;27(6):920-37.
[9] Li W, Huang P, Chen Z, Zheng X. Testing method of critical energy release rate for interfacial mode II crack. Engineering Fracture Mechanics. 2021;248:107708.
[10] Li W, Wang Y, Huang P, Li D, Zeng L, Guo X. Finite element analyses of failure of fiber reinforced polymer-concrete interface considering the concrete tension–compression softening effect. Theoretical and Applied Fracture Mechanics. 2024;131:104427.
[11] Täljsten B. Strengthening of concrete prisms using the plate-bonding technique. 1996.
[12] Li W, Huang P, Chen Z, Guo X, Wu B. The shear stress reverse phenomenon in FRP sheet–concrete interface. Construction and Building Materials. 2022;344:128192.
[13] Li W, Huang P, Chen Z, Cui H, Guo X, Wu B. Bond–slip model considering the interface shear stress reversal phenomenon and data dispersion for FRP–concrete interface. Engineering Fracture Mechanics. 2022;268:108492.
[14] Li W, Huang P, Chen Z, Yao G, Chen D. Single-side J-integral method for interfacial cracks. International Journal of Solids and Structures. 2022;241:111476.

Image Stitching Technology Based on Digital Image Correlation (DIC) for Measuring the Straightness of Long Components

.

*CHIA-HENG SUNG[1], ZI-LIANG TSENG[1], CHING-TSE CHUANG[1], TERRY YUAN-FANG CHEN[*2], MING-TZER LIN[*1]*

[1] *Graduate Institute of Precision Engineering, National Chung Hsing University, No.145 Xingda Rd., South Dist., Taichung City*
[2] *Department of Mechanical Engineering, National Cheng Kung University, No.1, University Rd., Tainan City 701, Taiwan*

1. Introduction

Many industrial manufacturing plants rely on manual visual inspection, which is inefficient and prone to errors due to worker fatigue, subjective judgment, and complex processes. Workforce changes and harsh environments further highlight the need for automated measurement technologies to enhance safety, stabilize quality, and boost efficiency. Smart manufacturing is transforming the industry, with machine vision driving automation. For example, Rao et al. [1] used machine vision to detect defects in steel processing, improving quality control by integrating material properties and process data. Similarly, Kamble et al. [2] developed automated optical systems for wire harness inspection. Residual stresses during manufacturing often cause deformation, such as warping or bending [3]. Traditional manual straightness inspection is time-consuming and imprecise. Automated detection can quantify defects, enabling efficient correction and enhanced quality control, applicable to timber [4], steel pipes [5], and T-beams [6].

2. Materials and methods

A systematic approach is required to achieve accurate image stitching using Digital Image Correlation (DIC), involving preparation, image preprocessing, DIC analysis, and alignment and validation. First, camera calibration is necessary to reduce lens distortion and ensure the accuracy of geometric transformations. Since the metal surface of the object already features a randomly speckled pattern, it is sufficient to facilitate correlation analysis. DIC analysis is then performed to calculate pixel displacements in the overlapping regions of adjacent images. The resulting displacement field determines the geometric transformation parameters required for alignment, including translation, rotation, and scaling. Once these parameters are established, the images are aligned and stitched into a complete image. Each image is mapped into a unified coordinate system based on the computed transformation parameters, ensuring a smooth transition between adjacent images.

3. Results and conclusions

Figure 1 shows the result of image stitching using DIC, where images from four cameras are combined to achieve a coverage of over eight meters. confounded by the experimental uncertainty. Therefore, the results were sorted out to determine a unique Table 1, which presents the results of

contour extraction and straightness calculation performed on the stitched images through image processing. The calculated straightness is compared with manual measurements.

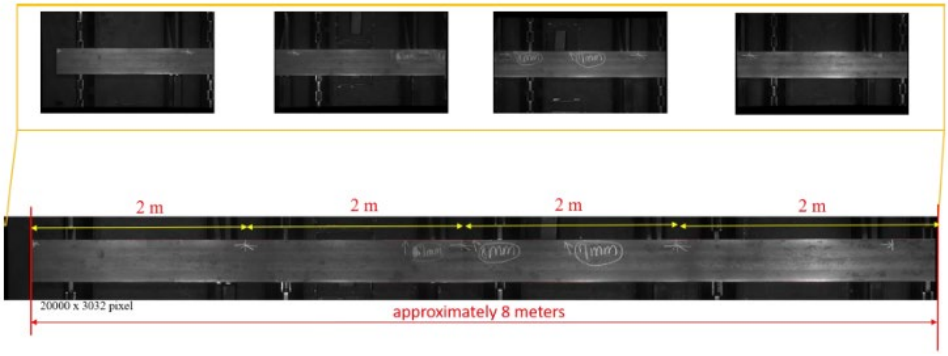

.

Fig. 1. Figure 1 shows the result of image stitching using DIC, where images from four cameras are combined to achieve a coverage of over eight meters.

	Upper edge
Manual measurement	8.0mm/ 8 m
Machine vision measurement	6.3 mm/8 m
Error	1.7 mm

Table 1. Comparison of Maximum Distortion Values for Concatenated Beam Steel Profiles

5. References

[1] [3] Changwoo Lee, C. (2018). Stresses and defects in roll products: A review of stress models and control techniques. *International Journal of Precision Engineering and Manufacturing, 19*(5), 781–789.

[2] [4] Hoang Tran, Keith Woeste, Bowen Li, Akshat Verma, & Guofan Shao. (2023). Direct measurement of timber straightness using automated image processing techniques. *Journal of Forestry Research, 34*, 1395–1405.

[3] [2] Kamble, S., & Kulkarni, A. (2021, July). Automatic Optical Inspection System for wiring harness using Computer Vision. Paper presented at the 2021 IEEE International Conference on Electronics, Computing and Communication Technologies (CONECCT), Bangalore, India.

[4] [5] Schmid-Schirling, T., Kraft, L., & Carl, D. (2021). Laser scanning-based straightness measurement of precision bright steel rods at one point. *The International Journal of Advanced Manufacturing Technology, 116*, 2511–2519.

[5] [6] Song, Y., & Yu, Z. (2013). Springback prediction in T-section beam bending process using neural networks and finite element method. *Archives of Civil and Mechanical Engineering, 13*(2), 229–241.

[6] [1] Rao, V., S., S., & Sudarsan, S. D. (2020, September). Machine Vision based Automation to Improve Process and Quality Control in Rolling Mills. Paper presented at the 2020 25th IEEE International Conference on Emerging Technologies and Factory Automation (ETFA), Vienna University of Technology.

DETERMINATION OF MULTIPLE WAVELENGTH PHOTOELASTIC CONSTANTS OF BIREFRINGENT MATERIALS BY USING A HYPERSPECTRAL CAMERA AND IMAGE ANALYSIS

Terry Yuan-Fang Chen[1], Tsai-Hsing Chang[1], and Ming-Tzer Lin[2]
[1]Department of Mechanical Engineering, National Cheng Kung University, Tainan, Taiwan, R.O.C.
[2]Graduate Institute of Precision Engineering, National Chung Hsing University, Taichung, Taiwan, R.O.C.

1. Introduction

Plastics and glass are widely used in a variety of systems, such as architecture, automobiles, and recent special applications in semiconductors, and optical systems. It is very important and indispensable for us to understand the photoelastic constant in the manufacturing process and finished products to control the quality of the final products. In photoelasticity, the similarity of stress distribution in birefringent material is often used to study the mechanical behavior of materials. Determination of material fringe value is essential for the photoelastic experiment. For most glasses, the double refraction is very weak, and it is often challenging and difficult to accurately measure it. A review of the methods for determining the photoelastic constant can be found in the literature [1].

Song et.al. [2] proposed a method called transmittance extreme photoelasticity theory (TEToP) by integrating white light photoelasticity and spectroscopy to measure stresses in low birefringence materials. Generally, various filters, spectrometers, or single-wavelength light sources are required to obtain photoelastic constants of multiple wavelengths. In digital photoelasticity, various methods to calibrate the photoelastic properties of glass have been discussed [3]. It is suggested that the use of phase shift and carrier stripe methods to accurately determine photoelastic constant in order to quickly calibrate glass specimens without residual force.

The appearance of hyperspectral cameras, which can record multiple wavelength images at one time and provide follow-up analysis. In this paper, a hyperspectral camera employed with digital image processing techniques was developed to determine the photoelastic constants of multiple wavelengths by using the four-point bending beam experiment. Test of the method on various birefringent materials was done. The measured photoelastic constant of multiple wavelengths is compared to the ones measured by using single-wavelength.

2. Materials and methods

A stressed model in a circular polariscope with the analyzer oriented at an arbitrary angle γ with respect to its dark position. The intensity of light emerging from the analyzer can be derived as,

$$I = K(1 - \cos 2\gamma \cos\Delta - \cos 2\alpha \sin 2\gamma \sin\Delta) \quad (1)$$

where K is the intensity of light, Δ is the relative retardation, and α is angle between the principal stress direction and the axis of polarizer. If $\alpha = 0$, subtraction of the two images captured at angles γ and $\gamma+90^o$, respectively, the following result can be obtained.

$$I_3 = I_{\gamma+90} - I_\gamma = K[\cos(\Delta - 2\gamma)]$$

The dark fringes occur when $\cos(\Delta - 2\gamma) = 0$, thus

$$\Delta = 2\pi m = 2\pi\left(\frac{N_3}{2} + \frac{\gamma}{\pi}\right), \quad (N_3 = 0.5,1.5,2.5 \ldots), \tag{2}$$

where m is the total fringe order. Figure 2 shows the schematic of a pure bending beam setup. In a circular polariscope, the relative retardation Δ at a point along near the central area of the beam can be related to the loading condition and geometry of bending beam as,

$$\Delta = \frac{2\pi C}{\lambda}\left(\frac{Fwy}{h^3/12}\right) = 2\pi m \tag{3}$$

where C is the photoelastic constant, λ is the wavelength, F is the applied force, w is the lever arm of the applied force, y is the distance from the neutral axis, and h is the specimen's height. As the fringe order m and the associated position y are determined, the photoelastic constant can be calculated from Eq. 3.

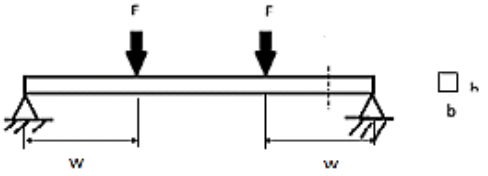

Fig. 1 Schematic of a pure bending beam setup.

The experimental system consists of a circularly polariscope and a digital imaging system with a hyperspectral camera. It operates in the VIS/NIR range (400 nm-1000 nm) with a resolution of 512 x 512 pixels. A halogen lamp is used as the light source. The test materials used are photoelastic material PSM1, Acrylic, and soda-lime glass with dimension of 100mm x 9.8mm x 3mm.

3. Results and discussion

Figure 2 shows the fringe images of wavelengths 475 nm, 545 nm and 601nm captured by the hyperspectral camera at analyzer angle γ of 0, and the fringe images of wavelengths 475 nm, 545 nm and 601nm captured by single wavelength light source and CCD camera at analyzer angle γ of 30 degrees, respectively. By subtraction of the two images captured at angles γ and γ +90°, the location of quarter-order fringe plus γ /π for each wavelength was determined by finding the minimum intensity along a line near the central area of the beam. Finally the photoelastic constant can be calculated from the Eq. 3. Figure 4-6 shows that the photoelastic constants determined in the wavelength range from 450nm to 800nm using the hyperspectral camera. Comparing to the results by using single wavelength, the difference between them is less than 3%.

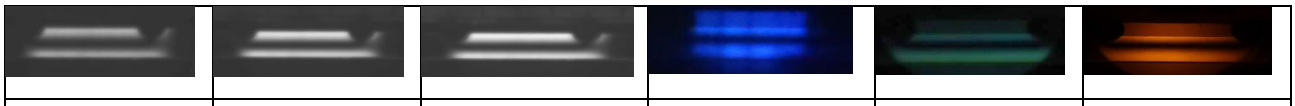

(a)475 nm, $\gamma = 0$	(b) 545nm, $\gamma = 0$	(c) 600nm, $\gamma = 0$	(d) 475 nm, $\gamma = 30$	(e) 545nm, $\gamma = 30$	(f) 600nm, $\gamma = 30$

Fig. 2 Fringe images of wavelengths (a) 475 nm, (b) 545 nm and (c) 600nm captured by the hyperspectral camera at analyzer angle γ of 0, and fringe images of wavelengths (d) 475 nm, (e) 545 nm and (f) 600nm captured with single wavelength light source and CCD camera at analyzer angle γ of 30 degrees, respectively.

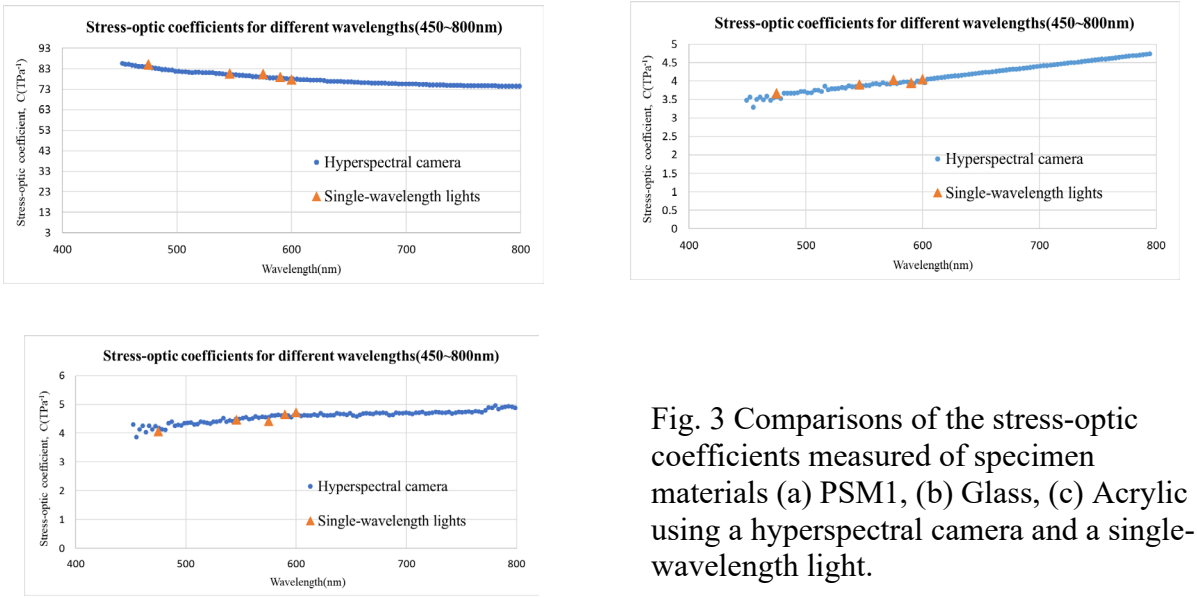

Fig. 3 Comparisons of the stress-optic coefficients measured of specimen materials (a) PSM1, (b) Glass, (c) Acrylic using a hyperspectral camera and a single-wavelength light.

4. Acknowledgements

The authors gratefully acknowledge the financial support provided to this study by the Ministry of Science and Technology of Taiwan under Grant No. MOST 111-2221-E-006-141 -.

5. References

[1] Ramesh K., V. Ramakrishnan, Digital photoelasticity of glass: A comprehensive review. Optics and Lasers in Engineering 87 (2016) 59 – 74.

[2] Sung PC, Wang WC, Chiang YA, Hung TH. Investigation of systematic relationship between spectroscopy and white light photoelasticity by regression analysis. J Strain Anal Eng Des 2015; 50(4):252 – 63. [1]

[3] Vivek R, Ramesh K.," A novel method for the evaluation of stress-optic coefficient of commercial float glass. Measurement 2016; 87:13 – 20. http://dx.doi.org/10.1016/j. measurement. 2016.03.14.

MECHANICAL PROPERTIES OF NOVEL NANO-CARBON PAPER REINFORCED CARBON FIBER COMPOSITE LAMINATES

Chin-Lung Chiang[1], Yu-Xiang Chiu[2], Ming-Yuan Shen[3,4]

[1]Department of Chemical and Materials Engineering, National Chin-Yi University of Technology, Taichung, Taiwan, R.O.C.
[2]Department of Mechanical Engineering, National Chin-Yi University of Technology, Taichung, Taiwan, R.O.C.
[3]Graduate Institute of Precision Engineering, National Chung-Hsing University, Taichung, Taiwan, R.O.C.
[4]Academy of Circular Economy, National Chung Hsing University, Nantou, Taiwan, R.O.C.

1. Introduction

Carbon atoms can be arranged in different ways to form different dimensions of nano-carbon materials, such as C60 (0D), carbon nanotubes (1D), graphene (2D), and nano-carbon aerogels (3D). Although they are all composed of carbon, their properties are very different. Figure 1 shows the different structures of nano-carbon materials.

The development of composite materials with superior mechanical properties has become a significant area of focus in material science, particularly for applications demanding high strength-to-weight ratios. Among these, carbon fiber-reinforced polymer (CFRP) composites have gained widespread attention due to their outstanding mechanical and thermal properties. However, the inherent brittleness and limited interfacial bonding between the matrix and fibers present challenges in maximizing their mechanical potential.

Recent advancements in nanomaterials, such as multi-walled carbon nanotubes (MWCNTs), graphene nanoplatelets (GNPs), and carbon aerogels, have shown promise in enhancing the performance of composite materials. These nanomaterials, characterized by high aspect ratios, exceptional strength, and unique surface properties, have been incorporated into polymer matrices to improve mechanical, thermal, and electrical characteristics. For example, MWCNTs have been demonstrated to significantly enhance tensile strength and fracture toughness when properly dispersed in epoxy matrices. Similarly, graphene nanoplatelets have shown notable improvements in thermal conductivity and flexural strength.

Despite these advantages, the integration of nanomaterials into composites is often hindered by issues such as poor dispersion, agglomeration, and limited interfacial compatibility with the matrix. Various methods, including ultrasonic dispersion, mechanical stirring, and surface functionalization, have been explored to address these challenges. While effective, these approaches are often time-consuming and complex, limiting their scalability for industrial applications.

To address these limitations, this study proposes a novel approach for the incorporation of nanomaterials into CFRP laminates. By utilizing diluted nanomaterial solutions to fabricate nano-carbon papers, which are subsequently integrated into carbon fiber prepregs, this method aims to achieve efficient reinforcement with minimal processing complexity. The primary objective is to

evaluate the effects of nano-carbon paper on the mechanical properties and synergistic enhancement of CFRP laminates, offering insights into scalable and effective reinforcement techniques.

2. Materials and methods

2.1 Materials

The materials employed in this study include unidirectional carbon fiber prepregs (T700, ECN271 TW37) supplied by Formosa Plastics Corporation, with a fiber areal weight of 100 g/m² and a resin content of 37 wt.%. The matrix material used was TPO-33X solvent-based epoxy resin (provided by YU PO CHEMICAL CO., LTD.), characterized by a viscosity of 20 – 30 MPa·s, a solid content of 60±2 wt.%, and a curing condition of 150°C for 30 minutes. Multi-walled carbon nanotubes (MWCNTs, LE-05) in a masterbatch form with a concentration of 1.5 wt.% and a density of 1.17 g/ml were provided by YSilicon Future Manufacturing Company Ltd. Regenerated carbon fiber paper (rCFP), with a fiber areal weight of 30 g/m² and a thickness of 0.18 mm, was sourced from Thermolysis Co., Ltd. Methyl ethyl ketone (MEK), used as a solvent for mixing and diluting nanomaterials with epoxy resin.

2.2 Preparation of Nano-Carbon Papers (NCPs)

Nano-carbon papers (NCPs) were prepared using a simple dispersion method using multi-walled carbon nanotubes (MWCNTs) impregnating with regenerated carbon fiber paper (rCFP). The process involved mixing MWCNTs with methyl ethyl ketone (MEK) at varying concentrations (0.1, 0.25, 0.5, and 0.75 wt.%). The solution was then uniformly sprayed onto both sides of the rCFP. After spraying, the samples were oven-dried at 80°C for 10 minutes to remove the solvent completely.

2.3 Layering Design of Nano-Carbon Papers

The prepared nano-carbon papers were incorporated into unidirectional carbon fiber prepregs (UD PPGs) at different stacking positions: middle (M), upper/lower (U/L), and upper/middle/lower (U/M/L). For 1-mm-thick CFRP, 12 layers of prepreg were used, and nano-carbon papers were inserted between specific layers: layers 6-7 for M, layers 3-4 and 9-10 for U/L, and layers 3-4, 6-7, and 9-10 for U/M/L. For 3-mm-thick CFRP, 36 layers of prepreg were stacked, and nano-carbon papers were placed between layers 18-19 for M, layers 9-10 and 27-28 for U/L, and layers 9-10, 18-19, and 27-28 for U/M/L. The layered structures were then placed in molds and processed using a hot press.

2.4 Fabrication of NCP/CFRP Laminates

The nano-carbon paper-reinforced CFRP laminates were fabricated via hot press molding. The prepared MWCNTs/rCFP/prepreg stacks were assembled in molds with perforated and non-perforated release films. The hot press process involved stepwise evacuation to incrementally increase the pressure (21, 35, 55, 70, 90, and 105 psi) with degassing at each step. Final curing was performed at 150°C for 30 minutes under the designated pressure. After curing, the molds were cooled to room temperature in a cold press. The cured laminates were removed from the molds and cut to specific dimensions using CNC machining for mechanical testing. The specimens were conditioned in a controlled temperature and humidity chamber before testing to ensure consistent results.

3. Results and conclusions

3.1 Morphology of MWCNTs and NCPs

Field Emission Scanning Electron Microscopy (FESEM) was used to analyze the morphology of the MWCNT masterbatch. As shown in **Fig. 1**, the MWCNTs exhibit a curled tubular structure with an average length of approximately 1 μm, confirming their characteristic morphology.

The attachment of MWCNTs onto regenerated carbon fiber paper (rCFP) was also examined via FESEM for varying MWCNT concentrations (0.1, 0.25, 0.5, and 0.75 wt.%). **Fig. 2** illustrates the fiber surface at a magnification of 3000×, where an increase in MWCNT attachment density is observed with higher concentrations. The MWCNTs appear well-distributed, particularly at 0.75 wt.%, highlighting the effectiveness of the dispersion and deposition method.

3.2 Mechanical Properties of NCP/CFRP Laminates

Tensile Properties of *NCP/CFRP Laminates*

The tensile strength and Young's modulus of CFRP laminates were significantly influenced by the addition of NCP. As presented in **Fig. 3**, the neat CFRP exhibited a tensile strength of 2389.66 MPa and a modulus of 106.49 GPa. The incorporation of NCP generally led to improvements in both properties. The optimal tensile strength of 3043.14 MPa, representing a 27.35% improvement, was achieved with 0.75 wt.% NCP at the Upper/Middle/Lower (U/M/L) stacking position. Similarly, the highest Young's modulus of 147.56 GPa, an enhancement of 38.56%, was recorded at 0.5 wt.% NCP under the same stacking configuration. The results indicate a clear trend of increasing tensile performance with higher MWCNT concentrations and optimized stacking positions.

Flexural Properties of *NCP/CFRP Laminates*

The flexural properties of CFRP laminates also benefited from MWCNTs/rCFP incorporation. **Fig. 4** illustrate the flexural strength and modulus for various MWCNT concentrations and stacking positions. Neat CFRP showed a baseline flexural strength of 1228.73 MPa and a modulus of 91.22 GPa. The highest flexural strength of 1561.10 MPa, a 27.05% improvement, was observed with 0.75 wt.% NCP at the U/M/L stacking position. The maximum flexural modulus of 115.27 GPa, a 26.27% enhancement, occurred with 0.25 wt.% NCP at the same stacking configuration. These results demonstrate that the MWCNT content and stacking arrangement significantly impact flexural performance.

Interlaminar Shear Strength (ILSS)

The interlaminar shear strength (ILSS) of CFRP laminates showed marked improvement with the addition of MWCNTs/rCFP. **Fig.5** present the ILSS results, highlighting a trend of increasing shear strength with higher MWCNT content and optimized stacking positions. Neat CFRP displayed an ILSS of 69.13 MPa, while the best performance of 87.27 MPa, representing a 26.25% improvement, was achieved with 0.75 wt.% MWCNTs/rCFP at the U/M/L position. The enhanced interfacial bonding due to MWCNTs is likely responsible for this improvement.

4. Acknowledgements

The authors would like to express their appreciation to the National Science and Technology Council for financial support of this study under Grant NSTC 112-2221-E-167 -036 -MY3.

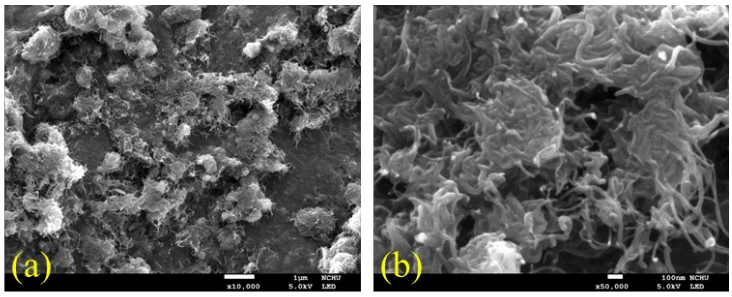

Fig. 1. SEM of MWCNTs masterbatch. (a) x10,000；(b) x50,000

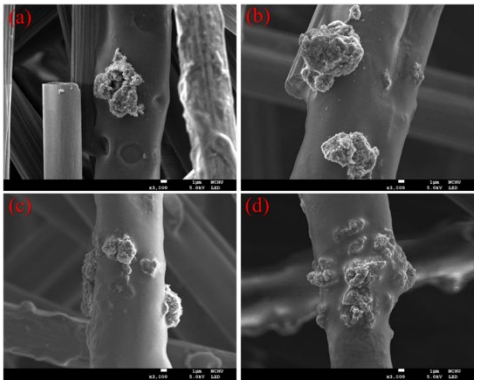

Fig. 2. SEM image of MWCNTs attached to rCFP surface. (a) 0.1 wt.%、（b）0.25 wt.%、（c）0.5 wt.%、（d）0.75 wt.%

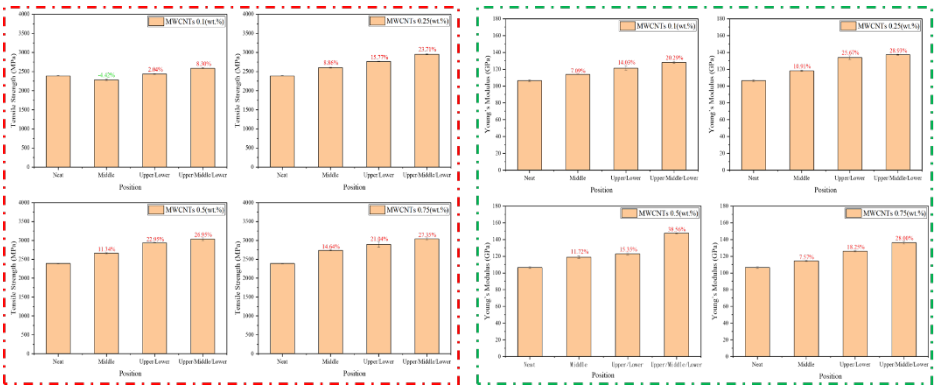

Fig. 3. Tensile properties of NCP/CFRP laminates.

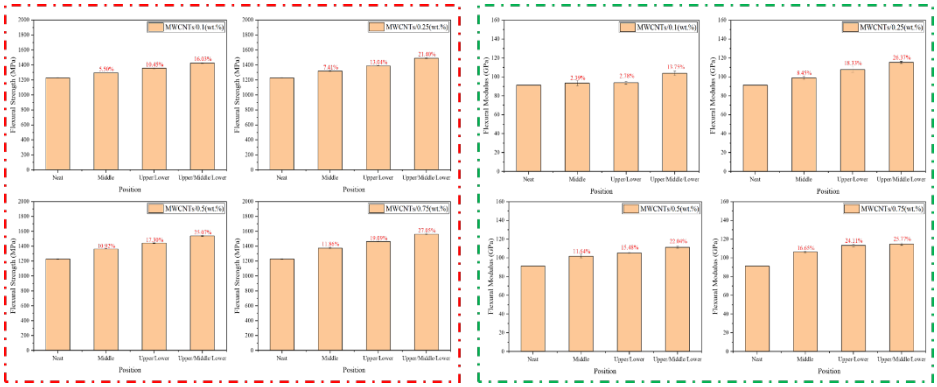

Fig. 4. Flexural properties of NCP/CFRP laminates.

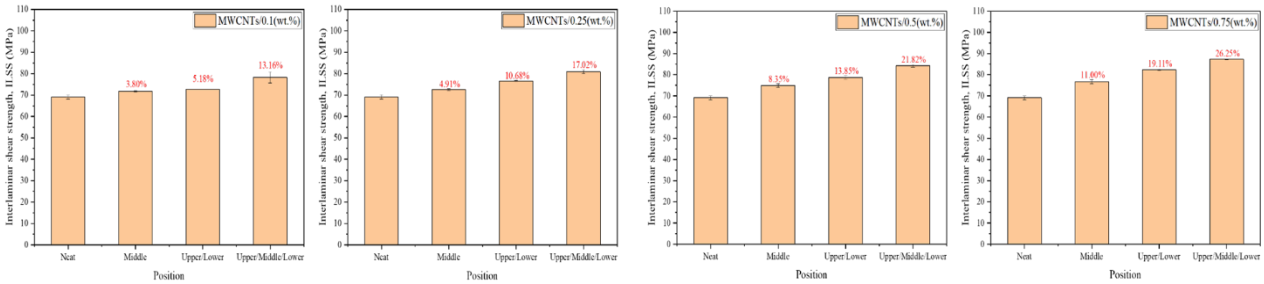

Fig. 5. ILSS of NCP/CFRP laminates.

5. References

[1] Ghosh, P. K., Kumar, K., & Chaudhary, N. (2015). Influence of ultrasonic dual mixing on thermal and tensile properties of MWCNTs-epoxy composite. Composites Part B: Engineering, 77, 139-144.

[2] Saboori, B., & Ayatollahi, M. R. (2017). Experimental fracture study of MWCNT/epoxy nanocomposites under the combined out-of-plane shear and tensile loading. Polymer Testing, 59, 193-202.

[3] Guo, J., Zhang, Q., Gao, L., Zhong, W., Sui, G., & Yang, X. (2017). Significantly improved electrical and interlaminar mechanical properties of carbon fiber laminated composites by using special carbon nanotube pre-dispersion mixture. Composites Part A: Applied Science and Manufacturing, 95, 294-303.

[4] Zheng, N., Huang, Y., Liu, H. Y., Gao, J., & Mai, Y. W. (2017). Improvement of interlaminar fracture toughness in carbon fiber/epoxy composites with carbon nanotubes/polysulfone interleaves. Composites Science and Technology, 140, 8-15.

[5] Xu, Jianwei.（2018）. Preparation and Mechanical Properties of Graphene Nanoplatelets/Epoxy Nanocomposite via Rapid Dispersion Process,Taiwan.

[6] Zhuang, ZW.（2018）.A Study on Mechanical Properties of Graphene Nanoplatelets/Glass Fiber Composite Laminates via Vacuum Assisted Resin Transfer Molding（VARTM）,Taiwan.

[7] Chiou, Y. C., Chou, H. Y., & Shen, M. Y. (2019). Effects of adding graphene nanoplatelets and nanocarbon aerogels to epoxy resins and their carbon fiber composites. Materials & Design, 178, 107869.

[8] Zarasvand, K. A., Golestanian, H., & Alasvand Zarasvand, K. (2019). Effects of arrangement and shape of MWCNT and GNP reinforcements on nanocomposite mechanical properties. Journal of Reinforced Plastics and Composites, 38(18), 846-859.

[9] Damnalı, O. F., & Eskizeybek, V. (2019). Synergistic impact of graphene and carbon nanotubes on waste paper for hybrid nanocomposite substrates. Cellulose, 26, 3935-3954.

[10] Shukla, M. K., & Sharma, K. (2019). Effect of carbon nanofillers on the mechanical and interfacial properties of epoxy based nanocomposites: A review. Polymer Science, Series A, 61, 439-460.

[11] Nguyen, S., Anthony, D. B., Qian, H., Yue, C., Singh, A., Bismarck, A., ... & Greenhalgh, E. S. (2019). Mechanical and physical performance of carbon aerogel reinforced carbon fibre hierarchical composites. Composites Science and Technology, 182, 107720.

[12] Raza, I., Hussain, M., Khan, A. N., Katzwinkel, T., & Feldhusen, J. (2021). Properties of light weight multi walled carbon nano tubes (MWCNTs) nano-composites. International Journal of Lightweight Materials and Manufacture, 4(2), 195-202.

Design and Prototyping of a High Force Density, Low-Cost Linear Electric Motor

H. Ouldhamrane[1], K. Touimi[1], Y. Achour[1] and A. Zaoui[2]
[1] Military Polytechnical School, UER- ELT, Algiers, Algeria
[2] National School of Advanced Technologies, Algiers, Algeria

1. Introduction

Linear switched reluctance motors (LSRMs) with transverse flux and EI-cores are emerging as a promising solution in the field of electromechanical systems due to their high force density, cost-effectiveness, and mechanical robustness [1]. Unlike conventional machines, these motors operate based on the principle of reluctance, which enables them to achieve high efficiency and precise control of mechanical forces, making them suitable for a wide range of industrial and commercial applications [2]. The unique design of the EI-core LSRM offers significant advantages in systems requiring high mechanical output in compact spaces. The motor's high force density, coupled with its relatively simple and cost-effective construction, makes it an ideal choice for demanding applications in automation, robotics, and transportation [3]. Despite the promising potential of these motors, their successful deployment requires a thorough understanding of their electromagnetic behavior and the precise control of the forces they generate. Simulation and modeling of the electromagnetic fields within the motor are crucial for optimizing design parameters and ensuring performance reliability [4]. To validate the performance of the EI-core LSRM, it is essential to employ advanced numerical techniques, such as 3D finite element analysis (FEA), alongside experimental testing to verify simulation results and refine motor designs for practical applications [5].

This research focuses on the comprehensive modeling, simulation, and experimental development of EI-core LSRMs with transverse flux. The goal is to deepen the understanding of their operating principles, simulate their electromagnetic behavior under various operational conditions, and validate the motor's performance through detailed experimental testing. The results will contribute to enhancing the practical application of these motors in high-performance, cost-sensitive industries, advancing their potential in precision motion control and actuation systems.

2. Design and realization of the experimental prototype

The present study focuses on the design, fabrication, and experimental validation of a linear switched reluctance motor (LSRM) with an EI-core. The design process, based on numerical simulations, defined parameters such as geometry, material selection, and component arrangement. The prototype consists of three main components: the stator, translation actuator, and winding structure, each selected to optimize performance and efficiency. Precision manufacturing ensured tight tolerances, minimizing mechanical losses. After assembly, the prototype underwent experimental tests, including inductance and force generation measurements, to validate its performance. The results were compared to simulations, confirming the design's accuracy. The developed prototype, shown in Fig. 1, demonstrates the successful implementation of the design. After the prototype was assembled, a series of experimental measurements were conducted to evaluate its performance. These tests included inductance measurements to assess the electromagnetic properties, as well as force generation tests to compare the actual force output with the theoretical predictions. The results from these tests were then analyzed and compared to the simulations to assess the accuracy of the design models.

(a) (b)

Fig. 1. Experimental prototype of the linear electrical motor

3. Results and conclusions

The developed prototype, shown in Fig. 1, was designed to evaluate the actuator's performance, generating forces along three axes: propulsion (F_x), traction (F_z), and lateral (F_y). The propulsion force (F_x) increased with current intensity, peaking at higher levels. The traction force profile, shown in Fig. 2 as a function of position for different current values, was stronger than the lateral force, which remained minimal due to the alignment of the mobile part and stator. A key challenge identified was that the high traction force could cause deviations in the mobile part, reducing the air gap and leading to friction-related mechanical issues. To address this, a rail and bearing system was added to stabilize the traction force. The experimental results validated the prototype's performance, closely matching theoretical predictions, and underscored the need for mechanical safeguards to ensure stable operation. These findings offer insights for future optimization and high-precision applications.

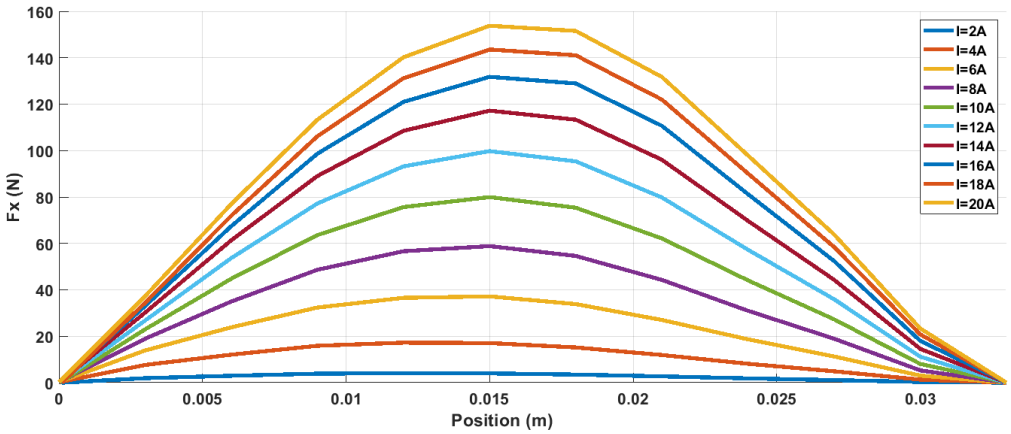

Fig. 2. Traction force as a function of position for various current values

4. References

[1] V.S. Murty, S. Jain, and A. Ojha (2023). Linear switched reluctance motor for traction propulsion system using configuration of electric locomotive, *Mechatronics*, **89**, 102916.

[2] J. Kunz, S. Cheng, Y. Duan, J.R. Mayor, R. Harley, and T. Habetler (2010). Design of a 750,000 rpm switched reluctance motor for micro machining, in 2010 IEEE Energy Conversion Congress and Exposition, *IEEE*, 3986–3992.

[3] A. Fenercioğlu and Y. Avşar (2015). Design and analysis of EI core structured transverse flux linear reluctance actuator, Turkish Journal of Electrical Engineering and Computer Sciences, 23(4), 945–955.

[4] A. Fenercioğlu (2010). Design and magnetically analysis of circular flux linear actuator, *Elektronika ir Elektrotechnika*, **101(5)**, 21–26.

[5] M. Dursun and A. Fenercioğlu (2011). Velocity control of linear switched reluctance motor for prototype elevator load, *Przeglad Elektrotechniczny*, **87(2a)**, 209–214.

Nanomechanical Sensors for Detecting Disease Early Detection

Qiubo Chen[1], Lin Zhang[1], Zihan Qiao[1], Yipeng Yang[1], Wenjie Wu[1], Chen Wang[1], Kainan Mei[1], Qingchuan Zhang[1]*, Shangquan Wu[1]*

[1] *Department of Modern Mechanics, University of Science and Technology of China, Hefei, China.*

1. Introduction

Cardiovascular disease (CVD) is the leading cause of death globally[1], with approximately 20.5 million fatalities in 2021, accounting for 32% of all deaths[2]. CVD typically presents as acute events caused by blockages that restrict blood flow to the heart or brain, significantly increasing mortality risk. Early diagnosis is crucial for effective management, which can substantially reduce cardiovascular mortality. If diagnosed early, the progression of CVD can be slowed or halted, minimizing damage to body tissues and improving patient survival and quality of life[3]. However, early diagnosis remains challenging due to the asymptomatic nature of CVD. To detect CVD biomarkers in blood samples, immunoassays like lateral flow assays (LFA) and enzyme-linked immunosorbent assays (ELISA) are commonly used[4], along with optical and electrochemical biosensors. Yet, these methods struggle with high-sensitivity detection of multiple targets in trace samples. The microcantilever biosensors is a high sensitivity and rapid response. These sensors detect target molecules through deflection caused by steric hindrance[5], but their effectiveness diminishes at low target concentrations. To address these limitations, we developed a magnetic nanomechanical sensor (MNS) that enhances sensitivity by using magnetic nanoparticles (MNP). The MNP, bound to microcantilevers via target molecules, generate magnetic forces that cause deflection, independent of sample complexity. This design allows effective detection using just a single drop of blood, achieving results in 10 minutes. Our MNS effectively combines the sensitivity of microcantilever arrays with the strong magnetic forces of MNP, enabling the simultaneous detection of multiple low-concentration targets.

2.Materials and Methods

This study proposes a method to drive microcantilever array to deflect using magnetic forces instead of intermolecular repulsive forces. The microcantilever array comprised a total of eight individual microcantilever, with four microcantilever (1, 3, 5, 7) designated as the experimental group (EG) and the other four (2, 4, 6, 8) serving as the control group (CG) (**Figure 1**). The experimental process is as follows: The immobilization of aptamer 2 onto the surface of the experimental microcantilever was achieved using a modification device (**Figure 1**).[34] Aptamer 2 is a single-stranded DNA that specifically binds to BNP. MNP has aptamer 1 on its surface, which also specifically binds to BNP. [35-36] When the target binds to both the microcantilever and the MNP, the MNP is connected to the microcantilever by a sandwich structure (**Figure 1**). In this way, MNP can be driven to deform the microcantilever by applying a magnetic field.

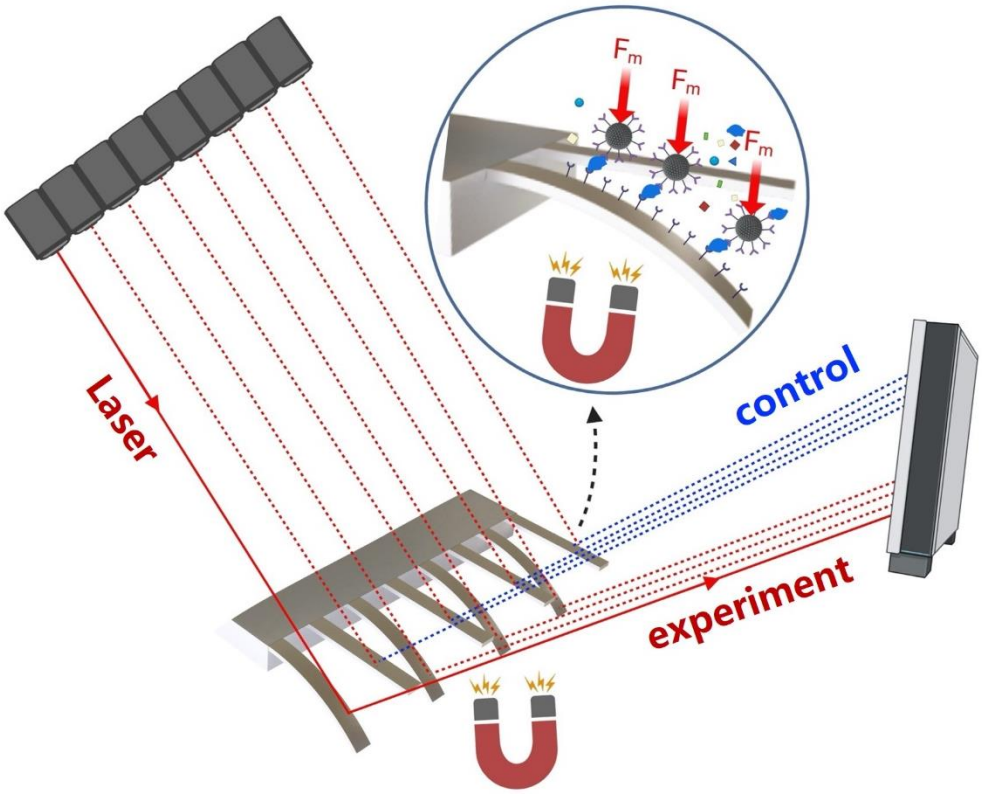

Figure 1. Schematic of magnetic force detection for CVD.

3.Result and conclusion

In this study, we have utilized MNS to achieve ultrasensitive and rapid detection of three CVD biomarkers in a single drop of blood. Due to its sensitive, selectivity and stability, MNS can also detect other molecules such as nucleic acids and ions after replacing the probe molecule. In our experiments, we found that the concentration of MNP has a great influence on the differential deflection of MNS. In addition, the position of the magnetic force also affects the detection results of MNS. This is a great inspiration for future optimization of similar mechanical biosensors. This study demonstrates the great potential for the development of magnetic-based microcantilever diagnostic tools for CVD and standard clinical practice.

4. Acknowledgements

The research presented in this paper has received funding from the National Natural Science Foundation of China (Grant Nos. 12222212 and 12072339).

5. References

[1] Yan S, Napiwocki B, Xu Y, et al. Wavy small-diameter vascular graft made of eggshell membrane and thermoplastic polyurethane[J]. Materials Science and Engineering: C, 2020, 107: 110311.

[2] Laranjo L, Lanas F, Sun M C, et al. World Heart Federation roadmap for secondary prevention of cardiovascular disease: 2023 update[J]. Global heart, 2024, 19(1).

[3] Leong, D. P., Joseph, P. G., McKee, M., Anand, S. S., Teo, K. K., Schwalm, J. D., & Yusuf, S. (2017). Reducing the global burden of cardiovascular disease, part 2: prevention and treatment of cardiovascular disease. Circulation research, 121(6), 695-710.

[4] Tang L, Yang J, Wang Y, et al. Recent advances in cardiovascular disease biosensors and monitoring technologies[J]. ACS sensors, 2023, 8(3): 956-973.

[5] G. Zhang, C. Li, S. Wu, Q. Zhang, *Sensors and Actuators B: Chemical,* **2018,** *260,* 42.

QUANTITATIVE FLOW VISUALIZATION OF TRANSONIC DIFFUSER FLOWS

H. Kodama[1], T. Yamashita[1], Nakao[1] and Y. Miyazato[1]
[1] Department of Mechanical Systems Engineering, The University of Kitakyushu, Japan

1. Introduction

In recent years, research on shock wave boundary layer interaction (SWBLI) in supersonic flow through a transonic diffuser has been actively pursued in connection with the development of next-generation supersonic transport (SST) engines. The flow field in which SWBLI occurs contains unsteady and complex shock waves, which cause vibration and noise generation in equipment and degrade engine performance [1]. Therefore, it is of great engineering and academic importance to study the unsteady properties of the SWBLI.

In many previous experimental studies, fluctuations caused by shock waves are measured by pressure sensors embedded in the wall surface. Ota et al. [2] measured shock wave oscillations in a transonic diffuser by Mach-Zehnder interferometry, high-speed laser schlieren, and pressure sensors installed flush to the wall surface of the diffuser. They concluded that the dominant frequency of the normal shock oscillation obtained from the high-speed Mach-Zehnder interferometry is in good quantitative agreement with that from the high-speed laser schlieren. In addition, the frequency of the oscillatory normal shock wave predicted from the wall pressure measurements is considerably lower compared to ones from the high-speed laser schlieren and high-speed Mach-Zehnder interferometry.

In this study, a transonic diffuser flow including oscillating shock waves is visualized quantitatively using high-speed Mach-Zehnder interferometry with the finite-fringe setting.

2. Experimental methods

Experiments were conducted in an intermittent compressible air facility. Compressed dry air from a high-pressure tank passes through a coupling and is discharged into the atmosphere through a transonic diffuser , which is fixed to a flange of the plenum chamber. The diffuser has an inlet height of 12 mm, a throat height of h^* = 4 mm, and an exit height of 8 mm, with a constant spanwise width of 10 mm from diffuser inlet to exit. The bottom wall of the diffuser is straight and the upper wall is a curve with a maximum divergence angle of 13 degrees just downstream of the throat.

The transonic diffuser was manufactured from a aluminum block using a cut-processing machine (Kitamura Machinery, Mycenter-3XG) with a positioning accuracy of ± 2 μm and a repeatability of ± 1 μ m. In the present experiment, the ratio of the plenum pressure p_{os} to back pressure p_b was adjusted by a solenoid valve to create a shock wave at a position downstream of the diffuser throat. The operating pressure ratio, p_{os}/p_b was 1.7, p_b = 101 kPa, and the ambient temperature was T_b = 298.1 K. The Reynolds number based on the height and flow properties at the diffuser throat is 5.0 $\times 10^5$.

Quantitative flow visualizations in the diffuser are performed using Mach-Zehnder interferometry with the finite-fringe setting. A He-Ne laser with a wavelength of 632.8 nm is utilized as a light source. A high-speed camera takes 3,000 interferogram images of the diffuser flow at an exposure time of

1/196,000 s (= approximately 5 μs) at 30,000 fps. The details of the method for the reconstruction of the density field are described in Yagi et al. [3].

3. Results and conclusions

An instantaneous density contour plot of a transonic diffuser flow is shown in Fig. 1 with the flow from left to right. The density fields are non-dimensionalized in terms of stagnation density ρ_{os} upstream of the diffuser, with minimum and maximum normalized densities of 0.1 and 0.8, respectively, with contours drawn every $\rho/\rho_{os} = 0.01$. A white vertical dashed line denotes the location of the throat. The spatial resolution of the present Mach-Zehnder interferometer is approximately 34 μm in the object plane, which can be evaluated based on the physical and image dimensions of the test diffuser. The origin of the coordinate system is the throat position. The x-axis is the distance downstream from the origin, and the y-axis is the vertical distance from the origin. Both axes are non-dimensionalized by a throat height of $h^* = 4$ mm.

Figure 1 shows a small normal shock at x/h^* = approximately 3 mm, which together with a large bifurcated shock on the upper wall side forms a λ-type shock. The freestream Mach number just upstream of the normal shock, which constitutes the λ-type shock, is around 1.93. On the diffuser upper wall, flow separation occurs from the foot of the leading shock of the bifurcated shock, forming a large separation region, and circular density fields caused by compression waves followed by expansion waves can be seen at x/h^* = around 4.2 and 5.3. Spectral analysis of the time-resolved density field of the diffuser flow demonstrated that the λ-shock wave oscillates back and forth in the flow direction with a standard deviation normalized by h^* of approximately 0.16 and a dominant frequency of about 50 Hz. The separation point at the foot of the leading shock also oscillates together in the same phase as the λ-shock.

In this study, the density field of a transonic diffuser flow with shock waves was captured using Mach-Zehnder interferometry with the finite fringe setting. The two-dimensional Fourier transform method was used to analyze the displacement of the interference fringes. It was shown that the complex density field of a time-resolved transonic diffuser flow, including a shock system and a large separation region, can be demonstrated quantitatively.

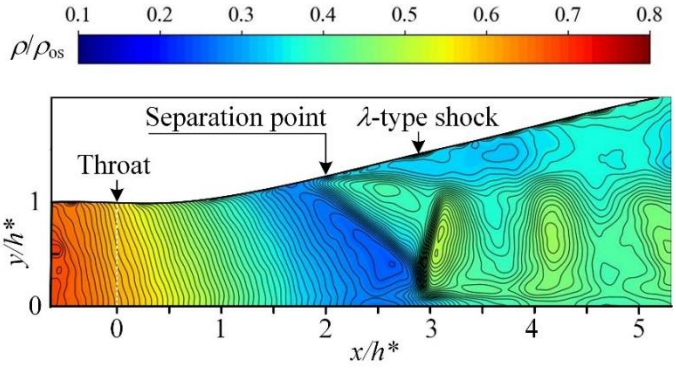

Fig. 1. Instantaneous density contour field of a transonic diffuser flow with a shock system

4. References

[1] K. Matsuo, Y. Miyazato, and H.D. Kim (1999). Shock train and pseudo-shock phenomena in internal gas flows, *Prog. Aerosp. Sci.*, **35**, 33-100.

[2] T. Ota, S. Nakao, D. Ono, and Y. Miyazato (2016). Optical measurements of shock wave oscillations in transonic diffusers by high-speed Mach-Zehnder interferometers, *AIAA Paper*, 1764.

[3] S. Yagi, S. Inoue, S. Nakao, D. Ono, and Y. Miyazato (2017).,Optical measurements of shock waves in critical nozzles at low Reynolds numbers, *J. Flow Control Meas. Visual.*, **5**, 36-50.

EVALUATION OF ULTRASHORT CREEP TESTS ON HYDRATING CEMENTITIOUS MATERIALS REQUIRES AN EVALUATION PROTOCOL ACCOUNTING FOR CREEP DURING LOAD APPLICATION

S.J. Schmid[1], L. Zelaya-Lainez[1], O. Lahayne[1], M. Peyerl[2], B. Pichler[1]
[1] Department of Civil and Environmental Engineering, TU Wien, Vienna, Austria
[2] ALAS Minerals GmbH, Ohlsdorf, Austria

1. Hourly three-minute creep testing under uniaxial compression

Hourly minute-long creep testing is well suited to provide access to the evolution of the viscoelastic properties of cementitious materials at early ages. Herein, we focus on uniaxial compression creep experiments. Each individual test probes a virtually constant microstructure, as hydration progresses minimally over a few minutes. Successive tests probe different microstructures due to the substantial advance of hydration within one hour. The tests are executed in a stress-controlled fashion. This includes load increase up to 15% of the compressive strength at the time of testing, followed by a three-minute load plateau, unloading, and a creep recovery phase. Deformations are measured using 6 displacement sensors which are evenly distributed around the specimen.

The evaluation of every minute-long creep test is aimed at quantifying the three viscoelastic properties intervening in a power-law creep function: the elastic modulus E, the creep modulus E_c, and the creep exponent β. In this context, Irfan-ul-Hassan et al. [1] introduced a two-step evaluation methodology. In step 1, the elastic modulus was refined based on the unloading modulus to avoid modeling of non-physical tensile creep strains right at the start of load application. In step 2, the creep modulus and the creep exponent were determined to minimize discrepancies between modeled and experimental strains during the load application phase and the subsequent three minutes of sustained loading. Inspired by a multiscale continuum micromechanics model for the non-aging basic creep of ordinary Portland cement (OPC) pastes by Königsberger et al. [2], Ausweger et al. [3] used a constant creep exponent of 0.25. The remaining viscoelastic properties, i.e. E and E_c, were identified in a single-step strategy, similar to the step 2 proposed in [1]. Herein, we report on a novel two-step strategy which allows for creep test evaluation without the need to make assumptions about any of the three target viscoelastic properties [4].

2. The new two-step creep test evaluation strategy

The linear theory of viscoelasticity, also referred to as Boltzmann's superposition principle, provides access to the modeled strain history ε:

$$\varepsilon(t) = \int_{-\infty}^{t} \left\{ \frac{1}{E} + \frac{1}{E_c} \left[\frac{t-\tau}{\tau_{ref}} \right]^{\beta} \right\} \frac{d\sigma}{d\tau} \, d\tau \,, \tag{1}$$

where t denotes the time, the term in the curly brackets is the power-law creep function which contains E, E_c, and β, as well as the reference time $\tau_{ref} = 1$ day, σ denotes the stress, and τ is the time variable resolving the stress history. Thus, $\frac{d\sigma}{d\tau}$ denotes the stress rate history. Introducing it as a piece-wise constant function of time [4], and solving the integral in Eq. (1) yields:

$$\varepsilon(t) = \sum_{i=1}^{4} \frac{\dot{\sigma}_i \langle t - t_i \rangle}{E} + \frac{\dot{\sigma}_i \tau_{ref}}{E_c (\beta+1)} \left[\frac{\langle t - t_i \rangle}{\tau_{ref}} \right]^{\beta+1}, \quad \text{with} \quad \langle t - t_i \rangle = \begin{cases} (t - t_i) \dots t \geq t_i \\ 0 \quad \dots t < t_i \end{cases} \tag{2}$$

where t_1, t_2, t_3, and t_4 denote the time instants at the start of (i) the load application phase, (ii) the load plateau, (iii) unloading, and (iv) the creep recovery phase, respectively. $\dot{\sigma}_1$, $\dot{\sigma}_2$, $\dot{\sigma}_3$, and $\dot{\sigma}_4$ denote the corresponding stress rates [4]. It is important to emphasize that Eq. (2) accounts for the fact that both elastic *and* time-dependent creep strains develop during the short phase of load application.

Test evaluation is aimed at quantifying E, E_c, and β such that the modeled strain history according to Eq. (2) closely matches the experimentally determined viscoelastic strain evolution. This is achieved in two steps [4]:

- **Step 1:** E_c and β are determined to ensure that the modeled strains run as parallel as possible to the experimentally determined viscoelastic strains during the three-minute load plateau. This is achieved by minimizing the root mean square deviation of the load plateau-related difference D of the modeled and experimentally determined viscoelastic strains, see Fig. 1(a).
- **Step 2:** E is quantified such that the load plateau-related average difference between modeled and experimentally determined viscoelastic strains is minimized, see Fig. 1(b).

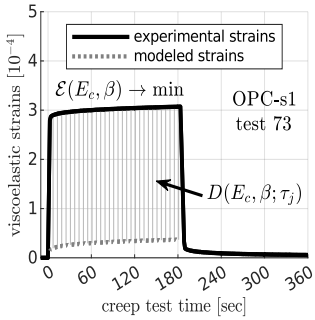

(a) Step 1: Identification of E_c and β

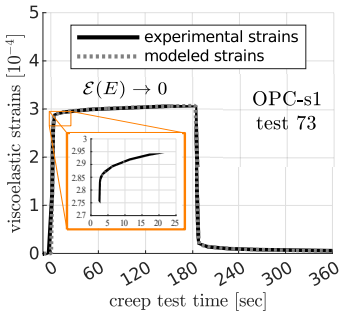

(b) Step 2: Identification of E

Fig. 1. Identification of viscoelastic properties from a test on an ordinary Portland cement paste

3. Results and Conclusions

The new two-step procedure allows for identification of viscoelastic properties from ultrashort creep tests without requiring any assumptions about the elastic modulus, the creep modulus, and the creep exponent. When performing hourly three-minute creep testing on hydrating cement pastes in the time interval from 1 to 7 days after material production, the used viscoelastic model, see Eqs. (1) and (2), clarifies that 20% to 60% of the creep deformation, which develops until the end of the three-minute load plateau, already develops during the short phase of initial load application [4]. Thus, to account for the fact that both elastic *and* time-dependent creep strains develop during fast load application is a conditio sine qua non for accurate quantification of the creep modulus and the creep exponent from a minutes-long creep test. It is also concluded that E and β are invariant with respect to different choices of the reference time τ_{ref}, while the interpretation of E_c does depend of the value assigned to τ_{ref} [4].

4. References

[1] M. Irfan-ul-Hassan, B. Pichler, R. Reihsner, C. Hellmich (2016). Elastic and creep properties of young cement paste, as determined from hourly repeated minute-long quasi-static tests. *Cement and Concrete Research*, **82**, 36–49.

[2] M. Königsberger, M. Irfan-ul Hassan, B. Pichler, C. Hellmich (2016). Downscaling based identification of nonaging power-law creep of cement hydrates. *Journal of Engineering Mechanics*, **142 (12)**, 04016106.

[3] M. Ausweger, E. Binder, O. Lahayne, R. Reihsner, G. Maier, M. Peyerl, B. Pichler (2019). Early-Age Evolution of Strength, Stiffness, and Non-Aging Creep of Concretes: Experimental Characterization and Correlation Analysis. *Materials*, **12 (207)**.

[4] S.J. Schmid, L. Zelaya, O. Lahayne, M. Peyerl, B. Pichler (2025). Hourly three-minute creep testing of an LC3 paste at early ages: Advanced test evaluation and the effects of the pozzolanic reaction on shrinkage, elastic stiffness, and creep. *Cement and Concrete Research,* **187**, 107705.

6-11 July 2025 ICEM21 Bologna
21st International Conference on EXPERIMENTAL MECHANICS

EXPERIMENTAL APROACH FOR THE ANALYSIS OF INTERNAL STRAIN MAPS ON A BOLTED CONNECTIONS USING DIGITAL IMAGE CORRELATION

A.J. Conde-Calabrús[1], L. Felipe-Sesé[1], A. Molina-Viedma[1], J.A. Almazán-Lázaro [1], E. López-Alba[2] and F.A. Diaz[2]
[1]Department Mechanical Engineering, EPS Linares, University of Jaén, Linares, Spain
[2]Department Mechanical Engineering, EPS Jaén, University of Jaén, Jaén, Spain

1. Introduction

The analysis of bolted connections is crucial in most sectors such as automotive, aerospace, construction and energy industry due to their significant impact on structural safety and performance [1]. Nowadays, different studies deal with the optimization of the bolt joint distribution, different failure mechanisms or the analysis of the loss in the tightening to ensure the reliability and safety of these structural elements [2,3]. In order to offer a new tool for those fields of research, this study proposes a new methodology for the analysis of the strain distribution inside the actual join together with the study of the interaction between applied torque, resulting preload, and friction coefficient key parameters for ensuring the reliability and durability of these connections.

Specifically, the proposed experimental approach employs Digital Image Correlation (DIC) [4] to precisely measure the strain maps induced during the tightening process. In this study, the strain distribution maps under various loading and lubrication conditions were calculated. The results were also useful to tune numerical prelaminar studies using the Finite Element Method.

2. Materials and methods

The experimental procedure in this work focused on analysing strain distribution within the mid-plane in bolted joints using the Digital Image Correlation 2D (2D-DIC) technique. This technique rely on the tracking of subsets of a speckle pattern sprayed on a flat surface to calculate displacement maps on it, from which strain maps can be also calculated. Therefore, in this work it was originally design a demonstrator of bolt joint. This joint was composed by two bolt-joined members, which, in turn, are composed of two transparent (methacrylate) elements.

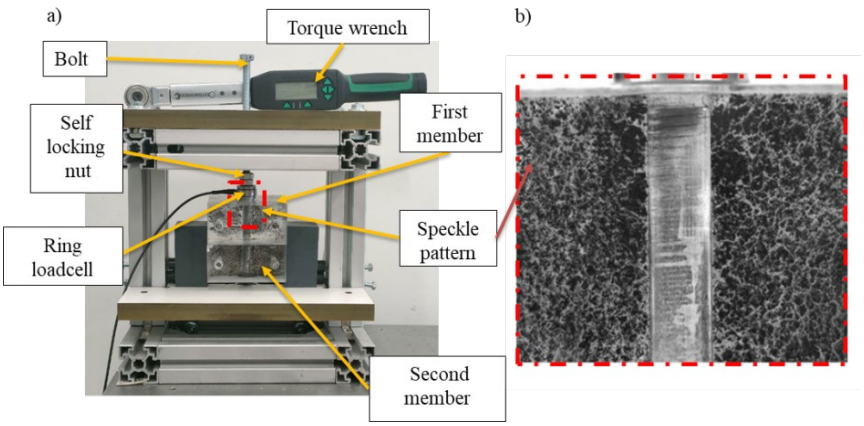

Figure 1. a) Measuring equipment. b) Digital Image Correlation 2D technique

Between these two elements, the speckle partner was applied by randomly distribute black powder (Figure 1.b) and then, both elements were glued together, leaving the speckle pattern in the middle of it. Same operation was performed with the second member of the join. Finally, a M8 hole going through both members was performed to allow a steel bolt to be used. This arrangement was placed on a frame which allows the tightening and the measurement of the torque (using a digital Stahlwille 713 torque wrench 3-60Nm) and the applied tightening force (using a HBK ring loadcell 0-60 kN) during the operation (Figure 1.a). The experimental campaign consisted of 4 tests on a unlubricated system and other 4 tests on a lubricated systems to observe differences. During the tightening, force and torque were measured. Additionally, at 4 torque steps, images of the joint's mid-plane was captured with a Allied Mako camera of 1.3 MP resolution. Images were processed using VIC 2D 7 from Correlated Solutions, Inc. to measure detailed strain maps. A FEM model was also performed using ANSYS considering the force measured by the load cell.

3. Results and conclusions

Figure 2 a) presents one graph showing the results of Torque vs Tightening load on the test on the unlubricated element. From that a friction coefficient of 0.23 was calculated [5]. In Figure 2 b), the different torque steps at which the strains measured were analysed are shown. The stiffness of the members of the joint was calculated, based on displacement, as 11.800 N/mm which shows a good agreement with the theoretical [5] value of 10.700 N/mm. As main conclusion, a novel tool for the understanding of internal behaviour was proposed, allowing further interesting research.

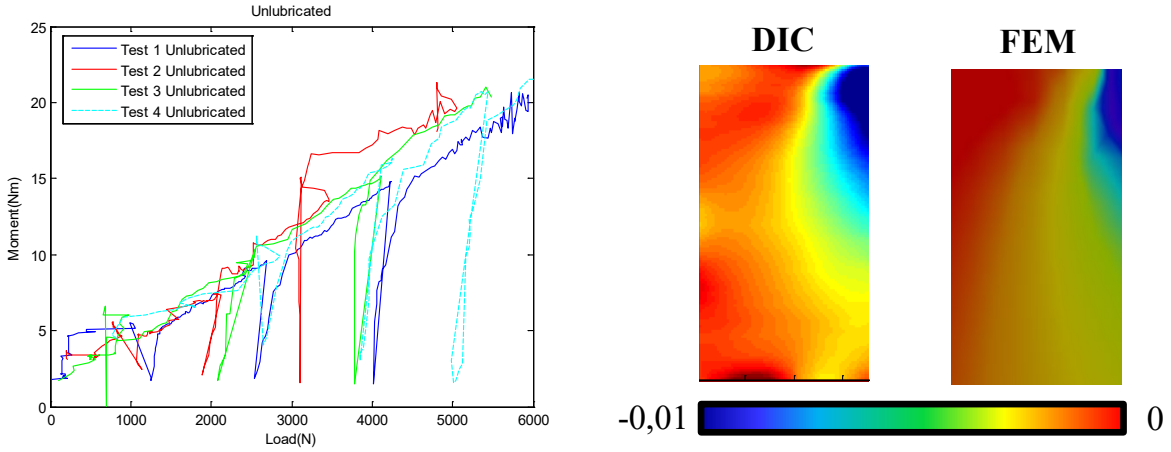

Figure 2. a) Torque vs tightening load. b) FEM and DIC ε_{yy} strains maps for 15N·m Torque.

4. Acknowledgements

This research has been funded by Ministerio de Ciencia e Innovación of the Spanish Government by the grant MCIN PID2022-141618OA-I00 "Integroptics"

5. References

[1] Croccolo, D., De Agostinis, M., Fini, S., Khan, M. Y., Mele, M., and Olmi, G., 2023, "Optimization of Bolted Joints: A Literature Review," Metals (Basel)., **13**(10), pp. 1–31.

[2] Croccolo, D., Agostinis, M. De, Fini, S., Scapecchi, C., Hassaan, M., Tariq, B., Mele, M., and Olmi, G., 2023, "Failure of Threaded Connections : A Literature Review."

[3] Pichoff, F., Kummel, M., and Schiff, M., 2018, "Dynamic Vibration Testing of Fasteners: Fastener Self-Loosening Theory, Vibration Testing Practical Applications," Mater. Tech., **106**(3).

[4] Schreier, H., Orteu, J.-J., and Sutton, M. A., 2009, *Image Correlation for Shape, Motion and Deformation Measurements*, Springer US, Boston, MA.

[5] Budynas, and Nisbett, 2006, "Shigley's Mechanical Engineering Design, Eighth Edition," Analysis, p. 1059.

6-11 July 2025 ICEM21 Bologna | 21st International Conference on EXPERIMENTAL MECHANICS

USE OF SHAPE MEMORY ALLOY FOR THERMAL STRAIN-ABSORPTION IN AEROSPACE APPLICATIONS

A.E. Berrocal-Coba [1a], M. Menegozzo [1b] , F.A. Just-Agosto [1b] , A. Cecchini-Brigi[2]
[1a] Engineering Sciences and Materials Department (CIIM); [1b] Mechanical Engineering Department (INME), University Puerto Rico-Mayaguez Campus, Mayaguez, PR, USA
[2] Mechanical Engineering Department, The University of Memphis, TN, USA

1. Introduction

Shape-Memory Alloys (SMAs) are well known for their ability to undergo large deformations and recover their original shape after unloading when the austenite-to-martensite transition temperature is reached [1]. This ability of SMAs has been used in numerous medical and aerospace applications [2]. However, the SMAs' capability for thermal strain absorption in mechanical shielding tile applications in aerospace structures has not been investigated yet. This may be potentially used in the design of a mechanical jointing device along with currently used adhesive mounting methods to increase the structural safety of hypersonic aircraft and spacecrafts during the atmospheric re-entry. In this work, the thermo-mechanical behavior of SMA NiTinol was experimentally and numerically characterized. The objective of this research is to design a joint in which a SMA NiTinol sheet is placed in the interface between two heterogeneous materials under a temperature gradient.

2. Materials and methods

NiTinol sheets manufactured by Kellogg's Research Labs, having an austenitic transformation temperature of 35°C were used. The thermomechanical response of the NiTinol was determined on test specimens according to the ASTM E8/E8M−13a standard. NiTinol specimens were tested under tension loading on an Instron testing machine with a customized furnace. Tests were conducted at a constant loading rate of 0.02 mm/s, producing an engineering strain rate of 0.03% strain/s, which is within the recommended range for quasi-static conditions (0.01-0.05% strain/sec) [3]. The thermomechanical training consisted of an austenitic isothermal process with 15 cycles at four different temperatures of 50, 60, 70 and 80°C. Figure 1 shows the stress versus strain curve corresponding to the last hysteresis cycle at each temperature.

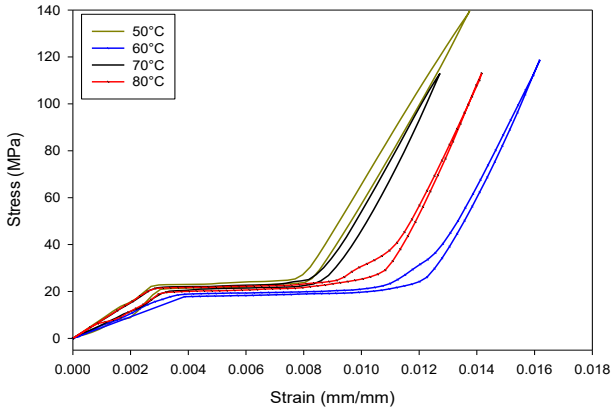

Figure 1. Stress-strain curves corresponding to the last loading cycle at different temperatures.

3. Results and conclusions

The experimental thermomechanical behavior of SMA NiTinol was used for calibration of the ANSYS Brinson's superelastic material model [4]. This allowed us to determine the different elastic properties and stress hysteresis where the transformation from austenite to martensite (critical stresses) occurs [5]. Experimental and numerical results show good correlation as shown in Figure 2.

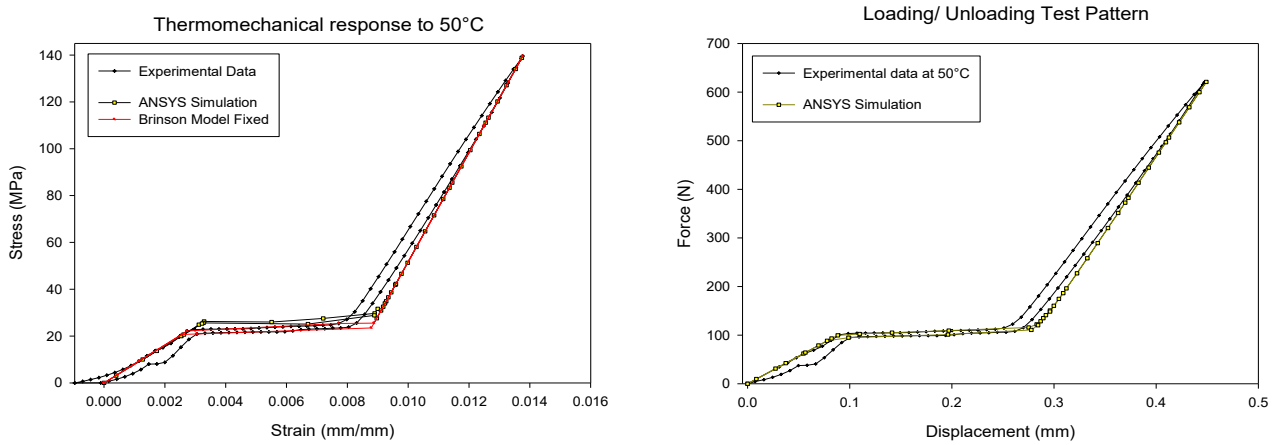

Figure 2. Comparison of experimental and numerical thermomechanical response of SMA NiTinol at 50°C.

4. Acknowledgements

The authors would like to acknowledge the support received from the Molecular Science Research Center of San Juan (US-PR), the Biodesign Institute of the Arizona State University, and the INME Department of UPRM, for the use of their facilities and equipment. We would also like to thank Dr. Oscar Marcelo Suárez (UPRM-CIIM) for his constructive conversations.

5. References

[1] P. S. Beato, G. Poologasundarampillai, A. Nommeots-Nomm, D. M. Kalaskar, 3 - Materials for 3D printing in medicine: metals, polymers, ceramics, and hydrogels, Editor(s): D. M. Kalaskar, In Woodhead Publishing Series in Biomaterials, 3D Printing in Medicine (2nd Edition), Woodhead Publishing, 2023, 59-103, ISBN 9780323898317.

[2] V. Brailovski, P. Terriault, T. Georges, D. Coutu, SMA actuators for morphing wings, Physics Procedia, Vol. 10, 2010, Pages 197-203, ISSN 1875-3892.

[3] D. C. Lagoudas, *Shape Memory Alloys: Modeling and Engineering Applications*. Springer US, 2008.

[4] T. M. Nguyễn, P. Hutapea, K. Darvish, and S. Pillapakkam, "MODELING OF THERMO-MECHANICAL BEHAVIOR OF NITINOL ACTUATOR FOR SMART NEEDLE APPLICATION", Temple University Libraries, [Philadelphia, Pennsylvania] TA - TT -, 2012.

[5] S. Miyazaki and K. Otsuka, "DEFORMATION AND TRANSITION BEHAVIOR ASSOCIATED WITH THE R-PHASE IN Ti-Ni ALLOYS.," *Metall. Trans. A, Phys. Metall. Mater. Sci.*, vol. 17 A, no. 1, pp. 53–63, 1986, doi: 10.1007/BF02644442.

EFFECT OF GEOGRID REINFORCEMNT IN THE GRANULAR CUSHION LAYER ON THE BEHAVIOUR OF DISCONNECTED PILED RAFT SYSTEM

Raut. S [1], Halder. P [2], Manna. B [1] and Shahu. J T [1]

[1] Department of Civil Engineering, Indian Institute of Technology Delhi, New Delhi, India
[2] Department of Civil Engineering, Indian Institute of Technology Jammu, J&K, India

1. Introduction

Despite the widespread use of connected piled raft (CPR) foundations in high-rise buildings [1, 2], the disconnected piled raft (DPR) has gained attention as an alternative solution to address some of the limitations inherent in CPR, particularly related to high shear and bending forces at the raft-pile connection and consequent structural failure of piles in the areas of high seismic activities [3]. In a DPR system, the piles are made structurally disconnected from the raft through a compacted granular cushion layer. The stiffness of this cushion layer serves as a key parameter regarding the load transfer process, redistribution of loads among piles, and defining the overall performance of a DPR system.

Therefore, the primary objective of the present study is to investigate the effect of cushion stiffness on the overall behavior of a vertically loaded DPR in cohesionless soil by incorporating single and multiple layers of geogrid within the granular cushion layer. The effects of this geogrid-reinforced cushion layer on load-settlement behavior of DPR, settlement efficiency, pile-raft load sharing, and pile's structural response are presented and discussed.

2. Materials and methods

Finite element-based platform PLAXIS-3D is used for numerical modelling and consequent parametric analyses of DPR as shown in Fig. 1(a). Fine Yamuna sand with a Young's modulus E_s = 10.3 MPa is used to model the bed material. The cushion beneath the raft consists of the same fine Yamuna sand, along with coarse Badarpur sand (E_c = 33 MPa) and medium crushed gravel (E_c = 60 MPa). Single and multiple layers of geogrid having an axial stiffness EA = 1100 kN/m are placed at different positions within the cushion.

After validation of the developed 3D numerical model with a published centrifuge test result [4], this study first discusses the basic differences in the responses between DPR and CPR system in cohesionless soil. Then, a systematic parametric study is carried out with different geogrid layers and their positions within the cushion layer of the DPR system. For a better understanding of the results, the response of CPR is also added here.

3. Results and conclusions

A typical variation of settlement efficiency (η) of DPRs with normalized cushion stiffness (E_c/E_s) is presented in Fig. 1(b). It can be observed that the η value increases with increasing cushion stiffness for both without and with geogrid conditions. However, after a normalized stiffness value of 3, the rate of enhancement in settlement efficiency decreases. Table 1 highlights the results regarding the effects of multiple layering of geogrid in DPR, with Badarpur sand used as the cushion material. Due to rigid structural connection between pile and raft, the CPR shows higher settlement efficiency

(63.6%) and pile load proportion (97.6%) as compared to DPR. The introduction of geogrid layers within the cushion significantly enhances its stiffness, improving the performance of DPR. A single geogrid layer increases settlement efficiency by nearly 20%, while multiple layers provide only marginal additional benefits.

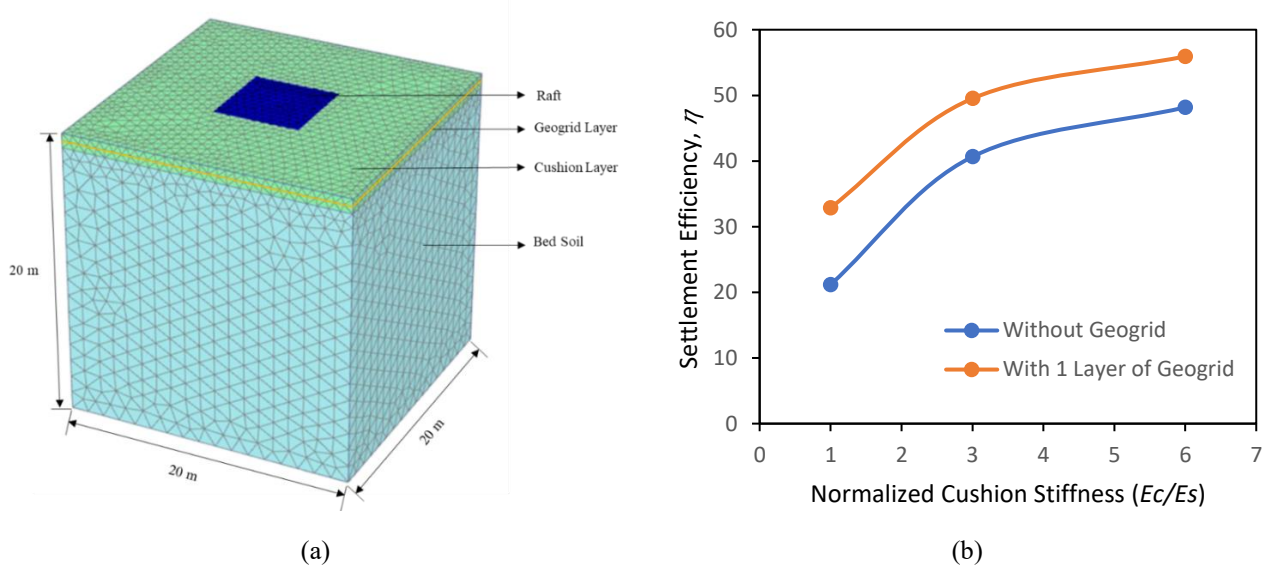

(a) (b)

Fig. 1. (a) FE model of disconnected piled raft system with geogrid layer, (b) Variation of η in DPR without and with geogrid for different cushion stiffness

Case	No. of Geogrid Layers	Settlemnt Efficiency (%)	Pile Load Proportion (%)
CPR	-	63.6	97.6
DPR	0	40.7	43.0
	1	49.0	43.8
	2	49.2	44.5
	3	49.5	45.8

Table 1. Effects of geogrid layering within the cushion on the performance of DPR

In summary, these results highlight the positive effect of geogrid reinforcement in the cushion layer, contributing to improved settlement behavior and more balanced load distribution across the piles, thereby enhancing the overall performance of the DPR system. The findings suggest that incorporating geogrid layers optimizes load transfer and improves foundation efficiency, making it a promising solution for medium to high-rise structures in cohesionless soils.

4. References

[1] Clancy P, Randolph MF. An approximate analysis procedure for piled raft foundations. Int. Journal of Numerical and Analytical Methods in Geomechanics, 1993, 17, p. 849-869.

[2] Katzenbach R, Leppla S, Choudhury D. Foundation systems for high-rise structures. CRC Press, Boca Raton, FL, 2016.

[3] Wong IH, Chang MF, Cao XD. Raft foundations with disconnected settlement reducing piles. Design application of raft foundations and ground slabs, Chap. 17, Thomas Telford, London, 2000, p. 469-486.

[4] Kumar A, Choudhury D, Katzenbach R. Effect of earthquake on combined pile–raft foundation. Int. J. Geomech. 2016;16(5):04016013.

Micromechanical Characterisation of Twinning and Detwinning during fatigue in Zirconium Using High-Resolution Electron Backscatter Diffraction and Digital Image Correlation Techniques

Weifeng Wan [a], Chaitanya Paramatmuni [b] and Xiaojun Yan [a]

[a] *School of Energy and Power Engineering, Beihang University, Beijing 100191, China*
[b] *Department of Materials Science and Engineering, The University of Sheffield, Mappin St, Sheffield, S1 3JD, United Kingdom*

1. Introduction

Zirconium is a typical HCP metal which has been widely used as claddings in nuclear industry [1]. Deformation twinning in HCP zirconium has been extensively studied. Under tensile stress along the direction of the c-axis, $\{10\bar{1}2\}<10\bar{1}1>$ twins are often activated in addition to limited activation of $\{11\bar{2}1\}<11\bar{2}\bar{6}>$ twins in HCP zirconium. On the other hand, $\{11\bar{2}2\}<11\bar{2}\bar{3}>$ twins at room temperature and $\{10\bar{1}1\}<\bar{1}012>$ twins at elevated temperature are observed under compression in the c-axis direction [2]. McCabe et al. [3] studied the deformation twinning in zirconium at low temperature (76K). They reported that for compression parallel to a primary c-axis texture prismatic slip and first generation $\{11\bar{2}2\}$ compression twinning were the dominant deformation mechanism with twinning accommodating roughly one third of the plastic strain, while for compression perpendicular to the primary c-axis texture, prismatic slip and first generation $\{10\bar{1}2\}$ tensile twinning are the dominant deformation mechanisms.

Most experimental and simulation studies to date have focused on twinning behaviour, with comparatively little attention given to detwinning in zirconium alloys. Detwinning can be treated as the reversal of twinning on a pre-twin, leading to an orientation identical to the original matrix, which is controlled by the migration of the twin boundaries [4,5]. Proust et al. [6] studied detwinning in high-purity zirconium at room temperature and liquid nitrogen temperature by using in-situ neutron diffraction technique. Their results show that detwinning of $\{10\bar{1}2\}<10\bar{1}1>$ tensile twins is favoured over the activation of a different twin variant in the parent grains. Chen et al. [7] found that the $\{10\bar{1}2\}$ tensile twins are activated during pre-compression of Zr702 plate along the rolling direction, while detwinning, instead of secondary tensile twinning, occurs when the pre-twinned sample is re-compressed along the normal direction.

In this study, a detailed microstructural characterisation on twinning and detwinning during short crack growth was conducted utilising scanning electron microscopy (SEM) and electron backscattered diffraction (EBSD) in a Zircaloy-4 with strong texture. Digital image correlation (DIC) technique has been employed to measure the strain distribution and subsequently calculate stress and stored energy density at the crack tip. This study provides a mechanistic understanding of twinning and detwinning behaviour at room temperature during fatigue short crack growth, laying the foundation for integrated investigations into the plasticity occurring locally near the crack tip.

2. Materials and methods

The Zircaloy-4 beam samples with 'blocky alpha' microstructures were subjected to force-controlled cyclic loading with a maximum force of 800 N or 850 N and a stress ratio of R = 0 using a three-point bend testing configuration. The fatigue tests were conducted using a Shimadzu universal testing machine as shown in Fig. 1(a). An edge-notch was created at the midpoint on the bottom of each beam sample using an electrical discharge machine. The schematics of the three-point bend testing configuration and the edge-notch geometry are shown in Fig. 1(b) and (c), respectively.

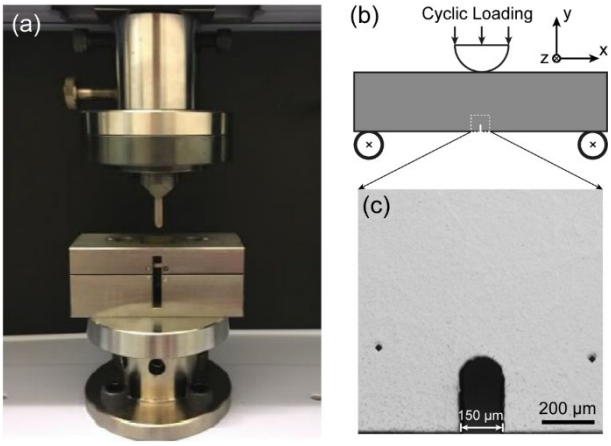

Fig. 1. Details of the experimental setup showing (a) Three-point bend testing setup; (b) schematic of cyclic loads on edge-notched beam sample; (c) optical microscope image showing the throughout edge-notch at the midpoint on the bottom of the Zircaloy-4 beam

The microstructural analyses were conducted using a Zeiss Sigma-300 scanning electron microscopy (SEM) equipped with a Bruker EBSD detector. For standard SEM imaging, graphs were captured at an accelerating voltage of 5 keV and a working distance of approximately 10 mm. In contrast, for the EBSD analysis, the SEM was operated at an accelerating voltage of 20 keV, with the sample surface tilted at 70 degrees relative to the horizontal plane. This setup allows for the determination of crystallographic orientation at each scanning point by automatically indexing the Kikuchi patterns. High-resolution EBSD technique was employed in this study to address crystallographic distortion by measuring the shift of region of interest (ROI) within the Kikuchi patterns. This technique allowed the subsequent calculation of full-field elastic strain and geometrically necessary dislocation (GND) density.

3. Results and conclusions

Fig. 2 compares SEM and EBSD results for Sample B at cycles 4000 and 4100, highlighting twinning-detwinning behaviour at a crack tip. Twins B1, B2, and B3 identified at cycle 4000 disappear by cycle 4100, indicating detwinning correlated with short crack growth. Detwinning at the crack tip is attributed to changes in stored energy density, represented by the plastic energy stored within local dislocation structures, particularly GND density. High-resolution EBSD reveals significant reductions in GND density between cycles, consistent with the disappearance of twins.

Stored energy density alone is insufficient to explain twinning-detwinning. In-situ DIC analysis of Sample B'' provides insight into stress-strain evolution during cyclic loading. Grain morphologies and crack paths (Fig. 3) indicate similarities between Samples B and B''. Plastic strain distributions (xx and yy) evolve as cracks propagate, forming wing-shaped patterns. Stress distribution near the

crack tip exhibits significant heterogeneity, transitioning between tensile and compressive states along specific paths, which may drive twinning and detwinning.

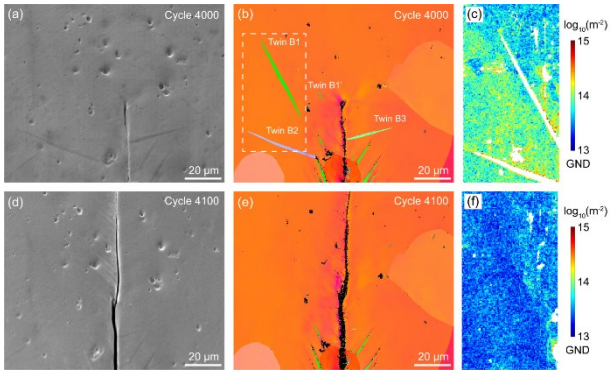

Fig. 2. The detailed analyses of twinning-detwinning in Sample B showing (a) SEM image of crack tip area at cycle 4000; (b) the corresponding IPFZ image showing twins near the crack tip; (c) GND density distribution in the selected area at cycle 4000; (d) SEM image of crack tip area at cycle 4100; (e) the corresponding IPFZ image showing detwinning; (f) GND density distribution in the selected area at cycle 4100

Local stress states influence twin formation and detwinning. High-resolution EBSD quantifies elastic strain and residual stresses at the crack tip. Analysis of Twin B1 (cycle 4000) shows stress heterogeneity, with stress (yy) potentially large enough to induce detwinning by stretching perpendicular to the c-axis. Fig. 4 illustrates twin boundary migration, driven by gradients in Twin-RSS, as a key factor in detwinning. Negative RSS during reverse loading may reverse twin boundaries, causing detwinning.

Slip traces, dislocation pile-up, and twin boundary interactions are critical. Fig. 4 highlights slip systems obstructed by twins, creating local stress heterogeneity. Twin boundaries act as barriers and facilitators of dislocation motion, influencing local stresses. Detwinning is associated with dislocation activity at twin boundaries, leading to boundary migration.

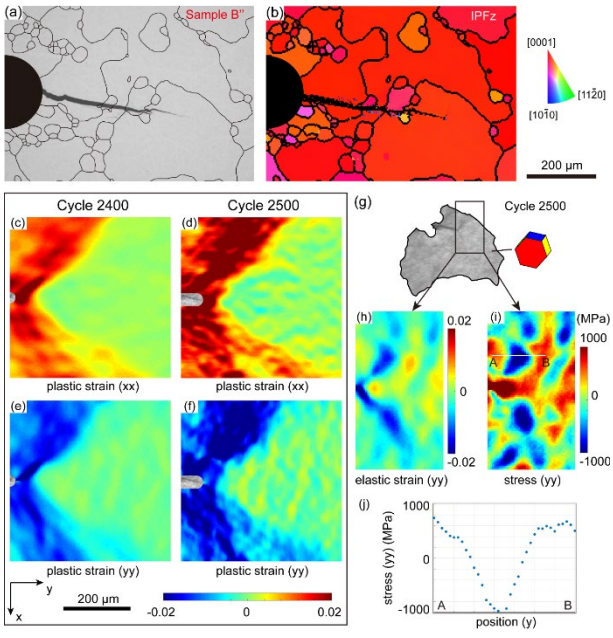

Fig. 3 The distribution of micromechanical fields within Sample B'': (a) optical microscope image showing the crack path and grain morphologies; (b) inverse pole figure maps showing the texture pole direction of Sample B'' aligned with the z-direction; plastic strain (xx) distribution (strain in the unloaded condition) at cycle 2400 (c) and cycle 2500 (d) in Sample B''; plastic strain (yy) distribution at cycle 2400 (e) and cycle 2500 (f); (g) selected grain with crystallographic orientation at the crack tip (cycle 2500) in Sample B''; elastic strain (yy) (h) and stress (yy) (i) distributions at peak load at cycle 2500; (j) the variation of stress (yy) along path A-B in (g)

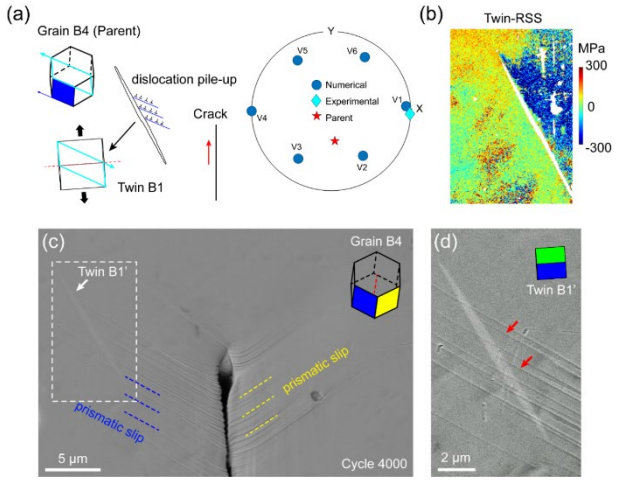

Fig. 4. (a) Pole figure showing the orientations of twin variants in Grain B1 with identified activated twinning plane (marked in cyan) and schematic showing the dislocation pile up at twin boundary along the prismatic slip plane (marked in blue) at cycle 4000 in Sample B; (b) relative Twin-RSS distribution of identified twin variant in (a); (c) slip traces and twinning at crack tip at cycle 4000 in Sample B; (d) enlarged SEM image of dashed white rectangular area in (c) showing slip traces partially impeded by Twin B1'

This study investigates fatigue short crack growth in Zircaloy-4 alloy, revealing phenomena of twinning and detwinning of $\{10\bar{1}2\}<10\bar{1}1>$ tensile type at the vicinity of the crack. Both twinning and slip contribute simultaneously to crack tip plasticity. Detwinning is induced by substantial changes in stress distribution at the crack tip, likely due to dislocation pile-up at the twin boundary during crack growth.

4. Acknowledgements

WW acknowledges the support from the National Natural Science Foundation of China (Grant No. 52101121).

5. References

[1] R.H. Nielsen, G. Wilfing, Zirconium and Zirconium Compounds, 2012. https://doi.org/10.1002/14356007.a28.
[2] E. Tenckhoff, Deformation mechanisms, texture, and anisotropy in Zirconium and Zircaloy, J. Chem. Inf. Model. (1988). https://doi.org/10.1017/CBO9781107415324.004.
[3] R.J. McCabe, G. Proust, E.K. Cerreta, A. Misra, Quantitative analysis of deformation twinning in zirconium, Int. J. Plast. 25 (2009) 454–472. https://doi.org/10.1016/j.ijplas.2008.03.010.
[4] C. Ma, H. Wang, T. Hama, X. Guo, X. Mao, J. Wang, P. Wu, Twinning and detwinning behaviors of commercially pure titanium sheets, Int. J. Plast. 121 (2019) 261–279. https://doi.org/10.1016/j.ijplas.2019.06.010.

[5] H. Yu, Y. Xin, H. Zhou, R. Hong, L. Zhao, Q. Liu, Detwinning behavior of Mg-3Al-1Zn alloy at elevated temperatures, Mater. Sci. Eng. A 617 (2014) 24–30. https://doi.org/10.1016/j.msea.2014.08.034.
[6] G. Proust, G.C. Kaschner, I.J. Beyerlein, B. Clausen, D.W. Brown, R.J. McCabe, C.N. Tomé, Detwinning of high-purity zirconium: In-Situ neutron diffraction experiments, Exp. Mech. 50 (2010) 125–133. https://doi.org/10.1007/s11340-008-9213-6.
[7] X. Chen, Q. Zeng, W. He, Q. Liu, Detwinning behavior in commercial pure zirconium during orthogonal re-compression after pre-compression and annealing, Mater. Sci. Eng. A 767 (2019) 138444. https://doi.org/10.1016/j.msea.2019.138444.

6-11 July 2025 ICEM21 Bologna
21st International Conference on EXPERIMENTAL MECHANICS

EFFECT OF INITITAL CONDITIONS ON PASSIVE SCALAIRE MIXING IN TURBULENT WAKES

M. Sehaba[1], A. Benaissa [2,1], J. Lemay[1]
[1]Department of Mechanical Engineering Laval University, Quebec, Canada.
[2]Department of Mechanical and Aerospace Engineering. Royal Military College of Canada, Kingston, Canada.

1. Introduction

In this work, we study the mixing of a passive scalar (temperature) in two wakes, one is a simple flat plate (1P) turbulent wake and the second is a more complex wake of two side-by-side flat plates (2P). For the one plate wake, the plate is heated slightly and for the two plates wake, one plate is heated and the other is cooled so that the temperature average presents an anti-symmetric profile. Along with the kinetic energy k budget, the temperature variance $\overline{\theta^2}/2$ budget is established in both wakes. From these budgets, kinetic energy and temperature variance dissipations were inferred. They were used to understand the small-scale dissipation of both kinetic energy and the scalar variance. The budget of the scalar for the one plate case was compared with published results of Antonia & Browne (1987). This simple flow is also considered as a test case to validate methods of simultaneously acquiring velocity and temperature data. The measurements were obtained with a combined CTA and CCA methods in the far wake where self-similarity solutions applied, and the scalar is passive ($Ri \leq 10^{-5}$).

2. Mathematical formulation for k and $\overline{\theta^2}/2$ budgets

$$0 = \underbrace{-\overline{U_j}\frac{\partial k}{\partial x_j}}_{C_k} \underbrace{-\overline{u_i u_j}\frac{\partial \overline{U_i}}{\partial x_j}}_{P_k} \underbrace{-\frac{1}{2}\frac{\overline{u_i u_i u_j}}{\partial x_j}}_{D_k} \underbrace{-\frac{1}{\rho}\frac{\partial \overline{p u_j}}{\partial x_j}}_{\Pi_k} \underbrace{-\frac{1}{2}\nu\left(\overline{\frac{\partial u_i}{\partial x_j}+\frac{\partial u_j}{\partial x_i}}\right)^2}_{\varepsilon_k} \tag{1}$$

$$k = \left(\overline{u^2}+\overline{v^2}+\overline{w^2}\right)/2 \tag{2}$$

The terms C_k, P_k, D_k, Π_k and ε_k, are respectively, convection, production, turbulent diffusion, pressure-diffusion, and the dissipation of the turbulent kinetic energy budget k. The term Π_k was not measured but replaced by a model [2] instead.

$$0 = \underbrace{-\overline{U_i}\frac{\partial \overline{\Theta^2}/2}{\partial x_i}}_{C_\Theta} \underbrace{-\overline{u_i\theta}\frac{\partial \overline{\Theta}}{\partial x_i}}_{P_\theta} \underbrace{-\frac{1}{2}\frac{\partial \overline{u_i\theta^2}}{\partial x_i}}_{D_\theta} \underbrace{-\alpha\overline{\frac{\partial\theta}{\partial x_i}\frac{\partial\theta}{\partial x_i}}}_{\varepsilon_\theta}. \tag{3}$$

All the terms in Eq.3 were measured and ε_θ obtained as a closing balance of the $\overline{\theta^2}/2$ budget. $C_\Theta, P_\Theta, D_\Theta$ and ε_θ are respectively, convection, production, turbulent diffusion and the dissipation of $\overline{\theta^2}/2$.

3. Flow Conditions

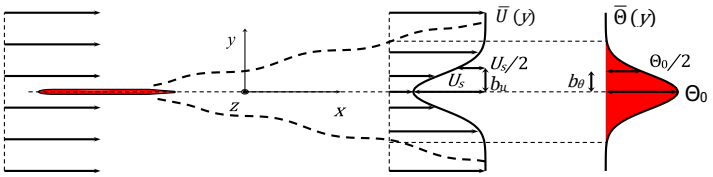

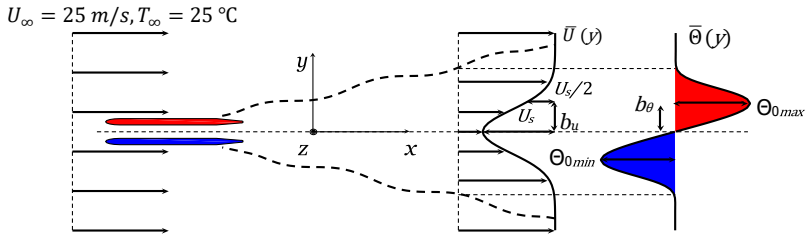

Fig. 1. Studied flows: one heated plate and two plates with anti-symmetrical temperatures.

As stated earlier, the plate in the 1P case was heated to a temperature of Θ_{1P} = 15 ℃, however, due to thermal capacity of the heat exchangers used, the level of heat allowed a temperature difference between the heated and cooled plate of $\Theta_{2P} = \pm 10$ ℃. Figure 1. shows both flow geometries with their normalization scales $(U_s, b_u, \Theta_0, b_\theta)$ of the mean velocity and scalar fields. Similarity between velocity profiles is observed while the temperature profiles are different with the 2P case showing an anti-symmetric profile. These conditions represent a novelty in scalar mixing research in turbulent flows. Boundary conditions for mean and temperature fluctuation in the two wakes are Θ_0 = 10℃ for 1P wake and $\Theta_{0min/max} = \pm 6$ ℃ for the 2P wake. The measurements were carried out at the same distance downstream from the plates, representing $x/\delta = 823$, for 1P and $x/\delta = 280$, for 2P.

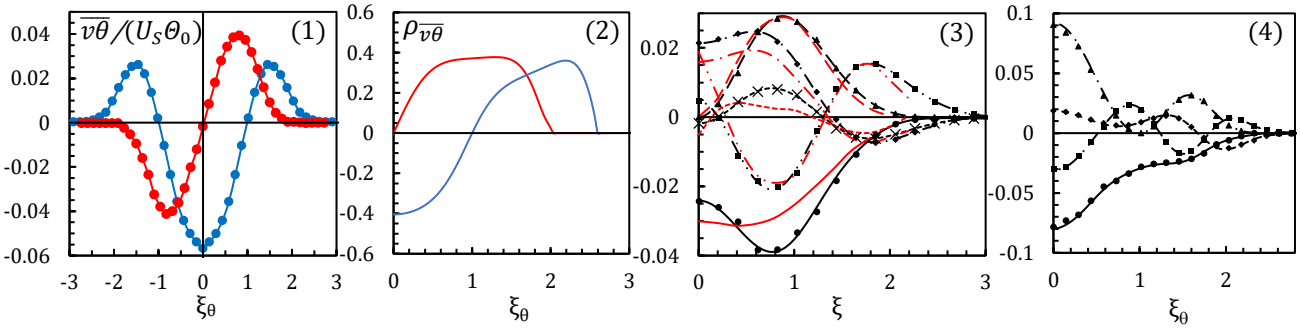

Fig. 2. (1) Scalar flux, $\overline{v\theta}/(U_S\Theta_0)$ (*: 1P, *: 2P); (2) the correlation coefficient $\rho_{\overline{v\theta}}$ (__ : 1P, __ : 2P); (3) k-budget (Present, ▲: P_k, ■: D_k, ×: Π_k, ♦ : C_k, ● : ε_k); [1], -.-: C_k, -..- : D_k, __ __ : P_k, -- : Π_k, __ : ε_k); (4) $\overline{\theta^2}/2$ budget (Present, ▲: P_θ, ■: D_θ, ♦ : C_θ, ● : ε_θ).

4. Results and conclusions

The heat flux measured in both flows (Fig. 2 (1)) reflects the alignment with the mean temperature gradient in each case. The correlation coefficient $\rho_{\overline{v\theta}}$ (Fig. 2 (2)) in the 2P wake presents a nonzero heat flux in the central region and a similar behaviour with 1P in the outer region. The normalised k-budget in 1P wake is in good agreement with [1] (Fig. 2 (3)) with a noticeable difference in the dissipation profile. The $\overline{\theta^2}/2$ budget (Fig. 2 (4)) shows a peculiar behaviour in the central region different from the 1P wake. A dominant production and dissipation characterise an intense transverse mixing. The diffusion and the convection mechanisms almost balance each other with an apparent equilibrium between the production and dissipation of the temperature fluctuation in the inner region.

5. References

[1] L. Browne, R. Antonia, D. Shah (1987). Turbulent energy dissipation in a wake. *Journal of Fluid Mechanics*. **179** 307–326.

[2] J.L. Lumley (1979) Computational modeling of turbulent flows. *Advances in applied mechanics*. **18** 123–176.

FATIGUE AND TENSIONAL FORCE DTEREMINATION ON THIN FILMS USED IN SEMICONDUCTOR MANUFACTURING

Y. C. Lee[1], M. and Y. W. Chen [2]
[1] Department of Mechanical Engineering, National Taiwan University of Science and Technology, Taipei, Taiwan
[2] Department of Mechanical Engineering, Southern Taiwan University of Science and Technology, Tainan, Taiwan

1. Introduction

The global thin film semiconductor deposition market has grown significantly in recent years owing to increasing demand for existing and emerging applications. High demand for product miniaturization and continuous advancement in technology such as IoT, 5G and autonomous driving have driven the global demand for functional special films and is expected to continue to drive development of thin film element devices including sensors, semiconductors, packaging, biomedicine, and medical treatment. There are two kinds of membrane structures, namely coated films and free-standing films. The first, used as conductive layers for electrodes or dielectric layers for capacitor components, will exceptionally high purity and favorable electrical properties. Over the following decades, numerous new thin film and substrate materials have been developed, showcasing their diverse range of applications, including solar energy, wearable devices, and human medical healthcare and son on. The second type has seen increased use in applications such as packing or protection. This also includes use in sensors, actuators, biomedical microchannels, microvalves, micropumps, optical thin film mirrors and the advanced semiconductor element. It is also referred to as the free-standing thin film structure, where one layer of thin film is the main component and the rest of the thin film layers or substrates are sacrificial layers [1-2], as shown in Fig. 1.

This paper will investigate the photomask protective film, a free-standing film that protects the integrated circuit (IC) features on the photomask [3-4]. Made of polymer membrane, it is stretched over an aluminum frame, mounted on the optical reticle. The analytic method proposed in this paper, namely stress analysis testing of the protective films, can be employed to not only protect the photomask and increase its lifespan, but also improve low wafer yield which is a thorn in the side of semiconductor manufacturers. A trial-and-error fitting method based on a simulation model of the modal analysis for the free-standing film is then employed to estimate the membrane tensional force which yields the natural frequencies of the free-standing film closest to the experimental measurement. Then, different fatigue experiments are built up to explore the shift of the natural frequencies of the film. Finally, these analytical results can be used as the replacement timing of the protective films on the production line.

2. Materials and methods

In this experiment, three commercial protective films with of identical size and material were employed from Micro Lithography, Inc. (MLI). Table 1 shows the film dimensions and mechanical parameters. Five points on the film surface are selected for measurement by confocal chromatic

sensor in order to prevent partial vibration frequencies from being unmeasurable due to film vibration nodal positions. In addition, these points are away from the edges of the outer frame to ensure that dynamic deflection can be measured. The center of the reticle protective membrane was taken as the origin, dividing it into four quadrants.

Photomask protective films				
Sample	Film size (length x width x thickness)	Young's modulus (GPa)	Poisson ratio	Density ρ(kg/m^3)
1、2、3	14.9 cm x 12.2 cm x 0.55μm	1.5	0.42	0.000203

Table 1. Dimensions and specifications of three samples used in experiment

3. Results and conclusions

A sweeping sinusoidal signal ranging from 1 to 1000 Hz generated by the speaker and applied continuously to the film surface for 1 h, 2 h, 4 h, and 1 day. The vibration frequency of the films tends to shift to the right as the time of fatigue testing increases, particularly at higher frequencies. The experimental results show that the tensional forces of the three protective films increase with increasing the deterioration time.

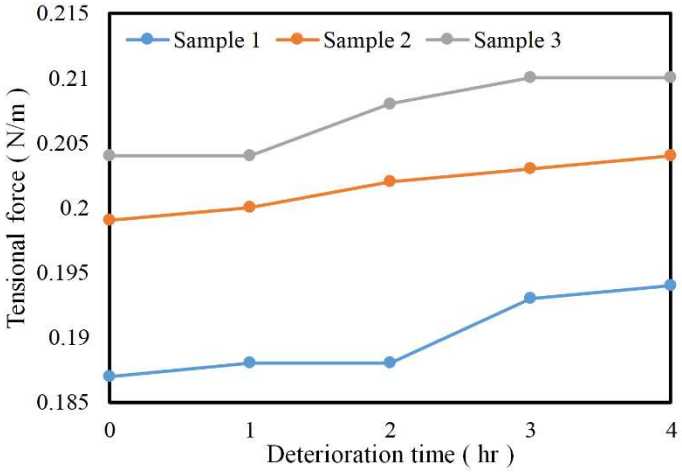

Fig. 1. Relationship between tensile force and deterioration time for three different samples

4. Acknowledgements

The authors gratefully acknowledge the financial support provided to this study by the Ministry of Science and Technology in Taiwan, ROC under Grant Number MOST 108-2218-E-218 -001-MY3..

5. References

[1] M. Schmotz, P. Bookjans, E. Scheer and P. Leiderer (2010). Optical temperature measurements on thin freestanding silicon membranes, *Rev. Sci. Instrum.*, **81**, 114903.

[2] K. Wang, Y. Song, Y. Zhang, Y. Zhang and Z. Cheng (2012). Quality Improvement of GaN Epi-layers Grown with a Strain-Releasing Scheme on Suspended Ultrathin Si Nanofilm Substrate, *Nanoscale Res. Lett.,* **17**, 1-6.

[3] E. S. Park, Z. H. Shamsi, J. W. Kim, D. G. Kim, J. G. Park, J. H. Ahn and H. K. Oh (2015). Mechanical deflection of a free-standing pellicle for extreme ultraviolet lithography, *Microelectron. Eng.*, **143**, 81-85.

[4] S. J. Wi, Y. J. Jang, D. G. Lee, S. Y. Kim and J. Ahn (2023). Investigating the Degradation of EUV Transmittance of an EUV Pellicle Membrane, *Membranes*, **13**, 5.

A Study on Seismic Resistance Analysis of A-Type Marble Storage Racks in Eastern Taiwan

J. T. Liu[1], H. W. Mo[1], C. S. Lin[1]* and C. F. Chen[2]
[1] Department of Mechanical Engineering, National Kaohsiung University of Science and Technology, Kaohsiung, Taiwan
[2] Stone & Resource Industry R&D Center, Hualien, Taiwan

1. Introduction

Taiwan is located in the Pacific Ring of Fire and suffers from frequent seismic activity, so earthquake engineering and disaster prevention are crucial. Hualien, located in eastern Taiwan, is rich in marble resources. Since the 1950s, the stone industry has been developed and has become a key industry in the region. The earthquake on April 3, 2024 (hereinafter referred to as 0403 Hualien earthquake) caused stone products in Hualien to collapse, damaged storage racks, crushing equipment, and halted production. The factory now faces the urgent task of cleaning up a large amount of damaged stone and finding ways to safely and properly store the marble in the future. Frequent and strong earthquakes in Taiwan pose a major challenge to the seismic resistance of marble storage racks.

This study uses computer-aided engineering analysis (CAE) and finite element method (FEM) to simulate typical seismic conditions to evaluate the structural performance and seismic resistance of stone storage racks. We only use the modal parameters obtained from the response data through experimental modal analysis (EMA) to verify the reliability of the FEM of the stone slab A-type storage rack, and then the corresponding strength analysis can be implemented.

2. Materials and methods

The aim of this study is to introduce modal testing techniques for the validation of the FEM of stone storage racks, in order to verify the results of finite element analysis (FEA) and further enhance the seismic performance of the racks during earthquakes. The reliability of the FEM will be validated using the modal parameters obtained from EMA, as well as harmonic analysis and modal analysis in ANSYS. Field measurements, combined with the results of EMA, will be used to appropriately adjust the geometry and contact conditions, enhancing the reliability of the FEM and the analysis results. By analyzing the structural strength of the storage rack, the consistency of failure locations will be examined, providing a reference for structural adjustments. In addition, we have also proposed improvements to original storage racks to significantly modify the seismic resistance of the stone storage racks.

3. Results and conclusions

A structural seismic strength analysis has been conducted using the 0403 Hualien earthquake signal as excitation, simulating the stress and deformation of the rack during an earthquake. The results of FEA show that the maximum stress of traditional A-type storage racks when stimulated by actual earthquake signals far exceeds the yield stress of the material, and the location of its occurrence is also consistent with the location of actual damage to the disaster-damaged storage rack. Finally, some proposed improvements to original storage racks effectively reducing the maximum stress of the stone storage rack to below the yield and tensile strength of the structural material.

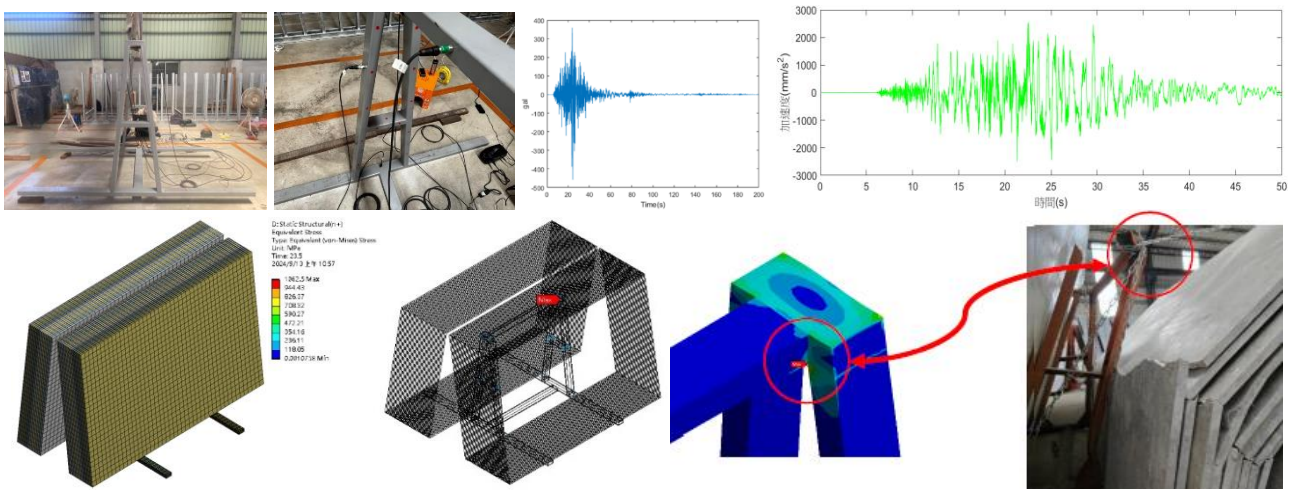

Fig. 1. EMA site, 0403 Hualien earthquake north-south signal and the location of its occurrence is consistent with the location of actual damage to the disaster-damaged A-type storage rack

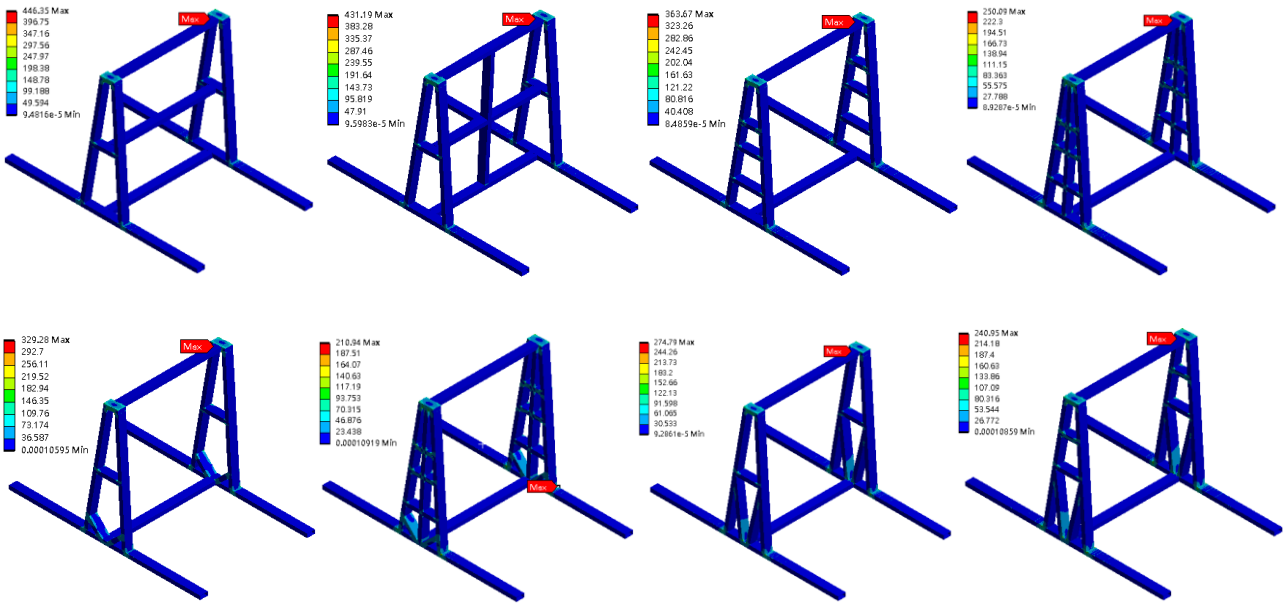

Fig. 2. A-type stone storage rack structure improvement and stress analysis

4. Acknowledgements

This research was supported in part by Stone & Resource Industry R&D Center of Taiwan under grant 113-B002-322A6-146 and 113-B002-322A6-205. The authors also wish to thank Sun Stone Company Ltd for providing the stone exhibition site in Kaohsiung and assistance to conduct the verification of the stone storage rack model in this study.

5. References

[1] Huang, T.-Y., "Updating Finite Element Model by Experimental Modal Data-The Technique and Application," Journal of Technology, Vol. **16**, No. 2. Pp. 335-344, 2001.

[2] Allemang, R. J., "The modal assurance criterion – twenty years of use and abuse," Sound and vibration, Vol. **37**, Iss. 8, pp. 14-23, 2003.

6-11 July 2025 ICEM21 Bologna
21st International Conference on EXPERIMENTAL MECHANICS

EXPERIMENTAL-COMPUTATIONAL APPROACH TO IDENTIFY THE TENSILE CURVE OF A MATERIAL DURING OPERATION

V. Chmelko[1], M.Šulko[1], M. Kučerková[1]

[1] Slovak University of Technology, Faculty of Mechanical Engineering, Namestie Slobody 17, 812 31 Bratislava, Slovakia

1. Introduction

Assessing the serviceability of structures after several years of operation requires knowledge and monitoring of the loading parameters, current properties and condition of the material. For the case of materials without the necessary documentation and for the need to know the actual strength properties of the material, a method to identify the actual tensile curve has been developed using a combination of experimental measurements and computer simulation.

The presented method is based on the association of the geometrical indentation parameters with the strength parameters of the tensile curve of the material. A suitable indenter for hardness testing is the sphere and thus the Brinell method (Fig. 1). The geometrical parameters of the indentation are mainly the diameter and the elevation angle of the material at the edge of the indentation.

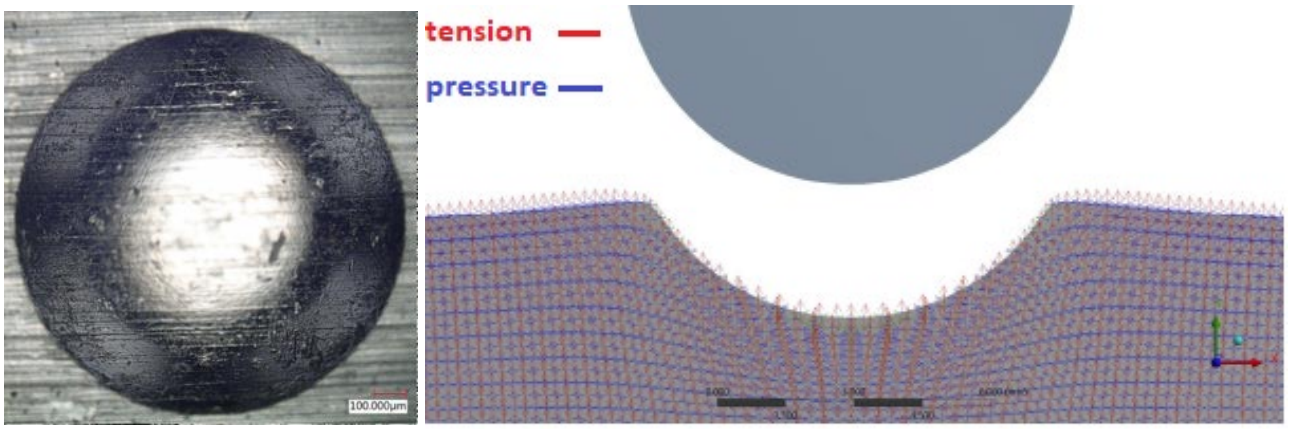

Fig. 1. Zones of tensile and compressive stresses after application of Brinell hardness measurement.

The parameters of the tensile curve, which are the target parameters of the identified material, are yield strength, ultimate strength and strain hardening modulus, which are to be obtained by successive computational iterations of the mathematical model of the indentor application process.

2. Methodology and results

The ball indentation (Brinell hardness) can be performed in laboratory conditions and also directly during operation (Fig.2). An important step is to image the geometry of the indentation as accurately as possible.

In the next step, this process has to be reproduced by FEM simulation in a number of iterations. The parameters of the iterations are, for a known value of Young's modulus, the yield stress, the ultimate strength and the strain hardening modulus (the secant modulus in the elastic-plastic region of the tensile curve).

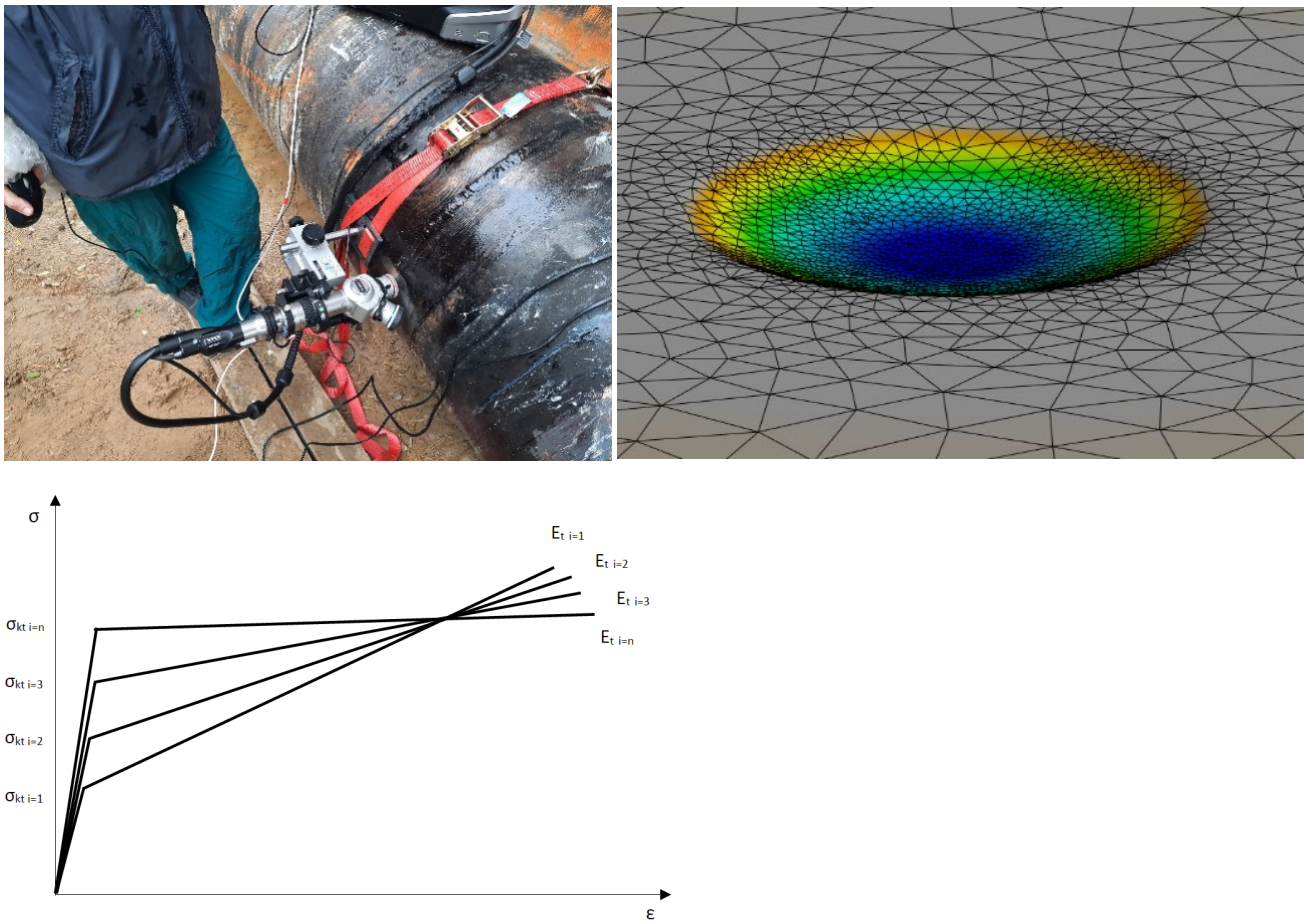

Fig.2 Insertion of an indenter in a pressurised pipeline during the operation and simulation of the indentation process for different combinations of tensile curve parameters.

3. References

[1] Liang Meng, Piotr Breitkopf, Balaji Raghavan, Gerard Mauvoisin, Olivier Bartier, et al.: Identification of material properties using indentation test and shape manifold learning approach. Computer Methods in Applied Mechanics and Engineering, 2015, 297

[2] Giuseppe Pintaude, Alessandro Roberto Hoechele: Experimental Analysis of Indentation Morphologies After Spherical Indentation, Materials Research. 2014; 17(1): 56-60

[3] Jianjun Wu, Mingzhi Wang, Yu Hui, Zengkun Zhang, He Fan.: Identification of anisotropic plasticity properties of materials using spherical indentation imprint mapping, Materials Science & Engineering A 723 (2018) 269–278

[4] Chmelko, V., Koščo, T., Šulko, M., Margetin, M., Škriniarová, J. Poisson's Ratio of Selected Metallic Materials in the Elastic–Plastic Region. Metals 2024, 14, 433.

6-11 July 2025 ICEM21 Bologna
21st International Conference on EXPERIMENTAL MECHANICS

DEVELOPMENT OF A BIOMECHANICAL EXPERIMENTAL ROBOT FOR HIGH FIDELITY CHARACTERIZATION OF FOOTWEAR TRACTION

A. Chanda[1,2] and S. Gupta[1]
[1] Centre for Biomedical Engineering, Indian Institute of Technology Delhi (IIT Delhi), India
[2] Department of Biomedical Engineering, All India Institute of Medical Sciences (AIIMS), Delhi, India

1. Introduction

In the workplace, slip-and-fall accidents occur frequently due to reduced traction at the region where the shoe and floor meet in presence of any contaminant (e.g., water or soap) [1]. However, due to a lack of public awareness, such events are frequently ignored, and the importance of appropriate footwear is frequently overlooked [2]. Mechanical slip and fall risk - assessment devices are used to evaluate the frictional measures at the shoe-floor interface. The existing devices in the market were developed for laboratories and are not capable of simulating slip biomechanics [3]. Additionally, it is expensive to use these instruments in low- or lower-middle-income nations where there is little to no information about slip testing.

In this study, a biomechanical, inexpensive robotic footwear traction characterization device was developed. For the application of normal load, slippage speed, and heel striking angle, a three-part modular subassembly was created. The performance of the experimental robot was thoroughly validated and examined utilizing 5 formal shoes on three different flooring surfaces in dry, wet (water), and lizol (floor cleaner) slippery conditions. The findings showed that the robot is able to effectively distinguish between a variety of combinations of shoes, contaminants, and floorings with accuracy, repeatability, and reliability. It was discovered that the slip tester's instrumentation performance could distinguish between different shoe tread patterns when fluid films were present. The developed device is projected to have a considerable influence, particularly in low- and middle-income countries, on the clinical, industrial, and commercial performance testing of the shoes to be labelled as slip-resistant. This device will make it possible for businesses or medical professionals to transport a device to the experimentation site in order to evaluate correct frictional characteristics under genuine slippery situations.

2. Materials and methods

In the experimental robot, the majority of the elements were generic mechanical components rather than specifically manufactured ones in order to assure ease of manufacturing due to the availability of the components. A modular design strategy was also used to provide simple assembly and disassembly for repair needs. As a result, the device was created in three sub-assemblies: a linear motion mechanism, a vertical motion mechanism, and an angle adjusting mechanism. The developed portable slip tester is depicted in Fig. 1. The device’s overall measurements were 400 mm in length, 400 mm in breadth, and 400 mm in height, and it weighed 55 kg (including two dumbbells of 20 kg each, used for dead load). Aluminum extrusion bars were used in the construction of the housing chassis (20 mm x 20 mm). Standard angle brackets were used in the chassis' construction, and additional support structures were added for stiffness. Four full-swivel load bearing wheels and two

nylon pulling handles were used to increase portability. Furthermore, to eliminate any vibrations during testing, treaded rubber pads were positioned beneath the chassis.

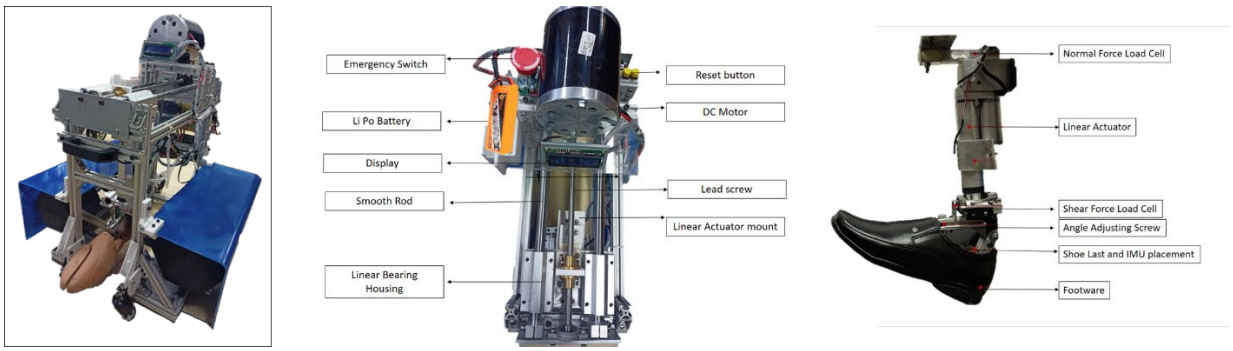

Fig. 1. Developed robot for experimental footwear traction characterization, with horizontal and vertical assemblies

It was evaluated how well the slip tester could differentiate between different pairs of shoes on contaminated flooring. Additionally, the performance of a slip tester was measured by putting the same pair of shoes under the same contaminated conditions on various floorings. Finally, the traction measured in terms of available coefficient of friction (ACOF) across shoes was also examined while maintaining the same contaminants and floorings.

3. Results and conclusions

It was found that the developed device complied with the realistic slip biomechanics (i.e., realistic normal load, slipping speed, and heel contact angle) seen during actual human slips [4]. The output normal load was observed to be within the designated range (500±25 N) (i.e., 500 N). The video analysis software and the sensors were found to have a high correlation and just mild vibration-related variations. The equipment was portable and easy for a person to carry to the location where the test will be conducted because of its lightweight construction. Additionally, the device was found to be repeatable across numerous trials (Fig. 2.), with values that were within about 5%. The robot's ability to differentiate between shoes under similar slipping circumstances, to record the performance trend of shoes over similar flooring, and to record the performance trend of shoes through similar contaminants was also validated.

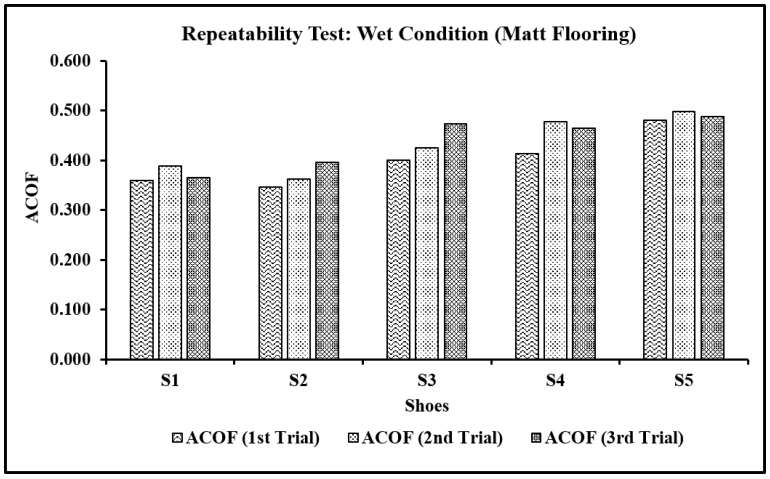

Fig. 2. Representative repeatability test results

4. Acknowledgements

The research presented in this paper has received funding from SERB-DST and IRD, IIT Delhi.

5. References

[1] Ricotti, R., Delucchi, M., & Cerisola, G. (2009). A comparison of results from portable and laboratory floor slipperiness testers. *International Journal of Industrial Ergonomics*, **39**, 353-357.

[2] Chanda, A., Gupta, S., & Chatterjee, S. (2023). Mechanical Footwear Traction Testing Methods. In Book Footwear Traction: Implications on Slips and Falls, *Springer Nature Singapore*, 49-63.

[3] Jones, T., Iraqi, A., & Beschorner, K. (2018). Performance testing of work shoes labeled as slip resistant. *Applied ergonomics*, **68**, 304-312.

[4] Iraqi, A., Cham, R., Redfern, M. S., Vidic, N. S., & Beschorner, K. E. (2018). Kinematics and kinetics of the shoe during human slips. *Journal of biomechanics*, **74**, 57-63.

Research on Shear Deformation Characteristics of Sandy Soil-Structure Interface

Xueying Yang[1,2*]

[1] School of Civil Engineering, Southeast University, Nanjing 211189, China
[2] School of Mechanics and Civil Engineering, China University of Mining and Technology, Jiangsu Xuzhou 221000, China
[*] Email: yxy411@seu.edu.cn

Abstract: Experimental researchs show the presence of a shear dislocation zone at the contact surface, which differs from conventional assumptions. In this paper, numerical simulations are conducted using ABAQUS software to analyze the mechanical characteristics of the contact surface. The analysis focused on shear dislocation, deformation, and strength properties based on variations in the size of the contact surface. The study highlights that the contact surface between sand and concrete structures is a unique shear dislocation zone with specific deformation properties different from the individual materials. The interface deformation is obviously divided into three regions: upper boundary influence, middle deformation, and lower dislocation. When the contact surface reaches the shear strength, the thickness of shear dislocation zone is approximately 30mm, and the corresponding dislocation displacement is about 1mm. In addition, the research addresses the influence of size effects on the mechanical properties of the contact surface between sand and concrete structures under shear load conditions. The length of the contact surface affects the shear stiffness and shear strength, and the height mainly affects the shear strength. The shear deformation characteristics of the contact surface have obvious size effect, while the shear strength characteristics have no size effect. These findings contribute to the understanding of the fundamentals of mechanical properties and contact surface deformation under loading situations. And it could enhance the recommendations for the shear experimental design with appropriate boundary effects.
Keywords**:** Interaction analysis;Shear test; Mechanical properties; Shear deformation; Interface thickness; Size effect

Optical Technics in Experimental Mechanics

6-11 July 2025 ICEM21 Bologna | 21st International Conference on EXPERIMENTAL MECHANICS

DEEP LEARNING-BASED PREDICTION OF RESIDUAL STRESSES OF A BIAXIALLY LOADED INFINTE PLATE WITH A CIRCULAR HOLE FROM PHOTOELASTIC IMAGES

D. W. Lee[1], H.J. An[2], T. Y. Kim[3], B. H. An[3], S. M. Lee[4], J. Oyebanji[1] and P. Balasubramanian1[1]
[1]Advanced Materials Research Center, Technology Innovation Institute, Abu Dhabi, UAE
[2]School of Industrial Engineering, Kumoh National Institute of Technology, Gumi, South Korea
[3]Civil Infrastructure and Environmental Engineering, Khalifa University of Science and Technology, Abu Dhabi, 127788, UAE
[4]Department of Biomedical Engineering and Healthcare Engineering Innovation Center, Khalifa University of Science and Technology, Abu Dhabi 127788, UAE

1. Introduction

Residual stress is one of the important factors which influences mechanical properties of materials such as strength, fracture toughness, ductility and brittleness. Photoelasticity, which describes the change in the optical properties of materials under deformation, is used to evaluate residual stresses. Photoelastic and photoelastic-coated materials exhibit fringe patterns under light rays when loaded, owing to their optomechanical property called birefringence. In this work, deep convolution neural network like Resnet is used to predict residual stresses of biaxially loaded infinite plates with the circular hole from isochromatic fringe pattern of photoelastic images.

2. Analytical solutions of the biaxially loaded infinite plate with circular hole

The residual stresses in the biaxial loaded infinite plate with the circular hole are analyzed by the superposition principle which is shown in Fig. 1. and it's radial normal (σ_r), tangential normal (σ_θ), and radial-tangential shear stress ($\tau_{r\theta}$) around the hole with far field stresses (principal stresses) σ_1 and σ_2 are given in [1],

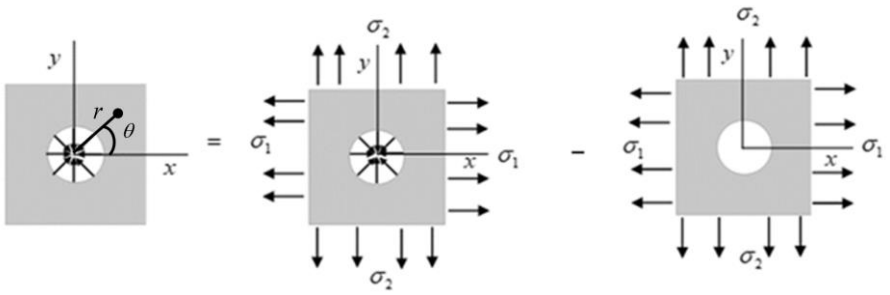

Fig. 1. Residual stresses obtained by the application of the superposition principle

3. Photoelastic images of the biaxially loaded infinite plate with circular hole

Maximum shear stresses (isochromatics) in two-dimensional problems can be visualized by photoelastic method. Isochromatic fringe is a locus of the points exhibiting the same value of maximum shear stress, so called isochromatic line. This isochromatic line has the same fringe order, which is proportional to the maximum shear stress. This relationship is expressed as $\tau_{max} =$

$(\sigma_{max} - \sigma_{min})/2 = nf_a/2$ in [2], where, σ_{max} and σ_{min} are the principal stresses, which are expressed by σ_r, σ_θ and $\tau_{r\theta}$ at point (r, θ) in the Fig. 1. n is the fringe order and f_a is the material stress fringe value and t is the plate thickness. f_a =23.6 (kPa-m/fringe) and t=6.35 (mm) are used in this work.

The synthetic isochromatic fringe pattern of photoelastic images of the infinite plate with circular hole, which is loaded by combining the uniform far field stresses σ_1 and σ_2, whic varies from 1 to 101 *MPa*. Some of them are shown in Fig. 2.

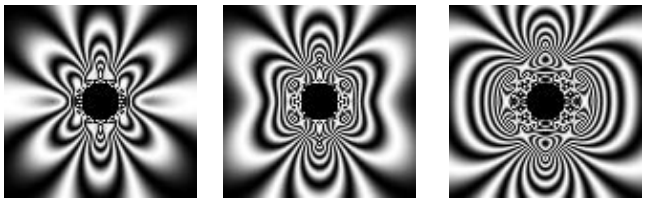

(a) (b) (c)

Fig. 2. Photoelastic images with σ_1 and σ_2**:** (a) 1, 26 (b) 26, 51 (c) 76, 101.

3. Results

The Resnet is modified to predict the residual stresses, and it uses 70% of 10201 photoelastic images for training and 30% for validation and testing. The training and validation loss and prediction of residual stress are shown in Fig. 3(a). Mean absolute error is 0.08. It shows very accurate predictions Fig. 3(b) and (c).

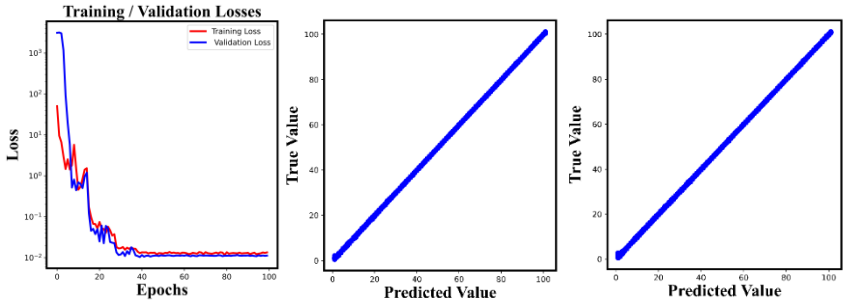

(a) (b) (c)

Fig. 3. (a) Training and validation loss and prediction of residual stresses (b) σ_1 (b) σ_2.

4. Conclusions

The photoelasticity is a powerful experimental tool to analyze stress-related problems such as residual stress, crack, fracture, fatigue, and structural health monitoring. An automatic photoelastic fringe analysis is required to achieve high accuracy and independence of the methodology. In this work, Resnet is employed to analyze the residual stresses from the synthesized photoelastic isochromatic fringe–pattern images of the analytical stress fields of infinite plate with hole. This method can be applied to any photoelastic related problems which we are working on.

5. References

[1] Cárdenas Garcia, J.F.(1999). Catalogue of photoelastic fringes for a biaxially loaded infinite plate with a hole. *Strain*, **35(3)**, 97-104.

[2] Durelli, A.J. and W.F. Riley (1965). Introduction to Photomechanics, Prentice-Hall .

6-11 July 2025 ICEM21 Bologna
21st International Conference on EXPERIMENTAL MECHANICS

Modal Characteristic Identification of Structure using High-Speed Digital Image Correlation Method

Xiongjie Che[1], Ruihai Xin[1], Nam Seo Goo[1]
[1] *Department of Mechanical and Aerospace Engineering, Konkuk University, South Korea*

1. Introduction

Aerospace structures are frequently exposed to complex and dynamic vibration environments, requiring accurate determination of their modal characteristics during the design and testing process. Accurate modal analysis is critical not only for ensuring structural reliability but also for optimizing performance under operational conditions [1]. Conventional vibration mode analysis techniques, such as those employing accelerometers or laser sensors, have inherent limitations, including restricted measurement ranges and the need for physical contact with the structure, which can influence the results and complicate experimental setups.

To overcome these limitations, this study proposes a novel, non-contact, full-field vibration mode analysis method that integrates the Digital Image Correlation (DIC) technique with Variational Mode Decomposition (VMD) [2,3]. The DIC technique, using high-speed cameras, enables full-field displacement measurements without the need for direct sensor contact, while the VMD algorithm effectively decomposes complex vibration signals into distinct modal components. This combined approach allows for detailed and accurate identification of modal characteristics across the entire structure.

2. Materials and methods

In this study, the vibration characteristics of an aluminum alloy specimen measuring 120 mm in length, 80 mm in width, and 1 mm in thickness were measured and analyzed using a high-speed camera. The experimental schematic diagram, as shown in Figure 1, was designed to capture and evaluate the specimen's vibration modes accurately [4]. The aluminum alloy specimen was first heated to a specified temperature using an infrared (IR) heater. And then a shaker was used to induce vibrations in the heated specimen. Two high-speed cameras captured the vibration response in real-time, and the data were analyzed using the DIC method to extract displacement fields.

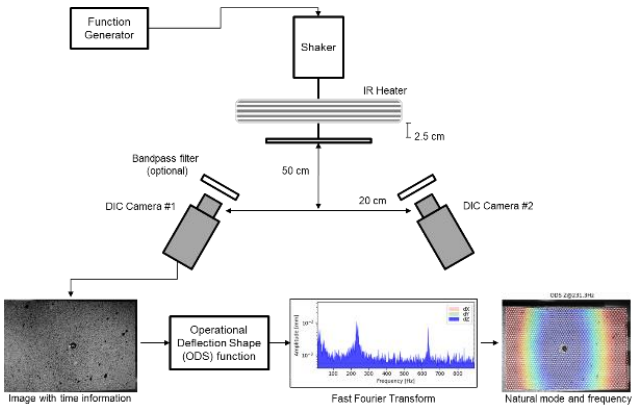

Fig. 1. Experimental schematic diagram

3. Results and conclusions

The vibration signals measured using the high-speed camera were analyzed with the Variational Mode Decomposition (VMD) method, as shown in Figure 2, to extract the natural frequencies and corresponding mode shapes. When compared to finite element analysis (FEA) results, both modes exhibited similar vibration frequencies and mode shapes, demonstrating strong consistency between experimental and simulation data. Furthermore, the Modal Assurance Criterion (MAC) values for both modes exceeded 0.9, indicating a high level of correlation and validating the accuracy of the experimental measurements.

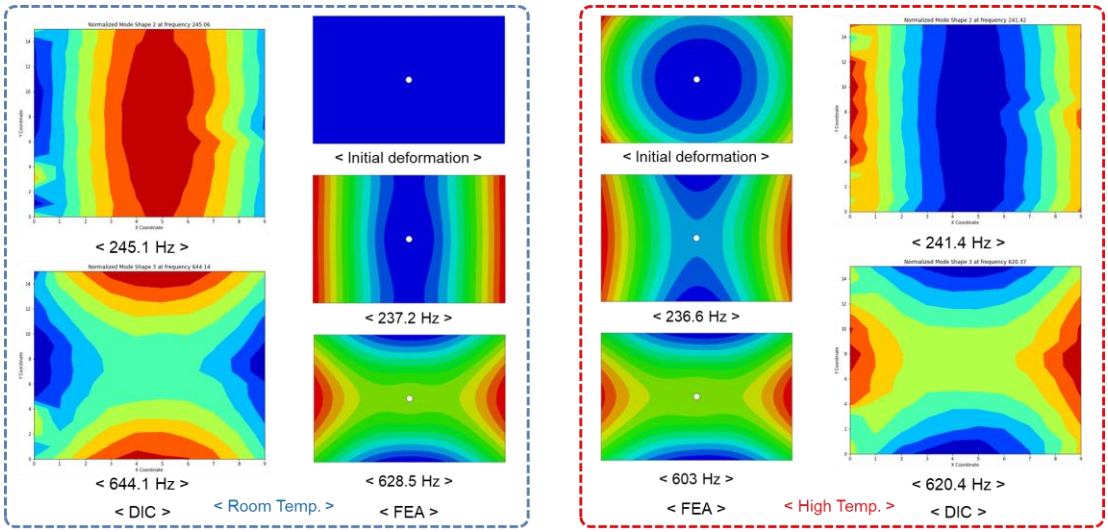

Fig. 2. Modal analysis comparison and mode shift effect of high temperature environment

In this study, the vibration mode analysis method was developed to measure the full-field vibration characteristics of structures accurately and efficiently. This method provides reliable data that can be applied to enhance the design and optimization of aircraft structures.

4. Acknowledgements

This research was supported by Basic Science Research Program through the National Research Foundation of Korea (NRF) funded by the Ministry of Education (NRF-2022R1I1A2055690).

5. References

[1] Tang S, Hu C. Design, preparation and properties of carbon fiber reinforced ultra-high temperature ceramic composites for aerospace applications: a review[J]. Journal of Materials Science & Technology, 2017, 33(2): 117-130.

[2] Peng, Fuhao, et al. "Variational mode decomposition framework for modal shape visualization of honeycomb sandwich structures for full-field vibration measurements in non-uniform temperature fields." Measurement 227 (2024): 114278.

[3] Dragomiretskiy, Konstantin, and Dominique Zosso. "Variational mode decomposition." IEEE transactions on signal processing 62.3 (2013): 531-544.

[4] Berke, R. B., et al. "High temperature vibratory response of Hastelloy-X: stereo-DIC measurements and image decomposition analysis." Experimental Mechanics 56 (2016): 231-243.

ETCHING SELECTION FOR PHASE ANALYSIS IN SUPER DUPLEX STAINLESS STEEL SAF2507

F. Sordetti[1,], A. Palombi[2], N. Picco[1], M. Magnan[1], C. Maranzana[3], A. Varone[2], A. Lanzutti[1]*

[1] *University of Udine, Polytechnic Department of Engineering and Architecture, Via delle Scienze 208, 33100 Udine (UD), Italy*
[2] *University of Rome "Tor Vergata", Department of Industrial Engineering Via del Politecnico 1, 00133 Roma, Italy*
[3] *Acciaieria Fonderia Cividale S.p.A., Via dell' Industria 40, 33043 Cividale (UD), Italy*
[*] *Corresponding author: e-mail: francesco.sordetti@uniud.it tel.: +39 0432 629972*

1. Introduction

Duplex stainless steels (DSS) are biphasic steels characterized by a microstructure consisting of a ferritic matrix and austenitic islands, typically equally distributed to optimize material properties [1]. Compared to ferritic (FSS) and austenitic (ASS) stainless steels, DSS have higher mechanical properties and corrosion resistance, in particular against pitting corrosion, stress corrosion cracking, intergranular corrosion, and crevice corrosion [2]. In DSS it is important to prevent the formation of secondary phases (σ, χ, carbides and nitrides) which lead to embrittlement and reduction of corrosion resistance [3]. Nitrides, carbides, σ and χ phases typically form at 700–1000°C, while spinodal decomposition of ferrite occurs between 300–600°C, reducing the maximum service temperature of DSS to about 300°C [4]. The σ-phase is particularly detrimental due to its rapid formation kinetics and stability. Even small amount of σ-phase significantly reduce toughness and corrosion resistance [5]. Solubilization annealing is required to remove these phases.
Accurate phase characterization in DSS is essential. Standard methods, e.g. ASTM E562-19e1, require a manual point counting, which is time-consuming and produce errors exceeding 10%. Alternative techniques include magnetic measurements, X-ray diffraction (XRD) and electron backscatter diffraction (EBSD), which offer high accuracy but are limited by sample size, preparation, and analysis speed. Metallographic analysis using chemical etching offers a faster and potentially more accurate approach [6].

2. Materials and methods

The material analyzed was SAF 2507 SDSS extracted from a solubilized cast and cut into 20x20x10 mm samples. To produce different amounts of σ-phase precipitation, the samples were heat treated in a furnace at 850°C for different holding times (5 min, 15 min, 30 min, 1 h, 5 h) and quenched in water. XRD was used to quantify the phase distribution, with patterns recorded in the range of 15–55° using Mo-Kα radiation (λ=0.0709 nm). Precision peak profiles were collected in steps of 0.005° with a counting time per step of 4 s to identify ferrite, austenite, and σ-phase, using the JCPDS database. After metallographic preparation the samples were chemically etched. Etchants were selected based on specific literature references (listed in Table 1) [7,8]. The samples were examined under an optical microscope at 100x magnification. Nine zones were identified on each sample using microhardness indentation. Images of these zones were analyzed to quantify the phase distribution using image analysis techniques and the results were averaged. Different numbers of images (1, 3, 6, and 9) were then analyzed to investigate the effect on the accuracy of the results. The images were processed using ImageJ. The quantitative phase distributions obtained by optical microscopy and image analysis were compared with the XRD results, which were used as a reference for the study.

Table 1: List of reagents and etching conditions

Reagent	Composition	Etching conditions
Beraha	20ml HCl, 80ml H_2O, 1g $K_2S_2O_5$	few seconds at room temperature
Carpenter	15ml HCl, 85ml ethanol	15 min, 30 min, 45 min and 60 min at room temperature
Groesbeck	4g $KMnO_4$, 4g NaOH, 100ml H_2O	10 min at 80°C
Kalling No2	5g $CuCl_2$, 100ml HCl, 100ml ethanol	few seconds at room temperature
LB1	20g NH_4FHF, 0.5 g $K_2S_2O_5$, 100ml hot H_2O	5 min at 35°C
Marble	4g $CuSO_4$, 20ml HCl, 20ml H_2O	from a few seconds to a few min time at room temperature
Murakami	10g NaOH or KOH, 10g $K_3Fe(CN)_6$, 100ml H_2O	5 min, 15 min and 30 min at 80°C
Vilella	1g picric acid, 5ml HCl, 100ml ethanol	1 min, 5 min, 15 min and 30 min at room temperature

3. Results and conclusions

This research defined a standardized method for estimating the phase volume fractions in SAF2507 SDSS. Different etchants were tested and optimized to improve the contrast between ferrite, austenite, and secondary phases. Beraha's reagent is the best etchant for identifying phases in the fully solubilized samples. Marble's and Groesbeck's reagents are suitable for detecting the σ-phase. Murakami's reagent is the best for highlighting all phases simultaneously. In particular, a 5 minute immersion in the reagent provides limited contrast between phaees in fully solubilized samples, while σ-phase is distinguishable only in low-content samples. Increasing the time to 15 minutes improves the phase contrast for fully solubilized and low σ-phase samples but remains insufficient for high σ-phase content. At 30 minutes of immersion, the contrast is excellent for all samples. The results of the image analysis of a 30 minute of immersion in Murakami's reagent is shown in Figure 1. Comparison of XRD and image analysis of samples etched with Murakami's reagent shows that this reagent overestimates ferrite and σ-phase and underestimates austenite, probably due to colour artefacts and the low resolution of light microscopy. Secondary austenite formed during σ phase precipitation also contributes to the underestimation of austenite.

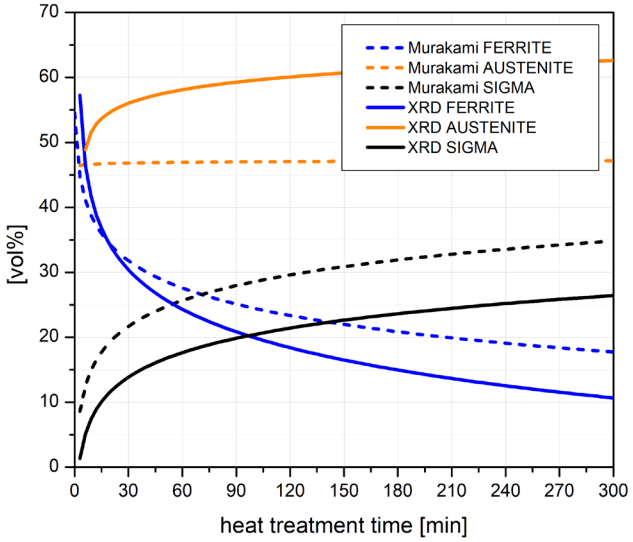

Figure 1: phase distribution of samples heat treated at 850 and etched with Murakami's reagent

In terms of accuracy of image analysis, Kalling's reagent was the best for quantifying ferrite and austenite. For the σ-phase quantification the Marble's reagent produced the most accurate results. Groesbeck's reagent is a good alternative. For a complete phase analysis the Murakami's reagent proved to be the most effective. A minimum of 3 images are required for accurate phase quantification, increasing to 6 for accurate evaluation with Marble's reagent.

4. References

[1] R.N. Gunn, Duplex Stainless Steels Microstructure, Properties and Applications, 1st ed., Woodhead Publishing, Cambridge, England, 1997. https://doi.org/10.1533/9781845698775.24.

[2] J. Charles, Super Duplex Stainless Steels-Structure and Properties, in: Conference of Duplex Stainless Stee, Les Editions de Physique, Les Ulis Cedex, France, 1991: pp. 3–48.

[3] J.M. Pardal, S. Souto, M. Tavares, M. Da Penha, C. Fonseca, J. Adailson De Souza, L. Menezes Vieira, H. Ferreira Gomes De Abreu, Deleterious Phases Precipitation on Superduplex Stainless Steel UNS S32750: Characterization by Light Optical and Scanning Electron Microscopy, 2010.

[4] E.M. Cojocaru, D. Raducanu, A. Nocivin, V.D. Cojocaru, Influence of ageing treatment temperature and duration on σ-phase precipitation and mechanical properties of UNS S32750 SDSS alloy, J Adv Res 30 (2021) 53–61. https://doi.org/10.1016/j.jare.2020.11.005.

[5] E.M. Cojocaru, D. Raducanu, A. Nocivin, I. Cinca, A.N. Vintila, N. Serban, M.L. Angelescu, V.D. Cojocaru, Influence of Aging Treatment on Microstructure and Tensile Properties of a Hot Deformed UNS S32750 Super Duplex Stainless Steel (SDSS) Alloy, Metals (Basel) 10 (2020) 353. https://doi.org/10.3390/met10030353.

[6] A. Fedorov, A. Zhitenev, D. Strekalovskaya, A. Kur, Quantitative Description of the Microstructure of Duplex Stainless Steels Using Selective Etching, in: The 1st International Electronic Conference on Metallurgy and Metals, MDPI, Basel Switzerland, 2021: p. 4. https://doi.org/10.3390/IEC2M-09387.

[7] N. Llorca-Isern, H. López-Luque, I. López-Jiménez, M.V. Biezma, Identification of sigma and chi phases in duplex stainless steels, Mater Charact 112 (2016) 20–29. https://doi.org/10.1016/j.matchar.2015.12.004.

[8] G.F. Vander Voort, Color Metallography, Micros Today 13 (2005) 22–27. https://doi.org/10.1017/S1551929500053943.

GENERALIZED CAMERA MODEL CALIBRATION METHOD BASED ON COLLIMATOR

Shunkun Liang[1], Banglei Guan[1*], Zibin Liu[1], Ang Su[1], Zhang Li[1], Yang Shang[1], Xiaolin Liu[2] and Qifeng Yu[1]

[1] College of Aerospace Science and Engineering, National University of Defense Technology, Changsha, China

[2] College of Physics and Optoelectronic Engineering, Shenzhen University, Shenzhen, China

** Corresponding Author*

1. Introduction

Optical measurement, characterized by its non-contact and high-precision attributes, has emerged as a pivotal technique in experimental mechanics. Camera calibration is a fundamental step in optical measurement of mechanics[1], with its accuracy directly influencing the final measurement results. In typical mechanical applications, such as high-temperature thermal deformation measurement[2] and wind tunnel deformation measurement[3], cameras are often required to measure workpieces through protective glass. However, the conventional pinhole camera model fails to account for the refractive effects induced by the glass, thereby reducing the accuracy of optical measurements. This study eschews the pinhole model in favor of a more comprehensive generalized camera model for camera representation. The generalized camera model is a non-parametric model that directly maps 3D spatial rays with 2D image pixels[4]. Consequently, this model is adept at encapsulating the glass refraction process in optical measurement contexts, thereby achieving better deformation measurement results.

Calibration methods for the generalized camera model have been explored in several studies[5,6]. For instance, Ramalingam et al. suggested employing a planar target to initially estimate the pose and then determine the direction of rays corresponding to each pixel[5,6]. This study presents a method for calibrating the generalized camera model using a collimator. The optical property of the collimator, which generates parallel light, provides additional geometric constraints for camera calibration. This reduction in the number of motion parameters to be computed results in more optimal calibration outcomes. This study applies the spherical motion constraints proposed by [7] to the calibration process of the generalized camera model, thereby proposing a novel calibration technique. Experimental calibration results demonstrate the advantages of the proposed collimator method

2. Methods

In simple terms, the main components of a collimator include a light source, a reticle lying on the focal plane and optical lens. By attaching a calibration pattern with encoding to the reticle, the camera can obtain calibration data by observing the pattern through the lenses. It has been proven in [7] that the relative motion between the pattern and camera is spherical motion, which can be expressed as:

$$\mathbf{T} = \begin{pmatrix} \mathbf{R} & -\mathbf{R}\mathbf{t} \\ \mathbf{0}_{3\times1} & 1 \end{pmatrix} \tag{1}$$

where $\mathbf{R}$ is a 3×3 rotation matrix, and $\mathbf{t}=(x,y,r)^T$ represents the position of the camera in the calibration target coordinate system.

Suppose a pixel in the image observes three points on calibration patterns with different poses, denoted as Q, Q' and Q''. Since the calibration pattern is artificially designed, the coordinates of these points in their respective local coordinate systems can be obtained. Selecting the coordinate frame of Q as the reference coordinate frame, the coordinate systems of Q' and Q'' can be transformed to the reference coordinate frame using the unknown rotation matrices $\mathbf{R}'$ and $\mathbf{R}''$ and the translation vectors $\mathbf{t}'$ and $\mathbf{t}''$. The points are all mapped to the reference frame, and their homogeneous coordinates are obtained, forming a 4 × 3 matrix as follows:

$$\begin{pmatrix} Q_1 & R'_{11}Q'_1+R'_{12}Q'_2+t'_1 & R''_{11}Q''_1+R''_{12}Q''_2+t''_1 \\ Q_2 & R'_{21}Q'_1+R'_{22}Q'_2+t'_2 & R''_{21}Q''_1+R''_{22}Q''_2+t''_2 \\ 0 & R'_{31}Q'_1+R'_{32}Q'_2+t'_3 & R''_{31}Q''_1+R''_{32}Q''_2+t''_3 \\ 1 & 1 & 1 \end{pmatrix} \tag{2}$$

Since rays corresponding to each pixel propagate along a straight line in 3D space, three points must be collinear. Hence, the determinant of all 3 × 3 submatrix is 0. Combining spherical motion constraints and three-point collinear constraints, two sets of rotation matrices and translation vectors can be calculate from multiple sets of points. Subsequently, the coordinates of the three points within the reference frame are known, and the corresponding ray for the pixel can be determined. Similarly, the light position of each pixel on the image can be calculated. For the sub-pixel coordinate, it can be obtained through spline interpolation of neighboring integer pixels.

3. Results and conclusions

This study performs calibration experiment using camera lenses with focal lengths of 8mm and 35mm (as shown in Fig. 1), respectively. The results were compared with the open-source code OpenCV[8] and the previous calibration methods for the generalized camera model [5]. Table 1 show that the collimator calibration method can achieve the best calibration accuracy.

Fig. 1. Calibration image observed through a collimator using 8mm (Left) and 35mm lenses (Right)

Algorithm	OpenCV[8]			Generic[5]			Collimator		
Error	Med	Avg	Max	Med	Avg	Max	Med	Avg	Max
8mm	0.0739	0.1012	1.1481	0.0522	0.0764	1.0223	**0.0520**	**0.0760**	**1.0081**
35mm	0.2664	0.3124	2.7768	0.2490	0.2932	**2.6373**	**0.2467**	**0.2896**	2.6767

Table 1. Reprojection error comparison for calibrating the cameras using different methods.

4. Acknowledgements

This research has been supported by the Hunan Provincial Natural Science Foundation for Excellent Young Scholars under Grant 2023JJ20045, and the National Natural Science Foundation of China under Grant 12372189.

5. References

[1] Z. Zhang (2000). A flexible new technique for camera calibration. IEEE Trans. Pattern Anal. Mach. Intell., 22, 1330-1334

[2] L. Yu, B. Pan (2021). Overview of high-temperature deformation measurement using digital image correlation. Experimental Mechanics, 61, 1121-1142.

[3] M. Gramola, P.J.K. Bruce, M. Santer (2019). Photogrammetry for accurate model deformation measurement in a supersonic wind tunnel. Exp. Fluids., 60, 1-11.

[4] M.D. Grossberg, S.K. Nayar (2001). A general imaging model and a method for finding its parameters. IEEE International Conference on Computer Vision. 2, 108-115.

[5] S. Ramalingam, P. Sturm (2016). A unifying model for camera calibration. IEEE Trans. Pattern Anal. Mach. Intell., 39,1309-1319.

[6] S. Ramalingam, P. Sturm, S.K. Lodha (2005). Towards complete generic camera calibration. IEEE Computer Society Conference on Computer Vision and Pattern Recognition, 1, 1093-1098.

[7] S. Liang, B. Guan, Z. Yu, et al (2024). Camera Calibration using a Collimator System. European Conference on Computer Vision.

[8] Gary Bradski (2000). The OpenCV Library. Dr. Dobb's Journal of Software Tools.

POLYMER CHARACTERIZATION USING LASER DOPPLER VIBROMETRY AND ULTRASONIC EXCITATION

N. Hasheminejad[1], N. Ghaderi[2] , A. Golmohammadi[1]
[1] SuPAR Research Group, Faculty of Applied Engineering, University of Antwerp, Belgium
[2] InViLab Research Group, Faculty of Applied Engineering, University of Antwerp, Belgium

1. Introduction

Polymeric materials, such as polymethyl methacrylate (PMMA), exhibit mechanical properties that vary significantly with temperature and strain rate, making accurate characterization essential in engineering applications [1]. Conventional methods, including temperature-frequency sweeps, are time-intensive and need to be performed in climate chambers. Other techniques such as the split Hopkinson pressure bar provide insights at high strain rates, but using contact-based sensors limits their spatial resolution and efficiency [2]. To overcome these limitations, non-contact optical measurement systems, such as cameras or Laser Doppler Vibrometers (LDV), have shown promise for rapid material characterization [3], [4]. LDVs in such experiments can measure surface vibrations at high spatial resolution, offering advantages over image-based methods, which require ultra-high-speed cameras and extensive processing. Scanning Laser Doppler Vibrometers (SLDV), in particular, enable vibration measurements across multiple points on a sample, facilitating comprehensive characterization of viscoelastic properties. Recent advancements integrate SLDV with high-power ultrasonic excitation and infrared thermography, allowing for rapid assessment of material properties without the need for traditional load cells [4]. This study uses a novel setup combining SLDV and ultrasonic excitation to characterize PMMA's storage modulus, rapidly producing a master curve over a range of temperatures and strain rates. This setup reduces measurement noise and improves efficiency, offering an advanced tool for high-speed material testing.

2. Materials and methods

This study used a laser-cut PMMA sample (54.3 mm x 3.0 mm x 11.6 mm) with a density of 1.19 g/cm3. The sample was painted white using Ardrox® 9D1B aerosol to optimize reflection for LDV measurements. As presented in Fig. 1, The experimental setup included a SynapTec high-power ultrasonic transducer, a Polytec VibroFlex Xtra LDV integrated with a Thorlabs GVS012 Galvanometric Scanning Mirror System, and a FLIR X6540sc IR camera for simultaneous thermal measurements. The transducer excited the sample near its first longitudinal natural frequency, at around 19.7 kHz, while the LDV measured vibrations across several points along the sample. Using this data, strain and stress as well as the storage moduli on several points along the sample were calculated. Meanwhile, thermal images were recorded simultaneously at 50 Hz and analyzed to provide temperatures corresponding to each calculated storage modulus. The combination of this data is used to form the master curve of storage modulus for this sample.

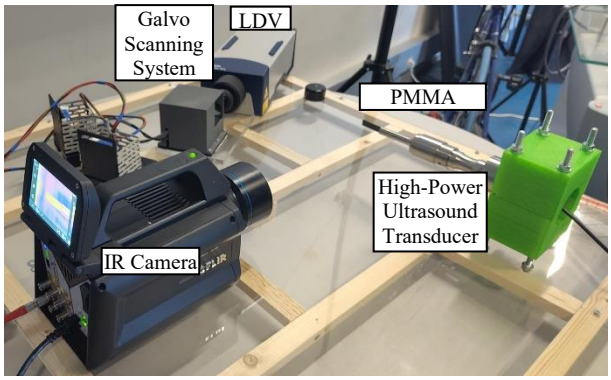

Fig 1: Experimental setup

3. Results and conclusions

As illustrated in Fig. 2, the storage modulus of PMMA was estimated across different strain rates and temperatures, yielding a master curve that aligns closely with a previous study [3]. The modulus decreased with increasing temperature and showed a slight increase at higher strain rates. Results highlight the effectiveness of the setup for characterizing viscoelastic materials, especially at high strain-rate levels.

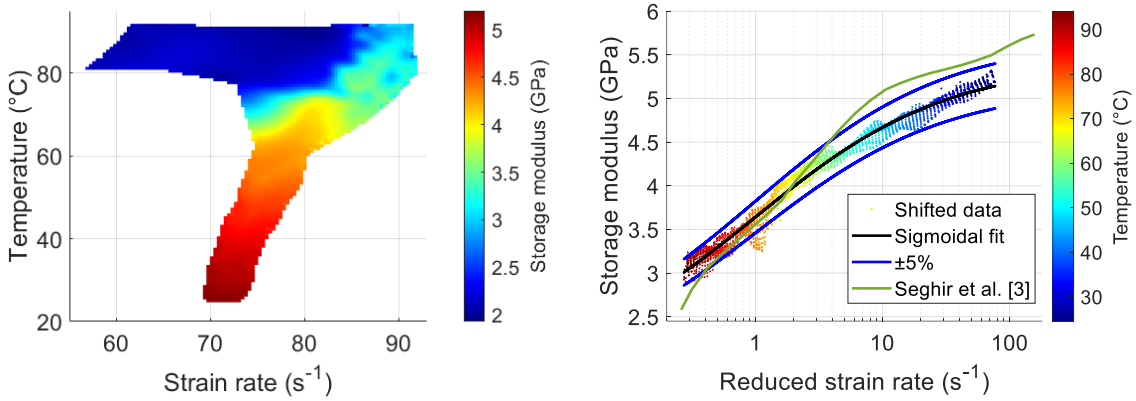

Fig 2: (Left) Smoothed storage modulus of sample at different conditions, (Right) Master curve of storage modulus estimated from the proposed method and compared with the image-based ultrasonic tests performed by [3].

4. Acknowledgements

The research presented in this paper has received funding from Fonds Wetenschappelijk Onderzoek – Vlaanderen (FWO) through the junior postdoc grant titled “BITuminous Mortars: an Accelerated testing APproach (BITMA²P).” number 12ZU123N.

5. References

[1] C. R. Siviour and J. L. Jordan, “High Strain Rate Mechanics of Polymers: A Review,” *Journal of Dynamic Behavior of Materials*, vol. 2, no. 1, pp. 15–32, 2016, doi: 10.1007/s40870-016-0052-8.

[2] J. Richeton, S. Ahzi, K. S. Vecchio, F. C. Jiang, and R. R. Adharapurapu, “Influence of temperature and strain rate on the mechanical behavior of three amorphous polymers: Characterization and modeling of the compressive yield stress,” *Int J Solids Struct*, vol. 43, no. 7–8, pp. 2318–2335, 2006, doi: 10.1016/j.ijsolstr.2005.06.040.

[3] R. Seghir and F. Pierron, “A Novel Image-based Ultrasonic Test to Map Material Mechanical Properties at High Strain-rates,” *Exp Mech*, vol. 58, no. 2, pp. 183–206, 2018, doi: 10.1007/s11340-017-0329-4.

[4] N. Hasheminejad, S. Vanlanduit, T. Ghalandari, F. Pierron, and C. Vuye, “Into a rapid polymer characterization employing optical measurement systems and high-power ultrasonic excitation,” *Polymer (Guildf)*, vol. 294, Feb. 2024, doi: 10.1016/j.polymer.2024.126730.

STUDY OF TRIANGULAR UNDEREXPANDED SONIC JETS

S. Kato[1], T. Miyaguni[1], S. Nakao[1] and Y. Miyazato[1]
[1] Department of Mechanical Systems Engineering, The University of Kitakyushu, Japan

1. Introduction

Supersonic jets have been used in aerospace engineering for applications such as attitude control of small satellites and reduction of jet engine exhaust noise, and have been the subject of numerous studies. However, most of the previous studies have focused on jets from round nozzles with a circular cross-sectional shape. On the other hand, non-circular supersonic jets are known to have many advantages over round supersonic jets, including noise reduction and enhanced mixing, but the reasons for this remain unclear. To investigate the three-dimensional structures of supersonic jets emerging from non-circular convergent nozzles, we have devised an optical system that incorporates tomographic elements into the conventional rainbow schlieren system. Gutmark et al. [1] performed non-reacting and combustion tests for subsonic, sonic, and supersonic conditions using non-circular injectors including square, equilateral-, and isosceles triangular-nozzles. The flow fields of the jets were investigated with hot-wire anemometry and spark schlieren photography and found that in the underexpanded supersonic jets, the shock structure determines the evolution of the jet and dominates the combustion. Umeda and Ishii [2] experimentally investigated the oscillation modes of underexpanded jets issuing from an equilateral triangular nozzle using the conventional spark schlieren technique and acoustic measurements. The experimental results showed that the oscillation modes are first axisymmetric and then sinusoidal with increasing nozzle pressure ratio, but the helical oscillation mode, which appeared for the underexpanded circular jet, is not observed. Sureshkumar and Sridhar [3] performed Pitot pressure surveys in the axial and lateral directions of the jet to investigate the decay and spread characteristics of an overexpanded triangular supersonic jet and concluded that the triangular jet has a shorter supersonic core than the comparable circular jet. Shock-containing triangular jets have experimentally been clarified only to a small extent due to difficulties in quantitative measurement techniques, despite their engineering and academic importance. In this study, the flow features of underexpanded jets emerging from a triangular-shaped convergent nozzle experimentally are investigated using rainbow schlieren tomography.

2. Experimental methods

Experiments were conducted in an intermittent compressed air facility. Dry air from two successive 1-m^3 high-pressure tanks, normally pressurized to 1.0 MPa, enters a plenum chamber through the coupling and is discharged into atmosphere through a flange-mounted test nozzle. The cross-section of the flow path at the nozzle exit is an equilateral triangle with one side 6.73 mm long and the equivalent diameter is D_{eq} = 5.0 mm. Quantitative flow visualization is performed using rainbow schlieren tomography. The ratio NPR (= p_{os}/p_b) of the pressure p_{os} in the planum chamber to the back pressure p_b was adjusted at 4.0 to produce underexpanded jets. The back pressure is p_b = 101.7 kPa and the ambient temperature is T_b = 297.1 K. In the present experiment, the test nozzle was

rotated from 0° to 180° at equal intervals of 5° to obtain a total of 37 rainbow schlieren images of the jet. Rainbow schlieren images with the horizontal setting were utilized to acquire the jet density field.

3. Results and conclusions

The density contour plots in the two distinct cross-sections, each of which contains an axis that passes through the location of the center of gravity in the channel cross-section, are shown in Fig. 1 where Figs. 1(a) and 2(b) denote the density fields in the top and side planes, respectively. The flow direction is from left to right. The density field is non-dimensionalized in terms of atmospheric density (ρ_b), with minimum and maximum normalized densities of 0.8 and 2.4, respectively, with contours drawn every $\rho/\rho_b = 0.1$. The spatial resolution of the present rainbow schlieren system is approximately 13 μm in the object plane, which can be evaluated based on the physical and image dimensions of the test nozzle. In addition, The isodensity line with ρ/ρ_b =1.2 indicates the sonic boundary of the jet, where the Mach number is unity. The density field in the top plane is approximately symmetrical about the nozzle center axis (z - axis). The shapes of the boundaries of the expansion and compression regions in the first shock-cell just downstream of the nozzle exit are approximately triangular, but their shapes change to round for downstream shock cells. In the first shock-cell, a short Mach stem can be observed at the outer boundary (z = about 5 mm) of the expansion and compression regions. The density field in the side plane is asymmetric with respect to the nozzle centerline (z-axis), and the sonic boundary of the jet is slightly downward with increasing streamwise distance. It was found that the structures of the shock wave, compression and expansion regions in the two characteristic cross sections inside the jet can be quantitatively revealed.

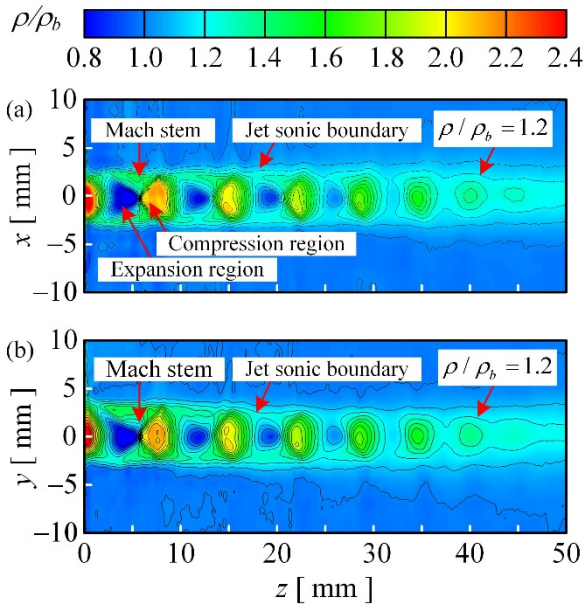

Fig. 1. Density contour plots in the (a) top plane and (b) side plane with the flow from left to right.

4. References

[1] E. Gutmark, K.C. Shadow, and K.J. Wilson (1991). Subsonic and supersonic combustion using noncircular injectors, *J. Propuls. Power*, **7**, 240-249.

[2] Y. Umeda and R. Ishii (1994). Oscillation modes of underexpanded jets issuing from square and equilateral triangular nozzles, *J. Acoust. Soc. Am.*, **95**, 1853-1857.

[3] A. Sureshkumar and B.T.N. Sridhar (2019). Experimental studies on decay and spread characteristics of an overexpanded triangular supersonic jet, *Fluid Dynamics*, **54**, 629-639.

STUDY OF DIAMOND UNDEREXPANDED SONIC JETS

K. Tanaka[1], T. Miyaguni[1], S. Nakao[1] and Y. Miyazato[1]
[1] Department of Mechanical Systems Engineering, The University of Kitakyushu, Japan

1. Introduction

Supersonic jets have been widely used in many industries, such as soot blowers for removing soot from the surface of heat transfer tubes in thermal power plants and gas-atomization for fine-graining metal powders. Numerous experimental, theoretical, and numerical simulation studies have been conducted on supersonic jets issuing from so-called axisymmetric nozzles with a circular cross-section. The diameter of the Mach disk and the position in the flow direction where the Mach disk occurs, the shock-cell spacings, and the noise characteristics caused by the shock wave have been clarified. To achieve a supersonic jet with superior mixing and noise characteristics without significant thrust loss, Alvi et al. [1] explored the possibility of a diamond-shaped nozzle. Using conventional schlieren and planar laser scattering flow visualizations, as well as Pitot pressure measurements, Alvi et al. experimentally investigated the flow and noise characteristics of supersonic jets emanating from a diamond-shaped nozzle with a design Mach number of 2.0, and found the presence of distinct structures in the shear layers that are not normally observed in ideally expanded axisymmetric and rectangular jets. Saleh et al. [2] investigated aeroacoustics of supersonic jets produced by a diamond-shaped Mach 2 nozzle operating at different nozzle pressure ratios ranging from highly overexpanded to moderately underexpanded. They found that the diamond jet exhibits a highly directional acoustic field with a distinct local minimum for sideline noise. In addition, screech behavior can be only observed in a narrow, overexpanded flow regime. Supersonic jets emerging from non-axisymmetric nozzles have been experimentally clarified only to a small extent due to difficulties in quantitative measurement techniques, despite their engineering and academic importance. In this study, the flow features of an underexpanded jet emerging from a diamond-shaped convergent nozzle have been experimentally investigated using rainbow schlieren tomography [3].

2. Experimental methods

Experiments were conducted in an intermittent compressed air facility. Dry air from two successive 1-m^3 high-pressure tanks, normally pressurized to 1.0 MPa, enters a plenum chamber through the coupling and is discharged into atmosphere through a flange-mounted test nozzle. The cross section of the flow path at the nozzle exit is diamond-shaped with semi-major and semi-minor axis lengths of 6.25 mm and 1.57 mm, respectively. The equivalent diameter of the cross section of the flow pass at the nozzle exit is D_{eq} = 5.0 mm. Quantitative flow visualization is performed using rainbow schlieren tomography. The ratio NPR (= p_{os}/p_b) of the pressure p_{os} in the planum chamber to the back pressure p_b was adjusted at 4.0 to produce underexpanded jets. The back pressure is p_b = 101.5 kPa and the ambient temperature is T_b = 297.9 K. In the present experiment, the test nozzle was rotated from 0° to 180° at equal intervals of 5° to obtain a total of 37 rainbow schlieren images of the jet. Rainbow schlieren images with the horizontal setting were utilized to obtain the jet density field.

3. Results and conclusions

The density fields in the major and minor axis planes are shown in Figs. 1(a) and 1(b), respectively, with the flow from left to right. The density fields are non-dimensionalized in terms of atmospheric density (ρ_b), with minimum and maximum normalized densities of 0.6 and 2.2, respectively, with contours drawn every $\rho/\rho_b = 0.1$. The spatial resolution of the present rainbow schlieren system is approximately 11 μm in the object plane, which can be evaluated based on the physical and image dimensions of the test nozzle. It should be noted that these figures are not integrated in the viewing direction, but are density fields in the cross section including the central axis of the jet. Thes density fields are expected to be useful for quantitative comparisons with density fields obtained by other measurement methods, such as the background oriented schlieren (BOS) and Mach-Zehnder interferometry, or for validation of density fields obtained by numerical simulations. In the density field in the minor-axis plane, upstream-curved shocks can be observed at z = approximately 5 mm and 12 mm. The width of the jet outer boundary is almost constant in the flow direction until about 20 mm from the nozzle exit, after which it gradually widens to about z = 30 mm and then becomes constant again in the flow direction. On the other hand, in the density field of the major axis plane, an incident shock extending from just after the nozzle exit lip to the central axis and its reflected shocks can be observed, which together form an approximately X-shaped shock. Immediately after this x-shaped shock, a reduced isodensity contour plot with an almost X-shaped shape is clearly visible. The width of the jet outer boundary decreases gradually in the flow direction from the nozzle exit. It was found that three-dimensional density field of a shock-containing triangular jet can be clarified quantitatively using rainbow schlieren tomography.

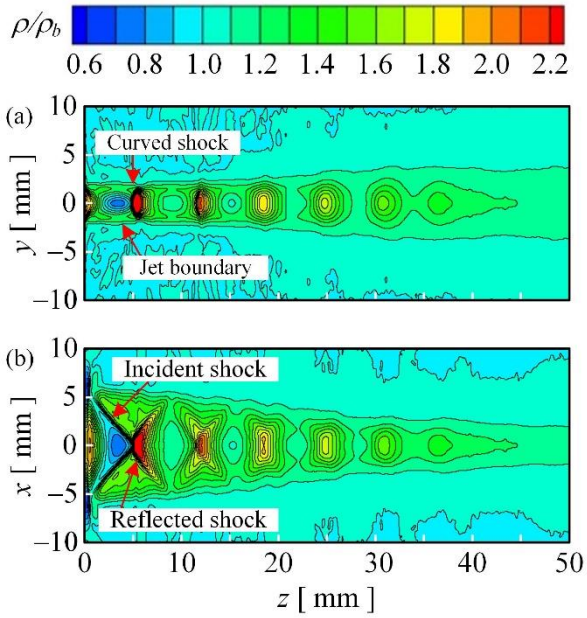

Fig. 1. Density contour plots in the (a) minor axis plane and (b) major axis plane.

4. References

[1] F.S. Alvi, A. Krothapalli, D. Washington, and C.J. King, (1996), Aeroacoustic properties of a supersonic diamond-shaped jet, *AIAA J.*, **34**, 1562-1569.

[2] Y. Saleh, P. Sellappan, and F.S. Alvi, A., (2023), Experimental characterization of supersonic diamond jet acoustics, *AIAA J.*, **61**, 4546-4555.

[3] T. Nagata, T. Sakashita, S. Nakao, and Y. Miyazato (2024). Three-dimensional flow features of underexpanded jets emerging from an elliptic convergent nozzle, *Exp. Fluids.*, **65**, 146.

SHOCK STRUCTURES IN NINJA-STAR UNDEREXPANDED SONIC JETS

R. Uchida[1], T. Miyaguni[1], S. Nakao[1] and Y. Miyazato[1]
[1] Department of Mechanical Systems Engineering, The University of Kitakyushu, Japan

1. Introduction

Supersonic jets have been widely used in many industries, such as soot blowers for removing soot from the surface of heat transfer tubes in thermal power plants and gas-atomization for fine-graining metal powders. Numerous experimental, theoretical, and numerical studies have been conducted on supersonic jets issuing from so-called axisymmetric nozzles with a circular cross-section. The diameter of the Mach disk and the position in the flow direction where the Mach disk occurs, the shock-cell spacings, and the noise characteristics caused by shock waves have been clarified. Menon and Skews [1] investigated underexpanded jets issuing from convergent nozzles with circular, elliptical and slotted cross sections using shadowgraph technique and Reynolds-averaged Navier-Stokes (RANS) simulation. Edgington-Mitchell et al. [2] experimentally investigated the unsteady characteristics of elliptic underexpanded sonic jets. Nagata et al. [3] quantitatively revealed the three-dimensional structure of the elliptical jet with shock waves using rainbow schlieren tomography [4]. On the other hand, Fukunaga et al. [4] have clarified the three-dimensional density field of underexpanded jets emerging from rectangular convergent nozzles. Supersonic jets emerging from non-axisymmetric nozzles other than rectangular and elliptical have been experimentally clarified only to a small extent due to difficulties in quantitative measurement techniques, despite their engineering and academic importance. In this study, the shock structures in an underexpanded sonic jet emerging from a ninja-star-shaped convergent nozzle are visualized quantitatively by rainbow schlieren tomography.

2. Experimental methods

The experiment is conducted in an intermittent compressible air facility. Compressed dry air from a high-pressure tank passes through a coupling and is discharged into the atmosphere through a test nozzle, which is fixed to a flange of the plenum chamber. The Cartesian coordinate system (x,y,z) is employed with its origin at the center of the nozzle exit plane and it has the x-axis in the horizontal axis direction, the y-axis in the vertical direction, and the z-axis in the flow direction. The flow path at the exit of the nozzle is a four-point ninja star, which is a square with a side of 2.68 mm surrounded by four equilateral triangles with a side of 2.68 mm. The equivalent diameter of the flow pass at the nozzle exit is D_{eq} = 5.0 mm. Quantitative flow visualizations are performed using rainbow schlieren tomography. The rainbow filter is placed parallel to the flow direction in the schlieren cutoff plane. The rainbow filter is calibrated prior to the experiment. The ratio NPR (p_{os}/p_b) of the stagnation pressure p_{os} in the plenum chamber to the back pressure p_b is adjusted at 4.0 to produce underexpanded jets with strong shocks. The back pressure is p_b = 102.1 kPa and the ambient temperature is T_b = 298.4 K, which is equal to the plenum temperature. The Reynolds number based upon the equivalent diameter and flow properties at the nozzle exit is 3.4 $\times 10^5$. In the present experiments, the nozzle is rotated from 0 to 90 at equal intervals of 5 to obtain a total of 19 rainbow

schlieren images of the jet. Since the test nozzle is symmetrical about the symmetric-axis plane, schlieren images of jets from 90 to 180 are replicated from the images obtained in the first quadrant. The convolution back projection method is used to reconstruct the jet three-dimensional density field. The spatial resolution of the present optical system is 13.3 μm in the object plane.

3. Results and conclusions

The magnitudes of the density gradient vectors are shown in Fig. 1 with the flow from left to right. This representation is useful in highlighting the physical structure of the shock wave and the root of expansion fan. The red dashed line parallel to the z-axis in each figure indicates the lip line. Figure 1 clearly shows the two-dimensional shock structures in the symmetric-axis and diagonal-axis planes of the ninja-star underexpanded sonic jet. Figure 1(a) clearly shows that an incident shock generated from the upper nozzle lip is reflected at the jet centerline, becoming a strong oblique shock that reaches the jet boundary and forms expansion waves. The width of the upper and lower jet boundaries gradually decreases in the flow direction. On the other hand, in the diagonal-axis plane, expansion waves from the lower nozzle lip are reflected at the opposite jet boundary to form compression waves, which accumulate to form an oblique shock. In this study, the three-dimensional density field of a shock-containing ninja-star jet was measured using rainbow schlieren tomography. In addition, the shock structures in the two characteristic cross sections inside the jet were revealed quantitatively.

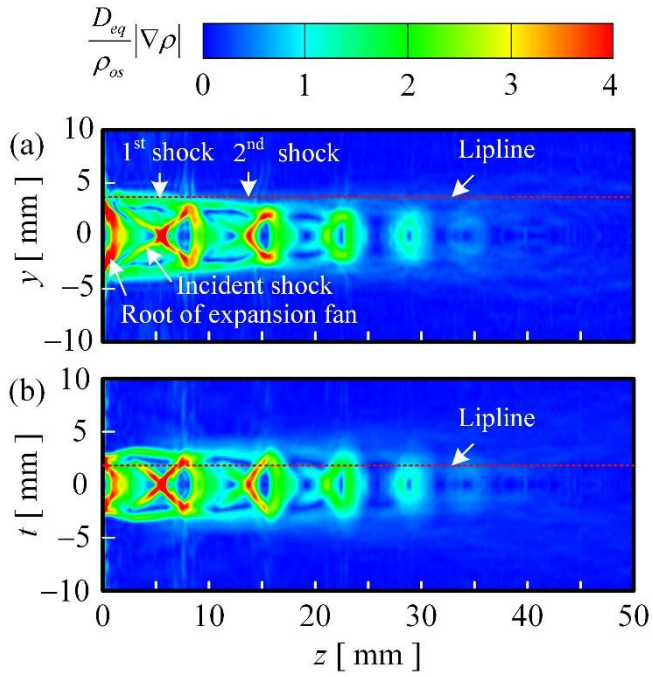

Fig. 1. Shock structures in the (a) symmetric-axis plane and (b) diagonal-axis plane

4. References

[1] N. Menon and B.W. Skews (2010). Shock wave configurations and flow structures in non-axisymmetric underexpanded sonic jets, *Shock Waves*, 20, 175-190.

[2] D.M. Edgington-Mitchell, D.R. Honnery, and J. Soria (2015).,Multimodal instability in the weakly underexpanded elliptic jet, *AIAA J.*, 53, 2739-2749.

[3] T. Nagata, T. Sakashita, S. Nakao, and Y. Miyazato (2024). Three-dimensional flow features of underexpanded jets emerging from an elliptic convergent nozzle, *Exp. Fluids.*, **65**, 146.

[4] R. Fukunaga, M. Ezoe, S. Nakao, and Y. Miyazato (2022). Application of rainbow schlieren tomography for shock-containing rectangular jets, *J. Vis.*,25, 687-695.

A calibration method of fringe projection profilemetry based on optical ray model correction

Wenxin Hu[1], Chen Xiong[2], Yan Liu[3]
[1] Artificial Intelligence Research Institute, Shenzhen MSU-BIT University, Shenzhen, China
[2] School of Intelligent Systems Engineering, Sun Yat-sen University, Guangzhou, China
[3] College of Physics and Optoelectronic Engineering, Shenzhen University, Shenzhen, China

1. Introduction

Accurate calibration is the prerequisite for the fringe projection profilometry [1,2] system to complete 3D reconstruction. Stereo vision calibration and phase 3D mapping calibration are two commonly used methods at present. The former treats the projector as an inverse camera, and forms a binocular system with the camera, and then uses the binocular vision principle to complete the calibration. Some related research focused on pattern design [3], parameter optimization [4] and error compensation [5]. The core of the latter is to accurately obtain the phase and three-dimensional coordinates of each pixel [6,7]. Researchers have proposed a series of methods such as projecting orthogonal fringes, using display instead of calibration board, B-spline interpolation, etc., but the process is relatively complicated. How to improve the efficiency of calibration algorithm without sacrificing accuracy is still a major research topic.

2. Methods

The present study propose a phase 3D mapping method based on camera ray model. Sinusoidal fringes are projected onto the chessboard under different positions. In order to establish the polynomial mapping relationship, the three-dimensional coordinates and absolute phase of a series of points on the ray passing through each pixel are calculated accurately. The three dimensional coordinates of the intersection points of the light ray and the checkerboard plane of each pose are converted to the reference plane by the conversion matrix, and corrected by the ray equation. Surface fitting method is adopted to improve the phase accuracy after four-step phase shifting calculation, and a fixed reference point is used to obtain absolute phase. This method does not need to accurately characterize the imaging process and distortion. The calculation process is simplified to some extent compared with the current advanced methods to find the corresponding points point by point or B-spline interpolation.

3. Results and conclusions

The results of the calibrated ray model are consistent with the imaging model of the camera, as shown in Fig.1. The error distribution of of the standard plane is shown in Fig.2, and the RMS error is 0.0374mm, which proves the effectiveness of the proposed method.

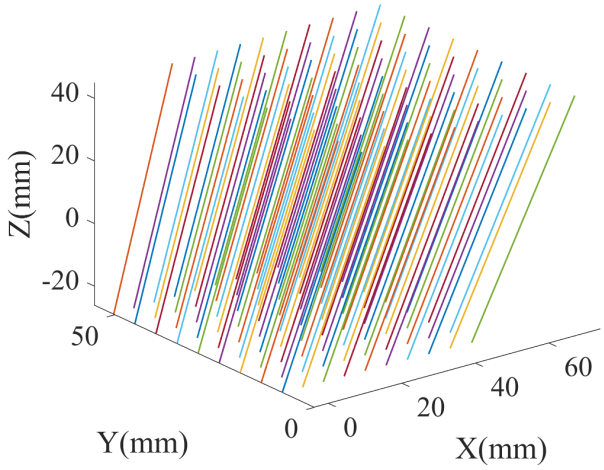

Fig. 1. Camera light calibration results

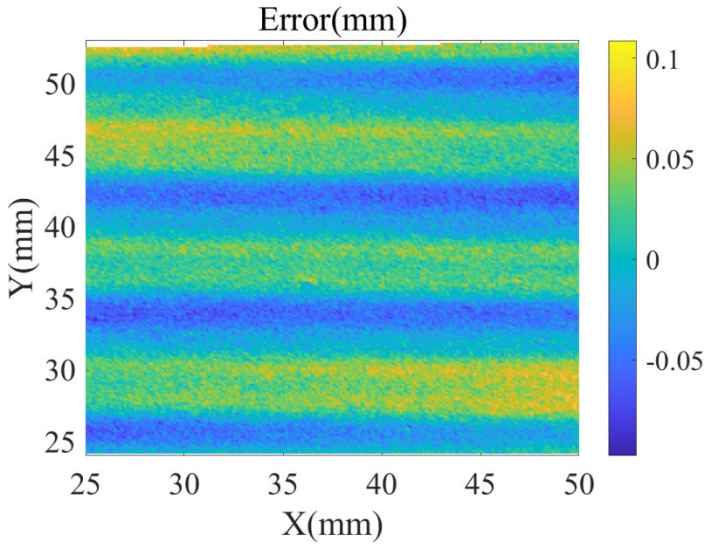

Fig. 2. Error distribution

4. Acknowledgements

The research presented in this paper has received funding from the National Natural Science Foundation of China No. 12102267.

5. References

[1] Lin J, Dou Q, Cheng Q, et al. (2025). Binocular composite grayscale fringe projection profilometry based on deep learning for single-shot 3D measurements. Optics and Lasers in Engineering, 185108701-108701.

[2] Xuan Li, Hongru Li, Hao Wei, Sha Wang, Songsong Zhu, Nan Jiang... & Guoliang Deng (2025). An improved quaternary complementary Gray code phase unwrapping method in fringe projection profilometry. Optics and Lasers in Engineering, 108680-108680.

[3] Ke F, Xie J, Chen Y, Zhang D, Chen B (2014). A fast and accurate calibration methodfor the structured light system based on trapezoidal phase-shifting pattern. Optik, 125(18): 5249-53.

[4] Yin Y, Peng X, Li A, Liu X, Gao BZ (2012). Calibration of fringe projection profilometrywith bundle adjustment strategy.Opt Lett, 37(4): 542-4.

[5] Lv S, Sun Q, Zhang Y, Jiang Y, Yang J, Liu J, et al. (2020). Projector distortion correctionin 3d shape measurement using a structured-light system by deep neural networks.Opt Lett, 45(1):204-7.
[6] Junlin Du, Xiaopeng Luo, Jiangping Zhu, Shiyong An, and Pei Zhou (2024). Flexible and accurate system calibration method in microscopic fringe projection profilometry. Appl. Opt., 63: 383-389.
[7] Qi, C., & Feng, P. (2024). Calibration method for fringe projection profilometry with complex distortion based on B-spline surface. Optics and Lasers in Engineering, 180: 108323.

TIME-GATED ACTIVE-IMAGING DIGITAL IMAGE CORRELATION: A NOVEL SOLUTION FOR ULTRA-HIGH TEMPERATURE DEFORMATION MEASUREMENT

Liping Yu[1], Ning Lu[1], Bing Pan[1]
[1] National Key Laboratory of Strength and Structural Integrity, School of Aeronautic Science and Engineering, Beihang University, Beijing 100191, China

1. Introduction

The ability to measure or monitor the deformation at elevated temperatures (ranging from 600°C to 3000°C) is of vital importance for the strength tests of various heat-resisting and thermal-protective materials/structures in aerospace and aero-engine industries. Conventional contacting approaches (e.g., high-temperature strain gages and high-temperature optical fiber sensors) measure the thermal deformation by physically attaching/bonding the sensors to the area of interest on the sample surface, which offer limited spatial resolution (pointwise in one individual direction), operate in a limited temperature range (usually below 800°C) and possess low measurement precision (require complex temperature compensation) in a high-temperature environment. By contrast, digital image correlation (DIC) can realize full-field measurement with wider applicable temperature and higher measuring accuracy, thus have been increasingly advocated for high-temperature deformation measurement of various materials and structures [1].

Being an image-processing technique in essence, DIC measurements rely heavily on the quality of the recorded images in terms of accuracy and precision. Usually, high-quality images with sufficient and stable intensity variations can be easily obtained by a conventional DIC system However, for the tests at higher temperatures or even ultra-high temperatures over 1000°C, the acquisition of digital images will be destroyed by the intensified thermal radiation of the heated sample and surrounding heating elements, the speckle pattern debonding problem and the heat haze. Among these challenges, the intensified thermal radiation bears the brunt as it may totally cover the speckle information on the specimen surface, leading to heavily saturated images. Currently, the most simple but effective approach to suppress the excess thermal radiation is integrating active image devices (bandpass filter and monochromatic light illumination) into conventional DIC systems [2]. This approach has been accepted as the standard routine for performing high-temperature DIC measurement. However, when the temperature of the object exceeds a certain value (i.e., 2000°C), neutral density filters, linear polarizing filters, or even an additional optical filter need to be manually added to the existing bandpass filter, which could induce additional artificial errors. Moreover, the active imaging method cannot adapt to rapidly changing thermal radiation from the heated sample and surrounding heating elements, particularly for the direct heating surface measurement under transient aerodynamic heating using quartz lamps and in an arc-heated wind tunnel.

Following the idea of active imaging, here we propose a novel time-gated active imaging digital image correlation method based on bandpass filtering and ultrafast gating techniques for high-temperature deformation measurement [3, 4]. The proposed method uses a powerful pulsed laser for illumination and then records the reflected pulsed laser light using a gated single-photon camera with an ultrashort exposure time, which is synchronized with the laser illumination device. As a result, the received radiation light from the heated object and the ambient light (including the reflection

lights from the environment and the surrounding heating elements) can be significantly reduced to a negligible level compared with the illumination light from the pulsed laser.

2. Methods

Figure 1 shows the schematic diagram of the ultraviolet time-gated active-imaging DIC system, which mainly includes a powerful pulsed laser (e.g., UV) that illuminates the heated sample with periodic short pulses, a bandpass optical filter, a lens, a gated single-photon camera a computer and the corresponding synchronization device for precisely controlling the emission of the laser and the gate open of the single-photon camera. As shown in Fig.1(a), when working, the pulsed UV laser was triggered by the single-photon camera through its built-in trigger output channel at the set frequency and timing, emitting periodic UV pulses with a pulse width of t_{pulse} (as shown in Fig.1(b)). The pulsed laser passes through the laser beam expander to form a uniform active illumination and illuminate the heated object surface. Then the reflected UV pulses, together with the intense thermal radiation and the ambient light, will be filtered by the UV bandpass optical filter. As a result, most of the pulsed UV laser and very limited thermal radiation/ambient light can enter the imaging lens, as shown in Fig.1(b). Later, the single-photon camera is timely activated with a time-gate (t_{gate}) close to t_{pulse}, and the filtered light rays are amplified by the image intensifier inside the single-photon camera and collected by the camera sensor. Note that the detector shutter will close immediately after this time-gate and only the light rays within this time-gate can be recorded by the camera. As shown in Fig.1(b), due to the strong peak power, the intensity of the pulsed UV laser (active illumination) distinctly overwhelms that of the filtered thermal radiation and the ambient light within each time gate. In summary, the enormous thermal radiation emitted from the heated sample can be suppressed to a negligible level by shielding the most transmitted wavelength using a UV bandpass optical filter in the spectral domain and dramatically reducing the exposure time with the gated single-photon camera in the time domain. Despite the use of a pulsed laser, the effective signal from the active illumination remains weak compared to conventional imaging systems with longer exposure times, typically in the tens of milliseconds. To address this, the image intensifier in the single-photon camera can enhance the received photons by amplifying the weak signals, ensuring clear and high-quality images. Following we will briefly introduce the mechanism of thermal radiation suppression in spectral and time domains.

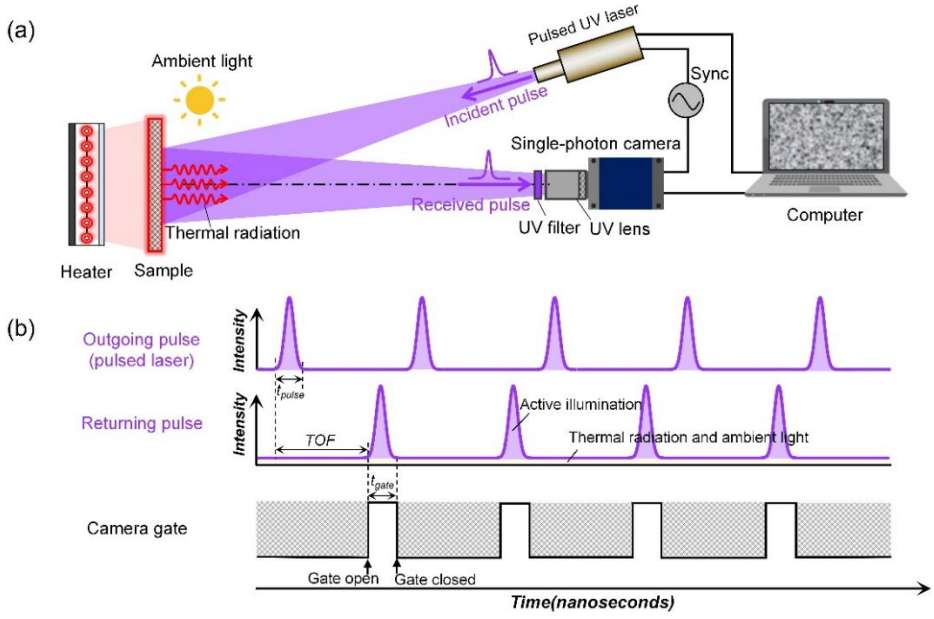

Fig.1 Schematic diagrams of (a) the ultraviolet time-gated active-imaging DIC system and (b) the principle of time-gated imaging.

3. Results and conclusions

To verify the effectiveness of the proposed ultraviolet time-gated active-imaging DIC system for ultra-high-temperature deformation measurement, we conducted a thermal expansion and tensile test on a carbon-carbon composite material sample. Fig. 2(a) depicts the carbon-carbon composite material sample, which has an overall length of 130 mm and a specific tensile section of approximately 40 mm. The specimen's diameter was measured as 8 mm. The experimental setup for high-temperature deformation measurement using the established system is illustrated in Fig. 2. As shown in the figure, only the central observation window was used for imaging the test sample through the ultraviolet time-gated active-imaging DIC system, while the pulsed UV laser illuminated the test sample from the right observation window. Thermal and mechanical loading during the high-temperature tensile test was performed using a high-temperature universal testing machine equipped with sealed chambers. The sealed chamber creates a vacuum environment, eliminating potential image distortion caused by heat haze between the specimen and the heating source.

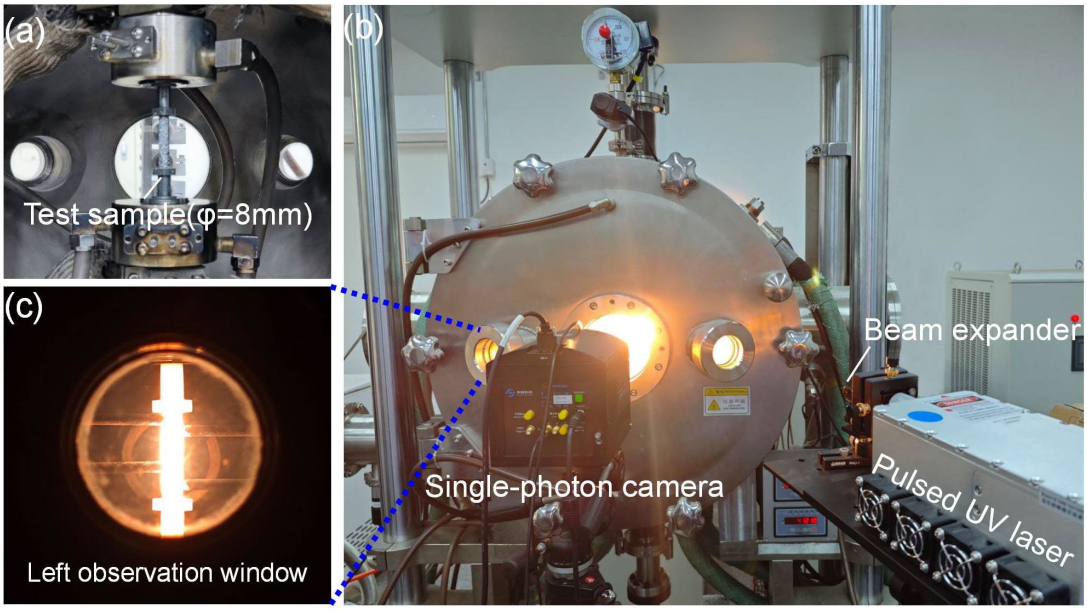

Fig.2 Experimental set-up for the high-temperature strain measurement using the established ultraviolet time-gated active-imaging DIC system.

Figure 3 presents images of the sample surface recorded by a normal camera at various temperatures and by the established ultraviolet time-gated active-imaging DIC system. Figure 4(a) illustrates the measured thermal strain along the vertical direction as a function of the applied temperature. The data indicate that the measured axial strain increases with the applied temperature, demonstrating a temperature-dependent thermal expansion property. Additionally, Figure 4(b) presents the Coefficient of Linear Thermal Expansion (CLTE) along the axial direction as a function of temperature. Below 1400°C, the CLTE value of the test sample stabilizes at approximately 0.55×10^{-6}/°C. As the temperature rises from 1400°C to 2400°C, the CLTE value shows a linear upward trend, reaching nearly 2×10^{-6}/°C at 2400°C. Beyond this temperature, the CLTE exhibits a significant increase with temperature. These observations lead to the conclusion that the CLTE of the tested carbon-carbon composite material is highly temperature-dependent. The underlying mechanism of this property is complicated and beyond the scope of this work.

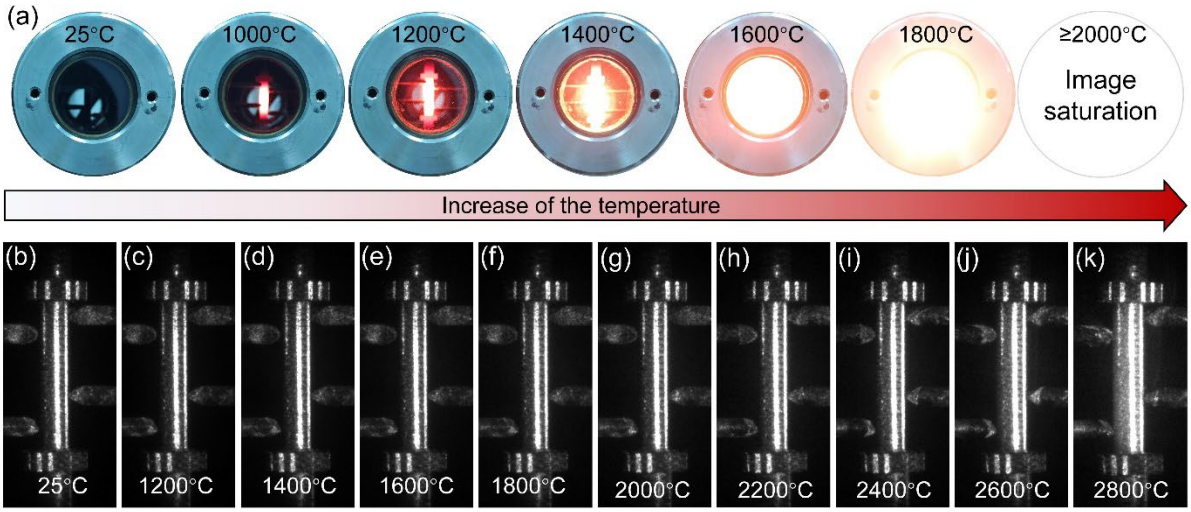

Fig.3 (a) images of the sample surface recorded by a normal camera at different temperatures, (b-k) the left sub-images of the test sample captured by the established ultraviolet time-gated active-imaging DIC system.

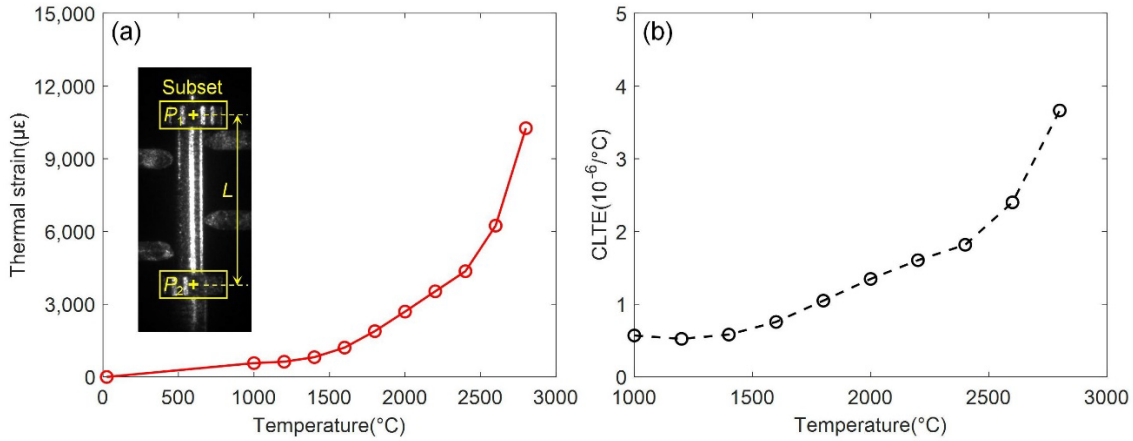

Fig.4 (a) The measured thermal strain along the vertical direction and (b) the determined coefficient of linear thermal expansion as a function of the applied temperature.

The proposed approach extends the temperature range and environmental resilience of DIC, positioning it as a powerful and novel solution for ultra-high temperature deformation measurement in aerospace and aero-engine applications. Future work may focus on further optimizing the system for even higher temperatures and enhancing the measurement accuracy, and exploring additional applications in various high-temperature environments.

4. Acknowledgements

This work is supported by the National Natural Science Foundation of China (Grant nos. 11925202 and 12102022)

5. References

[1] Lyons J S, Liu J, Sutton M A. High-temperature deformation measurements using digital-image correlation, *Exp. Mech.*, 1996, 36: 64-70.
[2] Grant B M B, Stone H J, Withers P J, et al. High-temperature strain field measurement using digital image correlation, *J. Strain Anal. Eng. Des.*, 2009, 44(4): 263-271.

[3] Yu L, Pan B. Time-gated active imaging digital image correlation for deformation measurement at high temperatures, *Extreme Mech. Lett.*, 2022, 54: 101767.
[4] Yu L, Lu N, Lu K, et al. Ultraviolet time-gated active-imaging digital image correlation: A novel solution for ultra-high temperature deformation measurement, *Opt. Laser Technol.*, 2025, 181: 111971.

6-11 July 2025 ICEM21 Bologna
21st International Conference on EXPERIMENTAL MECHANICS

COUPLING EFFECT BETWEEN DEFORMATION AND BLOOD CONDITION ON SKIN REFLECTANCE SPECTRUM IN-VIVO

Wang Shibin[1], Huo Zongze[1], Yu Qiaoyun[1],Ji Boyang[1], Wang Zhiyong[1], Li Chuanwei[1], Li Linan[1], Ma Jiangxiong[2]

[1] Department of Mechanics, School of Mechanical Engineering, Tianjin University, Tianjin, China
[2] Tianjin Hospital, Tianjin, China

1. Introduction

Skin reflectance spectra contain rich information about the body, and their understandings have developed various non-invasive diagnostic and health monitoring techniques. Hyperspectral imaging (HSI), by capturing a broad wavelength range, has expanded the scope for understanding physiological and physical properties about the body [2]. The dynamic skin spectral reflectance model (DSSR) quantifies skin deformation impacts on reflectance spectra through establish the relationship between reflectance, skin thickness and surface strain [3,4].

This study investigates the coupling effect between the skin strain change and the blood conditions on the reflectance spectrum, using HSI. The vein skin, compared to the non-vein skin, responds to strain with a different reflectance change. By introducing the relationship between skin thickness and blood volume fraction in to the DSSR model, we reveal the skin spectral response to surface strain and blood volume fraction. This understanding aids in non-invasive measurements measurement and health monitoring using optical sensing.

2. Materials and methods

We used a hyperspectral camera with a resolution of 387×696 pixels, capturing spectra from 377.70 to 1024.70 nm, illuminated by two 1000W halogen lamps, to measure forearm skin reflectance in vivo under strain. Reflectance calibration was done using a white board. A loading device with chutes and crossbars, affixed to the skin, facilitated deformation measurement. Figure 1(A-B) provide the experimental setup.

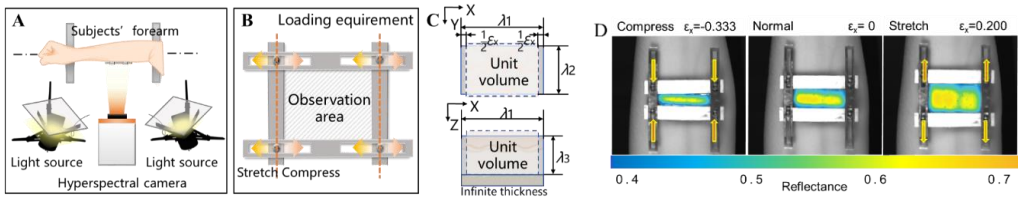

Figure 1. (A) Hyperspectral experimental setup. (B) Schematic of the experimental loading setup. (C) Schematic diagram of stretch ratios in the DSSR model. (D) Hyperspectral images of the spectral response of forearm skin under deformation in 850-1000 nm wavelength.

DSSR model describes how skin spectral reflectance R_{skin} changes with surface mechanical deformation ε_x, the stretch ratio direction as shown in Fig1 (C). It hypothesizes a rough epidermal surface and treats the epidermis and dermis as thin films, with the hypodermis as a semi-infinite body. $R_{skin}(\lambda)$ is the ratio of reflected to incident light intensity. The light escaping the skin includes direct epidermal reflection $R_{reflect}$ and light entering the skin, undergoing absorption and scattering by tissues, and then escaping $R_{scatter}$. Thus, we have

$$R_{skin}(\lambda,\varepsilon_x)=R_{reflect}(\lambda,\varepsilon_x)+(1-R_{reflect}(\lambda,\varepsilon_x))R_{scatter}(\lambda,\varepsilon_x) \quad (1)$$

$R_{reflect}$ is calculated by the Torrance–Sparrow model. $R_{scatter}$ can be expressed by the Kubelka-Munk theory, determined by the skin strain, wavelength, and the material compositions of each layer.

We introduce a hyper-elastic model to describe the relationship between the surface strain and thickness contains the vessels. Our model represents the skin as an orthotropic hyper-elastic material. It hypothesizes that the strain on the underlying dermis and hypodermis is the same as that of the epidermis. Thus, the thickness of the i-th layer h_i under strain ε_x is composed of the thickness of the skin matrix $h_{i,bs}$ and the thickness of the blood vessels $h_{i,blo}$, described as

$$h_i(\varepsilon_x)=h_{i,bs}(\varepsilon_x)+h_{i,blo}=h_{i,0}\cdot\lambda_3(\varepsilon_x) \quad (2)$$

3. Results and conclusions

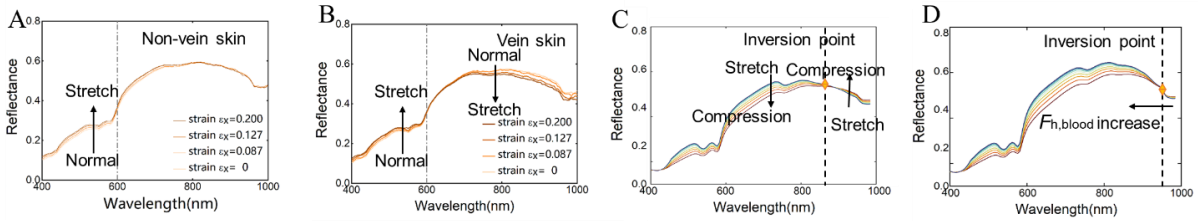

Figure 2. The experimental reflectance spectra of the skin stretched in (A) non-vein region and (B) vein region. The inversion point in spectral responses to strain, (C) indicates a reversal in spectra and (D) moves from higher to lower wavelengths with $F_{h,blood}$ increasing.

Figure2 (A) and (B) present the experimental spectra for both non-vein and vein skin under stretched in 400 to 1000 nm wavelength. Interestingly, while changes are consistent in the 400-700 nm range, they become subtler in non-vein skin in 700-1000 nm. In contrast, vein skin shows a reversal in trend from an increase to a decrease under stretch in 700-1000 nm wavelength. Through calibrating parameters and analysing the main factors, we introduce the "inversion point" as shown in Fig2 (C-D). It represents the reversal of the spectral trend. Fig 2(C) presents the reversal trend in inversion point. Fig 2(D) presents the shift trend of inversion point. As $F_{h,blood}$ increases, the inversion point shifts from higher to lower wavelength.

4. Acknowledgements

The research presented in this paper has received funding from the National Natural Science Foundation of China [Grant number 12472184].

5. References

[1] Z. Ou, Y. Duh, NJ. Rommelfanger, CHC. Keck, S. Jiang, Jr. Brinson K, S. Zhao, EL. Schmidt, X. Wu, F. Yang, B. Cai, H. Cui, W. Qi, S. Wu, A. Tantry, R. Roth R, J. Ding, X. Chen, JA. Kaltschmidt, ML. Brongersma and G. Hong (2024). Achieving optical transparency in live animals with absorbing molecules, *Science*, **385(6713)**, eadm6869.

[2] L. Bian, Z. Wang, Y. Zhang, L. Li, Y. Zhang, C. Yang, W. Fang, J. Zhao, C. Zhu, Q. Meng, X. Peng and J. Zhang (2024). A broadband hyperspectral image sensor with high spatio-temporal resolution, *Nature*, **635**, 73–81

[3] Z. Huo, S. Wang, H. Wei, X. Cheng, L. Li, C, L and Z. Wang (2024). A Dynamic Model for the Strain-Modulated Spectral Reflectance of the Human Skin in Vivo, *Biomed Opt Express*, **15(4)**, 2238-2250

[4] Z. Huo, H. Luan, H. Wei, S. Wang, X. Sun, L. Li, C, L and Z. Wang (2024). Research on Strain Modulation of Spectral Reflectance in Soft Materials, *Exp Mech*, **64**, 143–150

"DETERMINATION OF ISOCHROMATIC FRINGES USING MODIFIED MATLAB-BASED IMAGE PROCESSING TECHNIQUES"

Ramit Chugh[1], Shubhrata Nagpal [2], Shubhashis Sanyal [3]

1. *Ph.D. Research Scholar, Department of Mechanical Engineering, University Teaching Department, Chhattisgarh Swami Vivekanand Technical University, Bhilai, Chhattisgarh, India.*
2. *Professor, Department of Mechanical Engineering, Bhilai Institute of Technology, Durg, Chhattisgarh, India.*
3. *Professor, Department of Mechanical Engineering, National Institute of Technology, Raipur, Chhattisgarh, India.*

Abstract

The determination of isochromatic fringes is essential for understanding stress distribution in materials under load, particularly in photoelastic analysis. Previous research has highlighted challenges in threshold adjustment during fringe detection, which complicates image processing and reduces accuracy in stress analysis. Addressing these limitations, the current study utilizes MATLAB and introduces modified image processing techniques to enhance the determination of isochromatic fringes.

The advanced method simplifies the image processing workflow by implementing algorithms that dynamically adjust thresholds, minimizing manual intervention and ensuring more consistent results. By integrating these modifications, the approach effectively resolves issues related to noise and fringe order misinterpretation. High-precision epoxy models, fabricated through 3D printing, silicone moulding, and epoxy casting, were employed to validate the method, ensuring accurate and optically clear specimens.

Experimental results demonstrate the ability of the modified technique to reliably capture and interpret isochromatic fringes, particularly in geometries with intricate stress patterns. MATLAB's computational capabilities were leveraged to streamline image processing, automate fringe order identification, and enhance overall accuracy. Compared to traditional methods, this approach not only simplifies the process but also improves the resolution and clarity of fringe patterns.

This study offers a significant advancement in photoelastic analysis, addressing key challenges in threshold adjustment and image processing. The proposed method provides a robust framework for analyzing stress distribution in complex structures, with potential applications in engineering and material science research.

Keywords:
Photoelastic analysis, Isochromatic fringes, MATLAB, Image processing, Threshold adjustment, Stress distribution, Epoxy models, 3D printing, Silicone mould, Fringe detection.

INHOMOGENEOUS TENSILE DEFORMATION OF NITROGEN-ADDED Ti-Nb BASED SHAPE MEMORY ALLOYS

K. M. Golasiński[1], M. Maj[2], S. Musiał[2], W. Tasaki[3], E.A. Pieczyska[2] and H. Y. Kim[3]
[1] Multidisciplinary Research Center, Cardinal Stefan Wyszynski University in Warsaw, Warsaw, Poland
[2] Institute of Fundamental Technological Research, Polish Academy of Sciences, Warsaw, Poland
[3] Department of Materials Science, Institute of Pure and Applied Sciences, University of Tsukuba, Tsukuba, Ibaraki, Japan

1. Introduction

Ti-Nb based shape memory alloys (SMAs) exhibit shape memory effect or superelasticity due to the phase transformation from body-centered cubic β phase to orthorhombic α″ martensite [1, 2]. The addition of interstitial alloying elements, such as oxygen and nitrogen, can change the stress-strain response of these alloys [3, 4]. It is due to the formation of randomly distributed nanodomains. This strategy has been used to achieve and tailor specific properties of Ti-Nb SMAs, including superelastic deformation or invar-like behavior [4]. However, this class of SMAs has been seldom studied by means of digital image correlation (DIC), which can deepen the knowledge about the kinetics of deformation. The analysis of thermomechanical behavior of Gum Metal (Ti-23Nb-0.7Ta-2Zr-1.2O, at. %) under tensile loadings using infrared thermography and DIC did not present any local effects due to the high content of oxygen [5]. However, recent investigation of oxygen-added Ti-Nb SMAs in tension using DIC showed that the strain fields of these alloys are very inhomogeneous during the initial loading [6]. The objective of this study is to analyze and compare deformation fields of Ti-25Nb and Ti-25Nb-0.3N SMAs captured at selected stages of tension using DIC.

2. Materials and methods

The alloys were prepared by the Ar arc melting method using pre-melted sponges of Ti, pellets of pure Nb. The nitrogen concentrations of the alloys were adjusted by addition of TiN powder. The ingots were sealed in a vacuumed quartz tube and homogenized at 1273 K for 120 min with subsequent air-cooling. Then the ingots were cold-rolled with a reduction in thickness of 95%. Specimens for tensile tests were cut using an electro-discharge machine. Then, the specimens were solution-treated at 1173 K for 30 min in an Ar atmosphere, followed by water quenching. The damaged surface was removed by chemical etching at each step of the fabrication process. The surface of each specimen was first covered with soot and then small dots of white paint were sprayed onto the soot layer to obtain an adequate pattern for DIC. Displacement-controlled load-unload tensile tests of the SMAs specimens were carried out using an MTS 858 testing machine at room temperature. Maximal displacement of 0.35 mm and displacement rate of 0.12 mm/s were used. The gauge part of each specimen was 4 mm × 6 mm × 0.5 mm. Taking into account the specimen's geometry, an average strain rate of $2 \cdot 10^{-2}$ s^{-1} was applied. The deformation process of each specimen was monitored by a visible range (0.4 μm – 1 μm) sCMOS PCO Edge 5.5 camera for further DIC analysis.

3. Results and conclusions

True stress vs. true strain curves of Ti-25Nb and Ti-25Nb-0.3N SMAs under load-unload tension with ε_{yy} fields captured at selected stages of the deformation process are presented in Fig. 1(a) and 1(b), respectively. During the tension loading, the Ti-25Nb SMA exhibited a Lüders-type deformation via a development of macroscopic martensite bands at about 55° from the loading direction, which was clearly observed in ε_{yy} fields. The Ti-25Nb-0.3N SMA showed a different kind of deformation in a form of narrow bands with higher values of strain, which were perpendicular to the loading axis.

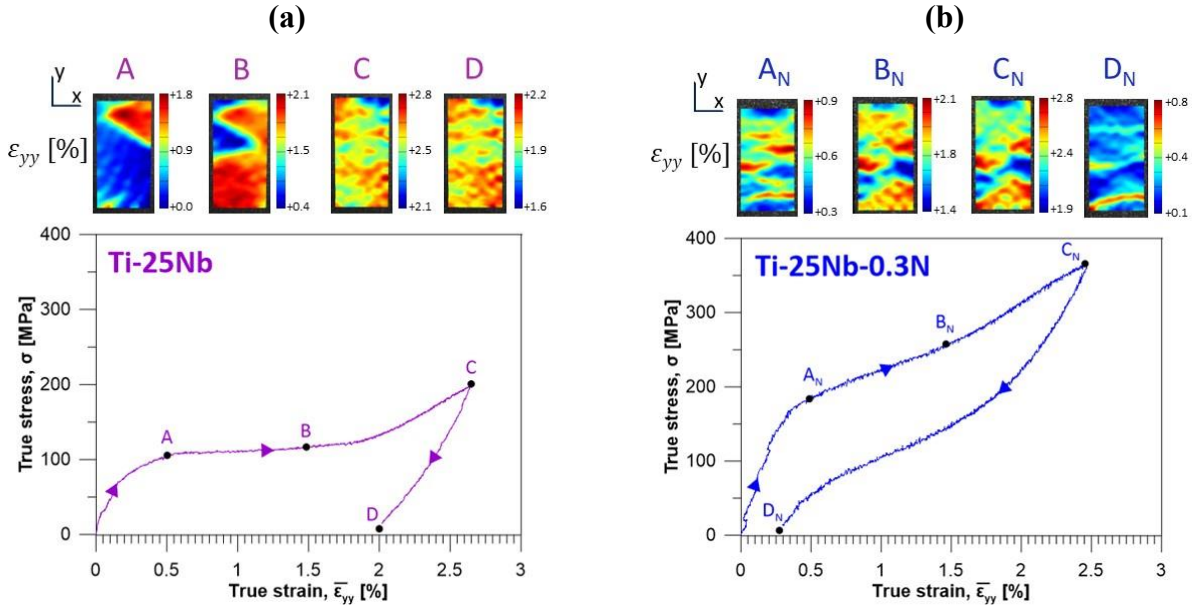

Fig. 1. True stress vs. true strain curves of (a) Ti-25Nb and (b) Ti-25Nb-0.3N SMAs under load-unload tension with ε_{yy} fields captured at selected stages of the deformation process.

4. Acknowledgements

Karol M. Golasiński acknowledges the support of the Japan Society for the Promotion of Science (JSPS) Postdoctoral Fellowship (ID No. P20812) and the National Science Centre, Poland through the Grant 2023/48/C/ST8/00038.

5. References

[1] H.Y. Kim, Y. Ikehara, J.I. Kim, H. Hosoda and S. Miyazaki (2006) Martensitic transformation, shape memory effect and superelasticity of Ti–Nb binary alloys. *Acta Mater.*, **54**, 2419-2429.

[2] M. Tahara, H.Y. Kim, H. Hosoda and S. Miyazaki (2009). Cyclic deformation behavior of a Ti–26 at.% Nb alloy. *Acta Mater.*, **57**, 2461–2469.

[3] M. Tahara, H.Y. Kim, H. Hosoda and S. Miyazaki (2009). Shape memory effect and cyclic deformation behavior of Ti–Nb–N alloys. *Funct. Mater. Lett.*, **2**, 79–82.

[4] S. Miyazaki (2017). My Experience with Ti–Ni-Based and Ti-Based Shape Memory Alloys. *Shap. Mem. Superelasticity*, **3**, 279–314.

[5] K. Golasiński, M. Maj, L. Urbański, M. Staszczak, A. Gradys and E.A. Pieczyska (2023) Experimental study of thermomechanical behaviour of Gum Metal during cyclic tensile loadings: the quantitative contribution of IRT and DIC. *Quant. InfraRed Thermogr. J.*, **21**, 259–276.

[6] K. Golasiński, M. Maj, W. Tasaki, E.A. Pieczyska and H.Y. Kim (2024) Full-Field Deformation Study of Ti–25Nb, Ti–25Nb–0.3O and Ti–25Nb–0.7O Shape Memory Alloys During Tension Using Digital Image Correlation. *Metall. Mater. Trans. A*, **55**, 2509–2518.

3D MOTION MEASUREMENT OF MOVING POINTS BASED ON A MONOCULAR CAMERA

Huayu Huang[1], Banglei Guan[1*], Zibin Liu[1], Ang Su[1], Zhang Li[1], Yang Shang[1], Xiaolin Liu[2] and Qifeng Yu[1]

[1] College of Aerospace Science and Engineering, National University of Defense Technology, Changsha, China

[2] College of Physics and Optoelectronic Engineering, Shenzhen University, Shenzhen, China

** Corresponding Author*

1. Introduction

The motion measurement of point targets constitutes a fundamental problem in photogrammetry, with extensive applications across various engineering domains. The conventional triangulation approach is geometrically sound and well-defined. Two lines of sight connecting the optical centers of the two cameras along with the baseline form a triangle, and the intersection of the two lines of sight is the position of the target point. This process is called triangulation. The triangulation technology of binocular vision has been systematically developed [1-2]. Unfortunately, the geometric constraint of triangulation becomes inapplicable when the point moves between image acquisitions. This situation is very common, because most artificial vision systems are monocular, and most real scenes contain moving targets [3- 4]. In this case, without reasonable assumptions about the target's motion, it is impossible to reconstruct the 3D trajectory of the target.

Motion measurement methods based on motion assumptions of the moving points have been explored in several studies [5-7]. For instance, Avidan et al. assumed the shape of the target trajectory as an additional constraint [5]. Park et al. Proposed to represent 3D trajectories using linear combinations of trajectory basis vectors [6]. This paper proposes a 3D trajectory reconstruction method of moving points based on a monocular camera. First, we use temporal polynomials to represent the point motion as an additional constraint and introduce ridge estimation to the least squares estimation system. Second, we propose an automatic selection algorithm for the degree of the temporal polynomials by minimizing an objective function of geometric error. Finally, we validate the efficiency, accuracy, and robustness of our method on both simulated data and real-world scenes.

2. Methods

Assuming that at the time t_i, the position of the camera is $\mathbf{C}_i = \begin{bmatrix} X_{Ci} & Y_{Ci} & Z_{Ci} \end{bmatrix}^{\mathrm{T}}$, which is accurately known. The position of the target is $\mathbf{P}_i = \begin{bmatrix} X_i & Y_i & Z_i \end{bmatrix}^T$. Let $\mathbf{P}_i$ be imaged as $\mathbf{p}_i = \begin{bmatrix} x_i & y_i \end{bmatrix}^{\mathrm{T}}$. The internal parameter $\mathbf{K}$ is calibrated in advance. The rotation matrix $\mathbf{R}_i$ of the camera can be calculated employing the technique of structure from motion within a given scene [2]. When the number of observations is N, the number of unknowns is $3N$, and the number of equations is $2N$. Therefore, utilizing the collinear equation to solve for the target position results in infinitely many solutions.

To calculate the position of the target, additional constraints must be imposed on its trajectory. We achieve this by expressing the target trajectory as polynomials of time:

$$\left(X_i = \sum_{k=0}^{K} a_k t_i^k \quad Y_i = \sum_{k=0}^{K} b_k t_i^k \quad Z_i = \sum_{k=0}^{K} c_k t_i^k \right), \tag{1}$$

where K is the degree of the polynomials. $a_k (k = \mathbf{0}, \mathbf{1}, \cdots, K)$, $b_k (k = \mathbf{0}, \mathbf{1}, \cdots, K)$, and $c_k (k = \mathbf{0}, \mathbf{1}, \cdots, K)$ are the motion parameters of the target that need to be solved. Combining Eq. (1) with the collinear equation, the number of unknowns is reduced to 3(K+1). When $\mathbf{2}N \geq \mathbf{3}(K + \mathbf{1})$N, the target position can be solved through the system of linear equations:

$$\mathbf{A}\boldsymbol{\beta} = \mathbf{B}, \tag{2}$$

Where $\boldsymbol{\beta}$ represents the motion parameters to be solved. However, under limited observation conditions, the 3D reconstruction error of the least squares estimation can be substantial or even cause degeneracies to occur. In such scenarios, the correlation of the observational data becomes significant, resulting in ill-conditioning of the system. This ill-conditioning severely undermines the accuracy and robustness of the estimation results. To address this issue and enhance the accuracy and stability of reconstruction results under limited observation conditions, we introduce ridge estimation. After adding the regularization term to the diagonal of the normal matrix of Eq. (2), the ridge estimation can be expressed as:

$$\boldsymbol{\beta} = (\mathbf{A}^{\mathrm{T}}\mathbf{A} - r\mathbf{I})^{-1}\mathbf{A}^{\mathrm{T}}\mathbf{B}, \tag{3}$$

Where r is the ridge parameter, and $\mathbf{I} \in \mathbb{R}^{\mathbf{3}(K+\mathbf{1})\times\mathbf{3}(K+\mathbf{1})}$ is the identity matrix. we adopt the Hoerl-Kennard-Baldwin ridge parameter selection method [8].

Our approach requires selecting the degree of the temporal polynomials, K. we propose an automatic selection algorithm for the degree of the temporal polynomials by minimizing an objective function of geometric error:

$$K_i^* = \underset{K_i}{\operatorname{argmin}} \sum_{j=\mathbf{1}}^{N} \| \hat{\mathbf{l}}_j - \mathbf{l}_j \|^2, \tag{4}$$

Where $\hat{\mathbf{l}}_j$ represents the direction vector from the camera's optical center to the reconstructed target.

3. Results and conclusions

The flight platform is equipped with a monocular RGB camera, which captures images at a spatial resolution of 1280 × 720 pixels and a temporal resolution of 25 Hz. We select three sequences of continuous observational imagery, each spanning approximately 30 seconds. We use the images to measure the motion parameters and trajectories of the target. The results were compared with the trajectory intersection method [7] (referred to as TI). Table 1 show that the proposed method can achieve the best calibration accuracy.

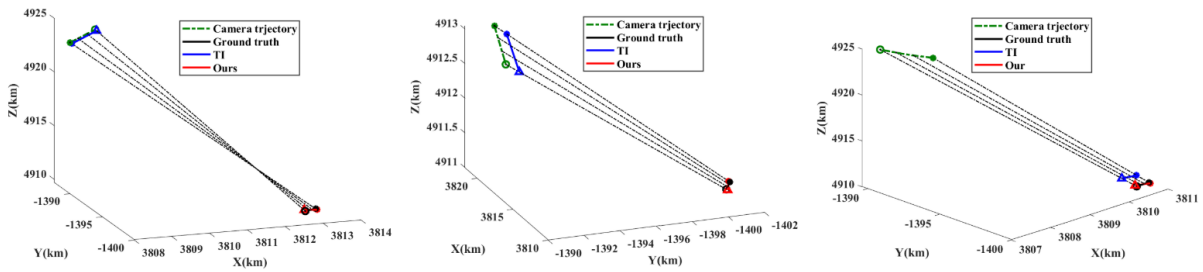

Fig. 1. Illustration of real-world experimental results

Group	a	b	c
TI method/m	16912.32	13258.37	908.36
Our method/m	**60.37**	**46.85**	**58.83**

Table 1. Localization error of flight experiments

4. Acknowledgements

This research has been supported by the Hunan Provincial Natural Science Foundation for Excellent Young Scholars under Grant 2023JJ20045, and the National Natural Science Foundation of China under Grant 12372189.

5. References

[1] H. C. Longuet-Higgins (1981). A computer algorithm for reconstructing a scene from two projections. Nature, 293, 133–135.

[2] R. Hartley, A. Zisserman (2004). Multiple view geometry in computer vision (2nd ed.). Cambridge university press.

[3] W. Tan, H. Liu, Z. Dong, G. Zhang, H. Bao (2013). Robust monocular slam in dynamic environments. IEEE International Symposium on Mixed and Augmented Reality (ISMAR), 209–218.

[4] M. R. U. Saputra, A. Markham, N. Trigoni (2018). Visual SLAM and structure from motion in dynamic environments: A survey. ACM Computing Surveys, 51, 1–36.

[5] S. Avidan, A. Shashua (2000). Trajectory triangulation: 3D reconstruction of moving points from a monocular image sequence, IEEE Trans. Pattern Anal. Mach. Intell., 22, 348–357.

[6] H. S. Park, T. Shiratori, I. Matthews, Y. Sheikh (2010). 3D reconstruction of a moving point from a series of 2d projections. European Conference on Computer Vision (ECCV), 6313, 158–171.

[7] Q. Yu, Y. Shang, J. Zhou, X. Zhang, L. Li (2009). Monocular trajectory intersection method for 3D motion measurement of a point target. Science in china Series E-Technological Sciences, 52, 3454–3463.

[8] A. E. Hoerl, R. W. Kannard, K. F. Baldwin (1975). Ridge regression: some simulations. Communications in Statistics-Theory and Methods, 4, 105–123.

APPLIED STRESS MODULATION OF BRILLOUIN OSCILLATIONS AT THE FILM-SUBSTRATE INTERFACE BY PICOSECOND ULTRASONICS

Yantao Zeng[1], Lin'an Li[1], Shibin Wang[1], Zhiyong Wang[1], Chuanwei Li[1]
[1] Department of Mechanics, School of Mechanical Engineering, Tianjin University, Tianjin, China

1. Introduction

With the rapid advancements in materials science and optoelectronic technologies, the non-destructive and precise characterization of interfacial properties at the microscopic level has emerged as a pivotal research focus. Picosecond ultrasonics is an ultrafast optical measurement technique that employs ultrashort laser pulses to generate and detect ultrasonic waves within materials [1]. This method is employed to investigate various characteristics of bulk and nanomaterials, ranging from elastic constants [2-3] to carrier diffusion [4]. It offers exceptionally high temporal and spatial resolutions, with temporal resolutions reaching femtoseconds to nanoseconds and spatial resolutions spanning nanometers to micrometers.

Brillouin oscillations are frequently observed in picosecond ultrasonics experiments. These oscillations primarily result from the interference between light reflected at the sample interface and light scattered by the acoustic pulses. In this study, based on picosecond ultrasonics, we investigate the relationship between Brillouin oscillation frequency and applied stress by combining the stress-optical effect and the acoustoelastic effect of the material. Additionally, this experimental phenomenon shows promise for development into a new method for measuring interfacial stress in film-substrate interfaces.

2. Materials and methods

Previous studies [1, 3, 5] have demonstrated that the Brillouin oscillation frequency f is dependent on the material's refractive index n, longitudinal sound velocity v, and the wavelength λ of the probe light, as shown in Eq. (1).

$$f = \frac{2nv}{\lambda} \tag{1}$$

Considering that the refractive index and longitudinal sound velocity of materials are modulated by applied stress σ, the Brillouin oscillation frequency will also vary with changes in the applied stress. Taking transparent glass materials as an example, our theoretical analysis led to the development of a linear model that describes the modulation relationship between the Brillouin oscillation frequency and the applied stress on the material, as shown in Eq. (2). To validate the accuracy of the model, experimental measurements were conducted on samples consisting of a 100 nm-thick chromium (Cr) film deposited on a high borosilicate glass (SiO_2) substrate, as shown in Fig. 1.

$$f = \frac{2n(\sigma)v(\sigma)}{\lambda} \approx A\sigma + B \tag{2}$$

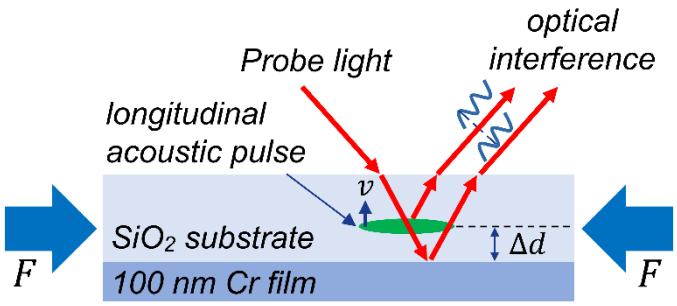

Fig. 1. Schematic diagram of the experimental setup.

3. Results and conclusions

Figure 2 shows the variation of the Brillouin oscillation frequency under three different compressive loads. The experimental results are in excellent agreement with our theoretical model, indicating that the Brillouin oscillation frequency can be used to quantify the internal stress distribution of the sample. Moreover, since the measurement region Δd is located near the interface, this method can also be applied to measure the stress near the thin film-substrate interface.

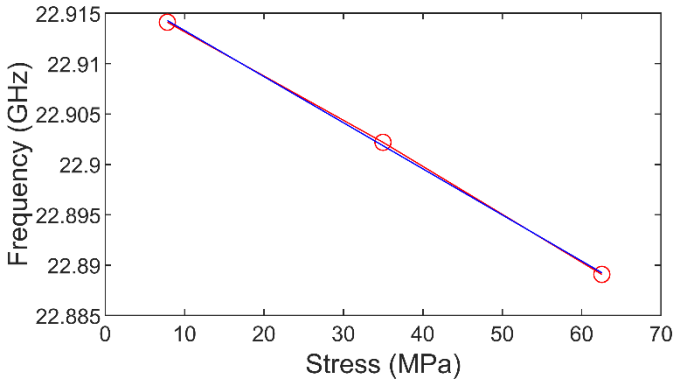

Fig. 2. Brillouin oscillation frequency variations of the sample under three different compressive loads.

4. Acknowledgements

The research presented in this paper has received funding from the National Natural Science Foundation of China (Project No. 12172251 and 12041201).

5. References

[1] O. Matsuda, M. C. Larciprete, Voti, R. Li, and O. B. Wright (2015). Fundamentals of picosecond laser ultrasonics, Ultrasonics, **56**, 3-20.

[2] P. A. Mante, S. Lehmann, N. Anttu, K. A. Dick, and A. Yartsev (2016). Nondestructive complete mechanical characterization of zinc blende and wurtzite GaAs nanowires using time-resolved pump–probe spectroscopy, *Nano Lett.*, **16**, 4792–4798.

[3] X. H. Tu, Y. T. Zeng, S. B. Wang, L. A. Li, et al (2022). Comprehensive characterization of thermal and mechanical properties in thin metal film-glass substrate system by ultrafast laser pump-probe method, *Optics Express*, **30**, 46193.

[4] O. B. Wright, B. Perrin, O. Matsuda, and V. E. Gusev (2001). Ultrafast carrier diffusion in gallium arsenide probed with picosecond acoustic pulses, *Phys. Rev. B*, **64**, 081202.

[5] Y. T. Zeng, L. A. Li, S. B. Wang, F. Y. Sun, et al (2024). Simultaneous measurement of cross-plane thermal conductivity and interfacial thermal conductance of nano-metal films on a low thermal diffusivity substrate using TDTR, *International Journal of Heat and Mass Transfer*, **227**, 125542.

6-11 July 2025 ICEM21 Bologna | 21st International Conference on EXPERIMENTAL MECHANICS

Electrowetting-actuated Liquid Iris for Switchable Aperture

C. Lee[1], S. Park[1], S. K. Chung[1] and J. Lee[2]
[1] *Department of Mechanical Engineering, Myongji University, Yongin, 17058, Republic of Korea*
[2] *Microsystems, Inc., Yongin, 17058, Republic of Korea*

1. Introduction

Conventional optical systems for imaging applications (camera modules and etc.) have faced significant challenges in miniaturization, due to bulky mechanical actuators made of solid elements. Specifically, a iris diaphragm with rotating blades is commonly used as a tuanble aperture to control image brightness and depth of focus. However, these components are susceptible to external shocks and material wear, resulting in reduced durability and a shorter operational lifespan. To solve these problems, the implementation of tunable optical devices made of liquid have received substantial attention from imaging applications. These liquid-based optical devices enable miniaturization by allowing precise control of liquid interfaces without eliminating the need for complex actuation mechanisms. Various technologies have been proposed for manipulating the shape or position of liquid droplets, including pneumatic pressure [1], magnetic actuation [2], and electrowetting [3-4]. Among these, electrowetting-based actuation is notable for its fast response times and low power consumption.

In this study, we present a novel microfluidic design and experimental results of a liquid-based optical iris with switchable aperture operated by electrowetting actuation (Fig. 1). The presented design achieves a compact structure and precise aperture control, providing the transition range of 2.5 to 5 mm in diameter for the aperture. Subsequently, the fabricated iris device was experimentally tested to investigate the behavior of a droplet inside a microchannel with different design variations and driving signals.

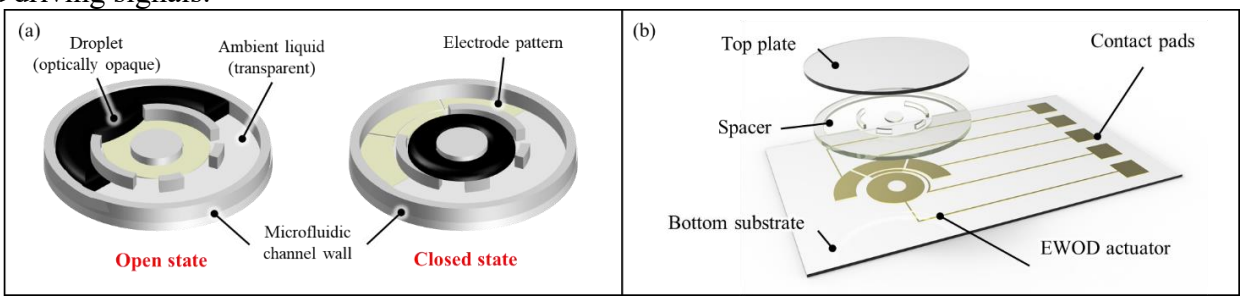

Fig. 1. (a) Schematic diagram of the proposed iris operated by EWOD actuation; (b) exploded diagram

2. Fabrication

The liquid-based iris was designed with a bottom glass substrate containing patterned electrodes, spacers to maintain the microchannel structure, and a top plate sealing the microchannel (Fig. 1 (b)). Inside the channel, optically transparent silicone oil and opaque liquid are contained. Sequential voltage application generates electromechanical force on the interface of the droplet, causing the opaque droplet to move toward the activated electrode and switch the aperture.

To fabricate this liquid-based optical iris, microfabrication techniques were employed to achieve a

compact structure and precise aperture control. First, a transparent indium tin oxide (ITO) thin film was sputtered onto a silicon wafer to serve as the bottom substrate, and electrode patterns were defined using photolithography. Dry film resist was then laminated and patterned to form 150 μm spacers, maintaining the shape of the microchannel. A parylene thin film was deposited via chemical vapor deposition (CVD) to provide electrical insulation, followed by a hydrophobic Teflon coating applied through spin-coating. Finally, the working fluid was introduced into the microchannel, and the top and bottom plates were bonded to seal the structure and complete the packaging (Fig. 2 (a)).

3. Performance test

To evaluate the driving conditions of the working fluid, the behavior of the droplets was analyzed under varying applied voltage magnitudes. Results showed that the contact angle decreased gradually with increasing voltage, stabilizing beyond a specific threshold.

Next, to evaluate the optical performance of the fabricated samples, the light transmittance as a function of dye concentration was measured by irradiating light with the iris closed and open. The results showed that the light transmittance decreased to less than 2 % in visible light at 400-1100 nm wavelength when the dye concentration was 50 wt.%.

Subsequently, the opening and closing response times of the iris were measured by applying voltages ranging from 40 to 120 V_{rms} at a frequency of 1 kHz, while recording real-time changes (Fig.2 (b)). The results indicated that at 120 V_{rms}, the iris required 3.8 seconds to close completely and 4.2 seconds to open.

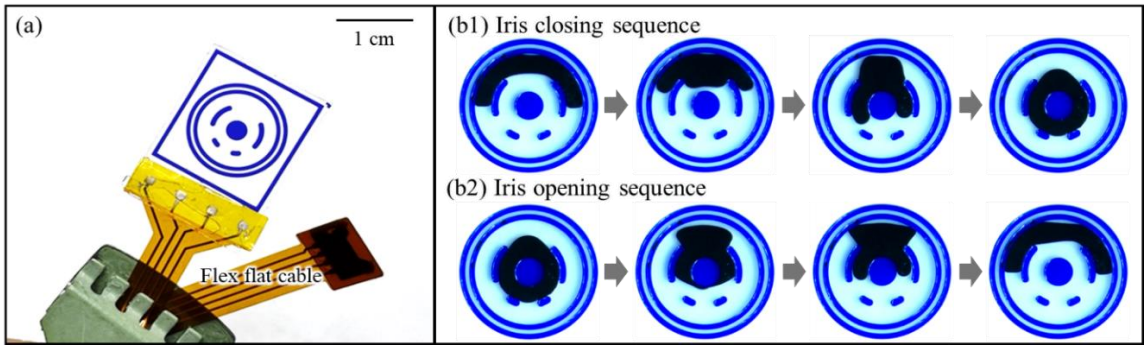

Fig. 2. Microfabricated liquid iris device: (a) Photograph of a device connected to a flexible flat cable; (b) Sequential snapshots of the device operated by electrowetting actuation

4. Conclusions

This paper presents a novel liquid iris design for miniature cameras, operating through electrowetting actuation. The presented iris demonstrates effective operation within a 150 μm channel thickness, achieving a compact structure and precise aperture control. The design provides an aperture transition range of 2.5 to 5 mm in diameter and demonstrates stable operation with consistent performance. These features make it suitable for miniaturized high-performance cameras and multifunctional optical systems.

5. References

[1] Li L, Liu C, Ren H and Wang Q-H (2013). Fluidic optical switch by pneumatic actuation, *IEEE Photonics Technology Letters,* **25,** 338–40.

[2] Oh S H, Rhee K and Chung S K (2016). Electromagnetically driven liquid lens, *Sens. Actuators A: Phys,* **240,** 153–9.

[3] Lee J, Park Y, Chung S K (2019). Multifunctional liquid lens for variable focus and aperture, *Sens. Actuators A: Phys,* **287,** 177–184.

[4] Lee J, Park Y, Jang D and Chung S K (2021). Switchable liquid shutter operated byelectrowetting for security of mobile electronics, *Review of Scientific Instruments*, **92,** 055009.

QUANTITATIVE MEASUREMENT THE WARPAGE OF PRINTED CIRCUIT BOARD UNDER THE ELECTRICITY ON BY UTILIZING LASER SPECKLE INTERFEROMETRY

Funjun Yang[1], Hanyang Jiang[2], Yinhang Ma[3], Xiangyang Xu[1]
[1] School of Civil Engineering, Southeast University, Nanjing, China
[2] College of Mechanical Engineering, Zhejiang University of Technology, Hangzhou, China
[3] College of Mechanical and Electronic Engineering, Nanjing Forestry University, Nanjing, China

1. Introduction

With the development of automotive electronics intelligence and interconnection, as well as meeting requirements for automotive active safety function, the reliability, quality and performance of automotive electronic products has become an important aspect of competition among automotive companies. At present, the microelectronic devices becomes light, small, high integration, thermal-mechanical reliability in microelectronic devices has become more and more important. Coefficient of thermal expansion mismatch in microelectronic devices or solder joint and printed circuit board induces deformation when these devices are subjected to thermal loading during manufacturing or everyday operation. Therefore, quantitative warpage measurement is critical in manufacture process or routine operation to improve product reliability and process yield, and determining overall thermal performance characteristics, and it also becomes very important to research and analyze this problem and find a solution to improve the reliability of electronic devices.

In this study, an electronic speckle pattern interferometry(ESPI) system was introduced to measure the full deformation and strain component of printed circuit boards(PCB). In this ESPI system, tri-wavelength lasers lights were used to independently sense two in-plane and out-of-plane deformation components, respectively. The three dimensional (3D) deformation information encoded by color speckle patterns was recorded by a 3CCD color camera. The color speckle interferograms were split into their red, green and blue components, and the 3D deformation data were quantitively determined by utilizing phase-shifting method and were furtherly denoised by phase filtering.

2. Methods

Two pair of separate symmetrical illuminating beams emitting from blue and green laser sources, respectively, and are then scattered from the surface of the specimen and then interfere without cross-talk and finally form coherent speckle patterns in blue and green respectively. These optical configurations can provid two sub-ESPI systems for measuring in-plane deformation. Based on michelson-interferometric setup and utilized red laser, another sub-ESPI system for out-of-plane deformation measurement is also established. These three sub-ESPI system are integrated with each other on a breadboard and one 3-sensor color camera is employed to image color speckle patterns. [1-4]. These speckle patterns contain essential information about the random phases, and consequently any change in the relative phase of the three patterns will give rise to intensity variations. Due to the observation direction being perpendicular to the specimen surface, the relative phase differences are therefore only sensitive to in-plane deformation in *x*- and *y*- directions for blue light and green light, respectively[5]. Owing to the illumination and observation vectors of red light both perpendicular to

the specimen surface, the relative phase difference of the red speckle patterns will only be out-of-plane-sensitive[5]. Quantitative phases related to three deformation components are retrieved by utilizing four-step phase-shifting technique.

3. Results and conclusions

Figure 1 shows color speckle pattern of the tested PCB specimen, which formed when the PCB is illuminated by tri-wavelength lasers, and the wrapped phase maps related to two in-plane displacement components *u* and *v* and out-of-plane deformation component *w* (warpage). The deformation is casued by thermal expansion during electronic device performance at room temperture (23ºC), the highest temperture of electronic component is 50ºC measured by infrared thermometer. The present interferometric method can precisely measure the deformation with the accuracy of sub-wavelength. Experimental results exhibit that the present ESPI system can simultaneously measure 3D deformation components, can become a practical application for measurement of 3D micro deformation.

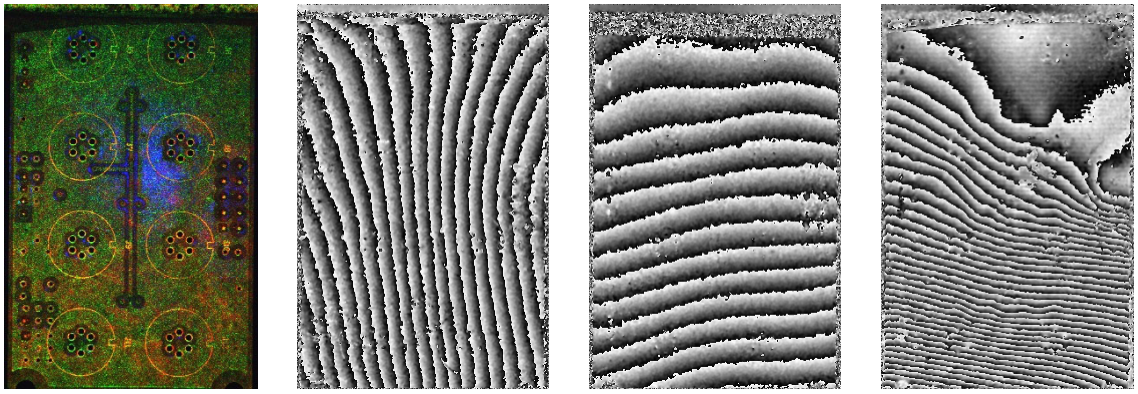

Speckle pattern *u* *v* *w*

Fig. 1 Color speckle pattern and Phase maps related to 3D displacement components

4. Acknowledgements

The research presented in this paper has received funding from National Natural Science Foundation of China the grant Nos. 12072073, 12202389, 11472081.

5. References

[1] Z. Li, P. Zhong, Y. Chen, et al. “Simultaneous measurement of three-dimensional deformation based on digital speckle pattern interferometry technology,” Opt. Comm. **480**(2021) ,12642

[2] YH Wang, CY Liu, SJ Wu, and WX Li, “Simultaneous measurement of three-dimensional displacement gradients using tri-color digital shearography,” Instruments and Experimental Techniques, 64(2021), 165–171

[3] Y Ye, X Li, Y Xu Y, et al, Simultaneous 3D measurement for infrared chips with speckle interferometry, Optics and Laser Technology. **153**(2022), 108199

[4] Wu M Y, Yang B S, Jiang H Y, et al. Simultaneous three-dimensional deformation measuring based on a simple phase-shift device combination with tri-wavelength and three-CCD camera[J], Optical Engineering 62(10) (2023**)**,104103-1

[5] J A Leendertz, Interferometric displacement measurement on scattering surfaces utilizing speckle effect, J. Phys. E **3**(1970), 214- 218

New Photoelastic Technology and Its Applications Based on Pixelated Polarization Camera and RGB Method

Fei SU and Qingyi LIU
School of Aeronautical Science and Engineering, Beihang University, P.R. China

1. Introduction

Traditional photoelastic systems are not only limited to laboratory applications, but their data processing is also very complex. With the emergence of pixel polarization cameras in recent years, polarization images corresponding to four different angles (0 degrees, 45 degrees, 90 degrees, and 135 degrees) can be obtained in one shot, thereby obtaining information on the phase retatdance and principal stress direction of the specimen. The advantages of this new photoelastic technology lie not only in its efficient testing, compact structure, and high sensitivity, but also in its simple post data processing: when the maximum value exceeds π/2, although the phase retardance also needs to be unwrapped, it is not affected by the principal stress direction data, and when the phase difference is less than π, the isochromatic-isoclinic interactions will not occur.

The unwrapping of phase retatdance in this case can only rely on the RGB method. We have two important improvement measures in this area. the first is to improve the content and search method of LUT, ensuring the spatial continuity of phase retardance field and the universality of LUT. The second is to remove the impact of phase retardance on the principal stress direction. After the methodology was set up, we conducted industrial application research on the new photoelastic method - online detection of stress in automotive glass.

2. Methodology

The optical path in the photoelastic method based on a pixelated polarization camera is illustrated in Figure 1. The polarizer and quarter-wave plate in Figure 1 were integrated with the LED light source, making the whole equipment very simple. Micro-polarizers made of nano-gratings with orientation of 0,45,90 and 135 degrees are placed in front of each pixel of the CCD target, pixels with the same grating orientation are picked up and reorganized as an image with specific polarization, as such, four images with different polarization can be obtained with one shot. the grayscale of the four polarization images can be given by:

$$I_{0^\circ}=\frac{1}{2}(1-\sin 2\theta\sin\delta), I_{45^\circ}=\frac{1}{2}(1+\cos 2\theta\sin\delta),$$
$$I_{90^\circ}=\frac{1}{2}(1+\sin 2\theta\sin\delta), I_{135^\circ}=\frac{1}{2}(1-\cos 2\theta\sin\delta) \quad (1)$$

Where δ is the phase retardance and θ is the principal azimuthal angle. If define

$$s_0=\frac{I_{0^\circ}+I_{90^\circ}}{I_{0^\circ}+I_{90^\circ}}, s_1=\frac{I_{0^\circ}-I_{90^\circ}}{I_{0^\circ}+I_{90^\circ}}, s_2=\frac{I_{45^\circ}-I_{135^\circ}}{I_{0^\circ}+I_{90^\circ}} \quad (2)$$

the phase retardance field δ(x,y) and principal azimuthal angle θ(x,y) of the sample can be obtained through mathematical calculations:

$$\sin\delta = \frac{\sqrt{(I_{0^\circ} - I_{90^\circ})^2 + (I_{45^\circ} - I_{135^\circ})^2}}{I_{0^\circ} + I_{90^\circ}} \tag{3-1}$$

$$\tan 2\theta = -\frac{I_{0^\circ} - I_{90^\circ}}{I_{45^\circ} - I_{135^\circ}} \tag{3-2}$$

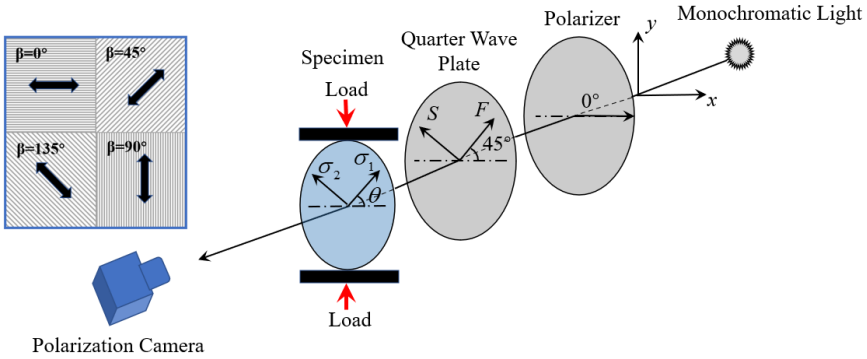

Figure 1. Schematic of the optical arrangement for stress birefringence measurements using a pixelated polarization CCD camera

Obviously, when δ>π/2, it cannot be uniquely determined based on the inverse function, and the next step is to use RGB solution wrapping. The approach of RGB method is to use a color camera to record these photoelastic fringes, and the camera decomposes the color image signal into three primary colors of varying intensities: red, green, and blue. RGB signal intensity corresponding to different phase retardance was determined through a four point bending experiment and recorded in a lookup table(LUT). When conducting formal testing, the intensity of the RGB signal at a point on the specimen was checked, and compared in the LUT table. Using the minimum value of ei in equation (4) as the criterion, group (Ri, G i, Bi) with the closest RGB signal was determined. Correspondingly,the phase retardance recorded in this group of data is determined as the measured value at that point.

$$e_i = \sqrt{(R - R_i)^2 + (G - G_i)^2 + (B - B_i)^2 + K \times [(\delta - \delta_L)^2 + (\delta - \delta_{UL})^2]} \tag{4}$$

δ_L and δ_{UL} are the phase retardance of the pixels on the left and up_left that has been determined, respectively, K is a coefficient. The last item under the squire root sympol implies spatial continuinty.

3. Results and conclusions

Firstly, the feasibility and correctness of the new method were confirmed through classic radial compression disk experiments, the results can be found in Fig.2. In this case, B&W CCD was employed while the color of light source were switched from Red to Green and Blue in sequence with the aid of computer, the duration of test was less than 2 minutes.

Fig 2 the phase retardacne and principal stress direction determined with the new methodolgy

Then the new system was applied to on-site stress evaluation of tempered glass around bolts. The experiment was performed in a lab with ample lighting but limited space, as shown in Fig. 3(a) , and some test results were shown in Fig.3(b), more details and applications will be shown in the formal paper.

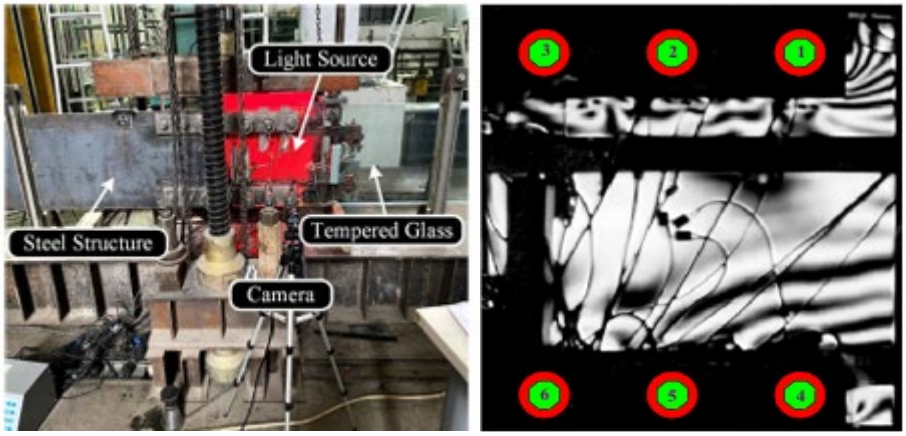

(a) Exoeriment environments (b) fringes of tempered glasss around bolts under the load of 10KN

In Summary: we introduced a new type of photoelastic technology that uses a pixel polarization camera to achieve dynamic phase shift, resulting in fast testing speed and simple structure, making it easy to apply in industrial fields. It uses the RGB method to deal with phase wrapping problem and achieves large-range of measurement scale, and it avoided the isochromatic-isoclinic interactions problems. Therefore, it is a highly promising photoelastic technology.

4. Acknowledgements x

The authors gratefully acknowledge financial support from the National Science Fund (grant no. 12072008 and 12102020) .

5. References

[1] Ramesh K, Sasikumar S. Digital photoelasticity: recent developments and diverse applications. Optics and Lasers in Engineering 2020; 135 :106186.
[2] Goldstein DH. Polarized Light . CRC press, Boca Raton, Florida, USA, 2017.
[3] Fei SU, Zijiao W. Error analysis and correction of a photoelastic method based on a pixelated polarization camera. Optics and Lasers in Engineering 2023; 161 :107374.

Determining the Heart Performance of Experimental an Animal Based on the Averaged Speed Using Digital Image Correlation Method

Chi Hung Hwang[1], Chun-Wei Lai[2], RongQing Qiu[1], Wei-Chung Wang[2], Yen-Pei Lu[1], Rui-Cian Weng[1]

[1] Taiwan Instrument Research Institute, National Applied Research Laboratories, Hsinchu, Taiwan
[2] Department of Power Mechanical Engineering, National Tsing Hua University, Hsinchu, Taiwan

1. Introduction

This study is inspired by studies conducted by Hokka et al. [1][2], which demonstrated the feasibility of using the digital image correlation (DIC) method during cardiopulmonary bypass surgery. The DIC method allows for measuring three-dimensional displacement and heart deformation every 0.1 seconds, even when the heart surface is moist, smooth, and has minimal features. Since DIC is an image-based feature-tracking method integrated with shape functions for calculating the deformation and the deformation gradient in directions, artificial or natural features on the object are essential. Therefore, in the studies of Hokka et al., it also commented that applying artificial features on the cardiac surface would significantly improve the displacement/ deformation measurement.

In addition to the studies of Hokka et al., Soltani et al. [3][4] also studied the displacement, total displacement, maximum and minimum principal strain, and time relationship for the three stages of cardiac surgery, saying before surgery, after weaning off the life support system, and after using theophylline, using the DIC approach. Soltani et al. used camera pairs installed above the operating room to capture 200 images stereoscopic dynamic images at 18 FPS. Different from Hokka's studies, Soltani et al. implemented surgical marker pen to create artificial features on the heart surface. Then, 3D DIC software analyzes the captured images to determine the displacement, total displacement, maximum and minimum principal strain, and time relationship.

Both teams installed the stereo-imaging system above the operation table on the cell, which introduced complex operation scenarios during surgery. Meanwhile, using surgical pens might introduce unnecessary mechanical touch to the organ. Therefore, this study proposes a movable imaging system with FDA-approved fluorescence medicine to generate an artificial feature on the cardiac surface for tracking. In this study, a single-camera stereo-imaging system is built to avoid the imaging synchronized problem of using two cameras. The stereo-imaging system is designed to enable the capture of images at a working distance of 500-600 mm with a 100 mm x 100 mm imaging area at a 40 FPS frame rate. Each captured image are automatically cropped into two images and then saved with time-tags and camera-view-labels as filenames. Fig. 1 shows the implemented stereo-imaging prototype[5]. The fluorescence medicine used for labeling can be excited by NIR light, and the emission light is also within NIR bandwidth, as shown in Fig. 2[5].

2. Material and Experimental Conditions

In this study, a 30.9 kg six-month-old female Sus scrofa is used. The animal experiment has been approved by the Institutional Animal Care and Use Committee of the National Laboratory Animal Center of National Applied Research Laboratories, Taiwan (IACUC No. NLAC-110-M-069). Typical images, as shown in Fig. 3[5], were captured using the developed single-camera stereo-imaging system with NIR fluorescence medicine sprayed on the cardiac surface as artificial features for tracking.

During the experiment, a veterinarian performed cardiac surgery, and the stereo-imaging system was installed aside from the operational table to image the heart directly. Saline was consistently applied to wet the cardiac surface; an artificial respirator controlled the breath twelve times per minute, recording body temperature and heartbeat rate every 15 minutes.

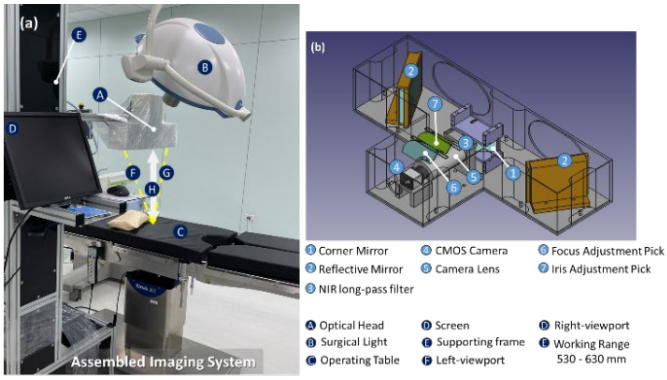

Fig. 1. Prototype of the developed a single-camera stereo-imaging system. (a) placed the prototype near the surgical table; (b) layout of the optical head used in single-camera stereo-imaging system.

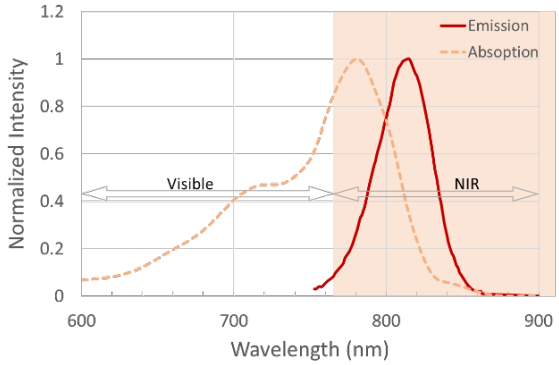

Fig. 2. Spectrum properties of FDA-approved fluorescence medicine. [5]

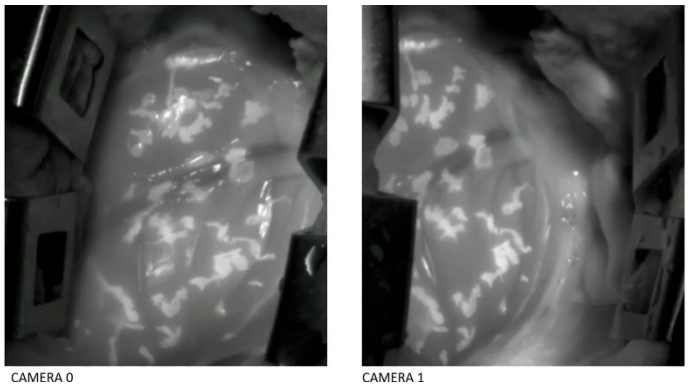

Fig. 3. Typical images taken using developed single-camera stereo-imaging system. [5]

3. Results and conclusions

Considering the cardiac is always beating during imaging, this would inevitably introduce two concerns: first, the imaging system could not be well synchronized with the heartbeat, so the heart behavior might be recorded as irregular behaviors of the heart; second, the reference image is difficult to define for DIC analysis. The 1st problem can be easily mitigated using a high frame-rate imaging system. In this study, the developed single-camera stereo-imaging system is operated at 40 FPS, which can take 2400 image pairs in a minute; the frame rate can record a maximum heartbeat rate of up to 1000 BMP based on the sampling principle.

Since DIC determines the displacement and strain based on tracking the features of two images captured at different statuses, which indicates the DIC-determined parameters, displacement, and stain, are status sensitive, the reference image is essential for heart study. Seeing this issue, in this study, two adjacent images would be used to determine the feature displacement between two frames to analyze the obtained cardiac images, which can be considered as motion velocity since the DIC determined displacement occurred during the frame time. Then, the displacement is reconstructed with a selected reference image so that the typical out-of-plane displacement of the heart can be obtained, as shown in Fig. 4. Comparing the result with typical DIC analysis (using the first frame as the reference image), the out-of-plan displacement reconstructed by using velocity almost the same, but the amplitude is relatively small. In this way, the out-of-plane velocity of heart motion can be determined; meanwhile, the reliable average heart displacement can be easily determined using numerical calculation once the reference image is selected. More details will be given at the conference.

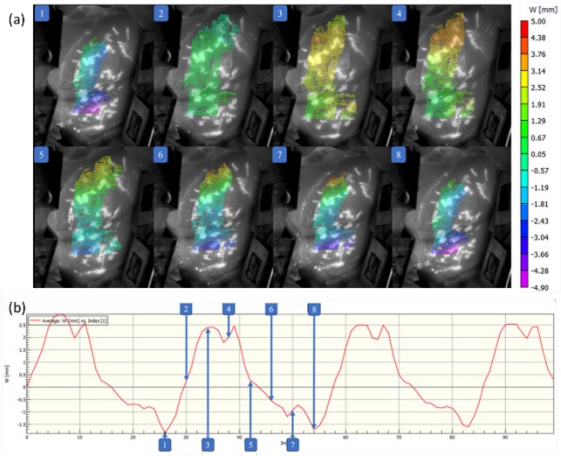

Fig. 4. Out-of-plane Displacement of heart determined using DIC

4. Acknowledgements

This work was sponsored in part by the National Science and Technology Council under contract number NSTC 108-2221-E-492-022-MY2 and NSTC 110-2221-E-492-011-MY3.

5. References

[1] M. Hokka, et al. "In-vivo deformation measurements of the human heart by 3D digital image correlation," Journal of biomechanics 48.10, pp. 2217-2220, (2015).

[2] M. Hokka, et al. "DIC Measurements of the Human Heart during Cardiopulmonary Bypass Surgery, " Mechanics of Biological Systems and Materials, Volume 6. Springer, Cham., pp. 51-59 (2016).

[3] A. Soltani, et al. "Digital Image Correlation Study of the Deformation and Functioning of the Human Heart during Open-Heart Surgery," Mechanics of Biological Systems, Materials and other topics in Experimental and Applied Mechanics, Volume 4, Springer, Cham, pp. 19-27 (2018).

[4] A. Soltani, J. Lahti, K. Järvelä, S. Curtze, J. Laurikka, M. Hokka, V. T. Kuokkala, "An Optical Method for the In-Vivo Characterization of the Biomechanical Response of the Right Ventricle," Scientific reports, 8(1), 6831 (2018).

[5] C. H. Hwang et al., "Tracking Fluorescent Artificial Features on Cardiac Surface for Evaluating Heart Function," 2024 IEEE International Instrumentation and Measurement Technology Conference (I2MTC), Glasgow, United Kingdom, 2024, pp. 1-6, doi: 10.1109/I2MTC60896.2024.10560677.

6-11 July 2025 ICEM21 Bologna
21st International Conference on EXPERIMENTAL MECHANICS

Snapshot full Stokes camera by RGB polarization camera for stress visualization

Yukitoshi Otani[1], Jessica Onaka[1], Nathan Hagen[1]
[1] Center for Optical Research and Education(CORE),
Utsunomiya University, Japan

1. Introduction

A Stokes polarimeter becomes more and more important in the field of optical science and engineering, especially in stress distributions and material testing by birefringence. A polarization camera makes a new technology for industrial applications. Its image sensor is attached linear mic ro-polarizer arrays with adjacent 4 pixels of a and aligned to 0, 45, 90 and 135º of azimuthal direction [1]. As it is based upon rotating polarizer, it can measure partial Stokes parameters. We have proposed for measuring full Stokes parameters by two polarization cameras. It is often used for video-rate measuring partial Stokes parameters but it is not so easy to measure full Stokes parameters. We have already proposed a full-Stokes polarimeter [2]. It also proposed it by RGB polarization cameras[3]. Research on the birefringence measurement by stress becomes widely known that certain types of polarization structure. In this paper, we propose a full Stokes imager and its application to detect polarization properties of stress mapping.

The first chapter should shortly view the background and introduce [2,4] the possibly unfamiliar read-er to the main subject of the research.

2. Materials and methods Snapshot full Stokes imager

Figure 1 shows an optical arrangement of a full Stokes imager by polarization cameras. An object with Stokes parameters S is imaged on to polarization cameras by a camera lens. The incident light is divided into two optical paths by a non-polarizing beam splitter (NPBS). The only reflected light passes through a retarder, used a quarter wave plate. The Stokes parameters is analyzed from 8 intensities with 4 different azimuthal angles of two polarization cameras. In addition, we propose a calibration method for errors of retardance and out of alignment of pixelated polarizers in advance. In addition, the measured accuracy is affected by birefringence of the non-polarizing beam splitter so that we also need to calibrate it. We succeeded to calibrate diattenuation and retardance of non-polarizing beam splitter (NPBS) and retardation of a quarter wave plate. We also applied a pixel interpolation proposed by Scott Tyo[4]. We can interpolate for the images of Stokes parameters as s_0, s_1 and s_2 after filtering in the Fourier domain.

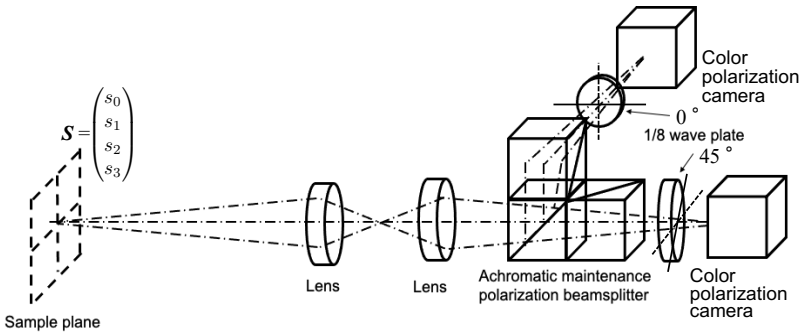

Fig.1 Optical setup of a full Stokes parameters by polarization cameras

A matrix of Stokes parameters $\boldsymbol{S}$ and a measured matrix $\boldsymbol{A}$ and a detected Stokes parameters by camera $\tilde{\boldsymbol{S}}$ is

expressed by Fig.(1), where s_{iCT}, $s_{iCR}(i = 0,1,2)$ are captured results of both transparent and reflection cameras. The phase difference Δ is set $\lambda/8$ of retardance.

$$\tilde{\boldsymbol{S}} = \boldsymbol{A} \cdot \boldsymbol{S}$$

$$\begin{bmatrix} s_{0CT} \\ s_{1CT} \\ s_{2CT} \\ s_{0CR} \\ s_{1CR} \\ s_{2CR} \end{bmatrix} = \begin{bmatrix} 1 & 0 & 0 & 0 \\ 0 & 1 & 0 & 0 \\ 0 & 0 & \cos\Delta & \sin\Delta \\ 1 & 0 & 0 & 0 \\ 0 & \cos\Delta & 0 & -\sin\Delta \\ 0 & 0 & 1 & 0 \end{bmatrix} \quad (1)$$

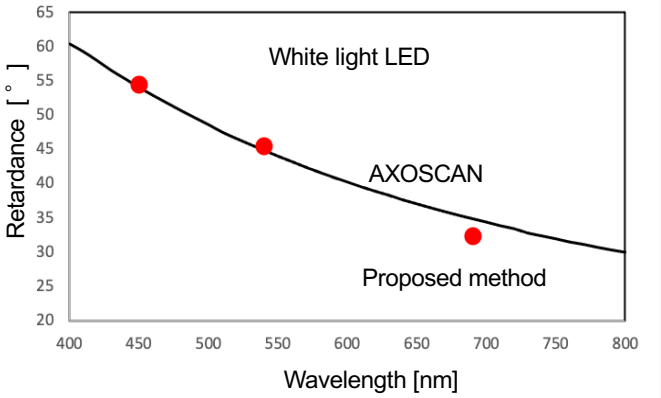

Fig.2 Evaluation of birefringence (retardance) comparing with commercioal polarimeter

By converting the measurement matrix $\boldsymbol{A}$ to the pseudo-inverse matrix $\boldsymbol{A}^{-1}$ and multiplying it by the Stokes parameter $\tilde{\boldsymbol{S}}$ obtained by the camera, the Stokes parameter $\boldsymbol{S}$ of the sample plane can be obtained. The use of a $\lambda/8$ plate allows the phase difference Δ of the one-eighth wavelength plate to be determined during the measurement.

$$\Delta = \cos^{-1}\frac{s_{2CT} + s_{1CR}}{s_{1CT} + s_{2CR}} \quad (2)$$

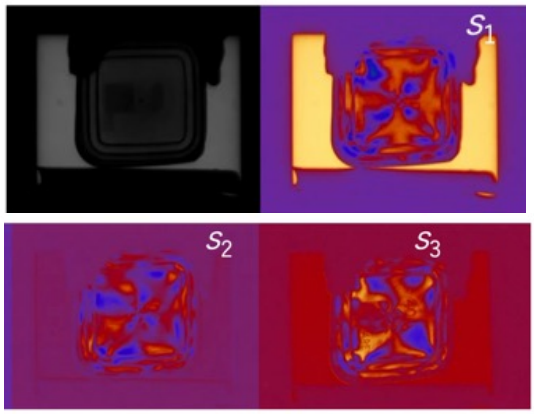

Fig.3 Stress birefringence distribution

Calibration of the extinction ratio [4] was applied to the Stokes parameters obtained by the camera. A halogen lamp, a diffuser, and a Glan Thomson prism were used. The Glan Thomson prism was set to 0 , 45, 90, and 135 °, and the micro-polarizer orientation α, linear double absorption D, and extinction ratio X were derived using the phase shift method. From the obtained parameters, the calibrated Stokes parameters were obtained by multiplying the measurement matrix by the polarizer's Muller matrix.

3. Experimental results of polarization effects of stress birefringence

Figure 2 shows a measured result of birefringence comparing with a commercial polarimeter, Axoscan. A sample is used as a $\lambda/8$ retarder by457 nm, 530 nm, 628 nm. Figure 3 shows Stokes parameters of a stress birefringence of a plastic plate.

4. Conclusion

We proposed a full-Stokes imager by polarization cameras. It is succeeded to reconstruct an image of full Stokes parameters in the video-rate. We also demonstrate to measure a stress birefringence.

5. References

[1] N.Hagen, S.Shibata, Y.Otani: Optical Engineering, 58,8, 082408 (2019).
[2] S.Shibata,N.Hagen, Y.Otani : Optics Letters,44, 4, 891-894 (2019).
[3] XingzhouTu et.al: Optics Express, 25, 26 33160 (2017).
[4] J.S.Tyo et.al:Opt.Lett(2009).

Thermal based techniques for materials and components analysis: applications and perspectives

ACTIVE AND PASSIVE THERMOGRAPHY FOR A NON-DESTRUCTIVE SURFACE TREATMENT CHARACTERIZATION IN SPUR GEARS

L. Corsaro, F. Curà and R. Sesana
Department of Mechanical and Aerospace Engineering (DIMEAS), Politecnico Di Torino, 10129 Torino, Italy

1. Introduction

The mechanical performance of gears is an important aspect in the power transmission field. The choice of appropriate materials and surface treatments determines their mechanical resistance under operating conditions. Typically, the mechanical properties produced by the surface treatment are evaluated through a rigorous inspection process before the components are put into service. For the specific topic of residual stresses evaluation, the analysis can be performed by using Destructive or Semi-Destructive methods [1-3]. For Destructive techniques [4], the residual stress analysis is conducted by perturbing the original equilibrium stress state of the material, resulting in relaxation of the original residual stresses, which can then be measured. In some cases, a reduction in the amount of damage during the measurement phase can be achieved with Semi-Destructive techniques.

An ever-expanding technique in the field of Non-Destructive measurement is InfraRed Thermography (IRT). Depending on the presence or absence of an external excitation source, it can be classified as Active (AT) or Passive (PT) Thermography. AT, also known as "Stimulated Thermography", was initially used to identify hidden defects and many papers described methods to improve the visibility of these defects [5-7]. Over the years, the capabilities of AT were also applied to other research areas, such as the characterization of materials and mechanical damages [8,9]. On the other hand, PT provides rapid and efficient non-invasive analysis by acquiring temperature data under operating conditions. One of the most important applications of PT in mechanical engineering was the well-known Thermography Method for estimating fatigue limits.

The objective of this work is to propose an alternative, rapid and Non-Destructive technique to characterize the surface treatment for gears, employing Thermography in both Active and Passive configurations. In particular, an AT based method was developed with the objective of properly characterizing the residual stresses produced by the surface treatment. To that aim, a dedicated Design of Experiment (DOE) was adopted for the identification of the optimal experimental set up. Then, a PT approach was utilized for the rapid estimation of the tooth root bending fatigue strength. For this purpose, a dedicated testing device was designed with the aim of performing Single Tooth Bending Fatigue (STBF) tests at a mechanical pulsator. The results are here presented for gears made of C45 steel, with and without an induction-hardening surface treatment.

2. Materials and methods

The proposed research was conducted on a set of two gears, both manufactured from the same C45 steel bar and with the same geometrical parameters. One of the gears was subjected to an induction hardening surface treatment, while the other was left untreated. Geometry and mechanical properties of the gear are resumed in Table 1. A complete mechanical property characterization was carried on

for each gear, with particular attention to both hardnesses and residual stresses. The analysis was performed with a classical hardness meter and an X-ray diffraction meter.

The residual stresses were characterized by means of an AT setup in reflection configuration, with a laser operating as the heating source [10]. An optical device, named F-theta lens, was utilized to localize the laser beam at the tip of the tooth. The heating phase was produced with a Lock-In technique, and the corresponding thermal responses were extracted from the tip of the tested tooth. The thermal diffusivity, determined through the Slope Method [11], was selected as thermal index for the residual stress characterization. Then, the thermal results were compared with the X-ray analysis. The bending fatigue strength evaluation was conducted using the thermal emission values produced during the fatigue tests. So, a thermal camera was positioned in front of the gear during the fatigue tests with the objective of acquiring thermal responses from the tested teeth. Then, the Two Curves Method (TCM) [12], widely used in literature for classical samples, was adopted and adapted for estimating the tooth root bending fatigue strength. More specifically, the stress level considered in the TCM routine was the tooth root stress, allowing the estimation of the permissible bending fatigue stress of the tested gear by identifying the intersection of the data approximating curves. Results obtained from the adapted TCM routine were then compared with the corresponding reference values provided by the ISO 6336 Standard [13,14].

C45 steel gear	
Geometry	Material
Modulus: 3 mm	$Rp_{0.2}$: 596 MPa
N° of teeth: 20	R_m: 760 MPa
Pressure angle: 20°	E: 196000MPa
Gear width: 28 mm	

Table 1. Geometry and material for gears.

3. Results and conclusions

The results of the surface treatment characterization are shown in Figure 1. In particular, the green colours represent the induction hardened gear, while the untreated gear (base material gear) is represented by red colours.

The thermal responses obtained from the AT analysis are shown in Fig. 1(a). More in detail, the phase profiles extracted from the tip of the tested tooth are compared for both treated (induction hardening) and untreated (base material) gears. On the other hand, the thermal emission analysis performed by using PT is shown in Fig. 1(b). In particular, the evolution of the thermal parameters for both treated (induction hardened) and untreated (base material) gears is compared for several tooth root stress conditions during the STBF tests. On the basis of the results proposed in Fig. 1, it can be noted that the presence of the surface treatment can be detected by thermal responses. In particular, an alteration of the heat propagation zone can be identified from the AT activity, allowing the residual stress characterization by means of the thermal index. On the other hand, a different evolution of the thermal parameters from the PT activity was detected for both tested gears, allowing the estimation of the bending fatigue strength by means of the TCM properly adapted to gears.

This way, the proposed Thermographic approach allowed a rapid and Non-Destructive characterization of the surface treatment by exploiting thermal response alterations caused by the microstructural modification resulting from the surface treatment.

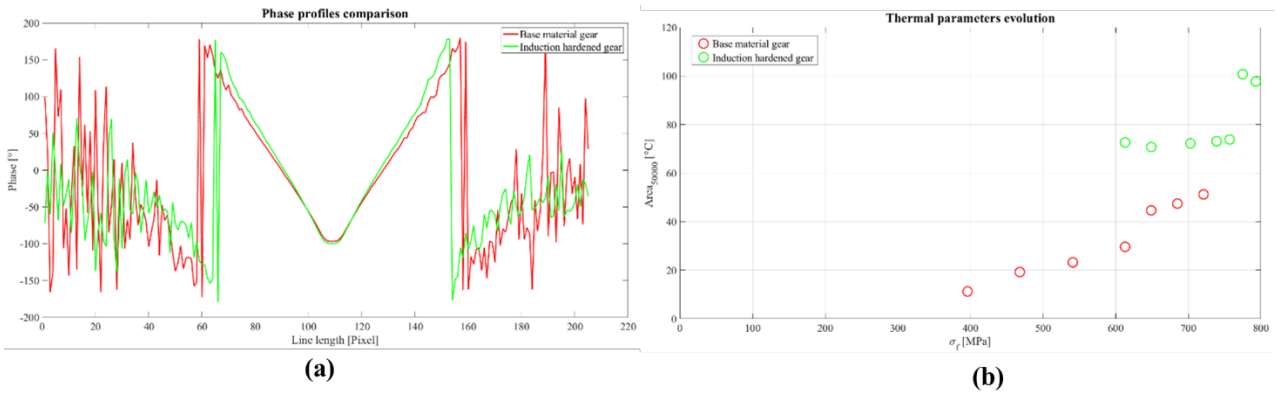

(a) (b)

Fig. 1. Surface treatment characterization: (a) AT, (b) PT

4. Acknowledgements

This research was funded by Fondazione Compagnia San Paolo. Proof of Concept project: "Sviluppo e set up di una metodologia basata sulla termografia attiva per la misura delle tensioni residue nei materiali e nei componenti metallici", 2023-2024.

5. References

[1] V. Savaria, H. Monajati, F. Bridier and P. Bocher (2015). Measurement and correction of residual stress gradients in aeronautical gears after various induction surface hardening treatments. *Journal of Materials Processing Technology*, **220**, 113-123.

[2] S. Denis, P. Archambault, E. Gautier, A. Simon and G. Beck (2002). Prediction of residual stress and distortion of ferrous and non-ferrous metals: Current status and future developments. *Journal of Materials Engineering and Performance*, **11(1)**, 92-102.

[3] G.E. Totten, M.A.H. Howes and T. Inoue T (2002). Handbook of residual stress and deformation of steel. *ASM International* (1st ed.).

[4] M. Honner, P. Litoš and M. Švantner (2004). Thermography analyses of the hole-drilling residual stress measuring technique. *Infrared Physics & Technology*, **45(2)**, 131-142.

[5] W. Ben Larbi, M. Klein, A. Bendada and X. Maldague (2009). Experimental Comparison of Lock-in and Pulsed Thermography for the Nondestructive Evaluation of Aerospace Materials. In *6th Int. Workshop, Advances in Signal Processing for Non Destructive Evaluation of Materials*, Ontario, Canada.

[6] J. Liu, W. Yang and J. Dai (2010). Research on thermal wave processing of lock-in thermography based on analyzing image sequences for NDT. *Infrared physics and technology*, **53(5)**, 348-357.

[7] C. Ibarra-Castanedo, J.M. Piau, S. Guilbert, N.P. Avdelidis, M. Genest, A. Bendada and X. Maldague (2009). Comparative Study of Active Thermography Techniques for the Nondestructive Evaluation of Honeycomb Structures. *Research in Nondestructive Evaluation*, **20(1)**, 1-31.

[8] F. Curà, R. Sesana, L. Corsaro, R. Mantoan (2022). Characterization of Thermal Barrier Coatings Using an Active Thermography Approach. *Ceramics*, **5(4)**, 848-861.

[9] F. Curà, R. Sesana, L. Corsaro (2023). Active thermography technique for fatigue damage characterization in gears. Experimental Mechanics in Engineering and Biomechanics – Proc. ICEM20 20th Int. Conf. on Experimental Mechanics, Porto.

[10] Curà. F., Sesana. R., Corsaro. L., Santoro. L., Metodo di rilevazione delle tensioni residue su materiali e componenti mediante tecniche di termografia attiva. Patent application for industrial invention n. 102023000003597, 2023.

[11] A. Mendioroz, R. Fuente-Dacal, E. Apiñaniz and A. Salazar (2009). Thermal diffusivity measurements of thin plates and filaments using lock-in thermography. *Review of Scientific Instruments*, **80(7)**.

[12] F. Curà, G. Curti, R. Sesana (2005). A new iteration method for the thermographic determination of fatigue limit in steels. *International Journal of Fatigue*, **27(4)**, 453–459.

[13] Standard ISO 6336, Calculation of Load Capacity of Spur and Helical Gears, Part 3 (2019). *International Standard Organization*.
[14] Standard ISO 6336, Calculation of Load Capacity of Spur and Helical Gears, Part 5 (2019). *International Standard Organization*.

6-11 July 2025 ICEM21 Bologna
21 st International Conference on EXPERIMENTAL MECHANICS

THERMOGRAPHIC ESTIMATION OF THE FATIGUE LIMIT OF A TITANIUM ALLOY

C. Colombo[1], A. Salerno[2], A. Teyssiéras[3], J. Fiocchi[4], C. Biffi[4]
[1] Department of Mechanical Engineering, Politecnico di Milano, Milan, Italy
[2] Department of Energy, Politecnico di Milano, Milan, Italy
[3] ISAE-ENSMA École Nationale Supérieure de Mécanique et d'Aérotechnique, Poitiers, France
[4] CNR ICMATE, National Research Council, Institute of Condensed Matter Chemistry and Technologies for Energy, 23900 Lecco, Italy

1. Introduction

The fatigue limit is the most meaningful parameter summarizing the fatigue performances of materials, interesting for many engineering applications. However, the experimental tests needed for its estimation, e.g., the Staircase method, require in general a very long time and many specimens to ensure repeatability and reliability. A valid alternative to this standardized method to estimate the fatigue limit is the thermographic approach proposed by many authors on homogeneous and composite materials [1,2]. The present work is aiming at using IR thermography to determine the fatigue limit of a titanium alloy; few thermographic works are present in the literature, mainly studying the amplitude of the second harmonic [3,4]. The present study will address this issue with a complex but efficient approach to process this quantity.

2. Materials and methods

The material object of the study is the Ti-6Al-4V alloy. After lamination, plates underwent a thermal treatment at 800°C for 1h and then they were water tempered. The mechanical properties were obtained from static tests according with ASTM E8-E8M standard: elastic modulus E =70958 MPa, yield stress YS= 458 MPa, ultimate tensile strength UTS =488 MPa.

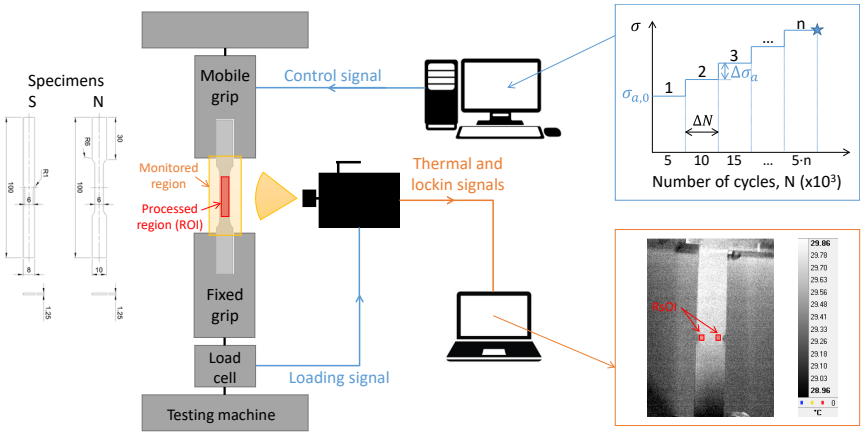

Fig. 1. Specimens, scheme of the setup and loading cycles.

Sinusoidal fatigue tests are performed at R=0.1 and *f*=15 Hz, progressively increasing the stress amplitude, e.g. stepwise tests. Two types of specimens are investigated, *S* smooth and *N* notched specimens. Those last specimens have fatigue stress concentration factor K_f = 1.86. The main parameters describing the fatigue cycle are: 1) the initial maximum stress σ_{max0}=180MPa for the S

specimens and 80MPa for the N-specimens; 2) the maximum stress step $\Delta\sigma_{max}$=15MPa; 3) the number of cycles for each loading block, ΔN=5000 cycles. Fig.1 schematizes the setup and the loading cycles.

The specimen's surface, black painted, is thermally monitored with the IR-camera FLIR Titanium, connecting the load cell to the lockin module. This allows analyzing the self-heating during the loading cycles. Thermograms and lockin signal are processed with the software Altair LI, allowing for the estimation of the second harmonic, named D-mode. Fig. 1 shows shematically the setup.

3. Results and conclusions

The analysis of the D-mode was particularly challenging and affected by noise. Therefore, the D-mode signal was furtherly processed as follows [5]: 1) calculate the average D-mode signal over an unloaded region; 2) subtract this value to the D-mode averaged over the ROI, e.g. the central portion of the *S* specimens and two regions of 2x2 pixels at the edges of the notch for the *N* specimens; 3) plot this value as a function of the applied stress amplitude; 4) fit the first 3 data with a linear regression, calculate the residuals and the standard deviation; 5) plot the residuals as a function of the applied stress amplitude; 6) define the threshold as six times the standard deviation. The first value of the D-mode residual is the proposed estimation of the fatigue limit. Fig.2 plots the residuals and shows the identification the fatigue limit for the two types of specimens.

The estimation of the fatigue limit is 264 MPa for the S specimens and 165MPa for the N specimens. Their ratio is K_f = 1.6, well aligned with the theoretical one. The proposed IR-based procedure proved to be a useful tool for quickly evaluating the fatigue limit, even in the presence of a stress gradient in the titanium alloy that made more challenging to capture accurately the thermal dissipation.

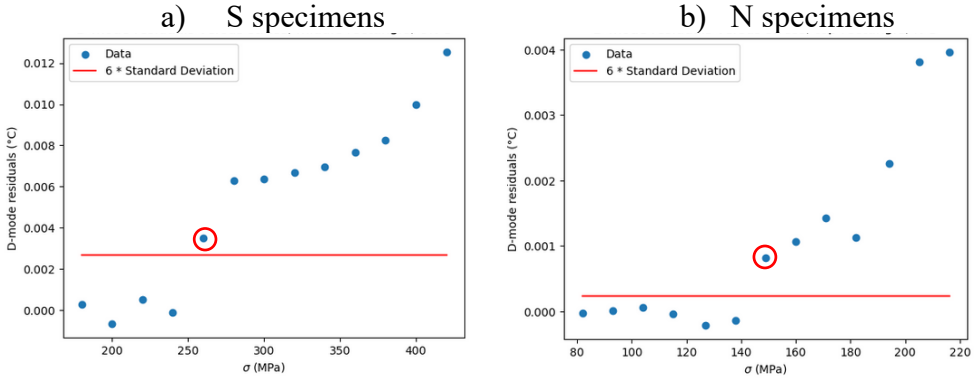

Fig. 2. Plot of the *D-mode* residuals as a function of the applied maximum stress. The red horizontal line identified the threshold. The first datum above it is the fatigue limit estimation (red circle).

4. References

[1] F. Curà, G. Curti, R. Sesana (2005). A new iteration method for the thermographic determination of fatigue limit in steels, *Int. J. Fatigue*, **27**, 453-459.

[2] L. Vergani, C. Colombo, F. Libonati (2014). A review of thermographic techniques for damage investigation in composites. *Fract. Struct. Integr.*. **27**, 1-12.

[3] I. Bustos, M. Bergant, A. Yawny (2023). On the suitability of applying thermographic methods for the rapid estimation of the fatigue limit of additively manufactured Ti-6Al-4V. *Int. J. Fatigue*, **174**, 107709.

[4] C. Colombo, A. Tridello, A.P. Pagnoncelli, C.A. Biffi, J. Fiocchi, A. Tuissi, L.M. Vergani, D.S. Paolino (2023). Efficient experimental methods for rapid fatigue life estimation of additive manufactured elements. *Int. J. Fatigue*, **167**, 107345.

[5] R. De Finis, D. Palumbo, F. Ancona, U. Galietti (2015). Fatigue limit evaluation of various martensitic stainless steels with new robust thermographic data analysis. *Int. J. Fatigue*, **74**, 88–96.

A MODEL FOR ASSESSING THE EFFECT OF THICKNESS ON APPARENT THERMAL DIFFUSIVITY IN LOCK-IN THERMOGRAPHY MEASUREMENTS

L. Santoro[1], R. Sesana[1], L. Tromba[1]
[1] Department of Mechanical and Aerospace Engineering, Politecnico di Torino, Italy

1. Introduction

Thermal diffusivity measurements are essential in many industrial applications, and various methodologies have been developed to accurately assess this parameter. However, measurement techniques often require a specimen to be extracted from the component, making it challenging to measure local properties in a non-destructive way. Common techniques, such as Hot Disk or Laser Flash, require destructive testing to obtain material specimens, compromising the component integrity. In contrast, Active Thermography enables testing directly on the part to be inspected, allowing for localized measurements at any position on the component.

Thermal diffusivity provides a wealth of information, not only about thermal properties but also about mechanical damage, the presence of flaws and defects such as porosities, and the metallurgical structure of the material. To this aim, laser thermography enables full-field, local, non-destructive, and non-contact pieces of information for dedicated analysis. In particular, Lock-In thermography is a well-known technique used for measuring thermal diffusivity. By applying a frequency-modulated heat source and analysing the frequency response of the material in Phase ϕ and Amplitude components $|T|$, it is possible to determine in-plane thermal diffusivity.

According to models in the literature [1], the main factors affecting the physical thermal response are the frequency of laser excitation f and the thermal diffusivity of the tested component D. The in-plane thermal diffusivity can be determined from the linear dependence of phase lag with the distance to the center point of laser beam, using the slope method [1]. The relevant equation is $\lambda = \sqrt{\left(\frac{D}{\pi f}\right)}$, where the parameter λ is the thermal diffusion length, and where the slope of the phase is $m_{\phi} = \frac{1}{\lambda}$.

This formulation is valid if assuming that the sample thickness $l >> \lambda$, condition for which the sample is considered 'thermally thick', and $l << \lambda$, condition for which the sample is considered 'thermally thin'. This distinction is crucial in thermography and thermal diffusivity measurements because it affects the behaviour of heat propagation and, thus, the measurement results.

The measurement of thermal diffusivity is then affected by the specimen thickness l and some studies [2] have shown a relation between thickness and thermal diffusivity, referring to this affected measurement as 'apparent thermal diffusivity'.

The present work aims at modelling the effect of thickness on thermal diffusivity measurement to provide researchers and scientists with a tool which can guide the selection of testing parameters when characterizing a new or unknown material or component.

2. Materials and methods

In the present work, the thermal diffusion equation has been reformulated in Hankel Space [3] for a laser Gaussian beam-shaped heat input and a uniform infinite slab. The equation has been solved for reflection mode. Although the equation has no analytical solution, it has been integrated using numerical methods through an in-house Python script, and the output has been evaluated and plotted.

Experimental tests were then performed to validate the model. More in detail, a combination of experimental measurements on six steel plates 50x50 mm of different thicknesses (2.5, 5, 7.5, 10, 12.5, 15 mm) is explored. The specimens were assumed to be made of steel with a thermal diffusivity of D_s = 22.8 mm^2/s and a thermal conductivity of K_s = 43 W/(m·K). The specimens were subjected to a laser heat source with a laser spot radius of a =0.7 mm, an absorbed power fraction of η =1, a power of P_0 = 7.5 W, and three different modulation frequencies of f = {0.2, 1, 5} Hz. The surrounding environment was assumed to be air with a thermal diffusivity of D_e = 19 mm^2/s and a thermal conductivity of K_e = 0.026 W/(m·K). The presented results are respectively Phase ϕ, Amplitude $|T|$, $ln\left(|T|\sqrt{\rho}\right)$ vs radial distance ρ from the central point of the laser beam and they provide insight into how these parameters of the thermal response vary with specimen thickness l, in reflection mode.

3. Results and conclusions

The thermal diffusion equation, reformulated in Hankel space [3] for a laser Gaussian beam-shaped heat input and a uniform infinite slab, does not have an analytical solution. In this work this equation has been integrated with numerical methods via an internal Python script and the numerical results, for the reflection configuration, are presented in Fig. 1. The three sets of graphs report the thermal parameters (Phase ϕ, Amplitude $|T|$, $ln\left(|T|\sqrt{\rho}\right)$) as a function of the radial distance ρ from the centre of the heating spot and normalized radial distance ρ/λ, where λ represents the thermal diffusion length. For specimens with a thickness less than the thermal diffusion length, the effect of thickness is evident, and this can be observed by the change in the slope of the curves. These results confirm the literature findings over the linear behaviour of amplitude and phase vs radial distance ρ from the centre point of the laser beam, however a difference in the slope, for the three modulation frequencies is observed. The phase measurement appears to the parameter more sensitive to thickness variation for lower values of excitation frequency.

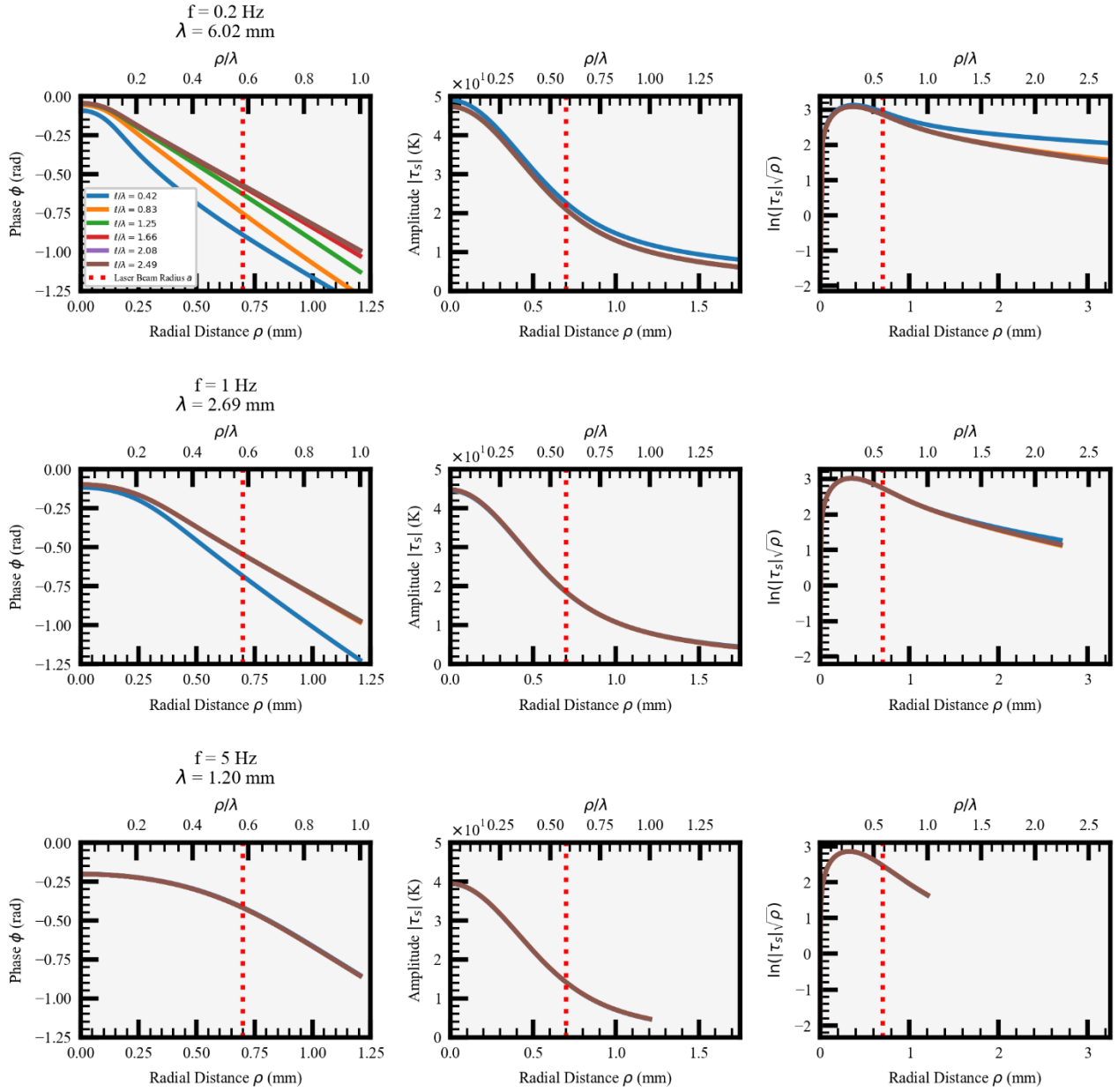

Fig. 1. Thermal response curves (Phase ϕ, Amplitude $|T|$, $ln(|T|\sqrt{\rho})$) for three different modulation frequencies f={0.2, 1, 5}Hz

4. Acknowledgements

The research has been conducted in J-Tech interdepartmental center laboratories from Politecnico di Torino. This publication is part of the project PNRR-NGEU which has received funding from the MUR–DM 630/2024.

5. References

[1] A. Mendioroz, R. Fuente-Dacal, E. Apianiz & A. Salazar (2009). Thermal diffusivity measurements of thin plates and filaments using lock-in thermography. *Review of Scientific Instruments,* **80.** doi:10.1063/1.3176467

[2] H. Kato, T. Baba, & M. Okaji (2001). Anisotropic thermal-diffusivity measurements by a new laser-spot-heating technique. *Measurement Science and Technology*, ***12*(12)**, 2074–2080. https://doi.org/10.1088/0957-0233/12/12/307

[3] W. B. Jackson, N. M. Amer, A. C. Boccara & D. Fournier (1981). Photothermal deflection spectroscopy and detection. *Appied Opt*ics, **20**, 8.

6-11 July 2025 ICEM21 Bologna
21st International Conference on EXPERIMENTAL MECHANICS

Novel Thermographic NDE Approach for Testing the Dispersion of Nanoparticles in Nanocomposites

Nicola Montinaro [1,2], Guglielmo Marchesa [1], Donatella Cerniglia [1], Antonio Pantano [1,]*

[1] *Department of Engineering, Università degli Studi di Palermo, 90128, Palermo, Italy*
[2] *National Institute for Astrophysics (INAF), Osservatorio Astronomico di Palermo, Piazza del Parlamento 1, Palermo, Italy*

**antonio.pantano@unipa.it*

1. Introduction

A non-destructive evaluation (NDE) technique capable of testing the dispersion of nanoparticles in a nanocomposite would be of great use to the manufacturing industry in verifying the quality of manufactured products and ensuring compliance with their specifications. At present there are very few NDE techniques in the literature capable of effectively assess such crucial parameter in a fast and comprehensive way [1-3]. In this work, a novel pulsed laser micro-thermography (PLMT) approach for the evaluation of carbon-based nanoparticles dispersion level is proposed.

2. Materials and methods

The technology involves nanoseconds laser pulsed excitation as heat source in combination with a cooled infra-red (IR) camera equipped with macro lenses in reflection mode. The methodology is tested on benchmark epoxy enriched carbon nanotubes (CNTs) samples produced with different dispersion grades of nanoparticles.

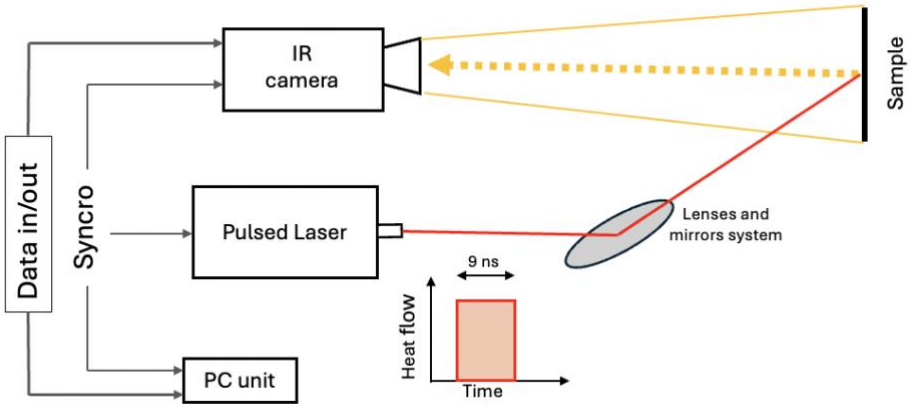

Fig 1. Experimental set-up for the PLMT technique.

3. Results and conclusions

The preliminary IR thermography outcomes indicate the presence of CNTs aggregates at the samples' surface and sub-surface. Also, the geometric and energetic resolution is further enhanced compared to previous works in the literature using a flash-based heat source [1-3]. Therefore, the technique could be employed for in-line inspection during the production of nanostructured parts, allowing for fast quality control of the manufactured, thus deploying the full potential of the material.

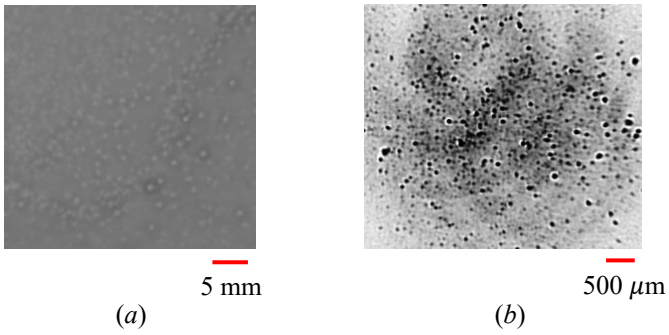

Fig. 2. IR frames showing CNTs aggregates in epoxy resin obtained with previous pulsed-flash thermography set-up (*a*) [2], and current pulsed-laser one (*b*).

4. Acknowledgements

The research presented in this paper has received funding from the project "SiciliAn MicronanOTecH Research And Innovation CEnter "SAMOTHRACE" (MUR, PNRR-M4C2, ECS_00000022), spoke 3 - Università degli Studi di Palermo "S2-COMMs - Micro and Nanotechnologies for Smart & Sustainable Communities"

5. References

[1] Montinaro N., Fustaino M., Bellisario D., Santo L., Quadrini F., Pantano A. "Testing the Dispersion of Nanoparticles in a Nanocomposite with an Ultra-Low Fill Content Using a Novel Non-Destructive Evaluation Technique", Materials, 15(3), 1208, 2022. DOI: 10.3390/ma15031208, ISSN: 19961944.

[2] Montinaro N., Fustaino M., Pantano A. "Carbon nanotubes dispersion assessment in nanocomposites by means of a pulsed thermographic approach", Materials, 13 (24), art. no. 5649, pp. 1-13, 2020. DOI: 10.3390/ma13245649, ISSN: 19961944.

[3] Pantano A., Montinaro N., Cerniglia D., Micciulla F., Bistarelli S., Cataldo A., Bellucci S., "Novel non-destructive evaluation technique for the detection of poor dispersion of carbon nanotubes in nanocomposites". Composites Part B: Engineering, Vol. 163, p. 52-58, 2019. DOI: 10.1016/j.compositesb.2018.10.097, ISSN: 1359-8368.

Energy-based approaches for a rapid fatigue characterisation of AlSi10Mg-AM

R. De Finis[1], D. Palumbo[2] and U. Galietti[2]
[1] Department of Engineering for Innovation (DII), University of Salento, Lecce, Italy
[2] Department of Mathematics, Mechanics and Management(DMMM), Polythecnic of Bari, Italy

1. Introduction

Additive manufacturing is a new material production technique that combines several technological advantages such as the ability to build complex-shaped components in a relatively short time and using a relatively circular process [1]. However, there are still many challenges to be overcome regarding structural integrity assessment and material characterization. Indeed, precisely with regard to the characterization of heterogeneous or anisotropic microstructure, the presence of residual stresses and induced defects, or the dependence of material properties of building direction and orientation may entail the definition of ad-hoc testing and analysis procedures. In particular, the dynamics involved in the fatigue behavior of these materials are not yet fully understood and therefore, new methodologies are needed to study the fatigue behavior and eventually estimate the material endurance limit in a rapid way [1-2].

The experimental mechanics provides invaluable support for both structural integrity checks and material characterization [3-9]. In particular, infrared thermography, which is used in the rapid characterization of materials, allows for the early detection of damage in the material and the study of damage in a relatively short time. By exploiting the material's self-heating [3-5], it is possible to assess the material's fatigue behavior from very low stress levels until failure. Energy-based methodologies [6-9], founded upon the evaluation of quantifiable variables such as temperature and strain, have exhibited their efficacy in the identification of damage, even in the presence of small surface defects, and in the separation of inelastic from anelastic material behavior. More in detail, in recent years, the estimation of energy dissipated during fatigue processes through the assessment of temperature fluctuations (second amplitude harmonics, or SAH [7-9]) has demonstrated considerable potential for the precise analysis of material behavior through the assessment of a parameter that is resistant to the influence of numerous disturbing noise factors.

This paper presents preliminary results of fatigue characterization of the AlSi10Mg-AM alloy produced by selective laser melting, using rapid methods. The SAH and the area under hysteresis loop are used as damage indices and to study the material behavior.

The results will also be analyzed in terms of material specificity: SAH will represent not only dissipative but also thermoelastic effects. This significantly complicates the assessment of material behavior.

2. Materials and methods

The present study dealt with AlSi10Mg-AM alloy produced by selective laser melting. The experimental plan investigated in was extended to the vertically and horizontally built heat-treated (age-hardening for 6 hours-T6). All samples were prepared by painting the surface with a matt black spray to enhance surface emissivity and make it uniform. All fatigue tests were performed on a servo-

hydraulic MTS 647 loading machine with a 100kN load cell. The tightness of the clamps was 6 MPa. The stepwise loading procedure [3-9] consists of a sequence of load blocks, each with the same duration of load cycles and fixed values for load frequency and stress ratio. The sequence of blocks is defined by incrementally increasing the applied stress level. Three acquisitions are carried out at each load step at 1000 and 15000 cycles respectively at a loading frequency of 15hz which is sufficiently high to avoid loss of adiabatic conditions. To acquire thermal data Flir X6540SC Infrared detector was adopted. In particular, the IR camera presented a cooled detector with 640*512 pixels matrix and a NETD lower than 25 mK. The adopted frame rate to obtain IR films was 200Hz. An extensometer MTS 634 (clip-on type with 25 mm gage length) acquired the strain data at 500 frame per second.

3. Results and conclusions

Figure 1 shows the curves of the second amplitude harmonic-SAH (Fig. 1a) and the area under the hysteresis loop-Wp (Fig. 1a) for the specimens built in the vertical direction.

As can be seen from Figure 1a, there is no real cut-off point in the thermal behaviour of the material as would be expected from the reference parameter (Figure 1b). This may be due to the superposition of reversible and irreversible effects in the thermal behaviour of the material. It should also be noted that aluminium does not have a true fatigue limit, but rather a fatigue strength at a given number of cycles. This will require future testing to better understand how to separate the two reversible and irreversible thermal contributions, as well as ad hoc processing procedures.

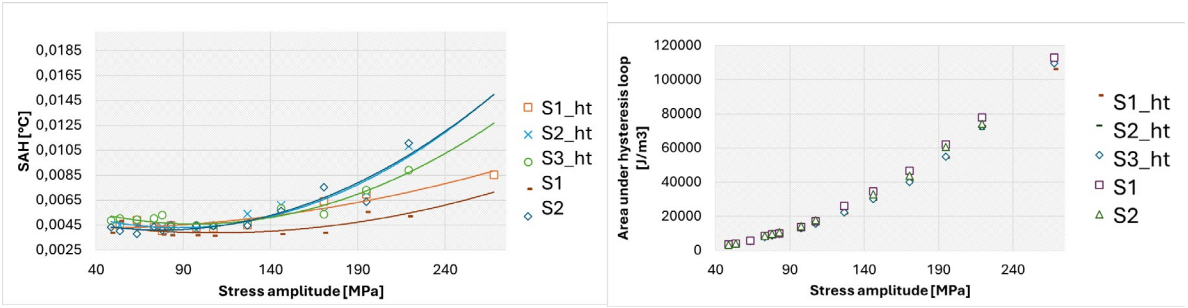

(a) (b)

Fig. 1. Curves for samples realized in z-direction with and without heat treatment (ht=heat treatment), (a) SAH , (b) area under hysteresis loop (Wp).

4. References

[1] Liu, H., Yu, H., Guo, C., Chen, X., Zhong, S., Zhou, L., Osman, A., & Lu, J. (2023). Review on Fatigue of Additive Manufactured Metallic Alloys: Microstructure, Performance, Enhancement, and Assessment Methods.

[2] Beretta, S., Gargourimotlagha, M., Folettia, S., du Plessisb, A., & Riccio, M. (2020). Fatigue strength assessment of as built AlSi10Mg manufactured by SLM with different build orientations.

[3] M.P. Luong, Fatigue limit evaluation of metals using an infrared thermographic technique, Mechanics of Materials, 28 (1998) 155-163.

[4] G. Fargione, A. Geraci, G. La Rosa, A. Risitano, Rapid determination of the fatigue curve by the thermographic method, International Journal of Fatigue, 24 (2002) 11-19.

[5] T. Boulanger, A. Chrysochoos, C. Mabru, A. Galtier, Calorimetric analysis of dissipative and thermoelastic effects associated with the fatigue behavior of steels, International Journal of Fatigue, 26 (2004) 221-229.

[6] F. Maquin, F. Pierron, Heat dissipation measurements in low stress cyclic loading of metallic materials: From internal friction to micro-plasticity, Mechanics of Materials, 41 (2009) 928-942.

[7] R. De Finis, D. Palumbo, U. Galietti, A multianalysis thermography-based approach for fatigue and damage investigations of ASTM A182 F6NM steel at two stress ratios, Fatigue & Fracture of Engineering Materials & Structures, 42 (2019) 267-283.

[8] G. Meneghetti, M. Ricotta, Estimating the intrinsic dissipation using the second harmonic of the temperature signal in tension-compression fatigue. Part II: Experiments, Fatigue & Fracture of Engineering Materials & Structures, 44 (2021) 2153-2167.
[9] R. De Finis, D. Palumbo, U. Galietti, On the relationship between mechanical energy rate and heat dissipated rate during fatigue for a C45 steel depending on stress ratio, Fatigue & Fracture of Engineering Materials & Structures, 44 (2021) 2781-2799.

STRESSES AND DEFORMATIONS INDUCED BY CURING IN EPOXY MATRIX CFRPs COMPOSITE LAMINATES

A. Mengozzi[1], M. Giacalone[1], E. Dolcini[2], S. Mantovani[1]
[1] Department of Engineering "Enzo Ferrari" (DIEF), University of Modena and Reggio Emilia, Modena, Italy
[2] Bucci Composites S.p.A. in Faenza, Italy

1. Introduction

Carbon Fiber-Reinforced Polymer (CFRP) laminate manufacturing may induce residual stresses and deformations, causing undesired dimensional deviations and formation of cracks [1][2]. These are induced by differential fibre-matrix thermal expansion and cure shrinkage. The latter is responsible for a volumetric reduction of the epoxy resin, which was quantified by Li *et al.* up to 7% [3]. The resulting deviations complicate assembly and increase production costs. The understanding of residual strains is crucial for producing high-quality composites.
This work presents a 3D multi-physics processing model, based on Finite Element Methods (FEM), to estimate the effects of the curing. A transient thermal load case is imposed on the model to simulate the laminate consolidation in the autoclave [4]. A kinetic phenomenological model describes the changes of polymeric phase with time under the influence of temperature. The investigation allowed to study the mechanical response of two laminates, with a stacking sequence of [0/0], [0/90].

2. Materials and methods

A 3D numerical model of a flat laminate was developed using FEM software Marc Mentat. Each ply has a thickness of 0.3 mm. The model was discretized using eight-node hexagonal elements. The mesh size (2 mm) was assigned after convergence tests. Each UniDirectional (UD) laminae was assigned orthotropic properties [5][6][7][8][9] (mechanical, thermal) according to the relative carbon fibre/epoxy matrix ratio, in accordance with micromechanics theory. Isostatic constraints were imposed on laminate, while a thermal face film was applied to describe the convective heat exchange between the environment and the laminate. At the kinetic level, the model responds to the Kamal-Sourour law [10]. Finally, a heat generation term, expressed as a function of cure rate and the total heat of reaction, is introduced to account for the heat emitted during the curing [11][12]. The simulation performed is of the coupled thermo-mechanical type in transient regime.

3. Results and conclusions

Awaiting experimental validation, the preliminary results of this computational study are shown in Fig. 1 and Fig. 2. At the material level, the fibre-matrix differential thermal contraction and the volumetric shrinkage of the epoxy due to cross-linking generate internal forces in the laminate that can be likened to membrane loads responsible for intra-plane deformations and out-of-plane bending. The curvature in Fig. 1 agrees with the classical laminate theory, according to which a laminate with an asymmetrical lamination sequence with respect to the mean plane, will have the coupling matrix terms, B11, B22, B12 different from zero. The data in the graphs of Figs. 2 are derived from a nodal sampling at the last increment of the analysis. This extremal node is located at the maximum x and y coordinate values, on the top face, belonging to the lamina with 0° orientation. It can be seen from

Fig. 1 that an increase in temperature induces rapid cross-linking. This demonstrates the direct proportionality of cure rate with Ki, the reaction rate constant, which, according to an Arrhenius-type trend, depends exponentially on temperature. A simultaneous increase in the degree of cure and volumetric shrinkage is observed until the degree of cure tends to one and the volumetric shrinkage value reaches a maximum (around 7.5%) [3] and remains constant until the end of the analysis. This trend reflects the theoretical principles. In fact, at the completion of cross-linking, all the reactive functional groups have reacted, resulting in the formation of a three-dimensional lattice. The formation of new covalent chemical bonds causes a reduction in the free volume between the polymer chains limiting their mobility.

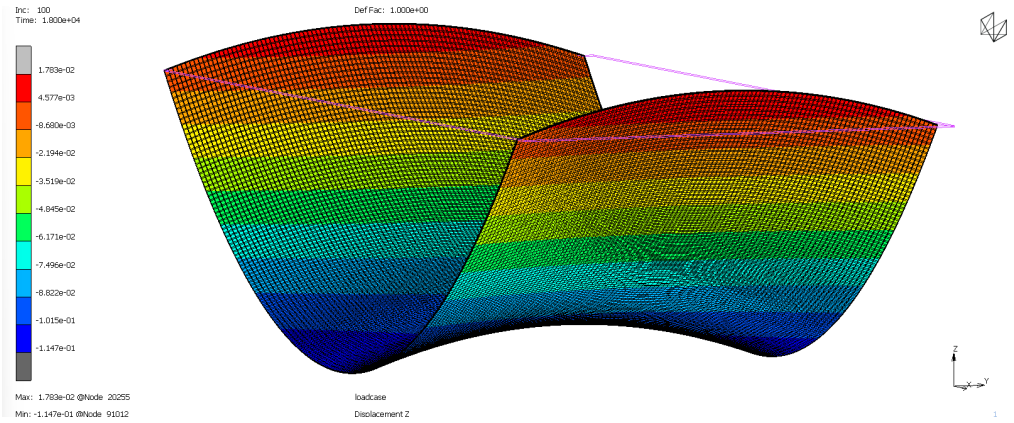

Fig. 1. Deformation of a laminate [0/90] at the end of cooling

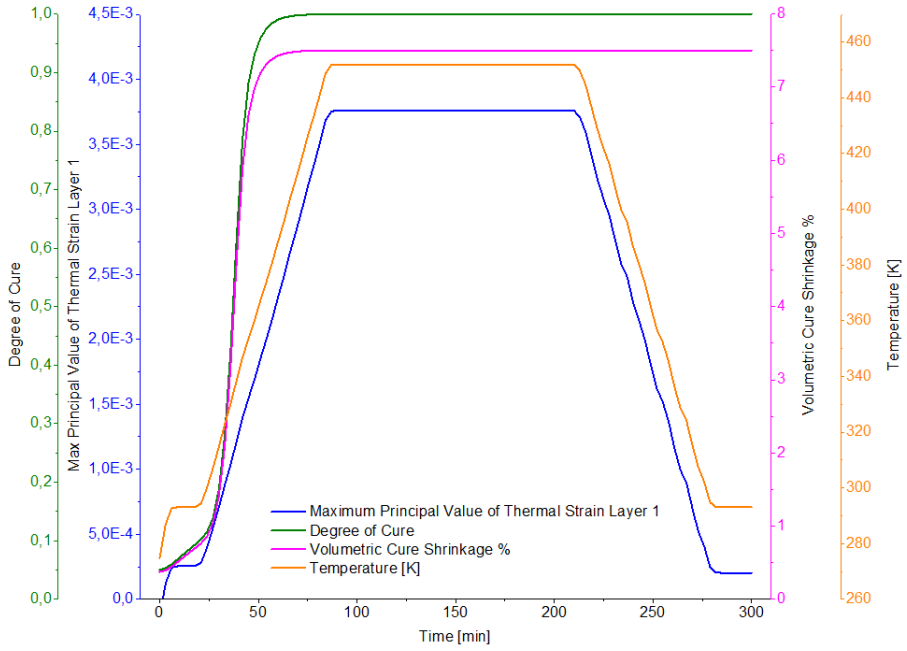

Fig. 2. Evolution of thermal profile, degree of cure, volumetric shrinkage and maximum thermal strain during curing simulation of a laminate [0/90]

4. Acknowledgements

The research presented in this paper has received funding from the Department of Engineering "Enzo Ferrari" (DIEF), University of Modena and Reggio Emilia. Special thanks to the company Bucci Composites S.p.A.

5. References

[1] Wisnom MR, Gigliotti M, Ersoy N, Campbell M, Potter KD. Mechanisms generating residual stresses and distortion during manufacture of polymer-matrix composite structures. Compos Part A Appl Sci Manuf 2006;37:522–9. https://doi.org/10.1016/j.compositesa.2005.05.019.

[2] White SR, Hahn HT. Journal of Composite Materials 1992. https://doi.org/10.1177/002199839202601604.

[3] Li C, Potter K, Wisnom MR, Stringer G. In-situ measurement of chemical shrinkage of MY750 epoxy resin by a novel gravimetric method. Compos Sci Technol 2004;64:55–64. https://doi.org/10.1016/S0266-3538(03)00199-4.

[4] Johnston A, Hubert P, Fernlund G, Vaziri R, Poursartip A. PROCESS MODELLING OF COMPOSITE STRUCTURES EMPLOYING A VIRTUAL AUTOCLAVE CONCEPT n.d.:235–52.

[5] Penn L. Chapter 3, Epoxy Resins, Handbook of Composites. Chapman Hall, 1998, p. 48–74.

[6] Lafdi K, Wright MA Chapter 9, Carbon Fibers, Handbook of Composites. Chapman Hall, 1998, p. 169-200.

[7] Gupta VB, Drzal LT, Lee CY-., Rich MJ. The temperature-dependence of some mechanical properties of a cured epoxy resin system. Polym Eng Sci 1985;25:812–23. https://doi.org/10.1002/pen.760251305.

[8] Simon SL, Mckenna GB, Sindt O. Modeling the evolution of the dynamic mechanical properties of a commercial epoxy during cure after gelation. J Appl Polym Sci 2000;76:495–508. https://doi.org/10.1002/(SICI)1097-4628(20000425)76:4<495::AID-APP7>3.0.CO;2-B.

[9] Dong C, Li K, Jiang Y, Arola D, Zhang D. Evaluation of thermal expansion coefficient of carbon fiber reinforced composites using electronic speckle interferometry. Opt Express 2018;26:531. https://doi.org/10.1364/oe.26.000531.

[10] Sourour S, Kamal MR. Differential scanning calorimetry of epoxy cure: isothermal cure kinetics. Thermochim Acta 1976;14:41–59. https://doi.org/10.1016/0040-6031(76)80056-1.

[11] Bogetti TA, Gillespie JW. Two-Dimensional Cure Simulation of Thick Thermosetting Composites. J Compos Mater 1991;25:239–73. https://doi.org/10.1177/002199839102500302.

[12] Loos AC, Springer GS. Curing of Epoxy Matrix Composites 1983;17:135–69.

INCREASING DAMAGE ASSESSMENT IN HYBRID WOVEN COMPOSITES USING A NOVEL THERMOGRAPHIC PROCEDURE

T. Matarrese[1], C. Sergi[2], D. Palumbo[1], F. Sarasini[2]and U. Galietti[1]
[1] Department of Mechanics, Mathematics and Management (DMMM), Polytechnic University of Bari, Bari, Italy
[2] Department of Chemical Engineering Materials Environment, University of Sapienza, Roma, Italy

1. Introduction

Currently, many researchers are studying innovative composite materials realized with natural, animal, or mineral fibers for minimizing the carbon footprint on the environment. However, the realization of these eco-friendly components yields it not suitable for structural applications [1-2].

In literature, an effective strategy adopted for enhancing poor mechanical properties is based on the hybridization approach. However, the structural integrity of these hybrid composites is significantly affected when are impacted at low velocity. In this work, pulsed active thermography techniques have been employed to characterize the damaged area of hybrid composites made of flax and basalt fibers impacted at the same energy level but with different masses (3-6-9 kg) [3-4].

These kinds of fibers have been employed as reinforcement of a polypropylene matrix with and without the addition of a coupling agent PP and PP_C, respectively.

The aim of this work is to develop a suitable procedure useful to enhance the assessment of the damaged area in hybrid composites [5]. In particular, for all the investigated specimens an estimation of the depth and extension of the damaged area has been performed and the obtained results have been compared and critically discussed.

2. Materials and methods

The laminates were manufactured by adopting a compression molding machine as shown in Figure 1 (a). The experimental tests were carried out in reflection mode with two flash lamps each one of 3000 J, in Figure 1 (b) [3-4]. The thermographic sequences were collected using the cooled IR camera A6751 by FLIR equipped with an FPA detector having a resolution of 640 × 512 pixels and a thermal resolution NETD < 20 mK. The geometrical resolution was 0.3 mm/pixel. Then, the software IR Max by FLIR was used for acquiring thermal sequences with a frame rate of 200 Hz.

3. Results and conclusions

A qualitative estimation of the extension and depth and damaged area for the PP_C specimen impacted to 3 J and 9 kg is shown in Figure 2 (a) and (b), respectively.

As can be seen, the damaged area appears as a cross shape. In Figure 2 (a) the upper part of the cross appears superficially damaged as it is detected around 2 - 4 s with respect to the down part of the cross that it is later detected. In Figure 2 (b) the extinction of the damaged area is assessed inside the red circle having the same dimension as the clamping system (~ 40 mm, i.e, 133 pixels). The damaged area is represented with white pixels, and it is equal to 30.6 %.

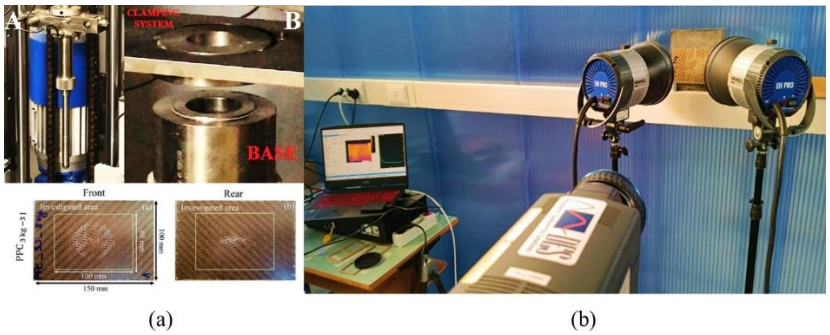

Fig. 1. (a) Drop weight tower and PP_C specimen impacted at 3 J and 9 kg. (b) Experimental set-up carried out in reflection mode.

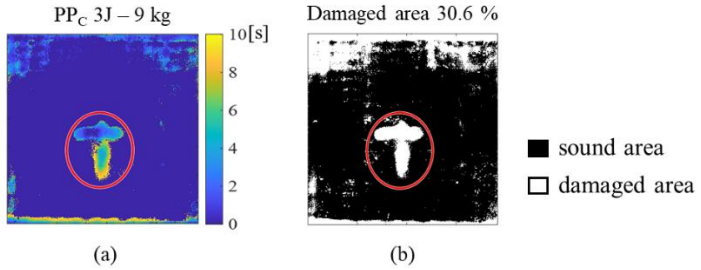

Fig. 2. Qualitative results for estimating (a) the depth and (b) the extension of the damaged area for the PP_C specimen subject to energy levels of 3 J and 9 kg.

Acknowledgements

Parts of the activities have been financed by the European Union – NextGenerationEU (National Sustainable Mobility Center CN00000023, Italian Ministry of University and Research Decree n. 1033 - 17/06/2022, Spoke 11 - Innovative Materials & Lightweighting). The opinions expressed are those of the authors only and should not be considered as representative of the European Union or the European Commission's official position. Neither the European Union nor the European Commission can be held responsible for them.

5. References

[1] A. Saleem; L. Medina; M. Skrifvars and L. Berglin (2020) Hybrid Polymer Composites of Bio-Based Bast Fibers with Glass, Carbon and Basalt Fibers for Automotive Applications - A Review, *Molecules*, **25**, 4933.

[2] F. Sarasini; J. Tirillò; L. Ferrante; C. Sergi; P. Russo; G. Simeoli; F. Cimino M.R. Ricciardi and V. Antonucci (2019), Quasi-Static and Low-Velocity Impact Behavior of Intraply Hybrid Flax/Basalt Composites, *Fibers,7, 26.*

[3] J. M. Roche and D. L. Balageas (2015). Common tools for quantitative pulse and step-heating thermography – part II: experimental investigation. *Quantitative InfraRed Thermography Journal*, **12**, 1–23.

[4] E. D'Accardi; F. Palano; R. Tamborrino; D. Palumbo; A. Tatì; R. Terzi and U. Galietti (2019). Pulsed phase thermography approach for the characterization of delaminations in CFRP and comparison to phased array ultrasonic testing. *Journal of Nondestructive Evaluation*, **38**,1-12.

[5] G. Poelman; S. Hedayatrasa; W. Van Paepegem and M. Kersemans (2023). Enhanced Thermographic Inspection of Woven Fabric Composites by k-Space Filtering, *Composites Part B: Engineering*, 252, 110508.

RAPID FATIGUE CHARACTERIZATION OF SINGLE ROW BOLTED LAP CFRP JOINTS VIA INFRARED THERMOGRAPHY

N. Manoharan[1] and S. Gururaja[1]
[1] *Department of Aerospace Engineering, Auburn University, Auburn, USA*

1. Introduction

Due to several advantages, including lightweight and tailored superior mechanical properties, polymer composites have replaced metals in aircraft structures. Since the 1960s, carbon fiber-reinforced polymer (CFRPs) composite usage in aircraft structures has gradually increased, with modern aircraft structures incorporating CFRP over 50% by weight. In such large structures, efficient load transfer under operation is vital. Mechanical joining has been the primary form of assembly in aerospace structures due to several advantages, such as ease of handling [1]. Specifically, single-row bolted lap joints have been predominantly used for in-plane load transfer applications. Under cyclic loading, such complex geometries show multi-step damage progression with varying failure modes such as bearing, net tension, cleavage, and shear-out. Understanding the cause of such different failure modes is necessary since catastrophic failures such as net tension should be avoided.

Additionally, to ensure the structural integrity of composite aircraft structures, adherence to 'no-growth' philosophy is a requirement [2]. Though traditional methods such as stress-life (S-N) curve approach are accurate, high time consumption and resource allocation are some major drawbacks. In addition, SN approach is heuristic, with no apparent correlation between the damage state and applied loads. Alternatively, passive infrared thermography, a rapid no-growth limit evaluation technique developed by La Rosa and Risitano in 1983 [3], has recently gained attention. The technique is based on the 'self-heating' phenomenon observed for all engineering materials under cyclic loads, where stabilized surface temperature behavior could be correlated to the material degradation. When plotted against the applied load levels, a bilinear trend could be observed for the stabilized mean surface temperature at increasing loads. The intersection point provided the no growth limit, thus ensuring fewer specimens and a huge reduction in testing time. In addition to its rapid nature, the technique has also gained attention for evaluating damage progression in the material by recording and analyzing thermal signals and their harmonic components.

In this study, the no-growth limit of aerospace-grade plain-weave CFRP single-row bolted lap joints was evaluated using IRT. Additionally, the first and second harmonic components of the recorded temperature signal were probed to understand the damage progression leading to varying failure modes. The first harmonic component represented the stress distribution across the specimens, while the second harmonic component map along the gage length represented the intrinsic dissipation. Thus, the observations from both maps provided insights into the damage state of the material. The thickness of the specimen blanks was varied, namely 8 and 12-ply specimens were tested to evaluate the effect of laminate thickness on the final failure mode and the no-growth limit.

2. Materials and methods

Plain-weave CFRP single-row bolted lap joints with two specimen blank thicknesses (8 and 12-ply) were tested under stepwise constant amplitude fatigue blocks with increasing loads. The specimen geometry was in accordance with ASTM D5961 standard, with a constant hole size of diameter (D) = 4.83 mm. The blanks were obtained by milling and mechanically joined by a titanium pin and aluminum alloy collar fastener system with a torque-off range of 2.82-3.95 N-m. By recording the stabilized mean surface temperature, the no-growth limit intersection for both configurations was evaluated using Huang's approach [4]. The first and second harmonic components of temperature signals in the gage section were plotted (pixelwise) for each thickness case and compared to understand the change in damage progression and final failure mode.

3. Results and conclusions

The no-growth limit evaluation for both configurations using IRT can be seen in Fig. 1. Approximately a 10 percent increase in the no-growth limit was evident with a reduction in thickness. This could be related to observations by Collings [5] where higher values of bearing strength were observed with a reduction in thickness. In addition, varying failure modes were observed between the two configurations, the temperature harmonic component maps were used to validate the damage progression in each case.

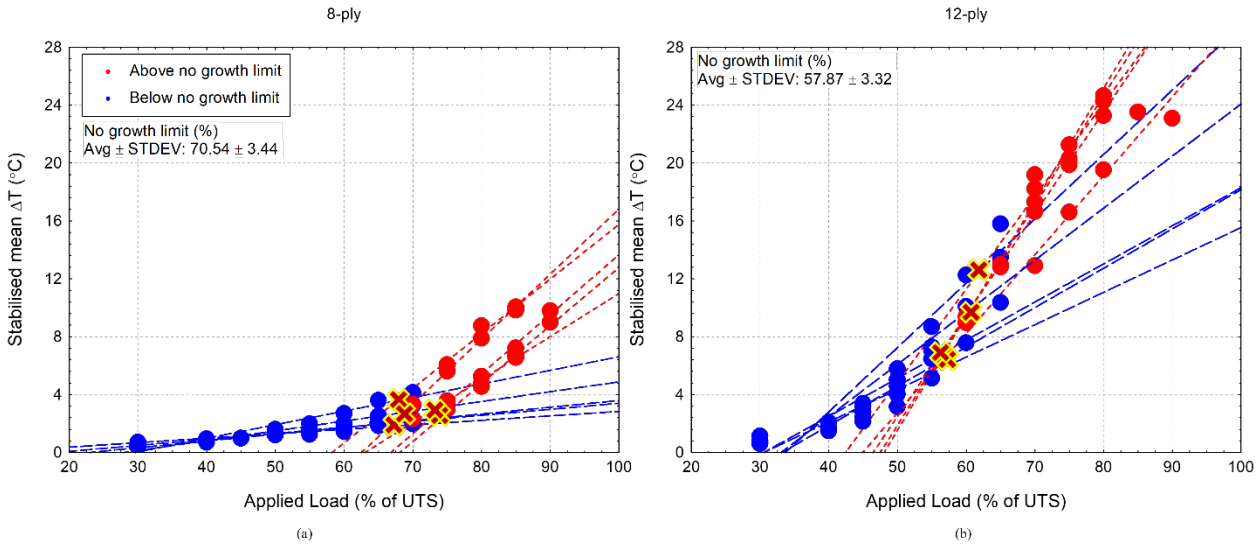

Fig. 1. No growth limit evaluation a) 8-ply, b) 12-ply configurations (intersection marked)

4. References

[1] S.D. Thoppul, J. Finegan, and R.F. Gibson (2009). Mechanics of mechanically fastened joints in polymer–matrix composite structures–a review. *Composites Sci. Tech.*, **69(3-4)**, 301–329.

[2] AC FAA (2009). AC 20-107B, Composite Aircraft Structure. *US Department of Transportation Federal Aviation Administration*.

[3] G. La Rosa and A. Risitano (2000). Thermographic methodology for rapid determination of the fatigue limit of materials and mechanical components. *Int. J. Fatigue*, **22**, 65–73.

[4] J. Huang, M.L. Pastor, C. Garnier, and X. Gong (2017). Rapid evaluation of fatigue limit on thermographic data analysis. *Int. J. Fatigue*, **104**, 293–301.

[5] T. A. Collings (1977). The strength of bolted joints in multi-directional CFRP laminates. *Composites*, **8**, 43–55.

Temperature harmonic analysis to investigate intrinsic dissipation of fatigue loaded Ti6Al4V produced by laser powder bed fusion

F.W. Panella[3], G. Pitarresi[1], D. Crisafulli[2], R. Penna[3], P. Leo[3], G. Pollara[1], G. Risitano[2], M. Tornabene[1]

[1] Dipartmento di Ingegneria, University of Palermo, Italy
[2] Dipartmento di Ingegneria, University of Messina, Italy
[3] Dipartimento di Ingegneria dell'Innovazione, University of Salento, Italy

1. Introduction

Laser-based powder bed fusion of metals (LPBF) is an additive manufacturing technology capable of producing complex parts using aerospace-grade metal alloys such as T6Al4V [1]. One crucial aspect that this technology needs to fully address to gain wider recognition in highly regulated industrial sectors is the ability to ensure adequate structural fatigue performance. The high porosity, inherent in this manufacturing process, can indeed reduce the domain of safe allowable stresses, thus compromising the lightweight potentials achievable with the LPBF manufacturing flexibility. Standard procedures to characterise the fatigue behavior of the material are time-consuming and require strict control of sample tolerances and surface finishes rarely met by the actual status of raw manufactured pieces, which then need further and intense post-processing treatments.

The present work explores the possibility of adopting Infrared Thermography for a rapid fatigue characterization of raw LPBF test coupons [2, 3]. This is based on the rationale that the rate of intrinsic dissipation of mechanical energy into heat rapidly increases above a certain cyclic stress amplitude. Such threshold stress amplitude can be interpreted as an intrinsic fatigue limit of the material. In this work, temperature metrics adopted to identify this threshold during stepwise fatigue tests are obtained from the temperature harmonic content [3]. This is extracted from temperature signals sampled at high framerate over short time intervals.

2. Methodology

The higher-order theory of the thermoelastic effects, applied to a tensile sample under uniaxial loading, predicts a temperature evolution that can be generally expressed as [4]:

$$\dot{T} = -T_o K_\omega \sigma_a \sin(\omega t) - T_o K_{2\omega} \sigma_a^2 \cos(2\omega t) \quad (1)$$

where K_ω and $K_{2\omega}$ are constants that depend on the material and the applied mean stress, σ_a is the applied stress amplitude, T_o is mean temperature and ω the angular loading frequency. Eq. (1) states that under linear elastic straining the material produces a temperature modulation with a well-predicted amplitude and phase at the load frequency (first harmonic, ω) and at twice the load frequency (second harmonic, 2ω). Some studies have evidenced that the first and second harmonics can be suitable temperature metrics to identify the intrinsic dissipation threshold [2,3]. This is due to the fatigue irreversible changes that arise in the material which leave a peculiar signature in the material thermoelastic response. In this work, harmonics are obtained by applying the Discrete Fourier Transform to the temperature acquired in a 5 s interval at a sampling rate of 200 Hz [3]. Temperature datasets are acquired on tensile samples under cyclic sinusoidal loading at 13 Hz, with load-ratio R=0.1.

Samples were produced using Ti6Al4V powder and an SLM 280HL machine [1]. Two sets of production parameters were used, with different values of supplied power, scanning velocity and line energy density (LED): 150 W, 1400 mm/s, 0.11 J/mm (for lot 1) and 350 W, 1400 mm/s, 0.25 J/mm (for lot 2). Net-shaped tensile samples were fabricated following ASTM E466 (see Fig. 1-left), with the lot produced at the higher LED having higher material density and smaller average pore size.

Figure 1 shows a map of the first harmonic amplitude from lot 1 and the trend of first and second harmonic amplitudes at different load steps, with $\Delta\sigma_a$=22.5 MPa. Each load step was applied for 5000 cycles, and harmonics were measured after 1000, 2500, and 4000 cycles within each step.

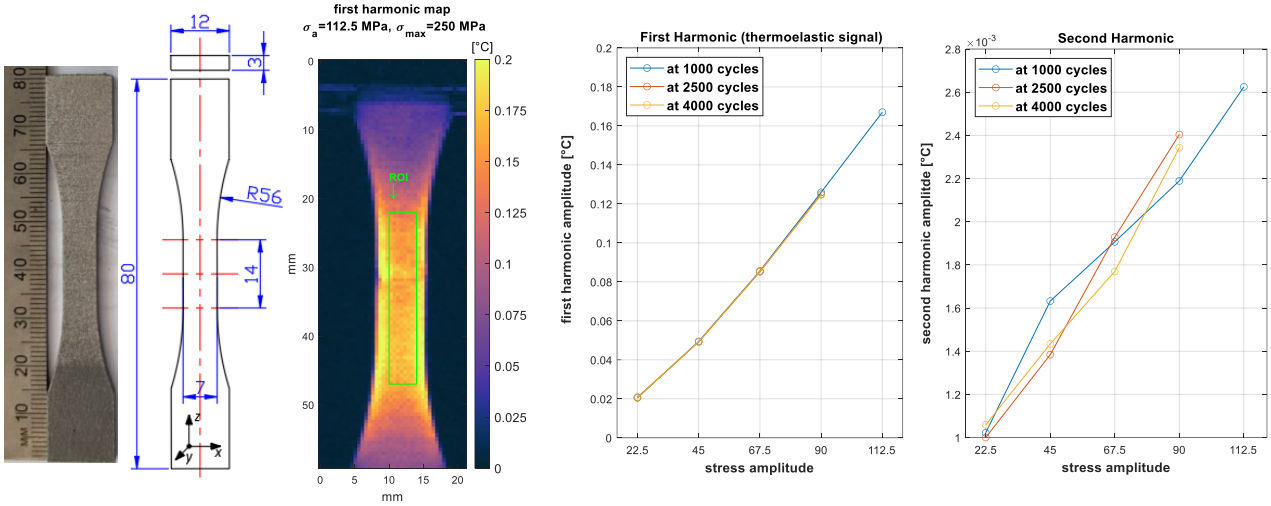

Fig. 1. (from left) sample drawing, thermoelastic map, plots of first and second harmonics.

3. Results and conclusions

Preliminary results show that although the sample had a brittle early failure before the onset of intrinsic dissipation (after 21600 cycles, i.e. during the fifth load step), the harmonic metrics acquired at different instants of each load-step showed similar values and trends. Future tests will be carried out measuring harmonics at an early stage, thus accumulating fewer loading cycles, with aim to reach higher stress levels before rupture. Moreover, samples will be tested after some post-processing treatments to explore if higher stress levels and intrinsic dissipation are reached.

4. Acknowledgements

The present research has received funding from the European Union's Framework Program for Research and Innovation - *Mission 4 - Component C2 Investment 1.1 (PRIN - 2022)* – project title MADforLIFE, code: 2022JE3LRA_001, CUP: B53D23006070006.

5. References

[4] G. Buffa, D. Palmeri, G. Pollara *et al.* (2024). Process parameters and surface treatment effects on the mechanical and corrosion resistance properties of Ti6Al4V components produced by laser powder bed fusion. *Prog Addit Manuf,* **9**, 151–167.

[1] R. Cappello, G. Meneghetti, M. Ricotta, G. Pitarresi (2022), On the correlation of temperature harmonic content with energy dissipation in c45 steel samples under fatigue loading. *Mechanics of Materials*, **168**.

[2] A. Wong, R. Jones, J. Sparrow (1987). Thermoelastic constant or thermoelastic parameter? *Journal of Physics and chemistry of solids* **48 (8)**, 749–753.

[3] M. Zaeimi, R. De Finis, D. Palumbo, U. Galietti (2024). Fatigue limit estimation of metals based on the thermographic methods: A comprehensive review. *Fatigue & Fracture of Engineering Materials & Structures* **47 (3)**, 611–646.

Thermoelastic Stress Analysis

Analysis of Stress Behavior in $Ti_{90}Al_{(10-x)}V_{(x)}$ Alloy for Medical Applications Using CASTEP Simulations.

Charef Azzeddine[1]* ,Karima Zitouni[1], Said Benramech[2].

[1]Institution : LEMOP Laboratory, Laboratoire d'Etude des Matériaux Optoélectronique et Polymères, Oran University. Address : Oran 31000 Algeria.

[2]Institution : Laboratoire de Physique Photonique et Nanomatériaux Multifonctionnels, LPPNM, Biskra University,Address : Biskra 07000 Algeria.

*Email: azzoucharef3@gmail.com

1. Introduction

The mechanical performance of titanium alloys is crucial for their use in orthopedic implants, where they must endure complex physiological stresses. This study utilizes first-principles calculations with CASTEP software to analyze the stress behavior of $Ti_{90}Al_{(10-x)}V_x$ alloys, focusing on compositions with x values from 1 to 9. Our findings reveal that the alloy with x=4 ($Ti_{90}Al_6V_4$) achieves an optimal balance of mechanical properties, positioning it as a promising candidate for biomedical applications [1]. Specifically, $Ti_{90}Al_6V_4$ shows a tensile strength of approximately 951 MPa and a Young's modulus of 110 GPa, closely aligning with the mechanical characteristics of human cortical bone [2]. This compatibility is vital to mitigate stress shielding, which can lead to bone resorption and implant failure [3]. In contrast, alloys with higher vanadium content (x=8 and x=9) exhibit increased tensile strength but also higher stiffness, which could worsen stress shielding [4]. Conversely, the alloy with x=1 displays lower tensile strength, potentially lacking sufficient mechanical support under physiological conditions [5]. Additionally, the $Ti_{90}Al_6V_4$ alloy demonstrates favorable deformation behavior under stress, with a yield strength of 880 MPa and an elongation at break of 12%, indicating good ductility [6]. These properties suggest that the alloy can effectively absorb and distribute mechanical loads, reducing the risk of implant failure due to brittle fracture. In conclusion, the $Ti_{90}Al_6V_4$ alloy provides a desirable combination of strength, stiffness, and ductility, meeting the mechanical requirements for orthopedic implants. This study offers valuable insights for further experimental validation and potential clinical use of this alloy in biomedical devices.

2. Materials and methods

This study uses CASTEP software to perform first-principles calculations, analyzing the stress behavior of $Ti_{90}Al_{(10-x)}V_x$ alloys, with x ranging from 1 to 9, to identify compositions that balance strength, stiffness, and ductility for orthopedic applications.

2.1 Simulation Parameters and Computational Setup

2.1.1 Computational Model: Density Functional Theory (DFT) within the Generalized Gradient Approximation (GGA) framework and Perdew-Burke-Ernzerhof (PBE) functional were used for accurate interatomic interaction representation.

2.1.2 Pseudopotentials: CASTEP's ultrasoft pseudopotentials were applied to enhance computational efficiency while maintaining precision in electronic and structural analysis.

2.2 Stress and Mechanical Property Calculations

2.2.1 Stress-Strain Analysis: CASTEP's stress-strain module evaluated tensile strength, Young's modulus, and yield strength, providing insight into each alloy's performance under physiological loads.

2.2.2 Ductility Analysis: Ductility was assessed by examining yield strength and elongation at break, focusing on compositions that withstand physiological stresses without fracturing.

3. Results and Discussion

The table below provides a summary of the tensile strength, Young's modulus, yield strength, and elongation at break for each $Ti_{90}Al_{(10-x)}V_x$ alloy composition:

Alloy Composition	Tensile Strength (MPa)	Young's Modulus (GPa)	Yield Strength (MPa)	Elongation at Break (%)
$Ti_{90}Al_9V_1$ (x=1)	685.55	92.82	649.58	15
$Ti_{90}Al_8V_2$ (x=2)	721.42	95.96	721.25	14
$Ti_{90}Al_7V_3$ (x=3)	823.98	101.09	803.74	13
$Ti_{90}Al_6V_4$ (x=4)	951.87	107.97	894.71	12
$Ti_{90}Al_5V_5$ (x=5)	1076.54	117.01	945.21	10
$Ti_{90}Al_4V_6$ (x=6)	1125.09	129.78	961.37	9
$Ti_{90}Al_3V_7$ (x=7)	1146.87	141.64	976.52	8
$Ti_{90}Al_2V_8$ (x=8)	1188.71	155.35	993.84	6
$Ti_{90}Al_1V_9$ (x=9)	1227.49	168.76	1017.54	5

Table 1 : Mechanical Properties of Ti90Al(10−x)Vx Alloys with Varying Vanadium Content (x = 1 to 9)

This table highlights the mechanical properties of Ti90Al(10−x)Vx alloys with varying vanadium content (x=1 to x=9). As vanadium content increases, both tensile strength and Young's modulus rise, indicating enhanced strength and stiffness. However, this increase in mechanical strength comes at the cost of reduced ductility, as shown by the decreasing elongation at break.

The alloy with x=4 (Ti90Al6V4) achieves a balanced combination of properties, with a tensile strength of 951.87 MPa and a Young's modulus of 107.97 GPa, values close to those of human bone.

This compatibility can help reduce stress shielding, a condition where excessive stiffness in implants causes bone loss around the implant site. Additionally, the alloy maintains good ductility, with an elongation at break of 12%, which is essential for absorbing physiological stresses.

In contrast, alloys with x=8 and x=9 have higher strength but low ductility (5-6%), increasing the risk of brittle fracture, which may limit their suitability for orthopedic implants.

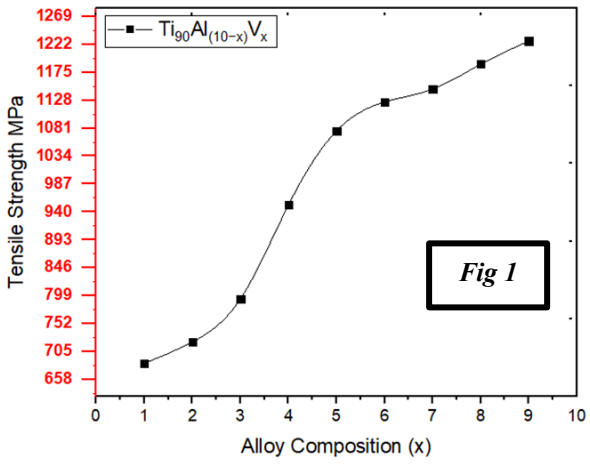

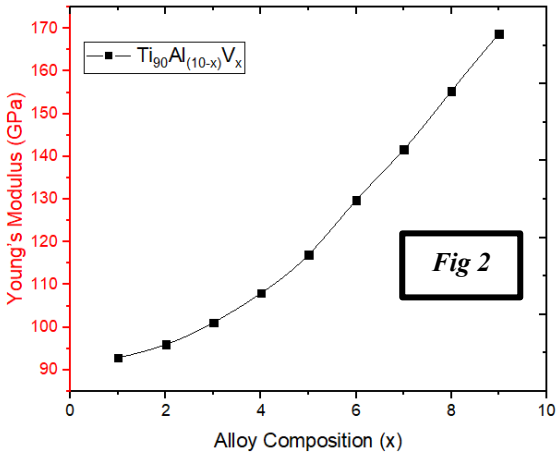

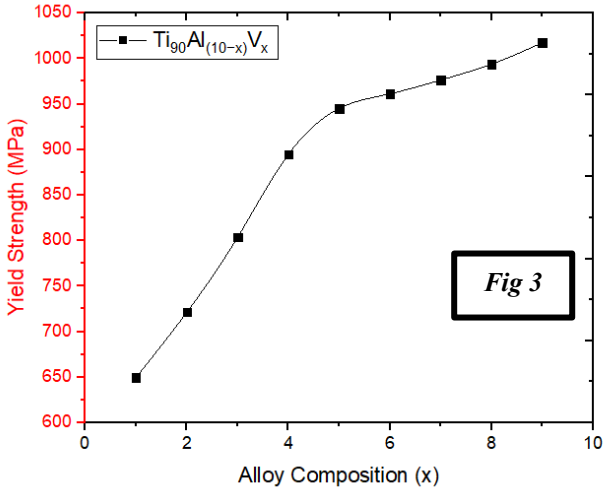

***Fig 1**:Tensile Strength Variation of $Ti_{90}Al_{(10-x)}V_x$ Alloys as a Function of Vanadium Content (x).*

***Fig 2:**Variation of Young's Modulus in $Ti_{90}Al_{(10-x)}V_x$ Alloys as a Function of Vanadium Content (x).*

***Fig 3:**Variation of Yield Strength in $Ti_{90}Al_{(10-x)}V_x$ Alloys as a Function of Vanadium Content (x).*

4. Conclusion

In conclusion, this study demonstrates that the Ti90Al6V4 alloy (containing 4% vanadium) is the optimal choice for medical applications, particularly for orthopedic implants [07]. This alloy effectively combines high strength, moderate stiffness, and appropriate ductility, making it a strong candidate for medical devices such as bone implants that require a balance between mechanical support and compatibility with natural bone properties [08]. The mechanical properties of this alloy, with a tensile strength of approximately 950 MPa and a Young's modulus of 110 GPa, closely align with the mechanical characteristics of human bone [09]. This compatibility reduces the phenomenon of "stress shielding," which occurs when there is a significant mismatch between implant stiffness and bone stiffness. Stress shielding leads to the implant absorbing most of the load, limiting the stimulation of the surrounding bone, ultimately causing bone resorption around the implant and potential implant failure [10]. Moreover, Ti90Al6V4 demonstrates relatively high ductility, with an elongation at break of around 12%, indicating its capability to absorb and distribute mechanical loads effectively [11]. This property is crucial for reducing the risk of brittle fracture, which can cause implant failure under the dynamic and repeated loads implants face in the body [12]. On the other hand, alloys with higher vanadium content, such as Ti90Al2V8 and Ti90Al1V9, exhibit greater stiffness, but their Young's modulus exceeds 150 GPa, increasing the likelihood of stress shielding [13]. Conversely, alloys with lower vanadium content, such as Ti90Al9V1, show

lower tensile strength, which may be insufficient to provide the necessary mechanical support for load-bearing implants [14].
Based on these findings, the Ti90Al6V4 alloy can be considered a balanced solution, meeting the essential requirements of orthopedic implants by offering load-bearing capacity while minimizing the risks of stress shielding [15]. However, further experimental validation is needed to confirm these results and ensure the long-term biocompatibility of the alloy in the human body. This study provides a robust theoretical framework for the development of innovative and effective bone implants and opens the door for the use of titanium alloys in future medical applications that enhance patient quality of life [16].

References :

1. Long, M., & Rack, H. J. (1998). Titanium alloys in total joint replacement—a materials science perspective. *Biomaterials*, 19(18), 1621-1639.
2. Niinomi, M. (1998). Mechanical properties of biomedical titanium alloys. *Materials Science and Engineering: A*, 243(1-2), 231-236.
3. Geetha, M., Singh, A. K., Asokamani, R., & Gogia, A. K. (2009). Ti based biomaterials, the ultimate choice for orthopaedic implants – A review. *Progress in Materials Science*, 54(3), 397-425.
4. Okazaki, Y., Rao, S., Ito, Y., & Tateishi, T. (1998). Corrosion resistance, mechanical properties, corrosion fatigue and cytocompatibility of new titanium alloys for medical implants. *Materials Science and Engineering: A*, 243(1-2), 250-256.
5. Abdel-Hady Gepreel, M., & Niinomi, M. (2013). Biocompatibility of Ti-alloys for long-term implantation. *Journal of the Mechanical Behavior of Biomedical Materials*, 20, 407-415.
6. Yang, C., Tian, X., Li, D., Wang, J., Tang, Y., & Zhao, K. (2015). Bio-functionalization of titanium surface with protein to improve the bioactivity and biocompatibility for medical application. *Scientific Reports*, 5, 9872.
7. Elias, C. N., Lima, J. H. C., Valiev, R., & Meyers, M. A. (2008). Biomedical applications of titanium and its alloys. *JOM*, 60(3), 46-49.
8. Leyens, C., & Peters, M. (2003). *Titanium and Titanium Alloys: Fundamentals and Applications*. John Wiley & Sons.
9. Froes, F. H. (2015). *Titanium: Physical Metallurgy, Processing, and Applications*. ASM International.
10. Boyer, R., Welsch, G., & Collings, E. W. (Eds.). (1994). *Materials Properties Handbook: Titanium Alloys*. ASM International.
11. Ahmed, N., & Galy, J. (2021). Modeling and experimental analysis of Ti-6Al-4V alloy for biomedical applications: mechanical properties, biocompatibility, and tribological behavior. *Journal of Alloys and Compounds*, 856, 158-167.
12. Kobayashi, E., Matsumoto, S., Yoneyama, T., & Hamanaka, H. (1995). Mechanical properties of the binary titanium-zirconium alloys and their potential for biomedical materials. *Journal of Biomedical Materials Research*, 29(8), 943-950.
13. Heinl, P., Müller, L., Körner, C., Singer, R. F., & Müller, F. A. (2008). Cellular Ti–6Al–4V structures with interconnected macro porosity for bone implants fabricated by selective electron beam melting. *Acta Biomaterialia*, 4(5), 1536-1544.
14. Levine, B. R., Della Valle, C. J., Jacobs, J. J. (2006). Applications of titanium in the orthopedic field. *Journal of the American Academy of Orthopaedic Surgeons*, 14(5), 239-248.
15. Wang, K. (1996). The use of titanium for medical applications in the USA. *Materials Science and Engineering: A*, 213(1-2), 134-137.
16. Sumner, D. R., & Galante, J. O. (1992). Bone ingrowth and stress shielding with a porous coated implant. *Clinical Orthopaedics and Related Research*, 274, 192-201.

NUMERICAL SIMULATION FOR THE THERMAL-MECHANICAL RESPONSE OF PBX-2 EXPLOSIVES AT DIFFERENT HEATING RATES*

***Xiaoli ZHANG*[1]**
[1] *Institute of Applied Physics and Computational Mathematics,*
Fenghao Donglu No.1, Haidian District, Beijing, P.R. China, 100094

1. Introduction

The ammunition can usually be heated by the unexpected thermal source. As a rule, the process is called “cookoff”. The heating can be rapid or very slow, or anything in between. The energetic material can be homogeneous, or it may have been damaged, either through thermal expansion and chemical processes or mechanically.

This paper is intended to study the thermal-mechanical response of the explosives in fast cookoff. The numerical simulation of the thermal-mechanical response of the PBX-2 explosives with steel confinement at different heating rates were carried out by means of LS-DYNA program.

2. Modeling

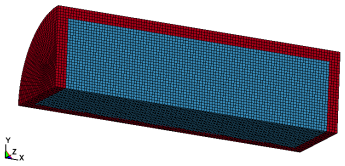

Figure 1. The calculation grid of model

The calculating model was established by means of ANSYS. The charge size isφ50mm×100mm and the thickness of the confinement is 4mm.The grid size is 1mm. The heating rates are respectively 1K·min^{-1}, 3K·min^{-1} and 10K·min^{-1}.

The calculating model equation as follows:

$$\rho c \frac{dT}{dt} = \lambda \nabla^2 T + S \tag{1}$$

It is the thermal conductive equation with source term. where ρis the density,c is specific heat at constant pressure, λ is the thermal conductivity; S is the heat source term of the explosive decomposing reaction.

The self-decomposing can be described by Arrhenius equation as follows[1] :

$$S = \rho Q Z \left(1-\alpha\right)^n \exp(-E/RT) \tag{2}$$

where S is the heating source term of decomposition reaction ; ρis the TNT density (kg·m^{-3}) ; Q is the reaction heat (J·kg^{-1}) ; Z is the frequency factor (s^{-1}) ; E is the activation energy (J·mol^{-1}) ; α is the reaction fraction; n is the reaction order. R is the gaseous constant (J·mol^{-1}·K^{-1}) .

* Corresponding author:Xiaoli ZHANG,E-mail:xiaoli_zhang79@yahoo.com

3. Results and discussions

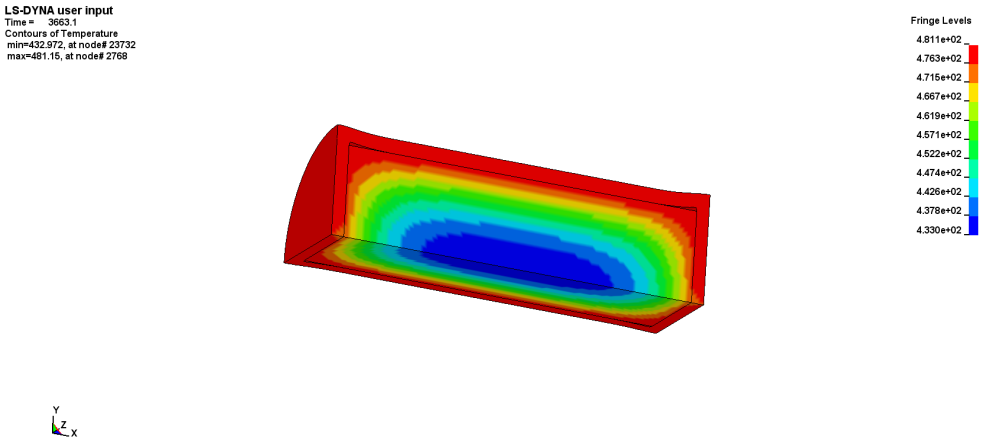

Figure 2. Temperature distribution and deformation on cookoff bomb at 3 $K \cdot min^{-1}$

Fig.2 shows the temperature distribution and deformation on cookoff bomb at 3 $K \cdot min^{-1}$. At 3663s ,the bomb burst. The ignition time of the calculating agrees with that of the experiment[2]. The ignition location is at the corner of the confinement and the explosive.The ignition time are respectively 9820s、3663s、1329s at 1 $K \cdot min^{-1}$、3$K \cdot min^{-1}$、10$K \cdot min^{-1}$.The ignition time decreases with the increasing of the heating rate. The maximum pressure of the selected elements are respectively 5.5MPa、12.5 MPa、37 MPa at 1 $K \cdot min^{-1}$、3$K \cdot min^{-1}$、10$K \cdot min^{-1}$. The maximum pressure is augmenting with the increasing of the heating rate.

4. Conclusion

The numerical simulation of the thermal-mechanical response of the PBX-2 explosives with steel confinement at different heating rates was carried out by means of LS-DYNA program. From the simulation result, we get some useful conclusions:

1）The ignition time are decreasing with the increasing of the heating rate.

2）The ignition location is at the corner of the explosive and confinement.

3）The maximum of the pressure and effective stress of the explosive are all at the location of the center of the cylinder and the center of the two ends of the explosive cylinder

4）The maximum radial displacement of the node is also at the location of the corner of the confinement and explosive, which is not exceeding 2mm.

5. References

[1] Wang Pei , Chen Lang , Wang Yan , et al. Numerical simulation of explosive cookoff at different heating rate‖Huang Ping , Wang Yajun , Li Shengcai. *Theory and Practice of Energetic Materials* , VOLVII. Beijing :Science Press ,2007 :701-704

[2] DAI Xiao-gan,LV Zi-jian,SHEN Chun-ying,etc. Slow cookoff experiments and the numerical simulation of the two charge sizes of JOB-9003 explosive.*The 8th Academic Conference of Explosion Mechanics of China*, Jiang xi province,September 2007, 29-32

OPERATIONAL MODAL SHAPES OF PLATES USING DIGITAL IMAGE CORRELATION AND TSA

A. Molina-Viedma[1], L. Felipe-Sesé[1], E. López-Alba[1], F. Díaz-Garrido[1]
[1] *Department of Mechanical and Mining Engineering, University of Jaén, Jaén, Spain*

1. Introduction

Optical techniques have experienced an increasing interest to the experimental mechanics community thanks to being non-invasive and providing dense information. In vibration analysis, the community has found the characterization of operational deflection shapes (ODS) as one of their strengths. ODSs are the shape or deformation experienced at a specific frequency, usually resonances.

Digital image correlation (DIC) has demonstrated its capability for ODS characterization. Both with high-speed cameras [1] and low-speed cameras but with higher sensitivity to displacements [2]. A sub-sampling strategy solved the limitation in the frame rate of low-speed cameras through the stroboscopic effect.

Recently, some studies have shown the interest of thermoelastic stress analysis (TSA) for stress measurement associated with ODSs through IR cameras. TSA has been traditionally employed for low-frequency harmonic excitation but those studies have proven its capability for higher frequencies, even over 2000 Hz [3].

Although it is possible to obtain strain and stress maps, under plane tension assumptions, by differentiation of displacement fields of DIC, this processing introduces high-frequency noise that might spoil the results, especially for low amplitude events under vibration. However, TSA provides stress information through a direct measurement.

Considering that DIC and TSA provide complementary results, this work shows a methodology to combine displacement and stress measurements of resonance ODSs in a dense mesh of virtual sensors through a spatial calibration of the vision systems of each technique.

2. Materials and methods

The specimen was a squared aluminum plate. It was coated with black paint and then sprayed with a random white speckle meeting both a random pattern for DIC and a high emissivity for TSA.

The first step was to identify the natural frequencies of the plate. Thus, the plate was excited by the shaker with a random signal and the frequency response function was measured. Some resonances were then selected in the frequency response function as peaks.

After the resonances identification, the operational deflection shapes were measured by the DIC camera system of two high-resolution cameras and the IR camera during a monotonic sinusoidal test, as shown in Fig 1. As the frequencies of the resonance overcome the frame rate of both vision systems, a subsampling strategy was employed. With this method, the signals have a frequency lower than the actual but they preserve the amplitude, which is the relevant information for the study. For DIC, the sequences had 500 frames. For TSA, the image sequences had 10.000 frames, much longer due to the weakness of the thermoelastic signal. Both sequences were analyzed using the Fourier transform to obtain the ODS of displacement and stress for the specific frequency.

Finally, with the calibration of DIC and IR vision systems, displacements and stress fields were combined and associated with the same measurement points on the plate by spatial triangulation.

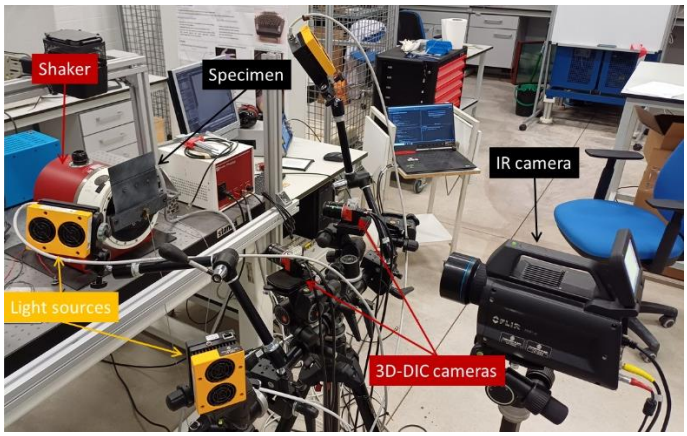

Fig. 1. Experimental setup for the integration of DIC and TSA.

3. Results and conclusions

As a result of the previous procedure, different ODSs of the plate were obtained through DIC and TSA. In Fig. 2, the displacement and stress ODS of a resonance at 1189 Hz is shown. Hence, with this methodology it is possible to characterize ODSs in terms of displacement and stress through a dense map of virtual sensors, providing an excellent tool for dynamic analysis and finite element model validation.

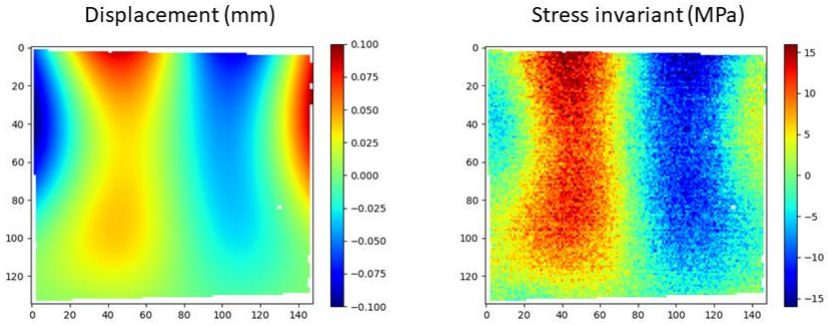

Fig. 2. Displacement and stress ODS at 1189 Hz of an aluminum plate obtained by DIC and TSA, respectively.

4. Acknowledgements

This research has been funded by Ministerio de Ciencia e Innovación of the Spanish Government through the R&D Projects through the grants PID2020-119107RA-I00 “Thermodop” and MCIN PID2022-141618OA-I00 “Integroptics”.

5. References

[1] A.J. Molina-Viedma, L. Felipe-Sesé, E. López-Alba and F.A. Díaz (2018). 3D mode shapes characterisation using phase-based motion magnification in large structures using stereoscopic DIC. *Mech. Syst. Signal Process.*, **108**, 140–155.

[2] P. Neri, A. Paoli, A.V. Razionale and C. Santus (2022). Low-speed cameras system for 3D-DIC vibration measurements in the kHz range. *Mech. Syst. Signal Process.*, **162**, 108040.

[3] A.J. Molina-Viedma, L. Felipe-Sesé, E. López-Alba and F.A. Díaz (2021). Thermoelastic effect in modal shapes at high frequencies using infrared thermography, *Measurement*, **176**, 109180.

THERMOELASTIC STRESS ANALYSIS SET UP OPTIMIZATION VIA ROBUST DESIGN

F. Di Carolo[1], U. Galietti[1]
[1] Department of Mechanics, Mathematics and Management, Polytechnic of Bari, Bari, Italy

1. Introduction

Thermoelastic Stress Analysis (TSA) is a thermographic technique for assessing surface stress states based on the thermoelastic effect caused by dynamic loads in the elastic field [1]. Advances in IR cameras have broadened TSA applications, including residual stress assessment [2], fracture mechanics [3], and fatigue characterization [4]. Calibration improves accuracy, but temperature-dependent material properties (e.g., in aluminum/titanium alloys) can introduce errors. Palumbo et al. proposed a correction for isotropic mono-axial loads [5], while Di Carolo et al. extended it to complex conditions with residual stresses [2]. This study uses a Robust Design-based approach [6][7] to analyze TSA errors under process variability, offering practical measurement guidelines.

2. Theory

In the case of a homogeneous and isotropic material, the TSA equation is[1]:

$$\frac{\Delta T}{T_0} = K_0 \cdot (\Delta\sigma_{11} + \Delta\sigma_{22}) \qquad \text{Eq.1}$$

ΔT in Eq 1 represents the temperature variation generated by the application of the loading system with principal stress sum $\Delta\sigma_{11} + \Delta\sigma_{22}$ at the same frequency. T_0 is the reference temperature and K_0 is the thermoelastic parameter, which depends on the material thermophysical properties.

The analytical model implemented in simulation is the TSA General Model [2], which includes the temperature dependency of mechanical properties and hence the effect of the mean load $\bar{\sigma}_m$. It is expressed by the following relation:

$$\Delta T = (\rho C_\varepsilon)^{-1} T_0 \left[\left(\bar{\bar{C}}^{-1} \left(\bar{\sigma}_m + \bar{\bar{R}} \bar{\sigma}_r \right) \right)^T \frac{\partial \bar{\bar{C}}^T}{\partial T} - \bar{\alpha}^T \bar{\bar{C}}^T \right] \bar{\bar{C}}^{-1} \Delta\bar{\sigma} \qquad \text{Eq.2}$$

Where:

- $\bar{\varepsilon}$, $\bar{\alpha}$ and $\bar{\bar{C}}$ represent respectively the state of deformation in a point, the vector of the linear thermal expansion coefficients and the material stiffness matrix.
- $\bar{\sigma}_r$ is the residual stress vector expressed in the principal system;
- the tensor $\bar{R}$ is the rotation matrix that allows writing $\bar{\sigma}_r$ in the equation reference system.

3. Materials and method

The aim was to identify the loading characteristics which ensure the more accurate and robust measurement of stresses by applying the classical TSA equation comparing three different calibration methods. The first calibration was simulated with free-residual stress samples, the second calibration was simulated considering a sample of the same material and the same residual stress conditions but with variable orientation for the residual stress principal system.

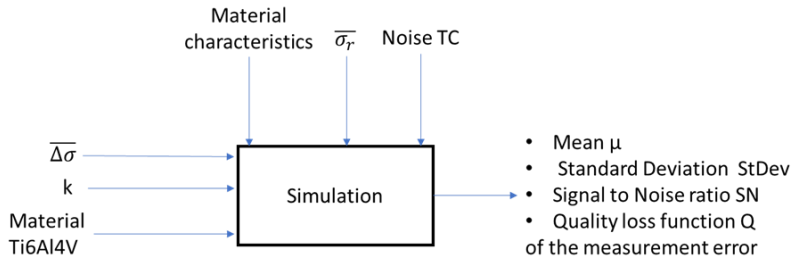

Fig. 1. Block diagram of the TSA stress measurement system

The study applied the Taguchi method, creating a control factors matrix with three values for each factor and an external matrix with two values for the material characteristics (Ti6Al4V alloy), three for the residual stress system characteristics, and three for IR camera noise. The only adjustable parameter for the operator is the ratio k, defined as the ratio between the mean and the load amplitude, constant for every pixel of the IR camera.

3. Results and conclusions

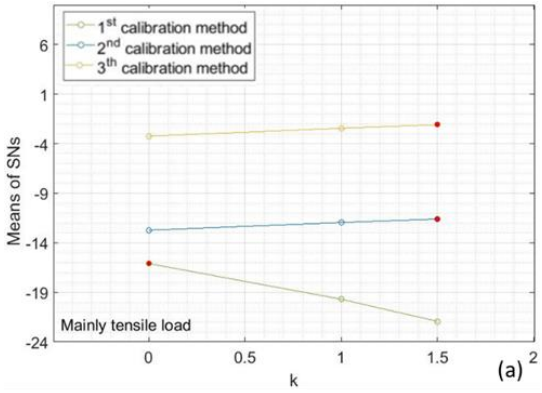

Fig. 2. Means of SNs of the relative error for each value of the control factor k and each calibration method

The plots of the *SN* (Fig. 2) how the quality of the measurement increases with the ratio k only with the first calibration, while for the two experimental calibration the mean load reduces the effect of the source of error due to residual stress. This latter effect is higher with the second calibration, when the calibration sample is relaxed end residual stress is completely neglected.

5. References

[1] N. Harwood, W.M. Cummings, Thermoelastic Stress Analysis, Adam Hilger: Philadelphia, PA, USA, 1991.

[2] F. Di Carolo, R. De Finis, D. Palumbo, U. Galietti, *A Thermoelastic Stress Analysis General Model: Study of the Influence of Biaxial Residual Stress on Aluminium and Titanium*, Metals 2019, 9, 671.

[3] D. Palumbo, F. Ancona, R. De Finis, U. Galietti, *Experimental study of the crack growth in stainless steels using thermal methods*, Procedia Engineering 109 (2015) 338 – 345.

[4] R. De Finis, D. Palumbo, U. Galietti, Mechanical behaviour of stainless steels under dynamic loading: An investigation with thermal methods, Journal of Imaging2(4),32.

[5] D. Palumbo, U. Galietti, Data correction for thermoelastic stress analysis on titanium components, Exp. Mech. 2016, 56, 451–462

[6] G. Taguchi, Introduction to Quality Engineering, Asian Productivity Organization (Distributed by American Supplier Institute Inc., Dearborn, MI) , 1986.

[7] S. M. Phadke, Quality Engineering Using Robust Design, Prentice Hall, Englewood Cliffs, N.J. , 1989

ASSESSMENT OF FATIGUE CRACK CLOSURE VIA WAVELET TRANSFORM OF INFRARED THERMOGRAPHY DATA

L. Bercelli[1], B. Levieil[1], C. Doudard[1] and S Calloch[1]
[1] ENSTA Bretagne, IRDL – UMR CNRS 6027, 29200 Brest, France

1. Introduction

The fatigue life of a structural component under cyclic loading can be distinguished in two phases: a crack initiation phase and a crack propagation phase. One phase might be neglected in the total life depending on the material properties, the component geometry and the nature of the loading. If the crack propagation phase is preponderant, the occurrence of a crack closure phenomenon (due to local stress state) can significantly affect the total fatigue lifetime [1]. Hence, its consideration in predictive models should improve fatigue life forecasts, provided that experimental data is made available. Although, the *in-situ* measurement of fatigue crack closure on full-scale structures remains a challenge. This study aims at introducing a new method for the *in-situ* observation and measurement of fatigue crack closure on structures via Thermoelastic Stress Analysis (TSA). This method is adapted to a wide range of scales and applicable with no prior knowledge of the position of cracks.

2. Materials and methods

The material of study is a DH36 naval-grade steel. In order to control the initiation site of fatigue cracks and their propagation in Mode I under cyclic loading, a notched sample was machined. Tests were performed using a hydraulic tensile testing machine at a constant stress range of $\Delta\sigma_{nom} = 128\,MPa$. A total of 72 loading configurations were explored, with loading ratios $R_{nom} = \frac{F_{min}}{F_{max}}$ ranging from 10 to -6, crack lengths ranging from 1 mm to 6 mm and mechanical frequencies ranging from 1 Hz to 10 Hz. The testing protocol is that of a conventional TSA test: the sample is coated with a high-emissivity black paint and infrared films are regularly recorded while under sine cyclic loading. An infrared camera of resolution 1536×1056 pixels (≈40 µm per pixel) is set with a sampling frequency of 100 Hz. Markers are added on the sample using low-emissivity paint to perform motion compensation of infrared films.

The TSA method relies on the post-processing of the temperature response linked to the thermoelastic coupling θ_{the}. For conventional steel under cyclic loading of mechanical frequency f_m, and supposing adiabatic conditions, the temperature response θ_{the} is also cyclic at frequency f_m, with an amplitude θ_{the}^{a} proportional to the amplitude of the first invariant of the stress tensor I_{1_a}.In practice, conduction effects are not negligible, hence the field of θ_{the}^{a} is a locally averaged image of the I_{1_a} field (Fig. 1.a). Although, TSA still allows the detection and monitoring of fatigue cracks due to their influence on the local stress field.

3. Results and conclusions

In the case of negative loading ratios R_{nom} (tension-compression), the fatigue crack alternatively opens and closes during one loading cycle, resulting in stress reversals close to the crack wake: from near-zero stress (open crack) to compressive nominal stress (closed crack). This induces discontinuities in the temperature response close to the crack wake, resulting in significative high-

frequency components. In that context, a Continuous Wavelet Transform (CWT) of the temperature signal is performed, decomposing the signal in a coherent time-frequency space, thus allowing to detect instants of stress-reversals [2]. From this information, a time of crack opening t_o can be measured, allowing for the definition of an effective stress range ratio $\tau_o = \frac{1-\cos(\pi f_m t_o)}{2}$ that links the nominal stress range $\Delta\sigma_{nom}$ to the effective stress range $\Delta\sigma_{eff} = \tau_o \Delta\sigma_{nom}$ (stress that effectively contributes to crack propagation). In the elastic case, τ_o^{th} can be directly linked to the loading ratio following $\tau_o^{th} = \frac{1}{1-R_{nom}}$. Measured values of τ_o at the crack wake are compared to τ_o^{th} both for perfect linear elastic simulation results (Fig. 1.b) and real experimental data (Fig. 1.c), considering the test configuration detailed above for a 3 mm long crack with $f_m = 10$ Hz. A very good agreement is found between the expected values τ_o^{th} and the measured values, both for perfect (noiseless) numeric data and experimental data. In practice, given the existence of crack tip plasticity, a gap can be found between τ_o^{exp} and τ_o^{th} for larger cracks, and a variation of τ_o^{exp} can be observed along the crack wake [3]. Nevertheless, simulation results validate the proposed method and experimental results gives good confidence in its applicability to more complex structures [4].

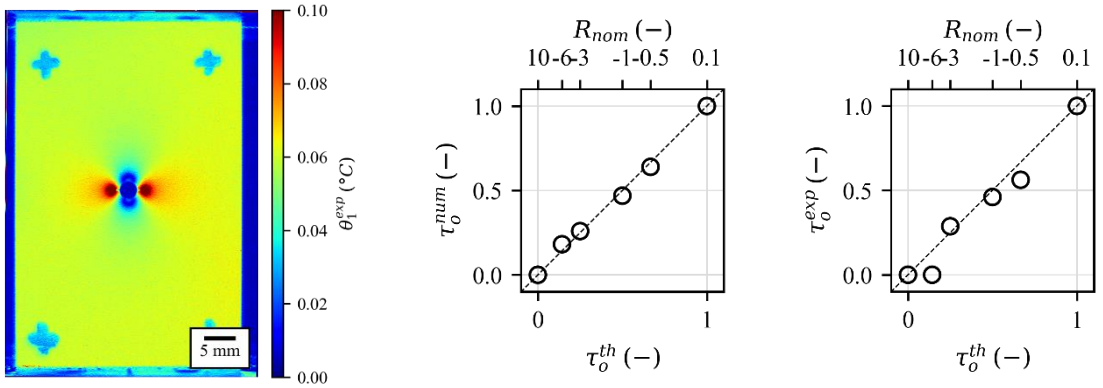

(a) (b) (c)

Fig. 1. Initial (crack free) field of the temperature first harmonic θ_1^{exp} (a) and values of τ_o^{num} for perfect thermoelastic simulation results (a) and τ_o^{exp} for experimental infrared data (b) plotted against the reference value τ_o^{th} for a 3 mm long crack with $f_m = 10$ Hz

4. Acknowledgements

A part of this study belongs to the "Self-Heating" ANR-Safran-Naval Group research chair (grant no. ANR-20-CHIN-0002), involving Safran Companies, Naval Group, ENSTA Bretagne (IRDL), and Institut.

5. References

[1] L. Bercelli, B. Levieil, C. Doudard, B. Malek, F. Bridier, and A. Ezanno, Use of infrared thermography to model the effective stress ratio effect on fatigue crack growth in welded T -joints, *Eng. Fract. Mech.*, vol. 279, no. September 2022, pp. 1–17, 2023.

[2] P. Du, W. A. Kibbe, and S. M. Lin, Improved peak detection in mass spectrum by incorporating continuous wavelet transform-based pattern matching, *Bioinformatics*, vol. 22, no. 17, pp. 2059–2065, 2006.

[3] L. Bercelli, B. Levieil, and S. Calloch, Fatigue crack closure assessment by wavelet transform of infrared thermography signals, vol. 190, no. October 2024, 2025.

[4] L. Bercelli, C. Guellec, B. Levieil, C. Doudard, F. Bridier, and S. Calloch, Stress ratio effect on fatigue crack growth assessment via thermoelastic stress analysis, *Procedia Struct. Integr.*, vol. 57, pp. 437–444, 2024.

OPTIMISED SAMPLING STRATEGIES FOR SELF-REFERENCED THERMOELASTIC STRESS ANALYSIS

G. Pitarresi[1], M. Tornabene[1], R. Cappello[1,2]
[1] Department of Engineering, University of Palermo, Italy
[2] Bristol Composites Institute, University of Bristol, UK

1. Introduction

The ability to analyze the temperature frequency content on materials under dynamic loading may enhance the analysis of thermomechanical couplings [1,2]. A peculiar signature in the frequency domain is indeed left by the thermoelastic effect, where elastic straining produces temperature variations. Other peculiar signatures may arise after the onset of damage, e.g.: stress relief following cracking, phase transitions, thermo-mechanical heat dissipation, etc. Specifically, Thermoelastic Stress Analysis (TSA) is renowned for providing quantitative stress parameters, subject to an accurate knowledge of the loading frequency, needed for an effective Temperature frequency demodulation. In the absence of such knowledge, coherent sampling cannot be ensured, potentially resulting in spectral leakage and poor noise filtering [3].

This study examines the conditions necessary to avoid spectral leakage and the risk of aliasing in self-referenced TSA. The impact of spectral leakage is evaluated with diverse signal processing techniques. The occurrence of aliasing collision frequencies is discussed concerning the choice of sampling parameters, and the role of synchronous and asynchronous sampling is discussed.

2. Materials and methods

TSA requires the filtering of harmonics from a temperature signal sampled over a time interval. Three signal processing schemes have been implemented: Digital Cross-Correlation (DCC) [2], Discrete Fourier Transform (DFT) [3] and Least Square Fitting (LSF) [1,4].

DCC provides the in-phase, X, and in-quadrature, Y, harmonic components with respect to a reference signal built upon the frequency being filtered:

$$X = \frac{2}{N} \cdot \sum_{j=1}^{N} T_j \cdot \sin\left(\frac{2\pi}{N} k \cdot j + \phi_r\right); \quad Y = \frac{2}{N} \cdot \sum_{j=1}^{N} T_j \cdot \cos\left(\frac{2\pi}{N} k \cdot j + \phi_r\right) \tag{1}$$

where N is the number of samples, ϕ_r is the phase shift between the self-reference signal and the initial sampling time [2], and $f_L = k \times f_f$ is the filtered frequency, with k being an integer multiple of the fundamental frequency $f_f = f_s/N$ and f_s the sampling frequency. The DFT formula of the k_{th} harmonic can be written as:

$$H_k = \sum_{j=1}^{N} T_j \cdot \left[\cos\left(\frac{2\pi}{N} k \cdot j\right) - i \cdot \sin\left(\frac{2\pi}{N} k \cdot j\right)\right] \tag{2}$$

where eqs. (1) and (2) are equivalent when k represents the frequency bin-number of the Fourier frequency domain. Finally, the implemented LSF is based on the minimisation of the sum of the square difference between the sampled temperature and its analytical model represented by:

$$T_{\mathrm{mod}}(t) = E \cdot \sin(2\pi f_L \cdot t + \phi_E) + D \cdot \sin(2\pi \cdot 2 f_L \cdot t + \phi_D) + \sum_{k=others} H_k \sin(2\pi \cdot n_k f_L \cdot t + \phi_k) \quad (3)$$

If k=0:(N-1)/2 terms are considered and an integer number of periods is included in the sampling time interval, then the LSF analytically coincides with the DFT [4].

The above signal processing schemes have been implemented to analyze a dog bone tensile specimen of stainless steel AISI 304l, under sinusoidal R=0.1 loading. The temperature is sampled with a FLIR X6540sc IR camera, with f_s=150 Hz.

3. Results and conclusions

A map of the thermoelastic signal amplitude ΔT and a table reporting average values obtained with varying N, f_L and k are reported in fig. 1.

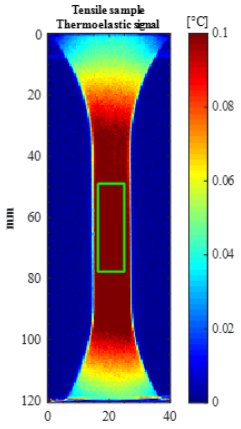

		f_L= (k-1)*fs/N			f_L=15 Hz			DCC with physical reference signal
		DFT	DCC	LSF	DFT	DCC	LSF	FLIR-THESA
N=4550 k=455 – f_L=15	ΔT [°C]	0.104	0.104	0.104	0.104	0.104	0.104	0.104
	St. dev [°C]	0.003	0.003	0.003	0.003	0.003	0.003	0.004
N=4553 k=455.3	ΔT [°C]	0.0894	0.0894	0.0894	×	0.125	0.104	
	St. dev [°C]	0.003	0.003	0.003	×	0.003	0.003	
	Err %	14.0	14.0	14.0	×	-20.2	0.0	
N=4555 k=455.5	ΔT [°C]	0.067	0.067	0.067	×	0.163	0.104	
	St. dev [°C]	0.002	0.002	0.002	×	0.003	0.003	
	Err %	35.6	35.6	35.6	×	-56.7	0.0	

Fig. 1. Thermoelastic map and thermoelastic signal values for different processing schemes, frequency bins and numbers of processed samples.

It is found that DCC and DFT produce different errors due to non-coherent sampling and spectral leakage. LSF is not affected by non-coherent sampling if it is performed knowing the correct loading frequency. For DCC and DFT to provide accurate results, the following coherent sampling conditions must be ensured:

$$\frac{f_L}{f_s} = \frac{(k-1)}{N} \quad \text{where } k \text{ and } N \text{ must be integers} \quad (4)$$

4. Acknowledgements

The present research has received funding from the European Union's Framework Program for Research and Innovation - *Mission 4 - Component C2 Investment 1.1 (PRIN - 2022)* – project title MAdforLIFE, code: 2022JE3LRA_001, CUP: B53D23006070006.

5. References

[1] J.C. Krapez, G Gardette, and D. Balageas (1995). Lock-In IR Thermography - advantages and problems of some approaches. Int. Workshop on Advanced Infrared Technologies and Applications.

[2] G. Pitarresi (2015). Lock-in signal post-processing techniques in infrared thermography for materials structural evaluation. Exp. Mech., **55**, 667–680.

[3] G. Pitarresi, R. Cappello and G. Catalanotti (2020). Quantitative thermoelastic stress analysis by means of low-cost setups. Optics and Lasers in Engineering, **134**, 106158, 11.

[4] U. Galietti, D. Modugno, and L. Spagnolo (2005). A novel signal processing method for tsa applications. Measurement Science and Technology, **16**, 2251–2260.

APPLICATION OF THERMOELASTIC STRESS ANALYSIS ON TITANIUM IN THE PRESENCE OF BIAXIAL STRESSES

D. Palumbo[1], R. De Finis[2]
[1]Department of Mechanics, Mathematics and Management, Politecnico di Bari, Via Orabona 4, 70125, Bari, Italy
[2] Department of Engineering for Innovation, Università del Salento, Via per Monteroni, 73100, Lecce, Italy

1. Introduction

Thermoelastic Stress Analysis (TSA) is a contactless, full-field technique used to assess superficial stresses in any material (metals and composites). Moreover, TSA can also provide damage parameters for investigating the fatigue behaviour of material and continuously monitoring crack growth [1]. The classic TSA theory [2] assumes that the effect of the mean stress can be neglected since the variations in Young's (E) and Poisson's (v) moduli with temperature are not significant [3], [4]. Several experimental works in the literature demonstrated that the effect of the mean stress cannot be neglected for some materials such as titanium and aluminium, so a new formulation needs to be adopted to avoid significant errors in stress assessment [3], [5].

The present works aim to investigate the effect of the means stress on the thermoelastic response of titanium material employing the extended TSA formulation and for a generic biaxial stress state [5]. In particular, a quantitative analysis was carried out to assess the effect of the mean stress on errors in stress evaluation by adopting the classical formulation.

2. Materials and methods

The tests were carried out on a TI6Al4V holed specimen applying a cyclic load with a sine wave in an elastic regime. The surface of the samples was painted matt black (Dupli-color, Special Thermo 800°C) to increase the emissivity. Three loading levels were applied at a mechanical frequency of 10Hz, characterized by a fixed amplitude and a variable mean load. The TSA data were acquired by a Deltatherm 1560 infrared camera with a focal plane array of 320*256 pixels, and NETD less than 18 mK. Thermal sequences were acquired at a frame rate of 153 frames per second for 2 minutes, setting the value of the "pixel integration time" equal to 75% [3]. The setup allowed a geometrical resolution of 0.27 mm/pixel. 1. A FEM analysis was carried out by using COMSOL® to estimate the stress behaviour of the material. The overall setup is represented in Figure 1.

3. Results and discussion

In Figure 2, experimental data obtained using the classical formulation and calibrated according to the classical approaches have been compared to numerical data considering a profile along a transverse direction through the centre of the sample.

The experimental data of the first stress invariant amplitude obtained using the classic thermoelastic formulation were affected by the mean stress, and a difference is observed between the experimental and FEM data, that the difference is likely due to the mean stress effect. In particular, the effect of the mean stress produced an overestimation of the measured stresses that was more evident in the proximity of the hole edges and increased as the mean stress increased.

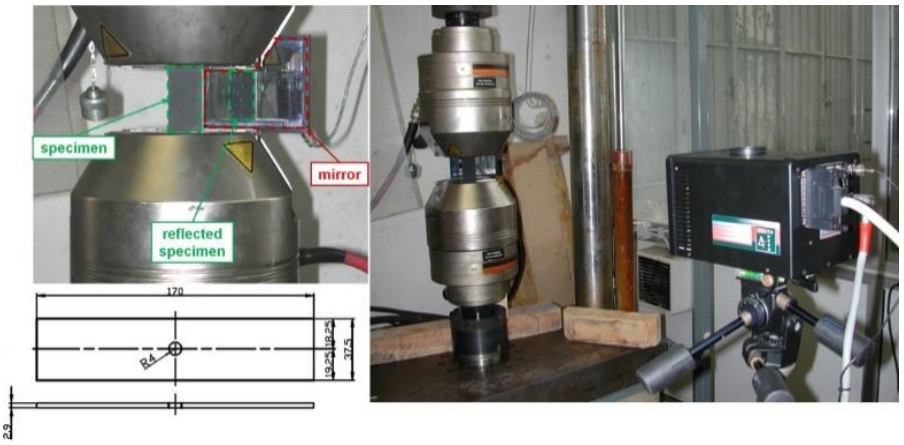

Fig. 1. Experimental set-up adopted for TSA tests and specimen geometry

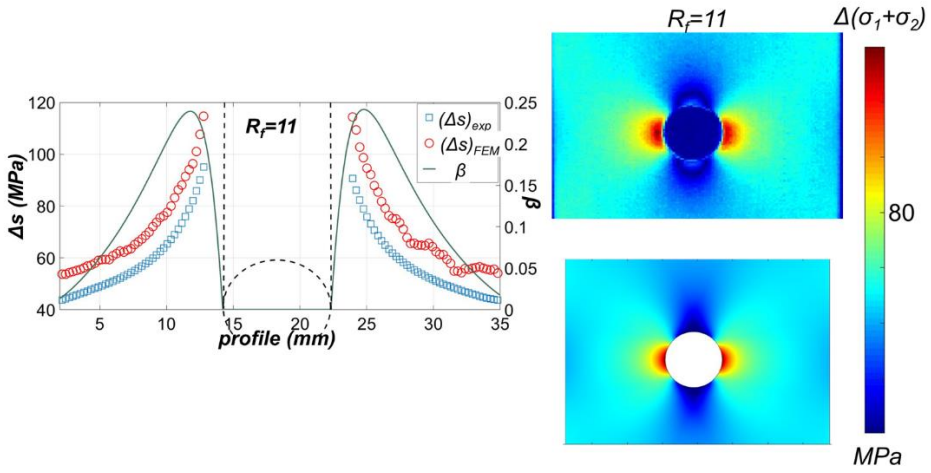

Fig. 2. Comparison between experiments and FEM data for a given level of stress ($\sigma m=253$ *MPa*)

4. Acknowledgements

Parts of the activities have been financed by the European Union – NextGenerationEU (National Sustainable Mobility Center CN00000023, Italian Ministry of University and Research Decree n. 1033 - 17/06/2022, Spoke 11 - Innovative Materials & Lightweighting). The opinions expressed are those of the authors only and should not be considered as representative of the European Union or the European Commission's official position. Neither the European Union nor the European Commission can be held responsible for them.

5. References

[1] JM. Dulieu-Barton, P. Stanley (1998). Development and applications of thermoelastic stress analysis. *J. Strain Analysis*, **33**, 93-104.

[2] G. Pitarresi, EA. Patterson (1999). A review of the general theory of thermoelastic stress analysis. *J. Strain Analysis*, **35**, 35-39.

[3] D. Palumbo, U, Galietti (2016). Data correction for thermoelastic stress analysis on titanium components. *Exp. Mech.*, **56**, 451–462.

[4] F. Di Carolo, R. De Finis, D. Palumbo, U. Galietti (2019). A thermoelastic stress analysis general model: Study of the influence of biaxial residual stress on aluminium and titanium. *Metals*, **9(6)**, 671.

[5] D. Palumbo, R. De Finis (2023). Thermoelastic Stress Analysis in the Presence of Biaxial Stresses in Titanium: Effect of the Mean Stress on Errors in Stress Evaluation. *Exp. Mech.*, **63 (8)**, 1335-1351

STRAIN EXPERIMENTAL MODAL ANALYSIS VIA A HIGH-SPEED THERMOELASTICITY-BASED APPROACH

L. Capponi[1], K. Zaletelj [1], G. Rossi[2], J. Slavič[1]
[1] Faculty of Mechanical Engineering, University of Ljubljana, Slovenia
[2] Department of Engineering, University of Perugia, Italy

1. Introduction

When a flexible structure is excited at or near one of its natural frequencies, resonance effects can arise, potentially resulting in vibration-induced fatigue damage [1]. To ensure structural integrity, health monitoring of such systems is essential, usually achieved through experimental measurements. Strain mode shapes provide valuable information for understanding the underlying structural dynamics of flexible structures, and, ultimately, reducing chances of unexpected fatigue failure [2]. Historically, strain gauges-based techniques have been the primary tools for this purpose. However, these methods often face limitations related to low spatial density, installation challenges, and vulnerability to environmental conditions. Over the past few decades, kinematic-based imaging has emerged as a promising alternative, offering non-invasive structural dynamics identification with enhanced spatial density [3]. Yet, accurately inferring full-field strain mode shapes using these techniques typically requires establishing a relationship between measured kinematic and stress/strain quantities. This process introduces uncertainties, especially when second-order spatial derivatives are involved.

Thermoelastic stress analysis, which operates in the infrared (IR) spectrum, has become a well-established method for measuring full-field stress and strain distributions in dynamically loaded structures. Its non-destructive nature makes it particularly effective for defect detection, fatigue crack monitoring, and investigating fatigue-related damage in the frequency domain [4]. While thermoelasticity has shown promise in these applications, its integration into strain experimental modal analysis (EMA) remains underexplored.

This study seeks to address this gap by developing a hybrid-EMA approach that leverages high-dynamic-range infrared sensors to capture, at high-speed, temperature variations on the surface of a flexible structure subjected to random excitation. Advanced thermoelasticity-based image processing algorithms are then employed to extract full-field strain mode shapes from the temperature data. The findings demonstrate that the hybrid-EMA method can accurately identify full-field strain mode shapes using IR imaging. The approach has been validated for materials such as aluminum and steel and provides insights into experimental design for achieving reliable results.

2. Materials and methods

The capabilities of the Telops FAST m3K high-speed thermal camera have been leveraged to measure temperature variations on the surface of a structure, undergoing a random load, with a Noise Equivalent Temperature Difference (NETD) of 32 mK, at 5 kHz sampling rate. The duration of the vibration test was 5 seconds, within which the excitation force was also measured. The Frequency

Response Functions were estimated, and the hybrid-EMA method was used to identify the thermoelasticity-based strain modal constants (see Fig 1).

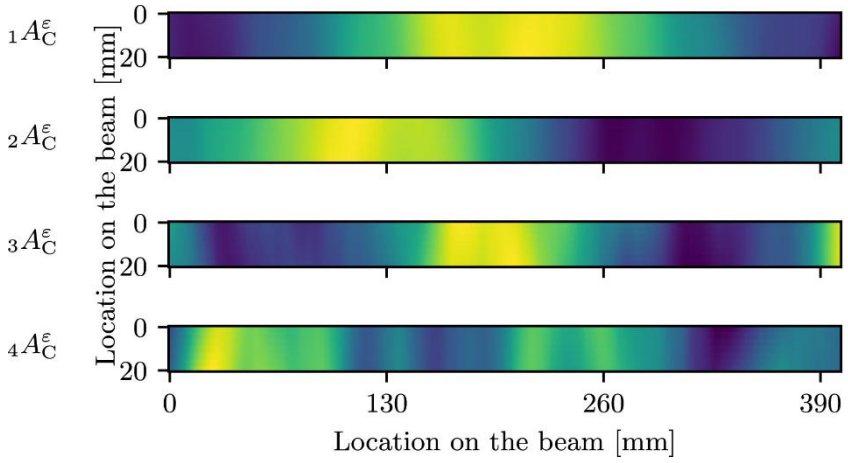

Fig. 1. First four full-field thermoelasticity-based strain modal constants A_C^ϵ

Finally, Modal Assurance Criterion (MAC) was employed to validate the results of the proposed methodology with the ones from established kinematic-based measurement techniques. The hybrid approach was shown to be essential for the identification of strain amplitudes below the noise floor of the IR-camera.

3. Acknowledgements

The research presented in this paper has received funding from the European Union's Horizon 2023 research and innovation programme under the MSCA grant ARTEMIDE, No. 101180595.

4. References

[1] D. Benasciutti, et al. (2015). Basic principles of spectral multi-axial fatigue analysis. *Procedia Engineering*, 101, 34-42.

[2] K. Zaletelj, et al. (2023). Strain experimental modal analysis of an Euler–Bernoulli beam based on the thermoelastic principle. *Mechanical Systems and Signal Processing,* 201, 110655.

[3] J. Javh, et al (2018). High frequency modal identification on noisy high-speed camera data. *Mechanical Systems and Signal Processing,* 98, 344-351.

[4] L. Capponi, et al. (2020). Thermoelasticity-based modal damage identification. *International Journal of Fatigue,* 137, 105661.

ALIASING INTERFERENCE AND SIGNAL UNDERSAMPLING IN THERMOELASTIC STRESS ANALYSIS

R. Cappello[1,2], G. Pitarresi[1]
[1] Department of Engineering, University of Palermo, Italy
[2] Bristol Composites Institute, University of Bristol, UK

1. Introduction

Thermoelastic Stress Analysis (TSA) relies on evaluating harmonic components of a temperature signal carrying temperature variations induced by cyclic elastic straining. These "thermoelastic" harmonics are typically modulated at frequencies f and $2f$, when f is the main loading frequency applied to the structure. Common algorithms to extract thermoelastic harmonics from a sampled temperature signal employ Discrete Fourier Transform (DFT) or Least Square Fitting based approaches [1]. These require the harmonic to be filtered to have at least four samples per cycle (reduced to two when the harmonic phase is known [1]), i.e. $f<4f_s$ and $2f<8f_s$ with f_s being the sampling frequency and f the load frequency. Thus, a thermoelastic "second harmonic" from a test performed with a 15 Hz loading would at least require f_s =120 Hz.

To the authors' knowledge, there are no works in the literature who have specifically evaluated thermoelastic harmonics by extracting their aliased waves. This possibility is of relevant interest since it would enable the possibility to use slower IR cameras (e.g. low cost microbolometers, [2,3]), and also provide strategies to investigate very high frequency loading scenarios.

This study examines the sampling conditions which enable the filtering of aliased waves in the TSA context. The analysis is performed by analyzing two scenarios: one where aliasing collision frequencies may arise [4], generating aliasing interference which may affect the accuracy in routine oversampled TSA, and the other one where aliased waves of the thermoelastic signals are instead detected by a properly and purposely designed undersampling strategy.

2. Methodology

The relationship that identifies aliased frequencies f_a when sampling a harmonic with frequency f at the sampling rate f_s can be written as [1]:

$$f_a = \left| f - m \cdot f_s \right| \quad \text{where } m \text{ is an integer ensuring that } f_a < f_s/2 = f_{ny} \tag{1}$$

The Nyquist frequency, f_{ny}, also known as the folding frequency, reflects aliased frequencies by mirroring frequency f about f_{ny} in a discrete Fourier spectrum.

If the frequencies carrying the thermoelastic harmonics are known, Eq. (1) can then be used to design a processing scheme which uses a subsampling frequency. In particular, Eq. (1) allows to determine the alias frequencies of the thermoelastic harmonics that will appear in the DFT spectrum of the subsampled signal.

A numerical example of a simulated temperature signal is here provided to proof the signal processing concept. Let's consider a generic signal of the likes:

$$T(t) = T_o + E\sin(2\pi f_E t + \phi_E) + D\sin(2\pi f_D t + \phi_D) + R\sin(2\pi f_R t + \phi_R) + whitenoise \tag{2}$$

where T_o= 23 °C, E=0.55 °C, f_E=15 Hz, D=0.05 °C, f_D =30 Hz, R= 0.01 °C, f_R =45 Hz. The phases ϕ can have any values and the term *whitenoise* adds uniformly distributed noise having a noise floor of about 0.001 °C. These figures well represent a typical TSA experiment. The E, D and R terms will also be referred to as *first*, *second* and *third harmonics*. In order to extract these from the signal, this is sampled and analysed by the DFT. Two different DFT spectrums are reported in Fig. 1, one obtained from sampling at 180 Hz and one obtained from sampling at 6.25 Hz (i.e. a typical frequency of a microbolometer [3]). In the first case (f_s=180 Hz), N=900 samples are processed, corresponding to an acquisition time window of 5 sec, while for the subsampling case (f_s=6.25 Hz), N=100 is chosen, corresponding to a time window of 16 sec.

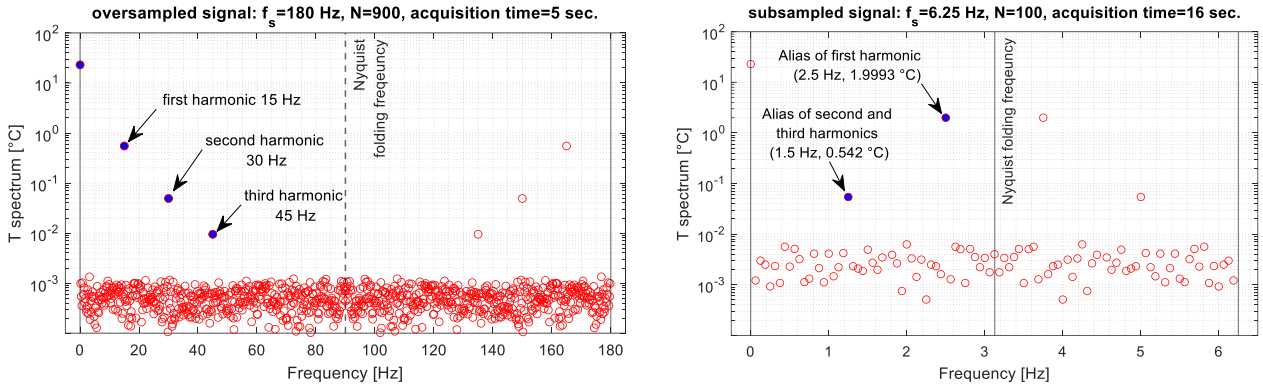

Fig. 1. DFT spectrums of the signal of Eq. (2). Left) oversampling case; Right) subsampling case.

3. Results and conclusions

From Eq. (1) it is found that the subsampled signal produces an alias of the first 15 Hz harmonic at 2.5 Hz, when m=2. The DFT in this case has evaluated an amplitude of E=0.552 °C which differs from the nominal one of only 0.36 %. It is noticed that the second 30Hz and third 45 Hz harmonics both have aliases at 1.5 Hz, for respectively m=5 and m=7. This is then a case where the presence of the third harmonic in the signal is producing an aliasing interference with the second harmonic. As a result, the amplitude of the second harmonic is now less accurate, with an error of 3.4 %.

It is also noticed that a careful choice of the number of processed samples (e.g. N=100) in the subsampling case yields coherent sampling, thus avoiding spectral leakage. It is also observed that the noise floor in the subsampling scheme is increased, although this can be reduce by extending further the acquisition time, that is anyway necessarily higher than that of the oversampling case.

4. Acknowledgements

The present research has received funding from the European Union's Framework Program for Research and Innovation - *Mission 4 - Component C2 Investment 1.1 (PRIN - 2022)* – project title MADforLIFE, code: 2022JE3LRA_001, CUP: B53D23006070006.

5. References

[1] O. Breitenstein, W. Warta, and M. Langenkamp (2010). Lock-in thermography: Basics and use for evaluating electronic devices and materials, volume 10. Springer, 2010.

[2] G. Pitarresi, R. Cappello and G. Catalanotti (2020). Quantitative thermoelastic stress analysis by means of low-cost setups. Optics and Lasers in Engineering, **134**, 106158, 11.

[3] I. Jiménez-Fortunato, D.J. Bull, O.T. Thomsen, J.M. Dulieu-Barton (2023). Quantitative microbolometer-based thermoelastic stress analysis. Optics and Lasers in Engineering, **160**, 107276.

[4] J.C. Krapez, G Gardette, and D. Balageas (1995). Lock-In IR Thermography - advantages and problems of some approaches. Int. Workshop on Advanced Infrared Technologies and Applications.

Wood Mechanics and Timber Engineering

BRAZILIAN NATIVE WOODS PILLARS STABILITY

R.M.L.R.F. Brasil[1], A.M. Wahrhaftig[2] and G.A. Pereira[1]
[1] Department of Structural and Geotechnic Engineering, University of São Paulo, São Paulo, Brazil
[2] Department of Construction and Structures, Federal University of Bahia, Salvador, Brazil

1. Introduction

We present results of an experimental study of the stability of Brazilian native woods slender pillars. We present comparisons of these results with values given by Brazilian Standards for Wooden Structures Design in their versions of 1997 and 2022, which are conceptually different on the subject of pillars stability. Theoretical critical loads given by classical references are also taken into consideration. Good agreement is obtained between all these sources when graphically compared.

2. Materials and methods

We present the results of a laboratory research on the instability loads of wooden pillars compared to the values recommended by the Brazilian Standard for Design of Wooden Structures [1-2].

A Brazilian native wood species called "Jatobá, *Hymenaea courbaril*, was chosen, which can be classified as Class D60, that is, dicotyledonous wood with characteristic resistance to compression in the direction of the fibers 60 MPa. The nondimensional slenderness of the specimens, λ, as defined in Eq. (1), was varied from 20 to 110, in increments of 10, and 6 specimens of each slenderness were made, a total of 60 specimens.

$$\lambda = L/\sqrt{I/A} \tag{1}$$

where I and A are the moment of inertia and area of the square cross sections, L the length of the simply supported specimens. Axial compression tests were carried out on the samples instrumented for lateral displacement at mid-span and for instability load. For each slenderness, mean and standard deviation of measured normal stress values were calculated. Non dimensional average values were computed by dividing these averages by the characteristic resistance 60 MPa.

Next, a comparison was made of the stress-slenderness curve obtained in the tests with the curves given by the Brazilian Standard for the Design of Wooden Structures, ABNT NBR 7190:1997 [1] and ABNT NBR 7190:2022 [2] versions, conceptually different. The former explicitly considers initial eccentricities of the loads, due to geometric imperfections and the presence of initial bending moments, augmented by the presence of axial loading and wood creep in time. The latter just gives closed form continuous formulas to compute resistance as a function of the slenderness and some other parameters. In both case, non-dimensional stress values were computed.

We also checked results with Euler's theoretical values, Eq. (2) [3], inside the linear elastic behavior regime, considering the elastic modulus E for stability computations as prescribed by NRB 7190:2022 [2].

$$\sigma = \frac{\pi^2 E}{\lambda^2} \tag{2}$$

3. Results and conclusions

Our results for slenderness versus non-dimensional stress are plotted in Fig. 1. Experimental results are shown in yellow, NBR 7190:1997 [1] in blue, NBR 7190:2022 [2] in orange and Euler's formula [3] in gray.

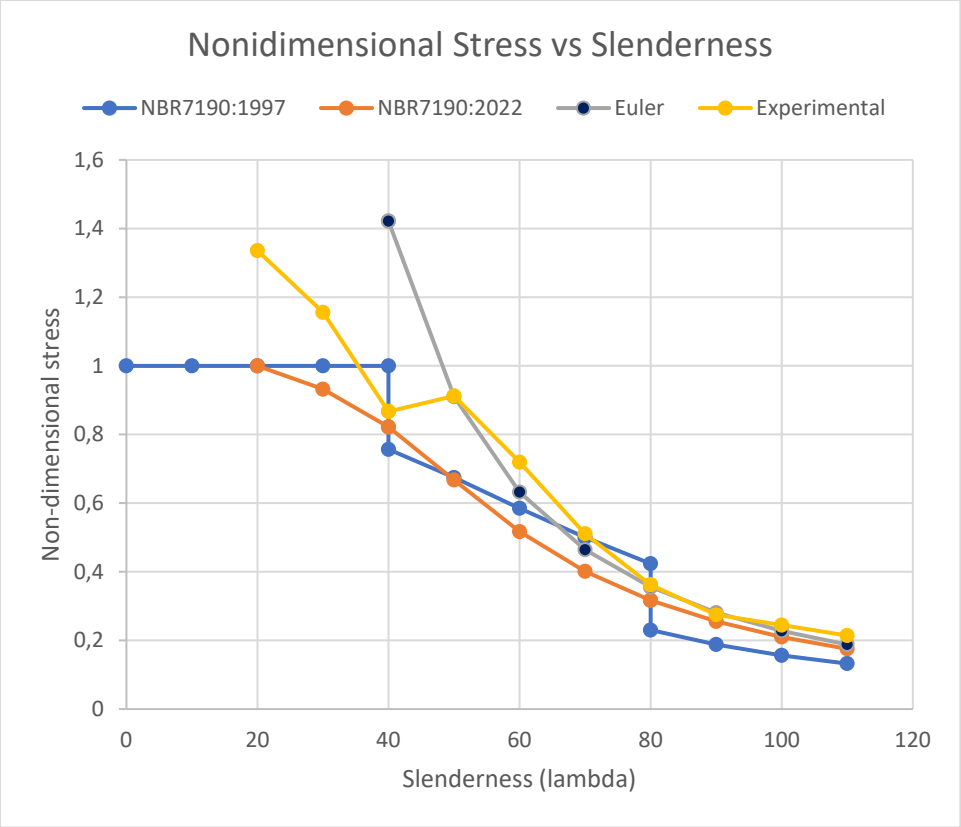

Fig. 1. Comparisons

Comparisons displayed in Fig. 1 led us to conclude that reasonable agreement was obtained between the 4 plotted curves, mainly for larger slenderness values, above usual design levels in excess of 60.

4. Acknowledgements

We acknowledge support from the CAPES and CNPQ, both Brazilian research funding agencies.

5. References

[1] ABNT Associação Brasileira de Normas Técnicas (1997). NBR 7190:1997. Projeto de Estruturas de Madeira. ABNT, Rio de Janeiro. (in Portuguese)
[2] ABNT Associação Brasileira de Normas Técnicas (2022). NBR 7190:2022 Projeto de Estruturas de Madeira. ABNT, Rio de Janeiro. (in Portuguese)
[3] S.P. Timoshenko, J.M. Gere (1989). Theory of Elastic Stability, 2nd Ed. McGraw-Hill, New York.

6-11 July 2025 ICEM21 Bologna
21st International Conference on EXPERIMENTAL MECHANICS

NUMERICAL SIMULATION OF CONTRIBUTION OF CONCRETE ANCHORAGE TO DUCTILITY OF SHEAR WALLS MADE OF CROSS LAMINATED TIMBER

P.Sejkot[1,2], A. Iqbal[3], G.Faraone[1]
[1] Department of Civil, Construction, and Environmental Engineering, San Diego State University, San Diego, California (United States of America)
[2] Klokner Institute, Czech Technical University in Prague, Prague, Czech Republic
[3] University of Northern British Columbia, Prince George, Canada

1. Introduction

This research aims to develop an enhanced seismic-resistant timber-concrete connection using replaceable ductile-anchor rods for rapid post-earthquake repair. The proposed timber-concrete connection mitigates seismic damage in timber structural components by dissipating energy in the anchor connecting timber to the concrete footing, allowing for easy replacement of the stretched anchor rod after damage. This solution enhances structural robustness, ductility, and strength, while accelerating post-earthquake repairs, helping to meet modern seismic design standards, especially post-earthquake occupancy and repairability. Unlike traditional solutions, it does not involve significant plastic deformations of fasteners and steel plates, and does not lead to timber damage.

The research objectives include investigating the seismic behavior and residual capacity of shear walls made of Cross-Laminated Timber (CLT) connected to a concrete foundation. Finite-element analyses will be used to numerically simulate seismic tests and design the anchors. Full-scale experimental testing will thereafter validate them. The outputs will provide modeling guidelines for practicing engineers to achieve ductile-anchor connections and analytical methods relating overall structural seismic demand to connection capacity.

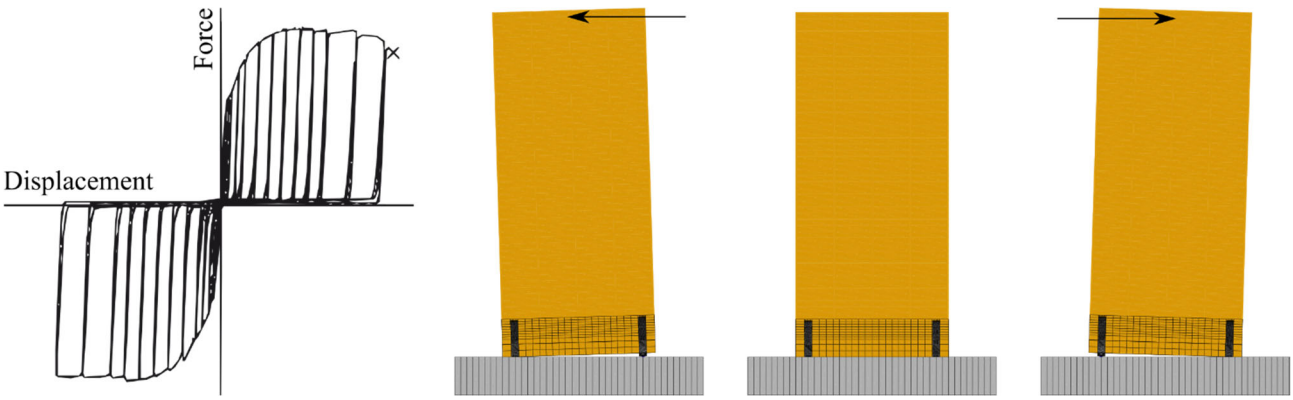

Fig. 1. Typical Force to Displacement response of CLT shear wall connected by hold-downs and anchors to concrete foundation subjected to horizontal cyclic external loading [1].

2. Materials and methods

Two numerical models were developed using Abaqus software. The first model (see Fig. 1.) focuses on obtaining the force-displacement response of a mechanical system consisting of a CLT shear wall connected by hold-downs and anchors to a concrete foundation subjected to horizontal

cyclic external loading. To be computationally efficient, the top part of the CLT wall is simulated by beam elements. Kinematic coupling is used to link it to the intermediate part, simulated by shell elements. Shell-to-solid coupling links it to the bottom part made of solid elements. Concrete is simulated by shell elements, and hold-downs by a combination of shell and solid elements. Nails connecting them to CLT and anchors connecting them to concrete are simulated by a combination of shell (head) and beam (shank) elements. Interaction between shanks and shell elements (CLT and concrete) is made by nonlinear springs. All other interactions (CLT to concrete, shanks to edges of holes, heads to surface of hold-downs) are made using general "hard" contact. Additionally, a detailed model of a hold-down connected to CLT and concrete (see Fig. 2.) subjected to external loading was developed to evaluate its stiffness and ductility. This combined approach aims to validate the numerical model against experimental data and expand the understanding of the connection's performance under various loading scenarios.

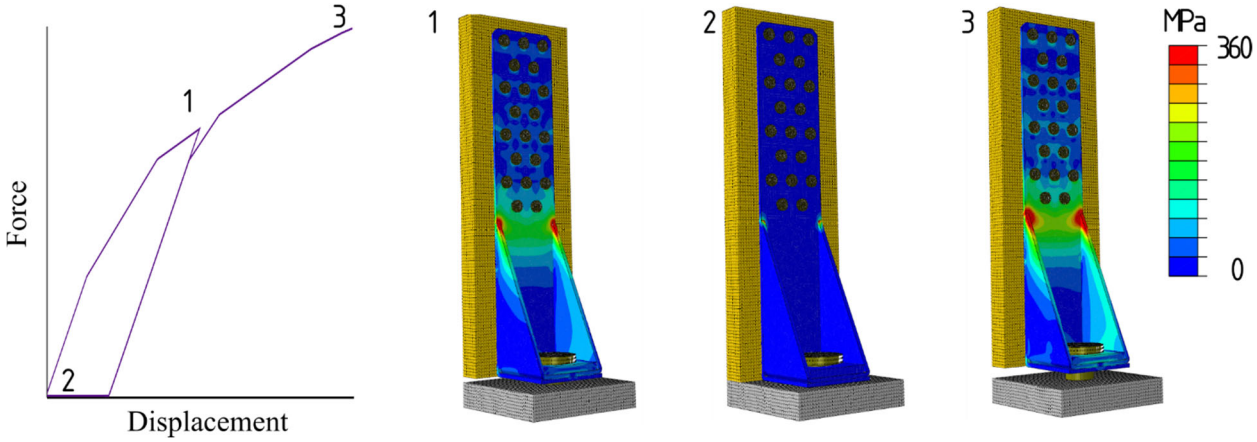

Fig. 2. Abaqus model of hold-down. 1- end of the first loading, 2-unloaded, 3-reloaded.

3. Results and conclusions

The numerical simulations provide a detailed understanding of the mechanical system's response to external loading, particularly how it is influenced by several interdependent factors, including the stiffness of the CLT shear wall, the plasticity in the contact between the CLT and concrete, and the stiffness of steel connectors and fasteners (nails, screws) used to connect them to the timber and concrete (anchors). Additionally, the results from the Abaqus simulations identified two critical components of the experimental setup that might be damaged during the planned experimental campaign. The first is the bottom corner of the CLT panel, where the contact between wood and concrete occurs (see Fig. 1). The second is the welded top of the reinforcing rib to the plate (see Fig. 2.). The findings highlight the importance of a holistic approach to designing these connections. With a well-informed choice of components, the anchor can become the most damaged part, which is easily replaceable, thereby facilitating rapid post-earthquake repair and enhancing the overall seismic resiliency of the structure.

4. Acknowledgements

This research project is partially funded through the National Science Foundation (NSF) Grant No. CMMI 2301691 project entitled ERI: Developing Ductility through Replaceable Concrete Anchorage Connections for Improved Seismic Performance of Mass Timber Structures and NSF Award No. 2129782.

5. References

[1] Gavric, I., Fragiacomo, M., & Ceccotti, A. (2015). Cyclic behaviour of typical metal connectors for cross-laminated (CLT) structures. *Materials and structures*, **48**, 1841-1857.

EuraSEM 6-11 July 2025 ICEM21 Bologna 21st International Conference on EXPERIMENTAL MECHANICS

AXIAL-SHEAR INTERACTION OF ANGLE BRACKETS IN CONNECTIONS OF CROSS-LAMINATED TIMBER

P.Sejkot[1], A. Aloisio[2], A. Iqbal[3]
[1] Klokner Institute, Czech Technical University in Prague, Prague, Czech Republic
[2] Department of Civil, Construction-Architectural and Environmental Engineering, Università degli Studi dell'Aquila, L'Aquila, Italy
[3] University of Northern British Columbia, Prince George, Canada

1. Introduction

Angle brackets with nails or screws are commonly used as anchoring systems in many timber buildings. These connections typically experience a biaxial stress state, with shear forces resulting from lateral actions (e.g., wind and earthquakes), and axial forces combining gravitational loads with those associated with rocking mechanisms, also induced by lateral actions. The interaction between shear and axial stresses is often expressed by the following equation:

$$\left[\frac{V_{Ed}}{V_{Rd}}\right]^n + \left[\frac{N_{Ed}}{N_{Rd}}\right]^n < 1$$

where V_{Ed} and N_{Ed} represent the design values of shear and axial forces, respectively, and V_{Rd} and N_{Rd} are the corresponding capacities. The goal of the research presented in this abstract is to estimate n by solving an optimization problem based on the values of V_{Rd} and N_{Rd} obtained from numerical simulations using a Monte Carlo approach. To this end, the authors developed finite element numerical models validated against experimental tests, aiming to estimate the exponent n, which describes the interaction domain while considering both modeling uncertainty and variability of the angle brackets.

2. Materials and methods

The conceptual approach of this research combines experimental testing and numerical modeling. Two loading scenarios were employed to estimate shear and axial capacities under given axial and shear forces, respectively. In the first scenario, an axial load was applied, followed by shear loading until failure. Conversely, a corresponding setup was used for shear capacity evaluation under axial forces.

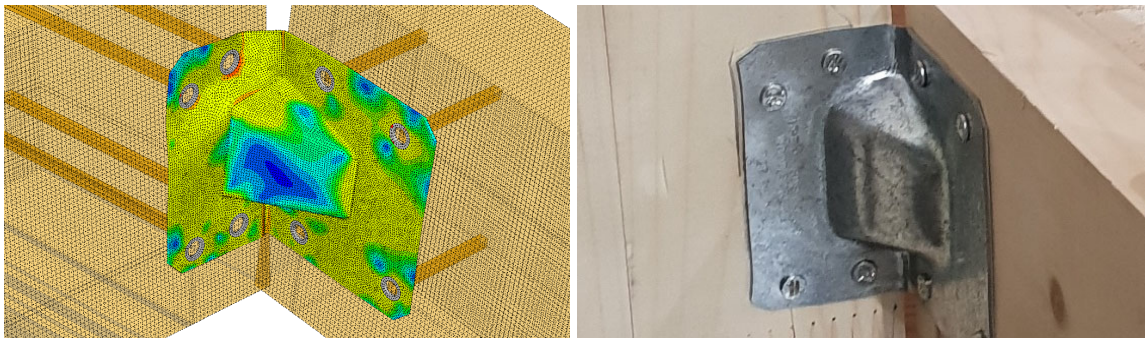

Fig. 1. Numerical simulations from Abaqus® (left), experimentally tested angle bracket (right).

3. Results and conclusions

This section presents the results of Monte Carlo analyses under axial and shear forces for three angle brackets (ABR9020, ABR105, and HGA10) at various shear and axial force levels, respectively. The aim is to estimate the axial-shear interaction domain point by point.

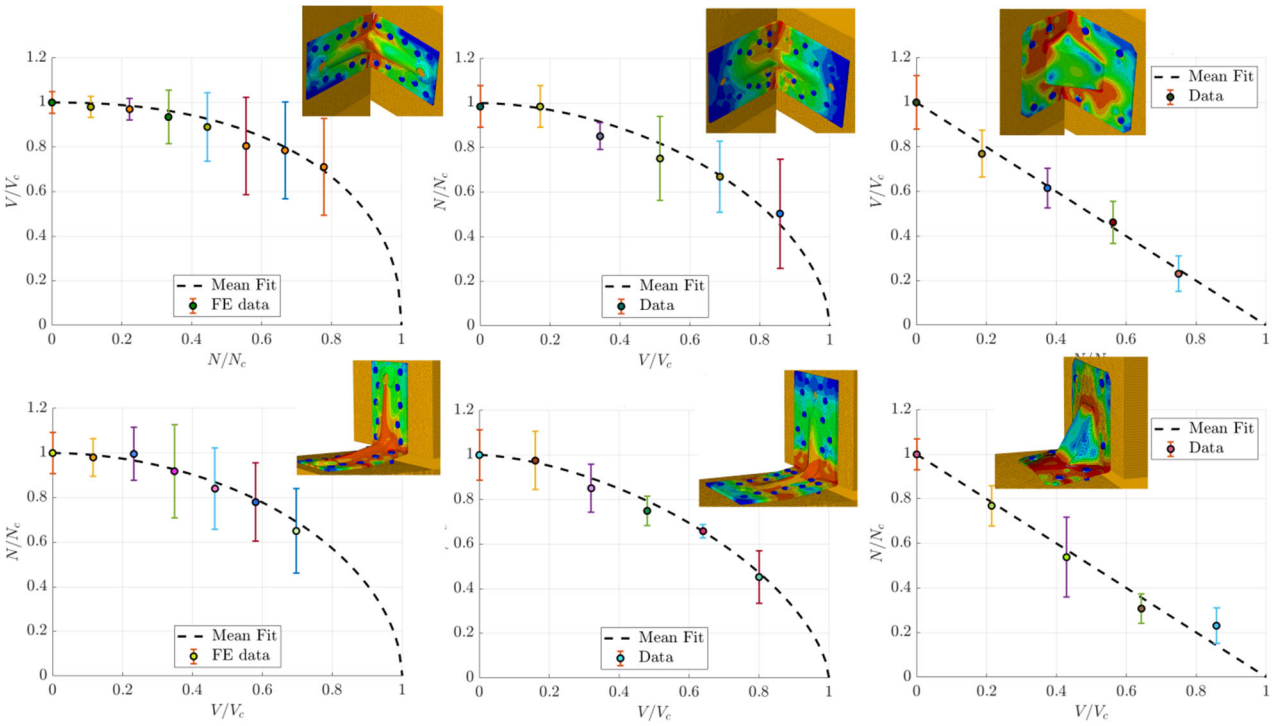

Fig. 2. Failure domain of the angle brackets, showing the simulated data points and the fitting curve.

The objective was to estimate the exponents of the interaction law that describes the axial-shear failure domain of these brackets. The results demonstrate that the axial-shear and shear-axial interaction domains are symmetric, as expected. Furthermore, the interaction behavior varies from quadratic (ABR9020) to linear (HGA10), with the ABR105 bracket exhibiting intermediate behavior. The failure domain was determined point by point, considering the uncertainty of the timber-nail interaction through a semi-empirical constitutive law. It was observed that the average interaction domains can be approximated as quadratic to linear domains depending on the contribution of the angle bracket or nails to failure.

The reasons for this variation lie in the failure mechanisms. Quadratic domains are predominantly associated with the yielding of the angle brackets, as steel materials typically exhibit a quadratic axial-shear interaction domain. Conversely, linear domains are characteristic of failure mechanisms governed by connection failure, such as nail withdrawal, which is dominated by frictional phenomena typically described by linear failure domains.

4. Acknowledgements

This work has been supported by the Ministry of Culture of the Czech Republic, research grant NAKI II DG18P02OVV012 – Sustainable Management of Historical Buildings.

5. References

[1] G. D'Arenzo, G. Rinaldin, M. Fossetti, M. Fragiacomo: An innovative shear-tension angle bracket for Cross-Laminated Timber structures: Experimental tests and numerical modelling. *Engineering Structures,* 197, p. 109434., 2019.

A NANOINDENTATION STUDY ON DIVERSE TECHNICAL LIGNINS FOR BIO-COMPOSITE APPLICATIONS

***Luis Zelaya-Lainez*[1], *Michael Schwaighofer*[2], *Markus Königsberger*[2], *Markus Lukacevic*[1], *Sebastián Serna-Loaiza*[3], *Florian Zikeli*[4], *Michael Harasek*[3], *Anton Friedl*[3], *Olaf Lahayne*[2], *Josef Füssl*[1]**

[1] *Christian Doppler Laboratory for Next-Generation Wood-Based Biocomposite, Institute for Mechanics of Materials and Structures, TU Wien, Karlsplatz 13/202, 1040, Vienna, Austria*
[2] *Institute for Mechanics of Materials and Structures, TU Wien, Karlsplatz 13/202, 1040, Vienna, Austria*
[3] *Christian Doppler Laboratory for Next-Generation Wood-Based Biocomposite, Institute of Chemical, Environmental and Bioscience Engineering, TU Wien, Getreidemarkt 9/166, 1060, Vienna, Austria*
[4] *Department for Innovation in Biological, Agro-Food and Forest Systems, University of Tuscia, Viterbo*

1. Introduction

Lignin, a cornerstone of wood and the second most abundant organic polymer on Earth is attracting increased attention as a renewable resource for sustainable materials. Specifically, its potential as a key component in bio-composites holds immense promise. However, the effective design and modeling of lignin-based bio-composites is hindered by a critical knowledge gap: a precise understanding of lignin's mechanical properties. This challenge is further compounded by the inherent variability of technical lignins derived from lignocellulosic biomass. Their chemical composition, molecular weight, degree of cross-linking, and functional group distribution are all influenced by the source material and the specific extraction and purification methods employed. To address this complexity, our study investigates the mechanical properties of five distinct hot-pressed lignins, each extracted from different raw materials using unique methods. We employ a microscopy-supported grid nanoindentation technique to provide a detailed analysis of their mechanical behavior.

2. Materials and methods

To investigate the influence of extraction method and source material on lignin properties, we prepared five technical lignins derived from hardwood (HW), softwood (SW), and grass (G) using three distinct processes: enzyme hydrolysis (E), organosolv (OS), and kraft pulping (K). These lignins were then processed into discs by hot-pressing at 90 °C under 108 MPa of pressure. For nanoindentation testing, each disc was embedded in a two-component resin and mounted on a microscope slide. The sample surface was meticulously polished using a rotating diamond head within an ultra-milling-sectioning system to ensure a smooth and flat surface. Nanoindentation measurements were conducted using a diamond Berkovich tip under load-controlled conditions. The indentation modulus, a key measure of material stiffness, was then determined from the resulting force-displacement curves using the Oliver-Pharr method.

3. Results and conclusions

The hot-pressing process used to fabricate the lignin discs resulted in a porous microstructure. To account for the influence of porosity on the nanoindentation measurements, we carefully mapped the

indent locations onto a light microscopy image of the indented area. This allowed us to identify and exclude indents located within pores, ensuring that only measurements representative of the bulk lignin were considered. Furthermore, by correlating the indentation modulus with the distance to the nearest pore, we observed a clear relationship between the measured properties and the proximity of a pore. This confirmed that the presence of pores significantly influenced the mechanical response, effectively creating a lignin-pore composite. To isolate the intrinsic stiffness of the lignin itself, we employed the Mori-Tanaka homogenization scheme, a well-established micromechanical model. This approach allowed us to deconvolute the contributions of the pores and the solid lignin matrix to the overall measured modulus. By fitting the model to our experimental data, we effectively back-calculated the stiffness of "pore-free" lignin, resulting in an estimated Young's modulus of 7.12 GPa [1]. The excellent agreement between the model and the experimental data, as depicted in Figure 1, supports our hypothesis that the intrinsic stiffness of the solid lignin is consistent across all five samples, irrespective of the extraction process or feedstock. This finding highlights the potential for a universal mechanical behavior of lignin, independent of its origin.

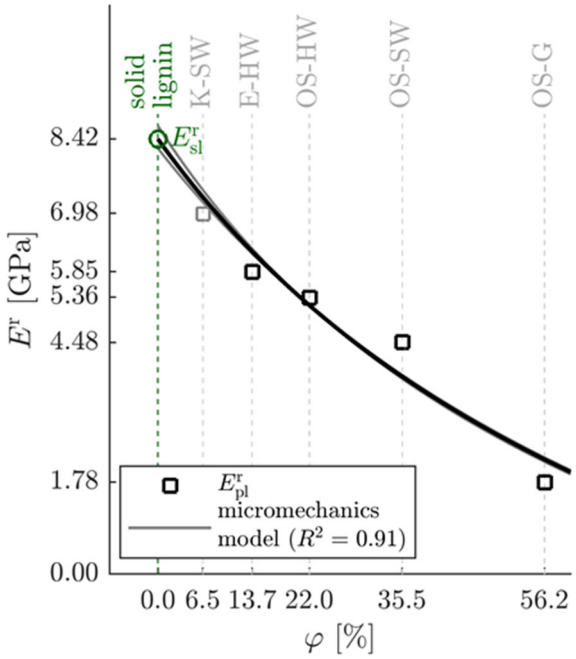

Fig 1: Porosity-dependent indentation moduli of porous and solid lignin

4. Acknowledgements

The financial support by the Austrian Federal Ministry of Labour and Economy, the National Foundation for Research, Technology and Development and the Christian Doppler Research Association is gratefully acknowledged. Furthermore, the authors would also like to express their gratitude to the CD laboratory company partner HS Timber for their financial support. The authors would also like to thank the support from the Austrian Science Fund (FWF) through the Y1093 START-project.”.

5. References

[1] Schwaighofer, M., Zelaya-Lainez, L., Königsberger, M., Lukacevic, M., Serna-Loaiza, S., Harasek, M., Lahayne, O., Senk, V., & Füssl, J. (2022). Characterization of mechanical properties of five hot-pressed lignins extracted from different feedstocks by microscopy-aided nanoindentation. *Materials and Design,* Volume 227, 111765

RESTARTING OF LONG-TERM MONITORING OF TWO EIGHT-STORY RESIDENTIAL CLT BUILDINGS

M. Dorn[1], C. Amaddeo[1], and E. Serrano[2]
[1] Department of Building Technology, Linnaeus University, Sweden
[2] Division of Structural Mechanics, Lund University, Sweden

1. Introduction

Construction with timber took up speed when regulations were adapted across Europe in the late 1990s, switching to performance-based regulations. Around the same time, CLT (cross-laminated timber) entered the market which started massive timber construction with prefabricated wall and floor elements. This allowed for new types of timber constructions, similar to the use of prefabricated concrete elements, for apartments and offices as well as for public buildings such as schools.

Nevertheless, the behavior of wood-based buildings was not fully known. Particularly its sensitivity to moisture was of concern – and still is. As a natural, plant-based material, wood is in continuous exchange with its surroundings and taking up water in humid conditions as well as releasing water in dry conditions, respectively. Most material properties are influenced by moisture content, e.g., density, strength, and stiffness, and it is swelling and shrinking with varying moisture content. When wood is exposed for long time to high moisture content, approx. above 16%, there is also risk for fungi to build up which may lead to decay of the material but may also be a health concern.

Long-term loading of wood is also an issue due to creep of the material. The creep compliance across fiber direction has to be taken into account in particular as the material itself is already comparably weak across fiber direction. This becomes an issue in platform-based constructions in tall buildings where a number of floor elements are loaded perpendicular to the fiber direction and experience significant permanent loading at the lower levels.

2. Materials and methods

The buildings at Limnologen in Växjö consist of four apartment blocks with 8 stories each with a total height of approx. 25 m. The bottom floor is made from cast in-situ concrete and the upper floors in timber, including the roof structure. CLT elements with thickness 85 mm are used for the outer and 95 mm for the internal walls. Non-load bearing walls are in a light-weight timber-frame system. The elevator shaft is made from CLT as well. Vertically, prestressing rods were used in the façade walls to stabilize the buildings.

During construction, permanent monitoring systems were installed in two of the houses [1]: in House 2, the vertical displacements along the façade were measured across the floor slabs. From a total of six potentiometers, the vertical movement could be tracked. In addition, temperature and humidity sensors were installed in two positions. In House 3, combined temperature and humidity sensors were installed, at three positions at the 2nd floor, and three at the upper most floor. At each position, the sensors were placed in 6 different depths of the walls to obtain the gradient.

Data were acquired between 2007 and 2017, when the logging system was removed. Analysis of the data was performed regularly and in particular the dry-out process of the wood as well as the

vertical displacements along the façade were shown [2]. During 2024, a new logging system was assembled since the old data logger was not available anymore and documentation was rudimentary preserved. In December 2024, the system was installed in the building and permanent measurements are running starting from January 2025.

The temperature and humidity data can be directly continued from the previous measurement series, as it represents absolute data (Fig. 1). However, during the first few months, it must be verified whether all sensors funct as intended and if any drift occurs. For the potentiometer readings, a longer time period is necessary in order to be able to continue the measurement series. Firstly, there is no absolute reading for the potentiometers after restarting; secondly, discontinuing the power supply resets the resistance readings. Therefore, the approach is to compare the long-term trends from both the old and new measurements in order to continue obtaining the offset value for displacements.

3. Results and conclusions

The buildings of Limnologen are approaching twenty years of ageand were one of the first CLT buildings of this size in the Nordic countries. Their intermediate age and exposure to these climatic conditions allows us to learn about the long-term behavior of CLT buildings. The seasonal variation in the vertical displacements is presumably still ongoing and it will be interesting to see if the magnitude remains consistent. Additionally, there is limited information available on creep over long time periods, making the results from Limnologen an important source of information.

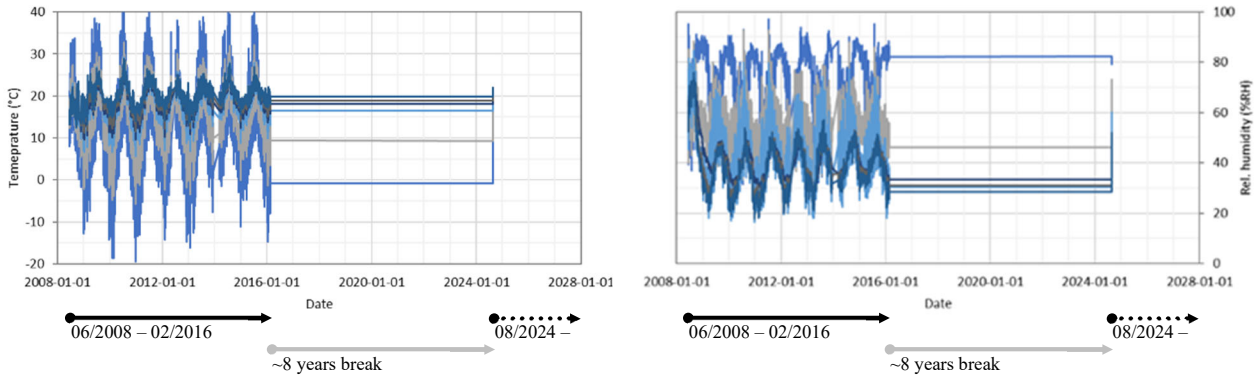

Fig. 1. Variation of temperature (left) and relative humidity (right) in one of the wall sections for the years 2008-2016 as well as momentarily in autumn 2024.

4. Acknowledgements

The research is made possible with support from the Södra Research Foundation (Södras Forskningsstiftelse; project number 2022-325) and is part of the project *Competitive timber structures* supported by the Knowledge Foundation (KK-stiftelsen; project number 20230005).

5. References

[1] Serrano, E. 2009. *Documentation of the Limnologen Project: Overview and Summaries of Sub Projects Results*. Technical Report #56. School of Technology and Design, Växjö University.

[2] Serrano, E., Enquist, B. and Vessby, J. 2014. Long term in-situ measurements of displacement, temperature and relative humidity in a multi-storey residential CLT building. *WCTE 2014 - World Conference on Timber Engineering* (2014).

Suitability of poplar rotary cut veneers as active layers in shape changing wood bilayers

S. Calvano[1], F. Negro[1], C. Cremonini[1], R. Zanuttini[1]
[1]Department of Agricultural, Forest and Food Science (DISAFA), University of Torino, Torino, Italy

1. Introduction

Wood bilayers are innovative composites that dynamically change shape in response to variations in relative humidity. They feature an asymmetric structure: the active layer, usually made from medium to high density wood veneers, allows bending in response to humidity changes; the passive layer, instead, has low reactivity and is essentially intended to provide support. The two layers are bonded with perpendicular grain orientation to activate the overall hygroscopic response [1]. Currently, wood bilayers can be classified as pre-industrial products with a Technology Readiness Level (TRL) of 4-5 [2]. While research has mainly focused on the use of medium to high density woods, such as beech, for the active layers, the present study explores the potential of poplar wood for this purpose. Poplar wood, characterized by a low density (350-400 kg/m^3), has long been the primary raw material for the Italian plywood sector, meeting over 90% of needs of the national plywood industry [3]. Nowadays, over 46,000 hectares are devoted in Italy to poplar cultivation, accounting for 48% of the national plantation area [4]. In this context, for the present study wood bilayers were manufactured from a combination of poplar (*Populus x canadensis* clone I-214) and cherry (*Prunus avium* L.) wood. Their change in curvature was evaluated after an absorption cycle. Overall, the aim is to provide novel insights into innovative shape-changing wood-based products, also to support the Italian poplar cultivation sector by offering an alternative approach to the valorization of poplar wood.

2. Materials and methods

Two bilayer configurations were manufactured by bonding an active layer of poplar rotary cut veneer (*Populus x canadensis* clone I-214, 1.8 or 2.5 mm thick) to a passive layer of cherry quarter cut sliced veneer (*Prunus avium* L., 0.5 mm thick). This resulted in bilayers 2.3 or 3.0 mm thick, bonded with orthogonal grain orientation using a commercially available, moisture-curing polyurethane adhesive. Ten replicas were produced for each configuration, for a total of 20 specimens of size 100 x 100 mm. They were subjected to an adsorption cycle (RH 30-80%; t=20°C) in a climatic chamber. During the cycle, weight and curvature were measured at 0, 1, 2, 3, 4, 6, 8 and 24 hours after the humidity change. The curvature was monitored by taking pictures, which were then processed with MATLAB software to determine the deformation curves over time. The experimental data were fitted using Eq. 1, proposed by [5]:

$$y = a \cdot e^{(-b \cdot x^{-c})} \qquad \text{Eq. 1}$$

where y = curvature (1/mm); x = time (h); a, b, c are specific constants derived from experimental data.

Finally, the average area under the curve (AUC) was calculated for each configuration, as an expression of the overall curvature of the bilayers. Statistical analysis was performed by t-test; normal distribution and homogeneity of variance were verified, and significance was set at the 0.05 level.

3. Results and conclusions

Changes in curvature over time for all bilayer configurations are presented in Fig.1. Statistical analysis revealed significant differences ($p<0.001$) depending on the thickness of the poplar layers. Both configurations exhibited moderate deformation, suggesting that poplar veneers might be suitable active layers in applications where modest deformation is both sufficient and desirable. These results allow further studies to evaluate the use of relatively thin poplar veneers as active layers, including comparisons between their behavior in adsorption and desorption, and modelling based on thickness.

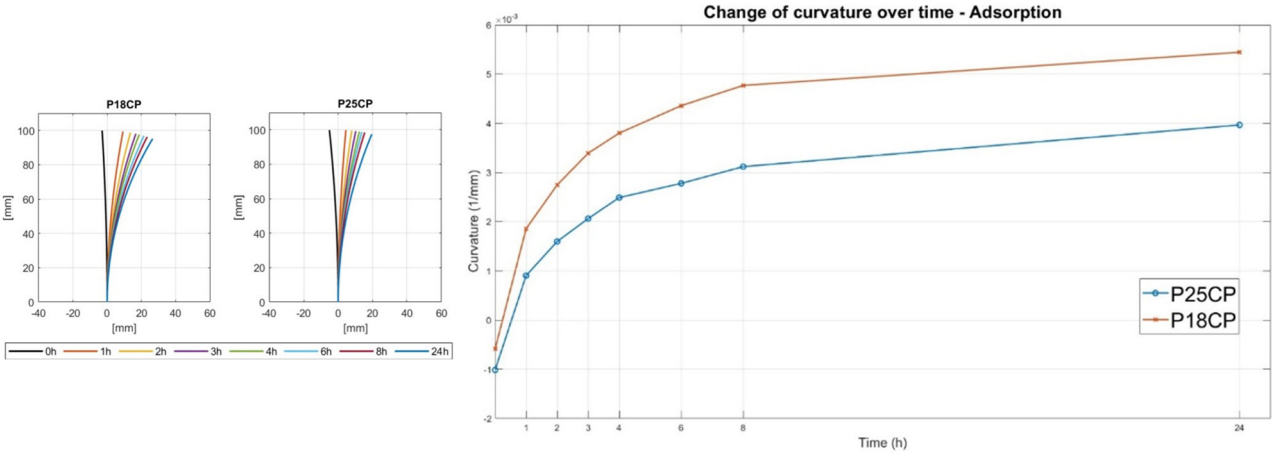

Fig. 1. Behavior of bilayers during the adsorption cycle. Left: visual representation of the average shape changes at different times. Right: average curvature (1/mm) at different times. P=poplar active layer; 25 or 18: thickness of the active layer; CP: polyurethane bonding.

4. References

[1] R. El-Dabaa, S. Abdelmohsen (2023). Hygroscopy and adaptive architectural façades: an overview, *Wood Science and Technology*, 57(3), 557-582.

[2] M. Togni (2022). Pannelli di legno decompensato. *Sherwood*, 233:27.

[3] G. Castro, G. Fragnelli, R. Zanuttini (2014). La pioppicoltura e il compensato di Pioppo dell'industria Italiana. Edizioni Lampi di Stampa, Milano, Italy.

[4] L. Cesaro, R. Romano, S. Marongiu (2019). RAF Italia - 2017-2018 Rapporto sullo stato delle foreste e del settore forestale in Italia. Compagnia delle Foreste S.r.l., Arezzo, Italy.

[5] F. Bianconi, M. Filippucci, G. Pelliccia, M. Fioravanti, M. Togni, G. Goli (2022). HYGROSCOPIC COFFER: Digital parametrization and realization of timber bilayer composites for passive dehumidification in built environments. *Interdisciplinary Perspectives on the Built Environment*, 2.1

EuraSEM 6-11 July 2025 ICEM21 Bologna | 21st International Conference on EXPERIMENTAL MECHANICS

IN SITU MONITORING OF A COMPLEX MODEL STRUCTURE BUILT WITH GREEN WOOD AND SUBMITTED TO REAL CLIMATE CONDITIONS

S. Bouhlel[1], A.Cointe[1], E. Maurin[2], A. Histace[3] and Y. Mélinge[2]
[1] Institute of Mechanics and Engineering (I2M), University of Bordeaux, France
[2] Historical Monuments Research Laboratory (LRMH), CRC - MNHN, CNRS, minister of culture-UAR3224, France
[3] ETIS UMR 8051, CY Cergy Paris University, ENSEA, CNRS, France

1. Introduction

Wood constructions made with green components evolve during the drying period and are very sensitive to local climate (relative humidity and temperature combination) which classically induces: thermal transfer, moisture transfer and the development of internal stresses. In the hygroscopic domain, these stresses result from differential shrinkage between the surface and the core of the wood pieces, because of non-linear and uneven distribution of moisture content. Considering the moisture gradients combined with the anisotropic properties of wood could help to better characterize the mechanical behavior of timber construction.

To evaluate the mechanical effect of drying on a green wood construction during the service life, a model of complex structure has been made. This model is a 1:3 scale replica of the ground floor of the timber heritage "Villereal Hall", built during the 16th century and located in the Lot-et-Garonne department. The studied structure, constructed using green oak wood, was built outdoors to expose it to natural weather variations. It was subjected to a mechanical loading to study its creep response.

2. Materials, model definition and methods

The experimental approach involves applying a constant surface load of approximately 486 kg.m^{-2} to the floor of a complex model structure made of green oak wood, exposed to real climatic conditions, as shown in Fig. 1. The loading began on March 28, 2024, and is ongoing, with monitoring scheduled to continue until the end of 2025. This methodology enables the long-term evaluation of the structural elements' response and aims to characterize the behavior of traditional assemblies under mechanical stresses and varying climatic conditions.

Fig. 1: Photograph of the 1:3 scale replica of "Villereal Hall"

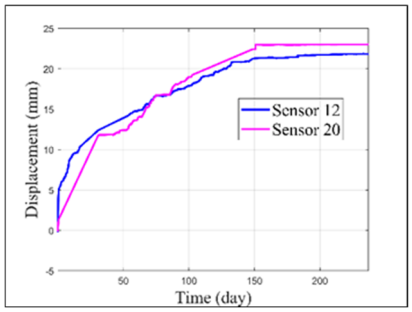

Fig. 2: Temporal evolution of deflection measurements recorded by sensors 12 and 20

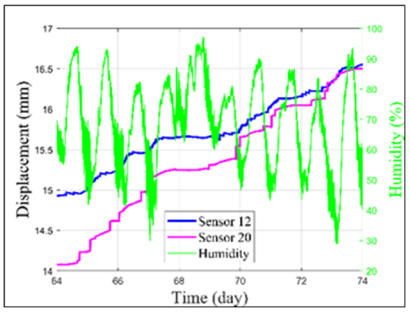

Fig. 3: Effect of daily fluctuations in relative humidity on the temporal behavior of deflection

The experimental setup includes 20 MMR10 potentiometric transducers to measure relative displacements between structural components, with 2 sensors specifically recording deflection. Two environmental sensors monitor ambient temperature and relative humidity. A data acquisition unit (imc SPARTAN), integrated with automated control software (imc STUDIO), records data at two-

second intervals. The collected data, including displacement, temperature, and humidity measurements, are processed and analyzed using MATLAB software.

3. Results and conclusions

The mechanosorptive behavior is monitored by analyzing the deflections recorded by sensors 12 and 20. The obtained results are presented in the Fig. 2. The presented behavior results from the coupling of mechanical stress (beam bending) and variations in relative humidity. The study highlights the instantaneous elastic effect induced by the constant loading, the hydric strains and the evolution of viscoelastic properties under mechanical loading, which are amplified by the mechanosorptive effect. The latter manifests as an increase in deformation during humidification phases, linked to the progressive softening of elastic properties caused by the moisture diffusion front. It is also manifested by the hygro-lock phenomenon (Fig.2 and Fig.3), characterized by a partial and temporary blocking of elastic deformations due to material stiffening during drying phases, followed by a resumption of creep during the re-wetting phase [1,2,3,4].

The amplified bending induces rotation in the tenon-mortise joint areas between the corner post (13x13 cm²) and the beam (9x10 cm²), leading to double shear of the dowels at the interfaces between the tenon cheeks and the mortise cheeks. This deformation mechanism, characterized by dowel shear, constitutes the main failure mode of the joint (Fig. 4 and Fig. 5).

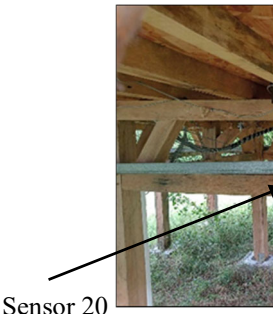

Fig. 4: Bending of the beam supported by two posts in the interior span

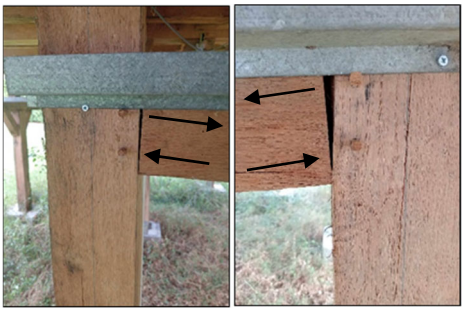

Fig. 5: Rotation of the joint area under the effect of bending

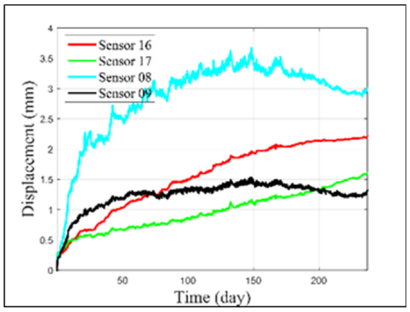

Fig. 6: Evolution of the relative displacement between two beams over time

The evolution of the relative displacement between two beams follows a characteristic creep kinetics, starting with an elastic response, followed by a transient phase with decreasing deformation rate, then a secondary phase with stable rate. This behavior results from the combination of longitudinal displacement due to the bending of one beam and the transverse shrinkage of the other. Figure 6 shows a more significant displacement measured by sensor 08 (3.5 mm) compared to sensors 09, 16, and 17 (1.9 mm). This difference is explained by the types of shrinkage measured: tangential for sensor 08, transverse for 09, and radial for 16 and 17.

By incorporating the effects of long-term thermo-hygro-mechanical coupling, the analysis of the assemblies highlights a significant sensitivity to hygrometric variations. This sensitivity is mainly manifested through volumetric deformation caused by shrinkage induced by the drying process, daily fluctuations resulting from the shrinkage and swelling of wood, and additional deformation linked to creep induced by sustained constant loading over time.

4. References

[1] F. Dubois, H. Randriambololona and C. Petit (2005) Creep in wood under variable climate conditions: numerical modeling and experimental validation, Mechanics of Time-Dependent Materials, Vol. 9, pp. 137-202.

[2] J. Gril (1988) Une modélisation du comportement hygro-rhéologique du bois à partir de sa microstructure, Thèse de doctorat de l'université Paris 6.

[3] O. Saifouni (2014) Modélisation des effets rhéologiques dans les matériaux: application au comportement mécanosorptif du bois, thèse de doctorat, Université Blaise Pascal.

[4] S.L. Nguyen (2017) Modélisation hydromécanique du bois: Application au sapin blanc du Massif Central, thèse de doctorat, Université Clermont Auvergne.

INFLUENCE OF MOISTURE ON BEECH AND BIRCH: COMPRESSION PERPENDICULAR TO GRAIN AND ROLLING SHEAR PROPERTIES

E. Binder[1], E. Kuck[2], C. Bertram[2], Z. Shehadeh[1], M. Schweigler[1], C. Sandhaas[2], T.K. Bader[1]
[1] Building Technology, Linnaeus University, Växjö, Sweden
[2] Timber Structures and Building Construction, Karlsruhe Institute of Technology KIT, Karlsruhe, Germany

1. Introduction

With the increasing interest in hardwood for structural purposes, this research aimed to extend the existing experimental database of the mechanical properties of beech and birch in the literature [1, 2]. The study investigated the rolling shear (RS) stiffness and the stiffness properties in compression perpendicular to the grain (CPG) at different, but constant relative humidity (RH) levels. In addition to the standard climate with 65% RH at 20 degrees Celsius, a dry climate with 40% RH and a wet climate with 85% RH at 20 degrees Celsius were investigated.

2. Materials and methods

RS and CPG stiffness values were tested on different scales, i.e., board level and material level, which required different experimental setups. The subsequent evaluation of RS and CPG stiffness values for both scales followed closely the EN 408 [3]. **CPG on the board level** was tested on prismatic specimens with a height of 90 mm, a width of 70 mm, and a thickness of 40 mm in a uniaxial testing machine, see Fig. 1(a). The required displacement measurement was done with LVDTs (linear variable differential transformers) on two sides. As for the **RS on the board level**, inclined 3-layer specimens were tested in a uniaxial testing machine, see Fig. 1(b). The specimens (150 mm / 18 mm / 100 mm) were prepared for an inclination of 14 degrees and displacements were measured digitally via a video extensometer. Investigating **RS and CPG on the material level** was done in a biaxial setup, see Fig. 1. The dog bone specimens with a neck width of 30 mm, a neck height and depth of 10 mm were clamped into the testing machine. For the CPG tests, the compressive force was applied in a vertical direction and the horizontal force was kept at zero. For the RS-tests, the shear force was applied via the horizontal load application and the vertical force was kept at zero. Displacements were measured by a digital image correlation (DIC) system. Hence, a speckle pattern was applied on the surface of the specimens.

3. Results and conclusions

CPG stiffness on the board level of the tested beech specimens increased by 7% for the dry climate (40% RH) and decreased by 13% for the wet climate (85% RH) compared to the standard climate (65% RH). On the material level, the CPG stiffness for beech increased by 17% for the dry climate and decreased by 3% for the wet climate. For birch CPG test results, see Fig. 1(a). RS stiffness of the beech specimens on the board level increased by 12% in the dry climate and decreased by 6% in the wet climate compared to results from the standard climate. On the material level, the RS stiffness for

beech increased by 11% for the dry climate and decreased by 14% for the wet climate. For birch RS test results, see Fig. 1(b). In general, the stiffness values determined on the board level were higher than on the material level for CPG and RS in all investigated climates. Only in the dry and the standard climate were beech RS stiffness values similar on both levels.

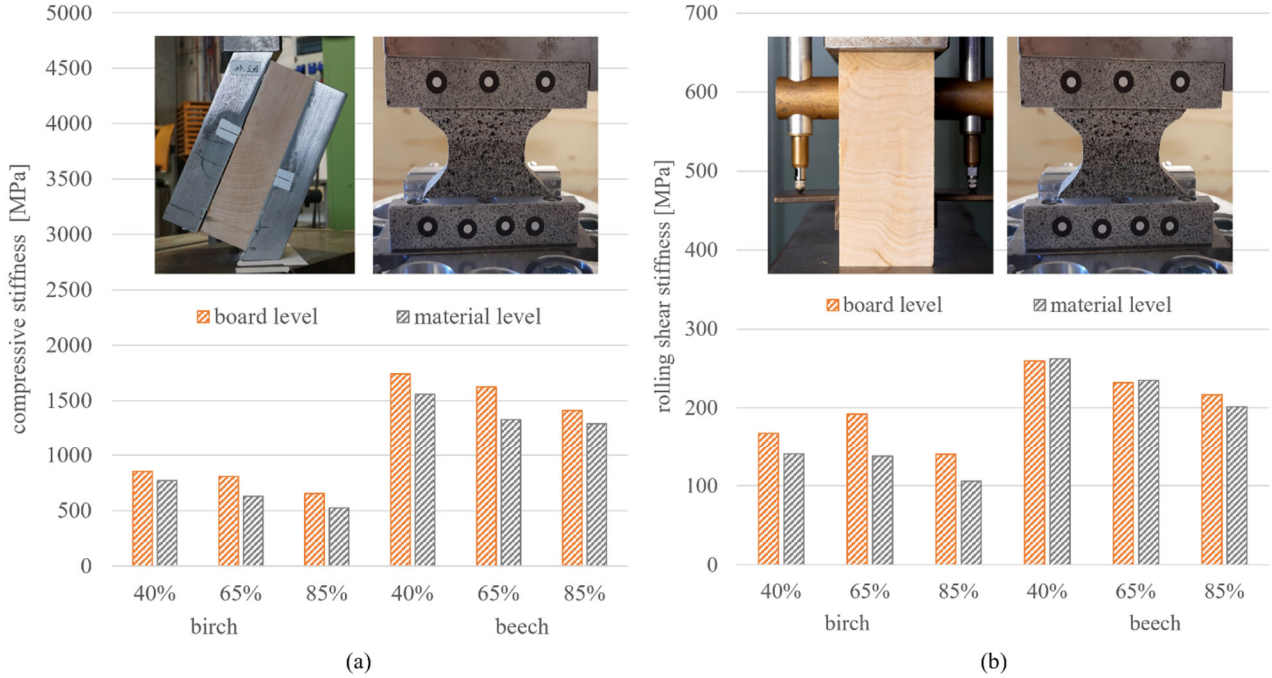

Fig. 1. Experimental setups and results for (a) compressive stiffness perpendicular to grain (CPG) and (b) rolling shear (RS) stiffness: comparison of different relative humidity levels and investigated scales (board and material level).

The expected influence of different climate conditions on the CPG and RS stiffness could be confirmed on the investigated board and material level, i.e., a dryer climate resulted in higher stiffness values, while a wetter climate led to reduced stiffness values. When comparing the results across different length scales, it seemed that the annual ring structure on the board level in general contributed positively to the RS and CPG stiffness.

4. Acknowledgements

The research presented in this paper has received funding from Södra's Research Foundation within the project 'Fukt- och tidsberoende egenskaper hos sydsvenskt lövträ för lastbärande konstruktioner'. Special appreciation goes to the colleagues in the laboratories at Karlsruhe Institute of Technology and Linnaeus University, Daniel Gustafsson and Anders Alrutz, for their support and help in the lab, particularly with preparing the specimens.

5. References

[1] T. Ehrhart, R. Brandner. "Rolling shear: Test configurations and properties of some European soft-and hardwood species." Engineering Structures **172** (2018), pp. 554-572.

[2] H. Al-Musawi, C. Huber, M. Grabner, B. Ungerer, T. Krenke, P. Matz, A. Teischinger, U. Müller. "Compressive strength of beech and birch at different moisture contents and temperatures." In: Journal of Materials Science **58** (35) (2023), pp.13994-14008.

[3] EN 408 (2010) "Structural timber and glued laminated timber. Determination of some physical and mechanical properties." European Committee for Standardization, (CEN), Brussels, Belgium.

MOISTURE PROTECTION TECHNIQUES FOR THE NARROW FACE OF CLT DURING THE CONSTRUCTION PHASE

M. Schweigler[1], M. Eveborn[2], M. Dorn[1], Z. Shehadeh[1] and T.K. Bader[1]
[1] Department of Building Technology, Linnaeus University, Växjö, Sweden
[2] Södra Building Systems, Växjö, Sweden

1. Introduction

Full coverage weather protection is commonly discarded in smaller building projects using cross-laminated timber (CLT), in order to be competitive with other building systems. However, building without full coverage weather protection raises the risk of water accumulation during the construction phase, and thus the risk of moisture related damages like mold growth. Thus, it is essential to apply local protection measures, like sealing with adhesive tapes, to minimize water absorption during the construction phase in sensitive areas, like at the narrow face of CLT elements at wall-to-floor joints.

Previous studies highlighted the importance of local protection measurements when full coverage weather protection is not used [1, 2, 3]. Especially the importance to cover the CLT narrow face, and to find cost-effective protection methods to seal these surfaces, were highlighted [3]. Furthermore, an increased risk of mold growth was shown in [4] if a CLT element is exposed over a longer period to a critical moisture content, which is commonly set at 18% and above.

In this contribution, the aim is to investigate by experiments the moisture absorption at visible CLT wall-to-floor joints using different protection methods at the CLT narrow face. The study aimed to serve as basis to assess the risk of mold growth as well as other moisture related damage scenarios. Based thereon, recommendations for the efficiency of the investigated protection methods to minimize the water absorption and related damages will be given.

2. Materials and methods

The water absorption through the narrow face of CLT elements was studied by T-shaped wall-to-floor joints as shown in Fig. 1. Non-edge glued, 5-layered CLT (20-20-20-20-20 mm) of C24 strength-graded Norway spruce was used for the CLT floor and wall elements. Wall elements were fixed with outside nail plates onto the floor elements. All open narrow faces of the CLT walls were sealed with silicon to avoid any moisture exchange with the surrounding air (see Fig. 1). Four different protection methods were applied, comprising, V1: taping method with a tape at the narrow face and 4 cm up to the wide face; V2: taping method with a tape only at the narrow face; V3: paint coating with a commercial wet room paint at the narrow face and 5 cm up to the wide face; V4: paint coating with a fossil free wood glazing at the narrow face and 5 cm up to the wide face; and V5: unprotected CLT narrow face (reference). One specimen each was studied. The specimens were placed in a roof-covered outdoor facility. Water was poured onto the CLT floor elements to give a constant water level of 3 cm for 2½ weeks on both sides of the walls. Two monitoring systems, based on (i) relative humidity and temperature measurements, and (ii) electrical resistance measurement, were applied. The moisture content was monitored in the first (outermost) layer, in the second layer, and in the third (middle) layer, at positions ranging from 50 to 320 mm from the CLT narrow face (see Fig. 1).

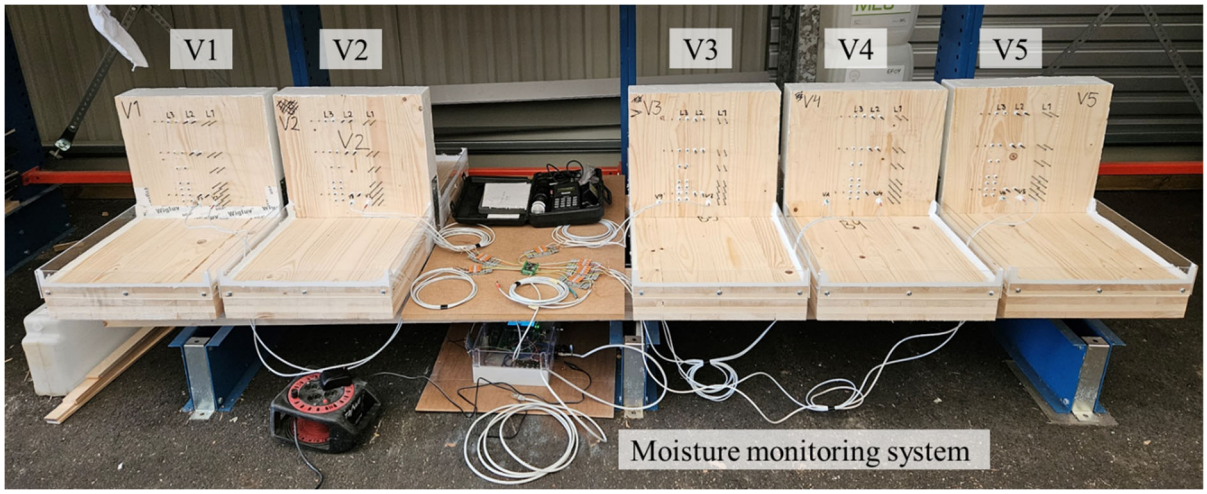

Fig. 1. Test setup for CLT wall-to-floor joints including the two applied moisture-monitoring systems. Specimens with different protection methods shown from left to right: V1: taping method 1; V2: taping method 2; V3: paint coating 1; V4: paint coating 2; and V5: unprotected (reference).

3. Results

In the abstract, results for the measurement points at a distance of 60 mm from the narrow face are presented. Protection measures V1, and both paint coating methods (V3 and V4) showed a moisture content (MC) well below 18% in all layers over the entire moisture exposure period, and thus a minimized risk for mold growth. Protection method V2 showed an immediate increase of the MC exceeding 18% in CLT wall layer 1 (outermost layer) already after one day of water exposure, while the MC in layer 3 (middle layer) stayed below 18%. For the unprotected specimen (V5), both, layer 1 and 3, exceeded a moisture content of 18% after 3 and 5 days, respectively.

4. Conclusions and recommendations

The indicative experimental study gave valuable insights on the moisture absorption of CLT wall-to-floor joints through the narrow face of CLT elements, utilizing different protection methods. The common taping method (V1) and both paint coating methods (V3 and V4) efficiently minimized the water absorption keeping the moisture content well below 18%, resulting in a reduced risk for mold growth. On the other hand, taping only at the narrow face (V2) and unprotected CLT (V5) showed unacceptable high moisture contents. Thus, methods V1, V3 and V4 can be recommended as efficient narrow face protection method, based on this indicative study. Furthermore, it is stressed that investigation of the dry-out period after moisture exposure is of highest relevance for those elements that exceeded a MC of 18%. This is important to assess the time period at which the CLT element exceeds this critical MC, in order to judge on the risk for mold growth. These investigations are still ongoing and will be added in the presentation.

5. Acknowledgements

The authors gratefully acknowledge the support from the Knowledge Foundation through the project ‘Competitive timber structures - Resource efficiency and climate benefits along the wood value chain through engineering design’ (grant number 20230005).

6. References

[1] E. Schmidt, M. Riggio, A. R. Barbosa, and I. Mugabo, Building and Environment, 148, 2019.
[2] BMTrada. Technical report, 2022.
[3] K. Kalbe, T. Kalamees, V. Kukk, A. Ruus, and A. Annuk, Building and Environment, 221, 2022.
[4] L. Olsson, L. Lång, G. Bok, and K. Mjörnell, Journal of Physics: Conference Series, 2654, 2023.

EFFECT OF WOOD DRYING ON AXIALLY LOADED SCREWS IN OAK

M. PILON[1], L. BLERON[1]
[1] LERMaB, INRAE, University of Lorraine, Epinal, France

1. Introduction

There is an important reserve of hardwood in Europe, in particular in France, where 70% of the forest area is made of deciduous trees. This resource is for a large part used for energy purposes as firewood. To achieve long-term carbon dioxide storage, more long-term uses should be chosen as a priority. The use of timber in construction as structural elements can reach this goal. Combined with the deficit of the French balance of trade regarding softwood for construction, it advocates for more uses of local hardwood in construction. Moreover, the use of green hardwood for structures was common in the past but is now forgotten. The main advantage is to save energy and cost of the drying operation, especially long and expensive with massive sections of hardwood.
Nowadays, self-tapping screws are widely used in modern carpentry or in rehabilitation. One part of screws is used in tension, as active element to connect several parts, or as passive element to avoid splinting, cracks formation or shrinkage strains. With the use of green timber, reinforcing screws can reduce cracks opening due to drying, especially in connections areas where cracks can be unsafe and difficult to take into account in the design. Reinforcing screws can also increase ductility of assembly made of dowel or bolt. The effect of wood moisture content on screw performance is known [1], but the effect of a moisture content variation on screws stiffness and strength is not well studied. Only one study on glulam element for softwood [2] and one on laminated veneer lumber of beech [3] could be found. The aim of this study is to analyse the effect of drying on the withdrawal stiffness, strength and ductility of screw in green hardwood.

2. Materials and methods

One type of self-tapping screw was tested (VGZH from Rothoblass), with an outer thread diameter of 8 mm, inner thread diameter of 5,9 mm, and zinc coating. This type of screw is specific to hardwood, due to the important ratio between the inner and the outer diameter. An ultimate tensile stress of the screw of 1435 MPa was obtained with 6 tensile tests. Timber specimens of Oak (*quercus robur* and *quercus petraea* without distinction) had a cross section of 52x104 mm (green dimension), and a length of 160 mm along the grain direction. One screw per specimen was fully inserted in the direction perpendicular to the grain, along the timber height of 104 mm, and extends beyond the opposite side. All specimens were predrilled with diameters equal to 6 mm, just prior the screw insertion.
According to the aims of this paper, three different conditions for the withdrawal test were used: (a) on green oak, (b) on dry oak with screw inserted in green timber, (c) on dry oak, with screw inserted in dry wood, immediately prior to testing. For the batch (b) and (c), drying with air condition corresponding to service class 1 was performed (temperature of 20°C and a relative humidity of 65%) during 7 months, until stabilization. In order to precisely compare conditions (b) and (c), samples were side by side in the board and dried together. Moisture content (M.C.) was measured with the

desiccation method of NF EN13183-1. For all batches, density was recalculated at 31% of M.C., corresponding to saturated point, to have comparable density.
The withdrawal performance was tested according to NF EN 1382, and loaded according to NF EN 26891. The displacement of the timber surface was not constrained in a distance of 35 mm from the screw axis. The withdrawal displacement was obtained with the mean of two displacement transducers (LVDT). Strength (f_{ax}) was computed as the failure force (F_{max}) divided by the height of the green specimen, the outer diameter of the screw and pi. Characteristic values are calculated with NF EN 14358, assuming log-normal distribution. Stiffness (K_{ser}) was calculated with a linear regression on the unloading and reloading steps with a load between 10% and 40% of the estimated failure load (20 kN for batch (a) and 25 kN for batch (b) and (c)). Ductility was defined here as the ratio of displacement at maximum load, over displacement at yield load. The yield load is obtained with the intersection of the line of elastic stiffness, and the line tangent of the force displacement curve, with a slope equal to one sixth of elastic stiffness.

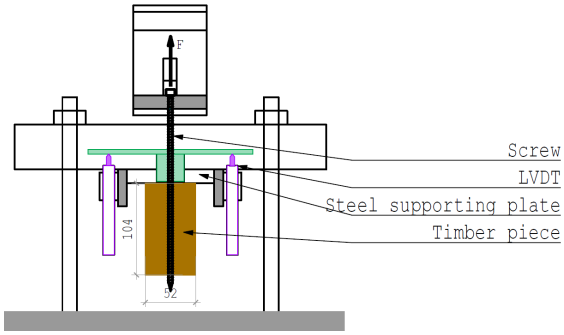

Fig. 1. Withdrawal test setup

Fig. 2. Sample

3. Results and conclusions

As shown in Fig. 3, before the withdrawal test, half specimens of batch (b) exhibited cracks due to drying and the corresponding blocks of batch (c) did not. The reason for this is that the screw retained the wood shrinkage, so the screw was compressed and timber was subjected to tension perpendicular to the grain, which corresponds to its lowest strength. For batch (c) the timber cross section height shrunk of 4,8% in average. The results of the withdrawal tests are summarized in table 1. It was noticed that during testing the cracks closed. For all specimens, wood failure occurs. Besides, corrosion appears on the screw for batch (b). The measurements of the screw outer and inner diameters show no impact on the screw cross section dimensions. Due to that, the decrease of resistance of batch (b) is assumed not to be related to corrosion.

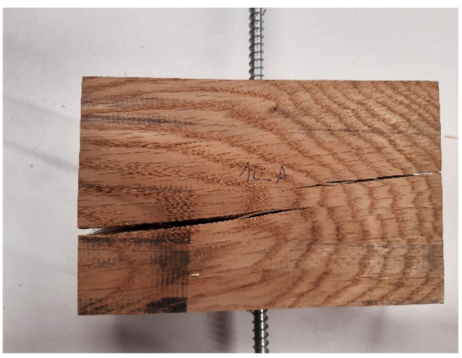

Fig. 3. Cracks after drying

Fig. 4. Corrosion on screw

Batch	No. of specimen	M.C. at test		Density at M.C.=31%		F_{max}		f_{ax}		K_{ser}		Ductility	
		mean	C.o.V	mean	C.o.V	mean	C.o.V	mean	fax,k	mean	C.o.V	mean	C.o.V
		[%]	[-]	[kg/m^3]	[-]	[kN]	[-]	[MPa]		[kN/mm]	[-]	[-]	[-]
a	26	71%	0,18	726	0,09	19,4	0,10	7,42	6,19	23620	0,11	2,91	0,08
b	21	14,6%	0,02	743	0,05	23,3	0,18	8,92	6,19	23920	0,28	3,06	0,30
c	21	14,6%	0,02	739	0,05	27,6	0,13	10,57	8,34	22960	0,13	2,09	0,09
Sub-group analysis													
b cracked	*10*	*14,5%*	*0,02*	*729*	*0,04*	*22,5*	*0,21*	*8,60*	*5,56*	*23090*	*0,32*	*3,16*	*0,33*
corresponding c	*10*	*14,5%*	*0,02*	*731*	*0,04*	*27,9*	*0,14*	*10,67*	*8,06*	*22840*	*0,17*	*2,07*	*0,08*
b uncracked	*11*	*14,7%*	*0,02*	*757*	*0,06*	*24,1*	*0,16*	*9,22*	*6,46*	*24680*	*0,25*	*2,97*	*0,28*
corresponding c	*11*	*14,7%*	*0,02*	*747*	*0,06*	*27,3*	*0,12*	*10,47*	*8,21*	*23070*	*0,08*	*2,1*	*0,09*

Table 1. Experimental withdrawal test results, and sub-group analysis for batch (b), according to presence or absence of cracks due to drying, and corresponding sub group of batch (c)

Comparing batches (b) and (c) allows to conclude that M.C. variation after screwing decreases significantly the strength: 16% for the mean value and the difference is even higher for the characteristic value (up to 26%) as it increases the strength variability. Moreover, M.C. variation increases the ductility of 46%, and has almost no influence on stiffness. Sub-group analysis according to the presence or absence of cracks shows a stronger impact on strength for sample with cracks. The tests on green timber (batch a) show a lower strength (around 30%), a higher ductility (42%) and an equivalent stiffness, compared to the tests in dry oak without moisture content variation after screwing (batch c). Assuming no influence above a saturated point around 31% M.C., and a linear influence from 31% to 14,5% of M.C, one can compute a rough ratio of 2,1% of strength reduction per percent of M.C. variation. This result is consistent with the result of 2,4% founded by Hübner in [1].

This study demonstrates an impact of moisture content variation on screw withdrawal resistance in timber and argue for more concern of this phenomena, especially for constructions using not dry hardwood. More studies should be performed, with different screw lengths, diameters, M.C. variations and timber species, to confirm this phenomena, to be able to predict strength decrease, and potentially to integrate it in design rules if needed.

4. Acknowledgements

The research presented in this paper is funded by the French State as part of France 2030 operated by ADEME. The authors would like to acknowledge Rothoblass company for providing screws.

5. References

[1] U. Hübner. Withdrawal strength of self-tapping screws in hardwoods (2013). *CIB-W18 conference, Vancouver*, **46**-7-4.

[2] A. Ringhofer, M. Grabner, C. V. Silva, J. Branco and G. Schickhofer (2014). The influence of moisture content variation on the withdrawal capacity of self-tapping screws. *Holztechnologie* **55-3**, 33-40.

[3] D. Gerstorfer, T. Forte, and J. Füssl (2021). Experimental and numerical determination of the screw deformation in laminated beech veneer lumber as a result of moisture-induced swelling. *Civil Engineering Design*, **3**, 171–178.

COMBINED EMBEDMENT AND AXIAL LOAD TESTS OF A STEEL DOWEL IN VARIOUS WOOD SPECIES

R. Lemaître [1], T.K. Bader[2], M. Schweigler[2]
[1] Fire Testing Centre, CERIB, Épernon, France
[2] Department of Building Technology, Linnaeus University, Växjö, Sweden

1. Introduction

In [1], the authors highlighted the influence of the interaction between the lateral embedment behavior and the axial withdrawal behavior of dowel-type fasteners, to numerically predict the mechanical behavior of steel-to-timber connections. Using different hypotheses about the friction between a steel dowel fastener and wood, they showed that the assumption of a linear increase of the coefficient of friction with increasing embedment displacement in the numerical model gave a good agreement with experimental results. There is however no experimental proof of this effect of an increasing coefficient of friction, while the influences of the moisture content, the sliding speed, wood species and roughness on the coefficient of friction between steel and wood materials are well known [2]. The influence of the drilling on the surface quality of the wood and the coefficient of friction was investigated in [3]. The aim of this experimental campaign was to investigate the mechanical response of combined axial and lateral loading of a steel dowel in various wood species.

2. Materials and methods

The tests were based on half-hole specimens following instructions from [4]. In this campaign, combined axial and lateral loading was carried out on a testing frame equipped with horizontal and vertical hydraulic servo actuators. This system allowed to independently move the horizontal and vertical sledges either in force or displacement control. The drill hole of the half-hole test specimens was produced with a 12 mm drill bit (hss steel). Wood pieces were first drilled and then cut with a bandsaw into two half-hole specimens. One dowel with a high steel quality and smoothed surface, with a measured average surface roughness of 1.14 µm, was used for all the tests. To avoid early brittle failure, specimens were reinforced with a 6 mm screw placed at 30 mm from the base of the specimen. Four wood species were tested (spruce, birch, oak solid wood and beech LVL) with a density range from 450 to 800 kg/m^3. The specimen's moisture contents were measured with the oven-dry method described in [5]. Specimen dimensions were chosen according to [4]. The relative axial and lateral displacements between the steel dowel and the specimen were measured by means of two cameras and then analyzed by a point tracking software based on digital image correlation techniques. Test series were performed along four different loading procedures with various combinations of axial and lateral loadings. For all series, first, vertical loading (force-controlled) by means of a loading-unloading cycle was applied up to a lateral embedment displacement of 0.2, 2.5, 5.5 or 14 mm. Then, horizontal loading (1 mm/min, displacement-controlled) was applied, while the lateral displacement was kept constant. In total, 128 combined lateral and axial load tests of steel dowels were carried out in the biaxial test setup.

3. Results and conclusions

In this contribution experimental results of the steel dowel-to-wood coefficient of dynamic friction, the static coefficient of friction, as well as axial and embedment stiffness properties are presented. The measured coefficients of dynamic friction for all four series and all four wood species are shown in Figure 1. For a lateral displacement of 0.2 mm, similar values were observed for spruce and birch solid wood and beech LVL, amounting to 0.3-0.5. However, results with oak solid wood showed a higher average value of around 0.6 which might be explained by the drilling quality of oak specimens [3]. For lateral displacements reached after local wood crushing below the dowel, no significant differences were observed between spruce and oak solid wood and beech LVL. For birch solid wood, higher variabilities and lower values of the coefficient of friction were observed. That can be explained by early cracks which appeared in the contact area despite the reinforcement of the specimens. The influence of the lateral load on the axial response of a 12 mm steel dowel in beech LVL, oak, birch and spruce solid wood was investigated. The results showed a non-linear trend (rising with an asymptote) of the coefficient of friction with the lateral embedment displacement. No significant differences were observed between the different wood species in exception of early cracked birch specimens. These experimental results could be used to improve design models such as the European Yield Model in Eurocode 5. Furthermore, these results could be used as input to numerically models simulating the mechanical response of dowel-type timber connections.

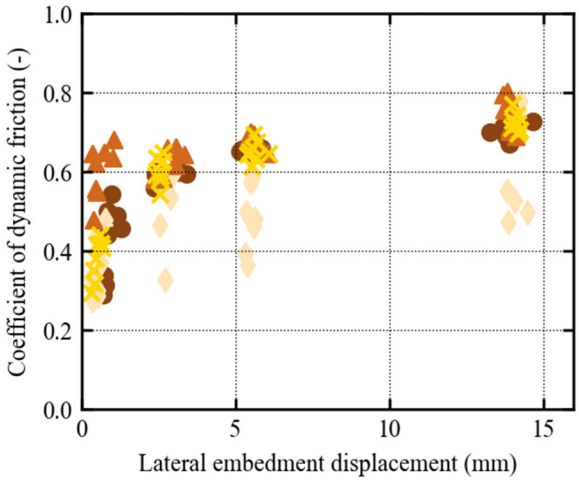

Fig. 1. Relationship between the measured coefficient of dynamic friction and the lateral embedment displacement for the four tested wood species (× spruce, ◇ birch and △ oak solid wood and ○ beech LVL).

4. Acknowledgements

This work has been carried out within the project *hardwood_joint*, which is supported under the umbrella of ERA-NET Cofund ForestValue by BMLFUW (AT), ADEME (FR), FNR (DE), Vinnova, Swedish Energy Agency and Formas (SE). ForestValue has received funding from the European Union's Horizon 2020 research and innovation programme under grant agreement N°773324.

5. References

[1] Schweigler, M., et al. (2021) INTER, paper 54-7-8.
[2] Mckenzie, W. M. and Karpovich, H. (1968) Wood Science and Technology, 2, 138–152.
[3] Dorn, M. (2012) PhD Thesis, Vienna University of Technology.
[4] ASTM D5764-97a (2018).
[5] EN 13183-1 (2002).

MECHANICS-BASED 3D MODELLING OF CNC-MADE CARPENTRY JOINTS USED IN CLT-GLULAM COMPOSITE FLOORING SYSTEMS

Y. Diao[1], C. Loss[1]

[1] SESS Lab, Department of Wood Science, Faculty of Forestry, University of British Columbia, Vancouver, Canada

1. Introduction

Carpentry joints have been integral to timber structures since the inception of low-rise wooden buildings. However, they were largely replaced by metal fasteners with the advent of modern building technologies. Now, in the fourth industrial revolution era, these traditional joints are making a resurgence. Advancements in computation-assisted design software and CNC manufacturing enable seamless customization and precise fabrication [1]. This new era highlights the potential of adapted CNC-made carpentry joints to meet modern construction demands.

Despite their promise, a comprehensive methodology is notably absent—one that considers practical design and structural performance, supported by mechanics-based simulation and experimental test data. While finite element analysis (FEA) has been applied to simulate joints in ancient timber pagodas, its application as a generalized methodology for modern timber structures remains underexplored. Challenges persist due to the intricate mechanics of localized fractures and surface friction, which are not yet fully understood [2-3]. Laboratory tests on small samples are limited by their direct applicability to full-scale structures. Validated 3D modeling, especially when informed by full-scale experimental data, plays a critical role in understanding the complex carpentry joint system.

This study addresses these gaps by proposing a simulation methodology within commercial FEA software that is validated through full-scale tests. The approach not only enhances understanding but also provides a scalable pathway for integrating CNC-made carpentry joints into modern timber structures.

2. Materials and methods

This study presents a modeling framework for CNC-fabricated carpentry joints adapted for use in CLT-glulam flooring systems. A full-scale 3D model was developed in the ANSYS workbench static analysis module. To optimize computational efficiency while maintaining accuracy, the geometry was simplified using two symmetric planes and partitioned to balance meshing quality with computational time. Fig 1 (a) shows the as-built model, created through the Application Programming Interface (API) of SpaceClaim, alongside the meshing results. Variable meshing densities were applied across different regions of the model, with finer meshes at the joint location and coarser meshes at the far ends. A 3D 20-node solid element was selected, combined with hexahedron meshing to capture the nonlinearity behavior. Mortise cut regions were modeled with full integration. The large deformation was activated.

Wood materials were modeled as orthotropic elastic with bilinear hardening, adopting Hill's yielding criteria. The stress-strain behavior was specifically calibrated for the compression quadrant, as the local materials predominantly experienced compressive stresses. Cohesive zone materials were assigned to areas prone to fracturing. The tenon and peg materials, fabricated from laminated bamboo lumber (LBL) and parallel strands bamboo (PSB), were modeled as orthotropic and transversely isotropic elastic materials, respectively. Hill's criteria were similarly applied according to [4-5]. Coulomb friction contacts between subassemblies were defined with a friction factor of 0.2. A pure penalty algorithm was used to model the normal contact between the mortise and tenon surfaces. The model was then calibrated with the double-shear plane push-out test results.

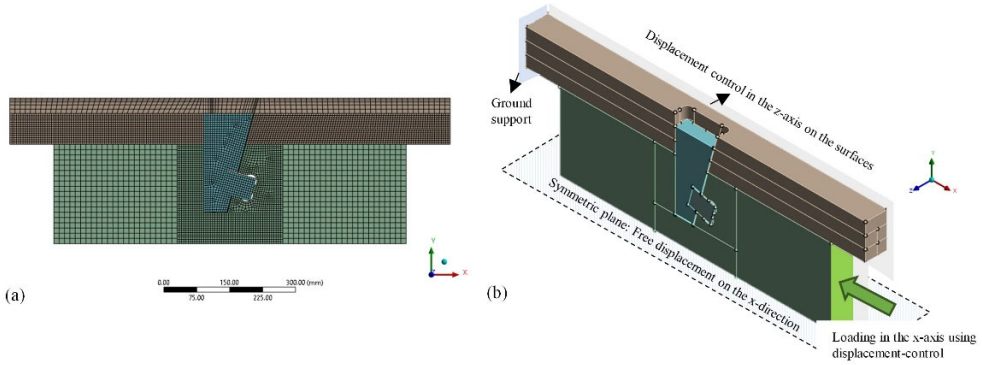

Fig 1. As-built model in ANSYS Workbench: (a) Mesh refinement result, (b) Boundary conditions

3. Results and Conclusions

The final state of the simulated deformation of the mortise on the CLT panel is presented in Fig. 2 (a). Fig. 2 (b) shows the observed local deformation after disassembly. The measured local mortise extension distance on the failed side ranged from 13 to 23 mm, which aligns with the directional result obtained from the current model. This agreement validates the proposed modeling methodology for CNC-made mortises.

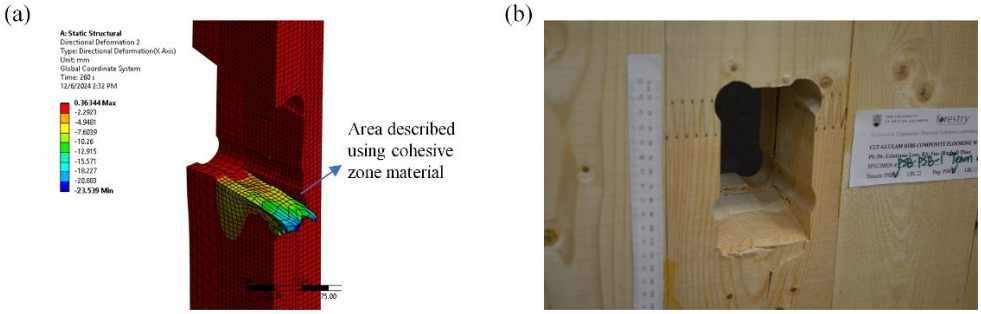

Fig. 2. Directional deformation of the mortise on the CLT panel: (a) Contour from the simulation; (b) Photograph taken after testing

As a key outcome of this research, practitioners can directly apply this methodology in advanced timber-to-timer simulations, leveraging the available tools in commercial FEA software.

5. Acknowledgements

The research presented in this paper has received funding from of the Government of British Columbia through an FII Wood First grant and the Natural Sciences and Engineering Research Council (NSERC) of Canada through the Discover Program grant number RGPIN-2019-04530, and Discovery Launch Supplement, grant number DGECR-2019-00265. The China Scholarship Council Doctoral Scholarships number 202006510006, awarded to Yue Diao, is also acknowledged. Great appreciation to MOSO International B.V. for sponsoring the engineered bamboo products.

6. References

[1] Forcael, E., Ferrari, I., Opazo-Vega, A., & Pulido-Arcas, J. A. (2020). Construction 4.0: A Literature Review. *Sustainability*, *12*(22), 9755.

[2] Smith, I., Landis, E., & Gong, M. (2003). *Fracture and fatigue in wood*. John Wiley & Sons.

[3] Xie, Q., Zhang, B., Zhang, L., Guo, T., & Wu, Y. (2021). Normal contact performance of mortise and tenon joint: Theoretical analysis and numerical simulation. *Journal of Wood Science*, *67*(1), 31.

[4] Huang, D., Bian, Y., Zhou, A., & Sheng, B. (2015). Experimental study on stress–strain relationships and failure mechanisms of parallel strand bamboo made from phyllostachys. *Construction and Building Materials*, *77*, 130–138.

[5] Tang, G., Yin, L., Li, Z., Li, Y., & You, L. (2019). Structural behaviors of bolted connections using laminated bamboo and steel plates. *Structures*, *20*, 324–339.

COMPARISON OF MECHANICAL PROPERTIES OF CROSS LAMINATED TIMBERPRESSED ON VACUUM AND HYDRAULIC PRESSES

W. Plowas[1], R. Hairstans[1], B. Shirley[2] and S. Hart[3]
[1] School of Computing, Engineering and The Built Environment, Edinburgh Napier University, Edinburgh, Scotland
[2] New Model Institute for Technology and Engineering, NMITE, Hereford, England
[3] Built Environment – Smarter Transformation, BE-ST, Hamilton, Scotland

1. Introduction

Cross Laminated Timber, often referred to as CLT, is a highly versatile engineered wood product used in construction. It consists of a minimum of three cross-bonded layers where at least 1 layer is orthogonally oriented to the two adjacent layers of timber boards. Bonding can be carried out on a hydraulic or vacuum presses, both of which apply pressure over the entire surface of the panel for several hours.

The product became increasingly popular in Europe, UK and America in the past decade. According to Forest Products Annual Market Review 2020-2021 [10] the global production capacity for CLT was estimated at 2.8 million m³ in 2020, with Europe accounting for 48%, North America 43%, Oceania 6%, and Asia 3%. Increased popularity of CLT resulted in development of ever more efficient manufacturing plants. Europe has the highest concentration of cross-laminated timber manufacturers, with 70 producers spread across 18 different countries [5]. The scale of operations and degree of automation among CLT plants worldwide vary significantly, with annual production volumes ranging from less than 500 m³ to over 125,000 m³ [8].

The two primary surface bonding machines used by CLT manufacturers are hydraulic presses and vacuum presses, which differ significantly in the bonding pressures they apply during panel formation. Hydraulic presses, are highly automatic, heavy and complex piece of machinery, designed to produce CLT panels quickly and efficiently, but they come at much higher price, require more space and thick concrete foundation. Vacuum presses, by comparison, are relatively light, versatile, simple and come at much lower cost, but they generally require more manual input, which could be reduced by introduction of lateral and longitudinal lamella feeding systems. Vacuum presses typically operate at pressures below 0.1 N/mm², while hydraulic presses usually exceed 0.4 N/mm² [9]. Several studies have examined the effect of bonding pressure on bonding quality. Knorz et al., [7] investigated the influence of bonding pressure (0.085 N/mm² vs. 0.8 N/mm²) on the delamination behavior of spruce CLT glued with one component PUR adhesive. Their findings indicate that pressure applied during manufacture had no effect on the delamination test results.

This publication presents the results of two research projects conducted by Edinburgh Napier University in 2014 and 2021 [4]. For both projects, a series of CLT specimens were manufactured and structurally tested in a laboratory setting. In each case, the baseline material was UK-grown Sitka Spruce. The key distinction between the two studies was that one set of samples was produced using a mechanical press, while the other was manufactured using a vacuum press.

2. Materials and methods

The material for both studies was supplied by BSW Timber Ltd and the species considered was Sitka spruce felled in Scotland. All boards used for the manufacture of test samples have been strength graded to C16 strength class, as per BS EN 338:2016 [1]. The dimensions and layouts of each CLT test specimen was determined from the geometrical constraints outlined in BS EN 16351:2021 [3] and BS EN 408:2010+A1:2012 [2]. For the comparison purposes CLT panels, consisting of 3 and 5 layers, were tested with load applied out-of-plane and in-plane of the panel to replicate slab-like and beam-like behaviour of the system.

The laboratory testing of bending properties (strength and stiffness) of 3ply and 5ply CLT panels was in accordance with BS EN 16351:2021. In all cases the load was applied across the whole width of the CLT sample at a constant rate, so adjusted that maximum estimated load was reached within 300 ± 120 s. Deformation of samples was measured using 3 LVDTs, 1 located at the centre span of the beam and a further 2 fixed to the cradle positioned either side of the beam on its neutral axis. For details regarding test setup see figure below.

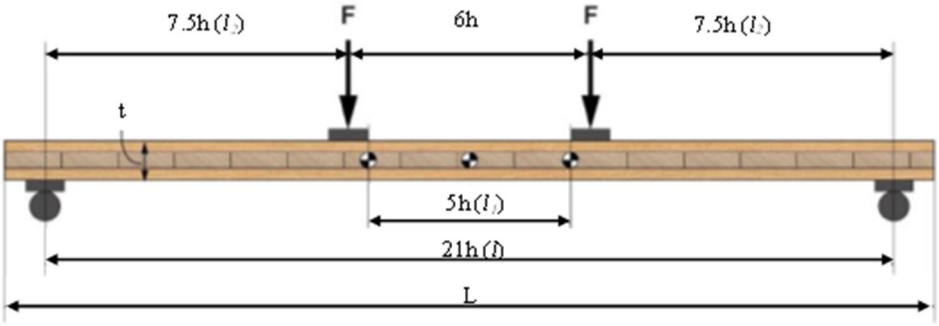

Figure 1. Test configuration for bending out-of-plane (CLT slabs)

3. Results and conclusions

The results from the bending tests are summarized in the figure below, providing a direct comparison of the bending properties—mean and characteristic values of modulus of elasticity and bending strength—of CLT panels manufactured from UK-grown resources in both studies conducted by ENU. The results are also compared with the properties of one of the most popular CLT panels currently available on the market, as declared in ETA-14/0349 [6].

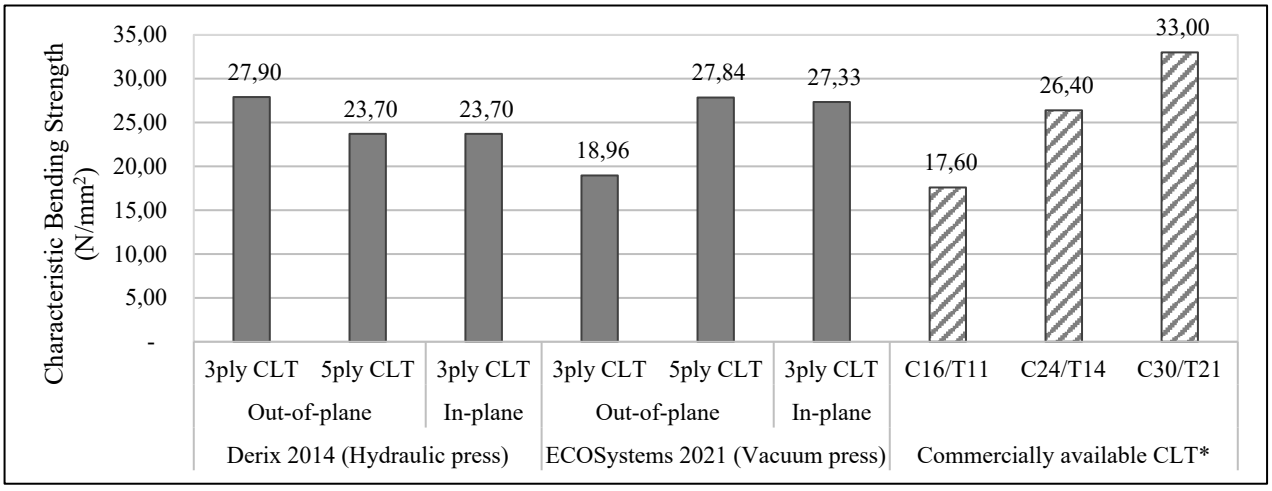

*As per values declared in ETA 14-0349 for panels made from C16/T11, C24/T14 and C30/T21 strength classes

Figure 2. Comparison and findings - characteristic bending strength

The results indicate that different pressing technologies have little effect on the mechanical performance of the panels. Although some differences were observed between panels pressed using vacuum and mechanical presses, these variations are most likely due to the relatively small sample size. It is expected that with larger testing programs, the structural evaluation outcomes for both mechanical and vacuum-pressed CLT panels would converge. Furthermore, panels produced using both pressing methods exhibited little to no delamination failures under severe loading conditions, indicating appropriate bond integrity in both cases.

4. Acknowledgements

The research outcomes presented in this publication are part of a larger project funded by UK Research and Innovation (UKRI-Innovate UK), under a grant valued at £1,450,138. The overarching project aim aligns with key themes of the UK Government's Clean Growth Strategy, particularly focusing on enhancing the benefits and value of our natural resources. The specific aspect of the research, as outlined in this publication, aimed to validate the use of homegrown mass timber construction products within the UK market, with emphasis on mechanical performance, engineering viability, productivity, and cost-effectiveness.

5. References

[1] BS EN 338:2016. (2016). Structural timber - Strength classes. *The British Standards Institution*.
[2] BS EN 408:2010+A1:2012. (2012). Timber structures - Structural timber and glued laminated timber - Determination of some physical and mechanical properties. *The British Standards Institution*.
[3] BS EN 16351:2021. (2021). Timber structures - Cross laminated timber - Requirements. *The British Standards Institution*.
[4] Crawford, D., Hairstans, R., Smith, S., & Papastavrou, P. (2015). Viability of cross-laminated timber from UK resources. *Proceedings of Institution of Civil Engineers: Construction Materials*, *168*(3), 110–120.
[5] De Araujo, V., & Christoforo, A. (2023). The Global Cross-Laminated Timber (CLT) Industry: A Systematic Review and a Sectoral Survey of Its Main Developers. *Sustainability (Switzerland)*, *15*(10).
[6] ETA-14/0349. (2023). European Technical Assessment - CLT - Cross Laminated Timber - Stora Enso Oyj. *Austrian Institute of Construction Engineering*.
[7] Knorz, M., Torno, S., & van de Kuilen, J. W. (2017). Bonding quality of industrially produced cross-laminated timber (CLT) as determined in delamination tests. *Construction and Building Materials*, *133*, 219–225.
[8] Muszynski, L., Larasatie, P., Guerrero, J. E., & Albee, R. (2020). Global CLT industry in 2020: Growth beyond the Alpine Region. *Proceedings of the 63rd International Convention of Society of Wood Science and Technology*.
[9] Purba, C. Y. C., Pot, G., Collet, R., Chaplain, M., & Coureau, J. L. (2022). Assessment of bonding durability of CLT and glulam made from oak and mixed poplar-oak according to bonding pressure and glue type. *Construction and Building Materials*, *335*.
[10] UN/FAO. (2021). *Forest Products Annual Market Review 2020-2021*. United Nations Publications.

INVESTIGATING THE INFLUENCE OF DELIGNIFICATION AND POLYMER INFILTRATION ON WOOD CELL WALL PROPERTIES VIA NANOINDENTATION

J. Schindler[1], M. Königsberger[1], L. Zelaya-Lainez[1], A. Mariani[2], D. Nuvoli[2], J. Füssl[1]

[1] Institute for Mechanics of Materials and Structures, TU WIEN, Vienna, Austria
[2] Department of Chemical, Physical, Mathematical and Natural Sciences, University of Sassari, Sassari, Italy

1. Introduction

Wood is an outstanding construction material, and due to the urgent need for environmentally friendly building materials, long-term approved materials, perfected by nature, are in high demand. To explore the structure of wood on a deeper level, it was made transparent in the early 90s by delignifying wood and infiltrating the scaffold with a polymer, having a matching refractive index to cellulose [1]. In the last decade, this material has been rediscovered as an alternative transparent material with excellent mechanical properties inherited from native wood [2-4]. However, the microscopic effects of various modifications on wood cell walls remain unexplored.

In this study, we investigate how delignification and polymer infiltration modify the mechanical properties of the wood cell walls, and thus aim to decipher the micromechanical properties of transparent wood. We rely on nanoindentation a method well established for wood testing [5-6]. We aim at using image-guided indentation [7] to specifically indent the S2 layer and the middle lamella of native wood to assess potential differences.

2. Materials and methods

To investigate the differences between native wood to transparent wood, nanoindentation was subjected to natural birch (NB) and delignified birch infiltrated with three different polymers (poly-methylmethacrylate (PMMA), poly-hydroxyethylmethacrylate (PHEMA), poly-isobornyl-acrylate, (PIOBA)). The latter is derived from camphene, a terpene obtained from wood, and is mainly used for varnish [8]. The samples were cut into smaller dimensions and embedded in Agra low-viscosity resin (Agar Scientific). The surfaces were smoothened with a Leica Ultracut machine using two different Diatome blades. This ensures that the probed regions of interest exhibit roughnesses as low as 10 to 20 nm. To take the hierarchical structure and transversely isotropic material behavior of the wood into account, the samples were tested in longitudinal and radial directions.

The tests were conducted on a Hysitron Triboindenter TI 950 and the indents were applied displacement-controlled with an indentation depth of 50 nm. Image guided test evaluation [7] allows to remove indents close to the phase boundaries, thus reducing the scatter and obtaining trustworthy mechanical properties of S2 layer and middle lamella respectively.

3. Results and conclusions

The histograms for the indentation modulus of native birch and delignified birch infiltrated with HEMA are shown in Figure 1. While the natural birch has an average indentation modulus of 15.7 ± 2.4 GPa, the transparent wood exhibits an indentation modulus of 18 ± 1.9 GPa.

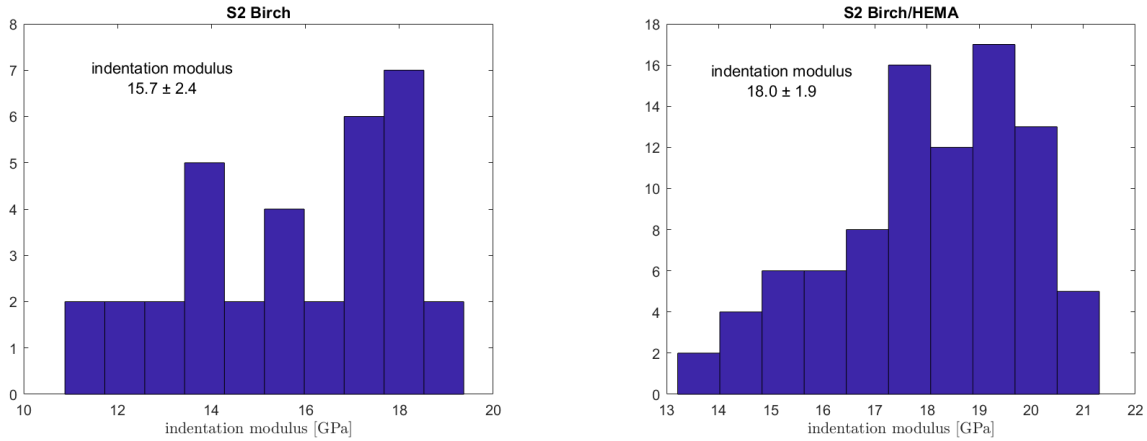

Figure 1: Histograms for indentation modulus for native birch (left) and for delignified birch infiltrated with HEMA (right)

As expected, the middle lamella is significantly softer than the S2 layer (in fiber direction). More importantly, the cell wall properties of the transparent wood are even higher than for native wood, as shown above. This indicates that despite the removal of lignin, which is considered the glue holding the cellulose together, the mechanical performance of the cell walls can be even further boosted by the consecutive infiltration with HEMA.

4. Acknowledgements

The AI-TranspWood project, HORIZON-CL4–2023-RESILIENCE- 01–23 (Grant Agreement 101138191), is gratefully acknowledged. This project is co-funded by the European Union. Views and opinions expressed are however those of the authors only and do not necessarily reflect those of the European Union or HaDEA. Neither the European Union nor the granting authority can be held responsible for them.

5. References

[1] S. Fink (1992). Transparent Wood – A New Approach in the Functional Study of Wood Structure, *Holzforschung,* **46**, 403 - 408.

[2] Y. Li et al. (2018). Optically Transparent Wood: Recent Progress, Opportunities, and Challenges, *Advanced Optical Materials*, **6**, 1800059.

[3] E. Jungsted et al. (2020). Mechanical properties of transparent high strength biocomposites from delignified wood veneer, *Composites Part A: Applied Science and Manufacturing.*, **133**, 105853.

[4] H. Yang et al. (2023). Light and wood: A review of optically transparent wood for architectural applications, *Industrial Crops and Products*, **204**, 117287.

[5] A. Jäger et al. (2011). Identification of stiffness tensor components of wood cell walls by means of nanoindentation, *Composites Part A: Applied Science and Manufacturing*, **42**, 2101 - 2109.

[6] J. Konnerth, W. Gindl (2006). Mechanical Characterization of wood-adhesive interphase cell walls by nanoindentation, *Holzforschung*, **60**, 429 - 433.

[7] M. Königsberger, L. Zelaya-Lainez (2021). Nanoindentation-probed Oliver-Pharr half-spaces in alkali-activated slag-fly ash pastes: Multimethod identification of microelasticity and hardness, *Mechanics of Advanced Materials and Structures,* **29:26**, 4878-4889

[8] F. Obermaier et al. (2024). Syntheses and polymerization of monoterpene-based (meth)acrylates: IBO(M)A as a relevant monomer for industrial applications, *Green Chemistry*, **26**, 4387 - 4416.

THE EFFECT OF CATENARY ACTION IN RESTRAINED AND REINFORCED GLUED LAMINDATED TIMBER MEMBERS

L. Esser[1], A. Frangi[1]
[1] Institute of Structural Engineering, ETH Zurich, 8093 Zurich, Switzerland

1. Introduction

Timber buildings are being built at an increased rate, driven by sustainability concerns related to the use of the popular construction materials steel and reinforced concrete [1]. As with such materials, modern mass timber can be used for high rise structures to a certain extent [2]. As the buildings get higher also does the necessity for a construction resistant to disproportional collapse, since the impact of structural failure also increases as the number of storeys increases.
Robustness is defined a structure's ability to resist collapse, given that damage an initial damage has already occurred to the structure [3]. Since timber has different material properties than steel and reinforced concrete, research that has been conducted in such fields cannot be transferred one-to-one for use in timber structural design. Different design strategies may be implemented to enhance a building's robustness and will be included in the next generation of the Eurocode 5 [4]. The research conducted here aims to better the understanding of catenary action which may be used to activate alternative load paths in damaged structures [5]. This effect can be compared to a taught rope being pushed down, which in turn activates the normal load resisting mechanism of the beam.
Timber is frequently used in combination with other materials to increase strength and promote certain, more ductile, failure modes [6]. Steel may be used to provide ductility in connections whilst the composite action between timber and concrete can increase stiffness and optimal utilisation of timber. The research into reinforcement of beams with fibre reinforcements gained traction in the 1970s [7].
Previous investigations by Cao et al. have shown that restraining both beam ends horizontally can activate catenary action in clear wood specimens [8]. Two types of tests were performed with different specimen types: standard three-point bending tests with the usual pinned and roller supports. The second tests were performed using two pinned supports at each beam end, allowing for tensile forces to occur in the beam. Cao et al. [8] found the combined bending and tensile action to be especially effective in beams with CFRP reinforcements, since the tensile side of the beam which is prone to brittle failure is reinforced and therefore this failure mode inhibited, allowing for a higher utilisation of the tensile strength of the carbon fibres. The aim of the outlined research in this abstract are to investigate whether the findings in the aforementioned paper can be applied for full-scale glued laminated (GLT) specimens.

2. Materials and methods

An experimental setup was designed to test full-scale GLT specimens under pinned support conditions, as well as a simply supported setup. Standard roller and pin supports were used for the 3-point bending tests. A hydraulic jack placed at the centre of the beam was connected to a servo-hydraulic system and used to push down the beam during testing using a displacement-controlled quasi-static loading protocol. For the restrained tests, a test setup was designed to resist horizontal forces up to 1400 kN. Each beam end was secured by means of ridged plates designed for tensile timber plates, these were pressed together using threaded rods, which also transferred shear forces to

the supports. This assembly was attached to hinges using additional steel plates and steel H-Beams. In turn, the hinge assembly at each beam end was attached to a shear wall secured to the strong-floor of the testing facility.
Two types of specimens were each tested in the three-point restrained and unrestrained test setups: unreinforced and reinforced GL24h members. These had cross-sections varying from 200 x 320 mm to 105 x 200 mm (b x h) and varying lengths from 4800 mm to 5900 mm. For the reinforced specimens, a pre-fabricated CFRP sheet of thickness 5 mm and the width of the beam was adhered to the underside of the beam using a PUR 1-K adhesive.
Measurements of deflections were performed using LVDTs at five points along each member. Due to the restraint of the beam, the normal force of the beam is also required to quantify the amount and effect of the catenary action. To measure these, strain gauges were adhered to the clamping system at both beam ends. This allowed for normal force measurements to be made after an initial calibration of the strain gauges performed by applying a tensile force to the clamps in a universal testing machine. Combined with an angle measurement of the clamp assembly by means of inclinometers and using analytical force decomposition, the proportion of force transferred by bending action and catenary action could be determined in post-processing.

3. Results and conclusions

Figure 1 shows the failure loads for specimens of different heights. The reinforced specimens were of constant 200 mm width whilst the height was varied between specimens. The mean total load (R-P) is 170 kN for the specimens with 320 mm height and 145 kN for the specimens with 240 and 280 mm heights. The bending component in the beams increases almost linearly with height increase, as a result the catenary action component is greatest for the h = 240 mm specimen, constituting 41% of the carried load. For the beams of 280 and 320 mm height, the proportions lie at 28 and 31%, respectively.

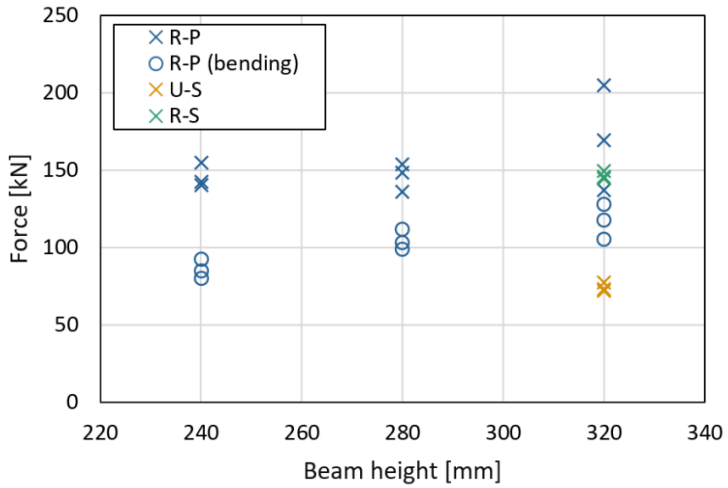

Fig. 1. Comparison of maximum forces of 200 mm wide specimens with reference tests.
R - reinforced, U – unreinforced, P – pinned supports, S – simply supported

In comparison to the reference tests (whose results were scaled due to a shorter specimen lengths/widths), the mean loads achieved in the restrained specimens for h = 320 mm specimens was 16% higher than the reinforced simply supported specimens. The activated mean bending component however lies below that of the maximum load of the reinforced simply supported beams, implying that the loss in bending action is compensated by the effect of catenary action. Compared to the simply supported unreinforced specimens, a strength increase of 130% was observed. This shows that catenary action can be activated to favourable effect in GLT members under idealized boundary conditions, however is also dependent on the reinforcement ratio of the beam.

4. Acknowledgements

The research presented in this abstract is part of the SNF project “Preventing disproportionate collapse in tall timber buildings” with grant number 219965.

5. References

[1] J. Abed, S. Rayburg, J. Rodwell, and M. Neave, ‘A Review of the Performance and Benefits of Mass Timber as an Alternative to Concrete and Steel for Improving the Sustainability of Structures’, *Sustainability*, vol. 14, no. 9, 2022, doi: 10.3390/su14095570.

[2] H. E. Ilgın, ‘High-Rise Residential Timber Buildings: Emerging Architectural and Structural Design Trends’, *Buildings*, vol. 14, no. 1, 2024, doi: 10.3390/buildings14010025.

[3] J. M. Adam, F. Parisi, J. Sagaseta, and X. Lu, ‘Research and practice on progressive collapse and robustness of building structures in the 21st century’, *Eng. Struct.*, vol. 173, pp. 122–149, Oct. 2018, doi: 10.1016/j.engstruct.2018.06.082.

[4] P. Palma, J. Munch-Andersen, and P. Dietsch, ‘Updating Eurocode 5 - Design guidance for increasing the robustness of timber structures’, in *World Conference on Timber Engineering (WCTE 2023), Oslo, 19th-22nd June 2023*, Oslo, Norwegen: Curran Associates, 2023, pp. 3054–3061. doi: 10.52202/069179-0398.

[5] U. Starossek, M. Asce, and M. Haberland, ‘Disproportionate Collapse: Terminology and Procedures’, *J. Perform. Constr. Facil. - J PERFORM CONSTR FACIL*, vol. 24, Dec. 2010, doi: 10.1061/(ASCE)CF.1943-5509.0000138.

[6] S. Pastori, E. Sergio Mazzucchelli, and M. Wallhagen, ‘Hybrid timber-based structures: A state of the art review’, *Constr. Build. Mater.*, vol. 359, p. 129505, Dec. 2022, doi: 10.1016/j.conbuildmat.2022.129505.

[7] K. Saad and A. Lengyel, ‘Strengthening Timber Structural Members with CFRP and GFRP: A State-of-the-Art Review’, *Polymers*, vol. 14, no. 12, 2022, doi: 10.3390/polym14122381.

[8] A. S. Cao, P. Grönquist, and A. Frangi, ‘Catenary action in strip-reinforced wood and timber beams’, *Constr. Build. Mater.*, vol. 385, p. 131422, 2023, doi: https://doi.org/10.1016/j.conbuildmat.2023.131422.

EuraSEM 6-11 July 2025 ICEM21 Bologna 21st International Conference on EXPERIMENTAL MECHANICS

FINITE ELEMENT MODELLING OF CLT-STEEL COMPOSITE SHEAR WALLS FOR MASS TIMBER BALLOON-TYPE CONSTRUCTION

C. Leong[1] and C. Loss[1]
[1] SESS Lab, Department of Wood Science, Faculty of Forestry, The University of British Columbia, Vancouver, Canada

1. Introduction

Recent studies on cross-laminated timber (CLT) have proven its capability to cover a large spectrum of structural applications – in fact, many wood buildings across the globe have been constructed using CLT shear walls and diaphragms as lateral force-resisting systems [1]. However, with the increased demand for taller buildings to address housing needs with minimal land use, a study from [2] has shown high wind/seismic drift demand in CLT shear walls of such buildings. To address this, either an increased number of shear walls in the building is required, reducing architectural freedom, or a combination of CLT with other lateral structural systems, such as steel or reinforced concrete, is needed. Regardless, advanced finite-element models are required to accurately represent the behaviour of such systems to ensure compliance with applicable codes and standards. This study proposes a CLT-steel composite shear wall system with enhanced stiffness compared to regular CLT shear walls, circumventing the need to modify the lateral system layout of the building. Numerical results between the proposed CLT-steel composite wall and a 5-ply CLT wall modelled using the general-purpose finite element analysis (FEA) program–ANSYS–are compared. While only results for a single wall case are presented, the approach is applicable to whole building analysis.

2. Materials and methods

A 4.57 m x 10.5m 5-ply grade E1 CLT wall was modelled using ANSYS's Static Structural module with the material elastic properties of each layer listed in Table 1 based on CSA O86-24 [3]. Each lamella is 35 x 175 mm and lumber boards are perfectly bonded, modelled with a 1 mm gap between one another similar to the modelling procedures in [4]. For the CLT-steel composite wall, 30 x 525 mm ASTM A572 Grade 50 (F_y = 345 MPa) steel plates are used. These plates are modelled at each end of the wall (4 total) and are bonded to the surface of the CLT. Both walls are fixed at the base and a 482 kN lateral load is applied to the top face of the walls, simulating the total seismic load acting on the wall in a 3-storey building located in Vancouver, BC.

Parameters		Longitudinal Boards (0°) 1950F_b-1.7E Spruce-Pine-Fir MSR lumber	Transverse Boards (90°) No. 3/Stud Spruce-Pine-Fir lumber
Modulus of elasticity about $x \mid y \mid z$ axis	$E_x \mid E_y \mid E_z$ (MPa)	390 | 11700 | 390	300 | 9000 | 300
Poisson's ratio about $xy \mid yz \mid xz$ axis	$\nu_{xy} \mid \nu_{yz} \mid \nu_{xz}$	0.083 | 0.462 | 0.255	0.083 | 0.462 | 0.255
Shear modulus about $xy \mid yz \mid xz$ axis	$G_{xy} \mid G_{yz} \mid G_{xz}$ (MPa)	731.25 | 731.25 | 73.125	562.5 | 562.5 | 56.25

Table 1. Material properties used in numerical model

Wood materials are modelled as orthotropic while steel is modelled as isotropic. Both materials are represented as solid-type elements with a mesh size of 500 x 500 mm. The longitudinal axis is defined as the y-axis, with longitudinal boards aligned parallel to it and transverse boards oriented perpendicular to it.

3. Results and conclusions

The FEA models and deformation results for the CLT and CLT-steel composite wall are found in Figure 1. A roughly 51% decrease in lateral deformation is seen with the addition of steel plates at the boundary zones of the CLT wall.

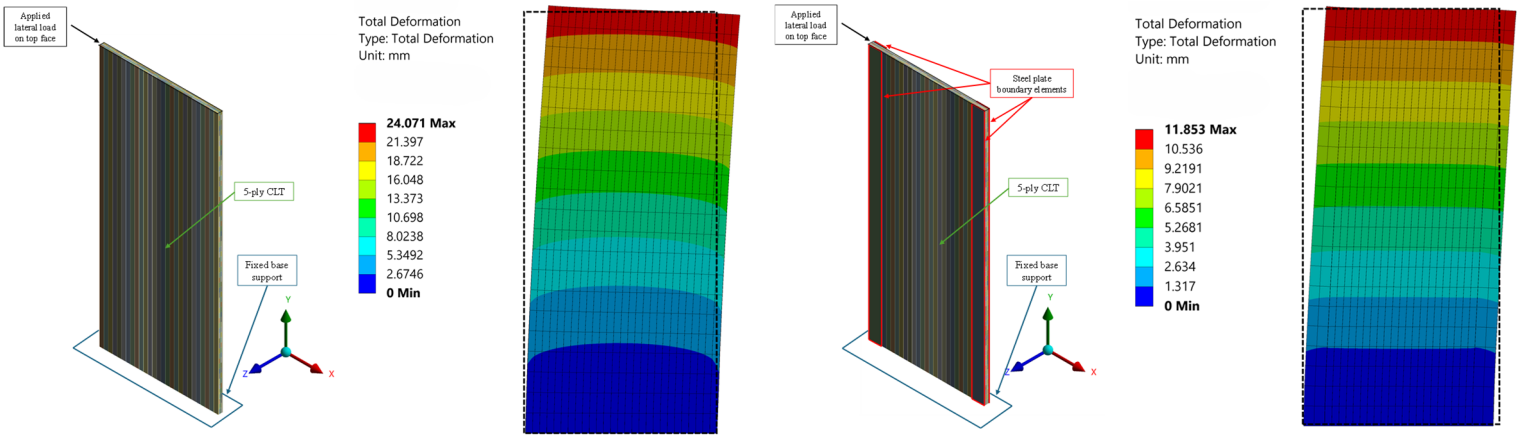

(a) (b) (c) (d)

Fig. 1. FEA models: a) CLT model, b) CLT deflection, c) CLT-steel model, d) CLT-steel deflection

4. Acknowledgements

The research presented in this paper has received funding from the Natural Sciences and Engineering Research Council (NSERC) of Canada through the Alliance Grants Program, grant number ALLRP 571090-21. The NSERC Graduate Scholarship – Masters' program, British Columbia Graduate Scholarship, UBC Faculty of Forestry Graduate Award, and Robert Kennedy Family Graduate Scholarship in Forestry, awarded to Christopher Leong, are gratefully acknowledged.

5. References

[1] Pei, S., Rammer, D., Popovski, M., Williamson, T., Line, P., & van de Lindt, J. W. (2016). An overview of CLT research and implementation in North America. *World Conference on Timber Engineering, WCTE 2016*, 22–25 August 2016, Vienna, Austria, 10 pp.

[2] Green, M. (2017). *The case for tall wood buildings: A new way of designing and constructing tall wood buildings* (2nd ed.).

[3] Canadian Standards Association. (2024). CSA O86-24: Engineering design in wood. Toronto, Canada: CSA Group.

[4] Jeleč, M., Danielsson, H., Rajčić, V., & Serrano, E. (2019). Experimental and numerical investigations of cross-laminated timber elements at in-plane beam loading conditions. *Construction and Building Materials*, *206*, 329–346. https://doi.org/10.1016/j.conbuildmat.2019.02.068.

Long-term analysis of steel-timber shear connectors for composite floors

M. Kamalinejad[1], C. Burigo[2], C. Loss[1] and I. Goingo[2]
[1] SESS Lab, Department of Wood Science, Faculty of Forestry, University of British Columbia, Vancouver, Canada
[2] Department of Civil, Environmental, and Mechanical Engineering, University of Trento, Italy

1. Introduction

Design for improving the strength and stiffness of structural systems and their components through material hybridization provides practitioners with a pathway to overcome the shortcomings of individual materials. Among those standardized hybrid systems, steel-timber composites (STC) stand out as engineered solutions for lightweight prefabricated floors, walls, and other timber-based structural elements obtained by incorporating steel members into timber assemblies. In STC floors, composite action is influenced by the performance and arrangements of the shear connectors. Despite the remarkable stiffness and strength of the STC floors under short-term loading, verified by numerous studies [1], the time-dependent behavior of the floorings and connectors still requires detailed investigations under moisture and temperature fluctuation. The long-term performance of timber members is usually a function of the wood species, dominant stresses, and environmental conditions [2]. The latter could emerge as a fluctuation of the equilibrium moisture content (EMC) below the fiber saturation point (FSP) due to temperature and humidity changes during service life. This can cause changes in the mechanical characteristics of timber elements, leading to an increase in joint slip. This study aims to provide valuable insights into the long-term behavior of shear connectors specifically developed for STC floors. To invistigate the moisture-time-dependant performance of such connectors under sustained loading, a computational framework is used and validated experimentally.

2. Materials and methods

Two shear connector types were investigated through long-term experimental tests conducted under sustained service loads in an environmentally controlled room. Figs. 1a and 1b illustrate the two connection types and layout of specimens. The first connection type (CV) consists of a perforated steel plate bonded to the CLT panel and welded to the steel member. The second type (DI) utilizes a thick steel plate welded to the steel member and connected to the CLT panel using inclined self-tapping screws (Φ=11mm). Fig. 1c shows the custom-designed testing apparatus used for this testing program. To complement the experimental study, a 3D finite element model (FEM) was developed, incorporating the rheological behavior of wood. The material laws governing wood behavior were implemented via a custom ANSYS-APDL subroutine using Torrati's model [3] based on Fick's law of diffusion. This model accounted for all time- and moisture-dependent components of strain, including elastic strain, creep strain, mechano-sorptive strain, nonlinear shrinkage, and thermal strain, ensuring a comprehensive representation of the long-term behavior of wood.

3. Results and conclusions

The fluctuation of the observed humidity and temperature is shown in Fig.1d. Slip change over time during the testing period is shown in Fig. 1e, including also the simulated numerical curves. Results show a remarkable increase of slip in the CV joint compared to the DI joint, with the tendency

of flattening early for the CV connections where bonded conditions between the steel and wood surfaces were achieved using an epoxy-based grout mixture. The specimens were unloaded on day 206, and measurement equipment continued daily readings for an additional twenty-five days in order to capture the residual deformation at the end of the tests. The analysis indicated that environmental factors, such as temperature and humidity, significantly impacted the wood's moisture content, altering the mechanical properties of the shear connectors over time. In addition, the results demonstrate an acceptable accuracy of the analytical method in predicting the connection's time- and moisture-dependent performance.

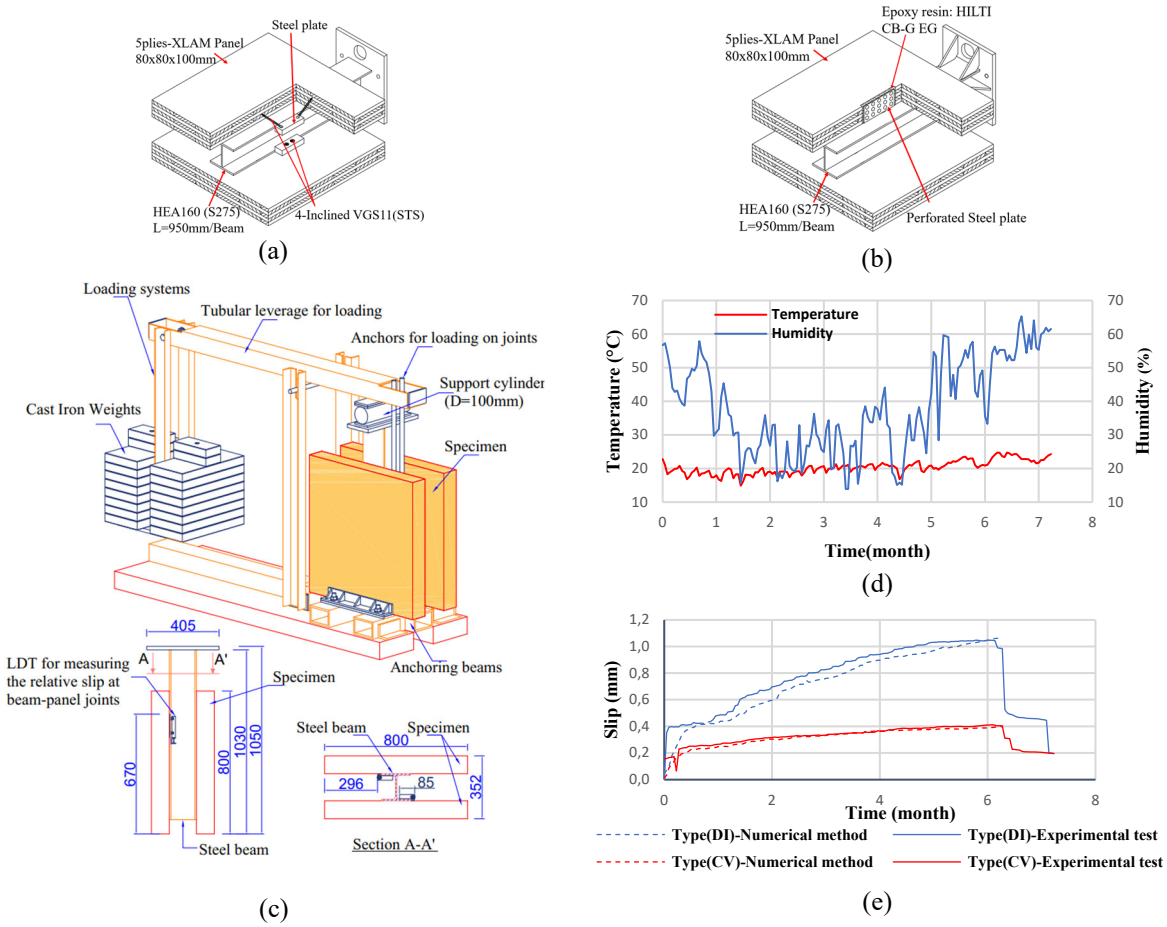

Fig. 1. Schematic of the DI-type specimen (a) and CV-type specimen (b), test setup apparatus (c), fluctuation of temperature and humidity during time (d), and experimental and numerical slips for specimens of CV and DI shear connectors (e).

4. Acknowledgements

The research presented in this paper has received funding from the Government of British Columbia through an FII Wood First grant and the Natural Sciences and Engineering Research Council (NSERC) of Canada through the Discover Program grant number RGPIN-2019-04530, and Discovery Launch Supplement, grant number DGECR-2019-00265.

5. References

[1] Loss, C., Piazza, M., & Zandonini, R. (2016). Connections for steel–timber hybrid prefabricated buildings. Part II: Innovative modular structures. *Construction and Building Materials*, *122*, 796-808.

[2] Chiniforush, A. A., Valipour, H. R., Bradford, M. A., & Nezhad, A. A. (2021). Experimental and theoretical investigation of long-term performance of steel-timber composite beams. *Engineering Structures*, *249*, 113314.

[3] Toratti T. Creep of timber beams in variable environment. Ph D Thesis, Helsinki 1992;182.

EFFECT OF INTERPOSED RESILIENT SOUNDPROOFING PROFILE ON TIMBER-TO-TIMBER STRUCTURAL CONNECTIONS

A. Morganti[1], L. Barbaresi[1], M. Benatti[2], P. Brugnara[3], M. Zoppè[3], C. Luzzani[3], L. Pozza[4]
[1] CIRI Buildings and Construction, University of Bologna, Bologna, Italy
[2] National Research Council (CNR), Roma, Italy
[3] Rotho Blaas srl, Cortaccia (BZ), Italy
[4] Department of Civil, Chemical, Environmental and Materials Engineering (DICAM), University of Bologna, Bologna, Italy

1. Introduction

In recent years, the use of timber as a construction material has increased due to its valued attributes. However, timber structures are characterized by critical acoustic performance levels and require effective sound isolation technologies. The most crucial elements when considering both acoustic and structural factors are the connections between the different structural components [2]. A valid constructive strategy involves the insertion of resilient strips as interlayers along joints. This approach limits the acoustic transmission through the connections and ensures satisfactory flanking noise reduction.

In this study, the results of an extended experimental campaign, supported by Rotho Blaas S.r.l. company, aimed at the experimental and theoretical characterization of timber-to-timber screwed connections with an interposed acoustic resilient strip are discussed. Experimental results were used for the calibration and subsequent validation of the analytical models available in literature, in order to consider the effects of the acoustic interlayer on the stiffness and load-carrying capacity of timber connections.

2. Experimental campaign and results

The experimental campaign investigated how the thickness of the soundproofing strip Xylofon 35 (6-12-18 mm) and the nominal diameter of the screws (HBS6-HBS8-HBS10) affect the stiffness and load-carrying capacity of timber-to-timber connections. A total of 9 different configurations of screwed connections with acoustic layer were tested under the application of monotonic loading and n. 3 repetitions were performed for consistency. The results, referred to the individual screw, were compared to two reference configurations, also tested with n. 3 repetitions, represented by the bare timber-to-timber connection and the air gap combined with Teflon spacer one. Samples are made of two GL24 timber elements joined at a 7° shear plane, fastened using three HBS screws aligned with the wood grain.

The setup details are illustrated in Fig. 1b and the various configurations tested are outlined in Fig. 1c. Fig. 2 presents the average force-displacement curves for each configuration, linearized according to the "method b" specified in EN 12512 [3]. The codes "NX_x" and "AIR_x_x" in Fig. 2 refer to the reference configurations.

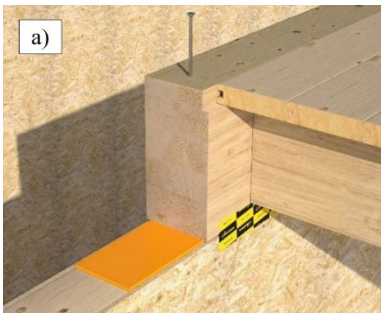

c)

Configurations under study

ID	Screw nominal diameter [mm]	Layer Type	Layer thickness [mm]
X35_6_6	6 (HBS6)	Xylofon 35	6
X35_6_12			12
X35_6_18			18
X35_8_6	8 (HBS8)	Xylofon 35	6
X35_8_12			12
X35_8_18			18
X35_10_6	10 (HBS10)	Xylofon 35	6
X35_10_12			12
X35_10_18			18

Fig. 1. a) Structural joint with acoustic interlayer; b) Specimens; c) Main configurations tested.

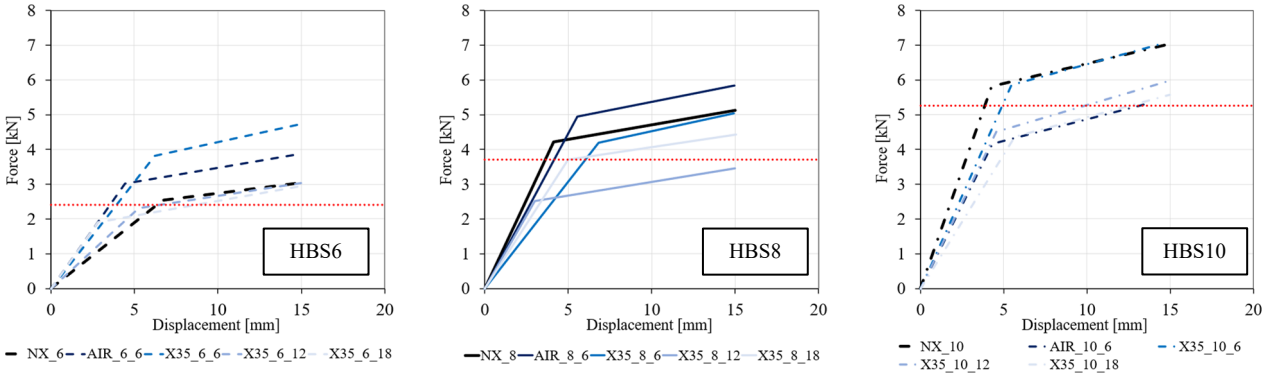

Fig. 2. Force-displacement curves superimposed to analitycal strength estimation (dotted red line).

As a result, the mechanical behavior of the connection primarily depends on screw diameter and, to a lesser extent, on the thickness of the resilient profile. Larger screw diameters lead to higher load-carrying capacity and reduced sensitivity to the thickness of the resilient profile. Analysis of the results presented in Fig. 2 reveals that the HBS6 and HBS8 configurations with a 6 mm thick profile exhibit greater resistance than the reference configuration without the interposed profile. As the thickness of the resilient profile increases, both the yield limit and the peak load tend to decrease nearing the values obtained from the reference configuration (air gap and Teflon). Furthermore, referring to the bare connection, including a resilient profile significally reduces the overall stiffness.

The experimental results were compared to the upgraded Johansen theory proposed by Blaß et al. [1]. The applicability of the theory was confirmed even if a proper calibration of the so called “rope effect” overtstrength contribution, accounting for the actual firctional properties of the interposed resilient profile, is necessary.

3. Conclusions

Results from experimental campaign demonstrate that the thickness and frictional properties of the acoustic interlayer plays a crucial role in fully understanding its structural influence. Specifically, it was observed that a thinner layer has a considerably lower impact compared to the influence exerted by a greater thickness. In fact, as the thickness increases, the reduction in joint stiffness becomes more pronounced. However, it was also found that the resistance remains largely unaffected thanks to the frictional properties of the interposed resilinet profile.

4. References

[1] H. J. Blaß e B. Laskewitz, «Load-carrying capacity of joints with dowel-type fasteners and interlayers» in International Council for Research and Innovation in Building and Construction, Delft, Olanda, 2000.

[2] Speranza, L. Barbaresi and F. Morandi, «Experimental analysis of flanking transmission of different connection systems for CLT panels» in World Conference on Timber Engineering, Vienna, Austria, 2016.

[3] UNI EN 12512, Timber structures - Test methods. Cyclic testing of joints made with mechanical fasteners, 2006.

X-ray & Neutron Tomography and Applications

TIME RESOLVED FAILURE PHYSICS TOMOGRAPHY (5D CT) ON THE DAMAGE BEHAVIORS BY MULTI-MODAL METHODS

S.C. Wu
State Key Laboratory of Rail Transit Vehicle System, Southwest Jiaotong University, Chengdu 610031, China

1. Introduction

Additive manufacturing (AM) processes result in complex internal architectures that lead to anisotropic mechanical properties. To identify damage origins, various microscopic techniques have been developed to gather damage evolution information. However, these slice-based techniques provide limited two-dimensional (2D) information, making it difficult to link surface features to internal events. To address this limitation, damage constitutive-informed mechanics enable the modeling of failure processes. For three-dimensional (3D) problems, advanced techniques, such as time-lapse X-ray tomography and neutron tomography/scattering can non-destructively probe critical failure events below the surface. Combining powerful computers, machine learning algorithms, and massive radiographs and images, we can reconstruct 3D renderings. Additionally, numerical modeling can visualize damage features and their evolution under real conditions, quantifying critical failure events and tailoring the fatigue resistance of AM materials. This work proposes a novel computational framework that integrates time-resolved damage physics-informed tomography mechanics (5D CT). The primary goal of tomography mechanics is to visualize vector damage fields in 3D solid problems, rather than relying on qualitative 2D images

This study will present both experimental and numerical methodologies mainly based on advanced X-ray and neutron tomography, illustrating their application through a representative example of AM materials and components. The discussion will conclude by identifying technological challenges that hinder the accurate quantification of degradation processes in AM materials.

2. Materials and methods

High-resolution tomography-driven damage mechanics offers a promising approach to directly quantify full-field damage evolution in large components subjected to diverse loading conditions and environmental temperatures. This innovative experimental damage mechanics methodology relies on three key components: 3D rendering of extensive scanned images, accurate constitutive relations and failure criteria, and advanced numerical simulation techniques. To illustrate this approach, three quantitative case studies are presented, mainly including Multi-modal imaging technology, Quantitative correlation characterization and Digital volume correlation technology. Meanwhile, integrating multi-modal data analysis with high-fidelity modeling, such as neutron and X-ray image-based finite element analysis, offers a powerful approach for mechanical engineers and scientists to precisely track critical events associated with specific features and establish comprehensive relationships between processing, microstructure, and service performance of AM components. This technique bridges the gap between qualitative tomographic data and quantitative, global damage evolution fields. The advent of advanced synchrotron X-ray and spallation neutron sources has

enabled both ex situ and in situ (or even operando) mechanical testing, pushing the boundaries of imaging resolution and sample size. This technological advancement, coupled with conventional mechanical tests (such as tensile, fatigue, fracture, and creep) and surface-based characterization techniques (TEM, SEM, OM), empowers researchers to delve deeper into the internal structures of novel materials and components. By integrating these experimental approaches with high-fidelity numerical simulations, a comprehensive understanding of material behavior and performance can be achieved, accelerating the development of innovative materials and structures for industrial applications. Six primary technological challenges hinder the advancement of X-ray tomography; achieving high contrast, reducing radiation dose, increasing span speed, improving resolution, eliminating artifacts, and automating data acquisition. Before embarking on multi-modal characterization, accurate feature segmentation is essential to identify internal structures and enable high-fidelity modeling. This section delves into the key challenges associated with implementing 5D CT.

3. Results and conclusions

Recent advancements in neutron and synchrotron X-ray sources, coupled with image-based numerical simulations and powerful computing capabilities, have enabled researchers to probe fine-scale features within materials, ranging from nanometers to micrometers, over time and under harsh conditions. Non-destructive neutron and X-ray tomography offers a significant advantage over post-mortem analysis by providing a window into the precise visualization and quantification of critical evolution events within opaque materials. To gain a deeper understanding of damage accumulation and accurately predict long-term service performance, multi-modal imaging characterization methods have been developed. These methods combine quantitative XCT (nanometer to micrometer scale) with surface-based examinations (SEM, OM, EBSD) and standard mechanical experiments. Leveraging these technological advancements, this paper proposes a time-resolved 3D CT methodology with intrinsic failure physics (5D CT) to directly acquire vector fields, including stress, damage, and lifetime, rather than relying solely on qualitative 2D images. This innovative approach aims to significantly reduce human intervention in big data processing by developing a self-contained plug-in software package. To realize this goal, several challenges, including feature segmentation, image-based high-fidelity modeling, correlative neutron and X-ray characterization, and limited angle reconstruction, must be addressed, and some points can be extended.

(1) To quantitatively characterize damage accumulation within AM materials and components, both X-ray computed image-based finite element modeling and EBSD-based crystal plasticity finite element modeling can bridge the gap between qualitative 2D images and quantitative 3D strain/stress distributions. Furthermore, neutron tomography-based numerical calculations can establish a reliable link between the internal features of small volumes and the mechanical properties of large samples.

(2) While DIC- and DVC-based finite element simulations can effectively quantify stress concentration regions as local or global field indicators, they may not accurately predict crack initiation and growth. The accuracy and validity of these simulations are heavily influenced by the internal architecture of the investigated object. However, as a crucial reference for in situ X-ray tomography, DVC results can significantly reduce the uncertainty in predicting crack paths, particularly in scenarios involving the competition between damage nucleation and coalescence.

(3) As in situ multi-field coupled mechanical experiments advance and spatial and temporal resolution limits are pushed, the generation of massive image data, particularly at large-scale science facilities, poses significant challenges for data cleaning and feature segmentation, including image noise and ring artifacts. To address these challenges, physics-informed machine learning methods, incorporating material constitutive equations and failure criteria, can be employed. Additionally, limiting the angular range of data collection, especially for in situ fatigue experiments, can offer a practical solution.

(4) As scientific instrumentation continues to advance, multi-functional devices are emerging to enable high-throughput characterization of microstructures, dislocations, residual stress, micro-hardness, and other properties. While each experimental method has its strengths and limitations, a judicious selection of techniques is essential to validate predictive models.

(5) By combining in situ neutron and X-ray tomography to precisely identify critical internal structures and their evolution with physics-informed machine learning for efficient processing of massive image data, we can generate explicit 3D visualizations of stress tensor fields within AM materials and components. This approach surpasses traditional qualitative 2D imaging techniques, such as TEM, EBSD, SEM, and OM. Through this experimental procedure, we can characterize multi-faceted, multi-scale, and multi-grade architectural scenarios in bulk materials under deformation and aggressive environments, gaining valuable insights into material behavior. This multi-modal data fusion methodology, rooted in tomography-driven damage mechanics, is increasingly valuable for material scientists and mechanical engineers to design new AM materials and structures and optimize their long-term performance, a concept we refer to as 5D CT.

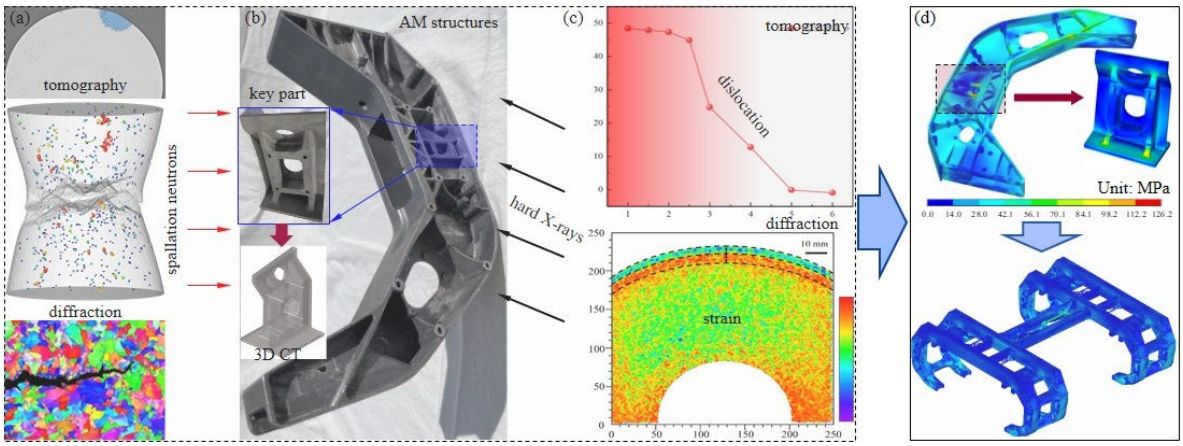

Fig. 1. Integrated approach to correlative neutron and X-ray characterization: (a) Hard X-ray tomography for defect evolution and diffraction for grain and strain; (b) AM AlSi10Mg structures; (c) Spallation neutron imaging and diffraction for dislocation and strain field; (d) Image-based finite element simulation of the mounting base and associated stress field.

4. Acknowledgements

I would like to acknowledge the support of the National Natural Science Foundation of China (52475167 and U2032121).

5. References

[1] K.J. Hemker, W.D. Nix. Nanoscale deformation: Seeing is believing (2008). Nat Mater **7**, 97.
[2] W.J. Qian, S.C. Wu, L.M. Lei, Q.D. Hu, C.K. Liu. Time lapse in situ X-ray imaging of failure in structural materials under cyclic loads and extreme environments (2024). J Mater Sci Technol **175**, 80-103.
[3] P.J. Withers, C. Bouman, S. Carmignato, V. Cnudde, D. Grimaldi, C.K. Hagen, et al. X-ray computed tomography (2021). Nat Rev Method Prime **1**, 18.
[4] Y.N. Hu, S.C. Wu, Y. Guo, Z. Shen, A.M. Korsunsky, Y.K. Yu, et al. Inhibiting weld cracking in high-strength aluminium alloys (2022). Nat Commun **13**, 5816.

EXPERIMENTAL AND COMPUTATIONAL ANALYSES OF HYDROGEN EMBRITTLEMENT BEHAVIOUR IN ALUMINIUM ALLOYS USING SYNCHROTRON-BASED MULTIMODAL MEASUREMENTS

H. Toda[1], Y. Wang[1], Z. Wu[1], H. Fujihara[1], M. Yamaguchi[2], T. Tsuru[3], K. Shimizu[4] and K. Hirayama[5]

[1] Department of Mechanical Engineering, Kyushu University, Fukuoka, Japan
[2] The Center for Computational Science and e-Systems, Japan Atomic Energy Agency, Ibaraki, Japan
[3] Nuclear Science and Engineering Center, Japan Atomic Energy Agency, Ibaraki, Japan
[4] Faculty of Engineering, Tottori University, Tottori, Japan
[5] Faculty of Engineering and Design, Kagawa University, Kagawa, Japan

1. Introduction

Various studies have been conducted on hydrogen embrittlement in terms of the inherent mechanism and it has still been the subject of controversy. Various industrial methods for preventing hydrogen embrittlement have been empirically derived from experimental trials. Given the absence of a universally accepted theory of the mechanism of hydrogen embrittlement, there appears to be a dearth of physical understanding of the mechanisms that prevent hydrogen embrittlement. Recently,

Tsuru et al. revealed the hydrogen embrittlement mechanism of Al-Zn-Mg alloys that coherent or semi-coherent interfaces between the η'/η precipitates and the aluminium matrix exhibits spontaneous interfacial decohesion [1]. Based on this understanding, an academic guiding principle for the prevention of hydrogen embrittlement were proposed, and several engineering methods for preventing hydrogen embrittlement were proposed [2, 3]. The basic idea is to add particles with higher hydrogen trapping energies than the coherent and semi-coherent interfaces between the precipitate and the aluminium matrix. This allows the majority of hydrogen in aluminium to be absorbed inside specific microscopic or nanoscopic particles. This in turn reduces the amount of hydrogen at the precipitate-aluminium coherent and semi-coherent interfaces, thereby suppressing hydrogen embrittlement of aluminium alloys.

In this presentation, the use of multimodal measurement combining X-ray CT and XRD will be introduced in details, with regard to the partitioning analysis of hydrogen in aluminium and the bridging between nano-level precipitate damage and macroscopic crack propagation, which formed the basis of a series of the studies.

2. Materials and methods

Multimodal measurements were performed, combining X-ray CT and DCT at the high-resolution imaging beamline of the synchrotron radiation facility SPring-8. The former was used to visualise the initiation and propagation of hydrogen embrittlement cracks, and the latter was used to visualise the polycrystalline microstructure before deformation in 3D. The 3D images were then combined to create a 3D image-based computational model. Utilising this model, multimodal simulations were performed, integrating crystal plasticity and hydrogen diffusion. Concurrently, the trajectories of tens of thousands of particles visible in the X-ray CT images were tracked, and plastic

strain mapping was conducted. From the absolute values of the plastic strain obtained, the 3D distributions of vacancy concentration and statistically accumulated dislocations were determined. Additionally, the gradient of the plastic strain was utilised to calculate the 3D distribution of geometrically necessary dislocations. This process ultimately resulted in the acquisition of the 3D distributions of nearly all the nanostructures capable of trapping hydrogen within the bulk tensile specimen. The hydrogen trap energies for each hydrogen trap site, as determined by first-principles calculations, were used to enable an examination of the local and dynamic partitioning of hydrogen to each hydrogen trap site.

3. Results and conclusions

It has been demonstrated that hydrogen concentrated in accordance with the distribution of hydrostatic tensile stress at the tip of a crack and at specific grain boundaries (Fig. 1(a)). A 3D map of the interfacial cohesive energy was obtained from the relationship between the nanoscopic hydrogen concentration and the interfacial cohesive energy at the precipitate/aluminium interface obtained by DFT (Fig. 1(b)). A strong correlation was observed between the measured hydrogen concentration and the actual crack propagation path, facilitating a connection between nano-level damage and macroscopic fracture behaviour.

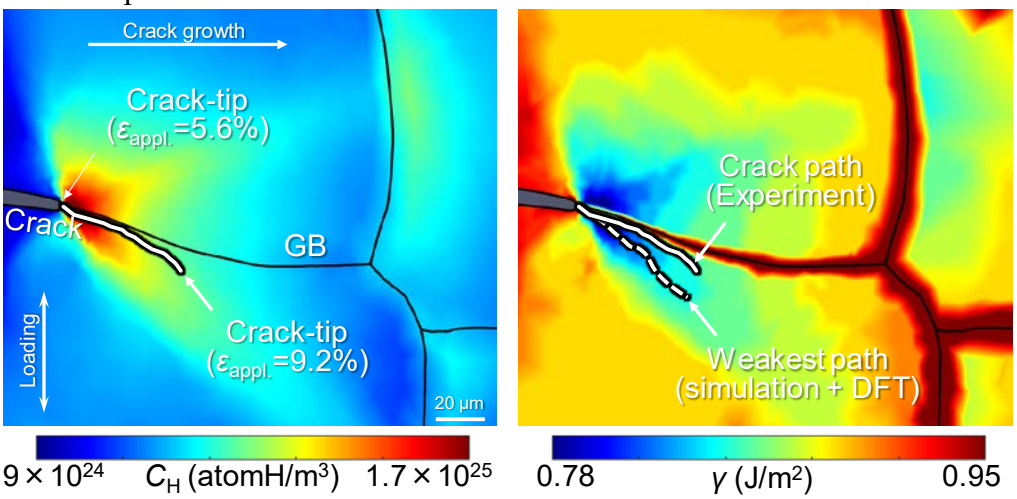

(a) Local hydrogen concentration map (b) Interfacial cohesive energy map

Fig. 1. 3D distributions of hydrogen concentration and interfacial cohesive energy.

4. Acknowledgements

This work was funded by JST Core Research for Evolutional Science and Technology (CREST) "Elucidation of nanoscale dynamic behaviour and mechanical property mechanisms for the creation of innovative mechanically functional materials".

5. References

[1] T. Tsuru, K. Shimizu, M. Yamaguchi, M. Itakura, K. Ebihara, A. Bendo, K. Matsuda and H. Toda (2020). Hydrogen-accelerated spontaneous microcracking in high-strength aluminium alloys, *Sci. Rep.*, **10**, 101998.

[2] Y. Wang, B. Sharma, Y. Xu, K. Shimizu, H. Fujihara, K. Hirayama, A. Takeuchi, M. Uesugi, G. Cheng, H. Toda (2022). Switching nanoprecipitates to resist hydrogen embrittlement in high-strength aluminum alloys, *Nat. Commun.*, **13**, 6860.

[3] H. Su, H. Toda, K. Shimizu, K. Uesugi, A. Takeuchi, Y. Watanabe. (2019). Assessment of hydrogen embrittlement via image-based techniques in Al-Zn-Mg-Cu aluminum alloys, *Acta Mater.*, **176**, 96 - 108.

[4] H. Toda, C. Koga, K. Hirayama, A. Takeuchi, M. Uesugi, K. Ishikawa, T. Yokoyama, H. Fujihara (2024). Multimodal assessment of mechanically induced transformation and damage in TRIP steels using X-ray nanotomography and pencil-beam diffraction tomography, *Acta Mater.*, **281**, 120412

CHARACTERIZATION OF INTERNAL DEFORMATION AND DAMAGE EVOLUTION IN MATERIALS UNDER EXTREME ENVIRONMENT BY USING X-RAY CT

Long Wang[1], Chuantao Hou[1], Ruisi Xing[1], Junbai Song[1], Wugang Liu[1], Yueping Zhang[1], Qiaoyu Liu[1] ,Fang Ren[1]and Shengchuan Wu[2]

[1] Science and Technology on Reliability and Environmental Engineering Laboratory, Beijing Institute of Structure and Environment Engineering, Beijing 100076, China

[2] State Key Laboratory of Rail Transit Vehicle System, Southwest Jiaotong University, Chengdu, 610031, China

1. Introduction

Understanding the internal deformation and damage evolution of materials is of crucial significance for the improvement of material processing, the optimization of structural design, the strength assessment and life prediction. With the increasing demand for materials to withstand extreme environments, such as ceramic composites [1-3] for the applications under extreme high temperature, aluminum alloy welded structure [4] used in extremely low temperature environment, solid propellants [5-7] used under high dynamic mechanical loads; the need for advanced characterization techniques becomes more prominent. X-ray CT, a non-destructive imaging method, has emerged as a powerful tool. It enables the visualization and quantification of the internal microstructure and the associated changes during deformation and damage processes. The internal deformation field could be measured by using the CT images captured before and after the deformation by using the Digital Volume Correlation (DVC) method [8-9]. The more accurate geometric models extracted from the CT images will also realize the assessment by using the Image-based Finite Element Method (IB-FEM) [5]. Thus this paper presents the advances and the applications of the above technologies involving the characterization of internal deformation and damage evolution in materials under extreme environment by using X-ray CT at the laboratory.

2. Materials and methods

A series of in-situ loading devices for X-ray CT have been developed at the laboratory in the past decade. They enable the mechanical loading (uniaxial tension and compression as well as fatigue loadings) being applied on the samples under extreme low (RT~-200℃) or extreme high (RT~ above 1200℃) temperatures with different gas atmospheres. The mechanical tests with in-situ observations by using X-ray CT are then carried out on C/SiC composite at extreme high temperature, on aluminum alloy welded sample at extreme low temperature, on Nitrate Ester Plasticized Polyether (NEPE) solid propellant with high-speed mechanical loading, with the above developed in-situ loading devices. The different microstructures and damages in the bulk of specimen are identified and segmented by using both the traditional methods based on threshold segmentation and the newly development recognition methods based on deep learning. A DVC software based on the layer-wise reliability-guided displacement tracking （LW-RGDT） strategy has also been developed at the laboratory for the internal deformation measurement. The FE model is established based on the quantitative statistical data from the CT images.

3. Results and conclusions

The representative results [1-9] for the development of in-situ loading devices for X-ray CT, the internal deformation and damage evolution in materials are shown in Fig. 1. The relationship between the microstructures, the damages and the internal mechanical field are thus established and will help understand the damage mechanisms in materials.

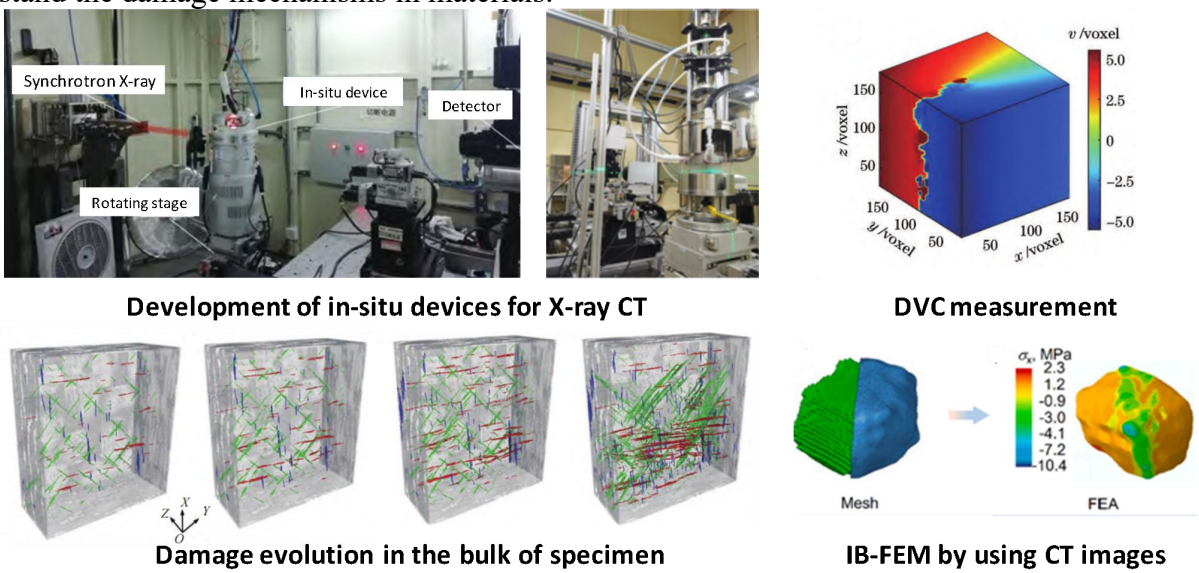

Fig. 1. Representative results for internal deformation and damage evolution in materials

4. Acknowledgements

The research presented in this paper has received funding from the National Natural Science Foundation of China (52202082). This work was carried out with the support of beamline 13HB and 16U2, Shanghai Synchrotron Radiation Facility (SSRF), China.

5. References

[1] L. Wang, W. Zhang, H. Li, et al (2020). 3D in-situ characterizations of damage evolution in C/SiC composite under monotonic tensile loading by using X-ray Computed Tomography. *Applied Composite Materials*, 27(3):119-130.

[2] L. Wang, K. Yuan, X. Luan, et al (2019). 3D characterizations of pores and damages in C/SiC composites by using X-ray Computed Tomography. *Applied Composite Materials*, 26(2):493-505.

[3] P. Chen, L. Wang, D. Zhang, et al (2024). Deep learning based tensile-shear damage evolution mechanism of quasi-isotropic satin weave C/SiC composites. *Acta Materiae Compositae Sinica*, 41(9): 4852-4862.

[4] Z. Wu, S. Wu, W. He, et al (2023). X-ray tomography of failure behaviors of arc welded AA2219 joints under tensile and cyclic loading. *Materials Characterization* 205, 113311

[5] Y. Liu, W. Qian, L. Wang, et al (2023). In situ X-ray tomography study on internal damage evolution within solid propellants of carrier rockets. *Materials Science and Engineering: A*, 145451.

[6] L. Wang, Y. Liu, S. Wu et al (2023). In-situ X-ray tomography based characterization of propellant damage evolution. *Acta Aeronauticaet Astronautica Sinica*, 44(7): 427022.

[7] R. Xing, L. Wang, F. Zhang, et al (2022). Mechanical behavior and constitutive model of NEPE solid propellant in finite deformation. *Mechanics of Materials* 172, 104383.

[8] L. Wang, Z. Gao, X. Zhang, et al (2024). Ex-situ Measurement of Internal Deformation in Ball Grid Array Package with Digital Volume Correlation. *Transactions of Nanjing University of Aeronautics and Astronautics*, (5): 609-620.

[9] B. Pan, X. Zhang, L. Wang (2024). Study on Gray Level Residual Field Calculation in Digital Volume Correlation. *Acta Optica Sinica*. 44（3）:0310001-1-10.

ANALYSIS OF DAMAGE EVOLUTION IN C/SIC COMPOSITE STRUCTURES WITH HOLE UNDER MONOTONIC TENSILE LOADING

Qiaoyu Liu[1], Long Wang[1], Chuantao Hou[1], Zhiqiang Li[1], Zhouxia Jia[1], Baorui Liu[1], Yao Li[1], Tongzhao Wang[1]

[1]Science and Technology on Reliability and Environmental Engineering Laboratory Beijing Institute of Structure and Environment Engineering, Beijing, China

1. Introduction

Carbon fiber reinforced silicon carbide (C/SiC) composites have attracted extensive attention in various engineering fields due to their excellent properties such as high specific strength, high temperature resistance, and good thermal shock resistance. In particular, the C/SiC composite structure with a central hole is commonly encountered in engineering applications, such as for riveted joint structures, which brings both challenges and research interests in understanding its mechanical behavior.The presence of a central hole significantly alters the stress distribution within the C/SiC composite. It induces stress concentrations around the hole periphery, which can lead to premature failure and affect the overall structural integrity and service life[1-4]. Understanding the damage evolution in the bulk the C/SiC composite structure with a central hole is crucial for optimizing the design and performance. Thus,the monotonic tensile loading with Synchrotron Radiation Computed Tomography (SR-CT) in-situ observations has been applied on the C/SiC composite structure with a central hole in order to reveal in the internal damage evolution in this paper, and the analysis were then performed by using the deep learning-based semantic segmentation algorithms, Digital Volume Correlation (DVC) and image-based finite element methods.

2. Specimen and methods

The C/SiC composite structures studied in this paper is produced by the Chemical Vapor Infiltration (CVI) process and designs. A dog-bone shaped specimenwith a central hole (Radius=1mm) is extracted from a (0°/90°) layered C/SiC composite material plate with a thickness of 4mm. The in-situ SR-CT test was carried out at the beamline 13HB of Shanghai Synchrotron Radiation Facility (SSRF) with a image resolution of 6.5 μm/voxel, and the monotonic tensile loading was applied by using Deben CT 5KN in-situ loading equipment.

3. Results and conclusions

Results of the damage identification by using deep learning method, image-based finite element methods and DVC measurement are shown in Fig.1. Machine learning is also used to analyze the distribution of the material's initial pores, which is similar to that of the damages, this phenomena indicates that damages are related to the stress concentrations caused by both the initial pores and the central hole. Image-based finite element methods and DVC measurement indicate significant stress and strain concentration in some region, where the damages occur under higher tensile stress.

This study demonstrates that X-ray CT in-situ tensile testing can track the propagation of damage, enabling qualitative analysis of the damage. The application of deep learning technology effectively identifies and extracts damage. Additionally, by combining DVC and image-based finite element techniques, insights into the initiation and evolution of internal damage within the material can be provided. The damage initiation in the(0°/90°) layered C/SiC specimens with a central circular hole is related to the stress concentrations caused by both the initial pores and the central hole.

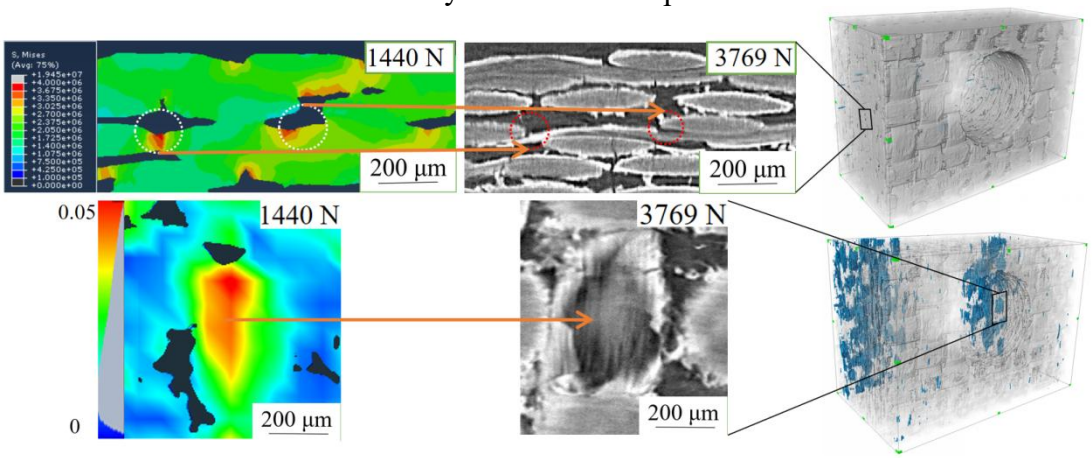

Fig. 1.Results of the damageidentification by using deep learning method, image-based finite element methods and DVC measurement

4. Acknowledgements

The research presented in this paper has received funding from the National Natural Science Foundation of China (52202082).This work was carried out with the support of beamline 13HB, Shanghai Synchrotron Radiation Facility (SSRF), China.

5. References

[1] Chen Y , Shi Y , Chateau C ,et al.In situ X-ray tomography characterisation of 3D deformation of C/C-SiC composites loaded under tension[J].Composites, Part A. Applied science and manufacturing, 2021(145-):145.

[2] Wang L , Zhang W , Li H ,et al.3D In-Situ Characterizations of Damage Evolution in C/SiC Composite under Monotonic Tensile Loading by Using X-Ray Computed Tomography[J].Applied Composite Materials, 2020, 27(1):1-12.

[3] L. Turpin, S. Roux, O. Caty, A. King, S. Denneulin, E. ´ Martin, In situ tomographic study of a 3D-woven SiC/SiC composite part subjected to severe thermomechanical loads, J. Synchrotron Radiat. 29 (Pt 2) (2022 Mar 1) 522–531.

[4] D. Zhang, Y. Liu, H. Liu, Y. Feng, H. Guo, Z. Hong, Characterisation of damage evolution in plain weave SiC/SiC composites using in situ X-ray micro-computed tomography, Compos. Struct. 275 (8) (2021) 114447.

VOID NUCLEATION AND GROWTH BEHAVIOR OF TIG WELDED AA2219 DEFORMED AT CRYOGENIC TEMPERATURES

Y.N. Hu[1], S.C. Wu[2], Z.Y. Wang[1], Y.L. Xue[3], Y.N. Fu[3], G.Z. Kang[1] and P.J. Withers[4]

[1] Applied Mechanics and Structure Safety Key Laboratory of Sichuan Province, School of Mechanics and Aerospace Engineering, Southwest Jiaotong University, Chengdu 611756, China
[2] State Key Laboratory of Rail Transit Vehicle System, Southwest Jiaotong University, Chengdu 610031, China
[3] Henry Royce Institute, Department of Materials, The University of Manchester, Manchester M13 9PL, UK
[4] Shanghai Synchrotron Radiation Facility, Shanghai Advanced Research Institute, Chinese Academy of Sciences, Shanghai 201204, China

1. Introduction

With the renewed interest in manned spaceflights, lunar landings, deep space exploration and national space stations, there is a big driver for reducing the weight and hence increasing the payload capacity of launch vehicles. In this regard the propellant tank is a critical component which contributes a significant portion to the overall weight. Furthermore, cryogenic liquid propellants including liquid hydrogen and liquid oxygen show great potential for longer-range and higher-payload missions, as compared to conventional propellants [1], because of their relatively high specific energy content. In addition, there is increasing focus on hydrogen for transportation, particularly to power the clean aircraft of the future. However, storing these cryogenic liquid hydrogen/oxygen propellants can pose a significant challenge in terms of material selection, manufacturing technology and cryogenic performance in order to guarantee reliable service under such low temperature environments.

Previous investigations on Al and Al welded joints under cryogenic conditions have focused mainly on the measurement of mechanical properties rather than the evolution of damage [2]. Furthermore, where damage accumulation studies have been done they have been limited to two-dimensional (2D) *in situ* scanning electron microscopy (SEM) or electron back scatter diffraction (EBSD) characterization [3]. Over the last two decades, *in situ* X-ray computed micro-tomography (μCT), and synchrotron X-ray μCT (SR-μCT) in particular, has emerged as an excellent means of tracking the sequence of damage accumulation events in three-dimensions (3D) over time (often termed 4D imaging or time-lapse imaging) [4]. Such experiments have shed much light on the ductile rupture process of void nucleation, growth, and coalescence of Al alloys [5]. However, damage evolution studies made by in situ SR-μCT have primarily focused on room and high-temperature environments [6]. Few publications have explored damage evolution at low temperatures, especially at 77 K or below [7].

The aim of this paper is to develop a picture of the damage accumulation during deformation at room and cryogenic temperatures in AA2219 TIG welded joints typical of cryogenic propellant tanks. To this end we have developed a dedicated in situ tensile testing machine that can be mounted on a SR-μCT beamline to study 3D damage evolution at low temperatures (down to 83 K). This has

enabled us to follow the internal damage accumulation process from void nucleation through growth to coalescence and failure as a function of temperature. The observed rate of damage evolution is then analyzed using an Eshelby approach to establish void nucleation and growth models along lines similar to those of the GTN model.

2. Materials and methods

The base metal (BM) comprised 8-mm thick 2219 Al alloy rolled plates having the following primary alloying constituents; 5.6-6.8 wt. % Cu, 0.2-0.4 wt. % Mn, and 0.10-0.25 wt. % Zr. A T87 heat-treatment process consisting of solution heat treatment, cold working and artificial aging was adopted. The AA2219-T87 rolled plates were butt-welded using ER2325 Al-Cu-Mn filler wire (1.6-mm diameter) containing 6.0-6.8 wt. % Cu and 0.2-0.4 wt. % Mn. A two-layer welding strategy was followed comprising direct current TIG helium-arc (DCTIG-He) welding without filler wire as the first layer (backing weld), and pulse variable polarity TIG argon-arc (VPTIG-Ar) welding with ER2325 filler wire as the second layer (capping weld).

A 1 kN load capacity tensile rig incorporating an environmental chamber allowing temperatures in the range from 573 K to 83 K was specially designed to be mounted on the 13 HB beam line (BL13HB) at the Shanghai Synchrotron Radiation Facility (SSRF), China, as shown in Fig. 1. The damage accumulation events from void nucleation through growth to coalescence and failure at 293 K and 123 K were observed in a time-lapse manner by in situ X-ray microtomography, where the load was held constant during each CT scan. The cross-head speed was 0.5 mm/min. Post-mortem fractography analysis was undertaken on a JSM-7800F SEM to identify the fracture mode.

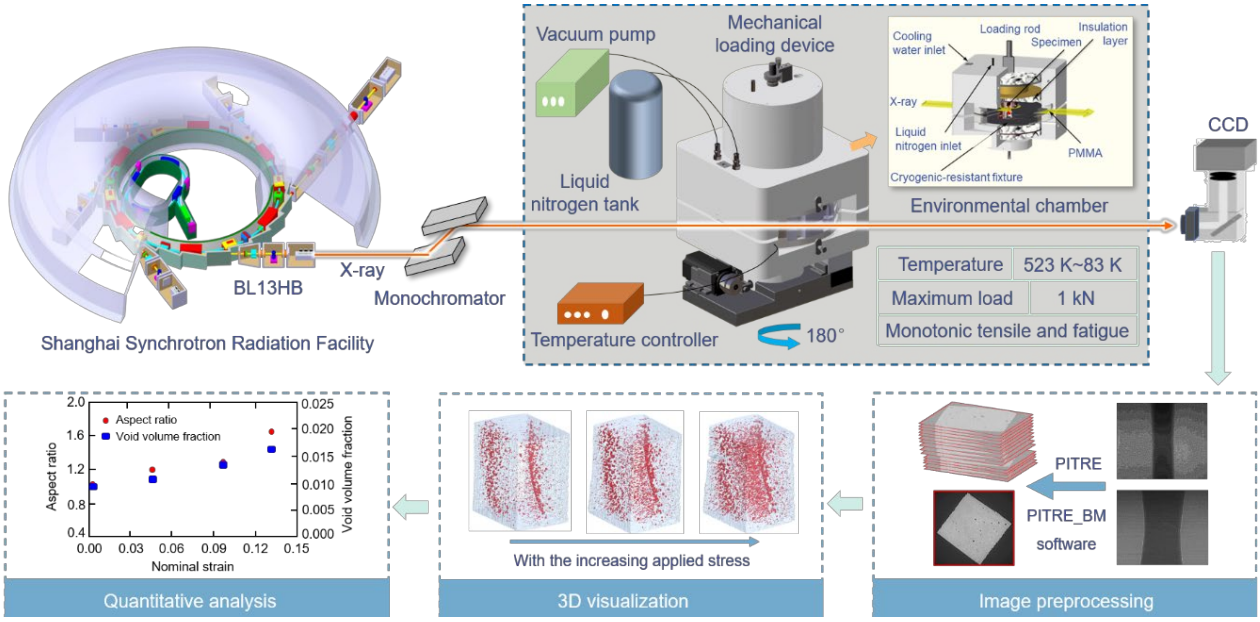

Fig. 1. A schematic of the void characterization workflow. An *in situ* tensile rig having an environmental chamber with an operating temperature range from 573 K to 83 K has been specially designed to be mounted on the BL13HB at the SSRF, to explore the impact of temperature on the internal damage evolution of capping welds through time-lapse in situ X-ray microtomography conducted during tensile straining at varying temperatures.

A 30 keV monochromatic X-ray beam was used for SR-μCT and the projections were recorded using a 2048 × 2048 pixel^2 Hamamastu Flash 4.0 sCMOS detector, coupled to a 2 × magnifying lens giving an effective pixel size of 3.25 μm. Each tomographic dataset comprised 720 projections recorded at angular increments of 0.25° over 180° using an exposure time of 30 ms such that each scan was collected in ~8 min. The 720 projections were subsequently reconstructed to obtain approximately 1080 slices by PITRE software. Graphical and quantitative post-processing of the CT images were carried out using the commercial software Avizo. Here the interactive thresholding technique (intensity range of 130~255) was employed for void segmentation within the matrix. The same segment threshold was adopted for all the loading stages during the *in situ* X-ray tomography experiment.

3. Results and conclusions

The results indicate that inherent manufacturing defects are mainly concentrated near the melt-pool boundary of the VPTIG-Ar capping weld. These defects can be divided into large near-spherical metallurgical gas pores and small elongated inter-dendritic shrinkage cavities. The capping weld is much softer than the base metal and, therefore, a location of strain concentration during tensile deformation. The strength and work hardening rate of the capping weld increases significantly from 293 K to 77 K.

An *in situ* tensile test rig, incorporating an environmental chamber with a temperature range down to 83 K, has been designed to be mounted on the X-ray tomography beamline. The nucleation, growth, coalescence, and rotation of voids in the capping weld has been tracked through time-lapse X-ray tomography during tensile straining. With increasing strain, numerous, closely spaced micro-voids nucleate by particle fracture and particle/matrix interface decohesion related to α-Al + θ (Al_2Cu) eutectic and θ (Al_2Cu) phases. Once nucleated, the voids together with the pre-existing welding defects grow predominantly extensionally, with the spherical defects growing faster than the pancake shaped inter-dendritic ones.

In terms of void nucleation by interface decohesion, the evolution of the probability density function for void nucleation as a function of the stress was calculated using the Eshelby approach. The threshold stresses for void nucleation at low temperatures are much higher due to the increasing matrix strength as a result of the higher work hardening rate, especially at 77 K, so that higher applied stresses are required to induce interface decohesion under cryogenic environments. The growth rate of the nucleated voids and as-manufactured defects was predicted using a framework similar to that of the Gurson-Tvergaard-Needleman model. This suggests that the pre-existing defects grow faster, but that the nucleated voids are so numerous, and their spacing so fine, that they play a very significant role in failure fracture.

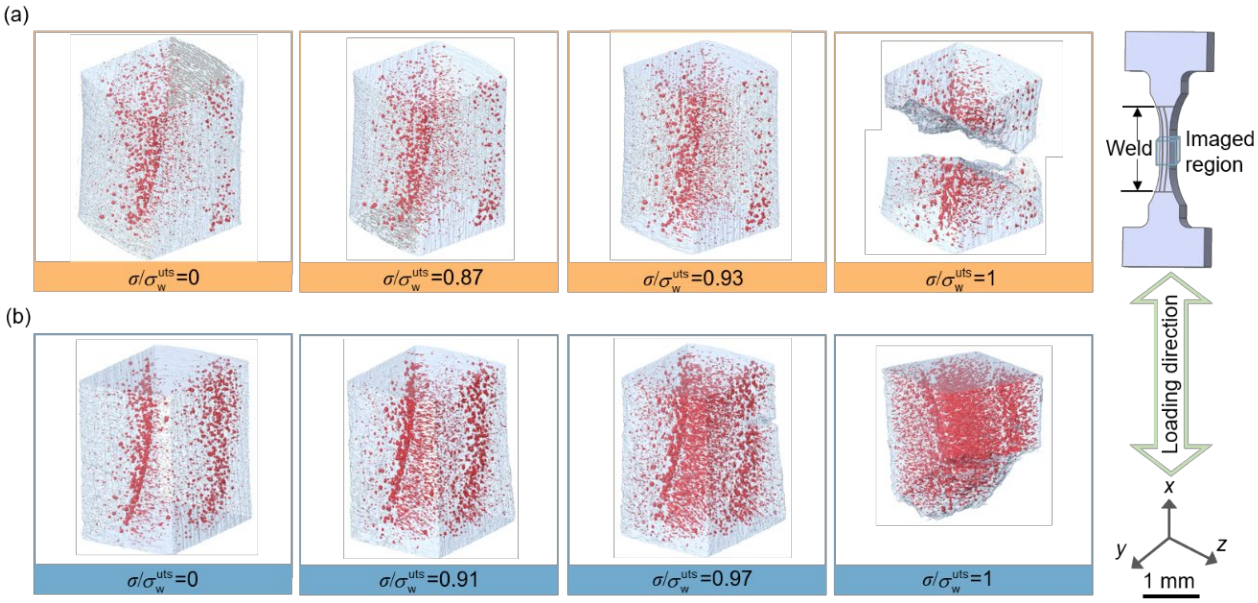

Fig. 2. 3D SR-μCT volume renderings of the central gauge segment of the in situ sub-scale welded joint test-pieces at different loading stages, deformed at (a) 293 K and (b) 123 K. Welding defects and newly nucleated voids larger than 8 cubic voxels are rendered red. The location of the region of interest relative to the weld and the test-piece is shown inset.

4. Acknowledgements

The research presented in this paper has received funding from the National Natural Science Foundation of China (12202369), and China Postdoctoral Science Foundation (2022TQ0263).

5. References

[1] N. Liu, B. Ma, F. Liu, W.X. Huang, B.S. Xu, L.J. Qu, Y.Z. Yang, Progress in research on composite cryogenic propellant tank for large aerospace vehicles, Composites Part A, 143 (2021) 106297.

[2] T. Yuri, T. Ogata, M. Saito, Y. Hirayama, Effect of welding structure on high-cycle and low-cycle fatigue properties for MIG welded A5083 aluminum alloys at cryogenic temperatures, Cryogenics, 41 (2001) 475–483.

[3] H. Gholipour, F.R. Biglari, K. Nikbin, Experimental and numerical investigation of ductile fracture using GTN damage model on in-situ tensile tests, International Journal of Mechanical Sciences, 164 (2019) 105170.

[4] S.C. Wu, T.Q. Xiao, P.J. Withers, The imaging of failure in structural materials by synchrotron radiation X-ray microtomography, Engineering Fracture Mechanics, 182 (2017) 127–156.

[5] C.S. Kaira, T.J. Stannard, V.D. Andrade, F.D. Carlo, N. Chawla, Exploring novel deformation mechanisms in aluminum–copper alloys using in situ 4D nanomechanical testing, Acta Materialia, 176 (2019) 242–249.

[6] J.G. Bao, S.C. Wu, P.J. Withers, Z.K. Wu, F. Li, Y.N. Fu, W. Sun, Defect evolution during high temperature tension-tension fatigue of SLM AlSi10Mg alloy by synchrotron tomography, Materials Science & Engineering A, 792 (2020) 139809.

[7] S.N. Li, P.J. Withers, S. Kabra, K. Yan, The behaviour and deformation mechanisms for 316L stainless steel deformed at cryogenic temperatures, Materials Science and Engineering: A, 880 (2023) 145279.

CARBON STEEL S38C AXLE RESIDUAL STRESS NEUTRON TESTING AND LIFE PREDICTION

Tianyu Qin[1], Feifei Hu[1], S. Yuhua Su[2], Pingguang Xu[3], Shengchuan Wu[1]
[1] State Key Laboratory of Rail Transit Vehicle System, Southwest Jiaotong University, Chengdu, China
[2] J-PARC center, Japan Atomic Energy Agency, Ibaraki, Japan
[3] Materials Sciences Research Center, Japan Atomic Energy Agency, Ibaraki, Japan

1. Introduction

In recent years, the operating speed of high-speed trains has steadily increased, extending their geographical coverage and subjecting them to increasingly harsh service conditions. This has placed higher demands on the reliability of key train components. The axle, as a critical load-bearing element, endures complex fatigue loads from both the wheel-rail interaction and the car body, and its structural integrity directly impacts the operational safety of the train. Consequently, surface strengthening technology has become widely adopted to enhance the structural strength and fatigue resistance of railway axles. One of the most successful applications of surface strengthening in high-speed railway axles is the carbon steel S38C axle, initially developed for the Japanese Shinkansen. Following induction hardening, the S38C axle develops a gradient structure with deep compressive residual stresses, significantly improving its wear resistance and fatigue performance. However, this also introduces challenges in accurately assessing the structural integrity of the strengthened axle. In this study, the advanced design concept of damage tolerance is applied to evaluate the structural integrity of S38C axles, considering the service environment and loading conditions of high-speed trains. Neutron scattering is employed to reveal residual stress distributions. Additionally, time-domain loads from train service are incorporated into the residual life assessment, thereby reducing uncertainties in the fatigue performance evaluation. A novel assessment method is proposed for reinforced axles, factoring in residual stress evolution and variable amplitude loading. These findings provide valuable insights for developing appropriate inspection cycles and extending the service life of surface-strengthened axles.

2. Materials and methods

The material used is from a real medium carbon steel S38C hollow axle, which has traveled about 3 million kilometers on the China railway network. After non-destructive testing, no surface damage or cracks were found on the axle body. The S38C axles are now used in Japanese Shinkansen trains and Chinese Harmony high-speed trains. The chemical compositions of the axle steel are listed in Table 1.

Table 1. The chemical compositions of S38C medium carbon steel for railway axles.

Element	C	Si	Cr	Mn	Mo	P	Al	S	Ni	Fe
wt.%	0.39	0.28	0.075	0.78	0.02	0.015	0.02	0.008	0.0072	Bal.

3. Results and conclusions

As shown in Fig. 1. Under the influence of residual stress, the crack propagation threshold size of the axle increases from 1.75 mm to 3 mm. However, once the crack depth exceeds 3 mm, the crack growth rate rapidly increases with the evolution of the residual stress state, significantly shortening the remaining life. The remaining life for a crack to propagate from 3 mm to 16 mm in depth decreases sharply from 624,800 km under a residual stress-free condition to 24,700 km, equivalent to less than 23 days of service. When the crack size is less than 2 mm, compressive residual stress at the crack tip still exists, preventing crack growth and failure. Notably, when the crack depth is 1 mm, there is still a considerable safety margin, and under economic considerations, the threshold for discard size can be appropriately relaxed.

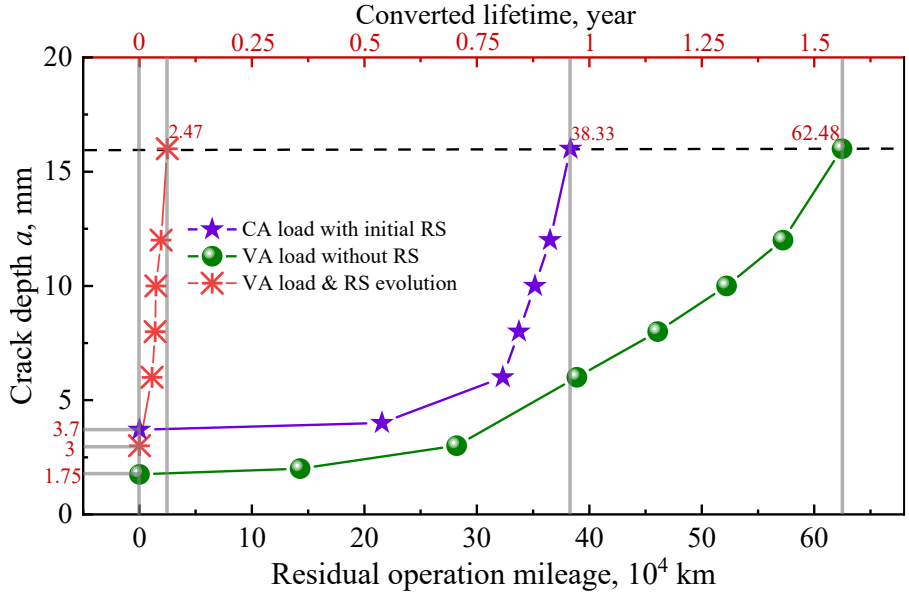

Fig. 1. The residual mileage and lifetime of S38C axles

4. Acknowledgements

The authors would like to express sincere thanks for the support from the National Natural Science Foundation of China (No. 52475167), National Key Research and Development Program of China (No. 2023YFA1609200). This work was performed under the Shared User Program of the JAEA Facility (JRR-3 No. 2022A-A07), with instrumental support from Dr. Satoshi Morooka at JAEA.

5. References

[1] Qin TY, Hu FF, Xu PG, et al. Gradient residual stress and fatigue life prediction of induction hardened carbon steel S38C axles: Experiment and simulation[J]. International Journal of Fatigue, 2024, 185: 108336.

[2] Hu FF, Qin TY, Ao N, et al. Gradient residual strain determination of surface impacted railway S38C axles by neutron Bragg-edge transmission imaging[J]. Engineering Fracture Mechanics, 2024, 306: 110267.

THE DIFFRACTION ELASTIC CONSTANTS OF RAILWAY WHEEL STEEL OF HIGH-SPEED TRAIN

X.X. Zhang
Institute of High Energy Physics, Chinese Academy of Sciences, Beijing 100049, People's Republic of China

1. Introduction

High-speed trains are a vital component of modern transportation systems. One critical aspect of their operation is the safety of the wheels. Residual stresses in railway wheels can lead to detrimental effects, such as promoting crack formation during service and reducing fatigue life. Consequently, it is essential to accurately determine the residual stresses in the wheels of high-speed trains.

The accurate determination of these residual stresses relies on the diffraction elastic constants (DEC), which are necessary for calculating residual stresses from the residual strains measured through diffraction techniques [1]. The DEC parameters depend on the chemical composition and microstructure. Assuming that strain measurements are accurate, any errors in the DEC directly influence the final calculated stress values. Therefore, precise measurements of the DEC are crucial, and the DEC values reported for different steel materials in the literature should be regarded as references only.

ER8 steel is a material actively used in high-speed trains, but its DEC values remain unknown [2]. ER8 steel predominantly consists of pearlite and ferrite, with the pearlite structure further composed of alternating layers of ferrite and cementite, the ferrite phase being the most prevalent. Thus, measuring the DEC of the ferrite phase is essential.

In this study, in-situ tensile experiments utilizing high-energy synchrotron radiation X-ray diffraction were conducted to measure the DEC for high-speed train wheel steel. This method minimizes uncertainties and errors associated with material performance parameters, establishing a robust foundation for the precise characterization of residual stress in the wheels of high-speed trains.

2. Materials and methods

The tensile specimen was cut from a new ER8 wheel for high-speed train using an electrical discharge machining method. It measures 50 mm in length and 1 mm in thickness, with the parallel section being 15 mm long and 4 mm wide. The specimen was subjected to tensile deformation using a tensile rig mounted on the sample table of the beamline.

The synchrotron X-ray diffraction experiments were conducted at the High Energy Materials Science (HEMS) beamline P07B of the Helmholtz-Zentrum Hereon at PETRA III, DESY. The X-ray energy at the P07B beamline is 87.01 keV, featuring a PerkinElmer XRD 1622 detector with a pixel resolution of 2048 × 2048, where each pixel measures 200 μm × 200 μm. High-energy X-rays penetrate the tensile samples, and the resulting diffraction patterns are collected using the

PerkinElmer detector. These diffraction patterns are analyzed along both the longitudinal direction and the transverse direction to calculate the lattice strain in each direction.

3. Results and conclusions

The results obtained for the *hkl*-dependent diffraction elastic parameters E_{hkl} and ν_{hkl} for the ferrite phase are presented in Fig. 1. The findings indicate that:

(1) The elastic modulus E_{222} for the 222 plane is the highest, while Poisson's ratio ν_{222} is the lowest. Conversely, the elastic modulus E_{200} for the 200 plane is the lowest, while the Poisson's ratio ν_{200} is the highest. The elastic moduli E_{hkl} and Poisson's ratios ν_{hkl} for the 110, 211, 220, and 321 planes are relatively similar.

(2) The parameters E_{hkl} and ν_{hkl} vary with depth. The elastic moduli E_{hkl} at depths of 1 mm and 2 mm from the tread surface are relatively high, following a decreasing trend with increasing depth. The measured Poisson's ratios ν_{hkl} for the 110, 211, 220, 310, and 321 planes are the highest at a depth of 15 mm.

These measurements differ from previously reported values. For instance, Dutta et al. [3] measured the diffraction elastic modulus of S690QL1 ferritic steel using in situ tensile experiments with synchrotron radiation X-ray diffraction. At room temperature, the values for E_{110}, E_{200}, E_{211}, and E_{220} were 213.3±0.6, 169.3±0.6, 221.5±0.6, and 218.2±0.6 GPa, respectively, while the values for ν_{110}, ν_{200}, ν_{211}, and ν_{220} were 0.244±0.003, 0.295±0.003, 0.227±0.003, and 0.239±0.003, respectively. Collins et al. [4] investigated the lattice stress of DX54 ferritic steel, where the elastic moduli E_{110}, E_{200}, and E_{211} for the 110, 200, and 211 planes were reported as 223, 134, and 223 GPa, respectively. Kumagai et al. [5] studied the residual stress in ferritic steel, where the elastic moduli for ferrite 110, 200, and 211 were reported as E_{110}, E_{200}, and E_{211} being 223.5, 169.3, and 223.5 GPa, respectively, with corresponding values of ν_{110}, ν_{200}, and ν_{211} being 0.273, 0.328, and 0.273.

It is clear that the reported diffraction elastic moduli for ferritic steels either reference older literature or are based on materials that do not correspond to the grade of high-speed train wheel materials, leading to inconsistencies among the reported parameters. This study provides accurate values for the *hkl*-dependent diffraction elastic parameters E_{hkl} and ν_{hkl} for the ferrite phase of the ER8 steel.

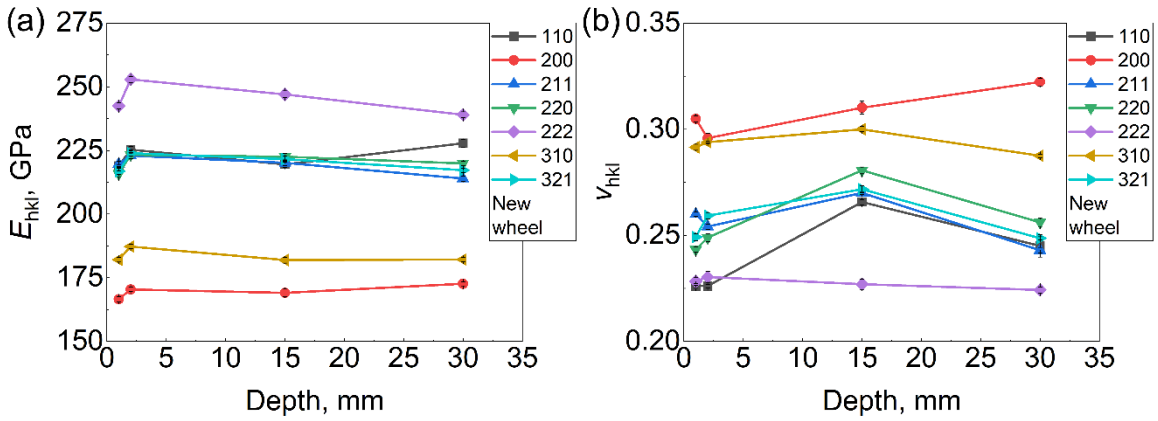

Fig. 1. Measurement results and measurement errors of the diffraction elastic modulus parameters (a) E_{hkl} and (b) ν_{hkl} at different depths from the tread surface. The measurement error bars are very small and are largely obscured by the data point markers.

4. Acknowledgements

I would like to acknowledge the support of the National Key R&D Program of China No. 2023YFA1609202.

5. References

[1] X.L. Liu, V. Luzin, H.L. Qin, Z.N. Bi, M.J. Li, Y.T. Liu, K. Sun, D.F. Chen, Mapping of three-dimensional residual stresses by neutron diffraction in nickel-based superalloy discs prepared under different quenching conditions, Mater. Today Commun. 32 (2022) 103876.

[2] G.-Z. Zhang, C.-P. Liu, R.-M. Ren, S. Wu, H.-X. Yin, T. Cong, X. Li, Effect of nonuniform microstructure on wear property of ER8 wheel steel, Wear 458 (2020).

[3] R.K. Dutta, R.M. Huizenga, M. Amirthalingam, A. King, H. Gao, M.J.M. Hermans, I.M. Richardson, In situ synchrotron diffraction studies on the temperature-dependent plane-specific elastic constants in a high-strength quenched and tempered structural steel, Scr. Mater. 69 (2013) 187-190.

[4] D.M. Collins, M. Mostafavi, R.I. Todd, T. Connolley, A.J. Wilkinson, A synchrotron X-ray diffraction study of in situ biaxial deformation, Acta Mater. 90 (2015) 46-58.

[5] M. Kumagai, S. Sato, S. Suzuki, M. Imafuku, H. Tashiro, S. Ohya, Residual Stress Analysis of Cold-drawn Pear lite Steel Wire Using White Synchrotron Radiation, ISIJ Int. 55 (2015) 1489-1495.

CHARACTERIZATION OF RESIDUAL STRESS FIELDS IN METALLIC MATERIALS: A COMBINED NEUTRON BRAGG EDGE IMAGING AND DIFFRACTION ANALYSIS

Y. Su[1], T. Shinohara[1], J.D. Parker[2], K. Oikawa[1], T. Kai[1], W. Gong[1], S. Harjo[1], K. Aizawa[1] and Y. Kiyanagi[3]

[1] J-PARC Center, Japan Atomic Energy Agency, Tokai, Ibaraki 319-1195, Japan
[2] Neutron Science and Technology Center, CROSS, Tokai, Ibaraki 319-1106, Japan
[3] Faculty of Engineering, Hokkaido University, Sapporo, Hokkaido 060-8628, Japan

1. Introduction

Fatigue damage poses a serious threat to the structural integrity of large-scale engineering components, making the analysis of fatigue crack growth essential for ensuring safety and reliability. The nonlinear distribution of strain and stress at crack tips plays a critical role in crack propagation, closure, and fracture, emphasizing the importance of understanding residual strain, stress, and microstructural evolution in the vicinity fatigue cracks. Accurate characterization of crack tip stress fields is crucial for interpreting experimental results, predicting failures, and optimizing engineering designs. Various techniques have been employed to study residual stress during fatigue crack propagation. Among these, the Finite Element Method, synchrotron X-ray diffraction, and neutron diffraction are commonly used. The emerging neutron Bragg edge imaging technique complements these methods by enabling two-dimensional (2D) strain mapping across thick specimens and larger areas, facilitating non-destructive bulk analysis [1, 2]. This study utilizes neutron Bragg edge imaging and neutron diffraction to characterize residual stress fields in steel materials. Bragg edge imaging provides through-thickness lattice strain maps, while neutron diffraction delivers detailed three-dimensional stress characterizations. The ultimate goal is to establish a non-destructive approach for monitoring internal stress-field evolution during fatigue loading under various conditions. This advancement enhances the understanding of crack propagation mechanisms in engineering materials and informs predictive models for the effects of variable amplitude loads on fatigue crack growth.

2. Materials and methods

The material used in this study is commercial SUS304, a typical austenitic stainless steel. Compact tension specimens, measuring 80 mm in width, 83.3 mm in length, and 6 mm in thickness, were prepared in accordance with ASTM E647-99. Fatigue tests on the compact tension specimens were conducted using a servo-hydraulic fatigue testing machine. As summarize in Table 1, three specimens (S1, S2, and S3) with different crack lengths were prepared for pulsed neutron experiments. The Bragg edge imaging experiments on the fatigued samples were carried out at BL22 RADEN in MLF/J-PARC [3]. A 2D counting-type detector with an area of 100 × 100 mm^2 and a spatial resolution of approximately 300 μm was used to acquire transmission data through the specimen thickness. The projection data of the atomic number density, lattice parameter, and crystallite size were determined via Bragg-edge spectral analysis using the GUI-RITS software. Time-of-flight neutron diffraction measurements were performed at BL19 TAKUMI in MLF/J-PARC. A neutron beam gauge volume

of $2 \times 2 \times 2$ mm^3 was utilized to scan the diffraction patterns along three orthogonal directions. Lattice parameters were determined by analyzing the diffraction patterns with Z-Rietveld software.

Specimens	Cycles (10^5)	Crack length (mm)	Stress intensity factor range, ΔK (MPa m$^{1/2}$)
SUS304_1 (S1)	2.01	23	30.3
SUS304_2 (S2)	2.9	38	58.7
SUS304_3 (S3)	2.95	Fracture	---

Table 1. Specimens prepared for pulsed neutron experiments

3. Results and conclusions

Figure 1 shows the measured and fitted transmission spectra, along with diffraction patterns, collected at locations approximately 2 mm and 20 mm from the crack tip of specimen S3. Both the Bragg-edge spectra and diffraction patterns confirm the presence of single-phase face-centered cubic (FCC) austenite in the specimen. Variations in the Bragg edge spectrum shapes and diffraction peak intensities between the two locations suggest texture evolution resulting from lattice rotation during plastic deformation near the crack tip. Peak shift and broadening were observed in enlarged views of the 200 diffraction peaks (Fig. 1b). 2D maps of the residual lattice strain and microstructure were obtained by Bragg edge spectral analysis. These results are consistent with neutron diffraction measurements, providing valuable insights into bulk microstructure changes near the crack tip and enhancing the understanding of crack propagation behavior in metallic materials.

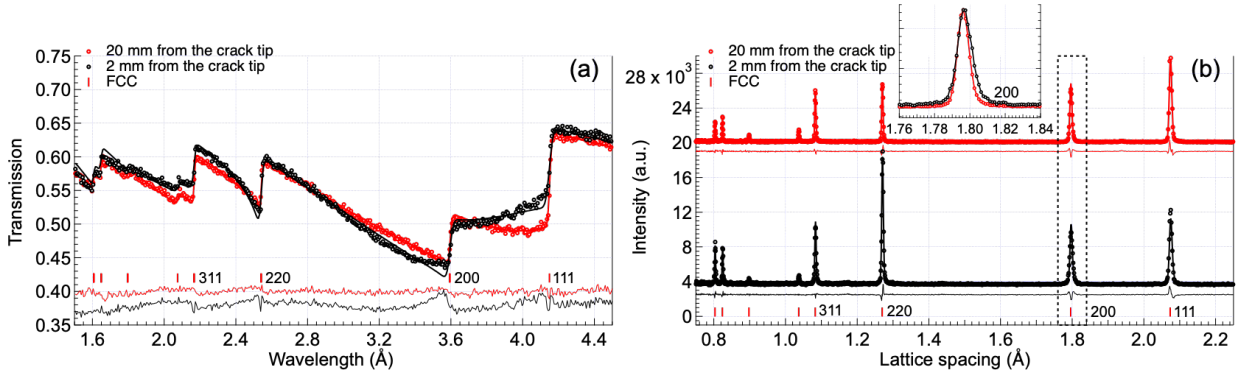

Fig. 1. Representative Bragg edge transmission spectra (a) and neutron diffraction patterns (b) collected at locations 2 mm and 20 mm from the crack tip for each

4. Acknowledgements

The neutron experiments at MLF J-PARC were conducted under proposal Nos. 2020B0236, 2020B0220, and 2022I0022.

5. References

[1] Y. Su, K. Oikawa, T. Shinohara, T. Kai, T. Horino, O. Idohara, Y. Misaka and Y. Tomota (2021). Neutron Bragg-edge transmission imaging for microstructure and residual strain in induction hardened gears. *Sci. Rep.*, **11**, 4155.

[2] Y. Su, K. Oikawa, T. Shinohara, T. Kai, T. Horino, O. Idohara, Y. Misaka and Y. Tomota (2023). Residual stress relaxation by bending fatigue in induction-hardened gear studied by neutron Bragg edge transmission imaging and X-ray diffraction. *Int. J. Fatigue*, **174**, 107729.

[3] T. Shinohara, T. Kai, K. Oikawa, T. Nakatani, M. Segawa, K. Hiroi, Y. Su, M. Ooi, M. Harada, H. Iikura, H. Hayashida, J.D. Parker, Y. Matsumoto, T. Kamiyama, H. Sato and Y. Kiyanagi (2020). The energy-resolved neutron imaging system, RADEN. *Rev. Sci. Instrum.*, **91**, 043302.

The Latest Progress of HEPS and Its Hard X-Ray Imaging Beamline

LI Gang*, ZHANG Weiwei, ZHANG Jie, WANG Yanping, GAO Lidan, SUN Rui, WANG Zhimao, HUANG Mei, DENG Tijian, WANG Lu, JIANG Xiaoming

High Energy Photon Source (HEPS), IHEP, CAS, Beijing, China

The High Energy Photon Source (HEPS), a 6 GeV green-field fourth-generation synchrotron light sources, is building in Beijing, China. Its storage ring is based on a modified hybrid seven-bend achromat (7BA) design, where bending magnets with reverse bending angles and longitudinal gradients are adopted to reach an ultralow natural emittance of 34.2 pm with a circumference of 1360.4 m. Moreover, alternating high- and low-beta sections are specially designed to generate and deliver X-ray synchrotron radiation with high brightness of 5x1022 photons s-1 mm-2 mrad-2 (0.1%bandwidth)-1.

Hard X-ray Imaging (HXI) beamline of HEPS is an almost ideal hard X-ray imaging system with the features that can achieve both the high sensitivity and deep penetration using high energy SRX phase contrast, the high spatial resolution and large FOV using super high pixel number detector.

To meet these contradictory requirements concurrent, we have designed and are constructing the HXI beamline of HEPS with the four considerations:

(1) Three IDs, one IAW, one CPMU, one MW (Mango Wiggler), already have developed in house, and the gap of each ID can be adjusted in a wide range. It allows the four parameters, the source size, the divergence angle, the characteristic energy, and the radiation power, can be adjusted in a large scale to satisfice the diversified requirements. Its energy range is 5 keV to 300 keV in pink mode.

(2) The distance between sample and source (Ds-s) is more than 330m for reducing the PSF of source to sample, expanding the spot size and increasing the spatial coherence length. The PSFs-s is much less than micron meter at 1m Ds-d for IAW/CPMU. The largest FOV is more than 300mm (H) x 100mm (V).

(3) It is the highest priority of HXI beamline design that the high uniformity and high stability of the X-Ray spot. The bending adjustable Laue twin crystal monochromator is designed to provide 40-200keV monochromatic hard X-ray with 100mm x 30mm size and the highest 5x10-4 energy resolution. The well screened set of filters, the scintillation crystals and the gap of IDs are carefully designed to obtain the SRX pink beam with high quality. The collimation CRLs and ultra-far aperture are working together with CPMU to provide high harmonic suppression ratio, high flux stability SRX spot.

(4) A series of SRX imaging detector with high pixel number, high resolution and high MTF have been developed in house. The detector with 6k x 6k pixel number and 0.8 μm resolution already has been developed 3 version and used in many experiments. The detector with 28k x10k pixels number is developing and will be available for testing in 2024. The detector with 30k x30k pixels number is developing too.

HEPS-HXI beamline will serve the large user community, including engineering materials, biomedicine, fossils and human heritage. The Commissioning and Day1 Experiment results will be introduced in details.

The HEPS-HXI beamlines photographs, IAW wiggler light source, the front end area, the FOE and beamline in experiment hall, the beamline in tunnel, the outside view of the experiment hutch, the inner view of the experiment hutch.

The HEPS-HXI beamlines photographs, IAW wiggler light source, the front end area, the FOE and beamline in experiment hall, the beamline in tunnel, the outside view of the experiment hutch, the inner view of the experiment hutch.

*** Contact: Li Gang, E-mail: lig@ihep.ac.cn**

4D microstructural characterization of corrosion fatigue crack initiation in high-strength aluminum ally

Ni Ao, Songquan Tang, and Shengchuan Wu
State Key Laboratory of Rail Transit Vehicle System, Southwest Jiaotong University, PR China

1. Introduction

7XXX aluminum alloys are widely used in aerospace applications due to their high specific strength, and good fatigue resistance. However, plenty of second-phase particles, they were susceptible to localized corrosion, including pitting, stress corrosion cracking and corrosion fatigue [1]. Corrosion fatigue crack initiation is closely related to the complex actions of corrosion damage geometry, localized stress concentration, and microstructures. Especially, the characteristics of the corrosion pits on the surface directly influenced the subsequent crack initiation [2]. Additionally, there is a limited understanding of pit to crack transition mechanism [2]. The spatio-temporal evolution for the crack initiating from pit is still unclear to date due to that most studies used two-dimensional (2D) destructive methods, such as confocal microscopy, optical microscopy, scanning electron microscopy (SEM).

Recently, synchrotron radiation X-ray computed microtomography (SR-μCT) has been emerged as an advanced technique to observe the three-dimensional (3D) microstructures and defects in the interior of opaque materials both in qualitative and quantitative manner [3,4]. In this study, a spatial-temporal characterization of corrosion pit growth and pit to crack transition in 7050 aluminum alloy in a saline environment is provided.

2. Materials and methods

A rolled 7050 aluminum alloy plate (overaging heat treatment) was used in this study. The sample used *in situ* corrosion fatigue testing, as depicted in Fig. 1(a), was machined from the as-received plate. Before in situ corrosion fatigue test, the sample was pre-exposed by immersing in 3.5 wt.% NaCl solution at 60 ℃ for a period of 24 h. The 3D tomography of pre-corrosion fatigue sample as shown in Fig. 1(b) demonstrates that dozens of pits was formed after pre-corrosion. Fig. 1(c) shows a variation of sphericity as a function of equivalent diameter for the pre-corrosion pits on the sample. The sphericity decreases with the decrease of equivalent diameter on the whole. Then an *in situ* corrosion fatigue test was performed based on SSRF.

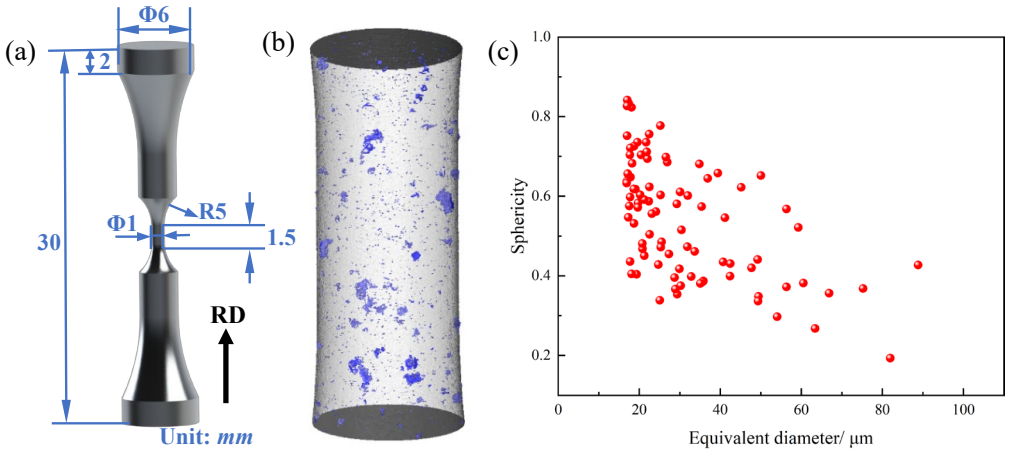

Fig. 1 (a) schematic and dimensions of in situ corrosion fatigue sample; (b) 3D tomography of pre-corrosion fatigue sample obtained from the working section; (c) Variation of sphericity as a function of equivalent diameter for the pre-corrosion pits.

3. Results and conclusions

The corrosion pit growth and pit to crack transition behaviors during corrosion fatigue loading in 7050 aluminum alloy is observed. Three ways for pit growth, including pit merges with original holes, pit merges with adjacent pits, and fall off of second-phase particles, are found. The spatial correlation among corrosion pits, cracks and corrosion products is illustrated (see Fig. 2). Subsequently, the pit to crack transition, crack initiation and growth behaviors are quantitatively studied.

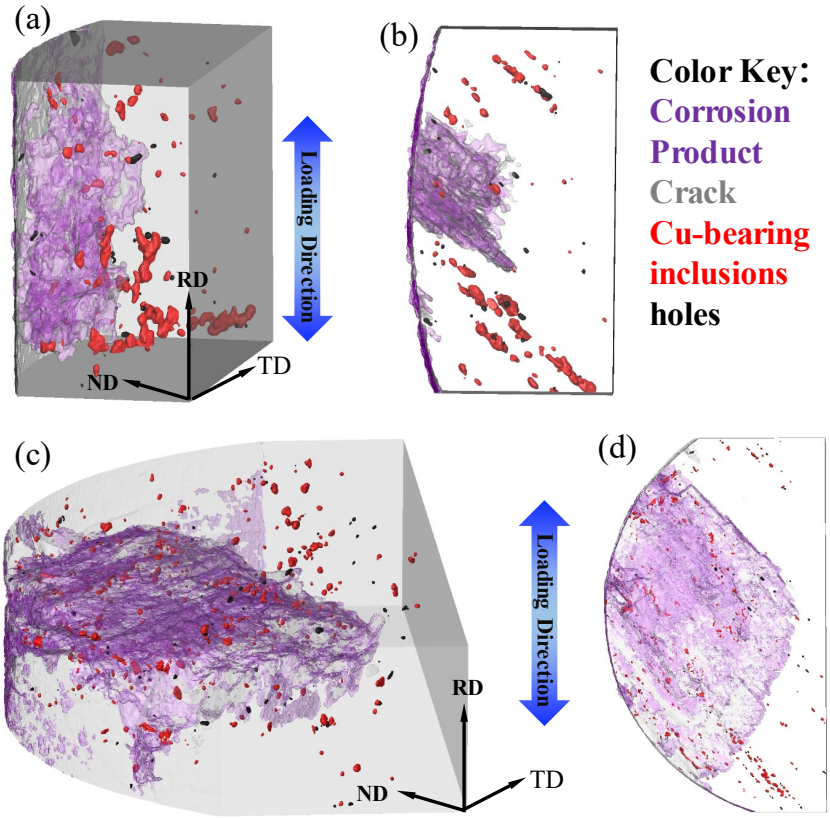

Fig. 2 (a, c) 3D segmented view of different corrosion regions in corrosion-fatigue fractured 7050 aluminum alloy; (b, d) 2D view of corrosion regions responding to (a) and (c) respectively.

4. Acknowledgements

The research presented in this paper has received funding from the National Natural Science Foundation of China (52305161) and China Postdoctoral Science Foundation (2024T170743).

5. References

[1] Y. Sun, Q. Pan, Y. Sun, W. Wang, Z. Huang, X. Wang, Q. Hu, Localized corrosion behavior associated with Al_7Cu_2Fe intermetallic in Al-Zn-Mg-Cu-Zr alloy, *J Alloys Comp.*, 2019, 783: 329–340.

[2] R.M. Katona, E.K. Karasz, R.F. Schaller, A Review of the Governing Factors in Pit-to-Crack Transitions of Metallic Structures, *Corrosion*, 2023,79: 72–96.

[3] H.A. Bale, A. Haboub, A.A. MacDowell, J.R. Nasiatka, D.Y. Parkinson, B.N. Cox, D.B. Marshall, R.O. Ritchie, Real-time quantitative imaging of failure events in materials under load at temperatures above 1,600 °C, *Nature Mater.*, 2013,12: 40–46.

[4] T.J. Stannard, J.J. Williams, S.S. Singh, A.S. Sundaram Singaravelu, X. Xiao, N. Chawla, 3D time-resolved observations of corrosion and corrosion-fatigue crack initiation and growth in peak-aged Al 7075 using synchrotron X-ray tomography, *Corro. Sci.*, 2018, 138: 340–352.

In situ X-ray tomography of failure criticality in μ-LPBF fabricated cellular lattice

Yuexun Liu[1], Shengchuan Wu[1] and Xu Song[2]
[1] State Key Laboratory of Rail Transit Vehicle System, Southwest Jiaotong University, Chengdu, China
[2] Department of Mechanical and Automation Engineering, The Chinese University of Hong Kong, Hong Kong, China

1. Introduction

Cellular lattices have great application potential in the aerospace and biomedical, due to high specific strength, energy absorption efficiency, and vibration dissipation performance [1]. According to the basic constituent elements, cellular lattices can be categorized into truss-lattices [2], shell-lattices [3], plate-lattices [4], and various hybrid lattices [5] with tuned mechanisms. Among them, truss-lattices and shell-lattices have received much attention. Laser powder bed fusion (LPBF) or selective laser melting (SLM), as an advanced metal Additive manufacturing (AM) route, produces high-resolution complex lattice structures and complete control over geometric features. Generally, deformation modes of classical cellular lattices include the bending, buckling, shearing, and folding [6]. Numerous experiments on lattices are typically conducted within multiple units, wherein loading initially leads to the local collapse of several individual lattices, followed by the gradual collapse at the overall scale, eventually leading to in macroscopic crushing or shear bands [7].

However, studies on the deformation and damage behavior of lattice materials have not yet addressed micro-scale lattices. These microlattices are of significant value in applications such as precision medical devices and complex electronic components. Micro laser powder bed fusion (μ-LPBF) technology makes the optimized design of microlattices feasible. Research on the mechanical properties of microlattices is scarce, and much of it is process-oriented. Due to their minuscule scale, traditional characterization methods struggle to assess the global and local deformation and damage behavior of micro-scale lattices. An in-depth experimental understanding of the intrinsic mechanical behavior of μ-LPBF lattices can provide a theoretical foundation for the application of microlattice metamaterials. In this work, we focus on the deformation and internal damage behavior of unit lattices, especially those of the most classical and widely studied cellular structures, therefore truss-lattices (BCC, FCC, Octet and RD) and shell-lattices (sheet-network TPMS: D, G and SplitP) were chosen for the study. With 2 characteristic dimensions, 14 lattices samples were obtained by μ-LPBF. *In situ* experimental mechanics methods were employed to reveal the mechanical response, deformation behavior and multiscale damage evolution behavior. This work reveals the typical failure modes of truss- and shell-lattices, providing a theoretical foundation for the integrity assessment of mechanical metamaterial based on these cellular types.

2. Materials and methods

μ-LPBF has become an ideal method to fabricate near-net-shape micro-scale lattices. In this work, the optimized parameters of Ti-6Al-4V materials for μ-LPBF include the laser power of 70 W, the scanning speed of 1300 mm/s, the hatch distance of 50 μm, the scanning rotation angle of 67 °, and

the layer thickness of 10 μm. The composition of the Ti-6Al-4V powder used is shown in Table 1. Note that the powders were examined for particle size, which was 6.8 μm for D10 and 20.9 μm for D90.

Element	Al	V	C	Fe	H	O	N	Ti
Value	6.36	4.01	0.01	0.18	0.002	0.1300	0.0174	Balance

Table 1. Chemical composition (wt.%) of Ti-6Al-4V powder

First, a Ti-6Al-4V plate was printed on the substrate, after which each lattice cell was uniformly printed on the Ti-6Al-4V plate at a certain interval. After printing, the pre-printed Ti-6Al-4V plate was cut from the substrate, and finally, the individual samples (Fig. 1 (a)) were separated from each other by a picosecond pulsed laser.

To understand the macroscopic mechanical properties of the lattices and their microscopic origins, in situ compressive tomography experiments were carried out at the BL16U2 beamline station at the SSRF, as shown in Fig. 1 (b).

In situ micromechanical test system is the core for conducting in situ mechanical experiments. Based on the test requirements and the test conditions of BL16U2, a new in situ mini tension/compression test system (Fig. 1 (c)) was developed by reference a prototype. The whole frame of the test system adopted a new design to optimize the load distribution and reduce the materials used. The field-of-view module of the test system was designed to be compression-ready by a customized PMMA cylinder with screw-in quick-release fasteners.

The monochromatic mode was chosen with absorption contrast and a certain phase contrast to help distinguish some features with similar absorption to X-rays. The photon energy was adjusted to 28 keV, the exposure time was only 20 ms, and the images were acquired using a Photron SA-Z high-speed camera with 2 μm/pixels. The steps of the *in situ* compression test was taken as a standard procedure. The initial state of the samples was scanned first, and then loaded in displacement-controlled mode, with a displacement step of 0.1 mm (10% strain) for each loading step, and the 3D scan was carried out with the load maintained, until the maximum displacement (0.7 mm). The flat-field and dark-field images were also acquired during the scanning process.

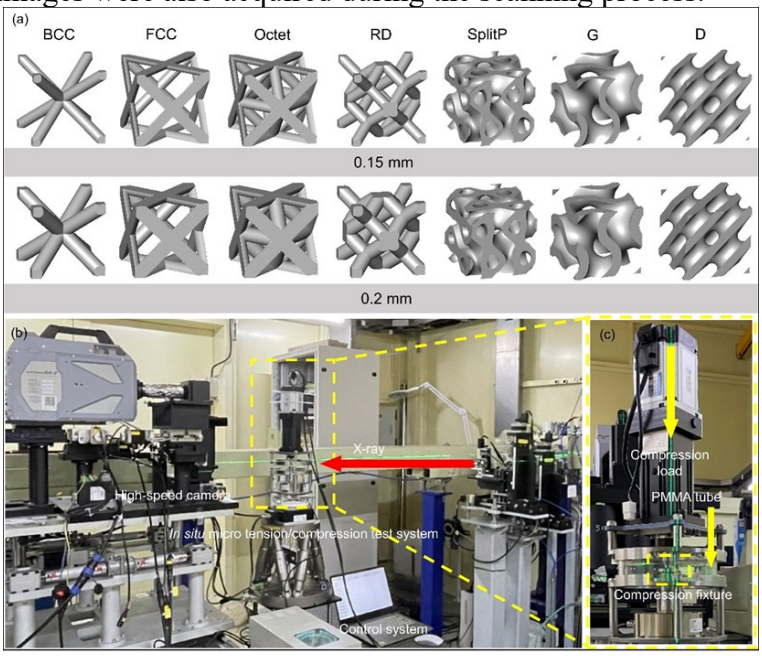

Fig. 1 (a) Geometry design of 7 classes lattice with 2 different characteristic dimensions, (b) and (c) in situ tension/compression testing setup at the BL16U2 station.

3. Results and conclusions

The EA and SEA properties of lattices can be obtained, as well as a wide variety of behavior modes. Nonetheless, an intrinsic perspective exists in all prior discussions, namely that various lattices exhibit distinct behaviors due to differing structural components, such as trusses and shells, as well as varying deformation modes, including bending-dominant and axial-dominant. Gibson-Ashby model [8] is widely used to describe the relationship between relative density and properties of porous structures:

$$\frac{\text{foam property}}{\text{cell wall property}} = C\left(\rho^*\right)^n \tag{1}$$

where C and n are material constants. The Gibson-Ashby model establishes a very simple but insightful relationship between the mechanical properties of a structure and its relative density.

As shown, Fig. 2 is the relationship between the EA, SEA and the relative density (without AM subscript), it should be noted that hereafter the relative densities are based on the experimental samples. It is clear that both the EA and SEA show an obvious positive correlation with the relative density, which is no longer affected by the different lattices and the different dominant modes. It is very clear that both the absorbed energy and the specific absorbed energy show such a behavior:

$$f \propto \left(\rho^*\right)^n \tag{2}$$

where f is the different physical properties, here including both EA and SEA. Exponent n, n>1 for total EA (n=2.33 in this work) and n=1 for SEA.

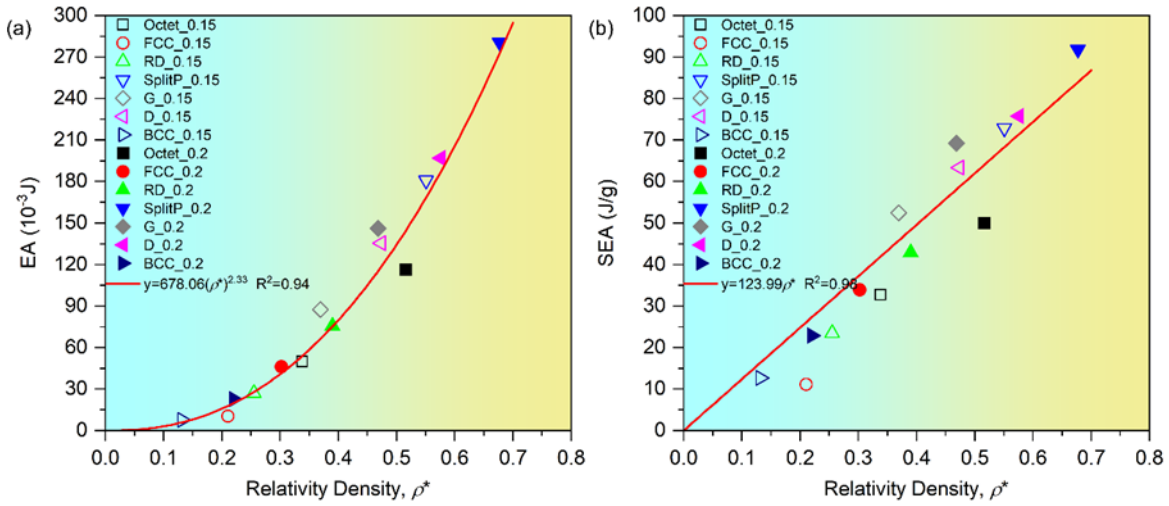

Fig. 2. The energy absorption properties of lattices: (a) EA and (b) SEA vs relative density.

With the benefit of synchrotron radiation *in situ* tomography experiments, we can elucidate the deformation behavior of lattice on different scales. From the macroscopic view, the deformation-to-failure phenomenon of the lattice can be extracted immediately.

The Octet lattice and SplitP lattice were selected as subjects for representative analysis due to their exceptional mechanical properties and energy absorption capabilities. Fig. 3 to Fig. 4 are 3D reconstructions of the deformation behavior of Octet (truss-lattice) and SplitP (shell-lattice) in the [001] and [100] directions. The two types of lattices have completely different deformation behaviors. For the Octet lattice, it can be seen that as the deformation increases, some of the trusses rotate around the nodes. For the shell-lattice, the significant shear can be observed in SplitP sample.

The evolution mode from deformation to failure can be obtained from the [100] direction. It can be seen that Octet lattice starts with several node fractures and then begins a gradual compression and densification process. In the SplitP lattice, as the loading process proceeds, cracks appear in certain

regions due to shear and gradually propagate, eventually leading to the separation of the whole lattice into two dislocated segments. Therefore, the final deformation state of the SplitP lattice is considerably distorted relative to the initial state.

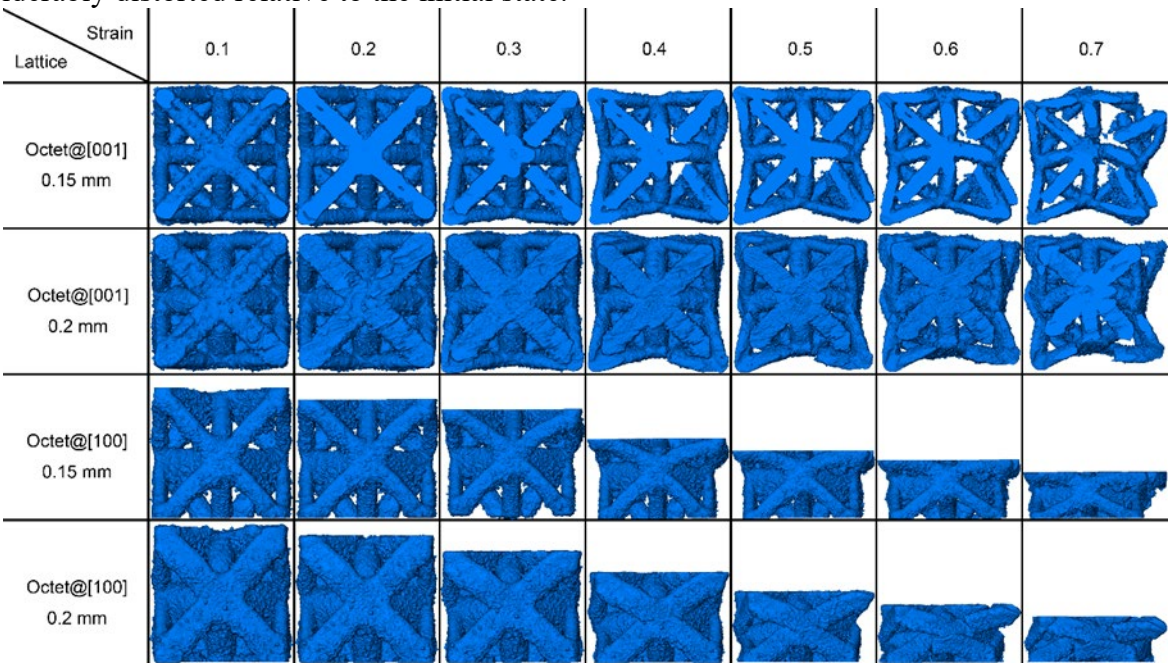

Fig. 3. Deformation behavior of the Octet lattice with 2 different characteristic dimensions at [001] and [100] directions.

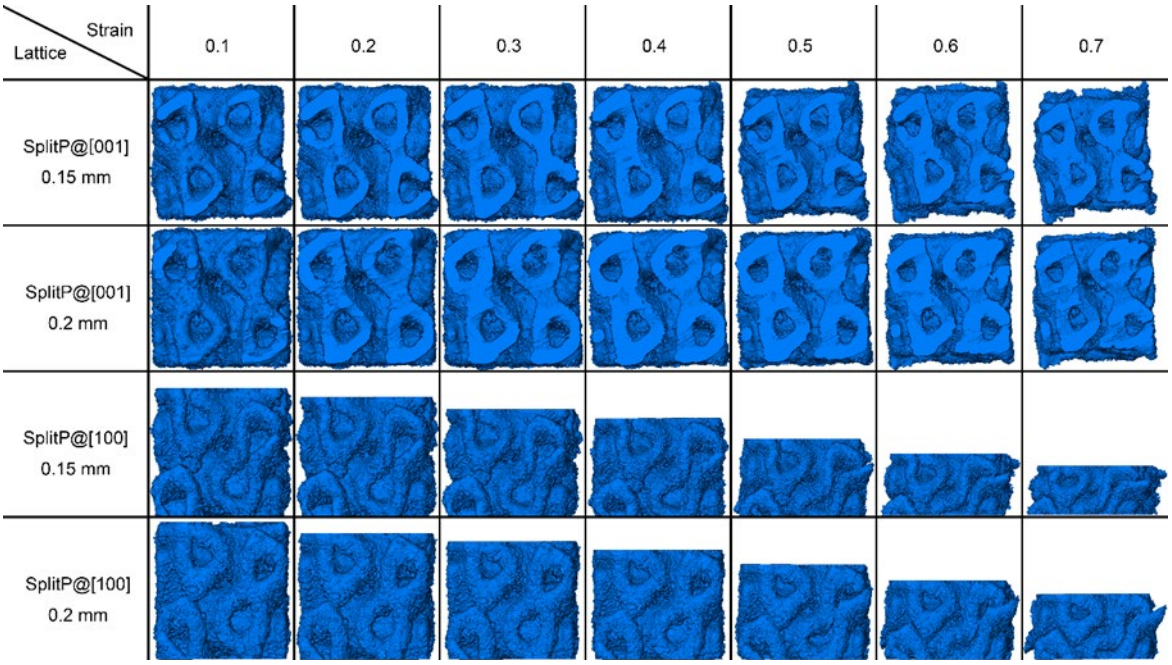

Fig. 4. Deformation behavior of the SplitP lattice with 2 different characteristic dimensions at [001] and [100] directions.

4. Acknowledgements

The research presented in this paper has received funding from the National Natural Science Foundation of China (U2032121 and U2341270).

5. References

[1] Li SC, Deng BL, Grinthal A, Schneider-Yamamura A, Kang JL, Martens RS, Zhang CT, Li J, Yu SQ, Bertoldi K, Aizenberg J. Liquid-induced topological transformations of cellular microstructures. Nature. 2021; 592(7854): 386-91.

[2] Tancogne-Dejean T, Spierings AB, Mohr D. Additively-manufactured metallic micro-lattice materials for high specific energy absorption under static and dynamic loading. Acta Materialia. 2016; 116: 14-28.

[3] Feng JW, Liu B, Lin ZW, Fu JZ. Isotropic porous structure design methods based on triply periodic minimal surfaces. Materials & Design. 2021; 210: 110050.

[4] Tancogne-Dejean T, Diamantopoulou M, Gorji MB, Bonatti C, Mohr D. 3D plate-lattices: an emerging class of low-density metamaterial exhibiting optimal isotropic stiffness. Advanced Materials. 2018; 30(45): 1803334.

[5] Zhang L, Song B, Choi SK, Shi YS. A topology strategy to reduce stress shielding of additively manufactured porous metallic biomaterials. International Journal of Mechanical Sciences. 2021; 197: 106331.

[6] Surjadi JU, Gao LB, Du HF, Li X, Xiong X, Fang NXL, Lu Y. Mechanical metamaterials and their engineering applications. Advanced Engineering Materials. 2019; 21(3): 1800864.

[7] Qi DX, Yu HB, Liu M, Huang H, Xu SC, Xia Y, Qian GA, Wu WW. Mechanical behaviors of SLM additive manufactured octet-truss and truncated-octahedron lattice structures with uniform and taper beams. International Journal of Mechanical Sciences. 2019; 163: 105091.

[8] Gibson IJ, Ashby MF. The mechanics of three-dimensional cellular materials. Proceedings of the royal society of London. A. Mathematical and Physical Sciences. 1982; 382(1782): 43-59.

MOVE CONTRAST X-RAY IMAGING FOR IN-SITU/IN-OPERANDO MECHANICAL TESTING WITH HIGH SENSITIVITY

T.Q. Xiao[1,2,3], F.X. Wang[1], K. Li[1], X.L. Ju[1,2,3], M.W. Xu[1,2,3], Z.H. Song[1,2,3], C.C. Ma[1,2,3]
[1] Research Center for Shanghai Synchrotron Radiation Facility, Shanghai Advanced Research Institute, Chinese Academy of Sciences, 201204 Shanghai, China
[2] Shanghai Institute of Applied Physics, Chinese Academy of Sciences, 201800 Shanghai, China
[3] University of Chinese Academy of Sciences, Chinese Academy of Sciences, 100049 Beijing, China

1. Introduction

X-ray imaging is extensively used for mechanical testing, but still confronted with a great challenge for imaging weak signals in complex systems during in-situ/in-operando mechanical testing. Complex systems are characterized by complex composition, structure and time-varying complexity. In the process of X-ray imaging, the structural information, motion artifacts and high-frequency noise formed by the objects of interest and the surrounding components are mixed, which cannot form obvious contrast due to mutual interference or weak signals, so that traditional direct imaging methods often cannot distinguish the objects of interest. Methods such as phase contrast, contrast labeling, K-edge subtraction, and time-subtraction are often used for contrast enhancement and extraction of weak signals in complex systems, but they are still prone to motion artifacts and high-frequency noises. When the signal of the object of interest in the complex system is too weak to form a resolvable contrast, the existing methods are no longer applicable.

Based on the demand of weak signal tracking imaging in complex systems, we invented the move contrast X-ray imaging (MCXI) method, which is based on a new contrast mechanism to achieve complex background noise suppression and highly sensitive tracking imaging for weak signal targets. A series of experimental results show that the MCXI method greatly improves the sensitivity of weak signal imaging in complex systems, and has more prominent advantages in situations where existing imaging methods cannot provide observable contrast [1~6]. We first introduce the principle of MCXI, then introduces the typical applications of X-ray imaging, including move contrast angiography, in situ dynamic study of plant microvessel water refilling, electrochemical reaction in an electrolytical cell, ultrafast cavitation evolution and one-pixel level nondestructive defect testing. Finally, we presented concluding remarks and perspectives.

2. Principle and method

The move contrast imaging is realized based on the frequency analysis of the pixel gray variation of the array detector with time, which is essentially the mapping of time domain spectrum signals to real space [3,4,5]. By combining the amplitude information representing the signal intensity of the moving target with the phase information representing timing characteristics of moving target under a specific frequency, the move contrast imaging of a specific system can be achieved. The detector collects a projection image sequence $g\ (x,\ y,\ t)$ within a certain time. In principle, the grayscale-fluctuation resulted time-domain frequency signal of the target is much more sensitive than the grayscale-variation in real space. Combined with frequency analysis, sensitivity of MCXI for in-situ/in-operando metrology can be improved significantly. The trajectory of the moving targets is

obtained based on the amplitude of move contrast, and the temporal information is obtained based on its phase. Accordingly, the move contrast image containing motion trajectory, direction and velocity information is obtained by image fusion. This means that MCXI is able to track sensitively the moving target in a complex background and find applications in in-situ/in-operando metrology including mechanical testing. Taking advantage of the relativity of motion, MCXI is also applicable for defect testing of materials.

3. Results and conclusions

A series of experiments show that the MCXI method greatly improves the sensitivity of weak signal imaging in complex systems, and has more prominent advantages in situations where existing imaging methods cannot provide observable contrast [1~6]. The experimental results include angiography with very low agent dose [1], sensitive tracking to ion migration in an electrolytic cell [2], ultrafast imaging of cavitation evolution [3], mass force field measurement of water refilling with MCXI-based tomography [4,5,6], and testing one-pixel-level micro-defects in high-noise and complex backgrounds. Shown in **Figure** 1 are the three-dimensional distribution of mass force field measured in-operando of water refilling in plant branch and sensitive in-situ testing of defects in an alloy steel pipe respectively. Results of this paper demonstrate that MCXI has the great potential for in-situ/in-operando mechanical testing with and without loading.

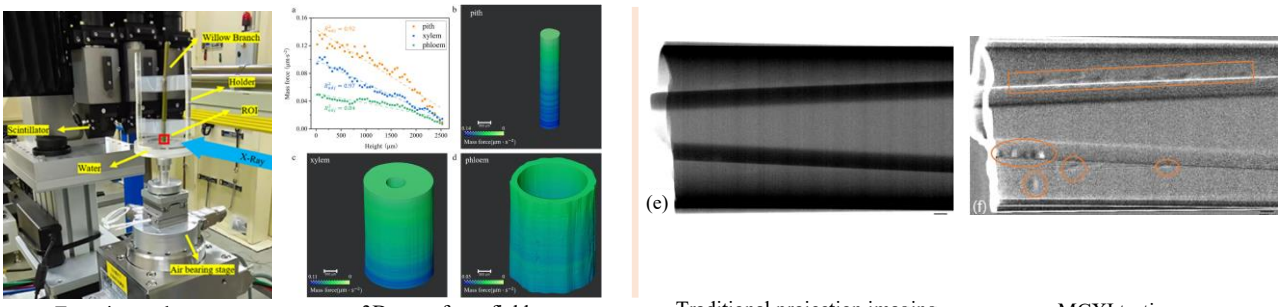

Fig. 1. Measurement of plant mass force field (left) and defect testing of an alloy steel pipe(right).

4. Acknowledgements

The National Key Research and Development Program of China (Grant Nos. 2022YFA1603601, 2021YFF0601203, 2021YFA1600703), the Young Scientists Fund of the National Natural Science Foundation of China (Grant No. 12205361,12405376).

5. References

[1] F.X. Wang, P.T. Zhou, K. Li, M. Mamtilahun, Y.H. Tang, G.H. Du, B. Deng, H.L. Xie, G.Y. Yang and T.Q. Xiao (2020). Sensitive imaging to intact microvessels in vivo with synchrotron radiation, *IUCrJ*, **7**,793–802

[2] X.L. Ju, K. Li, F.C. Yu, M.W. Xu, B. Deng, B. Li, T.Q. Xiao (2022). Move contrast X-ray imaging of electrochemical reaction processes in electrolytic cell. *Acta Physica Sinica*, **014**:071.

[3] F.X. Wang, K. Li, M.W. Xu, X.L. Ju, T.Q. Xiao (2023). Move contrast X-ray imaging and its applications, *Nuclear Inst. and Methods in Physics Research*, A **1055,**168560

[4] M.W. Xu, K. Li, Y.L. Xue, F.X. Wang, Z.X. Liu, Z.H Song and T.Q. Xiao (2023), Water refilling along vessels at initial stage of willow cuttage revealed by move contrast CT. *Front. Phys*. **11**,1174387

[5] M.W. Xu, K. Li, Y.L. Xue, F.X. Wang, Z.X. Liu, T.Q. Xiao (2024). Measurement of mass force field driving water refilling of cuttage. *Scientific Reports*.**14**(1):8947.

[6] K. Li, F.X. Wang, Y.L. Xue, S.Q. Huang, Z.X. Liu and T.Q. Xiao (2025). Move contrast X-ray imaging reveals wall infiltration along maize leaf vessels before water refilling. *Front. Phys*., **13**:1527070

POSTERS

EuraSEM 6-11 July 2025 ICEM21 Bologna 21st International Conference on EXPERIMENTAL MECHANICS

EFFECT OF THE GLASS AND PVB THICKNESS ON THE HEAD INJURY CRITERION

J. Kim[1], S. Ahn[1], J. Hwang[1] and H. Jung[1]
[1] Railroad Accident Research Department, Korea Railroad Research Institute, South Korea

1. Introduction

Laminated glass is widely utilized in automotive and architectural applications due to its superior safety features, which are primarily achieved through a polyvinyl butyral (PVB) interlayer that bonds multiple layers of glass. This construction provides the glass with enhanced impact resistance, which is essential for protecting passengers during accidents. The thickness of both the glass layers and the PVB interlayer has a significant effect on the head injury criterion (HIC), a metric that assesses potential head injuries from impacts. Recent studies have investigated the fracture mechanics and energy absorption properties of laminated glass under various impact scenarios, emphasizing the role of material thickness in improving safety outcomes.

Thicker glass layers are known to improve the structural integrity of laminated glass, delaying the initiation of cracks and mitigating the propagation of fractures upon impact. The PVB layer, when optimized for thickness, further contributes by distributing impact forces and preventing the glass from shattering. According to Müller-Braun et al. (2021), thicker PVB layers effectively maintain glass integrity under low-velocity impacts, thus reducing HIC values by allowing energy absorption to be spread across a larger area. Similarly, Dharani et al. (2003) demonstrated through finite element modeling that while PVB thickness impacts the post-impact behavior, initial crack patterns are more strongly influenced by the outer glass ply thickness and the velocity of the impact.

This study will focus on analyzing the effects of glass and PVB layer thickness on laminated glass's HIC response, providing insights that may inform future design optimizations for enhanced impact safety in railway applications.

2. Experimental methods

The head foam drop impact tester is as shown in Fig. 1. The maximum drop speed of the drop impact tester is 27.7 km/h. The headform used was a rigid aluminum headform from DTS. The test specimen was 1000x700 flat glass based on EN 15152, the technical standard of windshield for railroad applications.

Fig. 1. Headform drop tester(left) and laminated glass after impact test

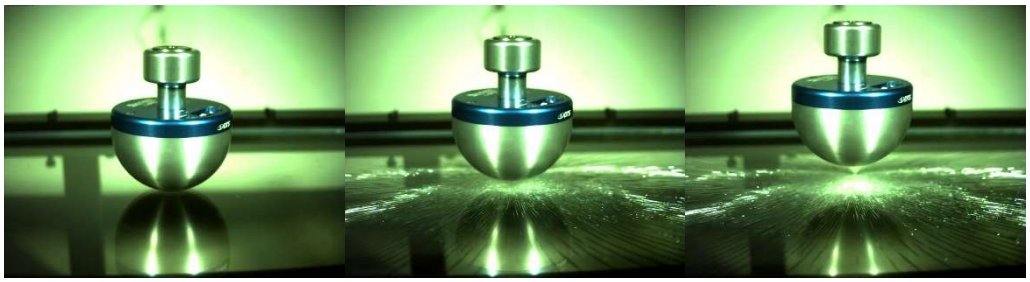

Fig. 2. Sequential impact images at the crack initiation point

3. Results and conclusions

Figure 3 shows the Head Injury Criteria and HIC values according to the headform's drop impact speed. The HIC value of the conventional laminated glass was 1236, exceeding the standard value of 1000 at 20 km/h, while the modified Laminated Glass whose strength was slightly weakened recorded 869, which was below the standard value of 1000 at 20 km/h. Among railroad vehicles, especially tram vehicles, the design of an appropriate front windshield is necessary to reduce damage in the event of a pedestrian crash accident.

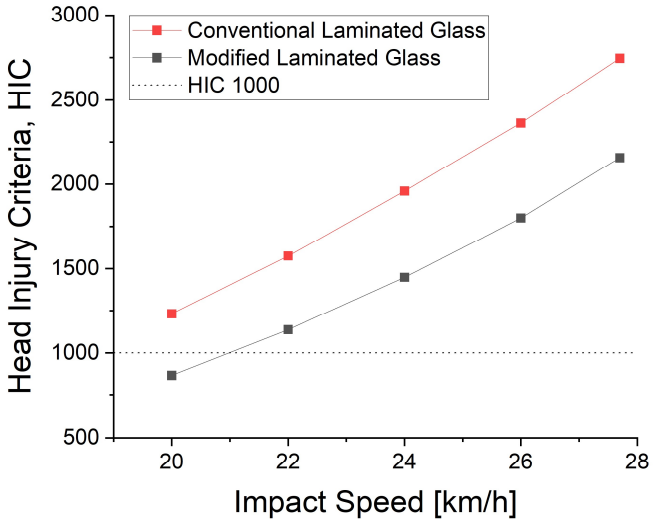

Fig. 3. HIC values with respect to the impact speeds

4. Acknowledgements

The research presented in this paper has received funding from the Korea Railroad Research Institute under the grant No. PK2403E2.

5. References

[1] Müller-Braun, S., et al. (2021). Strength of the individual glasses of curved, annealed, and laminated glass used in automotive windscreens. Engineering Failure Analysis, 123, 105281.

[2] L. R. Dharani, S. R. Mettu, S. Zhao, S. D. Barbat, and L. Chai (2003). Modeling Fracture in Laminated Automotive Glazing Impacted by Spherical Featureless Headform. *SAE Technical Papers, SAE International*, pp. 1225-1230.

[3] K. Osnes, O. S. Hopperstad, and T. Børvik (2020). Rate dependent fracture of monolithic and laminated glass: experiments and simulations. *Engineering Structures*, 212, 110516.

AI CLASSIFICATION OF FRACTURE MODES IN METALLIC COMPONENTS

R. Montanari[1], M. Sileo[2]
[1] Department of Industrial Engineering, University of Rome Tor Vergata, Via del Politecnico, 1- 00133 Rome, Italy
[2] SER TEC S.r.l., Via Lombardia 27/b, 40139, Bologna, Italy

Corresponding author: Mirko Sileo; Mail: mirko@sertec.it

1. Introduction

Scanning Electron Microscopy (SEM) is a technique of fundamental importance for investigating metallic fractures and damaged surfaces. Owing to its great resolution and field depth, it allows to study surfaces with complex morphology revealing details on nanometric scale. Through SEM observations relevant information has been achieved on the physical mechanisms underlying the fracture modes of metallic components subjected to different loads and aggressive environment in service conditions and a lot of scientific publications can be found in literature on individual cases. In the years the use of this technique moved from research labs to industrial practice, however the large variety of morphological features observed in fracture surfaces makes difficult the identification of the origin of a component failure from SEM micrographs and requires well trained personnel. Therefore, specific atlas of fracture surfaces have been published to help the comparison of what observed with some reference cases (see ref. [1]). The aim of present work was to develop a system based on Artificial Intelligence (AI) to automatically identify the most common types of fractures occurring in metals. The system has been trained through SEM images of ductile, brittle (transgranular and intercrystalline) and fatigue cracks. Some typical examples are shown in Fig. 1.

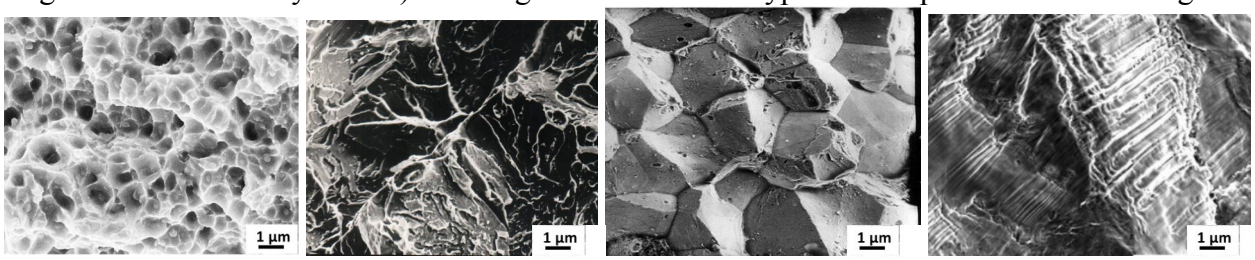

(a) (b) (c) (d)

Fig. 1- Most common types of fracture modes: ductile (a), transgranular brittle (b), intercrystalline (c) and fatigue (d).

2. The AI system

The AI based system involves artificial vision and the identification of objects and/or peculiar characteristics. A software for the automatic sampling of images from database of SEM micrographs was implemented, then a convolutional neural network (CNN) was developed for the detection of objects and the classification of images. It processes images with grid-like structures (e.g., images are made up of pixels) and its architecture is based on convolutional layers, which examine the image in small sections called "filters" or "kernels" for extracting specific features like edges, textures, or shapes. The system requires high-resolution SEM images to capture details on the microscopic scale

and make automatic, fast and accurate the inspection process. This is already used in industrial applications especially in the sectors where the quality of metal surface is critical, such as automotive, aerospace, and electronics manufacturing. The architecture of the neural network in computer vision is shown in Fig. 2.

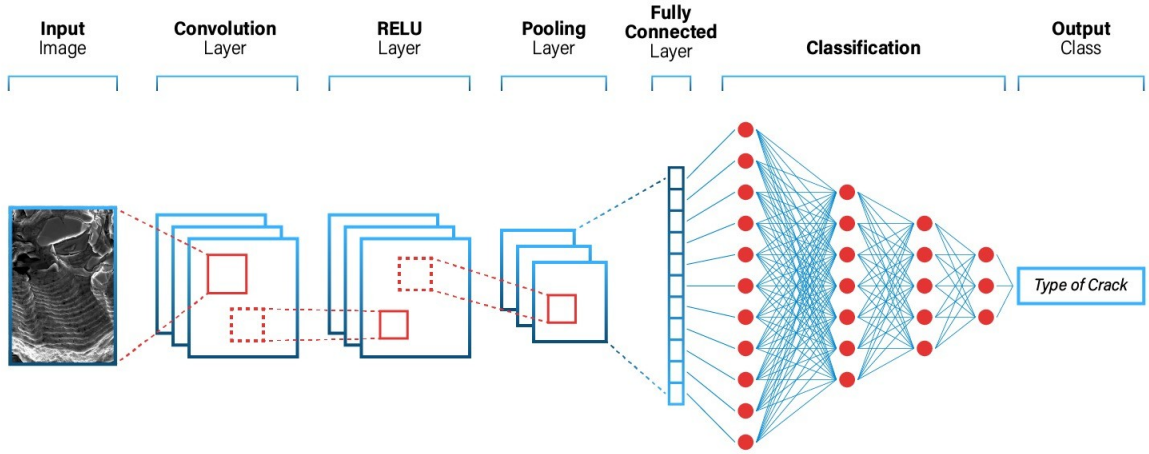

Fig. 2- Architecture of the neural network in computer vision developed for identifying the fracture modes in metallic components.

The key steps include: (i) collection and preprocessing of SEM micrographs; (ii) feature (edges, textures etc.) extraction by using convolutional layers, pooling, and activation functions (e.g., ReLU); classification of fracture modes and quantification of their areas when multiple modes coexist (e.g., see Fig. 3).

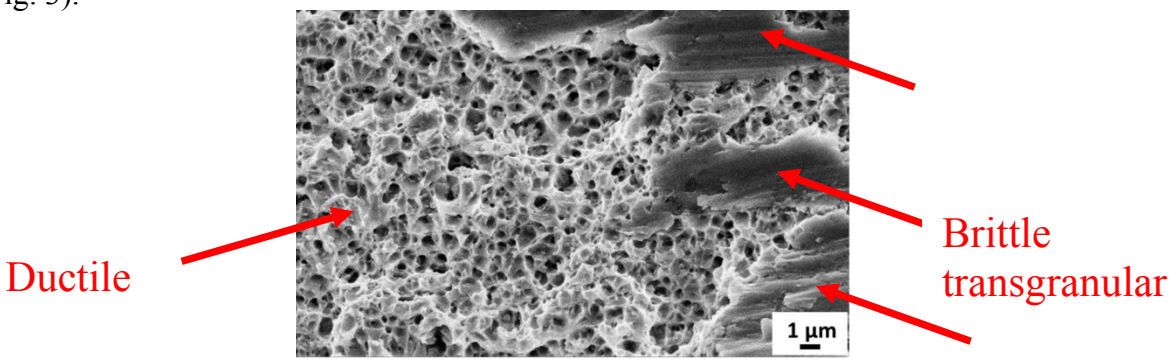

Fig. 3- Fracture surface of an ODS steel showing the features of both ductile e transgranular brittle modes [2].

The technologies employed in the system are: (i) Python that provides a flexible environment for development; (ii) OpenCV for image preprocessing (contour detection and feature extraction); (iii) Deep Learning (TensorFlow and YOLO) enabling real-time defect detection and high-speed classification. In conclusion the system allows the automatic classification of the main fracture typologies occurring in metallic components. At this stage of development the identification error is about 3-4 % but it will be further reduced by increasing the training dataset of micrographs.

3. References

[1] L. Engel, H. Klingele (1981). An Atlas of Metal Damage, Wolfe Science Books in association with Carl Hanser Verlag, Munich, Vienna.

[2] A. Fava, A. Mezzi, R. Montanari, C. Testani, A. Varone (2024) Influence of temperature on ductility of nano-ODS steel prepared by low-energy mechanical alloying, Materials Today Communications.

Development of an Organometallic Benzoxazine Composite for Dual Electromagnetic and Ballistic Shielding Applications

Abdelmalek Habes [a*], Oussama Mehelli [a], Mehdi Derradji [a,], Fouad Benaliouche [a], Slimane Abdous [a], M'hamed El Hadi Timtaoucine [a]

[a] *UER Procédés Energétiques, Ecole Militaire Polytechnique, BP 17, Bordj El-Bahri, Algiers Algeria.*

Corresponding author. Tel.: +213-556045225

Email : abdelmalekhbs@gmail.com

Abstract

This study focuses on the development of a novel organometallic benzoxazine (Bz-Al)-based composite for ballistic and electromagnetic shielding applications. The Bz-Al monomer was synthesized, and its structure was confirmed through ^{1}H NMR analysis. Thermal analysis (DSC, TGA) and conductivity measurements were conducted on the Bz-A and Bz-Al monomers, demonstrating that the Bz-Al monomer possesses significantly higher electrical conductivity, enhancing its effectiveness for electromagnetic interference (EMI) shielding. Composite plates were then fabricated by combining P(Bz-Al) with Kevlar fibers, and their properties were compared to those of P(Bz-A) plates. The ballistic performance of P(Bz-Al) plates was found to be good, closely matching those of P(Bz-A) composites. Furthermore, the P(Bz-Al) composites demonstrated excellent EMI shielding capabilities, which were not observed in the P(Bz-A) composites, highlighting their potential suitability for advanced protective gear.

Keywords:

Benzoxazine, organometallic monomer, aluminum, electromagnetic shielding, ballistic shielding**.**

Introduction

In recent years, the demand for multifunctional materials that provide both ballistic protection and electromagnetic interference (EMI) shielding has grown significantly, driven by advances in defense and electronic applications. Benzoxazine resins, known for their thermal stability, chemical resistance, and mechanical strength, have gained attention for their versatility in composite materials. However, traditional benzoxazines, such as P(Bz-A), lack the conductivity required for effective EMI shielding [1]. To address this limitation, organometallic modifications have emerged as a promising approach. In this study, we report the synthesis and characterization of a novel organometallic benzoxazine monomer, Bz-Al, specifically designed to combine high electrical conductivity with the intrinsic benefits of benzoxazines. By integrating Bz-Al with Kevlar fibers, we developed a composite that exhibits

promising ballistic and EMI shielding properties, thus advancing the potential for protective materials [2].

Materials

In this work, all chemicals were used without further purification. Aluminum powder was procured from Alfa Aesar, USA. Bisphenol A (Bpa) and paraformaldehyde (PFA) were sourced from Shanghai Aladdin Reagents, China, while tetrahydrofuran (THF) and dimethyl sulfoxide (DMSO) were supplied by VWR International, USA. Mercury (II) iodide (HgI_2) was obtained from Honeywell, USA. Kevlar fibers, selected for their excellent tensile strength and high impact resistance, were incorporated as reinforcing agents within the composite to enhance ballistic performance [3].

Experimental

Synthesis of Al-Bz-A and polymerisation

The synthesis reaction of the monomer (**Fig. 1**) was conducted using paraformaldehyde, aniline, and Al-Bpa in a respective molar ratio of (6:3:1) following the Mannich reaction, similar to ordinary benzoxazine. Initially, in a three-necked flask containing DMSO as the solvent, the entire mass of aniline was mixed with half of the total mass of paraformaldehyde for 2 hours at 70 °C then, the previously synthesized Al-Bpa was added to the resulting reaction mixture, along with the remaining amount of PFA, and the reaction was continued at 100 °C for 6 hours. Upon completion of the process, the monomer was recovered and subjected to filtration, followed by drying at 120 °C [4].

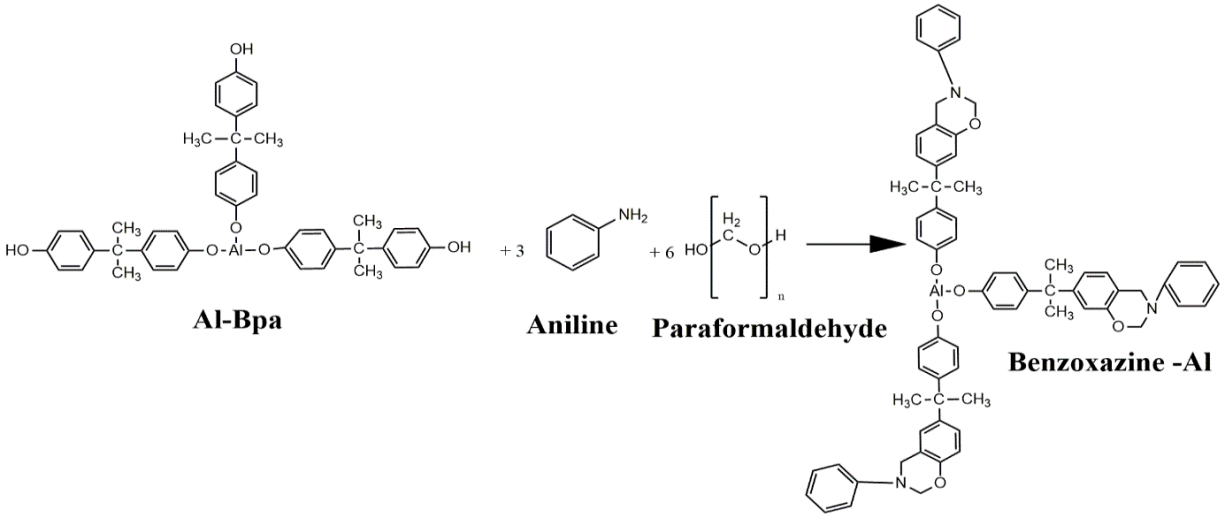

Fig. 1 Synthesis reaction of Bz-Al.

P(Bz-A) and P(Bz-Al) composites preparation:

To prepare the composite plates, the P(Bz-A) and P(Bz-Al) monomers were first dissolved in an appropriate solvent (THF) to create uniform solutions. Kevlar fibers, pre-cut to

dimensions of 10 cm by 10 cm, were then immersed in the monomer solutions for 15 minutes to ensure thorough impregnation. Following this, the fibers were placed in an oven to remove the solvent. Once dried, the impregnated Kevlar fibers were arranged in a metallic mold for the curing process. The curing was carried out in an oven for a total of 20 hours, beginning with an initial stage at 120 °C for 3 hours, followed by incremental temperature increases up to 200 °C. This gradual curing ensured optimal polymerization of the benzoxazine matrix and uniform distribution of the P(Bz-A) or P(Bz-Al) monomer within the composite structure, resulting in plates with enhanced structural integrity and performance.

Results

Ballistic and EMI shielding performance tests were conducted on P(Bz-A) (**Fig.2**) and P(Bz-Al) (**Fig.3**) composite plates (10 cm × 10 cm) using standard 9 mm full metal jacketed projectiles, following the National Institute of Justice (NIJ standard-0101.06-IIA). Both composites exhibited comparable ballistic resistance, effectively absorbing impact energy through mechanisms like tensile failure, elastic deformation, interlayer delamination, and shear. However, the P(Bz-Al) plates demonstrated superior dual functionality, excelling in electromagnetic interference (EMI) shielding (**Fig.4**) while maintaining ballistic integrity similar to P(Bz-A). This dual shielding capability in P(Bz-Al) plates is attributed to enhanced electrical conductivity, enabling the composite to serve in applications requiring both EMI and ballistic protection. The results highlight P(Bz-Al) as a promising material for advanced protective systems.

Fig. 2 P(Bz-A) plate before and after ballistic test.

Fig. 3 P(Bz-Al) plate before and after ballistic test.

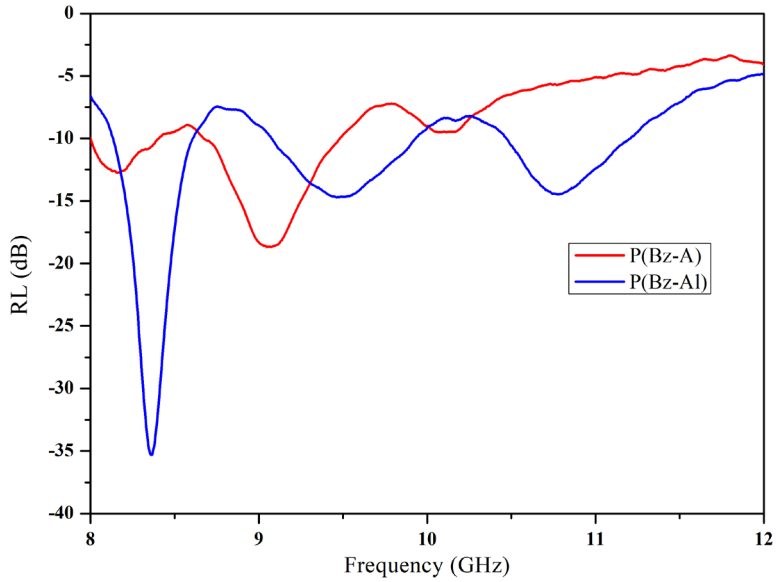

Fig. 4 EMI shielding performance of P(Bz-A) and P(Bz-Al) composites.

Conclusion

This work demonstrates the successful development of a dual-functional composite based on the novel organometallic benzoxazine monomer, Bz-Al. The P(Bz-Al) composites exhibit excellent electromagnetic interference (EMI) shielding capabilities while achieving ballistic performance comparable to that of P(Bz-A) composites. The incorporation of Bz-Al into Kevlar-reinforced plates has shown that this composite material effectively combines EMI shielding with impact resistance, making it highly suitable for advanced protective applications. These findings underscore the potential of organometallic benzoxazines as versatile materials for multi-functional protective systems.

References

[1] Zegaoui A, Derradji M, Dayo AQ, et al. High-performance polymer composites with enhanced mechanical and thermal properties from cyanate ester/benzoxazine resin and short Kevlar/glass hybrid fibers. High Perform Polym 2019; 31: 719–732.

[2] Ramadhan A, Talib AA, Rafie A, et al. High velocity impact damage in Kevlar-29/epoxy-Al2O3. J Adv Sci Eng Res 2012; 2: 138–154.

[3] Van Der Werff H and Heisserer U. High-performance ballistic fibers: ultra-high molecular weight polyethylene (UHMWPE). In: Chen X (ed) Advanced fibrous composite materials for ballistic protection. Amsterdam: Elsevier, 2016, pp. 71–107.

[4] Derradji M, Jun W and Wenbin L. Phthalonitrile resins and composites: properties and applications. Amsterdam: William Andrew, 2018.

6-11 July 2025 ICEM21 Bologna
21st International Conference on EXPERIMENTAL MECHANICS

SPEED-DEPENDENT CHARACTERISTICS MODEL OF RAILWAY BUFFERS USING DEEP LEARNING

Jun Hyeok Hwang[1], Hyun Seung Jung[1], Jin Sung Kim[1], Seung Ho Ahn[1]
[1] Railroad Accident Research Department, Korea Railroad Research Institute, Korea

1. Introduction

Train coupling and decoupling operations are conducted for various purposes, including formation change, rescue, and shunting. Due to their significant mass, trains possess considerable kinetic energy even at low velocities, which can lead to damage in the car body or couplers during low-speed impacts. To prevent such damage, energy-absorbing devices are integrated into couplers, and dynamic simulations replicating low-speed collisions with braked trains are conducted to verify that no damage occurs to the vehicle body or couplers.

Recently, high-capacity buffers exhibiting speed-dependent response characteristics, such as hydraulic dampers and hydrostatic buffers, have been employed as energy-absorbing devices in railway couplers [1]. The European standard EN15227 recommends that simulations take into account the characteristics of energy absorbers when such buffers are speed-dependent [2]. However, accounting for speed-dependent characteristics becomes challenging when a mathematical response function for the buffer is absent [3]. In this study, a response model was developed to calculate speed-dependent responses using a deep neural network (DNN) trained on test data and was applied to train coupling simulations to account for speed-dependent characteristics.

2. Materials and methods

In this study, a DNN-based response model was developed to represent the speed-dependent characteristics of buffers. Fig. 1 illustrates a schematic of the speed-dependent response model for a buffer. The characteristics of the buffer are classified into loading, transition, and unloading states, with the DNN specifically employed to compute responses in the loading state, which is highly dependent on speed.

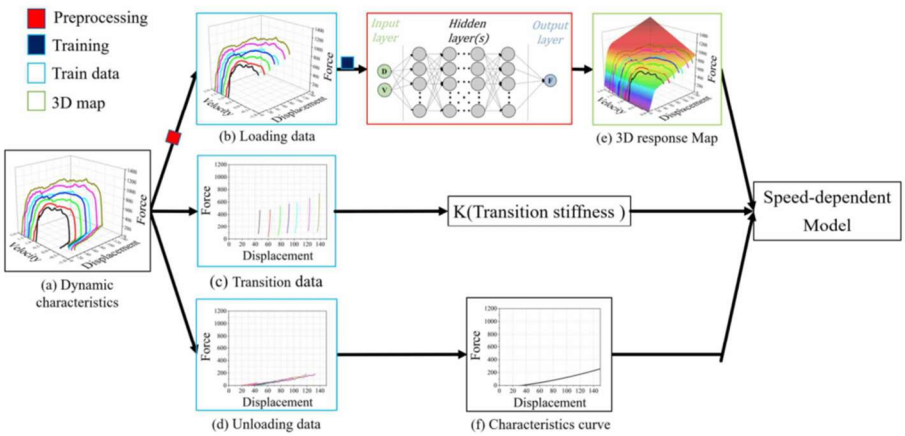

Fig. 1. The schematic of the speed-dependent response model

3. Results and conclusions

Rigid wall impact tests were performed to obtain the dynamic characteristics of the hydrostatic buffer. The experimental setup consisted of a rigid wall, a motor car, and a test vehicle. The motor car is utilized to accelerate the test car to a predetermined speed, after which the coupler is decoupled, resulting in the test car colliding with the rigid wall. The collected data were employed to train the response model, and its accuracy was validated through simulations of rigid wall impacts.

(a) (b) (c) (d)

Fig. 2. Experimental setup and results: (a) Rigid wall; (b) Test car; (c) Specimen; (d) Comparison of experiment and simulation

This study conducted a 10 km/h coupling simulation to evaluate coupling safety by applying both speed-dependent and speed-independent models of a hydrostatic buffer and analyzing the differences in results. Simulations without speed-dependent characteristics did not indicate hard contact in the hydrostatic buffer, but simulations incorporating speed dependency indicated hard contact and confirmed the potential for damage to the viscoelastic buffer. These results demonstrate that neglecting speed-dependent characteristics could limit the accurate assessment of potential damage to the train system.

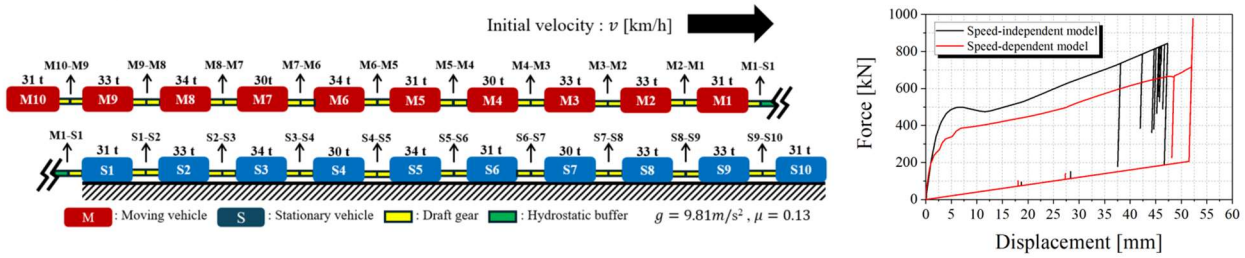

(a) (b)

Fig. 3. Coupling simulation: (a) Schematic of coupling scenario; (b) Force-displacement curve of hydrostatic buffer

4. Acknowledgements

The research presented in this paper has received funding from the R&D Program (PK2403E2) of the Korea Railroad Research Institute.

5. References

[1] J.H. Choi, H.G. Gil (2017). Performance simulation of high capacity hydrostatic buffer with silicon gum. *Journal of The Korean Society For Urban Railway*, **5(1)**, 791–800.

[2] BSI Standards Publication (2020). Railway applications - Crashworthiness requirements for railway vehicle bodies. **BS EN 15227:2020**. https://knowledge.bsigroup.com/products/railway-applications-crashworthiness-requirements-for-rail-vehicles/standard.

[3] N.W. Kim, Y.I. Park (2018). Collision tests and model development of a train coupling system using a high-capacity energy absorber. *Proceedings of the Institution of Mechanical Engineers, Part F: Journal of Rail and Rapid Transit,* **232(9)**, 2215–2227.

6-11 July 2025 ICEM21 Bologna
21st International Conference on EXPERIMENTAL MECHANICS

DEVELOPMENT OF AN IN-VITRO MODEL TO STUDY THE CERVICAL SPINE LOAD TRANSFER USING MOBI-C PROSTHESIS

A. Ramos[1], G. Costa[1], J. A. Ferreira[1], Y. Ledoux[2], and M. Mesnard[3]
[1] TEMA, Mechanical Engineering Department, University of Aveiro, Portugal
[2] Grenoble INP - Génie Industriel, Université of Grenoble, France
[3] I2M, Institut de Mécanique et d'Ingénierie, University of Bordeaux, France

1. Introduction

Spinal pathologies including degenerative disc disease are among the most common and critical worldwide [1].Several solutions can be employed to resolve the change in shape or loss of function of the deformed disc, the last is the disc replacement by a prosthesis [2]. The idea behind the replacement is to replicate the biomechanics of the natural disc using one of several concepts on the market [3]. The first prosthesis designs had high complication rates and more recent models have seen significant improvements, offering better clinical outcomes and lower risks of complications. Several experimental models have been developed to study the biomechanics of the cervical spine with in vitro and ex vivo models [4].

This study hypothesizes that cervical disc replacement influences the behavior of adjacent vertebrae. An in vitro model of the cervical spine between C5 and C6 was developed to comparatively evaluate the load transfer between the vertebrae after disc replacement.

2. Materials and methods

The Mobi-C Cervical Disc Prosthesis from Zimmer Biomet was selected, which is a semi-conditioned metal-on-plastic prosthetic disc for flexion, extension, rotation, and lateral flexion. Following on from the previous work [4] an experimental model was developed (figure 1) in an intact cervical spine and implanted between C5 and C6.

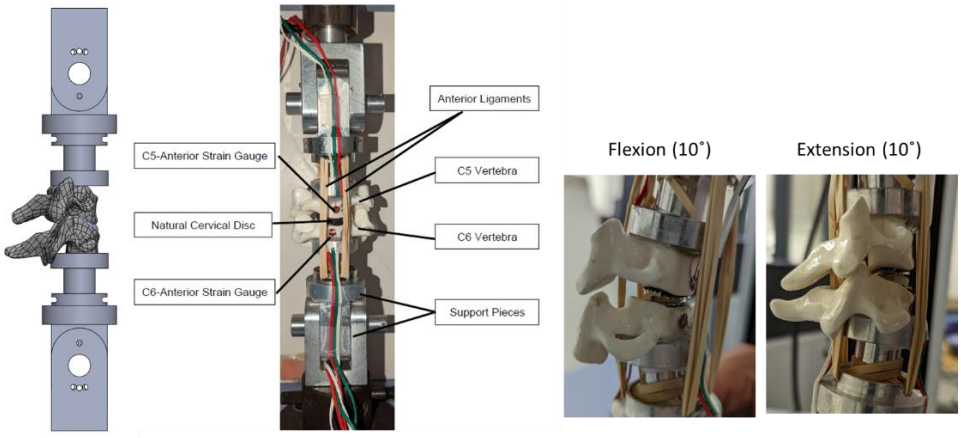

Figure1. Experimental design of cervical disc intact and with arthroplasty (CAD model).

The experimental model was developed based on CAD design, and the system includes the C5 and C6 vertebrae as a composite model, with the ligaments replaced by elastic bands in the posterior and anterior regions. This model allows the possibility to move in extension and flexion up to 10º. Strain gauges (KFG-1-120-D17-11L3M2S) were chosen to measure the strains in the anterior and posterior centers of the vertebral body of C5 and C6 and to evaluate the strains in the vertebrae.

3. Results and conclusions

The difference lies in the higher absolute strain values, which are higher in the natural state of the disc. The prosthetic disc allows the load to be distributed evenly over the outer part of the vertebral body, thus reducing the maximum strain in the sensor region. The prosthesis increases the strains in the posterior region of the vertebra, but this effect is influenced by the position of the prosthesis. This deduction results from the fact that cervical implants, regardless of their overall stiffness properties, redistribute the load over a larger part of the underlying vertebral body [5].

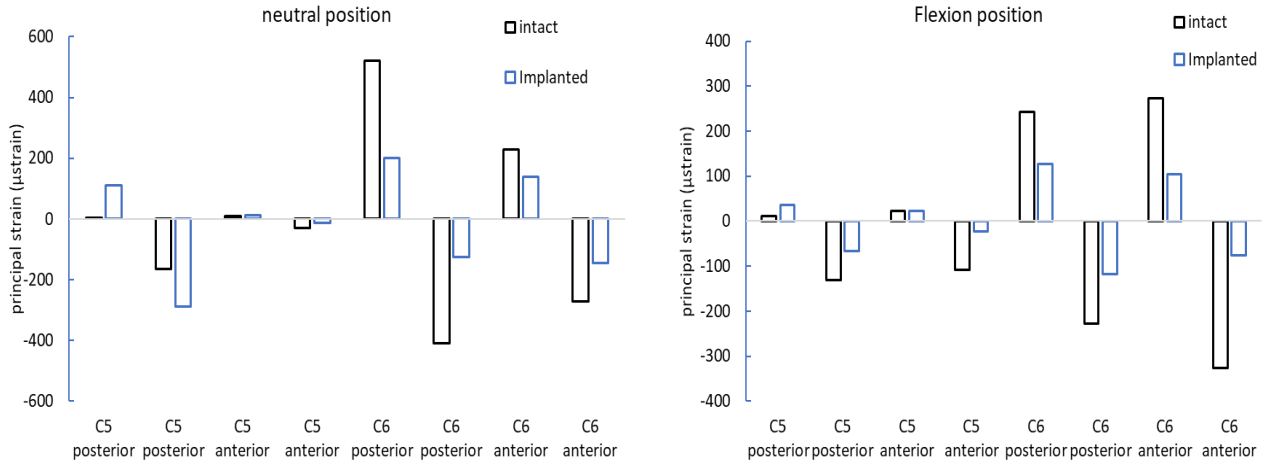

Fig. 1. Maximum and minimum principal strains in the rosettes

4. Acknowledgements

The work was founded by the Pessoa Program (FCT/Campus France)- 2023.09678.CBM.

5. References

[1] M. A. C. Negrelli, R. G. D. E. Oliveira, I. D. D. A. Rocha, A. F. Cristante, R. M. Marcon, and T. E. P. D. E. F. Barros, “Traumatic Injuries of the Cervical Spine: Current Epidemiological Panorama.,” Acta Ortop. Bras., vol. 26, no. 2, pp. 123–126, 2018.

[2] T. F. Fekete and F. Porchet, “Overview of disc arthroplasty-past, present and future,” Acta Neurochir. (Wien)., vol. 152, no. 3, pp. 393–404, 2010.

[3] Wellington, I. J., Kia, C., Coskun, E., Torre, B. B., Antonacci, C. L., Mancini, M. R., Connors, J. P., Esmende, S. M., & Makanji, H. S. (2022). Cervical and Lumbar Disc Arthroplasty: A Review of Current Implant Design and Outcomes. Bioengineering, 9(5), 227

[4] G. Costa, A. Ramos, M. Mesnard, Experimental Study of the Influence of Cervical Disc Mechanical Properties on the Strain Distribution in Adjacent Vertebrae, 2023.

[5] N. B. Bonnheim and T. M. Keaveny, “Load-transfer in the human vertebral body following lumbar total disc arthroplasty: Effects of implant size and stiffness in axial compression and forward flexion.,” JOR spine, vol. 3, no. 1, p. e1078, Mar. 2020.

EuraSEM 6-11 July 2025 ICEM21 Bologna | 21st International Conference on EXPERIMENTAL MECHANICS

NUMERICAL ANALYSIS OF FOUR TYPES OF STAR-SHAPED AUXETIC STRUCTURES BASED ON THE GEOMETRIC PARAMETERS OF THE 2D ARC-STAR-SHAPED STRUCTURE

V. Sinđelić[1], A. Nikolić[1], S. Ćirić Kostić[1], and N. Bogojević[1]
[1] Faculty of Mechanical and Civil Engineering in Kraljevo, University of Kragujevac, Serbia

1. Introduction

Mechanical metamaterials are artificially engineered materials designed to improve the mechanical properties of materials or add new properties of materials. Thanks to additive manufacturing technologies, it is possible to design various structural shapes to achieve new or improved mechanical properties. A special category of mechanical metamaterials includes auxetic materials (the term "auxetic" came from Greek word meaning retracted). A new property that auxetic materials impart to a structure is a negative Poisson's ratio (NPR in the further). Unlike conventional materials, auxetic materials has the ability to retract, under to external loading, as illustrated in Figure 1.

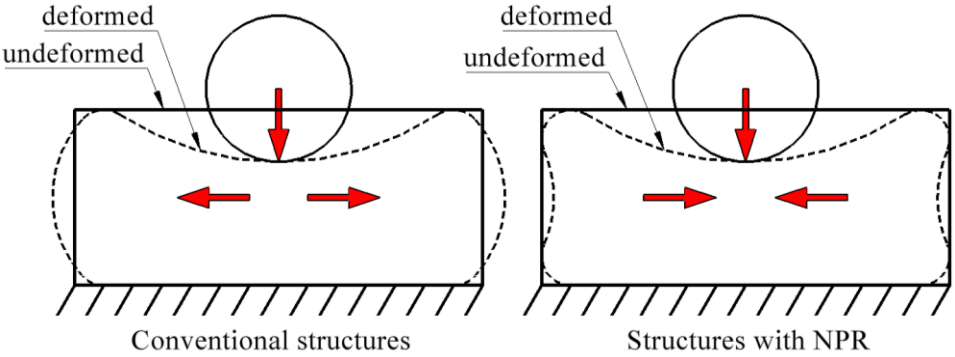

Fig. 1. The difference between conventional materials and materials with NPR [1]

A very popular structure is the Re-entrant honeycomb. This structure retracts in only one direction. By manipulating its geometry, a structure that retracts in both directions was developed and, due to its appearance, it was named the star-shaped structure. In this study, using the Finite Element Method (FEM), we investigated and compared the mechanical properties of four types of re-entrant star-shaped structures.

2. Design and numerical investigation of 2D arc-star-shaped structures

In a previous study published in [2], a redesign of the 2D arc-star-shaped structure (2D-AS) resulted in a new structure called the improved 2D arc-star-shaped structure (*i*2D-AS), which exhibited enhanced mechanical properties due to its geometry. By using the same geometric parameters a new structure called the tangent 2D arc-star-shaped structure (*t*2D-AS) was designed. Its mechanical properties, including relative density ρ_r, Poisson's ratio ν and Young's modulus E_Y, were compared with those of the 2D-AS and *i*2D-AS structures. Additionally, a comparison was made with the traditional star-shaped structure (2D-SS), see Fig.2. The FEM analysis was performed in ANSYS, with boundary conditions set to simulate Periodic Boundary Conditions (PBC).

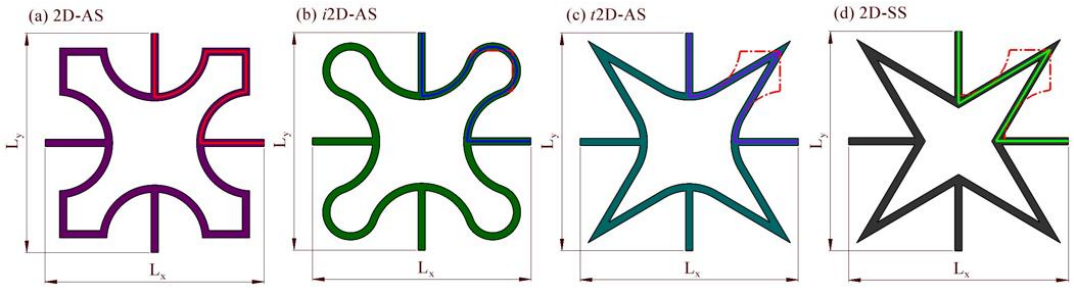

Fig. 2. Four types of 2D star-shaped: (a) 2D-AS [3]; (b) *i*2D-AS [2]; (c) *t*2D-AS; (c) 2D-SS

3. Results and conclusions

Fig.3 show the results of the mechanical properties for all four structures. The *t*2D-AS structure has the lowest values of ρ_r for the parameters given in reference [2-3]. Duo to its arches it was expected that *i*2D-AS would have the best values for Young's modulus, while 2D-SS exhibits the best values for the NPR.

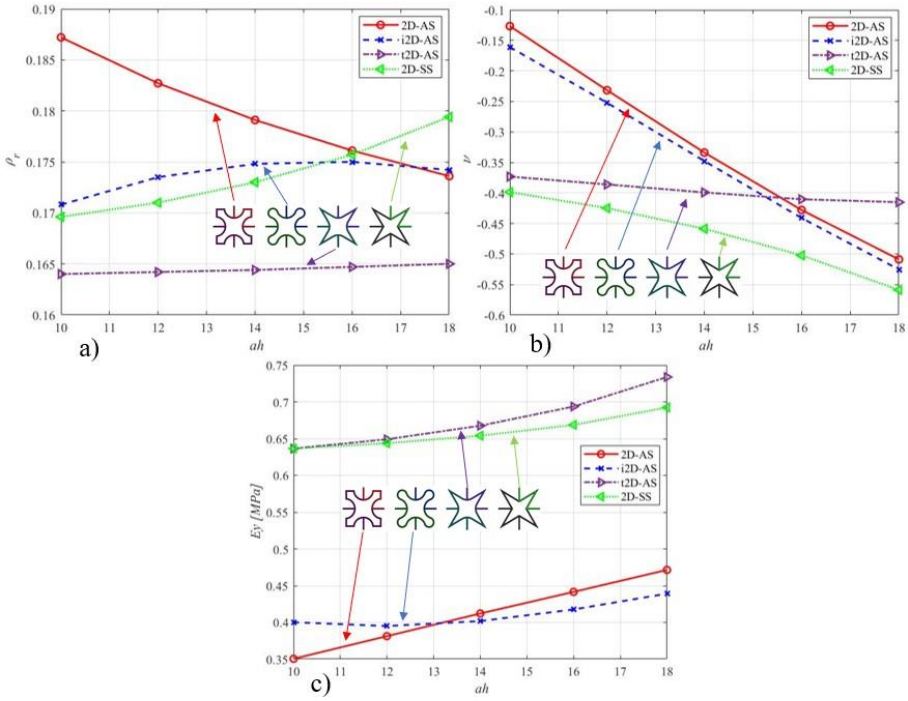

Fig. 3. Results of the mechanical properties of the structures

4. Acknowledgements

This research was supported under grant no. 451-03-68/2022-14/200108 by the Ministry of Education, Science and Technological Development of the Republic of Serbia.

5. References

[1] Sinđelić, V., Nikolić, A., Bogojević, N., Ćirić Kostić, S., Minak, G.: Analytical and numerical analysis of the modified 2D arc-star-shaped structure with negative Poisson's ratio. Engineering Today (2024).

[2] Sinđelić, V., Nikolić, A., Minak, G., Ćirić Kostić, S., Bogojević, N.: An improved 2D arc-star-shaped structure with negative Poisson's ratio: In-plane analysis. Materials Today Communication 36, Art. 107593 (1-12) (2023).

[3] Zhang, Z.Y., Li, J., Liu, H.T., Wang, Y.B.: Novel 2D arc-star-shaped structure with tunable Poisson's ratio and its 3D configurations. Materials Today Communication 30, Art. 103016 (1–13) (2022).

EFFECT OF STRAIN RATE ON COMPRESSIVE PROPERTIES OF HIGH CARBON CHROMIUM BEARING STEEL AND CHROMIUM MOLYBDENUM STEEL

K. Tateyama[1], R Kiya[2], H. Yamada[3] and H. Fujiki[1]
[1] College of Design and Manufacturing Technology, Muroran Institute of Technology, Muroran, Japan
[2] Division of Production Systems Engineering, Muroran Institute of Technology, Muroran, Japan
[3] Department of Mechanical Engineering, National Defense Academy, Yokosuka, Japan

1. Introduction

High carbon chromium bearing and chromium molybdenum steels are widely used in applications that are subject to high-rate loading due to their excellent mechanical properties and wear resistance. To effectively use these materials in such applications, it is essential to understand the stress-strain relationship during high-rate deformation. In general, the high-rate deformation properties of high-strength materials are evaluated for energy and toughness by Charpy impact testing. Therefore, the strain rate dependence of material strength based on the stress-strain relationship during high-rate deformation has been little studied. This is mainly because it is very difficult to experimentally obtain stress-strain data at high strain rates for high-strength materials.

The split Hopkinson pressure bar (SHPB) method is a widely used experimental method for accurately obtaining the stress-strain relationship of materials at high strain rates [1, 2]. The SHPB method uses two elastic bars as sensors and measures the propagation of stress waves passing through a test specimen placed between them, allowing the dynamic stress, strain, and strain rate of a material to be evaluated. However, when testing high-strength materials such as high carbon chromium bearing steel and chromium molybdenum steel, the elastic bar may undergo plastic deformation at the contact interface with the specimen, which may invalidate the basic principle of the SHPB method. To address this issue, it is necessary to fabricate the elastic bar from a material exceeding the yield strength of the specimen. In a previous study [3], the authors successfully developed an SHPB-based impact compression test apparatus that can evaluate high-strength materials using a cemented carbide round bar. In this study, the stress-strain relationship of high-strength materials under high-rate deformation was investigated using this testing apparatus.

2. Materials and methods

High carbon chromium bearing (100Cr6) and chromium molybdenum steels (34CrMo4) were used as specimens. The specimen shape was a cylinder with a diameter of 4 mm and a length of 6 mm, and both end faces were finished with Ra = 0.4 μm and parallelism of 10 μm or less. The quasi-static tests were performed using a universal testing machine (Instron 5566, Illinois Tool Works Inc.) at 298 K with strain rates of 1.0×10^{-3} s^{-1}, 1.0×10^{-2} s^{-1}, and 1.0×10^{-1} s^{-1}. The impact test was performed using the SHPB testing apparatus with strain rates of 1.0×10^{3} s^{-1}. A schematic diagram of the testing apparatus is shown in Fig. 1. The input and output bars were round cemented carbide bars (G2, Silveralloy Co., Ltd.) with a diameter of 20 mm and a length of 500 mm. They had a mass of 2.305 kg and a density of 14700 kg/m^3. The striker was a round bar made of 100Cr6 with a diameter of 20

mm and a length of 150 mm. The stress waves propagating through the input and output bars and the specimen were measured by strain gauges (KSP-1-350-E4, Kyowa Electronic Instruments Co., Ltd.) attached to the input and output bars, respectively. The strain gauges were attached 250 mm from the ends of the input and output bars, respectively. The signal obtained from the strain gauge was passed through a differential amplifier (5307, NF Corporation) and a Wheatstone bridge circuit and recorded on a digital oscilloscope (DL-750, Yokogawa Test & Measurement Corporation).

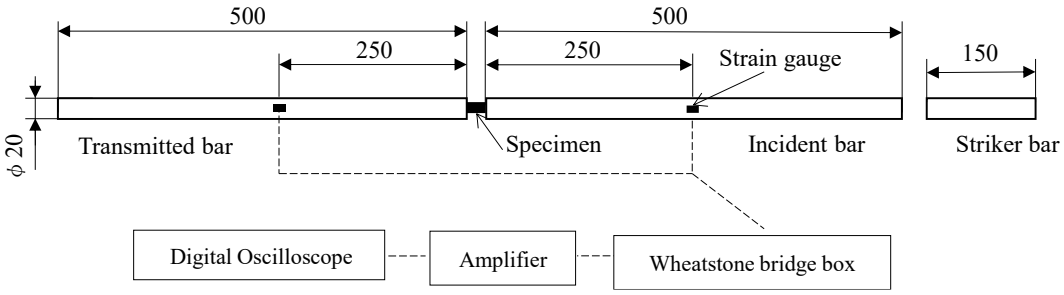

Fig. 1. Schematic diagram of the SHPB testing apparatus

3. Results and conclusions

Figure 2 shows typical stress-strain relationships at each strain rate at 298 K. The sudden drop in the stress-strain relationship in the impact test is due to the end of the stress wave duration and does not indicate fracture. It was found that 100Cr6 has a yield strength of approximately 3000 MPa and exhibits gradual work hardening. In comparison, 34CrMo4 has a yield strength of approximately 2000 MPa and shows a steeper work hardening slope than 100Cr6. An increase in flow stress was observed in the impact test results for both materials compared to the quasi-static tests, revealing that the material strength is depend on the strain rate.

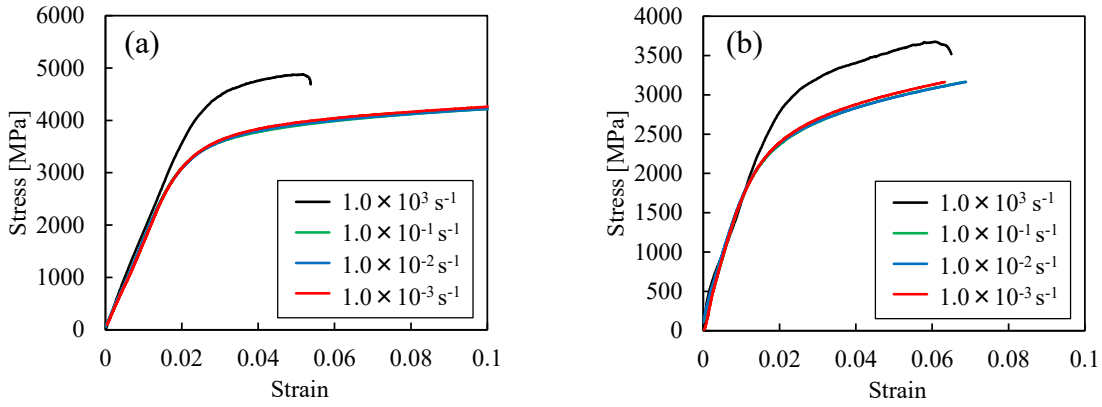

Fig. 2. Typical stress-strain relationships for (a) 100Cr6 and (b) 34CrMo4

4. References

[1] Kolsky H (1949). An investigation of the mechanical properties of materials at very high rates of loading. *Proc Phys Soc B*, **62,** 676700.

[2] Hopkinson B (1914). A method of measuring the pressure produced in the detonation of high explosives or by the impact of bullets. *Proc Royal Soc Lond Ser Containing Papers Math Phys Character* **89,** 411–413.

[3] K. Tateyama, H. Yamada and H. Kobayashi (2024). Effects of strain rate and temperature on plastic deformation behavior of molybdenum-based high-speed tool steel HS-6-5-2. *Journal of Dynamic Behavior of Materials*. In press.

EVALUATION OF THE RELATIONSHIP BETWEEN FATIGUE FRACTURE SURFACES IN ROTATING SHAFTS AND ACOUSTIC EMISSION GENERATION BEHAVIOR USING A NON-CONTACT AE MEASUREMENT SYSTEM

T.Matsuo[1], and Y. Abe[1]
[1] Department of Mechanical Engineering, Meiji University, Japan

1. Introduction

In recent years, ensuring high safety in aging industrial machinery and transportation equipment has become crucial and maintenance and management technologies for various machines have become increasingly important. Long-term operation of equipment causes component fatigue, which can lead to critical failures and accidents. Therefore, technologies that enable non-destructive inspection and safety evaluation are in demand. Currently, non-destructive inspections are primarily performed during equipment shutdowns. However, unexpected early failures often occur, making it difficult to determine optimal inspection intervals. This has created a demand for continuous monitoring methods capable of detecting structural defects at an early stage. Acoustic emission (AE) is a nondestructive monitoring technique that detects elastic waves generated by the release of strain energy during the initiation and propagation of microcracks in a material [1]. Conventional AE measurement uses piezoelectric sensors mounted on the surface of the test object. However, it is difficult to mount sensors on working parts such as rotating shafts that are prone to damage. Conventional methods involved placing sensors on bearing sections, but friction noise made it difficult to extract specific damage-related signals in real time. To overcome this problem, non-contact AE measurement techniques have been proposed [2]. Previous studies developed a non-contact AE measurement system using air-coupled ultrasonic sensor and demonstrated its effectiveness in detecting AE during rotating bending fatigue tests. These studies suggested that AE during such tests is primarily caused by contact between crack surfaces. However, AE was only detectable just prior to fracture.

In this study, the developed non-contact AE measurement system was used to monitor AE during rotating bending fatigue tests with various loads, and the relationship between the fracture surface features and AE parameters was evaluated. Then, the applicability of the AE method in monitoring fatigue damage of rotating shafts was investigated.

2. Non-contact AE measurement system and experimental setup

Figure 1 shows the experimental setup. This system causes fatigue damage to the specimen by four-point bending on the rotary shaft. The specimen is fixed with a collet and rotated at 700 rpm under a load. The AE monitoring system consisted of an air-coupled ultrasonic sensor (the ultran group: NCG100-D25, Resonant frequency: 100 kHz) and the digitizer with the noise reduction function [3]. A sensor is placed 5 mm above the specimen to detect AE, which is amplified (40 dB) and recorded on a PC. The specimens were 12 mm diameter aluminum alloy bars (JIS A2024) with a V-notch in the center all around the circumference. The results were compared across four different loading conditions: 44.1, 58.9, 83.4 and 93.2 N.

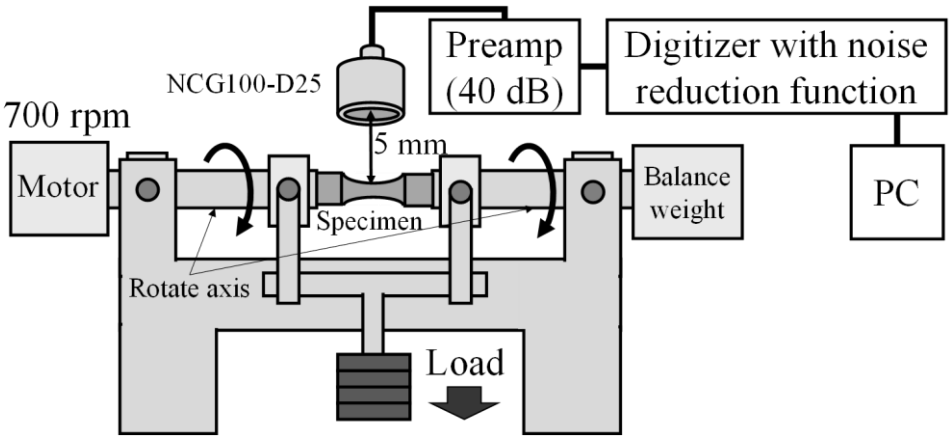

Fig.1. Experimental setup for monitoring AE signals during rotary bending fatigue test

3. Results and conclusions

Figure 2 shows fracture surface of the specimen with different load. Three types of fracture surface were identified: (a) final fracture surface, (b) fatigue fracture surface where striations were observed, and (c) wear surface where crack surface contact occurred. Fracture surfaces of the specimens subjected to the highest load of 93.2 N showed almost no wear surfaces, and the surfaces were almost smooth. However, the wear area increased as the load decreased, and approximately 60% of the wear surface was observed on the fracture surface of the specimen with the lowest load of 44.1 N. Table 1 shows a comparison of the number of cycles at each load and rupture, the total number of AE events, and the wear area. A correlation was found between the size of the wear area and the total number of AE events. This suggests that assessing fatigue damage in rotating shafts through AE monitoring with the developed system is influenced by the extent of wear on the fatigue fracture surface.

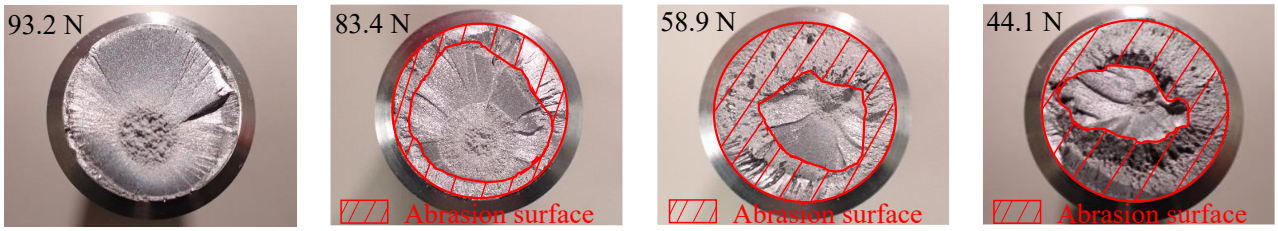

Fig.2. Fracture surface at various loads with V-notched specimens

Table 1. The monitoring results for each load

Load [N]	93.2	83.4	58.9	44.1
Cycle number [$\times 10^4$]	3.6	15.7	53.9	56.7
Abrasion area [%]	3	25	55	60
Total number of AE events	1	278	844	986

4. References

[1] Y.Mizutani ed. (2016). *Practical Acoustic Emission Testing*, Springer,
[2] T.Matsuo and D.Hatanaka (2019). Development of Non-Contact Fatigue Crack Propagation Monitoring Method, *Engin. Tran.*, **67**, 185-198.
[3] T.Matsuo and H.Cho (2012). Development of AE Monitoring System with Noise Reduction Function by Spectral Subtraction, *Mater. Tran.*, **53**, 342-348.

EXPERIMENTAL VERIFICATION OF THE FATIGUE STRENGTH OF A LOCOMOTIVE COMPOSITE DRIVE SHAFT

J. Chvojan[1] and J. Vaclavik[1]
[1] Research and Testing Institute in Pilsen, Pilsen, Czechia

1. Introduction

This paper contains a description of the performance of static and fatigue tests of the composite transmission shaft for locomotive, which is intended for torque transmission in traction bogie. The shaft is manufactured from glass fibre reinforced plastic composite. The aim is to assess the static and fatigue resistance of the composite shaft, to determine the values and stress distribution on the structure, the basis for the evaluation of fatigue life.

The verification of the drive was performed by a dynamic test under torque loading without rotation according to the test load block of 10 cycles, respecting the course of torques according to locomotive operation and its individual phases - starting, running at steady speed and braking, repeated to the total required number of cycles according to service life.

The data for the test were derived from the calculation of the tach gram of the train pulled by locomotive on the real with the two cities. Based on the given data of the distribution of moments and the length of the traveled distance, a block of 10 loading cycles is designed in the table, which will be repeated during the test until the required service life of 10 million cycles. The total number of cycles is divided into blocks of 6 and 2x 2 million cycles with increasing magnitude of forces with a multiplication factor of 1.2 and 1.4 in accordance with UIC 514-4. For the testing rig the special basic fixture for torsional moment loading was developed and was used for all tests for all versions of composite shaft.

2. Description of the testing rig and used sensor and equipment

The testing device for torque implementation using one force on the arm of the length 500 mm was used. The hydraulic servo-operated cylinder Schenck 630kN was used as the force acting from vertical position. The set of the whole testing rig is documented in Fig. 1. Two lower Schenck frames and one steel cube were used as the support for the test.

Five strain gauge rectangular rosettes TML FAER - 25R-35-S6EL were glued using the HBM adhesive to the upper line of the shaft body, see Fig. 2. Three of them will be on the composite glass epoxy middle part (R1 to R3) and two of them on the carbon-epoxy outer parts (R4, R5). One single strain gauge HBM 6LY11 (gauge length 6 mm) was positioned on the steel part in the place of stress concentration of the larger flange. The individual strain gauges of the rosettes (separated by the angle 45°) were marked as R_{ia}, R_{ib}, R_{ic}, in counterclockwise direction. The evaluated angle of the main principal stress is performed always from the strain gauge R_{ia}. Two inductive LVDT sensors were used for the measurement of the shaft twist in tangential direction (s1, s2). This will be performed using four small charcoals, glued to the composite body in one line. Two of them will be used for the

measurement of the twist of the composite body. One inductive LVDT sensor was used for the measurement of the shaft dimension in axial direction – was positioned on rear flange side.

Fig. 1. Test rig with the composite shaft

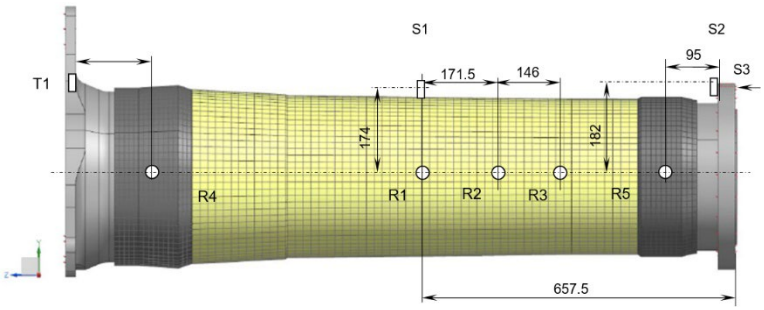

Fig. 2. Position of the sensors

During the experiments were evaluated the servo hydraulic cylinder force F, displacement (stroke) Z, torsional moment Mk, twist of the shaft using inductive sensors S1 (value y1) and S2 (value y2), axial shrinkage of the shaft using inductive sensor S3 (value x), strains at individual strain gauges of each rosettes ε R_{ia}, ε R_{ib}, ε R_{ic}, strains in principal directions ε R_{imax}, ε R_{imin}, the angle of the maximum principal direction measured from the rosette R_{ia}, strains in ±45°directions and temperature during fatigue test using manual infrared thermometer.

A static test was performed, static torsion using the comprehensive force F was performed in steps of 10 kNm up to 80 kNm and back to zero. At each step the time prolongation was 120 s. This test was three times repeated.

Fatigue was performed according given loading blocks comprising from 10 cycles, see Fig. 3 given in loading forces. A total of 1 million blocks obtained 10 million cycles was performed. The loading frequency was 2 Hz.

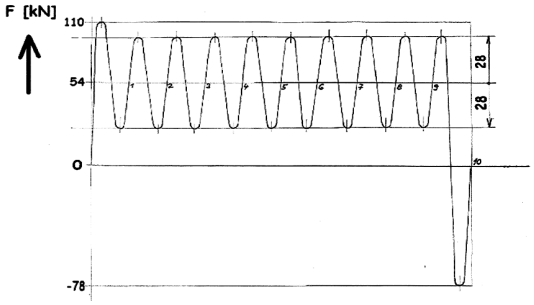

Fig. 3. Loading block

After the finishing of the dynamic test the static test was repeated – only one loading cycle.

3. Results and conclusions

During the static tests no substantial residual strains were observed. Short records of strains, displacement and loading force were measured during the fatigue test every 4 hours and recorded. The extreme values of strains, displacement and loading force were evaluated from these records. The time histories at the test beginning and at the test end are visualized in Fig. 4 to Fig. 5. No substantial changes occurred on the strain time histories as signal amplitude concerns. The mean value of the signals however was shifted.

The fatigue test was performed according to the design loading cycles. Summary 1×10^6 loading blocks was performed which corresponds to 10 000 000 cycles without destruction of the shaft. Some shift of the pre-stressed strain value was observed at the beginning of the test after 200 000 cycles at rosettes R4 and R5, which are situated on the black CFRP rings at the composite ends; it was not measured on the other rosettes on the composite surface.

Short delamination on the composite surface had occurred after say 5 million cycles, but it has not been observed their substantial extension during the last period of the test. The delamination was observed especially on the loaded side of the composite shaft. After the dynamic test the static test was repeated – measured values were in coincidence with those measured before the fatigue test.

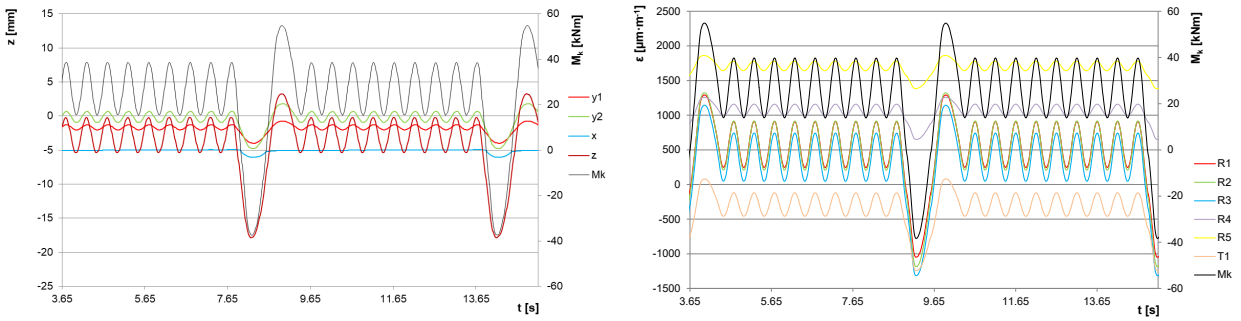

Fig. 4. Comparison of the displacement, actuator stroke, torsion at the beginning and end of tests

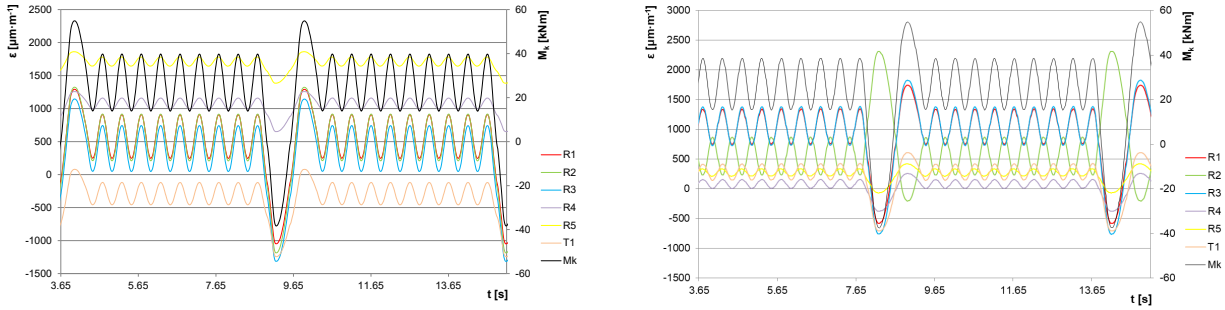

Fig. 5. Comparison of the principal strains and torsional moment at the beginning and end of tests

4. Acknowledgements

The research presented in this paper has received funding from National Centre of Competence of Jozef Bozek by Technological Agency of the Czech Republic of the Czech Ministry of Industry and Trade under the grant agreement No. TN 0100 0026.

5. References

[1] J. Vaclavik (2020). Project on the setup of a test stand and the investigated parameters of a composite shaft, VYZ-VZ-54/20/015, Research report, VZÚ Plzen, 2020.

6-11 July 2025 ICEM21 Bologna
21st International Conference on EXPERIMENTAL MECHANICS

EFFECT OF STRAIN RATE ON THE PULLOUT RESISTANCE OF GEOGRIDS

Harshal Verma[1], Bappaditya Manna[1], Partha Narayan Mishra[2], David Williams[2]
[1] Department of Civil Engineering, Indian Institute of Technology Delhi, India
[2] School of Civil Engineering, The University of Queensland, Australia

1. Introduction

The geogrid backfill interaction is vital for safe and effective design of reinforced structures such as reinforced walls, slopes and bridge abutments [1]. The pullout resistance depends on two major factors, bearing resistance and frictional resistance. Frictional resistance mainly depends on the type of backfill and geogrids but bearing resistance depends on several factors including confining pressure, the geometric characteristics of the geogrid, the ratio between the mean grain size of the backfill material and the size of the geogrid apertures [2]. The effect of strain rate on geogrid pullout behavior is a fundamental aspect of understanding the performance of geogrid-reinforced soil systems under different loading conditions. Strain rate influences the interaction mechanisms at the geogrid-soil interface, significantly affecting the pullout resistance

2. Materials and methods

The present study utilizes locally available sand as backfill material. The geotechnical properties of sand are shown in Table 1. The Specific gravity, grain size, minimum dry density and maximum dry density were investigated as per the ASTM standards. The shear behaviour was investigated based on direct shear test as per ASTM D3080/D3080M−11 [3] with displacement rate 0.01 mm/min. The biaxial PET geogrid with given strength od 60×40 kN/m was used for pullout test. The results of grain size analysis and tensile tests on geogrids are shown in Figure 1. The sand was characcterised as poorly graded sand.

Material properties	Value
G_s (g/cc)	2.6
$\gamma_{d(min)}$ (kN/m^3)	12.3
$\gamma_{d(max)}$ (kN/m^3)	16.8
k (cm/s)	0.003
φ^{peak} (°)	41
$\varphi^{residual}$ (°)	34

Table 1. Geotechnical properties of sand

The large scale pullout appearatus was used, the tests were performed as per ASTM [4]. Same appearatus has been previously used by Agarwal et al. [5], Pant et al. [6], Pant et al. [7] and Bansal et al. [8]. The pullout behaviour at three pullout rate 0.1 mm/min, 1 mm/min and 10 mm/min was investigated at normal stress of 50 kPa. A pneumatic compressor with air bag was used for applying the normal stress. The effevtive embedded length of geogrid was 600 mm with 300 mm width. The schematic of pullout appearatus is shown in Figure 2.

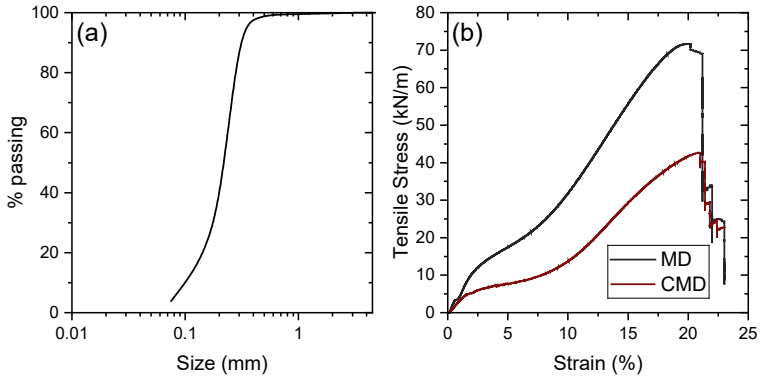

Fig. 1. (a) Grain size distribution of sand (b) Tensile test results of geogrid

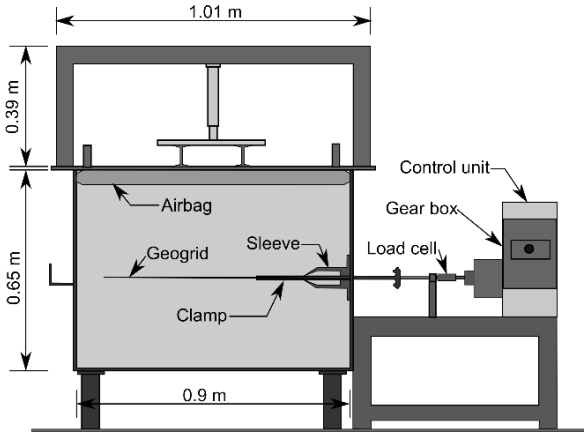

Fig. 2. Schematic representation of pullout apparatus

3. Results and conclusions

The pullout results of tests at different pullout rates are shown in Figure 3. Higher strain rates tend to increase the pullout resistance of geogrids due to the strain-rate dependency of soil and geogrid-soil interaction mechanisms.

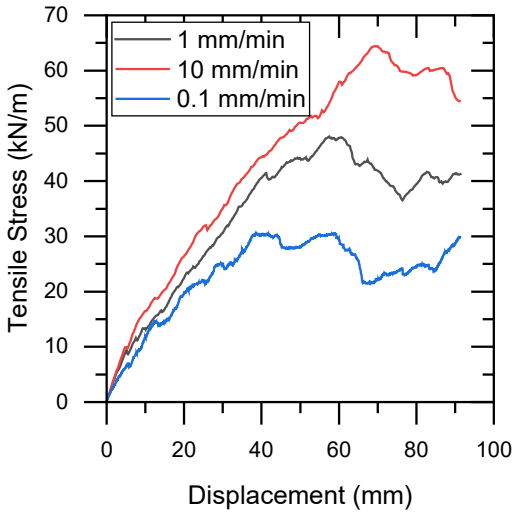

Fig. 3. Geogrid pullout results for different strain rates

At faster deformation rates, the soil surrounding the geogrid exhibits greater stiffness and less time for particle rearrangement, leading to enhanced frictional and interlocking resistance along the geogrid-soil interface. This phenomenon is particularly significant in coarse-grained soils, where interlocking plays a dominant role. Understanding these effects is essential for designing reinforced soil systems that account for both short-term dynamic loads and long-term creep behaviour.

Very high strain rates may introduce dynamic effects, such as localized soil failure, abrupt shear zone formation, or inconsistent stress distribution along the geogrid. At very low strain rates, time-dependent phenomena such as creep in both the soil and geogrid can dominate, reducing the pullout resistance over time. This knowledge is critical for designing durable geogrid-reinforced structures that perform reliably under both short-term and long-term stresses.

4. Acknowledgements

The research presented in this paper has received funding from the IIT Delhi-University of Queensland Research Academy.

5. References

[1] Palmeira, E.M (2009). *Soil–geosynthetic interaction: Modelling and analysis.* Geotextiles and Geomembranes. **27**(5): p. 368-390. https://doi.org/10.1016/j.geotexmem.2009.03.003

[2] Lopes, M.J. and M.L. Lopes (1999).*Soil-Geosynthetic Interaction - Influence of Soil Particle Size and Geosynthetic Structure.* Geosynthetics International. **6**(4): p. 261-282. https://doi.org/10.1680/gein.6.0153

[3] ASTM D3080/D3080M−11, (2012). Standard Test Method for Direct Shear Test of Soils Under Consolidated Drained Conditions, D3080/D3080M − 11, ASTM International. https://doi.org/10.1520/D3080_D3080M-11

[4] ASTM, (2021). Standard Test Method for Measuring Geosynthetic Pullout Resistance in Soil, D6706-01, ASTM International. https://doi.org/10.1520/D6706-01R21

[5] Agarwal, A., G.V. Ramana, M. Datta, N.K. Soni, and R. Satyakam (2023). *Pullout behaviour of polymeric strips embedded in mixed recycled aggregate (MRA) from construction & demolition (C&D) waste – Effect of type of fill and compaction.* Geotextiles and Geomembranes. **51**(3): p. 405-417. https://doi.org/10.1016/j.geotexmem.2023.01.004

[6] Pant, A., M. Datta, G.V. Ramana, and D. Bansal (2019) *Measurement of role of transverse and longitudinal members on pullout resistance of PET geogrid.* Measurement. **148**: p. 106944. https://doi.org/10.1016/j.measurement.2019.106944

[7] Pant, A., G.V. Ramana, M. Datta, and S.K. Gupta (2019) *Coal combustion residue as structural fill material for reinforced soil structures.* Journal of Cleaner Production. **232**: p. 417-426. https://doi.org/10.1016/j.jclepro.2019.05.354

[8] Bansal, D., G.V. Ramana, M. Datta, and G. Gupta (2023) *Characterization of MSW incineration bottom ash for use as structural fill in reinforced soil structures: Geoenvironmental, geotechnical and economical assessment.* Waste Management. **168**: p. 344-353. https://doi.org/10.1016/j.wasman.2023.06.024

FRACTURE TOUGHNESS DETERMINATION THROUGH RESISTANCE CURVE: A COMPARISON BETWEEN ASTM E1820 AND ISO 12135 STANDARDS

G. Coêlho[1], A. Guimarães[1], A. Silva[1], M. Dos Santos[1]
[1] Department of Mechanical Engineering, Federal University of Campina Grande, Campina Grande, Brazil

1. Introduction

Typically, structural steels exhibit elastic–plastic behavior and high toughness, requiring the assessment of their fracture toughness by deriving the materials' resistance curve. Worldwide commonly accepted standards for fracture toughness measurement are the ASTM 1820 [1] and the ISO 12135 [2] standards. Despite existing for quite some time, those standards have produced differences in determining the fracture toughness [3–6], with blunting (or construction) line slope, exclusion lines' distance, and fitting equations pointed out as the main reasons for the found differences. The main purpose of this study was to assess the differences in the estimation of the ASTM 1820 [1] and ISO 12135 [2] fracture toughness standards.

2. Materials and methods

ASTM A516 Gr.70 is a structural steel recommended for constructing pressure vessels with applications in moderate-to-low temperatures, and it is supplied as hot-rolled with no post-heat treatment normalization for plates up to 25 mm thickness. The experimental analysis consisted of metallographic analysis for microstructural characterization, tensile tests, and fracture toughness tests at room temperature.

3. Results and conclusions

ASTM E1820 [1] and ISO 12135 [2] have yielded different results for initiation CTOD regardless of notch orientation to the rolling direction and despite both standards using the same approach based on the interception of a 0.2 mm offset line with the same slope as the blunting line to the fitted resistance curve. The slope of the blunting line is precisely the justification for the different estimated initiation CTOD values. Since the ISO 12135 [2] blunting line exhibits a higher slope for the present material than the ASTM E1820 [1] blunting line, as observed in Figure 1(a), the initiation CTOD values estimated by the former are lower than the ones estimated by the latter, which has been an issue pointed out by some authors [3,4,6]. The estimated blunting lines for the ASTM A516 Gr.70 steel are shown in Figure 1(a) and were based on the initiation CTOD values estimated by the stretch zone width. This reinforces the necessity of a blunting line estimation based on the materials' deformation behavior since the slope also depends on the material's work hardening coefficient.

The fitted resistance curves are shown in Figure 1(b)-(d) for each standard fitting equation to allow their comparison. It can be noticed that both ASTM E1820 [1] and ISO 12135 [2] curves are very close for $\Delta a < 1$ mm and, in the current study, have almost no influence on the predicted initiation

fracture toughness values. This is also corroborated by the close mean values estimated by the width of the stretch zone.

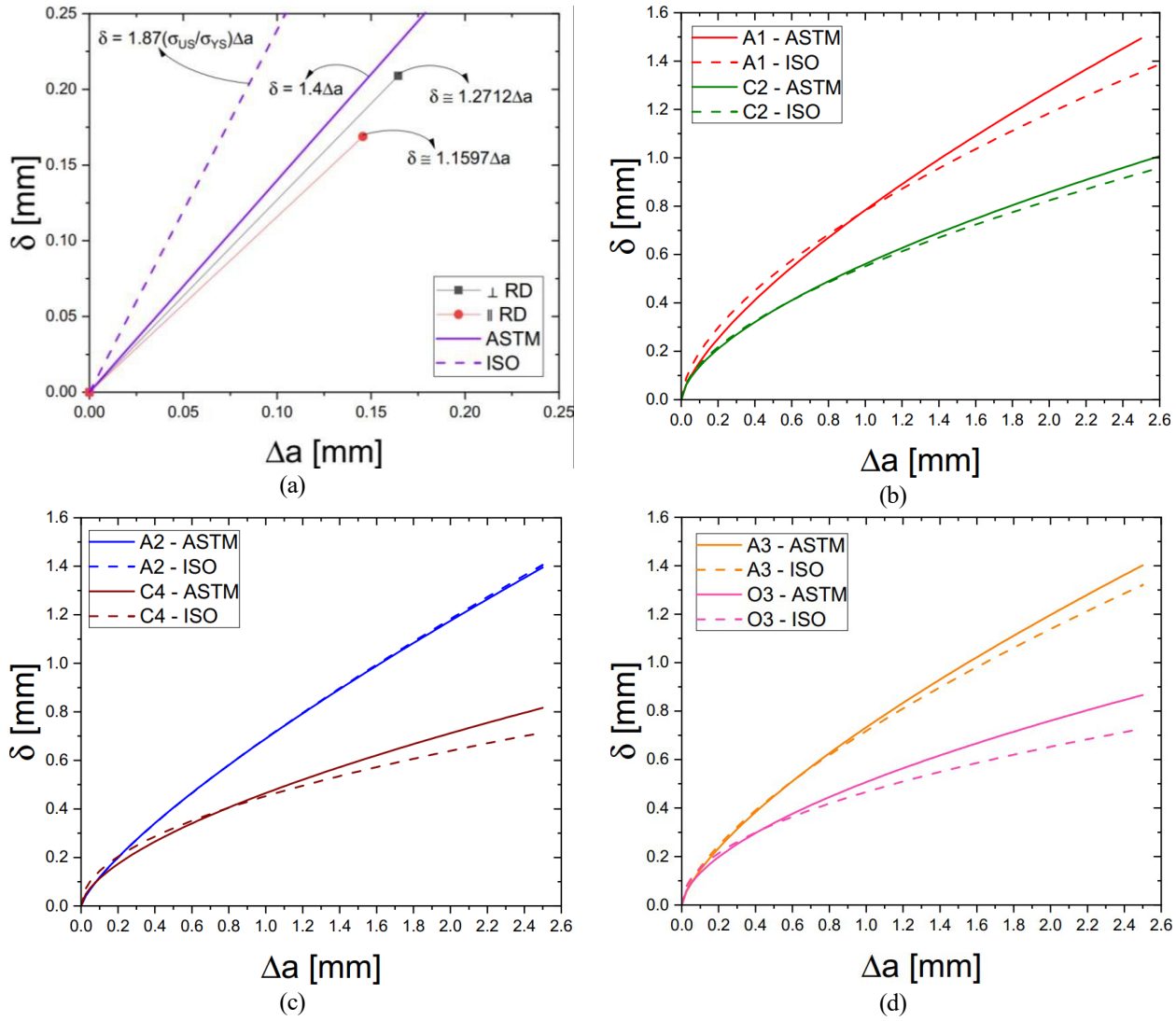

Fig. 1. Comparison between blunting lines and fitted resistance curves according to the ASTM E1820 and ISO 12135. (a) Blunting lines and fitted resistance curves for (b) A1 and C2; (c) A2 and C4; and (d) A3 and O3 specimens.

In conclusion, the initiation fracture toughness estimated by the ASTM E1820 and ISO 12135 standards led to different results, even considering the same orientation, and the values obtained with ISO 12135 were lower than the ones obtained by ASTM E1820. The difference is mainly attributed to the blunting line slope used on each standard. Regardless of the adopted standard, a concerning overestimation of the fracture initiation values was observed when compared to the initiation value estimated by the stretch zone measurement, which suggests the zone's dimension as a more real fracture toughness estimator.

4. Acknowledgements

This research was funded by the Brazilian National Council for Scientific and Technological Development (CNPq): grant number 408131/2018-7, and the Coordination for the Improvement of Higher Education Personnel (CAPES). The authors also would like to thank the Fracture, Fatigue and

Structural Integrity Research Group (NAFFIE) and the Laboratory of Vibrations and Instrumentation (LVI) for the support.

5. References

[1] ASTM, Standard test method for measurement of fracture toughness, (2022) 65. https://doi.org/10.1520/E1820-22E01.

[2] ISO, Metallic materials - Unified method of test for the determination of quasistatic fracture toughness, (2021) 98.

[3] J.D. Landes, Evaluation of the ISO J initiation procedure using the EURO fracture toughness data set, Int J Fract 145 (2007) 285–297. https://doi.org/10.1007/s10704-007-9118-x.

[4] K.S. Arora, H.W. Viehrig, Evaluation of the ASTM and ISO J initiation procedures by applying the unloading compliance technique to reactor pressure vessel steels, J Test Eval 39 (2011) 1. https://doi.org/10.1520/JTE103405.

[5] H.K. Khandelwal, R.N. Singh, J.K. Chakravartty, Fracture-toughness evaluation of solution heat-treated Zr-2.5 Nb alloys as per ASTM and ISO standards, J Test Eval 44 (2016) 1542– 1557. https://doi.org/10.1520/JTE20140329.

[6] X. Li, Z. Ding, C. Liu, S. Bao, Z. Gao, Evaluation and comparison of fracture toughness for metallic materials in different conditions by ASTM and ISO standards, International Journal of Pressure Vessels and Piping 187 (2020) 104189. https://doi.org/10.1016/j.ijpvp.2020.104189.

EFFECT OF CNF STRING ON TENSILE STRENGTH OF BIO-DEGRADABLE PARTS FABRICATED IN FUSED FILAMENT FABRICATION

T.Tateno[1], A. Nishida[2], Y. Kiminami[2]
[1] Department of Mechanical Engineering Informatics, Meiji University, Kanagawa, Japan
[2] Graduate School of Science and Technology, Meiji University, Kanagawa, Japan

1. Introduction

Additive Manufacturing (AM) is attracting attention as a manufacturing method that creates new product value because it has a high degree of freedom in design and an advantage in small-volume production. Fused Filament Fabrication (FFF) is one of the material extrusion-type AM, which is a method that adds material while melting a filament of resin material with heat. It has a simple structure and low equipment cost, so it is widely used as a modeling method in home and small business. However, since the material is limited to resin, there are problems in using it for mechanical parts that require high strength. To address this issue, some FFF machines were developed to treat a composite material of CFRP continuous fibers and resin, and some machines are on the market.

On the other hand, as interest in environmentally conscious product design, biodegradable materials have become an important topic. PLA is a thermoplastic resin often used in FFF and has biodegradable property since it is made from plants such as corn. Therefore, authors have developed a system [1] that uses FFF with a bio-degradable composite material using PLA as a matrix material and natural fibers such as cotton and linen as reinforcement. The composite was formed into a filament shape that can be printed using FFF. Additionally, as a new biodegradable and strong material, Cellulose Nanofiber (CNF) was focused on[2].

In this research, a composite material using PLA and CNF string was formed into filaments shape. By using the filament, rectangular shape test pieces were fabricated with FFF. Furthermore, tensile tests of these test pieces were conducted and the effect of CNF string on strength was evaluated.

2. Fabrication of Test piece and Experiment

Test pieces for tensile testing were fabricated with FFF using a composite filament of CNF and PLA. The manufacturing procedure is as follows. First, CNF aqueous solution is dried on a glass plate for three days to form a solid sheet. In this state, there are many air bubbles in the solid material. Second, it is soaked in water for 5 minutes and dried again. This process eliminates most air bubbles. Third, it is cut into 1mm width. This long and thin sheet is called CNF String. Fourth, a composite material filament is made by combining the CNF String and PLA. The filament forming method has been developed in their previous research. Finally, Test pieces are fabricated in FFF using the filament.

According to the above procedure, test pieces were made with two types of CNF composite filaments. One type contains one CNF string in the filament, and another contains five strings. Five test pieces were made with each type of filament. The test piece size was 80×11.2×0.9 mm (nominal dimensions). The tensile test was conducted with the two types of composite filament and the PLA filament without CNF for comparing.

3. Results and conclusions

Figure 1 shows that stress-strain curves of five tests for each type of filaments. In the region of small strain, there is a linear characteristic in all types of filaments. On the other hand, the breaking conditions were different. The test pieces of CNF string composite broke suddenly, whereas test pieces of PLA broke after being stretched significantly. It is thought that the test piece was broken by the impact of the CNF string breaking. Comparing the maximum strength, the test pieces using five strings composite showed the highest tendency, which means the CNF string reinforces the PLA matrix. On the other hand, the maximum strength of test pieces containing one string was similar to that of PLA. This seems to be due to the low composite rate.

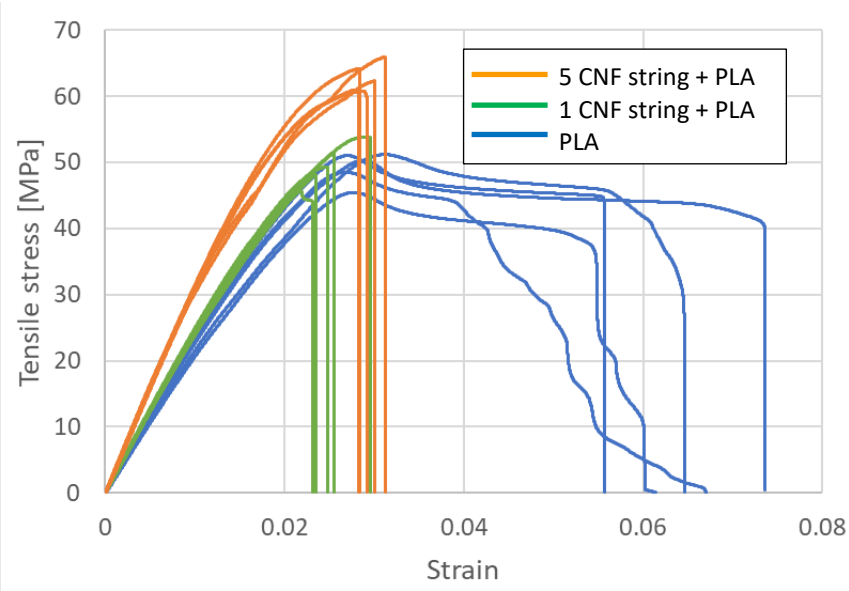

Fig.1 Stress-strain curves of test pieces fabricated with FFF

5. References

[1] Y.Yaguchi, K.Takeuchi, T.Waragai and T.Tateno (2020). Durability Evaluation of an Additive Manufactured Biodegradable Composite with Continuous Natural Fiber in Various Conditions Reproducing Usage Environment, *Int. J. of Automation Technology*, **14**, 6, 959-965.

[2] T.Tateno (2024). Environmentally Conscious Light-Weight Design and Fabrication with Continuous Cellulose Nanofiber String in Additive Manufacturing, *Proceedings of EcoDesign 2023 International Symposium*, #P3-2.

KINEMATIC ANALYSIS OF A 3-BAR MECHANISM FOR GMAW WELDING IN THE FLAT POSITION (G1)

***S. Cacpata*[1]**
[1] *Faculty of Mechanical Engineering, Escuela Politécnica Nacional EPN*

1. Introduction

A mechanism relies on linear and rotary motion that can be applied in the field of automation, requiring the development of a kinematic system. Ordaz et al. [1] propose a mechanical lever system driven by a linear actuator, simplifying control and improving functionality. This design allows for simulating the flexion and extension of fingers using mathematical relationships based on exponential and linear functions [2]. On the other hand, Ramírez and Rubiano [3] developed a mathematical model to solve direct and inverse kinematics problems using homogeneous transformation matrices and Denavit-Hartenberg parameters. Methods such as genetic algorithms, neural networks, and radial functions have improved precision, although inverse kinematics remains challenging due to multiple configurations and transcendental equations. The current approach seeks programmable and automatable models, addressing challenges such as accumulated errors and multiple configurations [4]. Cardoso et al. [5] validate a kinematic model through an experimental platform with microcontrollers, analyzing load capacity and employing methodologies like homogeneous transformation matrices and the Denavit-Hartenberg convention to describe robot configurations. They detail procedures to calculate positions, velocities, and orientations using matrix operations and geometric techniques, validating the model with simulations and physical tests. This highlights its applicability in welding, packaging, and painting processes [6]. Finally, Bamdad et al. [7] analyze hybrid manipulators suspended by cables, emphasizing their load capacity, large workspace, and cost-effective construction. Although they face limitations in the inclination of the actuator's end, hybrid systems combining serial and parallel manipulators are proposed to overcome these restrictions. Dynamic models developed using Newton-Euler and Lagrange methods allow precise control of position and orientation, demonstrating significant improvements in performance and flexibility through simulations [8].

2. Materials and methods

This study analyzes a 3-bar mechanism, beginning with an evaluation of its degrees of freedom to assess its mobility. The mechanism possesses two degrees of freedom. For the force analysis, the system motion matrix is explicitly determined. The direct kinematic solution defines the final position of the robot, taking into account homogeneous transformation matrices based on the Denavit-Hartenberg convention. The Ai matrix is a 4x4 array that contains the relative position and orientation information of the reference system associated with the manipulator iii-link in relation to the i−1 connection system. This matrix describes the position and orientation of the coordinate system S1 of the robot relative to S0. If S0 is located at the axis of the manipulator and S1 at the end of a link, the matrix characterizes the position of S1 in relation to the fixed coordinate system of the robot. The AnA_nAn matrix, where nnn is the degree of freedom, represents the final position of the manipulator relative to the reference system. This matrix, often referred to as T, is expressed through mathematical equations. Analytical methods are applied to determine endpoint values based on angular parameters, producing the desired results.

$$P_x = 0,30226\cos(\theta_1)\cos(\theta_2) + 0,285\cos(\theta_1)\cos(\theta_2)\cos(\theta_3) - 0,285\cos(\theta_1)\sin(\theta_2)\sin(\theta_3)$$

$$P_y = 0,30226\cos(\theta_2)\sin(\theta_1) + 0,285\cos(\theta_2)\cos(\theta_3)\sin(\theta_1) - 0,285\sin(\theta_1)\sin(\theta_2)\sin(\theta_3)$$

$$P_z = 0,30226\sin(\theta_2) + 0,285\cos(\theta_2)\sin(\theta_3) + 0,285\cos(\theta_3)\sin(\theta_2) + 0,28616$$

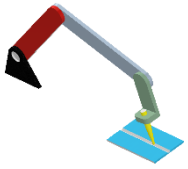

Fig 1. Assembly for motion analysis (Inventor)

Fig. 1 shows the simplified mechanism modeled in Inventor for their simulation.

3. Results and conclusions

The results for the position and velocity regarding the equations problem in Matlab and Inventor.

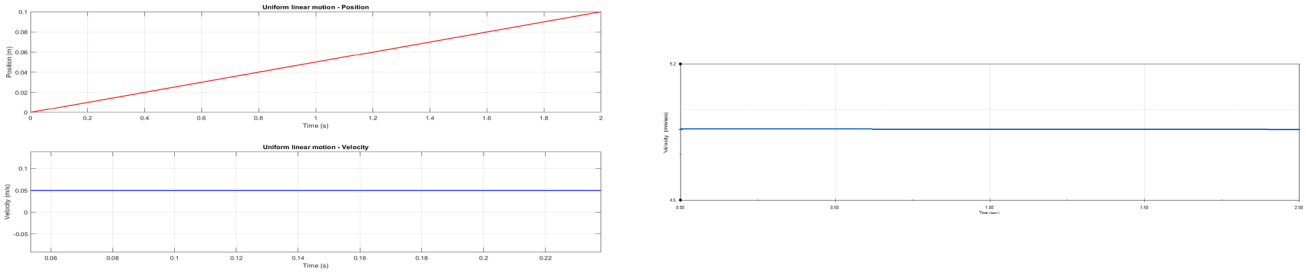

Fig 2. Results from motion analysis in MATLAB anda inventor

The results in Fig 2 show accurate motion analysis, illustrating a welding bead displacement of 100 mm at a constant velocity of 0.05 m/s. This is analyzed from the GMAW wire feed speed and the steady movement of the welding handle at approximately 300 m/min for flat plates. With constant speed, acceleration is zero in the graphs, as the movement is velocity-controlled. In the graphs generated with Inventor, a variation in link speed is observed. A more precise analysis is required to determine the cause of this variation, as the speed should remain constant. Variations result in acceleration, leading to non-uniform motion, potentially causing weld bead defects.

4. Acknowledgements

The research presented in this article has received funding from the National Polytechnic University in the research master's degree in mechanical engineering from Ecuador.

5. References

[1] J. Alberto, O. Rivera, E. Miguel, and S. García, “Análisis cinemático y síntesis de un sistema de palancas para la sub-actuación de un dedo artificial con 3 articulaciones,” no. 112, pp. 1134–1154, 2015.

[2] K. Sledziewska and R. Włoch, “How is production changing?,” 2021, pp. 77–117. doi: 10.4324/9781003144359-3.

[3] J. L. Ramirez Arias and A. Rubiano Fonseca, “Modelamiento Matem[Atico De La Cinemática Directa E Inversa De Un Robot Manipulador De Tres Grados De Libertad,” *Ing. Solidar.* , vol. 8, no. 15, pp. 46–52, 2012.

[4] L. Radavelli, D. Martins, E. De Pieri, and R. Simoni, “Cinemática Posicional de Robôs via Iteração e Quatérnios,” 2014. doi: 10.13140/2.1.1042.6563.

[5] E. Cardoso, A. Fernández, S. A. Marrero-Osorio, and P. F. Guardado, “Modelos cinemático y dinámico de un robot de cuatro grados de libertad,” *Rielac*, vol. XXXVIII, pp. 56–75, 2017.

[6] A. Trevisani, “Planning of dynamically feasible trajectories for translational, planar, and underconstrained cable-driven robots,” *J. Syst. Sci. Complex.*, vol. 26, no. 5, pp. 695–717, 2013, doi: 10.1007/s11424-013-3175-1.

[7] M. Bamdad, F. Taheri, and N. Abtahi, “Dynamic analysis of a hybrid cable-suspended planar manipulator,” *Proc. - IEEE Int. Conf. Robot. Autom.*, vol. 2015-June, no. June, pp. 1621–1626, 2015, doi: 10.1109/ICRA.2015.7139405.

[8] S. Lefrancois and C. Gosselin, “Point-to-Point Motion Control of a Pendulum-like 3-Dof Underactuated Cable-Driven Robot,” in *Proceedings - IEEE International Conference on Robotics and Automation*, 2010, pp. 5187–5193. doi: 10.1109/ROBOT.2010.5509656.

EuraSEM | 6-11 July 2025 ICEM21 Bologna | 21st International Conference on EXPERIMENTAL MECHANICS

KINEMATIC ANALYSIS OF A MECHANISM DESIGNED FOR A THUMB EXOSKELETON, INTEGRATING NUMERICAL, ANALYTICAL, AND SIMULATION METHODS INTO AUTODESK SOFTWARE

***D. García*[1]**
[1] *Mechanical Engineering Department, Escuela Politecnica Nacional University, Quito, Ecuador*

1. Introduction

Upper limb injuries frequently involve the fingers, accounting for approximately 2.6 million emergency hospital visits annually in the United States [1]. Additionally, degenerative diseases and cerebrovascular accidents significantly reduce the quality of life in adults over 40 years old [2]. Finger mobility recovery typically involves rehabilitation protocols aimed at partially restoring motor functions through accurate clinical evaluations by trauma specialists and the support of physiotherapists. The use of exoskeletal mechanisms facilitates repetitive treatments, effectively complementing conventional therapies. This approach to robotic rehabilitation has been the focus of active research [3]. However, due to patients' occupational demands and the financial burden of therapy, many rehabilitation programs remain incomplete. To address these challenges, recent studies have proposed the development of portable exoskeletal mechanisms as a feasible alternative [4].

This study complements the work presented by C. Brogi et al. [5] and focuses on the kinematic analysis of position, velocity, and acceleration using Autodesk and MATLAB software. Previous research optimized the dimensions of the robotic links for the thumb and constrained the angles of the physiological links, such as those of the metacarpophalangeal joint (MCP).

2. Materials and methods

This study focused on the natural movement of the thumb through a kinematic analysis using Autodesk parametric software and MATLAB. The work extends the study presented in [5], analyzing a mechanism composed of three robotic links (a, b, and c) and two physiological links (d and e), as simplified in Fig. 1. The degrees of freedom of the exoskeleton, calculated using the modified Grübler's formula, are m = 2. The state equations governing this mechanism are expressed as functions of the coordinates O1, O2, OEE, and O3, with link "e" considered as the fixed reference.

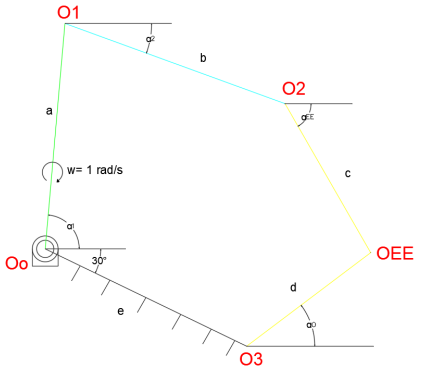

i – vector

$$a * \cos(\alpha_1) + b * \cos(\alpha_2) + c * \cos(\alpha_{EE}) = e * \cos(\psi) + d * \cos(\alpha_0)$$

j – vector

$$a * \mathrm{sen}(\alpha_1) + b * \mathrm{sen}(\alpha_2) + c * \mathrm{sen}(\alpha_{EE}) = e * \mathrm{sen}(\psi) + d * \mathrm{sen}(\alpha_0)$$

Fig. 1. Exoskeleton mechanism connected to the MCP (O3) and State Equations.

3. Results and conlusions

State equations are applied in MATLAB to simulate collision prevention using the Newton-Raphson method within the bounds of alpha angles (0 and 1), with the results validated using Autodesk software. To ensure the accuracy of the MATLAB simulation based on the Newton-Raphson numerical method, the results depicted in Fig. 2 are utilized to generate Table 1.

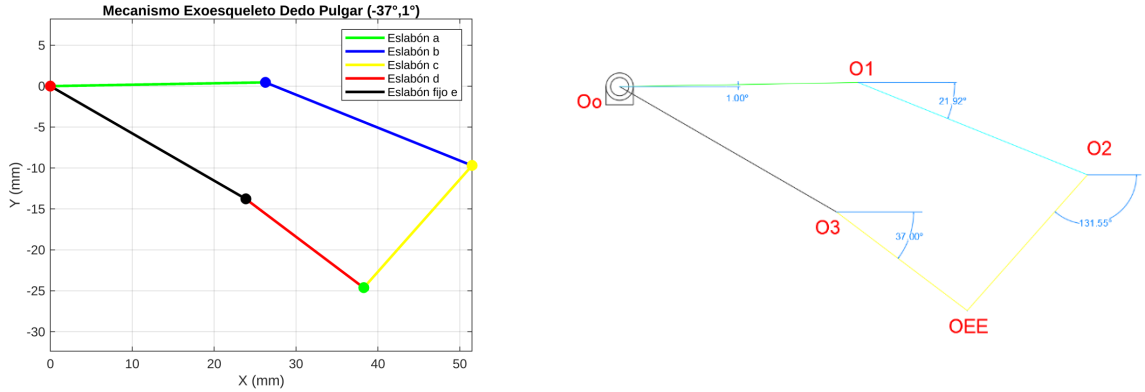

Fig. 2. Mechanism implemented in MATLAB (Left) and Autodesk Software (Right) for alpha (0) = -37° and alpha (1) = 1°.

KINEMATIC POSITION MATLAB VS AUTODESK SOFTWARE			
Alpha (0) = -37°		Alpha (1) = 1°	
MATLAB (NUMERICAL METHODS)			
Alpha (2) °	338,08	Alpha (EE) °	-491,55
SOFTWARE AUTODESK			
Alpha (2) °	21,92	Alpha (EE) °	131,55

Table 1. Comparison of Angles Obtained by Two Differents Software Tools.

4. Acknowledgements

The research presented in this document has been supported by the Master's Research Program of the Faculty of Mechanical Engineering, under Scholarship Contract No. VIIV-BM-20241059-2024-A.

5. References

[1] E. H. Lothet, A. J. Lacy, y E. B. Odom, «The Ten Test and Sensory Evaluation of Hand and Finger Injuries in the Emergency Department», *The Journal of Emergency Medicine*, nov. 2024, doi: 10.1016/j.jemermed.2024.10.008.

[2] G. Li, L. Cheng, y N. Sun, «Design, manipulability analysis and optimization of an index finger exoskeleton for stroke rehabilitation», *Mechanism and Machine Theory*, vol. 167, p. 104526, ene. 2022, doi: 10.1016/j.mechmachtheory.2021.104526.

[3] I. Jo, Y. Park, J. Lee, y J. Bae, «A portable and spring-guided hand exoskeleton for exercising flexion/extension of the fingers», *Mechanism and Machine Theory*, vol. 135, pp. 176-191, may 2019, doi: 10.1016/j.mechmachtheory.2019.02.004.

[4] G. Si, H. Zhang, Z. Zhang, y X. Zhang, «Enabling intuitive and effective micromanipulation: A wearable exoskeleton-integrated macro-to-micro teleoperation system with a 3D electrothermal microgripper», *Robotics and Autonomous Systems*, vol. 181, p. 104776, nov. 2024, doi: 10.1016/j.robot.2024.104776.

[5] C. Brogi, N. Secciani, y L. Bartalucci, «An original hybrid-architecture finger mechanism for wearable hand exoskeletons», *Mechatronics*, vol. 98, p. 103117, abr. 2024, doi: 10.1016/j.mechatronics.2023.103117.

DATA-MODEL COUPLING DRIVEN STRESS FIELD MEASUREMENTS FOR STRUCTURES WITH LOCALIZED DETERIORATION

Jian Zhao[1,2] and Guangbo Wang[1]
[1] School of Technology, Beijing Forestry University, Beijing, China
[2] Key Lab of State Forestry Administration on Forestry Equipment and Automation, Beijing, China

1. Introduction

Engineering structures often experience shape deformations and material property changes in localized areas during long-term service, posing a threat to their safety. Stress field measurement is crucial for structural health monitoring. Traditional methods rely on constitutive equations, which are often unknown in the deteriorated region, leading to modeling errors [1]. Data-driven methods, although avoiding constitutive equations, have high computational costs. Existing data-model coupling frameworks also have limitations [2].

This paper introduces a stress field measurement method within the data-model coupling framework. It aims to determine stress fields in isotropic materials with localized deterioration without relying on constitutive equations in the damaged area. The method combines measured strain fields with data-model coupling algorithms. By using the gradient and Canny operators, the deterioration region is located. An adaptive model building method and a dataset updating strategy based on the differential evolutionary algorithm are proposed. Validation against finite element method calculations shows that the method can accurately obtain the full-field stress of specimens with local degradation behavior, contributing to the field of intrinsic equation-free mechanics.

2. Methodology

2.1 Data-model coupling-driven computation. The structure's numerical model is discretized into data-driven (DD) and model-driven (MD) parts. Compatibility and equilibrium constraints are imposed. A local penalization objective function is introduced for DD elements, transforming the problem into a constrained optimization problem. The solution involves iterative projections between the dataset and the admissible set to determine the appropriate material state.

2.2 Area classification and adaptive model construction. Based on the characteristic of higher strain gradients in the deteriorated region, the strain field gradient and Canny operator are used to locate the boundaries and classify the region. The pixel coordinates are converted into node coordinates to construct quadrilateral plane strain elements. The computational type and material properties are set according to the node category, generating a coupling-driven model.

2.3 Dataset update strategy. To address the unknown material dataset of DD elements, an objective function is constructed using the variance between the coupled calculation strain field and the measured strain field. The differential evolution (DE) algorithm is employed to optimize the degradation factor and obtain the optimal material dataset. DE initializes the population and iteratively updates it through mutation, crossover, and selection operations.

2.4 Stress field measurement process. The measured strain field is input, the target area is classified, and the numerical model is constructed and discretized. The DE algorithm initializes the degradation factor population and constructs the material dataset. The penalty function and control equations are

constructed, and the stress-strain state is iteratively calculated. Convergence is judged, the objective function is calculated, and the population is updated. Finally, the stress field is obtained by interpolation.

3. Verification

A standard plate tension member with an elliptical deteriorated region is modeled by finite element simulation, and the strain field with added noise is used as input. The results show that the region classification and stress field prediction are basically accurate, but there are inaccuracies at the boundaries of the deteriorated region. Compared with other heuristic algorithms, the DE algorithm is less likely to fall into a local optimum when updating the degradation factor and can better update the population. The stress field obtained by this method can reflect the reference stress field well in both the stress concentration and non-concentration areas (as shown in Fig.1), but there are differences at the boundaries of the deteriorated region due to the poor transition of the quadrilateral mesh of the coupling-driven model. The relative error is mostly within 1% and the maximum is less than 4%, demonstrating the effectiveness of the method.

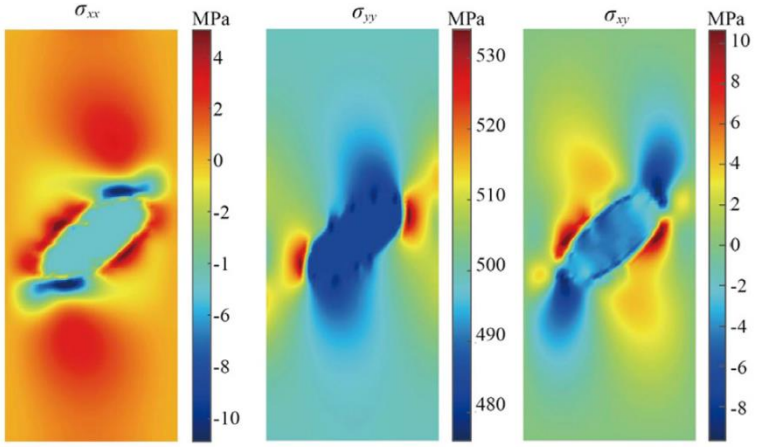

Fig. 1. Reconstructed stress field.

4. Conclusions

A stress field measurement method based on elastic strain fields is proposed. Non-contact methods like digital image correlation are used to obtain strain fields, which are then processed and classified to build the model. The dataset update strategy is used for stress field calculation. This method does not rely on constitutive equations and has advantages over traditional and pure data-driven methods. The feasibility of the method is verified by examples, and it can accurately reproduce the stress field of structures with deteriorated regions.

5. Acknowledgements

The research presented in this paper has received funding from the by the Fundamental Research Fund for the Central Universities (Grant No. BLX202226).

6. References

[1] J. Yang, W. Huang, Q. Huang and H. Hu (2022). An investigation on the coupling of data-driven computing and model-driven computing, *Comput. Methods Appl. Mech. Eng.*, **393**, 114798.

[2] S. Wattel, J. F. Molinari, M. Ortiz and J. Garcia-Suarez (2023). Mesh d-refinement: A data-based computational framework to account for complex material response. *Mech. Mater.*, **180**, 104630.

SYNTHETIC APERTURE X-RAY GHOST IMAGING: ENABLING SUB-MICRON PIXEL RESOLUTION

Nixi Zhao[1 2 3], Jie Tang[1 2 3], Changzhe Zhao[1 2 3], Jianwen Wu[1 2 3], Haipeng Zhang[2], Han Guo[2], Tiqiao Xiao[1 2 3] *

[1] Shanghai Institute of Applied Physics, Chinese Academy of Sciences, Shanghai 201800, China
[2] Shanghai Synchrotron Radiation Facility, Shanghai Advanced Research Institute, Chinese Academy of Sciences, Shanghai 201204, China
[3] University of Chinese Academy of Sciences, Beijing 100049, China

1. Introduction

Ghost imaging (GI) compresses target sample information into one-dimensional data and reconstructs a two-dimensional image computationally. Originating from quantum optics, GI has been extended to classical light sources and various particles, including X-rays. However, high-quality GI typically requires a large number of single-pixel samplings, limiting its practical application. SAXGI addresses this by using a bucket detector array generated through post-pixel-binning, enabling megapixel-level imaging with fewer samples. This study experimentally verifies SAXGI's potential for high-resolution X-ray imaging.

2. Experimental Methods and Setup

The SAXGI system uses a bucket detector array in the object arm and a high-magnification detector in the reference arm. The object arm uses a 2× magnification detector with 4×4 pixel binning, while the reference arm uses a 20× magnification detector without binning. This setup achieves a 40 ×40 block size in the reference arm compared to the object arm. The experiment was conducted at the Shanghai Synchrotron Radiation Facility, using a monochromatized X-ray beam modulated by a seven-layer sandpaper to create speckle patterns. The data acquisition system includes a scintillation crystal, an optical microscope, and a sCMOS detector.

3. Results and conclusions

The study demonstrates SAXGI imaging with 1960×1920 pixels resolution at 0.325 μm per pixel. The reconstructed images show detailed structural information not visible in the direct projection images, validating the sub-micron resolution capability of SAXGI. The results indicate that SAXGI can achieve high spatial resolution with fewer measurements compared to conventional GI methods. The study also examines the effects of X-ray energy, block size, binning mode, lens distortion, and sample complexity on imaging quality. Higher energy and larger block sizes result in lower signal-to-noise ratios. Accurate image registration between the reference and object arms is crucial for high-quality reconstruction.

The study develops protocols to improve SAXGI's experimental efficiency. By decoupling the sampling rate from the total number of pixels, SAXGI requires far fewer measurements for megapixel imaging. The data acquisition process is optimized to minimize vibration and interference, reducing

the total acquisition time to a few minutes. Pre-recording speckle patterns further reduces the experimental time, making SAXGI suitable for practical applications.

The study presents the first experimental implementation of SAXGI, achieving high-resolution X-ray imaging with fewer measurements. The results demonstrate the potential for sub-micron resolution imaging with large fields of view. Future work will focus on improving spatial resolution by enhancing experimental precision and optimizing image reconstruction algorithms. The SAXGI method is expected to contribute significantly to advanced X-ray imaging applications, including medical diagnostics.

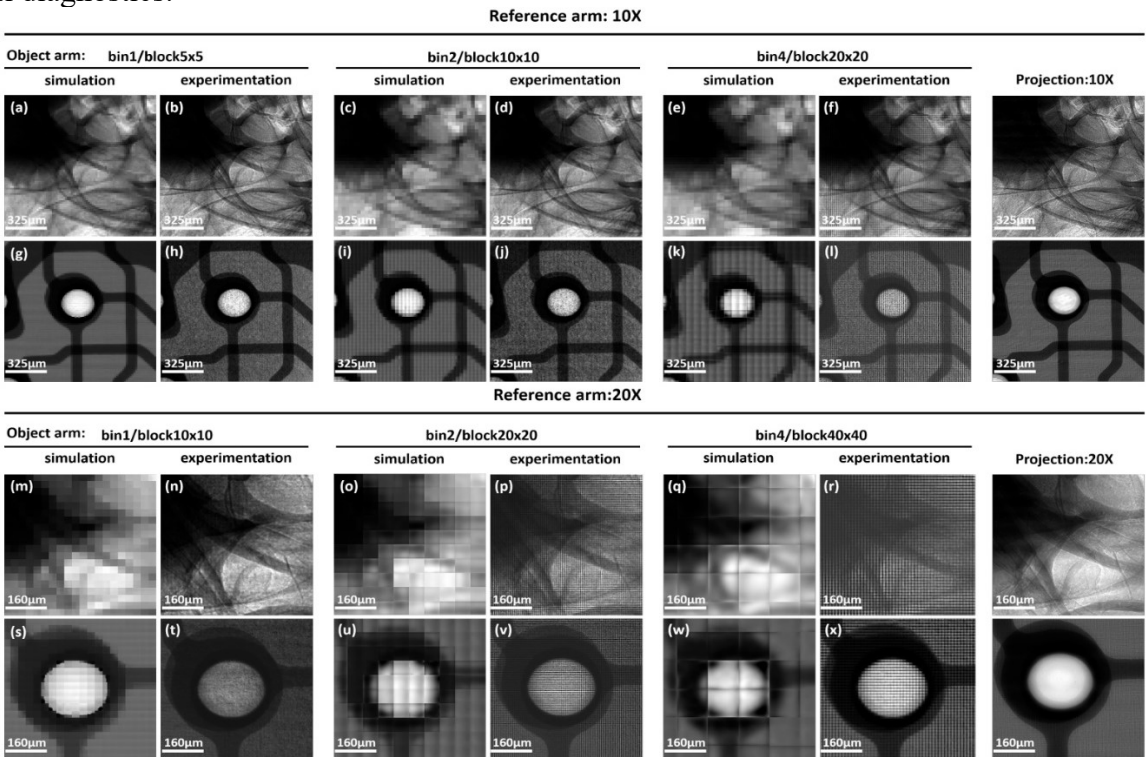

Fig. 1. Effect of block size, bin mode, lens distortion, experimental error and sample complexity on parallel ghost imaging

4. Acknowledgements

The research presented in this paper has received funding from National Key Research and Development Program of China (2022YFA1603601, 2021YFF0601203, 2021YFA1600703); the Young Scientists Fund of the National Natural Science Foundation of China (12205361).

5. References

[1] H. Yu, R. Lu, S. Han, et al. (2016). Fourier-transform ghost imaging with hard x rays. *Phys. Rev. Lett.*, **117(11)**, 113901.

[2] H. Zhang, K. Li, C. Zhao, et al. (2022). Efficient implementation of x-ray ghost imaging based on a modified compressive sensing algorithm. *Chin. Phys. B*, **31(6)**, 064202.

[3] H. Zhang, K. Li, F. Wang, et al. (2022). Megapixel x-ray ghost imaging with a binned detector in the object arm. *Chin. Opt. Lett.*, **20(3)**, 033401.

[4] C.-Z. Zhao, H.-P. Zhang, J. Tang, et al. (2024). X-ray ghost imaging with a specially developed beam splitter. *J. Synchrotron. Rad.*, **31(6)**, 1525–1533.

EXPERIMENTAL METHODOLOGY OF FAST X-RAY IMAGING BEAMLINE AT SSRF

Ke Li[1], Fei-Xiang Wang[1], Jianfeng Ji[1], Ya-Nan Fu[1], Guo-Hao Du[1], Biao Deng[1], Ti-Qiao Xiao[1], Hong-Lan Xie[*1]

[1] Shanghai Synchrotron Radiation Facility, Shanghai Advanced Research Institute, Chinese Academy of Sciences, Shanghai, 201204, China

1. Introduction

With the physical and chemical mechanisms being explored in depth, researchers are increasingly demanding higher spatial and temporal resolution for imaging in in-situ experiments. These experiments include studying the deformations and failures of materials under strong dynamic loads [1,2], as well as the high pressure and high-speed spray processes of fuel in automobile engines [3,4]. The current international X-ray imaging technology tends to have higher spatial resolution (nanometer scale) and faster temporal resolution (millisecond to hundred picosecond scale).

The fast X-ray imaging beamline (BL16U2) at Shanghai Synchrotron Radiation Facility (SSRF) is a new beamline that provides X-ray micro-imaging capabilities across a wide range of time scales, spanning from 100 ps to μs and ms. This beamline has been specifically designed to facilitate the investigation of a wide range of rapid phenomena, such as the deformation and failure of materials subjected to intense dynamic loads. Additionally, it enables the study of high-pressure and high-speed fuel spray processes in automotive engines. The light source of this beamline is a cryogenic permanent magnet undulator (CPMU) that is cooled by liquid nitrogen. This CPMU is able to generate X-ray photons within an energy range of 8.7-30 keV. The beamline has the capability to offer two modes of operation: monochromatic beam mode with a liquid nitrogen-cooled double-crystal monochromator (DCM) and pink beam mode with first crystal of the DCM out of beam path. Four X-ray imaging methods have been implemented in BL16U2, encompassing single-pulse ultrafast X-ray imaging, microsecond-resolved X-ray dynamic imaging, millisecond-resolved X-ray dynamic micro-CT, and high-resolution quantitative micro-CT. Furthermore, BL16U2 is equipped with various in-situ impact loading systems, such as a split Hopkinson bar system, a light gas gun, and a fuel spray chamber. Following the completion of the final commissioning in 2021 and subsequent trial operation in 2022, the beamline has been officially available to users in 2023.

2. Experimental methods

Several X-ray imaging methods have been established in BL16U2, encompassing a range of temporal scales from 100 picoseconds to milliseconds. These methods offer a spatial resolution at the micrometer scale and include single-pulse ultrafast X-ray imaging, microsecond-resolved X-ray dynamic imaging, millisecond-resolved X-ray dynamic micro-CT, and high-resolution quantitative micro-CT.

2.1 Single-pulse ultrafast X-ray imaging

Traditional X-ray imaging is dependent on the utilization of fast cameras with short gate times in order to prevent motion blur of the target. However, the minimum gate time of existing commercial fast cameras range from 2~3 ns to over one hundred nanoseconds. For a transient loading process with a velocity exceeding 1 km/s, even the shortest gate time will result in motion blur ranging from tens to hundreds of micrometers, leading to a significant degradation in spatial resolution. In contrast, single-pulse ultrafast X-ray imaging replaces the gate time of cameras with the temporal duration of the electron bunch in a storage ring as the exposure time for capturing an image. As depicted in the following Fig. 1, the storage ring contains a large bunch of electrons along with a sequence of small bunches. The duration of each bucket required for completing a full revolution in the storage ring is 1.44 μs. Additionally, there are no bunches present in the region 200 ns prior to and following the large bunch, which itself has a duration of only 60ps. Therefore, in theory, during a time period of up to 400 ns, only the central 60 ps will be utilized for the purpose of image exposure.

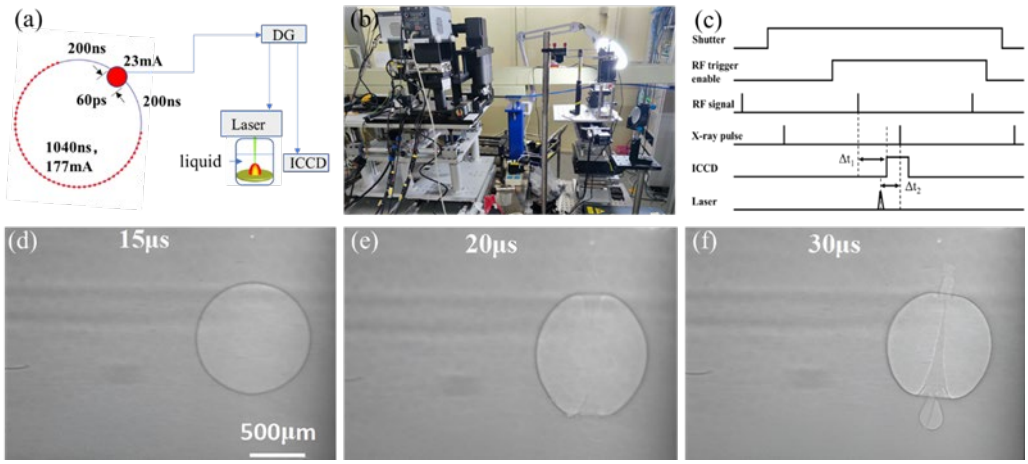

Fig. 1 single-pulse ultrafast X-ray imaging, (a) diagram of the experiment, (b)experimental setup, (c) a logical timing diagram for each key component, (d)-(f) bubble rupture and the generation of liquid jet captured using different Δt2.

2.2 Microsecond resolved X-ray dynamic imaging

X-ray 2D dynamic imaging is widely recognized as one of the most prevalent imaging techniques in the field. Thanks to the increased photon flux and improved detector conversion efficiency, the BL16U2 is capable of capturing a continuous series of images at a frame rate of 500,000 frames per second, while maintaining a micrometer scale spatial resolution. The experiment setup is very similar to single pulse X-ray imaging experiment in Fig. 1, except that one of the ICCD of the dual-channel ultrafast X-ray imaging detector was substituted with the Kirana 5M fast camera, as depicted in Fig. 2. The Kirana 5M camera has the capability to achieve a theoretical maximum frame rate of 5 million frames per second. In this experimental setup, the frame rate is configured at 500,000 frames per second (fps) in order to achieve a favorable signal-to-noise ratio.

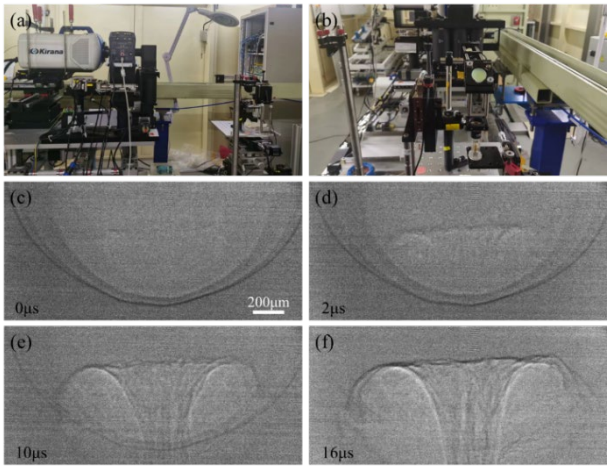

Fig. 2 Microsecond resolved X-ray dynamic imaging, (a) and (b) experimental setup, (c)-(f) images captured at the moment of 0 μs, 2 μs, 10 μs and 16 μs.

2.3 Millisecond resolved X-ray dynamic micro-CT

Dynamic micro-CT enables the acquisition of temporal changes in the three-dimensional spatial structure, making it an ideal tool for conducting in situ investigations into the mechanisms of system evolution. The CPMU light source of the BL16U2 beamline exhibits a significantly high pink beam flux, which allows for efficient flux even after being monochromatized by DCM. This process maintains a good monochromaticity level of 2×10^{-4}. Fig. 3 presents a validation experiment conducted using a fast-foaming polyurethane material system with a monochromatic beam of 15 keV and an effective pixel size of 2.2 μm.

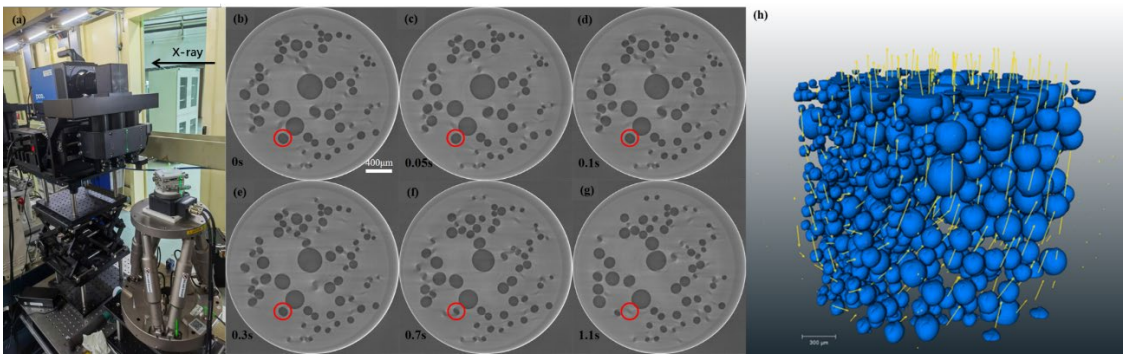

Fig. 3 Millisecond resolved X-ray dynamic micro-CT, (a) experimental setup, (b)-(g) the slices at the time of 0 s, 0.05 s, 0.1 s, 0.3 s, 0.7 s, 1.1s, (h) three-dimensional motion vector field of bubbles obtained by DVC analysis.

2.4 High-resolution quantitative micro-CT

Owing to the exceptional monochromaticity of DCM, it is possible to perform conventional in-line high-resolution quantitative micro-CT on BL16U2. The detector has effective pixel sizes of 3.25 μm, 1.625 μm, 0.65 μm, and 0.325 μm, which correspond to different optical lenses. An illustrative example utilizing this system is depicted in Fig. 4. The focus of this research is a C/C composite that is reinforced with fibers that are densely distributed. In this composite, the diameter of carbon fibers is about 7 μm, and the space between fibers is even smaller. Therefore, this particular composite necessitates a simultaneous high spatial and density resolution. As evident from the observation, carbon fibers can be extracted from the graphite matrix despite their close proximity to each other.

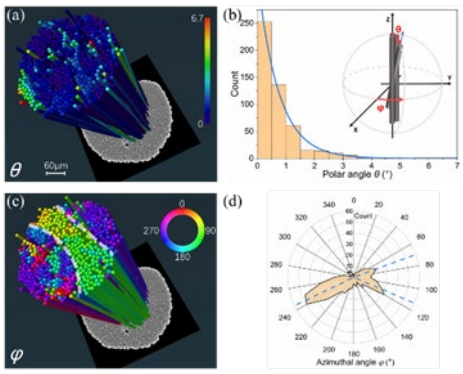

Fig. 4 Images and plots for the statistical analyses of fibers in the C/C composite, (a) and (b) the spatial distribution and histogram for the polar angle θ of each fiber, (c) and (d) the spatial distribution and histogram of the azimuthal angle φ of each fiber.

3. Summary and conclusions

The X-ray fast imaging beamline at SSRF is a new beamline which can provide X-ray micro-imaging at various time scales, ranging from 100 ps to μs and ms. This beamline is specifically designed to investigate rapid processes, including material deformations and failures under intense dynamic loads, as well as the high pressure and high-speed spray processes of fuel in automotive engines. A cryogenic permanent magnet undulator (CPMU) that is cooled by liquid nitrogen was chosen as the light source to generate X-ray photons within the energy range of 8.7-30 keV. The beamline offers two operational modes: pink beam mode and monochromatic beam mode. This is made possible by utilizing a liquid nitrogen cooled double-crystal monochromator. A variety of imaging detectors are currently accessible, offering spatial resolutions ranging from sub-micrometer to a few micrometers, as well as temporal capabilities spanning from 100 ps to milliseconds. Furthermore, BL16U2 is equipped with various in-situ impact loading systems, such as a split Hopkinson bar system, a vertical light gas gun, and a high pressure/speed fuel spray chamber. Four X-ray imaging methods have been implemented in BL16U2, encompassing 60 ps single-pulse ultrafast X-ray imaging, 2 μs time-resolved X-ray dynamic imaging, 50 ms time-resolved monochromatic X-ray dynamic micro-CT, and 0.325 μm/pixel quantitative micro-CT. The results obtained from the final commissioning demonstrate that all the measured specifications not only meet but also exceed the design values. Consequently, the fast X-ray imaging beamline is now fully prepared to accommodate users from all over the globe.

4. Acknowledgements

The research presented in this paper has received funding from CAS Project for Young Scientists in Basic Research (YSBR-096) and Young Scientist Fund of the National Science Foundation of China (Grant No. 12405376).

5. References

[1] M.Z. Mo, M.X. Tang, Z.J. Chen, et al (2022). Ultrafast visualization of incipient plasticity in dynamically compressed matter. *Nat. Commun*., **13**, 1055.
[2] Y.Y. Zhang, S. Chen, Y. Cai, et al (2020). Novel X-ray and optical diagnostics for studying energetic materials: a review. *Engineering*, **6**, 992-1005.
[3] Z.J. Wu, W.B. Zhao, Z.L. Li, et al (2019). A review of engine fuel injection studies using synchrotron radiation x-ray imaging. *Automotive Innovation*, **2**, 79-92..
[4] W.D. Huang, S. Moon, K. Ohsawa (2016). Near-nozzle dynamics of diesel spray under varied needle lifts and its prediction using analytical model. *Fuel*, **180**, 292-300.

EuraSEM 6-11 July 2025 ICEM21 Bologna 21st International Conference on EXPERIMENTAL MECHANICS

NUMERICALLY STUDY FOR ASSESSEMENT OF BALLISTIC EFFICIENCY OF HIGH HARDNES PERFORATED PLATES WITH UNCONVENTIONAL HOLES

A. Spoiala[1], A. N. Rotariu[1], L. C. Matache[1], E. Trana[1] and F. Bucur[1]
[1] *Military Technical Academy, Bucharest, Romania*

1. Introduction

Perforated plates made of high hardness steel, like bainitic steels, have benefited in recent years of ballisticians special attention as they have proven capable of ensuring the kinetic threats defeat, such as armor piercing (AP) bullets [1]. However, the perforated plates, due to their cellular structure, fall under the category of "statistical" armor because the impact effects on the bulled hardened core depend a lot on the point of impact. Numerous studies have shown that the most dramatic effects on the core (fragmentation and dispersion of the fragments) are obtained when the impact point is on the edge of a perforation. On the other hand, when the projectile hits normally in the center of the hole it is possible for the hardened core to pass the plate without being deflected, eroded or fragmented. Of course, the ballistic efficiency of such plates depends on several factors one of them being the shape of the perforations. Most studies have so far focused on plates in which the perforations are made in a direction normal to the plate. The present paper explores by numerical tools the possibility of improving the ballistic efficiency of such plates by creating perforations with an unconventional shape. In this sense, it is considered that the perforations are partially made on both side surfaces of the plate, but with an offset, so that they partially overlap, see Fig. 1 (right).

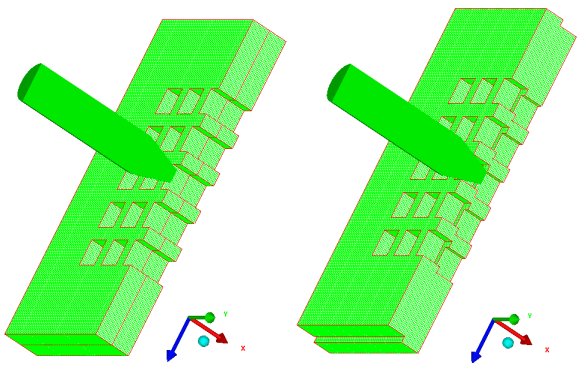

Fig. 1. Half of the model: reference configuration (left) and 1 mm offset configuration (right)

2. Numerically model

Numerical code used to build the model was ANSYS Autodyn. The bodies were built from several parts and discretized with the specific tools of the code. Three types of plates with square perforations were made: the first reference plate, with a thickness of 6 mm and square holes with a side of 4 mm, separated by ligaments of 2 mm, see Fig. 1 (left); the second plate with an offset of 1 mm on both sides of the hole, starting from the middle of the plate, see Fig. 1 (right); and a third plate with a similar offset of 2 mm. The projectile of 6 mm caliber, with an impact velocity of 870 m/s and a total

length of 26 mm, has a truncated tip of 2 mm in diameter. The impact point in all three simulations coincides with the center of the hole, see Fig. 1. For the material characteristics and failure/erosion limits, data from similar simulations were used [2, 3].

3. Results and conclusions

For both configurations with an offset the projectile was eroded and split into fragments, which does not happen in the first configuration, see Fig. 1. The parameters of interest for the relevant fragments resulting from the projectile in each of the simulations are reproduced in Table 1. From the obtained data it can be seen that an offset configuration eliminates the possibility of the projectile to pass through the plate in one piece and uneroded, without changing the total mass of the plate. The best results are obtained for the 2 mm offset, where the kinetic energy of the biggest fragment is just 32.2% of the projectile initial kinetic energy.

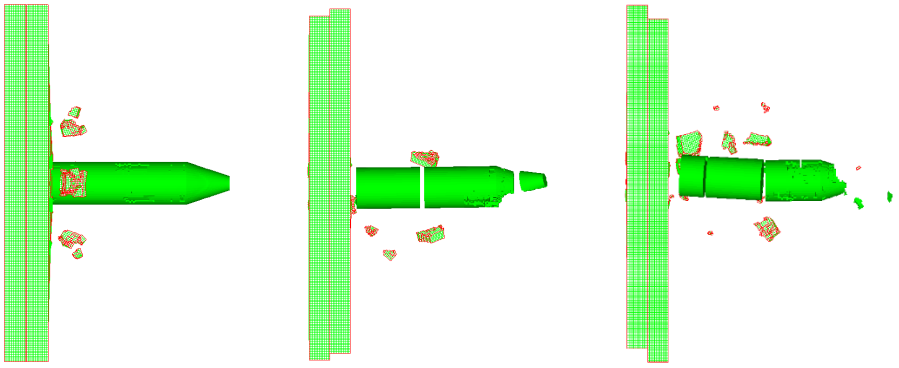

Fig. 2. Projectile status after impact: reference configuration (left) 1 mm offset configuration (center) and 2 mm offset configuration (right)

Configuration		Mass (g)	Velocity (m/s)	Kin. Energy (J)
Reference	Frag. 1	5.05	810	1,659
1 mm offset	Frag. 1	2.52	762	771
	Frag. 2	2.04	781	592
2 mm offset	Frag. 1	2.11	765	617
	Frag. 2	1.81	755	518
	Frag. 3	0.79	740	217

Table 1. Fragments parameters for the three simulated cases

4. Acknowledgements

This work was supported by a grant of the Ministry of Research, Innovation and Digitization, CCCDI - UEFISCDI, project number PN-IV-P6-6.3-SOL-2024-2-0254, within PNCDI IV.

5. References

[1] S. Balos, D. Howard, A. Brezulianu and D. L. Zlatanovic (2021). Perforated Plate for Ballistic Protection—A Review, *Metals*, **11**, 1-18.

[2] W. Burian, P. Zochowski, M. Gmitrzuk, J. Marcisz, L. Starczewski, B. Juszczyk and M. Magier (2019). Protection effectiveness of perforated plates made of high strength steel, *Int. J.Impact Eng.*, **126**, 27–39.

[3] T. Fras, A. Murzyn and P. Pawlowski (2017). Defeat Mechanisms Provided by Slotted Add-on Bainitic Plates against Small-calibre 7.62 mm 51 AP Projectiles. *Int. J. Impact Eng.*, **103**, 241–253.

NUMERICAL SIMULATION-BASED DETERMINATION OF THE VISCOSITY INFLUENCE OF MATERIALS SUBJECTED TO DYNAMIC LOADS AT HIGH STRAIN RATES

L.C. Matache[1], A.N. Rotariu[1], I.D. Pacurar[1], R.M. Mircioaga[1], C. Puica[2], M. Marmureanu[2] and P. Somoiag[1]

[1] Faculty of Integrated Armament Systems, Military Engineering and Mechatronics, Military Technical Academy „Ferdinand I", Bucharest, Romania

[2] Military Equipment and Technologies Research Agency, Bucharest, Romania

1. Introduction

The impact of kinetic penetrators on ballistic protection structures occurs at velocities exceeding 300 m/s, reaching in certain situations values of over 1000 m/s. This leads to the emergence of dynamic stresses with high strain rates, causing significant deformations [1] in the materials used. Therefore, materials employed in the field of ballistic protection must undergo dynamic testing in accordance with the type of application for which they are designed. These tests, which are costly and hazardous, must be combined with numerical simulation approaches, as the complexity of the processes involved makes it impossible to model these phenomena analytically.

The viscosity of materials plays an essential role in their behavior when subjected to dynamic loads with high strain rates. Under such conditions, materials can no longer be treated as purely elastic or plastic; instead, the viscous component of their response must also be taken into account [2].

At high strain rates, materials tend to exhibit stiffer and more brittle behavior, and viscosity becomes a critical factor in determining how energy is absorbed and distributed. For example, in the case of polymeric materials or composites, viscosity directly influences how they deform and fracture. Materials with higher viscosity tend to absorb more energy through viscous deformation, which can prevent the rapid propagation of cracks and improve impact resistance.

Thus, the viscosity of materials is a key parameter in determining their performance at high strain rates. By controlling and optimizing this property, engineers can develop safer and more efficient materials for applications involving extreme dynamic loads.

2. Description of the method used

The present paper aims to determine the influence of viscosity in materials subjected to dynamic loads at high strain rates, using numerical simulation of phenomena occurring in material specimens subjected to dynamic compression tests. For characterizing materials under dynamic conditions with high strain rates, three types of tests are used: impact tests, tests using Split Hopkinson Pressure Bars (SHPB), and tests with gas-dynamic guns [3]. Any of these can be used, but for illustration, we have chosen SHPB tests. To determine the influence of viscosity, at least two tests at different impact velocities are required.

Thus, after conducting the tests, a numerical simulation was performed using the Ls-Dyna software [4]. The numerical simulation was initially carried out without considering the influence of viscosity,

and by dividing the average impact stress obtained experimentally by the average impact stress obtained through numerical simulation, the viscosity function was determined. In the numerical simulation, two constitutive material models were used: Johnson-Cook and plastic kinematic with hardening plasticity, whose viscosity functions are expressed as follows:

$$f_v = \left(1 + C \cdot \ln \dot{\varepsilon}\right) \tag{1}$$

$$f_v = 1 + \left(\frac{\dot{\varepsilon}}{D}\right)^{\frac{1}{p}} \tag{2}$$

By solving the resulting system of equations, the coefficients of the viscosity function are determined, thereby establishing the influence of this material parameter in the case of dynamic loads with high strain rates.

3. Results and conclusions

The results obtained from the experimental tests and numerical simulation are presented in Fig. 1 for an impact velocity of 7.5 m/s.

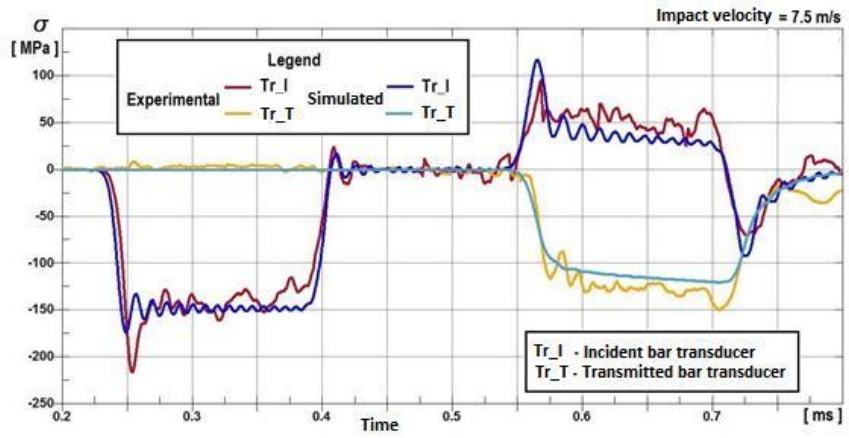

Fig. 1. Experimental and simulated stress in SHPB system for a metallic sample.

Similarly, the resulting stress from the impact with the incident bar is obtained for a velocity of 10 m/s, allowing the calculation of the coefficients of the viscosity function for the considered material:

$$C_1 = 0,0287 \;\; D = 3.8e6 \;\; p = 5.216 .$$

4. References

[1] Crouch I G2017 The Science of Armour Materials (Woodhead Publishing).
[2] National Research Council 2011 Opportunities in Protection Materials Science and Technology for Future Army Applications (WashingtonDC: Wiley–The National Academies Press)
[3] Yu, X., Chen, L., Fang, Q., Jiang X., Zhou Y., (2018). *A Review of the Torsional Split Hopkinson Bar*, Adv. in Civ. Eng., 1-17.
[4] Gavrus A, Bucur F, Rotariu A and Cananau S 2013 Analysis of metallic materials behavior during severe loadings using a FEM modeling of the SHPB test based on a numerical calibration of elastic strains with respect to the raw measurements and on the inverse analysis principle Key Eng Mat 554-557.

BL13HB：THE NEW X-RAY IMAGING AND BIOMEDICAL APPLICATION BEAMLINE AT SSRF

Y.L. Xue, H. Guo, G.H. Du, J.F. Ji, B. Deng, H.L. Xie, and T.Q. Xiao
Shanghai Synchrotron Radiation Facility, Shanghai Advanced Research Institute, Chinese Academy of Sciences, Shanghai 201204, China

1. Introduction

Shanghai Synchrotron Radiation Facility (SSRF) is a third-generation synchrotron light source using a 3.5 GeV storage ring and has 34 beamlines and 46 experimental hutches in service with the end of the phase-II construction project[1]. BL13HB [2]is one of the phase-II construction project.

Compared with the phase I BL13W1[3] wiggler beamline, a bending magnet light source was chosen for BL13HB to achieve a high photon flux density. A double multilayer monochromator is used instead of a double crystal monochromator, and the white beam mode is also provided to meet the needs of fast experiments with high photon flux density. The construction of BL13HB was completed in June 2021, and the beamline has been open to users since then. BL13HB is accessible through the sharing service platform of the Chinese Academy of Science Large Research Infrastructure Program.

2. Beamline characteristics and methods

The X-ray light source of BL13HB is a super-bending magnet with a magnetic field strength of 2.293 T, and the radius of the bending magnet is 5.09 m. With an energy range of 8–40 keV, the maximum photon flux occurs at approximately 15 keV, which corresponds to the critical energy. Within this energy range, the photon flux at each energy point wxceeds 1×10^{13} phs/s/0.1%BW and can meet most X-ray imaging experimental requirements for the energy range, photon flux, and beam size. The theoretical photon flux at 20 keV is 2.4×10^{13} phs/s/0.1%BW. The detailed technical specifications of BL13HB are listed in Table 1. BL13HB is equipped with multiple X-ray detectors designed for various X-ray imaging experiments.

Table 1. Technical specifications of the BL13HB beamline

BL13HB characteristics	Parameters
Light source	Super-bending magnet
Electron energy (GeV)	3.5
Magnetic field (T)	2.293
Beam current (mA)	300
Acceptance angle ($mrad^2$)	1.6×0.3
Energy range	8–20 keV (Ru/C); 20–40 keV (W/Si)
Energy resolution ($\Delta\Delta E/E$)	2.3% @20 keV
Flux density at sample	4.8×10^{11} phs/s/mm^2 @20 keV
Maximum beam size (mm^2)	48.5×5.2 mm

There are many experimental methods available at BL13HB, such as micro-CT, dynamic micro-CT, and pair distribution function. These methods constitute a powerful platform and means for

experimental mechanics research. For example, the relationship between material microstructure (such as grains, pores, cracks, etc.) and macroscopic mechanical properties is revealed. The deformation and damage evolution of materials under load were observed in situ and dynamically.

3. Results and conclusions

Using synchrotron radiation X-ray imaging technology, T.M. Wang et al.[4] addressed the “black box” problem in the alloy solidification process. In cooperation with enterprises, they established the world's first horizontal electromagnetic continuous casting production line of copper chromium-zirconium alloy, providing better copper contact line for Beijing-Shanghai high-speed railway. The speed of the pilot train on the Beijing-Shanghai high-speed railway reached 486.1 km/h, breaking the highest speed record of the world railway operation test.

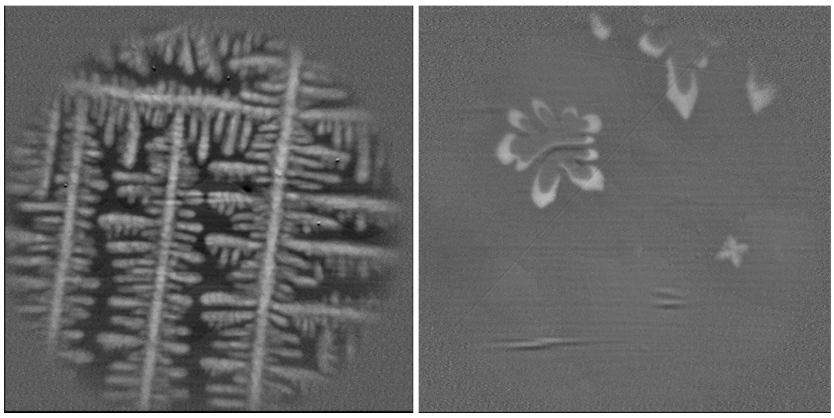

Fig1. Synchrotron radiation real-time imaging of dendrite growth during alloy solidification

Utilizing synchrotron radiation X-ray tomography, S.C. Wu et al.[5] traced the damage accumulation and evolution of SLM AlSi10Mg alloy over its entire fatigue life (ranging from 180 to 38,000 cycles) at 250 ℃ and pull-pull cyclic loading conditions in situ. Damage nucleation was identified, and a new joint manufacturing strategy wass proposed.

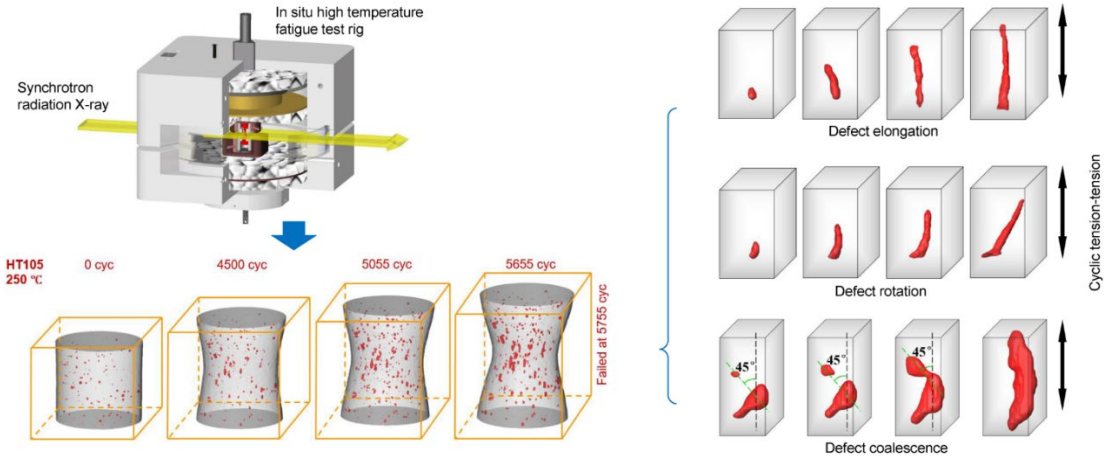

Fig2. Imaging of damage accumulation and evolution of alloy

The new X-ray imaging and biomedical applications beamline at SSRF, providing both white and monochromatic X-ray beam, serves as a powerful platform for research in materials science, biomedical science, paleontology, and industrial applications[6-8]. And it will make more contributions to experimental mechanics in future.

4. References

[1] R.Z. Tai, Z.T. Zhao (2024). Overview of SSRF phase-II beamlines, *Nuclear Science and Techniques*, **35**:137.

[2] J.F. Ji, H. Guo, Y.L. Xue, R.C. Chen, Y.N. Fu, G.H. Du, B. Deng, H.L. Xie and T.Q. Xiao (2023). The new X-ray imaging and biomedical application beamline BL13HB at SSRF, *Nuclear Science and Techniques*, **34**: 197.

[3] H.L. Xie, B. Deng, G.H. Du, Y.N. Fu, H. Guo, Y.L. Xue, G.Y. Peng, F.Tao, L. Zhang and T.Q. Xiao (2020). Methodology development and application of X-ray imaging beamline at SSRF, *Nuclear Science and Techniques*, **31**:102.

[4] T.M. Wang, J.J. Xu, T.Q. Xiao, H.L. Xie, J. Li, T.J. Li and Z.Q. Cao (2010). Evolution of dendrite morphology of a binary alloy under an applied electric current: An in situ observation, *Physical Review E,* **81**, 042601.

[5] Y.N. Hu, S.C. Wu, Y. Guo, et al. (2022). Inhibiting weld cracking in high-strength aluminium alloys, *Nature commun*., **13**: 5816.

[6] K. Du, M.W. Xu, Y.L. Xue, G.H. Du, B. Deng, H.L. Xie and T.Q. Xiao (2024). Time varying flat field correction of X-ray microtomography with an improved deep-learning method, *Optics Express*, **32**: 40136.

[7] L.L. Ye, Y.L. Xue, Y.D. Wang, J.C. Qi, and T.Q. Xiao (2017). Identification of ginseng root using quantitative X-ray microtomography, *J Ginseng Res,* **41**: 290-297.

[8] H.P. Xu, L. Wu, Y.L. Xue, T. Yang, T. Xiong, C.F. Wang, S.Y. He, H.Y. Sun, Z.Y. Cao, J. Liu, S.W. Wang, Z. Li, A. Naeem, X.Z. Yin and J.W. Zhang(2023). Advances in Structure Pharmaceutics from Discovery to Evaluation and Design, *Mol.Pharmaceutics*, **20**: 4404−4429.

DEVELOPMENT OF PTC-BASED COMPOSITE SURFACE HEATING TEXTILES: ENHANCED MECHANICAL RELIABILITY AND WASH DURABILITY THROUGH MWCNT COMPOSITING

Ji-Hyeok Choi[1], Sun Hee Kim[2,*]
[1] Department of Materials Science and Engineering, Gachon University, Seongnam, Gyeonggi-do, South Korea
[2] Department of Fashion Industry, Incheon National University, Incheon, South Korea

1. Introduction

Electronic textiles (e-textiles) represent a convergence of traditional garment aesthetics and form factors with contemporary information technology, evolving into high-performance wearable electronic systems. Among these, thermally active textiles were initially confined to niche applications in aerospace and military sectors; however, recent advancements in material science and significant reductions in production costs have accelerated their diffusion into broader consumer and industrial domains, including electric vehicle thermal management and personal wearable heating systems [1].

Conventional heating garments primarily employ heating elements exhibiting negative temperature coefficient (NTC) characteristics, wherein electrical resistance decreases with increasing temperature. This inherent trait leads to nonlinear power consumption and uncontrolled thermal escalation, which can pose safety risks such as localized overheating or low-temperature burns. Furthermore, the integration of external temperature regulation modules necessary to mitigate such risks inevitably increases the overall mass and volume of the garment, compromising user comfort and wearability.

To address these limitations, this study proposes a novel surface heating textile engineered with positive temperature coefficient (PTC) behavior, designed to ensure enhanced thermal self-regulation and structural stability. The heating element was fabricated via a composite paste consisting of multi-walled carbon nanotubes (MWCNTs) uniformly dispersed within a PTC-active ceramic matrix. This functional ink was deposited onto a highly stretchable textile substrate using precision screen-printing techniques. The resultant textile-based heater was systematically evaluated in terms of electrical power consumption, heat generation kinetics, and temperature-dependent resistance variation (i.e., PTC coefficient). Moreover, the impact of processing parameters on the electrothermal performance and applicability to wearable heating systems was thoroughly investigated.

2. Materials and methods

This work presents the development of a surface heating textile (SHT) exhibiting PTC behavior, achieved by applying a composite ink comprising commercial PTC carbon-based ink and MWCNTs onto highly elastic fabric substrates integrated with conductive yarn electrodes through screen-printing. The ink formulation, which excluded conventional binders, was homogenized via planetary mixing followed by sequential dispersion using a three-roll milling technique to enhance uniformity

and dispersion quality [1]. A dual-phase screen-printing procedure was employed to optimize the interfacial adhesion and surface morphology, succeeded by thermal drying and curing. To enhance durability and electrical insulation, the fabricated textile was encapsulated using laminated thermoplastic polyurethane (TPU) films, culminating in a flexible layered structure with an overall thickness of approximately 2.0 mm [2]. Mechanical stretching and washing tests were performed to assess the durability of the developed PTC-based surface heating textiles. Following each test, surface conductivity was evaluated via a four-point probe measurement, and the temperature-dependent resistance in the 25–55 °C range was recorded to examine the preservation of the material's PTC characteristics.

3. Results and conclusions

Cyclic tensile tests were conducted up to 7,000 cycles on two types of samples: those coated with PTC ink of varying thicknesses and those encapsulated as SHT using TPU. As illustrated in Fig.1(a), surface resistance was measured via a four-point probe for each configuration. The TPU-encapsulated samples, particularly those with thicknesses below 30-60 μm, exhibited superior mechanical durability compared to the directly coated PTC-SHTs. Furthermore, as shown in Fig.1(b), encapsulated samples designated T30, T60, and T90 demonstrated negligible variation in surface resistance after repeated washing cycles, confirming enhanced environmental stability.

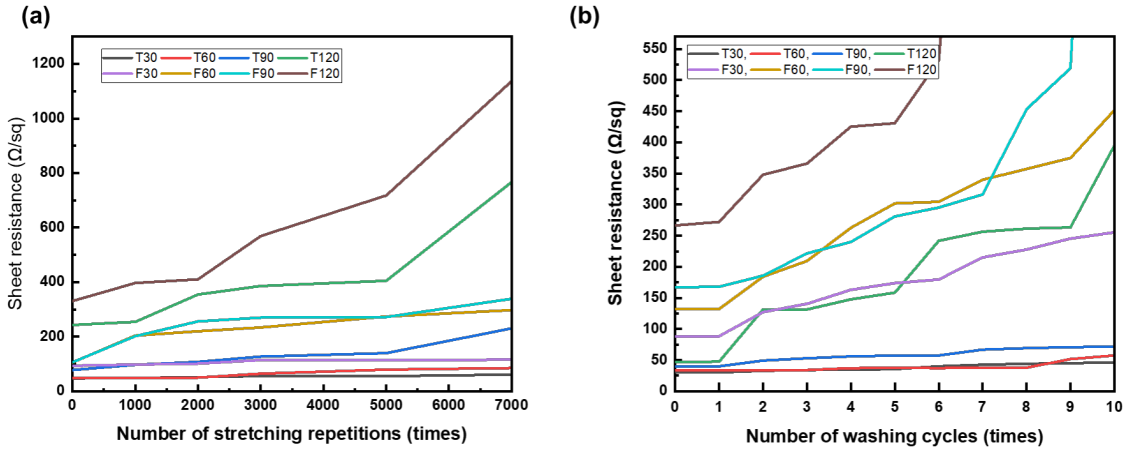

Fig. 1. (a) Surface resistance variation of PTC-SHT samples with different PTC ink thicknesses (30, 60, 90, and 120 μm) applied on fabric or encapsulated with TPU, measured during cyclic tensile testing up to 7,000 cycles. (b) Changes in surface resistance of the same samples (T30, T60, T90, T120) after repeated washing tests, demonstrating the effect of TPU encapsulation on wash durability.

In addition, the PTC characteristics of composites incorporating various weight ratios of MWCNTs into the PTC ink were evaluated. Fig.2(a) illustrates the temperature-dependent resistance behavior of the samples up to 55°C, which corresponds to the primary operating temperature range targeted in this study. As the weight fraction of MWCNTs increased, a noticeable attenuation in the intrinsic PTC behavior was observed across all samples. This degradation is attributed to the formation of continuous conductive pathways by the MWCNTs, which suppress the resistance increase typically induced by temperature. Furthermore, to assess the mechanical stability of the PTC

effect under dynamic conditions, PTC-MWCNT composite samples with a 1:1 weight ratio were subjected to cyclic tensile testing up to 7,000 cycles (Fig.2(b)). The results revealed no significant degradation in PTC behavior, indicating excellent electrothermal stability under repeated mechanical strain.

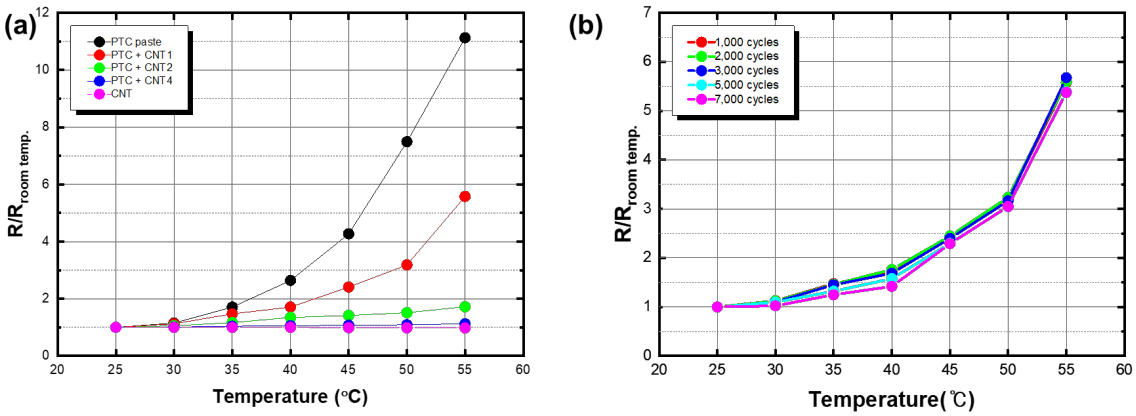

Fig. 2. (a) Resistance variation of composite samples as a function of the mixing ratio between PTC ink and MWCNTs. (b) Change in PTC characteristics of the composite sample with a 1:1 weight ratio of PTC ink to MWCNTs after cyclic tensile testing up to 7,000 cycles.

4. Acknowledgements

This work was supported by the Korea Planning & Evaluation Institute of Industrial Technology (KEIT) grant funded by the Korean government (MOTIE) (No. 20026439).

5. References

[1] Choi, J. H., Jee, S. H., Lee, Y. N., & Kim, S. H. A study on the exothermic behavior of ceramic composites with positive temperature coefficients for e-textiles. In Experimental Mechanics in Engineering and Biomechanics: Proceedings of ICEM20 – 20th International Conference on Experimental Mechanics, Porto, Portugal (2–7 July 2023).

[2] Choi, H. N., Jee, S. H., Ko, J., Kim, D. J., & Kim, S. H. (2021). Properties of surface heating textile for functional warm clothing based on a composite heating element with a positive temperature coefficient. *Nanomaterials*, *11*(4), 904.

CORROSION RESISTANCE EVALUATION AND BEHAVIOR ANALYSIS OF FE- AND NI-BASED ALLOYS FOR MOLTEN SALT REACTORS WITH MOLYBDENUM COATING APPLICATION

Su Hyeong Kim[1], Ji-Hyeok Choi[1], and Young Soo Yoon[1]
[1] Department of Materials Science amd Engineering, Gachon University, Seongnam-si, Republic of Korea

1. Introduction

As global warming intensifies, nuclear energy is gaining renewed attention as a viable alternative to fossil fuels due to its inherently low carbon emissions. Conventional nuclear reactors predominantly utilize solid fuels, with the fuel, cladding, and coolant maintained as discrete components. This separation renders the system vulnerable to core meltdown accidents under extreme conditions, thereby reinforcing public concerns regarding the intrinsic risks associated with nuclear energy. [1] Among the prospective designs for next-generation nuclear power systems, the Molten Salt Reactor (MSR) offers a paradigm shift by employing a mixed molten salt of fuel salt and coolant salt. This configuration fundamentally precludes the possibility of severe accidents such as a meltdown situation. The inception of MSR research dates back to the late 1950s at Oak Ridge National Laboratory (ORNL), where thermal-spectrum MSRs utilizing FLiNaK-based fluoride salts were first conceptualized and studied. [2,3] In recent years, escalating interest in fast-spectrum MSRs has led to increasing focus on chloride-based molten salts. Chloride salts offer several distinct advantages: they obviate the need for a moderator and exhibit higher solubility for actinides such as U(uranium) and Pu(plutonium) [4]. Moreover, compared to fluoride-based salt, chloride-based salts typically possess lower viscosities, higher operational temperatures, and the potential to facilitate hydrogen co-production. Despite these favorable properties, an optimal chloride-based salt composition—such as a definitive analogue to FLiNaK—has yet to be established. As a result, extensive studies are underway to investigate the corrosion behavior of various mixed chloride salts under representative reactor conditions. In the present study, a ternary eutectic mixture composed of NaCl-KCl-$CeCl_3$ (0.45 : 0.20 : 0.35 mol%) was employed, with $CeCl_3$ selected as a chemical surrogate for actinides like U and Pu. To further elucidate the impact of fission products on corrosion processes, tellurium (Te) was introduced, and the corrosion behavior in its presence and absence was systematically compared. Additionally, the efficacy of a protective molybdenum (Mo) coating was evaluated by comparing corrosion resistance with and without the Mo layer.

2. Materials and methods

The alloys employed in this study included a Fe-based alloy (SS316L) and two Ni-based alloys (Hastelloy C-276 and Hastelloy N). Each sample was machined into dimensions of 10 mm × 10 mm with a thickness of 1.5 mm. To ensure consistent surface roughness, all specimens were polished using SiC papers prior to the experiments. The chemical reagents used—NaCl, KCl, and $CeCl_3$—

were procured from Sigma-Aldrich. These were mixed in a molar ratio of 0.45 : 0.20 : 0.35 and subsequently subjected to a purification process at 300 °C for 12 hours to eliminate residual moisture and oxygen prior to use. A molybdenum (Mo) coating layer was deposited on selected samples using radio-frequency (RF) sputtering. The sputtering conditions were as follows: working pressure of 3.5 × 10^{-2} Torr, applied power of 100 W, and gas flow rate of Ar 20 sccm. Corrosion experiments were conducted inside a glove box maintained at an moisture and oxygen level of approximately 0.01 ppm. The specimens were immersed in the molten salt at 650 °C for a duration of 500 hours. Upon completion of the corrosion test and after complete cooling, the samples were retrieved, thoroughly cleaned, and subsequently analyzed.

	Hastelloy N	Hastelloy C-276	SUS 316L
Ni	Bal.	Bal.	~10–14
Cr	7.0	16	~16–18
Mo	16	16	~2.0–3.0
Fe	4.0	5.0	Bal.
Si	1.0	0.08	0.75
Mn	0.80	1.0	2.0
V	0.50	0.35	-
C	0.06	0.01	0.03
Co	0.20	2.5	-
Cu	0.35	0.50	-
W	0.50	4.0	-
Al+Ti	0.50	-	-
S	-	-	0.05
N	-	-	0.10

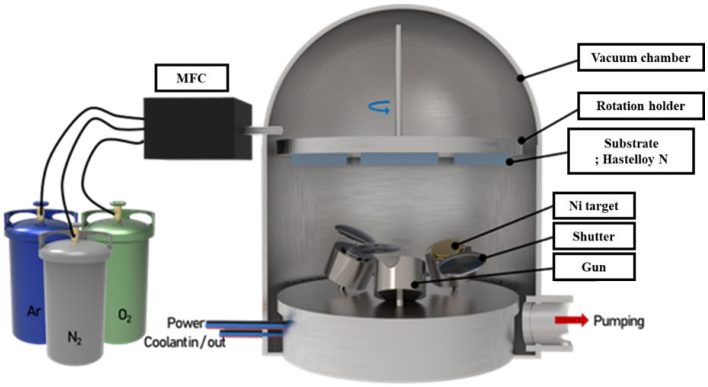

Figure 1. Elemental composition of the alloys and schematic diagram of the RF sputtering system employed for Mo coating deposition.

3. Results and conclusions

Figure 2 illustrates the corrosion rates of each alloy sample with and without the presence of tellurium (Te). As widely reported in the literature, SS316L exhibited the highest corrosion rate among the tested alloys. Bare samples, the corrosion rates followed the order: SS316L > Hastelloy C-276 > Hastelloy N. In all three alloys, the presence of Te resulted in a noticeable increase in the corrosion rate, indicating its detrimental influence under the given experimental conditions.

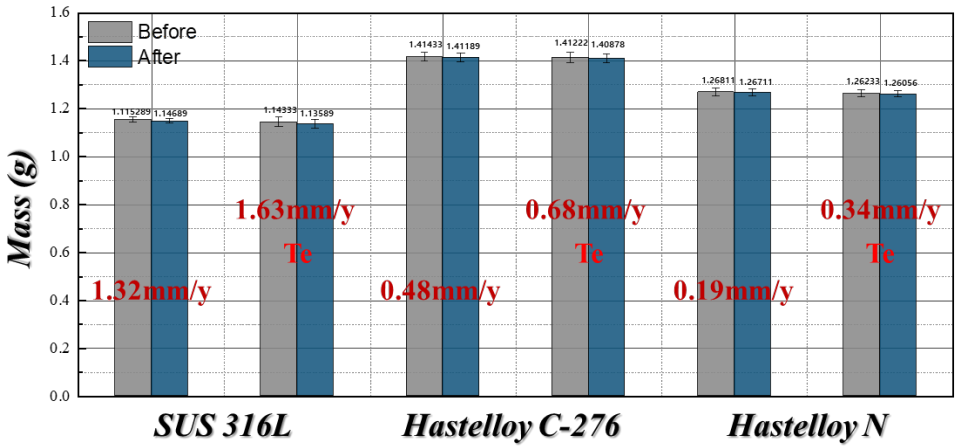

Figure 2. Corrosion rate of bare samples with and without Te.

Figure 3 presents the corrosion rates of samples coated with a molybdenum (Mo) protective layer. Unlike the uncoated samples, the corrosion trend was reversed, following the order: Hastelloy N > Hastelloy C-276 > SS316L. Notably, SS316L exhibited a significant reduction in corrosion rate upon Mo coating. Interestingly, in the cases of Hastelloy C-276 and Hastelloy N, the addition of Te resulted in lower corrosion rates compared to the non-Te condition. This suggests a possible interaction between Te and the Mo layer in Ni-based alloys, potentially forming a protective interfacial compound or altering the reaction kinetics. However, further in-depth analysis is necessary to elucidate the underlying mechanisms responsible for this unexpected behavior.

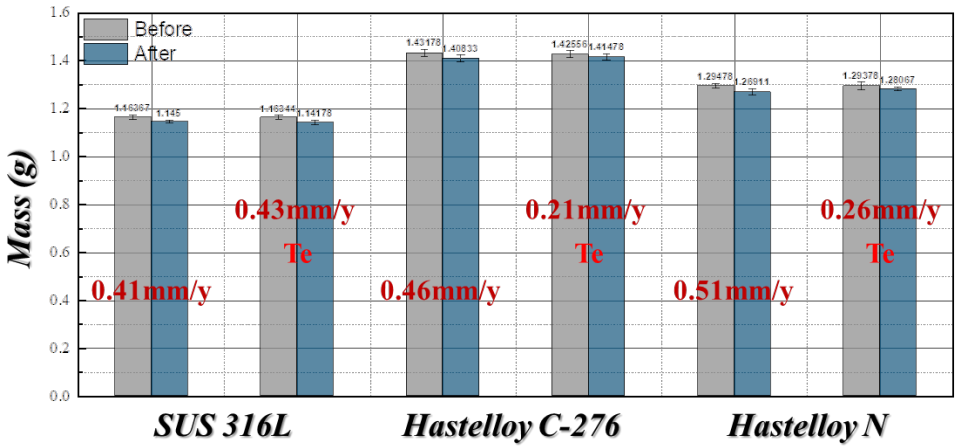

Figure 3. Corrosion rate of Mo-coated samples with and without Te.

4. Acknowledgements

This work was supported by a National Research Foundation of Korea (NRF) grant funded by the Korean government (MSIT) (No. NRF-2021M2D2A2076384)

5. References

[1] P.K. Vijayan, M.T. Kamble, A.K. Nayak, K.K. Vaze, R.K. Sinha, Safety features in nuclear power plants to eliminate the need of emergency planning in public domain, Indian Academy of Sciences. 38 (2013) 925–943.

[2] M.S. Sohal, M.A. Ebner, P. Sabharwall, P. Sharpe, Engineering Database of Liquid Salt Thermophysical and Thermochemical Properties, 2010. http://www.inl.gov.

[3] J. Serp, M. Allibert, O. Beneš, S. Delpech, O. Feynberg, V. Ghetta, D. Heuer, D. Holcomb, V. Ignatiev, J.L. Kloosterman, L. Luzzi, E. Merle-Lucotte, J. Uhlíř, R. Yoshioka, D. Zhimin, The molten salt reactor (MSR) in generation IV: Overview and perspectives, Progress in Nuclear Energy. 77 (2014) 308–319. https://doi.org/10.1016/j.pnucene.2014.02.014.

[4] M. Altmaier, E. Yalçıntaş, X. Gaona, V. Neck, R. Müller, M. Schlieker, T. Fanghänel, Solubility of U(VI) in chloride solutions. I. The stable oxides/hydroxides in NaCl systems, solubility products, hydrolysis constants and SIT coefficients, Journal of Chemical Thermodynamics. 114 (2017) 2–13. https://doi.org/10.1016/j.jct.2017.05.039.

INVESTIGATION OF 316L PRODUCED BY ADDITIVE MANUFACTURING FOR NUCLEAR APPLICATIONS

R. Montanari, A. Palombi, M. Richetta, A. Varone, A. Zahid*
Department of Industrial Engineering (DIN), University of Rome, Tor Vergata, Italy

1. Introduction

In recent years, extensive research is ongoing to investigate the feasibility of additive manufacturing (AM) for components of nuclear reactors. AM processes involve rapid cooling rate that causes metastable conditions: finer microstructure, secondary metastable phases, and residual stresses. This condition leads to mechanical properties matching or exceeding those obtained with traditional manufacturing processes. However, this metastable microstructure might evolve during service life compromising the required properties. Present work focuses on AM 316L steel to assess its thermal stability from room temperature up to 600 °C.

2. Materials and methods

Samples of 316L were manufactured using Laser Powder Bed Fusion (L-PBF) following the strategy described in [1]. The chemical composition of the alloy is reported in Table 1.

Table 1. Chemical composition of the 316L feedstock powder

C	Cr	Mo	N	Mn	Si	Ni	P	S	Fe
0.024	16.87	2.06	0.083	1.35	0.40	10.05	0.031	0.029	to balance

Mechanical spectroscopy (MS) experiments were performed on as-built samples to measure the dynamic modulus (E) from room temperature to 600 °C. The tests were carried out with a heating rate of 1.5 °C /minute through an automated vibrating reed analyzer (VRA 1604, CANTIL s.r.l.) [2] operating in resonance conditions. The dynamic modulus was determined from the resonance frequency f by the following equation:

$$E = \frac{48\pi^2 \rho L^2}{m^4 h^2} f^2 \tag{1}$$

where m = 1.875 is a constant, L and h the length and thickness of the sample, and ρ the material density.

The microstructure before and after MS test was investigated by using Light Microscopy (LM) and Scanning Electron Microscopy (SEM). X-ray diffraction (XRD) measurements were carried out on both materials in the as-built condition and after MS test by using the Mo-Kα (λ= 0.07093 nm) measurements in the 2Θ angular range 15°-50° with 2Θ steps of 0.05° and counting time of 5 s per step.

3. Results and conclusions

Figure 1(a) shows the cross-section of an as-built sample. Coarse columnar austenitic grains (~ 50 μm) are elongated in the building direction and not confined to a single deposited layer. Inside the grains there is a finer sub-structure of cells (less than 1 μm). After MS tests an evolution of microstructure was also observed: the melt pools disappear or are slightly visible and columnar grains are replaced by new equiaxed grains (Fig. 1b). Additionally, the cells of the sub-structure are coarser

(~ 5 μm) compared to that observed before the MS tests. The MS results in Fig. 1 (c) show that the dynamic modulus E progressively decreases with temperature due to anharmonicity effects (blue curve). However, after the first MS test run (heating to 600 °C/ cooling to room temperature) E results to be approximately 2% lower than its original value (E_0 =188 GPa).

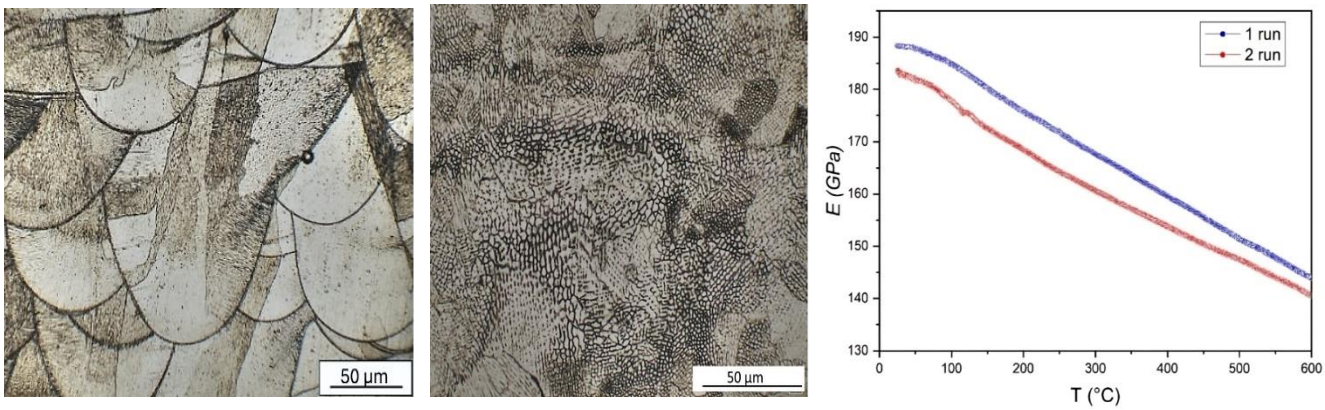

(a) (b) (c)

Fig. 1. Cross-section of an as-built sample before (a) and after (b) two MS test runs. Dynamic modulus E vs. temperature in two successive MS test runs (c).

The evolution of microstructure is also confirmed by XRD analysis, performed on the same sample before and after two MS test runs, involving changes in preferred grain orientation (Table 2).

	(111)	(200)	(220)	(311)	(222)	(400)
As-built	100	35	58	42	21	-
2 run	100	75	31	36	8	6
JCPDS-ICDD	100	45	26	30	12	3

Table 2. Relative intensities of the XRD peaks of a sample in as-built condition and after two MS test runs.

MS results can be interpreted by considering the Granato-Lücke model [3], which describes dynamic modulus in terms of dislocation density (ρ) and mean distance between dislocation pinning point (l):

$$\frac{\Delta G}{G} \cong -\Gamma \rho l^2 \qquad (2)$$

where $\Gamma \approx 1.67$ is a constant. Although Eq. (2) refers to the shear modulus G, the same effect occurs also for the dynamic modulus. Since heating does not increase the dislocation density the change of dynamic modulus depends on an increase of l. We suppose that the phenomenon could be related to the cell coarsening (see Fig. 1), anyway further analyses through XRD and transmission electron microscopy (TEM) are underway to get more specific information about the evolution of density and structure of dislocations.

4. References

[1] R. Montanari, A. Lanzutti, M. Richetta, J. Tursunbaev, E. Vaglio, A. Varone and C. Verona (2022). Plasma carburizing of laser powder bed fusion manufactured 316 L steel for enhancing the surface hardness. 2022. *Coatings* **12(2)**: p. 258.

[2] S. Amadori, E.G. Campari, A.L. Fiorini, R. Montanari, L. Pasquini, L. Savini and E. Bonetti (2006). Automated resonant vibrating-reed analyzer apparatus for a non-destructive characterization of materials for industrial applications. *Materials Science and Engineering: A*., **442**, 543–546.

[3] A.S. Nowick and B.S. Berry, Anelastic relaxation in crystalline solids. Academic Press New York and London 1972

Characteristics of LDHs grown on ECAP processed AZ31 alloy

Filippo Berto [1], Franco Bonollo [2], Alberto Fabrizi [2], Alessandra Fava [3], Paolo Ferro [2], Roberto Montanari [4], Riccardo Narducci [4], Ekaterina Pakhomova [5], Alessandra Palombi [4], Subhan Rasulzade[4], Maria Richetta [4], Alessandra Varone [4]

[1] *Department of Chemical Engineering Materials Environment, University of Rome "La Sapienza", Via Eudossiana 18, 00184 Roma, Italy*
[2] *Department of Management and Engineering, Padova University, Stradella San Nicola, 3, 36100 Vicenza, Italy*
[3] *ENEA, Department for Sustainability—Research Centre of Casaccia, Santa Maria di Galeria, 00123 Rome, Italy*
[4] *Department of Industrial Engineering, University of Rome Tor Vergata, Via del Politecnico 1, 00133 Rome, Italy.*
[5] *Department of Mechanical, Chemical and Materials Engineering, University of Cagliari, Via Marengo 2, 09123 Cagliari, Italy.*

1. Introduction

Magnesium alloys are gaining attention for biomedical applications, particularly in orthopedic implants, due to their favorable mechanical properties and biocompatibility. Their Young modulus closely matches that of human bone, reducing the risk of stress shielding, while their biodegradability eliminates the need of secondary surgery. However, their high corrosion rate in physiological environment can compromise implant integrity. To improve corrosion resistance, the attention has been focused on tailoring of alloy composition and microstructure, and on surface treatments. For istance, Equal Channel Angular Pressing (ECAP) refines the material microstructure, improving both mechanical and corrosion properties [1]. In addition to increase the corrosion resistance, Layered Double Hydroxide (LDH) coatings are of particular interest because they can to load and release drugs due to their tuneable structures and ion-exchange properties. This study investigated the deposition of LDHs on the AZ31 alloy treated with different ECAP passes to assess the effects of microstructural modifications on their nucleation and growth.

2. Materials and methods

The synthesis of LDHs was carried out on AZ31 substrate cut from billets (Dynamic Metals Ltd, Bedfordshire, UK) subjected to 0, 1, 2, and 4 ECAP passes. The ECAP process was carried out at 250 °C using route Bc. The in-situ LDH synthesis was performed by immersing the samples in a solution containing 5 mM zinc nitrate hexahydrate [$Zn(NO_3)_2*6H_2O$] and 15 mM urea in 150 mL of distilled water. The synthesis was made at 90 °C for 30 minutes. The samples were cooled to room temperature in the same solution. Once removed from the reactor, the samples were rinsed with demineralized water and ethanol, then air-dried. The AZ31 substrate has been characterized through X-Ray Diffraction (XRD), Light Microscopy (LM) and Scanning Electron Microscopy (SEM).

3. Results and conclusions

The XRD patterns of AZ31 substrate are reported in Fig.1 (a). From the spectra the I_{0002} / $I_{10\text{-}11}$ ratios have been calculated to get information about texture evolution and in particular about the fraction of basal planes (0002) parallel to the surface: the I_{0002} / $I_{10\text{-}11}$ ratio exhibits a maximum after 1 ECAP pass (Fig.1 b).

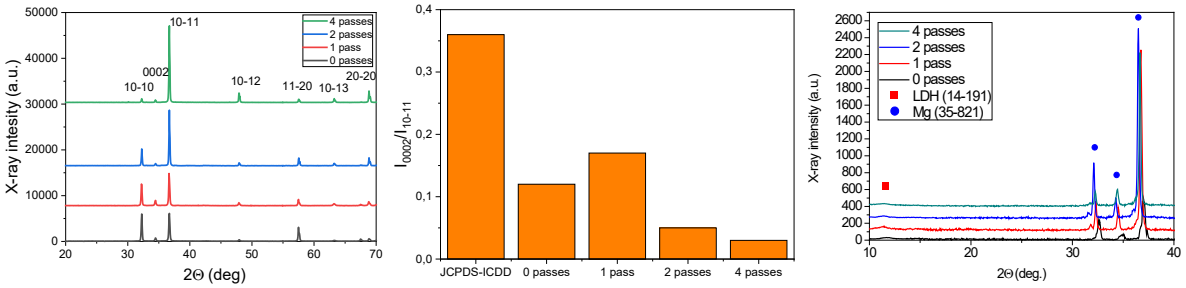

(a) (b) (c)

Fig. 1. XRD patterns of AZ31 substrate after different ECAP passes (a). Ratios I_{0002} / $I_{10\text{-}11}$ compared to that between the Mg peaks taken from JCPDS-ICDD database (b). XRD patterns after LDH synthesis (c).

LDH peaks are already visible after 30 minutes of synthesis (Fig.1 c) indicating the formation of such structures, that is also confirmed by SEM observations (Fig 2). LDHs are present on the surface of all the samples, but the morphologies vary significantly depending on the ECAP processing. Specifically, the LDH coating on the as-received alloy is incomplete (Fig. 2a). After 2 (Fig. 2c) and 4 ECAP passes (Fig. 2d), the surface is fully covered, however, the coating is not uniform and exhibits several clusters. On the contrary, the surface of the alloy subjected to 1 ECAP pass is the only one with a fine, homogeneous, and complete LDH coating (Fig. 2b).

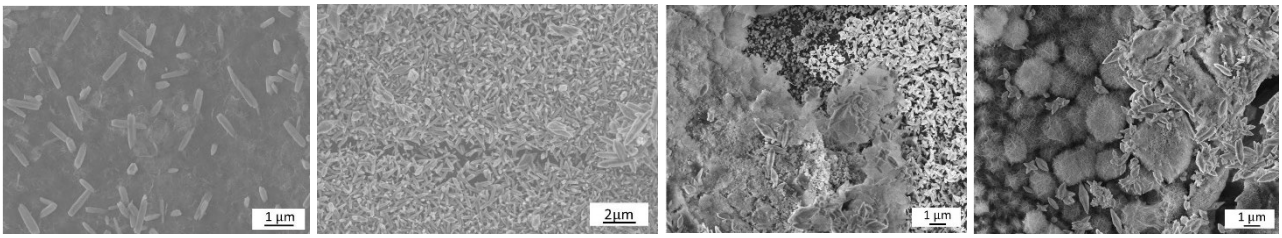

(a) (b) (c) (d)

Fig. 2**.** SEM images after LDH synthesis for 30 minutes: 0 (a), 1 (b), 2 (c) and 4 (d) ECAP passes.

The formation and growth of LDHs involves reactions between the nutrient solution and the metal surface. Forticaux et al. [2] found that LDHs preferentially nucleate on screw dislocations, so their distribution is the key factor in LDH coverage homogeneity. In the as-received material dislocations mainly lie on basal planes thus their distribution on the surface is not homogeneous leading to an incomplete coverage. On the contrary, after ECAP passes other slip systems are activated giving rise to a more homogeneous distribution of dislocations and consequently of LDHs. The petal-like clusters observed after 2-4 ECAP passes result from uncontrolled overgrowth in certain areas, depending on diffusion, which is slightly anisotropic in hcp Mg alloys thus texture is of fundamental importance in growth rate. In conclusion, the work demonstrated that AZ31 after 1 ECAP pass represents the optimal substrate for the deposition of LDH coatings.

5. References

[1] Varone, A., Fabrizi, A., Ferro, P. et al. J Mater Sci 60, 495–518 (2025).
[2] A. Forticaux, L. Dang, H. Liang, S. Jin. *Nano Lett.* **2015**, 15, 3403–3409.